Bulletin of the Geological Society of Greece
Volume L, Number 4
2016

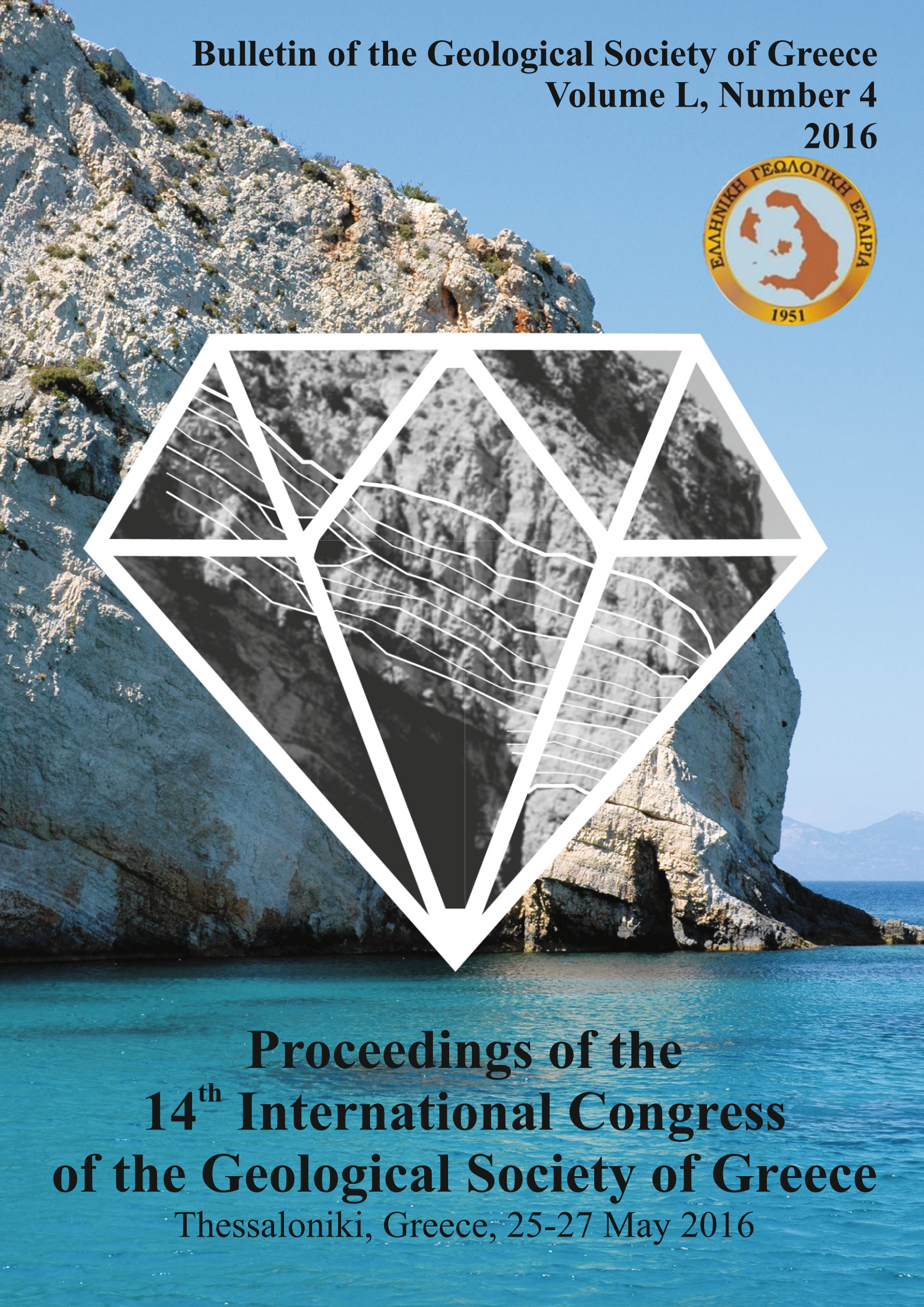

Proceedings of the 14th International Congress of the Geological Society of Greece

Thessaloniki, Greece, 25-27 May 2016

BULLETIN OF THE GEOLOGICAL SOCIETY OF GREECE

VOLUME L

14TH INTERNATIONAL CONGRESS OF THE GEOLOGICAL SOCIETY OF GREECE

Under the auspices of the Ministry of Education, Research and Religious Affairs

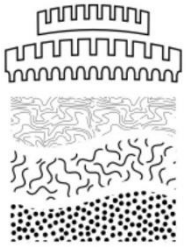

14th International Congress of the Geological Society of Greece

25-27 May 2016 Thessaloniki, Greece

PROCEEDINGS

EDITORS

KOUKOUSIOURA O.
CHATZIPETROS A.

SUPPORT TEAM

VARNAVA A.
GKEME A.
CHATZOPOULOU M.
DIMOU V.-G.
GEORGIOU S.
GRENDAS N.
KARAMITROS G.
KRIKONI C.
KYNIGOPOULOU Z.
KYRIAZIDOU E.
LAZOS I.
MYTIGLAKI C.
PANTAZOPOULOU Z.
PLASTIRAS C.-A.
THEODORIDOU S.
THOMAIDOU E.

Thessaloniki 2016

GEOLOGICAL SOCIETY OF GREECE

COUNCIL MEMBERS

(elected at the General Assembly of the members of the Society on April 2016)

PRESIDENT	PAVLIDES Spyridon, Professor *Aristotle University of Thessaloniki*
VICE-PRESIDENT	GANAS Athanassios, Dr. Geologist *Institute of Geodynamics*
SECRETARY GENERAL	KRANIS Haralambos, Dr. Geologist *National and Kapodistrian University of Athens*
EXECUTIVE SECRETARY	ANTONARAKOU Assimina, Associate Professor *National and Kapodistrian University of Athens*
TREASURER	MORAITI Eugenia, Dr. Geologist *Institute of Geology and Mineral Exploration*
TRUSTEE	LOUPASAKIS Konstantinos, Assistant Professor *National Technical University of Athens*
MEMBERS	ARVANITIS Apostolos, Dr. Geologist *Institute of Geology and Mineral Exploration* DRINIA Hara, Professor *National and Kapodistrian University of Athens* ECONOMOU George, Dr. Geologist *Institute of Geology and Mineral Exploration*

ORGANIZING COMMITTEE OF THE

14TH INTERNATIONAL CONGRESS OF THE GEOLOGICAL SOCIETY OF GREECE

CHAIRMAN

PAVLIDES Spyros – Professor, *School of Geology, Aristotle University of Thessaloniki*

SECRETARIAT

CHATZIPETROS Alexandros – Assistant Professor, *School of Geology, A.U.Th.*
KAKLIS Triantafyllos – Dr. Geologist, *School of Geology, A.U.Th.*
KOSTOPOULOS Dimitrios – Associate Professor, *School of Geology, A.U.Th.*
THOMAIDOU Effimia – Dr. Geologist, *School of Geology, A.U.Th.*

TREASURER

KANTIRANIS Nikolaos – Assistant Professor, *School of Geology, A.U.Th.*

MEMBERS

ANAGNOSTOPOULOU Christina – Assistant Professor, *School of Geology, A.U.Th.*
GALANAKIS Dimitrios – Dr. Geologist, *Institute of Geology and Mineral Exploration*
KOUKOUSIOURA Olga – Dr. Geologist, *School of Geology, A.U.Th.*
MICHAILIDIS Stylianos – Geologist, *Association of Greek Geologists*
MORAITI Eugenia – Dr. Geologist, *Institute of Geology and Mineral Exploration*
MOURATIDIS Antonios – Lecturer, *School of Geology, A.U.Th.*
SPYRIDIS Efthimios – Geologist, *Geotechnical Chamber of Greece*
VAMVAKARIS Dominikos – Dr. Geologist, *School of Geology, A.U.Th.*
VARGEMEZIS Georgios – Associate Professor, *School of Geology, A.U.Th.*
VAVELIDIS Michail – Professor, *Head of School of Geology, A.U.Th.*

CONGRESS SECRETARIAT AND SUPPORT TEAM

Koukousioura Olga
Thomaidou Effimia
Varnava Antriani
Gkeme Anastasia
Chatzopoulou Maria
Christoforidou Sofia
Dimou Vassiliki-Grigoria
Georgiou Sofia
Grendas Nikolaos
Ioakeimidis Ioakeim
Karamitros Ioannis
Ketikidou Sofia
Kordatos Nikolaos
Krikoni Christina
Kynigopoulou Zoe
Kyriazidou Eleni
Lazos Elias
Livas Agis
Mavrommatis Nikolaos
Michailidis Ioannis
Mytiglaki Christina
Ntona Marita
Pantazopoulou Zoe
Plastiras Christos-Alexandros
Spachos Georgios
Theodoridou Styliani
Vasiliadis Nikolaos

SPONSORS

Under the auspices of the
MINISTRY OF EDUCATION, RESEARCH
AND RELIGIOUS AFFAIRS

ΕΛΛΗΝΙΚΗ ΔΗΜΟΚΡΑΤΙΑ
Υπουργείο Παιδείας,
Έρευνας και Θρησκευμάτων

and the sponsorship of

Hellas GOLD
Ελληνικός Χρυσός Α.Ε.

HELLAS GOLD S.A.

ΕΓΝΑΤΙΑ ΟΔΟΣ Α.Ε.

EGNATIA ODOS S.A.

ΙΝΣΤΙΤΟΥΤΟ ΓΕΩΛΟΓΙΚΩΝ & ΜΕΤΑΛΛΕΥΤΙΚΩΝ ΕΡΕΥΝΩΝ
Ι.Γ.Μ.Ε

INSTITUTE OF GEOLOGY AND
MINERAL EXPLORATION

ΕΠΙΤΡΟΠΗ ΕΡΕΥΝΩΝ
ΑΡΙΣΤΟΤΕΛΕΙΟΥ ΠΑΝΕΠΙΣΤΗΜΙΟΥ ΘΕΣΣΑΛΟΝΙΚΗΣ

A.U.Th. RESEARCH COMMITTEE

Marathon Data Systems
e-mail: marathon@otenet.gr
www.marathondata.gr

MARATHON DATA SYSTEMS

ΓΕΩΤΕΧΝΙΚΟ
ΕΠΙΜΕΛΗΤΗΡΙΟ
ΕΛΛΑΔΑΣ

GEOTECHNICAL CHAMBER OF GREECE

ΜΕΤΡΟ ΘΕΣΣΑΛΟΝΙΚΗΣ
ΑΤΤΙΚΟ ΜΕΤΡΟ Α.Ε.

ATTICO METRO S.A.

Ο.Α.Σ.Π.
Οργανισμός Αντισεισμικού
Σχεδιασμού & Προστασίας

EARTHQUAKE PLANNING AND
PROTECTION ORGANIZATION

ΣΥΛΛΟΓΟΣ ΕΛΛΗΝΩΝ ΓΕΩΛΟΓΩΝ
1961

ASSOCIATION OF GREEK GEOLOGISTS

SCHEME OF PROCEEDINGS

VOLUME L/1

Structural Geology, Neotectonics, Paleontology, Stratigraphy

Earth Science and Society: *Geotopes, Teaching and Education, Sustainable Development*

Physical Geography, Sedimentology, Quaternary Geology, Karst and Speleology, Marine Geology, Oceanography

Special Session: Holocene Geomorphological Changes of Coastal Areas

Special Session: Earthquake-induced ground deformation Lefkada earthquake 2015

VOLUME L/2

Applied Geology

Engineering Geology, Hydrogeology, Urban Geology

Meteorology, Climatology, Atmospheric Environment

Special Session: Recent advances in Earth Sciences: monitoring networks, services and products – what do scientists deliver and what does society need

VOLUME L/3

Seismology, Geophysics, Physics of the Earth's Interior

Special Session: Statistical Seismology

Special Session: Probabilistic and deterministic seismic hazard, ground motion and permanent deformation assessment from strong earthquakes of the broader Aegean area

Special Session: Site characterization, estimate of seismic site response and its incorporation into the ground motion predictive models

Special Session: Geodetic methods for crustal deformation monitoring

Special Session: Modeling and monitoring crustal deformation and Aegean geodynamics using GPS/InSAR and geophysical/seismological methods

Remote Sensing and Information Technologies in Geosciences

Special Session: Geospatial technology in education, training, capacity building and outreach; towards STEM promotion and development of skills

Special Session: Geohazard analysis with Remote Sensing and GIS

VOLUME L/4

Mineral Sciences, Petrology, Geochemistry, Isotope Geology, Volcanology

Special Session: Environmental Geochemistry: mobility and speciation of chemical elements in the system rock-soil-water-plant (endorsed by SEGH)

Environmental Geosciences

Abstracts of Keynote Lectures

REVIEWERS

The Organizing Committee expresses special thanks for the valuable contribution of the reviewers for their assistance in producing high quality scientific proceedings.

Every paper was subjected to the scrutiny of at least two reviewers. The Organizing Committee is not responsible for the content of the papers, the statements made, or the opinions expressed in these volumes.

Aidona Eleni
Albanakis Konstantinos
Antoniou Vasileios
Argyraki Ariadne
Arvanitis Apostolos
Baziotis Ioannis
Bourliva Anna
Caroni Chrys
Chatzigogos Nikolaos-Panagiotis
Christanis Kimon
Christaras Basile
Christidis George
Doxani Georgia
Falcone Giuseppe
Filippidis Anestis
Gasparatos Dionisis
Georgiou Pantazis
Geraga Maria
Godelitsas Athanasios
Gruetzner Christoph
Hatzipanagiotou Konstantin
Iordanidis Andreas
Kalaitzidis Stavros
Kallioras Andreas
Kalogeras Ioannis
Kanellopoulos Christos
Kantiranis Nikolaos
Karagianni Eleni
Karagrigoriou Alex
Karakaisis George
Karakitsios Vasileios
Kassaras Ioannis
Kati Marianna
Kaviris George
Kazakis Nerantzis
Kelepertzis Efstratios
Kilias Adamantios
Kilias Stephanos
Kiratzi Anastasia
Koroneos Antonios
Koukousioura Olga
Kürçer Akın
Lambrakis Nikolaos
Loupasakis Constantinos
Magkanas Andreas
Makedon Thomas
Makri Kyriakoula
Marinos Vassilis
Massas Ioannis
Matiatos Ioannis
Mattas Christos
Melfos Vasilios
Melis Nikolaos
Mouratidis Antonios
Murru Maura
Nikolakopoulos Konstantinos
Nimfopoulos Miltiadis
Nomikou Paraskevi
Panagiotopoulos Dimitrios
Papachristou Maria
Papadopoulos Nikos
Papadopoulou Lambrini
Papanikolaou Dimitrios
Papanikolaou Ioannis
Papastergios Georgios
Papathanassiou George
Papazachos Costas
Papoulis Dimitrios
Papoutsis Ioannis
Paraskevopoulou Vasiliki
Parcharidis Issaak
Pavlides Spyros
Pertsinidou Christina Elisavet
Pikridas Christos
Pliakas Fotios-Konstantinos
Pomonis Panagiotis
Psimoulis Panos
Rhoades David
Rigopoulos Ioannis
Rotondi Renata
Roumelioti Zafeiria
Sabatakakis Nikolaos
Scordilis Emmanuel
Skarlatoudis Andreas
Skarpelis Nikolaos
Sokos Efthimios
Stamatis Georgios
Stathis Dimitrios
Steiakakis Emmanouil
Syrides Georgios
Thomaidou Effimia
Tolika Dia
Tranos Markos
Tsirambides Ananias
Tsodoulos Ioannis
Tsourlos Panagiotis
Tzanis Andreas
Tziritis Evangelos
Valkaniotis Sotiris
Vamvakaris Dominikos
Vargemezis George
Varini Elisa
Voudouris Konstantinos
Voudouris Panagiotis
Vouvalidis Konstantinos
Zotiadis Vassilis

THE CONGRESSES OF G. S. G.

1st MEETING, ATHENS, 1983, Bull. XVII
2nd MEETING, ATHENS, 1984, Bull. XIX
3rd CONGRESS, ATHENS, 1986, Bull. XX
4th CONGRESS, ATHENS, 1988, Bull. XXIII
5th CONGRESS, THESSALONIKI, 1990, Bull. XXV
6th CONGRESS, ATHENS, 1992, Bull. XXVIII
7th CONGRESS, THESSALONIKI, 1994, Bull. XXX
8th CONGRESS, PATRAS, 1998, Bull. XXXII
9th CONGRESS, ATHENS, 2001, Bull. XXXIV
10th CONGRESS, THESSALONIKI, 2004, Bull. XXXVI
11th CONGRESS, ATHENS, 2007, Bull. XXXX
12th CONGRESS, PATRAS, 2010, Bull. XLIII
13TH CONGRESS, CHANIA, 2013, Bull. XLVII

ΠΡΟΛΟΓΟΣ

Το 14ο Επιστημονικό Συνέδριο της Ελληνικής Γεωλογικής Εταιρίας, ολοκλήρωσε με επιτυχία τις εργασίες του και αποτελεί πλέον ιστορικό γεγονός. Στη μεγάλη αυτή εκδήλωση των Γεωεπιστημών, κορυφαία εκδήλωση της επιστημονικής Εταιρείας μας, περισσότεροι από **500 συμμετέχοντες**, μεταξύ των οποίων περισσότεροι από 200 φοιτητές και 80 νέοι επιστήμονες, παρακολούθησαν τις εργασίες ή ορισμένες ειδικές συνεδρίες (60% νέοι επιστήμονες), που αποτελούν και το μέλλον της γεωλογίας. Παρουσιάστηκαν **259 νέες επιστημονικές εργασίες**, με 170 προφορικές ανακοινώσεις και 89 επιστημονικά πόστερ.

Προσκεκλημένοι ομιλητές, πολλοί Έλληνες και ξένοι συνάδελφοι, αλλά κυρίως νέοι ερευνητές, νέοι επιστήμονες και Υποψήφιοι Διδάκτορες, παρουσίασαν με τον καλύτερο δυνατό τρόπο συμπεράσματα και αποτελέσματα στην πρωτοπορία της επιστημονικής έρευνας σήμερα παγκοσμίως. Παράλληλες εκδηλώσεις όπως οι προβολές ταινιών γεωλογικού περιεχομένου και οι "Στρογγυλές Τράπεζες", για τη διδακτική, του Συλλόγου Ελλήνων Γεωλόγων, για τα ενεργά ρήγματα, συμπλήρωσαν τις αυστηρά επιστημονικές παρουσιάσεις, όπου συνέκλιναν σχεδόν όλα τα αντικείμενα του ευρύτερου κύκλου των Γεωπιστημών, βασικών και εφαρμοσμένων. Για μια ακόμη φορά αποδείχθηκε το υψηλό επίπεδο της έρευνας των Ελλήνων γεωεπιστημόνων. Η Οργανωτική Επιτροπή προσπάθησε και οργάνωσε κατά τον καλύτερο δυνατό τρόπο το βήμα του Συνεδρίου. Το Συνέδριο όμως ανήκει σε αυτούς που το πλαισιώνουν, συμμετέχουν στο γίγνεσθαι της επιστήμης.

Το συνέδριο ανήκει σε όλους εσάς και οι οργανωτές καθώς και το Τμήμα Γεωλογίας του Α.Π.Θ. σας ευχαριστούν θερμά. Η επόμενη μεγάλη συνάντηση μας στην Αθήνα το 2019.

Εκ μέρους της Οργανωτικής Επιτροπής
Ο Πρόεδρος
Σπύρος Β. Παυλίδης
Καθηγητής Γεωλογίας
Αριστοτέλειο Πανεπιστήμιο Θεσσαλονίκης

PROLOGUE

The 14th International Congress of the Geological Society of Greece, successfully completed its works and is now a historical event. In this great event of Geosciences, the highest expression of our Scientific Society, more than **500 participants**, including more than 200 students and 80 young scientists, attended the congress works or specific sessions. 60% of young scientists, the future of geology. There were **259 new scientific papers presented**, 170 oral presentations and 89 scientific posters. Invited speakers, many Greeks and foreign colleagues, but especially young researchers, young scientists and PhD students, presented in the best possible way conclusions and results at the forefront of scientific research in the world today.

Parallel events, such as the geological films screenings and "Round Tables" for Geosciences in Education, of the Greek Association of Geologists, for Active Faults, completed the strictly scientific presentations, where almost all objects of the wider circle of Geosciences converged, basic and applied. Once again the high level of research of Geoscientists was demonstrated. The Organizing Committee tried and organized in the best possible way the step of the Congress. But the Congress belongs to those that surround it, and participate in science development.

The Congress belongs to all of you, and the organizers and the School of Geology of the Aristotle University of Thessaloniki thank you very much. Our next big meeting is in Athens in 2019.

On behalf of the Organizing Committee
The President
Spyros B. Pavlides
Professor of Geology
Aristotle University of Thessaloniki

CONTENTS

Volume L/4

Mineral Sciences, Petrology, Geochemistry, Isotope Geology, Volcanology

Special Session

Environmental Geochemistry: mobility and speciation of chemical elements in the system rock-soil-water-plant (endorsed by SEGH)

Conveners: Ariadne Argyraki, Athanasios Godelitsas

Environmental Geosciences

Abstracts of Keynote Lectures

Bulletin of the Geological Society of Greece

Proceedings of the 14th International Conference of the Geological Society of Greece

VOLUME L/4

Mineral Sciences
Petrology
Geochemistry
Isotope Geology
Volcanology

Δελτίο της Ελληνικής Γεωλογικής Εταιρίας, τόμος L, σελ. 1771-1780
Πρακτικά 14ου Διεθνούς Συνεδρίου, Θεσσαλονίκη, Μάιος 2016

Bulletin of the Geological Society of Greece, vol. L, p. 1771-1780
Proceedings of the 14th International Congress, Thessaloniki, May 2016

AESTHETIC CHARACTERISTICS OF GREEK ORNAMENTAL STONES ASSOCIATED WITH MINERAL, GEOCHEMICAL AND STRUCTURAL PROPERTIES

Badouna I.[1*], Koutsovitis P.[2*], Laskaridis K.[3*], Patronis M.[4*] and Papatrechas Ch.[5*]

[1]Geologist, MSc, ioannabad@hotmail.com, [2]Geologist, Ph.D., petroskoutsovitis@yahoo.com, [3]Geologist, Ph.D., laskaridis@igme.gr, [4]Mining Eng., Ph.D., patronis@igme.gr,

[5]Geologist, Ph.D., papatrechas@windowslive.com

**Institute of Geology and Mineral Exploration, 1st Spirou Louis St., Olympic Village, 13677, Acharnae, Greece*

Abstract

Commercial marble are almost ready-to-use materials with a high economic value for the building-construction industry. The most important ornamental stones in Greece include limestone and marble with notable qualitative features and are considered products of high commercial value. In this research, seventy-three carbonate samples (limestones, dolomites and marbles) from all over Greece have been studied to determine their macroscopic and petrographic features and to investigate their mineral chemistry and geochemistry. Their colors vary from whitish to gray due to their content of calcite and dolomite, black due to bitumens, yellow due to the presence of iron oxides and clay, red due to iron oxides and mixed phases of calcite- siderite, green-brownish due to the presence of iron oxides or muscovite and chlorite, giving schistosity to the rock. Scattered calcite and dolomite veins, as well as the occurrence of other minerals such as barite, epidote and magnetite, contribute to specific features, thus making their appearance unique. The particular characteristics of each stone depend highly upon the type of minerals present, their composition, grain size and extent of aggregation, their geochemistry and structure.
Keywords: *Ornamental stones, marble, aesthetic features, mineral chemistry, geochemistry.*

Περίληψη

Τα εμπορικά μάρμαρα αποτελούν υλικά που δεν απαιτούν ιδιαίτερη επεξεργασία με υψηλή οικονομική αξία για την κατασκευαστική βιομηχανία. Τα πιο σημαντικά διακοσμητικά πετρώματα στην Ελλάδα περιλαμβάνουν ασβεστόλιθους και μάρμαρα με ιδιαίτερα ποιοτικά χαρακτηριστικά και θεωρούνται προϊόντα ιδιαίτερης εμπορικής αξίας. Σε αυτή την εργασία μελετήθηκαν εβδομήντα τρία ανθρακικά δείγματα (ασβεστόλιθοι, δολομίτες και μάρμαρα) από όλη την Ελλάδα με σκοπό να καθοριστούν τα μακροσκοπικά και πετρογραφικά χαρακτηριστικά τους και να διερευνηθεί η ορυκτοχημική τους σύσταση και η γεωχημεία τους. Τα χρώματά τους ποικίλουν από λευκό έως τεφρό, εξαιτίας του περιεχομένου τους σε ασβεστίτη και δολομίτη, μαύρο σε βιτουμενιούχους ασβεστόλιθους, κίτρινο εξαιτίας της παρουσίας οξειδίων σιδήρου και αργιλικών ορυκτών, κόκκινο εξαιτίας των οξειδίων σιδήρου και μεικτών φάσεων

ασβεστίτη και σιδηρίτη, καστανοπράσινο εξαιτίας της εμφάνισης οξειδίων σιδήρου μαζί με χλωρίτη και μοσχοβίτη, προσδίδοντας σχιστότητα στο πέτρωμα. Διάσπαρτες ασβεστιτικές και δολομιτικές φλέβες, όπως επίσης και εμφάνιση άλλων ορυκτών φάσεων όπως βαρύτης, επίδοτο και μαγνητίτης συμβάλλουν στη δημιουργία ιδιαίτερων χαρακτηριστικών που προσδίδουν μοναδική εμφάνιση. Τα χαρακτηριστικά γνωρίσματα κάθε πετρώματος εξαρτώνται σημαντικά από το είδος των ορυκτών, τη σύσταση, κοκκομετρία και κατανομή τους, τη γεωχημεία και δομή τους.
Λέξεις κλειδιά: *Διακοσμητικά πετρώματα, μάρμαρα, αισθητικά χαρακτηριστικά, ορυκτοχημεία, γεωχημεία.*

1. Introduction

The aesthetic characteristics of marbles depend on their color variability, as well as on their mineralogy and physical features (texture, grain size and other structural features). These parameters can change even within the same pit environment causing color differences in quarried marble blocks. Differences in material content and metamorphic processes influence the final colors of marbles, whereas impurities in the original rock mass also contribute in the different color varieties. Iron-oxides in original rock mass for example result in forming yellow, yellowish or reddish marble types. Manganese-oxides and carbonic impurities in original rock mass cause the formation of dark bluish, violet or black colored marbles. After metamorphism, marbles as rock masses have not stayed static in their locations and they have been influenced by all types of structural defects. Most of the defects in marble mass involve discontinuities, some of which are open, disturbing the continuity of the marble blocks and others are filled with loose or compact materials. Compact filling materials cause color changes and provide additional structural features affecting marble appearance. The marble aesthetic characteristics are directly linked with their commercial final market price, which is decided by marble users and interior designers. (Brilli *et al.*, 2015; Directory of Greek Ornamental and Structural Stones, 2015; Ferrini *et al.*, 2012; Munyanyiwa *et al.*, 1988; Papatrechas, 2011).

In general commercial marbles include many others non-carbonate rocks capable of taking a polish. These rocks such as limestones, travertines, dolomites, marbles, granites, basalts, schists, sandstones, etc. are mined for the construction industry, especially to be used as decorative stones. In Greece, marble industry is one of the most effective forces in economy. In this paper, we present the aesthetic features of characteristic ornamental marbles from many areas of Greece in relation to their petrographic, mineralogical, chemical, and geochemical data.

2. Sampling and analytical methods

In this study, 73 samples have been analysed for mineralogical and geochemical investigations. For this purpose, 17 samples were collected from Eastern Macedonia, 6 samples from Central Macedonia, 4 samples from Western Macedonia, 9 samples from Peloponnesus, 4 samples from Thessaly, 1 samples from North Aegean, 2 samples from South Aegean, 7 samples from Crete, 15 samples from Sterea Ellada, 2 samples from Western Greece and 6 samples from Epirus.

Mineralogic and petrographic parameters (i.e. mineral association, grain size and structure, texture of samples) were examined under polarized light microscope using thin sections as well as with scanning electron microscopy–energy dispersive spectroscopy (SEM–EDS), using a JEOL JSM 5600 scanning electron microscope, equipped with an automated energy dispersive analysis system ISIS 300 OXFORD, with the following operating conditions: 20 kV accelerating voltage, 0.5 nA beam current, 20 s time of measurement and 5 μm beam diameter.

Qualitative mineralogical composition of the marble samples was determined with X-ray powder diffraction (XRD), using a Philips X'Pert Panalytical X-ray diffractometer, operating with Cu radiation at 40 kV, 30 mA, 0.020^{o} step size and 1.0 sec step time. The XRD patterns were evaluated using the DIFFRAC plus EVA software v.11 (Bruker-AXS, USA) based on the ICDD Powder Diffraction File

(2006). Major oxides and the trace elements analysis of all samples was carried out in the IGME laboratory. Samples were pulverized to <200 mesh in an agate mill, were digested with a mixture of $HCl–HNO_3–HF$ acids and were analyzed for a series of trace elements by Inductively Coupled Plasma-Atomic Emission Spectroscopy (ICP-MS) and for major elements by X-ray fluorescence (XRF).

3. Mineralogical and petrographic characterization of the samples

3.1 Macroscopic examination

Macroscopic investigations revealed that the marble samples can be grouped into eight types based on colo r features, crystal size, crystal boundaries and foliation. These groups are identified as (i) white, (ii) semi-w hite - light gray, (iii) beige-yellow, (iv) pink, (v) red, (vi) greenish, (vii) gray and (viii) blackish marbles.Th e ornamental marbles can be classified into three groups, based on their petrological characteristics . These groups are identified as **marbles** (AM_1- 17, KM_1-2, DM_1-4, P_1-2, TH_1-4, NA_1-2, STE_1-8, K_1-2), **limestones** (KM_3-6, P_3-6, BA_1, P_7, STE_9-11, DS_1-2, H_1-6, K_3-7) and **dolomites** (P_8-9, STE_12-15).

3.2 Microscopic and XRD examination

Microscopically, the marble groups display homeoblastic or heteroblastic mosaic texture, with vary ing crystal size. Larger crystal sizes appear in marbles from Macedonia, South Aegean and Sterea Ellada (cipolin marbles). The limestone-dolomite groups display a homeoblastic or heteroblastic te xture, with small crystal sizes.

Calcite and dolomite represent the major crystalline phases of the studied samples. Other minerals that participate in the mineralogical composition are quartz, muscovite, biotite, clinochlore, chlorit e, epidote, clay minerals (illite, kaolinite), magnetite, apatite, fluorite, sphalerite, etc. Calcite is the main mineral in samples AM_5, AM_8-11, AM_13, KM_1-6, DM_1-4, P_1-7, BA_ 1, TH_1-4, NA_1-2, STE_1-11, DS_1-2, H_1-6, K_1-7, while dolomite is the main mineral in samples AM_1-4, AM_6-7, AM_14-17, P_8-9, STE_12-1 5. Calcitic marbles mainly consist of 75-100% calcite and 0-20% dolomite, dolomitic marbles cons ist of 88-99% dolomite and 1-12% calcite, limestones consist of 85-100% calcite and 1% dolomite, and dolomites consist of 90-96% dolomite and 3-10% calcite. Calcite bearing rocks (both marbles and limestones) may also contain up to 15% micas.

The color presented by a marble, depends on its composition or its granulometry. White, semi-whit e, light gray and beige colors can be attributed either to pure calcite or dolomite. For example, the c alcitic marble NA_1 consists of 100% calcite (Fig. 1.1), while the dolomitic marble AM_3 consists mainly of dolomite (white crystalline mass), while calcite crystals are concentrated at few faint gra y areas (Fig. 1.2). At the semi-white calcite marble DM_3, the white crystalline mass consists of ca lcite and the gray strips consist of dolomite crystals with smaller size (Fig. 1.3). In the white calciti c marble DM_1, the white crystalline mass consists of calcite with granoblastic texture and the yell ow strips consist of smaller size calcite crystals mixed with clay minerals (Fig. 1.4). In the yellow-white calcitic marble AM_15, the crystalline mass comprises of small dolomitic crystals and a net work of yellow-red veins mainly of iron and manganese oxides (Fig. 1.5). Beige-yellow colors usu ally indicate the presence either of clay minerals or iron oxides. Pink and red marbles mainly attrib ute their color to iron and manganese impurities in the mass of calcite or dolomite, as calcium or m agnesium are substituted by these elements. In the pink calcitic marble TH_2, the crystalline mass consists of pink calcitic crystals of various sizes (Fig. 1.6), while the green-black veins consist of m uscovite, epidote and metallic minerals. In the red limestone STE_9 the color is attributed to the dif fusion of iron oxides in the micritic calcitic mass (Fig. 1.7). Green marbles on the other hand, like t he green cipolin marble STE_4, owe their darkest green color to layers of mica, epidote, titanite an d metallic minerals (Fig. 1.8). Blackish marbles like dolomite P_9 and limestone KM_3, owe their color to the presence of bitoumens (Fig. 1.9, 1.10). Moreover, in sample KM_3 concentrated micro crystals of iron-manganese oxides replace calcitic fossils (Fig. 1.10).

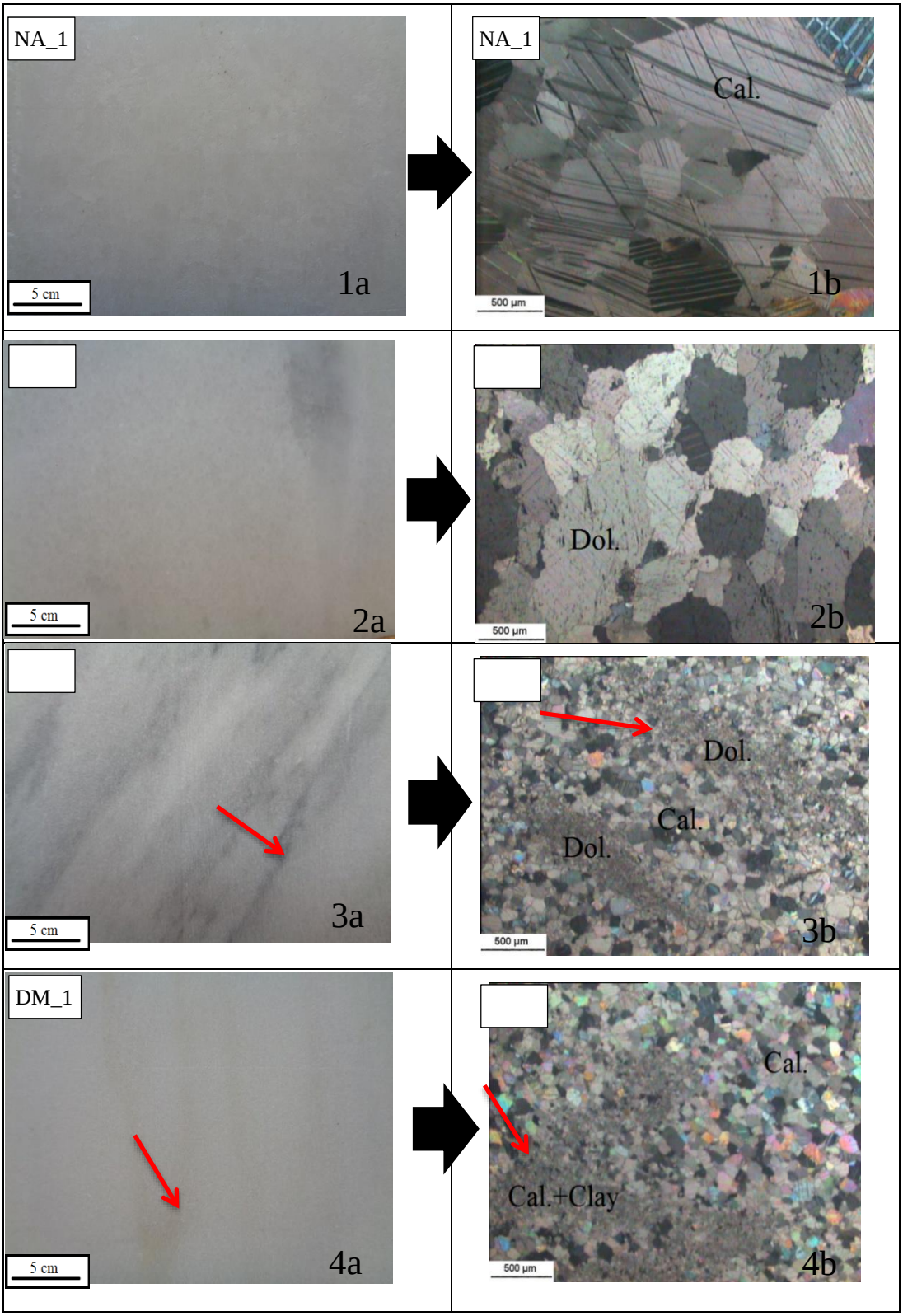
NA_1
5 cm
1a
NA_1
Cal.
500 µm
1b
5 cm
2a
Dol.
500 µm
2b
5 cm
3a
Dol.
Cal.
Dol.
500 µm
3b
DM_1
5 cm
4a
Cal.
Cal.+Clay
500 µm
4b

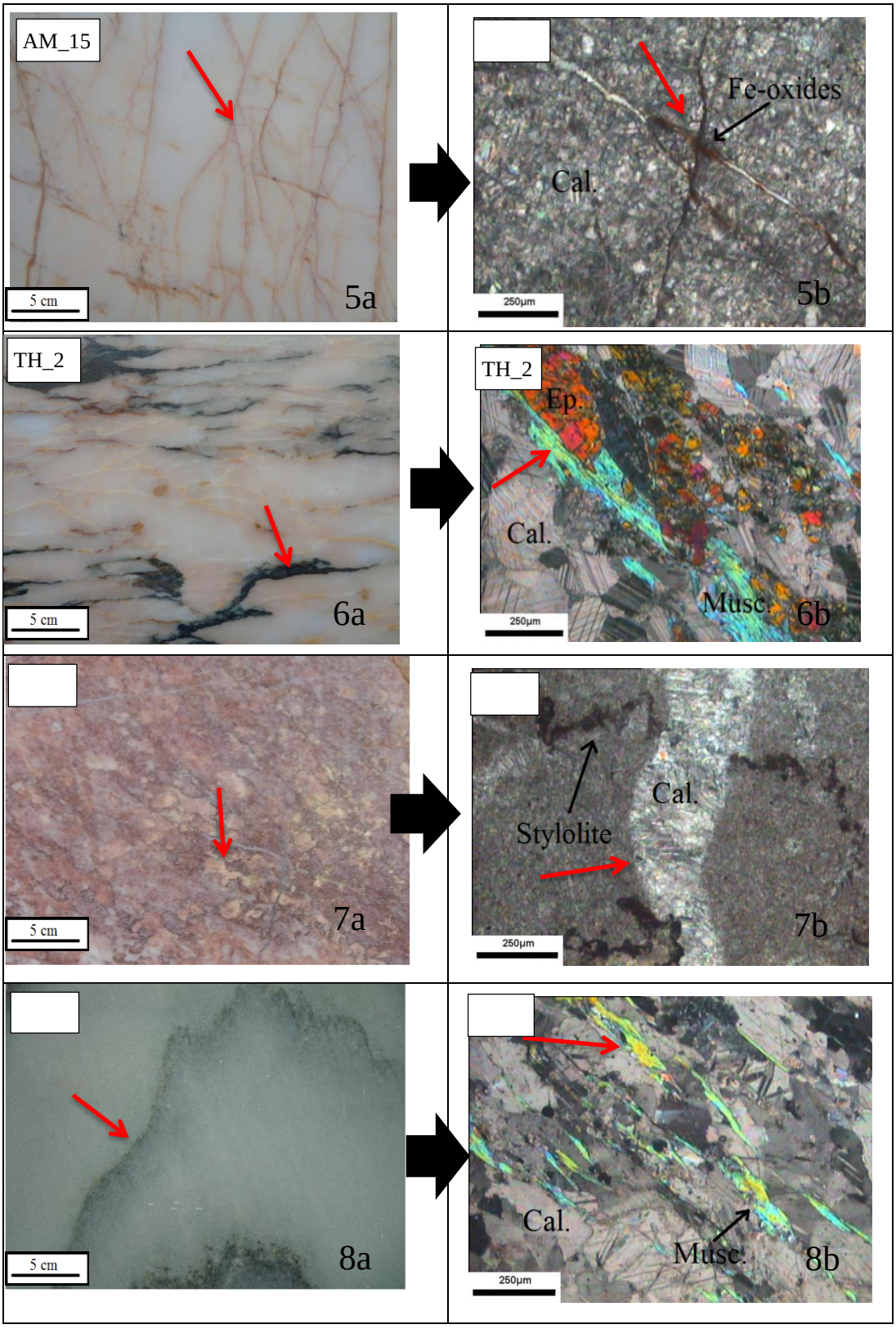
AM_15
5 cm
5a
Fe-oxides
Cal.
250µm
5b
TH_2
5 cm
6a
TH_2
Ep.
Cal.
Musc.
250µm
6b
5 cm
7a
Stylolite
Cal.
250µm
7b
5 cm
8a
Cal.
Musc.
250µm
8b

9a

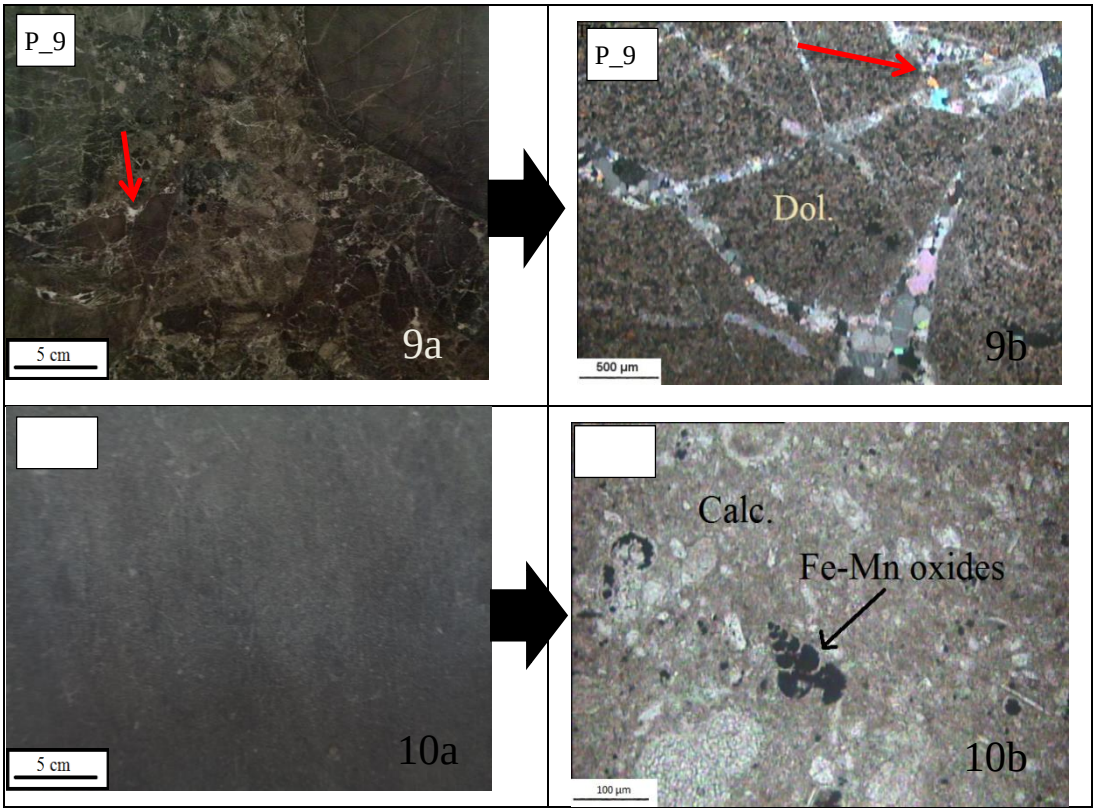

Figure 1 - Macroscopic image of the marble to the left and corresponding microscopic image of the marble to the right; calcitic marble NA_1 (1), dolomitic marble AM_3 (2), dolomitic-calcitic marble DM_3 (3), calcitic marble DM_1 (4), calcitic marble AM_15 (5), calcitic marble TH_2 (6), limestone STE_9 (7), cipolin marble STE_4 (8), dolomite P_9 (9), limestone KM_3 (10).

4. Geochemical analysis of the samples

Chemical analysis was performed in order to emphasize the differences or similarities in major and trace element trends between the marble groups studied. Major and trace element analyses results are given in table 1. Binary diagrams of the analyzed samples are shown in figure 3. In general, all marble groups display similar compositional distribution in terms of major oxide and trace element s. In this paper representative analyses of some samples are presented.

It is evident that all carbonate samples exhibit limited presence of major elements except Ca and Mg. The Mn, Ba and Sr elements and element ratios (i.e Mg/Ca, Mn/Sr, Ca/Sr) are much more useful than major elements alone for determining the geochemical affinities of rock (Koralaya *et al*., 2016; Lazzarini *et al*., 1980; Melezhik *et al*., 2001; Melezhik *et al*., 2008; Murra *et al*., 2011; Bağcı *et al*., 2010). In relatively pure marbles, the amounts of SiO2 and Al2O3 are very low and those of TiO2, Na2O and K2O are almost lacking. From the binary plots, it is shown a positive correlation between Na and K which is attributed to the limited presence of feldspars (Fig. 3g). All cipolin marbles are rich in Mn (STE_4, STE_5, STE_6, STE_7 and TH_4), a fact that is attributed to layers of mica and epidote crystals between calcitic crystals. Limestones from Epirus region (H_1-6), a limestone from Western Greece (DS-2) and limestones and marbles from Crete (K_1-4, K_7) are also Mn-rich. Cr3+ with ionic radius 0.62 Å substitutes Fe3+ (0.65 Å). Chromium is an element mainly connected to ultramafic rocks, especially in the grid of chromite or chromium silicate minerals (such as the chrome mica fuchsite). Samples from Peloponnesus (P_4, P_2, P_7), Thessaly (TH_3, TH_4) and central Macedonia (KM_3), appear to be rich in Cr3+. In the binary plots, there is a positive correlation between Ni and Cr observed

in the calcitic marbles, whereas in the dolomitic rocks the content of Ni does not seem to play any significant role in the extended presence of Cr. Dolomitic rocks contain minerals such as spinel in a standard amount; hence Ni and Cr cannot exceed a specific value. Moreover, there is a positive correlation between Cu and Zn in the calcitic marbles, whereas in the dolomitic rocks there is no statistically significant correlation between those two elements. As in the case of spinel, other similar heavy minerals that contain Cu and Zn have also a specific value range in dolomitic rocks.

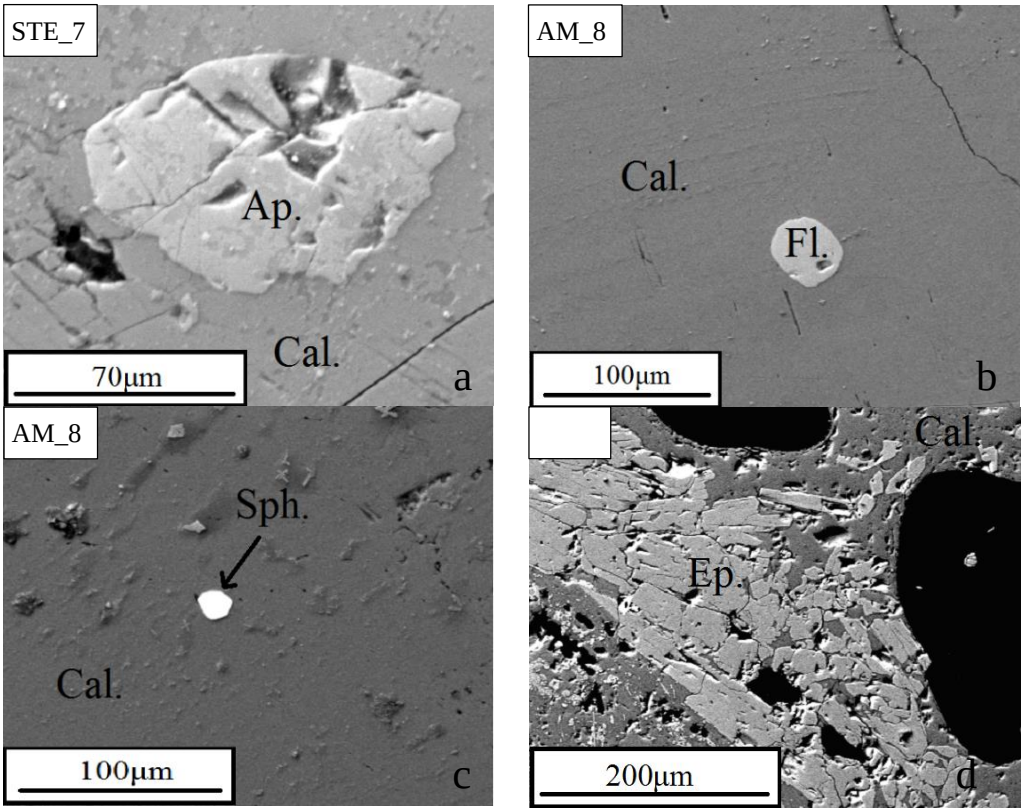

Figure 2 - SEM microphotographs of marble samples. Minerals such as apatite (sample STE_7a), fluorite (sample AM_8b), sphalerite (sample AM_8c) and epidote (sample TH_2d) participate also in the mineral composition of the samples.

High Sb content occurs in limestone sample from western Greece (DS_1: 6 ppm). Extremely high Ba co ntent has been found in samples from Sterea Ellada (calcitic-dolomitic marble STE_1: 4800 ppm, dolom ite STE_13: 6000 ppm) and in samples from Crete (dolomitic limestone K_5: 4200 ppm, calcitic marble K_1: 1600 ppm). As it is shown in the binary plots, there is a positive correlation between Ba and As, both in calcitic and dolomitic rocks, whereas there is no statistical correlation between Ba and Sr.

Strontium usually substitutes the Ca ions in dolomites due to its similar ion size. Thus it is expected that dolomitic rocks will present lower Sr contents than the calcitic rocks. Furthermore, the value range of Sr in calcitic rocks is higher than that in dolomitic, whereas marbles exhibit lower Sr value range compared to the non-metamorphic rocks (limestones, dolomites). Strontium is an indicator of diagenetic recrystallization in natural carbonate rocks. Its content decreases during dolomitisation and the subsequent replacement of calcite by dolomite (Shearman and Shirmohammadi, 1969; Garde, 1979). In addition, marbles that are in contact with schists tend to have slightly enriched Sr contents. The Sr/Ca ratio in seawater, the sedimentation environment, and biogenic factors affect strontium separation in biogenic carbonates and control the Sr/Ca ratio in marine carbonate rocks (Stoll and Schrag, 2001). Elements such as K, Na, Rb, and Sr are reported to be mobilized during sedimentation and

metamorphism. Since elements such as Th, Sc, and Y are least affected during sedimentation, they give more reliable information on the source properties (Chen *et al.*, 2002). The highest Rb contents appear in limestones (samples KM_5: 92 ppm, K_3: 92 ppm) and in calcitic marbles (sample K-5: 175 ppm). Rb^+ easily substitutes K^+ due to its chemical behavior and ion size (Rb^+: 1.52 Å, K^+:1.38 Å), so although Rb^+ does not form groundless minerals, it easily replaces K^+ in biotite and K-feldspars (Iliadou *et al.*, 2004).

Table 1 - Chemical composition of representative samples.

wt.%	**AM_13**	**STE_5**	**AM_17**	**AM_6**	**H_5**	**P_6**	**STE_13**
SiO_2	<0.10	4.20	0.18	<0.10	0.35	<0.05	0.30
Al_2O_3	<0.10	0.84	0.05	<0.10	0.08	<0.05	0.00
Fe_2O_3	<0.10	0.61	0.05	<0.10	0.20	<0.05	0.31
CaO	54.80	52.15	32.80	30.90	53.80	54.00	35.10
MgO	<0.05	0.80	19.80	21.10	0.30	0.65	17.80
MnO	<0.05	0.05	<0.05	<0.05	<0.05	<0.05	0.00
TiO_2	<0.10	<0.05	<0.05	<0.10	<0.05	<0.05	<0.05
K_2O	0.20	0.29	0.11	0.28	0.07	0.02	0.08
Na_2O	1.06	0.32	0.65	1.09	0.35	1.30	0.39
LOI	42.81	41.10	45.15	46.24	43.50	42.44	46.80
ppm							
Cr	25.00	26.00	6.00	24.00	11.00	45.00	28.00
Mn	15.00	425.00	7.00	12.00	135.00	65.00	35.00
Ni	13.00	26.00	10.00	8.00	16.00	30.00	24.00
Cu	2.30	40.00	3.00	2.00	32.00	7.00	41.00
Zn	14.00	28.00	4.00	21.00	26.00	25.00	53.00
As	1.50	1.50	1.00	1.30	2.00	2.00	370.00
Sr	150.00	430.00	20.00	16.00	385.00	158.00	220.00
Ba	28.00	75.00	12.00	6.00	38.00	67.00	6000.00
AM_13 & STE_5 = calcitic marbles, AM_17 & AM_6 = dolomitic marbles ,dolo							

5. Conclusions

Samples of ornamental stones from different areas of Greece are examined. They are classified into three main categories: marbles (calcitic and dolomitic), limestones and dolomites. Particular emphasis is given on the correlation between mineralogical composition and aesthetic characteristics. The constituents that are responsible for these special features are the Fe-Mn oxides and silicate minerals such as quartz, muscovite, biotite, clinochlore, chlorite, epidote, clay minerals (illite, kaolinite), etc. Oxides are either diffused to the whole rock mass or are concentrated in veins, while the silicate minerals usually appear in strips or agglomerates. Moreover, the geochemical characteristics of the marble groups show that those which have undergone higher diagenetic processes (i.e. calcitic and dolomitic marbles) exhibit lower Sr contents in comparison to non-metamorphic rocks (limestones and dolomites). Taking into consideration the fact that Sr substitutes only Ca, it is expected that all types of calcite-dominant rocks contain more Sr compared to the dolomitic ones. Positive correlations between Ba and As are observed in all studied groups, whereas there is no statistical correlation between Ba and Sr. Furthermore, it is concluded that dolomitic rocks show specific value ranges in their composition of the elements Ni, Cr, Cu and Zn, which cannot be correlated, while calcitic rocks show positive correlation and no limitation in their content. All these features affect marble appearance and contribute to their commercial final market price Considering also the fact that many of these ornamental stones have been used in architecture from ancient times as ornamental or building materials (statues, temples, emperors' residences, etc.), further investigation and research is required in order to enrich the existing database and archaeometric data which will be of immense importance for archeological and geoscience scientific fields.

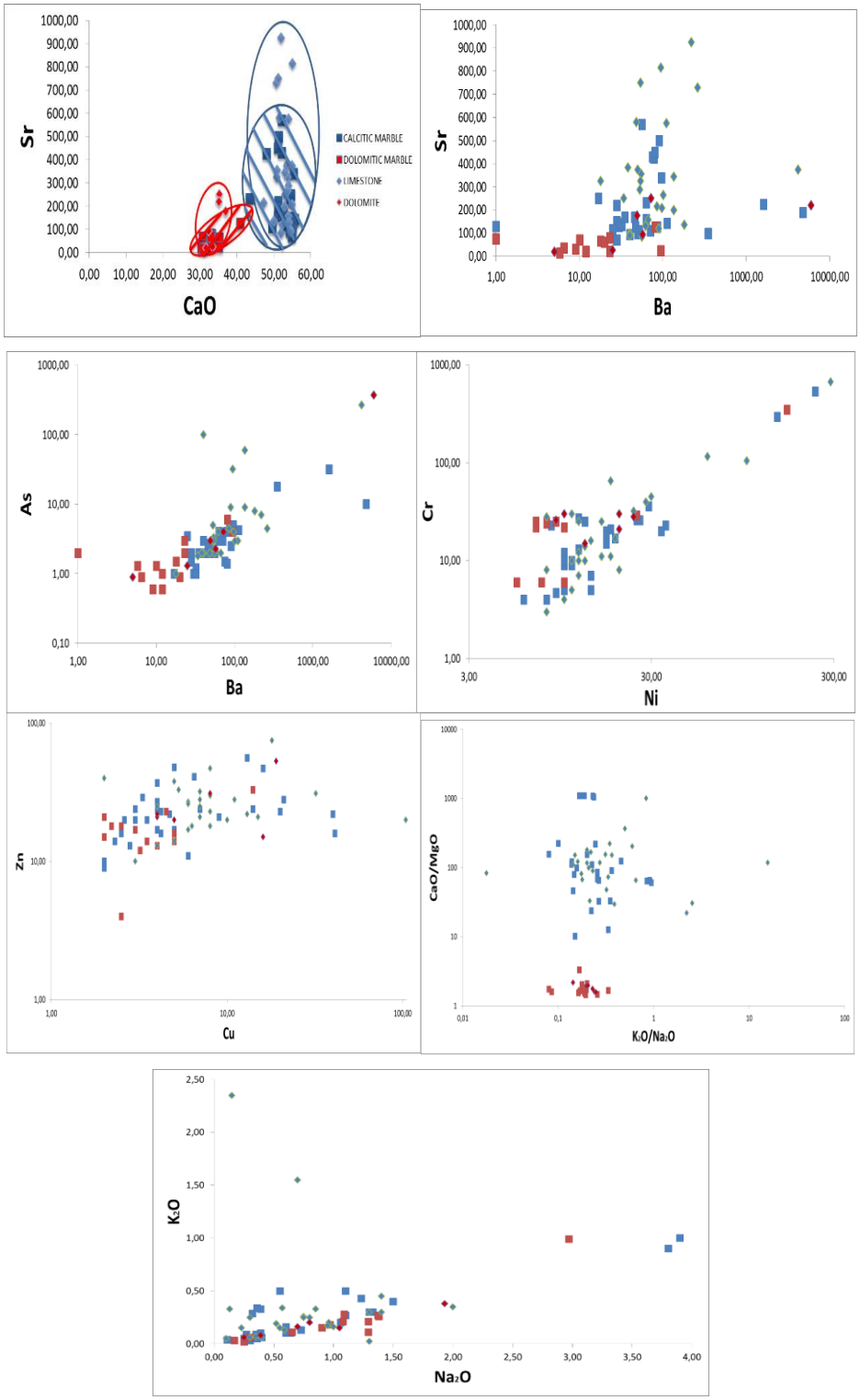

Figure 3 - Binary diagrams of analyzed samples. CaO-Sr (a), Ba-Sr (b), Ba-As (c), Ni-Cr (d), Cu-Zn(e), K_2O/Na_2O-CaO/MgO (f), Na_2O-K_2O (g). The legend of the first diagram is valid for all diagrams.

6. Acknowledgments

The authors express their sincere appreciation to I.G.M.E. and to its Director of Mineral Natural Resources Department Dr. George Economou for allowing them to examine the samples at the laboratories of Mineral Natural Resources Department. They also thank Yiannis Kouseris, Nikos Xirokostas, Efi Tsapara, Pantelis Patsis and Michalis Sakalis for their laboratory support. The study was funded by "Research And Evaluation Of Selected, Non-Energy, Primary Raw Materials Of The State, Aiming At The Sustainable Operation Of Mineral Industry (NEPRM)" project.

7. References

Bağcı, M., Kibici, Y., Yıldız, A. and Akıncı, Ö.T., 2010. Petrographical and geochemical ınvestigation of the Triassic marbles associated with Menderes Massif metamorphics, Kavaklıdere, Mugla, SW Turkey, *J. Geochem. Explor*., 107, 39-55.

Brilli M., Giustini F., Conte A., Mercadal P., Quarta G., Plumed H., Scardozzi G. and Belardi, G., 2015. Petrography, geochemistry, and cathodoluminescence of ancient white marble from quarries in the southern Phrygia and northern Caria regions of Turkey: Considerations on provenance discrimination, *J. of Archaeological Science*, 4, 124-142.

Chen, B., Jahn, B.-M. and Wei, C.-J., 2002. Petrogenesis of Mesozoic granitoids in the Dabie UHP complex, central China: trace element and Nd-Sr isotope evidence, *Lithos*, 60, 67-88.

Directory of Greek Ornamental & Structural Stones, I.G.M.E., 2015.

Ferrini, V., De Vito, C., Mignardi, S. and Fucinese, D., 2012. Archaeological carved slabs of the Langobard art in churches of Peligna Valley and Spoleto (Italy): provenance of the stones, *J. of Archaeological Science*, 39, 3505-3515.

Garde, A.A., 1979. Strontium geochemistry and carbon and oxygen isotopic compositions of lower Proterozoic dolomite and calcite marbles from the Marmoliric formation, West Greenland. *Precambrian Research*, 8, 183-199.

Iliadou, S., Tsirambidis, A., Kasoli- Fournaraki, A. and Michailidis, K., 2004. Petrographic and geochemical research of the carbonate rocks of the area of Vafiochori, Kilkis, *Bull. Geol. Soc. Greece*, 36(1), 10-18.

Koralaya, T. and Kılıncarslan, S., 2016. A multi-analytical approach for determining the origin of the marbles in Temple-A from Laodicea ad Lycum (Denizli-Western Anatolia, Turkey), *J. Cultural Heritage*, 42-52.

Lazzarini, L., Moschini, G. and Stievano, B.M., 1980. A contribution to the identification of Italian, Greek and Anatolian marbles through a petrological study and the evaluation of Ca/Sr ratio, *Archaeometry*, 22, 173-182.

Melezhik, V.A., Gorokhov, I., Fallick, A.F. and Gjelle, S., 2001. Strontium and carbon isotope geochemistry applied to dating of carbonate sedimentation: an example from high-grade rocks of the Norwegian Caledonides, *Precambrian Research*, 108, 267-292.

Melezhik, V.A., Bingen, B., Fallick, A.F., Gorokhov, I.M., Kuznetsov, A.B, Sandstad, J.S., Solli, A., Bjerkgard, T., Henderson, I., Boyd, R., Jamal, D. and Moniz, A., 2008. Isotope chemostratigraphy of marbles in northeastern Mozambique apparent depositional ages and regional implications, *Precambrian Research*, 162, 540-558.

Munyanyiwa, H. and Hanson, R., 1988. Geochemistry of marbles and calc-silicate rocks in the Pan-African Zambezi belt, Zambia, *Precambrian research*, 38, 177-200.

Murra, J., Bawo, K., Galindo, C., Casquet, C., Pankhurst, R., Rapela, C. and Dahlquist, J., 2011. Sr, C and O isotope composition of marbles from the Sierra de Ancasti, Eastern Sierras Pampeanas, Argentina: age and constraints for the Neoproterozoic-Lower Paleozoic evolution of the proto-Gondwana margin, *Geol. Acta*, 9, 1-23.

Papatrechas, Ch., 2011. Correlation of physicomechanical properties with grain size and mineralogical composition of the carbonate rocks of Eastern Macedonia (Greece), *PhD Thesis*, University of Thessaloniki.

Shearman, D.J. and Shirmohammadi, N.H., 1969. Distribution of strontium in dedolomites from the French Jura, *Nature*, 223, 606-608.

Stoll, H.M. and Schrag, D.P., 2001. Coccolith Sr/Ca as a new indicator of coccolithophorid calcification and growth rate, *Geochem. Geophys. Geosyst.*, 1, 1-24.

Δελτίο της Ελληνικής Γεωλογικής Εταιρίας, τόμος L, σελ. 1781-1788
Πρακτικά 14ου Διεθνούς Συνεδρίου, Θεσσαλονίκη, Μάιος 2016

Bulletin of the Geological Society of Greece, vol. L, p. 1781-1788
Proceedings of the 14th International Congress, Thessaloniki, May 2016

MINERALOGICAL AND GEOCHEMICAL CHARACTERIZATION OF ZEOLITES IN ALBANIAN OPHIOLITIC PLAGIOGRANITES

Goga Beqiraj E.[1], Muller F.[2] and Beqiraj A.

[1]*Polytechnic University of Tirana, Faculty of Geology and Mines, Rruga Elbasani, ea_beqiraj@yahoo.com*

[2]*Institut des Sciences de la Terre d'Orleans, Rue de la Férollerie Orleans, Cedex 2, France*

Abstract

The plagiogranites, that represent the uppermost part of the plutonic complex of the Albanian ophiolites, are intensively altered. They crop out in the north - eastern sectors of the Albanian ophiolitic complex presenting intrusive contacts with volcanic and gabbroic rocks. The zeolite, that is a typically secondary mineral, has filled thin veins and/or small vesicles of the rock. From the XRD, EMPA and microscopic analyses it is concluded that this zeolite belongs to the laumontite - leonhardite (LAU) series.
Keywords: *Laumontite, leonhardite, zeolites, plagiogranites, Kimza-Tuci.*

Περίληψη

Οι πλαγιογρανίτες, οι οποίοι αντιπροσωπεύουν το ανώτερο τμήμα του πλουτωνικού συμπλέγματος των Αλβανικών οφιολίθων, είναι έντονα εξαλλοιωμένοι. Εμφανίζονται στα βορειοανατολικά τμήματα του Αλβανικού οφιολιθικού συμπλέγματος παρουσιάζοντας επαφές διείσδυσης με ηφαιστειακά και γαβρικά πετρώματα. Ο ζεόλιθος, ο οποίος είναι ένα τυπικό δευτερογενές ορυκτό, έχει πληρώσει λεπτές φλέβες και/ή μικρές κοιλότητες του πετρώματος. Από τις αναλύσεις XRD, EPMA και μικροσκοπίας συμπεραίνεται ότι αυτός ο ζεόλιθος ανήκει στη σειρά λομοντίτη-λεονχαρδίτη.
Λέξεις κλειδιά: *Λομοντίτης, λεονχαρδίτης, ζεόλιθοι, πλαγιογρανίτες, Kimza-Tuci.*

1. Introduction

It is well known that zeolites are framework silicates consisting of interlocking SiO_4 and AlO_4 tetrahedrons. In order to be a zeolite the ratio (Si+Al)/O must be equal to 1/2. The alumino-silicate structure is negatively charged and attracts the positive cations that reside within it. Unlike most other tectosilicates, zeolites have large vacant spaces or cages in their structures that allow space for large cations such as sodium, potassium, barium and calcium and even relatively large molecule and cation groups such as water, ammonia, carbonate ions and nitrate ions (Gottardi and Galli, 1985; Baerlocher *et al.*, 2007). Therefore, zeolites were known to be able to act as ion exchangers of high ion exchange capacity (Soulaymana *et al*., 2004).

The zeolites in Albanian ophiolites are related with medium-acid volcanic rocks and with plagiogranites. Plagiogranites constitute the upper part of the plutonic sequence of the Albanian ophiolites and crop out among volcanic rocks (low-Ti basalts, andesites and dacites) (Shallo, 1995). Kimza-Tuci plagiogranitic unit consists of tonalites and trondhjemites. This unit is associated with microdiorites of small area.

The zeolites of the Kimza-Tuci plagiogranites have been scarcely studied (Kati, 1967). They occur as small and thin veins and/or vesicles within the above mentioned rocks. This study aims to further advance their mineralogical-chemical characterization based on the new analytical data.

2. Geological setting and sampling

The plagiogranites of Kimza-Tuci are located in the E-type ophiolites (Bebien *et al.,* 1997) in the north-eastern part of the Jurassic Mirdita ophiolitic complex, Albania (Fig. 1). The later represents an important segment of the Tethyan ophiolites in the Alpine orogenic system where two belts are distinguished: the "lherzolitic" western belt and "harzburgitic" eastern belt which show MORB and SSZ affinities, respectively (Shallo, 1992; Robertson and Shallo, 2000; Shallo and Dilek, 2003; Bortolotti *et al.,* 2005; Dilek *et al.,* 2007).

Western belt ophiolites compose an incomplete section which consists, from the bottom to the top, of ultramafic sequence (lherzolite-harzburgite, plagioclase lherzolite, plagioclase dunite, rare amphibole peridotite), overlain by limited and thin plutonic sequence (composed of troctolite, olivine gabbro, ferrogabbro, gabbro, rare amphibole gabbro and plagiogranite) and massive and pillow basalt, basalt-andesitic MORB type lavas (Shallo, 1994). On the contrary, a complete section is characteristic for the eastern belt ophiolite which consists of harzburgite, interbedded harzburgite-dunite, massive dunite, overlain by gabbronoritic sequence (layered and massive gabbronorite, gabbro, amphibole gabbro, quartz diorite and plagiogranite), on which lie a sheeted dyke complex and a basalt-dacitic (basalt, basalt-andesite, boninite, andesite, dacite, quartz dacite, rhyodacite) volcanic sequence (Shallo, 1994).

Quartz diorites and plagiogranites constitute the upper part of the plutonic sequence of the Albanian ophiolites and they are often accompanied by sheeted dyke complexes. They consist of plagiogranite and quartz diorite, while lateral sectors of the above magmatic bodies are represented by microdiorite. The plagiogranites contain zoned plagioclase, quartz, calcic pyroxene, amphibole and magnetite. Secondary alteration results in the development of albite, actinolite, chlorite, epidote and zeolite.

Seven samples were collected from plagiogranitic rocks of Kimza-Tuci region (Fig.1) which crop out among volcanic rocks (low-Ti basalts, andesites and dacites) and are intruded by low-Ti basaltic and andesitic dykes (Shallo, 1995). Kimza plagiogranitic unit consists of tonalities and trondhjemites associated with microdiorites of small area. These rocks contain a normally-zoned plagioclase (An_{50-15}), augite (Wo_{41} En_{39} Fs_{20}), ferro- edenitic amphibole, quartz, magnetite, ilmenite and abundant apatite (Bebien *et al.,* 1997).

Based on the geochemical data the tonalite - trondhjemite of Kimza shows a clear magmatic affinity with those from suprasubduction zone and are similar with sheeted dyke complexes and basalt-andesite volcanic rocks (Bebien *et al.,* 1995; Shallo, 1995). These leucocratic plutonic rocks reflect the diversity of the magmatic processes involved in the development of oceanic lithospheres near subduction zones (Bebien *et al.,* 1997). ^{40}Ar-^{39}Ar radiometric ages of the plagiogranite and quartz-diorite intrusions show rather similar ages of 160 Ma to 165 Ma (Dilek *et al.,* 2001, 2007).

3. Methods of study

Zeolite enriched samples were obtained by purification processes based on greater friability and lower density (de' Gennaro and Franco, 1979; de' Gennaro and Langella, 1996). Samples were

characterized by thin X-fluoresence, ICP-MS, thin section petrography, electron microprobe analysis (EMPA), X-ray diffraction (XRD).

Mineralogy of bulk and separated material was examined by X-ray diffraction using transmission geometry. The patterns were recorded in a 5° 2θ to 120° 2θ interval using a curved detector INEL, CPS 120 and a Co anticathode (λCoKα1 = 0.70926 Å). The powder samples were placed in capillary tubes (0.5 mm). Chemical analyses of zeolites and associated minerals were performed using CAMECA (CAMEBAX type) electron microprobe under the following operating conditions: accelerating voltage of 20kV, sample current of 10 nA and a beam diameter 7 μm to 10 μm. Microscopic observation was done using a Leitz Wetzlar microscope.

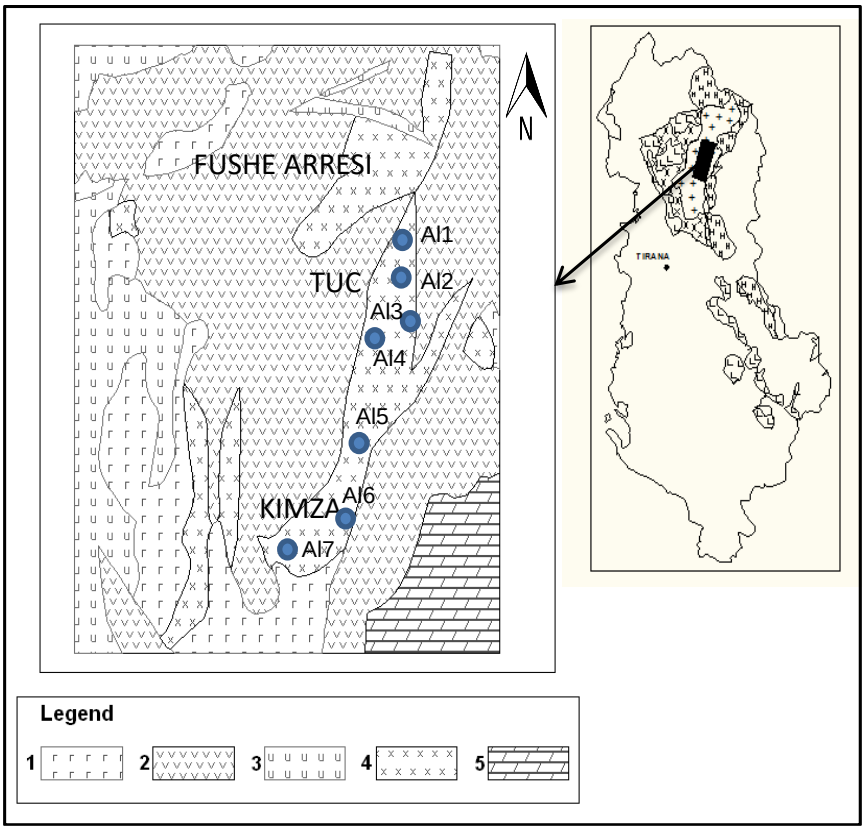

Figure 1 - Geological sketch of Kimza-Tuci region. Legend: 1. Gabbro, 2. Basalt - andesite, 3. Ultramafic rock, 4. Plagiogranite, 5. Limestone.

In particular, we focused on EMPA data which allow precise point analysis and thus correct characterization of minerals (Reed, 2005). This is important since many minerals show a wide variability in crystal size and composition and are not easy to be accurately determined with other methods. For example, feldspars, amphiboles or micas can incorporate many elements, which might be distinctive of certain rock types and genetic development. Apart from the methodological advantages, one of the strengths of the electron microprobe is the effective combination of back-scattered electron images (BSEI) and quantitative analyses (Ionescu *et al.*, 2011).

4. Results and discussion

The zeolitization represents one of the most developed secondary processes that affected the plagiogranitic rocks, thus generating the so-called mineralized zone (Kati, 1965). Macroscopically, the zeolitized plagiogranites are white to rouse and they are often friable. The zeolites occur as small

and thin veins and/or vesicles within the above mentioned rocks and, in some cases they cut the sulphide mineralized dykes. The thickness of the zeolite veins ranges from a few mm up to 2-3 cm.

Table 1 - Chemical analysis of zeolites from the Kimza-Tuci plagiogranites (oxides are in wt%, while REE in ppm).

Sample	Al1	Al2	Al3	Al4	Al5	Al6	Al7
SiO_2	68.98	69.71	67.63	50.79	55.10	62.99	53.04
Al_2O_3	13.05	11.84	12.03	18.35	18.80	13.59	20.47
Fe_2O_3	5.58	4.53	6.23	7.82	3.58	5.62	2.18
MnO	0.059	0.026	0.093	0.133	0.031	0.083	0.034
MgO	0.86	0.53	1.04	3.06	1.15	0.77	0.45
CaO	2.81	5.15	4.75	8.04	8.99	5.41	10.93
Na_2O	4.62	1.09	1.09	0.29	0.37	1.54	0.06
K_2O	0.17	0.09	0.09	0.16	0.21	0.41	0.16
TiO_2	0.467	0.351	0.427	0.587	0.301	0.376	0.153
P_2O_5	0.10	0.07	0.09	0.05	0.05	0.08	0.02
LOI	3.17	6.65	6.38	11.12	11.76	8.19	12.82
Total	99.87	100.03	99.84	100.4	100.34	99.06	100.31
Ba	13	3	Nd	4	4	7	Nd
Sr	38	32	42	68	69	27	59
Y	37	34	28	21	17	39	6
Zr	105	58	50	39	31	69	32
V	40	17	19	261	76	8	52
Co	9	5	7	22	10	5	13
Cr	129	59	91	39	27	44	15
Hf	3.4	1.7	2	1.1	1	2.1	Nd
Sc	16.7	15.8	19.2	27.9	14.4	17.2	7.9
La	3.3	4.7	3.8	2.4	2	4.8	1
Ce	10	12	11	6	5	13	Nd
Nd	8	8	5	Nd	Nd	9	Nd
Sm	2.9	2.6	2.3	1.6	1.5	2.7	0.6
Eu	0.8	0.6	0.7	0.6	0.4	0.8	0.2
Tb	Nd	0.9	0.5	Nd	Nd	0.7	Nd
Yb	4.8	4.1	4	2.6	2.2	4.5	1
Lu	0.72	0.62	0.6	0.41	0.33	0.69	0.15

Both major and trace elements were analyzed (Table 1). In the SiO_2-FeO_t/MgO plot (Fig. 2) all the plagiogranites of the Kimza-Tuci region plot in the tholeiitic field showing a wide range of SiO_2 (50-70 wt%). In addition, the FeO_t/MgO (FeO_t=total iron) is high and increases with increasing SiO_2 content. All the samples present very low K_2O content. They show positive MgO vs. TiO_2 and Co correlation and poor correlation of MgO vs. Cr, but no correlation was observed between MgO and CaO, Al_2O_3, Hf, Zr and Y. Geochemically, they are not very different from ocean ridge granites (Bebien *et al.*, 1997; Pierce *et al.*, 1984).

REE abundances of the Kimza-Tuci plagiogranites show two well differentiated patterns (Fig. 3). The first belongs to samples Al1, Al3 and Al5 which exhibit slightly LREE-depleted patterns, similar to plagiogranites from Cyprus and Oman ophiolites (Aldiss, 1981; Gillis and Coogan, 2002). Both show geochemical MORB affinity. On the contrary, the second group of samples (Al2, Al4 and Al6) exhibits highly HREE depleted patterns. Crystal fractionation of amphibole or partial melting of amphibolite can cause the enrichment of LREE in plagiogranite melt, because amphibole

has high partition coefficients for heavy REE (HREE) (Green, 1994). Finally, REE pattern of sample Al7 doesn't fit neither with the first group of samples nor with the second one.

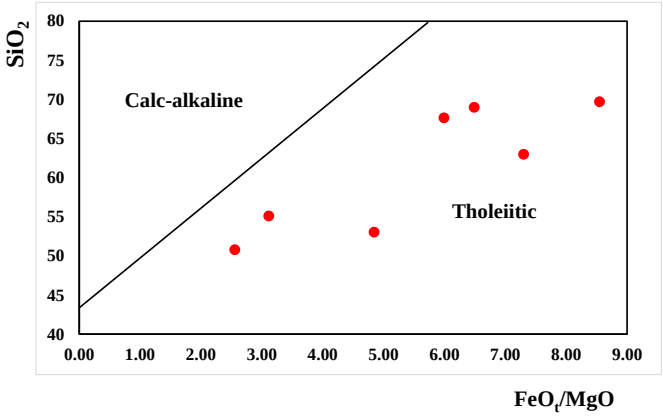

Figure 2 - Plot of SiO_2 versus FeO_t/MgO for lavas and dikes of the WMO and EMO. The boundary line between tholeiitic and calc-alkaline rock types is from Miyashiro (1974).

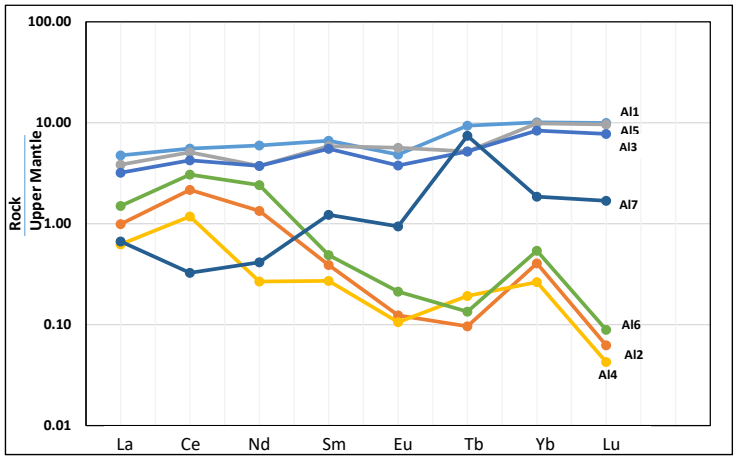

Figure 3 - Upper Mantle-normalized REE pattern of the plagiogranites. Normalized Upper Mantle values are taken from McDonough and Frey (1989).

The difference between the two groups of plagiogranites is evidence that ophiolites do not represent all kinds of ocean crust and that a greater range of magma compositions and/or conditions of magmatic differentiation is represented by the ocean crust (Aldiss, 1981).

Based on XRD, EMPA, DTA and optical observation the mineralogical composition of the studied plagiogranites mainly consists of plagioclase and quartz (55-60%), followed by LAU-type zeolite (30-35%) and subordinate amphibole and chlorite (10%) (Fig. 4).

From the thin section petrography it was found that plagiogranites are fine to medium-grained rocks with subhedral granular and intergranular textures that contain plagioclase, quartz and minor amounts of amphibole and chlorite. In addition scarce quantities of epidote and magnetite are observed. Zeolites are represented by laumontite which belongs to two structural types: the first type was formed by replacement of albite and the second was formed through filling of the fractures and veins. They are slightly colored (grey, beige). Biotite is partly transformed into chlorite.

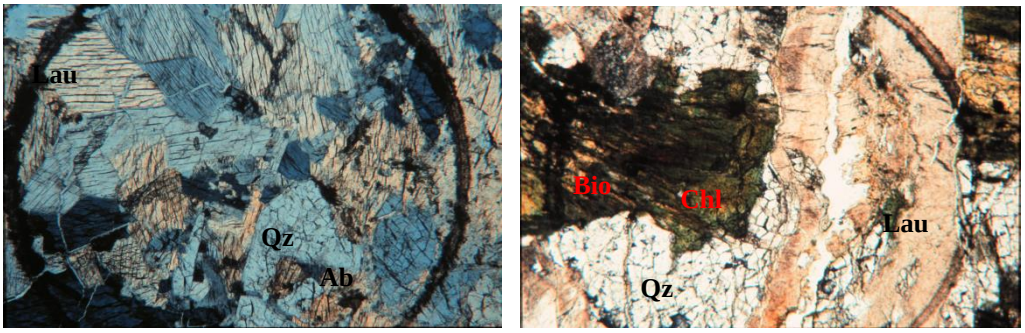

a **b**

Figure 4 - Microphotographs from plagiogranites showing the zeolitization process. (a. Zeolite-free plagiogranite - PL, 6.3x; b. Zeolite-bearing plagiogranite - PL, 6.3x; Lau=Laumontite; Qz=Quartz; Ab=Albite; Bio=Biotite; Chl=Chlorite).

Fig. 2 shows X-ray diffraction of three (of seven samples analyzed by XRD) powdered zeolite-bearing plagiogranite samples (Al2, Al3, Al7). X-ray diffraction analysis revealed the presence Laumontite-Leonhardite series which corresponds to peaks d=9.41 Å and d=4.15 Å. As it can be seen by diffraction spectra of the samples studied, there is no differences between them with respect to zeolite phase.

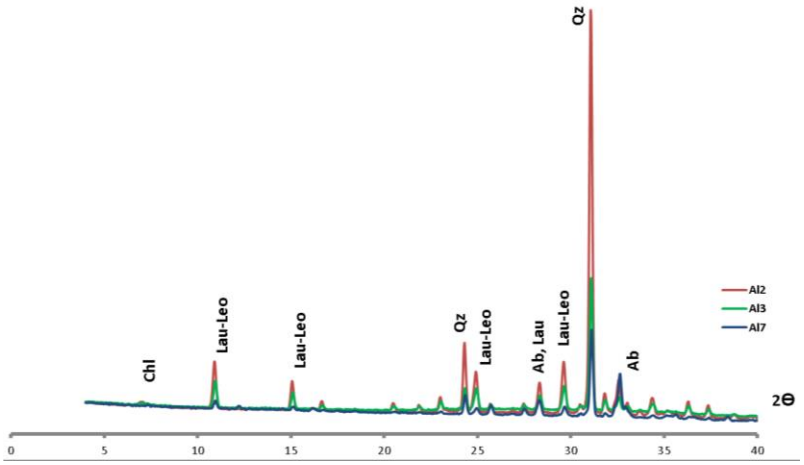

Figure 5 - X-ray diffraction pattern of Al2, Al3 and Al7 samples (Chl - chlorite; Lau-Leo - Laumontite-Leonhardite; Qz - Quartz; Ab - Albite).

The non-zeolitic phase consists of quartz which corresponds to peaks d=3.34 Å and d=4.25Å; albite (d=3.65 Å and 3.18 Å).It was also observed the presence of chlorite that corresponds to very weak peaks (d=14.28 Å) in the sample Al3, Al7 and are quite similar with corresponding peaks in samples Al 4, Al5 and Al6 (not shown).

From the EMPA analytical data (Table 2) it is concluded that the chemical composition of laumontite is normally near to its stoichiometric formula: $Ca_{0.9}Al_{2.1}Si_{4.0}O_{12}$ $4H_2O$ (Al1), $Ca_{1.0}Al_{2.0}Si_{4.0}O_{12}$ $4H_2O$ (Al2, Al3), $Ca_{0.9}Al_{2.0}Si_{4.1}O_{12}$ $4H_2O$ (Al4, Al5, Al6, Al7). The content (as a.f.u.) of the principal constituents ranges within the intervals 14.90-16.20%, 7.91-8.49% and 2.8-3.8% for Si, Al and Ca, respectively. All the analyses show the presence of a Ca highly rich

laumontite as it could be expected from the strong calc-alkaline affinity of the host rocks (plagiogranites).

Table 2 - Selected microprobe analysis of LAU zeolites from the studied samples (wt%).

Sample	Al1	Al2	Al3	Al4	Al15	Al6	Al7
SiO2	47.94	53.48	53.12	51.22	51.58	51.05	51.71
FeO	0.00	0.075	0.15	0.00	0.11	0.49	0.00
Na2O	0.027	0.00	0.04	0.058	0.02	0.01	0.00
K2O	0.125	0.101	0.12	0.42	0.45	0.44	0.14
Al2O3	21.74	23.049	22.44	21.48	21.70	21.31	21.72
MnO	0.098	0.00	0.02	0.00	0.014	0.00	0.02
MgO	0.00	0.00	0.00	0.00	0.00	0.44	0.00
CaO	10.65	11.19	11.24	10.62	10.53	10.37	10.88
TiO2	0.00	0.00	0.04	0.033	0.00	0.00	0.00
Total	80.58	87.90	87.18	83.83	84.41	84.13	84.47

5. Conclusions

The plagiogranitic rocks from Kimza-Tuci region, northern Albania, are intensively altered and contain veins and vesicles filled with zeolites. Their mineralogical composition consists of plagioclase and quartz (55-60%), followed by zeolites (30-35%) and subordinate amphibole and chlorite (10%).

They show geochemical signatures that are similar to those of oceanic granites.

The existing zeolite belongs to the LAU type where the Ca highly rich laumontite predominates as it could be expected from the strong calc-alkaline affinity of the host rocks (plagiogranites).

6. Acknowledgments

We appreciate the help of Dr. Tonin Deda who accompanied us during the sampling.

7. References

Aldiss, D.T., 1981. Plagiogranites from the ocean crust and ophiolites, *Nature*, 289, 577-579.

Baerlocher, Ch., McCusker and Olson, D.H., 2007. Atlas of zeolite framework types, Sixth Revised Edition, *Elsevier*, 405 pp.

Bebien, J., Shallo, M. and Karadumi, A., 1995. Intrusive ultramafic rocks in Albanian ophiolites, *EUG*-8.

Bébien, J., Dautaj, N., Shallo, M., Turku, I. and Barbarin, B., 1997. Diversity of ophiolitic plagiogranites: the Albanian example, Comptes Rendus de l'Academie des Sciences Series IIA, *Earth and Planetary*, 324, 875-889.

Bish, D.L. and Ming, D.W., 2001. Natural zeolites: Occurrence, Properties, Applications, *Reviews in Mineralogy and Geochemistry*, 45, USA, 654 pp.

Bortolotti, V., Marroni, M., Pandolfi, L. and Principi, G., 2005. Mesozoic to Tertiary tectonic history of the Mirdita ophiolites, northern Albania, *Island Arc*, 14, 471-493.

de' Gennaro, M. and Franco, E., 1979. Arrichimento e separazione delle zeoliti di rocce piroclestiche, *Ind. Minerals*, 30, 329-336.

de' Gennaro, M. and Langella A., 1996. Italian zeolitized rocks of technological interest, *Miner. Deposita*, 31, 452-472.

Dilek, Y., Furnes, H. and Shallo, M., 2007. Geochemistry of the Jurassic Mirdita Ophiolite (Albania) and the MORB to SSZ evolution of a marginal basin oceanic crust, *Lithos*, 01618, 36 pp.
Gillis, K.M. and Coogan, L.A., 2002. Anatectic migmatites from the roof of an ocean ridge magma chamber, *J. Petrology*, 43, 2075-2095.
Green, 1994. Experimental studies of trace-element partitioning applicable to igneous petrogenesis - Sedona 16 years later, *Chemical Geology*, 117, 1-36.
Gottardi, G. and Galli, E., 1985. Natural Zeolites, *Springer, Editors, A.EI Goresy, W von Engelhardt, T. Hahn.* 391 pp.
Ionescu, C., Hoeck, V. and Ghergari, L., 2011. Electron microprobe analysis of ancient ceramics: A case study from Romania, *Appl. Clay Science*, 53(3), 466-475.
Kati, P., 1965. Ceolitizimi i shkembinjve plagjeogranitike ne rajonin e Tucit, *Permbledhje studimesh*, 43-49.
McDonough, W.F. and Frey, F.A., 1989. Rare earth elements in upper mantle rocks. *In*: Lipin, B.R. and McKay, G.A., *eds*, Geochemistry and mineralogy of rare earth elements. *Mineralogical Society of America*, Washington D.C., 21, 99-145.
Miyashiro, A., 1974. Volcanic rock series in island arcs and active continental margins, *American Journal of Science*, 274, 321-355.
Pierce, J.A., Harris, N.B.W. and Tindle, A.G., 1984. Trace element discrimination diagrams for the tectonic interpretation of granitic rocks, *J. Petrology*, 25, 956-983.
Reed, S.J.B., 2005. Electron Microprobe Analysis and Scanning Electron Microscopy in Geology, *Cambridge University Press*, 206 pp.
Robertson, A.H.F. and Shallo, M., 2000. Mesozoic-Tertiary tectonic evolution of Albania in its regional Eastern Mediterranean context, *Tectonophysics*, 316, 197-254.
Robinson, S.M., Kent, T.E. and Arnold, W.D., 1993. Natural Zeolites 93. *In*: Ming, D.W. and Mumpton, F.A., *eds*, *International Communication of Natural Zeolites*, Brockport, NY, 1995, 579 pp.
Shallo, M., 1992. Geological evolution of the Albanian ophiolites and their platform periphery, *Geologische Rundschau*, 81(3), 681-694.
Shallo, M., 1994. Outline of the Albanian ophiolites, *Ofioliti*, 19, 57-75.
Shallo, M., 1995. Volcanics and sheeted dykes of the Albanian SSZ ophiolites, *Bull. Shk.Gjeol.*, 1, 99-118
Shallo, M. and Dilek, Y., 2003. Development of the ideas on the origin of Albanian ophiolites. *In*: Dilek, Y. and Newcomb, S., *eds*, Ophiolite Concept and the Evolution of Geological Thought. *Geological Society of America Sp. Paper*, 373, 351-364.
Soulaymana, S.S., Mkamib, H.E. and Smith, G.M., 2004. EPR investigation of two types of Syrian's natural zeolites, *J. of Physics and Chemistry of Solids*, 65, 1779-1783.

Δελτίο της Ελληνικής Γεωλογικής Εταιρίας, τόμος L, σελ. 1789-1798
Πρακτικά 14ου Διεθνούς Συνεδρίου, Θεσσαλονίκη, Μάιος 2016

Bulletin of the Geological Society of Greece, vol. L, p. 1789-1798
Proceedings of the 14th International Congress, Thessaloniki, May 2016

ON THE RELATIVELY COMPOSITIONAL HOMOGENEITY OF ALBANIAN EASTERN OPHIOLITIC BELT

Çina A.

Institute of Geosciences, Energy, Water and Environment, Polytechnic University of Tirana, Str. Don Bosko, Nr 60, Tirana, Albania, aleksandercina@gmail.com.

Abstract

Ophiolitic formation of Albanides, named as Mirdita zone, represents a compact segment of oceanic lithosphere of Middle-Upper Jurassic. Based on petrographic, geochemical and metalogenical features two types of belts are distinguished: western MORB and eastern SSZ types. In fact, structural and geological units as well as many other elements have shed light on lack of a sharp separation between the two belts.
Recent investigations have evidenced that different ultramafic massifs of western ophiolitic formation, represent an evident variation of their composition from harzburgite to lherzolitic -types. This composition reflects a different grade of partial melting of upper mantle. Peridotites show a high variability, from 0.3 - 3.8 wt.% Al_2O_3, varying from small to highly extreme depleted peridotite.
On the contrary, Albanian eastern belt, it seems to be formed by a more homogeneous hartzburgitic mantle.
Detailed petrologic and metallogenic investigations have evidenced that this belt changes also from one massif to another, naturally at a smaller level, therefore it is easier to be named relatively homogeneous. It is distinguished by a higher melting degree, chiefly of hartzburgitic-type, characterized by whole and thick ultramafic section, as well as by metalogenic variety, mostly of metallurgic-type of chromite mineralization. It is supposed that rock-forming and mineraluzation processes have been developed not uniformly along the ophiolitic belt.
Keywords: *Chromite, ophiolite section, SSZ-type.*

1. Introduction

Albanides, the geological structure of Albania situated in south of Shkodra-Peja transversal fault, as a segment of Dinarides-Hellenides arc, are characterized by the presence of the ophiolitic formation.

The most important of geological event of Albania during Jurassic has been ocean spreading in Mirdita zone. Western belt is thought to have been composed by an ocean ridge, the eastern one by development of an immature island arc (Beccaluva *et al.*, 1994; Shallo *et al.*, 1995; Kodra *et al.*, 1995). During Middle Jurassic, intraoceanic subduction was associated with formation of metamorphic sole. In the Early Tithonian, due to the compression regime, overlapping (obduction) of ophiolite occur.

The Albanian ophiolite formation has classically divided into western and eastern belts. The western ophiolitic belt, similar to western Mediterranean type as MORB-type ophiolite, is characterized by presence of lherzolite ± hartzburgite type, plagioclase - rich basal cumulates, TiO_2 - rich basaltic lavas (1.5 - 2% TiO_2), and by scarce chromite mineralization, chiefly of Al - rich refractory type. A particular Fe - Ti mineralization, related to Fe-gabbro, is also present. For this belt is characteristic

the crystallization order: olivine+chromite+plagioclase+clinopyroxene and geochemical features of association high-Ti basalts, that an oceanic spreading system without any influence of subdacted related processes (Beccaluva *et al.*, 1994; Shallo *et al.*, 1995; Hoeck *et al.*, 2002). The western ophiolite belt is originated from magmatic source that was less depleted, 5-10% (Koller *et al.*, 2009; Çina, 2010).

The eastern belt is si milar to eastern Mediterranean-type, as IAT-boninitic, SSZ setting of ophiolite-type, is characterized by presence of hartzburgitic-type mantle, pyroxene-rich basal cumulates and by TiO_2 poor lavas of boninitic affinity with range down of 0.3%.

This ophiolitic belt is particularly distinguished by high potential chromite-bearing mineralization of Cr-rich metallurgic type. Other types of mineralizations are occur also such as PGM and Ni-sulfide, associated with PGE. As is suggested by Nicolas *et al.* (1999), the slow spreading, oxygen fugacity and the cool action of overlayered crust have played their role in high chromite concentration.

The eastern belt is most depleted, about 25%. This belt, the petrologic characteristics of the cumulate sequence, and the strongly underlying depleted mantle tectonics, along with geochemical features of lavas, indicate a suprasubduction generation of parental magmas (Beccaluva *et al.*, 1994; Shallo *et al.*, 1995). Their crystallization order is olivine + chromite, followed by clinopyroxene and/or orthopyroxene and then plagioclase. Generation of such magmatic system implies intra-oceanic subduction of a pristine lithosphere.

2. Geological setting

The Albanian ophiolitic formation is situated in eastern part of Albania, about 250 km long. Its northern part is bounded by Shkoder - Peja transform fault. The Labinot - Diber transversal fault zone separates the northern and southern ophiolitic formation.

The Albanian ophiolite formation is situated in the western flank of Korabi - Pelagonian microplate. The contact zone of this formation is usually marked by a narrow belt of metamorphic rocks of amphibolites, green schist facies and pre-ophiolitic volcano-sedimentary series.

The primary sedimentary cover of Albanian ophiolite consists of Late Jurassic radiolarian charts and flyschoidal sediments of Tithonian to Early Cretaceous age (Shallo *et.al*., 1995; Kodra *et al.*, 1995). According to recent micro-paleontological investigations (Chiari *et al.*, 2004) radiolarian chart formation located on top and within volcanics, in upper part is older than Upper Bajocian and younger than Lower Oxfordian, therefore it is thought to be of Middle Jurassic. The age of Albanian ophiolite calculated by K - Ar method, is 160 ± 7.5 ml years, and by Rb - Sr method is 158 ± 4.1 ml years (Tashko *et al.*, 1990, CRPG, Nancy, France).

3. Petrological and metalogenic features

Eastern ophiolitic belt consists of some ultramafic massifs, from Tropoja - Has of northeastern area, to the south and southeast, where are situated Kukes, Lura, Bulqiza, Shebenik-Pogradec massifs and some other occurrances in Bitincka, Devolli area (Figure 1).

Based on geophysical measurements, ophiolitic formation of eastern belt is very thick, 5 - 7 to 10 - 12 km toward northeast.

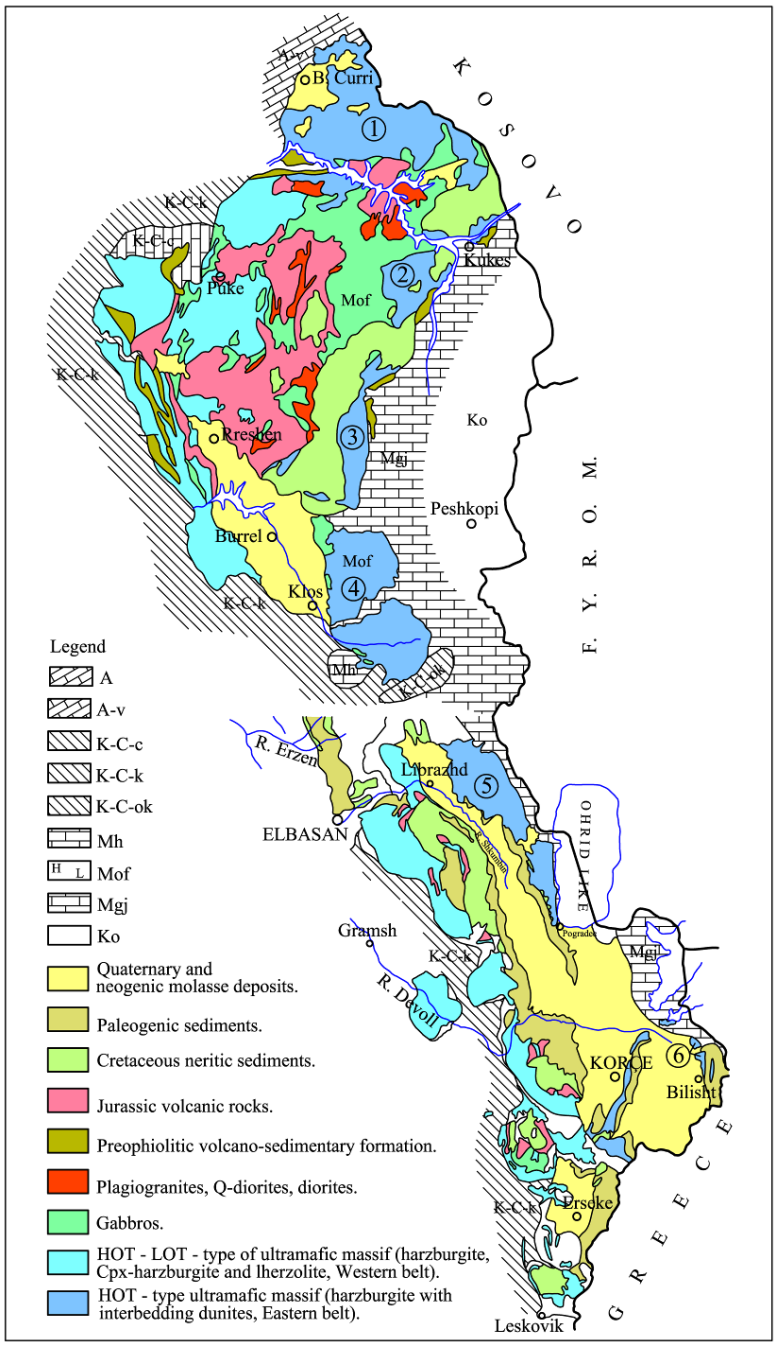

Figure 1 - Albanian ophiolitic formation. A-Albanian Alps; K-C- Krasta-Cukali zone; M-Mirdita zone: M-of- Mirdita ophiolites; Ko-Korabi zone. Ultramafic massifs, eastern ophiolitic belt: 1-Tropoja-Has, 2-Kukesi, 3-Lura, 4-Bulqiza, 5-Shebenik-Pogradeci, 6-Bitincka.

Dominated rocks of this area are mantle ultramafics, chiefly mantle harzbugites, less dunites and transition zone dunites. Ultramafic cumulates, dunites, pyroxenites and wehrlites are thin, about 50 – 200 m. Other part of crust sequence, the mafic, is very thick, about 1500 - 1800 m. It should be noticed that in northeastern zone, occurs a large gabbro massif, named Kaptena, which covers a

territory of 350 km^2. This sequence is composed by different gabbro rocks, even amphibole gabbro and quartz gabbro. Small quartz diorite and plagiogranite massifs have intruded in gabbro sequence and in lower part of volcanic unit (Figure 2).

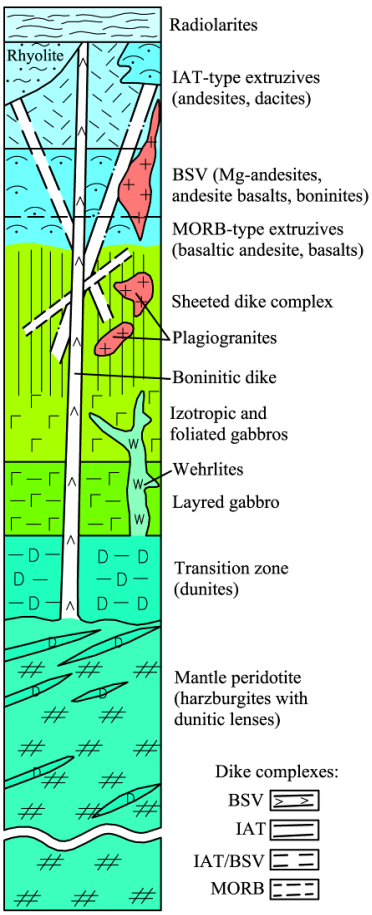

Figure 2 - Generalized column of eastern Albanian ophilitic belt.

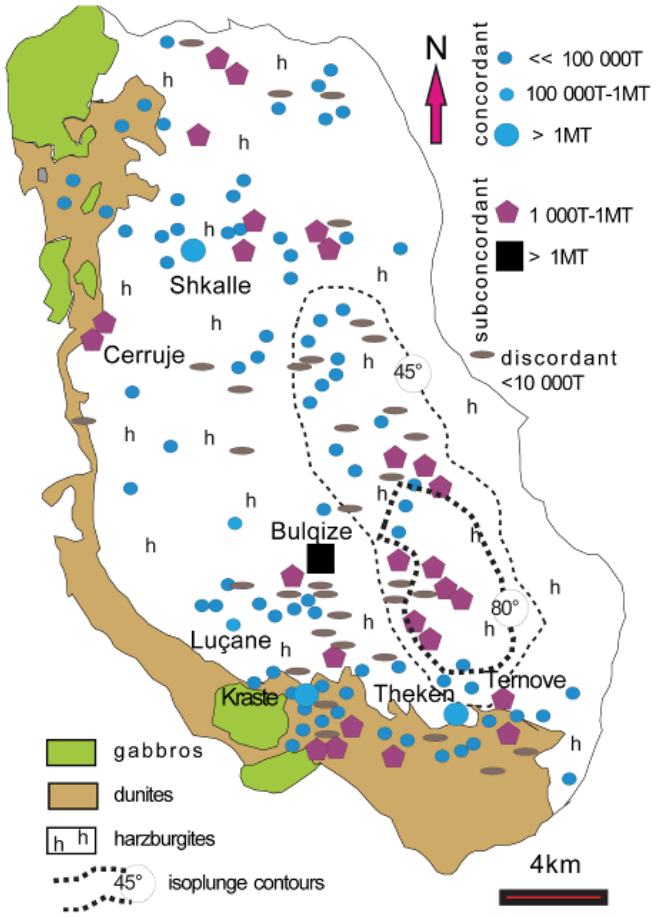

Figure 3 - Distribution of chromite ore bodies and their structural types of Bulqiza massif.

Extrusive volcanic rocks of IAT- type, with a considerable thickness of 1500 - 2200 m, are represented by basalts, basalt andesites, boninites, dacites and rhyolites.

Presence of sheeted dyke complex is another distinctive feature of eastern belt. It is situated in northeastern axial part wth 1000 - 1200 m thickness. They perform an IAT boninitic affinity, but are also of MORB type (Manika, 1994; Shallo *et al.*, 1995). Presence of boninites in eastern belt represents a significant petrologic interest.

Some ultramafic massifs show a relative variation regarding to rock-types, thickness of their sequences, metallogenic features, mineralization types, their potential and shapes of ore bodies. General characteristics of eastern belt are hartzburgite composition of mantle, highly magnesium composition of rock-forming minerals, of enstatite $En_{90\text{-}92}$, as well as forsterite Fo_{90-93}, a few Al_2O_3 and CaO (tenths of %) and very stable composition of chromite ores.

3.1. Tropoja-Hasi massif

Tropoja - Hasi ultramafic massif has a special position, since it appears as a common node for two belts. This massif is large and is composed by mantle hartzburgites, as well as by transition zone

dunites. In the central part of the massif occur pyroxenites and gabbro dykes. Main mineral is chromite, related to mantle hartzburgites and dunites of super-MOHO zone. Many occurrences with some average size and some deposits from 0.5 to 1 milion ton reserves occur. Ore bodies have lenticular - platy shapes and composed by ores with varied textures, whereas chromite itself belongs to Cr-rich type with high grade metallurgic ores. Average chemical indicators are as following (Table 1): Cr/ (Cr + Al) = 0.79-0.82, while Mg/ (Mg + Fe^{2+}) = 0.60 - 0.65. Some occurrences of chromite, related to relatively deeper mantle hartzburgites, belong to Al-rich-type with (Cr/ (Cr +Al) about 0.65. A special chromite type is that of schlieren chromite, associated by pyroxenite veins, distinguished for euhedral crystals of chromite, at size of some mm, and with highly Fe content Mg/ (Mg + Fe^{2+}) = 0.40 – 0.45 and FeO^{tot} = 27.4 – 31.5wt.%. Another metalogenic distinction of Tropoja - Hasi massif is presence of unique mineralization in Albanian ophiolites, such as PGE, which occurs within schlieren chromite related to pyroxenite veins and magmatic brecciated dunites (Bregu i Bibes, Zherge, Shpati i Dajcit deposits).

Albanian eastern ophiolite belt; 1, 4, 6, 7, 9 and 10- chromite related to mantle hartzburgites and transition zone dunites from ultramafic massifs; 2- Fe-rich chromite PGE-bearing ores; 3- Al-rich chromite related to deeper Cpx-hartzburgites; 5 and 8- Al-rich chromite related to cumulate ultramafics; 11- Al-rich chromite related to lherzolite western belt massifs (Çina *et al.*, 1986; Çina 2010); Vourinos (Greece) massif: 12-Xerolivado (Economou *et al.*, 1986).

Table 1 - Representative electron microprobe analyses of chromite.

	1	**2**	**3**	**4**	**5**	**6**	**7**	**8**	**9**	**10**	**11**	**12**
SiO_2	0.05	0.06	0.09	0.08	0.06	0.07	0.05	0.06	0.05	0.06	0.05	0.25
Al_2O_3	10.12	9.38	21.49	9.91	13.68	10.26	10.06	22.97	10.72	9.92	23.43	9.85
Cr_2O_3	59.06	50.74	46.7	59.22	52.52	60.45	60.45	42.92	58.76	60.66	44.53	59.58
Fe_2O_3	3.96		5.2	4.3	4.18	2.03	1.85	4.18	5.62	2.57	2.88	4.78
TiO_2	0.05	0.15					0.2	0.26	0.06	0.15	0.19	0.18
MgO	15.32	7.54	17.35	14.88	13.57	14.84	14.62	15.81	16.58	12.79	15.71	10.87
FeO	11.02	31.3*	8.32	11.69	15.74	12.58	12.92	12.86	7.9	13.20	12.40	13.05
MnO	0.16	0.4	0.31				0.2	0.17	0.37	0.33	0.16	0.66
NiO	0.05	0.18	0.05			0.1	0.16	0.17	0.06	0.13	0.22	0.13
Total	99.99	99.75	99.51	100.1	99.75	99.8	99.95	99.54	100.1	99.81	99.57	99.35
Al	3.083	2.887	6.113	3.037	4.2	3.151	3.066	6.595	3.095	3.033	6.769	2.968
Cr	12.07	11.05	8.908	12.135	10.928	12.451	12.363	8.261	11.78	12.42	8.630	12.043
Fe^{3+}	0.77	2.018	0.949	0.838	0.828	0.398	0.36	0.766	1.068	0.501	0.531	0.920
Ti	0.039	0.028					0.039	0.048	0.011	0.03	0.070	0.069
Mg	5.59	3.114	6.213	5.459	4.799	5.432	5.406	5.675	6.228	4.957	5.452	4.667
Fe^{2+}	2.358	4.815	1.674	2.466	3.201	2.536	2.698	2.6	1.667	2.941	2.474	3.142
Mn	0.011	0.097	0.064				0.044	0.035	0.08	0.074	0.032	0.161
Ni	0.020	0.035	0.01			0.032	0.033	0.034	0.012	0.028	0.042	0.030
Cr#	0.8	0.8	0.6	0.8	0.72	0.8	0.8	0.53	0.79	0.8	0.55	0.80
Mg#	0.7	0.39	0.78	0.67	0.60	0.68	0.66	0.68	0.78	0.63	0.56	0.60

The PGE amount is about 2000 ppb up to over 10.000 ppb (Ohnenstetter *et al.*, 1991; Neziraj, 1992). PGM are dominated by Pt + Fe alloys, commonly isoferroplatinum and tetraferroplatinum, while other minerals as alloys of PGE + BME are less contained. The other characteristic of this mineralization is elevated content of Rh (4-5%). The composition of olivine: from mantle hartzburgites Fo=91.53-91.83; from mantle dunites Fo=91.32-92.93; Opx of mantle hartzburgites En=89.33-90.77; Cpx Wo=47.2-49.6, En=49.65-49.96.

Some quartz-sulfide veined mineralizations of Cu and several lens-like ore bodies of Cu - Ni sulfide-type are related with gabbro - norite massifs.

3.2. Kukesi massif

The following ultramafc massif, Kukesi massif further south, is smaller, about 80 km^2. In northern and western side it contacts with gabbro rocks, while to the east occur Triassic and Cretaceous limestones.

The distinguishing feature of this eastern ophiolitic massif is specific formational composition. It is composed partly by mantle harzburgites, but is dominated by dunite of transition zone, up to 800 m thick. Between dunite and gabbro massifs is observed a thin belt of 100m thickness, composed mostly of wehrlites.

Kukesi ultramafic massif is also chromite-bearing. Several occurrences and any small chromatic deposit are situated within mantle hartzburgites. On the contrary, higher chromite-bearing potential belongs to thick dunitic sequence. There are also evidenced some horizons of layered bodies, composed of disseminated, schlieren and banded ores, with micro to fine-grained texture. Chromite belongs to Cr-rich metallurgic type, while its ore is low grade, containing 15 - 25% Cr_2O_3. Disseminated and banded chromitic ores of like-layered shape ore bodies are observed also in thick dunite lenses, situated in upper parts of hartzburgite - dunite sequence. The size of some chromitite ore bodies reach to 1000 m in strike, and perform a gentle dip. In dunite, close to the contact with gabbro massifs is observed Ni - As maucherite mineralization.

3.3. Lura massif

Lura massif, situated in the south, is also small. It covers an area less than 100 km^2. It is bounded to the east by Triassic limestone, whereas to the west is covered by Cretaceous limestones. This massif, consist mainly of mantle hartzburgites while dunites of the transition zone are very limited. Its chromite-bearing potential is limited, since there are only some occurrences and any small chromite deposit. The chromite belongs to Cr-rich metallurgic type (Table 1).

3.4. Bulqiza massif

Bulqiza ultramafic massif is situated at the west of Korabi microplate. The contact zone is usually marked by narrow belt of ultrametamorphic rocks of amphibolites and green-schist facies. The western flank is covered by molasse sediments of Burreli depression, whereas in southwestern flank, are located Triassic limestones. Further south, the Labinot - Diber transverse zone divides the Mirdita ophiolite belt in two sectors.

This massif covers a large territory, about 350 km^2 while the ultramafic section is very thick about 3-5 km.This massif is dominated by mantle hartzburgites with any dunitic lens. The upper part of hartzburgite sequence switches to a hartzburgite - dunite composition, and above continue dunites of transition zone, situated on southern and western part of the massif. This sequence has a considerable thickness, about 300 - 500 m. Further on are observed cumulate ultramafics, plagioclas dunites, pyroxenites and wehrlites, not very thick (50 - 150 m). Some small massifs of gabbro rocks occur in the western edge of the massif. In addition to these, for Bulqiza massif is characteristics presence of intrusive ultramafic wehrlitic bodies (Bebien *et al.*, 1995).

There is a high level of magnesium in Bulqiza massif composition since rock-forming minerals are orthopyroxene and olivine. In addition, they are enstatite En_{90-92} and forsterite Fo_{90-93} mineral-types respectively, whereas olivine of chromitite is extremely forsteritic Fo_{93-96}.

The grade of partial melting of mantle, results to be very high about 25% (Beqiraj *et al.*, 2001). Another distinguishing feature of Bulqiza ultramafc massif is its metallogeny, which can be proved by presence of highly intensive chromite mineralization, as well as some other mineralizations, such as PGE and Ni-S (Karaj, 1992; Çina, 2010). Chromite mineralization is related with some sequences of ultramafic section, concretely in mantle hartzburgite, hartzburgite - dunite/or mantle dunite - hartzburgite, dunite of transisition zone and in ultramafic cumulate sequence. Thin Cr-picotite bands are observed also in troctolites.

In Bulqiza massif occur many occurrences and some middle sized, large and very large chromite deposits. Among them can be mentioned Bulqiza deposit, which in resources and extraction reaches about 25 milion ton. The highest chromite mineralization is related mainly to mantle hartzburgites and partly with dunites of transition zone. Ore bodies are lens-like - platy shaped, whereas some other ore bodies are platy folded (Bulqiza deposit) and pencil-like (Shkalla deposit). They are very large: ore bodies of Bulqiza - Batra deposit are 5 km in strike and 500 - 1200 m dip. Ore bodies are exploited from an altitude of 1570 m, down to 200 m, though resources are located down to 300 m below sea level. The principal ore body of Shkalla deposit is oval - shaped of horizontal section, about 25 m, whereas in dip 1500m. In dunite sequence of transition zone are observed some horizons of layered bodies, composed by low grade, disseminated, schlieren and banded ores (Krasta deposit). According to structural classification are evidenced concordant, subconcordant and discordant chromite ore bodies (Meshi *et al.*, 2005; Çina and Meshi, 2013) (Figure 3).

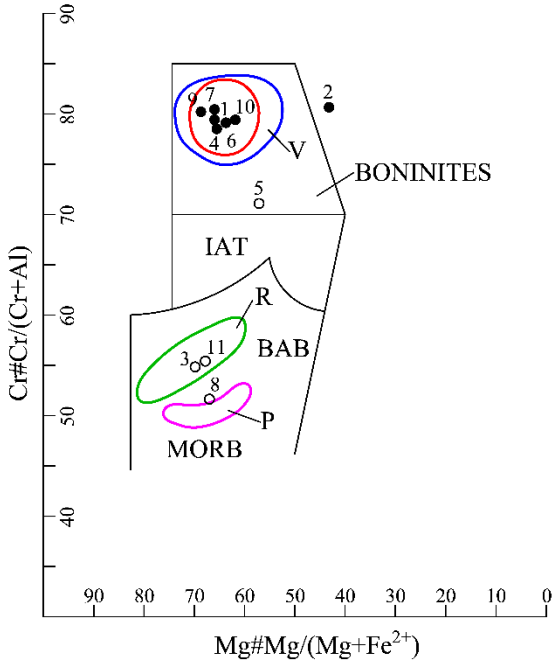

Figure 4 - Cr# versus Mg# of chromite from Albanian chromitite, eastern ophiolitic belt (1- 11) and average composition of Vourinos massif (V), Rodiani (R) area and Pindos massif (P) (Economou *et al.*, 1986) with reference to boninitic lavas from western Pacific, IAT, BAB and MORB environments (after Dick and Bullen, 1984).

Almost on the whole chromite of this massif belongs to Cr-rich metallurgic type, with Cr/(Cr + Al) averagely 0.78-0.82 and Mg/ (Mg + Fe^{2+}) averagely 0.61-0.68 (Figure 4). Difference is at The

chromite of deposits occur in cumulate ultramafics is composed by A-rich type, Cr/(Cr + Al), about 0.52 (Çina *et al.*, 1986; Çina 2010). Olivine of mantle hartzurgites Fo=90.80-91.60 and from mantle dunites Fo=91.73-92.74; Opx of mantle hartzburgites En=89.5-91.0 and Cpx Wo=47.08-47.75 En=49.09-49.7; olivine of chromitites Fo=93.98-96.59.

Another characteristics of Bulqiza massif, is presence of Ni-S, pentlandite mineralization, occurs as disseminations in dunite + chromite sequence of transition zone. With this mineralization are associated PGE in high quantity, reaching to 2200 ppb (Krasta deposit). Similarly another mineralization is that of chromite, associated with Ni - sulfide and PGE, reaching to 9000 ppb. This mineralization is related with cumulate ultramafites of western side of the massif were occur Cerruja, Rrasa Martin, Kunji i Gjate deposits (Ohnenstetter *et al.*, 1991; Karaj, 1992).

3.5. Shebenik-Pogradeci massif

At southeastern end of ophiolitic belt, is situated Shebenik - Pogradec ultramafic massif, dominated by mantle hartzburgites. Other rock components, dunite of transition zone, are limited. This massif contains some chromite occurrences and deposits with reserves vary from 0.5 to 1 mln ton, composed by average to high grade ores (Katjel and Pojska deposits). This mineralization is related with mantle hartzburgites and only some chromite occurrences occur in dunites of transition zone. Chromite, for both groups of mineralizations, belongs to Cr-rich type, Cr/ (Cr + Al) = 0.80 – 0.81, whereas Mg/ (Mg + Fe^{2+}), 0.63 – 0.68. This area of Librazhd-Pogradeci is distinguished also for presence of a large Fe – Ni mineralization and particularly of Ni-silicate lateritic type.

4.6. Vourinos massif

In Greek territory as the continuation of Albanian eastern ophiolitic belt is situated the largest Vourinos ultramafic massif covering an area of 450 km^2.

Based chiefly on geochemical investigations (Beccaluva *et al.*, 1984; Konstantopoullo and Economou-Eliopoulos, 1990), the Jurassic ophiolites have been proposed as supra-subduction and island arc composition.

The Vourinos ophiolite contains the largest producing chromite mines in Greece. Chromite ores are related with tectonite and cumulate parts of ophiolite section. Here ores occur as minor layers in dunite bases.The grade of Cr_2O_3 in chromitite ores vary from 12-18-25%. As for disseminated and schlieren ores, is 35 - 50%. All economic concentrations are found in 2-3 km thick stratigraphic zones at the below the cumulate-tectonite contact. Chromite deposits are related with dunite host rocks of two types, as following: cumulate rocks, associated with ophiolitic magmatic suite and deformed bodies within mantle level sequence of ultramafic tectonites (Economou *et al.*, 1986; Rassios *et al.*, 1990).

In Vourinos massif, most of chromite mineralization belongs to C-rich type with Cr/ (Cr + Al) 0.79 - 0.82, whereas Mg/ (Mg + Fe^{2+}), averagely 0.62 - 0.68 whereas some other types related with cumulates, are composed of chromite of Al-rich type with ratio Cr/ (Cr + Al) 0.58, Mg/(Mg + Fe^{2+}) 0.63. Chemical composition of chromite ores leads to the idea, that Vourinos is formed from an environment, characterized by a higher grade of partial melting, that's why this eastern ophiolite zone contains Cr-rich type chromite ore (Economou *et al.*, 1986). The PGE content, related to chromitite, is very low, about 100 - 200 ppb, whereas the Chondrite normalized patterns show similarity for chromitite of Bulqiza, Vourinos, Turkey and Oman (Economou, 1983, 1986; Ohnenstetter *et al.*, 1991; Alliu *et al.*, 1994).

The Pindios massif as southern continuation of Albanian western ophiolitic belt contains a few of Al-rich chromite occurrances (Economou-Eliopolis and Vacandios, 1995) any of them are metamorphoused (Kapsiotis *et al.*, 2007).

5. Conclusions

The Albanian eastern ophiolitic belt is formed by relatively homogenous hartzburgite mantle, nevertheless its evident the lithofacial and metallogenic variation along north-south direction.

This relatively variation of Albanian eastern ophiolitic belt was conditioned to a certain grade of different degree of partial melting of upper mantle, from the various intensity of mantle-peridotite residue action, by degree of development of magmatic cameras and from diverse activity of magmatic and post magmatic mineralizing processes.

The high chromite-bearing potential and the Cr-rich-type is conditioned by chiefly high magnesium and hartzburgitic composition of upper mantle as well as by high grade of its melting. The slow spreading, oxygen fugasity and the cool action of over layered crust have played also their role for this high chromite concentration.

6. References

Alliu, I., Beccaluva, L., Çina, A., Coltorti, M., Dobi, A., Gjata, K., Gjoni, V., Halku, A., Kodra, A., Premti, I., Saccani, E., Shallo, M., Siena, F., Stermasi, Sh. and Tashko, A., 1994. The Skanderbeg and Bulqiza mafic-ultramafic ophiolitic complexes and their relationship with chromititic ore deposits, *Ofioliti*, 19(1), 27-55.

Bebien, I. and Shallo, M., 1995. Intrusive ultramafic rocks in Albania ophiolites, EUG. 8, Strasbourg (abstract volume).

Beccaluva, L., Ohnenstetter, D., Ohnenstetter, M. and Paupy, A., 1984.Two magmatic series with island-arc affinity within the Vourinos ophiolite, *Contribution to Mineralogy and Petrology*, 85, 253-271.

Beccaluva, L., Coltorti, M., Saccani, E., Siena, F. and Zeda, O., 1994. Midocean ridge and suprasubduction affinities in the ophiolite belts of Albania, *Ofioliti*, 19(1), 77-97.

Beqiraj, A., Masi, U. and Violo, M., 2001. Geochemical characterization of podiformchromite ores from the Bulqiza ultramafic massif and hits for prospection, *Journal of Exploration and Maining Geology*, 9(2), 268-276.

Chiari, A., Marcucci, M. and Prela, M., 2004. Radiolarian assemblages from the Jurassic charts of Albania: new data, *Ofioliti*, 29(2), 95-105.

Çina, A., Casli, H. and Goci, L., 1986. Chromites in the ophiolites ofAlbanides. *In: "*Chromites", UNESCO)'s IGCP 197 project, *Metallogeny of Ophiolites*, Theophrastus Publ., Athens, 107-126.

Çina, A., 2010. Mineralogy of chromitite, Bulqiza ultramafic massif, Albanian ophiolitic complex, 12th International Congress of the Geological Society of Greece, Patras, XLlII/5, 2577-2587.

Çina, A., 2010. Pentlandite mineralization related to Albanian ophiolites, XIX Congress of the Carpathian-Balkan Geological Association, Greece, 110, 317-323.

Çina, A. and Meshi, A., 2013. Later chromitites from ophiolites of Albania. *In:* Basalt 2013, Cenozoic Magmatism in Central Europe, 43-44.

Dick, H.J. and Bullen, T., 1984. Chromian spinel as a petrogenetic indicator in abyssal and Alpine-type peridotite and specially associated lavas, *Contribution to Mineralogy and Petrography*, 86, 54-76.

Economou, M., 1983. Platinum group metals in chromite ores from the Vourinos ophiolite complex, Greece, *Ofioliti*, 8(3), 339-356.

Economou, M., Dimou, E., Economou, G., Migiros, G., Vacondios, I., Grivas, E., Rassios, A. and Dabitzias, S., 1986. Chromite deposits of Greece. *In: "*Chromites", UNESCO's IGCP 197 project, *Metallogeny of ophiolites*, Theofrastus publication, Athens, 129-159.

Economou-Eliopoulos, M. and Vacandios, I., 1995. Geochemistry of chromitites and host rocks from the Pindos ophiolite complex, northwestern Greece, *Chemical Geology*, 122, 99-108.

Hoeck, V., Koller, F., Meisel, T., Onuzi, K. and Kneringer, E., 2002. The Jurassic South Albanian Ophiolites: MOR-vs SSZ-type ophiolites, *Lithos*, 65, 143-164.

Kapsiotis, A., Tsikouras, B., Grammatikopoulos, T., Karipi, S. and Hatzipanagiotou, K., 2007. On the metamorphic modification of Cr-spinel compositions from the ultrabasic rocks of the Pindos ophiolite complex (NW Greece), *Bulletin of the Geological Society of Greece, Procedings of the 11th International Congress*, XXXX, 781-793.

Karaj, N., 1992. Repartition des platinoides des chromites et sulfures dans le massif de Bulqiza, Albanie. Incidence sur les proccesus métallogeniques dans les ophiolites, Thèse, Univ. d'Orléèans, 400 pp.

Kodra, A., Gjata, K. and Bakalli, F., 1995. The Mirdita oceanic basin from rifting to the closure. *In:* Workshop on Albanian ophiolites and related mineralizations, Documents du BRGM 244, Edition BRGM, France, 9-26.

Koller, F., Hoeck, V., Ionescu, C. and Onuzi, K., 2009. Contrasting mantle section in Albanian ophiolites: evidences from mineral and bulk rock composition. *In;* MinPet 2009 and 4th Mineral sciences in the Carpathians Conference, Budapest, Band, 155, 84.

Konstantopoulou, G. and Economou-Eliopoulos, M., 1990. Geochemistry of the Vourinos chromite ores, Greece. *In:* Ophiolites, Oceanic crustal Analogues, Symposium "Trodoos 1987*",* Nicosia, Cyprus, 605-613.

Manika, K., 1994. Pétrologie du massif ophiolitique de Shebenik, Albanie, Thèse, Univ. de Paris-Sud, 297 pp.

Meshi, A., Hoxha, I. and Milushi, I., 2005. Chromitites in Mirdita ophiolite (Albania); Structure and genetic implications, *Journal of Alpine geology*, 49, 1-29.

Neziraj, A., 1992. Etude pétrologique et métallogenique du massif ophiolitique de Tropoja, Albanie. Reference particuliere aux gisements de chromite et éléments du group du platine, Thèse, Univ. d'Orléans, France, 544 pp.

Nicolas, A., Boudier, F. and Meshi, A., 1999. A slow spreading accretionin the ophiolite of Mirdita (Albania), *Journal of Geophysical Researcher*, 104(87), 15155-15167.

Ohnenstetter, M., Karaj, N., Neziraj, A., Johan, Z. and Çina, A., 1991. Le potential platinifere des ophiolites: minéralisations en éléments du group du platine (PGE) dans les massifs de Tropoja et Bulqiza, Albanie, *C.R. Acad. Sci. Fr.*, 313(II), 201-208.

Rassios, A. and Kostopoulos, D., 1990.The geochemistry of dunite and its relation to the position of chromitites in the Vourinos, Ophiolite complex, Greece, *In:* Ophiolites, Oceanic Crustal Analogues, Symp. "Trodoos 1987", Nicosia, Cyprus, 593-603.

Shallo,M., Çina, A. and Turku, I., 1995.Outline of the metallogeny of the Albanian MOR and SSZ-type ophiolites. *In:* Workshop on Albanian ophiolites and related mineralizations, Documents du BRGM244, editions of BRGM, France, 27-46.

Tashko, A. and Gjata, K., 1990. Rreth gjeokronologjise absolute te masiveve ultrabasike te Albanideve, *Bul. Shkenc. Gjeol.*, 1, 39-50.

Δελτίο της Ελληνικής Γεωλογικής Εταιρίας, τόμος L, σελ. 1799-1808
Πρακτικά 14ου Διεθνούς Συνεδρίου, Θεσσαλονίκη, Μάιος 2016

Bulletin of the Geological Society of Greece, vol. L, p. 1799-1808
Proceedings of the 14th International Congress, Thessaloniki, May 2016

GEOCHEMISTRY OF THE GAS MANIFESTATIONS OF GREECE: METHANE AND LIGHT HYDROCARBONS

Daskalopoulou K.[1], D'Alessandro W.[2], Cabassi J.[3], Calabrese S.[1], Fiebig J.[4], Grassa F.[2], Kyriakopoulos K.[5], Parello F.[1] and Tassi F.[3]

[1]*Università degli Studi di Palermo, Dipartimento della Terra e del Mare, via Archirafi, 36, 90123, Palermo, Italy, kyriaki.daskalopoulou@unipa.it, sergio.calabrese@gmail.it, francesco.parello@unipa.it*

[2]*Istituto Nazionale di Geofisica e Vulcanologia, via Ugo la Malfa 153, 90146, Palermo, Italy, walter.dalessandro@ingv.it, fausto.grassa@ingv.it*

[3]*Università degli Studi di Firenze, Dipartimento della Terra, via G. La Pira 4, 50121, Florence, Italy, jacopo.cabassi@unifi.it, franco.tassi@unifi.it*

[4]*Goethe-Universität, Institut für Geowissenschaften, Altenhöferallee 1, 60438 Frankfurt am Main, Germany, Jens.Fiebig@em.uni-frankfurt.de*

[5]*National and Kapodistrian University of Athens, Department of Geology and Geoenvironment, Panepistimioupolis, Ano Ilissia, 15784, Athens, Greece, ckiriako@geo.uoa.gr*

Abstract

Greece has a very complex geodynamic setting deriving from a long and complicated geological history being characterized by intense seismic activity and enhanced geothermal gradient. This activity, with the contribution of an active volcanic arc, favours the existence of many gas manifestations. Depending on the prevailing gas species, the latter can be subdivided in three main groups: CO_2-, N_2- and CH_4-dominated. In the present work, we focus on methane and light hydrocarbons (C_2-C_6) to define their origin. CH_4 concentrations (<2 to 915,200 μmol/mol) and isotopic ratios ($\delta^{13}C$ -79.8 to +16.9 ‰, δD -298 to +264‰) cover a wide range of values indicating different origins and/or secondary post-genetic processes. Samples from gas discharged along the Ionian coast and in northern Aegean Sea have a prevailing microbial origin. Cold and thermal gas manifestations of central and northern Greece display a prevalent thermogenic origin. Methane in gases released along the active volcanic arc is prevailingly abiogenic, although thermogenic contributions cannot be excluded. Gases collected in the geothermal areas of Sperchios basin and northern Euboea are likely affected by strong secondary oxidation processes, as suggested by their highly positive C and H isotopic values (up to +16.9‰ and +264‰ respectively) and low $C_1/(C_{2+}C_3)$ ratios.

Keywords: *Hellenic territory, hydrothermal gases, cold gas emissions, origin of hydrocarbon gases.*

Περίληψη

Το σύνθετο γεωδυναμικό καθεστώς της Ελλάδας πηγάζει από την πολύπλοκη γεωλογική της ιστορία, η οποία χαρακτηρίζεται από έντονη σεισμική δραστηριότητα και ενισχυμένη γεωθερμική βαθμίδα. Αυτή η δραστηριότητα σε συνδυασμό με το ενεργό

ηφαιστειακό τόξο, ευνοεί την ύπαρξη πολλών εκπομπών αερίων, με αποτέλεσμα την κατηγοριοποίηση σε CO_2-, N_2- και CH_4- αέρια, ανάλογα με το επικρατών είδος. Η παρούσα εργασία επικεντρώνεται στο μεθάνιο και τους ελαφρούς υδρογονάνθρακες (C_2-C_6) με σκοπό τον προσδιορισμό της προέλευσή τους. Οι συγκεντρώσεις του CH_4 (<2 έως 915,200 μmol/mol) και η ισοτοπική του αναλογία ($\delta^{13}C$ -79.8 έως +16.9 ‰, δD -298 έως +264‰) καλύπτουν ένα ευρύ φάσμα τιμών, που υποδεικνύει διαφορετικές προελεύσεις ή/και δευτερογενείς μεταγενετικές διεργασίες. Δείγματα εκφορτισμένων αερίων που συλλέχθηκαν στις ακτές του Ιονίου Πελάγους και στο Βόρειο Αιγαίο, δείχνουν να επικρατεί η μικροβιακή προέλευση ενώ στις ψυχρές και θερμές εκπομπές αερίων της κεντρικής και βόρειας Ελλάδας η θερμογενετική. Το μεθάνιο που απελευθερώνεται από τα αέρια του ηφαιστειακού τόξου είναι κυρίως αβιογενές, αν και οι θερμογενετικές συνθήκες δεν μπορούν να εξαιρεθούν. Τα συλλεγμένα αέρια των περιοχών της κεντρικής Ελλάδας (λεκάνη Σπερχειού και βόρεια Εύβοια) πιθανά επηρεάστηκαν από έντονες δευτερογενετικές οξειδωτικές διεργασίες, όπως φαίνεται από τις υψηλές θετικές ισοτοπικές τιμές των C και H (έως +16.9‰ και +264‰ αντίστοιχα) και από τις χαμηλές αναλογίες των $C_1/(C_{2+}C_3)$.
Λέξεις κλειδιά: *Ελληνική περιοχή, υδροθερμικά αέρια, εκπομπές ψυχρών αερίων, προέλευση υδρογονανθράκων.*

1. Introduction

The Hellenic territory has a complex geodynamic setting deriving from a long and complicated geological history. Due to this specific geological background, conditions for the formation of many thermal springs were favoured (D'Alessandro *et al.*, 2006, 2008, 2010, 2011; Kyriakopoulos *et al.*, 2010). The major geodynamic activity in macroscale gave rise to a geological evolution which is expressed in volcanism, orogenetic processes and active tectonics. Widespread volcanic activity in the Aegean Sea started in the Oligocene and continues to the present. Two major phases took place. The first one was developed in the North Aegean area from the Oligocene to the Middle Miocene and the second started in the Pliocene forming the active South Aegean Volcanic Arc. During the Oligocene – Miocene volcanic phase the volcanic activity occurred in an East to West oriented zone from Thrace to the Central Aegean. Many places of the Aegean region (North Euboea, Tinos, Sikinos, Patmos and Samos Islands) were affected by this activity. Chemical- physical conditions related to the recent volcanism, coupled with the major faults were the fundamental causes for the warming and uplift of deep thermal waters, resulting in this discharge at the surface thermal springs (Fytikas *et al.*, 1984; Pe-Piper *et al.*, 1989).

Geochemical studies based on the isotopic composition of carbon and hydrogen, along with helium isotopic ratios have become a good indicator of the origin of the gas. The isotopic ratio $^{13}C/^{12}C$ of CO_2 expressed in $\delta\ ^{13}C$ (‰), may provide important information about the amount of CO_2 released from the Earth's crust or mantle. Carbon and hydrogen isotopic compositions and $C_1/(C_2+C_3)$ hydrocarbon ratios can characterize the origin of methane. In sedimentary environments, CH_4 is primarily produced by 1) processes related to metabolic and biosynthetic activity of biological organisms (biogenesis), and 2) decomposition of organic matter buried in sediments at T>150 °C (thermogenesis) (Schoell, 1980, 1988; Whiticar *et al.*, 1986; Galimov, 1988; Welhan, 1988; Whiticar and Suess, 1990; Whiticar, 1999). Helium isotopic ratios provide additional information about crustal or mantle origin of the gas.

This study is focusing on methane and light hydrocarbons and is having as an aim the identification and the characterization of methane's origin and the identification of post-genetic processes affecting hydrocarbon gases.

2. Geodynamic setting and volcanism of Greece

The Hellenides are the result of the collision of several microcontinental fragments with the margin of Eurasia through the Cretaceous and Paleogene (van Hinsbergen *et al.*, 2005). After the collision, the Hellenides have been characterized by widespread extension, particularly since the Miocene, as a result of subduction rollback from the oceanic crust of the African plate. The modern fault pattern is a result of the westward and southwestward motion of the Aegean-Anatolian microplate with respect to the Eurasian plate.

The Paleogene Hellenide orogeny of Greece and its eastward continuation into western Turkey resulted from the collision of the Apulian microcontinental fragment in the Eocene to Oligocene with the Pelagonian, Rhodope, and Serbo-Macedonian fragments, which had previously accreted to the southern margin of Eurasia in the Cretaceous. Subsequent extension in the Aegean was rapid, likely due to subduction rollback over residual oceanic crust of the African plate, whereas Anatolia had been bounded by African continental crust south of Cyprus since the Early Miocene. This regional extension and the thermal effects of asthenospheric upwelling, related to changes in the geometry of subducting slabs, have been interpreted as causing magma genesis principally within the lithospheric mantle (Pe- Piper and Piper, 2002).

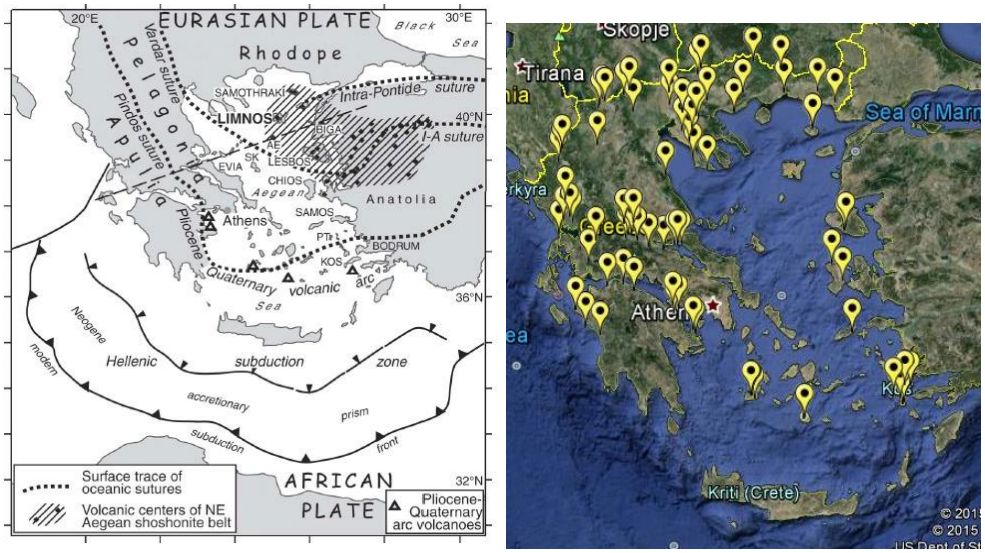

Figure 1 – a) Map that shows the plate boundaries and the geodynamic pattern of Greece and the Ionian and Aegean Seas (Pe-Piper, 2006). This map was the criteria used for the categorization of the samples collected in the Hellenic territory as seen in Figure b.

At the south Aegean Volcanic Arc the activity started during the Upper Pliocene (Fytikas *et al.*, 1986) and is currently active at solfataric stage. The calc-alkaline volcanic activity of Southern Aegean region developed in various volcanic centers from Sousaki to Nisyros through Methana-Poros, Milos and Santorini. The volcanic products are dominated by lava domes and lava flows with associated minor pyroclastic breccias and felsic ignimbritic covers (Mitropoulos *et al.*, 1987). The final activity of this orogenic cycle is characterized by the presence of K-rich shoshonites and latites with ultrapotassic character.

On the basis of the previous description of the Hellenic geodynamic setting, the whole territory has been subdivided into 5 homogeneous areas (see map of fig. 1a): Apulia, Pelagonia, Rhodope, North Aegean and South Aegean active volcanic arc. The results of the present study will be discussed in the light of such subdivision.

3. Fluid emissions in Greece

Greece, like many other Mediterranean countries (e.g. Italy and Turkey) has a significant geothermal potential, since most areas of the country are geodynamically active as a result of the movement of the African plate towards the Eurasian plate. Heat flow higher than 80 m/Wm^2 characterize several regions, mainly in the internal Hellenides and the Aegean Sea. Such an intense volcanotectonic activity caused the geological conditions for accumulation of heat energy, as testified by the occurrence of low-medium and high enthalpy hydrothermal systems. The most important high-enthalpy geothermal fields are located in the Southern Aegean, along the active volcanic arc (Milos, Nisyros), whereas medium and low enthalpy reservoirs are mostly associated with grabens (Central Aegean) and post-orogenic sedimentary molassic basins (southern boundaries of the Rhodope and Servo-Macedonian Massifs) (Fytikas *et al.*, 2005).

4. Materials and Methods

Bubbling gases were sampled using an inverted funnel positioned above the bubbles, whereas soil gases were collected by inserting a pipe in the soil and driving the gas by a syringe and a 3-way valve. Gases were collected in 12 ml Exetainer® vials (only for hydrocarbons) and glass sampling bottles equipped with two vacuum stopcocks.

In the laboratory, samples were analyses for He, H_2, O_2, N_2, CH_4 and CO_2 by gas-chromatography (Perkin Elmer Clarus500 equipped with a double Carboxen 1000 columns, TCD-FID detectors) using argon as the carrier gas. Analytical uncertainties were ± 5%. Hydrocarbon analysis, were performed with a Shimadzu 14a gas-chromatograph equipped with a Flame Ionization Detector (FID) using helium as the carrier gas. The analytical error was ≤5%. The $^{13}C/^{12}C$ ratios of CO_2 (expressed as $\delta^{13}C$-CO_2‰ V-PDB) were measured with a Finnigan Delta S mass spectrometer after purification of the gas mixture by standard procedures using cryogenic traps (precisions ±0.1‰). Carbon and hydrogen isotopic compositions of CH_4 were measured using a Thermo TRACE GC and a Thermo GC/C III interfaced to a Delta Plus XP gas source mass spectrometer. $^{13}C/^{12}C$ ratios are reported here as $\delta\,^{13}C$ values (±0.2 ‰) with respect to the V-PDB standard. H/D ratios are reported here as δD values (±2 ‰) with respect to the V-SMOW standard.

5. Results and discussion

The gas samples collected in the Hellenic territory (Fig 1b) display a large variability in the chemical composition. Helium ranges from 0.10 to 3372 ppm and shows a fair positive correlation with N_2. Almost 112 samples out of 399 have detectable H_2 (>2 ppm) concentrations ranging from 3.50 up to 149,100 ppm. O_2 concentrations range from below the detection limit (<200 ppm - 45 samples) up to 192,700. The concentrations of N_2, CH_4 and CO_2 range from 600 up to 995,100 ppm, from less than 2 up to 915,200 ppm and from less than 50 up to 999,900 ppm. The last three species represent always the main gas component and all the samples can be subdivided in N_2-, CH_4- or CO_2- dominated gases.

The O_2- N_2- CO_2 triangular graph (Fig. 2a) reveals that only few samples plot close to the point representing atmospheric air excluding important contaminations for most of the samples. The majority of the gases display N_2/O_2 ratios less than air or Air Saturated Waters (ASW), which is indicating that the atmospheric component of meteoric water has been modified by redox reactions that took place either in the subsoil or in the aquifers. Furthermore, most of the samples show a strong contribution of helium deriving either from a crustal or mantle sources.

As shown by the CH_4- N_2- CO_2 triangular plot (Fig 2b), only few samples, mostly from Apulia, display a CH_4- dominated composition. In general, the collected samples can also be subdivided in 3 groups:

a) CO_2- dominated, consisted of the samples collected in the Volcanic Arc and a part of Pelagonia and Aegean,

b) N_2- dominated, consisted of a part of the samples collected in Pelagonia and Rhodope

c) CH_4- dominated, consisted of the samples mainly collected in Apulia (Fig 2a, 2b).

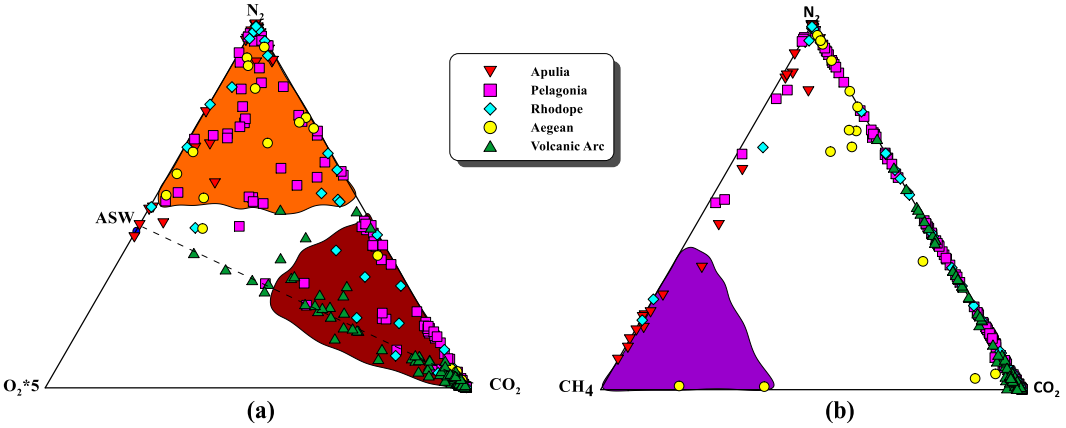

Figure 2 - Ternary plots of a) O_2- N_2- CO_2, b) CH_4- N_2- CO_2 in which are plotted the samples divided by geographic areas. The polygons represent the dominant gas: CO_2- dominated, red, N_2- dominated, orange, CH_4- dominated, purple.

He isotopic values, expressed as $^3He/^4He$ ratio, normalized to the atmospheric one ($Ra=1.386*10^{-6}$), range from 0.03 to 6.70 R/Ra. Measured values corrected for the atmospheric contamination of the sample on the base of its $^4He/^{20}Ne$ ratio (Sano and Wakita, 1985) display a similar range (Rc/Ra 0.02 – 6.73). Such a wide range is indicative of different sources for He in the studied gases.

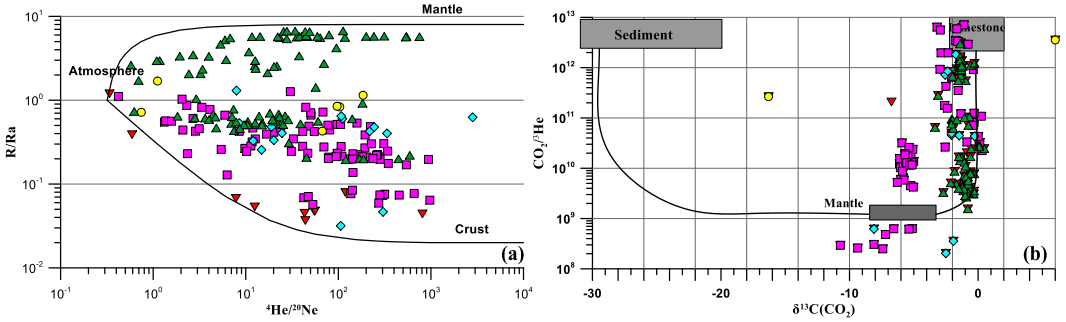

Figure 3 - a) Binary plot of R/Ra vs. $^4He/^{20}Ne$ of the natural gas manifestations of Greece. Atmosphere, Mantle and Crust represent three possible end-members: atmospheric air, MORB-like mantle and crust. The mixing lines between Atmosphere and Mantle and between Atmosphere and Crust are also plotted, b) Binary plot of $CO_2/^3He$ vs. $\delta^{13}C(CO_2)$ of natural gas manifestations of Greece. The end-member compositions for Sediments, MORB-like Mantle and Limestones are $\delta^{13}C(CO_2)$ = -30‰, -5‰ and 0‰ and $CO_2/^3He = 1*10^{13}$, $2*10^9$ and $1*10^{13}$, respectively (Sano and Marty, 1995).

On Fig. 3a, the measured values of R/Ra are plotted against the $^4He/^{20}Ne$ ratio. Only few samples plot close to the atmospheric end member, confirming that the atmospheric contribution is negligible. The majority of the samples collected in the Volcanic Arc display high contributions of mantle component, as shown by the highest Rc/Ra ratios (up to 6.73) found at the islands of Kos and Nisyros. Samples collected in Apulia show a prevailingly crustal component with Rc/Ra ratios <0.1. The

remaining samples (Pelagonia, Rhodope, Aegean) show a mixed mantle-crustal composition with Rc/Ra ratios up to 2.15.

The carbon isotopic composition of CO_2 of the free gas samples displays a wide range from -16.5 to +6.0‰ (vs. V-PDB) although the majority falls in a narrower range (from -6.0 to +0.0 $\delta^{13}C(CO_2)$ ‰). By taking into account the $\delta^{13}C(CO_2)$ values and the $CO_2/^3He$ ratios (Fig. 3b), it is noticed that the majority of the collected samples is a mixture of mantle and limestone end-members, whereas the contribution of the sedimentary organic member to the fluids deriving from the descending slab is considered to be insignificant. However, a small contribution from organic sediments can be detected in the CO_2- dominated gases of Apulia deriving from crustal sources. On the contrary, CH_4 and N_2- dominated gases display sometimes a strong organic contribution and low $CO_2/^3He$ ratios (samples collected in Pelagonia and Rhodope) probably due to CO_2- depleting processes (CO_2 dissolution in groundwater, carbonate precipitation, CO_2 reduction, etc.).

Thermogenic CH4 has been reported to exhibit δ13C(CH4) values ranging from -50 up to -30‰ V-PDB, whereas microbial CH4 usually has δ13C(CH4) values <-50‰ V-PDB (e.g., Whiticar, 1999; McCollom and Seewald, 2007). However, these limit values may vary depending on processes occurring during gas migration, such as isotopic fractionation by diffusion (Prinzhofer and Battani, 2003), secondary methanogenesis and anaerobic biodegradation (Dimitrakopoulos and Muehlenbachs, 1987; Pallasser, 2000; Etiope *et al*., 2009). Gases produced by the decay of organic matter at T > 150 °C (thermogenic gases) are commonly characterized by CH4/(C2H6+C3H8) concentration ratios (the so called "Bernard parameter") <100, whereas higher ratios (>1000) are expected when hydrocarbon production derives exclusively from microbial activity (Whiticar and Suess, 1990; Jenden et al., 1993). As previously pointed out, concentrations of CH4 as well as its isotopic composition cover a wide range (<2 to 915.200 μmol/mol and δ13C from -79.8 ‰ to +16.9 ‰, δD from -298 ‰ to +264 ‰ respectively) indicating different origins and/or secondary post genetic processes. On Fig. 4a and 4b, it is shown that samples from gas discharge located in Apulia and North Aegean likely have a microbial origin, as suggested by the low δ13C(CH4) values (down to -79.8 ‰ for Apulia and down to -45.9 ‰ for Aegean) and high C1/(C2+C3) ratios (highest values reaching up to 9000). The cold and thermal manifestations of Rhodope and a part of Apulia and Pelagonia seem to display a thermogenic origin. CH4 released along the Volcanic Arc, seems to be prevailingly abiogenic (Fiebig *et al*., 2009; Tassi *et al*., 2012, 2012) according to the high δ13C(CH4) values (> -25‰) and high C1/(C2+C3) ratios (up to 16,000), although thermogenic contribution cannot be excluded. Some of the remaining gases of Apulia and Pelagonia are affected by secondary oxidation processes, as highlighted by their high isotopic values of H and C (up to +16.9 ‰ and +264 ‰ respectively) and their low C1/(C2+C3) ratios. Incubation experiments on waters and sediments of some of these springs, showed that the oxidation of CH4 is generally microbially driven.

As shown in Fig. 5, the CH4/C2H6 concentration ratios of the studied gases vary by more than three orders of magnitude, whereas the ratios between the light hydrocarbons (C2H6, C3H8 and C6H6) vary by less than two orders of magnitude. As far as this evidence is concerned, the redox processes between CO2 (CO) and CH4, which likely controls the CH4 abundance in volcanic-hydrothermal fluids, does not affect the higher alkanes whose origin could be entirely related to thermal degradation of organic matter. At the same time, the residual methane seems to retain its primary carbon isotopic composition due to the possible low degree of polymerization. This could also explain why there is no significant correlation between the carbon isotopic composition of methane and the CH4/(C2H6+C3H8) values for gases from volcanic environments (Fig. 5a and 5b), whose δ13C (CH4) seems to be controlled by δ13C (CO2) and temperature. In addition, methane polymerization may explain why volcanic-hydrothermal gas emissions exhibit a spread to much lower CH4/(C2H6+C3H8) concentration ratios than the geothermal discharges.

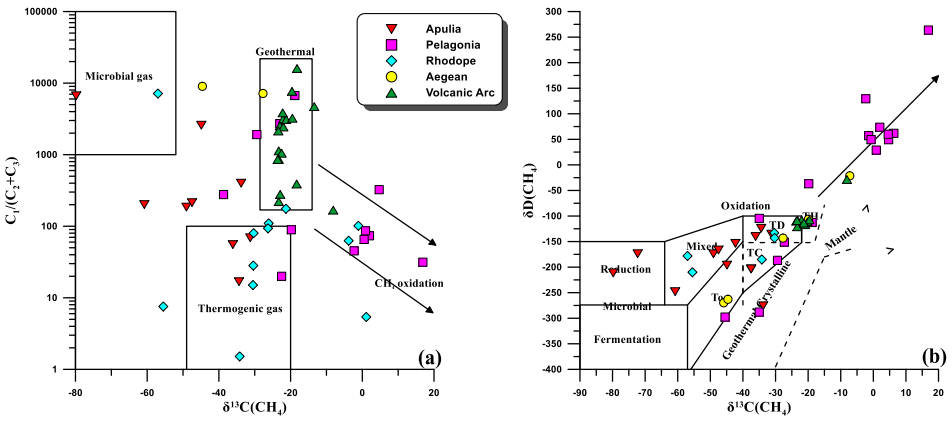

Figure 4 – a) $C_1/(C_2+C_3)$ vs $\delta^{13}C(CH_4)$ and b) $\delta D(CH_4)$ vs $\delta^{13}C(CH_4)$ diagrams for the Hellenic gas discharges.

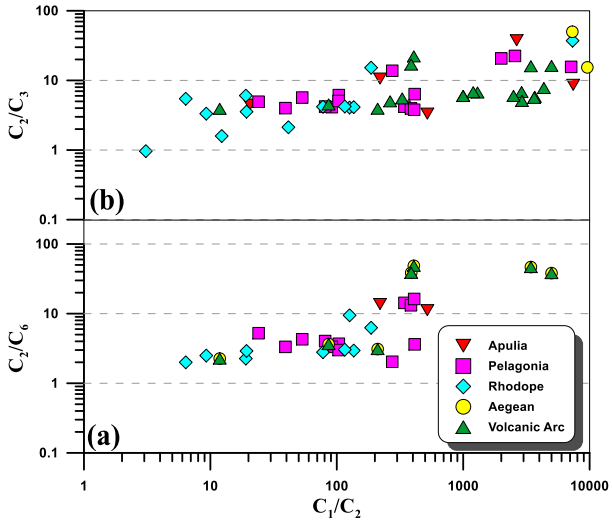

Figure 5 – a) CH_4/C_2H_6 vs. C_2H_6/C_3H_8 and b) CH_4/C_2H_6 vs. C_2H_6/C_6H_6 binary plots for the Greek gas discharges.

6. Conclusions

The chemical and isotopic compositions of CH_4 indicate that this gas has different primary sources and is significantly affected by secondary post-generic processes (oxidation). The preliminary results of this study show that the Hellenic territory can be subdivided in 4 groups according to the gas compounds dominating the chemical composition of gas emissions (Fig. 6) as follows:

a) along the Volcanic arc, gases are CO_2-dominated, with CH_4 showing a hydrothermal origin (abiotic and / or thermogenic) and a prevailing mantle component for He and CO_2.

b) the Apulia region shows N_2- CH_4- dominated gases with a biogenic origin for CH_4 and a dominant crustal component for He.

c) Pelagonia, Rhodope and Aegean regions show variable composition (CO_2, CH_4 and N_2-dominated) with a mixed crustal component for He, whereas CH_4 is mainly thermogenic.

d) in the Sperchios Basin and northern Evia area (Pelagonia), the CH_4 is strongly affected by oxidation processes probably microbial driven.

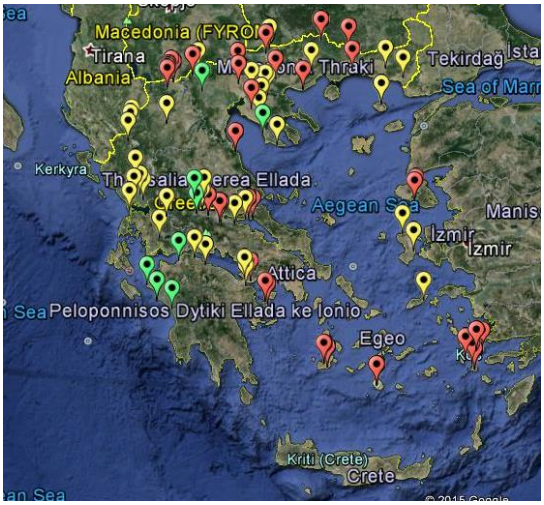

Figure 6 – Map of the Hellenic territory with the dominated gases in the sampled regions, with red color are shown the CO2 dominated sampling points, with yellow the N2 and with green the CH4.

7. References

Andritsos, N., Dalampakis, P., Karydakis, G., Kolios, N. and Fytikas, M., 2007. Update and characteristics of low-enthalpy geothermal applications in Greece, Proceedings, European Geothermal Congress EGC 2007, May 30 - June 1, 2007, Unterhaching, Germany.

D'Alessandro, W., Brusca, L., Kyriakopoulos, K., Rotolo, S., Michas, G., Minio, M. and Papadakis, G., 2006. Diffuse and focussed carbon dioxide and methane emissions from the Sousaki geothermal system, Greece, *Geophys. Res. Lett*., 33, L05307, doi: 10.1029/2006GL025777.

D'Alessandro, W., Brusca, L., Kyriakopoulos, K., Michas, G. and Papadakis, G., 2008. Methana, the westernmost active volcanic system of the south Aegean arc (Greece): insight from fluids geochemistry, *J. Volcanol. Geotherm. Res*., 178, 818-828.

D'Alessandro, W., Bellomo, S., Brusca, L., Fiebig, J., Longo, M., Martelli, M., Pecoraino, G. and Salerno, F., 2009. Hydrothermal methane fluxes from the soil at Pantelleria Island (Italy), *J. Volcanol. Geotherm. Res*., 187, 147-157.

D'Alessandro, W., Brusca, L., Martelli, M., Rizzo, A. and Kyriakopoulos, K., 2010. Geochemical characterization of natural gas manifestations in Greece, Proceedings of the 12th International Congress of the Geological Society of Greece, Patras, May 2010, *Bulletin of the Geological Society of Greece*, 43(5), 2327–2337.

D'Alessandro, W., Bellomo, S., Brusca, L., Karakazanis, S., Kyriakopoulos, K. and Liotta, M., 2011. The impact on water quality of the high carbon dioxide contents of the groundwater in the area of Florina (N. Greece). *In*: Lambrakis, N., Stournaras, G. and Katsanou, K., *eds*., Advances in the research of aquatic environment, Springer, Berlin, 2, 135-143.

D'Alessandro, W., Brusca, L., Kyriakopoulos, K., Bellomo, S. and Calabrese, S., 2014. A geochemical traverse along the "Sperchios Basin - Evoikos Gulf" graben (Central Greece): Origin and evolution of the emitted fluids, *Marine and Petroleum Geology*, 55, 295-308, doi: 10.1016/j.marpetgeo.2013.12.011.

Dimitrakopoulos, R. and Muehlenbachs, K., 1987. Biodegradation of petroleum as a source of 13C enriched carbon dioxide in the formation of carbonate cements, *Chemical Geology*, 65, 283-291.

Etiope, G., Feyzullayev, A., Milkov, A.V., Waseda, A., Mizobe, K. and Sun, C.H., 2009. Evidence of subsurface anaerobic biodegradation of hydrocarbons and potential secondary methanogenesis in terrestrial mud volcanoes, *Marine and Petroleum Geology*, 26, 1692-1703.

Evans, W.C., White, L.D. and Rapp, J.B., 1998, Geochemistry of some gases in hydrothermal fluids from the southern Juan de Fuca ridge, *Journal of Geophysical Research*, 15, 305-313.

Fiebig, J., Chiodini, G., Caliro, S., Rizzo, A., Spandenberg, J. and Hunziker, J.C., 2004. Chemical and isotopic equilibrium between CO2 and CH4 in fumarolic gas discharges: generation of CH4 in arc magmatic-hydrothermal systems, *Geochimica et Cosmochimica Acta*, 68, 2321-2334.

Fiebig, J., Woodland, AB., D'Alessandro, W. and Puttmann, W., 2009. Excess methane in hydrothermal emissions is abiogenic, *Geology*, 37(6), 495-8.

Fytikas, M., Innocenti, F., Manetti, P., Mazzuoli, R., Peccerillo, A. and Villari, L., 1984. Tertiary to Quarternary evolution of volcanism in the Aegean region, *Geological Society of London, Special Publications*, 17, 687-699.

Fytikas, M., Innocenti, F., Kolios, N., Manetti, P. and Mazzuoli, R., 1986. The Plio- Quaternary volcanism of the Saronikos area (western part of the active Aegean volcanic arc), *Annales Geologique des Pays Helleniques*, 33, 23-45.

Fytikas, M., Andritsos, N., Dalabakis, P. and Kolios, N., 2005. Greek Geothermal Update 2000-2004, Proceedings of the World Geothermal Congress-2005, 24-29 April 2005, Antalya-Turkey (invited paper).

Galimov, E.M., 1988. Sources and mechanisms of formation of gaseous hydrocarbons in sedimentary rocks, *Chemical Geology*, 71, 77-95.

Jenden, P.D., Hilton, D.R., Kaplan, I.R. and Craig, H., 1993. Abiogenic hydrocarbons and mantle helium in oil and gas fields. *In*: Howell, D.G., *ed*., The Future of Energy Gases: US Geological Survey Professional Paper, 1570, 31–56.

Kyriakopoulos, K, 2010. Natural degassing of carbon dioxide and hydrogen sulphide and its environmental impact at Milos island, Greece. In: Proceedings of 12th international congress, Patras, May 2010, *Bull Geol Soc Greece*.

McCollom, T.M. and Seewald, J.S., 2007. Abiotic synthesis of organic compounds in deep sea hydrothermal environments, *Chemical Reviews*, 107, 382-401.

Mitropoulos, P., Tarney, J., Saunders, D. and Marsh, N., 1987. Petrogenesis of Cenozoic volcanic rocks from the Aegean Island Arc, *Journ. Volcanology and Geothermal Research*, 32, 177-193.

Pallasser, R.J., 2000. Recognising biodegradation in gas/oil accumulations through the δ13C compositions of gas components, *Organic Geochemistry*, 31, 1363-1373.

Pe-Piper, G. and Piper, D.J.W., 2006. Unique features of the Cenozoic igneous rocks of Greece. In: Dilek, Y. and Pavlides, S., eds., Postcollisional tectonics and magmatism in the Mediterranean region and Asia, *Geological Society of America, Special Paper*, 409, 259-282.

Prinzhofer, A.A. and Battani, A., 2003. Gas isotopes tracing: an important tool for hydrocarbon exploration, *Oil and Gas Science and Technology*, 58(2), 229-311.

Sano, Y. and Marty, B., 1995. Origin of carbon in fumarolic gas from island arcs, *Chemical Geology*, 119, 265-274.

Sano, Y. and Wakita, H., 1985. Geographical distribution of 3He/4He in Japan: implications for arc tectonics and incipient magmatism, *Journal of Geophysical Research*, 90, 8729-8741.

Schoell, M., 1980. The hydrogen and carbon isotopic composition of methane from natural gases of various origins, *Geochimica et Cosmochimica Acta*, 44, 649-661.

Schoell, M., 1988. Multiple origins of methane in the Earth, *Chemical Geology*, 71, 1-10.

Tassi, F., Fiebig, J., Vaselli, O. and Nocentini, M., 2012. Origins of methane discharging from volcanic-hydrothermal, geothermal and cold emissions in Italy, *Chem. Geol*., 310-311, 36-48. http://dx.doi.org/10.1016/j.chemgeo.2012.03.018.

Tassi, F., Bonini, M., Montegrossi, G., Capecchiacci, F., Capaccioni, B. and Vaselli, O., 2012. Origin of light hydrocarbons in gases from mud volcanoes and CH4-rich emissions, *Chem. Geol*., 294-295, 113-126.

van Hinsbergen, D.J.J., Langereis, C.G. and Meulenkamp, J.E., 2005. Revision of the timing, magnitude and distribution of Neogene rotations in the western Aegean region, *Tectonophysics*, 396, 1-34, doi: 10.1016/j.tecto.2004.10.001.

Vaselli, O., Tassi, F., Montegrossi, G., Capaccioni, B. and Giannini, L., 2006. Sampling and analysis of volcanic gases, *Acta Volcanol*., 18, 65-76.

Whiticar, M.J., Faber, E. and Schoell, M., 1986. Biogenic methane formation in marine and freshwater environments: CO2 reduction vs. acetate fermentation - isotopic evidence, *Geochimica et Cosmochimica Acta*, 50, 693-709.

Whiticar, M.J. and Suess, E., 1990. Hydrothermal hydrocarbon gases in the sediments of the King-George Basin, Bransfield Strait, Antarctica, *Applied Geochemistry*, 5, 135-147.

Whiticar, M.J., 1999. Carbon and hydrogen isotope systematics of bacterial formation and oxidation of methane, *Chemical Geology*, 161, 291-314.

Welhan, J.A., 1988. Origins of methane in hydrothermal systems, Chemical Geology, 71, 183-198.

Zhang, J., Quay, P.D. and Wilbur, D.O., 1995. Carbon isotope fractionation during gas-water exchange and dissolution of CO2, *Geochimica et Cosmochimica Acta*, 59, 107-114.

Δελτίο της Ελληνικής Γεωλογικής Εταιρίας, τόμος L., σελ. 1809-1819
Πρακτικά 14ου Διεθνούς Συνεδρίου, Θεσσαλονίκη, Μάιος 2016

Bulletin of the Geological Society of Greece, vol. L, p. 1809-1819
Proceedings of the 14th International Congress, Thessaloniki, May 2016

APPLICATIONS OF THE HELLENIC NATURAL ZEOLITE (HENAZE) AND SPECIFICATIONS OF ZEOLITIC TUFFS

Filippidis A.

Aristotle University of Thessaloniki, Faculty of Sciences, School of Geology, Department of Mineralogy-Petrology-Economic Geology, 54124 Thessaloniki, Greece, anestis@geo.auth.gr

Abstract

The Hellenic Natural Zeolite (HENAZE) is free of fibres and contains 89 wt% clinoptilolite, 3 wt% mica + clay minerals, 3 wt% quartz, 2 wt% cristobalie ± tridymite and 3 wt% feldspars. HENAZE do not meet the requirements of the EU Regulation No 651/2013, and thus cannot be used as feed additive for all animal species and consequently as nutrition supplement, since it contains 3 wt% quartz. HENAZE is suitable for use as soil conditioner, since the concentration of trace elements are lower than the maximum allowable concentrations in agricultural soils (EU Directive 278/1986). HENAZE as soil conditioner: a) improved the pH of acid soils by 47-55%, b) reduced the leaching of metals by 33-71% from contaminated soils, c) reduced the Hg concentration by 47-78% in shoots and roots of plants, d) increased the production of agricultural products by 17-95%, e) decreased the plant-losses in new vineyard by 12% and f) improved the quality of tomato by 4-46%. The HENAZE neutralized sewage-sludge (producing zeo-sewage-sludge), industrial-sludge (producing zeo-sludge), battery solid waste and mine solid wastes (mine-tailings). The zeo-sewage-sludge and zeo-sludge are odorless, cohesive and suitable for safe deposition. The treatment of sewage-sludge and industrial-sludge with the HENAZE, reduced the leaching of metals by 91-100% and of NO_3^- by 81-82%. Depending on the trace element contents, the zeo-sewage-sludge can be used as soil conditioner. HENAZE sorbed-removed 37-92% of metals, radionuclides and cyanobacteria from their solutions and waters. The treatment of wastewaters (urban, dyeing-industry, industrial area and tanning-work) with HENAZE, improved the quality characteristics by 48-99%. The HENAZE reduced the NO_3^- load by 54-94% in groundwater, nitrate-solutions, industrial and urban wastewaters. Considering, the European, Global and Greek legislation, the mineralogical, chemical, morphological and radiological characteristics, as well as the leachability and bioavailability of chemical elements, the specifications for the different applications-uses of the zeolitic tuffs are defined.

Keywords: *Clinoptilolite, feed additive, nutrition supplement, soil conditioner.*

Περίληψη

Ο Ελληνικός Φυσικός Ζεόλιθος (ΕΛΦΥΖΕ) είναι ελεύθερος από ίνες και περιέχει 89% κ.β. κλινοπτιλόλιθο, 3% κ.β. μαρμαρυγία + αργιλικά ορυκτά, 3% κ.β. χαλαζία, 2% κ.β. χριστοβαλίτη ± τριδυμίτη και 3% κ.β. αστρίους. Ο ΕΛΦΥΖΕ δεν πληρεί τις απαιτήσεις του κανονισμού αριθ 651/2013 της ΕΕ, και ως εκ τούτου δεν μπορεί να χρησιμοποιηθεί ως πρόσθετη ύλη ζωοτροφών για όλα τα ζωικά είδη, και κατά συνέπεια, ως συμπλήρωμα διατροφής, δεδομένου ότι περιέχει 3% κ.β. χαλαζία. Ο ΕΛΦΥΖΕ είναι κατάλληλο για χρήση ως εδαφο-βελτιωτικό, δεδομένου ότι οι συγκεντρώσεις των ιχνοστοιχείων είναι χαμηλότερες από τις μέγιστες επιτρεπόμενες συγκεντρώσεις στα

αγροτικά εδάφη (οδηγία ΕΕ 278/1986). Ο ΕΛΦΥΖΕ ως εδαφοβελτιωτικό: α) βελτίωσε το pH των όξινων εδαφών κατά 47-55%, β) μείωσε την έκπλυση μετάλλων κατά 33-71% από τα ρυπασμένα εδάφη, γ) μείωσε τη συγκέντρωση Hg κατά 47-78 % στους βλαστούς και ρίζες φυτών, δ) αύξησε την παραγωγή γεωργικών προϊόντων κατά 17-95%, ε) μείωσε τις απώλειες φυτών σε νέο αμπελώνα κατά 12% και στ) βελτίωσε την ποιότητα της τομάτας κατά 4-46%. Ο ΕΛΦΥΖΕ αδρανοποιεί τη λυματολάσπη (παράγοντας τη ζεο-λυματολάσπη), τη βιομηχανική-λάσπη (παράγοντας τη ζεο-λάσπη), τα στερεά απόβλητα μπαταριών και μεταλλείων (τέλματα). Η ζεο-λυματολάσπη και η ζεο-λάσπη είναι άοσμες, συνεκτικές και κατάλληλες για ασφαλή απόθεση. Η κατεργασία της λυματολάσπης και της βιομηχανικής λάσπης με τον ΕΛΦΥΖΕ, μείωσε την έκπλυση μετάλλων κατά 91-100% και των NO_3^- κατά 81-82%. Ανάλογα με την περιεκτικότητα των ιχνοστοιχείων, η ζεο-λυματολάσπη μπορεί να χρησιμοποιηθεί ως εδαφο-βελτιωτικό. Ο ΕΛΦΥΖΕ δέσμευσε-απομάκρυνε 37-92% των ιχνοστοιχείων, ραδιονουκλιδίων και κυανοβακτηρίων από τα διαλύματά τους και τα ύδατα. Η κατεργασία υγρών αποβλήτων (αστικών, βαφείων, βιομηχανικών ζωνών και βυρσοδεψείων) με ΕΛΦΥΖΕ, βελτίωσε τα ποιοτικά χαρακτηριστικά κατά 48-99%. Ο ΕΛΦΥΖΕ μείωσε το φορτίο των NO_3^- κατά 54-94% σε υπόγειο νερό, διαλύματα, βιομηχανικά και αστικά υγρά απόβλητα. Λαμβάνοντας υπόψη, την ευρωπαϊκή, παγκόσμια και ελληνική νομοθεσία, τα ορυκτολογικά, χημικά, μορφολογικά και ραδιολογικά χαρακτηριστικά, καθώς και την εκπλυσιμότητα και βιοδιαθεσιμότητα χημικών στοιχείων, καθορίζονται οι προδιαγραφές για τις διάφορες εφαρμογές-χρήσεις των ζεολιθικών τόφφων.
Λέξεις κλειδιά: *Κλινοπτιλόλιθος, πρόσθετο ζωοτροφής, συμπλήρωμα διατροφής, εδαφοβελτιωτικό.*

1. Introduction

The Zeolitic volcaniclastic rock deposit corresponds to a rock which contains high amounts of one or more from the different (>65) phases of zeolites. The zeolite with the numerous applications is the HEU-type zeolite (clinoptilolite-heulandite) that shows tabular crystals and contains micro/nano-pores in a framework of channels with 10- and 8-member rings, in dimensions of 7.5x3.1 Å, 4.6x3.6 Å and 4.7x2.8 Å. Only clinoptilolite of sedimentary origin with ≥80 wt% clinoptilolite, ≤20 wt% clay minerals, free of fibres and quartz, can be used as feed additive for all animal species (EU Regulation No 651/2013) and consequently as nutrition supplement. In humans and animals, inhaled or injected or swallowed, fibrous zeolites (erionite, mordenite, etc), as well as the SiO_2 minerals (quartz, cristobalite, tridymite), are toxic, carcinogenic and highly pathogenic (e.g., Davis, 1993; Driscoll, 1993; Saffiotti *et al*., 1993). The Maximum Allowable Concentrations (MAC) of the trace elements in soils, are specified as limit values for concentrations of heavy metals in soil, in the ANNEX IA of the EU Directive 278/1986.

In the Ntrista stream location (concession of GEO-VET N. Alexandridis & Co O.E.) of Petrota village has been identified a clinoptilolite deposit, specific layers of zeolitic tuffs (Filippidis and Kantiranis, 2002; Filippidis, 2005), named the Hellenic Natural Zeolite (HENAZE) (e.g., Filippidis *et al*., 2007, 2008a,b,d-g, 2009a,b, 2010a,b, 2011a-c, 2014, 2015c; Filippidis, 2010a,b; Vogiatzis, *et al*. 2012). The aim of the present study is to investigate the quality characteristics and applications of the HENAZE, to evaluate its potential use as feed additive (in accordance with the EU Regulation No 651/2013), as nutrition supplement and as soil conditioner in agriculture (in accordance with the EU Directive 278/1986) and define the specifications of the zeolitic tuffs for the different uses.

2. Materials, Methods and Quality characteristics

The Hellenic Natural Zeolite (HENAZE) samples was supplied by GEO-VET N. Alexandridis & Co O.E. Different granulates (8-4, 4-1.5, <1.5, <0.5 mm) of the HENAZE were used in different

applications. The petrographic investigation of the HENAZE was performed on thin and polished thin sections. The combined methods of SEM-EDS (microanalyses), thermal treatment at 450o C for 8 hours and X-Ray Diffraction (XRD), revealed that the HEU-type zeolite in the HENAZE, in two samples presents characteristics of group I zeolite (clinoptilolite) and in one sample of group II (intermediate heulandite). The morphology and the microanalyses of the minerals were studied by Scanning Electron Microscopy-Energy Dispersive Spectroscopy (SEM-EDS) with Link-AN 10000 EDS system. The microscopic examination of the thin sections revealed a fine-grained vitroclastic texture containing shards (0.1-2.0 mm in size), angular to subangular quartz and feldspars and tabular mica crystals. The lath-tabular shaped crystals of clinoptilolite (~5-50 μm in size) are abundant as interstitial cements and as polycrystallites in the shards. The peripheral zone of the shards is a very thin rim of clay minerals. The chemical formulae of the minerals are: clinoptilolite $Ca_{1.8}K_{1.1}Mg_{0.7}Na_{0.5}Al_{6.4}Si_{29.6}O_{72}.21H_2O$, mica $Mg_{1.4}Fe_{1.1}K_{0.8}Na_{0.1}Mn_{0.1}Ti_{0.3}Al_{1.4}Si_{2.6}O_{10}(OH)_2$, clay mineral $Fe_{1.0}K_{0.9}Mg_{0.4}Ca_{0.2}Al_{2.4}(Al_{0.2}Si_{7.8})O_{20}(OH)_4 \cdot 2.9H_2O$, alkali-feldspar (sanidine) $K_{0.6}Na_{0.4}Al_{1.0}Si_{3.0}O_8$, plagioclase (andesine) $Na_{0.5}Ca_{0.5}Al_{1.4}Si_{2.6}O_8$ and quartz, cristobalite, tridymite SiO_2. Cell parameter refinements were performed with XRD-data, using the 30 strongest and well defined reflections. The cell dimensions of clinoptilolite (monoclinic, C2/m) are: a = 17.663 Å, b = 17.917 Å, c = 7.406 Å, V = 2099.64 Å3 and β = 116o38'.

The mineralogical composition of six samples of HENAZE were determined by the X-Ray Diffraction (XRD) method. The semi-quantitative mineralogical composition was measured, using the intensity (counts) of certain reflections, the density and the mass absorption coefficient of the identified minerals for CuKα radiation, the software MAUD-Material Analysis Using Diffraction with the RIETVELD method. Clay mineralogy was identified from air-dried, glycolated and heat-treated oriented samples. The ammonia ion exchange capacity (sorption ability) was determined according to the Ammonium Acetate Saturation (AMAS) method (Filippidis and Kantiranis, 2007). On average, the HENAZE shows sorption ability of 187 meq/100g and contains 89 wt% clinoptilolite (Table 1).

Table 1 - Mineralogical composition (wt%) of the Hellenic Natural Zeolite (HENAZE).

Samples	**EN 1**	**EN 2**	**EN 3**	**EN 4**	**EN 5**	**EN 6**	**Average (range)**
Clinoptilolite	83	89	89	89	90	91	89 (83-91)
Mica + Clay minerals (smectite, illite, celadonite)	4	4	3	3	2	2	3 (2-4)
Quartz	4	2	3	3	4	3	3 (2-4)
Cristobalite ± tridymite	2	2	1	3	2	2	2 (1-3)
Feldspars (alkali-feldspar + plagioclase)	7	3	4	2	2	2	3 (2-7)
Total	100	100	100	100	100	100	100
Sorption ability (meq/100g)	175	186	187	190	191	191	187 (175-191)

The chemical composition (major and trace elements) of the HENAZE (Tables 2 and 3) was determined by FUS-ICP (Fusion-Inductively Coupled Plasma), FUS-MS (Fusion-Mass Spectrometry), TD-ICP (Total Digestion-Inductively Coupled Plasma), INAA (Instrumental Neutron Activation Analysis) and FA (Fire Assay). The contents of the trace elements Cd, Cr, Cu, Hg, Ni, Pb and Zn are ≤46 ppm, all values are lower than the limit values in soil (EU Directive 278/1986) (Table 2).

The leachability of the main exchangeable cations from the HENAZE is very low: Mg (0%), Ca (0%), K (0.0020%) and Na (0.0467%). The agricultural applications were applied in fields and greenhouses, always compared to a control. The wastewaters were treated in batch-type experiments, under continuous stirring and at the final stage, coagulants were added.

Table 2 - Chemical composition of the Hellenic Natural Zeolite (HENAZE).

HENAZE						Limit Values in Soil*
SiO_2 wt%	66.79	CaO wt%	2.71	Cd	<0.5 ppm	1 – 3 ppm
TiO_2	0.17	Na_2O	1.23	Cr	23 ppm	50 – 150 ppm
Al_2O_3	12.07	K_2O	2.37	Cu	2 ppm	50 – 140 ppm
$Fe_2O_{3\ t}$	1.22	P_2O_5	0.02	Hg	0.006 ppm	1 – 1.5 ppm
MnO	0.03	LOI	12.39	Ni	4 ppm	30 – 75 ppm
MgO	0.92	Total	99.92	Pb	41 ppm	50 – 300 ppm
*) EU Directive 86/278/EEC 1986				Zn	46 ppm	150 – 300 ppm

Table 3 - Trace element contents of the Hellenic Natural Zeolite (HENAZE).

(ppm)	Method	Det. limit	HENAZE	(ppm)	Method	Det. limit	HENAZE
Ag	FUS-MS	0.5	<0.5	Mo	FUS-MS	2	<2
As	INAA	2	4	Nb	FUS-MS	0.2	15.0
Au	INAA	0.005	<0.005	Nd	FUS-MS	0.1	19.9
Ba	FUS-ICP	3	172	Ni	TD-ICP	1	4
Be	FUS-ICP	1	6	Pb	FUS-MS	5	41
Bi	FUS-MS	0.1	0.2	Pr	FUS-MS	0.01	7.08
Br	INAA	1	<1	Rb	FUS-MS	1	150
Cd	TD-ICP	0.5	<0.5	Sb	FUS-MS	0.2	0.2
Ce	FUS-MS	0.1	64.4	Sc	INAA	0.1	3.0
Co	FUS-MS	1	8	Se	INAA	3	<3
Cr	INAA	1	23	Sm	FUS-MS	0.01	3.52
Cs	FUS-MS	0.1	8.9	Sn	FUS-MS	1	4
Cu	TD-ICP	1	2	Sr	FUS-ICP	2	1104
Dy	FUS-MS	0.01	3.44	Ta	FUS-MS	0.01	1.13
Er	FUS-MS	0.01	2.29	Tb	FUS-MS	0.01	0.24
Eu	FUS-MS	0.005	0.294	Th	FUS-MS	0.1	30.5
Ga	FUS-MS	1	14	Tl	FUS-MS	0.05	1.29
Gd	FUS-MS	0.01	3.12	Tm	FUS-MS	0.005	0.367
Ge	FUS-MS	0.5	1.4	U	FUS-MS	0.01	8.56
Hf	FUS-MS	0.1	4.3	V	FUS-ICP	5	17
Hg	FA	0.005	0.006	W	FUS-MS	0.5	3.7
Ho	FUS-MS	0.01	0.72	Y	FUS-MS	0.5	20.4
In	FUS-MS	0.1	<0.1	Yb	FUS-MS	0.01	2.52
Ir	INAA	0.005	<0.005	Zn	TD-ICP	1	46
La	FUS-MS	0.1	37.1	Zr	FUS-ICP	2	137
Lu	FUS-MS	0.002	0.409				

FUS-MS: Fusion Mass Spectrometry, FUS-ICP: Fusion Inductively Coupled Plasma, INAA: Instrumental Neutron Activation Analysis, TD-ICP: Total Digestion ICP, FA: Fire Assay

3. Agricultural, Industrial and Environmental Applications

The Hellenic Natural Zeolite (HENAZE) as soil conditioner (500 kg/acre) increased the initial pH (3.8-4.0) of soil to 5.6-6.0 after 16 days (improvement 47-50%) and to 5.8-6.2 after 5 years (improvement 53-55%). The use of HENAZE (500kg/acre) for the reclamation of contaminated soils reduced the seepage of Cd by 33%, of Cs by 39%, of Pb by 44%, of Zn by 52% and of Ni by 60%, also for the reclamation of mine land reduced the seepage of Cd by 43%, of Pb by 52% and Zn by 71%. The use of HENAZE (600kg/acre) reduced the Hg concentration in the trifolium by 77% in the shoots and 53% in the roots, while in the grass by 78% in the shoots and 47% in the roots. The HENAZE as soil conditioner improves the physicochemical and nutritious abilities of soils, reinforces the root-system of the plants, improves the quality of tomato by 4-46%, decreases the plant-losses in new vineyard by 12% and increases the crops yield of agricultural products on average by 17-95% (Table 4).

Table 4 - Hellenic Natural Zeolite (HENAZE) (200-600 kg/acre) in agricultural soils.

Product (area)	Production increase (%)				
	*	**	***	This study	Average
Barley, Gefyra (Thessaloniki)	-	-	-	95	95
Potato, Gefyra	-	-	-	94	94
Grapes, Ag. Athanasios (Thessaloniki) & Gefyra	73	-	48, 66	25, 65, 99	63 (25-99)
Maize	-	50	-	-	50
Tomato, Aspro (Pella) & Gefyra	48	52	-	96, 39, 50, 11	49 (11-96)
Actinides, Livadochori (Serres)	45	-	-	-	45
Wheat, Gefyra & Livadochori	-	29, 57	-	-	43 (29-57)
Apples, Naousa (Imathia)	-	-	-	33, 37	35 (33-37)
Rice, Chalastra (Thessaloniki)	-	34	-	-	34
Garlic, Gefyra	-	-	-	33	33
Peaches, Naousa	-	-	-	31, 35	33 (31-35)
Cotton, Livadochori	17	-	-	-	17
Carnation florescence increase, Sidirokastro (Serres)	25	-	-	40	33 (25-40)
Decrease of plant-losses in new vineyard, Gefyra	-	-	-	12	12

*) Filippidis 2007, **) Filippidis et al. 2007, ***) Filippidis 2010a

The HENAZE effectively neutralize sewage-sludge, industrial area sludge, dangerous industrial solid wastes, such as battery solid waste, mine solid wastes (mine-tailings) and also the acid mine drainage. The HENAZE-treatment of the different solid wastes gave odorless and cohesive materials (zeo-sewage sludge, zeo-sludge, etc.) which are suitable for safe deposition since the fixation of dangerous species into the HENAZE, prevents the seepage by runoff or leaching, thus protecting the quality of soils, surface and groundwaters. The seepage of Mn, Ni, Cr and NO_3^- from sewage-sludge was 7-100%, while that from the zeo-sewage-sludge 0-19%. The seepage of Cr and NO_3^- from dyeing-industry-sludge was 40-100%, while that from the zeo-sludge 0-18%. The treatment of sewage-sludge and industrial sludge with HENAZE, reduced the nitrate leaching by 81% and 82%, respectively (Table 5). The HENAZE in batch treatments, reduced the nitrate load by 55% in groundwater (Lagkadas, Thessaloniki), by 57% in nitrate-solutions, by 54-70% in Sindos industrial area wastewaters (Thessaloniki), by 86-92% in Kilkis city urban wastewaters and by 94% in Thessaloniki dyeing industry wastewater (Table 6).

Table 5 - Seepage of NO_3^- and metals from sewage-sludge(SS), zeo-sewage-sludge (ZSS), dyeing-industry-sludge (DIS) and zeo-sludge (ZS).

*)	SS (mg/kg)	Seepage water from SS (mg/L)	Seepage (%)	ZSS (mg/kg)	Seepage water from ZSS (mg/L)	Seepage (%)
NO_3^-	19.92	19.92	100	65.08	12.40	19
Cr	0.08	0.02	25	0.10	Bdl	0
Fe	0.18	0.04	22	0.22	0.02	9
Ni	0.20	0.02	10	0.22	Bdl	0
Mn	0.28	0.02	7	0.30	Bdl	0
**)	**DIS (mg/kg)**	**Seepage water from DIS (mg/L)**	**Seepage (%)**	**ZS (mg/kg)**	**Seepage water from ZS (mg/L)**	**Seepage (%)**
NO_3^-	26.64	26.56	100	73.48	13.22	18
Cr	0.05	0.02	40	0.06	Bdl	0

*) Filippidis et al. 2015a, **) Filippidis et al. 2015b, Bdl: Below detection limit (<0.02)

Table 6 - Nitrate (NO_3^-) reduction by Hellenic Natural Zeolite (HENAZE).

	Initial concentration (mg/L)	HENAZE ± coagulants (C)	Reduction (%)
Groundwater (Lagkadas, Thessaloniki)[1]	98	HENAZE	55
Nitrate-solutions [2]	100	HENAZE	57
Sindos industrial area wastewater (Thessaloniki)[3]	35	HENAZE+C	54-70
Urban wastewater (Kilkis city) [4]	42.30-75.70	HENAZE+C	86-92
Dyeing industry wastewater (Thessaloniki) [5]	78.36	HENAZE+C	94

[1]) Filippidis 2010a; Filippidis et al. 2006, [2]) Filippidis 2007, 2010a, [3]) Filippidis et al. 2011b,c, 2013, 2014, 2015c, [4]) Filippidis 2008, 2009, 2010a; Filippidis et al. 2008e, 2012, 2015a; Filippidis and Tsirambides 2012, [5]) Filippidis et al. 2015b.

The HENAZE is suitable for the sorption-removal of trace elements, radionuclides and cyanobacteria from their solutions and waters. Depending on the initial concentration, the HENAZE removed 37-87% of metals (Cd, Hg, Ag) and 37-70% of radionuclides (Th, U, Cs) (Table 7). The sorption-removal of cyanobacteria from Lake water and culture by the HENAZE, reached values of 51-92% (Table 8).

Table 7 - Sorption (removal) of metals and radionuclides by Hellenic Natural Zeolite (1 g of HENAZE with grain-size <0.5 mm) from their solutions (100 mL).

Initial concentration (mg/L)	Sorption – Removal (%)					
	Cd	Hg	Ag	Th	U	Cs
1000	37	70	84	-	-	-
500	56	82	87	-	-	60
100	-	-	-	55	37	70
50	-	-	-	58	40	-

Table 8 - Cyanobacteria removal by Hellenic Natural Zeolite (HENAZE)*.

	Cyanobacteria	Removal after HENAZE treatment (%)
Doirani Lake water	*Colonial Microcystis*	51
	Filamentous	75
Culture	*Chroococcus*	91 and 92
Starting water: 70-200mL. HENAZE: 0.2-1.75g (grain-size < 0.5, <1.5mm). Contact time: 60min		

*) Filippidis et al. 2010a, 2011a

The treatment of wastewaters (urban, textile industry, industrial area and tanning-work) with HENAZE and coagulants, resulted to production of clear water, free of odors, control the pH to neutral and improved the quality characteristics (on average) by 48-99% (Tables 9 and 10). All values of the clear water quality parameters, after repeated treatments, can be within the required limits for disposition as downstream, irrigation, swimming and fish waters.

Table 9 - Purification of urban (U) and dyeing industry (DI) wastewaters by HENAZE and coagulants in batch-type experiments. Starting wastewater: 300 mL. Average (range).

	Improvement in U* (%)	Improvement in DI** (%)
pH	11 (7-18)	7 (5-9)
Color	93 (88-97)	97
Suspended particles	94 (87-98)	92 (91-93)
Chemical Oxygen Demand (COD)	94 (89-97)	90 (74-95)
P_2O_5	97 (91-99)	98
NH_4	98 (97-99)	98
NO_3^-	90 (86-92)	94
Cr	86 (83-90)	75
HENAZE (6-7.7*g, 10-12.5**g), Grain-size (<0.5, <1.5mm), Stirring time (2-60*min, 2**min)		

*) Filippidis et al. 2008a-f, 2009a,b, 2010b, 2012, 2015a; Filippidis 2010b, 2013

**) Filippidis et al. 2008d,e,g, 2015b; Filippidis 2013

Table 10 - Purification of industrial area (I) and tanning-work (T) wastewaters by HENAZE and coagulants in batch-type experiments. Starting wastewater: 300 mL. Average (range).

	Improvement in I* (%)		Improvement in T** (%)
pH	5 (4-6)	pH	18
Color	93	Color	98
Chemical Oxygen Demand	74 (69-77)	Suspended particles	99
P_2O_5	97	P_2O_5	99
NO_3^-	60 (54-70)	HENAZE (0.1-6.4* g, 7.5** g), Grain-size (<0.5* mm, <1.5** mm), Stirring time (3* min, 2** min)	
Cr	85 (77-88)		
Pb	48 (33-50)		

*) Filippidis et al. 2011b,c, 2013, 2014, 2015c, **) Filippidis et al. 2008a; Filippidis 2013

Aquaculture: Cleaning the water and reducing ammonia by 90% by crossing three (3) sequential filters of HENAZE (grain size 1-8 mm). Air purification in fish feed plant: The strong odor reduction was achieved by passing the air through two (2) sequential filters (20 cm in thickness) of HENAZE (grain size 8-25 mm). The addition of HENAZE in mortar mixtures of sand and portland cement leads to a decrease of up to 18% unit weight. The increase of the HENAZE proportions increases

the porosity and water absorption of the lighter mortar and at the same time, decreases the uniaxial compressive strength (Vogiatzis *et al*., 2012).

4. Discussion and Conclusions

Only clinoptilolite of sedimentary origin (clinoptilolitic zeolitic tuffs) with ≥80 wt% clinoptilolite, ≤20 wt% clay minerals, free of fibres and quartz, can be used (in powder form) as feed additive for all animal species (EU Regulation No 651/2013) and consequently as nutrition supplement for humans. In humans and animals, inhaled or injected or swallowed, fibrous zeolites (mainly erionite and mordenite, and to a lesser extent roggianite and mazzite), as well as the SiO_2 minerals (quartz, cristobalite, tridymite), are toxic, carcinogenic and highly pathogenic (e.g., Davis, 1993; Driscoll, 1993; Saffiotti *et al*., 1993). The Hellenic Natural Zeolite (HENAZE) on average, contains 89 wt% clinoptilolite, <3 wt% clay minerals, is free of fibres (fibrous zeolites), but unfortunately is not free of quartz. Mineralogically, HENAZE do not meet the requirements of the EU Regulation No 651/2013, and thus cannot be used as feed additive for all animal species and consequently as nutrition supplement, since it contains 3 wt% quartz and 2 wt% cristobalite±tridymite. Chemically, the HENAZE is suitable for use as soil conditioner, since the concentration of trace elements (Cd, Cr, Cu, Hg, Ni, Pb, Zn) are lower than the maximum allowable concentrations in agricultural soils (EU Directive 278/EEC 1986). The HENAZE is of very high quality clinoptilolitic zeolitic tuff. The sorption and fixation of the different components from their solutions by the micro/nano-pores of clinoptilolite, as well as the meso- and macro-pores of the HENAZE, is attributed to absorption (ion exchange), adsorption and surface precipitation processes. The clinoptilolite, because of the existence in its structure, of the Brønsted acidic active sites and the Lewis basic active sites, reacts with the positively or/and negatively charged chemical components, even with molecules in gas condition. These chemical processes are related to sorption and fixation physicochemical phenomena of ions and molecules, and concerns both the structural void spaces (micro/nano-pores) and the surface of the clinoptilolite crystals, consequently the meso- and macro-pores of the HENAZE. The HENAZE shows an ability to neutralize the pH of acidic and basic waters, acting either as a proton acceptor or donor, exhibiting thus an amphoteric character (Misaelides *et al*., 1995; Godelitsas *et al*., 2003; Filippidis and Kantiranis, 2007; Filippidis, 2010a, 2013).

Considering among others, EU Regulation No 651/2013, EU Directives 278/EEC 1986 and 98/83/EC/1998, the high toxicity in animals and humans of fibrous zeolites and crystalline silica (e.g., Davis, 1993; Driscoll, 1993; Saffiotti *et al*., 1993), the pozzolanic activity of minerals, the bioavailability of elements, the trace elements and radionuclides (radioactivity) of zeolitic tuffs, the observed negative-zero performance in greenhouse crops (lettuce and peppers), in the field (maize), in the removal of metals from wastewater and drinking water, due to the addition of low quality zeolitic tuff (40% clinoptilolite) (Gkertsis, 2008; Marantos and Angelatou, 2009), the low quality zeolitic rock (70% clinoptilolite) proved to be insufficient for nitrate retention (Mazeikiene *et al*., 2008) and the performance-yield and the cost in all type of uses, it is very important to emphasize the quality characteristics of the zeolitic tuffs, in relation to different uses. The specifications for the various uses of HEU-type (clinoptilolite-heulandite) zeolitic tuffs are:

(1st) The zeolitic tuff, for all uses, must be free of fibres (EU Regulation No 651/2013) and consequently fibrous zeolites and other fibrous minerals (tiny needles). The presence of fibrous zeolites (e.g., erionite, mordenite, roggianite, mazzite) is inhibitory for the use of zeolitic tuffs, **(2nd)** The zeolitic tuff must be free of quartz for use (in powder form) as feed additive for all animal species (EU Regulation No 651/2013). The zeolitic tuff must be free of quartz, cristobalite and tridymite (crystalline SiO_2-phases, tiny insoluble axes) for use as feed additive for all animal species and consequently for humans as nutrition supplement. The same applies to the use as livestock floor materials, in case the animals are used to consume materials from the floor, **(3rd)** The content of the HEU-type zeolite (clinoptilolite-heulandite) in the zeolitic tuff, for all uses, should be ≥80 wt%, **(4th)** The content of the clay minerals in the zeolitic tuff, should be ≤20 wt%. Particular care is required (zero or very low content) for the swelling clay minerals (high pozzolanic activity, equivalent in

action to the cement), **(5th)** The zeolitic tuff should not be burdened or contaminated with major elements, trace elements and radionuclides (radioactivity) and their concentrations should not exceed the Maximum Allowable Concentrations (MAC) of trace elements in agricultural soils, according to the World, European and Greek legislation, and also should not be enriched compared to the average values of the rocks and the Earth's crust, **(6th)** The bioavailability and leachability of dangerous-harmful metals, trace elements, radionuclides and chemical compounds of the zeolitic tuff, should be zero or extremely low. The metals, trace elements and radionuclides should be located within the crystal structure of the zeolite (absorption) rather than the surface of the zeolite crystals (adsorption, surface precipitation), **(7th)** The main exchangeable cations of the HEU-type zeolite (clinoptilolite-heulandite) contained in the zeolitic tuff, should be K, Ca, Mg and Na, **(8th)** The sorption-uptake ability (ion exchange capacity) of the zeolitic tuff, should be >170 meq/100g, **(9th)** The granulation of the zeolitic tuff for different uses, should consider the size of the shards and the type of application and **(10th)** The Correlation of the cost, the economic and environmental benefits, always should seriously be considered.

The great majority (>99%) of zeolitic tuffs are unsuitable and/or dangerous for consumption from animals and humans. Even if the zeolitic tuffs fulfill all the above mineralogical, chemical, morphological and radiological conditions, particular care is needed for those who take medicines, because the zeolitic tuffs as a material with high adsorption capacity, can bind, inactivate and remove the beneficial medicine from the human body, with consequent harm.

5. Acknowledgments

Thanks to GEO-VET N. Alexandridis & Co O.E. for the supply of the HENAZE samples.

6. References

Davis, J.M.G., 1993. In vivo assays to evaluate the pathogenic effects of minerals in rodents. *In:* Health Effects of Mineral Dusts. MSA, Washington DC, *Reviews in Miner.*, 28, 471-487.

Driscoll, K.E., 1993. In vitro evaluation of mineral cytotoxicity and inflammatory activity. *In:* Health Effects of Mineral Dusts. MSA, Washington DC, *Reviews in Miner.*, 28, 489-511.

EU Directive 278/1986. Council Directive 86/278/EEC of 12 June 1986 on the protection of the environment, and in particular of the soil, when sewage sludge is used in agriculture.

EU Directive 83/1998. Council Directive 98/83/EC of 3 November 1998 on the quality of water intended for human consumption.

EU Regulation No 651/2013. Commission Implementing Regulation (EU) No 651/2013 of 9 July 2013 concerning the authorisation of clinoptilolite of sedimentary origin as a feed additive for all animal species and amending Regulation (EC) No 1810/2005.

Filippidis, A., 2005. Study: Mineralogy and physico-chemical characteristics of five natural zeolite samples on behalf of N. Alexandridis & Co OE (in Greek), Thessaloniki, 10 pp.

Filippidis, A., 2007. Zeolites of Trigono Municipality of Evros Prefecture in industrial, agricultural, cattle-raising and environmental technology (in Greek), *Proc. of the Sci. Meet. Develop. Perspectives of Northern Evros*, Petrota, 4 August, 89-107.

Filippidis, A., 2008. Treatment and recycling of municipal and industrial waste waters using Hellenic Natural Zeolite: A Review. *Proc. of the AQUA 3rd Int. Conf.* Athens, 16-19 Oct., 5 pp.

Filippidis, A., 2009. Management of urban and industrial wastewaters using Hellenic Natural Zeolite. Review article (in Greek with English abs), *Proc. of the Congr. Integrated Manag. Water Resources*, Volos, 27-30 May, II, 829-836.

Filippidis, A., 2010a. Environmental, industrial and agricultural applications of Hellenic Natural Zeolite, *Hellenic Journal of Geosciences*, 45, 91-100.

Filippidis, A., 2010b. Purification of municipal wastewaters and production of odorless and cohesive zeo-sewage sludge, using Hellenic Natural Zeolite, *Sci. Annals, Geology, AUTh*, 100, 55-62, 2010.

Filippidis, A., 2013. Industrial and municipal wastewater treatment by zeolitic tuff, *Water Today*, Jan., V/X, 34-38.

Filippidis, A. and Kantiranis, N., 2002. Study: Morphology, mineralogy, chemistry, mineral-chemistry and ion exchange capacity of five natural zeolite samples on behalf of N. Alexandridis & Co OE (in Greek), Thessaloniki, Greece, 5 pp.

Filippidis, A. and Kantiranis, N., 2007. Experimental neutralization of lake and stream waters from N. Greece using domestic HEU-type rich natural zeolitic material, *Desalination*, 213, 47-55.

Filippidis, A. and Tsirambides, A., 2012. Quality characteristics of the Greek zeolites, environmental, industrial, agricultural and aquacultural uses of Hellenic natural zeolite: A review (in Greek with English abs), *Sci. Annals, Geology*, AUTh, 101, 125-133.

Filippidis, A., Kantiranis, N., Drakoulis, A. and Vogiatzis, D., 2006. Improvement and protection of the lake Koronia using natural zeolite (in Greek with English abs), *Proc. of the 2nd Congr. Aristotle Univ. Envir. Council*, Thessaloniki, 1-4 June, 273-279.

Filippidis, A., Siomos, A., Barbayiannis, N. and Filippidis, S., 2007. Agricultural and environmental applications using Hellenic Natural Zeolite of Petrota (Evros) (In Greek with English abs), *Proc. of the Jean Monnet Congr.*, Veria, 30 November - 1 December, 557-569.

Filippidis, A., Apostolidis, N., Filippidis, S. and Paragios, I., 2008a. Purification of industrial and urban wastewaters, production of odorless and cohesive zeo-sewage sludge using Hellenic Natural Zeolite, *Proc. of the 2nd Int. Conf. Wastewater Treat. Plants*, Skiathos, 2-4 May, 403-408.

Filippidis, A., Apostolidis, N., Filippidis, S. and Paragios, I., 2008b. Purification of urban wastewaters, production of odorless and cohesive zeo-sewage sludge using Hellenic Natural Zeolite (in Greek with English abs), *Proc. of the 8th Int. Hydrogeol. Congr.* Athens, 7-10 October, 2, 789-798.

Filippidis, A., Apostolidis, N., Paragios, I. and Filippidis, S., 2008c. Zeolites clean up, *Industrial Minerals*, 485 (April), 68-71.

Filippidis, A., Apostolidis, N., Paragios, I. and Filippidis, S., 2008d. Purification of dye-work and urban wastewaters, production of odorless and cohesive zeo-sewage sludge, using Hellenic Natural Zeolite, *Proc. of the 1st Int. Conf. Hazardous Waste Manag.*, Chania, 1-3 October, 8 pp.

Filippidis, A., Apostolidis, N., Paragios, I. and Filippidis, S., 2008e. Safe management of sewage sludge, produced by treatment of municipal sewage with Hellenic Natural Zeolite, *Proc. of the AQUA 3rd Int. Conf.* Athens, 16-19 October, 5 pp.

Filippidis, A., Apostolidis, N., Paragios, I. and Filippidis, S., 2008f. Production of odorless sewage sludge, purification of dye-work and urban waste-waters, using Hellenic Natural Zeolite (in Greek with English abs), *Proc. of the 3rd Macedonia Envir. Congr.*, Thessaloniki, 14-17 March, 8pp.

Filippidis, A., Apostolidis, N., Paragios, I. and Filippidis, S., 2008g. Purification of dye-work wastewaters and production of cohesive zeo-sludge using Hellenic Natural Zeolite (in Greek with English abs), *Proc. of the 8th Int. Hydrogeol. Congr.*, Athens, 7-10 October, 2, 783-788.

Filippidis, A., Apostolidis, N., Filippidis, S. and Paragios, I., 2009a. Purification of sewage effluents and production of odourless-cohesive sewage sludge, using Hellenic Natural Zeolite (in Greek with English abs), *Honorary to Prof. Tzimopoulos, YDROGAIA*, 425-434.

Filippidis, A., Papastergios, G., Apostolidis, N., Paragios, I., Filippidis, S. and Sikalidis, C., 2009b. Oderless and cohesive zeo-sewage sludge produced by Hellenic Natural Zeolite treatment, *Proc. of the 3rd AMIREG Int. Conf.* Athens 7-9 September, 96-100.

Filippidis, A., Moustaka-Gouni, M., Papastergios, G., Katsiapi, M., Kantiranis, N., Karamitsou, V., Vogiatzis, D. and Filippidis, S., 2010a. Cyanobacteria removal by Hellenic Natural Zeolite. *Proc. of the 3rd Int. Conf. Wastewater Treat. Plants*, Skiathos, 14-16 May, 383-387.

Filippidis, A., Papastergios, G., Apostolidis, N., Filippidis, S., Paragios, I. and Sikalidis, C., 2010b. Purification of urban wastewaters by Hellenic Natural Zeolite, *Bull. Geol. Soc. Greece*, 43(5), 2597-2605.

Filippidis, A., Moustaka-Gouni, M., Katsiapi, M. and Filippidis, S., 2011a. Cyanobacteria removal by Hellenic Natural Zeolite (in Greek with English abs), *Proc. of the 4th Macedonia Envir. Conf.*, Thessaloniki, 18-20 March, 9 pp.

Filippidis, A., Tsirambides, A., Kantiranis, N., Tzamos, E., Vogiatzis, D., Papastergios, G., Papadopoulos, A. and Filippidis, S., 2011b. Purification of wastewater from Sindos industrial area of Thessaloniki (N. Greece) using Hellenic Natural Zeolite. Environ, Earth Sci., Springer, Berlin, *Advances in the Research of Aquatic Environment*, 2, 435-442.

Filippidis, A., Tsirambides, A., Tzamos, E., Vogiatzis, D., Papastergios, G., Georgiadis, I., Papadopoulos, A. and Filippidis, S., 2011c. Purification of wastewater from Thessaloniki industrial area using Hellenic natural zeolite (in Greek with English abs), *Proc. of the 21st Panhel. Chem. Congr.*, Thessaloniki, 9-12 Dec., 8 pp.

Filippidis, A., Kantiranis, N., Vogiatzis, D., Tzamos, E., Papastergios, G. and Filippidis, S., 2012. Odourless-cohesive zeosewage sludge production and urban wastewater purification by natural zeolite, *Proc. of the XI Int. Conf. Prot. Restor. Enviv*, Thessaloniki, 3-6 July, 582-588.

Filippidis, A., Godelitsas, A., Kantiranis, N., Gamaletsos, P., Tzamos, E. and Filippidis, S., 2013. Neutralization of sludge and purification of wastewater from Sindos industrial area of Thessaloniki (Greece) using natural zeolite, *Bull. Geol. Soc. Greece*, 47(2), 920-926.

Filippidis, A., Kantiranis, N., Tziritis, E., Tzamos, E., Vogiatzis, D. and Filippidis, S., 2014. The use of Hellenic Natural Zeolite (HENAZE) in the purification of Thessaloniki industrial area wastewaters, *Proc. of the 10th Intern. Hydrogeol. Congr.*, Thessaloniki, 8-10 Oct., 187-193.

Filippidis, A., Kantiranis, N., Papastergios, G. and Filippidis, S. 2015a. Safe management of municipal wastewater and sludge by fixation of pollutants in very high quality HEU-type zeolitic tuff, *Journal of Basic and Applied Research International*, 7(1), 1-8.

Filippidis, A., Papastergios, G., Kantiranis, N. and Filippidis, S., 2015b. Neutralization of dyeing industry wastewater and sludge by fixation of pollutants in very high quality HEU-type zeolitic tuff, *Journal of Global Ecology and Environment*, 2(4), 221-226.

Filippidis, A., Tziritis, E., Kantiranis, N., Tzamos, E., Gamaletsos, P., Papastergios, G. and Filippidis, S., 2015c. Application of Hellenic Natural Zeolite in Thessaloniki industrial area wastewater treatment, *Desalination and Water Treatment*, doi: 10.1080/19443994.1103314.

Gkertsis, A.K., 2008. Evaluation of zeolitic tuffs, vermiculite and wet fly ash as soil conditioners (in Greek), IGME Final Report, Athens, 75 pp.

Godelitsas, A., Charistos, D., Tsipis, C., Misaelides, P., Filippidis, A. and Schindler, M., 2003. Heterostructures patterned on aluminosilicate microporous substrates: Crystallisation of cobalt (III) tris(N,N-diethyl-dithiocarbamato) on the surface of HEU-type zeolite, *Microp. & Mesop. Mat.*, 61, 69-77.

Marantos, I. and Aggelatou, V., 2009. Evaluation of natural zeolites to improve the quality of drinking water, the sorption of heavy metals from wastewaters and the quality improvement of soils (in Greek), IGME Final Report, Athens, 21 pp.

Mazeikiene, A., Valentukeviciene, M., Rimeika, M., Matuzevicius, A.B. and Dauknys, R., 2008. Removal of nitrates and ammonium ions from water using natural sorbent zeolite (clinoptilolite), *J. Envir. Eng. Landsc. Manag.*, 16, 38-44.

Misaelides, P., Godelitsas, A., Filippidis, A., Charistos, D. and Anousis, I., 1995. Thorium and uranium uptake by natural zeolitic materials, *Sci. Total Environment*, 173/174, 237-246.

Saffiotti U., Daniel L.N., Mao Y., Williams O., Kaighn M.E., Ahmed N. and Knapton A.D., 1993. Biological studies on the carcinogenic mechanisms of quartz. *In:* Health Effects of Mineral Dusts. MSA, Washington DC, *Reviews in Miner. 28*, 522-544.

Vogiatzis, D., Kantiranis, N., Filippidis, A., Tzamos, E. and Sikalidis, C., 2012. Hellenic Natural Zeolite as a replacement of sand in mortar: Mineralogy monitoring and evaluation of its influence on mechanical properties, *Geosciences*, 2, 298-307.

Δελτίο της Ελληνικής Γεωλογικής Εταιρίας, τόμος L, σελ. 1820-1828
Πρακτικά 14ου Διεθνούς Συνεδρίου, Θεσσαλονίκη, Μάιος 2016

Bulletin of the Geological Society of Greece, vol. L, p. 1820-1828
Proceedings of the 14th International Congress, Thessaloniki, May 2016

THE MINERALOGICAL COMPOSITION OF THRACE ZEOLITIC ROCKS AND THEIR POTENTIAL USE AS FEED ADDITIVES AND NUTRITION SUPPLEMENTS

Filippidis A., Kantiranis N. and Tsirambides A.

Aristotle University of Thessaloniki, Faculty of Sciences, School of Geology, Department of Mineralogy-Petrology-Economic Geology, 54124 Thessaloniki, Greece, anestis@geo.auth.gr, kantira@geo.auth.gr, ananias@geo.auth.gr

Abstract

Thirty two (32) locations of zeolitic rocks from Thrace (29 from Evros prefecture and 3 from Rhodope prefecture) were investigated for their mineralogical composition by X-Ray Diffraction (XRD) method. According to EU Regulation No 651/2013, clinoptilolite of sedimentary origin (zeolitic tuffs) with ≥80 wt% clinoptilolite, ≤20 wt% clay minerals, free of fibres and quartz, can be used as feed additive for all animal species. The zeolitic rocks of Thrace on average contain, 23-89 wt% HEU-type zeolite (clinoptilolite-heulandite), 8-45 wt% mordenite (ten locations), 24 wt% analcime (one location), 1-11 wt% mica, 1-11 wt% clay minerals, 3-37 wt% quartz, 2-29 wt% cristobalite, 3-34 wt% feldspars and 0-22 wt% amorphous materials. Only one location contains 89 wt% HEU-type zeolite (clinoptilolite-heulandite), 2 wt% clay minerals, is free of fibres, but unfortunately it contains 3 wt% quartz and 2 wt% cristobalite. Considering the mineralogical composition, the zeolitic rocks of Thrace do not meet the requirements of the EU Regulation No 651/2013, and thus cannot be used as feed additives for all animal species and consequently as nutrition supplements, since the zeolitic rocks in all locations, contain on average 3-37 wt% quartz, 2-29 wt% cristobalite, 8-45 wt% mordenite (fibrous zeolite) in 10 locations, 24-65 wt% zeolites (HEU-type ± mordenite ± analcime) in 28 locations, 74 wt% HEU-type zeolite in 2 locations and 77 wt% HEU-type zeolite in 1 location.
Keywords: *HEU-type zeolite, fibrous zeolites, mordenite, analcime.*

Περίληψη

Τριάντα δύο (32) θέσεις ζεολιθικών πετρωμάτων της Θράκης (29 της ΠΕ Έβρου και 3 της ΠΕ Ροδόπης) μελετήθηκαν ως προς την ορυκτολογική τους σύσταση με την μέθοδο της περιθλασιμετρίας ακτίνων Χ (XRD). Σύμφωνα με τον Κανονισμό της ΕΕ αριθ. 651/2013, κλινοπτιλόλιθος ιζηματογενούς προέλευσης (ζεολιθικοί τόφφοι) με ≥80% κ.β. κλινοπτιλόλιθο, ≤20% κ.β. αργιλικά ορυκτά, χωρίς ίνες και χαλαζία, μπορεί να χρησιμοποιηθεί ως πρόσθετη ύλη ζωοτροφών για όλα τα ζωικά είδη. Τα ζεολιθικά πετρώματα της Θράκης κατά μέσο όρο περιέχουν, 23-89% κ.β. ζεόλιθο τύπου- HEU (κλινοπτιλόλιθο-ευλανδίτη), 8-45% κ.β. μορντενίτη (δέκα θέσεις), 24% κ.β. ανάλκιμο (μία θέση), 1-11% κ.β. μαρμαρυγία, 1-11% κ.β. αργιλικά ορυκτά, 3-37% κ.β. χαλαζία, 2-29% κ.β. χριστοβαλίτη, 3-34% κ.β. αστρίους και 0-22% κ.β. άμορφα υλικά. Μόνο μία θέση περιέχει 89% κ.β. ζεόλιθο τύπου-HEU (κλινοπτιλόλιθο-ευλανδίτη), 2% κ.β. αργιλικά ορυκτά, είναι χωρίς ίνες, αλλά δυστυχώς περιέχει 3% κ.β. χαλαζία και 2% κ.β. χριστοβαλίτη. Λαμβάνοντας υπόψη την ορυκτολογική σύσταση, τα ζεολιθικά

πετρώματα της Θράκης δεν πληρούν τις απαιτήσεις του Κανονισμού της ΕΕ αριθ. 651/2013, και γι' αυτό δεν μπορούν να χρησιμοποιηθούν ως πρόσθετη ύλη ζωοτροφών για όλα τα ζωικά είδη και επομένως ως συμπληρώματα διατροφής, επειδή τα ζεολιθικά πετρώματα όλων των θέσεων, περιέχουν κατά μέσο όρο 3-37% κ.β. χαλαζία, 2-29% κ.β. χριστοβαλίτη, 8-45% κ.β. μορντενίτη (ινώδη ζεόλιθο) σε 10 θέσεις, 24-65% κ.β. ζεόλιθους (τύπου-HEU ± μορντενίτη ± ανάλκιμο) σε 28 θέσεις, 74% κ.β. ζεόλιθο τύπου-HEU σε 2 θέσεις και 77% κ.β. ζεόλιθο τύπου-HEU σε 1 θέση.
Λέξεις κλειδιά: *Ζεόλιθος τύπου-HEU, ινώδεις ζεόλιθοι, μορντενίτης, ανάλκιμο.*

1. Introduction

The zeolitic volcaniclastic rock deposit corresponds to a rock which contains high amounts of one or more from the different (>65) phases of zeolites. The zeolite with the numerous applications is the HEU-type zeolite (clinoptilolite-heulandite) that shows tabular crystals and contains micro/nano-pores in a framework of channels with 10- and 8-member rings, in dimensions of 7.5x3.1 Å, 4.6x3.6 Å and 4.7x2.8 Å (Baerlocher *et al.* 2007; Mitchell *et al.*, 2012). Only zeolitic tuffs with ≥80 wt% clinoptilolite, ≤20 wt% clay minerals, free of fibres and quartz, can be used as feed additives for all animal species (EU Regulation No 651/2013) and consequently as nutrition supplements. In humans and animals, inhaled or injected or swallowed, fibrous zeolites (mainly erionite and mordenite, and to a lesser extent roggianite and mazzite), as well as the SiO_2 minerals (quartz, cristobalite, tridymite), were found to be toxic, carcinogenic and highly pathogenic (Davis, 1993; Driscoll, 1993; Ross *et al.*, 1993).

The zeolitic volcaniclastic rocks of Thrace have been investigated for their mineralogy, petrology and geochemistry by many authors (e.g., Tsirambides *et al.*, 1989, 1993; Kirov *et al.*, 1990; Tsolis-Katagas and Katagas, 1990; Filippidis, 1993; Koutles *et al.*, 1995; Stamatakis *et al.*, 1996; Kassoli-Fournaraki *et al.*, 2000; Barbieri *et al.*, 2001; Kantiranis *et al.*, 2006a; Filippidis *et al.*, 2007; Marantos *et al.*, 2008; Tzamos *et al.*, 2011). Zeolitic volcaniclastic rocks of Thrace have been tasted in different industrial, environmental and agricultural applications (e.g., Misaelides *et al.*, 1995; Filippidis and Kantiranis, 2007; Filippidis *et al.*, 2008, 2010, 2013, 2015a, b; Filippidis, 2010, 2013; Tsirambides and Filippidis, 2012; Vogiatzis *et al.*, 2012). Some studies concern the use of Thrace zeolitic rocks as feed additives in hens, pigs and lambs (e,g., Tserveni-Gousi et al, 1997; Yannakopoulos *et al.*, 2000; Deligiannis *et al.*, 2005).

The aim of the present study is to investigate the mineralogical composition of the zeolitic rocks from thirty-two (32) locations of Thrace and evaluate their potential use as feed additives (in accordance with the EU Regulation No 651/2013) and as nutrition supplements.

2. Materials and Methods

Four (4) to ten (10) representative samples were collected from each zeolitic tuff location of Thrace. The mineralogical composition was determined by the X-Ray Diffraction (XRD) method. The XRD analysis was performed using a Philips PW1710 diffractometer with Ni-filtered CuK_α radiation on randomly oriented powder samples. The counting statistics were: start angle 3°, end angle 63° and in few samples 43° (2θ), step size 0.02° (2θ), time per step 1 sec and scan speed 0.02°/sec. Semi-quantitative estimates of the abundance of the mineral phases were derived from the XRD data, using the intensity (counts) of certain reflections, the density and the mass absorption coefficient of the identified minerals for CuK_α radiation, the software MAUD-Material Analysis Using Diffraction with the RIETVELD method. The semi-quantitative estimation of the percentage of total amorphous materials was achieved by comparing the area of each broad background hump, which represents the amorphous materials in each sample, with the analogous area of standard mixtures of minerals with different contents of natural amorphous material, scanned under the same conditions (Filippidis and Kantiranis, 2007; Kantiranis *et al.*, 2004, 2005, 2006b).

3. Results

The semi-quantitative mineralogical composition of the zeolitic rock samples are presented in Tables 1-6 and Figures 1 and 2.

In the Petrota area of Evros prefecture, from the 11 locations, the zeolitic rocks contain on average, 47-89 wt% HEU-type zeolite in 10 locations and 45 wt% mordenite in 1 location (Table 1, Figure 1). Only in the Ntrista Stream location, the zeolitic rock contains ≥80 wt% HEU-type zeolite (on average 89 wt%), ≤20 wt% clay minerals (on average 2 wt%), is free of fibres (fibrous zeolites such as mordenite), but unfortunately is not free of quartz (SiO_2), containing 3 wt% quartz and 2 wt% cristobalite (SiO_2).

Table 1 - Semi-quantitative mineralogical composition (wt%) of zeolitic rocks from Petrota locations (Evros). HEU-type zeolite: Clinoptilolite-heulandite. Average (range).

Location (no. of samples)	HEU-type zeolite	Mord-enite	Mica	Clay minerals	Quartz	Cristo-balite	Feld-spars	Amor-phous
Lefki Stream (4)	60 (53-64)	-	1 (1-2)	2 (1-2)	8 (6-9)	2 (1-3)	27 (24-35)	-
Tympanistis (4)	57 (50-62)	-	3 (2-4)	1 (1-2)	9 (7-10)	3 (2-4)	27 (23-32)	-
Livadakia (4)	52 (42-60)	-	11 (9-12)	6 (5-7)	11 (8-14)	4 (2-6)	16 (7-23)	-
Paliovouni (4)	52 (39-63)	-	2 (1-3)	4 (3-5)	5 (4-8)	4 (2-6)	19 (14-27)	14 (11-17)
Paliodasos (4)	60 (57-63)	-	1 (1-2)	2 (1-3)	6 (4-8)	2 (1-4)	17 (14-20)	12 (7-18)
Fylakio Omega (4)	-	45 (41-49)	2 (1-2)	3 (2-4)	10 (7-13)	15 (13-17)	21 (18-24)	4 (3-6)
Mavri Petra (6)	65 (42-79)	-	3 (2-6)	2 (1-3)	5 (2-6)	6 (2-12)	16 (8-30)	3 (0-9)
Kokkalo (6)	47 (44-56)	-	2 (1-2)	3 (2-4)	5 (3-6)	4 (3-8)	17 (14-21)	22 (14-27)
Aloni (4)	59 (55-63)	-	2 (1-2)	3 (2-4)	4 (3-6)	4 (2-5)	14 (12-19)	14 (6-21)
Ntrista Stream (6)	89 (83-91)	-	1 (1-2)	2 (1-3)	3 (2-4)	2 (1-3)	3 (2-7)	-
Gkazomylos (10)	60 (47-76)	-	2 (1-3)	3 (2-11)	7 (3-14)	7 (2-15)	15 (11-21)	6 (0-20)

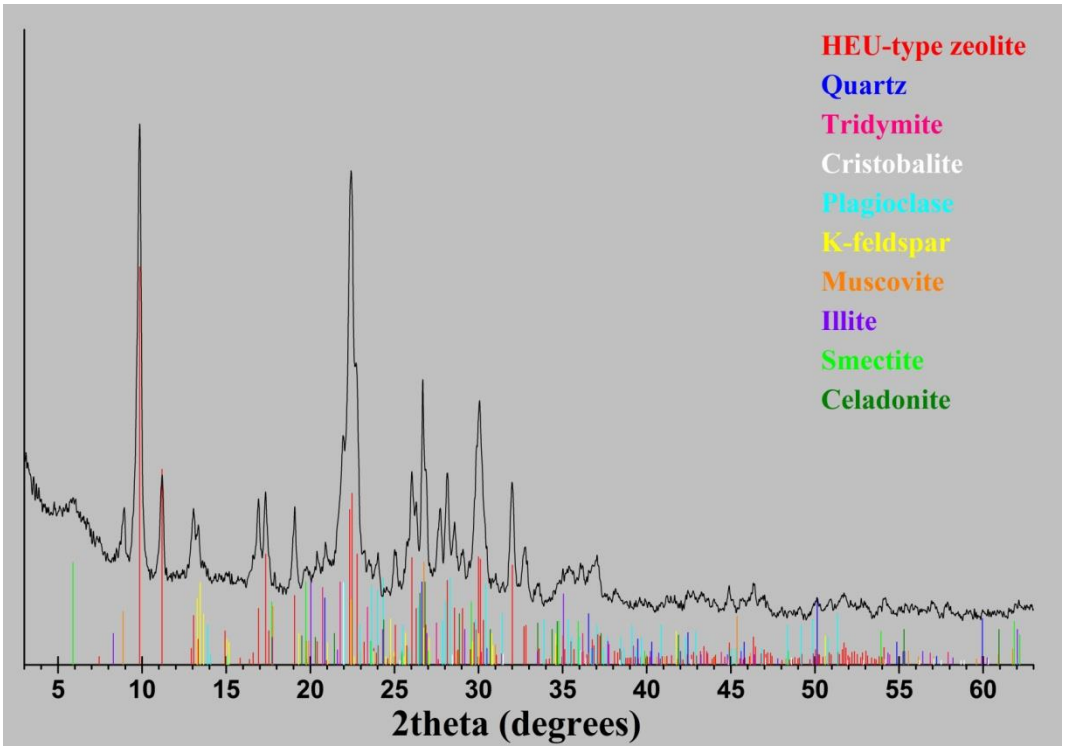

Figure 1 - X-Ray Diffraction pattern of zeolitic rock from Ntrista Stream (Petrota, Evros prefecture).

In the Pentalofos area of Evros prefecture, the zeolitic rocks in all 4 locations contain on average, 55-77 wt% HEU-type zeolite (clinoptilolite-heulandite), 4-7 wt% quartz and 3-7 wt% cristobalite (Table 2).

Table 2 - Semi-quantitative mineralogical composition (wt%) of zeolitic rocks from Pentalofos locations (Evros). HEU-type zeolite: Clinoptilolite-heulandite. Average (range).

Location (no. of samples)	HEU-type zeolite	Mica	Clay min-erals	Quartz	Cristo-balite	Feld-spars	Amor-phous
Palestra (4)	55 (49-62)	3 (2-4)	2 (1-3)	7 (5-9)	7 (4-10)	20 (18-27)	6 (2-10)
Kapsali Rachi (4)	74 (70-77)	3 (2-4)	2 (1-3)	5 (3-7)	4 (3-6)	8 (6-10)	4 (0-6)
Kyries Toumbes (4)	74 (71-77)	6 (3-10)	3 (1-5)	4 (2-6)	3 (2-6)	6 (2-10)	4 (3-5)
Tympano (6)	77 (68-86)	5 (2-11)	5 (2-7)	4 (2-5)	3 (2-4)	6 (3-8)	-

In the Metaxades area of Evros prefecture, the zeolitic rocks in all 3 locations contain on average, 53-55 wt% HEU-type zeolite (clinoptilolite-heulandite), 7-12 wt% quartz and 6-21 wt% cristobalite (Table 3).

Table 3 - Semi-quantitative mineralogical composition (wt%) of zeolitic rocks from Metaxades locations (Evros). HEU-type zeolite: Clinoptilolite-heulandite. Average (range).

Location (no. of samples)	HEU-type zeolite	Mica	Clay minerals	Quartz	Cristo-balite	Feld-spars	Amor-phous
Xerovouni (4)	55 (38-63)	7 (4-10)	8 (5-11)	7 (6-9)	6 (3-10)	17 (6-41)	-
Gourounorema (5)	55 (42-69)	4 (2-5)	6 (2-11)	12 (4-22)	12 (7-23)	11 (4-17)	-
Paliouri (4)	53 (28-67)	2 (1-3)	3 (2-5)	8 (6-12)	21 (14-35)	13 (4-22)	-

In the Dadia-Lefkimmi area of Evros prefecture, the zeolitic rocks in all 3 locations contain on average, 51-53 wt% HEU-type zeolite (clinoptilolite-heulandite), 6-9 wt% quartz and 23-29 wt% cristobalite (Table 4).

Table 4 - Semi-quantitative mineralogical composition (wt%) of zeolitic rocks from Dadia-Lefkimmi locations (Evros). HEU-type zeolite: Clinoptilolite-heulandite. Average (range).

Location (no. of samples)	HEU-type zeolite	Mica	Clay minerals	Quartz	Cristo-balite	Feld-spars	Amor-phous
Synoro (4)	53 (46-60)	2 (1-3)	3 (2-4)	6 (3-8)	25 (19-30)	11 (6-23)	-
Xephoto (5)	51 (44-58)	2 (1-3)	4 (2-5)	7 (5-10)	29 (20-34)	7 (4-16)	-
Stavros (4)	51 (43-59)	3 (2-4)	4 (2-6)	9 (4-11)	23 (18-29)	10 (4-21)	-

Table 5 - Semi-quantitative mineralogical composition (wt%) of zeolitic rocks from Feres-Kirki locations (Evros). HEU-type zeolite: Clinoptilolite-heulandite. Average (range).

Location (no. of samples)	HEU-type zeolite	Mord-enite	Mica	Clay min-erals	Quartz	Cristo-balite	Feld-spars	Amor-phous
Makrylofos (7)	36 (30-46)	13 (11-15)	1 (1-3)	6 (2-13)	21 (14-30)	2 (1-4)	13 (6-15)	8 (2-23)
Kavissos (4)	38 (29-50)	25 (22-28)	2 (2)	9 (7-12)	16 (5-25)	3 (1-6)	3 (0-5)	4 (0-7)
Aspra Chomata (7)	-	32 (11-49)	2 (1-3)	6 (1-16)	18 (9-30)	2 (1-5)	31 (18-43)	9 (0-21)
Laka (4)	56 (46-66)	8 (6-10)	2 (1-3)	2 (1-4)	9 (7-13)	3 (2-5)	17 (14-22)	3 (0-5)
Kapsala (4)	23 (19-27)	21 (15-28)	1 (0-3)	3 (1-4)	19 (17-21)	4 (2-6)	19 (13-26)	10 (0-21)
Nipsa (4)	33 (30-36)	18 (15-21)	1 (0-3)	8 (6-10)	4 (2-6)	4 (2-5)	29 (26-32)	3 (2-5)
Aetochori (4)	25 (23-28)	8 (6-10)	1 (0-2)	11 (7-13)	15 (13-17)	4 (2-6)	34 (32-37)	2 (0-4)
Kirki (4)	49 (39-68)	-	2 (1-3)	6 (2-7)	10 (8-12)	10 (6-12)	23 (14-29)	-

In the Feres-Kirki area of Evros prefecture, the zeolitic rocks in all 8 locations contain on average, 23-56 wt% HEU-type zeolite (clinoptilolite-heulandite) + 8-25 wt% mordenite in 6 locations, 32 wt% mordenite in 1 location and 49 wt% HEU-type zeolite in 1 location (Table 5). The zeolitic rocks of all locations contain on average, 4-21 wt% quartz and 2-10 wt% cristobalite (Table 5).

In the Skaloma-Darmeni area of Rhodope prefecture, the zeolitic rocks in all 3 locations contain on average, 23-30 wt% HEU-type zeolite (clinoptilolite-heulandite) + 20-33 mordenite in 2 locations and 24 wt% analcime in 1 location (Table 6, Figure 2). The zeolitic rocks of all locations contain on average 10-37 wt% quartz and 4-16 wt% cristobalite (Table 6).

Table 6 - Semi-quantitative mineralogical composition (wt%) of zeolitic rocks from Skaloma-Darmeni locations (Rhodope prefecture). HEU-type zeolite: Clinoptilolite-heulandite. Average (range).

Location (no. samples)	HEU-type zeolite	Mord-enite	Anal-cime	Mica	Clay-min-erals	Qua-rtz	Cristo-balite	Feld-spars	Amor-phous
Skaloma: Avraam (4)	30 (27-33)	33 (22-40)	-	2 (1-3)	6 (2-15)	10 (7-16)	4 (2-9)	9 (4-12)	6 (0-11)
Skaloma: NE (5)	23 (20-30)	20 (17-27)	-	1 (0-5)	11 (1-15)	11 (8-13)	16 (9-19)	14 (12-15)	4 (2-6)
Darmeni: Voukefalo (4)	-	-	24 (19-29)	1 (0-3)	9 (5-20)	37 (29-41)	5 (2-8)	12 (9-14)	12 (7-14)

4. Discussion and Conclusions

Only clinoptilolite of sedimentary origin (clinoptilolitic zeolitic tuffs) with ≥80 wt% clinoptilolite, ≤20 wt% clay minerals and free of fibres and quartz, can be used (in powder form) as feed additive for all animal species (EU Regulation No 651/2013) and consequently as nutrition supplements. Clinoptilolite of sedimentary origin, belonging to the additive category "technological additives" and to the functional groups "binders" and "anticaking agents", is authorised as an additive in animal nutrition with the conditions laid in the EU Regulation No 651/2013, which is binding in its entirely and directly applicable in all Member States. The EU Regulation No 651/2013, also defines the X-Ray Diffraction (XRD) as analytical method for the determination of clinoptilolite. In humans and animals, inhaled or injected or swallowed, fibrous zeolites (mainly erionite and mordenite, and to a lesser extent roggianite and mazzite), as well as the SiO_2 minerals (quartz, cristobalite, tridymite), were found to be toxic, carcinogenic and highly pathogenic (Davis, 1993; Driscoll, 1993; Ross *et al.*, 1993).

The 32 locations of Thrace (29 in Evros prefecture and 3 in Rhodope prefecture) of zeolitic rocks can be grouped as follows: a) Twenty one locations contain (average values) 47-89 wt% HEU-type zeolite (clinoptilolite-heulandite), b) Eight locations contain 23-56 wt% HEU-type zeolite + 8-33 wt% mordenite, c) Two locations contain 32 & 45 wt% mordenite, d) One location contains 24 wt% analcime. In all 32 locations the zeolitic rocks contains 3-37 wt% quartz, 2-29 wt% cristobalite and 1-11 wt% clay minerals.

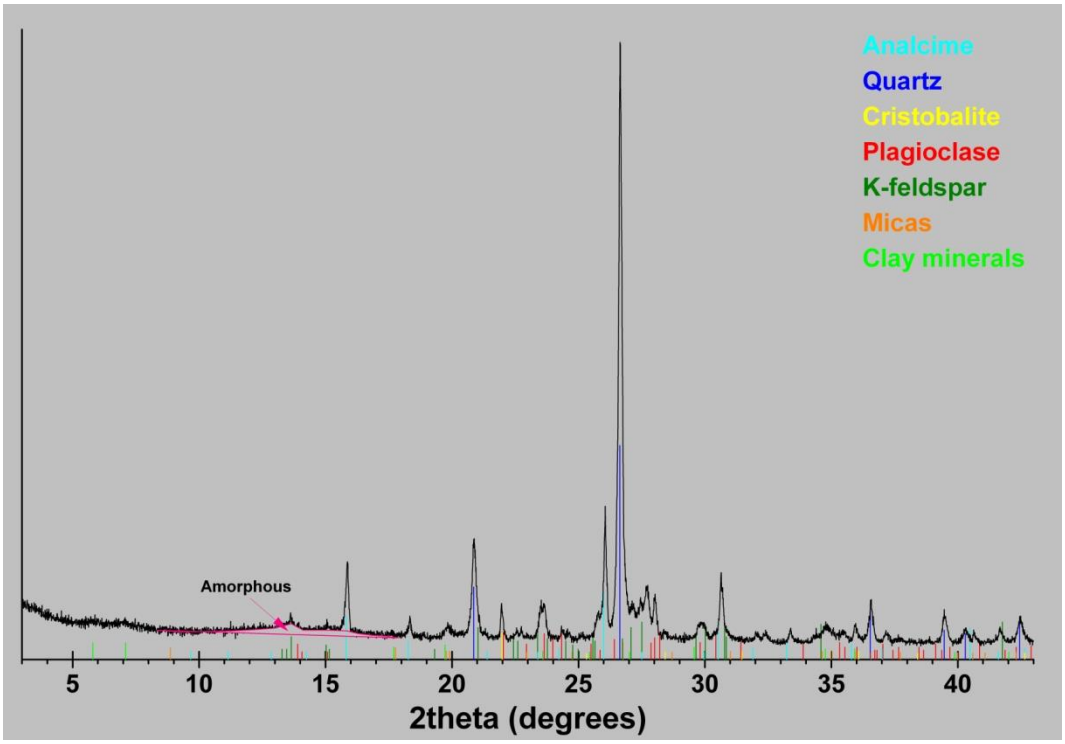

Figure 2 - X-Ray Diffraction pattern of zeolitic rock from Darmeni (Rhodope prefecture).

Only in one location (Ntrista Stream, Petrota, Evros) the zeolitic rock contains ≥80 wt% HEU-type zeolite (clinoptilolite-heulandite) (on average 89 wt%), ≤20 wt% clay minerals (on average 2 wt%), is free of fibres (fibrous zeolites such as mordenite), but unfortunately contains 3 wt% quartz and 2 wt% cristobalite. Concerning the total average zeolite content, one location (Ntrista Stream of Petrota) contains 89 wt%, another one (Tympano of Pentalofos) contains 77 wt%, two (Kapsali Rachi and Kyries Toumpes) contain 74 wt% and the rest 28 locations of Thrace contain 24-65 wt% zeolites.

Considering the mineralogical composition described above and presented in Tables 1-6, none of the zeolite rocks of Thrace meet the requirements of the EU Regulation No 651/2013, and thus cannot be used as feed additives for all animal species and consequently as nutrition supplements, since all of them contain on average 3-37 wt% quartz, 2-29 wt% cristobalite, 8-45 wt% mordenite (fibrous zeolite) in 10 locations, 24-65 wt% zeolites (HEU-type ± mordenite ± analcime) in 28 locations, 74 wt% HEU-type zeolite in 2 locations and 77 wt% HEU-type zeolite in 1 location.

5. Acknowledgments

The authors wish to thank the GEO-VET N. Alexandridis & Co O.E., for the supply of the zeolitic tuff samples from Ntrista Stream location of Petrota (Evros).

6. References

Baerlocher, Ch., McCuster, L.B. and Olson, D.H., 2007. Atlas of Zeolite Framework Types, Amsterdam, Elsevier, 301 pp.

Barbieri, M., Castorina, F., Masi, U., Garbarino, C., Nicoletti, M., Kassoli-Fournaraki, A., Filippidis, A. and Mignardi, S., 2001. Geochemical and isotopic evidence for the origin of rhyolites

from Petrota (Northern Thrace, Greece) and geodynamic significance, *Chemie der Erde*, 61, 13-29.

Davis, J.M.G., 1993. In vivo assays to evaluate the pathogenic effects of minerals in rodents. *In:* Guthrie, G.D.Jr. and Mossman, B.T., *eds.*, Health Effects of Mineral Dusts. Mineralogical Society of America, Washington DC, *Reviews in Mineralogy*, 28, 471-487.

Deligiannis, K., Lainas, Th., Arsenos, G., Papadopoulos, E., Fortomaris, P., Kufidis, D., Stamataris, C. and Zygoyiannis, D., 2005. The effect of feeding clinoptilolite on food intake and performance of growing lambs infected or not with gastrointestinal nematodes, *Livestock Production Science*, 96, 195-203.

Driscoll, K.E., 1993. In vitro evaluation of mineral cytotoxicity and inflammatory activity. *In:* Guthrie, G.D.Jr. and Mossman, B.T., *eds.*, Health Effects of Mineral Dusts, Mineralogical Society of America, Washington DC, *Reviews in Mineralogy*, 28, 489-511.

EU Regulation No 651/2013. Commission Implementing Regulation (EU) No 651/2013 of 9 July 2013 concerning the authorisation of clinoptilolite of sedimentary origin as a feed additive for all animal species and amending Regulation (EC) No 1810/2005.

Filippidis, A., 1993. New find of moissanite in the Metaxades zeolite-bearing volcaniclastic rocks, Thrace County, Greece, *Neues Jahrbuch fur Mineralogie Monatshefte*, 11, 521-527.

Filippidis, A., 2010. Environmental, industrial and agricultural applications of Hellenic Natural Zeolite, *Hellenic Journal of Geosciences*, 45, 91-100.

Filippidis, A., 2013. Industrial and municipal wastewater treatment by zeolitic tuff, *Water Today*, Jan., V/X, 34-38.

Filippidis, A. and Kantiranis, N., 2007. Experimental neutralization of lake and stream waters from N. Greece using domestic HEU-type rich natural zeolitic material, *Desalination*, 213, 47-55.

Filippidis, A., Kantiranis, N., Stamatakis, M., Drakoulis, A. and Tzamos, E., 2007. The cation exchange capacity of the Greek zeolitic rocks, *Bull. Geol. Soc. Greece*, 40(2), 723-735.

Filippidis, A., Apostolidis, N., Paragios, I. and Filippidis, S., 2008. Zeolites clean up, *Industrial Minerals*, 485, 68-71.

Filippidis, A., Papastergios, G., Apostolidis, N., Filippidis, S., Paragios, I. and Sikalidis, C., 2010. Purification of urban wastewaters by Hellenic Natural Zeolite, *Bull. Geol. Soc. Greece*, 43(5), 2597-2605.

Filippidis, A., Godelitsas, A., Kantiranis, N., Gamaletsos, P., Tzamos, E. and Filippidis, S., 2013. Neutralization of sludge and purification of wastewater from Sindos industrial area of Thessaloniki (Greece) using natural zeolite, *Bull. Geol. Soc. Greece*, 47(2), 920-926.

Filippidis, A., Kantiranis, N., Papastergios, G. and Filippidis, S. 2015a. Safe management of municipal wastewater and sludge by fixation of pollutants in very high quality HEU-type zeolitic tuff, *J. Basic and Applied Research International*, 7(1), 1-8.

Filippidis, A., Papastergios, G., Kantiranis, N. and Filippidis, S., 2015b. Neutralization of dyeing industry wastewater and sludge by fixation of pollutants in very high quality HEU-type zeolitic tuff, *J. Global Ecology and Environment*, 2(4), 221-226.

Kantiranis, N., Georgakopoulos, A., Filippidis, A. and Drakoulis, A., 2004. Mineralogy and organic matter content of bottom ash samples from Agios Dimitrios power plant, Greece, *Bull. Geol. Soc. Greece*, 36(1), 320-326.

Kantiranis, N., Filippidis, A. and Georgakopoulos, A., 2005. Investigation of the uptake ability of fly ashes produced after lignite combustion, *J. Environmental Management*, 76, 119-123.

Kantiranis, N., Chrissafis, C., Filippidis, A. and Paraskevopoulos, K., 2006a. Thermal distinction of HEU-type mineral phases contained in Greek zeolite-rich volcaniclastic tuffs, *European J. Mineralogy*, 18(4), 509-516.

Kantiranis, N., Filippidis, A., Mouhtaris, T., Paraskevopoulos, K.M., Zorba, T., Squires, C. and Charistos, D., 2006b. EPI-type zeolite synthesis from Greek sulphocalcic fly ashes promoted by H_2O_2 solutions, *Fuel*, 85, 360-366.

Kassoli-Fournaraki, A., Stamatakis, M., Hall, A., Filippidis, A., Michailidis, K., Tsirambides, A. and Koutles, Th., 2000. The Ca-rich clinoptilolite deposit of Pentalofos, Thrace, Greece. *In*:

Colella, C. and Mumpton, F.A., *eds.*, Natural Zeolites for the Third Millennium, Napoli, De Frede, 193-202.

Kirov, G.N., Filippidis, A., Tsirambidis, A., Tzvetanov, R.G. and Kassoli-Fournaraki, A., 1990. Zeolite-bearing rocks in Petrota area (Eastern Rhodope Massif, Greece), *Geologica Rhodopica*, 2, 500-511.

Koutles, Th., Kassoli-Fournaraki, A., Filippidis, A. and Tsirambides, A., 1995. Geology and geochemistry of the Eocene zeolitic-bearing volcaniclastic sediments of Metaxades, Thrace, Greece, *Estudios Geologicos*, 51, 19-27.

Marantos, I., Markopoulos, Th., Christidis, G.E. and Perdikatsis, V., 2008. Geochemical characteristics of the alteration of volcanic and volcaniclastic rocks in the Feres Basin, Thrace, NE Greece, *Clay Minerals*, 43, 575-595.

Misaelides, P., Godelitsas, A., Filippidis, A., Charistos, D. and Anousis, I., 1995. Thorium and uranium uptake by natural zeolitic materials, *The Science of the Total Environment*, 173/174, 237-246.

Mitchell, S., Michels, N.L., Kunze, K. and Perez-Ramirez, J., 2012. Visualization of hierarchically structured zeolite bodies from macro to nano length scales, *Nature Chemistry*, 4, 825-831.

Ross, M., Nolan, R.P., Langer, A.M. and Cooper, W.C., 1993. Health effects of various mineral dusts other than asbestos. *In:* Guthrie, G.D.Jr. and Mossman, B.T., *eds.*, Health Effects of Mineral Dusts, Mineralogical Society of America, Washington DC, *Reviews in Mineralogy*, 28, 361-407.

Stamatakis, M.G., Hall, A. and Hein, J.R., 1996. The zeolite deposits of Greece, *Mineralium Deposita*, 31, 473-481.

Tserveni-Gousi, A.S., Yannakopoulos, A.L., Katsaounis, N.K., Filippidis, A. and Kassoli-Fournaraki, A., 1997. Some interior egg characteristics as influenced by addition of Greek clinoptilolitic rock material in the hen diet, *Archiv fur Geflugelkunde*, 61(6), 291-296.

Tsirambides, A. and Filippidis, A., 2012. Exploration key to growing Greek industry, *Industrial Minerals*, 533, 44-47.

Tsirambides, A., Kassoli-Fournaraki, A., Filippidis, A. and Soldatos, K., 1989. Preliminary results on clinoptilolite-containing volcaniclastic sediments from Metaxades, NE Greece, *Bull. Geol. Soc. Greece*, 23(2), 451-460.

Tsirambides, A., Filippidis, A. and Kassoli-Fournaraki, A., 1993. Zeolitic alteration of Eocene volcaniclastic sediments at Metaxades, Thrace, Greece, *Applied Clay Science*, 7, 509-526.

Tsolis-Katagas, P. and Katagas, C., 1990. Zeolitic diagenesis of Oligocene pyroclastic rocks of the Metaxades area, Thrace, Greece, *Mineralogical Magazine*, 54, 95-103.

Tzamos, E., Kantiranis, N., Papastergios, G., Vogiatzis, D., Filippidis, A. and Sikalidis, C., 2011. Ammonium exchange capacity of the Xerovouni zeolitic tuffs, Avdella area, Evros Prefecture, Greece, *Clay Minerals*, 46, 179-187.

Vogiatzis, D., Kantiranis, N., Filippidis, A., Tzamos, E. and Sikalidis, C., 2012. Hellenic Natural Zeolite as a replacement of sand in mortar: Mineralogy monitoring and evaluation of its influence on mechanical properties, *Geosciences*, 2, 298-307.

Yannakopoulos, A., Tserveni-Gousi, A., Kassoli-Fournaraki, A., Tsirambides, A., Michailidis, K., Filippidis, A. and Lutat, U., 2000. Effects of dietary clinoptilolite-rich tuff on the performance of growing-finishing pigs. *In*: Colella, C. and Mumpton, F.A., *eds.*, Natural Zeolites for the Third Millennium, Napoli, De Frede, 471-481.

Δελτίο της Ελληνικής Γεωλογικής Εταιρίας, τόμος L, σελ. 1829-1837
Πρακτικά 14ου Διεθνούς Συνεδρίου, Θεσσαλονίκη, Μάιος 2016

Bulletin of the Geological Society of Greece, vol. L, p. 1829-1837
Proceedings of the 14th International Congress, Thessaloniki, May 2016

THE INTERDEPENDENCE OF MECHANICAL PROPERTIES AND PETROGRAPHIC CHARACTERISTICS OF ULTRAMAFIC ROCKS FROM GERANIA OPHIOLITIC COMPLEX

Giannakopoulou P.P.[1], Tsikouras B.[1,2] and Hatzipanagiotou K.[1]

[1]*University of Patras, Department of Geology, Section of Earth Materials, 265 00, Patras, Greece*

[2]*Universiti Brunei Darussalam, Faculty of Science, Physical and Geological Sciences, Jalan Tungku Link,Gadong BE1410, Bandar Seri Begawan, Brunei Darussalam*

Abstract

Ultramafic rocks from the Gerania Mountain ophiolite were tested as aggregates. Petrographic study through polarizing microscope enabled us to determine the presence of dunite, harzburgite and lherzolite. A series of mechanical tests were carried out in order to determine the suitability of these rocks in a wide range of applications. Dunite and harzburgite samples show higher values of uniaxial compression strength than the lherzolites, as the presence of joints and the higher degree of alteration significantly affects negatively this mechanical property in the last rock-type. The same factors influence the point load index, too. Serpentinization and the presence of soft and laminate minerals also exert a negative influence on the resistance on abrasion and attrition, as well as the grinding of the rocks. The same factors influence negatively the point load index, too.
Keywords: *Aggregates, Mechanical properties, Lherzolite, Dunite, Harzburgite.*

Περίληψη

Στα πλαίσια αυτής της εργασίας πραγματοποιήθηκε δειγματοληψία έξι υπερβασικών πετρωμάτων με σκοπό να εξεταστεί η χρήση τους ως αδρανή υλικά. Τα υπό εξέταση πετρώματα συλλέχθηκαν από το οφιολιθικό σύμπλεγμα των Γερανείων Ορέων το οποίο ανήκει στην Πελαγονική ζώνη. Αρχικά πραγματοποιήθηκε πετρογραφική μελέτη, μέσω της οποίας καθορίστηκαν οι εξής λιθότυποι: δουνίτες, χαρτσβουργίτες και λερζόλιθοι. Εν συνεχεία, προσδιορίστηκε μια σειρά από μηχανικές ιδιότητες, με σκοπό τον προσδιορισμό της καταλληλότητάς τους για ένα μεγάλο εύρος εφαρμογών. Παρατηρήθηκαν διαφορές στις τιμές των μηχανικών παραμέτρων μεταξύ δειγμάτων ίδιας λιθολογίας, για τον λόγο αυτό στραφήκαμε στα πετρογραφικά χαρακτηριστικά και στο κατά πόσο επηρεάζουν τη μηχανική συμπεριφορά των υπό μελέτη δειγμάτων. Θα πρέπει να σημειωθεί ότι η επίδραση της ορυκτολογίας και ειδικότερα η δράση της σερπεντινίωσης και η παρουσία ορυκτών όπως του χλωρίτη και του ακτινόλιθου επηρεάζουν αρνητικά την ανθεκτικότητα των πετρωμάτων σε τριβή, φθορά και κρούση. Είναι, επίσης, αξιοσημείωτο το γεγονός ότι η παρουσία διακλάσεων αλλάζει δραματικά την αντοχή των πετρωμάτων σε μονοαξονική θλίψη καθώς και το δείκτη σημειακής φόρτισης.
Λέξεις κλειδιά*: Αδρανή, Μηχανικές ιδιότητες, Λερζόλιθος, Δουνίτης, Χαρτσβουργίτης.*

1. Introduction

Ophiolites are products of complex tectonic and magmatic processes that operated during the initial rifting through seafloor spreading to subduction-facilitated emplacement stages of ancient oceanic lithospheres. The investigation of the mechanical properties of ophiolitic aggregates is of high significance because of their use in numerous applications, such as concrete, mortar, road bases and sub-bases, bituminous mixtures, railway track ballast, filters and armourstone. Differences in mineralogical and textural characteristics influence the mechanical properties, which vary from excellent to fair (Tugrul and Zarif 1999; Akesson *et al.*, 2001; Lundqvist and Goran, 2001; Miskovsky *et al.*, 2004; Zorlu *et al.*, 2004; Al-Oraimi *et al.*, 2006; Pomonis *et al.*, 2007; Tamrakar *et al.*, 2007; Rigopoulos *et al.*, 2010). This research focuses on the investigation of the mechanical properties of ultramafic rocks, including dunite, lherzolite and harzburgite, and the influence of the modification of their primary petrographic characteristics, due to ocean-floor metamorphism (serpentinization) from Gerania Mountains.

2. Geological Setting

Gerania Mountains belong to the Pelagonian geotectonic zone of the internal Hellenides and comprise, from bottom to top, the following succession: a) Sedimentary and volcanic rocks of Permian age (Bornovas *et al.*, 1984); b) a 500 m thick Upper Triassic-Lower Jurassic unit of dark grey neritic limestones and dolomites (Clement, 1971); c) an upper Jurassic succession overlain by either Ammonitico Rosso of Bathonian-Oxfordian age or radiolarian sediments (Clement, 1983); d) ophiolite-derived turbidites (Beotian flysch), occasionally with manganese ore deposits at its bottom; and e) an ophiolite sequence (Fig. 1). The ophiolite is a NE-trending rhomb-shaped outcrop, with approximately 10 km length and 5 km width, representing an incomplete and dismembered ophiolite sequence consisting mainly of serpentinized harzburgite, lherzolite and dunite (Fig. 1). Dunite is present at the hypsometrically higher places and is characterized by variable degrees of serpentinization commonly showing a 2-3 cm thick brown crust due to weathering. Harzburgite comprises a dark lithology affected by variable degrees of alteration and/or weathering, as well as by intense tectonic stress. Lherzolite, which constitutes the dominant lithology of the Gerania peridotites, shows variable but intense serpentinization and contains pyroxenitic dykes 3-4 cm thick. These serpentinized peridotites are interrupted by gabbro dykes, some of which have been transformed to rodingites. The Gerania ophiolite sequence lacks lavas, cumulates and other lithologies of a typical ophiolitic complex. Fragments of lavas, cumulates and oceanic sediments were found within the melange outcrops and in the detritus in Neogene basins (Kaplanis *et al.*, 2012). An ophiolite mélange that includes fragments of lavas, serpentinized peridotites, gabbros, oceanic sediments, as well as an amphibolite metamorphic sole tectonically underlie the ophiolite. The root zone of the Gerania ultramafic rocks (i.e. Pindos or Axios) and its geochemical signature is poorly constrained (Vacondios, 1997; Danelian and Robertson, 1998).

3. Analytical methods

Six polished-thin sections were prepared in order to investigate the mineralogical and textural characteristics of the ultramafic samples using a polarizing microscope. Scanning electron microscopic (SEM) observations and microanalyses were carried out at the Laboratory of Electron Microscopy and Microanalysis, University of Patras, using a Jeol JSM- 6300 SEM, equipped with EDS and WDS and a THETA software in order to determine the chemical composition of primary and secondary minerals. Operating conditions were accelerating voltage 15kV and beam current 3.3nA with 4μm diameter beam. Subsequent laboratory tests were performed using the counterpart material of the investigated polished-thin sections. Samples were crushed in a laboratory jaw crusher Retsch BB200 Mangan and they were sieved in order to reach the desired fraction for the LA test, according to ASTM using “B” gradation (ASTM C-131).

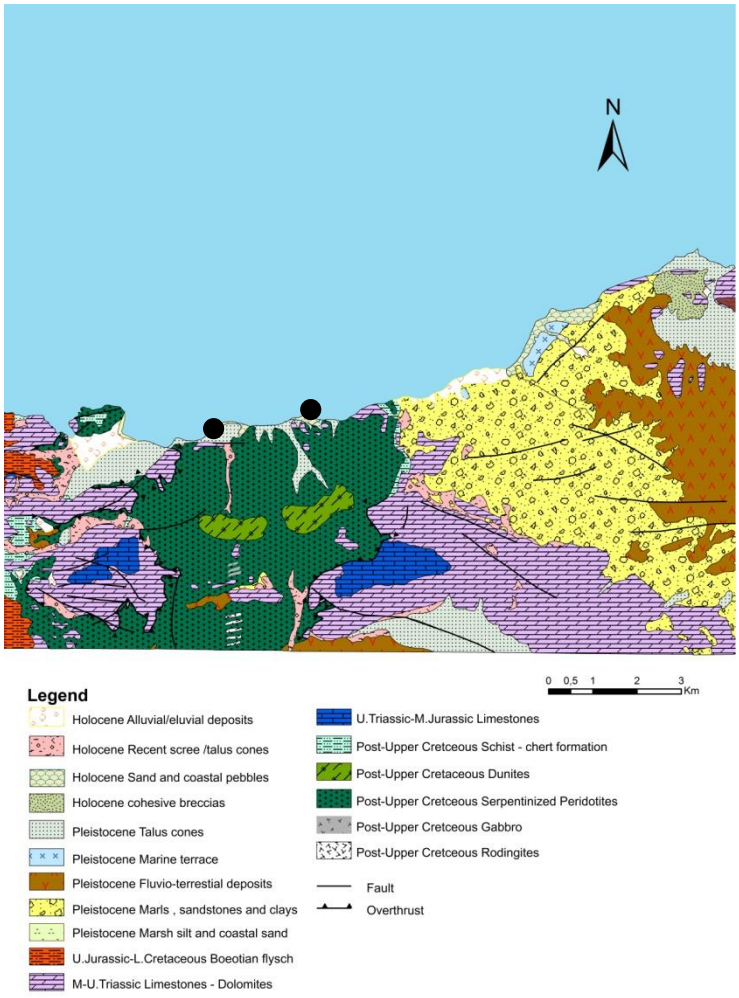

Figure 1 - Geological map of the studied area (Gerania Mountain).

Furthermore, 6 cylindrical rock specimens were prepared with height/diameter ratio between 2 and 3, and their diameters ranging from 51 to 54 mm (ASTM D-2938) for the elaboration of uniaxial compressive strength test, and the average values were used for each set of specimens. Six cylindrical and cubic specimens were also prepared for each sample in order to be used for the calculation of the point load index (ISMR (1985).

4. Results

4.1 Petrographic characteristics

The studied ultramafic samples comprise dunite, harzburgite and lherzolite with variable degrees of serpentinization and deformation. The dunite presents cataclastic and locally granular textures whereas the serpentinized samples show mainly mesh, as well as, local ribbon and interwoven textures. Primary assemblage includes mostly olivine (forsteritic) and scarce relic crystals of orthopyroxene (Figure 2a, b). Infrequent opaque minerals (mainly chromite) are present, too. Serpentine, up to 42 %, forms mesh and ribbon textures and is the dominant secondary mineral. It

is accompanied by chlorite and minor talc; chlorite is frequently observed to surround crystals of chromite.

The harzburgite presents mainly porphyroclastic texture. Its primary assemblage includes olivine, orthopyroxene (most of them with exsolution lamellae of clinopyroxene) and rare clinopyroxene (Figure 2c). Olivine appears as porphyroclasts, which present strong deformation (strain lamellae, kink banding and undulate extinction), as well as small-sized unstrained neoblasts (Figure 2c). Frequent replacement of orthopyroxene from olivine neoblasts is also observed. Chromite is present in small amounts, some of which display rims altered to secondary spinel-type minerals. A dense network of joints occurs in the harzburgite. The serpentine (12%) comprises the commonest secondary phase presenting ribbon texture; minor chlorite occurs, too.

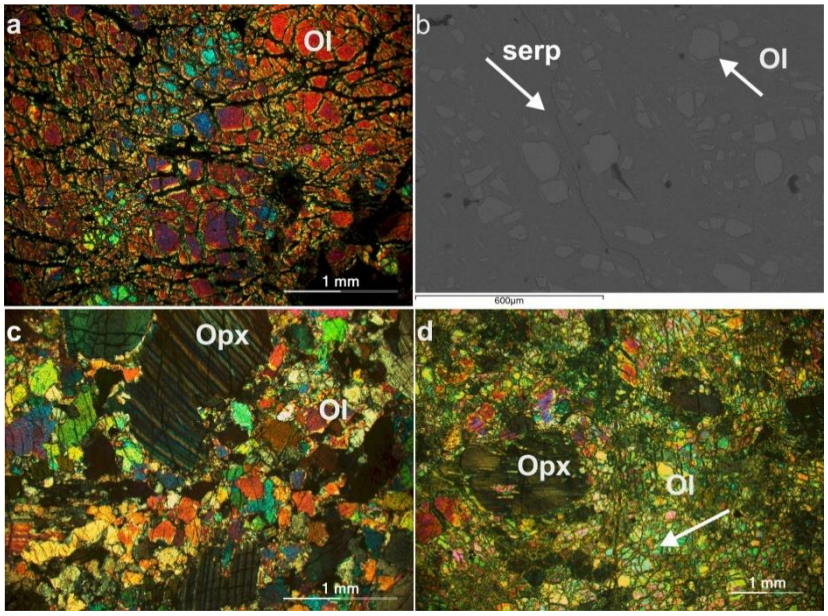

Figure 2 - Petrographic characteristics of the peridotites from the Gerania ophiolite: a. Photomicrograph (XPL) of a dunite (GE 34). b. Backscattered electron image of a serpentinized dunite (GE 17). c. Photomicrograph (XPL) of a harzburgite with strained orthopyroxene crystals (sample GE 28). d. Photomicrograph (XPL) of cataclastic olivine surrounding a relic porphyroclast of orthopyroxene in a lherzolite from Gerania (sample GE 30).Abbreviations: Ol: olivine, Opx: orthopyroxene, serp: serpentine.

The lherzolite shows cataclastic, porphyroclastic and locally protogranular textures, with the primary assemblage including olivine (forsteritic), orthopyroxene and clinopyroxene (Figure 2d). Opaque minerals (mainly Al-spinel) are present in small amounts. Evidence of high-temperature plastic deformation is shown in strained olivine and orthopyroxene porphyroclasts, which display undulate extinction, strain lamellae and kink banding in both orthopyroxene and clinopyroxene (Figure 3a, b). Serpentine is the main secondary mineral ranging from 12 to 75 % of the mode, which shows mostly mesh and ribbon textures (Figure 3c). The effect of serpentinization also leads to the replacement of orthopyroxene from bastite. Some orthopyroxene and clinopyroxene crystals are additionally replaced by chlorite and actinolite. A dense network of joints is also observed in lherzolite (Figure 3d).

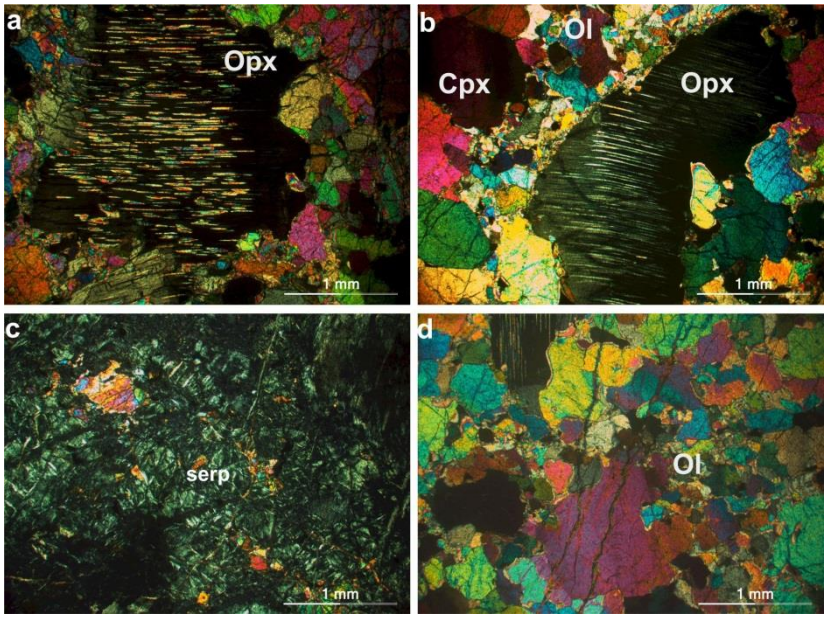

Figure 3 - a. Photomicrograph (XPL) of a lherzolite where exsolution lamellae of clinopyroxene from orthopyroxene is shown (sample GE 36). b. Photomicrograph (XPL) of a lherzolite showing undulate extinction, strain lamellae and kink banding in crystals of orthopyroxene and clinopyroxene (sample GE 36). c. Photomicrograph (XPL) of a serpentinized lherzolite, with relic olivine and serpentine with mesh texture (sample GE 26). d. Photomicrograph (XPL) of lherzolite transected by an intense network of joints, showing olivine with characteristic undulate extinction (sample GE 36).Abbreviations: Ol: olivine, Opx: orthopyroxene, Cpx: clinopyroxene, serp: serpentine.

4.2 Mechanical tests

The mechanical properties of ultramafic samples were determined by a number of laboratory tests, including the uniaxial compressive strength (UCS), the Los Angeles abrasion value and the point load index. Peridotites with various degrees of serpentinization were chosen in order to study the influence of alteration on their mechanical behaviour. Six cylindrical specimens from each sample were tested for uniaxial compressive strength and the average value was calculated (Table 1). Dunite and harzburgite samples differ from lherzolites in having distinctively higher UCS values. Among lherzolites, the least serpentinized sample GE 30 shows the highest UCS value, while the lherzolitic sample GE 36 presents the lowest value of UCS. However, the most serpentinized dunite GE 17 shows higher value of UCS relative to the fresher GE 34 sample, hence indicating an inconsistent behaviour in terms of alteration.

Table 1 – Results of mechanical tests in the ultramafic rocks from Gerania.

Samples	UCS (MPa)	LA (%)	$Is_{(50)}$ (MPa)	Serpentine (%)
Dunite (GE 17)	93.05	20.30	3.46	41.26
Dunite (GE 34)	88.86	17.51	5.38	28.15
Harzburgite (GE 28)	86.20	15.73	2.28	12.00
Lherzolite (GE 26)	66.00	19.63	3.50	75.01
Lherzolite (GE 30)	75.00	16.61	3.84	28.48
Lherzolite (GE 36)	50.00	23.29	1.15	12.15

The Los Angeles (LA) abrasion test measures the resistance of an aggregate to impact, abrasion, attrition and grinding. As shown in the Table 1, the results of the LA test range between 15.73 and 23.29 %. The harzburgite, as well as the fresh dunite and lherzolite are clearly the most durable samples while the serpentinized peridotites show higher LA values (Table 1). Point load index is considered to be an indirect measurement of the uniaxial compressive strength of samples. Generally, there is a sympathetic relationship of this index to the UCS values in the investigated samples as the fresher ones, with high UCS, show also the highest Is_{50} values (Table 1).

5. Discussion

In this study, mechanical properties of the investigated ultramafic rocks are correlated with petrographic characteristics using diagrammatic representation and regression analysis (Figure 3 a, b, c). Samples GE 26 and GE 36, which are the most altered peridotites, with quite abundant serpentine, actinolite and chlorite, present very low UCS, and $Is_{(50)}$, as well as high LA values. This fact strongly suggests that alteration has a negative effect on the mechanical performance of the rocks as the secondary minerals tend to reduce the coherence of rocks. GE 36, which is the most vulnerable sample includes moreover a dense network of joints, which further lower its quality. Furthermore, the fresh GE 34 dunite displays lower UCS than the altered GE 17 indicating the significant negative influence of the joints in the samples. This is in line with other micropetrographic studies, which have shown that intensely tectonized samples present low values of strength regardless if they are affected by alteration of their primary assemblages or not (Rigopoulos, 2010).

Serpentinization negatively affects the resistance to abrasion, attrition and grinding in our samples as it appears that the highly altered ones show higher LA values as well. Sample GE 36, which is a moderately altered lherzolite, shows the worst LA value, which is assigned to the additional effect of intense fatigue that it has experienced from the occurrence of dense joints. The existence of soft and laminate minerals such as serpentine, chlorite and talc, which behave differentially relative to the hard, prismatic primary minerals (olivine, orthopyroxene, clinopyroxene) explains well the weaker resistance to abrasion, attrition and grinding. The more plastic behaviour of these soft minerals likely absorbs the shocks during the conduction of the LA test, contrary to the hard and brittle primary minerals, hence leading to easier disintegration of the aggregate particles. The variable behaviour of the largely transected samples GE 34 and GE 36, which show low and high LA values, respectively, suggests that the existence of joints doesn't play a determinant role in LA values. This can be explained by the fact that the particles, which are prepared for the conduction of the test, are mostly devoid of joints as these planes of weakness determine the shape of the particles.

Regression analysis was applied for the investigation of the interdependence of the mechanical properties of these ultramafic rocks. Linear regression was used based on the linearity assumption and the determination coefficients R^2 and equations of the fitted lines were calculated by the "least squares" method. Other types of relationships were also tested (e.g. logarithmic, power, etc.) but it is always observed that the linear model fits best, giving the highest R^2 values. Los Angeles coefficient tended to increase with decreasing uniaxial compressive strength (Fig. 4a) and their correlation is described by the equation:

$$LA = -0.1088 \times UCS + 27.171, \; R^2 = 0.4057$$

The negative correlation between the LA coefficient and the UCS in mafic and ultramafic rocks has also been reported previously (e.g. Rigopoulos *et al.*, 2006, 2010) and it indicates that the resistance of the peridotites in attrition and grinding is a linear function of their strength.

Moreover, rather poor correlation exists between LA and $Is_{(50)}$, which are related through the equation:

$$Is50 = 0.2550 \times LA + 8.091, \; R^2 = 0.2468$$

This negative correlation suggests generally that the less resistant to abrasion and attrition rocks are also weaker under point load. However, other factors are likely involved in order to explain the poor

relationship. Although the degree of alteration is a dominant factor that exerts a negative influence on the LA and $Is_{(50)}$ values, as it has been described by several authors (e.g. Rigopoulos, 2006), the differential impact of joints on the two tests, cannot be ignored. As it was mentioned above LA is not affected by the presence of joints, however, these definitely affect negatively the $Is_{(50)}$ values of the rocks(Fig. 4b). Hence, it is concluded that the combined effect of alteration and jointing is responsible for the poor correlation shown by LA and $Is_{(50)}$ tests.

Uniaxial compression strength and point load index show a moderate correlation which can be described by the equation (Fig. 4c):

$UCS = 0.0543 \times Is50 - 0.8874$, $R^2=0.3809$

Similar positive correlations have been observed also for other ultramafic rocks and several authors have recommended that there is a direct and strong correlation between these two mechanical parameters in rocks (Kurtulus *et al.*, 2011), hence an indirect estimation of one from the other can be made. The moderate correlation shown for the Gerania peridotites indicates that such an estimation involves large errors. This may also be explained by the presence of dense joints and mainly their variable orientation may lead to largely different results particularly for the point load test in the same sample. Mechanical weakness is also largely affected by the presence of actinolite, which is a hard mineral but shows a brittle behavior under stress due to its fibrous crystal habit and its very good cleavage along (110) planes (Rigopoulos *et al.*, 2009). Thus the presence or not and the variable amounts of actinolite in the secondary assemblage of the investigated peridotites is another factor that prevents a good correlation between mechanical properties of the rocks.

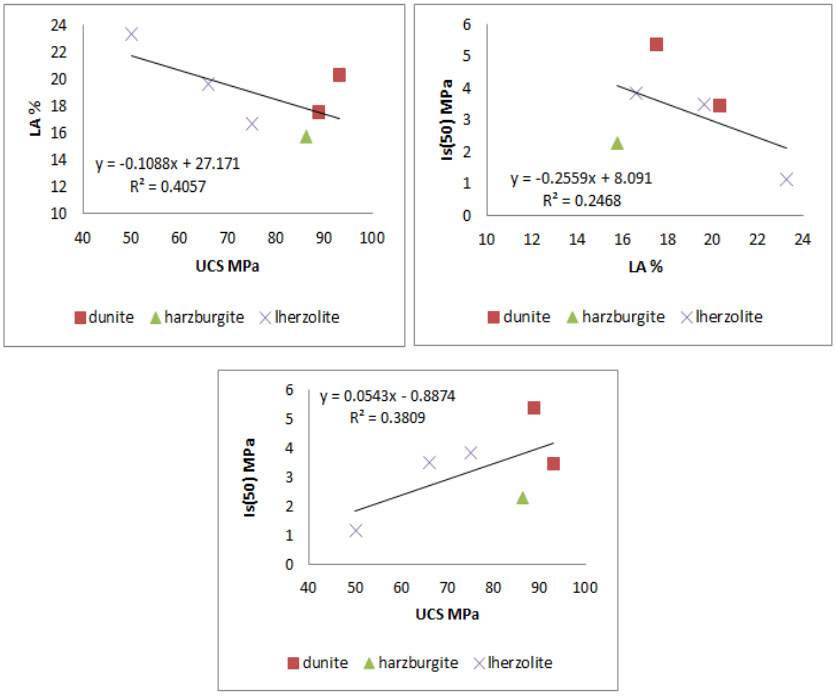

Figure 4 - Correlation of mechanical properties of ultramafic rocks from Gerania: (a) Uniaxial compressive strength (UCS) vs. Los Angeles abrasion value (LA), (b) LA vs. point load index (Is (50), (c) UCS vs. Is (50).

6. Conclusions

- Increasing serpentinization and ocean floor alteration affects negatively the mechanical performance of ultramafic rocks.
- Rocks which contain laminate and soft minerals like chlorite and talc or hard but very brittle phases like actinolite present worse mechanical properties.
- Brittle deformation of rocks affect variably their mechanical strength but it does not play an important role to their resistance to abrasion, attrition and grinding of rocks as the shape of the aggregates is controlled and determined by the original planes of weakness in the rocks.
- Study of the microtextural and mineralogical characteristics of rocks is a determinant factor for the prediction of their mechanical behaviour.

7. References

Akesson, U., Lindqvist, J.E., Göransson, M. and Stigh, J., 2001. Relationship between texture and mechanical properties of granites, central Sweden, by use of image-analysing techniques, *Bull. Eng. Geol. Environ*., 60, 277-284.

Al-Oraimi, S.K., Taha, R. and Hassan, H.F., 2006. The effect of the mineralogy of coarse aggregate on the mechanical properties of high-strength concrete, *Constr. Build. Mater*., 20, 499-503.

Bornovas, J., Gaitanakis, P. and Spiridopoulos, A., 1984. Geological Map of Greece, 1:50000, Perachora sheet, IGME.

Clément, B., 1971. Découverte d'un flysch éocrétacé en Béotie (Grèce continentale), *CR Acad. Sci*., 272, 791-792.

Clément, B., 1983. Evolution géodynamique d'un secteur des Hellénides internes: l'Attique-Béotie (Gréce continentale), Thesis Univ Lille I (unpublished).

Danelian, T. and Robertson, A.H.F., 1998. Palaeogeographic implications of the age of radiolarian-rich sediments in Beotia (Greece), *Bull. Geol. Soc. Greece*, 32, 21-29.

Dilek, Y., Furnes, H. and Shallo, M., 2007. Suprasubduction zone ophiolite formation along the periphery of Mesozoic Gondwana, *Gondwana Res*., 11, 453-475.

Kaplanis, A., Koukouvelas, I., Xypolias, P. and Kokkalas, S., 2012. Kinematics and Ophiolite obduction in the Gerania and Helicon Mountains, Central Greece, *Tectonophysics*, 215-234.

Kurtulus, C., Bozkurt, A. and Endes, H., 2011. Physical and Mechanical Properties of Serpentinized Ultrabasic Rocks in NW Turkey, *Pure Appl. Geophys*.

Lundqvist, S. and Göran, M., 2001. Evaluation and interpretation of microscopic parameters versus mechanical properties of Precambrian rocks from the Stockholm region, Sweden. *In*: *Proceedings of 8th Euroseminar on microscopy applied to building materials*, 4-7 Sept, Athens.

Miskovsky, K., Taborda Duarte, M., Kou, S.Q. and Lindqvist, PA., 2004. Influence of the mineralogical composition and textural properties on the quality of coarse aggregates, *J. Mater. Eng. Perform*., 13, 144-150.

Pomonis, P., Rigopoulos, I., Tsikouras, B. and Hatzipanagiotou, K. 2007. Relationships between petrographic and physico-mechanical properties of basic igneous rocks from the Pindos ophiolitic complex, NW Greece, *Bull. Geol. Soc. Greece*, 40, 947-958.

Rigopoulos, I., Tsikouras, B., Pomonis, P. and Hatzipanagiotou, K. 2006. Comparative Evaluation of Dolerites from the Pindos and Vourinos Ophiolitic Rocks for their Use as Aggregates, *Tech. Cron. Sci. J. TCG*, I, No 3.

Rigopoulos, I., Tsikouras, B., Pomonis, P. and Hatzipanagiotou, K. 2010. The influence of alteration on the engineering properties of dolerites: the examples from the Pindos and Vourinos ophiolites (northern Greece), *Int. J. Rock Mech. Min. Sci*., 47, 69-80.

Tamrakar, N.K., Yokota, S. and Shrestha, S.D. 2007. Relationships among mechanical, physical and petrographic properties of Siwalik sandstones, Central Nepal Sub-Himalayas, *Eng. Geol*., 90, 105-123.

Tuğrul, A. and Zarif, I.H., 1999. Correlation of mineralogical and textural characteristics with engineering properties of selected granitic rocks from Turkey, *Eng. Geol*., 51, 303-317.
Vacondios, I., 1997. Etude metallogenique des chromites liees aux ophiolites de type Mediterranee occdentale ou orientale: le chromites de Tinos et des Gerannees, Ph.D. thesis, Patras, 98 pp.
Zorlu, K., Ulusay, R., Ocakoglu, F., Gokceoglu, C. and Sonmez, H., 2004. Predicting intact rock properties of selected sandstones using petrographic thin-section data, *Int. J. Rock Mech. Min. Sci*., 41(1), 93-98.

Δελτίο της Ελληνικής Γεωλογικής Εταιρίας, τόμος L, σελ. 1838-1848
Πρακτικά 14ου Διεθνούς Συνεδρίου, Θεσσαλονίκη, Μάιος 2016

Bulletin of the Geological Society of Greece, vol. L, p. 1838-1848
Proceedings of the 14th International Congress, Thessaloniki, May 2016

MUDPOTS AT STEFANOS HYDROTHERMAL CRATER OF NISYROS VOLCANO. AN INSIGHT AT THE HYDROTHERMAL PROCESSES OF AN ACTIVE VOLCANO

Kanellopoulos C.[1*] and Xirokostas N.[2*]

[1]*Geologist, Ph.D., ckanellopoulos@gmail.com*

[2]*Chemical Engineer, Ph.D., nikosxirokostas@yahoo.com*

**Institute of Geology and Mineral Exploration, 1st Spirou Louis St., Olympic Village, 13677, Acharnae, Greece*

Abstract

On Nisyros island as a result of the volcanic activity and active tectonic, a hydrothermal system develops and it is expressed by 5 types of surface manifestations: i) thermal springs, ii) fumaroles iii) hydrothermal craters, iv) hot grounds and v) mudpots. In general, a mudpot could be described as an acidic hot spring and fumarole with limited water which it is formed in high-temperature geothermal areas. Water sample and depositions of mudpots collected, analyzed and studied from Stefanos hydrothermal crater, which is the only site on Nisyros Island, where mudpots occur. Mudpots water is very acidic (pH=2.4), with high sulfate concentration (1375mg/L), due to the $H_2S_{(gas)}$ and temperature near the boiling point. As a result, elemental sulfur is found inside the depositions alongside with products of the hydrothermal alteration of the surrounding rocks. In the water and in the depositions were found high concentrations in several elements (e.g. in water: 55mg/L Fe; 19.5mg/L Zn, in depositions: 430mg/Kg Pb; 72mg/Kg Cu; 60mg/Kg Cr) reflecting the alterations processes which are taking place.

Keywords: *mudpots, hydrothermal systems, volcano, Nisyros, Greece.*

Περίληψη

Στο νησί της Νισύρου, σαν αποτέλεσμα της ηφαιστειακής δραστηριότητας και των ενεργών τεκτονικών διεργασιών, αναπτύσσεται ένα υδροθερμικό σύστημα, το οποίο παρουσιάζει πέντε τύπων επιφανειακές εκδηλώσεις: α) θερμές πηγές, β) ατμίδες γ) υδροθερμικούς κρατήρες, δ) θερμά εδάφη και ε) αναβράζουσες ηφαιστειακές λίμνες λάσπης. Οι αναβράζουσες ηφαιστειακές λίμνες λάσπης μπορούν να περιγραφούν και σαν όξινες θερμές πηγές ή ατμίδες, με περιορισμένη ποσότητα νερού, σε υψηλής θερμοκρασίας ηφαιστειακά περιβάλλοντα. Κατά την παρούσα μελέτη, ελήφθησαν δείγματα νερού και αποθέσεων από τον υδροθερμικό κρατήρα του Στέφανου. Η περιοχή του κρατήρα είναι το μόνο σημείο στο οποίο εμφανίζονται αναβράζουσες ηφαιστειακές λίμνες λάσπης στη Νίσυρο. Το νερό είναι ιδιαιτέρα όξινο (pH=2.4), με υψηλές συγκεντρώσεις θεϊκών (1375mg/L), λόγω του αερίου H2S) και θερμοκρασία κοντά στο σημείο βρασμού. Αποτέλεσμα του γεγονότος αυτού είναι η δημιουργία του στοιχειακού θείου σε κρυστάλλους που εντοπίζεται στις αποθέσεις. μαζί με προϊόντα της υδροθερμικής εξαλλοίωσης των περιβαλλόντων πετρωμάτων. Κατά τη χημική ανάλυση του νερού και των αποθέσεων εντοπίστηκαν υψηλές συγκεντρώσεις σε μια σειρά

στοιχείων (π.χ. στο νερό: 55mg/L Fe; 19.5mg/L Zn, στις αποθέσεις: 430mg/Kg Pb; 72mg/Kg Cu; 60mg/Kg Cr) σαν αποτέλεσμα των διεργασιών της υδροθερμικής εξαλλοίωσης που λαμβάνει χώρα στην περιοχή.
Λέξεις κλειδιά: *αναβράζουσες λίμνες λάσπης, υδροθερμικά συστήματα, ηφαίστειο, Νίσυρος, Ελλάδα.*

1. Introduction

Nisyros Island is located in southeastern part of Aegean Sea and geologically belongs to the South Aegean active volcanic arc. The whole island forms a calc-alkaline stratovolcano, which is built at various explosive activities in the last 150,000 years; it has a 3.8 km diameter caldera (Di Paola, 1974; Keller *et al*., 1990; Vougioukalakis, 1993; Francalanci *et al*., 1995) and is currently classified in the "Very High Threat" category (Kinvig *et al*., 2010).

As a result of the volcanic activity and active tectonic, a hydrothermal system occurs. The presence of hydrothermal activity on Nisyros is expressed by five types of surface manifestations: i) the thermal springs distributed along the northern and southern coasts of the island, ii) the large fumarolic field located mainly in the southern Lakki plain, iii) the hydrothermal craters, iv) the hot grounds and v) the mudpots located in the center of Stefanos hydrothermal crater (Fig. 1, 2). In the Lakki area, different hydrothermal eruptions took place recently until the historical times (Marini *et al.*, 1993). Also, changes in the composition of the fumaroles recorded recently (1995-1998) and they were associated with episodes of intense seismicity and ground deformation (Chiodini *et al*., 2002; Caliro *et al*., 2005; Shimizu *et al*., 2005), during a volcanic unrest period.

In general, mudpot or mud pool could be described as an acidic hot spring or a fumarole with limited water. It usually takes the form of a pool of bubbling mud. The acid fluids and microorganisms alter the surrounding rock into clay and mud. The mud of a mudpot usually takes the form of a viscous, often bubbling slurry. As the boiling mud is often squirted over the brims of the mudpot, a sort of mini-crater of mud could build up (Clynne *et al.*, 2003).

Mudpots are forming high-temperature geothermal areas where water is in short supply. The little water that is available rises to the surface usually at spots where are rich in volcanic ash, clay and other fine particulates. The thickness of the mud usually changes along with meteoric phenomena, i.e. rain. On Nisyros Island mudpots were detected only at Stefanos hydrothermal crater (Fig. 2) and their size depends on climate conditions i.e. the rain in the Stefanos and surrounding plain and caldera area.

The aim of this paper is to study the chemical composition of the mudpots and the mineralogical and geochemical composition of their depositions and relate them with the hydrothermal processes of Nisyros volcano.

2. Geological setting

Nisyros island (42 km^2 in surface) is a small and young composite volcano with a central caldera (Keller, 1971; Di Paola, 1974; Vougioukalakis, 1984, 1993; Limburg, 1986; Limburg *et al*., 1986; Bohla and Keller, 1987; Lodise, 1987; Seymour and Vlassopoulos, 1992; Wyers and Barton, 1989; Keller *et al*., 1990; Papanikolaou *et al*., 1991; Limburg and Varekamp, 1991; Gansecki, 1991; Francalanci *et al*., 1995; Volentik *et al*., 2002) (Fig. 1). The topography resembles the shape of a truncated cone with a basal diameter of 8 Km and a central caldera depression of 4 Km diameter. The post-caldera domes (youngest volcanic products) excel the caldera rim (~ 450 m high) and the internal domes arrive at a maximum height of 698 m. The whole island is entirely buildup of volcanic products, deposited on a basement consisting of Mesozoic limestone and Neogene sediments (Barberi *et al*., 1988; Varekamp, 1992; Nis-1 well report - Geotermica Italiana, 1983).

Two eruptive cycles are distinguished in the evolution of Nisyros volcanic activity: the first cycle includes the cone-building eruptive activity and the second one the caldera-forming eruptive activity. The second cycle consists of two different phases. Each phase commenced with a low intensity - low magnitude phreato-magmatic explosion fed by rhyolitic magmas. This triggered a central calderic collapse that was followed by extrusion of rhyolitic-dacitic domes and lava flows.

The existing radiometric ages (K-Ar, ^{14}C), tephro-stratigraphy and the absence of the Kos Plateau Tuff deposits suggest that the actual subaerial part of Nisyros was built up during the last 160,000 years. The available radiometric ages of Nisyros rocks are difficult to correlate and still leave some open questions about the time frame of volcanic eruption. K/Ar ages of 66.4 and 24 ka were obtained on the uppermost products of the cone building activity (Rehren, 1988). According to these data, the earliest caldera collapse should have an age < 24 ka. Nevertheless, ages > 44 ka were obtained with different methods for the Nisyros Upper Pumice deposits, whereas the age of the Yali Upper Pumice that postdate the last Nisyros caldera collapse is 31 ka (Yali C deep ash layer of Federman and Carey, 1980).

All the historically registered explosions at Nisyros (1873-1887) are hydrothermal and created three small craters in the west area of the caldera floor (Gorceix, 1873, 1874; Martelli, 1917). The presence of more than 8 older hydrothermal explosion craters in the caldera floor, with a maximum diameter of 300m, indicate that this type of activity was frequent in the past few thousand years. The island is today a site of intense hydrothermal activity which feed many fumaroles in the caldera floor area and hot springs along the coast, hosting a high enthalpy geothermal field (fluids with more than 400^{o}C at 1800m depth; Geotermica Italiana, 1983).

Active tectonics is prominent on the Nisyros island group. Some of the active faults have been reactivated during seismic crisis manifested in the last century. During the last 1995-1997 volcanic unrest shallow earthquake activity, two of these fractures trending N-S and NW-SE were opened on Nisyros and Yali, respectively (Vougioukalakis *et al*., 1998).

Nisyros is characterised by a nearly continuous series of rocks, from basaltic andesites to rhyolites. Basaltic andesites and most of andesites are CA, whereas dacites and rhyolites plot along the boundary between CA and HKCA series.

3. Materials and methods

3.1. Groundwater and depositions sampling and analysis

From mudpots, which are located at the Eastern part of Stefanos hydrothermal crater (Fig. 2), one hot groundwater sample and several wet and dry samples from the depositions were collected. The groundwater sample was vacuum filtered and stored in polyethylene bottles and preserved in a refrigerator. Part of it was acidified to a final concentration of 2% nitric acid. Sampling was conducted on June 2015.

About the groundwater sample, the major elements and ion concentrations were measured by spectrophotometry, or/and titration or/and AAS or and ICP-OES (Table 1). The trace element concentrations were measured using ICP-MS (Table 1).

Depositions from active (wet) and dry mudpots were collected. The deposition samples were dried in an oven at a temperature of 40^{o}C and afterwards pulverized to <200 mesh in an agate mill. Representative samples were digested with a mixture of HCl-HNO_3-HF acids and were analysed for a series of trace elements by ICP-MS and a series of major elements by ICP-OES after fusion. In order to determine the mineralogical composition of the samples, a number of thin sections were prepared and investigated under optical microscope and powder X-ray diffraction (XRD) analyses were conducted. The XRD study was carried out using a Philips X'Pert Panalytical X-ray diffractometer, operating with Cu radiation at 40 kV, 30 mA, 0.020^{o} step size and 1.0 s steptime. The XRD patterns were evaluated using the EVA ver. 11 software. All samples were analyzed in the Laboratories of Institute of Geology and Mineral Exploration (I.G.M.E.) in Athens.

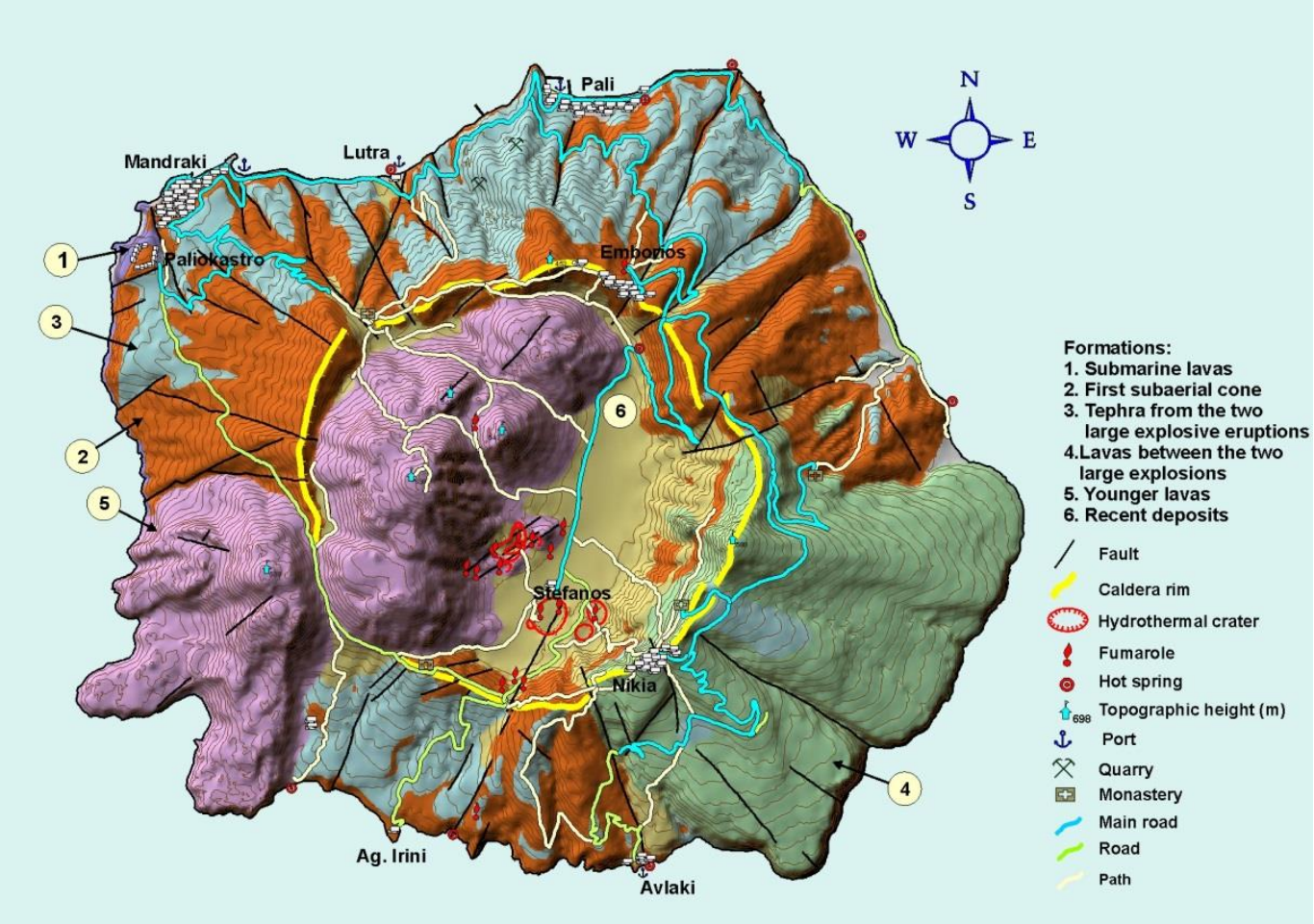

Figure 1 - 3D simplified geological map of Nisyros Island (Vougioukalakis and Androulakakis, 2008).

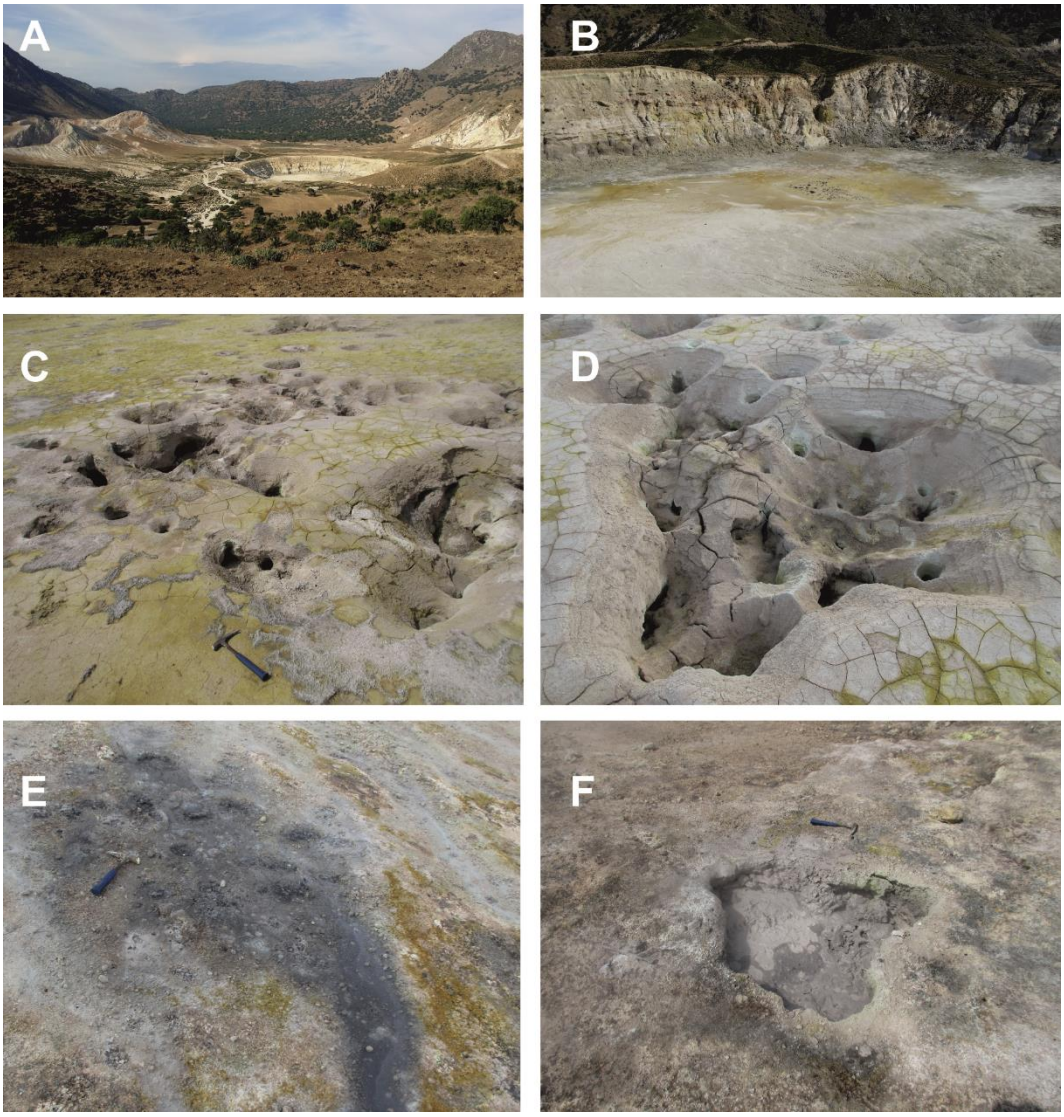

Figure 2 - (A) General view of the Nisyros caldera from the North. (B) General view of the Stefanos hydrothermal crater, with characteristic white-yellowish altered rocks. (C) and (D) Dry mudpots. (E) Steaming ground with limited water supply. (F) Active boiling mudpot.

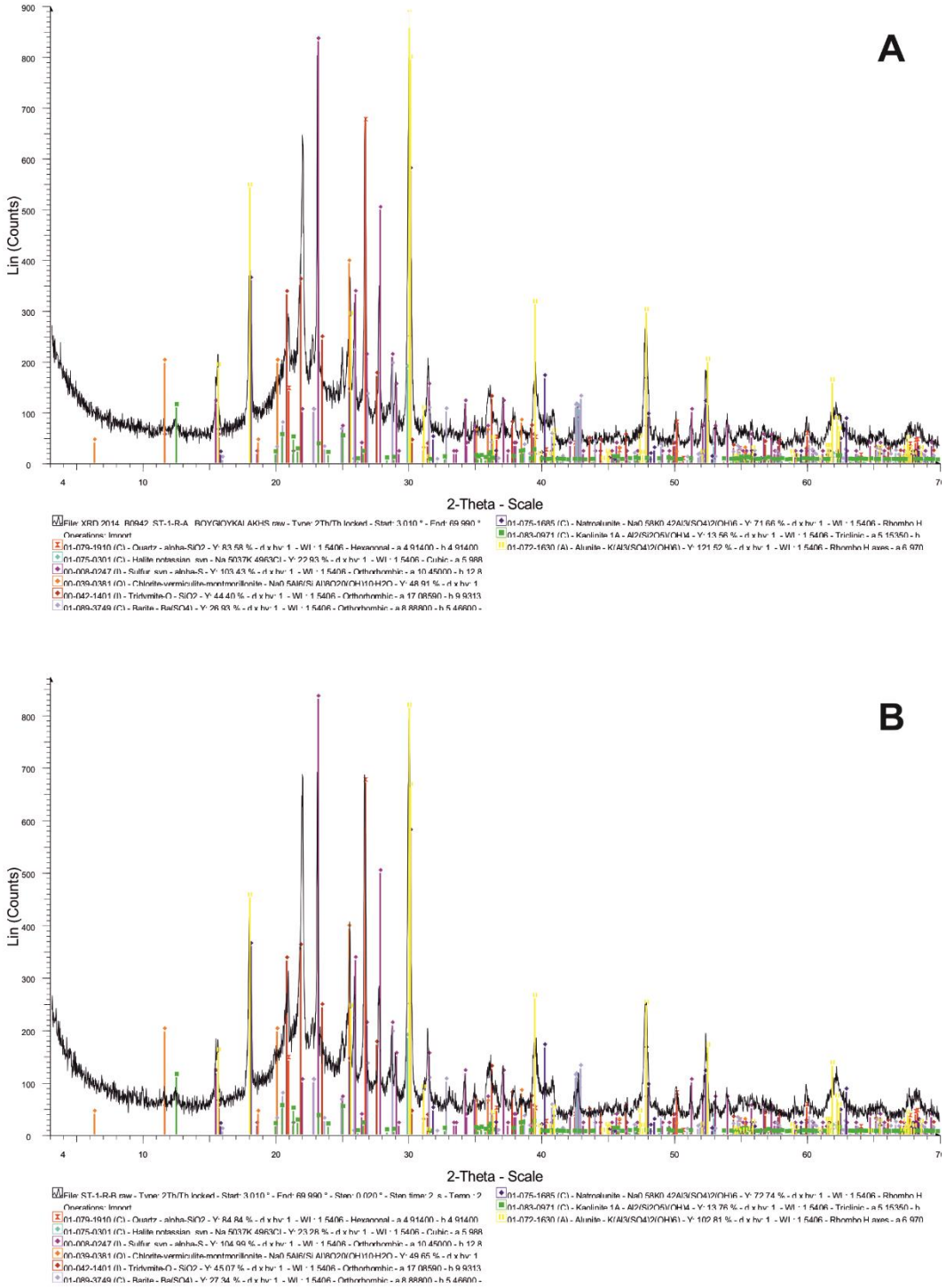

Figure 3 - Evaluated XRD pattern from mudpot depositions of Nisyros.

Table 1 - Concentrations of major and trace elements in water sample.

		ST-1-W
pH		2.4
Al	**mg/L**	72
Ca	**mg/L**	190
Mg	**mg/L**	10.1
Na	**mg/L**	21.2
K	**mg/L**	2.74
HCO_3	**mg/L**	bld
Cl	**mg/L**	4.25
SO_4	**mg/L**	1375
NO_2	**mg/L**	<0,050
NO_3	**mg/L**	<5,0
NH_4	**mg/L**	70.5
SiO_2	**mg/L**	277
Ag	**µg/L**	<5
As	**µg/L**	<100
B	**µg/L**	41
Ba	**µg/L**	16
Be	**µg/L**	<5
Br	**µg/L**	-
Cd	**µg/L**	<5
Co	**µg/L**	<10
Cr	**µg/L**	40
Cu	**µg/L**	<10
F	**µg/L**	1340
Fe	**µg/L**	55000
Hg	**µg/L**	<0,5
I	**µg/L**	-
Li	**µg/L**	11
Mn	**µg/L**	190
Mo	**µg/L**	<10
Ni	**µg/L**	26
Pb	**µg/L**	9
Rb	**µg/L**	60
Sb	**µg/L**	<5
Se	**µg/L**	11
Sr	**µg/L**	480
U	**µg/L**	<5
V	**µg/L**	120
Zn	**µg/L**	19500

Table 2 - Concentrations of major and trace elements in deposition samples.

		ST-1-A-R	ST-1-B-R
SiO_2	**%**	52.35	52.65
Al_2O_3	**%**	1.95	2
Fe_2O_3	**%**	0.25	0.15
CaO	**%**	0.1	0.1
MgO	**%**	<0,01	<0,01
TiO_2	**%**	0.25	0.25
MnO	**%**	<0,01	<0,01
K_2O	**%**	1.6	1.55
Na_2O	**%**	1.8	0.95
S	**%**	14.7	14.7
L.O.I.	**%**	26.7	26.7
V	**mg/Kg**	92	86
Cr	**mg/Kg**	56	60
Co	**mg/Kg**	1	1
Ni	**mg/Kg**	14	16
Cu	**mg/Kg**	72	44
Zn	**mg/Kg**	35	29
As	**mg/Kg**	37	22
Rb	**mg/Kg**	12	18
Sr	**mg/Kg**	300	275
Mo	**mg/Kg**	5	5
Cd	**mg/Kg**	<1	<1
Ba	**mg/Kg**	1290	1150
Pb	**mg/Kg**	430	400
U	**mg/Kg**	1	1
Sc	**mg/Kg**	7	7
Y	**mg/Kg**	7	7
La	**mg/Kg**	14	15
Ce	**mg/Kg**	26	27
Pr	**mg/Kg**	3	3
Nd	**mg/Kg**	10	10
Sm	**mg/Kg**	3	3
Eu	**mg/Kg**	1	1
Gd	**mg/Kg**	2	2
Tb	**mg/Kg**	<1	<1
Dy	**mg/Kg**	1	1
Ho	**mg/Kg**	<1	<1
Er	**mg/Kg**	<1	<1
Tm	**mg/Kg**	<1	<1
Yb	**mg/Kg**	<1	<1
Lu	**mg/Kg**	<1	<1
Th	**mg/Kg**	5	5

4. Analytical results

The analysed chemical parameters are presented in Table 1 and 2. The studied water sample is very acidic (pH = 2.4) with high concentration of sulfate (1375 mg/L), silica (277 mg/L SiO_2), calcium (190 mg/L) and aluminum (72 mg/L). It presents also high concentrations of metallic elements like Fe (55 mg/L) and Zn (19.5 mg/L).

The mineralogical and geochemical compositions of depositions, from the active and dry mudpots, are similar. The mineralogical composition of the depositions is quartz, tridymite, alunite, elemental sulfur, chlorite-vermiculite-montorillonite, kaolinite, barite and halite (Fig. 3). The bulk geochemical analysis (Table 2) of the studies depositions shown high concentrations to major elements like 55 % to SiO_2 and 14.7 % to S and between 1 to 2 % to Al_2O_3, K_2O and Na_2O. High concentrations were found in a series of trace elements and some REE like Pb (up to 430 mg/Kg), Cu (up to 72 mg/Kg), Cr (up to 60 mg/Kg), As (up to 37 mg/Kg), Zn (up to 35 mg/Kg), Ni (up to 16 mg/Kg), Ce (up to 27 mg/Kg), La (up to 15 mg/Kg), Nd (up to 10 mg/Kg) and Th (up to 5 mg/Kg).

5. Discussion - conclusions

Nisyros Island is young composite volcano with a central caldera. Underneath, it develops a hydrothermal system, with circulation of meteoric and sea water. Surface manifestations of the hydrothermal system are the hot springs, the fumaroles, the hydrothermal craters, the hot grounds and the mudpots. The present study shows and evaluates for the first time the chemical composition of the active mudpots of Nisyros and the mineralogical and geochemical composition of their depositions.

On Nisyros, meteoric and sea water goes deep underground using permeable rock, fractures, fault systems and boundaries between volcanic flows. Once deep underground, the water is heated. The heat source is a body of magma or a body of solid but still very hot rock related to recent quite active volcanism. This heat source is probably located at a depth of 4-6 km. When water penetrates the hot rock surrounding the heat source, it is heated by conduction. Hydrochloric acid, sulfurous gases and other volatiles emitted by the body of magma or hot rock dissolve in the water as it is heated. Because it is less dense than cold water, the heated water rises by convection. As the water rises, acids react with surrounding rocks, enriching the water in dissolved silica (SiO_2) and metals. The chemically evolving hot water rises, where it saturates permeable rock and accumulates in fractures beneath the thermal features creating a geothermal reservoir. Based on the two deep geothermal wells drilled on the island by PPC (Public Power Company, Geotermica Italiana, 1983, 1984; Marinelli *et al*., 1983; Chiodini *et al*., 1993) two main hot aquifers were identified. The first one in ~250-700 m and the second one from ~1000 to 1500 m depth, with temperatures 120-180 ºC and 290 °C respectively (Marini *et al*., 1993; Ambrosio *et al*., 2010).

When rising hot water reaches a depth where the pressure of overlying fluid (hydrostatic pressure) has decreased, boiling occurs. Bubbles of steam rise through the water and migrate to the surface, carrying most of the gases that were dissolved in the water (carbon dioxide, hydrogen sulfide, hydrogen, nitrogen and helium).

Steam and non-condensable gasses reaches the surface through fractions and creates the fumaroles. It may also condense and heat groundwater near the surface. The condensed steam and heated water may boil at the water table, creating the boiling mudpots. Hydrogen sulfide gas is oxidized in this near-surface, oxygen-rich environment to form elemental sulfur and sulfuric acid, producing waters that are acidic (low pH) and have a high sulfate concentration. Stefanos mudpots water have pH = 2.4, 1375 mg/L of sulfate and temperature near the boiling point. Also, hydrogen sulfide gas is one of the main components of the fumaroles in Nisyros volcano (Teschner *et al*., 2005; Tassi *et al*., 2013). For that reason, also the studied water present very high sulfate concentration (1375 mg/L) and crystals of elemental sulfur found inside the studied depositions. The water is also enriched in

dissolved silica (277 mg/L SiO_2) and metals (e.g. 55 mg/L Fe; 19.5 mg/L Zn). High concentrations of major and trace elements like Ca (190 mg/L), Al (72 mg/L), Sr (480 μg/L) etc reflecting the alterations processes which are taking place.

Inside Stefanos hydrothermal crater characteristic is the view of white-yellow altered rocks (Fig. 2A, B, C). Hydrothermal alteration occurs when acidic hot water chemically changes minerals in rocks. The final product of such alteration in volcanic rocks is usually white material rich in kaolinite clay and silica; this material is abundant at Nisyros caldera and especially at Stefanos hydrothermal crater. More specifically, the mineralogical study reveals that the studied depositions comprise of quartz, tridymite, alunite, elemental sulfur, chlorite-vermiculite-montorillonite, kaolinite, barite and halite as main mineral phases. In agreement to the mineralogical results are the results of the chemical analysis. The highest concentrations are presented to SiO_2 and S (52 % and 14.7 % respectively) and follow Al_2O_3, K_2O and Na_2O with concentrations between 1 to 2 %. It is interesting the enrichment of the depositions in metals like Pb (up to 430 mg/Kg), Cu (up to 72 mg/Kg), Cr (up to 60 mg/Kg), As (up to 37 mg/Kg), Zn (up to 35 mg/Kg), Ni (up to 16 mg/Kg) and in some REE like Ce (up to 27 mg/Kg), La (up to 15 mg/Kg), Nd (up to 10 mg/Kg) and Th (up to 5 mg/Kg).

Even though the presented data are limited, allow as insights of the hydrothermal processes of Nisyros volcano. In order to have a better picture, a further more systematic study of the mudpots is needed i.e. including chemical and isotopic analysis of the gas and isotopic analysis of the water. Several studies have conducted concerning Nisyros, but still many open questions remain to be answered. More data concerning the reservoir, the circulation and the composition of the fluid below the surface will be valuable. They could reveal the detail hydrothermal processes which are taking place and allow us to compare them with old-not active systems, estimate geothermal potentials of the system etc. Also, the surface manifestations of the system create an extreme environment in which unstudied geological and biological processes take place alongside.

6. Acknowledgements

This study was funded by the National Strategic Reference Framework (NSRF, 350913). The authors would like to thank Dr. George Vougioukalakis who critically commented on an earlier version of this manuscript and the local population for their co-operation during the field work.

7. References

Ambrosio, M., Doveri, M., Fagioli, M., Marini, L, Principe, C. and Raco, B., 2010. Water-rock interaction in the magmatic-hydrothermal system of Nisyros Island (Greece), *J. Volcanology and Geothermal Research*, 192, 57-68.

Bohla, M. and Keller, J., 1987. Petrology of plinian eruptions of Nisyros volcano, Hellenic arc, *Terra cognita*, 7, 171 pp.

Bohla, M. and Keller, J., 1987. Petrology of Plinian eruptions of Nisyros volcano, Hellenic Arc, *Terra Cognita*, 7, 171.

Bonadonna, C., Ernst, G.G.J. and Sparks, R.S.J., 1998. Thickness variations and volume estimates of tephra fall deposits: the importance of particle Reynolds number, *Journal of Volcanology and Geothermal Research*, 81, 173-187.

Caliro, S., Chiodini, G., Galluzzo, D., Granieri, D., La Rocca, M., Saccorotti, G. and Ventura, G., 2005. Recent activity of Nisyros volcano (Greece) inferred from structural, geochemical and seismological data, *Bull. Volcanol*., 67, 358-369.

Chiodini, G., Brombach, T., Caliro, S., Cardellini, C., Marini, L. and Dietrich, V., 2002. Geochemical indicators of possible ongoing volcanic unrest at Nisyros Island (Greece), *Geophys. Res. Lett.*, 29(16), doi: 10.1029/2001GL014355.

Clynne, M.A., Janik, C.J. and Muffler, L.P., 2003. "Hot Water" in Lassen Volcanic National Park-Fumaroles, Steaming Ground, and Boiling Mudpots, *U.S. Geological Survey Fact Sheet*, 101-02, 4 pp.

Di Paola, G.M., 1974. Volcanology and petrology of Nisyros Island (Dodecanese, Greece), *Bull. Volcanol*., 38, 944-987.

Federman, A.N. and Karey, S.N., 1980. Electron microprobe correlation of tephra layers from Eastern Mediterranean abyssal sediments and the Island of Santorini, *Quat.Res.*, 13, 160-171.

Francalanci, L., Varekamp, J.C., Vougioukalakis, G., Defant, M.J., Innocenti, F. and Manetti, P., 1995. Crystal retention, fractionation and crustal assimilation in a convecting magma chamber, Nisyros Volcano, Greece, *Bull. Volcanol*., 56, 601-620.

Gansecki, C., 1991. Petrology of the domes and inclusions of Nisyros volcano, Dodecanese island, Greece, BA Thesis, Wesleyan University, Middletown, CT, 97 pp.

Geotermica Italiana, 1983. Nisyros 1 geothermal well, Unpublished PPC-EEC report, 106 pp.

Geotermica Italiana, 1984. Nisyros 2 geothermal well, Unpublished PPC-EEC report, 44 pp.

Gorceix, M.H., 1873. Sur l' eruption boueuse de Nisyros, *Centre de Recherche Academie de Paris*, LXXVII(X, XI, XII), 1474-1477.

Gorceix, M.H., 1874. Sur l'etude des fumerolles de Nisyros et de quelques-uns des produits de l'eruption de 1873, *Centre de Recherche Academie de Paris*, LXXVIII(X,XII), 1309-1311.

Keller, J., 1971. The major volcanic events in recent eastern mediterranean volcanism and their bearing on the problem of Santorini ash layers, *Int. Sci. Congr. Volcano Thera*, 1, 152-169.

Keller, J., Rehren, T. and Stadlbauer, E., 1990. Explosive volcanism in the Hellenic Arc: a summary and review. *In*: Hardy, D.A., Keller, J., Galanopoulos, V.P., Flemming, N.C. and Druitt, T.H., *eds*., Thera and the Aegean World, *Proc. 3d Int. Congr*., The Thera Foundation, 13-26.

Kinvig, H.S., Winson, A. and Gottsmann, J., 2010. Analysis of volcanic threat from Nisyros Island, Greece, with implications for aviation and population exposure, *Natural Hazards Earth System Sciences*, 10, 1101-1113.

Limburg, E.M., 1986. Young pyroclastics on Nisyros, Greece: Physical studies, B.A. thesis, Wesleyan Un., Middletown, CT, 104 pp.

Limburg, E.M., Lodice, L. and Varekamp, J.C., 1986. Volcanology and Petrology of Nisyros, Greece. *In*: Sigurdson,H., Ed., Enviromental Impact of Volcanism, *Norman Watkins Symposium*, Un. of Rhode Island, Narrangansett, RI, 47-49.

Limburg, E.M. and Varekamp, J.C., 1991. Young pumice deposits on Nisyros, Greece, *Bull. Volc.* 54, 68-77.

Lodise, L., 1987. Petrology and geochemistry of Nisyros volcano (Dodecanese, Greece), MS Thesis, Wesleyan University, Mddletown, CT, USA, 245 pp.

Marini, L., Peincipe, C., Chiodini, G., Cioni, R., Fytikas, M. and Marinelli, G., 1993. Hydrothermal eruptions of Nisyros (Dodecanese, Greece). Past events and present hazard, *J. Volc. And Geothermal Research*, 56, 71-94.

Martelli, A., 1917. Il gruppo eruttivo di Nisiro nel mare Egeo, *Societa dei XL*, ser. 3, XX, 79-165.

Papanikolaou, D.J., Lekkas, E.L. and Sakellariou, D., 1991. Geological structure and evolution of the Nisyros Volcano, *Bull. Geol. Soc. Greece* XXV, 405-419 (In Greek, with English abstract).

Rehren, T., 1988. Geochemie und Petrologie von Nisyros, PhD thesis. Univ. Freiburg.

Seymour, K. and Vlassopoulos, D., 1992. Magma mixing at Nisyros volcano, as inferred from incompatible trace-elements systematics, *J. Volcanol. Geotherm. Res*., 50, 273-299.

Shimizu, A., Sumino, H., Nagao, K., Notsu, K. and Mitropoulos, P., 2005. Variation in noble gas isotopic composition of gas samples from the Aegean arc, Greece, *J. Volcanol. Geotherm. Res*., 140, 321-339.

Tassi, F., Vaselli, O., Papazachos, C.B., Giannini, L., Chiodini, G., Vougioukalakis, G.E., Karagianni, E., Vamvakaris, D. and Panagiotopoulos, D., 2013. Geochemical and isotopic changes in the fumarolic and submerged gas discharges during the 2011-2012 unrest at Santorini caldera (Greece), *Bulletin of Volcanology*, 75, 711.

Teschner, M., Vougioukalakis, G.E., Faber, E., Poggenburg, J. and Hatziyannis, G., 2005. Real time monitoring of gas-geochemical parameters in Nisyros fumaroles. *In*: Developments in Volcanology, 7, 247-254.

Varekamp, J.C.R., Kreulen, R., Poorter, R.P.E. and Van Bergen, M.J., 1992. Carbon sources and arc volcanism, with implications for the carbon cycle, *Terra Nova*, 4(3), 363-373, doi: 10.1111/j .1365-3121.1992.tb00825.x.

Volentik, A., Vanderkluysen, L. and Principe, C., 2002. Stratigraphy of the caldera walls of Nisyros volcano, Greece, *Eclogae Geol. Helv*., 95, 223-235.

Vougioukalakis, G. and Androulakakis, N., 2008. Presenting the Volcano of Nisyros. http://nisyros.igme.gr/nisyros/index.php?option=com_content&task=view&id=12&Itemid=26, Athens, IGME.

Vougioukalakis, G., 1984. Studio vulcanologico e chimico-petrografico dell'isola di Nisyros (Dodecanneso, Grecia), Tesi di laurea, Universita di Pisa.

Vougioukalakis, G., 1998. Blue volcanoes: Nisyros, Regional Council of Mandraki.

Vougioukalakis, G.E., 1993. Volcanic stratigraphy and evolution of Nisyros Island, *Bull. Geol. Soc. Greece*, XXVII, 239-258 (In Greek, with English abstract).

Wyers, G.P. and Barton, M., 1989. Polybaric evolution of calc-alkaline magmas from Nisyros, Southeastern Hellenic Arc, Greece, *J. Petrol*., 30, 1-37.

Δελτίο της Ελληνικής Γεωλογικής Εταιρίας, τόμος L, σελ. 1849-1858
Πρακτικά 14ου Διεθνούς Συνεδρίου, Θεσσαλονίκη, Μάιος 2016

Bulletin of the Geological Society of Greece, vol. L, p. 1849-1858
Proceedings of the 14th International Congress, Thessaloniki, May 2016

RESERVES ESTIMATION OF A MARBLE QUARRY USING QUALITY INDICATORS

Kapageridis I.[1] and Albanopoulos C.[2]

[1]*Technological Educational Institute of Western Macedonia, Department of Environmental and Pollution Control Engineering, Koila, 50100, Kozani, Greece, ikapa@teiwm.gr*

[2]*Iktinos Hellas SA, 11th Aeshilou St., 66100, Drama, Greece, albanopoulos@iktinos.gr*

Abstract

The use of standard estimation and modelling software tools in estimating marble quarry reserves poses a number of challenges. Marble quarry reserves are based on marble quality categories, almost unique for each quarry/deposit considered. These categories represent visual and physical aspects of marble such as colour, texture and fractures. Classification of marble to one of the categories is performed by experienced personnel and is based on samples much smaller in area than the blocks of marble which are potentially exploited. The available information is, also, mostly qualitative leading to further complications in the application of geomathematical estimation methods. The estimation of marble reserves described in this paper is based on interpolating quality indicator values from drillhole and quarry face samples to blocks in three dimensions. The procedure is applied in all working quarries of Iktinos Hellas SA and is based on Maptek Vulcan Quarry Modeller, a mine planning package adapted for quarrying. Its application and results is demonstrated using a case study from one of the quarries in NE Greece.
Keywords: *inverse distance weighting, quality indicators, reserves estimation, marble quarrying.*

Περίληψη

Η χρήση τυπικών εργαλείων λογισμικού εκτίμησης και μοντελοποίησης στην εκτίμηση αποθεμάτων λατομείων μαρμάρου παρουσιάζει κάποιες προκλήσεις. Τα αποθέματα λατομείων μαρμάρου βασίζονται σε κατηγορίες ποιότητας μαρμάρου, σχεδόν μοναδικές για κάθε εξεταζόμενο λατομείο/κοίτασμα. Οι κατηγορίες αυτές αποδίδουν οπτικές και φυσικές ιδιότητες του μαρμάρου όπως το χρώμα, την υφή και τα ραγίσματα. Η ταξινόμηση του μαρμάρου σε μια από τις κατηγορίες γίνεται από έμπειρο προσωπικό και βασίζεται σε δείγματα κατά πολύ μικρότερα σε εμβαδό από τα μπλοκ μαρμάρου που ενδεχομένως εκμεταλλεύονται. Οι διαθέσιμες πληροφορίες είναι, επίσης, κυρίως ποιοτικές γεγονός που οδηγεί σε επιπρόσθετες δυσκολίες στην εφαρμογή γεωμαθηματικών μεθόδων εκτίμησης. Η εκτίμηση αποθεμάτων μαρμάρου που περιγράφεται σε αυτή την εργασία βασίζεται στην παρεμβολή τιμών δεικτών ποιότητας από γεωτρητικά δείγματα και τομές στα μέτωπα του λατομείο σε μπλοκ τριών διαστάσεων. Η διαδικασία εφαρμόζεται σε όλα τα ενεργά λατομεία της Ικτίνος Ελλάς ΑΕ και βασίζεται στο Maptek Vulcan Quarry Modeller, ένα πακέτο μεταλλευτικού σχεδιασμού προσαρμοσμένου για λατομεία. Η εφαρμογή και τα αποτελέσματα της παρουσιάζονται μέσω ενός παραδείγματος εφαρμογής σε ένα από τα λατομεία στη ΒΑ Ελλάδα.
Λέξεις κλειδιά: *ζύγιση αντιστρόφου αποστάσεως, ποιοτικοί δείκτες, εκτίμηση αποθεμάτων, λατομεία μαρμάρου.*

1. Introduction

The reserves estimation procedure discussed in this paper concerns the Platanotopos quarry of Iktinos Hellas SA (Figure 1) - similar procedures are applied to the other quarries of the company. Specialised mine planning software (Maptek Vulcan Quarry Modeller) was used in all estimation and reporting stages. Data was provided by Iktinos Hellas SA personnel, including samples quality characterisation. A technical report was issued on behalf of Iktinos Hellas SA (Kapageridis, 2015). Similar computerised estimation efforts are reported by Forlani *et al.,* 2000, Careddu *et al.,* 2010, and Abdollahisharif *et al.,* 2012.

1.1. Location

The quarry area is located in the Municipal District of Platanotopos of the Piereon Municipality of Kavala Prefecture, approximately 1.5km NNE of the Platanotopos village and 2km SW of the Mesoropi village (Figure 1). The quarry area under exploration is 88.649m^2. The quarry area is in public forest land between 380 and 540m elevation covered by bushes, and administered by Kavala Prefecture Authorities and Kavala Forest Inspection Authorities.

Figure 1 - Location of Platanotopos quarry near Platanotopos village.

1.2. Geological Background and Production History

The area belongs to the Rodopi Metamorphic Mass, extending from Thrace to part of Central Macedonia, with characteristic metamorphic geological formations and in particular marble horizons (metamorphic limestones) with gneissic background. Generally, the wider area is characterised by horizons and outcrops of white - semi-white and grey marbles, locally subject to quarrying. In the quarry area we meet calcitic and dolomitic marbles, gneiss and gneissic schists. Calcitic marbles, gneiss and gneissic schists have no use and are not targeted for quarrying.

Interest is focused on dolomitic marbles which are enclosed and protected as a lens by alternating gneissic schist layers and calcitic marbles. The horizons orientation is constant with a bearing NNW-SSE and dipping between 25º-30º ESE. As already mentioned, marbles in the area are lens-like white dolomitic microcrystallic rocks (marbles). They are characterised as solid white fine grained, with evident spider net fractures which are red-yellow as they are filled with iron oxides and hydroxides.

This rare combination of white fine grained marble which is fractured and filled with secondary material which gives back the cohesion to the marble, constitutes this dolomitic appearance particularly interesting for quarrying. Marbles are solid and allow recovery of large healthy volumes, raising the level of recovery of the quarry and limiting the production of waste material. Close to

the surface, the marble deposit is covered by a weathered layer of marble, 1-2m thick, which has a low recovery factor for marketable marble.

Given the geological, mineralogical, and climate characteristics and the quarrying equipment of the quarry, production is scheduled for 7000-10000m^3 per annum and at this rate, the life of the quarry is estimated at 15 years. Marbles extracted are known as Golden Spider and are characterised as fine grain white dolomitic marble with spider net red-yellow fractures, filled with iron oxides and hydroxides (Figure 2). They present very good physical and mechanical properties and can take very fine polishing (Table 1). Historical production of the quarry is given in Table 2.

Figure 2 - Appearance of marble volumes of Platanotopos quarry.

Table 1 - Physical and chemical properties of marble from Platanotopos quarry.

Specific gravity	2.850	Bending strength (dry condition) DIN 52112	11.31
Open porosity factor wt% DIN 52102	0.60	Bending strength Mpa** (wet condition) DIN 52112	8.25
Absorption factor wt% DIN 52103	0.21	Compressive strength after freezing and thaw cycles	81.25
Elasticity Gpa ASTM C-170	42	Abrasion wearing mm DIN 52108	2.06
Compressive strength N/mm^2** (dry condition)DIN 52105	120.6	Impact strength cm UNI-U 32.07.248.0	29
Compressive strength N/mm^2** (wet condition) DIN	146.3	**1MPa=1N/mm^2 = 10.2kp/cm^2	

2. Marble Blocks Quality Characterisation

2.1. Colour and Texture

Quality grading of Golden Spider marble is initially based on colour and in the following categories: G - Golden, Y - Yellow, R - Red. Grading based on spider texture is in one of 4 categories as described in the following table. Colour and texture combinations are presented in Figure 3.

Table 2 - Production history of Platanotopos quarry between 2010-2014.

	2014		2013		2012		2011		2010	
	m^3	%	m^3	%	m^3	%	m^3	%	m^3	%
Extraction	77,617		92,668		89,929		73,533		34,618	
Production	13,494	17	20,657	22	19,905	22	21,151	29	13,409	39
A1	353	3	915	5	1,014	5	1,367	6	1,290	10
A2	1,835	14	2,136	10						
AB	3,423	25	3,981	19	4,684	24	5,135	24	4,100	31
B	7,246	54	11,509	56	10,011	50	8,833	42	5,630	42
BB	636	5	2,116	10	4,196	21	5,816	27	2,390	18

Table 3 - Volume texture categories of Platanotopos marbles.

1	Classic Spider, even net, clear background (classic type)
2	Relatively even spider with local strong concentrations (logs), or unclearly constructed net (few spiders) or very few areas of dense net (standard type)
3	Dense spider, or many continuous brown lines, (heavy type)
4	Absence of spider, many white parts or with minimum net, (white type)

2.2. Volume Defects

Based on defects (fractures, dendrite zones, brown lines, discolourings or marks etc.) each volume is classified using the 4 categories in Table 4 and final volume quality is assigned according to Table 5.

Table 4 - Categories based on defects of Platanotopos marble.

1	Solid volume with no evident defects or defects to less than 10% of each slab which is handled with a -3% or -6% discount
2	One or two defects up to 20-25% of each slab
3	Defects up to 30-35% of each slab
4	Defects up to 50% of each slab

Table 5 - Platanotopos marble quality based on defects and texture/colour categories.

Rectangular (Length >180, Height > 120)	**1** - No defects	**2** - Defects 25-35% of each	**3** - Defects 25-35% of each	**4** - Defects 35-50% of each
Classic type 1	1-1=A1	1-2=A2	1-3=AB	1-4=B
Standard type 2	2-1=A2	2-2=AB	2-3=B	2-4=BB
Heavy type 3	3-1=AB	3-2=B	3-3=BB	3-4=BB
White type 4	4-1=B	4-2=BB	4-3=BB	4-3=BB

1	Classic Spider, even net, clear background (classic type)
	
2	Relatively even spider with local strong concentrations (logs), or unclearly constructed net (fuzzy spider) or uneven zones of dense/coarse net, (standard type)
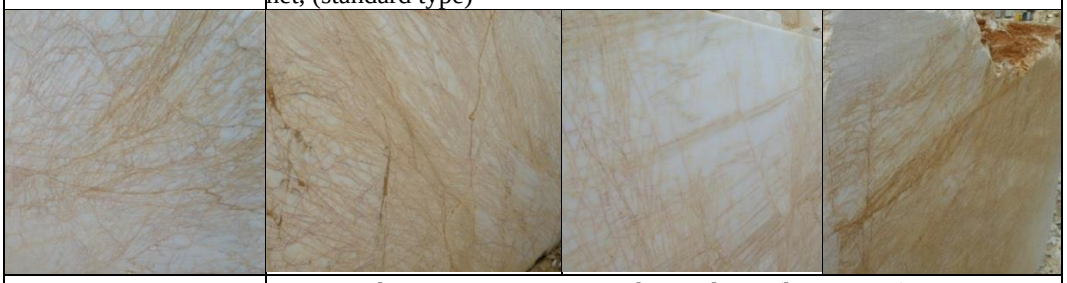	
3	Dense spider, or many continuous brown lines, (heavy type).
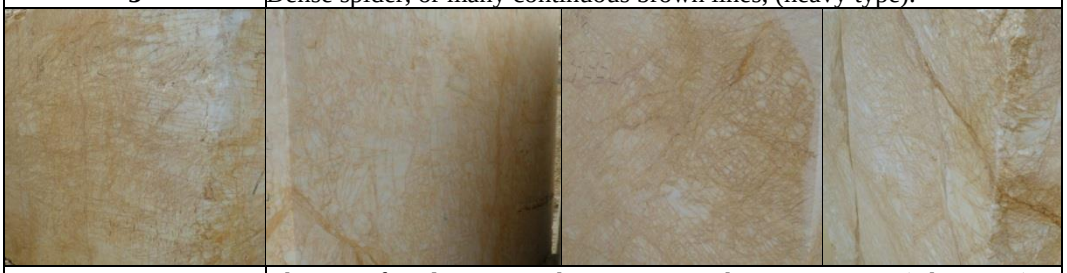	
4	Absence of spider, many white parts or with minimum net, (white type)
	

Figure 3 - Colour and texture categories of Platanotopos marbles.

3. Reserves Estimation Data

Data used in the reserves estimation of each quarry includes the original as well as the current topography of the quarry area based on the quarrying activities up to the date of the study. It also includes diamond drillhole samples and sections on quarry faces, which are analysed per meter as to the marble quality characteristics. A separate data folder was created for quarry with a separate database for topographical/vector data and one for drillhole/section data. An effort was made to maintain a systematic naming of all files of databases and models created during modelling and estimation. Topographical data were provided in AutoCAD™ (DWG, DXF) file format and were imported to Maptek Vulcan Quarry Modeller software and stored to appropriate layers. Drillhole data were provided in Microsoft Excel™ file format and were imported to specialised samples

databases in Maptek Vulcan Quarry Modeller. In the following paragraphs we discuss briefly the data provided for each quarry.

3.1. Topographical Data

For the Platanotopos quarry, two layers were provided with the minor and major contours every 4 and 20 meters respectively. The exploitation limits were given as a separate layer as shown in Figure 4. The contours covered an area much larger than the quarry area and had very good detail, suitable for reserves estimation. The current morphology of the quarry was also provided in two separate layers for crests and toes.

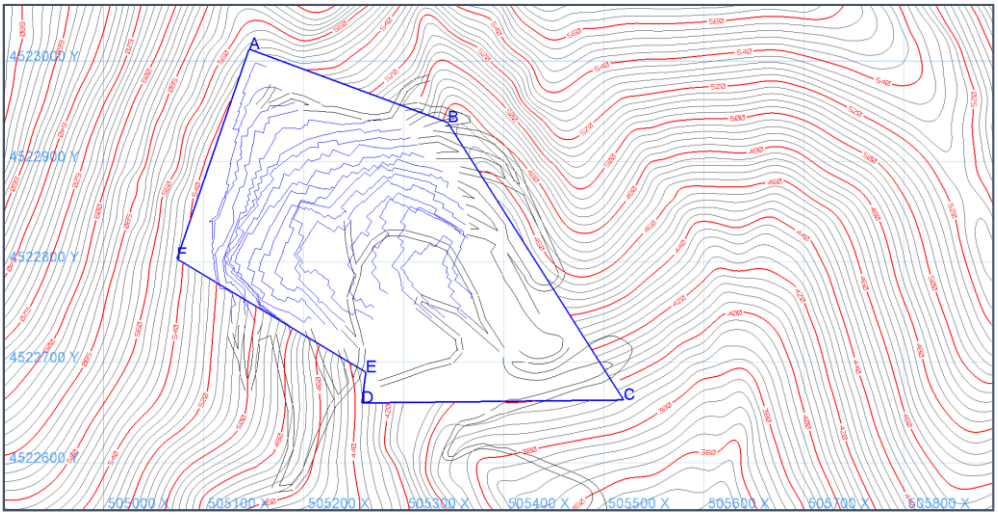

Figure 4 - Original topography contours, current pit and exploitation limits of the Platanotopos quarry.

3.2. Drillholes and Quarry Face Sections

A total of 92 drillholes and sections were provided for the Platanotopos quarry (47 sections and 45 drillholes), giving a total of 1,684 one-meter samples used in reserves estimation of the quarry. This data covers sufficiently the space of the estimated final excavation as show in the following figure. The data was validated using the software for collar location and overlapping intervals.

3.3. Quarry Volumetric Model

The estimated volume of the final excavation was designed per bench (level) starting from the existing quarry morphology. The design of each of the 16 benches was modelled as a solid triangulation which was used in reserves estimation (Figure 6). These solids were visually checked and validated using triangulation topology checks (self-crossing, opening, inconsistencies) to ensure that they can be used for valid volumetric calculations.

4. Methodology

4.1. Samples Database Processing

The drillhole and section samples database was configured with extra fields to allow the interpolation of arithmetic values in space. Specifically, fields were added which represent the different marble qualities based on original colour, texture, fracture and tectonism fields. These fields take only two values, 0 or 1, based on if whether the specific sample belongs or not to the particular marble quality, which is based on criteria which are specific for each quarry. As shown in

Figure 7, at the Platanotopos quarry, if a sample has lithology value LITHO = “SPIDER” and spider type SPTYP = 1 and fractures BACKRO = 1 then it belongs to quality A1.

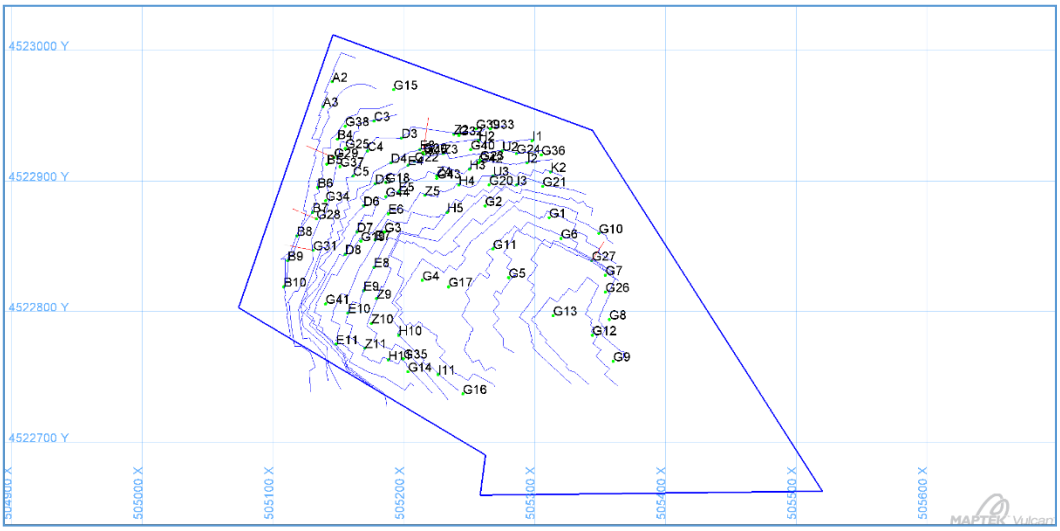

Figure 5 - Plan view of drillhole and face section locations.

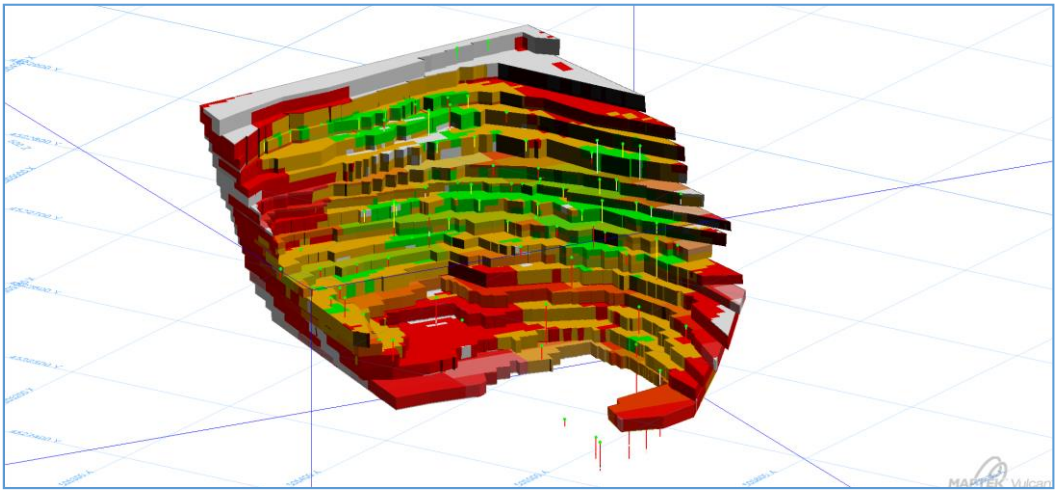

Figure 6 - Solid triangulation models of the final excavation benches of the Platanotopos quarry coloured by reserves classification (green = proved reserves, orange = probable reserves, red = inferred resources).

This logic leaves out of the definition of initial quality the large scale tectonism (represented by a solidity field called SYNOXH), which affects the final quality after it is estimated separately with its own class fields. In other words, as with the different initial quality classes (A1, A2, etc.), a number of fields are defined for the different tectonism categories. The reason for handling tectonism separately is the different orientation of large scale tectonism requiring a different search ellipsoid orientation during estimation to the one used for all other fields. It is combined with initial qualities to derive the final ones with degrading wherever necessary based on the estimated value of this field.

In other words, if the original field SYNOXH (solidity) has a value of 1, then the field SN1_PR receives the value of 1, if it has a value of 2, then field SN2_PR receives the value of 1 and so on. The original quality class fields and the additional tectonism field are combined after interpolation in space to receive

the final qualities. The need to interpolate tectonism separately is due to its different spatial distribution, i.e. the different orientation of this parameter in space compared to other parameters.

Condition	Field	Equation
LITHO == "SPIDER" AND SPTYP == 1 AND BACKRO == 1	A1_PR	1
LITHO == "SPIDER" AND ((SPTYP + BACKRO) == 3) AND A1_PR == 0	A2_PR	1
LITHO == "SPIDER" AND SPTYP == 2 AND BACKRO == 2 AND (A1_PR + A2_PR == 0)	AB_PR	1
LITHO == "SPIDER" AND (SPTYP == 3 OR SPTYP == 4) AND BACKRO == 1 AND (A1_PR + A2_PR + AB_PR == 0)	B_PR	1
LITHO == "SPIDER" AND BACKRO < 4 AND SPTYP < 5 AND (A1_PR + A2_PR + AB_PR + B_PR == 0)	BB_PR	1
	W_PR	1 - A1_PR - A2_PR - AB_PR - B_PR - BB_PR

Figure 7 - Quality class fields calculation based on original colour, texture and fracture fields for the Platanotopos quarry.

After calculation of initial quality class fields and tectonism categories, a secondary process of the database is performed in order to calculate the location of each sample (XYZ coordinates at the centre of each sample) and assign a weighting factor to the samples. This factor takes the value of 1 if the sample is from a section on the face of the quarry, and 0.5 if the sample comes from a drillhole. Essentially, more weight is given to face sections as their quality assessment is performed on a surface larger than the drillholes and therefore better approaches the actual quality of the marble in the specific location. These weight factors are used to further weight samples during interpolation.

4.2. Qualities Estimation

Interpolation of quality class field values was performed using the inverse distance squared method as implemented by Maptek Vulcan Quarry Modeller software on the basis of a block model. The estimated volume is divided in blocks of the same size. For Platanotopos quarry, a block model with rotation around Z axis was constructed that covered the entire quarry volume and current sampling. The model specifications are given in Table 6. Block dimensions were configured based on the marble volumes that are extracted separately at the given quarry. In each block, the percentage of each marble quality was estimated using the method analysed earlier using neighbouring samples.These samples are selected around each block using search ellipsoids which are oriented according to the geological features of the particular deposit.

Table 6 - Block model specifications of the Platanotopos quarry.

Origin	X	505,460
	Y	4,522,340
	Z	290.5
Model dimensions	X	582
	Y	728
	Z	350
Block dimensions	X	6
	Y	2.8
	Z	7
Orientation	X-axis azimuth	28
	X-axis rotation	0
	Y-axis rotation	0
Block count		1,261,000

Ellipsoid parameters are given in Table 7. Block estimation in Platanotopos quarry was different to the other quarries as the ellipsoids had different orientation in each block due to the folding of the deposit. Thus, a special function of the software was used before estimation that calculates the appropriate ellipsoid orientation for each block, taking in to account reference surfaces that define folding (Figure 8).

In the case of Iktinos Hellas SA quarries, the modifying factors for converting marble resources to reserves include the limitation of resources inside a technicallly feasible excavation as designed by the company's personnel (mining and legal factors), inside the exploitation license limits (legal, environmental and governmental factors). Classification based on the three categories of mineral resources was performed during three stages of block estimation, using ellipsoids of different dimensions and different sample count requirements (Table 7).

Table 7 - Platanotopos quarry estimation parameters.

	Measured (Proved) Reserves	Indicated (Probable) Reserves	Inferred In-Pit Resources	SYNOXH
Major Axis (m)	15	30	50	50
Semi-major Axis (m)	15	30	50	50
Minor Axis (m)	5	10	15	10
Azimuth	Variable	Variable	Variable	330
Plunge	Variable	Variable	Variable	0
Dip	Variable	Variable	Variable	70
Minimum Number of Samples	8	8	4	4
Maximum Number of Samples	20	20	20	20
Maximum Samples per Drillhole	4	4	4	4
Blocks estimated	1342	9754	26259	37355

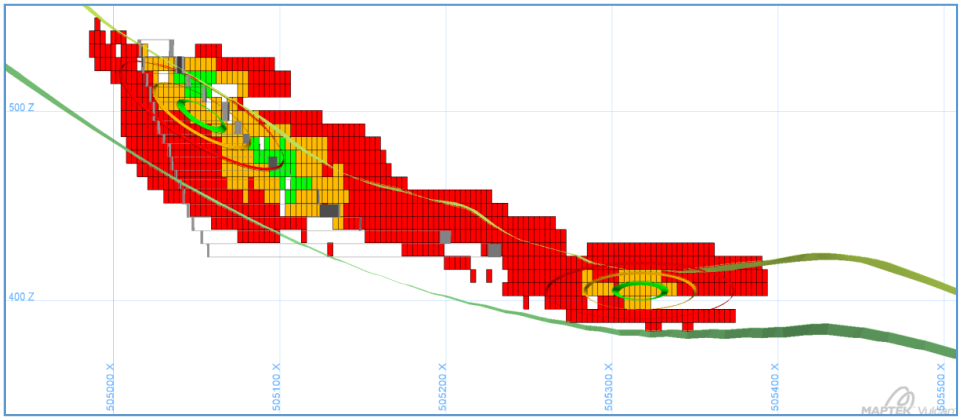

Figure 8 - Cross section through block model and resource classification ellipsoids following the deposit folding of the Platanotopos quarry (smaller to larger - measured, indicated, inferred).

5. Results and Conclusions

5.1. Reserves Estimates

Table 8 gives the results of the reserves calculation. For each reserve category, three generalised qualities are reported. Generalising of qualities was considered necessary as the limited sampling does not allow more detailed analysis of reserves to the original A1, A2, AB, B, and BB qualities produced by the particular quarry. Therefore, reported quality A corresponds to quantities A1 and A2, AB is reported on its own, while B quality contains both B and BB. Reported waste quantities are the remaining bench volume which cannot be estimated using the available sampling and the limitations

set by the reserve categories as to ellipsoid dimensions and minimum sample count. As a result, a considerable part of the waste and the inferred resources can be upgraded potentially in the future with additional drilling which will provide a clearer picture in areas with no samples currently.

Table 8 - Reserves estimation results for the Platanotopos quarry.

		Measured (Proved) Reserves (m^3)			Indicated (Probable) Reserves (m^3)			Inferred In-Pit Resources (m^3)				
Bench	**Elevation**	**A**	**AB**	**B**	**A**	**AB**	**B**	**A**	**AB**	**B**	**Waste**	**Total**
P11	423	296	227	242	2,753	8,229	14,236	4,443	18,843	27,146	130,896	207,312
P10	430	140	128	337	3,942	7,863	12,088	7,094	19,414	41,562	92,659	185,228
P09	437	43	68	51	3,402	11,166	16,313	5,460	21,649	39,272	68,859	166,283
P08	444	28	156	708	2,078	13,171	25,174	4,088	16,381	34,392	59,047	155,222
P07	451	204	1,993	4,101	2,590	12,393	36,991	4,506	11,370	32,786	59,560	166,494
P06	459	336	1,548	4,253	2,444	7,987	24,850	2,485	5,618	12,518	31,392	93,432
P05	464	600	1,718	5,871	2,405	7,263	25,625	2,194	5,335	12,740	26,246	89,998
P04	469	722	2,351	9,020	2,116	7,906	30,162	2,530	6,826	18,035	30,793	110,460
P03	476	771	2,019	8,445	1,059	5,642	28,002	1,554	7,095	20,281	26,147	101,015
P02	483	398	1,031	4,824	465	2,732	18,544	573	5,367	16,006	18,327	68,267
P01	488	227	644	5,839	443	2,927	22,082	277	5,568	23,672	25,995	87,676
P00	495	1	826	5,230	358	2,691	28,704	177	5,356	29,298	38,795	111,435
P-01	505	165	818	3,063	343	2,376	20,618	104	3,624	18,147	22,949	72,207
P-02	513	118	253	2,536	298	2,012	11,791	134	2,634	17,007	14,016	50,801
P-03	520	17	19	192	198	1,022	14,530	82	1,034	10,987	20,008	48,090
P-04	529				-	22	1,240	89	139	8,449	18,125	28,063
Total		**4,068**	**13,801**	**54,713**	**24,894**	**95,402**	**330,951**	**35,790**	**136,251**	**362,299**	**683,814**	**1,741,983**

5.2. Conclusions

This paper discussed a reserves estimation procedure applied at the Platanotopos marble quarry of Iktinos Hellas SA. Reserves estimation was performed using specialised software. Original sample quality values were converted to indicator values to allow interpolation to a block model using inverse distance weighting. This procedure provides Iktinos Hellas SA and potentially other marble quarrying companies with a solid method to produce reliable results according to international standards of resources/reserves reporting.

6. References

Abdollahisharif, J., Bakhtavar, E., Alipour, A. and Mokhtarian, M., 2012. Geological Modeling and Short-term Production Planning of Dimension Stone Quarries Based on Market Demand, *Journal of Geological Society of India*, 80, September 2012, 420-428.

Careddu, N., Siotto, G. and Tuveri, A., 2010. Evolution of a Marble Quarry: From Open Cast to Underground Exploitation, *Proceedings of Global Stone Congress 2010, Alicante, Spain*.

Forlani, G. and Pinto, L., 2000. Monitoring Marble Extraction in Open Cast Quarries, *International Archives of Photogrammetry and Remote Sensing*, XXXIII/B4, Amsterdam, 2000, 283-289.

Kapageridis, I., 2015. Iktinos Hellas SA Quarries - Marble Reserves Estimation Technical Report, September 2015, Maptek Pty Ltd.

Δελτίο της Ελληνικής Γεωλογικής Εταιρίας, τόμος L, σελ. 1859-1866
Πρακτικά 14ου Διεθνούς Συνεδρίου, Θεσσαλονίκη, Μάιος 2016

Bulletin of the Geological Society of Greece, vol. L, p. 1859-1866
Proceedings of the 14th International Congress, Thessaloniki, May 2016

GEOCHEMICAL ANALYSIS OF SILICEOUS SEDIMENTS FROM VASILIKA, NORTHERN GREECE

Karageorgiou S.[1], Vavelidis M.[1], Andreou S.[2] and Melfos V.[1]

[1]*Aristotle University of Thessaloniki, School of Geology, Department of Mineralogy-Petrology-Economic Geology, 54124, Thessaloniki, Greece, matina_mk@hotmail.com, vavelidi@geo.auth.gr, melfosv@geo.auth.gr*

[2]*Aristotle University of Thessaloniki, Faculty of Philosophy School of History and Archaeology, 54124 Thessaloniki, Greece,* andrest@hist.auth.gr

Abstract

The present paper presents new mineralogical and geochemical data of the siliceous sediments from the region of Vasilika in northern Greece. The studied material consists of reddish and brownish cherts and jaspers containing mostly microcrystalline quartz and Fe-oxides. Chemical analysis has been carried out, including the identification of major oxides, trace elements and REE, in order to determine their geotectonic affinity based on the correlation of immobile trace element distribution. The geochemical features combined with the mineralogical composition of these siliceous sediments indicate that they were formed as the result of a hydrothermal circulating convection system near a mid-ocean ridge. Rare earth elements (REE) are regarded as the most reliable immobile elemental components in the complex geological process of the sedimentary cycle because they are relatively stable during post-depositional processes such as diagenesis, alteration and weathering. In addition Ce anomaly can help to establish the marine environment in which cherts were formed.

Keywords: *chert, jasper, Ce anomaly, REE, hydrothermal sediments.*

Περίληψη

Στην παρούσα μελέτη παρουσιάζονται νέα ορυκτολογικά και γεωχημικά δεδομένα των πυριτικών ιζημάτων που προέρχονται από την περιοχή των Βασιλικών, στην βόρεια Ελλάδα. Το υλικό που μελετήθηκε περιλαμβάνει ερυθρούς και καστανούς πυριτόλιθους και ιάσπιδες, αποτελούμενοι κυρίως από μικροκρυσταλλικό χαλαζία και Fe-οξείδια. Έγινε χημική ανάλυση, η οποία περιελάμβανε την αναγνώριση των κυρίων οξειδίων, των ιχνοστοιχείων και των σπάνιων γαιών, με σκοπό τον προσδιορισμό της γεωτεκτονικής συνάφειας βασισμένη στην συσχέτιση με την κατανομή των σταθερών ιχνοστοιχείων. Τα γεωχημικά χαρακτηριστικά σε συνδυασμό με τα ορυκτολογικά χαρακτηριστικά των ιζημάτων αυτών υποδεικνύουν πως αυτά έχουν σχηματιστεί ως αποτέλεσμα επίδρασης υδροθερμικού συστήματος κοντά σε μεσο-ωκεάνια ράχη. Οι σπάνιες γαίες (REE) θεωρούνται ως τα πιο αξιόπιστα σταθερά χημικά στοιχεία κατά τις ιζηματογενείς διαδικασίες καθώς τα στοιχεία αυτά παραμένουν σταθερά κατά τις μετά-αποθετικές διαδικασίες όπως διαγένεση, εξαλλοίωση, αποσάθρωση. Ακόμη, η ανωμαλία Ce βοηθά στον προσδιορισμό του θαλάσσιου περιβάλλοντος στο οποίο και σχηματίστηκαν οι πυριτόλιθοι.

Λέξεις κλειδιά: πυριτόλιθος, ίασπις, ανωμαλία Ce, σπάνιες γαιές, υδροθερμικά ιζήματα.

1. Introduction

Siliceous sediments are dominantly composed of SiO_2 minerals such as quartz, chalcedony and opal. These sedimentary rocks are very hard and fine-grained. The term chert is used as a group name for siliceous sedimentary rocks (Boggs, 2005). Chert is a high-silica rock, consisting mainly of cryptocrystalline or microcrystalline quartz. Other siliceous sediments such as flint, jasper, and chalcedony are considered to be chert, despite the distinct differences among them (Cradell, 2005). Chert and other related siliceous sediments were among the first raw materials utilized in prehistory for the manufacture of knapped tools (Rapp, 2009).

In this study siliceous sediments from the region of Vasilika, in northern Greece are studied in terms of mineralogy and geochemistry. In this location there is evidence for prehistoric quarrying activity and exploitation of these raw materials for the construction of knapped tools. Such evidence is mentioned by Grammenos *et al*. (1992) at a distance of approximately 2.5 km north of the Neolithic settlement of Thermi, in the site of Kiparissi. A link between the settlement of Thermi and the quarrying activity in Vasilika in Neolithic (7,000-3,000 BCE) and Early Bronze Age (3,000-1,800 BCE), has been suggested for the procurement of chert.

The aim of this study is to identify the geochemical context of these raw materials and examine especially the distribution of the rare earth elements (REE) and how they can be applied for the identification model of the formation of these sediments.

2. Geological setting

The area of Vasilika is located 28 km southeast of the city of Thessaloniki, at the upstream part of the Anthemountas basin, at the boundary between the Vardar zone and the Circum Rhodope belt. The area is dominated by an ophiolite outcrop, part of the Chalkidiki ophiolite complex. This ophiolite complex has a NW-SE direction and is considered as a detached block of the Vardar oceanic crust, consisting of dismembered bodies which display tectonic contacts with the country rocks. Other ophiolites outcrops occur in Triadi, Galatista, Vavdos, Gerakini, Metamorphosis and Toroni, in Chalkidiki. The Vasilika ophiolite includes mainly pyroxenites, dunites, peridotites, gabbros and serpentinites, with magnesite and chromium occurrences (Fig.2). Chromium deposits are hosted in the ultramafic unit of the ophiolitic complex forming mainly massive stratiform ore bodies in dunites (Christodoulou and Michailidis, 1990). Dunites are the dominant ultramafic rocks in Vasilika area and are serpentinized (Christofides *et al*., 1994).

The emplacement of the Vardar oceanic crust on to the continental margin took place in the Upper Jurassic-Lower Cretaceous, which is confirmed by the existence of fossils in the sediments which interfere in pillow lavas (Spray *et al*., 1984). The tectonic contacts between ophiolites and the neighbouring rock formations represent thrust faults. According to Jung *et al*. (1980) the ophiolite complex is considered to be allochthonous. However, it has also been proposed a theory of autochthonous character (Bebien *et al*., 1986).

3. Materials and Methods

Twelve samples of siliceous sediments were collected from the study area after a regional fieldwork focusing on a geological-archaeological survey in the frame of a combined project at Anthemountas basin, among the Aristotle University of Thessaloniki, the Ephorate of Antiquities of Thessaloniki City and the *Poznań University (Poland)*. The samples represent the raw materials that prehistoric man utilized for the manufacture of lithic tools and they are connected with the quarrying activity at the region.

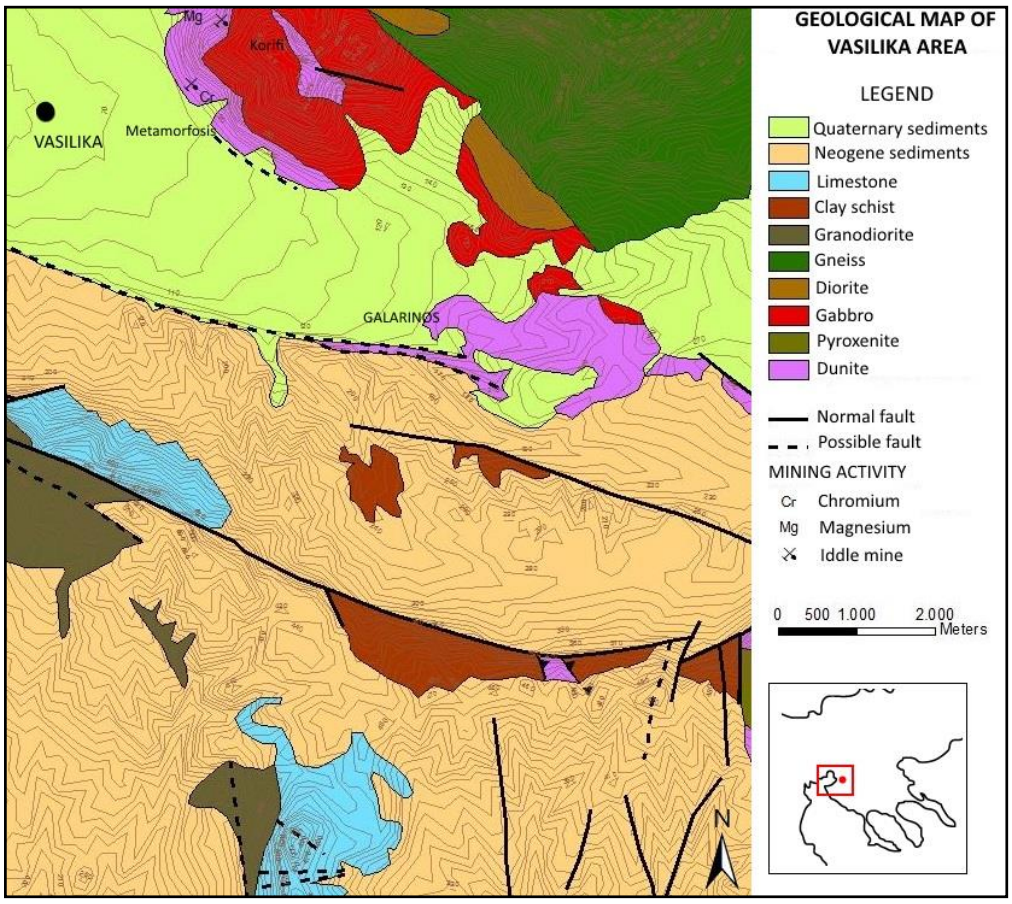

Figure 1 - Geological map of Vasilika region. Modified after Mollat *et al.* (1978).

The macroscopic examination of the sediments was mainly based on colour, texture and translucency characteristics of the rock samples. The colour characterization was based on the Munsell soil colour chart. In order to identify the mineralogical composition and the rock textures of the cherts optical microscopy was applied by using a polarizing microscope at the Department of Mineralogy-Petrology-Economic Geology at the School of Geology, Aristotle University of Thessaloniki.

The determination of the major, trace and rare earth elements (REE) was achieved by inductively coupled plasma mass spectrometry (ICP-MS) at the ACME Analytical Labs (Bureau Veritas), in Vancouver, Canada. This method is mainly preferred due to the effective detection abilities. For this study the samples were dissolved by using multiple acids (multi-acid digestion) with Ultra Trace ICP-MS analysis. The quantity of each sample was 0.5 gr. The samples were heated at t = 150°C in a solution form, using HNO_3-HF-$HCLO_4$. After drying, the residual samples were dissolved in 6 N HCL. The REE concentrations of the analysed cherts were normalized compared to the prototype sample of PAAS (Post-Archaean Australian Shale Average) which is the most common standard for modern sea water and ocean sediments.

X-ray fluorescence (XRF) analysis was applied in order to identify the major oxides in the cherts. The samples were pulverized and then were prepared in order to construct fused beads. The powder was mixed with Li_2B4O_7 and was fused at a temperature of 1100°-1200°C. The ratio of each sample in the Li borate was 1:8.

4. Results

The colour characterization of the studied cherts showed four main categories which are: (i) reddish brown-dark reddish brown, (ii) brown, (iii) yellow-red and (iv) dusky red (Fig.2). The most prominent type is brown-dark reddish brown, with 8 out of 12 samples. The samples with a lighter colour, such as yellow-red colour, include darker veins which consist of Fe and Mn oxides. Five out of twelve samples have dark spots on the surface indicating a thermal effect. This could be the result of a heat treatment applied by prehistoric man during the process of collecting raw materials or during manufacturing lithic tools, or because of an accidental fire.

Mineralogical and petrographic analysis under the polarizing microscope showed that the cherts are fine-grained consisting mainly of microcrystalline quartz and some chalcedony spheroids. The grain size of the quartz grains range from 1 to 10 μm. Additionally, there are minor accessory minerals consisting of Fe-oxides. Due to the presence of Fe-oxides, the microcrystals of quartz have acquired a reddish hue (Fig.3).

The analytical results for the studied cherts show that SiO_2 varies between 88 and 92 wt % whereas FeO ranges from 4 to 10 wt%. SiO_2 is negatively correlated to Al_2O_3. The Si-Al diagram proposed by Crerar *et al*. (1982) shows that the Vasilika chert samples are connected with a hydrothermal source (Fig.4). The ratio of Al/(Al+Fe+Mn) is 0.08-0.13 which shows the correlation of the cherts to a hydrothermal circulating convection system. According to Yamamoto (1986) these value of Al/(Al+Fe+Mn) ratio indicate a hydrothermal contribution to the ocean sediments. Trace element geochemistry of the cherts is dominantly based on the study of Cu, Co, Ni, As, Ag, Ba, B, Sb and U (Junguo *et al*., 2011). The maximum value of Ni/Co ratio for cherts of a hydrothermal origin is 3.6 (Crerar *et al*., 1982). The Ni/Co ratio of the Vasilika chert is 3.0.

The $Al_2O_3/(Al_2O_3+Fe_2O_3)$ ratio is from 0.11 to 0.19 indicating a mid-ocean ridge geotectonic environment (Murray *et al*., 1990). The discrimination diagrams of $100x(Fe_2O_3/SiO_2)$ versus $100x(Al_2O_3/SiO_2)$ (Fig.5), $Fe_2O_3/(100-SiO_2)$ versus $Al_2O_3/(100-SiO_2)$ (Fig.6) and Fe_2O_3/TiO_2 versus $Al_2O_3/(Al_2O_3+Fe_2O_3)$ (Fig.7) show the plot areas of siliceous sediments at various geotectonic environments such as continental margins, ocean ridges and ocean basins, according to Murray (1994). The chert samples from Vasilika plot in the ocean ridge areas of these diagrams, or very close to them. The high SiO_2 content and the very low concentrations of the rest elements affect the plot of the samples in these diagrams and so a slight deviation may be observed in the diagrams.

Figure 2 - Raw materials of reddish brown cherts from Vasilika.

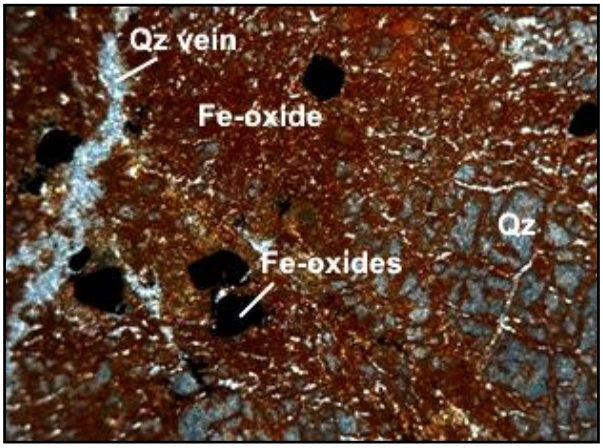

Figure 3 - Thin section of chert from Vasilika, under crossed polarized light. Chert mainly consists of microcrystalline quartz and Fe-oxides (magnification x5, the large side of the photo corresponds to 2.8mm).

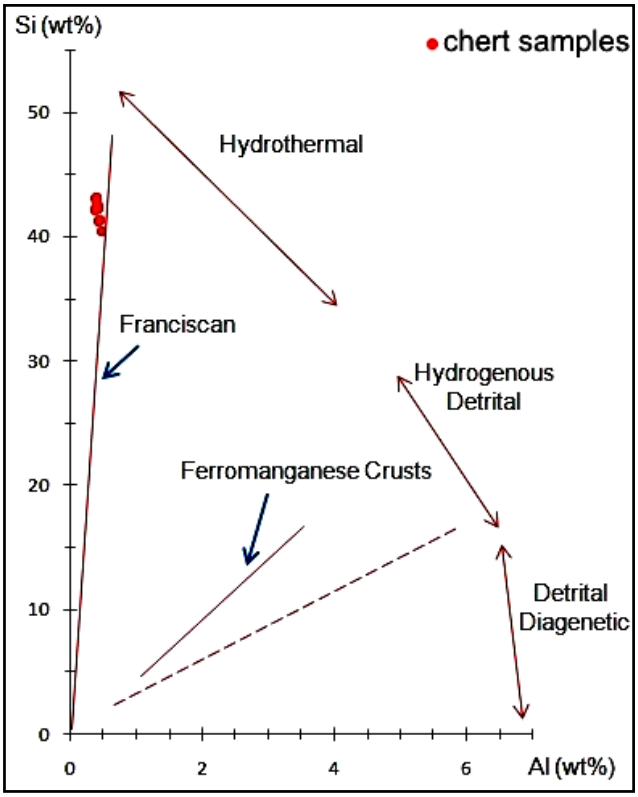

Figure 4 - Si-Al diagram (modified after Crerar *et al.*, 1982). Cherts from Vasilika are connected to a hydrothermal system.

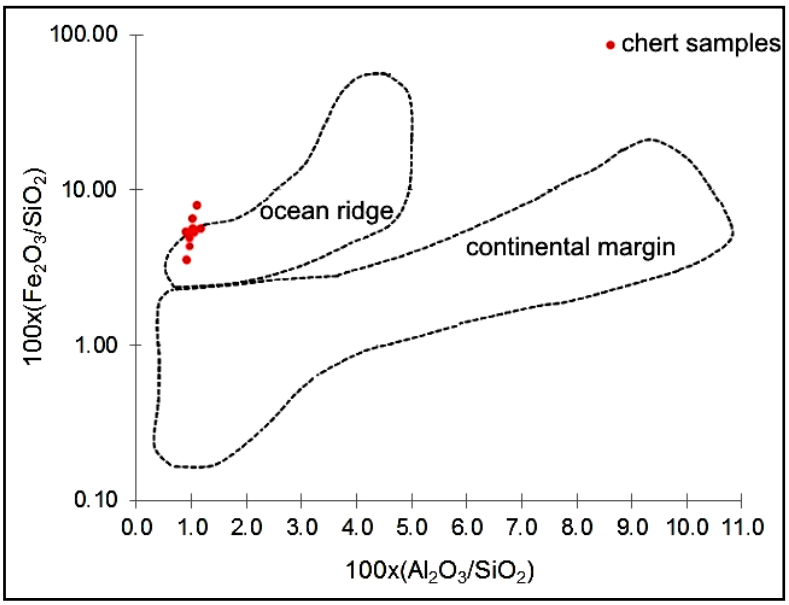

Figure 5 - 100x(Fe_2O_3/SiO_2)-100x(Al_2O_3/SiO_2) diagram (modified after Murray, 1994) showing samples from Vasilika related to ocean ridge area.

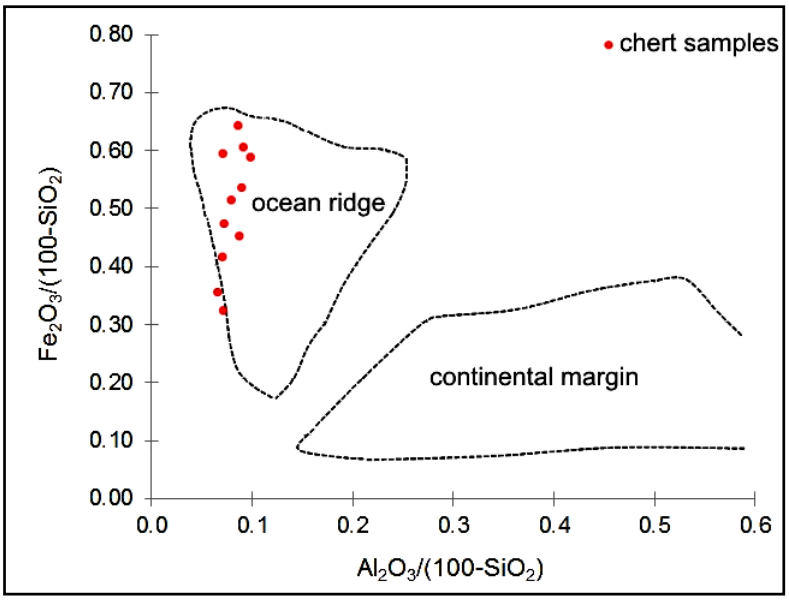

Figure 6 - $Fe_2O_3/(100-SiO_2)$-$Al_2O_3/(100-SiO_2)$ diagram (modified after Murray, 1994). The samples appear at the ocean ridge province of the diagram.

The study of the REE in these cherts is mostly based to the estimation of Ce anomaly. Ce^{3+} has low ionization potential and as a result the cerium's behaviour differs from the rest REE. The Ce anomaly is defined by the equation: $Ce/Ce^*= Ce_N/[(La_N)(Pr_N)]^{1/2}$ where Ce* is the hypothetical concentration of Ce^{3+} or: $Ce/Ce^*= 2Ce_N/(La_N+Pr_N)$ (Kato et al., 2009). N stands for the normalized values. The ratio of Ce/Ce* for the cherts from Vasilika is 0.62-1.78 (Tab.1). Due to the capture of tetravalent Ce by the Fe-Mn nodules there is a negative Ce anomaly in the sea water and a positive anomaly in the Fe-Mn minerals. Cerium anomaly is negative when siliceous sediments have been separated from the Fe-Mn minerals (Junguo *et al*., 2011).

Table 1 - Ratios related to the REE study of cherts from Vasilika.

	ΣREE	LREE	HREE	LREE/HREE	Ce/Ce*
17LV-1	0.17	0.09	0.08	1.21	1.32
17LV-2	0.06	0.02	0.04	0.62	1.38
17LV-4	0.01	0.01	-	-	1.44
17LV-5	0.07	0.03	0.04	0.87	0.62
17LV-6	0.16	0.03	0.13	0.26	0.77
17LV-7	0.01	0.01	-	-	1.78
17LV-8	0.02	0.02	-	-	1.39
17LV-9	0.09	0.03	0.06	0.52	1.37
17LV-10	0.11	0.07	0.04	2.06	1.25
17LV-11	0.08	0.05	0.02	2.52	0.69
17LV-12	0.11	0.06	0.06	0.97	0.72

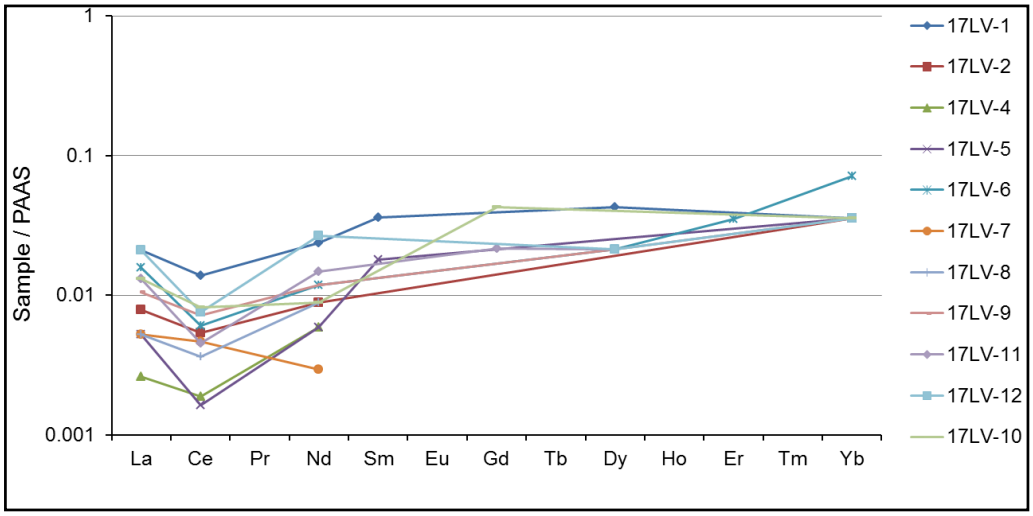

Figure 7 - REE diagram of Vasilika samples.

When there is mixing of the two, Ce-anomaly may be slightly negative up to slightly positive, as it has been identified in the case of the samples from Vasilika. Table 1 shows the sums and the ratios related to the REE study. When the HREE values are higher than the LREE, it is more likely for the silicate sediments to be related to an ocean basin. However, in the studied case, the LREE values are similar to the HREE although HREE are slightly more depleted than LREE. That is also an indicator of hydrothermal activity. ΣREE is controlled by the influence degree of a continental input. The values of ΣREE tend to get higher from a mid-ocean ridge to a continental environment (Junguo *et al*., 2011). The depositional rate minimizes the exposure time of cherts to seawater and consequently the adsorption of REE resulting lower ΣREE (Murray *et al*., 1990). Samples from Vasilika have low ΣREE values which indicate low terrigenous content with a higher depositional rate in mid-ocean ridge.

5. Conclusions

After the petrographic and geochemical study of the siliceous sediments from Vasilika in northern Greece it was concluded that these are mainly reddish-brownish cherts which consist mainly of microcrystalline quartz with minor Fe-oxides. Major, trace and rare earth elements indicate the

hydrothermal origin of these cherts. There is a correlation with a hydrothermal source near a mid-ocean ridge geotectonic environment. The Ce anomaly reveals the mixing between siliceous sediments and Fe-Mn oxides, and its value differs, depending on the related geotectonic environment. Because of REE's immobility, these are used as geochemical tracers, giving a safe consideration on the origin of siliceous sediments.

6. References

Bebien, J., Baroz, J., Caperdi, S. and Venturelli, G., 1986. Magmatisme basique associe/es a l'ouverture d'un basin marginal dans les Hellenides internes au Jurassic, *Ofioliti*, 12, 53-70.

Boggs, S.J., 2005. Petrology of Sedimentary Rocks, Second Edition, Cambridge.

Christodoulou, C. and Michailidis, K., 1990. Petrology of the plutonic suites from the Chalkidiki ophiolites, Northern Greece. Implications for parental magma characteristics and tectonic provenance, *Ofioliti*, 15(1), 17-44.

Christofides, G., Thimiatis, G., Koroneos, A., Sklavounos, S. and Eleftheriadis, G., 1994. Mineralogy and chemistry of Cr-chlorites associated with chromites from Vavdos and Vasilika ophiolite complexes (Chalkidiki, Macedonia, N. Greece), *Chemie der Erde*, 54, 151-166.

Cradell, O., 2005. Macroscopic analysis and characterization of chert from Transylvania for provenance purposes, *Sargetia*, 33.

Crerar D.A., Namson, J., Chyi, M.S., Williams, L. and Feigenson, M.D., 1982. Manganiferous cherts of the Franciscan assemblage. I. General geology, ancient and modern analogues, and implications for hydrothermal convection at oceanic spreading centers, *Economic Geology*, 77, 519-540.

Grammenos, D.V., Pappa, M., Ourem-Kotsos, N., Skourtopoulou, K., Giannouli, E., Maraggou, C., Valamoti, S., Syrides, G., Makri, E. and Christidou, P., 1992. Excavation of the Neolithic settlement Thermi B and Byzantine installation despite the prehistoric settlement of Thermi A. Excavation period 1989, *Macedonika KH*, 381-50.

Jung, G., Mussallam, K., Burgath, K., Kockel, F., Mohr, M. and Raschka, H., 1980. Ulramafic and related rocks of Chalkidiki, *Proc. Internat. Symp. Metals in Mafic and Ultramafic Complexes, vol. 3. Inst. Geol. Mining Research*, Athens, Greece, 24-42.

Junguo, H., Yongzhang, Z. and Hongzhong, L., 2011. Study on geochemical characteristics and depositional environment of Pengcuolin chert, Southern Tibet, *Journal of Geography and Geology*, 3(1), 178-188.

Kato, Y. and Isozaki, Y., 2009. Comment on "Evaluation of palaeo-oxygenation of the ocean bottom cross the Permian-Triassic boundary" by Kakuwa (2008): Was the Late Permian deep-super-ocean really oxic? Global and Planetary change, *Elsevier*, 69, 79-81.

Mollat, H., Antoniades, P. and Ricou, L.E., 1978. Geological Map of Greece, Vasilika sheet, Institute of Geological and Mining Research, IGME.

Murray, R.W., 1994. Chemical criteria to identify the depositional environment of chert: general principles and applications, *Sedimentary Geology*, 90, 213-232.

Murray, R.W., Jones, D.L., Gerlach, D.C. and Russ, G.P., 1990. Rare Earth Elements as Indicators of Different Marine Depositional Environments in Chert and Shale, *Geology*, 18(3), 268-271.

Rapp, G., 2009. Archaeomineralogy, *Natural sciences in archaeology*, Second Edition, Springer.

Spray, J.G., Bebien, J., Rex, D.C. and Roddick, J.C., 1984. Age constraints on the igneous and metamorphic evolution of the Hellenic - Dinaric ophiolites, Dixon, J.E. and Robertson, A.H.F., *eds*., The geological evolution of the Eastern Mediterranean, *Geological Society*, London, Special Publications, 17, 619-627.

Yamamoto, K., 1986. Geochemical characteristics and depositional environments of cherts and associated rocks in the Franciscan and Shimanto terranes, *Sedimentary Geology*, 51, 65-108.

Δελτίο της Ελληνικής Γεωλογικής Εταιρίας, τόμος L, σελ. 1867-1877
Πρακτικά 14ου Διεθνούς Συνεδρίου, Θεσσαλονίκη, Μάιος 2016

Bulletin of the Geological Society of Greece, vol. L, p. 1867-1877
Proceedings of the 14th International Congress, Thessaloniki, May 2016

PETROLOGICAL, MINERALOGICAL AND GEOCHEMICAL DATA FROM THE EOHELLENIC OPHIOLITIC NAPPE IN THE ISLAND OF SKYROS, GREECE

Karkalis C.[1], Magganas A.[1] and Koutsovitis P. [2]

[1]Faculty of Geology and Geoenvironment, National & Kapodistrian University of Athens. Panepistimioupolis, Athens, GR-15784

[2]IGME, 1st Spirou Louis St., Olympic Village, Acharnae, GR, 13677, chriskarkalis@gmail.com, amagganas@geol.uoa.gr, petroskoutsovitis@yahoo.com

Abstract

The ophiolite of Skyros mainly consists of serpentinized harzburgites, gabbroic rocks, dolerites, tholeiitic basaltic lavas, rodingites, as well as ophicalcites. This ophiolitic sequence comprises of an ophiolitic mélange of pre-Upper Cretaceous age belonging to the Eohellenic nappe, has been affected by low to moderate metamorphic and metasomatic processes. Their mineral chemistry as well as their whole rock chemistry suggests that these ophiolitic rocks are associated with supra-subduction related processes. The presence of vesuvianite crystals in rodingites, as well as the occurrence of relict spinels within serpentinitic rocks, further confirms this assumption. Geochemical and petrological comparison between Skyros ophiolitic rocks and similar rocks of the Eohellenic nappe in East Thessaly and other N. Sporades islands, reveal that they all share many petrogenetical features. These east-central Greece Eohellenic ophiolites, and the ophiolitic rocks of the upper tectonic unit of the Attico-Cycladic Zone may possibly form an elongated ophiolitic zone associated to the hanging wall of the North Cycladic Detachment System.
Keywords: *Metasomatism, metamorphism, vesuvianite, rodingite, subduction.*

Περίληψη

Οι οφιόλιθοι της νήσου Σκύρου αποτελούνται κυρίως από σερπεντινιωμένους χατρζβουργίτες, γαββρικά πετρώματα, δολερίτες, θολεϊτικές βασαλτικές λάβες, ροδιγκίτες και οφειτασβεστίτες. Αυτή η οφιολιθική ακολουθία περιλαμβάνει ένα οφιολιθικό mélange προ-Ανωκρητιδικής ηλικίας το οποίο ανήκει στο Ηωελληνικό Κάλυμμα που έχει υποστεί χαμηλού έως μέσου βαθμού μεταμορφικές και μετασωματικές διεργασίες. Τα ορυκτοχημικά και γεωχημικά δεδομένα καταδεικνύουν τη σχέση αυτών των πετρωμάτων με ένα περιβάλλον διάνοιξης υπεράνω ζώνης υποβύθισης (SSZ). Η παρουσία βεζουβιανίτη στους ροδιγκίτες καθώς και η ύπαρξη υπολειματικών σπινέλιων στους σερπεντινίτες, επιβεβαιώνουν περεταίρω την εν λόγω υπόθεση. Η σύγκριση γεωχημικών και πετρολογικών στοιχείων των οφιολιθικών πετρωμάτων της Σκύρου, με ανάλογα πετρώματα από την Ανατολική Θεσσαλία και από άλλα νησιά των Βορείων Σποράδων δείχνει ότι υπάρχουν κοινά πετρογενετικά χαρακτηριστικά. Αυτά τα Ηωελληνικά οφιολιθικά πετρώματα της Κεντρικής Ελλάδας μαζί με ανάλογης σύστασης, προέλευσης και εξέλιξης οφιλίθους της ανώτερης τεκτονικής ενότητας της Αττικο-Κυκλαδικής Ζώνης πιθανά αποτελούν μια ενιαία

επιμηκυμένη ζώνη σχετιζόμενο με το υπερκείμενο τέμαχος του Συστήματος Αποκόλλησης των Βορείων Κυκλάδων.

Λέξεις κλειδιά: *Μετασωμάτωση, μεταμόρφωση, βεζουβιανίτης, ροδιγκίτης, υποβύθιση.*

1. Introduction

Jurassic ophiolites in Greece are mostly exposed in its Central and Northern parts forming two subparallel zones which trend NNW-SSE (Stampfli *et al.*, 2003; Robertson, 2004; Papanikolaou, 2009; Ferrière *et al.*, 2012). Ophiolitic rocks, independently of zone of their occurrence, show as prevailing petrological and geochemical characters either those related to a subduction setting or those of a ridge one. For example, the ophiolitic sequences of Pindos, Koziakas and West Othris present mostly MORB and back-arc basin (BAB) affinities (e.g. Pomonis *et al.*, 2007; Pelletier *et al.*, 2008; Whattam and Stern, 2011), whereas the ophiolitic sequences of East Othris, Vourinos, Rhodiani and Evros are supra-subduction zone (SSZ) ophiolites (Beccaluva *et al.*, 1984; Magganas, 2002; Saccani *et al.*, 2008; Magganas and Koutsovitis, 2015). The Skyros ophiolitic rocks, occurring within the eastern zone and along with schists, phyllites and marbles, are part of the Eohellenic tectonic nappe (Harder *et al.*, 1983).

Here we present our initial results from evaluation of new petrographical, mineralogical and whole-rock major and trace chemical element data of the main magmatic rock types of the Skyros ophiolite in order to contribute to the gap existing in their petrologic knowledge and in general on the geology of the Eohellenic nappe (Fig. 1), which is also exposed in other islands of North Sporades as well as in Eastern Thessaly and Central Macedonia regions. Moreover, our conclusions may provide constrains on the development and closure of the Mesozoic Tethyan oceanic and continental strands that these ophiolitic rocks were formed and emplaced, as well as on their petrogenetic processes and metasomatic/metamorphic evolution.

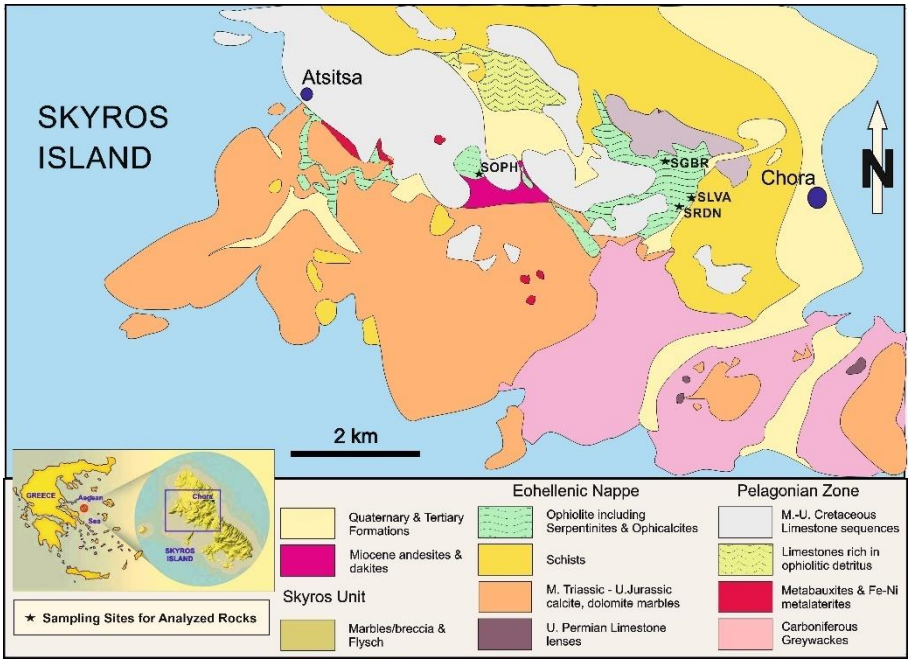

2. Geological Setting

Skyros Island is located in the central Aegean Sea and belongs to the group of North Sporades islands (Fig. 1). It consists of the Pelagonian Zone (mostly metamorphosed sedimentary rocks), the Eohellenic tectonic nappe and the Skyros Unit (consisting of marbles and breccia with flyschoid members). The Pelagonian Zone is regarded as being part of the Internal Hellenides and is distinguished into two distinct metamorphic and non-metamorphic parts (Katsikatsos, 1992; Papanikolaou, 2009). In Skyros Island, the Pelagonian Zone is located mostly in the southern and north-western region.

The Eohellenic nappe was emplaced during the Late Jurassic to Early Cretaceous overthrusting Palaeozoic-Middle Jurassic Pelagonian basement rocks, and in Skyros it mainly consists of an ophiolitic mélange (Katsikatsos, 1992; Pe-Piper and Piper, 2002). This ophiolitic formation is mostly located in the central and eastern parts of the island and to a lesser extent in the western part. The Skyros ophiolite includes massive or highly deformed serpentinite, which locally in its margin change to talc schist or in other places intruded by rodingitic dykes, massive gabbroic rocks, dolerite dykes intruded by quartz and epidote rich veins, massive lavas of basaltic composition and ophicalcite. According to Pe-Piper and Piper (2002) K-Ar dating on a gabbroic rock (diorite) of the ophiolitic formation located at mountain Notos, yields for the Skyros ophiolite a Lower Cretaceous age (125 ± 8 Ma). In contact to ophiolitic rocks thin slices of massive or brecciated deep sea cherts of red colour rarely occur. As the Skyros ophiolitic rocks are usually found in a chaotic mixture they constitute an ophiolitic melange. This melange is usually found above a volcano-sedimentary metamorphosed sequence which includes marbles, calc- and mica-schists, phyllites, meta-greywacke and blueschists (Harder *et al.*, 1983; Baltatzis, 1984; Katsikatsos, 1992). On top of some serpentinite erosion surfaces dark brown Fe-rich lateritic horizons cover by transgressive Upper Cretaceous, usually rudist bearing, limestones, also occur. The Skyros Unit, which consists of coarse grained marbles, breccia and flysch, is emplaced above the Eohellenic tectonic nappe (Jacobshagen and Matarangas, 2004).

In eastern Thessaly, the Eohellenic Nappe is metamorphosed and was emplaced during Upper Jurassic to Lower Cretaceous, overthrusting the pre-upper Cretaceous Pelagonian zone rocks (Migiros, 1986). The ultrabasic rocks of the Eohellenic nappe in eastern Thessaly are mainly serpentinized hartzburgites, with serpentinized dunite bodies in the uppermost parts which contain small tectonized and broken chromite lenses (Migiros and Economou, 1988). In the North Sporades islands such as Skiathos (Heinitz and Heinitz-Richter, 1983) and Skopelos (Matarangas, 1992), the main tectono-stratigraphic units include the Pelagonian unit, Eohellenic nappe relics and the Mesoautochthonous complex (Jacobshagen and Matarangas, 2004). In Alonnisos island, the Eohellenic nappe also overthrusts the Pelagonian unit, whereas in Kyra Panagia the basaltic andesites seem to also be part of the Eohellenic nappe (Pe-Piper *et al.*, 1996).

3. Sampling and analytical methods

Samples were collected from Northern part of Skyros and more specifically from areas between the Skyros town and the Atsitsa village. Twelve samples were collected and petrographically studied. These include four serpentinites (samples SOPH, SSRP, SRPD, SDUN), one ophicalcite (sample SOPH2), one rodingite (sample SRDN), two lavas (samples SLVA, SLVA2) three dolerites (samples SMLE, SMLE2, SMLE3) and one gabbro (SGBR). Mineral chemistry analyses were conducted in two basaltic lavas (samples SLVA, SLVA2), one rodingite (sample SRDN), one serpentinite (sample SOPH), and one gabbro (sample SGBR).

Whole-rock analyses (Table 1) were carried out at Acme Analytical Laboratories in Canada with the use of ICP-MS 4A-4B for major elements, trace elements and REE and included one lava, one dolerite, one rodingite and one serpentinite sample. Low Detection Limits range from 0.002% to 0.04% and High Detection Limits are all 100% for major oxides. The Low Detection Limits range

from 0.5 ppb to 20 ppm and the High Detection Limits range from 50 ppm to 50000 ppm for the trace elements. For REE the Low Detection Limits range from 0.01 ppm to 30 ppm and the High Detection Limits range from 50000 ppm to 10000 ppm. Mineral chemistry analyses (Table 2) were obtained using a SEM JEOL JSM-5600 equipped with an Oxford LinkISIS 300EDX microanalysis system, at the University of Athens, Department of Mineralogy and Petrology.

4. Results

4.1. Petrography and mineral chemistry

Serpentinite presents mesh textural features with slip-fiber (Fig. 2a) and cross-fiber chrysotile veins. Their mineral assemblage mainly consists of serpentine (mainly antigorite and few chrysotile) and orthopyroxene bastites, which indicates their harzburgitic origin. A few relict spinels with quite low Cr# (38.18-38.87) and moderate TiO_2 (0.14-0.25 wt.%) contents, have been identified, while some of them are classified as Fe-chromite with high Cr# (92.69) and FeO (51.88 wt.%) values and low MgO (4.45 wt.%) and Al_2O_3 (1.5 wt.%) contents. Secondary minerals include magnetite (Fig. 2b), derived from spinel and olivine alteration, as well as magnesite in veinlets. Ophicalcite also shows mesh texture. It mainly consists of serpentine and calcite, the former sometimes in the form of bastite after orthopyroxene and as chrysotile veinlets. Magnetite also occur. Gabbro is medium grained with secondary quartz veins. It mostly consists of saussuritized plagioclase and amphiboles.

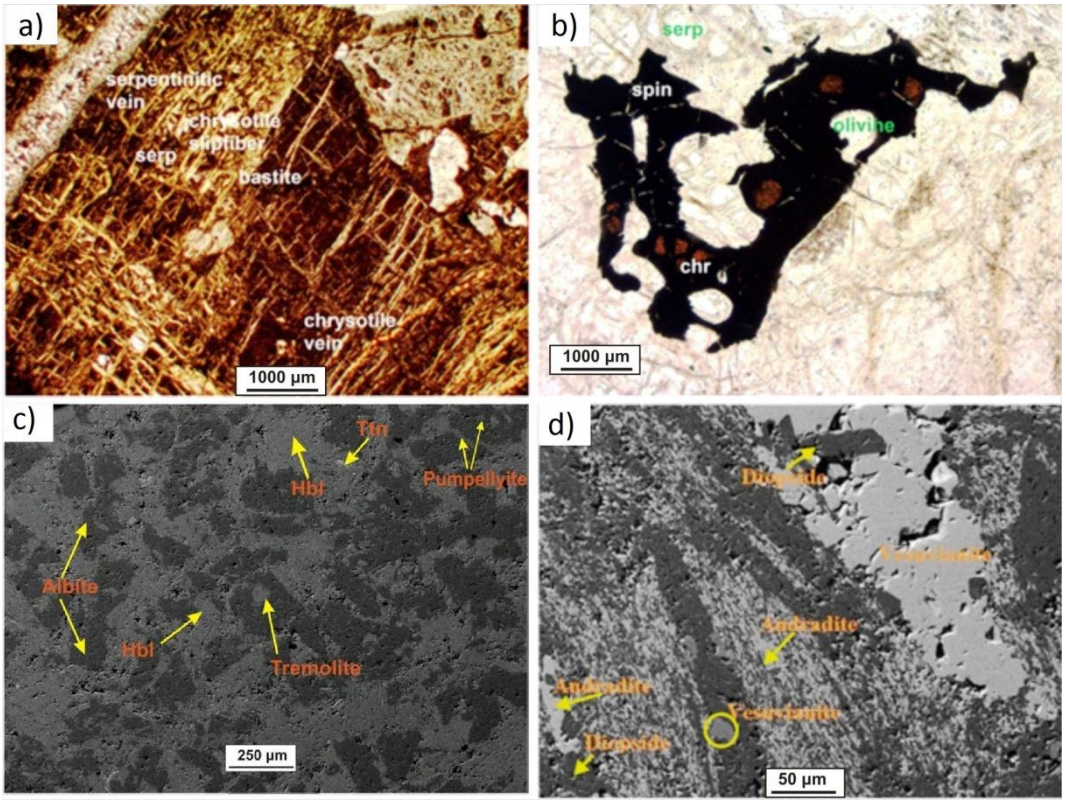

Figure 2 - a. Serpentinite sample (SOPH) including slip-fiber chrysotile and hourglass/mesh antigorite as well as some bastites; b. Serpentinite sample (SOPH) with serpentine surrounding xenomorphic spinel (magnetite with residue olivine) grain and relict chromite patches preserved in the core; c. Dolerite sample (SMLE3). Subophitic texture with amphiboles (hornblende and tremolite), albite, titanite and pumpellyite. d. Rodingite sample (SRDN) consisting of diopside, vesuvianite and hydroandradite grains.

Amphiboles can be separated into two groups. The first group includes hornblende with relatively high Al_2O_3 (5.86-5.11wt.%), TiO_2 (1.62-1.52wt.%) and Na_2O (1.01-1.09 wt.%) contents, which possibly indicates a magmatic origin (cf. Koutsovitis, 2012), while the second group includes metamorphic hornblende with lower Al_2O_3 (4.43-4.65wt.%), TiO_2 (0.55-0.58 wt.%) and Na_2O (0.62-0.65 wt.%) contents. Basic plagioclase was not recognized having being replaced by albite. Secondary minerals also include clouded epidote and zoisite. Opaque minerals include Fe-Ti-oxides and hematite.

From the above petrographic and mineral chemistry data, the abundance of hornblende and the absence of any clinopyroxene crystal the original rock can be characterized as hornblende gabbro. The basaltic lava, which shows aphyric, intergranular, intersertal and micro-porphyritic textures, mainly consists of secondary minerals and some few relics of clinopyroxene microphenocrysts. Secondary minerals include almost pure albite ($Ab_{99.7-98.7}$), Mg-rich chlorites (brunsvigites), epidote, titanite, pumpellyite and quartz as interstitial mass or late veins. On the other hand, dolerites present mostly subophitic textures (Fig. 2c). They mainly consist of albitized plagioclase ($Ab_{98.5-99.2}$) and amphiboles, which can be distinguished into hornblende and secondary tremolite and actinolite. Some hornblende and plagioclase can be observed as inclusions in each other, clearly indicating their syncrystallization. Secondary minerals also include epidote, zoisite, titanite, quartz and chlorite. Opaque minerals include Fe-Ti-oxides.

Rodingite sample (Fig. 2d) SRDN consists of hydrogarnets, vesuvianite, chlorite (brunsvigite), diopside and prehnite. Hydrogarnets mostly appear as hydroandradites ($Alm_{0.00}Adr_{61.33-67.43}Grs_{28.25-35.16}$Prp0.10-2.49$Sps_{0.00-0.33}Uv_{0.41-2.75}$), but there are also accessory uvarovite crystals ($Alm_{0.00}Andr_{38.94}Grs_{19.95}Prp_{1.07}Sps_0Uv_{40.05}$). The uvarovite Cr-bearing crystals (Cr_2O_3: 10.34 wt.%), most likely formed at the expense of spinel. The clinopyroxenes are appearing as diopside grains ($En_{48.53-49.89}Wo_{47.56-48.10}Fs_{2.32-3.33}Mg_{93.96-96.28}$), exhibiting high Mg# values (89.71-93.56) and low TiO_2 (0.00-0.04 wt.%), Al_2O_3 (0.00-0.61 wt.%), Na_2O (0.00-0.01 wt.%) and Cr_2O_3 (0.00-0.06 wt.%) values. Vesuvianite presents highly ranging TiO_2 values (0.02-0.59 wt.%) while the MgO range from 2.78 to 3.33 wt.%.

Table 1 - Representative average mineral chemistry analyses.

Rock Type	**Rodingite**			**Serpen-tinite**	**Basaltic Lava**		**Dolerite**				**Gabbro**			
Miner.	**H-gt**	**Cpx**	**Vez**	**Sp**	**Plag**	**Epd**	**Plag**	**Epd**	**Amph**	**Pump**	**Plag**	**Epd**	**Amph**	**Pump**
SiO_2	37.42	55.67	37.40	0.22	68.40	38.10	68.11	38.22	52.49	37.49	68.75	39.43	50.58	37.38
TiO_2	0.14	0.05	0.23	0.20	0.08	0.08	0.02	0.11	2.81	0.01	0.16	0.05	1.21	0.05
Al_2O_3	5.18	0.18	16.42	35.16	18.94	22.33	19.08	25.06	3.37	24.56	18.92	27.84	5.25	24.82
FeO	18.34	0.93	3.00	15.40	0.47	13.05	0.05	9.65	11.92	2.11	0.00	6.51	10.53	2.45
MnO	0.29	0.12	0.09	0.12	0.03	0.36	0.00	0.12	0.25	0.09	0.14	0.00	0.14	0.10
MgO	0.17	10.78	3.07	15.25	0.00	0.00	0.00	0.00	16.77	3.37	0.00	0.00	16.90	2.95
CaO	32.37	14.56	34.56	0.00	0.12	23.05	0.22	23.17	10.99	22.40	0.03	23.40	11.09	22.72
Na_2O	0.00	0.00	0.51	0.00	10.79	0.01	11.03	0.10	0.57	0.09	10.99	0.03	0.33	0.03
K_2O	0.00	0.00	0.12	0.00	0.04	0.03	0.01	0.01	0.10	0.10	0.00	0.14	0.18	0.09
Cr_2O_3	2.36	0.03	0.12	32.86	0.02	0.00	0.05	0.00	0.12	0.11	0.07	0.00	0.20	0.04
NiO	0.02	0.00	0.47	0.00	0.00	0.00	0.00	0.00	0.01	0.09	0.00	0.00	0.09	0.00
Total	96.06	100.02	95.20	99.20	98.88	96.82	98.60	96.92	97.37	90.44	99.06	97.38	97.08	90.62

4.2. Whole Rock Chemistry

For classification of the basic rocks, due to their high percentage of secondary minerals and LOI values, we base mostly on relatively immobile elements diagrams. So, using the plot of Zr/Ti vs. Nb/Y (Fig. 3a) both lava and gabbro samples plot within the basaltic field, indicating secondary silicification of the rocks. In addition, both of these studied rocks plot in the tholeiitic field (Fig. 3b). From REE/MORB

normalized patterns the tholeiitic basalt exhibits a slight fractionation between the LREE and HREE, however all REE values being constantly near MORB ones. The gabbro presents moderate to low LREE values, slightly higher MREE and even higher HREE patterns (Fig. 4a). The $(La/Yb)_{MORB-N}$ values are quite similar for the basalt and gabbro (1.22 and 1.4 respectively), with the basalt exhibiting lower $(La/Sm)_{MORB-N}$ values compared to gabbro (1.36 and 2.41 respectively) (Fig. 4a), while the Eu anomalies vary from negative to slightly positive (Eu_N/Eu^*= 1.03 and 0.76 respectively). Diorite from Skyros Island (Pe-Piper and Piper, 2002) presents subparallel LREE patterns with basalt and gabbro respectively (Fig. 4a). Its MORB normalized multi-trace element pattern is almost identical with Skyros gabbro (Fig. 4b) suggesting a same source of the rocks. The MORB normalized multi-trace element of the gabbro and lava samples show that the normalized Th and U values are much higher compared to those of Nb. Both samples have noticeable positive Sr and Pb anomalies, as well as slight negative Zr anomalies (Fig. 4b). Low Ti tholeiitic volcanic rocks from Kyra Panagia and Alonnisos ophiolites (Pe-Piper et al., 1996) exhibit high U, Th and K values, while their Sr positive anomaly is also observed in basalt, gabbro and diorite samples (Fig. 4b).

Table 2 - Whole Rock major (wt.%) and trace element (ppm) compositions of serpentinite (SOPH), rondigite (SRDN), gabbro (SGBR) and lava (SLVA), -: below detection limit.

SiO_2	39.66	43.49	50.37	56.76	La	0.3	20.2	1.4	1.8
TiO_2	0.01	0.04	0.23	0.93	Ce	0.3	43	2.3	4.4
Al_2O_3	1.39	9.43	17.06	15	Pr	-	4.64	0.34	0.73
Fe_2O_3	8.39	3.45	5.67	11.98	Nd	-	16	1.4	4.1
MnO	0.11	0.16	0.11	0.15	Sm	-	3.49	0.61	1.39
MgO	34.79	10.2	9	3.04	Eu	-	0.45	0.21	0.63
CaO	0.44	29.59	9.98	5.81	Gd	-	4.27	1.13	2.48
Na_2O	0.02	-	2.8	2.47	Tb	-	0.76	0.22	0.43
K_2O	0.01	-	0.81	0.01	Dy	-	5.32	1.61	3.6
P_2O_5	-	0.04	0.02	0.07	Ho	-	1.04	0.37	0.69
Cr_2O_3	0.462	0.027	0.076	-	Er	0.04	3.62	1.2	2.41
LOI	14.4	3.4	3.8	3.7	Tm	-	0.48	0.18	0.3
TOT/C	0.11	0.18	0.03	0.02	Yb	0.08	2.87	1.22	1.8
TOT/S	0.06	-	-	-	Lu	0.02	0.45	0.17	0.3
TOTAL	99.85	100.01	99.96	99.94	Mo	-	-	-	-
Ba	5	5	34	7	Cu	7.7	200.1	15.2	20.7
Be	-	5	-	-	Pb	1	2.1	1.4	2.2
Co	111.5	23.9	30.7	26.2	Zn	16	7	7	73
Cs	-	-	0.2	-	Ni	2458.5	124.4	111.1	18.5
Ga	-	3.8	8.5	12.2	As	0.8	0.5	2.3	0.6
Hf	-	2.9	0.5	1.2	Cd	-	0.3	-	-
Nb	-	17.8	0.1	0.3	Sb	-	-	-	-
Rb	0.1	-	11	-	Bi	-	-	-	-
Sn	-	-	-	1	Ag	-	-	-	-
Sr	3.5	17.6	193	236.5	Au	1.3	11.7	-	-
Ta	-	1.2	-	-	Hg	0.11	0.09	0.12	0.08
Th	-	8.2	-	0.4	Tl	-	-	-	-
U	0.2	1	0.1	0.1	Se	-	-	-	-
V	40	25	177	134	Sc	15	7	41	32
Zr	0.6	74.1	11.4	32	Y	0.5	31.1	10	20.1

On the other hand, low Ti tholeiitic rocks from East Thessaly ophiolites (Migiros, 1986) exhibit a positive Pb anomaly, similar to that of lava, gabbro and rodingite sample respectively (Fig. 4b). They also present high Th values and negative Ti anomalies (Fig. 4b). Rodingite sample displays a high fractionation between the LREE and the HREE patterns (Fig. 4a). Its MREE and HREE patterns seem to be subparallel to those of gabbro and lava samples. It presents $(La/Yb)_N$= 8.59 and

$(La/Sm)_N$= 6.09 (Fig. 4a) and negative Eu anomaly (Eu_N/Eu^*=0.35). MORB normalized multi-trace element show a clear Ba and Sr enrichment and strong Ti, Sr, K negative anomalies, while their U, Nb and LREE values are quite high (Fig. 4b).

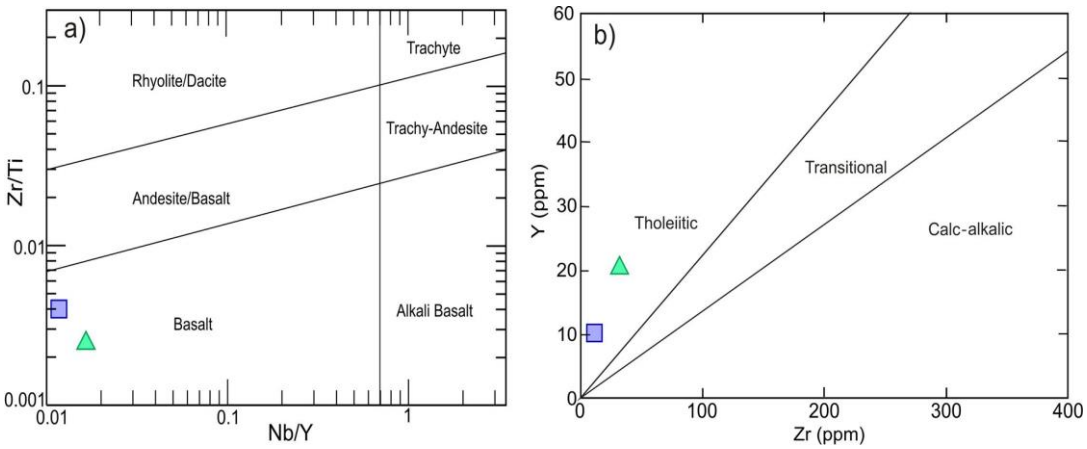

Figure 3 - a). Binary classification diagram of Zr/Ti vs. Nb/Y (Winchester and Floyd, 1977, modified by Pearce 1996) for basaltic lava (triangle) and gabbro (square) samples. b). Y (ppm) vs Zr (ppm) magmatic affinity distinguishing diagram (Barrett and Maclean, 1999).

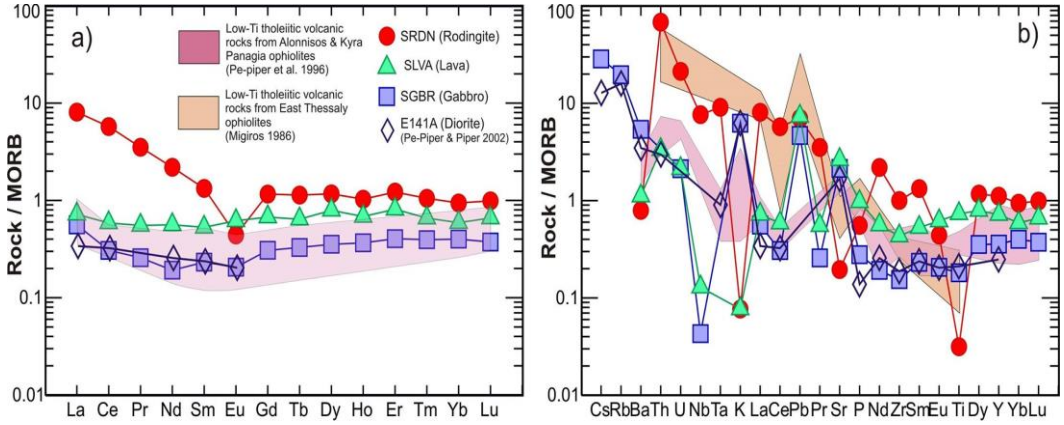

Figure 4 - MORB-normalized REE patterns [normalization factors after Pearce and Parkinson (1993)] of rodingite (SRDN), gabbro (SGBR), basaltic lava (SLVA) samples from Skyros. b) MORB-normalized multi-trace element patterns. For comparison, diorite (E141A) is from Skyros (Pe-Piper and Piper, 2002), volcanic rocks from Kyra Panagia ophiolites (Pe-Piper et al., 1996) and volcanic rocks from E. Thessaly ophiolites (Migiros, 1986).

5. Discussion

5.1. Metamorphic and metasomatic processes

Ophiolites are often exposed to orogenic and/or oceanic metamorphism and metasomatism which may be associated with subduction and subsequent exhumation processes and also the hydrothermal fluids circulation (e.g. Manning and Bird, 1995; Magganas and Koutsovitis, 2015 and references therein). During the exhumation stage circulating subduction related fluids and/or oceanic thermal waters may alter the ophiolitic rocks. Serpentinization and rodingitization of the ultramafic and basic rocks respectively are two of the most usual alteration processes. The mineralogy of the Skyros ophiolitic rocks imply for an intense alteration, which due to the absence of strong or pervasive

foliation in all magmatic rocks is assumed to have been developed mostly during oceanic metamorphism and metasomatism. In particular, the basaltic and gabbroic rocks have been subjected from medium to very low grade oceanic metamorphism (lower amphibolite to prehnite-pumpellyite facies), as noticed by clinopyroxene alteration, and the abundance of secondary minerals such as hornblende, albite, chlorite, epidote, prehnite and pumpellyite. Similarly, ultramafic rocks have been subjected to intense serpentinization, noticed by the predominance of serpentine (antigorite), but also by the replacement of pyroxenes to bastites and spinel alteration to magnetite. The presence of quartz and epidote-rich late veins within dolerite points also for alteration induced by low T oxidized silica-rich hydrothermal fluids. However, the role of subduction originated fluids to this alteration needs more data to be clearly evaluated for these rocks.

The formation of rodingite can be ascribed to intense metasomatic processes, either associated with sea but possibly also with subduction related fluids (e.g. Li *et al.*, 2004; Tsikouras *et al.*, 2009; Koutsovitis *et al.*, 2013). The main rodingitization stages are interpreted by the Coleman reactions (1967) as seen below:

(1) $1.5An + 0.5Ca^{+2} + 1.5H_2O \rightarrow Prh + 0.5Al_2O_3 + H^+$,

(2) $2Prh + 2Ca^{+2} \rightarrow 2Hgrs + Si^{+4}$

(3) $An + 2Ca^{+2} + 3H_2O + 0.5SiO_2 \rightarrow 2Hgrs + 4H^+$

Most garnets are hydroandradites, while there are some small sized Cr-bearing hydrogarnets crystals (Cr_2O_3= 10.34wt.%). Li *et al*. (2008) explains the formation of hydrogarnet with clinopyroxene and water participation in the reaction with plagioclase, whereas Cr-bearing hydrogarnets formation is related with Cr release from serpentinites (Li *et al.*, 2004). The vesuvianite was most likely formed in very low CO_2 conditions with water rich fluids, at 300-400^{o}C (Li et al., 2004, Hatzipanagiotou *et al.*, 2003, Li *et al.*, 2008, Koutsovitis *et al.*, 2013). Nevertheless, in a lower T stage and during the ophicalcite formation the chemistry of pore waters were enriched in CO_2.

As the ophiolitic rocks clearly escaped any post-Cretaceous high pressure event of regional metamorphism, whereas their underlying metamorphosed rocks of the Eohellenic nappe were probably involved in it (presence of blueschist facies assemblages), the former can correspond to the analogous rocks of the upper tectonic unit (UTU) of the Attico-Cycladic Zone (e.g. those occur in Tinos Island) and the latter to the lower blueschist tectonic unit (BTU) of the Cyclades. In such case, we suggest provided the tectonic contact between Skyros ophiolitic rocks and underlying schists and marbles interpreted as a low-angle detachment zone, then it maybe represents part of the northward extension of the North Cycladic Detachment System (NCDS) (Jolivet *et al.*, 2010).

5.2. Geotectonic setting

Based upon the geochemical data of the basalt and gabbro samples (Fig. 4), it is evident that these have been affected by subduction-related processes. This can be observed by the La/10-Y/15-Nb/8 ternary diagram (Fig. 5) in which the studied samples plot within the island arc settings field. On the other hand, the Nb/Th ratio has been used by researchers (e.g. Pearce and Peate 1995; Koutsovitis, 2012) to characterize the tectonic settings of volcanic rocks, with the values lower than '4' characterizing arc-related rocks. Thus, the very low Nb/Th ratios (0.5-0.75) strongly suggests subduction processes, which are further confirmed by their slightly enriched Th/Yb ratios (0.17-0.23; for MORB ~0.05, Pearce, 2008). Furthermore, the high MORB-normalized Th and U values compared to those of Nb for the gabbro and basalt samples (Fig. 4b), may account for influence of subduction processes (Pearce and Peate, 1995; Campbell, 2001).

Small negative Zr anomalies may be either related to subduction or may be attributed to source depletion. The observed positive Pb and Sr anomalies favor subduction; however, secondary processes most likely affected their original magmatic values. Crustal contamination processes most likely did not take place due to the tholeiitic affinity of the studied mafic rocks. On the other hand, the types of hydrogarnet and vesuvianite crystals found within the rodingites are indicative for the involvement of subduction-related fluids during the formation of the rodingites (Koutsovitis *et al.*, 2013). In addition, the chemistry of spinels in serpentinites (TiO_2=0.14-0.25 wt.%, Al_2O_3=35.1-

35.21 wt.%, Cr#=37.38-38.87), shows that their harzburgitic protoliths plausibly resemble back-arc basin peridotites (Kamenetsky *et al.*, 2001). These implications seem to correspond to those of Skyros high Mg and Al chromitites whose petrological and geochemical features indicate a supra-subduction zone (SSZ)/back arc basin environment (Economou *et al.*, 1999). Looking on the geochemistry of the ophiolitic volcanics of the Eohellenic nappe in other parts of east central Greece a general similarity is noted. In particular, the low-Ti tholeiitic volcanic rocks from Alonnisos and Kyra Panagia ophiolites (Pe-Piper *et al.*, 1996) exhibit subparallel MORB-normalized multi-trace element patterns with our studied gabbro and basalt (Fig. 4b). Based upon their trace element and REE geochemistry the majority of Alonnisos and Kyra Panagia rocks formed in an arc related environment (Pe-Piper and Piper, 2002) which corresponds to Skyros subduction related geochemical features. Furthermore, low-Ti tholeiitic volcanic rocks from East Thessaly ophiolites (Migiros, 1986) present subparallel MORB-normalized patterns with Skyros rodingites, exhibiting Ti negative anomalies (Fig. 4b), which further confirm the assumption that Eohellenic nappe ophiolitic rocks from all North Sporades Islands and East Thessaly probably formed within the same supra-subduction zone geotectonic environment of the Jurassic – Lower Cretaceous Vardar Ocean. In addition, certain similarities in tectonic and stratigraphic position, petrogenetical evolution and metamorphism (up to greenschist facies) of these east-central Greece Eohellenic ophiolites and the ophiolitic rocks of the upper tectonic unit of the Attico-Cycladic Zone indicate that they may establish an elongated ophiolitic zone, which, hosting dispersed and small in volume ophiolitic complexes of Vardar Ocean origin, can be associated to the hanging wall of the northward extension of the North Cycladic Detachment System. However many more data are needed in order this hypothesis to be confirmed.

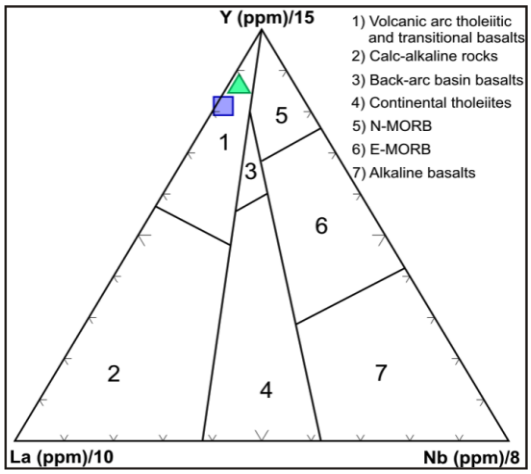

Figure 5 - Ternary diagram La/10-Y/15-Nb/8 for geotectonic environment discrimination of basaltic to felsic rocks (after Cabanis and Lecolle, 1989).

6. Conclusions

The studied rocks occurring on top of the Eohellenic nappe in Skyros mainly consists of serpentinized harzburgite, gabbroic rocks, dolerites, tholeiitic basalt and rodingite. Based on their mutual contacts, which mostly are tectonic and the co-occurrence of ophicalcite, lateritic ores and cherts these magmatic rocks constitute an ophiolitic mélange of probably Upper Jurassic – Lower Cretaceous age. The rocks of the mélange have been affected by low to moderate metamorphic and metasomatic processes; however, some of their magmatic features have been preserved, especially in gabbroic rocks and basalt. Their mineral chemistry as well as their whole rock chemistry suggests that these ophiolitic rocks are associated with subduction-related processes. The presence of vesuvianite crystals in rodingites, as well as the occurrence of relict spinels within serpentinitic rocks, further supports this assumption. Taking into account a geochemical and petrological comparison

between Skyros ophiolitic rocks and similar rocks of the Eohellenic nappe in East Thessaly and other N. Sporades islands we suggest that they all share many petrogenetical and evolutionary features. On the other hand, a similar origin and evolution may exist and with analogous rocks occurring in the upper tectonic unit of the Attico-Cycladic Zone.

7. References

Baltatzis, E., 1984. A new occurrence of rodingite from Skiros island, Greece, *N. Jb. Mineral. Mh*., 317-322

Barrett, T.J. and MacLean, W.H., 1999. Volcanic sequences, lithogeochemistry, and hydrothermal alteration in some bimodal volcanic-associated massive sulfide systems, in Volcanic Associated Massive Sulfide Deposits: Processes and Examples in Modern and Ancient Environments, *Society of Economic Geologists, Reviews in Economic Geology*, 8, 101-131.

Beccaluva, L., Ohnestetter, D., Ohnestetter, M. and Paupy, A., 1984. Two magmatic series with island arc affinities within the Vourinos ophiolites, *Contrib. Mineral. Petrol.*, 85, 253-271.

Cabanis, B. and Lecolle, M., 1989. The La/10-Y/15-Nb/8 diagram; a tool for distinguishing volcanic series and discovering crustal mixing and/or contamination, *Comptes Rendus de l'Academie des Sciences*, 309, 2023-2029 (in French with an English abstract).

Campbell, I.H., 2001. Identification of ancient mantle plumes. *In*: Ernst, R.E. and Buchan, K.L., *eds.*, Mantle plumes: their identification through time, *Geological Society of America Special Paper*, 352, 5-21.

Coleman, R.G., 1967. Low-temperature reaction zones and alpine ultramafic rocks of California, Oregon and Washington, *U.S. Geological Survey Bulletin*, 1247, 1-49.

Economou-Eliopoulos, M. and Eliopoulos, D.G., 1999. Significance of a Spatial Association of High-Cr and High-Al Chromites for Their Genesis and Exploration, *Extrait du Bulletin T. CXIX de l' Académie Serbe des Sciences et des Arts, Classe des Sciences mathématiques et naturelles, Science naturelles*, 39, 123-140.

Ferrière, J., Chanier, F. and Ditbanjong, P., 2012. The Hellenic ophiolites: eastward or westward obduction of the Maliac Ocean, a discussion, *International Journal of Earth Sciences*, 101, 1559-1580.

Harder, H., Jacobshagen, V., Skala, W., Arafeh, M., Berndsen, J., Hofmann, A., Kusserow, H. and Schedler, W., 1983. Geologische Entwicklung und Struktur der Insel Skyros, Nordsporaden, Griechenland, *Berliner geowissenschaftliche Abhandlungen*, 48(A), 7-40.

Hatzipanagiotou, K., Tsikouras, B., Migiros, G., Gartzos, E. and Serelis, K., 2003. Origin of rodingites in ultramafic rocks from Lesvos island (NE Aegean, Greece), *Ofioliti*, 28, 13-23.

Heinitz, W., and Richter-Heinitz, I., 1983. Geologische Unteersuchungen im Nordost-Teil der Insel Skiathos (Griechenland), *Berliner geowissenschaftliche Abhandlungen Berlin*, 48(A), 41-63.

Jacobshagen, G. and Matarangas, D., 2004. Nappe structure of the North Sporades (Greece): on the geological evolution of Alonissos island, *Bull.* Geol. Soc. Greece, 36/4, 1636-1642.

Jolivet, L., Lecomte, E., Huet, B., Denele, Y., Lacombe, O., Labrousse, L., Le Pourhiet, L. and Mehlet, C., 2010. The North Cycladic Detachment System, *Earth and Planetary Science Letters*, 289, 87-104.

Kamenetsky, V.S., Crawford, A.J. and Meffre, S., 2001. Factors controlling chemistry of magmatic spinel: an empirical study of associated olivine, Cr-spinel and melt inclusions from primitive rocks, *Journal of Petrology*, 42(4), 655-671.

Katsikatsos, G.H., 1992. Geology of Greece, Patra, University Publications, 451 pp.

Koutsovitis, P., 2012. Gabbroic rocks in ophiolitic occurrences from East Othris, Greece: petroge-netic processes and geotectonic environment implications, *Mineralogy and Petrology*, 104(3), 249-265.

Koutsovitis, P., Magganas, A., Pomonis, P. and Ntaflos, T., 2013. Subduction-related rodingites from East Othris, Greece: Mineral reactions and physicochemical conditions of formation, *Lithos*, 172-173, 139-157.

Li, X.P., Rahn, M. and Bucher, K., 2004. Metamorphic Processes in Rodingites of the Zermatt-Saas Ophiolites, *International Geology Review*, 46, 28-51.

Li, X.P., Rahn, M. and Bucher, K., 2008. Eclogite facies metarodingites: phase relations in the system SiO2–Al2O3–Fe2O3–FeO–MgO–CaO–CO2–H2O: an example from the Zermatt-Saas ophiolite, *Journal of metamorphic Geology*, 26, 347-364.

Manning, C.E. and Bird, D.K., 1995. Porosity, permeability and basalt metamorphism. *In*: Schiffman, P. and Day, H.W., *eds*., *Geological Society of America Special Paper,* 296, 123-140.

Matarangas, D., 1992. Geological investigations of Skopelos island (North Sporades, Greece), *Berichte des Forschungszentrums Jülich*, 2684, 157.

Magganas, A., 2002. Constraints on the petrogenesis of Evros ophiolite extrusives, NE Greece, *Lithos*, 65, 165-182.

Magganas, A. and Koutsovitis, P., 2015. Composition, melting and evolution of the upper mantle beneath the Jurassic Pindos ocean inferred by ophiolitic ultramafic rocks in East Othris, Greece, *International Journal of Earth Sciences*, 104, 1185-1207.

Migiros, G., 1986. The ophiolites of East Thessaly, *IGME Geol. & Geoph. Special Issue*, Athens, 249-268.

Migiros, G. and Economou, G.S., 1988. Chromites in the ultrabasic rocks East Thessaly Complex (Central Greece), *Ofioliti*, 13, 127-136.

Papanikolaou, D., 2009. Timing of tectonic emplacement of the ophiolites and terrane paleogeography in the Hellenides, *Lithos*, 108, 262-280.

Pearce, J.A. and Parkinson, I.J., 1993. Trace element models for mantle melting: application to volcanic arc petrogenesis. *In*: Pichard, H.M., Alabaster, T., Harris, N.B.W., Neary, N.B.W., *eds*., Magmatic Processes and Plate Tectonics, *Geol. Soc. London Sp. Pub.*, 76, 373-403.

Pearce, J.A., 1996. A user's guide to basalt discrimination diagrams. *In*: Wyman, D.A., *ed*., Trace element geochemistry of volcanic rocks: applications for massive sultide exploration, *Geological Association of Canada, Short Course Notes*, 12, 79-113.

Pearce, J.A. and Peate, D.W., 1995. Tectonic implications of the composition of volcanic ARC magmas, *Annual Review of Earth and Planetary Sciences*, 23, 251-285.

Pearce, J.A., 2008. Geochemical fingerprinting of oceanic basalts with applications to ophiolite classification and the search for Archean oceanic crust, *Lithos*, 100, 14-48.

Pelletier, L., Vils, F., Kalt, A. and Gméling, K., 2008. Li, B and Be Contents of Harzburgites from the Dramala Complex (Pindos Ophiolite, Greece): Evidence for a MOR-type Mantle in a Supra-subduction Zone Environment, *Journal of Petrology*, 49(11), 2043-2080.

Pe-Piper, G., Matarangas, D. and Jacobshagen, V., 1996. The Mesozoic metavolcanics rocks of Alonnisos and Kyra Panagia islands, Sporades, Greece, *N. Jb. Miner. Mh*, 6, 251-263.

Pe-Piper, G. and Piper, D.J.W., 2002. "The Igneous rocks of Greece: the anatomy of an orogen", Gebrüder Borntraeger, Stuttgart, 573 pp.

Pomonis, P., Tsikouras, B. and Hatzipanagiotou, K., 2007. Petrogenetic evolution of the Koziakas ophiolite complex (W. Thessaly, Greece), *Mineralogy and Petrology*, 89, 77-111.

Robertson, A.H.F., 2004. Development of concepts concerning the genesis and emplacement of Tethyan ophiolites in the Eastern Mediterranean and Oman regions, *Earth-Science Reviews*, 6, 331-387.

Saccani, E., Photiades, A. and Beccaluva, L., 2008. Petrogenesis and tectonic significance of Jurassic IAT magma-types in the Hellenide ophiolites as deduced from the Rhodiani ophiolites (Pelagonian zone, Greece), *Lithos*, 104, 71-84.

Stampfli, G.M., Vavassis, I., de Bono, A., Rosselet, F., Matti, B. and Bellini, M., 2003. Remnants of the Palaeotethys oceanic suture-zone in the western Tethyan area, *Bolletino della Società Geologica Italiana*, Volume speciale, 1-24.

Tsikouras, B., Karipi, S., Rigopoulos, I., Perraki, M., Pomonis, P. and Hatzipanagiotou, K., 2009. Geochemical processes and petrogenetic evolution of rodingite dykes in the ophiolite complex of Othrys (Central Greece), *Lithos*, 113, 540-554.

Whattam, S.A. and Stern, R.J., 2011. The 'subduction initiation rule': A key for linking ophiolites, intra-oceanic forearcs and subduction initiation, *Contributions to Mineralogy and Petrology*, 162, 1031-1045.

Winchester, J.A. and Floyd, P.A., 1977. Geochemical discrimination of different magma series and their differentiation products using immobile elements, *Chem. Geol.*, 20, 325-343.

Δελτίο της Ελληνικής Γεωλογικής Εταιρίας, τόμος L, σελ. 1878-1886
Πρακτικά 14ου Διεθνούς Συνεδρίου, Θεσσαλονίκη, Μάιος 2016

Bulletin of the Geological Society of Greece, vol. L, p. 1878-1886
Proceedings of the 14th International Congress, Thessaloniki, May 2016

DETERMINATION OF SILICA POLYMORPHS AND FELDSPARS IN INDUSTRIAL SAMPLES OF BENTONITE AND PERLITE

Kaza T. and Stamatakis M.G.

National and Kapodistrian University of Athens, Department of Geology, Panepistimiopolis, Ano Ilissia, 157 84, Athens, Greece, kaza.triada@hotmail.com, stamatakis@geol.uoa.gr

Abstract

The aim of the present study is to apply a fast and reliable XRD method to identify the percentage of silica polymorphs and feldspars that industrial bentonite and perlite may contain, because these gangue minerals influence the quality of the final products. The current research was implemented by selecting of appropriate almost pure reference samples of bentonite and perlite in which specific amount of silica polymorphs and feldspars was added. The selection of all samples was based on the X-ray diffraction patterns. The synthetic mixtures produced were either with bentonite or perlite with a single added mineral or with two of them in percentages up to 10%. The minerals added to the reference samples were distinguishable in the XRD patterns in different percentages for each mineral added, but also in the two different reference samples. After evaluating of the XRD patterns of a series of samples, it was concluded that the lowest percentage of silica polymorphs and albite that was detected in the reference bentonite was 0.5% quartz, 1% cristobalite 10% opal-CT, and 1% albite, whereas the percentages for the reference perlite was 1% quartz, 2% opal-CT, 1% cristobalite and 0.5% albite. This method can be applied to any commercial bentonite and perlite bulk sample to define its purity concerning its silica polymorph and feldspar content.
Keywords: *Quartz, Opal-CT, Cristobalite, Albite, XRD.*

Περίληψη

Στόχος της συγκεκριμένης εργασίας είναι η εφαρμογή μιας ταχείας και αξιόπιστης μεθόδου XRD για τον υπολογισμό % περιεκτικότητας πολύμορφων της πυριτίας και αστρίων, σε δείγματα μπεντονίτη και περλίτη. Τα συγκριμένα ορυκτά επηρεάζουν άμεσα την ποιότητα των τελικών βιομηχανικών προϊόντων. Η διαδικασία που ακολουθήθηκε αφορά την επιλογή, με βάση την αποτίμηση των ακτινοδιαγραμμάτων XRD, κατάλληλων δειγμάτων αναφοράς μπεντονίτη και περλίτη, στα οποία προστέθηκε ένα συγκεκριμένο ποσοστό πολύμορφων SiO_2 και αστρίων. Οι συνθετικές αναμείξεις δημιουργήθηκαν με μπεντονίτη ή περλίτη, με ένα ή δύο από τα παραπάνω ορυκτά, σε συνολικό ποσοστό < 10%. Τα ορυκτά που προστέθηκαν στα δείγματα αναφοράς ήταν διακριτά στα ακτινοδιαγράμματα, τα οποία με την σειρά τους διαφοροποιούνταν όχι μόνο σε σχέση με τα διαφορετικά ποσοστά των ίδιων προστιθέμενων ορυκτών αλλά και σε σχέση με τα δύο αρχικά υλικά. Από την αποτίμηση των ακτινοδιαγραμμάτων που προήλθαν από την μέθοδο XRD, τα χαμηλότερα ποσοστά των πολύμορφων πυριτίας και του αλβίτη που ανιχνεύθηκαν στον μπεντονίτη ήταν 0,5% για τον χαλαζία, 1% για τον χριστοβαλίτη, 10% για τον οπάλιο-CT, και 1% για τον αλβίτη, ενώ για τον περλίτη τα ποσοστά διαφοροποιούνται ως εξής: 1% για τον χαλαζία, 1% για τον χριστοβαλίτη, 2%

για τον οπάλιο-CT και 0,5% για τον αλβίτη. Η συγκεκριμένη μέθοδος μπορεί να εφαρμοστεί σε δείγματα μπεντονίτη και περλίτη, για να καθοριστεί η καθαρότητα του σε σχέση με το περιεχόμενο τους σε πολύμορφα πυριτίας και αστρίους.
Λέξεις κλειδιά: *Χαλαζίας, Οπάλιος-CT, Χριστοβαλίτης, Αλβίτης, XRD.*

1. Introduction

Bentonite and perlite are important industrial minerals since they have qualitative and quantitative characteristics that justify economic interest for their use in a series of industrial and agricultural sectors, trade and generally in human activities (Harben and Kuzvart, 1997).

1.1. Bentonite

Bentonite is a rock consisting of aluminosilicate minerals of the group of smectites and its main component is the mineral clay montmorillonite, which is found at a rate of over 80%. Montmorillonite, as well as other minerals of the smectite group, belongs to the phyllosilicates minerals with a 2:1 layer structure and consist of two silica tetrahedral layers between which an aluminum octahedral layer is located (Eisenhour *et al.,* 2009).

Bentonite is used for its rheological**,** bonding and sorptive properties,as well as its impermeability and large surface area. The main uses include drilling mud, foundry sands, iron ore pelletizing, absorbent granules (litter), various invasive agents, sealants, ingredients in cosmetics, pharmaceuticals and medical applications, fire protection materials, animal food (feed supplement-pelletizing process), additives in ceramics to increase the plasticity, the paper industry and agriculture (Grim *et al.*, 1978).

In Greece, the most important bentonite deposits, with the largest production are in Milos and Kimolos, while minor deposits with no commercial interest occur in Lesvos, Chios and Evros. The deposits of Milos and Kimolos are mainly Ca-bentonites (Francalanci *et al.*, 2008).

Bentonites from Milos (mainly in the eastern and northeastern part of the island) have been formed by transgenic alteration pyroclastic layers, with a composition between Pliocene rhyolite and andesite, which took place in an underwater environment and low temperature conditions (Chrisitids *et al.*, 1995). Bentonite from Milos is mostly calcium with varying percentages of quartz, potassium feldspars and plagioclase. Mineralogical studies have shown that the dominant component of all the deposits is the dioctaedral smectite, while there are also significant percentages of opal, zeolite, alunite, barite, gypsum, sulfides and oxides of iron and titanium (Stamatakis *et al*., 1996).

In Kimolos the most significant reserves are detected in the northeastern part of the island and include the deposits of Prassa and Loutra (Christidis *et al.*, 1995). The bentonites of Kimolos are mainly calcareous, while it is worth noting that contain significant amounts of cristobalite. The only deposit that is exploited is that of Prassa, since it consists of white high quality bentonite.

Greece conceives the 3rd place in world production of bentonite with extraction of 1.011.485 t/yr, (USGS 2014). The extraction is mostly in Milos by IMERYS and in smaller quantities in Kimolos by BENTOMINE S.A Company. In a global scale, large bentonite deposits are located in USA and Turkey [1st and 2nd producer respectively], and in China, Italy, Spain, Germany, Cyprus, Bulgaria, Australia, Algeria, Morocco and South Africa (Harben and Kuzvart, 1997; USGS, 2014).

1.2. Perlite

The term perlite refers to a vitreous acidic volcanic rock which contains 72-76% SiO_2 and 2.6% H_2O^+. The composition is commonly rhyolitic. However some perlites have dacitic or andesitic composition. Most perlites consist almost entirely of a glassy groundmass, in which scattered phenocrysts and microcrystals of quartz, feldspar, biotite and other mafic minerals are found. The presence of phenocrysts, which are found in varying amounts, depreciate their quality since the swelling capacity of the perlite is reduced as the presence of phenocrysts increases (Breese *et al.*, 1994). The age of

perlite deposits formation is relatively young in geologic time, mostly earlier than Tertiary, since over time lavas undergoes devitrification, partly or completely losing their ability to swell.

Perlite is used in the construction industry as lightweight aggregate and insulation agent, in agricultural applications as soil amendment and in hydroponics, in liquid filtration, in chemical industries, and in environmental applications such as waste filtration, binding of contaminated subsoil, absorption of industrial oil spills and hazardous liquids in contaminated areas (Austin *et al.*, 1995).

Greece ranks 1st in the European and global arena since 2002, with a production of about 876.396 t/yr of perlite in 2012, followed by the US and China with production rate reaching only 21% compared to 38% in Greece (Bolen, 2013). Perlite is currently mined in Milos Island, in the north coast at Trahilas and in the south coast at Tsigrado by IMERYS SA, and on the islet of Gyali that is located close to Kos and Nisyros islands by the PERLITES AEGEAN SA. In the island of Milos, the formation of perlites is due to the Pliocene volcanic activity and it has created acidic tuffs, tuffites and ignimbrites with an extrusive phase represented by blocks and lava flows of andesite, dacite and rhyolite. In Kos, the volcanic activity is characterized by Upper-Miocene to Pleistocene volcanic products, while Nisyros is a stratovolcano structured by Pliocene volcanic products that consist mainly of andesites and basaltic andesites on which is deposited calcalcaline volcanic products of dacitic-ryodacitic composition in the form of pyroclastic deposits, lava flows and lava structures. Perlite deposits of minor importance occur also in Kimolos, Kos and Lesbos islands.

2. Materials and Methods

In order to select the purest minerals to use as reference samples, a series of raw materials were run by XRD, with the exception of perlite extracted from Turkey that was already tested for its purity by Dr D. Alfieris, resources development geologist in IMERYS SA. For bentonite, nine samples derived from different regions of Turkey and Romania was tested, whereas the silica polymorphs and feldspars were derived from different regions of Greece.

2.1. Materials

2.1.1. Bentonite Sample

The sample selected comes from the area Seyitgazi (39 ° 26'44 "N 30 ° 41'38" E) in central Turkey. The central city of Seyitgazi is 43km to the south of the capital of the Eskisehir Province. The area consists of Miocene metamorphic, ophiolitic and carbonate, as well as by Neogene volcanic and sedimentary rocks. More specifically, the background of the given area is represented by Mesozoic carbonate rocks, mélange with sandstones, clays and marls and ophiolites. These rocks are covered by Neogene carbonate rocks, lavas and tuffs (Aydar *et al.*, 2013).

2.1.2. Perlite Sample

The perlite sample used was derived from the region Nevsehir (38° 46' 54" N, 34° 41' 17" E) a city and the capital of the prefecture of central Turkey. The Nevsehir Plateau belongs to the Central Anatolian Volcanic Province (CAVP) and includes the Cappadocian Volcanic Province (CVP) that is characterized by the development of stratovolcanoes and the presence of thick layers of ignimbrite (Le-Pennec *et al.*, 1994; Lepetit *et al.*, 2007).

2.1.3. Quartz Samples

Two quartz samples were analyzed to make the selection of the suitable one. The QUARTZ CRETE sample comes from Kissamos Bay, Chania and it comes from beach sand. The second sample, QUARTZ, comes from quartz veins of milky quartz running through metamorphic rocks of Hymettus Mountain in Attica.

2.1.4. Opal-CT Samples

Based on previous surveys, two samples of opal-CT were tested. The sample OPAL KIM comes from the island of Kimolos and is associated with hydrothermal alteration of volcanic rocks, mainly in the area of Prassa. The sample OPAL EVIA comes from Evia Island and is associated with the formation of stockwork magnesite in ultrabasic rocks (Sample provided by Dr. I. Mitsis).

2.1.5. Albite Sample

The albite sample also comes from the island of Crete and more specifically Western Crete, and is associated with the tectonic cover of phyllite-quartzite series (Fytrolakis, 1978).

2.1.6. Cristobalite Sample

The sample of cristobalite is a commercial sample imported from Italy, in powder form.

2.2. Analytical Techniques

All samples were ground, homogenized, in an agate mile, and analyzed by X-ray diffraction twice, (Siemens Model 5005 X-ray diffractometer, Cu-Ka rad., 40 kV, 40mA, NKUA) and evaluated by use of the EVA 10.0 program.

The methodology initially involved selecting of reference samples for the minerals: quartz, cristobalite, opal-CT and albite, known for their clarity and the absence of impurities. The purity of the samples was defined by evaluating their X-ray diffraction patterns. Afterwards, the corresponding selection of suitable bentonite sample was made with the same procedure, which led to the selection of the appropriate sample with the highest percentage of smectite and low percentage of impurities.

Subsequently, the selection of the reference samples, involves the creation of synthetic mixtures of different percentages of bentonite and perlite with quartz, opal-CT, cristobalite and albite. This process also included the weighing, using the electronic precision balance, and the co-grinding of blends. Finally, the valuation of these X-ray diffraction patterns of the mixtures, allows us to find the lowest percentage of silica polymorphs [quartz, opal-CT, cristobalite] and feldspars [albite].

3. Results and Discussion

3.1. Selection of the reference samples

3.1.1. Bentonite

In Table 1, the mineralogical composition of the bentonite samples studied is shown.

Table 1 - XRD analysis of the bentonite samples studied.

Bentonite Samples	Minerals								
	QZ	ILL	CRS/ OCT	MO	VG	ALB	CL	TRD	SN
B13352_06	TR	TR	TR	MJ		TR			
B13352_07	MJ	MD	MD	MD		MD		TR	
B13352_14	MD	MD	MD	MJ		TR			TR
B13352_40	MD	TR	MJ	MJ	MJ	MD		MJ	
B07209_03	MD	MJ		MD		MD	MD		
B07225_01	TR		MD	MJ		TR			
B07226_01	TR		MD	MJ					
B09416_03	TR		MJ	MJ		MD			

Explanatory Notes: **QZ**: Quartz, **ILL**: Illite, **CRS/OCT**: Cristobalite/Opal-CT, **MO**: Montmorillonite, **VG**: Volcanic Glass, **ALB**: Albite, **CL**: Clinoptilolite, **TRD**: Tridymite, **SN**: Sanidine, **MJ**: major, **MD**: medium, **TR**: trace.

From the above nine bentonite samples, B13352_06 was chosen as appropriate for establishing the laboratory part of the work. Through the process of XRD, it was able to determine the structure and composition of the samples. Therefore, the purity of the sample and the absence of impurities have led us to the given selection.

3.1.2. Perlite Sample

The XRD image of the perlite sample reveals that it is exclusively composed of volcanic glass.

3.1.3. Quartz Sample

Of the two quartz samples tested, sample QUARTZ CRETE was selected, as the assessment of its X-ray diffraction patterns points us to a high purity sample.

3.1.4. Opal-CT Sample

From the two opal-CT samples, the sample: OPAL_EVIA was selected, containing only traces of quartz. By contrast the OPAL_KIM, eventhough rich in opal-CT, it contains higher amounts of quartz and minor tridymite (Figure 1).

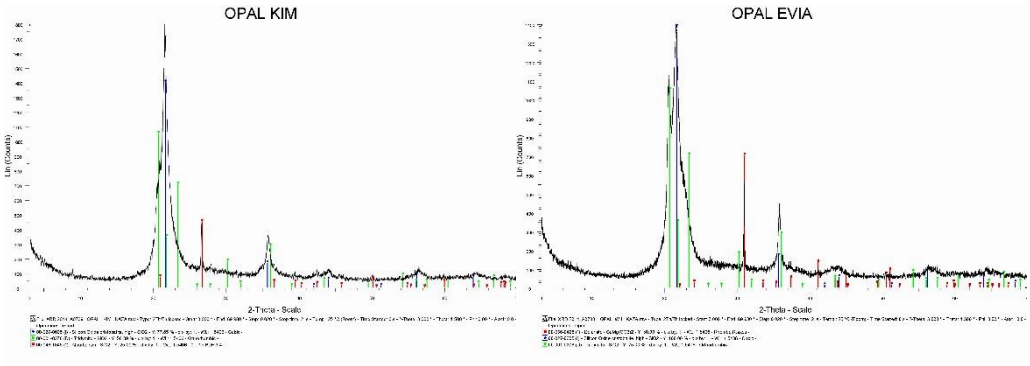

Figure 1 - X-ray diffraction patterns of the opal-CT samples tested.

3.1.5. Albite Sample

The feldspar sample selected was identified by XRD as pure albite.

7.1.6. Cristobalite Sample

The XRD pattern of cristobalite sample showed that cristobalite is the predominant mineral phase, accompanied by only negligible amount of microcline and quartz.

3.2. Mixture preparation and XRD analysis

Mixtures of the two aforementioned reference raw materials with silica polymorphs and albite were prepared. In order to achieve qualities of commercial bentonite and perlite, the percentage of the added minerals was <10% in total. The selection of the specific mixtures is shown in Tables 2 and 3.

3.2. Bentonite Mixtures Results

Bentonite-Quartz: These blends were prepared by adding of 2% and 0.5% g of quartz (Figure 2). It is perceived, therefore, that the addition of 2% quartz creates a characteristic peak that stands out compared to the X-ray diffraction pattern of pure bentonite. In contrast, the addition 0.5% quartz

generates a peak that barely stands out from that of pure bentonite, resulting in the rate of 0.5% quartz being considered the lowest.

Table 2 - Artificial Mixtures of Bentonite.

Serial Number	Bentonite (%)	Quartz (%)	Cristobalite (%)	Opal-CT (%)	Albite (%)
1	98	2			
2	96	2	2		
3	98			2	
4	98		2		
5	98				2
6	99.5	0.5			
7	90			10	
8	99		1		
9	99				1
10	99.5				0.5

Table 3 - Artificial Mixtures of Perlite.

Serial Number	Perlite (%)	Quartz (%)	Cristobalite (%)	Opal-CT (%)	Albite (%)
1	98	2			
2	96	2	2		
3	98			2	
4	98		2		
5	98				2
6	99.5	0.5			
7	90			10	
8	99		1		
9	99				1
10	99	1			
11	99,5				0,5

Bentonite-Opal-CT: These blends were prepared by adding of 10% and 2% opal-CT. The addition of 2% in the first mixing had no difference with the pure bentonite, thus leading to the creation of a new mixture by adding 10% opal-CT. In the X-ray diffraction pattern of the second mixing, a small difference was observed, concluding that the lower percentage in the case of opal-CT is 10%.

Bentonite-Cristobalite: These blends were prepared by adding of 2% and 1% cristobalite. The initial addition of 2% cristobalite resulted in the creation of a peak with a greater height than that of pure bentonite. Then, a mixture with 1% cristobalite was created and 1% was considered the lowest percentage.

Bentonite-Albite: These blends were prepared by adding of 2%, 1% and 0.5% of albite. This specific mixture exhibited diverse results for each of the two runs at percentages of 0.5% adding of albite. Controversial results were obtained in a second badge of analyses of the same sample, so we conclude that albite is clearly detectable at the rate of >1%.

3.3. Perlite Mixtures Results

Perlite-Quartz: These blends were prepared by adding of 2%, 1% and 0.5% quartz (Figure 3). The process began with the creation of a mixture containing 2% quartz, resulting in the creation of an

intense XRD peak at 26.6º degrees. By contrast, negative results were obtained using the mixture with 0.5% quartz. The XRD pattern created with this mixture was not different from that of pure perlite. A 3rd mixture was introduced, therefore with 1% added quartz. In the XRD pattern of this mixture, quartz was detectable.

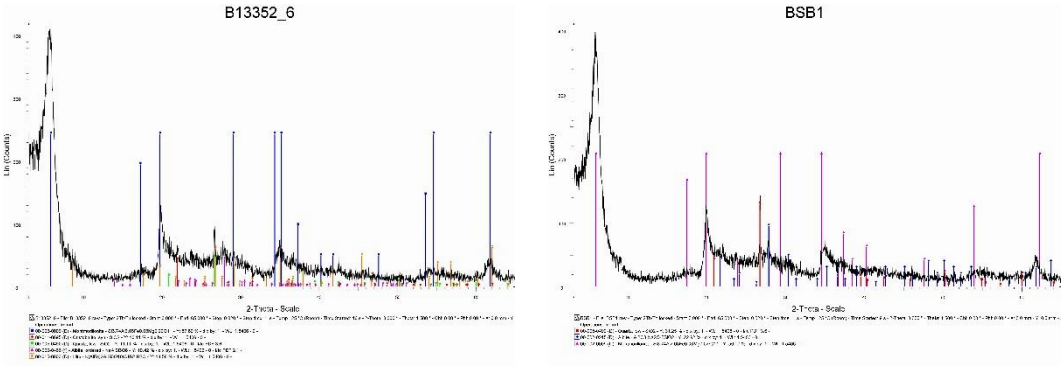

Figure 2 - X-ray diffraction patterns of a) the bentonite sample and b) the mixture of bentonite and quartz.

Perlite-Quartz: These blends were prepared by adding of 2%, 1% and 0.5% quartz (Figure 3). The process began with the creation of a mixture containing 2% quartz, resulting in the creation of an intense XRD peak at 26.6º degrees. By contrast, negative results were obtained using the mixture with 0.5% quartz. The XRD pattern created with this mixture was not different from that of pure perlite. A 3rd mixture was introduced, therefore with 1% added quartz. In the XRD pattern of this mixture, quartz was detectable.

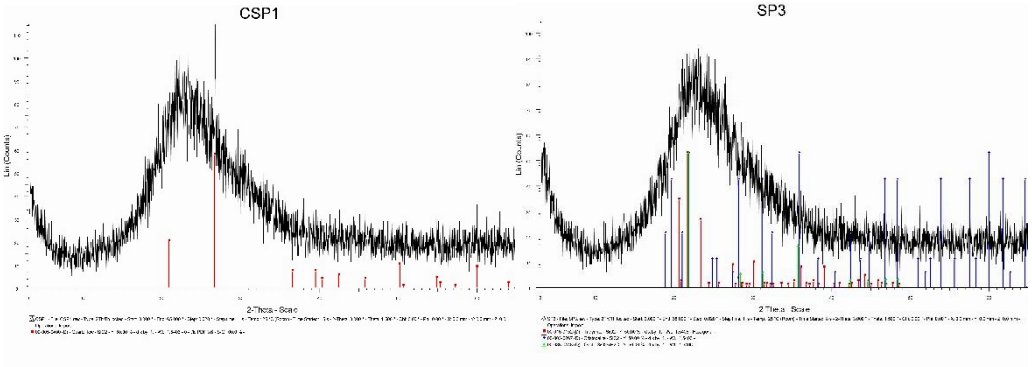

Figure 3- X-ray diffraction patterns of the mixtures of a) perlite and quartz and b) perlite and opal-CT.

Perlite–Opal-CT: These blends were prepared by adding of 10% and 2% of opal-CT (Figure 3). In the XRD pattern, when 10% was added, a sharp change occurs to hump shape. It is more intense in relation to the XRD patterns of pure perlite and perlite with the addition of 2% opal-CT. However, the lowest detectable percentage of opal-CT addition in perlite was 2%. The semi-crystalline opal and amorphous perlite create an effect in which the difference between XRD patterns is not certain.

Perlite-Cristobalite: These blends were prepared by adding of 2% and 1% of cristobalite. The study of the above X-ray diffraction patterns shows clear results, concluding that the lower percentage of cristobalite reaches 1%.

Perlite–Albite: These blends were prepared by adding of 2%, 1% and 0.5% of albite. The evaluation of the above X-ray diffraction patterns led to the conclusion that the lowest detectable percentage of albite in perlite is 0.5%.

4. Conclusions

In the present work, the identification of significantly low levels of silica polymorphs and feldspars in bentonite and perlite samples was achieved, using XRD techniques. Concerning the bentonite sample, percentages are identified as follows: 0.5% for quartz, 10% for the opal-CT, 1% for cristobalite and 1% for albite, while the percentages for perlite are to be differentiated as follows: 1% for quartz, 2% for opal-CT, 1% for cristobalite and 0.5% for albite. The above results are justified by the crystalline nature of quartz and cristobalite, while differentiated in the case of opal-CT, which is semi-crystalline. Still, in line with the material safety data sheet, which determines the quality of perlite in the proportion of crystalline minerals, which must be less than 1% in quartz. It should also be noted that especially in the case of bentonite, the lowest percentage of opal-CT that was identified is close to 10%, since the insertion of semi-crystalline mineral below this percentage is not shown because of the shape of the XRD pattern. The use of reference artificial samples as prototypes is a fast and accurate method for detection of trace amounts of accessory minerals and the quality control of any perlite and bentonite sample of unknown composition. Similar trials but only with quartz in perlite have been done by McKee *et al.* (1990). Comparing with Reitveld method the proposed technique is less complicated, since latter requires in each new sample the interference of internal standard of either ZnO or Al_2O_3. Furthermore, the estimation of mineral content, especially in low percentages in samples that contain mainly amorphous phases or smectites is unsafe by Reitveld method. Concerning the estimation of smectite content of bentonite samples using the Cation Exchange Capacity [CEC] method, it is also less accurate in cases of presence of other micro- and mesoporous minerals, i.e., opal-CT, zeolites, other clay minerals, etc. Future plans include the addition and estimation of their detection limit of other undesirable minerals in bentonite, i.e. pyrite, gypsum, alunite, but also clinoptilolite that is frequently determined in some bentonite deposits, like those of Kimolos Island, Bulgaria and Turkey.

5. Acknowledgments

The authors would like to express their appreciation to Dr. Dimitris Alfieris, IMERYS SA (former S&B Industrial Minerals SA), for providing us all bentonite and perlite samples. Additionally, we would like to thank Dr. George Economou, IGME, for sample preparation, and Dr. Ioannis Mitsis UoA, for helping in XRD analysis.

6. References

Austin, G.S. and Barker, J.M., 1995. Production and Marketing of perlite in the western United States, *In*: Tabilio, M. and Dupras, D.L., *eds*., *Proceedings, 29th Forum on the Geology of Industrial Minerals, California Division of Mines and Geology*, Special Publication, 110, 39-68.

Aydar, E., Çubukcu, H.E., Şen, E. and Akin, L., 2013. Central Anatolian Plateau, Turkey: incision and paleoaltimetry recorded from volcanic rocks, Department of Geological Engineering, Hacettepe University, Ankara, Turkey, *Turkish Journal of Earth Sciences*, 22, 739-746.

Bolen, W.P., 2013. Perlite Mininig Engineering, U.S. Geological Survey: National Minerals Information Center, 72-73.

Breese, R.O.Y. and Barker, J.M., 1994. Perlite, Industrial Minerals and Rocks, 6th ed. Society for Mining, Metallurgy and Exploration, Littleton, Colorado, Carr, L., *ed*., 735-749.

Christidis, G.E., Scott, P.W. and Marcopoulos, T., 1995. Origin of the Bentonite Deposits of Eastern Milos, Aegean, Greece: Geological, Mineralogical and Geochemical Evidence, *Clays and Clay Minerals*, (43), 63-77.

Eisenhour, D.D. and Brown, R.K., 2009. Bentonites - Versatile Clays: Bentonite and Its Impact on Modern Life, *ELEMENTS*, 5(2), 83-88.

Francalanci, L., Vougioukalakis, G.E. and Fytikas, M., 2008. Petrology and Volcanology of Kimolos and Polyegos volcanoes within the context of the South Aegean Arc, *Greece. Geol. Soc. Am*., Spec. Paper (481), 33-65.

Fytrolakis, N., 1978. Contribution to the geological survey of Crete, *Bull. Geol. Soc*., Greece, XIII/2, 101-115 (in Greek).

Grim, R.E. and Güven, N., 1978. Bentonites: Geology, Mineralogy, Properties and Uses. Developments in Sedimentology, 24, Amsterdam, Elsevier scientific publishing company.

Harben, P.W. and Kuzvart, M., 1997. Industrial minerals - global geology, Industrial Minerals Information Ltd. (IMIL), Worcester Park, Surrey, UK. Annex.

Le-Pennec, J.L., Bourdier, J.L., Froger, J.L., Temel, A., Camus, G. and Gourgaud, A., 1994. Neogene ignimbrites of the Nevsehir plateau, Elsevier, Amsterdam, Netherlands.

Lepetit, P., Viereck- Goette, L. and Gurel, A., 2007. Neogene Stratigraphyn of the Nevsehir Plateau, Cappadoca, Turkey, Geological Background in Field Guide to the Excursion on the Geology of the Nevsehir Plateau and the historical cultural.

McKee, Ch., Renault, J. and Barker J., 1990. Quantitative analysis of quartz in perlite by X-ray diffraction, *Prepr. Soc. Min. Eng. Aime*, Soc of Mining Engineers of Aime, Littleton, CO, (USA), 11-166.

Stamatakis, M., Lutat, U., Regueiro, M. and Calvo, P.J., 1996. Milos-The mineral island, Industrial Minerals, No 341.

USGS, 2014. Mineral Commodity Summaries, *Clays*, 44.

Δελτίο της Ελληνικής Γεωλογικής Εταιρίας, τόμος L, σελ. 1887-1894
Πρακτικά 14ου Διεθνούς Συνεδρίου, Θεσσαλονίκη, Μάιος 2016

Bulletin of the Geological Society of Greece, vol. L, p. 1887-1894
Proceedings of the 14th International Congress, Thessaloniki, May 2016

GEOCHEMICAL CHARACTERISTICS OF THE MAFIC ENCLAVES AND THEIR HOSTS FROM NEOGENE ERENLERDAGI VOLCANITES, AROUND YATAGAN VILLAGE AND SAĞLIK TOWN (KONYA), CENTRAL TURKEY

Koçak K.[1]

[1]*Selcuk University Konya, TURKEY, Department of Geology, 54124, Konya, TURKEY, kkocak@yahoo.com, kkocak@selcuk.edu.tr*

Abstract

Late Miocene to Pliocene volcanism is represented by development of lava domes, nuée ardentes and pyroclastic fall and flow (ignimbrites) deposits in the WSW and NW of Konya city. The lava dome contains various mafic microgranular enclaves (MMEs), which have various size (a few cm to a few meters), shape (ellipse/sphere to rounded), with a well-developed chilly zone. The MMEs samples are situated on mostly basaltic andesite and andesite, and a few MME samples on basaltic trachy-andesite area while the host rocks are concentrated on dacite and andesite areas. The felsic samples have more fractionated chondrite-normalised REE pattern (La/Yb_N: 9.5-18.1) than MMEs (6.7-16.0) ones, but both have slightly developed negative Eu anomaly (Eu/Eu: 0.67-0.89 in felsic rocks, 0.68-0.87 in MMEs). In primitive mantle-normalized spider diagram, the MMEs and felsic rocks have negative Nb, Ta, P and Ti anomalies, indicating some subduction component in their genesis. Based on geochemical data, the MMEs are suggested to have been formed by hybridization of basic magma mingled with partially crystallized felsic magma.*
Keywords: *Erenlerdagı, volcanism, Mafic enclaves.*

1. Introduction

Widespread volcanic activity developed in Turkey during the Neotectonic period, producing volcanic rocks covered an area of about 85,000 km^2 in East, Central and West Anatolia (Ketin, 1983). In Central Anatolia, calc-alkaline volcanic units are exposed in large areas situated in the WSW and NW of Konya city (Figure 1), in where transtensive and transpressive tectonic regimes have been effective since the Late Miocene (Kempler and Garfunkel, 1991). The volcanism took place between Late Miocene 11.9 Ma. to Pliocene 3.35 Ma (Keller *et al.*, 1977).

Pre-Mesozoic basement is represented by ophiolitic complex, phyllite, schist, quartzite and dolomi tic limestone, metavolcanic rocks, diorite, diabase, gabbro, peridodite and serpantinite (Özcan ve d iğ., 1990; Eren, 1993; Kurt, 1994). It is unconformably overlain by Upper Miocene-Lower Pliocen e Ulumuhsine formation (Eren, 1993), which is made up by limestone, limestone-mudstone alterna tion and marl. The pyroclastic rocks, which consist of volcanic breccia, agglomerate, tuffite and tuf fs, conformably overlaid the Ulumuhsine formation. The youngest volcanic rocks are andesite, dac ite, and basaltic andesite. Lower Pliocene Yürükler formation overlies unconformably volcanic roc ks, and contains red conglomerate and caliche nodulled mudstone deposits.

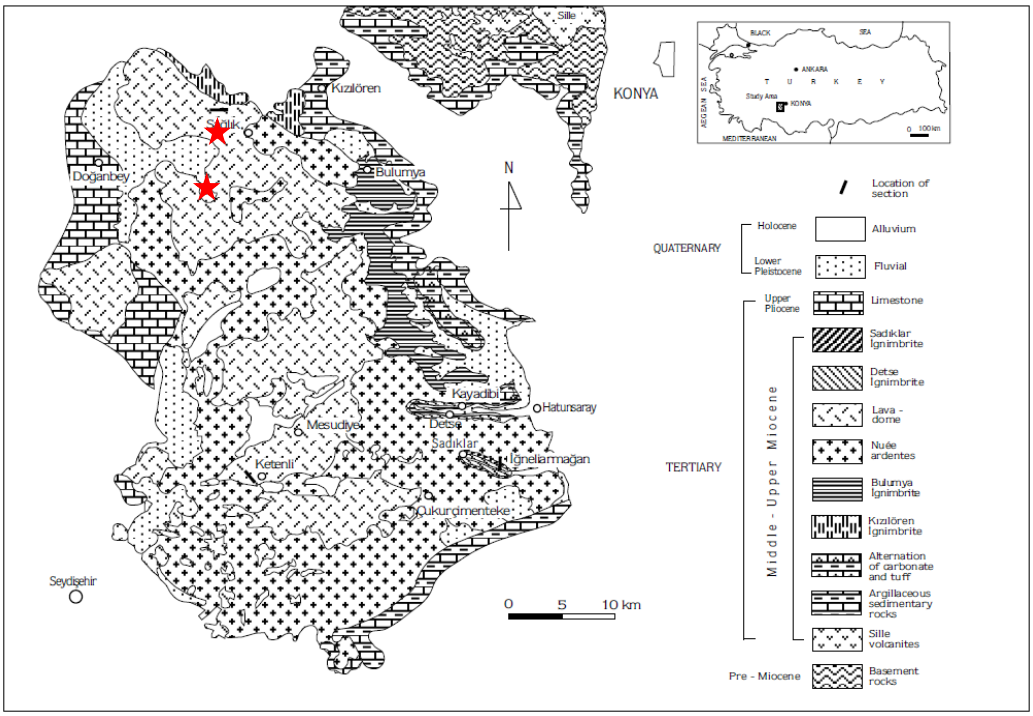

Figure 1 - Location and geological map of the study area (modified from Keller *et al.*, 1977). ★: Rock quarries studied.

The study aims to explain the origin of and importance of mafic magmas In Erenlerdagi volcanics. To do so, the study was performed at a rock quarry, in where mafic and felsic magma interactions can be observed very well. The dom contains various mafic microgranular enclaves (MMEs), whic h have various size (a few cm to a few meters) and shape (ellipse/sphere to rounded).

2. Materials and Methods

The MMEs samples were analyzed to determine contents of major oxides, trace and rare earth elem ents (REE) by ICP-MS at ACME Analytical laboratories in Canada.

3. Geochemistry

Bulk rock chemical analyses of the MMEs and three additional MMEs from previous studies (Tem el *et al.*, 1996) are presented in Table 1, with host lava samples (Table 2, Kocak and Zedef, 2016). In an AFM ternary diagram (Figure 2a), the samples clearly define a calc-alkaline trend.

The samples are concentrated on high K calc-alkaline series (Figure 2b), but some MME samples were also found on calc-alkaline areas in a SiO_2 vs K_2O diagram. In a Na_2O+K_2O vs SiO_2 diagram, the MMEs samples are situated on mostly basaltic andesite and andesite areas, and a MME sample on basaltic trachy-andesite area while the host rocks are found on dacite and andesite areas (Figure 3a). In Figure 2 and 3a, there is almost no compositional gap between mafic and felsic rocks. In Harker diagram, the SiO_2 increases generally with decreasing TiO_2, FeOt, MgO, CaO and Co (not shown), suggesting fractional crystallization of pyroxene (±olivine), ilmenite and magnetite. Primitive mantle normalized spider trace element diagram of the samples from Sağlık lava domes, the MMEs (Figure 3b) are characterized by an enrichment in large ion litophile elements (LILE), particularly Cs, Ba and Th, and depletion in high field strength elements (HFSE). The rocks show progressively decreasing negative Nb, Ta, P and Ti anomalies, which are typical of subduction-

related magmas (Pearce, 1983). Chondrite-normalized REE patterns (Figure 4a) for the three rock groups usually exhibit a strongly fractionated REE pattern with high LREE/ HREE for the rocks. In general, all samples are LREE enriched with $(Ce / Sm)_N$=2.54-4.54, which are similar to those of subduction-related magmas (Pearce 1982, 1983). The more fractionated and LREE-enriched character of the volcanic rocks indicates that the evolution of the rocks involved continental crust (Watters and Pearce, 1987). Plagioclase fractionation is evident from the slight-moderate development of a negative Eu anomaly ($(Eu/Eu^*)_N$:= 0.68-0.86, Figure 4a). The MMEs have les fractionated REE pattern than their hosts. Figure 4 b-c shows that both MMEs and their hosts have mostly volcanic arc geotectonic setting.

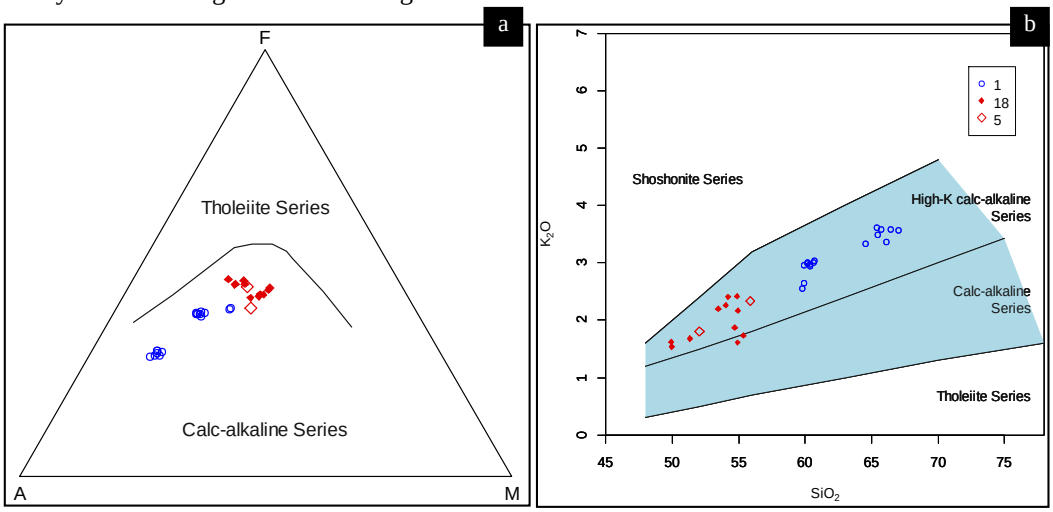

Figure 2 - a) AFM classification of the samples (Irvine and Baragar, 1971), b) SiO_2 vs K_2O diagram of the samples (after Peccerillo and Taylor, 1976). Symbols; 1: Sağlık lava domes, 18: MMEs, 5: MMEs (Temel *et al.*, 1996)

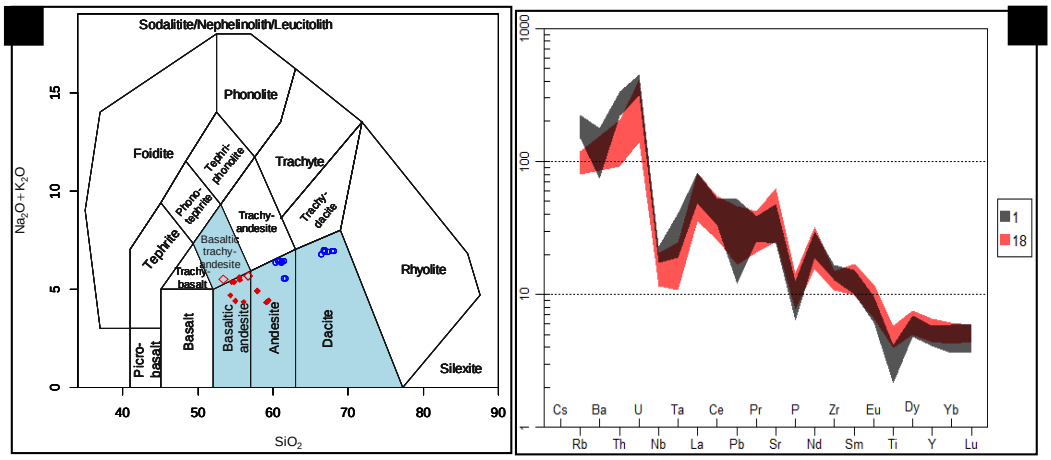

Figure 3 - a) Total alkaline vs SiO_2 diagram (Middlemost, 1994) of the samples b) Primitive mantle normalized spider trace element diagram (McDonough and Sun, 1995). Symbols; 1: Sağlık lava domes, 18: MMEs, 5: MMEs (Temel *et al.*, 1998).

Table 1 - Results of the geochemical analyses of the samples from MMEs.

Samples	5A	8A	4A	42A	43A	41A	1A	40A	2A	47A	9A	Temel *et al.*, 1998		
												KO-39	KO-50	KO-53
SiO_2	49.92	49.95	51.33	53.46	54.02	54.19	54.71	54.88	54.93	54.94	55.35	55.89	52.06	50.54
TiO_2	0.81	0.8	0.9	1.17	1.14	1.11	0.93	1.11	0.89	1.13	0.87	0.83	0.86	0.76
Al_2O_3	14.66	14.79	15.4	17.59	17.53	17.94	16.19	17.69	16.17	17.73	16.1	16.24	16.4	14.31
Fe_2O_3	6.23	6.2	7.22	8.54	8.37	8.16	7.4	8.18	7.1	8.08	6.69	7.33	8.41	8.61
MgO	3.5	3.65	4.24	3.79	3.9	3.08	4.31	3.49	4.2	3.44	4.01	4.57	4.13	1.09
CaO	11.93	10.91	8.06	7.91	7.98	7.21	6	7.61	5.3	7.74	5.72	7.79	9.82	9.39
Na_2O	2.68	2.45	2.29	3.05	3.02	3.05	2.76	3.12	2.41	3.23	2.38	3.23	3.54	2.2
K_2O	1.62	1.54	1.68	2.2	2.26	2.41	1.87	2.42	1.61	2.17	1.73	2.34	1.81	1.31
P_2O_5	0.17	0.16	0.2	0.28	0.27	0.3	0.16	0.27	0.17	0.29	0.17	0.27	0.27	0.24
MnO	0.37	0.4	0.23	0.13	0.13	0.13	0.18	0.12	0.18	0.13	0.15	0.123	0.193	0.17
LOI	7.8	8.9	8.2	1.5	0.9	2	5.2	0.7	6.8	0.7	6.5	0.98	1.87	0.83
Sum	99.74	99.75	99.72	99.58	99.55	99.58	99.71	99.58	99.73	99.58	99.73	99.59	99.36	99.25
Ni	2.2	1.4	2.3	2.6	2.9	2.2	2.9	2.4	2.8	2.1	2.4	10.8	19.1	184.5
Co	14.4	13.6	15.8	21.9	21.2	20.6	16	21.3	15.5	20.1	15.2	34.4	27.6	46.9
Pb	4.4	2.7	5.5	2.9	2.6	2.9	5.4	2.5	6.1	2.9	6.9			
Rb	57.3	47.9	57.2	62.2	65	70.5	66.6	71	50.4	63.5	52.2	62.2	51.5	25.9
Sr	615.3	548.6	577.1	1213	1221	1222	635.5	1207	495.9	1249	541.5	1195	637.7	1162
Hf	3.6	2.4	3.2	4.1	3.6	4.8	3.2	3.9	3.3	4.3	3.6			
Nb	8.7	7.6	9.1	11.6	11.8	11.9	10.2	10.3	8.4	13.6	8.1	9.2	14.7	5.3
Ta	0.7	0.4	0.5	0.5	0.6	0.7	0.5	0.9	0.5	0.8	0.6			
Th	8.5	7.5	7.3	14.4	16.2	16.4	8	15.7	8.9	16.2	9			
U	8.3	3	3.5	3.8	5	4.5	4.3	4.5	2.8	5.4	2.8	175.5	153.9	164.4
Zr	128.7	113.3	125.2	148.7	152.7	156.5	116.8	149.2	115	151.7	124	150	113.5	127.6
Y	23.3	20.3	24.2	24.9	25.1	28.4	23.2	22.8	18.9	23.8	20.2	21.1	30.5	16.4
La	25.8	24.6	28.4	47.3	49.1	53.7	25.7	46.2	22.8	49.2	25.4			
Ce	46.6	43.6	53.2	81.8	86.8	91.4	50	85.3	45.9	87.4	48.1			
Pr	5.39	5.25	6.29	9.8	10.11	10.73	5.87	9.82	5.25	10.28	5.66			
Nd	22.7	23.3	26.6	40.6	39.7	38.7	21.6	32	19.3	37.9	23.2			
Sm	4.12	4.01	4.84	6.68	6.87	6.76	4.62	6.66	4.27	6.73	4.57			
Eu	1.11	1.04	1.27	1.67	1.59	1.83	1.26	1.71	1.11	1.65	1.01			
Gd	3.99	3.58	4.68	5.36	6.09	6.19	4.4	5.63	3.89	5.65	4.48			
Tb	0.63	0.6	0.72	0.82	0.82	0.83	0.69	0.81	0.59	0.81	0.65			
Dy	4.09	3.52	4.28	4.23	4.47	5.09	4.04	4.23	3.37	4.16	3.76			
Ho	0.79	0.79	0.91	0.89	0.8	1	0.89	0.92	0.71	0.82	0.72			
Er	2.28	2.14	2.62	2.68	2.82	2.96	2.61	2.49	2.13	2.52	2.33			
Tm	0.3	0.29	0.34	0.39	0.36	0.39	0.42	0.4	0.32	0.35	0.31			
Yb	2.13	1.87	2.34	2.38	2.64	2.26	2.6	2.36	2.09	2.68	2.17			
Lu	0.38	0.3	0.35	0.34	0.35	0.33	0.4	0.32	0.32	0.35	0.34			

Table 2 - Results of the geochemical analyses of the samples from the lava domes (Kocak and Zedef, 2016)

Samp	1B	2C	3B	4B	5B	7B	8B	9C	11B	40B	41B	42B	43B	44B	46B	47B
SiO2	66.11	59.9	67	64.57	65.75	65.44	65.39	59.76	66.46	60.18	60.35	60.69	60.38	60.67	60.15	59.89
TiO2	0.45	0.8	0.45	0.47	0.47	0.47	0.48	0.83	0.43	0.8	0.79	0.79	0.78	0.79	0.8	0.83
Al2O3	15.52	15.91	15.23	15.43	15.39	15.15	15.24	16.07	15.54	16.94	17.07	16.64	16.53	16.8	16.94	16.97
Fe2O	3.76	6.3	3.68	3.74	3.78	3.84	3.95	6.27	3.57	6.11	5.99	5.95	6.12	6.04	6.01	6.19
MgO	1.61	3.37	1.58	1.54	1.7	1.56	1.73	3.33	1.42	2.54	2.45	2.39	2.51	2.38	2.61	2.69
CaO	3.73	5.26	3.44	4.73	4.1	4.48	4.01	5.38	3.51	5.93	5.77	5.68	5.88	5.77	5.78	6.04
Na2O	3.39	2.73	3.26	3.22	3.27	3.26	3.23	2.84	3.19	3.39	3.39	3.3	3.33	3.33	3.4	3.34
K2O	3.37	2.64	3.57	3.34	3.58	3.49	3.62	2.56	3.58	2.99	2.97	3.04	2.94	3	3.01	2.96
P2O5	0.17	0.13	0.16	0.17	0.18	0.18	0.18	0.16	0.16	0.25	0.24	0.24	0.25	0.26	0.25	0.25
MnO	0.08	0.13	0.07	0.1	0.08	0.1	0.1	0.12	0.07	0.11	0.11	0.1	0.11	0.11	0.11	0.11
LOI	1.6	2.6	1.3	2.4	1.4	1.8	1.8	2.4	1.8	0.4	0.5	0.9	0.8	0.5	0.6	0.4
Sum	**99.75**	**99.79**	**99.75**	**99.75**	**99.75**	**99.75**	**99.75**	**99.74**	**99.75**	**99.64**	**99.65**	**99.67**	**99.66**	**99.66**	**99.65**	**99.65**
Ni	3.4	2.1	3.2	3	3.4	3.2	3.5	2.6	3.2	2	1.9	2.4	2.6	2.3	1.8	1.9
Co	6.7	12.2	7.7	8.7	8.4	7.3	7.7	14.3	8	14.6	13.7	12.8	14	14.7	13.8	14.1
Hf	4	4	4.1	3.5	4.7	4.1	4.8	4.3	4.2	3.9	5	4.5	4.4	5.2	5.2	4.1
Nb	13.9	12.8	14.6	14.1	15	14.1	13.4	12.2	13.3	12.5	13.5	13.1	12.1	12.6	13.8	11.4
Rb	125.9	93.4	130.5	115.2	131.6	122.7	130.4	99.6	135.3	92.3	91.9	95.5	94.4	96.9	93	90.3
Ba	1024	490	1027	984	1015	980	988	621	981	1151	1103	1055	1120	1176	1134	1087
Sr	529.2	524.9	501.8	514.5	503.7	541	479.4	577.4	518.8	949.5	906.7	858.2	906.4	878.4	900.7	925.6
Pb	3.2	5.4	3.5	2.4	2.8	3.5	2.5	5	7.8	2.3	1.9	1.8	1.8	1.9	2	2.1
Zn	27	35	23	30	31	25	26	39	35	19	15	17	20	18	16	14
Ta	1.3	1	1.5	1.1	1.4	1.2	1.3	1	1.2	1	0.7	1.2	1	1	0.9	0.9
Th	23.3	20.4	26.8	23.7	26.7	24.4	24.6	17.7	25.7	21.2	21.3	20.7	22	22.3	21.3	20.7
U	7.7	6.3	8.8	7.7	9	8.9	9	7.3	8.1	6.6	6.3	6.3	6.2	6.5	6.5	6.4
Zr	151.2	133.7	166.7	143.6	168.6	155.5	170.3	146.1	157.6	173.2	168.1	164.1	174.5	175.2	170.2	164.5
Y	17.5	21.2	18.5	18.6	19.1	18.2	18.6	23.2	17.8	23.9	24.9	21.6	22.1	25.1	21.9	22.8
La	42.5	31.6	46.9	42.8	46.6	44.1	41.4	32	42.1	49.1	51.4	46	49	53	51.4	49.8
Ce	71.5	56.7	80.9	75.2	82	76.9	72	58.8	73	86.4	84.6	83.1	84.4	86.7	88.4	85
Pr	7.3	6.32	8.32	7.83	8.47	7.96	7.56	6.49	7.38	9.6	9.35	9	9.26	9.75	9.51	9.41
Nd	28.6	23.7	26.8	26.9	29.8	26.8	25.8	23.9	27.3	37.1	33.8	34.6	34.1	35.5	35.5	36.3
Sm	4.41	4.25	4.48	4.41	4.79	4.09	4.7	4.48	4.2	5.94	5.54	5.71	5.78	6.16	5.82	5.69
Eu	1.04	1.1	0.97	0.97	1.03	0.96	0.97	1.02	0.95	1.42	1.37	1.38	1.42	1.49	1.45	1.4
Gd	3.88	4.07	4.22	4.14	4.49	3.86	4.09	4.32	3.64	5	5.07	4.95	5.3	5.22	5.08	5.08
Tb	0.54	0.64	0.59	0.56	0.6	0.57	0.58	0.68	0.53	0.7	0.7	0.67	0.72	0.77	0.7	0.73
Dy	3.3	3.71	3.76	3.46	3.21	3.43	3.47	4.18	3.3	3.84	3.93	4.15	3.58	4.68	3.62	3.79
Ho	0.6	0.88	0.58	0.56	0.65	0.64	0.68	0.84	0.56	0.8	0.86	0.69	0.79	0.98	0.81	0.77
Er	1.96	2.32	2.03	1.92	1.91	1.74	1.92	2.63	1.91	2.23	2.74	1.98	2.29	2.36	2.49	2.42
Tm	0.27	0.4	0.27	0.29	0.29	0.34	0.3	0.33	0.26	0.31	0.37	0.31	0.36	0.38	0.32	0.36
Yb	1.6	2.2	1.99	1.69	1.87	1.88	1.77	2.12	2	2.31	1.91	2.23	2.21	2.59	2.23	2.3
Lu	0.29	0.41	0.33	0.31	0.33	0.29	0.28	0.39	0.25	0.32	0.33	0.32	0.3	0.35	0.33	0.39

4. Discussions and Conclusions

The MMEs have relatively low SiO_2 content (50-56%) and intermediate to high molar Mg# (20-55), which is inconsistent with partial melting of the mafic lower crustal rocks, and requires a mantle-derived component. As a whole, existence of colinear variations in Harker diagrams and minor Eu anomaly indicate that fractional crystallization was substantial in the petrogenesis of the Erenlerdagi Volcanites. In contrast, in A/CNK and Y vs SiO_2 diagrams (Figure 5) two distinct group appears, which is evident also in Lu vs La, vs #mg diagrams (not shown). Existence of MMEs suggests mafic–felsic interaction and mingling (Barbarin and Didier, 1992; Kocak, 2006) by injection hot mafic magma injected into felsic magma. Accordingly, Temel *et al.* (1998) suggest a mix of mantle and crustal sources for the Erenlerdagı volcanites based on an isotopic study.

The Konya volcanites are characterized by intermediate to high K_2O (1.31-3.62 wt.%), Rb (26-135 ppm), Ba (490-1176 ppm), K_2O/Na_2O (0.5-1.1) and FeOt/MgO (1.44-7.11) ratios, which is similar to Andean type andesites series formed in relation with subduction event, which is evident in some geotectonic setting diagrams. It is likely that the volcanics may have been produced by assimilation-fractional crystallisation process in relation with the collision of Eurasian and Arabian plates.

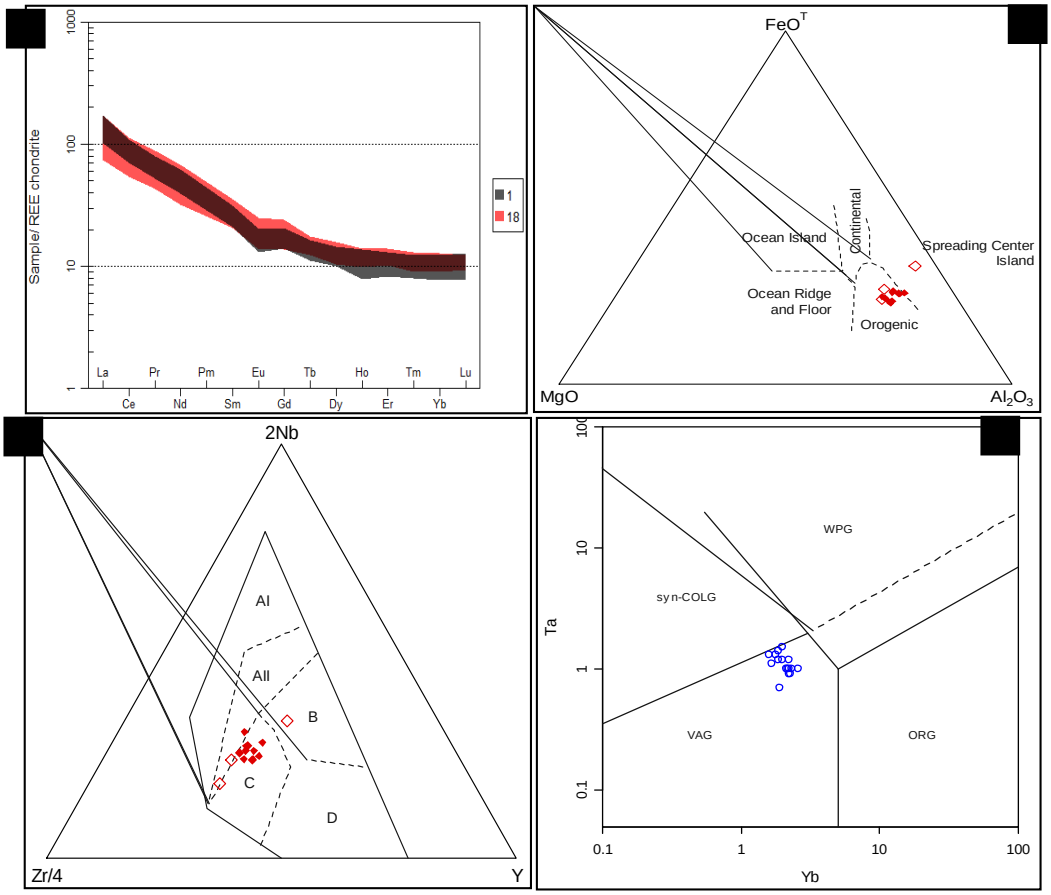

Figure 4 - a) Chondrite normalized REE pattern of the Sağlık lava domes (1), Takkeli tepevolcanics (2) and sill (3). Normalized values are from Boynton, 1984, b)FeOt-MgO-Al_2O_3 ternary diagram (Pearce *et al.*,1977), c) Zr/4-Y-2Nb (Meschede, 1986) (samples with high SiO2(>55) are excluded). AI-II: WP alkaline, AII-C: WP Tholeiitic, B: E-MORB, D: N-MORB, C-D: VAB, d) Ta vs Yb diagram (after Pearce *et al.*, 1984). Symbols; 1: Sağlık lava domes, 18: MMEs, 5: MMEs (Temel *et al.*, 1996).

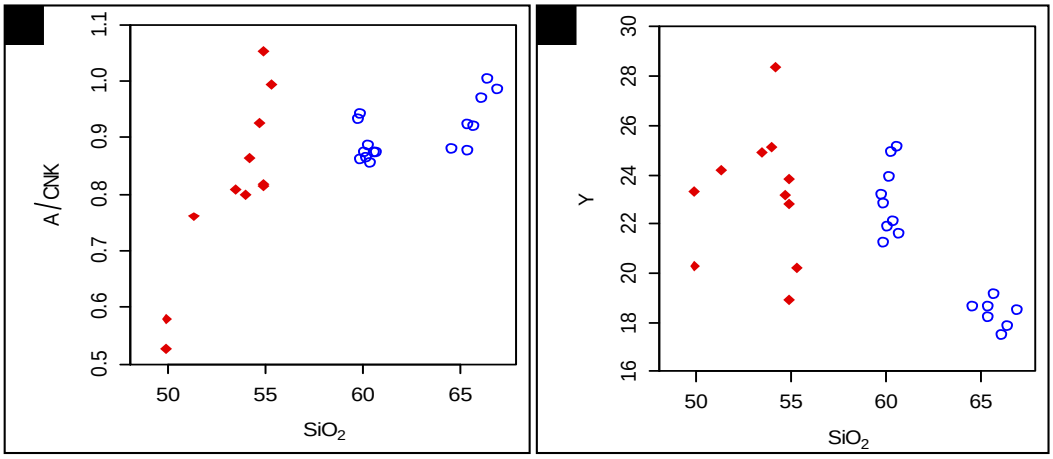

Figure 5 - a)A/CNK vs SiO_2, b) Y vs SiO_2. Symbols; 1: Sağlık lava domes, 18: MMEs, 5: MMEs (Temel et al., 1996).

8. Acknowledgements

Thanks to Selcuk University (BAP, Konya/Turkey) Research Fund for the financial support of the study.

6. References

Temel, A., Gundogdu, M.N. and Gourgaud, A., 1998. Petrological and geochemical characteristics of cenozoic high-K calc-alkaline volcanism in Konya, central Anatolia, Turkey, *Journal of Volcanology and Geothermal Research*, 85, 327-354.

Barbarin, B. and Didier, J., 1992. Genesis and Evolution of Mafic Microgranular Enclaves through Various Types of Interaction between Coexisting Felsic and Mafic Magmas, *Transactions of the Royal Society of Edinburgh-Earth Sciences*, 83,145-153.

Boynton, W.V., 1984. Cosmochemistry of the rare earth elements: meteorite studies. *In*: Henderson, P., *ed*., Rare earth elements, Elsevier, 63-114.

Eren, Y., 1993. Eldes - Derbent - Tepeköy - Söğüttözü (Konya) arasinin jeolojisi, Doktora Tezi, 5, Fen Bilimleri Enstitüsü, Konya, 224 pp. (yayinlanmamis).

Irvine, T.N. and Baragar, W.R., 1971. A guide to the chemical classification of the common igneous rocks, *Canadian Journal of Earth Sciences*, 8, 523-548.

Keller, J., Jung, D., Burgath, K. and Wolf, F., 1977. Geologie und petrologie des Neogenen kalkalkali-vulkanismus von Konya (Erenler Dağ-Alaca Dağ-Massiv Zentral-Anatolian), *Geo. Jb. B.*, 25, 37-117.

Kempler D. and Garfunkel, Z., 1991. The northeast Mediterranean triple junction from a plate kinematics point of view, *Bull. Tech. Univ*., Istanbul, 44, 203-232.

Ketin, İ., 1983, Türkiye Jeolojisine Genel Bir Bakış Istanbul Technical Univercity, Publications, Istanbul, 595 pp.

Kocak, K., 2006. Hybridization of mafic microgranular enclaves: mineral and whole-rock chemistry evidence from the Karamadazi Granitoid, Central Turkey, *International Journal of Earth Sciences*, 95(4), 587-607.

Kocak, K. and Zedef, 2016. Geochemical characteristics of the lava domes in Yatagan village and Sağlik town, from Erenlerdagi (Konya, Central Turkey) volcanites, *Acta Geobalcanica*, 2(1), 7-19.

Kurt, H.K., Özkan, A.M. and Kocak, K., 2003. Geology, Petrography and Geochemistry of the Subduction Related Volcanic Rocks, West of Konya, Central Anatolia, *Geological Bulletin of Turkey*, 46(2), 39-51.

Kurt, H., 1994. Petrography and geochemistry of Kadinhani (Konya) area, Central Turkey, PhD th esis, Glasgow University (unpublished), UK, 191 pp.

McDonough, W.F. and Sun, S.-S., 1995. Composition of the Earth, *Chemical Geology*, 120, 223-253.

Meschede, M., 1986. A method of discriminating between different types of mid-ocean ridge basal ts and continental tholeiites with the Nb-Zr-Y diagram, *Chemical Geology*, 56, 207-208.

Middlemost, E.A.K., 1994. Naming materials in the magma/igneous rock system, *Earth Science Reviews*, 37(1), 215-224.

Özcan, A., Göncüoglu, M.C., Turhan, N., Sentürk, K., Uysal, S. and ve Isık, A., 1990. Konya- Kad ınhanı-Ilgın dolayının temel jeolojisi, *M.T.A. Rapor*, No: 9535 (in Turkish, unpublished).

Pearce, T.H., Gorman, B.E. and Birkett, T.C., 1977. The relationship between major element chemistry and tectonic environment of basic and intermediate volcanic rock, Earth and Planetary Science Letters, 36, 121-132.

Pearce, J.A., 1982. Trace element characteristics of lavas from destructive plate boundaries; 525-548, *In:* Thorp, R.S., *ed*., Andesites: Orogenic Andesites and Related Rocks, John Wiley and Sons, New York, 724 pp.

Pearce, T.H., Gorman, B.E. and Birkett, T.C., 1977. The relationship between major element chemistry and tectonic environment of basic and intermediate volcanic rock, *Earth and Planetary Science Letters*, 36, 121-132.

Pearce, J.A., Harris, N.B.W. and Tindle, A.G., 1984. Trace element discrimination diagrams for the tectonic interpretation of granitic rocks, *Journal of Petrology*, 25, 956-983.

Pearce, J.A., 1983. Role of the sub-continental lithosphere in magma genesis at acrive continental margins: p. 230-249. *In:* Hawkesworth, C.J. and Norry, M.J., *eds*., Continental Basalts and Mantle Xenoliths, Shiva Publishing Ltd., Cambridge, Mass., 272 pp.

Peccerillo, A. and Taylor, S.R., 1976. Geochemistry of Eocene calcalkaline volcanic rocks from the Kastamonu area, northern Turkey, *Contrib Mineral Petrol*, 58, 63-81.

Temel, A., Gündoğdu, M.N. and Gourgaud, A., 1998. Petrological and geochemical characteristics of Cenozoic high-K calc-alkaline volcanism in Konya, Central Anatolia, Turkey, *J. Volcanol. Geotherm. Res*, 85, 327-354.

Watters, B.R. and Pearce, J.A., 1987. Metavolcanic rocks of La Ronge domain in the Churchill Province, Saskatchewan: geochemical evidence for a volcanic arc origin, *Geol. Soc. Lond*., 33, 167-182.

Δελτίο της Ελληνικής Γεωλογικής Εταιρίας, τόμος L, σελ. 1895-1902
Πρακτικά 14ου Διεθνούς Συνεδρίου, Θεσσαλονίκη, Μάιος 2016

Bulletin of the Geological Society of Greece, vol. L, p. 1895-1902
Proceedings of the 14th International Congress, Thessaloniki, May 2016

ATTAPULGITE CLAY OF THE VENTZIA BASIN, WESTERN MACEDONIA, GREECE, AS TEMPLATE IN SYNTHESIZING AMORPHOUS CARBON NANOTUBES

Koukakis P.[1], Tsakiridis P.[1], Ntziouni A.[2], Kordatos K.[2] and Perraki M.[1]

[1]*National Technical University of Athens, School of Mining and Metallurgical Engineering, 15780, Athens, Greece, koukakispanos@gmail.com, ptsakiri@central.ntua.gr, maria@metal.ntua.gr*

[2]*National Technical University of Athens, School of Chemical Engineering, 15780, Athens, Greece, kordatos@central.ntua.gr, ntziouni@central.ntua.gr*

Abstract

Attapulgite from the Ventzia Basin, Western Macedonia, Greece, was used as a template for preparing amorphous carbon nanotubes by vapor deposition polymerization (VDP) method and two different alcohols, furfuryl alcohol and ethylene glycol, as carbon source. The morphology and structure of the as-prepared carbon nanotubes were investigated by means of scanning electron microscopy and a transmission electron microscopy. X-ray diffraction and Raman spectroscopy were additionally employed. The amorphous nature of the carbon nanotubes has been confirmed by the XRD and the SAED pattern, as well as the Raman spectrum. No noticeable difference was observed in the morphology and structure of the as-prepared carbon nanotubes regarding the type of alcohol used as carbon source. However, a difference in the quantity of the produced carbon nanotubes was noticed, with the furfuryl alcohol, as carbon source, producing a larger amount of carbon nanotubes than the ethylene glycol.
Keywords: attapulgite, clay mineral, carbon nanotubes, *Ventzia basin.*

Περίληψη

Στην παρούσα εργασία χρησιμοποιήθηκε ατταπουλγίτης από τη λεκάνη των Βεντζίων, στη Δυτική Μακεδονία, Ελλάδα, ως υπόστρωμα για τη σύνθεση άμορφων νανοσωλήνων άνθρακα με τη μέθοδο πολυμερισμού εναπόθεσης ατμών (VDP) και με τη χρήση δύο διαφορετικών αλκοολών, της φουρφουρυλικής αλκοόλης και της αιθυλενογλυκόλης, ως πηγές άνθρακα. Η μορφολογία και η δομή των νανοσωλήνων άνθρακα μελετήθηκαν με ηλεκτρονιακό μικροσκόπιο σάρωσης (SEM) και με ηλεκτρονιακό μικροσκόπιο διερχόμενης δέσμης (TEM). Επιπρόσθετα, χρησιμοποιήθηκε περίθλαση ακτινών Χ (XRD) και φασματοσκοπία σκέδασης Raman. Η άμορφη δομή των νανοσωλήνων επιβεβαιώθηκε από τα φάσματα του XRD και του SAED, όπως επίσης και από το φάσμα Raman. Δεν παρατηρήθηκε καμία αξιοσημείωτη διαφορά στη μορφολογία και τη δομή των νανοσωλήνων άνθρακα όσον αφορά τον τύπο της αλκοόλης που χρησιμοποιήθηκε ως πηγή άνθρακα. Ωστόσο, παρατηρήθηκε διαφορά στην ποσότητα των νανοσωλήνων που συντέθηκαν, με τη φουρφουρυλική αλκοόλη, ως πηγή άνθρακα, να συνθέτει μεγαλύτερη ποσότητα νανοσωλήνων άνθρακα από την αιθυλενογλυκόλη.
Λέξεις κλειδιά: *ατταπουλγίτης, αργιλικό ορυκτό, νανοσωλήνες άνθρακα. Λεκάνη Βεντζίων.*

1. Introduction

Attapulgite is a hydrated magnesium phyllosilicate ($[Mg(Al_{0.5\text{-}1}Fe_{0\text{-}0.5})]Si_4O_{10}(OH).4H_2O$) with magnesium partially replaced by aluminium or, to a lesser extent, iron (Bish and Guthrie, 1993), named after the U.S. town of Attapulgus, in southwest Georgia, where the mineral is abundant. The synonym palygorskite is derived from a deposit found at Palygorskaya on the Popovka River, Middle Urals, Russia. The attapulgite used in this paper, provided by GEOHELLAS S.A. is a commercial product and therefore the term attapulgite is used instead of the synonym palygorskite. Its structure consists of long double chains of silica tetrahedra which run parallel to the fiber axis. These chains are joined by magnesium and aluminum octahedra to produce strips similar in structures to the three-layer minerals. These three-layer strips are joined at the corners by Si-O-Si bonds into a structure resembling a checkerboard in cross-section, with free channels of about 3.7 by 6.0 Å in cross-section running the length of the needles (Haden, 1963). These channels can collapse when attapulgite is dehydrated. The reason being the open-channel structure is stabilized by the water of composition which completes the edges of the octahedral strips (Preisinger, 1963). This collapse of the channels during dehydration is the probable cause of the abrupt decrease of the mineral's surface area from about 190 to 125 m^2/g (Barrer and Mackenzie, 1954). Suitable acidification treatment or heat treatment of attapulgite could increase its surface area, pore volume and amount of active Si-OH bonds (Sun *et al*., 2012).

The important applied properties of attapulgite are a direct result of its needle-like structure. The attapulgite needle is commonly about 1μm in length and approximately 10nm across. The properties of attapulgite are rarely determined by these tiny channels. The external surface of the needles and the arrangement of the needles in gross particles are of primary importance (Haden, 1963).

Attapulgite is being used in a wide variety of applications, both in heavy industry and in every-day life. Recent studies have shown that attapulgite can be used to synthesize carbon nanotubes, taking advantage of its fibrous morphology and diameter in nanoscale.

Recently, amorphous carbon nanotubes (ACNTs) have become a core research because of their low temperature synthesis process and large production yield. The walls of the ACNTs are composed of many carbon clusters featuring short-distance order and long-distance disorder. Amorphous carbon has both sp^2 and sp^3 bonding and contains parts of the properties of both diamond and graphite, which distinguish their properties from crystalline single-walled and multi-walled carbon nanotubes (Sun *et al*., 2012).

In this paper, a template synthesis technique was utilized to prepare ACNTs, using attapulgite as template and both furfuryl alcohol and ethylene glycol as carbon sources. This technique features the virtue of low cost and wide source of raw materials, its simple and easily reached process conditions, which may redeem some drawbacks of the commonly-used methods.

2. Materials and Methods

2.1. Analytical Methods

X-Ray Diffraction patterns were obtained with a Bruker D8 Focus diffractometer in a θ-θ configuration employing CuKα radiation (λ = 1.5406 Å) with a fixed divergence slit size of 0.5° and a rotating sample stage. The samples were scanned between 4 and 70° 2θ. The step size and time per step were set to 0.017° 2θ and 80 s, respectively. Scanning Electron Microscopy (SEM) was performed using a JEOL 6380LV-SEM equipped with an Oxford EDS-WDS. Transmission Electron Microscopy was performed with a JEOL 2100 HR–TEM at 200kV. A Renishaw's inVia-micro-RAMAN (532 nm excitation laser wavelength) was also employed to study the carbon products.

2.2. Raw Attapulgite

Attapulgite from the Ventzia basin, Western Macedonia, Greece, was provided by GEOHELLAS S.A. which has exploited the attapulgite deposit since 2003.

2.3. Synthesis Process

The raw attapulgite was treated in 0.5 M HCl solution for 120min under refluxing and magnetic stirring, then washed with distilled water to pH=7 and dried at 105°C overnight.

The carbon nanotubes were synthesized through a vapor deposition polymerization (VDP) method. 2.0g of acid-attapulgite were placed in a Teflon container, and t hen placed into a stainless steel autoclave. 3mL of furfuryl alcohol were additionally added into the Teflon container. The high pressure autoclave was sealed and transferred into a homogeneous reactor at 180°C for 6h (over the boiling point of furfuryl alcohol which is 170°C). Thereafter, the furfuryl alcohol-attapulgite mixture was carbonized in a horizontal furnace under Ar_2 atmosphere. The heating protocol rate was 60 min from room temperature to 300°C, 60 min from 300°C to 600°C, held at 600°C for 2h, 40 min from 600°C to 800°C and held at 800°C for 2h to get the carbon-attapulgite hybrid material. Then, the carbonized black powders were stirred in HF (40 wt.%) solution for 15h in a fume cupboard at room temperature to dissolve the mineral template completely. Next, the resulting insoluble carbon based materials were filtered and washed by distilled water several times. Finally, the carbon based materials were treated with HCl (37 wt.%) solution under stirring at room temperature for 2h to purify them, followed by filtering, washing with distilled water and drying in an oven at 105°C overnight (Sun *et al.*, 2012).

The synthesis process using ethylene glycol as carbon source was similar apart from the following points: a) 5mL of ethylene glycol were added in the Teflon container and b) the high pressure autoclave was transferred in a homogeneous reactor at 200°C (over the boiling point of ethylene glycol which is 197°C) for 6h.

3. Results and Discussion

3.1. Raw attapulgite

XRD pattern of the raw attapulgite can be seen in Figure 1. It exhibits the characteristic attapulgite diffraction peaks at d=10.79 Å, *hkl* (110), d=4.4 Å, *hkl* (040) and at d=3.5 Å, *hkl* (400). The intense, sharp and symmetric peak at d=10.79 Å indicates highly-crystalline pure attapulgite (Yan *et al.*, 2013). The presence of quartz was verified in the studied samples by its typical diffraction peaks at d=~3.34 Å *hkl* (101) and d=~4.25 Å *hkl* (100).

Study by Scanning Electron Microscopy (SEM) showed a fibrous and sheet-like morphology for the attapulgite crystals whilst their length ranges from 1μm to 10μm (Figure 2). The EDS point analyses revealed an average attapulgite chemical formula of $(Si_{7.72}Al_{0.28})(Al_{0.77}Fe_{0.91}Mg_{2.52})_{4.20}Ca_{0.04}Na_{0.02}K_{0.09}O_{20}(OH)_2(OH_2)_4$ (Kastritis *et al.*, 2003).

Thermogravimetric (TG), Differential Thermal Gravimetric (DTG) and Differential Thermal analysis (DTA) curves of the raw attapulgite are given in Figure 3. As can be seen in the respective DTA curve attapulgite shows characteristic endothermic peaks. The first peak, at 120°C, is due to the abortion of the surface absorbed water and part of the zeolitic water which exists in the canals of the attapulgite crystal. The second peak, at 300°C, is due to the abortion of all the zeolitic water and part of the bound water. The third peak is wider, from 420°C to 600°C, and indicates that all the water has been aborted and also the formation of anhydride. Around the temperature of 800-870°C the structure of the attapulgite completely collapses. The exothermic peak at ~845°C is attributed to the formation of enstatite ($MgSiO_3$) (Che *et al.*, 2011).

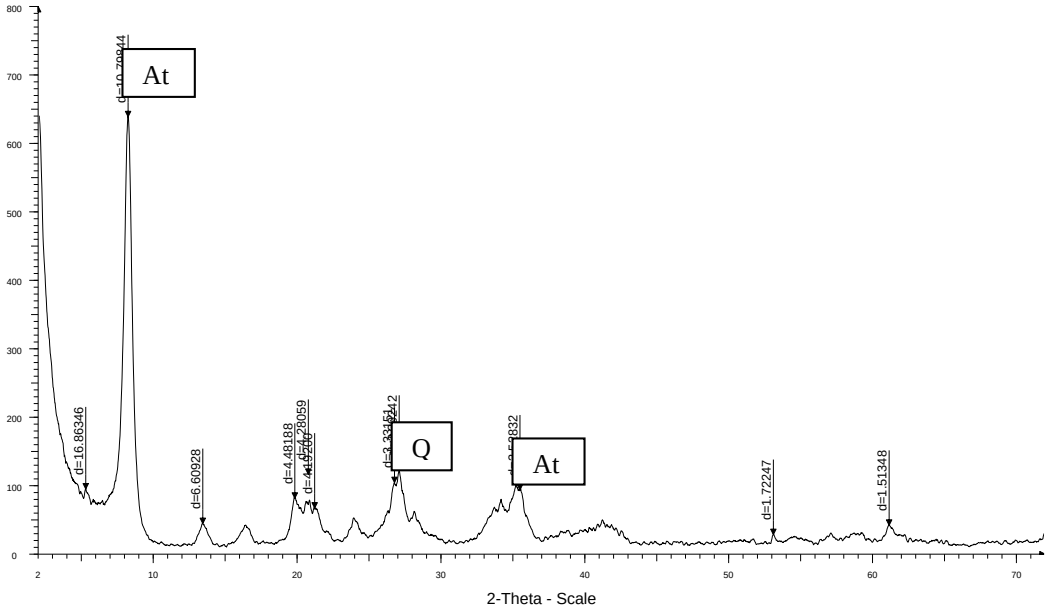

Figure 1 - A representative XRD pattern of the raw attapulgite studied herein.

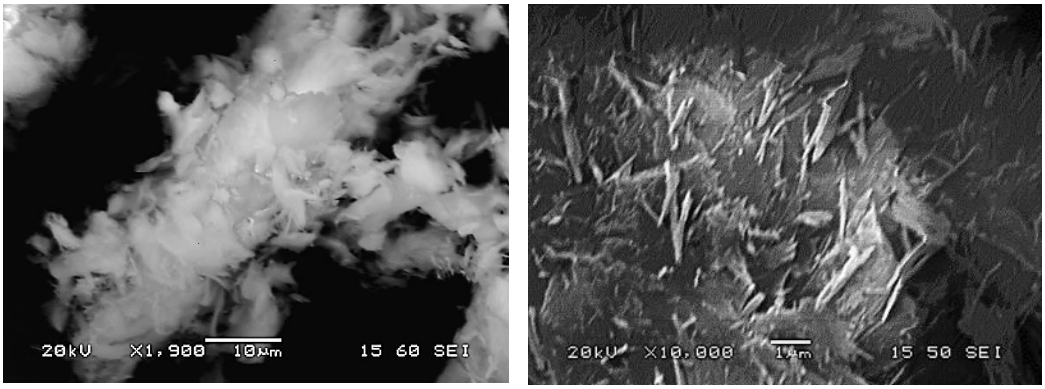

Figure 2 - SEM images of the attapulgite template.

3.2. Products

As can be seen, in the respective XRD patterns of the final product (Figure 4), the characteristic XRD peaks of the attapulgite have been disappeared, indicating that the mineral template has been completely removed. At around $2\theta=26.3^{o}$ a very weak and wide peak is observed, possibly corresponding to the (002) plane of the carbon (Sun *et al*., 2012). The low intensity and width of the peak show that the as-prepared carbon nanotubes are amorphous.

In the SEM images of the as-prepared carbon nanotubes (Figure 5), it can be seen that the morphology is fibrous and sheet-like, similar to that of the attapulgite template, indicating that most of the carbon was deposited onto the surface of the template. In the case of the carbon nanotubes which were synthesized with ethylene glycol as carbon source, their morphology is more sheet-like.

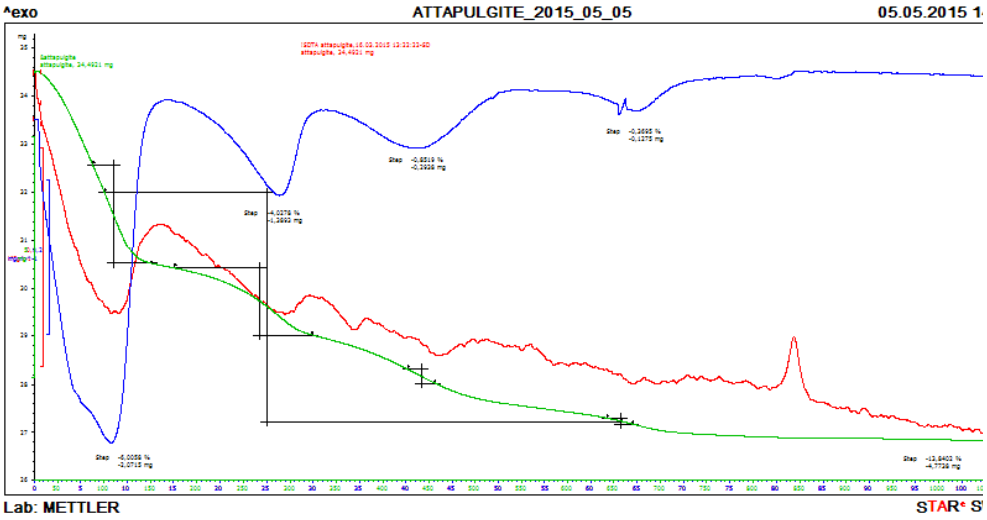

Figure 3 - TG/DTG/DTA curves of the studied raw attapulgite.

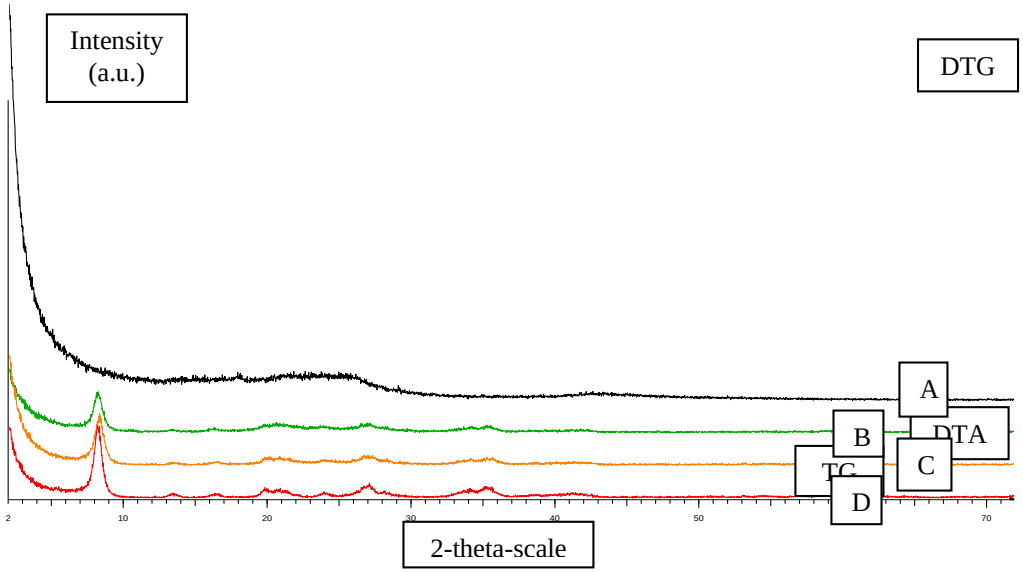

Figure 4 - XRD patterns of A) the as-prepared carbon nanotubes B) attapulgite treated with 0.5M HCl for 2h C) attapulgite treated with 0.5M HCl for 1h and D) raw attapulgite.

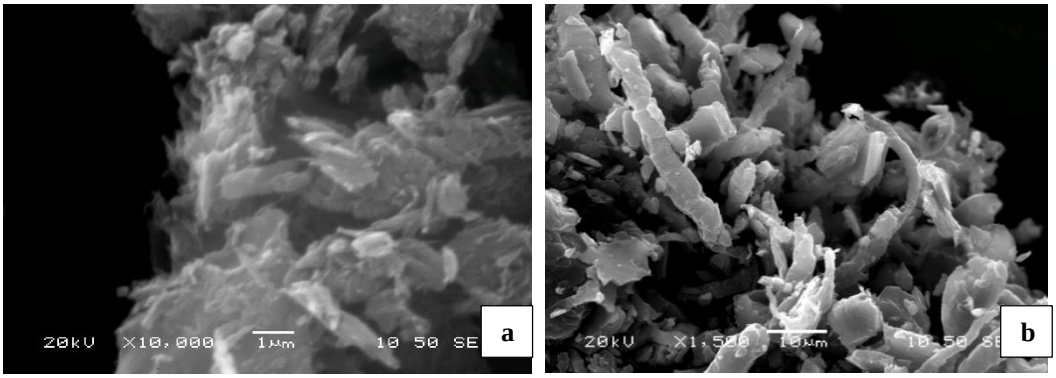

Figure 5 - SEM images of the as-prepared carbon nanotubes using a) furfuryl alcohol and b) ethylene glycol as carbon sources, respectively.

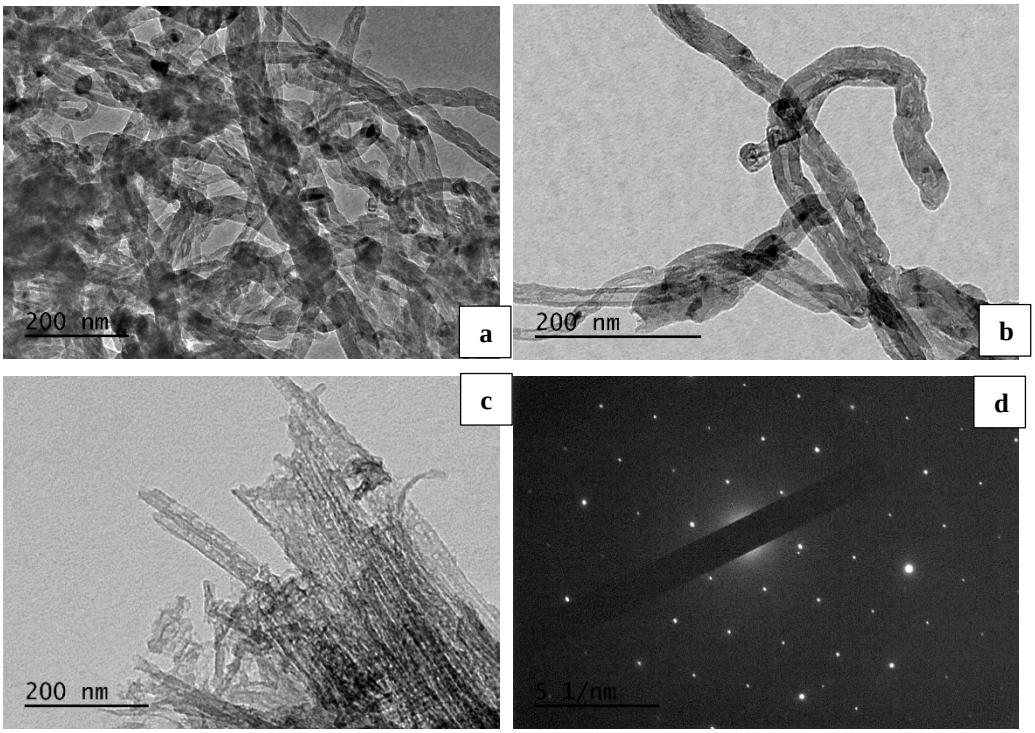

Figure 6 - TEM images (a,b,c) and SAED (d) pattern of the as-prepared carbon nanotubes using furfuryl alcohol as carbon source.

The morphology of the as-prepared carbon nanotubes was observed with Transmission Electron Microscopy (TEM) (Figures 6, 7). The ACNTs are similar in shape and diameter to the attapulgite template. The Selected Area Electron Diffraction (SAED) pattern, in agreement with the XRD study, shows a featureless pattern which is indicative of the amorphous structure of the as-prepared carbon nanotubes.

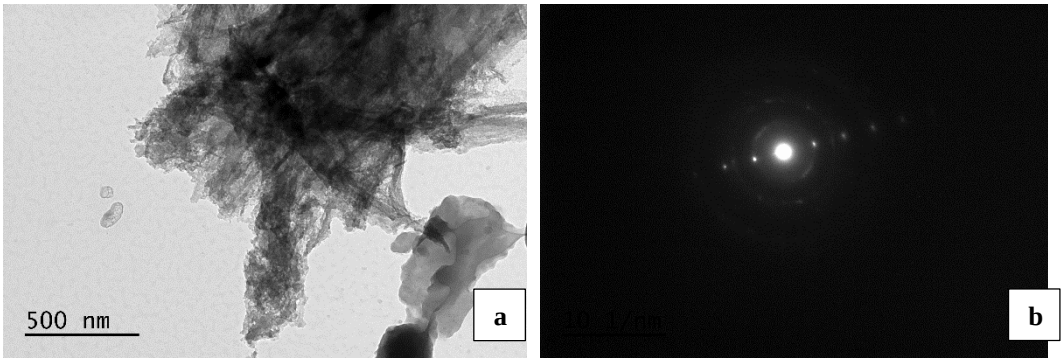

Figure 7 - TEM image (a) and SAED pattern (b) of the as-prepared carbon nanotubes usin g ethylene glycol as carbon source.

In Figure 8 a representative Raman spectrum of the carbon nanotubes is given. As can been seen the Raman features confirmed that the as-prepared carbon nanotubes are highly amorphous, as indicated by the two wide peaks at 1307 cm^{-1} and 1597 cm^{-1} (Chen, 2008).

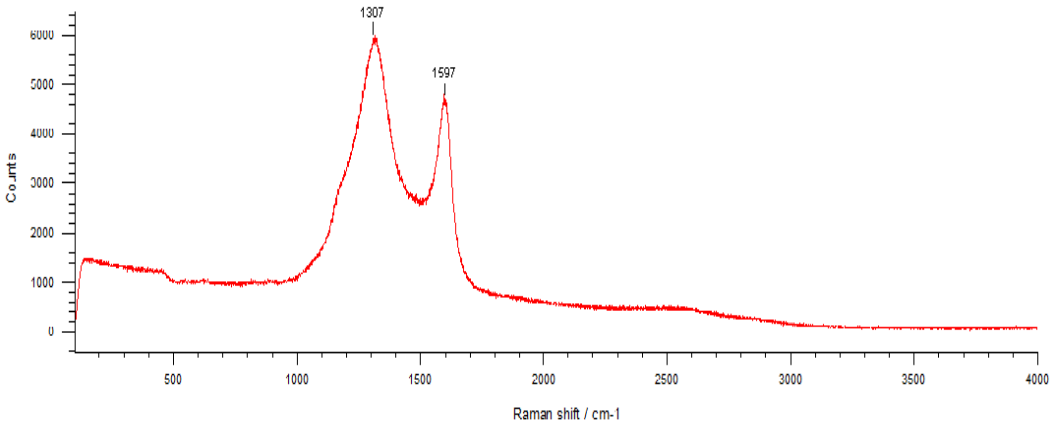

Figure 8 - Raman spectrum of the as-prepared carbon nanotubes.

4. Conclusions

Attapulgite from the Ventzia Basin, Western Macedonia, Greece, proved to be a suitable template for preparing amorphous carbon nanotubes by vapor deposition polymerization (VDP) method and furfuryl alcohol or ethylene glycol as carbon sources. The as-prepared carbon nanotubes were investigated by means of a scanning electron microscope and a transmission electron microscope to obtain information on their morphology and structure. X-ray diffraction and Raman spectroscopy were additionally employed. The amorphous nature of the carbon nanotubes has been confirmed by the XRD and the SAED pattern, as well as the Raman spectrum. No noticeable difference was observed in the morphology and structure of the as-prepared carbon nanotubes regarding the type of alcohol used as carbon source. However, a difference in the quantity was noticed as the furfuryl alcohol, as carbon source, produced a larger amount of carbon nanotubes than the ethylene glycol.

5. Acknowledgments

GEOHELLAS S.A. is thanked for providing the attapulgite sample. Vasilis Skliros is cordially thanked for his support in the Raman analysis of the samples.

6. References

Barrer, R.M. and Mackenzie, N., 1954. Sorption by attapulgite, Part 1, Availability of intracrystalline channels, *The Journal of Physical Chemistry*, 58, 560-568.

Bish, D.L. and Guthrie, G.D.Jr., 1993. Mineralogy of clay and zeolite dusts (exclusive of 1:1 layer silicates). *In*: Guthrie, G.D.Jr and Mossman, B.T., *eds*., Reviews in Mineralogy, Health Effects of Mineral Dusts, Chelsea, MI, Book Crafters, 28, 139-184.

Che, C., Glotch, D.T., Bish, L.D., Michalski, R.J. and Xu, W., 2011. Spectroscopic study of the dehydration and/or dehydroxylation of phyllosilicate and zeolite minerals, *Journal of Geophysical research, Planets*, 116, Issue E5.

Chen, Y.-C., 2008. Raman spectroscopic studies on single-walled carbon nanotubes (SWNTs) and SWNT/Ag nanostructure, *PHD thesis submitted to the University of Manchester, Faculty of Engineering and Physical Sciences*, 205 pp.

Christidis, G.E., Katsiki, P., Pratikakis, A. and Kacandes, A., 2010. Rheological properties of palygorskite-smectite suspensions from the Ventzia basin, W. Macedonia, Greece, *Bulletin of the geological Society of Greece*, Proceedings of the 12th International Congress, Patras, 2562-2569.

Haden, W.L.Jr., 1963. Attapulgite: properties and uses: in Clays and Clay Minerals, lOth Conf., Pergamon Press, New York, 284-290.

Kastritis, I.D., Kacandes, G.H. and Mposkos, E., 2003. The palygorskite and Mg-Fe smectite clay deposits of the Ventzia basin, western Macedonia, Greece, *Mineral Exploration and Sustainable Development*, Eliopoulos *et al*., *eds*., Millpress, Rotterdam, 891-894.

Preisinger, A., 1963. Sepiolite and related compounds: its stability and application, *Clay and Clay Minerals*, 10, 365-371.

Sun, L., Yan, C., Chen, Y., Wang, H. and Wang, Q., 2012. Preparation of amorphous carbon nanotubes using attapulgite as template and furfuryl alcohol as carbon source, *Journal of Non-crystalline Solids*, 358, 2723-2736.

Yan, W., Yuana, P., Chena, M., Wang, L. and Liu, D., 2013. Infrared spectroscopic evidence of a direct addition reaction between palygorskite and pyrometallitic dianhydride, *Applied Surface Science*, 265, 585-590.

Δελτίο της Ελληνικής Γεωλογικής Εταιρίας, τόμος L, σελ.1903-1912
Πρακτικά 14ου Διεθνούς Συνεδρίου, Θεσσαλονίκη, Μάιος 2016

Bulletin of the Geological Society of Greece, vol. L, p. 1903-1912
Proceedings of the 14th International Congress, Thessaloniki, May 2016

MINERALOGICAL, PETROLOGICAL AND GEOCHEMICAL FEATURES OF THE UNIQUE LAPIS LACEDAEMONIUS (KROKEATIS LITHOS) FROM LACONIA, GREECE: APPROACH ON PETROGENETIC PROCESSES WITHIN THE TRIASSIC VOLCANIC CONTEXT

Koutsovitis P.[1*], Kanellopoulos C.[1], Passa S.[1], Foni K.[2], Tsapara E.[1], Oikonomou G.[1], Xirokostas N.[1], Vallianatou K.[1] and Mouxiou E.[1]

[1]Institute of Geology and Mineral Exploration, 1st Spirou Louis St., Olympic Village, Acharnae, GR, 13677

[2]Faculty of Geology and Geoenvironment, National & Kapodistrian University of Athens. University Campus- Zografou, Athens, GR, 15784 petroskoutsovitis@yahoo.com, ckanellopoulos@gmail.com, passa@upatras.gr, kallirroe.f@gmail.com, efi.tsapara@gmail.com, georgeoik7@gmail.com, nikosxirokostas@yahoo.com, kalliav@yahoo.com, elenimouxiou@yahoo.com

Abstract

The Lapis Lacedaemonius (krokeatis lithos) is a well-known meta-volcanic rock of great historical importance. Petrographic observations, mineral chemistry data, as well as geochemical analysis of selected samples, reveal that these rocks are porphyritic metabasaltic rocks which have been significantly affected by saussuritization and also by restricted silicification processes. They represent subduction related calc-alkaline volcanic rocks which also appear in the adjacent Hellenic Triassic volcanic outcrops, and appear to be associated with the rift/drift phase within the Pindos oceanic realm. The unique features of the Lapis Lacedaemonius, when compared to geochemically similar volcanic rock outcrops, are mainly attributed to their distinct porphyritic textures, predominantly with microlithically textured groundmass along with the coarse grained plagioclase, and to saussuritization processes. The Lapis Lacedaemonius seems to have been formed in a sub-volcanic system closely associated with epidosites, suggesting that metasomatism occurred within hydrothermal upflow zones.
Keywords: *Lapis Lacedaemonius, Krokeatis lithos, Saussuritization, Subduction, Triassic volcanism.*

Περίληψη

Ο Κροκεάτης Λίθος είναι ένα ευρέως γνωστό μετα-ηφαιστειακό πέτρωμα με μεγάλη ιστορική σημασία. Οι πετρογραφικές παρατηρήσεις, τα ορυκτοχημικά δεδομένα καθώς και οι γεωχημικές αναλύσεις επιλεγμένων δειγμάτων, δείχνουν ότι το πέτρωμα αυτό είναι πορφυρικός μεταβασάλτης ο οποίος έχει επηρεαστεί σημαντικά από διεργασίες σωσσυριτίωσης, καθώς και από περιορισμένου βαθμού δευτερογενή πυριτίωση. Αντιπροσωπεύουν ασβεσταλκαλικά ηφαιστειακά πετρώματα που σχετίζονται με διεργασίες υποβύθισης, ανάλογα των πετρωμάτων που εμφανίζονται και σε άλλες Τριαδικές ηφαιστειακές σειρές του Ελλαδικού χώρου, οι οποίες σχετίζονται με την διάνοιξή του

ωκεανού της Πίνδου αλλά και υποβύθισης σε αρχικά στάδια. Τα μοναδικά χαρακτηριστικά του Κροκεάτη Λίθου, σε σχέση με ηφαιστειακά πετρώματα παρόμοιας χημικής σύστασης, οφείλονται στις πορφυρικές δομές που αναπτύσσονται ανάμεσα στη μικρολιθική θεμελιώδη μάζα και τους αδροκοκκώδεις φαινοκρυστάλλους πλαγιοκλάστου, καθώς και στις διεργασίες σωσσυριτίωσης. Ο Κροκεάτης Λίθος φαίνεται ότι σχηματίστηκε σε ένα υπο-ηφαιστειακό σύστημα άμεσα σχετιζόμενο με επιδοσίτες, υποδεικνύοντας ότι η μετασωμάτωση πραγματοποιήθηκε σε ζώνες ανόδου υδροθερμικών ρευστών.
Λέξεις κλειδιά: *Lapis Lacedaemonius, Κροκεάτης Λίθος, Σωσσυριτίωση, Υποβύθιση, Τριαδική ηφαιστειότητα.*

1. Introduction

Lapis Lacedaemonius (Krokeatis lithos) is a well-known volcanic rock since the ancient times. Although it was very difficult material to processes, in antiquity it was used for the manufacture of vases, seals and for the decoration of buildings. It is referred by Pausanias who noted the outcrops locality, as well as its importance in ancient times, since it had been used as raw material since the Minoan period. Later on, the Romans largely extracted this stone for decorative elements. Few of the noteworthy monuments where the Lapis Lacedaemonius has been found are: the ancient acropolis of Mycenae, the palace of King Minos (Knossos, Crete), the baths next to the temple of Poseidon (Corinth), Basilica of Saint Peter, (Rome), Agia Sofia church (Constantinople), Westminster Abbey (London), the ruins of ancient Pompeii and Saint Marc church (Venice). Consequently, it is known with several names; Krokeatis lithos, Porfido verde antico, Marmor Lacedaemonium, Spartan basalt, green stone from Taygetus, Green Porphyry, Viride or Porfido serpentino verde, Krokeischer Stein (e.g. Zezza and Lazzarini, 2002; Wilson, 2013; Kokkorou-Alevra, 2014). The only known occurrence of Lapis Lacedaemonius is near the village of Krokees (old name Levetsova) in Laconia, Northern Southern Peloponnese.

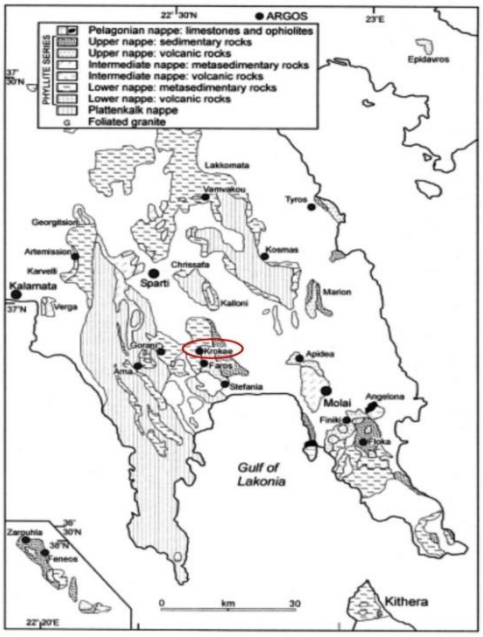

Figure 1 - Simplified geological map of Triassic volcanic rocks in the southern Peloponnese (Pe-Piper and Piper, 2002).

Figure 2 - Hand specimen of Lapis Lacedaemonius presenting characteristic porphyritic texture.

From a geologic aspect, this metavolcanic rock occurrence is part of the Triassic volcanism, which is widespread throughout the mainland of Greece, as part of the Sub-Pelagonian Zone. These volcanic occurrences, which mostly include pillow lavas and massive flows, are associated with the rift/drift phase within the Pindos oceanic realm. In the past, several studies were conducted focusing mostly to the entire Triassic volcanism of the area (Panagos, 1979; Thiebault, 1982; Pe-Piper *et al.*, 1982; Gerolymatos, 1994; Pe-Piper and Piper, 2002). The current study aims to characterize mineralogically and geochemically the Lapis Lacedaemonius (Krokeatis lithos), in an attempt to interpret from a geological scope the reasons for its uniqueness and its absence in other Triassic volcanic localities. In order to accomplish the aforementioned, scientists with different scientific specialization have collaborated to achieve a multidiscipline approach.

2. Geological Setting

Lapis Lacedaemonius is an altered porphyritic basaltic rock which occurs near the village of Krokees (Fig. 1) and is considered as being part of the rift/drift related Triassic volcanism of the Hellinides, which in geotectonic terms may be considered as part of the Sub-Pelagonian Zone (Sharp and Robertson, 2006). The Triassic nappes in the region are termed as the Phyllite-Quarzite Series (Thiebault, 1982; Pe-Piper and Piper, 1991, 2002). These include Paleozoic to Early Triassic pelagic brecciated limestones/marbles and metasedimentary rocks (phyllites, metaconglomerates, metasandstones). The overlaying Tyros beds, mostly exposed in Lakonia, comprise a volcanic and sedimentary sequence, which includes altered basaltic/andesitic pillows, thick pyroclastic series, as well as minor basaltic, dacitic or rhyolitic massive flows and hypabyssal intrusions, while the sedimentary rocks include minor dolomite, sandstone and shale fragments (Gerolymatos, 1994; Pe-Piper and Piper, 2002 and references therein). This nappe is locally conformably overlain by Triassic limestone, passing up into the Tripolitsa limestone (Thiebault, 1982). The volcanic rocks in Lakonia and subsequently in Krokees are basaltic rocks that have undergone low-grade metamorphism (Fig. 2) and are often accompanied by epidosites, which formed by pervasive alteration of the basalts. These volcanic rocks lack significant penetrative deformation features (Thiebault, 1982; Gerolymatos, 1994).

3. Materials and Methods

Thin polished sections were made from three selected samples and examined by transmitted light mic roscopy and scanning electron microscopy-energy dispersive spectroscopy (SEM-EDS), using a JEO L JSM 5600 scanning electron microscope, equipped with an automated energy dispersive analysis s ystem ISIS 300 OXFORD, with the following operating conditions: 20 kV accelerating voltage, 0.5 n A beam current, 20 s time of measurement and 5 μm beam diameter. The spectra were processed usin g the ZAF program (3 iterations). The mineralogical composition of the samples was also investigated by powder X-ray diffraction (XRD). The XRD study was carried out using a Philips XPert Panalytical X-ray diffractometer, operating with Cu radiation at 40 kV, 30 mA, 0.020 step size and 1.0 sec step time. The XRD patterns were evaluated using the DIFFRACplus EVA software v.11 (Bruker-AXS, USA) based on the ICDD Powder Diffraction File (2006). Part of these three samples were pulverized to <200 mesh in an agate mill and were digested with a mixture of HCl-HNO_3-HF acids and was analyzed for a series of trace elements by Inductively Coupled Plasma-Atomic Emission Spectroscopy (ICP-MS) and a series of major elements by X-ray fluorescence (XRF). All samples were analyzed at the Laboratories of the Institute of Geology and Mineral Exploration (I.G.M.E.).

4. Results and Discussion

4.1. Petrography and mineral chemistry

The Lapis Lacedaemonius samples consist of altered prismatically lath-shaped subhedral plagioclase phenocrysts, with their size reaching up to 2 cm, as well as of a groundmass exhibiting microphitic or symplectitic textures (Fig. 3). Based upon petrographic observations (Fig. 3), XRD peak patterns (Fig. 4) and mineral chemistry (Table 2), it is determined that the groundmass consists

mainly of albite, clinopyroxene, epidote, magnetite, quartz, titanite and rare devitrified glass composed of chlorite. In particular, clinopyroxene grains are found only within the groundmass and are classified as augite, exhibiting moderate TiO_2 (0.35-0.72 wt. %), Al_2O_3 (1.75-2.28 wt.%) and low Na_2O and Cr_2O_3 contents (representative analyses in Table 2). The groundmass along with the coarse grained plagioclase crystals forms characteristic porphyritic and also glomeroporphyritic textures. The medium to coarse grained plagioclase crystals have undergone extensive saussuritization processes, including albite/oligoclase relicts, epidote, pumpellyite, sericite, quartz and magnetite. Epidote and prehnite, pumpellyite are more frequent within the cores of the former basic plagioclase feldspars but they also appear within the groundmass. The occurrence of epidote, pumpellyite, prehnite, pumpellyite and sericite strongly suggests that these rocks underwent low-grade metamorphic/metasomatic processes. Despite the prevailing metasomatism, metamorphic degrees are restricted, which is confirmed by the absence of secondary amphibole. Secondary amygdales (1-2 mm) are filled with mixtures of epidote, chlorite, pumpellyite and rarely calcite (Figure 3B, C).

Table 1 - Representative microanalyses of Lapis Lacedaemonius samples.

Mineral	**Cpx**	**Cpx**	**Ab**	**Olig**	**Ser**	**Ep**	**Pmp**	**Prh**	**Chl**	**Ttn**
Sample	KR1	KR3	KR3	KR1	KR3	KR3	KR1	KR2	KR1	KR2
Comments	*within matrix*	*within matrix*	*within matrix*	*within PL*	*within PL*	*Sec. amygd.*	*within PL*	*within PL*	*Sec. amygd.*	*within matrix*
SiO_2	51.87	51.62	67.47	62.16	45.87	37.84	38.84	44.82	28.38	29.88
TiO_2	0.58	0.46	-	-	0.17	0.3	-	-	-	33.29
Al_2O_3	1.72	2.13	20.56	23.43	35.31	22.34	26.97	25.29	19.54	2.25
FeO_t	11.74	11.76	0.21	0.37	1.98	11.22	3.93	3.26	22.74	4
MnO	0.24	0.31	-	0.08	-	-	-	0.29	0.12	-
MgO	14.81	15.34	-	0.15	1.56	1.81	1.77	-	15.91	0.19
CaO	18.91	18.67	2.17	4.88	0.76	22.4	21.33	20.78	0.34	26.79
Na_2O	0.35	0.23	9.84	9.26	0.79	0.38	0.03	0.89	-	0.63
K_2O	0.04	0.1	0.29	0.1	10.27	0.08	0.32	0.18	-	0.16
Cr_2O_3	0.25	0.2	-	-	-	0.09	0.27	-	0.1	0.18
NiO	0.24	0.08	-	-	-	0.04	0.02	-	0.04	-
Total	100.75	100.9	100.54	100.43	96.71	96.5	93.48	95.51	87.18	97.37
Atoms										
Si	1.924	1.908	2.968	2.734	3.030	2.982	3.138	3.076	2.935	1.016
Ti	0.016	0.013	0.000	0.000	0.008	0.018	0.000	0.000	0.000	0.851
Al	0.075	0.093	1.066	1.214	2.749	2.075	2.568	2.046	2.395	0.090
Fe	0.364	0.363	0.008	0.014	0.109	0.739	0.266	0.168	1.966	0.114
Mn	0.008	0.010	0.000	0.003	0.000	0.000	0.000	0.017	0.011	0.000
Mg	0.819	0.845	0.000	0.010	0.154	0.213	0.213	0.000	2.452	0.010
Ca	0.752	0.739	0.102	0.230	0.054	1.892	1.847	1.528	0.038	0.976
Na	0.025	0.016	0.839	0.790	0.101	0.058	0.005	0.118	0.000	0.042
K	0.002	0.005	0.016	0.006	0.865	0.008	0.033	0.016	0.000	0.007
Cr	0.007	0.006	0.000	0.000	0.000	0.000	0.000	0.000	0.008	0.005
Ni	0.007	0.002	0.000	0.000	0.000	0.000	0.000	0.000	0.003	0.000
tot. cat.	4.00	4.00	5.00	5.00	7.07	7.98	8.07	6.97	9.81	3.11
tot. oxy.	6	6	8	8	11	12	12.5	11	14	5

Note: Pl: plagioclase; Ab: albite; An25: oligoclase; Cpx; clinopyroxene, Ep: epidote; Ser: sericite; Chl: chlorite; Mag: magnetite; Pmp: pumpellyite; Prh: prehnite; Qrz: quartz; Aug: augite.

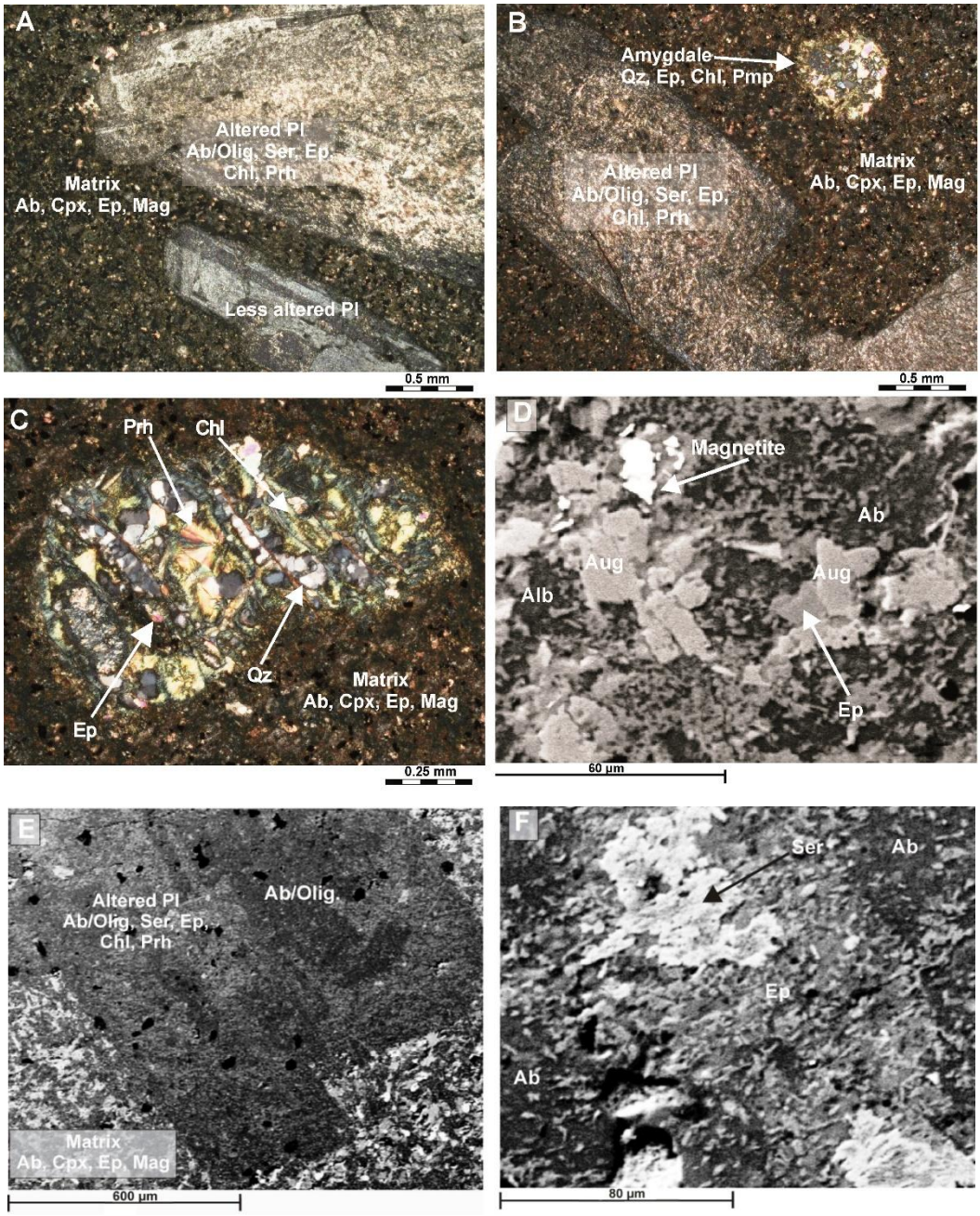

Figure 3 - Photomicrographs and back-scattered electron (BSE) images of Lapis Lacedaemonius samples; (A) Altered plagioclase phenocrysts within the micritic groundmass; (B) Altered plagioclase phenocrysts and amygdale within the groundmass; (C) Amygdale within the groundmass. (D) Micritic groundmass area; (E) Altered plagioclase phenocrysts with relict albite; (F) BSE image within the center of the plagioclase phenocryst.

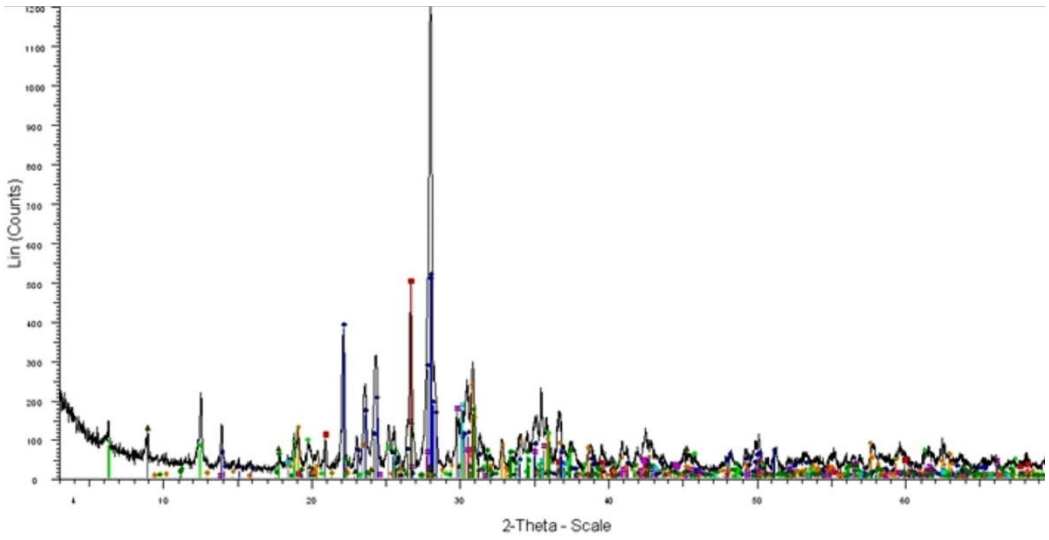

Figure 4. Evaluated XRD pattern of representative Lapis Lacedaemonius.

4.2. Whole-rock geochemistry

Rock classification of the studied metavolcanic Lapis Lacedaemonius (Krokeatis lithos) samples was based upon the binary diagram of Winchester and Floyd (1977), modified by Pearce (1996), which incorporates relatively immobile elements, since Lapis Lacedaemonius have been affected by low-grade metamorphic and metasomatic processes. Based upon this diagram (Fig 5A) and on their petrographic features, samples are classified as porphyritic basalts. These rocks are regarded by many authors (e.g. Pe-Piper *et al.*, 1982; Zezza and Lazzarini, 2002) as porphyritic andesites. However, this classification has been based upon their silica and alkali contents that were affected by metamorphic and metasomatic processes. On a volatile free basis, the rocks of this study have relatively high Al_2O_3 contents (19.39-19.93 wt. %), as well as rather high TiO_2 (0.84-0.89 wt. %) and low MgO (3.45-3.68 wt. %) contents. Their TiO_2 contents, as well as their relatively high FeO_t/MgO ratio values (2.35-2.37), can classify them as being Fe-Ti-rich, based upon the criteria of Melson *et al.* (1976) and Sinton *et al.* (1983) (FeO_t/MgO>1.75). Their relatively high SiO_2 contents (53.33-54.24 wt. %) and the occurrence of CIPW normative quartz, would classify these rocks as andesites, however, this is most likely the result of restricted silification, as confirmed from the petrographic observations. Their geochemical character can be regarded as transitional calc-alkaline, as shown on the Y vs. Zr binary plot (Fig. 5B).

Their MORB-normalized MREE and HREE patterns are subparallel (0.66-1.90 and 0.50-0.77xMORB respectively; Fig. 5C), while their LREE are moderately enriched [$(La/Yb)_{MORB}$=0.66-1.90] (Fig. 5C). Eu anomalies vary from moderate to significant negative (Eu_{MORB}/Eu^{*}=0.66-0.84) which may be due to plagioclase fractionation, changes in $f\,O_2$ conditions or crustal contamination of the source. The Middle to Upper Triassic calc-alkaline rocks from Lakmon (Pindos region), Gionna (Central Greece), Glykomilia (Koziakas region) (Magganas *et al.*, 1997; Pomonis *et al.*, 2004), South Othris (Koutsovitis *et al.*, 2009), as well as from the eastern and south-western Peloponnese region (villages of Platano and Kokkino respectively) (Pe-Piper and Piper 1991, 2002) show similar and subparallel REE patterns, although the latter seem to be more comparable. On the other hand, the MORB-normalized incompatible trace element patterns (Fig. 5D) reveal that Th and K have higher normalized values than Nb and Ta. Zr exhibits significant negative anomalies, while Ti shows moderate negative anomalies. Furthermore, the incompatible Cs and Rb are relative to other elements enriched. The calc-alkaline rocks from the referred adjacent localities present comparable enrichments and depletions, especially regarding the immobile elements.

4.3. Geotectonic and Mantle source interpretations

In the MORB-normalized incompatible trace element patterns of the studied samples (Fig. 5D), the higher normalized values of Th and K relative to Nb and Ta most likely account for influence of subduction or crustal contamination processes (Pearce and Peate, 1995). Negative HFSE anomalies, such as those of Ti and Zr, most often point to supra-subduction zone magmas (e.g. Saunders *et al.*, 1991; McCulloch and Gamble, 1991). Similar assumptions can be inferred from the LILE Cs and Ba enrichments; however, secondary processes most likely affected their original magmatic values. The Ti–V–Sm ternary discrimination diagram (after Vermeesch, 2006; Fig. 5E), which incorporates immobile elements, clearly suggests that subduction related processes had a significant effect during rock-formation. Similar assumptions can be made from the binary diagram of Th/Yb vs. Nb/Yb (Fig. 5F), in which the studied samples plot above the MORB-OIB mantle array, but also from the strikingly low Nb/Th ratio values, which are below the value of 4, characterizing arc-related rocks (Sun and McDonough, 1989). From the same binary diagram, apart from the effect subduction, it seems that the samples were derived from an enriched mantle source.

The occurrence of alkaline and E-MORB lavas along with the calc-alkaline basalts and trachyandesites in Triassic localities in Greece, such as in Pindos (Pe-Piper and Piper, 2002; Pe-Piper *et al.*, 2004), Koziakas (Magganas *et al.*, 1997; Pomonis *et al.*, 2004) and South Othris (Koutsovitis *et al.*, 2012), further supports this assumption. In addition, the Zr/Nb ratios of the studied samples, which are almost independent from fractional crystallization and slab dehydration processes (e.g. Thirlwall *et al.*, 1994; Pearce and Peate, 1995; Kamber and Collerson, 2000), may provide information concerning the nature of the mantle source. In particular, their Zr/Nb ratios range between 10.9 and 15.2, which may be considered as very low, pointing to derivation from an enriched mantle source. This enriched source is most likely linked to the Early Triassic upwelling of plume-related asthenospheric OIB melts, shown by the high estimated mantle potential temperature (~1,370°C; Magganas and Koutsovitis, 2015). Addition of slab related sedimentary components seems to have also taken place as implied by the relatively high Th/La ratios (0.25-0.41) (Plank, 2005). A plausible scenario to interpret the geotectonic setting for the formation of the Triassic studied rocks, as well as other comparable Triassic calc-alkaline lavas, is the occurrence of intra-oceanic local compressional tectonics, possibly related with a breakup of the early formed oceanic crust forming an infant subduction zone. This scenario has successfully interpreted the unusual Triassic ultramafic-mafic-felsic suite in Othris (Koutsovitis *et al.*, 2012).

4.4. Unique features of the Lapis Lacedaemonius

The question which obviously arises is what are the reasons for the unique appearance of the Lapis Lacedaemonius (Krokeatis lithos) and why is it absent in other Triassic volcanic localities. The fact that this rock occurrence presents obvious geochemical similarities with other Triassic calc-alkaline volcanics reported throughout the Hellenic mainland, makes it even more difficult to interpret. Small differences in their chemistry and possibly variability in the influence of subduction or sediment components cannot explain this alone. What makes the Lapis Lacedaemonius unique compared to the other Triassic calc-alkaline volcanic rocks is the absence of K-feldspar, the presence of fewer clinopyroxene crystals and the higher modal composition of the groundmass, the larger in size plagioclase phenocrysts, the silicification processes and also the infrequency of calcite in comparison to sericite. The most reasonable explanation that can be given is related to the fact that the other Triassic calc-alkaline volcanic rocks appear mostly in the form of pillow lavas, whereas the Lapis Lacedaemonius seems to be part of a subvolcanic suite. Thus, large sized plagioclase crystals were most likely formed in relatively deeper levels before being brought to shallower levels by a differentiated melt. Their association with epidosites in veins and crosscutting intrusions indicates that metasomatism occurred within hydrothermal upflow zones, comparable to those occurring in sheeted dykes of SSZ ophiolites (Banerjee *et al.*, 2000; Gillis, 2002).

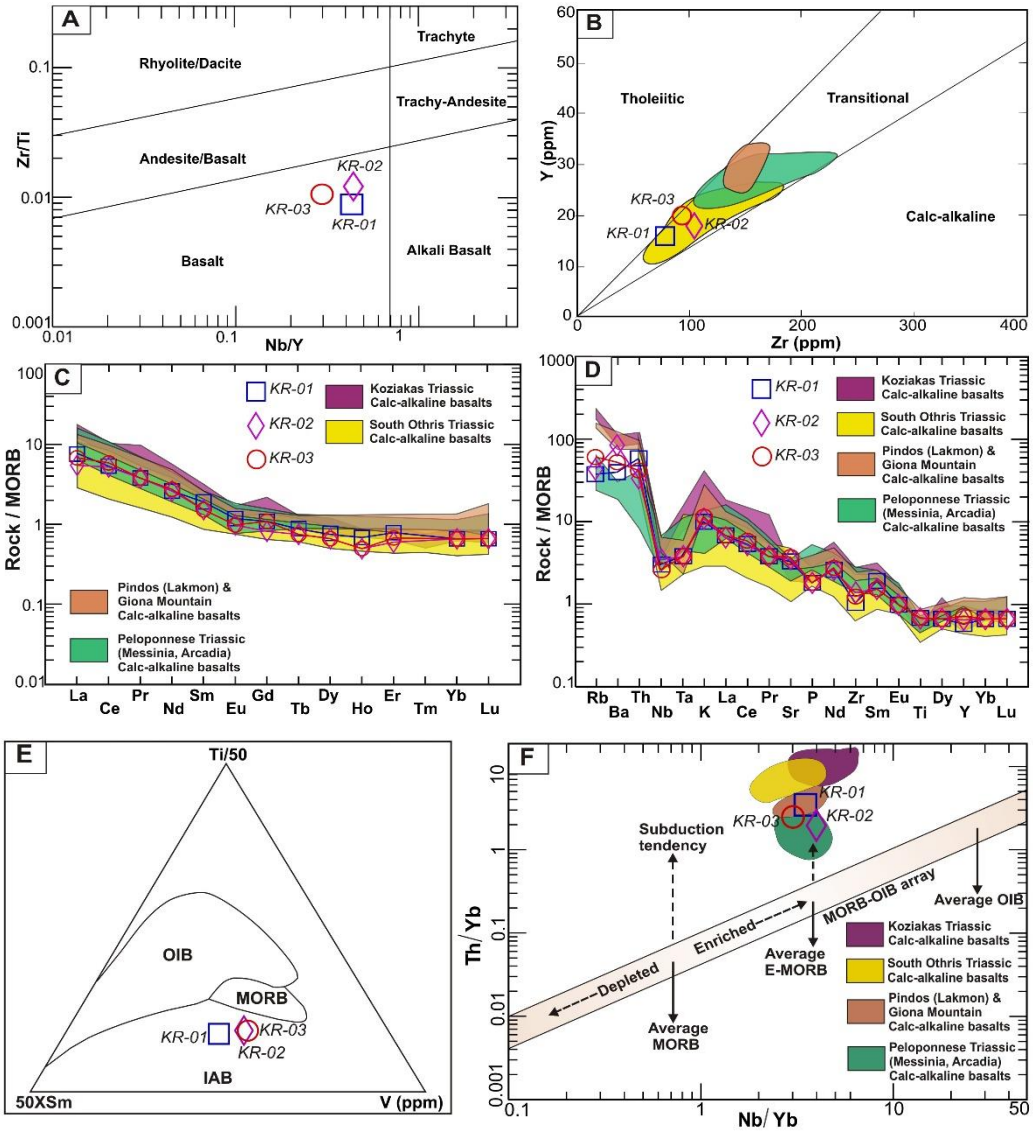

Figure 5. Lapis Lacedaemonius samples plotted on the: (A) Zr/Ti vs. Nb/Y diagram (Winchester and Floyd, 1977, modified by Pearce, 1996). (B) Y (ppm) against Zr (ppm) diagram (Barrett and Maclean, 1999). (C) MORB-normalized REE patterns. (D) MORB-normalized incompatible trace element patterns [normalization factors after Pearce and Parkinson (1993)]. (E) Ti–V–Sm diagram (after Vermeesch, 2006); (F) Th/Yb vs. Nb/Yb diagram (after Pearce, 2008). Triassic calc-alkaline volcanic rocks from Koziakas (Magganas *et al.*, 1997; Pomonis *et al.* 2004), South Othris (Koutsovitis *et al.*, 2009), Pindos (Lakmon) and Giona Mountain (Pe-Piper and Piper, 1991, 2002), Peloponnese (Messinia-Kokkino, Arcadia-Platanos villages) (Pe-Piper and Piper, 1991, 2002) are shown.

5. Conclusions

The Lapis Lacedaemonius (Krokeatis lithos) is a meta-volcanic rock of great historical importance. Its impressive and unique appearance was known even since the Minoan period and was used throughout ancient and medieval times as a raw material source. The studied samples reveal that

Lapis Lacedaemonius is a subduction affected, transitional calc-alkaline basalt, formed during the Triassic volcanic period.

They exhibit many similarities compared with other Triassic calc-alkaline volcanic rocks from adjacent localities, showing that they were formed after interaction between E-MORB type volcanism and subduction related processes. Their differences which make the Lapis Lacedaemonius unique are mostly petrographic, accommodating higher modal plagioclase phenocrysts and micritic groundmass, both affected by saussuritization and restricted silicification processes, as well as the absence of clinopyroxene phenocrysts. It seems to have formed in a subvolcanic system closely associated with epidosites in the area, indicating that metasomatism occurred within hydrothermal upflow zones. In order to confirm these assumptions a more detailed study is anticipated in the short future so as to further investigate and unravel these processes.

6. Acknowledgments

We would like to express our thanks to an anonymous reviewer for the useful comments which helped to improve this paper. We express our appreciation to the Museum of Mineralogy and Petrology, at University of Athens and its Director Prof. Athanasios Katerinopoulos for allowing us to study one of the Lapis Lacedaemonius samples. Many thanks go to Pantelis Patsis, Michalis Sakalis and Dimitris Tarenidis of the Institute of Geological and Mineralogical Exploration (IGME) for their laboratory support.

7. References

Banerjee, N.R., Gillis, K.M. and Muehlenbachs, K., 2000. Discovery of epidosites in a modern oceanic setting, the Tonga forearc, *Geology*, 28(2), 151-154.

Barrett, TJ. and Maclean, WH., 1999. Volcanic sequences, lithogeochemistry, and hydrothermal alteration in some bimodal volcanic-associated massive sulfide systems. *In*: Barrie, C.T. and Hannington, M.D., *eds*., Volcanic-Associated Massive Sulfide Systems: Processes and Examples in Modern and Ancient Settings, *Reviews in Economic Geology*, 8, 101-131.

Gerolymatos, I., 1994. Metamorphose und Tektonik der Phyllit- Quartzit-Serie und der Tyros Formation auf dem Peloponnes und Kythira, *Berliner Geowiss. Abh*., 164-161.

Gillis, K.M., 2002. Root-zones of a fossil oceanic hydrothermal system exposed in the Troodos Ophiolite, *The Journal of Geology*, 110, 57-74.

Kamber, BS. and Collerson, KD., 2000. Zr/Nb Systematics of Ocean Island Basalts Reassessed-the Case for Binary Mixing, *Journal of Petrology*, 41(7), 1007-1021.

Kokkorou-Alevra, G., Poupaki, I., Efstathopoulos, A. and Hatzikonstantinou, A., 2014. Corpus of Ancient Greek Quarries. University of Athens, 350 pp. (In Greek).

Koutsovitis, P., Magganas, A. and Katerinopoulos, A., 2009. Calc-alkaline volcanic rocks in mélange formations from the South Othris region, Greece: petrogenetic and geo-tectonic implications, *Geochemistry, Mineralogy, Petrology*, 47, 79-95.

Koutsovitis, P., Magganas, A. and Ntaflos, T., 2012. Rift and intra-oceanic subduction signatures in the Western Tethys during the Triassic: the case of ultramafic lavas as part of an unusual ultramafic-mafic-felsic suite in Othris, Greece, *Lithos*, 144-145,177-193.

Magganas, A. and Koutsovitis, P., 2015. Composition, Melting and Evolution of the Upper Mantle beneath the Jurassic Pindos Ocean Inferred by Ophiolitic Ultramafic Rocks in East Othris, Greece, *International Journal of Earth Sciences*, 1-23.

Magganas, A., Kyriakopoulos, K. and Lekkas, E., 1997. Early Alpine Rift Volcanism in Continental Greece: the Case of Glykomilia Area (Koziakas Mountain), *Chemie der Erde*, 57, 243-255.

McCulloch, M.T. and Gamble, A.J., 1991. Geochemical and geodynamical constraints on subduction zone magmatism, *Earth and Planetary Science Letters*, 102, 358-374.

Melson, W.G., Vallier, T.L., Wright, T.L., Bryerly, G. and Nelson, J., 1976. Chemical diversity of abyssal volcanic glass erupted along the Pacific, Atlantic, and Indian Ocean seafloor

spreading centers. *In*: Sutton, G., Manghari, M.H. and Moberly, R., *eds*., The geophysics of the Pacific Ocean Basin and its margins, *Geophysical Monograph,* 12, 351-367.
Panagos, A., Pe, G.G., Piper, D.J.W. and Kotopouli, C.N., 1979. Age and stratigraphic subdivision of the phyllite series, Krokee region, Peloponnese, Greece, *Neu. Jb. Geol.-Paläont.,* Mh., 3, 181-190.
Pearce, J.A., 1996. A users guide to basalt discrimination diagrams. *In*: Wyman, D.A., *ed*., Trace Element Geochemistry of Volcanic Rocks: Applications for Massive Sulphide Exploration, Geological Association of Canada, Short Course Notes, 12, 79-113.
Pearce, J.A., 2008. Geochemical fingerprinting of oceanic basalts with applications to ophiolite classification and the search for Archean oceanic crust, *Lithos*, 100, 14-48.
Pearce, J.A. and Parkinson, I.J., 1993. Trace element models for mantle melting: application to volcanic arc petrogenesis. *In*: Prichard, H.M., Alabaster, T., Harris, N.B.W. and Neary, C.R., *eds*., Magmatic Processes and Plate Tectonics, Geological Society, *London, Special Publications*, 76, 373-403.
Pearce, JA. and Peate, D.W., 1995. Tectonic Implications of the Composition of Volcanic ARC Magmas, *Annu. Rev. Earth Planet Sci.*, 23, 251-285.
Pe-Piper, G., 1982. Geochemistry, tectonic setting and metamorphism of the mid-Triassic volcanic rocks of Greece, *Tectonophysics*, 85, 253-272.
Pe-Piper, G., Panagos, A.G., Piper, D.J.W. and Kotopouli, C.N., 1982. The (?) mid Triassic volcanic rocks of Lakonia, Greece, *Geological Magazine*, 119, 77-85.
Pe-Piper, G. and Piper, D.J.W., 1991. Early Mesozoic oceanic subduction- related volcanic rocks, Pindos Basin, Greece, *Tectonophysics*, 192, 273-292.
Pe-Piper, G. and Piper, D.J.W., 2002. The Igneous Rocks of Greece, *Borntraeger, Stuttgart*, 1-645.
Pe-Piper, G., Tsikouras, B. and Hatzipanagiotou, K., 2004. Evolution of boninites and island-arc tholeiites in the Pindos Ophiolite, Greece, *Geol Magazine*, 141, 455-469.
Plank, T., 2005. Constraints from thorium/lanthanum on sediment recycling at subduction zones and the evolution of the continents, *Journal of Petrology*, 46, 921-944.
Pomonis, P., Tsikouras, B. and Hatzipanagiotou, K., 2004. Comparative geochemical study of the Triassic trachyandesites of Glykomilia and alkalibasalts from the Koziakas ophiolite mélange (W. Thessaly): implications for their origin, 10th G.S.G. Congress 2004, *Bulletin of the Geological Society of Greece*, 36, 587-596.
Saunders, A.D., Norry, M.J. and Tarney, J., 1991. Fluid influence on the trace element compositions of subduction zone magmas, Philosophical Transactions of the Royal Society of London, A335, 377-392.
Sharp, I.R. and Robertson, A.H.F., 2006. Tectonic-sedimentary evolution of the western margin of the Mesozoic Vardar Ocean: evidence from the Pelagonian and Almopias zones, northern Greece, *Geol. Soc. London Spec. Publ.*, 260, 373-412.
Sinton, J.M., Wilson, D.S., Christie, D.M., Hey, R.N. and Delaney, J.R., 1983. Petrologic consequences of rift propagation on oceanic spreading ridges, *Earth and Planetary Science Letters*, 62, 193-207.
Sun, S.S. and McDonough, W.F., 1989. Chemical and isotopic systematics of oceanic basalts: implications for mantle composition and processes. *In*: Saunders, A.D. and Norry, M.J., *eds*., Magmatism in the Ocean Basins, *Geol. Soc., London, Spec. Publ.*, 42, 313-345.
Thiebault, F., 1982. Evolution geodynamique des Hellenides externs en Peloponnese meridional (Greece), *Soc. Geol. Nord*, 6, 1-574.
Thirlwall, M.F., Upton, B.G.J. and Jenkins, C., 1994. Interaction between continental lithosphere and the Iceland plume-Sr-Nd-Pb isotope geochemistry of Tertiary basalts, NE Greenland, *Journal of Petrology*, 35, 839-879.
Vermeesch, P., 2006. Tectonic discrimi-nation diagrams revisited, *Geochem. Geophys. Geosyst*., 7.
Wilson, N., 2013. Encyclopedia of Ancient Greece, Hoboken, Taylor and Francis, 1-800.
Winchester, J.A. and Floyd, P.A., 1977. Geochemical discrimination of different magma series and their differentiation products using immobile elements, *Chemical Geology*, 20, 325-343.
Zezza, U. and Lazzarini, L., 2002. Krokeatis Lithos (Lapis Lacedaemonius): source, history of use, scientific characterization'. *In*: Lazzarini, L., *ed*., Interdisciplinary Studies on Ancient Stone, ASMOSIA VI, Padua.

Δελτίο της Ελληνικής Γεωλογικής Εταιρίας, τόμος L, σελ. 1913-1922
Πρακτικά 14ου Διεθνούς Συνεδρίου, Θεσσαλονίκη, Μάιος 2016

Bulletin of the Geological Society of Greece, vol. L, p. 1913-1922
Proceedings of the 14th International Congress, Thessaloniki, May 2016

ASSESMENT OF THE QUALITY OF METAMORPHIC AND IGNEOUS ROCKS FROM TERPNI (SERRES, NORTH GREECE) FOR THEIR USE AS RAW MATERIALS IN THE PRODUCTION OF STONEWOOL

Lampropoulou P.[1], Papoulis D.[1], Metaxa E.[1], Tsikouras B.[2], Hatzipanagioutou K.[1], Tzevelekou Th.[3] and Karageorgis A.[3]

[1]University of Patras, Department of Geology, Section of Earth Materials, 265 04, Patras, Greece, p.lampropoulou@upatras.gr, papoulis@upatras.gr, eygenia1990_@hotmail.com, k.hatzipanagiotou@upatras.gr

[2]University of Brunei Darussalam, Faculty of Science, Physical and Geological Sciences, JalanTungku Link, Gadong BE1410, Bandar Seri Begawan, Brunei Darussalam,basilios.tsikouras@ubd.edu.bn

[3]Hellenic Research Centre for Metals S.A. (ELKEME), 56th km Athens - Lamia National Road, 32011 OinofytaViotias, Greece, ftzevelekou@elkeme.vionet.gr, akarageorgis@elkeme.vionet.gr

Abstract

Metamorphic and igneous rocks of Terpnis' Serres in N. Greece have been studied. Nowadays these metamorphic rocks are used as raw materials in stone wool production, by Fibran industry, whilst the studied plutonic samples with lower content of iron oxide are proposed as alternative raw material for the production of new lightly colored stone wool, according to the market demands.

Selected epidote amphibolites and quartz diorite samples were analyzed by ICP-OES, AAS, XRD, Petrographic microscopy, and SEM.

The epidote-amphibolites show some evidence of weathering leading to sericitic-saussuritizated plagioclase crystals and secondary smectite and chlorite nanocrystals. Phyllosilicates affect positively the grinding procedure and melting of the raw materials under industrial conditions of stone wool production, due to its lower hardness and melting point compared to that of the primary hornblende.

The chemical and major mineralogical composition, the heterogeneous characteristics of textures as well as the frequent presence of phyllosilicates, due to the weathering of the plutonic studied samples, are expected to contribute to the easier grinding and melting of rocks under industrial conditions as well as to the production of a new light colored and competitive stone wool product.

Keywords: *thermal insulation, mineralogy, microstructure, natural stone.*

Περίληψη

Από την περιοχή της Τερπνής Σερρών στη Β. Ελλάδα, μελετήθηκαν δείγματα μεταμορφωμένου πετρώματος αμφιβολίτη, το οποίο χρησιμοποιείται στην Ελληνική βιομηχανία από την εταιρία Fibran ως πρώτη ύλη για την παραγωγή πετροβάμβακα. Παράλληλα μελετήθηκαν και δείγματα από γειτονική εμφάνιση πετρωμάτων χαλαζιακού διορίτη, ως εναλλακτική πρώτη ύλη με χαμηλότερη περιεκτικότητα σιδήρου

για την παραγωγή νέου ανοιχτόχρωμου μονωτικού υλικού πετροβάμβακα σύμφωνα με τις ανάγκες της αγοράς.
Τα δείγματα του επιδοτιτικού αμφιβολίτη και χαλαζιακού διορίτη μελετήθηκαν πετρογραφικά, με πολωτικό μικροσκόπιο σάρωσης καθώς και με ηλεκτρονικό μικροσκόπιο σάρωσης (SEM), περιθλασιμετρία Ακτινών-Χ, φασματοσκοπία ατομικής εκπομπής με πλάσμα (ICP-OES) και φασματοφωτομετρία ατομικής απορρόφησης (AAS).
Η ανάλυση του επιδοτιτικού αμφιβολίτη παρουσίασε ενδείξεις αποσάθρωσης σε χλωρίτη καθώς επίσης και των πλαγιοκλάστων σε σερικίτη και σμεκτίτη. Τα φυλλοπυριτικά ορυκτά που βρίσκονται στα πετρώματα αυτά επιδρούν θετικά κατά τη διαδικασία θραύσης, ανάμιξης και τήξης των πρώτων υλών κατά την παραγωγική διαδικασία του πετροβάμβακα.
Η χημική, η κύρια ορυκτολογική σύσταση, ο ετεροκοκκώδης ιστός του χαλαζιακού διορίτη αλλά και η συχνή εμφάνιση φυλλοπυριτικών λόγω αποσάθρωσης, αναμένεται να συμβάλλουν θετικά τόσο κατά την παραγωγική διαδικασία (άλεση και τήξη) όσο και στην ποιότητα νέων περισσότερο ανοιχτόχρωμων και ανταγωνιστικότερων προϊόντων πετροβάμβακα.
Λέξεις κλειδιά: *θερμομόνωση, ορυκτολογία, φυσικές πρώτες ύλες, μικροδομή, μονωτικό υλικό.*

1. Introduction

In the middle of 19th century, in Hawaii, American geologists discovered woolen strings of stone lying on the ground. That was made after volcanic eruption. The inhabitants used them to reinforce their homes and called them Pele's hair.

Stone wool consists of fibers with an average length of 4-20μm, are inflamed and derive from rock melting at 1450-1600ºC (Blagojevic *et al*., 2004; Ecofys, 2012). Their chemical composition is dominated by the presence of aluminum-silicon oxides and their colour is amber.

The most important use of stone wool is in construction, because it exhibits insulation's unique fire-retardant properties (Karamanos *et al*., 2004; Karamanos *et al*., 2005), sound absorption/insulation (Antonio *et al*., 2003) and water repellence. Also stone wool is well known for its external uses (in insulation, external façades and roofs (Yang and Zhang, 2012) and for bio-solubility in the body (*Bomberg and Onysko, 2015).* Stone wool materials are also used in industrial applications, particularly at relatively high temperatures up to 1000 °C as a casing material in furnaces and fireplaces as well as in agriculture as a substrate in hydroponic applications.

Worldwide basalts, metabasalts, diabases, gabbros, bauxites, anorthosites, limestones and carbonate minerals are used as raw material to produce mineral wool (Papadopoulos, 2005). The main chemical compounds included in the composition of these raw materials are oxides of silicon, aluminum, calcium, magnesium and iron. Greece is the only country that uses amphibolites as the major raw material.

This study aims at evaluating the quality of metamorphic and igneous rocks of Terpnis' Serres in N. Greece (Figure 1a) as raw materials in stone wool production. The relation between the mineralogical, geochemical and microstructural characteristics of these rocks, with the properties of the stone wool products as well as the production procedure were also investigated.

2. Geological Settings

The studied area (Terpni Serres) is located in northern Greece (Figure 1a) and belongs to the Serbo-Macedonian massif. The Serbo-Macedonian massif is divided into two units, the lower (Kerdilion) and the upper (Vertiskos) (Mountrakis, 2010). The main rocks of lower unit are gneisses while in the studied area they coexist with diorites, amphibolites and conglomerates (Figure 1b).

3. Materials and Methods

A representative epidote amphibolitic sample and three quartz diorite samples were analyzed and studied in this work. Currently the metamorphic studied rocks are used as raw materials in the industrial production of stone wool materials by the Greek company Fibrangeo, whilst the adjacent quartz diorite rocks are studied as an alternative physical raw material. The chemical analysis of major and trace elements was conducted at the Analytical Chemistry laboratory of the Hellenic Research Centre for Metals by ICP-OES (Inductively Coupled Plasma Optical Emission Photometer) and AAS (Atomic Absorption Spectroscopy). The composition of bulk-rock mineralogy and of clay fractions (2-20 μm) was determined by X-Ray powder Diffraction (Bruker, D8 Advance Diffractometer equipped with a LynxEye®detector) at the Dept. of Geology, Univ. of Patras. Conditions for the XRD analysis on bulk-rock mineralogy were CuKα radiation (40kV and 40mA), in the range 2-70 °2θ, with a scanning angle step of 0.015° and a time step of 0.3s. For the identification of clay minerals standard procedures have been applied, oriented samples of the <20μm size-fractions extracted by sedimentation, in the air-dried state and after ethylene glycol solvation was used. The mineral phases were detected using the DIFFRACplus EVA® software (Bruker-AXS, USA) based on the ICDD Powder Diffraction File. Petrographic, fabric and microstructure observations were performed on polished thin sections and fracture surfaces, using a Leica DM LSP polarizing microscope equipped with a digital imaging system (at the Dept. of Geology, Univ. of Patras) and Scanning Electron Microscope equipped with an Energy Dispersive Spectrometer (EDS) (SEM JEOL 6300 at the Laboratory of the Electron Microscopy and Microanalysis, Univ. of Patras and LEO SUPRA 3VP at the Institute of Chemical Engineering Sciences (ICE-HT), Patras), respectively.

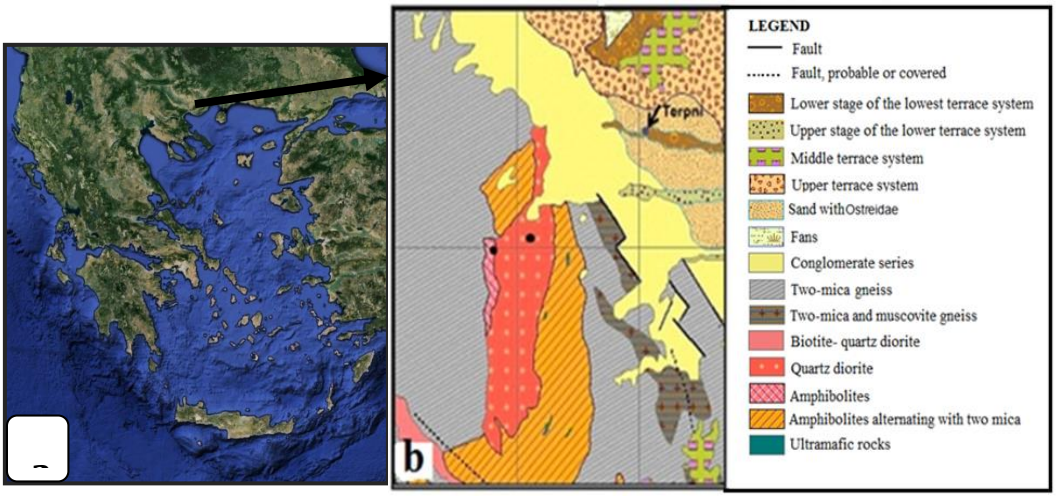

Figure 1 - (a) Map of the Greece area, (b) Modified geological map by GIS from the issue of IGME "SOHOS". The black dots show the sampling points, amphibolitic (left) and quartz diorite (right) rocks.

4. Results and discussion

4.1. Chemistry

Representative chemical analyses of studied epidote amphibolitic and quartz dioritic rocks are presented in Table 1. The igneous rocks showed lower contents of iron, calcium and magnesium oxides and higher content of silicon oxide than those in the metamorphic ones. According to the industrial market demands for light colored stone wool products, the lower content of iron in the latter rocks was the first criterion for studying these as alternative raw materials.

Table 1 - Representative chemical analyses of studied samples (ICP-OES).

Sample	Epidote amphibolitic rock	Quartz dioritic rock
%wt oxides		
SiO_2	49.14	63.79
TiO_2	1.98	0.44
Al_2O_3	13.71	13.83
Fe_2O_3	12.07	6.48
MnO	0.13	0.06
MgO	5.98	2.71
CaO	11.71	4.83
Na_2O	2.03	2.25
K_2O	0.59	1.53
LOI	2.66	4.06
Total	100.01	99.97

4.2. Mineralogy and Microstructure

The major mineral phases of the epidote amphibolitic rock (S1) that were detected are magnesiohornblende (Figure 2), feldspar (oligoclase and Na feldspar, Figure 3) and epidote. In some cases it shows evidence of weathering (and probably hydrothermal alteration also) leading to sericitic-saussuritizated plagioclase crystals and secondary smectite or rarely chlorite nanocrystals (Figures 4, 5, 6). Due to the large available space for the growth of clay minerals, the orientation of clay particles is random and the rock's porosity high (Keller, 1978), as it is evident by clay minerals morphology. The rock's texture is characterized by fine grained inoblastic hornblende and granoblastic feldspars (Figure 5).

The mineralogical compositions as well as the microstructural characteristics of the studied plutonic samples (quartz diorite rocks) (Figures 4, 7, 8), revealed the presence of some unaffected rocks (S2) as well as low to medium altered ones (S3) and highly altered samples (S4) after weathering (Velde, 1995; Meunier, 2005). Biotite, hornblende and plagioclase are dominant in unaffected rocks. Deficient secondary chlorite nanocrystals, smectite and cauliflower hematite are present in the slightly and medium altered rocks, whilst well formed chlorite nanocrystals as rosettes occur in the completely altered rocks (Figure 8). S2 sample contains oligoclase and andesine plagioclase which are substituted by albite as they are altered (S3, S4, Figure 3). The amphibole in the quartz diorite samples is characterized as magnesio- hornblende (Figure 2). Several microanalyses of secondary chlorite revealed the occurrence of pycnochlorite in sample S2, while diabantite seems to be dominant in the chemically affected samples (S4). The texture of these specimens could be characterized as dissimilar coarse to medium grained.

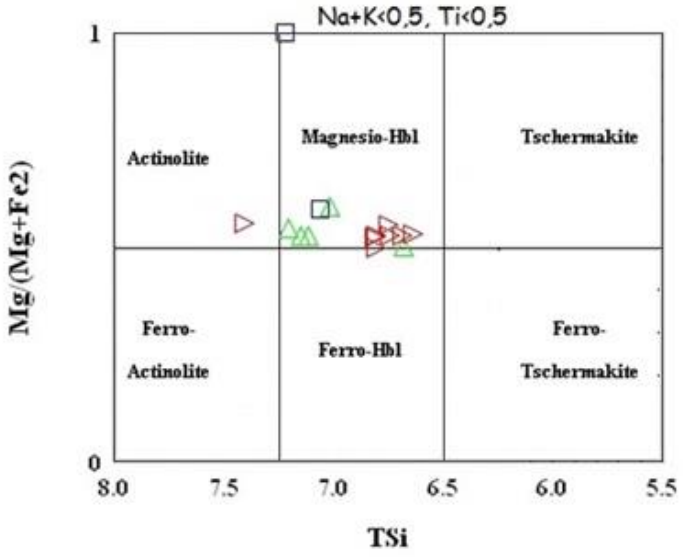

Figure 2 - Chemical classification diagram for the amphiboles (Leake *et al.*, 1997) Legend: ▷: Epidote amphibolitic rock, ∆: Quartz diorite rock, □ : Altered Quartz diorite.

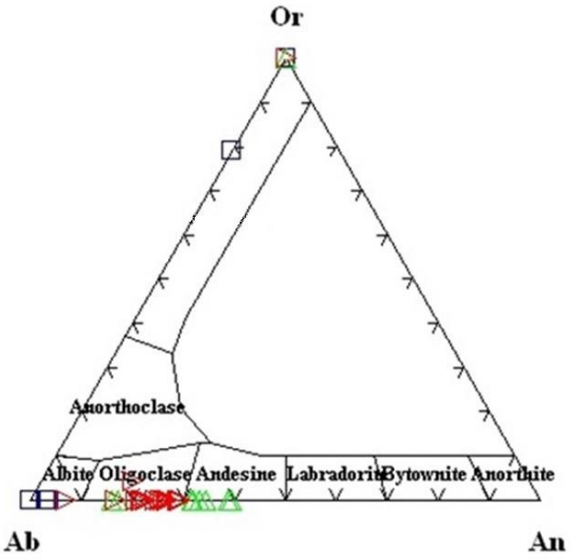

Figure 3 - Chemical classification diagram for the plagioclase in epidote amphibolitic and quartz diorite rock. Legend: ►: Epidote amphibolitic rock, ∆: Quartz diorite rock, □: Altered Quartz diorite.

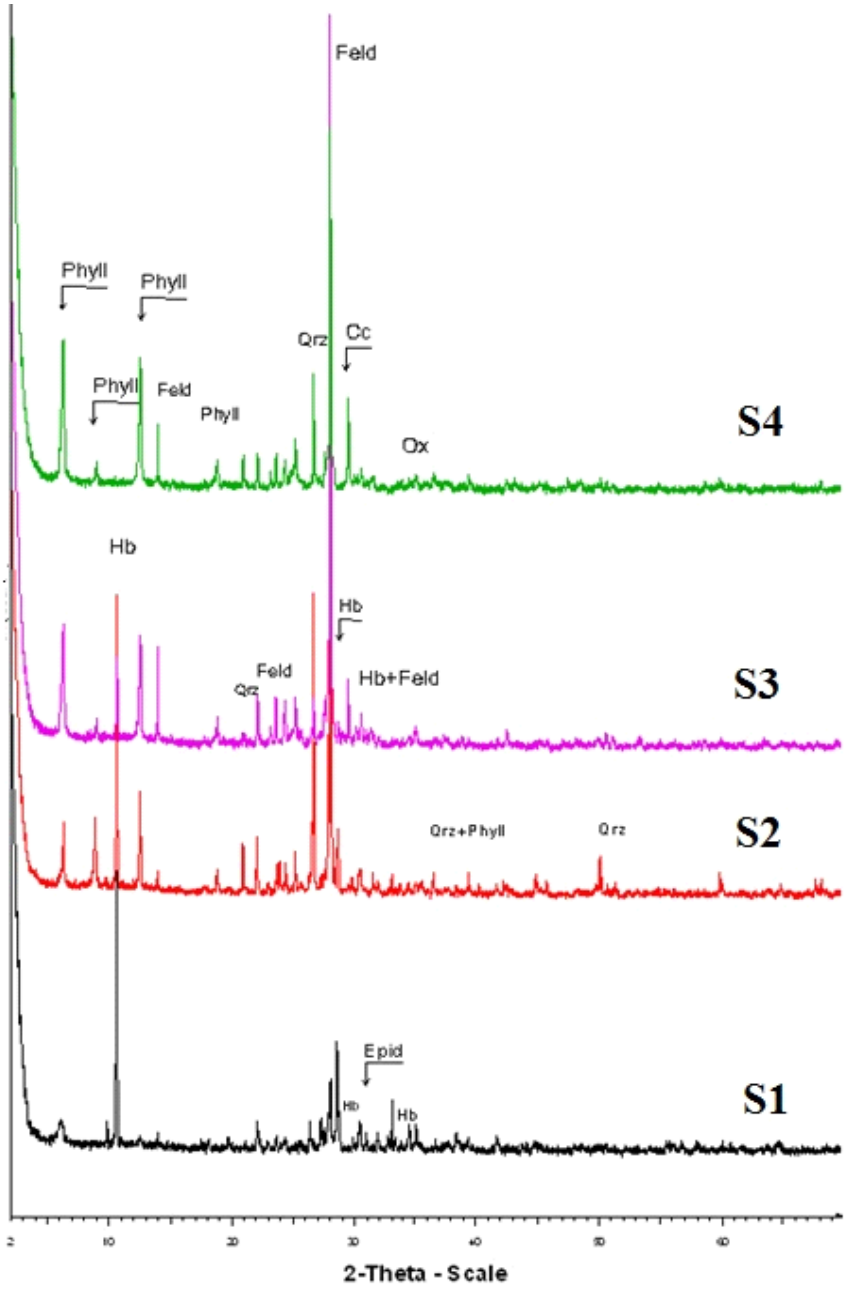
Feld
Phyll
Phyll
Qrz
Cc
Phyll
Feld
Phyll
Ox
S4
Hb
Hb
Feld
Qrz
Hb+Feld
S3
Qrz+Phyll
Qrz
S2
Epid
Hb
Hb
S1
2-Theta - Scale

a

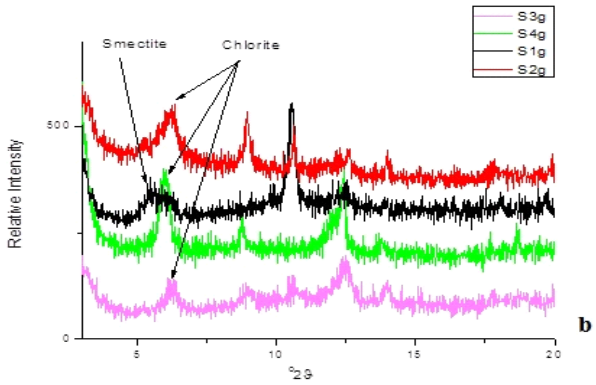

Figure 4 - (a) X-ray diffraction patterns of bulk studied samples. feldspar (Feld), phyllosilicates (Phyll), hornblende (Hb), epidote (Ep), quartz (Qrz), calcite (Cc), oxides (Ox), (b) X-ray patterns of clay fraction of the studied samples (S1-4) after ethylene-glycol treatment (g). S1: Epidote amphibolitic rock; S2: Unaffected Quartz diorite rock; S3: Medium altered Quartz diorite rock; S4: Highly altered Quartz diorite rock.

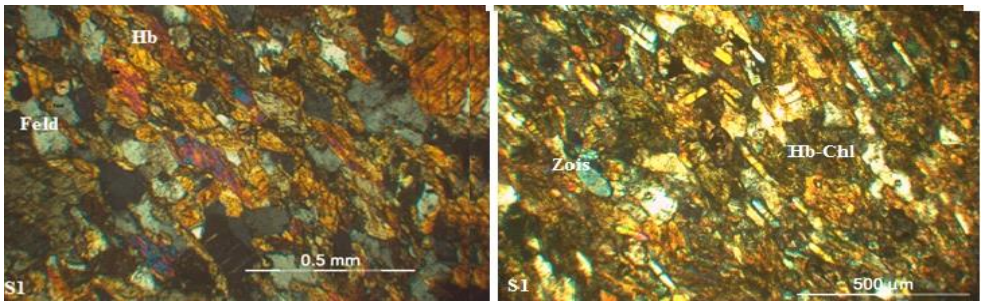

Figure 5 - Photomicrographs in crossed polars (XPL) of S1 sample showing the presence of feldspar (Feld), hornblende (Hb), zoisite (Zois) and chlorite (Chl).

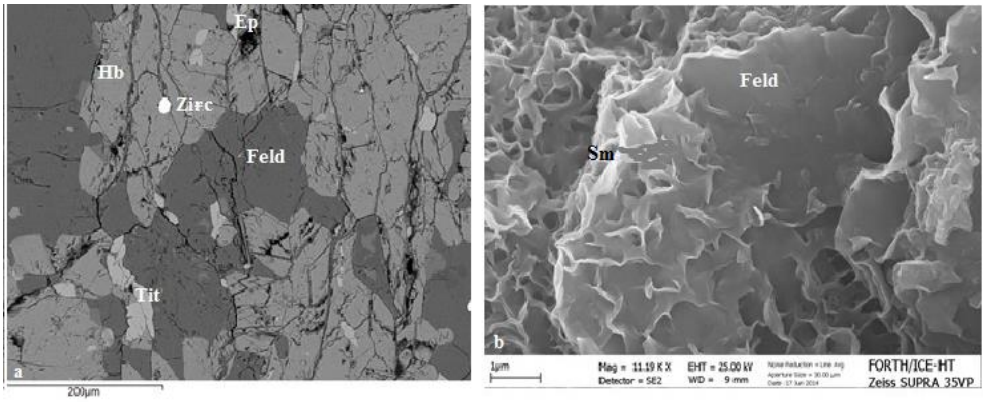

Figure 6 - (a) Backscattered electron image of the epidote amphibolitic rock microstructure (S1) and (b) secondary electron image on fracture surface of S1 sample showing a feldspar surface altered to smectite flakes. feldspar (Feld), hornblende (Hb), epidote (Ep), zircon (Zirc), titanite (Tit), smectite (Sm).

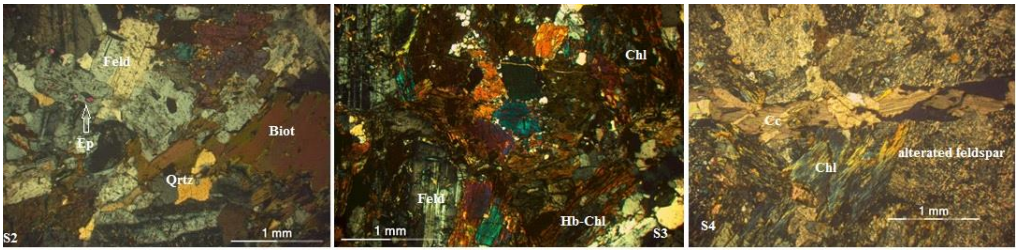

Figure 7 - Photomicrographs in crossed polars (XPL) of S2, S3, S4 microstructures. feldspar (Feld), hornblende (Hb), biotite (Biot), epidote (Ep), quartz (Qrtz), chlorite (Chl), calcite (Cc).

The typical industrial mixture of the raw materials (epidote amphibolitic rock, bauxite, lime and dolomite) that is currently implemented by FIBRAN in the production of advanced stone wool materials, demands a specific chemical composition (Table 2). The fine grained texture and the major mineralogical composition of quartz diorite rocks in combination with the presence of smectite and chlorite (with lower hardness and melting point than that of the primary hornblende) promote the grinding procedure and melting of raw materials under industrial conditions.

The results of the studied plutonic rocks revealed that these materials do not vary significantly in chemical and mineralogical composition from the metamorphic ones. So the addition of an appropriate ratio of quarz dioritic rock instead of epidote-amphibolitic could lead to a new prepared mixture of raw materials with a lower FeO content, preserving simultaneously the standard industrial recipe (Table 2). Furthermore, the dissimilar coarse to medium grained texture in these specimens (S2, S3, S4) as well as the presence of chlorite nanocrystals and other secondary clay minerals anticipate for the easier grinding and melting of rocks. According to the above, these igneous rocks could be tested in a pilot laboratory scale as an alternative raw material for the production of new, light-colored and global competitive stone wool with no increase of industrial economy cost.

Table 2 - Typical industrial major chemical composition of raw materials mixture for stone wool production.

Oxides	%wt
SiO_2	~37
CaO+ MgO	>26
Al_2O_3	~18
FeO_x	~6-11

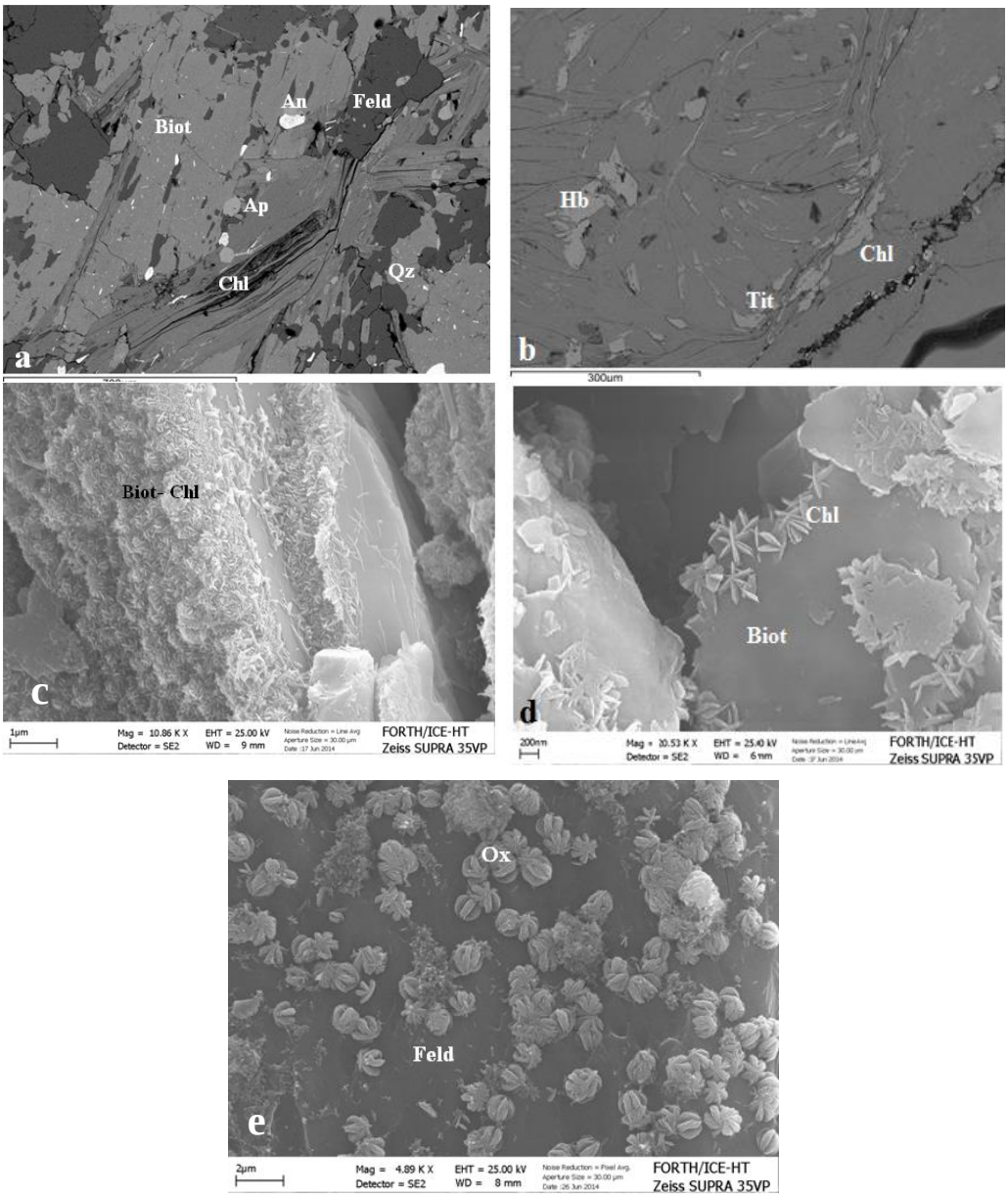

Figure 8 - (a) and (b) Representative backscattered electron images of S2 and S4 microstructures, respectively; (c) Secondary electron image on fracture surface of S2 sample: Biotite altered to chlorite; (d) Magnification of Figure 8 (c); (e) cauliflower hematite on feldspar surface in S4 sample feldspar (Feld), hornblende (Hb), biotite (Biot), chlorite (Chl), quartz (Qrz), anatase (An), titanite (Tit), apatite (Ap), oxides (Ox) (cauliflower hematite).

5. Conclusions

- The metamorphic rocks consist of magnesiohornblende, feldspar (oligoclase and Na-feldspar) and epidote in a fine grained inoblastic to granoblastic texture. Low amounts of secondary smectite and nano-chlorite crystals due to weathering are also detected.

- Biotite, magnesiohornblende and plagioclase (oligoclase and andesine) are mainly detected in unaffected plutonic studied samples. Biotite and magnesiohornblende are almost absent in the altered rocks while deficient secondary chlorite nanocrystals, smectite and cauliflower hematite are present.

- The presence of secondary phyllosilicates in both studied metamorphic and igneous rocks is expected to affect positively the industrial production processes of stone wool.

- The quartz diorite rocks are proposed as an alternative raw material in the production of new, light-colored and advanced stone wool materials.

6. Acknowledgments

We would like to thank E. Kotsopoulou from the laboratory of Electron Microscopy and Microanalysis, University of Patras and V. Drakopoulos from Institute of Chemical Engineering Sciences (ICE-HT), Patras, for his assistance with the EDS microanalyses and SEM photomicrographs. Special thanks to Fibran industry for their collaboration Rock.FeNi.Al research project "914-BET-2013", supported and funded by the Development Program for Industrial Research and Technology PAVET 2013, ESPA 2007-2013, European Regional Development Fund ERDF. The authors would also like to thank anonymous Reviewer for helping improving our manuscript.

7. References

Blagojevic, B., Sirok, B. and Stemfelj, B., 2004. Simulation of the effect of melt composition on mineral wool fibre thickness, *Ceramics-Silikaty*, 48(3).

Bomberg, M. and Onysko, D., 2015. Walls of Canadian Houses: A Review of the Historic Basis for Current Practices, *Journal of Building Physics*, *EE9-1 Innovative Materials: Bio-Fiber Batts and Boards.*

Ecofys/Fraunhofer, 2012. Methodology for the free allocation of emission allowances in the EU E TS post 2012, Sector report for the mineral wool industry, By order of the European Comm is-sion, Institute for Systems and Innovation Research, Oko-Institut, 20 pp.

Antonio, J.M.P., Tadeu, A. and Godinho, L., 2003. Analytical evaluation of the acoustic insulation provided by double infinite walls, 114-129.

Karamanos, A., Papadopoulos, A. and Anastasellos D., 2004. Heat transfer phenomena in fibrous i nsulating materials Laboratory of Heat Transfer and Environmental Engineering, Departme nt of Mechanical Engineering Aristotle University Thessaloniki, 26 pp.

Leake, B.E., Woolley, A.R., Arps, C.E.S., Birch, W.D., Gilbert, M.C., Grice, J.D., Hawthorne, F.C., Kato, A., Kisch, H.J., Krivovichev, V.G., Linthout, K., Laird, J., Mandarino, J., Maresch, W.V., Nickel, E.H., Rock, N.M.S., Schumacher, J.C., Smith, D.C., Stephenson, N.C.N., Ungaretti, L., Whittaker, E.J.W. and Youzhi, G., 1997. Nomenclature of amphiboles: report of the subcommittee on amphiboles of the International Mineralogical Association Commision on new minerals and mineral names, *Min. Mag*., 61, 295-321.

Meunier, A., 2005. Clays, Springer-Verlag Berlin Heideblberg 2005.

Mountrakis, D., 2010. Geology and tectonic evolution of Greece, University Studio Press, 2010.

Velde, B., 1995. Origin and Mineralogy of Clays, Springer-Verlag Berlin Heideblberg 1995.

Yang, S. and Zhang, L., 2012. Research on Properties of Rock- Mineral Wool as ThermalInsulation Material for Construction.

Karamanos, A., Papadopoulos, A. and Anastasellos, D., 2005. Comparative Evaluation of stonewool and extruded Polystyrene, Department of Mechanical Engineering, Aristotle Uni versity Thessaloniki, 11 pp.

Keller, W.D., 1978. Classification of kaolins exemplified by their textures in scan electron micrographs, *Clays and Clay Minerals*, 26, 1-20.

Papadopoulos, A.M., 2005. State of the art in thermal insulation materials and aims for future developments, Energy and Buildings, 37, 77-86.

Δελτίο της Ελληνικής Γεωλογικής Εταιρίας, τόμος L, σελ. 1923-1932
Πρακτικά 14ου Διεθνούς Συνεδρίου, Θεσσαλονίκη, Μάιος 2016

Bulletin of the Geological Society of Greece, vol. L, p. 1923-1932
Proceedings of the 14th International Congress, Thessaloniki, May 2016

PHOSPHORUS ZONING FROM SECONDARY OLIVINE IN MANTLE XENOLITH FROM MIDDLE ATLAS MOUNTAINS (MOROCCO, AFRICA): IMPLICATIONS FOR CRYSTAL GROWTH KINETICS

Mavrogonatos K.[1,2], Flemetakis S. [1,2], Papoutsa A. [1], Klemme S.[3], Berndt J.[3], Economou G.[4], Pantazidis A.[1], Baziotis I.[1] and Asimow P.D.[5]

[1]*Department of Natural Resources Management and Agricultural Engineering, Agricultural University of Athens, Iera Odos 75, 11855 Athens, Greece, ibaziotis@aua.gr*

[2]*Faculty of Geology and Geoenvironment, National and Kapodistrian University of Athens, Panepistimiopolis, Zografou 15784 Athens, Greece*

[3]*Institut für Mineralogie, Universität Münster, Corrensstrasse. 24, 48149, Münster, Germany*

[4]*Institute of Geology and Mineral Exploration, Olympic Village Acharnae, Athens, Greece, P.C. 13677*

[5]*California Institute of Technology, Division of Geological and Planetary Sciences, Pasadena California 91125, USA*

Abstract

Mantle xenolith samples in contact with basalt flows were collected from the Tafraoute maar in Morocco. Discrete melt veins are present in one xenolith sample, crosscutting primary layering and foliation. We used both optical microscopy and electron microprobe analysis to characterize the glasses and minerals in the melt veins. The melt veins consist of glass and crystals of olivine, clinopyroxene, plagioclase, spinel and apatite. The olivine in the melt veins is quite distinct from the same mineral within the matrix due to its characteristic P-enriched rims (up to 0.3 wt.%). Correlations between Al and P, as well as experimentally determined partition coefficient for P, point towards non-equilibrium partitioning during rapid crystal growth at the end of crystallization.
Keywords: *melt vein; boundary layer enrichment; Tafraoute maar.*

Περίληψη

Συλλέχθηκαν δείγματα μανδυακών ξενολίθων σε επαφή με βασάλτες από το μάαρ Tafraoute του Μαρόκκου. Διαπιστώθηκε η ύπαρξη φλεβών τήγματος που τέμνουν την πρωτογενή στρωμάτωση και σχιστότητα. Για τον πετρογραφικό και χημικό χαρακτηρισμό των φλεβών τήγματος, εφαρμόστηκαν οι τεχνικές της οπτικής μικροσκοπίας και ηλεκτρονικής μικροανάλυσης. Οι φλέβες αποτελούνται από ύελο και κρυστάλλους ολιβίνη, κλινοπυροξένου, πλαγιοκλάστου, σπινελίου και απατίτη. Ο ολιβίνης είναι πλούσιος στην περιφέρειά του σε φώσφορο ~0,3 %κ.β. (εκπεφρασμένο ως P_2O_5). Correlations between Al and P, as well as experimentally determined partition coefficient for P, point towards non-equilibrium partitioning during rapid crystal growth at the end of crystallization. Βασιζόμενοι σε συντελεστές κατανομής φωσφόρου μεταξύ ολιβίνη και τήγματος, και τη σχέση του αργιλίου με το φώσφορο,

καταλήγουμε σε κατανομή σε συνθήκες μη ισορροπίας κατά τη διάρκεια ταχύτατης ανάπτυξης στο τέλος της κρυστάλλωσης.
Λέξεις κλειδιά: *φλέβα τήγματος; εμπλουτισμός οριακού στρώματος; Tafraoute μάαρ.*

1. Introduction

Mantle xenoliths provide critical information on the geological history of the Earth's mantle lithosphere, including - in principle - the durations and rates of chemical and thermal events. The mineral chemistry of such xenoliths, and in particular the presence of phosphorus (P)-a moderately incompatible and very slowly diffusing element - may preserve the history of mineral growth and constrain timescales of pre-eruption petrogenetic processes (e.g. Boesenberg and Hewins, 2010). P-rich zones in olivine may reflect incorporation of P in excess of equilibrium partitioning during rapid growth, in which case zoning patterns primarily record crystal growth rate variations, or they may be related to other processes such as non-equilibrium incorporation, melt composition, temperature, oxygen fugacity, or apatite saturation conditions (Toplis and Caroll, 1995; Milman-Barris *et al.*, 2008; Mallmann *et al.*, 2009; Boesenberg and Hewins, 2010; Grant and Kohn, 2013; Welsch *et al.*, 2014).

In this study we report the results of detailed micro-scale analyses of the constituent minerals and glass in and around melt veins from one xenolith sample from the Tafraoute maar (Morocco). Sample MA-1 contains spinel-bearing lherzolite and orthopyroxenite layers, crosscut by veins that are dominated by glass and secondary phases. Although, the host lava is present on the margins of the recovered hand sample specimen, it was not included in our thin section. However, the xenolith-bearing flows in the broad Tafraoute maar area include nephelinites, basanites and alkaline basalts (El Azzouzi *et al.*, 1999, 2010; El Messbahi *et al.*, 2015) and we expect our xenolith's host to be in this compositional range.

We used both optical microscopy and electron microprobe (EMP) analysis to characterize the glasses and minerals in the melt veins. This paper focuses most intently on the exotic second-generation P-rich zoned olivines found in the melt veins. We examine whether the P concentrations are anomalous given the overall budget of P in the melt veins. Finally, we propose a zonation model for the olivine to infer constraints on the growth processes and to assess the extent of disequilibrium relative to the associated glass.

2. Sampling areas - Description

2.1. Geological Setting

The Tafraoute maar is located in Morocco (Figs. 1, 2), situated at the NW termination of the NE-SW North Middle Atlas Fault, which separates the "folded" Middle Atlas to the southeast from the "tabular" Middle Atlas to the northwest. The tectonic framework of the area is associated with a NE-SW oriented strip of thin lithosphere that is expressed at the surface by a series of intraplate alkaline volcanic centers (Lenaz *et al.*, 2014 and references therein). The Middle Atlas basaltic province comprises the largest and youngest volcanic fields (strombolian cones and maars) in Morocco with an age range spanning from Miocene to Quaternary (0.6-0.5 Ma). The Tafraoute maar may be a distal and attenuated expression of the mantle upwelling centered on the Bou Ibalghatene maar, about 45 km to the southwest, and bordered by the Middle Atlas Fault on the southeast. The Tafraoute maar is thought to record various stages of deformation associated with decompression and lithospheric thinning (El Messbahi *et al.*, 2015).

2.2. Mantle xenoliths

Several of the middle Atlas maar outcrops contain ultramafic xenoliths with a variety of lithologies, including a full spectrum of fertility from harzburgites through spinel lherzolites and wehrlites to pyroxenites. We collected several mantle xenoliths during the post-conference field trip to the

Middle Atlas after the 6th Orogenic Lherzolite Conference in Marrakech, 2014. The criteria for the selection of the studied xenolith were freshness and integrity of specimen and the presence of an obvious melt vein crosscutting the layering of the xenolith.

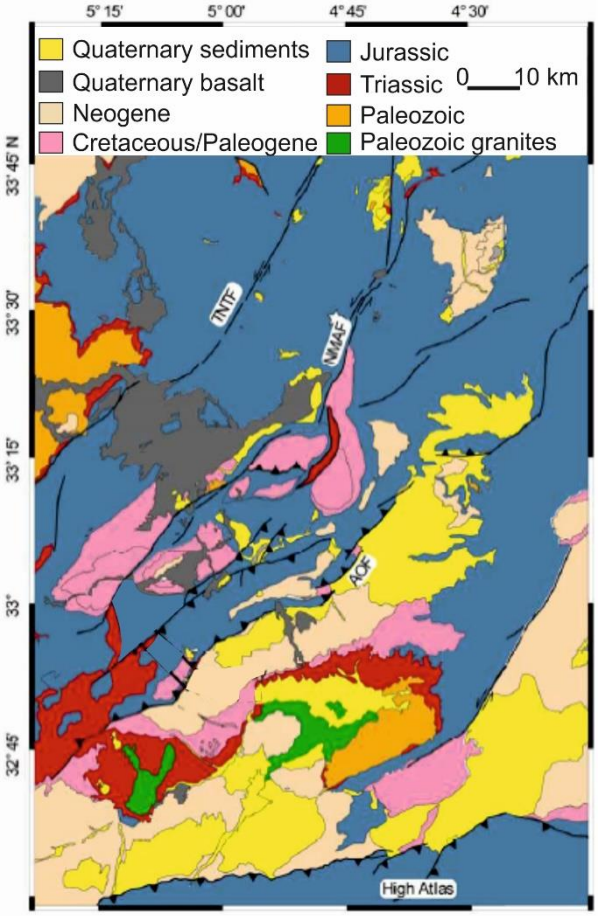

Figure 1 - Geologic map of the Middle Atlas Mountains. Labeled structures include AOF - Ait Oufella Fault, TNTF - Tizi-n-Tretten Fault, and NMAF - North Middle Atlas Fault. Study area is outlined by a black box. Figure adapted from Gomez *et al.* (1998).

3. Analytical Methods

3.1. Major elements

Major element compositions of minerals were determined in polished thin section using a JEOL JXA8530F EMP equipped with five wavelength-dispersive spectrometers (WDS) and one energy-dispersive spectrometer (EDS) at the Institut für Mineralogie, University of Münster, Germany. All analyses used 15 kV accelerating potential. For minerals, a 20 nA beam current and 20 s counting time on peak position were used. For glass analyses, a slightly defocused beam with 5 µm diameter and 10 s counting time were used, in order to avoid volatilization of lighter elements such as Na. Natural minerals were used as standards: albite (Na, Si, Al), wollastonite (Ca), olivine (Mg), almandine (Fe), spessartine (Mn), orthoclase (K), apatite (P), rutile (Ti), chromite (Cr) and Ni-oxide (Ni). Representative olivine and glass compositions are given in Table 1.

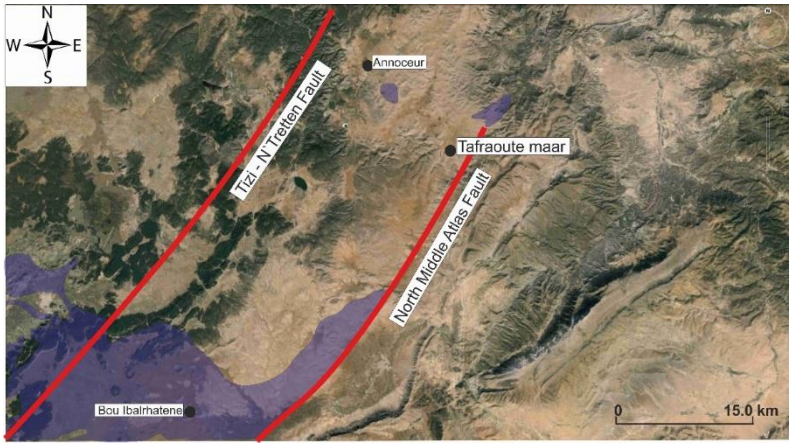

Figure 2 - Sketch map (from *Google Earth*) showing the location of Tafraoute maar (33˚31´10.20´´N-4˚41´37.60´´W). Purple fields indicate lava flows. Red lines are major faults.

Table 1 - Representative olivine and glass compositions (in wt.%) from the studied mantle xenolith.

Olivine	**Ol1-8***	**Ol1-9***	**Ol2-9***	**Ol1-13***	**Ol-2****	**Ol-3****	**Glass**	**12**	**14**	**16**	**20**	**25**
SiO_2	37.9	37.1	39.2	38.9	40.6	40.5	SiO_2	45.6	49.6	46.2	46.4	45.2
TiO_2	0.06	0.12	0.05	0.06	-	0.01	TiO_2	2.65	2.84	3.14	3.5	3.3
Al_2O_3	0.04	0.15	0.02	0.19	-	0.01	Al_2O_3	16.8	19.3	16.9	17.8	17.1
Cr_2O_3	0.04	0.01	0.02	0.01	0.01	-	Cr_2O_3	0.00	0.05	0.00	0.00	0.00
FeO	17.9	21.9	16.3	16.0	10.5	10.1	FeO	9.87	8.2	10.2	8.24	8.45
MnO	0.33	0.42	0.25	0.30	0.19	0.18	MnO	0.18	0.12	0.22	0.12	0.11
MgO	42.7	38.3	43.3	43.8	48.9	49.4	MgO	2.73	1.61	2.72	1.89	2.32
NiO	0.11	0.12	0.18	0.35	0.37	0.32	NiO	0.03	0.04	0.00	0.00	0.00
CaO	0.43	0.45	0.23	0.31	0.02	0.03	CaO	7.88	6.76	7.50	8.81	9.39
P_2O_5	0.15	0.21	0.04	0.30	-	-	Na_2O	5.78	1.28	5.06	6.14	5.48
Total	99.6	98.7	99.5	100.1	100.6	100.5	K_2O	2.32	2.26	2.06	2.23	2.37
*: Secondary; **: matrix							P_2O_5	1.52	1.10	1.45	1.15	1.33
							Total	95.4	93.1	95.4	96.3	95.0

4. Petrographic and Analytical Results

4.1. Matrix petrography

The studied mantle xenolith was recovered from the contact with the host lava, which is presumed to be alkalic like other analysed xenolith-bearing lavas in the region. The xenolith contains spinel-bearing lherzolite and orthopyroxenite layers displaying a coarse to porphyroclastic texture (Harte, 1975). The lherzolite is amphibole-free, and dominated by euhedral to subhedral olivine crystals and subhedral orthopyroxene and clinopyroxene. The orthopyroxenite layer is composed of large, euhedral to subhedral orthopyroxenes. Some finer-grained areas are composed of small olivine and interstitial spinel crystals.

4.2. Melt vein and veinlets petrography

Discrete dark-coloured melt veins about ~100 μm wide on average penetrate the lherzolite and orthopyroxenite layers; some of these veins clearly crosscut the foliation and lithologic layering,

whereas others are parallel to layering (Fig. 3). Lacking analysis of the host lava, we cannot say at this time whether there is a cogenetic relationship between host lava and melt veins in the xenolith.

Figure 3 - Hand-specimen image of sample MA-1 xenolith from Tafraoute maar. A melt vein with phosphorus-rich olivines is indicated by the white rectangle.

The studied melt veins are generally composed of olivine (Fig. 4a) + clinopyroxene + plagioclase + spinel + glass ± apatite. Plagioclase occurs as prismatic, flow-oriented crystals parallel or sub-parallel to the layering (Fig. 4b). Although some olivine grains are free of inclusions, others may contain rounded glass (quenched melt) inclusions (Fig. 4c) or subhedral inclusions of spinel or ilmenite. The olivines are generally found in contact with plagioclase and glass. The abundance of glass in several studied veins varies from ~5 to 15 vol.%; the largest volume fractions are observed only in the large cross-cutting melt vein highlighted in Fig. 3. Where vein glass is in contact with matrix olivine, mineral-melt reaction is indicated by Fe-rich outer rims on the olivine. Spinel shows both anhedral and euhedral shapes and occurs both as inclusions in olivine and as discrete grains associated with plagioclase and glass. Where spinel is in contact with glass, it presents a spongy outer rim and a normal zonation with progressively more Fe-rich compositions towards the rim. Clinopyroxene is present both as isolated subhedral to euhedral crystals within the melt layer and as replacive rims where matrix orthopyroxene and olivine have reacted with the melt. Very fine-grained clinopyroxene crystals indicative of quench (up to 10 μm in width and dendritic shape) are also present (Fig. 4d). Apatite is found mostly as very small crystals embedded in glass.

4.5. Analytical results

The melt veins contain olivines ($Fo_{72.1\text{-}83.4}$) with 0.02-0.3 wt.% P_2O_5; the P-rich olivines (P_2O_5>0.1 wt.%) are $Fo_{75.3}$ to $Fo_{82.8}$. The glass has variable composition with P_2O_5 up to 1.52 wt.%, K_2O 1.65-2.37 wt.%, CaO 6.39-9.55 wt.%, Na_2O 0.78-6.70 wt.% and SiO_2 45.2-49.6 wt.% (Table 1). In MgO variation diagrams, the glass compositions appear to display a coherent single trend group for all oxides, with the exception of a discrete low-Na group containing four to six analyses (Fig. 5).

In olivine, P is correlated negatively with Si^{4+}, poorly with the divalent cations (Mg+Fe+Ca) and positively with Al^{3+} (Fig. 6; R is >0.7 showing that the correlation is statistically significant). These correlations suggest that the predominant substitution is: $2^{IV}Si^{4+} = {}^{IV}P^{5+} + {}^{IV}R^{3}$, where IV refers to tetrahedral sites and R^{3+} to trivalent cations like Al^{3+}, Cr^{3+} and Fe^{3+}. Furthermore, P is concentrated mainly at the rim of the olivine, in contact with the surrounding glass. In particular, individual rim-rim profiles show maximum P_2O_5 content up to 0.25 wt.% at the rims of the crystals (Fig. 6).

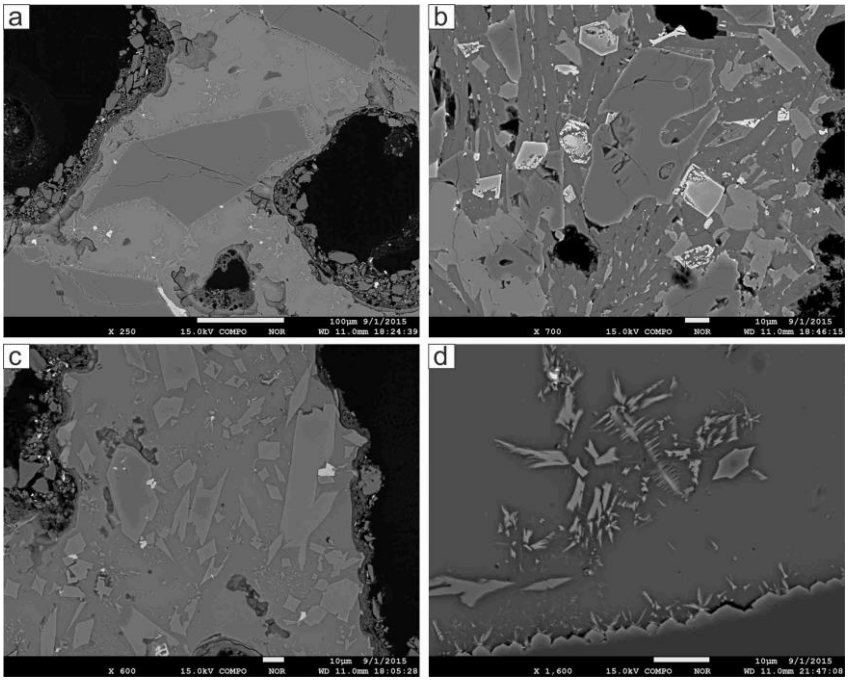

Figure 4 - a) Large P-poor subhedral olivine embedded in melt vein. b) Melt vein with plagioclase as flow-oriented crystals and euhedral zoned spinel. A large subhedral olivine hosts a melt inclusion. c) Small euhedral to subhedral olivine and clinopyroxene crystals in melt vein. At left, an euhedral P-rich olivine with Fe-rich rim, d) Small clinopyroxene quenched crystals in melt vein.

5. Discussion

In the literature, $D_P^{ol/melt}$ has been reported in the range 0.02 to 1.6, with the lowest numbers thought to represent equilibrium conditions and higher values usually attributed to non-equilibrium partitioning via processes such as solute trapping during rapid growth (Reitano *et al.*, 1994; Grant and Kohn 2013). According to Jambon *et al.* (1992), P-Al-rich areas of olivine may grow in minutes, whereas P-Al-poor zones represent a few weeks. Furthermore, high-resolution X-ray mapping of P in olivine reveals narrow P-rich bands parallel to rim of the crystals (Fig. 7). The imperfect correlation between P and Al in our data implies either diffusive relaxation of Al gradients or, judging by dynamic experiments (Grant and Kohn, 2013), cooling rates ~1-10°C/h that generate disequilibrium solute trapping of P but near-equilibrium incorporation of Al. Early-crystallized olivine grew slowly enough to incorporate only quantities of P consistent with equilibrium partitioning, suggesting that no P-rich boundary layer developed despite the slow diffusion of P in melts. Afterwards, during crystallization of olivine rim, the process was rapid enough to over-enrich P; the increase in P at the rim is too large in amplitude and too abrupt to be consistent with simple concentration of P in a decreasing mass of residual melt (Watson *et al.*, 2015; Baziotis *et al.*, 2016). The apparent partition coefficient between olivine rims and adjacent melt suggests $D_P^{ol/melt}$ in the range 0.13-0.19.

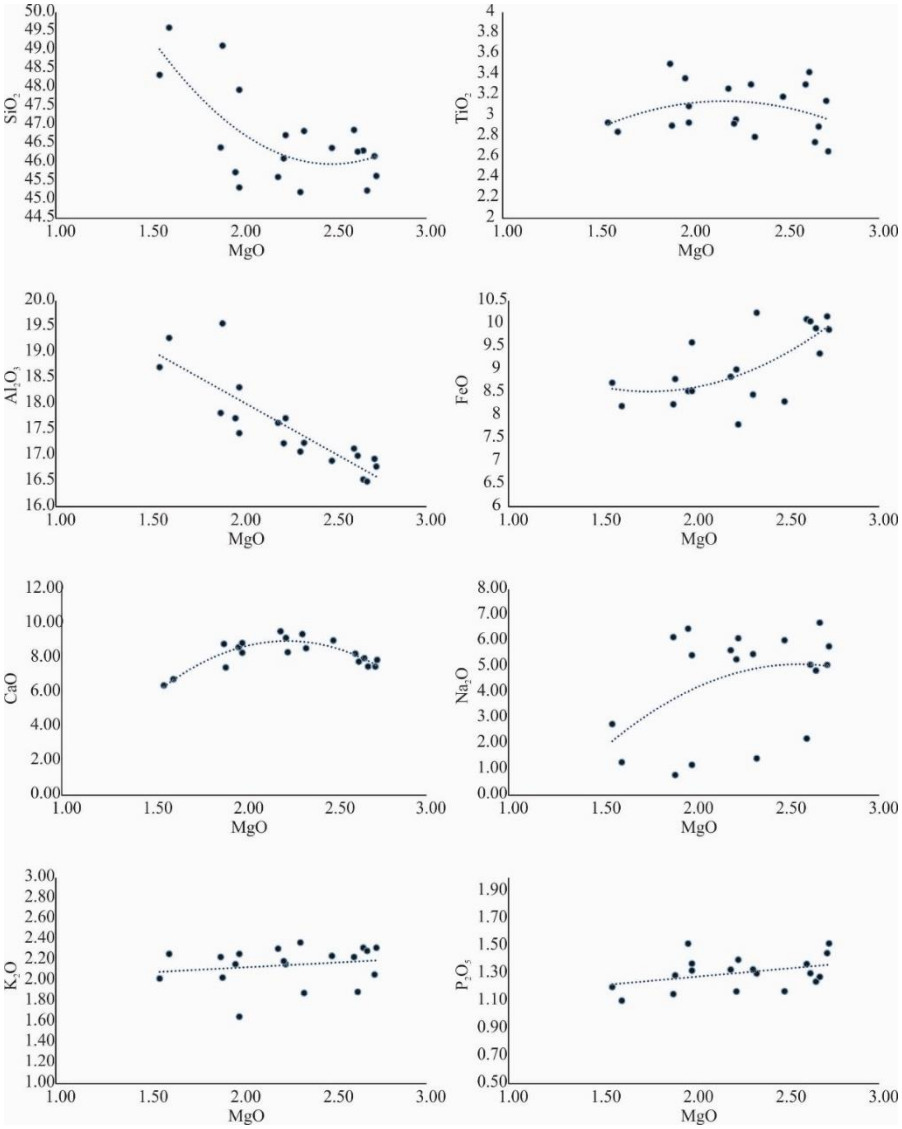

Figure 5 - Glass compositions correlating MgO with major oxides (all in wt.%). The dotted lines or curves are linear or quadratic trendlines based on least squares method.

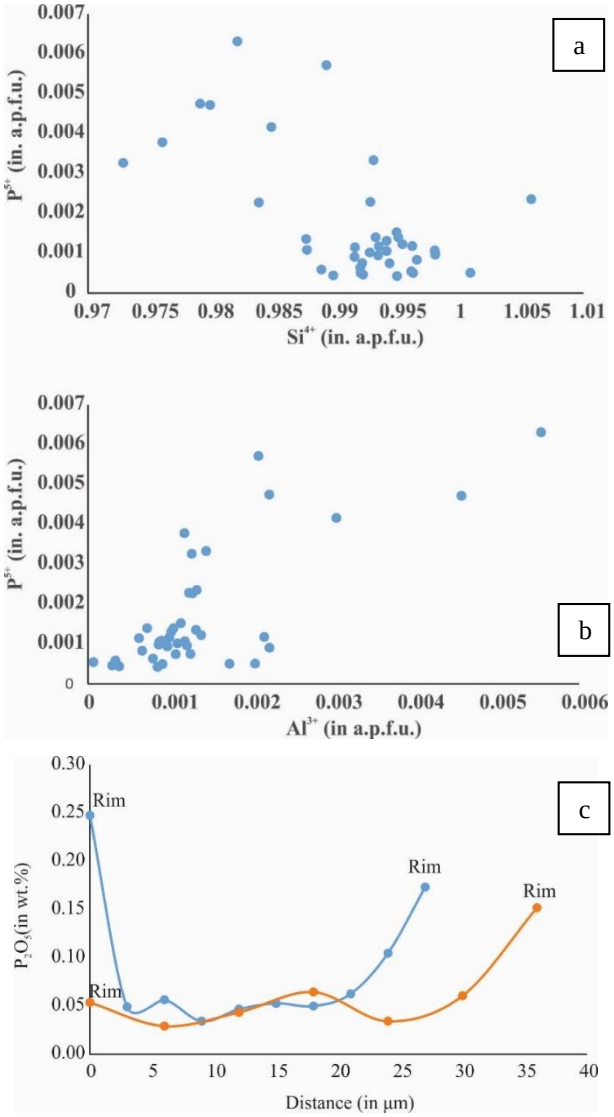

Figure 6 - Correlation of olivine P with (a) Si^{4+} and (b) Al^{3+}. (c) Two compositional rim-rim profiles across a particular olivine grain, as indicated in figure 7 (A-B profile in blue; C-D profile in orange).

6. Conclusions

A mantle xenolith sample was collected in contact with an alkali basalt flow from the Tafraoute maar in Morocco. Melt veins appear to locally crosscut the layering and the foliation of this rock. Within these veins, zoned olivine appears to be P-enriched towards the rims. Correlations between the chemistry of olivine and experimentally determined partition coefficients for P suggest that crystallization of P-poor olivine cores was rather slow, as to incorporate only minor amounts of this component. Enrichment in P, on the other hand, was facilitated by non-equilibrium partitioning during rapid crystal growth. The latter is further suggested by the imperfect correlation between P and Al in olivine.

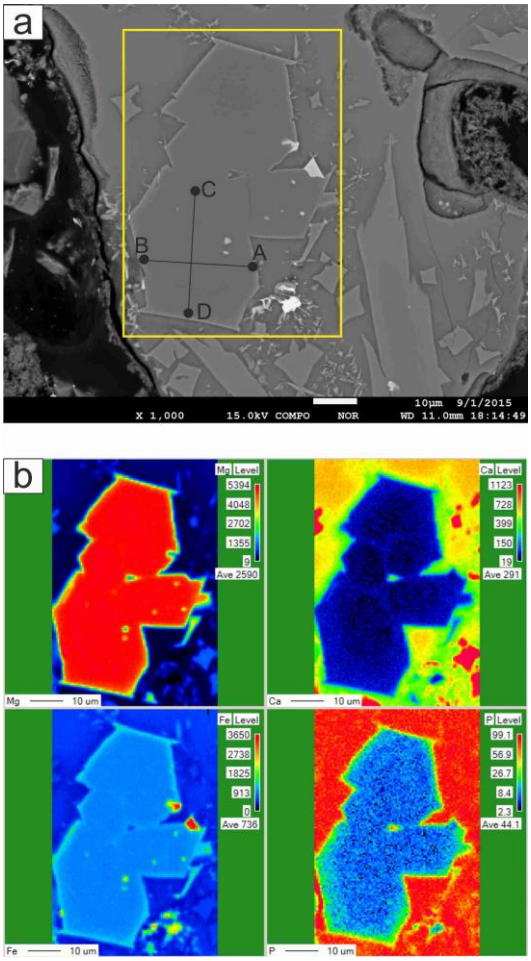

Figure 7 - a) Cluster of P-rich olivine grains embedded in melt vein. b) X-ray maps for Mg, Ca, Fe, and P of the olivine indicated in (a). The Ca map delineates grains within the cluster.

7. Acknowledgments

I.B. was supported by research funding implemented within the framework of the «IKYDA» programme 242, based on a bilateral agreement between the State Scholarships Foundation (IKY) and Deutscher Akademischer Austausch Dienst. Additional funds to I.B. implemented within the framework of the Action «Supporting Postdoctoral Researchers» of the Operational Program "Education and Lifelong Learning" (Action's Beneficiary: General Secretariat for Research and Technology), and is co-financed by the European Social Fund (ESF) and the Greek State. PDA is supported by the US NSF through award GI-1226270. We would like to thank an anonymous reviewer for his constructive comments and Prof Alexandros Chatzipetros for his editorial handling.

8. References

Baziotis, I., Asimow, P.D., Ntaflos, T., Boyce, J.W., McCubbin, F.M., Koroneos, A., Perugini, D., Flude, S., Storey, M., Liu, Y.S., Klemme, S., Berndt, J. and Stolper, E.M., 2016. Phosphorus zoning as a recorder of crystal growth kinetics: application to secondary olivine and pyroxene in mantle xenoliths from Cima Volcanic Field, *Journal of Petrology*, Under Review.

Boesenberg, J.S. and Hewins, R.H., 2010. An experimental investigation into the metastable formation of phosphoran olivine and pyroxene, *Geochimica et Cosmochimica Acta*, 74, 1923-1941.

El Azzouzi, M., Bernard-Griffiths, J., Bellon, H., Maury, R.C., Piqué, A., Fourcade, S., Cotten, J. and Hernandez, J., 1999. Evolution des sources du volcanisme marocain au cours du Néogène, *C. R. Acad. Sci. Paris*, 329, 95-102.

El Azzouzi, M., Maury, R.C., Bellon, H., Youbi, N., Cotten, J. and Kharbouch, F., 2010. Petrology and K-Ar chronology of the Neogene-Quaternary Middle Atlas basaltic province, Morocco, *Bull. Soc. Géol. Fr.*, 181, 243-257.

El Messbahi, H., Bodinier, J.L., Vauchez, A., Dautria, J.M., Ouali, H. and Garrido, C.J., 2015. Short wavelength lateral variability of lithospheric mantle beneath the Middle Atlas (Morocco) as recorded by mantle xenoliths, *Tectonophysics*, 650, 34-52.

Gomez, F., Allmendinger, R., Barazangi, M., Er-Raji, A. and Dahmani, M., 1998. Crustal shortening and vertical strain partitioning in the Middle Atlas Mountains of Morocco, *Tectonics*, 17, 520-533.

Grant, T.B. and Kohn, S.C., 2013. Phosphorus partitioning between olivine and melt: An experimental study in the system Mg_2SiO_4-$Ca_2Al_2Si_2O_9$-$NaAlSi_3O_8$-$Mg_3(PO_4)_2$, *American Mineralogist*, 98, 1860-1869.

Harte, B., 1977. Rock nomenclature with particular relation to deformation and recrystallization textures in olivine-bearing xenoliths, *The Journal of Geology*, 85, 279-288.

Jambon, A., Lussiez, P., Clocchiatti, R., Weisz, J. and Hernandez, J., 1992. Olivine growth rates in a tholeiitic basalt: An experimental study of melt inclusions in plagioclase, *Chemical Geology*, 96(3), 277-287.

Lenaz, D., Youbi, N., De Min, A., Boumehdi, M.A. and Abbou, M.B., 2014. Low intra-crystalline closure temperatures of Cr-bearing spinels from the mantle xenoliths of the Middle Atlas Neogene-Quaternary Volcanic Field (Morocco): Mineralogical evidence of a cooler mantle beneath the West African Craton, *American Mineralogist*, 99(2-3), 267-275.

Mallmann, G., O'Neill, H.C.St. and Klemme, S., 2009. Heterogeneous distribution of phosphorus in olivine from otherwise well-equilibrated spinel peridotite xenoliths and its implications for the mantle geochemistry of lithium, *Contributions to Mineralogy and Petrology*, 158, 485-504.

Milman-Barris, M.S., Beckett, J.R., Baker, M.B., Hofmann, A.E., Morgan, Z., Crowley, M.R., Vielzeuf, D. and Stolper, E., 2008. Zoning of phosphorus in igneous olivines, *Contributions to Mineralogy and Petrology*, 155, 739-765.

Reitano, R., Smith, P.M. and Aziz, M.J., 1994. Solute trapping of group III, IV, and V elements in silicon by an aperiodic stepwise growth mechanism, *Journal of Applied Physics*, 76(3), 1518-1529.

Toplis, M.J. and Carroll, M.R., 1995. An experimental study of the influence of oxygen fugacity on Fe-Ti oxide stability, phase relations, and mineral-melt equilibria in ferro-basaltic systems, *Journal of Petrology*, 36, 1137-1170.

Watson, E.B., Cherniak, D.J. and Holycross, M.E., 2015. Diffusion of phosphorus in olivine and molten basalt, *American Mineralogist*, 100, 2053-2065.

Welsch, B., Hammer, J. and Hellebrand, E., 2014. Phosphorus zoning reveals dendritic architecture of olivine, *Geology*, 42, 867-870.

Δελτίο της Ελληνικής Γεωλογικής Εταιρίας, τόμος L, σελ. 1933-1942
Πρακτικά 14ου Διεθνούς Συνεδρίου, Θεσσαλονίκη, Μάιος 2016

Bulletin of the Geological Society of Greece, vol. L, p. 1933-1942
Proceedings of the 14th International Congress, Thessaloniki, May 2016

ASSESSMENT ON HYDROTHERMAL PARTICLE CHEMISTRY FROM A SHALLOW VENTING SYSTEM OFFSHORE KOS, AEGEAN SEA

Megalovasilis P.

University of Patras, Department of Geology, 26504, Patras, Greece, pmegal@upatras.gr

Abstract

Shallow submarine hydrothermal vents along Hellenic Volcanic Arc transfer significant quantities of particles enriched in basic metals. Fluids collected by scuba diving from two shallow hydrothermal venting areas on Kos Island in the Aegean Sea in East Mediterranean. Samples were filtrated and membrane filters leached with a mixture of acids. Chemical analysis performed in suspended particles for Fe, Mn, Cu, Pb, Cd, Ca, Ba, Sr, Li, Al and Si. The suspended particulate matter (SPM) flux varied from 0.93 to 8.64 mg/l and between 0.21 and 20.94 mg/l in two sites. Metal/Al ratios also vary significantly within a short distance. The pH of hydrothermal waters was from 5.50 to 5.95 in Kephalos Bay and from 6.09 to 6.53 in Bros Thermi suggesting gases CO_2 and H_2S may control pH values. Particles were dominated by Fe, Ca, Si and Al and strongly enriched in Mn, Cu, Pb and Ba. Three geochemical groups were identified being associated with distinct hydrothermal processes concerning sulphide minerals, carbonate substrate and deeper Al-Silicate rock basement.

Keywords: *particulate matter, basic metals, vents, Hellenic Volcanic Arc.*

Περίληψη

Οι υδροθερμικές πηγές ρηχών περιοχών του Ελληνικού Ηφαιστειακού Τόξου μεταφέρουν σημαντικές ποσότητες σωματιδίων εμπλουτισμένων με βασικά μέταλλα. Υδροθερμικά ρευστά συλλέχθηκαν από δύο ρηχές υδροθερμικές περιοχές Κόλπος Κέφαλος και Μπρος Θέρμη στην Κω στην Ανατολική Μεσόγειο. Τα δείγματα νερού διηθήθηκαν με φίλτρα μεμβράνης και το υλικό που κατακρατήθηκε αφού διαλύθηκε από μίγμα οξέων αναλύθηκε για Fe, Mn, Cu, Pb, Cd, Ca, Ba, Sr, Li, Al και Si. Η εκροή αιωρούμενου υλικού (SPM) ροή κυμάνθηκε από 0,93 έως 8,64 mg/l και μεταξύ 0,21 και 20,94 mg/l στις δύο περιοχές μελέτης, ενώ οι λόγοι Metal/Al διέφεραν με την απόσταση. Το pH των υδροθερμικών νερών ήταν από 5,50 έως 5,95 στον Κόλπο Κέφαλο και 6,09 έως 6,53 στην Μπρος Θέρμη πιθανολογώντας ότι η συγκέντρωση αερίων όπως CO_2 και H_2S ελέγχει τις τιμές του. Το αιωρούμενο υλικό αποτελείται κυρίως από Fe, Ca, Si και Al είναι όμως και εμπλουτισμένο σε Mn, Cu, Pb και Ba. Τρεις γεωχημικές ομάδες εντοπίστηκαν που φαίνεται να συνδέονται με διαφορετικές υδροθερμικές διεργασίες των θειούχων, ανθρακικών και αργιλλοπυριτικών φάσεων του γεωλογικού υποβάθρου.

Λέξεις κλειδιά: *αιωρούμενο υλικό, μέταλλα, πηγές, Ελληνικό Ηφαιστειακό τόξο.*

1. Introduction

The seafloor hydrothermal vent systems influence marine chemistry in every timescale and in large extent (Von Damm, 1990; Parson *et al.*, 1995; Von Damm, 2001). The spatial evolution of magmatic-hydrothermal systems very often presents great extent of several kilometres into the crust and the formation of hydrothermal plumes on sea column (Humphris *et al.*, 1995; Lupton, 1995; Edmonds and German, 2004). The hydrothermal fluid phase such as gases, water, solutes and particulate matter. Particulate matter indeed is an important constituent of hydrothermal fluids and actually it represents sedimentary material in early stage of formation (Whittield and Turner, 1987). The compositional variability of suspended particulate matter (SPM) depends upon a number of factors such and the nature of chemical reactions taking place in the substrate the prevailing physico-chemical and oceanographic conditions, the amount of dissolved oxygen, other gas content and the rate of mixing of hydrothermal fluids with seawater (Von Damm *et al.*, 1985). Particulate Fe and Mn was found in unusually high concentrations in South Aegean Sea, comparing to other straits of Mediterranean and their origin was attributed to hydrothermal sources (Balopoulos *et al.*, 1999). Furthermore, particulate matter distribution in Aegean Sea seawater is influenced mainly by three factors such as the proximity to the initial sources, the water circulation patterns prevailing and the topography of sea-bottom, while resuspension phenomena affect sediment depositional geochemistry of surface sediments (Karageorgis and Anagnostou, 2001). Moreover, the shallow submarine hydrothermal venting related to the Hellenic Volcanic Arc and its influence on seabed and seawater chemistry has been well investigated (Dando *et al.*, 2000; Price *et al.*, 2013; Yücel *et al.*, 2013), while controls local marine sediment geochemistry have been also attributed (Megalovasilis, 2014, Megalovasilis and Godelitsas, 2015). There are few studies on particle emission in submarine hydrothermal areas in Aegean (Varnavas *et al.*, 1998; Varnavas *et al.*, 2000; Megalovasilis, 2007; Megalovasilis, 2015a; Megalovasilis, 2015b). In this work, statistical data are presented and an assessment on elemental interrelationships between hydrothermal particulates is attempted. Such a research is important because it provides further information on the geochemical influence of hydrothermal fluids along the Hellenic island volcanic arc.

2. Materials and Methods

Sampling was carried out in Kephalos Bay and Bros Thermi. Interactions between hydrothermal fluids and oxygenated seawater result in various precipitates settling to the sea bottom around the venting seeps influence strongly local sediment geochemistry (Megalovasilis and Godelitsas, 2015). Fe oxides and hydroxides are observed both in Kephalos Bay and Bros Thermi. A variety from brown-red Fe oxides to yellowish Sulphur and metal-sulphides phases together with white silica - bacterial mat are observed around the seeps but in lesser extent than those recognised in Milos (Dando *et al.*, 1998; Godelitsas *et al.*, 2015). Samples obtained by scuba diving using fluid samplers consisted of two double plastic bags connected by a Y-shaped selectable plastic connector to a plastic funnel, applied on the top of the venting outlet. All parts were laboratory ultra pure acid cleaned. The first bag was used for collecting primary wastes (sand and seawater) while second bag collection was timed. The volume of gas+water and only water was measured with the Archimedes method of water displacement (Dando *et al.*, 1995). Water samples were transferred in glass bottles. The H_2S was detected in all samples by its characteristic smell. The hydrothermal waters were filtered in the field setup laboratory using a vacuum pump system and with the aid of Millipore Sterifil Aseptic System Holder and Millipore 0.45μm pre-weighted membrane filters while both the ending tube and the top funnel were sealed with plastic covers (Loring and Rantala, 1992). After filtration the sample-filters were then dried in an evacuated desiccator over silica gel and stored in acid-cleaned individual Petri slides. After weighing, the suspended particulate matter on the membrane filters was subjected to chemical leaching (Landing and Lewis, 1991), with the addition of 20 ml of extra high purity 2M HCl-1M HNO_3 mixture, samples left for 4 hours at room temperature. Flasks were put afterwards on a hot plate at 65^{o}C near dryness and after they were cool, 5ml of mixture 0.5M HCl-0.1M HNO_3 were added. All reagents and stock standards for AAS were of extra high purity commercially obtained (Merck), while 3-distilled water

used for preparation of all reagents and working standards, and for rinsing all glassware which previously had been immersed for 2 days in 10%wt HNO_3. Aliquots of the samples were analysed for Fe, Mn, Cu, Pb, Cd, Ca, Ba, Sr, Li, Al and Si, applying Atomic Absorption Spectrometry with Graphite furnace technique (GFFAS) using Perkin Elmer 2100 AAS and 701HGA Graphite Furnace. The operational parameters applied were of these from manufacturer and modified depending on the element (Loring and Rantala, 1992). Accuracy checked with the sensitivity check standards found better than ±5% while analytical precision was checked with replicate analyses and found varied from ±5 to ±10%.

2.1. Geological setting

The Hellenic volcanic arc (HVA) in east Mediterranean region, is part of the pre-Alpine to Quaternary continental crust of the Hellenic subduction zone (Pichon and Angelier, 1979) and is a rather young (5 Ma) volcanic arc in the pre-Alpine to Quaternary continental crust of the Hellenic subduction zone (R oyden and Papanikolaou, 2011). It is the result of northward subduction of the last remnant of the oceanic crust of the African plate beneath the southern edge of the active margin of the European plate (Pichon and Angelier, 1979). The volcanoes of the HVA occur onshore the peninsula of Methana, and offshore the islands of Poros in the west, Milos and Santorini in the centre, and on Nisyros and Kos in the east (Fig. 1). Many submarine volcanoes have been discovered recently including Paphsanias near Methana, the volcanic domes to the east of Antimilos near Milos, and the Christiana domes and Kolumbo near Santorini (Nomikou *et al.*, 2013). A great explosion occurred before 161 ka between Nisyros and Kephalos Bay producing >60 km^3 of volcanic material which covered half of the island of Kos. Mainly the western part covered with a layer of ash and pumice of about 30 meters in thickness. This formation is unconformably overlying or concordant with older stratified sediment in west Kos basin of thickness more than 100 m. Kos Plateau Tuff (KPT) eruption was the largest eruption in the Pliocene-Quaternary in Hellenic volcanic arc (Pe-Piper *et al.*, 2005). Kos is controlled by WNW-ESE and NE-SW faults systems, which are related to extensional processes and volcanic activity during the Pleistocene and Pliocene (Papanikolaou and Lekkas, 1990; Lagios *et al.*, 1998). The Kos-Nisyros volcanic center is a Plio-Pleistocene magmatic system which characterized by magmas with variable composition of basaltic andesite to high-SiO_2 rhyolite, formed during last 3-4 Ma (Bachmann *et al.*, 2012). Geothermal manifestations on the island are found in various locations such as the hot spring of cape Agios Fokas (Ruffa *et al.*, 1999) in the NE part called Empros Thermes (Bros Thermi in modern Greek), where there is active flow of warm water into the beach of Thermes with temperature of 47 ^oC (Varnavas *et al.*, 1998) and the hot spring of Agia Irini (Piso Thermes), which is easily accessible by boat, with fluid temperature of 45 ^oC. Also, there are other hot spring at Kokkinonero found southwest of the Asclepeion archaeological site where water is ferruginous (red in colour) and rich in carbon oxides (CO, CO_2) with a temperature of 22.5^oC (Hatzivasileiou, 2013). Finally there is the Volcano hot spring containing muddy mineral water and the hot spring of Kokkinonero nearby (Ruffa *et al.*, 1999). A famous submarine hydrothermal site is the Paradise Beach on Kephalos Bay and together with Bros Thermi they gain a lot of attraction from tourists. Previous research on hydrothermal gas chemistry showed that springs onshore and offshore contain CO_2 (93-99%), H_2S (<0.005%), H_2(<0.001%), CH_4 (0.008-0.362%), N_2 (1.10-4.82%), O_2 and Ar (0.030-0.912%) (Minissale *et al.*, 1997).

The Kos-Nisyros volcanic activity presents great variation with time the last 3 Ma (Bachmann *et al.*, 2012). Although recent and present times are not characterized by any volcanic activity, active onshore fumaroles and shallow submarine hydrothermal fields are found around Nisyros and Yali islands and along the southern coast of Kos (Varnavas and Cronan, 1991), particularly near shore in Kephalos Bay (Paradise bubble beach) in south-west and Bros Thermi in northeast (Megalovasilis and Godelitsas, 2015). At Bros Thermi, seawater moving downwards being modified by water-rock interactions and circulates with Mg and K losses, reaching 110^oC close to sea bottom while meteoric water contribution has been found in other geothermal sites in Kos (Ruffa *et al.*, 1999). Details on physiographic characteristics of submarine study areas (i.e bathymetry etc.), can be found in previous research (Megalovasilis and Godelitsas, 2015).

3. Results

3.1. Kephalos Bay

The geochemical data obtained show a significant variability in all parameters (Table 1). The water flux varied from 60 to 122 l/h and the gas flux values varied from 2 to 126 l/h while the gas/water ratio found between 0.03 and 1.30. The hydrothermal suspended particulate matter (SPM) varied from 0.93 - 8.64 mg/l with an average of 4.32 mg/l. The pH in vent waters found between 5.50-5.95 and conductivity was 56.7-57.5 mS/cm. Fe concentrations in SPM were from 8.7-87.2 μg/l, Mn 0.14-2.33 μg/l, Cu 0.01-0.34 μg/l, Pb 0.05-0.52 μg/l, and Cd found only in few samples being 0.001-0.015 μg/l. Ca varied from 16.9 to 215 μg/l, Ba from 0.16 to 1.46 μg/l and Sr 0.12-2.07 μg/l. Li varied from 0.01-0.28 μg/l, Al 4.83-90.25 μg/l and Si 1.23-112.5 μg/l. SPM concentrations are well correlated (correlation coefficient $0.70<r<0.98$) with all elements except Cu, Cd and Si. Based on average values of hydrothermal water flux obtained and on the number of vents studied an estimation of annual fluxes can be deduced (i.e. water average discharge/h x hours of year x number of vents). Consequently annual flux of SPM also can be calculated based on annual water discharge. The annual hydrothermal water flux is estimated 819 m^3/y, the annual gas flux 636m^3/y and annual production of SPM to 24,749 g/y. Actual fluxes should be at least 2 orders of magnitude much more because the total number of observed hot spots is much higher than those studied. Many seeps are not even visible continuously, because gas effluence which gives the visual character of outflow is intermittent.

3.2. Bros Thermi

Significant variability is also observed in this submarine hydrothermal field. The water flux varied from 16.5 to 96 l/h and the gas flux values varied from 4.5 to 60 l/h while the gas/water ratio was between 0.18 and 1.14. The SPM flux varied from 0.21 - 20.94 mg/l with an average of 6.06 mg/l.

The pH in vent waters found between 6.09-6.53. Fe concentrations in SPM were from 6.5-229 μg/l, Mn 0.05-2.17 μg/l, Cu 0.10-1.01 μg/l, Pb 0.08-1.34 μg/l, and Cd recorded in most samples being 0.001-0.038 μg/l. Ca found between 14.6 and 182 μg/l, Ba from 0.09 to 0.91μg/l and Sr 0.13-1.19 μg/l. Finally Li varied from 0.01-0.85 μg/l, Al 1.53-192 μg/l and Si 0.56-105 μg/l. SPM concentrations are very well positively correlated ($0.70<r<0.99$) with all elements studied and moderate positively with Cd ($r=0.54$). Analytical results are presented in Table 1. On the basis of average values and the number of submarine hydrothermal vents studied, annual values can be estimated. Thus, the total hydrothermal water flux is estimated 418 m^3/y, gas flux 216 m^3/y and for SPM 40,540 g/y. For similar reasons as in Kephalos Bay the actual outflow should be two orders of magnitude higher.

3.3. Element to Al ratios

To examine the origin of particulate metals from another view element/Al ratios of their concentrations in SPM were estimated (Table 2). Remarkably, differences on time and space compositional variability of SPM were observed. In Bros Thermi Vent B1 showing higher values for Fe/Al, Cu/Al, Pb/Al, Cd/Al and Ca/Al where Kephalos Bay vents are presenting elevated Mn/Al, Ba/Al and Si/Al ratios considering all analytical data obtained.

The present data strongly suggest that elements are concentrated in different phases in which they are held. The inter-element correlations of particulate elements imply not only a hydrothermal origin, for some particulates (e.g. Ba, Si) but also a biological affiliation of biogenic debris, or calcareous and siliceous tests. A further mineralogical investigation should be performed in order to clarify the above hypothesis. Notably the metal/Al varies significantly from vent to vent within a short distance, both in Kephalos Bay and in Bros Thermi.

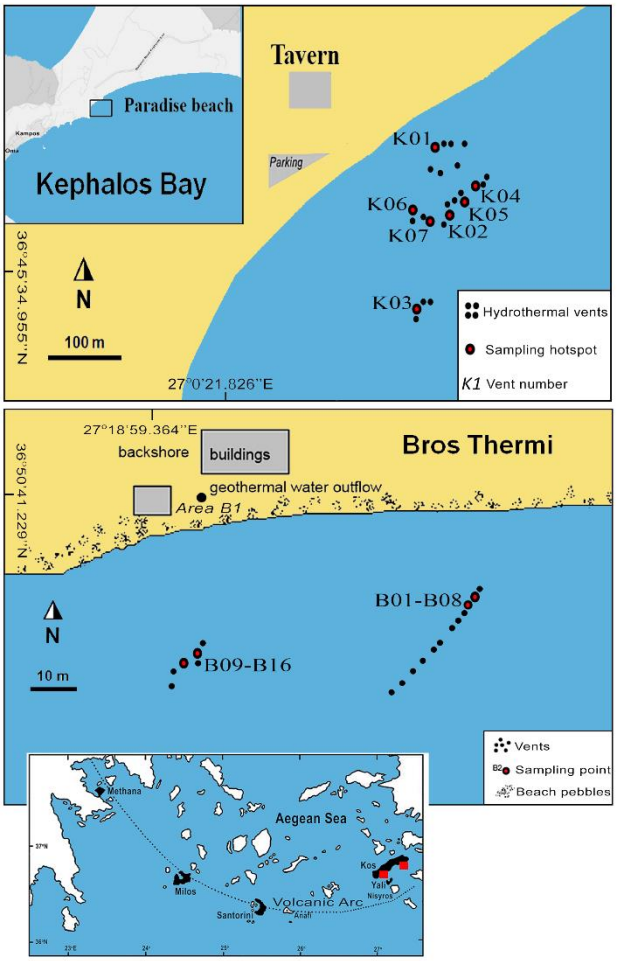

Figure 1 – Study area and sampling sites.

Although Fe/Al and Mn/Al follow different trends between the two hydrothermal fields, the Cu/Al, Pb/Al and Cd/Al are showing quite similar correlation indicating a possible common hydrothermal phase. Moreover, Ca/Al, Ba/Al and Sr/Al are very well and positively correlated. Probably they are concentrated in the same phase, while dissolved Ca derived from the dissolution of carbonates during hydrothermal leaching may form particles of secondary minerals such as anhydrite or clay minerals (Von Damm *et al.*, 1985). Furthermore, particulate Sr should be incorporated in anhydrite as well. Finally, Li/Al and Si/Al are found to be correlated positively only in Kephalos vents. The Fe/(Fe+Mn+Al) ratio and especially that of Al/(Fe+Mn+Al) can be used as an indication of hydrothermal versus detrital sediment inputs. Values being below 0.60 is considered as an indication of hydrothermal versus detrital sediment inputs while values below 10 or even 20 are strongly related to submarine hydrothermalism or volcanism (Bostrom *et al.*, 1969; Edmonds and German, 2004). In Kos hydrothermal particles the Al/(Fe+Mn+Al) ratio varied between 0.16-0.62 and an average 0.29 in Kephalos Bay and from 0.03-0.53 with an average 0.29 in Bros Thermi (Table 2). Furthermore, the fluctuation of Fe/(Fe+Mn+Al) ratio found to be above 0.50 in most samples with only one exception in Bros Thermi and one in Kephalos.

3.4. Factor analysis

R-Mode statistical analysis was performed for SPM elemental data using SPSS 18. In Kephalos Bay

2 factors were account for 73.31 % of total variance and in Bros Thermi 2 factors 87.72%. In Kephalos Bay Factor 1, which described 55.0 % of the total variance, presents high loadings for Mn, Pb, Ca, Ba, Sr Li and Al. The second factor consists from Cu and Si account for 18.3% of the total variance. SPM in this site consist mainly of hydrothermal oxides and hydroxides of Fe, Mn, and Pb but contains also a lithogenic mixture of Ca, Ba and Sr linked with the limestone substrate and also Li-Al fraction which can be attributed to a deeper volcanic rock origin. Cu and Si relationship can be attributed to oxidation of Cu sulphide by exposure to hydrothermal fluids and forming secondary Cu-Si mineral such as Chrysocolla (complex hydrated copper aluminum silicate). Further analysis might need to confirm this. In Bros Thermi Factor 1 described 52.6 % of the total variance presenting high loadings in Fe, Mn, Cu, Pb, Ca, Ba, Al and Si and moderate loadings for Sr and Li. The second factor presents high loadings in SPM, Cd, Li and moderate loadings in Cu, Pb, Ca, Ba, Sr, Al and Si. The different geochemical groups observed within the data from two sites also agree with other recent research on Bros Thermi local sediments and hydrothermal venting additions (Megalovasilis and Godelitsas, 2015).

Table 1 – Summary results of submarine hydrothermal SPM, Kos Aegean Sea.

	Gas	Water	G/W	pH	SPM	Fe	Mn	Cu	Pb	Cd	Ca	Ba	Sr	Li	Al	Si
Kephalos Bay	l/h	l/h			mg/l	µg/l	µg/l	µg/l	µg/l	µg/l	µg/l	µg/l	µg/l	µg/l	µg/l	µg/l
min	2.00	60.00	0.030	5.50	0.93	8.7	0.14	0.01	0.05	0.001	16.89	0.16	0.12	0.01	4.83	1.23
max	126.00	121.50	1.300	5.95	8.64	87.2	2.33	0.34	0.52	0.015	215.38	1.46	2.07	0.28	90.25	112.50
geomean	48.26	90.55	0.525	5.66	3.43	34.8	0.67	0.10	0.17	0.002	62.05	0.54	0.48	0.04	15.46	10.20
average	72.64	93.46	0.769	5.66	4.32	44.5	0.96	0.14	0.21	0.004	87.57	0.67	0.75	0.08	27.20	29.05
stdev	37.76	23.89	0.432	0.15	2.91	28.9	0.77	0.11	0.15	0.005	69.96	0.44	0.72	0.09	31.23	40.29
Bros Thermi																
min	4.50	16.50	0.180	6.09	0.21	6.5	0.05	0.10	0.08	0.001	14.58	0.09	0.13	0.01	1.53	0.56
max	60.00	96.00	1.140	6.53	20.94	228.8	2.17	1.01	1.34	0.038	181.82	0.91	1.19	0.85	191.95	104.77
geomean	20.62	43.52	0.474	6.23	2.89	55.6	0.43	0.23	0.37	0.006	47.11	0.26	0.37	0.09	18.41	7.98
average	24.71	47.70	0.544	6.23	6.06	80.2	0.66	0.30	0.47	0.011	62.08	0.33	0.48	0.23	53.25	23.15
stdev	14.79	20.20	0.296	0.13	6.88	59.5	0.56	0.25	0.34	0.012	47.79	0.24	0.36	0.28	62.58	29.48

Table 2 – Metal/Al ratios of submarine hydrothermal SPM, Kos Aegean sea.

	Fe/Al	Mn/Al	Cu/Al	Pb/Al	Cd/Al	Ca/Al	Ba/Al	Sr/Al	Li/Al	Si/Al	Fe/Fe+Mn+Al	Al/Fe+Mn+Al
Kephalos Bay												
min	0.58	0.026	0.002	0.005	0.0000	2.39	0.013	0.023	0.002	0.212	0.36	0.16
max	5.03	0.090	0.030	0.029	0.0030	9.45	0.131	0.056	0.006	5.769	0.82	0.62
geomean	2.25	0.043	0.006	0.011	0.0001	4.02	0.035	0.031	0.003	0.660	0.65	0.29
average	2.66	0.048	0.012	0.013	0.0006	4.44	0.046	0.033	0.003	1.384	0.67	0.32
stdev	1.43	0.023	0.012	0.009	0.0011	2.42	0.040	0.012	0.002	2.043	0.15	0.15
Bros Thermi												
min	0.88	0.006	0.002	0.004	0.0001	0.64	0.003	0.005	0.003	0.042	0.47	0.03
max	38.92	0.063	0.122	0.144	0.0202	18.43	0.087	0.122	0.012	2.916	0.97	0.53
geomean	3.02	0.023	0.013	0.020	0.0004	2.56	0.014	0.020	0.004	0.434	0.69	0.23
average	5.56	0.030	0.031	0.039	0.0018	4.39	0.026	0.035	0.005	0.698	0.71	0.29
stdev	9.16	0.019	0.042	0.044	0.0050	4.87	0.028	0.035	0.002	0.813	0.17	0.17

4. Discussion – Conclusions

Different gas content equilibrium, pH and redox conditions of hydrothermal fluids together with different rock basement and water source result in various particulate matter types containing diverse crystal forms and aggregates (Chester and Jickells, 2012). The elemental geochemistry of SPM presents some similarities but also differentiations between study areas were observed. Fe particulate correlates well with Mn, Cu and Pb particles suggesting a common sulphide source. Also Ca, Ba and Sr particulate concentrations are well correlated linked with dissolution of carbonate substrate maybe forming secondary minerals such as anhydrite $CaSO_4$, $BaSO_4$ and $SrSO_4$. Finally the particulate concentrations of Al, Si and Li being also well correlated, forming the "lithogenic" group of hydrothermal particles (Fig. 2).

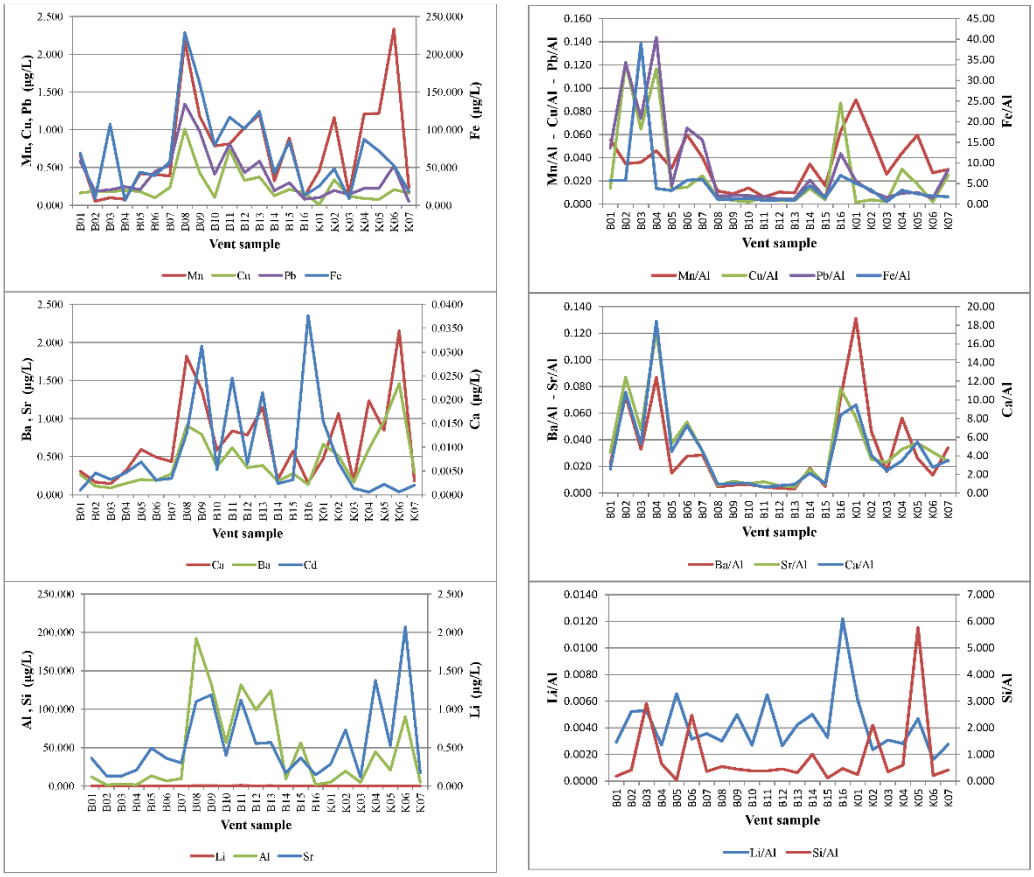

Figure 2 – Elemental concentration variability in hydrothermal SPM, Kos Aegean Sea.

Kephalos Bay hydrothermal site presents higher gas and water flux compared with Bros Thermi but gas/water ratio is similar. Periodicity in sediment temperature caused by tidal and barometric pressure affect pore pressure in sediment and consequently controls flux of nutrients and metals. As a consequence, bacterial mats morphology and expansion around seeps vary with time.(Aliani *et al.*, 2004). The SPM concentration is higher in Bros Thermi than in Kephalos coupled with higher levels of Mn, Cu and Fe. Both fields present same levels of concentrations in Mn, Si and Ca. Higher concentrations are observed in Bros Thermi for Fe, Cu, Cd, Li, Pb and Al, while increased concentrations in Ba and Sr found in Kephalos Bay (Fig. 2). Particulate Fe is associated in a different way with specific elements, such as with Cu on the two hydrothermal areas, presenting no distinct trend in Kephalos while the opposite is observed in Bros Thermi. Furthermore, Fe presents similar positive concentrations trends with Mn and with Pb and Al on both fields. In many environments Ca, Ba and Sr are very well geochemically correlated and coupled because of similarities on their geochemical propertied despite possible different sources and biogenic affiliations. In Kos their concentrations are quite similar in both areas indicating a common carbonate substrate beneath the island, leached by the hydrothermal ascending fluids. A barite ($BaSO_4$), source for Ba is also possible. Lithogenic elements in SPM present different relationships in their concentrations such as between Si and Al while they follow similar interrelationships with Li in both areas studied. Si and Al in Kephalos only show more distinguishable trend (Megalovasilis, 2015b). There are only a few studies for hydrothermal particulate matter along the Hellenic volcanic arc Comparing with existing literature, Kos submarine hydrothermal SPM levels are below the Milos SPM (Palaeochori Bay) concentrations and similar with other submarine hydrothermal areas in Milos such as Voudia Bay

and Adamas Bay (Varnavas *et al.*, 2000; Megalovasilis, 2007). Notably particulate Fe is exhibiting high concentrations only in Bros Thermi while Mn particulate is high in both fields and both elemental concentrations are comparable with Milos Palaeochori Bay. In addition, the strong influence of sedimentary substrate is imprinted with the very high levels of particulate Ca being the highest observed along the volcanic arc. Elevated particulate Sr is also observed in Kos and remarkably high particulate Al are found in Bros Thermi suggesting strong Al-Silicate mineral assemblages underneath the hydrothermal site. Previous research on sediments deposited near the venting area of Bros Thermi suggested the possible existence of significant metallic sulphide deposits of hydrothermal origin at depth beneath Kos (Megalovasilis and Godelitsas, 2015). It is quite difficult if not impossible to compare fully hydrothermal particulate concentrations of elements in all marine environments such as the shallow vents and hydrothermal fields of open oceans; because of huge differences on sampling procedures and the actual dispersion of plumes in the water column. When scuba diving is involved, sampling results in more condense and isolated hydrothermal fluid component while niskin bottle sampling (or in situ pumping of seawater), over hydrothermal plumes and submarine volcanoes with hydrothermal activity, contains more diluted hydrothermal component altered by the prevailing oceanographic conditions. Summarising, particle chemistry from the submarine vents studied were dominated by Fe, Ca, Si and Al and strongly enriched in Mn, Cu, Pb and Ba. Data are indicating that hydrothermal vents are major sources for basic metals and trace elements such as Fe, Mn, Cu, Pb and Cd. The different elemental associations in the two study sites are attributed mainly to the different geologic type of substrate petrology rather than in very different hydrothermal processes prevailing. But because the two study sites presented differences in their pH, gas flux, water flux and gas/water ratio a different hydrothermal reactivity between the two sites is assumed. Particulate matter originating from hydrothermal vents plays important role in local marine sediments geochemistry and it seems is ruled by the geochemistry of the geologic basement and the water-rock interactions taking place beneath in the substrate. Long-term or short-term time series or even periodical sampling of hydrothermal fluids are of prime importance in furthering our understanding on shallow-sea hydrothermal systems and strongly suggested. Furthermore, future investigations should incorporate study of both dissolved and particulate species together with mineralogical analysis and SEM images in order to access the geochemistry of these vents in total.

5. Acknowledgments

I want to thank divers P. Tsarpalis, K. Romeos for their excellent work during all the submarine research, Prof. P. Dando and Prof. S. Varnavas for providing the opportunity to collect and perform chemical analyses on samples. Part of this work had been funded by the EU MAST programme, Contract No. MAST2-CT94-0101.

6. References

Aliani, S., Meloni, R. and Dando, P.R., 2004. Periodicities in sediment temperature time-series at a marine shallow water hydrothermal vent in Milos Island (Aegean Volcanic arc, Eastern Mediterranean), *Journal of Marine Systems*, 46(1-4), 109-119.

Bachmann, O., Deering, C.D., Ruprecht, J.S., Huber, C., Skopelitis, A. and Schnyder, C., 2012. Evolution of silicic magmas in the Kos-Nisyros volcanic center, Greece: cycles associated with caldera collapse, *Contributions to Mineralogy and Petrology*, 163(1), 151-166.

Balopoulos, E.T., Theocharis, A., Kontoyiannis, H., Varnavas, S., Voutsinou-Taliadouri, F., Iona, A., Souvermezoglou, A., Ignatiades, L., Gotsis-Skretas, O. and Pavlidou, A., 1999. Major advances in the oceanography of the southern Aegean Sea-Cretan Straits system (eastern Mediterranean), *Progress in Oceanography*, 44(1-3), 109-130.

Bostrom, K., Peterson, M.N.A., Joensuu, O. and Fisher, D.E., 1969. Aluminum-poor ferromanganoan sediments on active oceanic ridges, *Journal of Geophysical Research*, 74(12), 3261-3270.

Chester, R. and Jickells, T.D., 2012. Marine Geochemistry, 3rd Edition. Wiley-Blackwell.
Dando, P.R., Hughes, J.A., Leahy, Y., Niven, S.J., Taylor, L.J. and Smith, C., 1995. Gas venting rates from submarine hydrothermal areas around the island of Milos, Hellenic Volcanic Arc, *Continental Shelf Research*, 15(8), 913-929.
Dando, P.R., Thomm, M., Arab, H., Brehmer, M., Hooper, L.E., Jochimsen, B., Schlesner, H., Stohr, R., Miquel, J.C. and Fowler, S.W., 1998. Microbiology of shallow hydrothermal sites off Palaeochori Bay, Milos (Hellenic Volcanic Arc), *Cahiers de Biologie Marine*, 39(3-4), 369-372.
Dando, P. R., Aliani, S., Arab, H., Bianchi, C.N., Brehmer, M., Cocito, S., Fowler, S.W., Gundersen, J., Hooper, L.E., Kolbl, R., Kuever, J., Linke, P., Makropoulos, K.C., Meloni, R., Miquel, J.C., Morri, C., Muller, S., Robinson, C., Schlesner, H., Sievert, S., Stohr, R., Stuben, D., Thomm, M., Varnavas, S.P. and Ziebis, W., 2000. Hydrothermal studies in the aegean sea, *Physics and Chemistry of the Earth, Part B: Hydrology, Oceans and Atmosphere*, 25(1), 1-8.
Edmonds, H.N. and German, C.R., 2004. Particle geochemistry in the Rainbow hydrothermal plume, Mid-Atlantic Ridge, *Geochimica et Cosmochimica Acta*, 68(4), 759-772.
Godelitsas, A., Price, R.E. Pichler, T., Amend, J., Gamaletsos, P. and Goettlicher, J., 2015. Amorphous As-sulfide precipitates from the shallow-water hydrothermal vents off Milos Island (Greece), *Marine Chemistry*, 177(5), 687-696.
Hatzivasileiou, V., 2013. History of Island of Kos Ancient, Medieval and Modern, Municipality of Kos, Kos Greece.
Humphris, S.E., Zierenberg, R.A., Mullineaux, L.S. and Thomson, R.E., 1995. Seafloor Hydrothermal Systems:Physical, Chemical, Biological, and Geological Interactions, AGU Monograph 91 American Geophysical Union, Willey, Washington, DC. 466.
Karageorgis, A.P. and Anagnostou, C.L., 2001. Particulate matter spatial-temporal distribution and associated surface sediment properties: Thermaikos Gulf and Sporades Basin, NW Aegean Sea, *Continental Shelf Research*, 21, 2141-2153.
Lagios, E., Galanopoulos, D., Hobbs, B.A. and Dawes, G.J.K., 1998. Two-dimensional magnetotelluric modelling of the Kos Island geothermal region (Greece), *Tectonophysics*, 287(1-4), 157-172.
Landing, W.M. and Lewis, B.L., 1991. Collection, processing and analysis of marine particulate and colloidal material for transition metals. *In:* Marine Particles: Analysis and Characterization, Spencer, D. and Hurd, D., *eds*., *Geophys. Monog. AGU*, 63, 263-272.
Loring, D.H. and Rantala, R.T.T., 1992. Manual for the geochemical analyses of marine sediments and suspended particulate matter, *Earth Sciences Reviews*, 32, 235-283.
Lupton, J.E., 1995. Hydrothermal plumes: near and far fields. *In*: Humphries, S.E., Zierenberg, R.A., Mullineaux, L.S., *et al*., *eds*., Seafloor Hydrothermal Systems: Physical, Chemical, Biological and Geological Interactions, American Geophysical Union 91, Washington D.C., 317-346.
Megalovasilis, P., 2007. Geochemical research on sediments and waters in submarine hydrothermal areas along the Aegean Volcanic Arc (in Greek with English Abstract) Ph.D, Thesis, Athens, National and Kapodistrian University of Athens.
Megalovasilis, P., 2014. Partition geochemistry of hydrothermal precipitates from submarine hydrothermal fields in the Hellenic Volcanic Island Arc, *Geochemistry International*, 52(11), 992-1010.
Megalovasilis, P. and Godelitsas, A., 2015. Hydrothermal influence on nearshore sediments of Kos Island, Aegean Sea, *Geo-Marine Letters*, 35(2), 77-89.
Megalovasilis, P., 2015a. Evaluation of hydrothermal SPM inputs in Aegean Sea. *In*: 11th Panhellenic Symposium on Oceanography and Fisheries, «Aquatic Horizons: Challenges & Perspectives», *Hellenic Centre for Marine Research*, 1, 365-368.
Megalovasilis, P., 2015b. Hydrothermal fluid particle geochemistry of submarine vents in Kos Island, Aegean Sea East Mediterranean, *Journal of Marine Systems*, Submitted: 1-25.
Minissale, A., Duchi, V., Kolios, N., Nocenti, M. and Verrucchi, C., 1997. Chemical patterns of thermal aquifers in the volcanic islands of the Aegean Arc, Greece, *Geothermics*, 26(4), 501-518.
Nomikou, P., Papanikolaou, D., Alexandri, M., Sakellariou, D. and Rousakis, G., 2013. Submarine volcanoes along the Aegean volcanic arc, *Tectonophysics*, 597-598(0), 123-146.

Papanikolaou, D. and Lekkas, E., 1990. Miocene tectonism in Kos, Dodecanese islands, *IESCA Abstract*, 179-180.

Parson, L., Walker, C.L. and Dixon, D.R.E., 1995. Hydrothermal vents and processes. *Geological Society London.*

Pe-Piper, G., Piper, D.J.W. and Perissoratis, C., 2005. Neotectonics and the Kos Plateau Tuff eruption of 161 ka, South Aegean arc, *Journal of Volcanology and Geothermal Research*, 139(3-4), 315-338.

Pichon, X.L. and Angelier, J., 1979. The Hellenic arc and trench system: a key to the neotectonic evolution of the eastern mediterranean area, *Tectonophysics*, 60(1-2), 1-42.

Price, R.E., Savov, I., Planer-Friedrich, B., Bühringa, S.I., Amendb, J. and Pichlera, T., 2013. Processes influencing extreme As enrichment in shallow-sea hydrothermal fluids of Milos Island, Greece, *Chemical Geology*, 348, 15-26.

Royden, L.H. and Papanikolaou, D.J., 2011. Slab segmentation and late Cenozoic disruption of the Hellenic arc, *Geochemistry, Geophysics, Geosystems*, 12(3), 1-24.

Ruffa, G.L., Panichi, C., Kavouridis, T. *et al*., 1999. Isotope and chemical assessment of geothermal potential of Kos Island, Greece, *Geothermics*, 28(2), 205-217.

Varnavas, S., Megalovasilis, P., Panagiotaras, D. *et al*., 1998. Compositional and morphological characterisation of particulate matter in hydrothermal fields of the Hellenic Volcanic arc, *In*: XXIII General Assembly of European Geophysical Society (EGS), Part II Hydrology, Oceans & Atmospere, European Geophysical Society, *Annales Geophysicae*, Supplement II to Volume 16, 16, C 744.

Varnavas, S., Panagiotaras, D. and Megalovasilis, P., 1998. Chemical characteristics of a submarine hydrothermal system offshore Kos island, on the Hellenic Volcanic Arc. *Rapports et Procès-Verbaux de la Commission Internationale Pour L'Exploration Scientifique de la mer Mediterranee, 35th CIESM Congress,*, 35(1), 104-105.

Varnavas, S.P. and Cronan, D.S., 1991. Hydrothermal metallogenic processes off the islands of Nisiros and Kos in the Hellenic Volcanic Arc, *Marine Geology*, 99(1-2), 109-133.

Varnavas, S.P., Panagiotaras, D. and Megalovasilis, P. *et al*., 2000. Compositional characterization of suspended particulate matter in hellenic volcanic arc hydrothermal centres, *Physics and Chemistry of the Earth, Part B: Hydrology, Oceans and Atmosphere*, 25(1), 9-18.

Von Damm, K.L., Edmond, J.M., Measures, C.I., *et al*., 1985. Chemistry of submarine hydrothermal solutions at Guaymas Basin, Gulf of California, *Geochim. Cosmochim. Acta*, 49, 2221-2237.

Von Damm, K.L., 1990. SeaSoor hydrothermal activity: black smoker chemistry and chimneys, *Annual Review of Earth and Planetary Science*, 18, 173-204.

Von Damm, K.L., 2001. Chemistry of hydrothermal vent fluids. *In*: Steele, J.H., *ed*., Encyclopedia of Ocean Sciences, Academic Press Oxford, 3, Cambridge, Massachusetts USA, 1246-1253.

Whittield, M. and Turner, R.D., 1987. The role of particles in regulating the composition of sea water. *In*: Stumm, W., *ed*., Aquatic Surface Chemistry: Chemical Processes at the Particle - Water Interface, *John Wiley N.Y., New York*, 457-493.

Yücel, M., Sievert, S.M., Vetriani, C. *et al.*, 2013. Eco-geochemical dynamics of a shallow-water hydrothermal vent system at Milos Island, Aegean Sea (Eastern Mediterranean), *Chemical Geology*, 356(0), 11-20.

Δελτίο της Ελληνικής Γεωλογικής Εταιρίας, τόμος L, σελ. 1943-1951
Πρακτικά 14ου Διεθνούς Συνεδρίου, Θεσσαλονίκη, Μάιος 2016

Bulletin of the Geological Society of Greece, vol. L, p. 1943-1951
Proceedings of the 14th International Congress, Thessaloniki, May 2016

MARIALITIC SCAPOLITE OCCURENCES FROM THE KIMMERIA-LEFKOPETRA METAMORPHIC CONTACT, XANTHI (N. GREECE)

Mouchos E.[1,2], Papadopoulou L.[1], Williamson B.J.[2] and Christofides G.[1]

[1]*Aristotle University of Thessaloniki, Department of Geology, 54124, Thessaloniki, Greece, lambrini@geo.auth.gr, christof@geo.auth.gr*

[2]*Camborne School of Mines, University of Exeter, Penryn, Cornwall, TR10 9FE, UK, em415@exeter.ac.uk, b.j.williamson@exeter.ac.uk*

Abstract

Emplacement of the Xanthi Plutonic Complex within the Rhodope Massif of N. Greece created an extensive metamorphic aureole around the plutonite. The aureole contains two areas of intense scapolitization in the contacts between granodiorite and biotite-gneiss and between monzonite and sandstone, the latter cross-cut by andesite dykes. This paper reports the results of a mineralogical and geochemical study into the formation of the scapolites and particularly the nature of the plutonite-derived hydrothermal fluids from which scapolites were formed.
Keywords: *Xanthi Plutonic Complex, scapolitization, marialite.*

Περίληψη

Η διείσδυση του πλουτωνίτη της Ξάνθης στην μάζα της Ροδόπης στη Β. Ελλάδα δημιούργησε μια εκτεταμένη μεταμορφική άλω γύρω από τον πλουτωνίτη. Η άλω περιέχει δυο περιοχές έντονης σκαπολιθίωσης στις επαφές μεταξύ γρανοδιορίτη και βιοτιτικού γνεύσιου και μεταξύ μονζονίτη και ψαμμίτη στον οποίο διεισδύουν ανδεσιτικές φλέβες. Η παρούσα εργασία παρουσιάζει τα αποτελέσματα ορυκτολογικής και γεωχημικής έρευνας για το σχηματισμό των σκαπόλιθων και ιδιαίτερα για τη φύση των υδροθερμικών ρευστών προερχόμενων από τον πλουτωνίτη από τα οποία σχηματίστηκαν οι σκαπόλιθοι.
Λέξεις κλειδιά: *Πλουτωνίτης της Ξάνθης, σκαπολιθίωση, μαριάλιθος.*

1. Introduction

Scapolite-group minerals are tetragonal framework aluminosilicates with a general formula: $M_4T_{12}O_{24}A$, where M = Ca, Na, K and Sr, T = Si and Al and A = Cl, CO_3, and SO_4 (Deer *et al.*, 2013). Their compositions vary between the end-members marialite ($Na_4(Al_3Si_9O_{24})Cl$) and meionite ($Ca_4(Al_6Si_6O_{24})CO_3$) which are not found in nature but can be synthesized (e.g. Eugster and Prostka, 1960; Eugster *et al.*, 1962; Goldsmith and Newton, 1977; Sokolova *et al.*, 1996; Sherriff *et al.*, 2000). In natural systems, the composition of Cl-bearing scapolite ranges between three end-members: $Na_4(Al_3Si_9O_{24})Cl$, $Na_3Ca(Al_4Si_8O_{24})Cl$, and $NaCa_3(Al_5Si_7O_{24})CO_3$ (Pan, 1998). Scapolite has no industrial uses but is a minor gemstone that exhibits chatoyancy, creating a cat's eye effect when cut *en cabochon* (Bonewitz, 2005).

Scapolite is found in a wide range of geological settings but most commonly in metamorphic and metasomatic rocks. Its presence has been described in low-pressure skarns, low to medium pressure regional metamorphic rocks, medium to high pressure/depth assemblages of amphibolite and granulite facies and even in kimberlites and basalts (Baker and Newton, 1994 and references therein). It is also thought to occur as a primary mineral in alkaline igneous rocks (Larsen, 1981; Goff *et al.*, 1982). Well-known occurrences of scapolite in Greece include the Serifos Island skarn (Mposkos, 1978), the Kerdillion Unit amphibolites of the Serbo-Macedonian Massif (Rentina and Stratoni areas) (Kassoli-Fournaraki, 1981), the Chalkidiki peninsula quartz amphibolites (Sarti area) (Kassoli-Fournaraki, 1991) and the eastern Rhodope amphibolitized eclogites (Organi-Kimi area) (Mposkos and Mpaziotis, 2005).

Where scapolite occurs proximal to magmatic intrusions, its formation is likely to be due to metasomatic processes (Deer *et al.*, 2013). Scapolitization can occur sequentially or contemporaneously with other metasomatic processes like albitization, as both require saline fluids (Touret and Nijland, 2013). However, why scapolitization occurs instead of other metasomatic processes remains unclear. An obviously important control is the nature of the hydrothermal fluid from which it forms. To investigate this we have carried out a case study in the metamorphic aureole of the Xanthi Plutonic Complex (XPC), Rhodope Massif, Greece, where scapolite is particularly well developed and it has a clear spatial and temporal association with intrusive magmatic rocks (Christofides, 1977). The objective of this study was to carry out mineralogical and geochemical studies on scapolite to investigate the nature of metasomatic fluids responsible for its formation.

2. Geological Setting

The evolution of the Rhodope Massif during the Oligocene to Miocene was heavily influenced by the presence of fault-controlled sedimentary basins (Caracciolo *et al.*, 2011; Kilias *et al.*, 2011) and calc-alkaline to high-K calc-alkaline intrusive and extrusive magmatism. Intrusive rocks include those of the XPC which were emplaced into gneisses, mica schists, amphibolites, calc-silicate rocks, marbles and Eocene-Oligocene sedimentary rocks of the Rhodope Massif (Fig. 1). To the south, the XPC has a fault contact with Neogene and Quaternary rocks (Christofides *et al.*, 2010). From geophysical data (Maltezou and Brooks, 1989; Tsokas *et al.*, 1996), the XPC is a laccolith-shaped body that extends several kilometers to the south.

The 40 km^2 (10.5 km length and 4.5 km width) XPC mainly consists of two rock groups: an 'acid' group containing granodiorites grading into monzogranites, with microgranular mafic enclaves of quartz diorite composition; and a 'basic' group composed of monzonite/quartz monzonite, quartz monzodiorite and subordinate monzogabbro and olivine gabbro. The SiO_2 content of the XPC ranges from 62-69 wt.% for the 'acid' group and 44-61 wt.% for the 'basic' group (Christofides *et al.*, 2010). The age of the XPC has been estimated at 25-29 Ma (Liati, 1986; Bigazzi *et al.*, 1994), however Christofides *et al.* (2012) recently determined an age of 34.3±0.5 Ma for the granodiorite rock type.

Christofides *et al.* (2010), estimated that the XPC initially crystallized under relatively dry conditions at 5.8 kbar pressure and 1300°C maximum temperature. This temperature reflects the initial crystallization of the gabbroic magma immediately after emplacement. In a subsequent phase, the water content of the melt increased (to more than 4 wt.%) at an average temperature of 870°C. The increase in melt-water content allowed magma to reach higher crustal levels at lower pressure (average of 1.8 kbar). The 'acid' group crystallized under oxidizing conditions at 729°C average temperature and 0.7 kbar pressure (Christofides *et al.*, 2010). These P/T conditions are significantly lower compared to those of the 'basic' group. This fact potentially suggests a different origin and/or evolution of the 'acid' and 'basic' group.

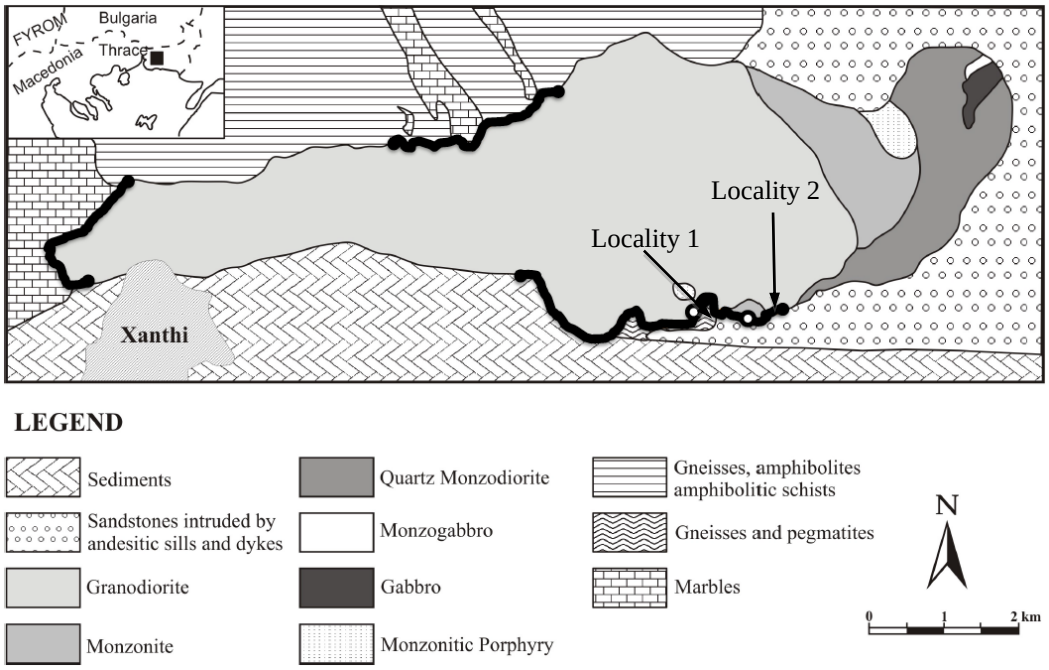

Figure 1 - Geological map of the Xanthi Plutonic Complex (modified after Christofides *et al.*, 2010). The contact metamorphic aureole surrounds the plutonite but is more intense and visible in the bold areas. The two points indicate the positions of the scapolite occurrences. Scapolite at Locality 1 occurs at the contact between granodiorite and biotite-gneiss whereas that at Locality 2 is at the contact between monzonite and sandstones (intruded by andesitic dykes).

The XPC, which is mostly undeformed and unweathered, has an extensive (around 300m thick) contact metamorphic aureole that is mostly visible in contact with marbles and contains a massive Au-bearing skarn-type mineralization, a Mo-Cu-Bi-W vein mineralization and a magnetite ore deposit (Christofides, 1977; Liati, 1986; Vavelidis *et al.*, 1990; Skarpelis and Liati, 1991; Voudouris *et al.*, 2010; Melfos and Voudouris, 2012). Scapolite mostly occurs in the southern part of the complex, best seen north of Lefkopetra village (Fig. 1), at the 'Kimmeria-Lefkopetra' contact, between the granodiorite and biotite-gneiss (Locality 1) and monzonite and sandstones (intruded by andesite dykes) (Locality 2).

3. Materials and Methods

Scapolite samples were analyzed using a Philips PW1820/00 X-ray diffractometer equipped with a PW1710/00 microprocessor (CuKα radiation, Ni filter, 35 kV and 25 mA) at the Department of Mineralogy-Petrology-Economic Geology, School of Geology, Aristotle University of Thessaloniki (AUTh). Samples were typically scanned at room temperature over angles of 3-63° 2θ with a 1.2° 2θ minimum scan velocity. The resulting patterns were interpreted using PC-APD (1994) software by matching peaks with those for minerals in the ICDDPDF database. Imaging in backscattered electron mode (BSE, for average atomic number contrast) and chemical analyses were performed on polished thin sections and resin blocks in a JEOL JSM-840A scanning electron microscope (SEM) with energy dispersive X-ray spectrometer (EDS) at the Interdepartmental Laboratory of Electron Microscopy of AUTh. The analyses were undertaken at an accelerating voltage of 20 kV and a probe current of 0.4 mA.

4. Results

Scapolite showed very different crystal sizes at the two locations in Fig. 1, reaching up to 10 cm in length at Locality 1 but being microscopic at Locality 2. In both locations, scapolite in hand specimen ranged from white to grey or colorless. Powdered samples analyzed by XRD had a marialite composition (Fig. 2). Rock samples from Locality 1 were composed of actinolite-clinopyroxene-scapolite-white mica, whilst those from Locality 2 were consisted of plagioclase-scapolite-clinopyroxene-titanite (Fig. 3). Scapolite from both localities is colorless in PPL, with low relief and poor {100} to indistinct {110} cleavage. Crystals from Locality 1 are often poikilitic containing inclusions of clinopyroxene. Those from Locality 2 surround and often partially replace primary plagioclase (by scapolitization). Where still present, the plagioclase is cloudy in appearance, which, from SEM-EDS analysis, is due to the presence of fine-grained (from less than 100 μm to a few mm) alteration phases including scapolite, calcite, white mica and orthoclase (Fig. 4). From semi-quantitative SEM-EDS analysis of scapolite from Locality 1 and 2, it can be classified as marialite, containing approximately 11.5 and 8 wt.% NaCl, respectively.

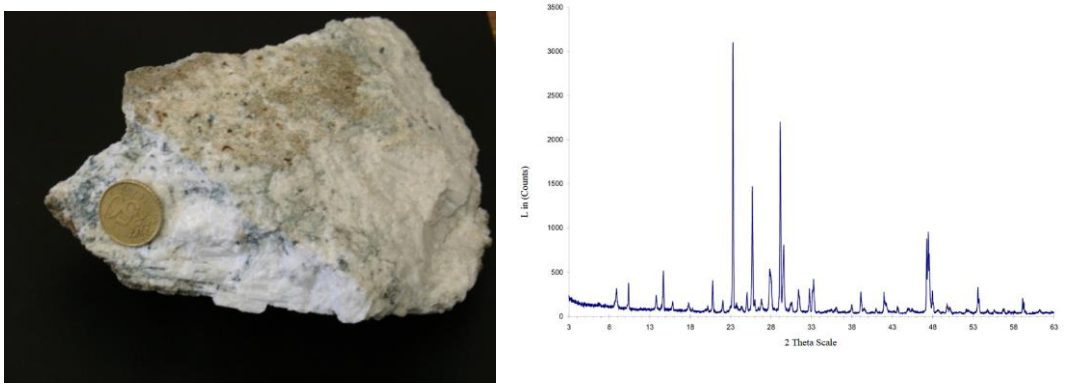

Figure 2 - Photograph of scapolite from Locality 1 (left) and its XRD pattern (right).

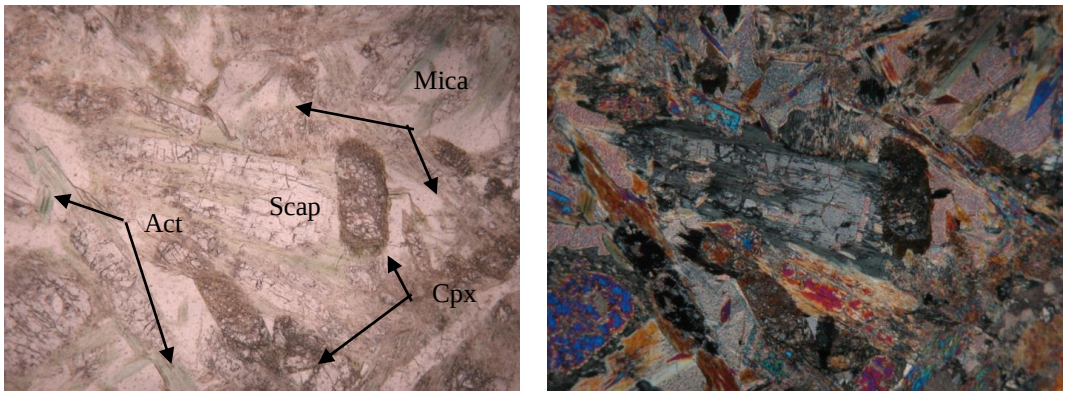

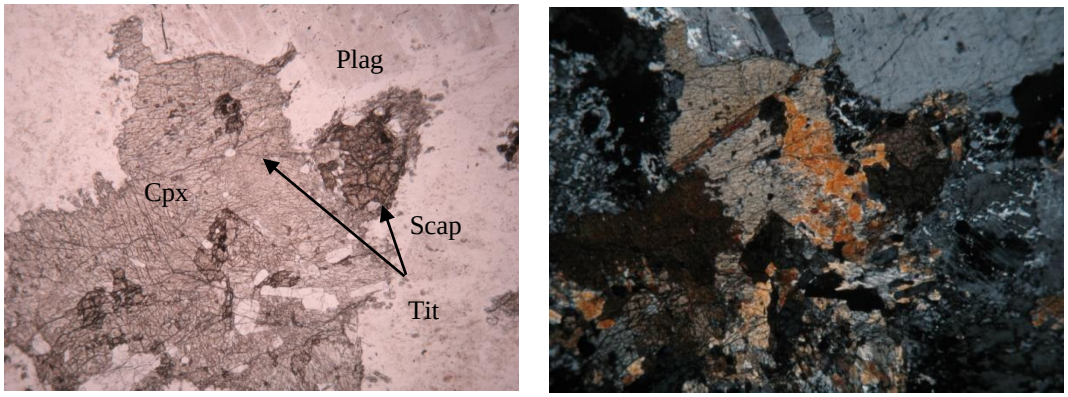

Figure 3 - Photomicrographs (40x) of scapolite from Locality 1 (upper) and 2 (lower) in plane- (PPL, left) and crossed-polarized light (XPL, right). Act = actinolite, Cpx = clinopyroxene, Mica = white mica, Plag = plagioclase, Scap = scapolite, and Tit = titanite.

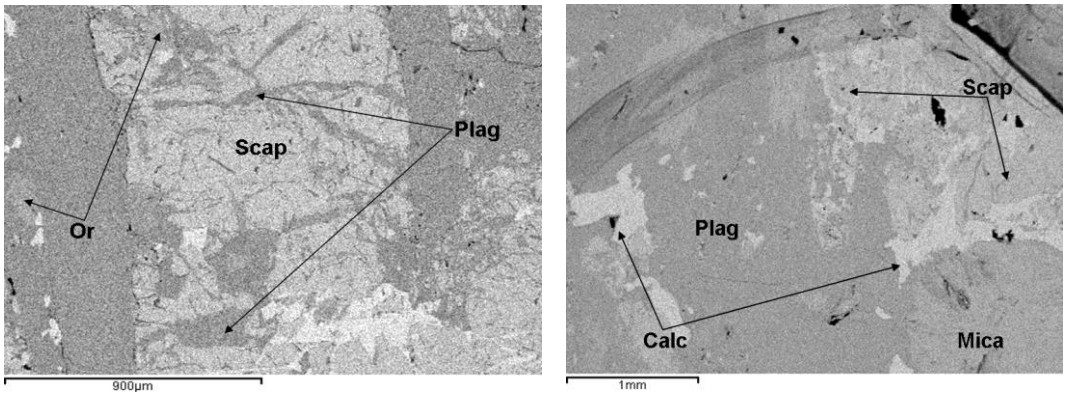

Figure 4 - BSE-SEM images of scapolite from Locality 2. Scap = scapolite, Plag = plagioclase, Calc = calcite, Mica = white mica and Or = orthoclase.

5. Discussion

Scapolite within skarns almost invariably shares its host's metasomatic origin, formed due to the action of metasomatic fluids expelled during the emplacement and crystallization of proximal magmatic intrusions (Einaudi *et al.*, 1981). In most circumstances, scapolite forms by replacement of plagioclase due to the process of scapolitization. Such replacement is thought to be driven by interaction of plagioclase with fluids containing Cl^-, CO_2, SO_3 and Na^+, rather than by isochemical transformation (*Kullerud and Erambert, 1999*). When the fluids contain high concentrations of SO_2 and CO_2, the formation and stabilization of meionite (Ca-rich scapolite) is favoured. On the contrary, a Cl-rich fluid phase favours the formation and stabilization of marialite (Na-rich scapolite). The composition of scapolite is largely controlled by the following linked substitutions: $Na^+ \leftrightarrow Ca^{2+}$, $Al^{3+} \leftrightarrow Si^{4+}$ and $Cl^- \leftrightarrow CO_3^{-2}$. All three substitutions are active in Na-rich scapolite [Ca/(Ca+Na)<0.75], whereas Cl is completely replaced by CO_3 in Ca-rich scapolite [Ca/(Ca+Na)>0.75] and hence the chemical reaction is controlled only by the NaSi↔CaAl double substitution (Strauss, 2003).

Scapolite can be a potential indicator for the activity of volatiles during various processes that take place in the Earth's crust. This is because of its ability to incorporate volatile elements and compounds such as Cl, CO_2 and SO_3, and due to the fact that scapolite can equilibrate in a wide range of pressure and temperature environments. There are many papers in the literature that contain

quantitative calculations on the volatile activity of metamorphic fluids based on the chemistry of scapolite (e.g. Ellis, 1978; Moecher and Essene, 1991; Harley *et al.*, 1994; Gómez-Pugnaire *et al.*, 1994). Nowadays, there are two diametrically opposed views on the distribution of volatile components between scapolite and fluids. The first one suggests that the Cl content of scapolite is heavily dependent on the limitations imposed by the cationic lattice in the balance of valences (Pan *et al.*, 1994). The second one claims that Cl content of scapolite is mainly controlled by the activity of NaCl in fluids that are in equilibrium with the mineral (Jiang *et al.*, 1994).

In addition to this, F and Cl are ubiquitous (in various amounts from ppm to wt.%) in fluids at all crustal levels (Markl and Piazolo, 1998). These two elements occur in many metamorphic rock-forming minerals and consequently can be determined in order to estimate their ratios in metamorphic fluids (Munoz and Swenson, 1981; Zhu and Sverjensky, 1991; Harley and Buick, 1992; Markl and Bucher, 1998). As a result, the chemistry of scapolite, and particularly its Cl and CO_2 contents, in relation to the Cl and F content of other coexisting common metamorphic rock-forming minerals, such as amphibole, mica, apatite and titanite, can be used as tracers for the chemical composition of the metamorphic fluid (Ellis, 1978; Munoz and Swenson, 1981; Binder and Troll, 1989; Mora and Valley, 1989; Kullerud, 1996; Rebbert and Rice, 1997; Markl and Bucher, 1998; Kullerud and Erambert, 1999; Yardley *et al.*, 2000; Svensen *et al.*, 2001).

The formation of marialite requires saline (around 20 wt.% NaCl) metasomatic fluids (Vanko and Bishop, 1982), which means that Cl-rich scapolite is an indicator of high NaCl activity during crystallization (Orville, 1975; Ellis, 1978; Vanko and Bishop, 1982). NaCl may have been original to the system or may have been derived from an external source (such as nearby sedimentary rocks, halite-bearing rocks or brines) through fluid migration. Fluid inclusion studies indicate that the salinity of metamorphic fluids ranges from 0-6 wt.% in pelitic schists and gneisses, 20-25 wt.% in calcareous rocks and up to 50 wt.% NaCl equivalent in evaporates (Mora and Valley, 1989, and references therein). However, when scapolite contains low levels of NaCl (<20 wt.%), as in those from both localities, it is unclear if it is formed from low salinity magmatic fluids, ingress of saline meteoric waters or a mixture of both, which can cause a decrease in fluid temperature and salinity.

Finally, NaCl-rich scapolite was synthesized at temperatures higher than 700-800ºC and at low to high pressure (Eugster and Prostka, 1960; Newton and Goldsmith, 1975). This temperature range is not significantly different from the crystallization temperature of granodiorite and monzonite. Hence, it can be considered that scapolite from Locality 1 formed at 729ºC and 0.7 kbar, and in equilibrium with the fluid phase, as it seems that the plutonic plagioclase was completely replaced by scapolite. Incomplete scapolitization at Locality 2 took place at 870ºC and approximately 1.8 kbar pressure. Scapolitization at both localities occurred under the influence of magmatic fluids emanating from crystallizing magma that formed the XPC, particularly after the initial stage of cooling when melt-water contents increased allowing the magma to reach shallower emplacement levels.

6. Conclusions

Scapolite in the case study was formed and developed by replacement of igneous plagioclase through metasomatic reactions within the contact aureole of the XPC. Complete scapolitization at Locality 1 took place at 729ºC and 0.7 kbar by interaction of the cooling granodiorite with fluids containing 11.5 wt.% NaCl. On the other hand, incomplete scapolitization at Locality 2 occurred at slightly higher temperatures and pressures (870ºC and 1.8 kbar) and during interaction with lower salinity (8 wt.% NaCl) fluids during the cooling of monzonite. Differences in the chemistry of scapolite from Locality 1 and 2, with varying substitution of $Na^{+} \leftrightarrow Ca^{2+}$, $Al^{3+} \leftrightarrow Si^{4+}$ and $Cl^{-} \leftrightarrow CO_3^{-2}$, are likely to reflect slight differences in the salinity of the metasomatic fluids from which they were formed. However, the cause of the variations in the temperature and salinity of the metasomatic fluids remains to be determined. Further to this, the reasons for the abrupt end to the scapolitization process

at Locality 2, as well as the role of the nearby sediments and andesitic intrusions as a potential source for NaCl-rich fluids, requires further research.

7. References

Baker, J. and Newton, R.C., 1994. Standard thermodynamic properties of meionite, $Ca_4Al_6Si_6O_{24}CO_3$, from experimental phase equilibrium data, *American Mineralogist*, 79, 478-484.

Bigazzi, N.S.G., Christofides, G., Del Moro, A. and Kyriakopoulos, K., 1994. A contribution to the evolution of the Xanthi pluton (Northern Greece): The apatite fission track analysis, *Bull. Soc. Geol. It.*, 113, 243-248.

Binder, G. and Troll, G., 1989. Coupled anion substitution in natural carbon-bearing apatites, *Contrib. Mineral. Petrol.*, 101, 394-401.

Bonewitz, R.L., 2005. Smithsonian Rock and Gem: The definitive guide to rocks, minerals, gems, and fossils, D.K. Publishing Inc./Smithsonian Institution and Dorling Kindersley Limited, 254 pp.

Caracciolo, L., Critelli, S., Innocenti, F., Kolios, N. and Manetti, P., 2011. Unraveling Provenance From Eocene-Oligocene Sandstones Of The Thrace Basin, North-East Greece, *Sedimentology*, 58, 1988-2011.

Christofides, G., 1977. Contribution to the study of plutonic rocks in the area of Xanthi, PhD thesis, Aristotle University of Thessaloniki, 249 pp. (In Greek).

Christofides, G., Papadopoulou, L., Soldatos, T., and Koroneos, A., 2010. Crystallization conditions of the Xanthi Plutonic Complex (Rhodope Massif, N. Greece): geothermometry and geobarometry, Scientific Annals, School of Geology, Aristotle University of Thessaloniki, *Proceedings of the XIX CBGA Congress*, Thessaloniki, Greece, Special volume 99, 199-207.

Christofides, G., Pipera, K., Koroneos, A. and Papadopoulos, A., 2012. New geochronological data from the Xanthi pluton: Constraints on the Nestos thrust dating, The School of Prof. Zhivko Ivanov, International Conference: Exhumation of High-grade Metamorphic Rocks (MCC), Magmatic Arc Systems and Strrike-slip Zones, 49-52.

Deer, W.A., Howie, R.A. and Zussman, J., 2013. An introduction to the rock-forming minerals, 3rd ed., The Mineralogical Society, London. 498 pp.

Einaudi, M.T., Meinert, L.D. and Newberry, R.J., 1981. Skarn deposits, *Econ. Geology*, 75th Anniversary Volume, 317-391.

Ellis, D.E., 1978. Stability and phase equilibria of chloride and carbonate bearing scapolites at 750°C and 4000 bar, *Geochimica et Cosmochimica Acta*, 42, 1271-1281.

Eugster, H. and Prostka, H.J., 1960. Synthetic scapolites, *Geological Society of America Bulletin*, 71, 1858.

Eugster, H., Prostka, H.J. and Appleman, D.E., 1962. Unit cell dimensions of natural and synthetic scapolites, *Science*, 137, 853-854.

Goff, F., Arney, B.H. and Eddy, A.C., 1982. Scapolite phenocrysts in a latite dome, northwest Arizona, U.S A, *Earth and Planetary Science Letters*, 60, 86-92.

Goldsmith, J.R. and Newton, R.C., 1977. Scapolite-plagioclase stability relations at high pressures and temperatures in the system $NaAlSi_3O_8$-$CaAl_2Si_2O_8$-$CaCO_3$-$CaSO_4$, *Am. Mineral*, 62, 1063-1081.

Gómez-Pugnaire, M.T., Franz, G. and Sanchez-Vizcaino, V.L., 1994. Retrograde formation of NaCl-scapolite in high pressure metaevaporites from the Cordilleras Beticas (Spain), *Contrib. Mineral. Petrol.*, 116, 448-461.

Harley, S.L. and Buick, I.S., 1992. Wollastonite-scapolite assemblages as indicators of granulite pressure-temperature-fluid histories: the Rauer Group, East Antarctica, *Journal of Petrology*, 33, 693-728.

Harley, S.L., Fitzsimons, I.C.W. and Buick, I.S., 1994. Reactions and textures in wollastonite-scapolite granulites and their significance for pressure-temperature-fluid histories of high-grade terranes, *Precambrian Research*, 66, 309-323.

Jiang, S.-Y., Palmer, M.R., Xue, C.-J. and Li, Y.-H., 1994. Halogen-rich scapolite-biotite rocks from the Tongmugou Pb-Zn deposit, Qinling, north-western China: Implications for the ore-forming processes, *Mineral. Mag.*, 58, 543-552.

Kassoli-Fournaraki, A., 1981. Contribution to the mineralogical and petrological study of amphibolitic rocks of the Serbomacedonian massif. PhD thesis, Aristotle University of Thessaloniki, 231 pp. (In Greek).

Kassoli-Fournaraki, A., 1991. Ca-rich scapolite in quartz amphibolites from the Sarti area, northern Greece, *Eur. J. Min.*, 3, 887-94.

Kilias, A., Falalakis, G., Sfeikos, A., Papadimitriou, E., Vamvaka, A. and Gkarlaouni, Ch., 2011. Architecture of Kinematics and Deformation History of the Tertiary Supradetachment Thrace Basin: Rhodope Province (NE Greece), *In:* New Frontiers in Tectonic Research - At the Midst of Plate Convergence, In Tech, 241-268.

Kullerud, K., 1996. Chlorine-rich amphiboles: Interplay between amphibole composition and an evolving fluid, *European Journal of Mineralogy*, 8, 355-370.

Kullerud, K. and Erambert, M., 1999. Cl-scapolite, Cl-amphibole, and plagioclase equilibria in ductile shear zones at Nusfjord, Lofoten, Norway: Implications for fluid compositional evolution during fluid-mineral interaction in the deep crust, Geochimica et Cosmochimica Acta, 63, 3829-*3844.*

Larsen, J.G., 1981. Medium pressure crystallization of a monchiquitic magma: Evidence from megacrysts of Drever's block, Ubekendt Ejland, West Greenland, *Lithos*, 14, 241-262.

Liati, A., 1986. Regional metamorphism and overprinting contact metamorphism of the Rhodope Zone, near Xanthi (N. Greece): petrology, geochemistry, geochronology, PhD thesis, Techn. Univ. Braunschweig, 186 pp.

Maltezou, F. and Brooks, M., 1989. A geophysical investigation of post-Alpine granites and Tertiary sedimentary basins in northern Greece, *Journal of the Geologial Society*, London, 146, 53-59.

Markl, G. *and Bucher, K.*, 1998. *Composition of fluids in the lower crust inferred from metamorphic salt in lower crustal rocks, Nature*, 391, 781-*783.*

Markl, G. and Piazolo, S., 1998. Halogen-bearing minerals in syenites and high-grade marbles of Dronning Maud Land, Antarctica: monitors of fluid compositional changes during late-magmatic fluid-rock interaction processes, *Contributions to Mineralogy and Petrology*, 132, 246-268.

Melfos, V. and Voudouris, P.C., 2012. Geological, Mineralogical and Geochemical Aspects for Critical and Rare Metals in Greece, *Minerals*, 2, 300-317.

Moecher, D.P. and Essene, E.J., 1991. Calculation of CO_2 activities using scapolite equilibria: Constraints on the presence and composition of a fluid phase during high grade metamorphism, *Contrib. Mineral. Petrol*., 108, 219-240.

Mora, C.I. and Valley, J.W., 1989. Halogen-rich scapolite and biotite: Implications for metamorphic fluid-rock interactions, *Am. Mineral*., 74, 721-737.

Mposkos, E. and Baziotis, I., 2005. Petrology and geochemistry of amphibolitized eclogites and trondhjemitic dykes from Organi-Kimi area of Eastern Rhodope, 2nd conference of the Committee of Economic Geology, Mineralogy and Geochemistry of the Geological Society of Greece, 259-268 (In Greek).

Mposkos, E., 1978. Scapolite of Seriphos and the garnet composition of several garnetites of the island, *Bull. Soc. Geol. Greece*, 13(2), 34-45 (In Greek).

Munoz, J.L. and Swenson, A., 1981. Chloride-hydroxyl exchange in biotite and estimation of relative HCl/HF activities in hydrothermal fluids, *Econ. Geol.*, 76, 2212-21.

Newton, R.C. and Goldsmith, J.R., 1975. Stability of the scapolite meionite ($3CaAl_2Si_2O_8{\cdot}CaCO_3$) at high pressure and storage of CO_2 in the deep crust, *Contributions to Mineralogy and Petrology*, 49, 49-62.

Orville, P.M., 1975. Stability of scapolite in the system Ab-An-NaCl-$CaCO_3$ at 4kb and 750° C, *Geochimica et Cosmochimica Acta*, 39, 1091-1095.

Pan, Y., Fleet, M.E. and Ray, G.E., 1994. Scapolite in two gold deposits: Nickel Plate, British Columbia and Hemlo, Ontario, *Canadian Mineral*, 32, 825-837.

Pan, Y., 1998. Scapolite in skarn deposits: Petrogenetic and geochemical ignificance. *In:* Mineralized Intrusion-Related Skarn Systems, Lentz, D.R., *ed*., *Mineralogical Association of Canada Short Course Series*, 26, 69-109.

Rebbert, C.R. and Rice, J.M., 1997. Scapolite-plagioclase exchange: Cl-CO_3 scapolite solution chemistry and implications for peristerite plagioclase, *Geochim. Cosmochim. Acta*, 61, 555-567.

Sherriff, B.L., Sokolova, E.V., Kabalov, Y.K., Jenkins, D.M., Kunath-Fandrei, G., Goetz, S., Jäger, C. and Schneider, J., 2000. Meionite: Rietveld structure-refinement, ^{29}Si Mas and ^{27}Al Satras NMR spectroscopy, and comments on the marialite-meionite series, *Can. Mineral*, 38, 1201-1213.

Skarpelis, N. and Liati, A., 1991. Wollastonite and associated copper mineralization in the contact metamorphic aurole of Kimmeria, Xanthi, N. Greece, *Bulletin of the Geological Society of Greece*, 25(2), 369-377.

Sokolova, E.V., Kabalov, Y.K., Sherriff, B.L., Teertstra, D.K., Jenkins, D.M., Kunath-Fandrei, G., Goetz, S. and Jäger, C., 1996. Marialite: Rietveld structure-refinement and ^{29}Si Mas and ^{27}Al satellite transition NMR spectroscopy, *Can. Mineral*., 34, 1039-1050.

Strauss, T.A.L., 2003. *The geology of the Proterozoic Haveri Au-Cu deposit, Southern Finland,* PhD thesis, Rhodes University.

Svensen, H., Jamtveit, B., Banks, D.A. and Austrheim, H., 2001. Halogen contents of eclogite facies fluid inclusions and minerals: Caledonides, western Norway, *Journal of Metamorphic Geology*, 19, 165-178.

Tsokas, G.N., Christofides, G.C. and Papakonstantinou, C., 1996. A geophysical study of the granites and the sedimentary basins of the Xanthi area (N. Greece), *"PAGEOPH"*, 146, 2, 365-392.

Touret, J.L.R. and Nijland, T.G., 2013. Prograde, peak and retrograde metamorphic fluids and associated metasomatism in upper amphibolite to granulite facies transition zones. *In:* Harlow, D. and Austrheim, H., *eds*., Metasomatism and the Chemical Transformation of Rocks, Lecture Notes in Earth System Science. Springer, Berlin-Heidelberg, 415-471.

Vavelidis, M., Michailidis, K., Christofides, G. and Boboti, I., 1990. Geochemical study of placer gold and the gold bearing skarn type mineralization of the Kimmeria area, Xanthi district, NE Greece, *Geologica Rhodopica*, 2, 297-308.

Vanko, D.A. and Bishop, F.C., 1982. Occurrence and origin of marialitic scapolite in the Humbold lopolith, N.W. Nevada, *Contributions to Mineralogy and Petrology*, 81, 277-289.

Voudouris, P., Melfos, V., Moritz, R., Spry, P.G., Ortelli, M. and Kartal, T., 2010. Molybdenite Occurrences in Greece: Mineralogy, Geochemistry and Rhenium Content, *In:* Scientific Annals of the School of Geology AUTH, *Proceedings of the XIX Congress of the Carpathian-Balkan Geological Association*, Thessaloniki, Greece, 23-26 September 2010, 369-378.

Yardley, B., Gleeson, S., Bruce, S. and Banks, D., 2000. Origin of retrograde fluids in metamorphic rocks, *J. Geochem. Explor.*, **69**, 281-285.

Zhu, C. and Sverjensky, D.A., 1991. Partitioning of F-Cl-OH between minerals and hydrothermal fluids, *Geochimica et Cosmochimica Acta*, 55, 1837-1858.

Δελτίο της Ελληνικής Γεωλογικής Εταιρίας, τόμος L, σελ. 1952-1958
Πρακτικά 14ου Διεθνούς Συνεδρίου, Θεσσαλονίκη, Μάιος 2016

Bulletin of the Geological Society of Greece, vol. L, p. 1952-1958
Proceedings of the 14th International Congress, Thessaloniki, May 2016

EASILY LEACHABLE RARE EARTH ELEMENT PHASES IN THE PARNASSUS-GIONA BAUXITE DEPOSITS, GREECE

Mouchos E.[1], Wall F.[1], Williamson B.J.[1] and Palumbo-Roe B.[2]

[1]Camborne School of Mines, University of Exeter, Penryn, UK, em415@exeter.ac.uk, f.wall@exeter.ac.uk, b.j.williamson@exeter.ac.uk

[2]British Geological Survey, Environmental Science Centre, Keyworth, Nottingham, UK, bpal@bgs.ac.uk

Abstract

The Parnassus-Giona karst bauxite deposits contain significant concentrations of rare earth elements (400-500 ppm). Preliminary results from a pilot leaching study show that between 19 and 47% of rare earth elements in the bauxite are easily leachable using ion exchange agents such as ammonium sulphate.
Keywords: *Rare earth element leaching, bauxite, Parnassus-Giona.*

Περίληψη

Τα κοιτάσματα καρστικού βωξίτη Παρνασσού-Γκιώνας περιέχουν σημαντικές συγκεντρώσεις σπανίων γαιών (400-500 ppm). Τα πρώτα αποτελέσματα από μια πιλοτική έρευνα ανάκτησης δείχνουν ότι μεταξύ 19 και 47% των σπανίων γαιών στο βωξίτη ανακτώνται εύκολα με χρήση ιοντοανταλλακτών όπως το θειικό αμμώνιο.
Λέξεις κλειδιά: *Ανάκτηση σπανίων γαιών, βωξίτης, Παρνασσός-Γκιώνα.*

1. Introduction

Rare earth elements (REE) have been recently classed as "critical metals" because of rising global demand, due to their use in many new, green and emerging technologies (EC, 2014), and because of a near monopoly (~97%) in supply from China (Chakhmouradian and Wall, 2012; Kynicky *et al.,* 2012). Other countries producing REE, in order of decreasing production are USA, India, Australia, Russia, Thailand, Malaysia and Vietnam (USGS, 2015). In addition there are currently extremely low rates of recycling, less than 1 % (Chakhmouradian and Wall, 2012). These factors increase the urgency to identify alternative REE resources. Most of the world's supply of heavy REE (HREE) comes from around 200 mines working so-called ion-adsorption deposits (or weathered crust elution-deposited rare earth ores) across southern China (Jiangxi, Hunan, Guangdong, Guangxi and Fujian provinces) (Bao and Zhao, 2008; Chi and Tian, 2008). These deposits were formed by *in situ* lateritic weathering of REE rich felsic rocks (mainly granites), which led to the formation of weathered profiles containing residual REE-clays (Kynicky *et al.,* 2012; Moldoveanu and Papangelakis, 2012). A proportion of the REE in these deposits is adsorbed onto the surfaces of clays. REE can be easily removed from the clays using ion exchange agents such as magnesium chloride, EDTA or ammonium sulphate.

Laterites and bauxites are ores formed in tropical soils by weathering processes and are enriched in iron and aluminum, respectively (Retallack, 2010). Some lateritic deposits are also mined for their nickel, gold, niobium, phosphorus and REE concentrations (Freyssinet *et al.,* 2005; Wall, 2014).

Although laterites and bauxites of Central Greece contain REE (Valeton *et al.,* 1987), they are not mined for REE because their concentrations are relatively low. The aim of the current study was to assess the concentrations and leachability of REE in Greek bauxites, which are currently being mined as a commercial source of aluminum, and for which Greece has large reserves (9th country worldwide and 1st in the EU according to the USGS (2015)). Although there have been few studies on the REE potential of Greek bauxites, a number have found significant concentrations in the red mud waste from their processing using the Bayer Process (e.g. Ochsenkühn-Petropulu *et al.,* 1994; Deady *et al.,* 2014; Borra *et al.,* 2015; Gamaletsos *et al.,* 2016).

The main differences between bauxite, red mud waste and ion-absorption clays is that bauxite contains significantly lower concentrations of Si compared with ion-absorption clays, and significantly higher levels of Al compared with red mud. Fulford *et al.* (1991) developed a protocol for the extraction of REE from Jamaican red mud waste using sulphur dioxide. Although this method showed that REE appear to be readily leachable from red mud waste using diluted mineral acids, they cannot be leached from bauxite under the same experimental conditions (Fulford *et al.,* 1991; Binnemans *et al.,* 2013). However, Gamaletsos *et al.* (2016) recently achieved a significant recovery of REE from both Greek bauxites and red muds using acetic acid. The aim of this paper is to present preliminary results from a pilot leaching study of Greek bauxite using an ammonium sulphate [$(NH_4)_2SO_4$] solution as leaching agent.

2. Greek Bauxite Characteristics

The most economically important bauxite deposits in Greece are those of the Parnassus-Giona area (B3 or 3rd bauxite horizon). These belong to the Mediterranean-type allochthonous karst bauxites, which occur as layers or pockets and were formed by lateritic weathering processes (Valeton *et al.*, 1987; Tsirambides and Filippidis, 2012). The mineralogy of these bauxites is dominated by the aluminium oxide monohydrates boehmite [(γ-AlO(OH)] and diaspore [(α-AlO(OH)], the iron oxides hematite (Fe_2O_3) and goethite [FeO(OH)], the titanium oxide anatase (TiO_2), and secondary minerals including kaolinite [$Al_2Si_2O_5(OH)_4$] among others (Valeton *et al.,* 1987; Tsirambides and Filippidis, 2012). The Parnassus-Giona bauxite contains up to 5% of kaolinite as well as lesser amounts of other clay minerals such as illite and chamosite (Tsirambides and Filippidis, 2012; Laskou and Economou-Eliopoulos, 2013). Kaolinite occurs locally as mixtures with Al hydroxides. Low pressure/low temperature alteration of bauxite grains and matrix, possibly aided by down-flowing siliceous waters through pores, cracks and fissures, results in kaolinisation (Dangić, 1988).

Greek bauxite deposits contain an average of approximately 400-500 ppm REE (Ochsenkühn-Petropoulou *et al.,* 1994; Deady *et al.,* 2014). REE are found at both detrital and authigenic REE-bearing minerals in bauxite. The latter are significantly more abundant and usually minute in size (<1 μm), occasionally forming larger aggregates or occurring as micropore and fissure fillings (Maksimović and Pantó, 1996). The authigenic REE-bearing minerals reported at the Parnassus-Giona bauxite are LREE fluorocarbonate minerals of the bastnäsite ($(Ce,La)CO_3F$) and parasite ($Ca(Ce,La)_2(CO_3)_3F_2$) group (Gamaletsos et al., 2011; 2016). On the other hand, the detrital ones are the LREE phosphates rhabdophane ($(Ce,La)PO_4{\cdot}(H_2O)$) and florencite ($CeAl_3(PO_4)_2(OH)_6$), and the Y-phosphates churchite ($YPO_4{\cdot}2(H_2O)$) and xenotime (YPO_4) (Laskou and Andreou, 2003). The crystallisation of authigenic REE-bearing minerals towards the base of the bauxite deposits occurs due to the downward transport of relatively mobile elements (including the REE) (Valeton *et al.*, 1987; Ochsenkühn *et al.,* 1991; Maksimović and Pantó, **1996;** Deady *et al.,* 2014**)**. Although *per descensum* enrichment results occasionally in very high REE concentrations near the limestone bedrock, it is not a standard feature of every bauxite deposit.

3. Materials and Methods

Bauxite samples were collected from the upper parts of Delphi-Distomon S.A. (subsidiary of Aluminium of Greece S.A.) underground mines and were analyzed for their trace element contents by ICP-MS. The B3 (3rd bauxite horizon) active mines were selected due to their importance for the

bauxite exploitation in Greece. Samples Baux 1 and Baux 2 were collected at an altitude of 577 m and 500 m, and at 4.5 m and 9.5 m above the chamber floor respectively. However, both profiles have a greater depth given that "room-and-pillar" mining progresses vertically following the slope of the deposit. Preparation of the samples was carried out at the Camborne School of Mines (Penryn, UK), whilst sample preparation, by lithium borate fusion followed by acid digestion protocol (LF100 analysis for refractory elements and REEs), and ICP-MS analysis was carried out at Acme Labs (Canada).

In order to investigate the potential presence of adsorbed REE cations in bauxite the ammonium sulphate extraction method from the sequential extraction procedure presented in Sanematsu *et al.* (2013) was used. Sanematsu *et al.* (2013) used a modified BCR method of Rauret *et al.* (1999, 2000) for ion-adsorption clays in Thailand. More precisely, they substituted the first step of the BCR method for one using ammonium sulphate, which is also used for cation exchange at many of the mines in China. The first step was carried out at a slightly acidic pH that may also dissolve some of the carbonate. Preparation and analysis of the leachates was carried out at the British Geological Survey (Keyworth, UK). The REE leaching protocol used in the current paper is the following:

1. 1 g of sample is placed in a 50 ml centrifuge tube
2. 40 ml ± 0.1 ml volume of 0.5 M $(NH_4)_2SO_4$ solution added
3. Tube shaken to achieve a suspension
4. Adjust the pH to 4 by adding H_2SO_4
5. 16 h end-over-end shaking
6. Centrifugation of tubes for 20 mins at 3000 rpm (or until supernatant/solid separation is obtained)
7. Allow any residual suspended solid to settle for 15 mins
8. An aliquot from the tube is sampled and the sampled eluate is filtered through a 0.45 μm filter
9. The filtered solution is acidified using HNO_3 and analysed for REE with ICP-MS

4. Results

The two Greek bauxite samples are enriched in light REE (LREE) with approximately 600 ppm of REE in total. The extraction by 0.5 M $(NH_4)_2SO_4$ at pH4 leached 19% (114 ppm) and 47% (278 ppm) of total REE from Baux 1 and Baux 2 samples, respectively (Table 1). Chondrite normalized REE patterns of both bauxite samples and their leachates show a positive Ce anomaly and a negative Eu anomaly, which seem to be common in the Parnassus-Giona bauxites and red muds (Ochsenkühn-Petropulu *et al.*, 1994; Laskou and Andreou, 2003; Deady *et al.*, 2014). Chondrite-normalized data plotted on a graph also show that a higher proportion of LREE can be leached compared with HREE (Figure 1). Leaching results show that the two samples have significant differences in the proportion of the REE being leached. More precisely, ammonium sulphate leached almost the same proportion of HREE (19%) from the two bauxite samples, whereas it leached higher amounts of LREE from Baux 2 sample (52%) compared with those of Baux 1 sample (19%). Nevertheless, the total REE amount leached does not reach the 500 ppm of leachable REE that is required by Bao and Zhao (2008) to satisfy the definition of ion-adsorption ore.

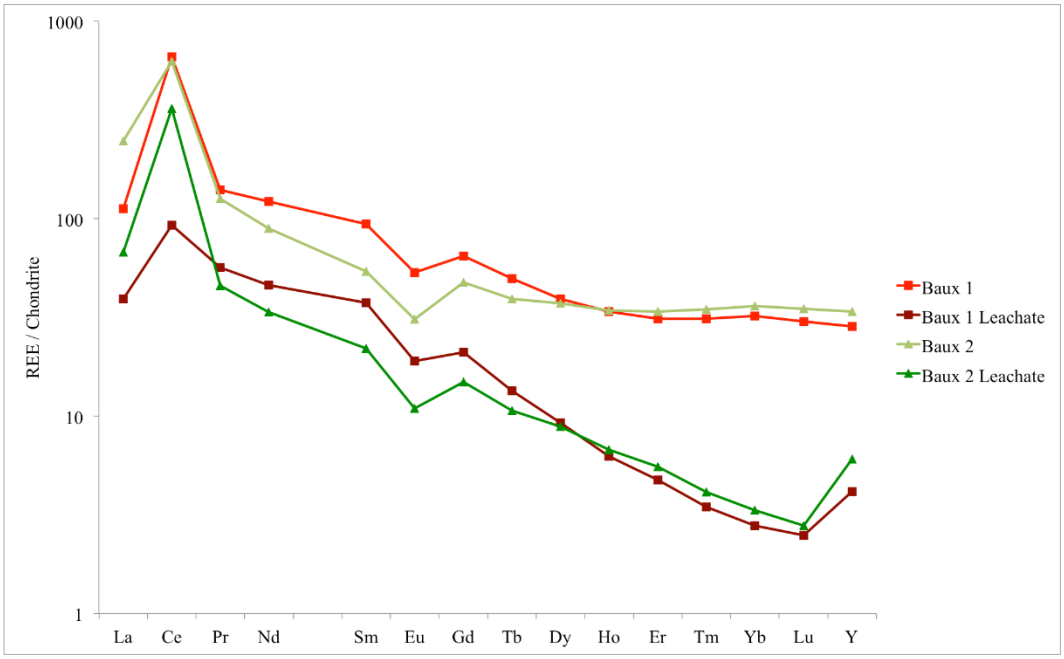

Figure 1 - Chondrite-normalized (McDonough and Sun, 1995) REE patterns in Greek bauxite samples and leachates.

LREE occur as very fine, crystalline, slightly soluble LREE carbonate/hydroxycarbonate minerals in the bauxite samples leached, usually forming clusters or filling micropores and fissures (Figure 2). Ammonium sulphate is supposed only to exchange cations from the surface of minerals and not dissolve them. However, at the leaching experimental conditions of this study (pH 4), it may have caused some dissolution of these minerals. Consequently, preferential LREE fractionation into solution, relative to HREE, may have been caused by a partial dissolution of the LREE minerals in the bauxite. In addition the lanthanide contraction that controls the grouping of LREE and HREE into different mineral hosts may also have an effect on the cation exchange behaviour.

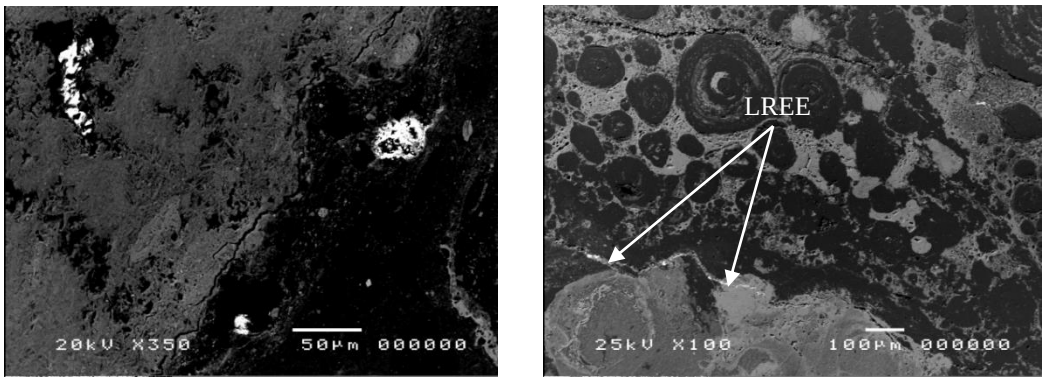

Figure 2 - BSE-SEM images of LREE carbonate/hydroxycarbonate minerals in Greek bauxite samples (Wall *et al.*, 2014).

5. Discussion

Concentrations of REE in Greek bauxite and red muds are low (usually <1,000 ppm) compared with carbonatite deposits such as Mountain Pass and Mount Weld, which have grades of around 80,000 ppm REE (Wall, 2014). They are more comparable to those in lower grade Chinese ion-adsorption

clay deposits that usually contain 500-2,000 ppm REE (Kynicky *et al.*, 2012; Moldoveanu and Papangelakis, 2012). Heterogeneity and differences in the chemistry of bauxite and red mud make it difficult to develop a common REE leaching method that can extract 100% of REE from bauxite or its by-products. Currently, the focus of REE extraction is mainly on red mud as it has double the REE concentrations compared with the initial bauxite (Ochsenkühn-Petropoulou *et al.*, 1994). Various studies have achieved significant results towards this direction using acids (e.g. Ochsenkühn-Petropoulou *et al.*, 1996; Borra *et al.*, 2015; Gamaletsos *et al.*, 2016), but these still need more development in order to be economically feasible and able to be established as parts of aluminium's industry.

Table 1 - Leaching results for REE, showing the leached amounts of REE after using a protocol based on Sanematsu *et al.* (2013).

	Baux 1 (ppm)	Baux 1 Leachate (ppm)	Baux 1 REE % Leached	Baux 2 (ppm)	Baux 2 Leachate (ppm)	Baux 2 REE % Leached
La	26.70	9.31	34.88	58.80	16.01	27.22
Ce	404.20	56.82	14.06	384.80	221.84	57.65
Pr	13.01	5.24	40.28	11.68	4.25	36.41
Nd	55.80	21.09	37.80	40.70	15.36	37.74
Sm	13.91	5.55	39.91	7.99	3.26	40.81
Eu	3.01	1.07	35.48	1.74	0.61	35.31
Gd	12.88	4.19	32.55	9.47	2.96	31.21
Tb	1.80	0.48	26.91	1.42	0.38	27.03
Dy	9.68	2.27	23.46	9.16	2.18	23.84
Ho	1.85	0.34	18.44	1.87	0.37	19.72
Er	4.99	0.76	15.27	5.40	0.89	16.41
Tm	0.77	0.09	11.10	0.86	0.10	11.87
Yb	5.18	0.45	8.67	5.82	0.54	9.20
Lu	0.74	0.06	8.27	0.86	0.07	7.97
Y	44.60	6.52	14.62	53.20	9.50	17.86
ΣREE	599.12	114.25	19.07	593.77	278.32	46.87
ΣLREE	513.62	98.01	19.08	503.97	260.72	51.73
ΣHREE	85.50	16.24	18.99	89.80	17.60	19.60

Note: ΣREE are La-Lu and Y, LREE are La-Sm and HREE are Eu-Lu and Y (Wall, 2014)

Our preliminary results suggest that up to ~50 % of the total REE in bauxite (especially in the upper parts of the weathered profile) could be leached easily using ammonium sulphate (Table 1 and Figure 1). Consequently, leaching 100-300 ppm of REE directly from bauxite results in consuming fewer and cheaper reagents compared with red muds, where large amounts of strong acids and long digestion time periods are needed to leach high proportions (almost 80%) of REE (e.g Borra *et al.*, 2015). The high costs of acids needed for leaching as well as the low HREE contents of Greek red muds seem problematic for an economically feasible REE extraction. Moreover, the disposal of the acids used may have important environmental implications. The most important benefit of the suggested method is that it is less likely to interfere with the Bayer process because it may be easy to install and run in the plant at the point where bauxite is gathered, right before passing through the Bayer process.

The preliminary results presented in this study also indicate that the easily leachable REE in Greek bauxite, extracted using ammonium sulphate, may occur as ion-adsorbed phases, i.e. mainly as ions

adsorbed onto phases such as kaolinite, illite and chamosite, which are present in Greek bauxite (Tsirambides and Filippidis, 2012; Laskou and Economou-Eliopoulos, 2013). These REE phases will not be retained in the solid phase after the bauxite passes the Bayer process, due to the ore processing in a concentrated sodium hydroxide (NaOH) solution at various temperatures and pressures (Power *et al.*, 2011; Binnemans *et al.*, 2015). It is therefore likely that an ammonium sulphate leaching method may not be efficient in removing REE for red mud waste.

6. Conclusions

Our pilot study suggests that some amounts of REE could be leached in a simple and cheap way by taking advantage of some easily leachable REE phases occurring in bauxite. Even if those amounts are relatively small, application of this method could result in further income for Aluminium of Greece S.A., in addition to the induction of Greece and hence EU in the rare earth oxide (REO) production chain. However, further research focused on improved characterization of bauxite and red mud waste phases, selective mining of REE enriched bauxites, and the development of efficient REE recovery techniques from bauxites and red muds, is required to fully assess these potentially important resources.

7. Acknowledgements

The authors would like to thank Delphi-Distomon S.A. (subsidiary of Aluminium of Greece S.A.) for permitting the collection of bauxite samples. The British Geological Survey (BGS) laboratories are also gratefully acknowledged.

8. References

Bao, Z. and Zhao, Z., 2008. Geochemistry of mineralization with exchangeable REY in the weathering crusts of granitic rocks in South China, *Ore Geology Reviews*, 33, 519-535.

Binnemans, K., Jones, P.T., Blanpain, B., Van Gerven, T. and Pontikes, Y., 2015. Towards zero-waste valorisation of rare-earth-containing industrial process residues: a critical review. *Journal of Cleaner Production*, 99, 17-38.

Binnemans, K., Pontikes, Y., Jones, P.T., Van Gerven, T. and Blanpain, B., 2013. Recovery of rare earths from industrial waste residues: a concise review. *In*: *Proceedings of the 3rd International Slag Valorisation Symposium: The Transition to Sustainable Materials Management*, Leuven, Belgium, 191-205.

Borra, C.R., Pontikes, Y., Binnemans, K. and Van Gerven, T., 2015. Leaching of rare earths from bauxite residue (red mud), *Minerals Engineering*, 76, 20-27.

Chakhmouradian, A.R. and Wall, F., 2012. Rare earth elements: minerals, mines, magnets (and more). *Elements: an international magazine of mineralogy, geochemistry, and petrology*, 8, 333-340.

Chi, R. and Tian, J., 2008. Weathered crust elution-deposited rare earth ores, New York, *Nova Science Publishers*, 288 pp.

Dangić, A., 1988. Kaolinization of bauxite: a study of the Vlasenice bauxite area, Yugoslavia, II. Alteration of oolites, *Clays and Clay Minerals*, 36(5), 439-447.

Deady, É., Mouchos, E., Goodenough, K., Williamson, B. and Wall, F., 2014. Rare earth elements in karst-bauxites: a novel untapped European resource? ERES 1st European Rare Earth Resources conference, Milos, Greece.

European Commission, 2014. Report on critical raw materials for the EU. Report of the Ad Hoc Working Group on defining critical raw materials, 41 pp.

Freyssinet, Ph., Butt, C.R.M. and Morris, R.C., 2005. Ore-forming processes related to lateritic weathering, *Econ. Geol*., 100th Anniversary Volume, 681-722.

Fulford, G.D., Lever, G. and Sato, T., 1991. Recovery of rare earth elements from red mud, BR9001453A.

Gamaletsos, P., Godelitsas, A., Mertzimekis, T.J., Göttlicher, J., Steininger, R., Xanthos, S., Berndt, J., Klemme, S., Kuzmin, A. and Bárdossy, G., 2011. Thorium partitioning in Greek industrial bauxite investigated by synchrotron radiation and laser-ablation techniques. *Nuclear*

Instruments and Methods in Physics Research Section B: Beam Interactions with Materials and Atoms, 269, 3067-3073.

Gamaletsos, P.N., Godelitsas, A., Kasama, T., Kuzmin, A., Lagos, M., Mertzimekis, T.J., Göttlicher, J., Steininger, R., Xanthos, S., Pontikes, Y., Angelopoulos, G.N., Zarkadas, C., Komelkov, A., Tzamos, E. and Filippidis, A., 2016. The role of nano-perovskite in the negligible thorium release in seawater from Greek bauxite residue (red mud), *Sci. Rep*., 6, 21737, doi: 10.1038/srep21737.

Kynicky, J., Smith, M.P. and Xu, C., 2012. Diversity of rare earth deposits: the key example of China. *Elements: an international magazine of mineralogy, geochemistry, and petrology*, 8, 361-367.

Laskou, M. and Andreou, G., 2003. Rare earth element distribution and REE-minerals from the Parnassos-Ghiona bauxite deposits, Greece, Biennial Society for Geology Applied to Mineral Deposits Meeting, 7th, Mineral Exploration and Sustainable Development, Athens, Greece, 2003, *Conference Proceedings*, 89-92.

Laskou, M. and Economou-Eliopoulos, M., 2013. Bio-mineralization and potential biogeochemical processes in bauxite deposits: genetic and ore quality significance, *Mineralogy and Petrology*, 407(4), 171-186.

MacDonough, W.F. and Sun, S.-S., 1995. The composition of the Earth, *Chemical Geology*, 120, 223-253.

Maksimović, Z. and Pantó, G., 1996. Authigenic rare earth minerals in karst-bauxites and karstic nickel deposits. *In*: Jones, A.P., Wall, F. and Williams, C.T., *eds*., Rare earth minerals, chemistry, origin and ore deposits, Chapter 10, 257-279.

Moldoveanu, G. and Papangelakis, V.G., 2012. Recovery of rare earth elements adsorbed on clay minerals: I. Desorption mechanism, *Hydrometallurgy*, 117-118 71-78.

Ochsenkühn-Petropoulou, M., Lyberopoulou, Th. and Parissakis, G., 1994. Direct determination of lanthanides, yttium and scandium in bauxites and red mud from alumina production, *Analytica Chimica Acta*, 296(3), 305-313.

Ochsenkühn-Petropulou, M., Ochsenkühn, K. and Luck, J., 1991. Comparison of inductively coupled plasma mass spectrometry with instrumental neutron activation analysis for the determination of rare earth elements in Greek bauxites, *Spectrochim. Acta*, 46, 51-65.

Ochsenkühn-Petropulu, M., Lyberopulu, T., Ochsenkühn, K.M. and Parissakis, G., 1996. Recovery of lanthanides and yttrium from red mud by selective leaching, *Analytica Chimica Acta*, 319, 249-254.

Power, G., Gräfe, M. and Klauber, C., 2011. Bauxite residue issues: I. Current management, disposal and storage practices, *Hydrometallurgy*, 108, 33-45.

Rauret, G., López-Sànchez, J.F., Sahuquillo, A., Barahona, E., Lachica, M., Ure, A.M., Davidson, C.M., Gomez, A., Lück, D., Bacon, J., Yli-Halla, M., Muntau, H. and Quevauviller, Ph., 2000. Application of a modified BCR sequential extraction (three-step) procedure for the determination of extractable trace metal contents in a sewage sludge amended soil reference material (CRM 483), complemented by a three-year stability study of acetic acid and EDTA extractable metal content, *J. Environ. Monit*., 2, 228-233.

Rauret, G., López-Sánchez, J.F., Sahuquillo, A., Rubio, R., Davidson, C., Ure, A. and Quevauviller, Ph., 1999. Improvement of the BCR three step sequential extraction procedure prior to the certification of new sediment and soil reference materials, *J. Environ. Monit.*, 1, 57-61.

Retallack, G.J., 2010. Lateritization and bauxitization events, *Economic Geology*, 105, 655-667.

Sanematsu, K., Kon, Y., Imai, A., Watanabe, K. and Watanabe, Y., 2013. Geochemical and mineralogical characteristics of ion-adsorption type REE mineralization in Phuket, Thailand, *Miner. Deposita*, 48, 437-451.

Tsirambides, A. and Filippidis, A., 2012. Metallic mineral resources of Greece, *Central European Journal of Geosciences*, 4(4), 641-650.

U.S. Geological Survey, 2015. Mineral commodity summaries 2015. Reston, VA, U.S. Geological Survey, 196.

Valeton, I., Bierman, M., Reche, R. and Rosenberg, F.F., 1987. Genesis of nickel laterites and bauxites in Greece during the Jurassic and the Cretaceous and their relation to ultrabasic rocks, *Ore Geol. Rev*., 2, 359-404.

Wall, F., 2014. Rare earth elements. *In*: Gunn, G., Critical Metals Handbook, Chapter 13, 312-339.

Wall, F., Mouchos, E. and Loye, E., 2014. Processing weathered REE deposits. Geology to Metallurgy of Critical Rare Earths (GEM-CRE). Workshop 3, Camborne School of Mines, UK.

Δελτίο της Ελληνικής Γεωλογικής Εταιρίας, τόμος L, σελ. 1959-1968
Πρακτικά 14ου Διεθνούς Συνεδρίου, Θεσσαλονίκη, Μάιος 2016

Bulletin of the Geological Society of Greece, vol. L, p. 1959-1968
Proceedings of the 14th International Congress, Thessaloniki, May 2016

THE KONDAROS-KATSIMOUTI INTERMEDIATE-SULFIDATION EPITHERMAL PB-ZN-AG-MN MINERALIZATION, WESTERN MILOS, GREECE: NEW MINERALOGICAL AND GEOCHEMICAL DATA

Papavasiliou K.[1], Voudouris P.[2], Kanellopoulos C.[3], Alfieris D.[4] and Xydous S.[2]

[1]*Faculty of Geology and Geoenvironment, University of Athens, Department of Economic Geology & Geochemistry, Panepistimiopolis A. Ilisia 15784 Athens/Greece, papavas@geol.uoa.gr*

[2]*Faculty of Geology and Geoenvironment, University of Athens, Department of Petrology, Panepistimiopolis A. Ilisia 15784 Athens/Greece, voudouris@geol.uoa.gr, stxydous@geol.uoa.gr*

[3]*Institute of Geology and Mineral Exploration, 1st Spirou Louis St., Olympic Village, 13677, Acharnae, Greece, ckanellopoulos@gmail.com*

[4]*Imerys Filtration, 15A Metaxa Street, Kifisia 14564, Greece, Dimitris.Alfieris@imerys.com*

Abstract

The metallic mineralization in Kontaros-Katsimouti area is an epithermal Pb-Zn-Ag mineralization located along the NW-trending Kondaros-Katsimouti-Vani fault, NW Milos Island, Greece. It is hosted within propylitically and argillically altered dacitic flow dome and volcaniclastic sandstone and shows features typical of intermediate sulfidation deposits like colloform banding, cockade breccias and gangue adularia, Mn-rich carbonates and amethystine quartz. The Kondaros-Katsimouti system evolves at higher elevation into the Vani Ag-Pb mineralization, which occurs proximal to the Vani manganese deposit. The metallic mineralogical assemblage at Kondaros-Katsimouti includes mainly galena and sphalerite and minor pyrite. Silver is present in the form of Ag-(Cd)-rich tetrahedrite (up to 23.1 wt. % Ag) and polybasite included in galena. Bulk ore analyses indicate enrichment in W (up to 424 mg/kg) and Mo (up to 24 mg/kg), similarly to the other neighboring mineralizations in western Milos (e.g. Vani, Triades-Galana). This enrichment suggests a magmatic-hydrothermal contribution to the ore fluids, probably from a buried granitoid at depth. Boiling, in addition to mixing processes between magmatic- and seawater, resulted in pH increase, oxidation and temperature decrease, and resulted into ore deposition.
Keywords: *Silver sulfosalts, tungsten, epithermal, boiling-mixing, Milos island.*

Περίληψη

Η επιθερμική μεταλλοφορία Pb-Zn-Ag στο Κοντάρο-Κατσιμούτι, αναπτύσσεται κατά μήκος του ΒΔ κατεύθυνσης ρήγματος Κοντάρος-Κατσιμούτι-Βάνι στη ΒΔ Μήλο. Πετρώματα ξενιστές αποτελούν προπυλιτιωμένοι έως αργιλλικά εξαλλοιωμένοι δόμοι δακιτικής λάβας και ηφαιστειοκλαστικοί ψαμμίτες. Η μεταλλοφορία Κοντάρου-Κατσιμουτίου παρουσιάζει χαρακτηριστικά τυπικά των επιθερμικών κοιτασμάτων ενδιάμεσης θείωσης,όπως ζωνώδης ανάπτυξη των φλεβών, υδροθερμικά λατυποπαγή, καθώς και παρουσία αδουλάριου, Mn-ούχου ασβεστίτη και αμέθυστου μεταξύ των σύνδρομων ορυκτών. Το σύστημα Κοντάτου-

Κατσιμουτίου εξελίσσεται σε υψηλότερα τοπογραφικά επίπεδα, στη μεταλλοφορία Ag-Mn του Βανίου, η οποία γειτνίαζει με το κοίτασμα Mn του Βανίου. Η μεταλλική ορυκτολογική παραγένεση στο Κοντάρο-Κατσιμούτι περιλαμβάνει κυρίως γαληνίτη και σφαλερίτη και σε μικρότερο ποσοστό σιδηροπυρίτη. Ο άργυρος απαντά σε μορφή Ag-(Cd)-ούχου τετραεδρίτη (έως 23.1 % κβ Ag) και πολυβασίτη που εγκλείονται στον γαληνίτη. Χημικές αναλύσεις μεταλλεύματος παρουσιάζουν εμπλουτισμό σε βολφράμιο (έως 424 mg/kg) και Mo (έως 24 mg/kg) αντίστοιχα με γειτονικά κοιτάσματα της Δ. Μήλου (Βάνι, Τριάδες-Γαλανά). Οι γεωχημικές αυτές ανωμαλίες υποδεικνύουν ένα ποσοστό μαγματικής-υδροθερμικής συνεισφοράς στα ρευστά, πιθανόν από γρανιτική διείσδυση στο βάθος. Βρασμός και ανάμειξη μεταξύ μαγματικών και θαλασσινών νερών, οδήγησαν σε αύξηση του pH, οξείδωση και μείωση της θερμοκρασίας, με τελικό αποτέλεσμα την απόθεση της μεταλλοφορίας.
Λέξεις κλειδιά: *Θειοάλατα αργύρου, βολφράμιο, επιθερμική, βρασμός-ανάμειξη, Μήλος.*

1. Introduction

Milos Island is one of the most densely mineralized areas in Greece, characterized by epithermal Au-Ag and base metal deposition within a Plio-Pleistocene volcanic edifice. Metallic mineralization on western Milos was the subject of several mineralogical and geochemical studies, with base- and precious metal mineralization having been classified as either Kuroko- (Hauck, 1988; Vavelidis and Melfos, 1998), seawater-dominated epithermal (Kilias *et al.*, 2001; Liakopoulos *et al.*, 2001; Marchik *et al.*, 2010), shallow submarine epithermal- (Alfieris, 2006; Stewart and McPhie, 2006; Alfieris *et al.*, 2013), or hybrid volcanogenic massive sulfide (VMS)-epithermal types (Naden *et al.*, 2005). A modern analogue for the setting of epithermal-style mineralization in western Milos is the shallow submarine Kolumbo hydrothermal vent field located 7 km NE of Santorini Island in the Hellenic arc (Kilias *et al.*, 2013). Along the NW-trending Kondaros-Katsimouti fault a base metal and Ag-bearing epithermal mineralization was found (Alfieris and Voudouris, 2005). This vein-system extends NW towards Cape Vani, and includes the Kondaros-Katsimouti Pb-Zn-Ag±Cu±Mn intermediate-sulfidation epithermal system (Alfieris and Voudouris, 2005) and the Vani Ag-Pb epithermal prospect, which is proximal to the Vani manganese deposit, and is highly enriched in Ag-bearing phases (e.g. native silver, argentite/acanthite, silver halides, argentian covellite) (Voudouris *et al.*, 2014). Already Alfieris and Voudouris (2005) suggested that epithermal banded quartz-chalcedony-barite-Mn-Fe veins at Katsimoutis represent feeder zones to the Vani stratiform Mn-Ba-Pb-Zn mineralization, described by Hein *et al.* (2000), Liakopoulos *et al.* (2001) and Glasby *et al.* (2005). Under this respect the Kondaros-Vani fault, played a major role in the formation of the Vani manganese deposit, since manganese deposition represents the final hydrothermal manifestation of the major Pb-Zn-Ag epithermal system. The latter also represents the sub-seafloor feeder zones of the stratiform Mn-Ba-Pb-Zn deposit that formed on the sea floor at Cape Vani (Alfieris and Voudouris, 2005).

The aim of the current study is to present new data on the metallic mineralization at Kontaros-Katsimouti area, to describe its mineralogical and geochemical characteristics and discuss the role of various physico-chemical mechanisms in its formation by comparing it with other mineralized areas in western Milos and elsewhere.

2. Geological setting and mineralization

Milos Island forms part of the Cycladic Blueschist in the Attico-Cycladic massif, a polymetamorphic terrane within the Alpine orogen of the Hellenides (Jolivet and Brun, 2010; Papanikolaou, 1987; Ring *et al.*, 2010). Miocene extension in the Aegean Sea was accompanied by the intrusion and extrusion of magmatic rocks at upper crustal levels (Altherr and Siebel, 2002). Milos is located in the central part of the Lower Pliocene to Recent South Aegean Active Volcanic Arc, which includes a belt of calc-alkaline volcanic centers (Sousaki, Aegina, Methana, Poros, Milos, Santorini, Kos,

and Nisyros) consisting mainly of basalts, andesites, dacites, and rhyolites (Fytikas *et al.*, 1986). It comprises mainly Neogene sediments and volcanic rocks overlying a metamorphic basement that consists of eclogites, glaucophane schists and mica schists (Fytikas *et al.*, 1986; Stewart and McPhie, 2006; Fig. 1). The Upper Miocene to Lower Pliocene sedimentary sequence contains basal conglomerates, shallow marine carbonates and sandstones from the base to top with minor intercalations of tuffs, and is succeeded by volcanic rocks that can be subdivided into four main phases from Middle to Upper Pliocene (3.5 Ma) to Pleistocene (0.08 Ma) (Alfieris *et al.*, 2013; Fytikas *et al.*, 1986; Stewart and McPhie, 2006): The earliest volcanic episode (Middle to Upper Pliocene, 3.5-3.0 Ma) produced a succession of felsic submarine units including pumice flows, tuffs and pumice rich pyroclastic flows, with locally intrusive subvolcanic bodies, lavas and/or hyaloclastites. Some volcanosedimentary products have been deposited in E-W directed graben structures from 3.0 to 2.7 Ma. The subsequent phase of submarine volcanism (Upper Pliocene-Lower Pleistocene, 2.7-1.4 Ma) is characterized by the emplacement of dacitic/andesitic domes, plugs and lava flows along a system of mainly NE-trending faults, and subordinately along NW-SE to E-W directions. These domes intruded and disrupted the still unconsolidated volcanosedimentary unit, suggesting contemporaneous emplacement in a shallow seawater environment. Hyaloclastitic margins around a flow banded coherent core and talus breccias characterize the subvolcanic emplacement of this volcanic rock into sediments. Based on SHRIMP U–Pb in zircon, Stewart and McPhie (2006) dated submarine dacite lavas at 2.18± 0.09 Ma and submarine to subaerial dacitic–rhyodacitic flow banded domes and their autobreccias at 1.44± 0.08 Ma (both at Triades). The effusive activity was accompanied locally by explosive episodes, which locally produced bedded pumiceous tuff cones and/or pyroclastic flows and breccias in submarine and partially subaerial environments. During Lower to Middle Pleistocene (1.4-0.5 Ma), intense shallow marine to subaerial pyroclastic activity associated with rhyolitic domes and lavas was developed in the eastern and northeastern part of the island.

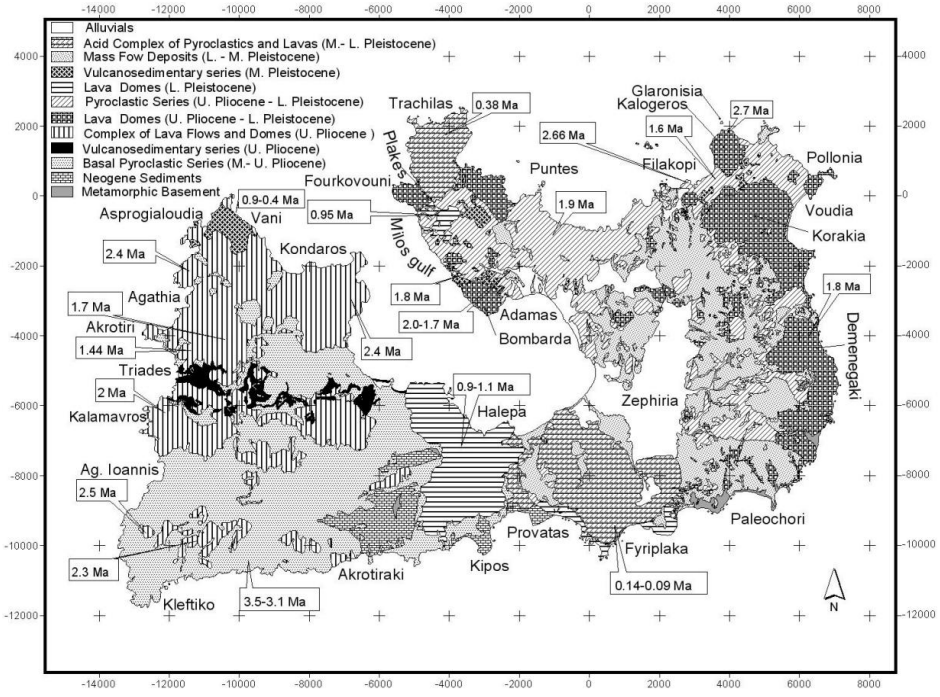

Figure 1 - Geological map of Milos Island showing the distribution of the main volcanic phases, metamorphic and sedimentary units, as well as geochronological data (after Fytikas *et al.*, 1986; Alfieris, 2006).

The most recent volcanic activity on Milos is concentrated along the eastern coast of Milos gulf, where there are felsic centres with ages of 0.38-0.08 Ma (Middle-Upper Pleistocene). At Milos Island, Miocene to Pliocene extensional tectonics resulted in four main fault sets trending NW, N, NE, and E.

The studied metallic mineralization is located along the NW-trending Kondaros-Katsimouti fault. The mineralization is hosted within propylitically and argillically altered dacitic flow dome and volcaniclastic sandstone and shows features typical of intermediate sulfidation deposits, like colloform banding and cockade breccias (Fig. 2a-c). The mineralized system consists of banded veins (up to 1 m thick and up to 100 m length) and stockworks, including alternating bands of quartz-chalcedony with galena, sphalerite and minor pyrite, hematite, chalcopyrite and silver-bearing sulfosalts (e.g. tetrahedrite and polybasite) (Fig. 2 and Table 1). Quartz, calcite, Mn-rich calcite, barite and adularia (e.g. sanidine) are the gangue minerals (Table 1).

3. Materials and methods

Fourty five thin- and polished-sections of the sulfide mineralization were prepared from eight samples of Kondaros-Katsimouti area: KO1A, KO1B, KO2, KA1, KA2 and KA3 along the NW-trending fault and KA4 and KA4Q located within the NE-trending Triades-Galana-Katsimouti fault. KO1 and KO2 represent a hydrothermal breccia composed of milky and amethystine quartz fragments within a matrix of sulfides, carbonates and barite. KA1 consists of epithermal vein material showing initial deposition of sulfides plus minor barite (KA1A) followed by colloform banded chalcedony, aragonite and hydrothermal manganese oxides (KA1B). KA2 represent epithermal vein composed of sulfides and barite cross cutting propylitized lavas as in KA1 but without the final stage of deposition of hydrothermal manganese oxides. KA3 is epithermal vein-material of manganese oxides, aragonite and minor barite cross cutting propylitized lavas. Finally, KA4 and KA4Q are quartz veins enriched in pyrite, galena, sphalerite and minor chalcopyrite.

The samples were studied by optical microscopy and a JEOL JSM 5600 scanning electron microscope, equipped with back-scattered imaging capabilities, at the Department of Mineralogy and Petrology, University of Athens. The chemical compositions of sulfides and sulfosalts were determined with a JEOL JSM 5600 scanning electron microscope, equipped with an automated energy dispersive analysis system ISIS 300 OXFORD, with the following operating conditions: accelerating voltage 20 kV, beam current 0.5 nA, time of measurement 50 s and beam diameter 1-2 mm. The spectra were processed using ZAF software. The mineralogical composition of the samples was also investigated through powder X-ray diffraction (XRD). The XRD study was carried out using a Siemens Model 5005 X-ray diffractometer in combination with the DIFFRAC plus software package. The diffractometer was operated using CuKα radiation at 40 kV and 40 mA and employing the following scanning parameters: step size 0.020° and step time from 1.0 to 20.0 sec. The raw files (XRD diagrams) were evaluated with the EVA 10.0 software (Table 1).

Table 1. Semi-quantitative (XRD) mineralogical estimation of the samples from Kondaros (KO) and Katsimouti (KA) area.

*Mineral abundances: ***** =dominant; **** = abundant; ***common; ** = minor; * = rare.*

	Barite	Sanidine	Quartz	Sphalerite	Galena	Pyrite	Calcite	Mn-calcite	Hematite
KA-1A	**	**		*****	***	*	*****	****	
KA-1B			*				*****	*****	**
KA-2	***		***	*****	***	**	****	*	
KA-3							*****	*****	
KA-4			*****	***	*	*			*
KA-4Q			*****	***	*	*			*
KO-1		**	***	****	*****	**	**	**	
KO-2	**	*	*****	***	**				

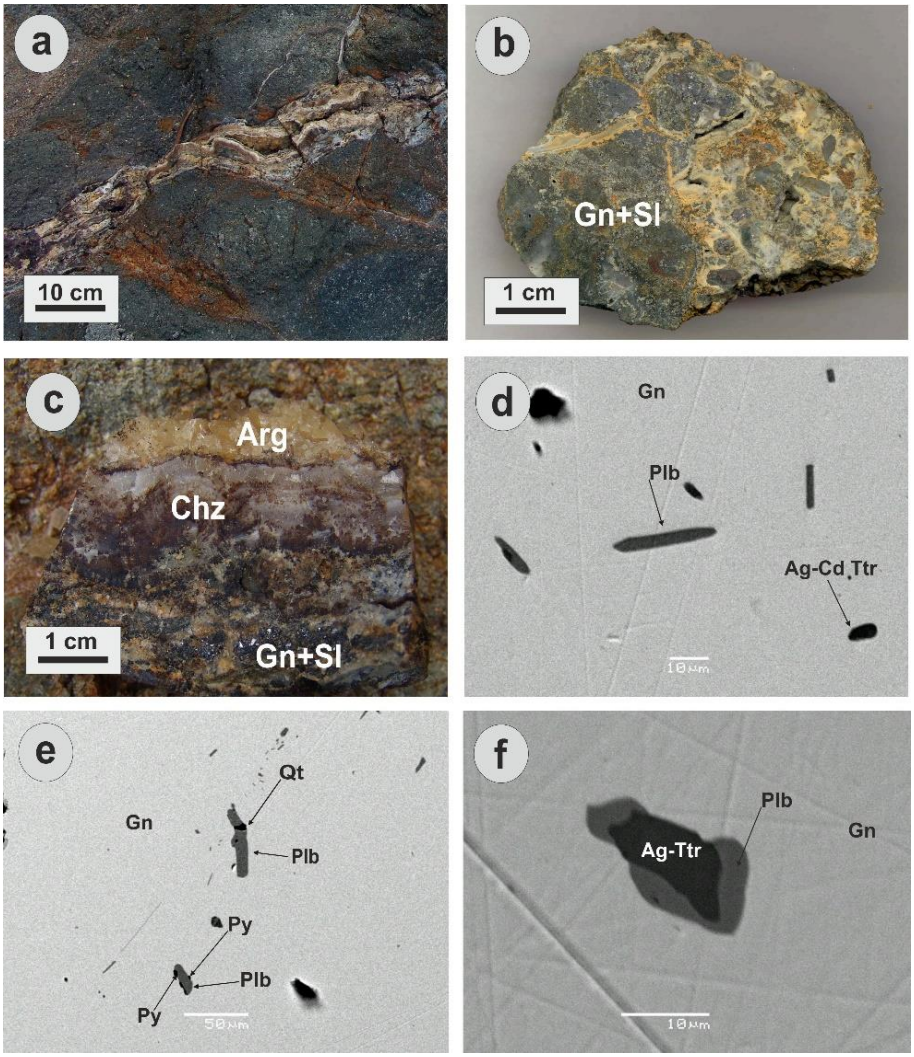

Figure 2 - Macroscopic photographs (a to c) and (d to f) SEM-BSE images demonstrating ore assemblages at Kontaros-Katsimouti metallic mineralization: (a) colloform-banded quartz-chalcedony-sulfide vein crosscutting propylitic altered dacite, (b) hand specimen of cockade breccia with subangular galena-sphalerite (Gn-Sl) fragments, surrounded by aragonite, (c) banded vein, with early deposition of Galena-sphalerite, followed by chalcedony (Chz) and then by aragonite (Arg), (d) polybasite (Plb) and Ag-Cd-rich tetrahedrite (Ag-Cd-Ttr) included in galena (Gn), (e) polybasite, pyrite (Py) and quartz (Qt) included in galena, (f) Ag-rich tetrahedrite (Ag-Ttr) surrounded by polybasite and included in galena.

Part of the samples were also digested with a mixture of $HClO_4$-HNO_3-HF acids and were analyzed for a series of trace elements using Inductively Coupled Plasma-Atomic Emission Spectrometry (ICP-AES) and Inductively Coupled Plasma-Atomic Emission Spectroscopy (ICP-MS) and a series of major elements by Inductively Coupled Plasma-Optical Emission Spectrometry (ICP-OES) at the Department of Chemistry, University of Gottingen, Germany.

4. Analytical results

4.1 Sulfide-sulfosalt mineralogy and mineral chemistry

Representative microanalyses of metallic mineral phases are presented in Table 2 and all data of the Ag-bearing sulfosalts are plotted in Figure 3. The metallic mineral phases at Kontaros-Katsimouti area show the following characteristics:

Galena is major constituent of the metallic mineralization assemblage of Kondaros-Katsimouti (Fig. 2). Galena is the main host of Ag-sulfosalts, which usually appear as inclusions. Paragenetic relations suggest contemporaneous deposition of galena with sphalerite (Fig. 2b, c). The Ag, Bi and Sb content in galena are below detection limit (Table 2).

Sphalerite forms skeletal intergrowths with galena and pyrite. It is iron-poor (less than <0.71 wt. %) and contains minor Cd, Mn and up to 0.3 wt% In (Table 2).

Tetrahedrite-freibergite solid solution is present in the form of up to 10 μm inclusions in galena, usually associated with polybasite (Fig. 2d, f). High contents of Ag (up to 23.06 wt %), are detected in the solid solution, substituting for Cu, whereas Pb (up to 6.57 wt %) and Cd (up to 5.39 wt %) are substituting for Zn and Fe respectively (Table 1).

Polybasite accompanies Ag-bearing tetrahedrite in the mineralization. It occurs either as isolated grains in galena or rimming pyrite and Ag-rich tetrahedrite (Fig. 2d to f). The composition is almost matching with the ideal Sb-endmember, as indicated by the negligible As content (up to 0.30 wt %), substituting for Sb in the structural formula (Table 2, Fig. 3).

4.2 Geochemical study

Selected bulk ore geochemical analyses from the Kondaros-Katsimoutis epithermal quartz-carbonate veins and breccias are presented in Table 3. Alfieris *et al.* (2013) identified a molybdenum geochemical anomaly (up to 176 mg/kg) along two major NE trending lineaments, which also control the surface distribution of silicic- and advanced argillic alteration in northwestern Milos (Triades-Katimouti area). According to the above authors there is also a positive correlation between Mo and W geochemical anomalies.

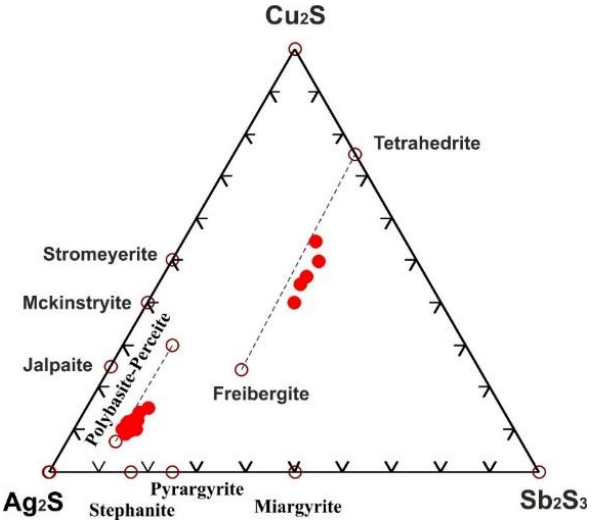

Figure 3 - Chemical composition of Ag-bearing sulfosalts from Kondaro and Katsimouti area in terms of the Ag-Cu-(Sb+As) ternary diagram (after Alfieris *et al.*, 2013). Theoretical compositions are shown as open circles. Compositional ranges of tetrahedrite-freibergite and polybasite-pearceite solid solution are shown by dashed lines for reference.

Table 2 - Representative microanalyses of galena (1), sphalerite (2-3), tetrahedrite (4-6) and polybasite (7-11) from Kondaros-Katsimouti, (values in %, (-): not detected).

	1	2	3	4	5	6	7	8	9	10	11
Cu	-	-	-	18.13	22.19	24.87	4.55	6.09	5.23	5.81	6.22
Ag	-	-	-	23.06	20.01	16.9	69.3	69.54	70.18	69.42	69.06
Fe	-	0.29	0.11	1.50	1.44	1.17	-	-	-	-	-
Zn	-	65.93	65.46	2.89	1.49	4.58	-	-	-	-	-
Sb	-			6.57	27.03	28.48	10.69	10.07	9.83	10.71	9.99
As	-	-	-	0.04	0.14	0.24	0.10	0.22	0.06	0.14	0.30
Hg	-	-	-	-	-	-	-	-	-	-	-
Cd	-	0.69	0.91	-	5.39	-	-	-	-	-	-
Pb	87.17	-	-	6.57	-	-	-	-	-	-	-
Mn	-	-	-	-	-	-	-	-	-	-	-
S	13.46	31.76	33.06	20.57	21.82	23.47	14.6	14.94	16.02	15.27	14.51
Bi	-	-	-	-	-	-	-	-	-	-	-
In	-	0.31	-	-	-	-	-	-	-	-	-
Total	100.63	98.96	99.38	98.88	99.51	99.71	99.25	100.86	101.31	101.36	100.08
Atoms	**2**	**2**	**2**	**29**	**29**	**29**	**29**	**29**	**29**	**29**	**29**
Cu	0.000	0.000	0.000	5.672	6.597	7.059	1.647	2.152	1.818	2.039	2.227
Ag	0.000	0.000	0.000	4.248	3.503	2.825	14.801	14.468	14.358	14.346	14.591
Fe	0.000	0.003	0.002	0.534	0.487	0.38	0.000	0.000	0.000	0.000	0.000
Zn	0.000	1.002	0.98	0.879	0.432	1.261	0.000	0.000	0.000	0.000	0.000
Sb	0.000	0.000	0.000	4.266	4.190	4.217	2.024	1.856	1.78	1.96	1.865
As	0.000	0.000	0.000	0.011	0.035	0.058	0..032	0.064	0.017	0.04	0.087
Hg	0.000	0.000	0.000	0.000	0.000	0.000	0.000	0.000	0.000	0.000	0.000
Cd	0.000	0.006	0.008	0.000	0.905	0.000	0.000	0.000	0.000	0.000	0.000
Pb	1.001	0.000	0.000	0.629	0.000	0.000	0.000	0.000	0.000	0.000	0.000
Mn	0.000	0.000	0.000	0.000	0.000	0.000	0.000	0.000	0.000	0.000	0.000
S	0.500	0.984	1.095	12.757	12.847	13.198	10.495	10.457	11.026	10.611	10.28
Bi	0.000	0.000	0.000	0.000	0.000	0.000	0.000	0.000	0.000	0.000	0.000
In	0.000	0.003	0.000	0.000	0.000	0.000	0.000	0.000	0.000	0.000	0.000

This study demonstrates Mo- and tungsten-enrichment (up to 24 mg/kg and 424 mg/kg respectively) along the NW-trending Kondaros-Katsimouti fault. The studied samples are also highly enriched in Pb and Zn with concentrations of up to 31.8 wt % and 16.5 wt % respectively. The presence of Cd in the structural formula of low-Fe sphalerite and Cd-Ag-rich tetrahedrite (Table 2) is reasonable for the elevated Cd concentrations in the bulk geochemical analyses (Kondaros: up to 247 mg/kg Cd; Katsimouti: up to 769 mg/kg Cd, Table 3). Similarly, the presence of Sb-bearing sulfosalts with minor As-content are responsible for the relevant concentrations in the bulk geochemical analyses (Kondaros: up to 243 mg/kg Sb and up to 36 mg/kg As; Katsimouti: up to 178 mg/kg Sb and up to 42 mg/kg As, Table 3). Bi, up to 1 mg/kg, may indicate the presence of minor Bi-sulfosalts in the mineralization.

5. Discussion and conclusions

The western Milos ore deposits have been formed under transitional shallow submarine to subaerial conditions (Alfieris *et al.*, 2013; Naden *et al.*, 2005). Alfieris *et al.* (2013) and Voudouris *et al.* (2014) listed a number of mineralogical characteristics, which strongly support sub-seafloor deposition for the base- and precious metal mineralization along the NW-trending Kondaros-Katsimouti-Vani fault. Our mineralogical data (e.g. presence of adularia, hematite associated with sulfides, and amethystine quartz) verify previous work of Alfieris *et al.* (2013), and suggest boiling and fluctuating oxidizing-reducing conditions for the formation of the Kondaros-Katsimouti metallic mineral assemblage. Amethyst requires oxidizing conditions to obtain its colour, and this may be resulted by either mixing of oxidized meteoric and/or seawaters with upwelling hydrothermal fluids or boiling processes (Fournier, 1985). It is considered that the deposition of the metallic mineral phases at Kondaros-Katsimouti took place due to increasing pH and oxidation (as a result of boiling and mixing of fluids, respectively) and by temperature decrease from above 300º to below 200 ºC (Alfieris, 2006; Alfieris *et al.*, 2013). These temperatures were estimated using the geothermometer of coexisting polybasite-pearceite and tetrahedrite-group minerals in the presence of sphalerite (Sack 2005). The lowest temperatures (<180 ºC) predicted for coexisting sulfosalts in Kondaros-Katsimoutis could represent equilibration temperatures after cooling. Polybasite and argentian tetrahedrite-freibergite are the main silver minerals at Kondaros-Katsimoutis mineralization, and most probably they represent exsolved grains from a galena solid solution (Alfieris *et al.*, 2013).

The metallic mineralization in Kondaros-Katsimouti area is highly enriched in W (up to 439 mg/kg) and in lesser amounts of Mo (e.g. 24 mg/kg), in common to other mineralization in northwestern Milos. Already Glasby *et al.* (2005) reported extremely high-enrichment (up to 2870 mg/kg W) for the Vani exhalative/inhalative manganese deposit and Alfieris *et al.* (2013) reported on a tungsten anomaly (up to 677 mg/kg) related to Mo anomaly along the NE-trending Triades–Katsimoutis lineament.

They considered elevated contents of Mo and W at Triades–Galana–Kondaros, to be related to a buried granite at depth that fed volatiles and metals into the magmatic-hydrothermal system, consistent to Mo-enrichment in VMS deposits (Mercier-Langevin *et al.*, 2011). Although exhalative processes are considered previously to be genetically connected to the transport of B and W and to the formation of syngenetic/syndiagenetic tungsten mineralization (Raith, 1988; Spry *et al.*, 2000), new in-situ U-Pb age data confirm formation of tungsten mineralization from magmatic-hydrothermal fluids during granitoid emplacement (Raith, 2013).

Mineralization at Kondaros-Katsimouti resembles other intermediate-sulfidation mineralizations elsewhere, as for example Tonopah Ag-Zn-Pb deposit, Nevada (Sillitoe and Hedenquist, 2003), as well as epithermal deposits in Baia Mare polymetallic district, where tungsten in the form of wolframite and scheelite occurs in early stages of ore deposition associated with Fe-oxides (Grancea *et al.*, 2002). Towards Vani, and at higher leves, the Kondaros-Kastimouti ore system becomes more Ag-rich (eg. Vani Ag-Pb deposits; Voudouris *et al.*, 2014), probably as a result of combined action of increasing mixing- (between magmatic and seawater) and boiling processes.

Table 3 - Representative bulk ore geochemical analyses from Kondaros-Katsimouti.

		KA-1A	KA-1B	KA-2	KA-3	KA-4	KA-4Q	KO-1	KO-2
Na_2O	%	0.17	0.05	0.08	0.81	0.17	0.06	0.05	0.03
K_2O	%	0.31	0.06	0.24	0.16	0.14	0.09	0.06	0.03
MgO	%	0.25	0.46	0.17	0.53	0.03	0.02	0.16	0.01
CaO	%	15.24	47.54	13.39	45.61	0.03	0.03	3.67	0.12
Al_2O_3	%	0.65	0.10	0.62	0.08	0.61	0.44	0.23	0.11
TiO_2	%	0.01	bdl	0.01	bdl	bdl	bdl	bdl	bdl
MnO	%	0.99	8.32	0.73	10.15	0.06	0.03	0.73	0.04
Fe_2O_3	%	1.82	1.86	2.97	1.56	1.15	1.73	2.13	0.11
Zn	%	16.5	0.15	14.2	0.12	8.17	4.38	6.70	1.52
Pb	%	2.65	0.03	2.83	0.05	29.8	0.75	21.8	0.36
Cu	%	0.04	0.002	0.05	0.002	0.08	0.03	0.03	0.002
Ba	%	0.01	0.003	0.01	0.02	0.002	0.001	0.001	0.21
As	mg/kg	14	4	42	4	8	18	36	1
Sb	mg/kg	68	1	42	0	178	94	243	46
Ni	mg/kg	22	16	24	16	26	27	26	27
Co	mg/kg	31	30	42	18	22	98	20	123
W	mg/kg	49	26	159	bdl	94	439	2	424
Cd	mg/kg	769	7	622	3	410	207	247	86
Mo	mg/kg	23	4	24	4	10	5	9	2
Tl	mg/kg	0.26	0.30	0.26	0.10	0.54	0.05	0.62	0.01
Bi	mg/kg	0.03	bdl	0.05	bdl	0.26	0.01	1.05	bdl

bdl: below detection limit.

6. References

Alfieris, D., 2006. Geological, geochemical and mineralogical studies of shallow submarine epithermal mineralization in an emergent volcanic edifice, at western Milos island, Greece. PhD thesis, University of Hamburg, Germany, 211 pp.

Alfieris, D. and Voudouris, P., 2005. Ore mineralogy of transitional submarine to subaerial magmatic-hydrothermal deposits in W. Milos, Greece. *In:* Cook, N.G. and Bonev, I., e*ds*., Au-Ag-Te-Se deposits, *Geochemistry, Mineralogy and Petrology*, 43, Sofia, 1-6.

Alfieris, D., Voudouris, P. and Spry, P.G., 2013. Shallow submarine epithermal Pb-Zn-Cu-Au-Ag-Te mineralization on western Milos Island, Aegean Volcanic Arc, Greece: Mineralogical, Geological and Geochemical constraints, *Ore Geology Reviews*, 53, 159-180.

Altherr, R. and Siebel, W., 2002. I-type plutonism in a continental back-arc setting: Miocene granitoids and monzonites from the central Aegean Sea, Greece, *Contrib. Mineral. Petrol*., 143, 397-415.

Fournier, R.O., 1985. The behaviour of silica in hydrothermal solutions, *In:* Berger, B.R. and Bethke, P.M., *eds*., Geology and geochemistry of epithermal systems, *Rev. Econ. Geol.*, 2, 45-61.

Fytikas, M., Innocenti, F., Kolios, N., Manneti, P., Mazzuoli, R., Poli, G., Rita, F. and Villari, L., 1986. Volcanology and petrology of volcanic products from the island of Milos and neighbouring islets, *J. Volcanol. Geotherm. Res*., 28, 297-317.

Glasby, G.P., Papavassiliou, C.T., Mitsis, J., Valsami-Jones, E., Liakopoulos, A. and Renner, R.M., 2005. The Vani manganese deposit, Milos island, Greece: a fossil stratabound Mn-Ba-Pb-Zn-As-Sb-W-rich hydrothermal deposit. *In:* Fytikas, M. and Vougioukalakis, G.E., e*ds.*, The South Aegean Active Volcanic Arc: Present Knowledge and Future Perspectives. Developments in Volcanology, 7. Elsevier, 255-291.

Grancea, L., Bailly, L., Leroy, J., Banks, D., Marcoux, E., Milési, J.P., Cuney, M., André, A.S., Istvan, D. and Fabre, C., 2002. Fluid evolution in the Baia Mare epithermal gold /polymetallic district, Inner Carpathians, Romania, *Mineral. Deposita*, 37, 630-647.

Hauck, M., 1988. Kuroko-type ore deposits on the Aegean Islands, Greece. *In:* Friedrich, G.M. and Herzig, P.M., e*ds*., Base metal sulfide deposits. Springer Verlag, Berlin, 216-228.

Hein, J.R., Stamatakis, M.G. and Dowling, J.S., 2000. Trace metal-rich Quaternary hydrothermal manganese oxide and barite deposit, Milos Island, Greece, *Trans Inst Min Metall*, 109, 67-76.

Jolivet, L. and Brun, J.P., 2010. Cenozoic geodynamic evolution of the Aegean region, *Int. J. Earth Sci.*, 99, 109-138.

Kilias, S.P., Naden, J., Cheliotis, I., Shepherd, T.J., Constandinidou, H., Crossing, J. and Simos, I., 2001. Epithermal gold mineralisation in the active Aegean volcanic arc: The Profitis Ilias deposit, Milos Island, Greece, *Miner. Deposita*, 36, 32-44.

Kilias, S.P., Nomikou, P., Papanikolaou, D., Polymenakou, P.N., Godelitsas, A., Argyraki, A., Carey, S., Gamaletsos, P., Mertzimekis, T.J., Stathopoulou, E. and Goettlicher, J., 2013. New insights into hydrothermal vent processes in the unique shallow-submarine arc-volcano, Kolumbo (Santorini), Greece, *Scientific Reports*, 3, 2421, 1-13.

Liakopoulos, A, Glasby, G.P., Papavassiliou, C.T. and Boulegue, J., 2001. Nature and origin of the Vani manganese deposit, Milos, Greece: an overview, *Ore Geol. Rev.*, 18, 181-209.

Marschik, R., Bauer, T., Hensler, A.S., Skarpelis, N. and Holzl, S., 2010. Isotope Geochemistry of the Pb-Zn-Ba (-Ag-Au) Mineralization at Triades-Galana, Milos Island, Greece, *Res. Geology*, 60, 335-347.

Mercier-Langevin, P., Hannington, M.D., Dubé, B. and Bécu, V., 2011. The gold content of volcanogenic massive sulfide deposits, *Miner. Deposita*, 46, 509-539.

Naden, J., Kilias, S.P. and Darbyshire, D.B.F., 2005. Active geothermal systems with entrained seawater as analogues for transitional continental magmato-hydrothermal and volcanic-hosted massive sulfide mineralization-the example of Milos Island, Greece, *Geology*, 33, 541-544.

Papanikolaou, D.J., 1987. Tectonic evolution of the Cycladic blueschist belt (Aegean Sea, Greece). *In:* Helgeson, H.C., e*d.*, Chemical transport in metasomatic processes: NATO ASI series, 218, 429-450.

Raith, J.G., 1988. Tourmaline rocks associated with stratabound scheelite mineralization in the Austroalpine crystalline complex, Austria, *Mineral. Petrol*., 39, 265-288.

Raith, J.G., 2013. Stratabound tungsten deposits in the Alps revisited in the light of new age data, *Geophysical Research Abstracts*, Vol. 15, EGU2013-5095, 2013 EGU General Assembly.

Ring, U., Glodny, J., Will, T. and Thomson, S., 2010. The Hellenic subduction system: high pressure metamorphism, exhumation, normal faulting, and large-scale extension, *Ann. Rev. Earth Planet. Sci*., 38, 45-76.

Sack, R.O., 2005. Internally consistent database for sulfides and sulfosalts in the system Ag_2S-Cu_2S-ZnS-FeS-Sb_2S_3-As_2S_3: Update, *Geoch. Cosmoch. Acta*, 69, 1157-1164.

Sillitoe, R.H. and Hedenquist, J.W., 2003. Linkages between volcanotectonic settings, ore-fluid compositions, and epithermal precious-metal deposits, *Soc. Econ. Geol., Special Publ*., 10, 315-343.

Spry, P.G., Peter, J.M. and Slack, J.M. 2000. Metaexalites as exploration guides to ores, *Rev. Econ. Geol.*, 11, 163-201.

Stewart, A.L. and McPhie, J., 2006. Facies architecture and Late Pliocene-Pleistocene evolution of a felsic volcanic island, Milos, Greece, *Bull. Volcanol*., 68, 703-726.

Vavelidis, M. and Melfos, V., 1997. Two plumbian tetrahedrite-tennantite occurrences from Maronia area (Thrace) and Milos island (Aegean Sea, Greece), *Eur. J. Mineral*., 9, 653-657.

Vavelidis, M. and Melfos, V., 1998. Fluid inclusion evidence for the origin of the barite silver-gold-bearing Pb-Zn mineralization of the Triades area, Milos Island, Greece, *Bull. Geol. Soc. Greece*, 32, 137-144.

Voudouris, P., Xydous, S., Alfieris, D., Veligrakis, Th., Papavasiliou, C., Kanellopoulos, C. and Falalakis, G., 2014. Silver-rich sulfide mineralization at Vani, western Milos Island, Greece: New mineralogical evidence for epithermal ore deposition in a shallow submarine environment, *Proceedings of XX CBGA Congress*, Tirana, *Albania. Bul. Shk. Gjeol*., 1/2014, 187-190.

Δελτίο της Ελληνικής Γεωλογικής Εταιρίας, τόμος L, σελ. 1969-1979
Πρακτικά 14ου Διεθνούς Συνεδρίου, Θεσσαλονίκη, Μάιος 2016

Bulletin of the Geological Society of Greece, vol. L, p. 1969-1979
Proceedings of the 14th International Congress, Thessaloniki, May 2016

MINERALOGY AND GEOCHEMISTRY OF THE TRIADES-GALANA PB-ZN-AG-AU INTERMEDIATE-HIGH SULFIDATION EPITHERMAL MINERALIZATION, MILOS ISLAND, GREECE

Papavasiliou K.[1], Voudouris P.[2], Kanellopoulos C.[3], Alfieris D.[4] and Xydous S.[2]

[1]*Faculty of Geology and Geoenvironment, University of Athens, Department of Economic Geology* and *Geochemistry, Panepistimiopolis A. Ilisia 15784 Athens/Greece, papavas@geol.uoa.gr*

[2]*Faculty of Geology and Geoenvironment, University of Athens, Department of Petrology, Panepistimiopolis A. Ilisia 15784 Athens/Greece, voudouris@geol.uoa.gr, stxydous@geol.uoa.gr*

[3]*Institute of Geology and Mineral Exploration, 1st Spirou Louis St., Olympic Village, 13677, Acharnae, Greece, ckanellopoulos@gmail.com*

[4]*Imerys Filtration, 15A Metaxa Street, Kifisia 14564, Greece, Dimitris.Alfieris@imerys.com*

Abstract

The Triades-Galana Pb-Zn-Ag-Au mineralization is a shallow-submarine epithermal mineralization located along NE-trending faults, NW Milos Island, Greece. It is hosted in 2.5–1.4 Ma pyroclastic rocks and is genetically related to andesitic/dacitic lava domes. Mineralization occurs as breccias, quartz-barite-galena veins and stockworks within sericite-adularia or kaolinitic altered rocks. The mineralization is enriched in Mo, W and base- and precious metals (e.g. Pb, Zn, Ag) similarly to the neighbouring mineralization at Kondaros-Katsimouti and Vani, indicating common source of metals from a deep buried granitoid feeding western Milos with metals and volatiles. Paragenetic relations suggest early deposition of pyrite, followed by famatinite, polybasite and Ag-rich tetrahedrite, and then by enargite, suggesting fluctuating sulfidation states during ore formation. The evolution from Sb- towards As-rich enrichment indicate a renewed magmatic pulse (probably in the form of magmatic gases) in the hydrothermal system. Silver is present in the structure of sulfosalts (up to 66.2 wt.% in polybasite-pearceite, 15.1 wt.% in tetrahedrite and 60 wt. % in pyrargyrite). Boiling processes (as evidenced by the presence of adularia accompanying intermediate-sulfidation ore) and mixing with seawater (presence of hypogene lead chlorides) and contemporaneous uplift, contributed to ore formation.
***Keywords**: Silver mineralogy, epithermal, Triades-Galana, Milos Island*

Περίληψη

Η μεταλλοφορία Pb-Zn-Ag-Au Τριάδων-Γαλανών στη ΒΔ Μήλο, αποτελεί μία επιθερμική μεταλλοφορία ρηχού θαλάσσιου περιβάλλοντος που αποτέθηκε κατά μήκος ρηγμάτων ΒΑ διεύθυνσης. Πετρώματα ξενιστές είναι πυροκλαστικά ηλικίας 2.5-1.4 εκ. χρόνων και ανδεσιτικοί/δακιτικοί δόμοι λάβας, με τους οποίους και συνδέεται γενετικά. Η μεταλλοφορία απαντά υπό μορφή λατυποπαγών, φλεβών και πλέγματος φλεβιδίων χαλαζία-βαρίτη-γαληνίτη εντός πετρωμάτων εξαλλοιωμένων σε σερικίτη-αδουλάριου και καολινίτη. Η μεταλλοφορία είναι εμπλουτισμένο σε Mo, W, καθώς και σε βασικά

και πολύτιμα μέταλλα (e.g. Pb, Zn, Ag), όπως και οι γειτονικές μεταλλοφορίες του Κοντάρου-Κατσιμουτίου και Βανίου, υποδεικνύοντας μία κοινή μαγματική πηγή στο βάθος που τροφοδότησε τις μεταλλοφορίες αυτές σε μέταλλα και πτητικά συστατικά. Παραγενετικά δεδομένα υποδεικνύουν αρχική απόθεση σιδηροπυρίτη, και στη συνέχεια φαματινίτη, πολυβασίτη, πυραργυρίτη και Ag-ούχου τετραεδρίτη, και τέλος εναργίτη, παρέχοντας ενδείξεις μεταβαλλόμενων συνθηκών θείωσης κατά τη διάρκειας της μεταλλοφορίας. Η εξέλιξη των ρευστών πλούσιων σε Sb στα αρχικά στάδια πρός As-ούχα ρευστά στα τελευταία στάδια, αποτελεί ένδειξη μιάς νέας μαγματικής συνεισφοράς (πιθανόν υπό μορφή μαγματικών αερίων) στο υδροθερμικό σύστημα. Ο άργυρος απαντά στη δομή των θειοαλάτων (έως 66.2 % κ.β. στον πολυβασίτη, 15.1 % κ.β. στον τετραεδρίτη και 60 % κ.β. στον πυραργυρίτη). Διαδικασίες βρασμού (όπως υποδεικνύει η παρουσία αδουλάριου στη παραγένεση ενδιάμεσης θείωσης), και ανάμειξης με θαλασσινό νερό (παρουσία υπογενετικού χλωριδίου του μολύβδου), σύγχρονες με ανάδυση της περιοχής, έχουν συνεισφέρει στην απόθεση του μεταλλεύματος.
Λέξεις κλειδιά: *Ορυκτολογία αργύρου, επιθερμική, Τριάδες-Γαλανά, Δυτική Μήλος.*

1. Introduction

Milos Island is one of the most densely mineralized areas in Greece, characterized by epithermal Au-Ag and base metal deposition within a Plio-Pleistocene volcanic edifice. Metallic mineralization on Milos was the subject of several mineralogical and geochemical studies, with base- and precious metal mineralization in western Milos Island having been classified as either Kuroko- (Hauck, 1988;Vavelidis and Melfos, 1998), seawater-dominated epithermal (Kilias *et al.*, 2001; Liakopoulos *et al.*, 2001; Marchik *et al.*, 2010), shallow submarine epithermal- (Alfieris, 2006; Stewart and McPhie, 2006; Alfieris *et al.*, 2013), or hybrid volcanogenic massive sulfide (VMS)-epithermal types (Naden *et al.*, 2005). A modern analogue for the setting of epithermal - style mineralization in western Milos is the shallow submarine Kolumbo hydrothermal vent field located 7 km NE of Santorini Island in the Hellenic arc (Kilias *et al.*, 2013). As suggested by Plimer (2000) and Stewar t and McPhie (2006), the Triades-Galana mineralization represents sub-seafloor/seafloor stockwor k zones, which formed in a shallow submarine setting. The Triades-Galana system is classified as i ntermediate- to high-sulfidation epithermal type (Alfieris and Voudouris, 2005; Marschik *et al.*, 20 10). Probable resources of the Galana mine, according to Liakopoulos *et al.* (2001), were estimated to be 10 million tones with a mean concentration of Ag of 500 mg/kg. Reported indicative resource s at Triades-Galana are 1.2 Mt at 1 g/t Au and 124 g/t Ag (Stewart and McPhie, 2003). Since there is no detail exploration in this area until now, all the above estimations are very approximate.

The aim of the current study is to present new data on the metallic mineralization at Triades-Galana area, to describe its mineralogical and geochemical characteristics and discuss the role of various physico-chemical processes (e.g. boiling, mixing, etc.) in its formation by comparing it with other mineralized areas in western Milos and elsewhere.

2. Geology and mineralization

Milos Island forms part of the Cycladic Blueschist in the Attico-Cycladic massif, a polymetamorphic terrane within the Alpine orogen of the Hellenides (Jolivet and Brun, 2010). Miocene extension in the Aegean Sea was accompanied by the intrusion and extrusion of magmatic rocks at upper crustal levels (Altherr and Siebel, 2002). Milos is located in the central part of the Lower Pliocene to Recent South Aegean Active Volcanic Arc, which includes a belt of calc-alkaline volcanic centers consisting mainly of basalts, andesites, dacites, and rhyolites (Fig. 1, Fytikas *et al.*, 1986). It comprises mainly Neogene sediments and volcanic rocks overlying a metamorphic basement that consists of eclogites, glaucophane schists and mica schists (Alfieris *et al.* 2013; Fytikas *et al.*, 1986; Stewart and McPhie, 2006). The earliest volcanic episode (Middle to Upper Pliocene, 3.5-3.0 Ma) produced a succession of felsic submarine units including pumice flows, tuffs and pumice rich

pyroclastic flows, with locally intrusive subvolcanic bodies, lavas and/or hyaloclastites. Some volcanosedimentary products have been deposited in E-W directed grabens from 3.0 to 2.7 Ma. The subsequent phase of submarine volcanism (Upper Pliocene-Lower Pleistocene, 2.7-1.4 Ma) is characterized by the emplacement of dacitic/andesitic domes, plugs and lava flows along a system of mainly NE-trending faults, and subordinately along NW-SE to E-W directions. These domes intruded and disrupted the still fluid and unconsolidated volcanosedimentary unit, suggesting contemporaneous emplacement in a shallow seawater environment. Based on SHRIMP U–Pb in zircon, Stewart and McPhie (2006) dated submarine dacite lavas at 2.18± 0.09 Ma and submarine to subaerial dacitic-rhyodacitic flow banded domes and their autobreccias at 1.44± 0.08 Ma (both at Triades). The effusive activity was accompanied locally by explosive episodes, which locally produced bedded pumiceous tuff cones and/or pyroclastic flows and breccias in submarine and partially subaerial environments. The dominant structural features on western Milos Island are a series of steep, NE trending structures, which are characterized by left lateral strike–slip and dip–slip motion, and from the other side, a series of dilational NW trending lineament zones, into which composite volcanic centers, domes, and collapsed calderas developed. These zones limited the magmatic-hydrothermal fluid flow, producing zones of intense silicification, brecciation, and veining.

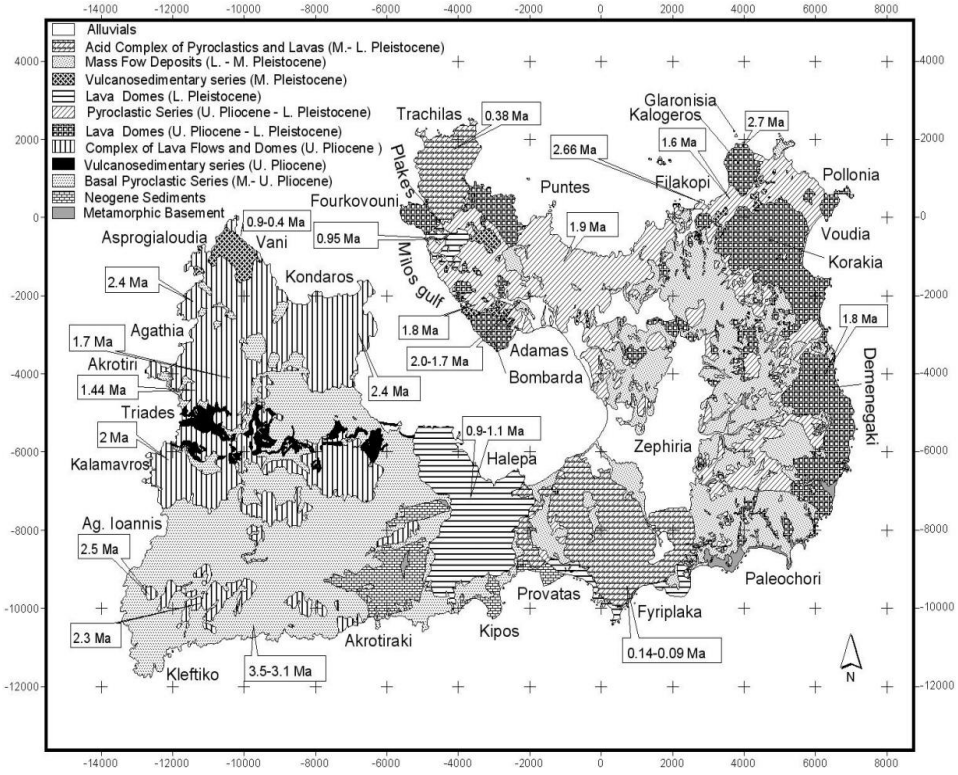

Figure 1 - Geological map of Milos Island showing the distribution of the main volcanic phases, metamorphic and sedimentary units, as well as geochronological data (after Fytikas *et al.*, 1986; Alfieris, 2006).

The Triades-Galana area is located along the NE-trending Triades-Katsimoutis lineament. The host rocks to the mineralization are submarine ash flow tuffs, fossil-bearing tuffs, tuffaceous and epiclastic marine sediments, as well as andesitic or dacitic flow domes. The flow domes are genetically related to the mineralization, and were subject to kaolinite-sericite and alunitic alteration. In the Galana area, the dominant alteration is quartz-sericite-pyrite. The mineralization and associated hydrothermal alteration are spatially related to NE-trending faults and occurs as breccia

zones and quartz–barite–galena veins or stockworks, crosscutting quartz-sericite-kaolinite and quartz–kaolinite/alunite altered breccia fragments (Alfieris *et al.*, 2013). Barite, kaolinite, sericite, adularia and quartz are the gangue minerals. The textural features of the Triades-Galana ore indicate early deposition of pyrite with inclusions of bornite+digenite and Fe-poor sphalerite. This was succeeded by a metallic mineral assemblage composed of galena, tetrahedrite-tennantite, chalcopyrite, enargite, famatinite, pyrargyrite, polybasite, and covellite (Alfieris *et al.*, 2013).

3. Materials and methods

The mineralogical composition of nineteen samples was investigated by reflected light microscopy (Leica DM 2500P), powder X-ray diffraction (XRD) and scanning electron microscopy-equipped with energy dispersive spectroscopy (SEM–EDS). The Triades samples included TR-1 (silicified and pyritized breccia, containing barite); TR-2 (argillized, silicified and sulfur impregnated dacite); TR-3 (quartz-barite±sphalerite vein cutting through a dacite; malachite staining is present); TR-4 (quartz-barite vein with sphalerite); TR-5 (galena-sphalerite mineralized, silicified dacite with veinlets of barite); TR-6 (quartz-barite veinlets and crustiform/colloform chalcedony veinlets cutting through a silicified dacite); TR-7 (quartz-sphalerite±barite vein cutting through a chalcedony/silicified volcaniclastic sandstone); TR-8 (silicified hyaloclastite containing fine-grained pyrite, marcasite and barite); TR-9 (hyaloclastite fragments impregnated with barite, silica and sphalerite, galena); TR-10 (hyaloclastite fragments impregnated with barite, silica and sphalerite, galena); TR-11 (fragments of silicified hyaloclastite containing pyrite-marcasite and barite); TR-12 and TR-13 (hyaloclastite fragments impregnated with galena, barite and sphalerite within a silicified matrix); The Galana samples included GA-1 (silicified, brecciated contact between a dacite intruded through mudstones); GA-2 (brecciated and silicified dacite-hyaloclastite); GA-3 (silicified dacitie with some oxidation most probably of pyrite. Barite is present); GA-4 and GA-5 (silicified dacite with sphalerite and barite); GA-6 (argillized and partially silicified dacite with disseminated spalerite, barite).

The XRD study was carried out using a Siemens Model 5005 X-ray diffractometer in combination with the DIFFRAC plus software package. The diffractometer was operated using Cu Kα radiation at 40 kV and 40 mA and employing the following scanning parameters: step size 0.020° and step time from 1.0 to 20.0 sec. The raw files (XRD diagrams) were evaluated for mineralogical identifications using the EVA 10.0 software. For microprobe analyses and SEM imaging we used a JEOL JSM 5600 scanning electron microscope, equipped with an automated energy dispersive analyses system ISIS 300 OXFORD, with the following operating conditions: accelerating voltage 20 kV, beam current 0.5 nA, time of measurement 50 s and beam diameter 1-2 mm. The spectra were processed using the ZAF software.

Samples were also digested with a mixture of HClO4-HNO3-HF acids and were analysed for a series of trace elements using Inductively Coupled Plasma-Atomic Emission Spectrometry (ICP-AES) and Inductively Coupled Plasma-Atomic Emission Spectroscopy (ICP-MS) and for a series of major elements by Inductively Coupled Plasma-Optical Emission Spectrometry (ICP-OES) at the Department of Chemistry, University of Gottingen, Germany.

4. Analytical results

4.1. Mineralogy and mineral chemistry

The main mineralogical composition of the studied samples (XRD analysis) are presented in Table 1. Representative microanalyses of metallic mineral phases are presented in Table 2 and all data of Ag-bearing sulfosalts are plotted in figure 3. Table 1 demonstrates abundance of galena, sphalerite and pyrite accompanying quartz, adularia and sericite in all samples. In sample TR-3 the rare sulfosalt watanabeite (e.g. Shimizu *et al.*, 1993) was detected, however, this could not be verified by the microprobe analyses. It follows a description of the metallic mineral phases in Triades-Galana area:

Galena is a major constituent of the metallic mineralization assemblage at the Triades-Galana. Galena is the main host of Ag-sulfosalts, which usually, appear as inclusions (Fig. 2). It contains up to 0.09 wt. % Sb and no Ag and Bi (Table 2).

Sphalerite replaces galena, is Fe-poor (< 0.71 wt. %) and contains Cd and Mn (up to 0.2 wt. %; Table 2).

Pyrite is associated with polybasite, pyrargyrite and Ag-rich tetrahedrite, included in galena (Fig. 2b to d).

Enargite is a common mineral in the metallic paragenesis of Triades; it postdates galena and Ag-tetrahedrite (Fig. 2e). The analysed grains contain up to 2.57 wt. % Ag (Table 2). Alfieris *et al.* (2013) reported enargite with up to 7.1 wt. % Ag.

Famatinite, the Sb-analogue to enargite, is a common mineral at Triades. It appears either as isolated crystals or in association with polybasite and tetrahedrite, both included in galena (Fig. 2f, g). The analyzed famatinites contain up to: 3.3 wt. % Ag, 0.39 wt. % Zn, 1 wt. % As, 0.18 wt. % Cd and 0.71 wt. % Fe (Table 2).

Tetrahedrite accompanies Sb-bearing sulfosalts (e.g. polybasite, pyrargyrite and famatinite) in the mineralization (Fig. 2). Already Vavelidis and Melfos (1997) presented Ag-rich and Pb-rich tetrahedrite in the area, and Alfieris *et al.* (2013) reported both tennantite and tetrahedrite coexisting in the same sample, with a dominance of tennantite over tetrahedrite, especially during late-stage ore deposition**.** Although previously only zincian tetrahedrite varieties have been reported (Alfieris *et al.*, 2013), this study also demonstrates Cd- and Hg- tetrahedrite varieties with up to 7.37 wt. % Cd and up to 7.42 wt % Hg respectively (Table 2). Ag content up to 15.07 wt. % and Pb up to 9.34 wt. % were also detected (Table 2). Cd, Hg and Pb substitute for Zn in the fahlore structure.

Pyrargyrite-proustite solid solution has reported by many researchers in Triades-Galana (Vavelidis and Melfos, 1997, 1998; Liakopoulos *et al.*, 2001; Alfieris *et al.*, 2013). Based on the microanalyses conducted during the present study, only pyrargyrite was found (Table 2, Fig. 3). It occurs in association with tetrahedrite as inclusion in galena (Fig. 2b, c, g, h).

Polybasite-pearceite solid solution occurs either as monomineralic rounded and/or lath-shaped grains included in galena, or in assemblages with Ag-tetrahedrite and pyrite or famatinite (Fig. 2a, b, d). Polybasite-pearceite solid solution contains up to 4.76 wt. % As (Table 1, Fig. 3).

Lead chloride with a structural formula $PbCl_2$ was found at Triades in the form of subrounded inclusions in galena (Fig. 2i).

4.2. Bulk ore geochemistry

Selected bulk geochemical analyses from epithermal veins and silicified and/or adularia-sericitic altered samples, rich in metallic mineral phases i.e. galena, sphalerite are presented in Table 3. The Triades samples are enriched in molybdenum (up to 265 mg/kg), above the molybdenum geochemical anomaly (up to 176 mg/kg) identified by Alfieris *et al.* (2013) along two NE-trending Triades-Katsimouti lineament, which controls the surface distribution of silicic- and advanced argillic alteration in northwestern Milos Island. The studied samples from both areas are enriched in tungsten (e.g. Triades up to 848 mg/kg and Galana up to 440 mg/kg).

Table 1 - Semi-quantitative (XRD) mineralogical estimation of the samples from Triades (TR) and Galana (GA) area.

	Bar	San	Cris	Qz	Sph	Gal	Pyr	Wat	Ill	Alu	Tetr
TR-1	**	****		*****							
TR-2			**	*****						***	
TR-3	*****			*****	*	*		***			**
TR-4	*			*****	**	*	*				
TR-5	**	*		****	****	**					
TR-6	****			***	**	*					
TR-7	**	*		*****	***	**					
TR-8	***			*****							
TR-9	*****			****	****	**	*				
TR-10	****			*****	***	**	*				
TR-11	***			*****	*		**				
TR-12	*****			****	***	**	*				
TR-13	***	*		****	***	**	*				
GA-1		**		*****					*		
GA-2		*****		**					***		
GA-3	***	***	***	*****					***		
GA-4	tr.	**		*****	***	*	*		*		
GA-5		**		*****	***	*			**		
GA-6	*	**		*****	****				tr.		

*Mineral abundances: ***** = dominant; **** = abundant; ***=common; ** = medium; * = minor; tr. = trace; - = not detected;*

Abbr.: Bar=Barite; San=Sanidine; Cri=Cristobalite; Qz= Quartz; Sph=Sphalerite; Gal=Galena; Pyr=Pyrite; Wat=Watanabeite; Ill=Illite; Alu=Alunite; Tetr=Tetrahedrite.

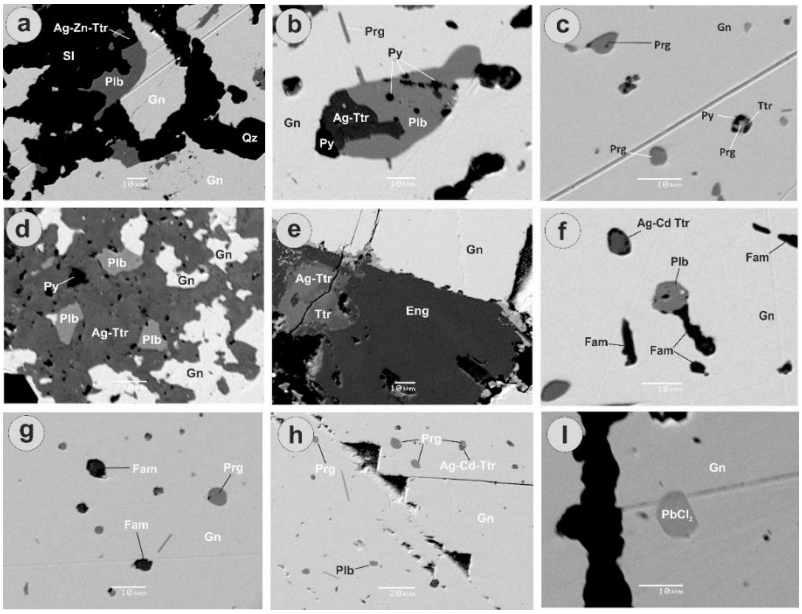

Figure 2 - Photomicrographs (SEM-BSE images) demonstrating ore assemblages at Triades-Galana mineralization: (a) Galena (Gn), polybasite (Plb) and Ag-Zn-rich tetrahedrite (Ag-Zn-Ttr) are replaced by sphalerite (Sl). Quartz (Qz) is also present, (b) Pyrite (Py) associated with polybasite and Ag-rich tetrahedrite, and pyrargyrite (Prg) are included in galena, (c) Pyrite associated with pyrargyrite and tetrahedrite are included in galena, (d) Polybasite-galena intergrowths are replaced by Ag-rich tetrahedrite. Pyrite is also present, (e) Galena is surrounded by Ag-rich tetrahedrite and enargite (Eng), (f) Famatinite (Fam) intergrown with polybasite and Ag-Cd-rich tetrahedrite (Ag-Cd-Ttr) are included in galena, (g) Famatinite and pyrargyrite are included in galena, (h) Pyrargyrite, polybasite and Ag-Cd-rich tetrahedrite are included in galena, (i) Lead chloride is included in galena.

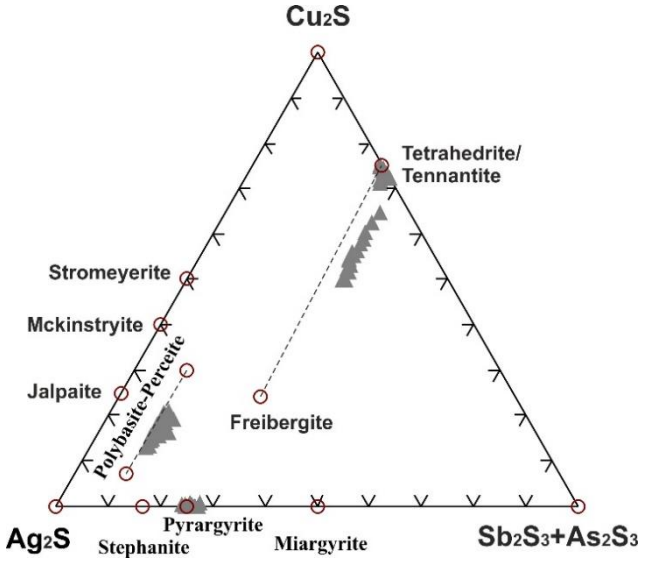

Figure 3 - Chemical composition of Ag-bearing sulfosalts in terms of the Ag-Cu-(Sb+As) ternary diagram (after Alfieris *et al.*, 2013). Theoretical compositions are shown as open red circles. Filled triangles represent composition of the tetrahedrite-group minerals from Trades-Galana area. Compositional ranges of tetrahedrite-freibergite and polybasite solid solution are shown by dashed lines for reference.

Table 2 - Representative microanalysis of galena (1-2), sphalerite (3), enargite (4), polybasite-pearceite (5-8), famatinite (9), tennantite-tetrahedrite series (10-14) and pyrargyrite (15-17).

	1	2	3	4	5	6	7	8	9	10	11	12	13	14	15	16	17
Cu	-	-	-	46.34	9.23	9.85	9.67	10.64	41.57	41.27	20.57	32.41	23.1	21.14	-	-	0.17
Ag	-	-	-	0.38	65.56	66.18	61.84	55.78	1	3.3	13.77	9.76	15.07	14.16	57.38	59.67	60.07
Fe	-	-	0.13	0.2	-	-	-	-	0.04	0.03	-	0.3	0.18	2.47	-	-	-
Zn	-	-	66.55	-	-	-	-	-	-	0.19	-	6.75	0.72	1.11	-	-	-
Sb	-	0.09	-	4.33	3.5	2.84	10.98	14.42	27.69	25.61	23.42	21.25	25.84	23.39	23.35	22.23	21.05
As	-	-	-	16.6	4.76	3.66	0.47	0.02	1.01	0.04	0.57	5.39	0.16	0.54	0.01	-	-
Hg	-	-	-	-	-	-	-	-	-	-	7.42	-	-	-	-	-	-
Cd	-	-	0.18	-	-	-	-	-	-	-	4.07	-	7.37	4.74	-	-	-
Pb	86.49	86.08	-	-	-	-	-	-	-	-	9.34	-	7.31	8.35	-	-	-
Mn	-	-	0.02	-	-	-	-	-	-	-	-	-	-	1.00	-	-	-
S	13.32	13.34	32.4	31.36	15.52	16.17	16.55	17.01	28.45	28.68	19.76	24.04	21.78	22.97	18.68	18.3	18.11
Total	99.82	99.51	99.27	99.22	98.59	98.72	99.52	99.87	99.77	99.13	98.95	99.91	101.53	99.86	99.39	100.2	99.4
Ato	**2**	**2**	**2**	**8**	**29**	**29**	**29**	**29**	**8**	**8**	**29**	**29**	**29**	**29**	**7**	**7**	**7**
Cu	0.000	0.000	0.000	2.958	3.170	2.764	3.300	3.639	2.920	2.905	6.771	8.674	6.974	6.261	0.000	0.000	0.015
Ag	0.000	0.000	0.000	0.014	13.259	13.227	12.424	11.243	0.042	0.137	2.671	1.537	2.680	2.471	2.894	2.964	3.005
Fe	0.000	0.000	0.002	0.015	0.000	0.000	0.000	0.000	0.003	0.002	0.000	0.093	0.061	0.829	0.000	0.000	0.000
Zn	0.000	0.000	1.002	0.000	0.000	0.000	0.000	0.000	0.000	0.014	0.000	1.757	0.212	0.319	0.000	0.000	0.000
Sb	0.000	0.086	0.000	0.145	0.626	0.505	1.955	2.575	1.015	0.941	4.022	2.967	4.069	3.613	1.028	0.979	0.933
As	0.000	0.000	0.000	0.899	1.386	1.056	0.136	0.060	0.061	0.002	0.157	1.224	0.041	0.133	0.001	0.000	0.000
Hg	0.000	0.000	0.000	0.000	0.000	0.000	0.000	0.000	0.000	0.000	0.800	0.000	0.000	0.000	0.000	0.000	0.000
Cd	0.000	0.000	0.002	0.000	0.000	0.000	0.000	0.000	0.000	0.000	0.000	0.000	0.000	0.792	0.000	0.000	0.000
Pb	1.002	0.998	0.000	0.000	0.000	0.000	0.000	0.000	0.000	0.000	0.942	0.000	0.658	0.760	0.000	0.000	0.000
Mn	0.000	0.000	0.004	0.000	0.000	0.000	0.000	0.000	0.000	0.000	0.000	0.000	0.000	0.342	0.000	0.000	0.000
S	0.997	1.000	0.994	3.486	10.559	10.872	11.188	11.533	3.960	3.999	12.896	12.748	13.030	13.476	3.123	3.058	3.047

Table 3 - Representative bulk geochemical analyses from Trades-Galana area.

		TR-1	TR-2	TR-3	TR-4	TR-5	TR-6	TR-7	TR-8	TR-9	TR-10	TR-11	TR-12	TR-13	GA-1	GA-2	GA-3	GA-4	GA-5	GA-6
Zn	%	0.01	0.003	0.88	2.99	15.0	0.39	9.14	0.15	3.80	3.36	0.43	2.56	3.92	0.08	0.02	0.06	1.73	3.01	4.10
Pb	%	0.05	0.002	0.50	0.45	0.71	0.09	0.86	0.16	0.58	3.27	0.31	1.44	0.81	1.05	0.27	2.13	1.46	0.75	1.99
Cu	%	0.002	0.001	3.28	0.14	0.07	0.04	0.13	0.005	0.11	0.03	0.02	0.11	0.08	0.08	0.02	0.01	0.08	0.04	0.03
As	mg/kg	1210	33	7090	705	65	106	316	342	392	78	2040	281	278	305	43	19	32	15	21
Sb	mg/kg	317	2	22300	563	379	151	562	348	339	136	515	691	519	33	34	49	78	27	32
W	mg/kg	113	79	145	848	300	171	508	474	296	419	459	195	239	268	71	440	450	348	342
Cd	mg/kg	16	0.37	107	215	2370	15	665	4	219	203	16	109	297	2	2	4	106	236	225
Mo	mg/kg	265	bdl	42	5	41	17	21	99	28	7	92	22	44	9	4	8	7	7	10
Tl	mg/kg	55500	1730	724	1420	1040	1100	4690	12400	27900	705	89000	3290	4090	1270	2420	922	952	840	1670
Bi	mg/kg	0.178	0.022	0.001	0.795	0.019	0.011	0.024	0.005	0.011	0.017	0.003	0.010	0.005	0.090	0.186	0.058	0.056	0.040	0.084

bdl: below detection limit.

Based on the geochemical data presented on Table 3, the samples from Triades are enriched in base metals (up to 15 wt. % Zn, up to 3.27 wt. % Pb, up to 3.28 wt. % Cu) compared to those from Galana.

The presence of Cd-bearing low-Fe sphalerite (Table 1) most probably could explain the elevated Cd concentrations in the bulk rock geochemical analyses (Triades: up to 2370 mg/kg Cd; Galana: 225 mg/kg Cd, Table 3). Similarly, the presence of abundant As- and Sb-bearing sulfosalts (e.g. enargite, famatinite, Ag-rich phases, etc.) at Triades compared to Galana are responsible for the elevated concentrations in the bulk rock geochemical analyses (Triades: up to 0.7 wt. % As; up to 2.2 wt. % Sb, Galana: up to 305 mg/kg As and up to 78 mg/kg Sb, Table 3). Tl with up to 89 mg/kg is highly enriched in Triades compared to Galana. Thallium-bearing sulfides and/or sulfosalts were not detected during our study, and most probably thallium is structurally bound in pyrite as suggested for Palaeochori, southern Milos by Katsouri *et al.* (2004) and Kati *et al.* (2015).

5. Discussion - conclusions

Precious metal-rich mineralization in western Milos Island was formed during the Upper Pliocene to Lower Pleistocene during the emplacement of three successive magma pulses (submarine to subaerial rhyodacite, andesite-dacite) in an emergent volcanic edifice (Alfieris *et al.*, 2013; Kilias *et al.*, 2001; Marchik *et al.*, 2010; Naden *et al.*, 2005). Mineralogical data indicate common features among the Profitis Ilias-Chondro Vouno, Kondaros-Katsimoutis-Vani and Triades-Galana mineralizations, all of them characterized by intermediate-sulfidation epithermal ore assemblages (e.g. Einaudi *et al.*, 2003) including galena, iron-poor sphalerite, minor chalcopyrite and barite–adularia–sericite (±calcite). At Triades-Galana fluctuations between intermediate- and high-sulfidation states are indicated by the presence of enargite and famatinite in the mineralization (Alfieris *et al.*, 2013). This study verifies earlier work by Alfieris (2006) and Alfieris *et al.* (2013) and suggests a common paragenetic sequence for both Triades and Galana with early deposition of pyrite followed by galena with tetrahedrite, polybasite, famatinite inclusions plus minor chalcopyrite, then by sphalerite and finally by a high-sulfidation ore assemblage composed of enargite, tennantite, hypogene covellite and late pyrite. Late pyrite occurs as colloform banded pyrite and framboids and is indicative of mineral deposition in a submarine environment (Vavelidis and Melfos 1998; Alfieris *et al.*, 2013). Enargite was deposited during late introduction of As-bearing solutions in the mineralization, as is the case in other submarine settings (e.g. Brothers Volcano/Offshore New Zealand, Wetar island/Indonesia, etc.), where enargite is reported either as an early or late mineral (Sillitoe *et al.*, 1996; de Ronde *et al.*, 2011).

Naden *et al.* (2005) and Alfieris *et al.* (2013) suggest that metallic mineralization in western Milos Island formed under shallow water and partially emergent conditions that were the products of the mixing of seawater and magmatic water derived from subvolcanic sources. The seawater was sufficiently shallow near the top of the domes to allow boiling of ascending fluids (e.g. precipitation of adularia), and the formation of stockwork mineralization beneath the sea-floor. In common to other mineralization in northwestern Milos (e.g. Kondaros-Katsimouti and Vani; Alfieris *et al.*, 2013; Glasby *et al.*, 2005), the metallic mineralization in Triades-Galana area is highly enriched in Mo and W up to 265 and 848 mg/kg, respectively. This enrichment extends over a surface area of about 15 km^2 and is attributed to a buried granite at depth that fed volatiles and metals into the magmatic-hydrothermal system (Alfieris *et al.*, 2013). Tungsten (e.g. scheelite) and Mo-bearing minerals (molybdenite) were not detected in the studied samples, however it is believed that they occur as early, high-temperature phases in the mineralizations. The subsequent evolution of the mineralization from Sb-, towards As-enrichment, may suggest a renewed magmatic pulse in the hydrothermal system associated with an input of As-rich magmatic gases. This evolution was consistent from early reduced and lower sulfidation, towards more oxidized and high-sulfidation conditions and took place under sub-seafloor to seafloor conditions respectively. The presence of lead chlorides included in galena, indicates involvement of seawater (in addition to magmatic water) for the mineralization.

6. References

Alfieris, D., 2006. Geological, geochemical and mineralogical studies of shallow submarine epithermal mineralization in an emergent volcanic edifice, at western Milos island, Greece, PhD thesis, University of Hamburg, Germany, 211 pp.

Alfieris, D. and Voudouris, P., 2005. Ore mineralogy of transitional submarine to subaerial magmatic-hydrothermal deposits in W. Milos, Greece, *In:* Cook, N.G. and Bonev, I., e*ds.*, Au-Ag-Te-Se deposits, *Geochemistry, Mineralogy and Petrology*, 43, Sofia, 1-6.

Alfieris, D., Voudouris, P. and Spry, P.G., 2013. Shallow submarine epithermal Pb-Zn-Cu-Au-Ag-Te mineralization on western Milos Island, Aegean Volcanic Arc, Greece: Mineralogical, Geological and Geochemical constraints, *Ore Geology Reviews*, 53, 159-180.

Altherr, R. and Siebel, W., 2002. I-type plutonism in a continental back-arc setting:Miocene granitoids and monzonites from the central Aegean Sea, Greece, *Contrib.Mineral.Petrol*., 143, 397-415.

de Ronde, C.E., Massoth, G.J., Butterfield, D.A., Christenson, B.W., Ishibashi, J., Ditchburn, R.G., Hannington, M.D., Brathwaite, R.L., Lupton, J.E., Kamenetsky, V.S. and Graham, I.J., 2011. Submarine hydrothermal activity and gold-rich mineralization at Brothers Volcano, Kermadec Arc, New Zealand, *Mineralium Deposita*, 46(5-6), 541-584.

Einaudi, M.T., Hedenquist, J.W. and Inan, E.E., 2003. Sulfidation state of fluids in active and extinct hydrothermal systems: Transitions from porphyry to epithermal environments. *In:* Simmons, S.F. and Graham, I., *eds.*, Volcanic, Geothermal, and oreforming fluids: Rulers and witnesses of processes within the Earth, *Soc. Econ. Geol., Special Publication*, 10, 285-313.

Fytikas, M., Innocenti, F., Kolios, N., Manneti, P., Mazzuoli, R., Poli, G., Rita, F. and Villari, L., 1986. Volcanology and petrology of volcanic products from the island of Milos and neighbouring islets, *J. Volcanol. Geotherm. Res*., 28, 297-317.

Glasby, G.P., Papavassiliou, C.T., Mitsis, J., Valsami-Jones, E., Liakopoulos, A. and Renner, R.M., 2005. The Vani manganese deposit, Milos island, Greece: a fossil stratabound Mn-Ba-Pb-Zn-As-Sb-W-rich hydrothermal deposit. *In:* Fytikas, M. and Vougioukalakis, G.E., e*ds*., The South Aegean Active Volcanic Arc: Present Knowledge and Future Perspectives, *Developments in Volcanology*, 7, Elsevier, 255-291.

Hauck, M., 1988. Kuroko-type ore deposits on the Aegean Islands, Greece. *In:* Friedrich, G.M. and Herzig, P.M., *eds.*, Base metal sulfide deposits, Springer Verlag, Berlin, 216-228.

Jolivet, L., and Brun, J.P., 2010. Cenozoic geodynamic evolution of the Aegean region, *Int. J. Earth Sci.*, 99, 109-138.

Kati, M., Voudouris, P., Valsami-Jones, E., Magganas, A., Baltatzis, E., Kanellopoulos, C. and Mavrogonatos, C., 2015, April. Cinnabar, arsenian pyrite and thallium-enrichment in active shallow submarine hydrothermal vents at Paleochori Bay, Milos Island, Greece, *EGU General Assembly Conference Abstracts*, 17, 13046 pp.

Katsouri, S., Scott, S.D., Gorton, M.P., Magganas, A., Valsami-Jones, E., Baltatzis, E. and Kati, M., 2004. Formation of hydrothermal sulphides in active shallow water systems: the role of freshwater vs seawater, SEG Eugen Stumpfl Memorial Symposium, *Predictive Mineral Discovery Under Cover. Seccion*, 1, 220-223.

Kilias, S.P., Naden, J., Cheliotis, I., Shepherd, T.J., Constandinidou, H., Crossing, J. and Simos, I., 2001. Epithermal gold mineralisation in the active Aegean volcanic arc: the ProfitisIlias deposit, Milos Island, Greece, *Miner. Deposita*, 36, 32-44.

Kilias, S.P., Nomikou, P., Papanikolaou, D., Polymenakou, P.N., Godelitsas, A., Argyraki, A., Carey, S., Gamaletsos, P., Mertzimekis, T.J., Stathopoulou, E. and Goettlicher, J., 2013. New insights into hydrothermal vent processes in the unique shallow-submarine arc-volcano, Kolumbo (Santorini), Greece, *Scientific Reports*, 3, 2421, 1-13.

Liakopoulos, A., Glasby, G.P., Papavassiliou, C.T. and Boulegue, J., 2001. Nature and origin of the Vani manganese deposit, Milos, Greece: an overview, *Ore Geol Rev*, 18, 181-209.

Marschik, R., Bauer, T., Hensler, A.S., Skarpelis, N. and Holzl, S., 2010. Isotope Geochemistry of the Pb-Zn-Ba(-Ag-Au) Mineralization at Triades-Galana, Milos Island, Greece, *Res. Geology*, 60, 335-347.

Naden, J., Kilias, S.P. and Darbyshire, D.B.F., 2005. Active geothermal systems with entrained seawater as analogues for transitional continental magmato-hydrothermal and volcanic-hosted massive sulfide mineralization-the example of Milos Island, Greece, *Geology*, 33, 541-544.

Plimer, I., 2000. Milos Geologic History. KOAN Publishing House, Athens, 262 pp.

Scotney, P.M., Roberts, S., Herrngton, R.J., Boyce, A.J. and Burgess, R., 2005. The development of volcanic hosted massive aulfide and barite gold orebodies on Wetar Island, Idonesia, *Mineralium Deposita*, 40, 76-99.

Shimizu, M., Kato, A., Matsubara, S., Criddle, A.J. and Stanley, C.J., 1993. Watanabeite, $Cu_4(As,Sb)_2S_5$, a new mineral from the Teine mine, Sapporo, Hokkaido, Japan, *Mineral. Mag.*, 57, 643-649.

Sillitoe, R.H., Hannington, M.D. and Thompson, J.F.H., 1996. High-sulfidation deposits in the volcanogenic massive sulfide environment, *Econ. Geol.*, 91, 204-212.

Stewart, A.L. and McPhie, J., 2003. Setting of epithermal Au deposits in a modern volcanic island arc setting, Milos, Greece: Implications for mineral exploration, *Mineral Exploration and Sustainable Development. Millpress*, Rotterdam, 533-536.

Stewart, A.L. and McPhie, J., 2006. Facies architecture and Late Pliocene-Pleistocene evolution of a felsic volcanic island, Milos, Greece, *Bull. Volcanol.*, 68, 703-726.

Vavelidis, M. and Melfos, V., 1997. Two plumbian tetrahedrite-tennantite occurrences from Maronia area (Thrace) and Milos island (Aegean Sea, Greece), *Eur. J. Mineral.*, 9, 653-657.

Vavelidis, M. and Melfos, V., 1998. Fluid inclusion evidence for the origin of the barite silver-gold-bearing Pb-Zn mineralization of the Triades area, Milos Island, Greece, *Bull. Geol. Soc. Greece*, 32, 137-144.

Δελτίο της Ελληνικής Γεωλογικής Εταιρίας, τόμος L, σελ. 1980-1988
Πρακτικά 14ου Διεθνούς Συνεδρίου, Θεσσαλονίκη, Μάιος 2016

Bulletin of the Geological Society of Greece, vol. L, p.1980-1988
Proceedings of the 14th International Congress, Thessaloniki, May 2016

IMPLICATIONS OF PETROGRAPHY AND GEOCHEMISTRY OF ATHINIOS METAMORPHIC UNITS USING PXRF AND GIS ANALYSES IN THERA (SANTORINI, GREECE).

Pasqualon N.G.[1], Santos K.N.S.[2], Marsellos A.E.[3] and Kyriakopoulos K.[4]

[1]*Universidade Federal do Rio Grande do Sul (UFRGS), Av. Bento Gonçalves, 9500 - Agronomia, Porto Alegre - RS, Brazil, 90650-001, nati_pasqualon@yahoo.com.br*

[2]*Universidade Federal do Rio de Janeiro (UFRJ), Av. Athos da Silveira, 274, Campus Ilha do Fundão, Rio de Janeiro-RJ, Brazil, 21949-900, kathelynunes@gmail.com*

[3]*Hofstra University, Hempstead, New York, U.S.A., 11549-1000, antonios.marsellos@hofstra.edu*

[4]*National & Kapodistrian University of Athens, Zografou, Athens, Greece, 157 84, ckiriako@geol.uoa.gr*

Abstract

Santorini metamorphic basement is part of the metamorphic complex known as Cycladic Massif, which was formed during the subduction of the Mediterranean lithosphere underneath the Aegean microplate. The two main components of the exposed basement are a complex of low-grade schists and phyllites, which are well exposed in Athinios harbour and overlaid by the crystalline limestones exposed in Mount Profitis Ilias and Mount Mesa Vouno. The Eocene and Miocene metamorphic units present evidence of dynamic metamorphism, and possibly are influenced by a granitic intrusion in Miocene. In this study, a new methodology was developed to study the two units exposed at Athinios. Structural data and rock samples were analysed using a Portable X-Ray fluorescence (PXRF) spectrometer analysis at Athinios and integrated in aGIS (Geographical Information System) software to understand the spatial geochemical variations in the area. PXRF results for the two metamorphic units showed similar geochemical patterns. However, a contour map of TiO_2 (%) for the metamorphic rocks of the Athinios area presented intermittent zones of high and low TiO_2 concentrations which could indicate hydrothermal remobilization of light elements and an enrichment in Ti. Petrography and geochemistry results suggest the local existence of a ductile-brittle shear zone between the two metamorphic units.

Keywords: *Petrography, geochemistry, Athinios, Eocene and Miocene metamorphic units, Santorini ductile-brittle shear zone.*

1. Introduction

The Hellenic Volcanic Arc tectonics has been influenced by the interaction between the northward subducting African plate and the overriding Aegean micro-plate. Santorini Island belongs to the Hellenic volcanic arc located at the South Aegean Sea. Santorini metamorphic basement is part of the metamorphic complex called Cycladic Massif. In the study area, a metamorphic unit with Miocene cooling ages is juxtaposed structurally below an Eocene metamorphic unit (Marsellos *et al.*, 2013). Both units have undergone two stages of the Alpine metamorphism: at Eocene

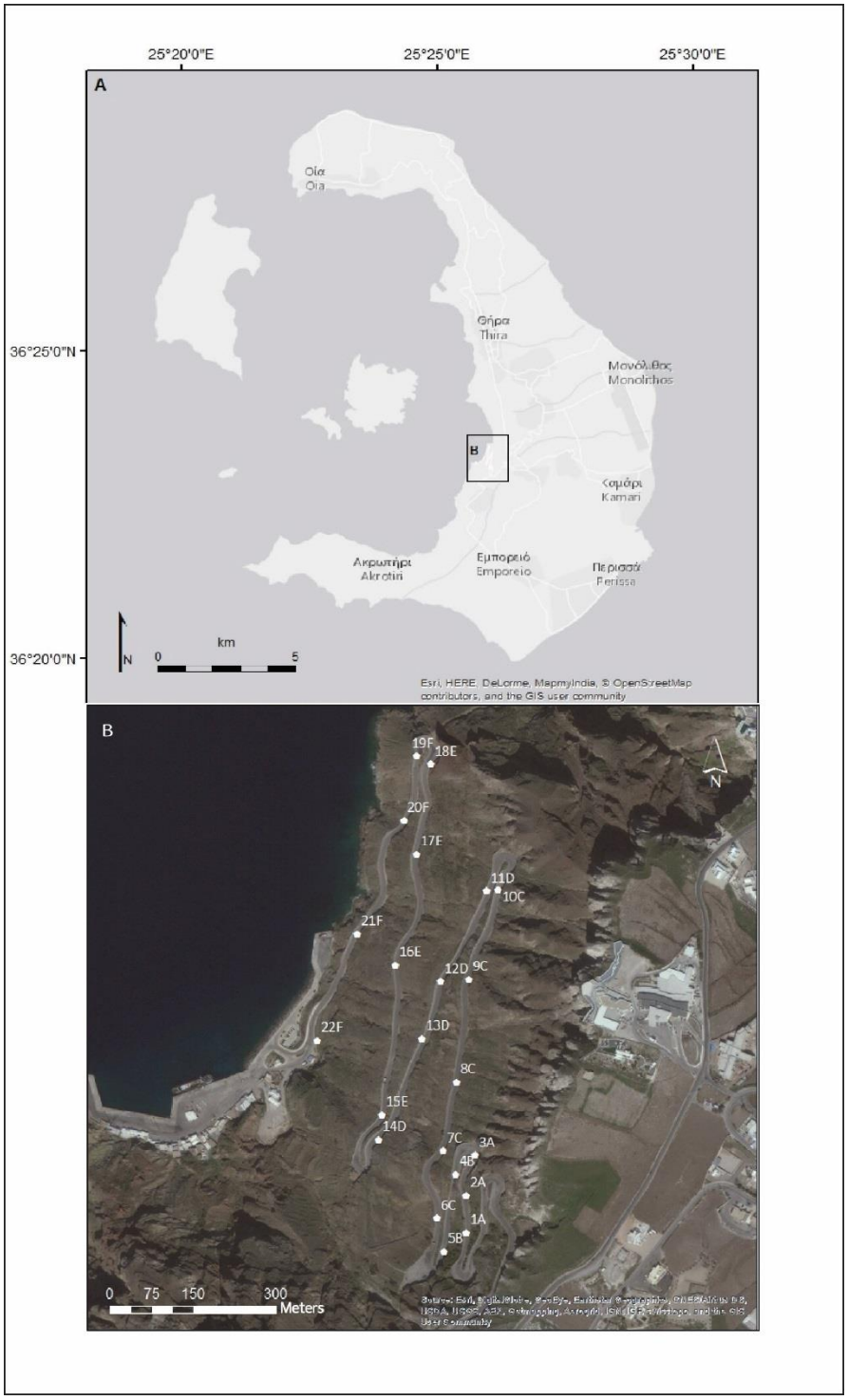

Figure 1 - A) Athinios harbour location within Santorini. B) Map of samples collected for petrography in Athinios. Each letter corresponds to a road-segment following a descending direction where the sample was collected.

high-pressure event producing blueschist-facies assemblages and a Miocene medium-pressure event producing greenschist-facies assemblages (Altherr *et al.*, 1982 Andriessen *et al.*, 1979). The two metamorphic units are composed of low-grade metapelites and were exhumed during multiple events and via multiple detachment faults as previously described in other areas in the Aegean as well (e.g. Lister *et al.*, 1984; Fassoulas *et al.*, 1994; Thomson *et al.*, 1999; Ring *et al.*, 2010; Keay *et al.*, 2001; Jolivet *et al.*, 2003; Marsellos *et al.*, 2010). The Santorini metamorphic rocks have shown an interesting petrography and geochemistry (e.g. Davis and Bastas, 1978 and Skarpelis and Liati, 1990). This work presents a petrographic and geochemical study of the two metamorphic units exposed along the road of Athinios harbour (Fig.1) through the use of optical microscopy, PXRF (Portable X-ray Fluorescence) and GIS (Geographical Information System) analyses. A discussion follows about the interesting petrographic, geochemical, and structural patterns of the two metamorphic units.

2. Santorini tectonic and geological setting

The Hellenic Volcanic Arc tectonics (Fig.2) has been influenced by the interaction of the northward African subducting slab and the overriding Aegean plate. The African plate experiences episodic rollback (Ring *et al.*, 2010; Marsellos *et al.*, 2012), and the overriding Aegean plate follows a back arc extension. The Aegean Sea is an excellent example of episodic extension and exposes a wide range of regional detachment faults (e.g. Fassoulas *et al.*, 1994; Thomson *et al.*, 1999; Jolivet *et al.*, 2003; Marsellos and Kidd, 2008; Ring *et al.*, 2010; Skourtsos and Lekkas, 2011) and localized multi-detachments with episodic extension direction as observed in Kythera and Peloponnese. The Hellenic arc has recorded a local arc-parallel extension along a

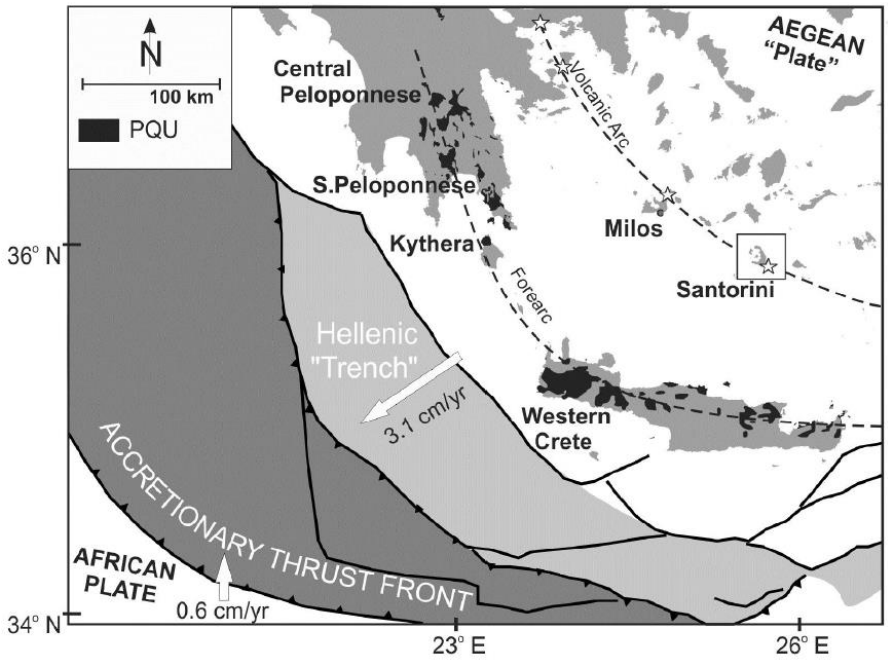

Figure 2 - Tectonic setting of the Hellenic volcanic arc and forearc which are the result of the interaction between the northward African subducting plate and the overriding Aegean microplate. Present GPS Eurasia-Africa relative velocity and average western Hellenic Arc-Africa relative velocity (derived from the average of five stations in western-central Crete, Kythera, and south Peloponnese) after McClusky *et al.* (2000).

NW-SE direction from southeastern Peloponnese through Kythera and western Crete (Marsellos and Kidd, 2008). In the Hellenic Trench the tensional field causes low dip angle thrust faults trending NW-SE and dipping NE (Fytikas and Vougioukalakis, 2005), while in the volcanic arc the crust is dominated by a tensional field with a NW-SE direction, resulting in normal faults which strike NE-SW. (e.g. Jolivet *et al.*, 2003; Papazachos *et al.*, 2005). In Santorini, the exposed schists and phyllites at Athinios have shown Miocene (10.9 ± 0.7Ma, ZFT; 9.4 ± 0.3 Ma, AHe) and Eocene (46.3± 2.8 Ma, ZFT; 49.34 ± 2.9 Ma, AHe) exhumation ages (Marsellos *et al.*, 2013) implying a thermal reset in Miocene which is possibly related to a granitic intrusion that took place at 9.5 Ma (Skarpelis *et al.*, 1992).

3. Methodology

3.1. Sample locations

The occurrence of metamorphic rocks in Santorini Island is restricted to the localities of Perissa in the southeast, to the outer rim of the island and to the caldera walls at Athinios harbour. The area chosen for this work within Santorini Island is Athinios harbour, which is located in the eastern portion of the island (Fig.1A) and shows very well preserved metamorphic rocks and structures for a length of at least 3 km and a height of 215 m. For the PXRF analysis, 132 sites were selected within 20-30 m intervals along the 3 km descending road towards Athinios harbour (Fig. 3) and 22 sites for microscopic analysis of rock thin sections.

3.2. Geochemistry and Petrography

For the petrographic work a Nikon Eclipse E400 microscope was used, with an attached Nikon E995, 34.4 megapixel Digital camera for the photomicrographs. Analysis was completed with 22 thin sections from Athinios metamorphic rock units. PXRF analysis performed in 132 samples during three days using the battery-powered portable x-ray fluorescence spectrometer X-MET 5100 - Oxford Instruments. The modes of operation were standard element ('soil') and the light element analysis programme (LEAP) which provided analyses for Al, Si, P, S, Cl, K, Ca, Na, Mg, Ti, Cr, Mn, Fe, Cu, Zn, As, Rb, Sr, Pb. Each of the 132 samples was analysed 3 times using count times of 60 seconds per measurement. The ppm values obtained were inserted in an Excel file, the average value for the 3 measurements was taken and the final values were converted to oxide percentages. Finally, a series of graphs and contour maps were generated through a GIS software for the spatial analysis of major, minor and trace elements.

3.3. Geographical Information System (GIS)

PXRF measurements with sample coordinates, altitude, lineations and element analysis was imported in a GIS software (ArcGIS 10.2 by ESRI) to study the spatial distribution of major and minor elements in the area. Using a previous methodology of k-means cluster analysis in a GIS software (Marsellos *et al.*, 2013) the two metamorphic units were separated through their stretching lineations (with clusters at NNW-Miocene and at NNE-Eocene) values. A representative average of the major elements geochemistry of each unit was calculated, which is summarized in Table 1.

4. Results

4.1. Petrology

The Miocene unit rocks show a gray to pale green colour, a prominent foliation with a stretching lineation trending NNW, and mineral composition of chlorite, muscovite, quartz, albite and minor calcite. Some outcrops presented alternation between schists and layers from 0,5 up to 2 m thick of marbles, which have light gray colour and granoblastic texture, composed mostly of fine calcite grains. The Eocene unit has an orange-reddish colour due to alteration and where best preserved, a pale green colour, with a silky luster at its surface composed of very fine grains barely identified by

the naked eye. On the foliation surface a stretching lineation trending NNE was identified. Both metamorphic units present sets of faults filled in by quartz and calcite and dynamic metamorphism features such as quartz and albite porphyroclasts and aggregates. It was possible to find within the two units chlorite-quartz-mica schists, mica-calcite-quartz schists to quartzites, phyllites, calc-phyllites and calcite marbles (Fig.4).

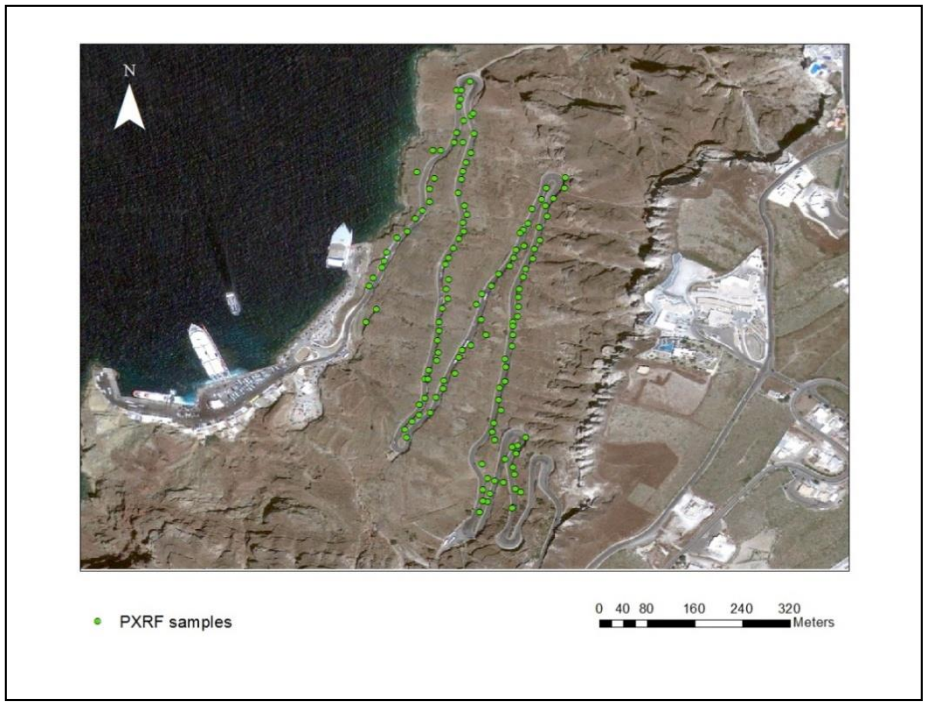

Figure 3 - Location of 132 samples collected in Athinios for PXRF analysis.

In general, schists and phyllites from both metamorphic units host a well-developed foliation, with a visible crenulation cleavage and a main mineralogical composition of quartz, muscovite, albite, chlorite, biotite, calcite, and rutile and iron oxides as accessory phases. Rocks present a granolepidoblastic texture; micas and chlorite aligned in a preferential direction define the lepidoblastic texture and phyllites' optical fissility, while quartz, calcite and feldspar define the granoblastic texture.

Marble lenses are located within the schists and phyllites of Athinios. They are composed of fine to medium grain granoblastic calcite and they may also contain a few percentage of quartz and white mica.

Quartz occurs as porphyroclasts and as recrystallized polycrystalline quartz in the matrix of the phyllites or schists. Quartz porphyroclasts have an undulose extinction (Fig.4h), with a sub-angular shape. Quartz porphyroclasts have been fractured or rotated showing bookshelf structures. Some grains also present deformation bands and gradual evolution to sub grains in the external portion (Fig.4f). The recrystallized quartz grains in the matrix show a homogeneous grain size and vary from almost undeformed to very well oriented and present irregular grain boundaries. Albite has been identified in the matrix with quartz, and some of them are substituted by calcite and sericite and albite porphyrclasts presented polysynthetic twinning, sub to well-rounded shape, and it is possible to observe that they suffered rotation within the matrix (Fig.4e). Micas are aligned in a preferred orientation defining the lepidoblastic texture of the rocks (Fig.4b and 4c). C-S structures marked by muscovite surrounding feldspar porphyroclasts were observed. Chlorite occurs with a lamellar habit and dark green to brownish pleochroism under plane polarized light. Most of chlorite

was found within mica domains in the matrix. Calcite appears substituting plagioclase in the matrix or cementing the grains with an anhedral shape and lamellar twinning, with high order birefringence colors. In the marble lenses calcite presented a rhombohedral cleavage and lamellar mechanic twinning (Fig.4d).

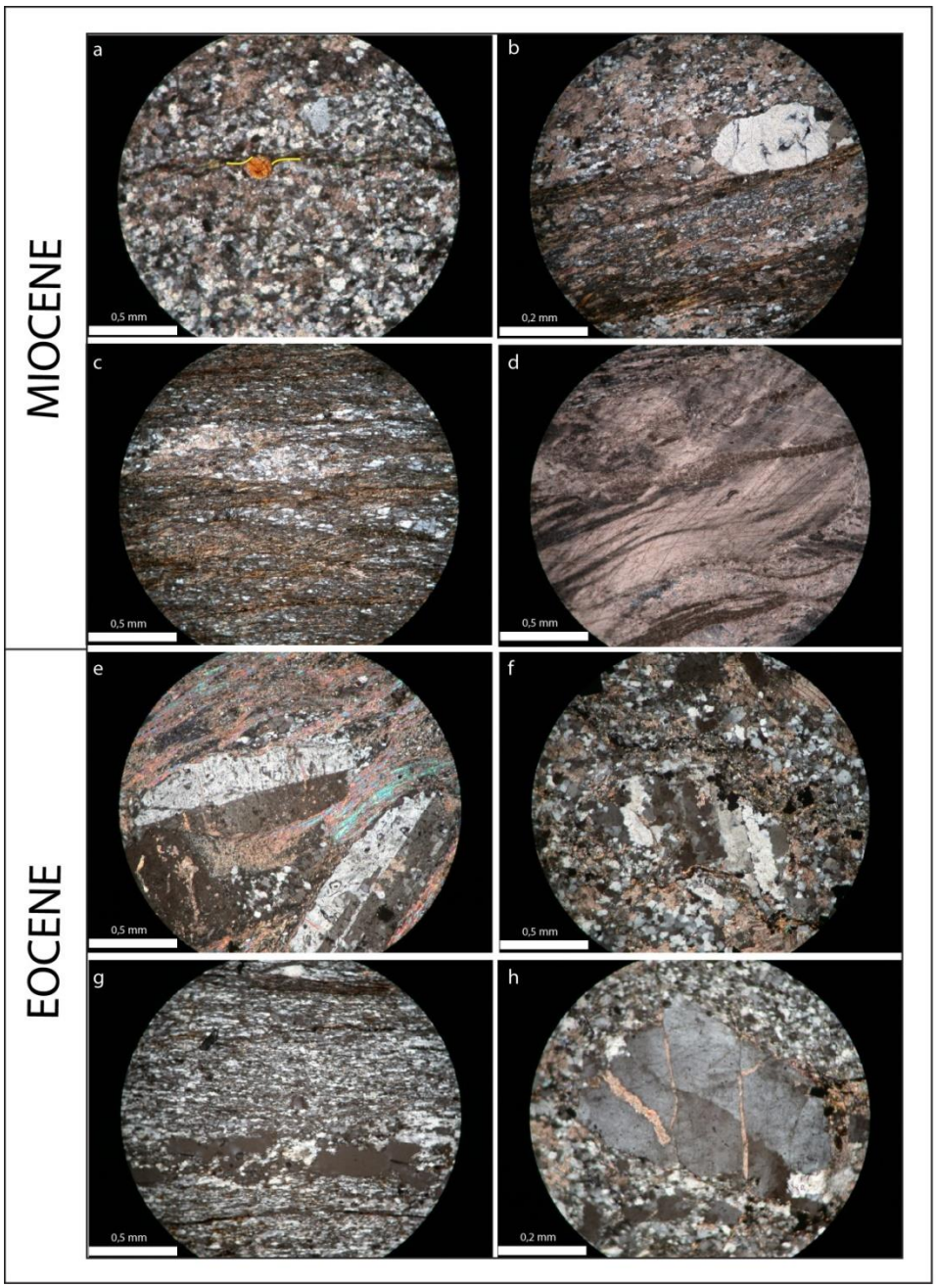

Figure 4 - Representative thin sections under cross polarized light (XPL) from Miocene and Eocene units. Miocene: a) Mica-calcite-quartz schist to quartzite (site 2A); b) and c) Calc-phyllites (site 12D); d) Calcite marble lense within phyllites in plane polarized light (site 15E). Eocene: e) Chlorite-mica shicst (site 9C); f) and h) Mica-calcite-quartz schists to quartzites (site 18E); g) Phyllite (site 19F).

4.2. Geochemistry, structural data and GIS analysis

PXRF measurements with sample coordinates, altitude, lineations and element analysis was imported in a GIS software (ESRI) to study the spatial distribution of major and minor elements in the area. Using a previous methodology (Marsellos *et al*., 2013) of separating the two metamorphic units through their stretching lineation (NNW-Miocene and NNE-Eocene) values, we calculated a representative average of the major elements geochemistry of each unit, which is summarized in Table 1. In the GIS software using the kriging function, a series of major and minor elements contour maps were created. TiO_2 showed quantile QQ-plots with values closer to a normal distribution of the data, and resulted in the most significant contour map. In TiO_2 contour map it is possible to distinguish two zones of titanium concentrations, regions in green that show concentrations from 0-1,51% of TiO_2 while regions in yellow show values higher than 1,51% (Fig.5).

Table 1 - Average concentrations (% percentages) of major elements for Eocene and Miocene samples. *FeO is the total iron content.

Metamorphic unit	SiO_2	Al_2O_3	FeO*	MnO	MgO	CaO + Na_2O	K_20	TiO_2	Total
Miocene N = 83	49.16	21.26	12.09	0.41	2.27	5.17	7.01	1.97	99.34
Eocene N = 49	50.14	20.82	10.6	0.48	2.09	7.36	6.59	1.68	99.76

5. Discussion and conclusions

Miocene and Eocene units at Athinios harbour show similar petrographic and geochemical features, being distinguished only by their different stretching lineations and thermochronological ages, which suggest that both units have undergone the same stages of metamorphism, but were exhumed at different times. We confirm that Miocene unit was affected by arc-parallel extension while Eocene unit by arc-normal extension during its exhumation.

Analysing the petrography of the schists and phyllites, it is possible to note evidences of dynamic metamorphism. Microstructures and features such as quartz porphyroclasts showing undulose extinction, sub-grains formation and deformation bands, C-S structures marked by micas, rotated albite porphyroclasts and calcite deformed crystals showing twinning are indicators of plastic deformation mechanisms. The formation of some of these microstructures is due to the recovery process, in which, in order to decrease the strain/energy in crystal lattice, dislocations become rearranged and destroyed. During this process of recovery, dislocations align and create dislocation walls, which form sub-grains and undulose extinction. Recrystallized quartz grains express the process in which deformed grains with many dislocations are substituted by grains with few dislocations. In some of the samples analysed, recrystallized quartz presents an equigranular aspect, with no preferred orientation which indicates static recrystallization or annealing process, while in other samples quartz grains show alignment, evidence of recrystallization under differential stress. The deformation of phyllosilicates in framework phyllosilicate bands are also indicators of ductile deformation because under high temperatures/pressures these minerals rotate to align with the band and generate barriers to the fluid flow.

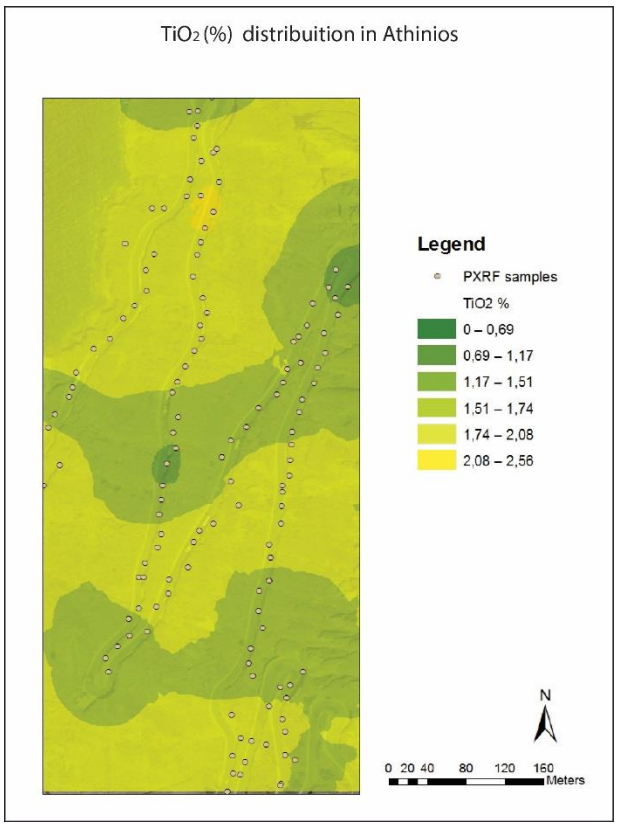

Figure 5 - TiO_2 contour map. Dark green represents lower percentages of TiO_2 and light green and yellow represent higher percentages.

Geochemistry values, together with petrography, suggest pelitic, calc-silicate and silisiclastic sedimentary rocks as protholiths for both units. TiO_2 contour map shows a surprising pattern in which well delimited zones with high and low values of TiO_2 concentration can be explained due to the geochemical behaviour of this element. Ti behaves as a high field strength element (HFSE) (Salters, 1998), hence it would not be easily remobilized even under hydrothermal alteration. Zones with a TiO_2 enrichment would represent areas in which other elements were remobilized by hydrothermal fluids. Therefore, through TiO_2 contour map and evidences of dynamic metamorphism found in petrography, it is possible to infer the presence of a ductile-brittle shear zone that, when active in Miocene, allowed fluids to go through its brittle portions and remobilize light elements provoking Ti enrichment and lead plastic deformation to occur in greater depth.

6. Acknowledgments

This work is a result of the Brazilian exchange program Science without Borders, sponsored by CNPq. Funding for sample analysis with PXRF and thin sections was provided by University of Brighton in United Kingdom. We thank Peter Lyons, Norman Moles, Martin Smith and Stewart Ullyott from University of Brighton for the support with sample analysis and advices. Part of the conference expenses are covered by ELKE of EKPA of University of Athens and by the Hofstra University.

7. References

Altherr, R., Kreuzer, H.A.N.S., Wendt, I., Lenz, H., Wagner, G.A., Keller, J., Harre, W. and Hohndorf, A., 1982. A late Oligocene/early Miocene high temperature belt in the Attic-Cycladic crystalline complex (SE Pelagonian, Greece), *Geologisches Jahrbuch E.*, 23, 97-164.

Andriessen, P.A.M., Boelrijk, N.A.I.M., Hebeda, E.H., Priem, H.N.A., Verdurnen, E.T. and Verschure, R.H., 1979. Dating the events of metamorphism and granitic magmatism in the Alpine Orogen of Naxos (Cyclades, Greece), *Contributions to Mineralogy and Petrology*, 69(3), 215-225.

Davis, E.N. and Bastas, C., 1978. Petrology and geochemistry of the metamorphic system of Santorini. In Thera and the Aegean World. 1, 61 pp.

Fassoulas, C., Kilias, A. and Mountrakis, D., 1994. Post-nappe stacking extension and exhumation of the HP/LT rocks in the island of Crete, Greece, *Tectonics*, 13, 127-138.

Fytikas, M. and Vougioukalakis, G., *eds*., 2005. The South Aegean Active Volcanic Arc: Present Knowledge and Future Perspectives, 7, Elsevier.

Jolivet, L., Faccenna, C., Goffé, B., Burov, E. and Agard, P., 2003. Subduction tectonics and exhumation of high-pressure metamorphic rocks in the Mediterranean orogens, *American Journal of Science*, 303(5), 353-409.

Keay, S., Lister, G. and Buick, I., 2001. The timing of partial melting, Barrovian metamorphism and granite intrusion in the Naxos metamorphic core complex, Cyclades, Aegean Sea, Greece, *Tectonophysics*, 342, 275-312.

Lister, G.S. and Snoke, A.W., 1984. SC mylonites. *Journal of Structural Geology*, 6(6), 617-638.

Marsellos, A.E. and Kidd, W.S.F., 2008. Extension and exhumation of the Hellenic forearc ridge in Kythera, *The Journal of Geology*, 116(6), 640-651.

Marsellos, A.E., Kidd, W.S.F. and Garver, J.I., 2010. Extension and exhumation of the HP/LT rocks in the Hellenic forearc ridge, *American Journal of Science*, 310(1), 1-36.

Marsellos, A., Foster, D.A., Kamenov, G.D. and Kyriakopoulos, K., 2012. Detrital zircon U-Pb data from the Hellenic south Aegean belts: constraints on the age and source of the South Aegean basement, *Journal of the Virtual Explorer*, 42, 1-12.

Marsellos, A., Foster, D.A., Min, K., Kidd, W.S.F., Garver, J.I. and Kyriakopoulos, K., 2013. An application of GIS analysis on structural data from metamorphic rocks in Santorini Island, *Bulletin of the Geological Society of Greece*, 47.

McClusky, S., Balassanian, S., Barka, A., Demir, C., Ergintav, S., Georgiev, I. and Kastens, K., 2000. Global Positioning System constraints on plate kinematics and dynamics in the eastern Mediterranean and Caucasus. *Journal of Geophysical Research: Solid Earth*, 1978-2012, 105(B3), 5695-5719.

Papazachos, B.C., Dimitriadis, S.T., Panagiotopoulos, D.G., Papazachos, C.B. and Papadimitriou, E.E., 2005. Deep structure and active tectonics of the southern Aegean volcanic arc, *Developments in Volcanology*, 7, 47-64.

Ring, U., Glodny, J., Will, T. and Thomson, S., 2010. The Hellenic subduction system: high-pressure metamorphism, exhumation, normal faulting, and large-scale extension, *Annual Review of Earth and Planetary Sciences*, 38, 45-76.

Salters, V.J.M., 1998. Elements: High Field strength. *In*: Marshall, C.P. and Fairbridge, R.W., *eds*., 1999, *Encyclopedia of Geochemistry, Springer Science and Business Media*, 21, 209-210.

Skarpelis, N. and Liati, A., 1990. The prevolcanic basement of Thera at Athinios: metamorphism, plutonism and mineralization, *Thera and the Aegean World III*, 2, 172-82.

Skarpelis, N., Kyriakopoulos, K. and Villa, I., 1992. Occurrence and $^{40}Ar/^{39}Ar$ dating of a granite in Thera (Santorini, Greece), *Geologische Rundschau*, 81/3, 729-735, Stuttgart 1992.

Skourtsos, E., and Lekkas, S. (2011). Extensional tectonics in Mt Parnon (Peloponnesus, Greece). *International Journal of Earth Sciences*, 100(7), 1551-1567.

Thomson, S.N., Stockhert, B. and Brix, M.R., 1999. Miocene high-pressure metamorphic rocks of Crete, Greece: rapid exhumation by buoyant escape, *In*: Ring, U., Brandon, M., Lister, G.S., and Willet, S.D., *eds*., Exhumation Processes: Normal Faulting, Ductile Flow and Erosion, *Geological Society, London, Special Publication*, 154, 87.

Δελτίο της Ελληνικής Γεωλογικής Εταιρίας, τόμος L, σελ. 1989-1998
Πρακτικά 14ου Διεθνούς Συνεδρίου, Θεσσαλονίκη, Μάιος 2016

Bulletin of the Geological Society of Greece, vol. L, p. 1989-1998
Proceedings of the 14th International Congress, Thessaloniki, May 2016

COMPARATIVE STUDY OF PHYSICOMECHANICAL PROPERTIES OF ULTRABASIC ROCKS AND ANDESITES FROM CENTRAL MACEDONIA (GREECE)

Petrounias P.[1], Rogkala A.[1], Kalpogiannaki M.[1], Tsikouras B.[1,2] and Hatzipanagiotou K.[1]

[1]*University of Patras, Department of Geology, Section of Earth Materials, 265 00, Patras, Greece*

[2]*Universiti Brunei Darussalam, Faculty of Science, Physical and Geological Sciences, Jalan Tungku Link,Gadong BE1410, Bandar Seri Begawan, Brunei Darussalam*

Abstract

Petrographic, geochemical and physicomechanical features were determined and inter-correlated in two representative ultrabasic samples from the Veria-Naousa ophiolite and two Pliocenic andesite samples, occurring at the east of the above complex. Results show that mineralogical and textural features are major factors affecting the physicomechanical properties in both lithotypes. The ultrabasic rocks display higher resistance to attrition and abrasion and lower water absorption values relative to the intermediate volcanic rocks, hence the first are predicted to show better in-service engineering performance. However, the degree of serpentinisation is detrimental, as a highly serpentinised ultrabasic sample yielded poor results, analogous to the andesites, in certain laboratory tests. Ophiolite complexes in Greece are abundant and they are distributed along several mainland areas. Hence setting evaluation criteria for their quality is important as they can potentially replace limestones, which are less resistant and durable, in several environmental and industrial applications.

Keywords: *aggregates, physicomechanical properties, andesites, serpentinite, harzburgite, ophiolite.*

Περίληψη

Προσδιορίστηκαν πετρογραφικά, γεωχημικά και φυσικομηχανικά χαρακτηριστικά σε δυο αντιπροσωπευτικά δείγματα υπερβασικών πετρωμάτων από το οφιολιθικό σύμπλεγμα Βέροιας-Νάουσας και δυο δείγματα Πλειοκαινικών *ανδεσιτών οι οποίοι απαντούν στα ανατολικά του παραπάνω συμπλέγματος. Τα αποτελέσματα υποδεικνύουν ότι τα ορυκτολογικά και ιστολογικά χαρακτηριστικά και των δυο λιθοτύπων είναι σημαντικοί παράγοντες που επηρεάζουν τις φυσικομηχανικές τους ιδιότητες. Οι υπερβασικοί λιθότυποι παρουσιάζουν υψηλότερη αντοχή σε φθορά από τριβή και κρούση με την μηχανή* Los Angeles *και μικρότερες τιμές υδαταπορροφητικότητας σε σχέση με τα ενδιάμεσα ηφαιστειακά πετρώματα. Όμως, ο βαθμός σερπεντινίωσης παίζει αρνητικό ρόλο καθώς παρατηρήθηκε ότι ένα έντονα σερπεντινιωμένο δείγμα έδωσε πτωχές τιμές, ανάλογες με αυτές των ανδεσιτών, σε συγκεκριμένες εργαστηριακές δοκιμές. Οφιολιθικά πετρώματα αφθονούν στον Ελληνικό χώρο καταλαμβάνοντας μεγάλες εκτάσεις σε περιοχές της ηπειρωτικής χώρας. Για το λόγο αυτό θεωρούμε σημαντικό να καθοριστούν κριτήρια εκτίμησης της καταλληλότητάς*

τους, καθόσον δυνητικά μπορούν να αντικαταστήσουν τα ασβεστολιθικά πετρώματα, τα οποία γενικά παρουσιάζουν χαμηλότερη αντοχή και ανθεκτικότητα, σε διάφορες περιβαλλοντικές και βιομηχανικές εφαρμογές.
Λέξεις κλειδιά: *αδρανή υλικά, φυσικομηχανικές ιδιότητες, ανδεσίτες, σερπεντινίτες, χαρτσβουργίτες, οφιολιθικό σύμπλεγμα.*

1. Introduction

Research of the engineering properties of ophiolitic and acidic to intermediate volcanic rocks, for industrial purposes, shows an increasing interest. Basic and ultrabasic rocks find a wide variety of uses as aggregates for antiskid road surfacing, concrete, railway ballast, etc. (French and Gammond, 1989; Tsikouras *et al.,* 2005; Pomonis *et al.,* 2007; Rigopoulos *et al.,* 2010), whereas those of acidic-intermediate composition comprise very good mortar aggregates for various uses (Miskovsky *et al.,* 2004; Zorlu *et al.,* 2004). Use of petrography as a tool in the assessment of aggregates quality dates back to the early part of the 20th century (Knight and Knight, 1935; Griffiths, 1989; Rhoades and Mielenz, 1946). The influence of alteration on strength and durability properties of rocks has been discussed by many researchers in recent years and various micropetrographic and weathering indices have been proposed (Harben and Bates, 1990; Irfan *et al.,* 1978; Mendes *et al.,* 1966).

The present paper aims at the comparison of the physicomechanical properties and engineering performances of ultrabasic rocks (from the Veria-Naousa ophiolitic complex) and andesites (from a Pliocene intrusive series at the east of the complex). Moreover, we intend to investigate the influence of their petrographic characteristics to their mechanical behaviour and to assess their quality.

2. Geological setting

The Veria-Naousa ophiolite represents a dismembered ophiolite unit, which is superimposed on a basement consisting of rocks belonging to the Pelagonian and Axios (Almopias subzone) isopic zones in northern Greece (Fig. 1).

The ophiolite is obducted onto Cretaceous platform carbonates and a flysch succession of the Pelagonian Zone during Upper Jurassic to Lower Cretaceous time (Mercier *et al.,* 1975; Economou, 1983; Michailidis, 1990; Economou-Eliopoulos, 2003; Tsoupas and Economou-Eliopoulos, 2008). The ophiolite suite includes, from bottom to top, serpentinised lherzolite and harzburgite, intruded by a sparse network of pyroxenitic dykes, gabbro, diabase and pillow basalts. Field work revealed that it is an incomplete and dismembered suite, due to intensive tectonism. The serpentinised peridotites are intensely tectonised, showing a dense network of joints. Rare rodingite dykes occur in the serpentinised ultramafic rocks. The ophiolite is unconformably overlain by sediments (conglomeratic limenstone, flysch).

Pliocenic volcanic rocks of the Almopias subzone ranging in composition fromtrachyte to trachyandesite occur to the east of the ophiolitic complex. Nd/Sr isotopic data indicate that these rocks are associated with melting of the mantle wedge in supra-subduction zone regime (Eleftheriadis *et al.,* 2003).

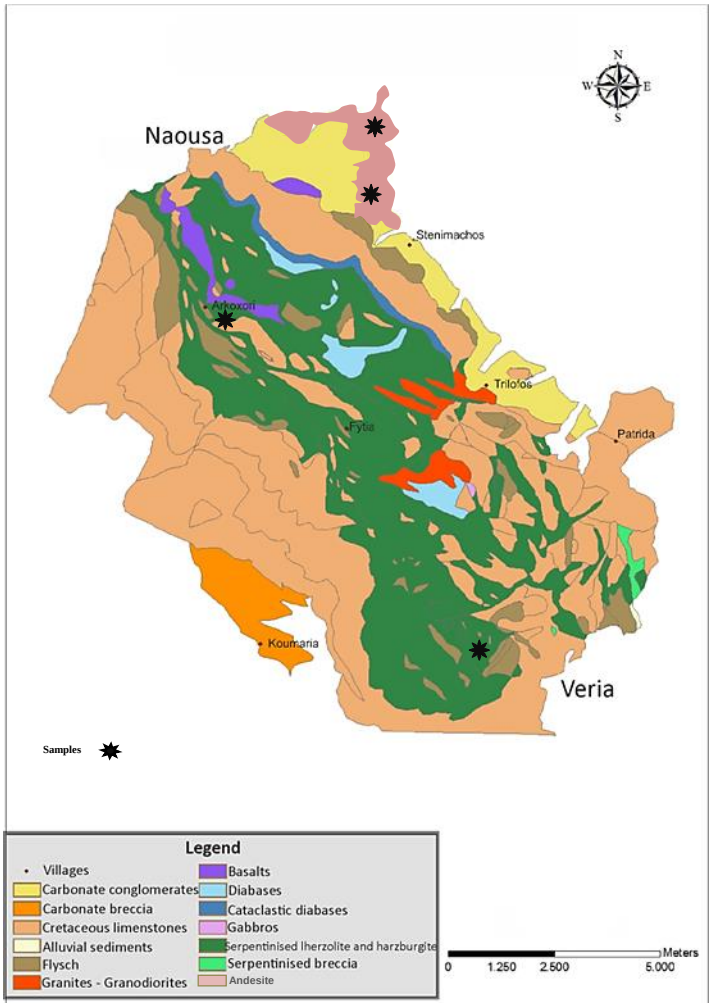

Figure 1 - Geological map of Veria-Naousa region.

3. Analytic methods

The mineralogical and textural characteristics of the samples were studied in polished-thin sections using polarising and scanning electron microscopes (SEM). SEM operating conditions were accelerating voltage 15 kV and beam current 3.3 nA, with 4 μm beam diameter. Whole-rock chemical analyses for major and trace elements were performed at ACME Analytical Laboratories LTD in Canada. Whole-rock major element analyses were carried out using an XRF spectrometer and a sequential spectrometer (ICP-OES). Trace elements were determined on totally digested samples by inductively coupled plasma-mass spectrometry (ICP-MS). Detection limits for major elements is 0.01 wt. %. The analytical precision calculated from replicate analyses is better than 3% for most major elements and better than 5% for trace elements. Laboratory tests for the determination of physicomechanical properties were conducted according to international standards and included: flakiness index (I_F; B5 812:105:01), moisture content (w; AASHTO T255), water absorption (w_a; ΕΛΟΤ EN 1097-06), Los Angeles (LA; ASTM C 131), uniaxial compressive strength (USC; ASTM D 2938), Schmidt Hammer Value (SHV; ISRM 1985) and soundness (S; ΕΛΟΤ EN 1367-2).

4. Results

4.1. Petrographic Features

4.1.1. Serpentinised Harzburgite

The serpentinised harzburgite shows mainly cataclastic texture, due to intense brittle deformation and a variety secondary textural features. Its primary modal mineralogical composition includes relics of orthopyroxene, Cr-spinel, as well as rare olivine, and scarce clinopyroxene. Orthopyroxene appears as subhedral porphyroclasts and most of them show exsolution lamellae of clinopyroxene, typical feature of Upper Mantle peridotites. Serpentine is the major secondary phase showing typical mesh (Fig.2a, b), local bastite after orthopyroxene (Fig. 2c) and ribbon (Fig. 2d) textures. Chlorite and magnetite are also products of hydrothermal alteration of the harzburgite. Magnetite commonly fills microcracks of or rims Cr-spinel crystals. Brittle deformation is expressed mainly by intense of fragmentation of spinel as well as by intergranular microcracks.

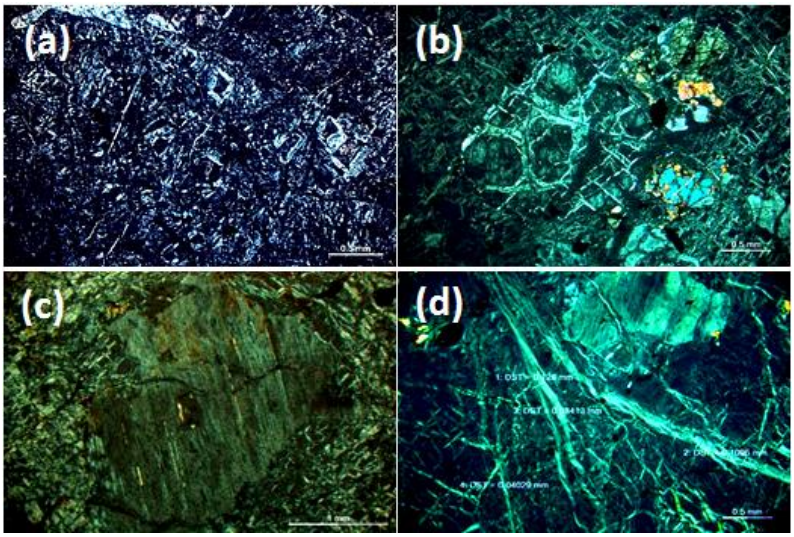

Figure 2 - Photomicrographs (XPL) of textural characteristics of the serpentinised harzburgite from the Veria-Naousa ophiolite: a and b. serpentine mess texture (samples BE.12 and BE.01, respectively), c. orthopyroxene porphyroclast with exsolution lamellae of clinopyroxene (sample BE.12), d. ribbon texture in serpentinised mass (sample BE.01).

4.1.2. Andesite

The collected andesite samples are vesicular and have porhyritic texture with phenocrysts of plagioclase, up to 1 cm, biotite (rarely phlogopite) and lesser clinopyroxene surrounded by a microcrystalline and amorphous groundmass in places with flow structure (Fig. 3). Locally, plagioclase phenocrysts are surrounded by sanidine. Plagioclase phenocrysts are optically zoned showing both normal and oscillatory reverse zoning (Fig. 3c, d). Accessory minerals commonly include apatite, titanite, zircon and magnetite. Alteration products in the andesites include clay minerals, albite, chlorite, Fe-oxides and calcite. Numerous intergranular cracks are present as a result of brittle deformation.

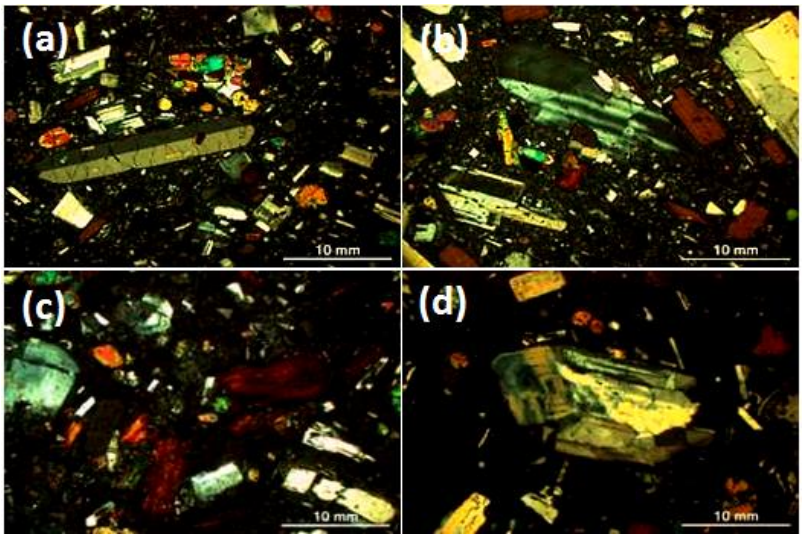

Figure 3 - Photomicrographs (XPL) of the characteristic of the Pliocene andesites from Edessa: a and b. porhyritic texture with plagioclase and clinopyroxene phenocrysts; biotite is present in b, too (sample BE.81), c. phenocrysts of oxidised biotite and zoned plagioclase in a microcrystalline to glassy groundmass (sample BE.82), d. phenocryst of a zoned and altered to albite plagioclase surrounded by glassy groundmass (sample BE.82).

4.2. Geochemical features

Whole-rock composition of representative andesites and ultrabasic rocks from the Veria-Naousa ophiolitic complex are listed in Table 1. SiO_2 in the serpentinised harzburgites typically ranges from 39.82% to 40.95% and Fe_2O_3 from 8.06% to 8.86%. The high degree of serpentinisation is reflected by high loss-on-ignition (LOI) values (13.50%-14.60%).

Table 1 - Whole-rock geochemical analyses of representative serpentinised harzburgites from the Veria –Naousa ophiolite and Edessa andesites.

	Serpentinised Harzburgite		Andesite			Serpentinised Harzburgite		Andesite	
	BE.01	BE.12	BE.81	BE.82		BE.01	BE.12	BE.81	BE.82
Major elements (wt. %)					Trace elements (ppm)				
SiO_2	39.82	40.95	60.91	56.39	Zn	8.00	26.00	43.00	26.00
TiO_2	*	*	0.52	0.63	Rb	0.40	0.40	220.60	203.50
Al_2O_3	1.01	1.11	17.32	17.;84	Sr	2.00	0.70	1101.40	1896.20
$Fe_2O_3^t$	8.86	8.06	3.94	5.91	Y	0.90	33.00	20.10	27.00
MnO	0.11	0.13	0.10	0.09	Zr	0.10	0.10	305.60	290.50
MgO	34.17	34.81	1.50	2.25	Nb	0.30	*	21.60	20.60
CaO	0.10	0.21	3.93	5.28	Pb	21.70	4.60	20.60	50.00
Na_2O	*	*	4.12	3.78	Ba	1.00	3.00	1591.00	2020.00
K_2O	*	*	5.24	4.80	V	60.00	33.00	86.00	115.00
P_2O_5	*	*	0.35	0.39	Sc	11.00	11.00	8.00	12.00
LOI	14.60	13.50	1.6	2.0	Ga	3.10	3.30	20.40	20.00
Total	98.67	98.77	99.53	99.36	Hf	*	*	7.70	7.40
Trace elements (ppm)					Ta	*	*	1.20	1.20
Cr	2963.00	2792.00	*	*	Th	*	*	61.70	62.70
Co	91.10	102.80	9.50	17.30	U	0.20	*	16.60	17.80
Ni	2655.80	2481.30	9.20	11.60	MgO/FeO^t	4.29	4.80	0.42	0.42
Cu	12.90	7.50	19.70	29.50					

* Below detection limit

The andesites show expectedly higher SiO2 contents (56.39%-60.91%). High Na2O, CaO and Al2O3 percentages in them reflect the participation of plagioclase in these rocks. They show low loss-on-ignition (LOI) values (1.60%-2.00%) due to the restricted participation of hydrous minerals.

4.3. Physicomechanical properties

The results of the determined geometrical, physical, mechanical and physicomechanical properties from the serpentinised harzburgites and andesites are listed in Table 2. The tested peridotites are mechanically stronger than the andesites, showing higher uniaxial compressive strength (UCS), Schmidt hammer value (SHV) and lower Los Angeles (LA) values (Table 1). Soundness test (S) and water absorption (w_a) values are largely different in the two ultrabasic rocks, as sample BE.01 appear much less durable and more absorbent than BE.12 (Table 2). The lower UCS and S and the higher LA values of sample BE.12 reflect its higher degree of serpentinisation relative to sample BE.01. Moisture contents (2.94%-3.35%) and water absorption (5.54%-5.9%) values are slightly higher whereas flakiness index is much lower (15.42%-16.91%) in the andesites than the serpentinised harzburgites (Table 2). The two andesite samples show rather consistent S values of 67.4% and 77.5%, analogous to the relatively fresher peridotite sample.

Table 2 - Results of physicomechanical tests in the Veria-Naousa ultrabasic rocks and Edessa andesites.

Sample No		*Uniaxial compression strength*	*Los Angeles*	*Schmidt hammer value*	*Moisture contect*	*Water absorption*	*Soundness test*	*Flakiness index*
		UCS (Mpa)	*LA (%)*	*SHV*	*W (%)*	*W_a (%)*	*S (%)*	*I_F (%)*
Serpendinised harzburgite	**BE.01**	75.62	19.20	60.90	2.58	4.40	75.34	42.10
	BE.12	56.40	25.16	60.00	2.18	1.68	18.05	37.20
Andesite	**BE.81**	34.52	37.93	49.00	2.94	5.90	77.50	15.42
	BE.82	35.62	39.41	50.30	3.35	5.54	67.40	16.91

4.4. Correlations of physicomechanical properties

Regression and factor analyses were applied to test the acquired results and to detect the interrelationships between their geometrical, physical and mechanical properties (Fig.4). Evidently, the two different rock-types cluster at different areas on the correlation diagrams, apparently due to their considerably dissimilar values in certain tests. Decoupling of the ultrabasic samples in some diagrams results from their different strength and durability, owed to the different degree of serpentinisation. However, all samples form cohesive trends that can be described by statistical equations and important correlations can be obtained.

Linear regression was used based on the linearity assumption and the determination coefficients R^2 and equations of the fitted lines were calculated by the "least squares" method. Other types of relationships were also tested (e.g. logarithmic, power, etc.) but it is always observed that the linear model fits best, giving the highest R^2 values. Uniaxial compression strength and Schmidt hammer

value show excellent negative linear correlations with Los Angeles coefficient (Fig. 4a, b), which can be described by the equations:

$$UCS = -1.9488 \times LA + 109.83, \; R^2 = 0.9665$$

$$SHV = -0.6184 \times LA + 73.864, \; R^2 = 0.9432$$

Los Angeles shows excellent negative and good positive linear correlations with Flakiness index and moisture content, respectively (Fig. 4c, d) and these relationships can be modelled with the following equations:

$$LA = -0.7097 \times I_F + 50.232, \; R^2 = 0.9782$$

$$LA = 15.65 \times w - 12.808, \; R^2 = 0.6311$$

Soundness test demonstrate an excellent positive linear relationship with water absorption (Fig. 4e), which can be described by the equation:

$$S = 13.589 \times w_a + 0.0506, \; R^2 = 0.8582$$

Flakiness index shows an excellent positive linear relationship with uniaxial compressive strength (Fig. 4f) and the relationship is given by the equation:

$$I_F = 0.6779 \times UCS - 6.3523, \; R^2 = 0.9298$$

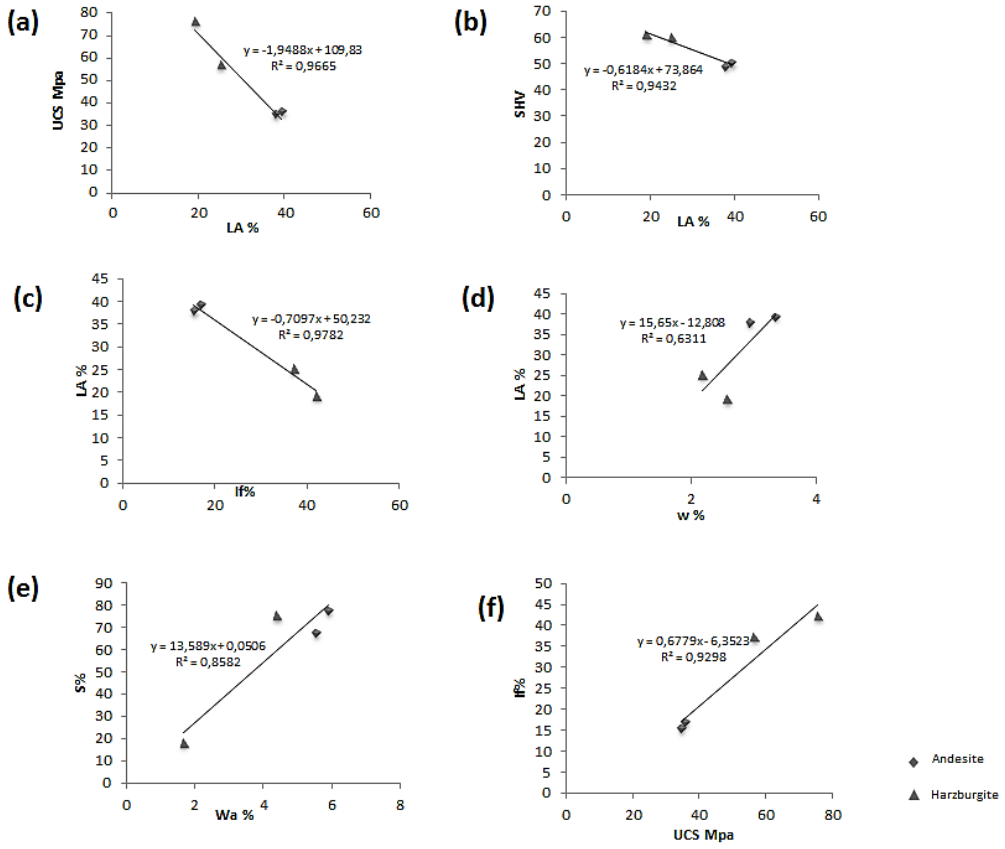

Figure 4 - Correlations of physicomechanical properties of the ultrabasic rocks from the Veria-Naousa ophiolite and the Edessa andesites.

5. Discussion

5.1. The Influence of Alteration on the Engineering Properties of the Rocks

Mineralogical composition, textural features, degree of alteration/deformation and weathering are the main factors which affect the physicomechanical properties and consequently the suitability of aggregates in industrial applications (Hartley, 1974; Brattli, 1992). Primary assemblages of ultramafic rocks are often converted to secondary mineral phases as a result of ocean-floor metamorphic process. Ocean-floor metamorphism has variably affected the collected ultrabasic samples and despite the fact that we present a limited number of samples, it is evident that serpentinisation has a negative influence on the engineering behaviour of these rocks, as sample BE.12 is clearly weaker and less durable relative to the less serpentinised sample BE.01; similar results have been previously proposed by other authors, too (Rigopoulos *et al.,* 2010; Smith and Collins, 2001). The much lower hardness of the secondary minerals (serpentine polymorphs and chlorite) relative to the primary relics (olive and pyroxenes) results in differential mechanical behaviours, thus contributing to the weakness and easier deterioration of the rocks under stress and subsequently during their in-service. This is assigned to the fact that the secondary minerals have substantially different mechanical behaviour compared with the primary ones, leading to a modification of rock strength (Rigopoulos *et al.,* 2010).

The andesites include secondary clay minerals as a result of plagioclase alteration. These clay minerals have the ability to absorb water within their structure, therefore, even present in low amounts, they contribute to the disintegration and low coherence of the rocks. The andesites have been greatly affected by brittle deformation, as it is deduced by a dense network of cracks and joints in their mass. This feature along with their vesicular structure are considered as the main factors for their reduced strength and durability relative to the significantly altered serpentinised harzburgites.

5.2. Interdependence of Physicomechanical Properties

Regression analysis indicate significant interrelationships between the physicomechanical properties in both the ultrabasic and andesitic rocks. Inverse correlation of LA with UCS and SHV, suggest that the resistance of these rocks in attrition and grinding is a linear function of their strength. Similar correlations have been previously reported for mafic and ultramafic rocks, too (Rigopoulos *et al.,* 2006; Rigopoulos *et al.,* 2009; Davis, 2002; Räisänen, 2004) but from this research it is concluded that such a relationship can be extended to other rock types like intermediate volcanic rocks.

The flakiness index is a critical factor for the quality of aggregates as flaky particles may have adverse effects in several applications and impair the durability of constructions. The significantly higher I_F of the serpentinised samples can be explained by the large amount of secondary serpentine and chlorite (both of the phyllosilicate subclass) thus affecting their intrinsic mechanical properties. The andesites, which contain mostly prismatic and squat crystals as well as glass and lack abundant phyllosilicate minerals exhibit better I_F values. However, this coefficient shows a negative correlation with LA and a positive one with UCS suggesting that the adverse influence of the flaky shape of the aggregates is surpassed by other factors and most likely the mineralogical composition and texture as well as the brittle deformation of the rocks; the last appears to have a stronger influence on the quality of the aggregates.

Water absorption and moisture content are two parameters that are commonly considered to relate with open pores and the presence of minerals that have the capability to sequester water (like serpentine, chlorite and clay minerals). The positive correlations of S and LA with w_a and w, respectively, can be interpreted that open spaces (voids and/or joints) are detrimental to the mechanical strength and durability of both the ultrabasic and andesitic rocks. The later contain much lesser amounts of clay minerals than the amount of serpentine (and chlorite) in the ultrabasic lithologies, therefore it is plausible to assume that porosity and fracturing is a more important factor

than the presence of water adsorbing minerals. These open spaces accommodate water and can host the crystallisation of salts, which are well-known disadvantageous factors for the engineering performance of rocks.

6. Conclusions

Ultrabasic and andesitic lithologies were studied and significant relationships are found between them. The ultrabasic rocks are variably serpentinised, a feature that influences negatively their performance. The sheet-like and soft character of the secondary minerals, as well as the coexistence of harder primary minerals contribute to the disintegration of the altered peridotites. Although the andesites show smaller degree of alteration, their tectonic disturbance and high porosity are extremely a negative factors for their in-service performance, contributed by the minor occurrence of secondary clay minerals, too. These factors cause a dramatic deterioration of their strength and durability as aggregates, hence the andesites show eventually worse engineering properties than the serpentinised peridotites. These low quality andesites are considered unsuitable for most industrial and construction applications, however they may be suitable for the production of mortars where high w and w_a values are favoured. The significant correlations observed between several physicomechanical parameters suggest the strong interdependence of these properties in a broad range of lithologies, like peridotites and andesites. Certain coefficients can be predicted from others and their determination coupled with petrographic information can assist to the explanation of the engineering behaviour of the rocks.

7. References

Brattli, B., 1992. The influence of geological factors on the mechanical properties of basic igneous rocks used as road surface aggregates. *Eng. Geol.*, 33:31-44.

Davis, G.H., 2002, Tentative correlation between the pl(pla-gioclase) normin and L.A. Wear Percent in Precambrian mid-continent granites [abs.], *In*: Seeger, C.M., *eds.*, Forum on the Geology of Industrial Minerals, 38th, St. Louis, Mo, *Proceedings*: Jefferson City, Missouri Division of Geology and Land Survey, 48 pp.

Economou, M., 1983. A short note on the evolution of the Vermion ophiolite complex (Macedonia-Greece), *Ofioliti*, 8, 333-338.

Economou-Eliopoulos, M., 2003. Apatite and Mn, Zn, Co-enriched chromite in Ni-laterites of northern Greece and their genetic significance, *Journal of Geochemical Exploration*, 80, 41-54.

Griffiths, J., 1989. Olivine, volume the key to success, *Ind. Minerals*, 1, 25-36.

Harben, P.W. and Bates, R.L., 1990. Industrial minerals, geology and world deposits, London: Industrial Minerals Division, *metal Bulletin Plc.*, 312.

Eleftheriadis, G., Castorina, F., Soldatos, T. and Masi, U., 2003. Geochemical and Sr-Nd isotopic evidence for the genesis of the Late Cainozoic Almopia Volcanic rocks (Central Macedonia, Greece), *Miner. Petrol.*, 78, 21-36.

Hartley, A., 1974. A review of the geological factors influencing the mechanical properties of road surface aggregates, *Quaterly Journal of Eng. Geol.*, 7, 69-100.

Irfan, T.Y. and Dearman, W.R., 1978. The engineering petrography of a weathered granite in Cornwall, England, *Q. J. Eng. Geol.*, 11, 233-44.

Knight, B.H. and Knight, R.G., 1935. Road aggregates, their uses and testing. London, Edward Arnold.

Miskovsky, K., Taborda Duarte, M., Kou, S.Q. and Lindqvist, P.A., 2004. Influence of the mineralogical composition and textural properties on the quality of coarse aggregates, *J. Mater. Eng. Perform.*, 13, 144-150.

Mendes, F.M., Aires-Barros, L. and Rodrigues, FP., 1966. The use of modal analysis in the mechanical characterization of rock masses. *In*: *Proccedings of first congress, international society for rock mechanics*, Lisbon, 217-233.

Mercier, J., Vergely, P. and Bebien, J., 1975. Les ophiolites helleniques “obductees” au Jurassique superieur sont-elles les vestiges d’ un ocean tethysien ou d’ une mer marginale perieuropeenne. *C.R. Somm. Soc. Geol.*, France, 17, 108-112.

Michailidis, K.M., 1990. Zoned chromites with high Mn-contents in the Fe-Ni-Cr-laterite ore deposits from the Edessa area in Northern Greece, *Mineral. Deposita*, 25, 190-197.

Pomonis, P., Rigopoulos, I., Tsikouras, B. and Hatzipanagiotou, K. 2007. Relationships between petrographic and physicomechanical properties of basic igneous rocks from the Pindos ophiolitic complex, NW Greece, *Bull. Geol. Soc. Greece*, 40, 947-958.

Räisänen, M., 2004. Relationships between texture and mechanical properties of hybrid rocks from the Jaala-litti complex, southeastern Finland, *Eng. Geol.*, 74, 197-211.

Rhoades, R. and Mielenz, R.C., 1946. Petrography of concrete aggregate, *Proc Am Concr Inst.*, 42, 581-600.

Rigopoulos, I., Tsikouras, B., Pomonis, P. and Hatzipanagiotou, K. 2006. Comparative Evaluation of Dolerites from the Pindos and Vourinos Ophiolitic Rocks for their Use as Aggregates, *Tech. cron. Sci. J. TCG*, I, No3.

Rigopoulos, I., 2009. Correlation between petrographic and physico-mechanical properties of the Pindos and Vourinos ophiolitic rocks and assessment of their suitability as aggregates in construction-industrial uses, PhD thesis, University of Patras.

Rigopoulos, I., Tsikouras, B., Pomonis, P. and Hatzipanagiotou, K., 2010. The influence of alteration on the engineering properties of dolerites: the examples from the Pindos and Vourinos ophiolites (northern Greece), *Int. J. Rock Mech. Min. Sci.*, 47, 69-80.

Smith, M.R. and Collis, L., 2001. Aggregates: sand, gravel and crushed rock aggregates for construction purposes, *Spec. Publ.*, 17, Geol. Soc. London.

Tsikouras, B., Pomonis, P., Rigopoulos, I. and Hatzipanagiotou, K., 2005. Investigation for the suitability of basic rocks from Mikrokleisoura, Grevena, for their use as antiskid aggregates and railway ballast, *Proc. 2nd Congress of Committee of Economic Geology, Mineralogy, and Geochemistry of the Geological Society of Greece*, 347-356

Tsouras, G. and Economou-Eliopoulos, M., 2008. High PGE contents and extremely abundant PGE-minerals hosted in chromitites from the Veria ophiolite complex, Northern Greece, *Ore Geol. Rev.*, 33, 3-19.

Tugrul, A. and Gurpinar, O., 1997. The effect of chemical weathering on the engineering properties of Eocene basalts in northeastern Turkey, *Environ. Eng. Geosci.*, 3, 225-34.

Zorlu, K., Ulusay, R., Ocakoglu, F., Gokceoglou, C. and Sonmez, H., 2004. Predicting intact rock properties of selected sandstones using petrographic thin-selection data, *Int. J. Rock Mech. Min. Sci.*, 41(1), 93-98.

Δελτίο της Ελληνικής Γεωλογικής Εταιρίας, τόμος L, σελ. 1999-2008
Πρακτικά 14ου Διεθνούς Συνεδρίου, Θεσσαλονίκη, Μάιος 2016

Bulletin of the Geological Society of Greece, vol. L, p. 1999-2008
Proceedings of the 14th International Congress, Thessaloniki, May 2016

PETROGENETIC SIGNIFICANCE OF SPINELS FROM SERPENTINISED PERIDOTITES FROM THE VERIA-NAOUSA OPHIOLITE

Rogkala A.[1], Petrounias P.[1], Tsikouras B.[1,2] and Hatzipanagiotou K.[1]

[1]*University of Patras, Department of Geology, Section of Earth Materials, 265 00, Patras, Greece*

[2]*Universiti Brunei Darussalam, Faculty of Science, Physical and Geological Sciences, Jalan Tungku Link, Gadong BE1410, Bandar Seri Begawan, Brunei Darussalam*

Abstract

The Veria-Naousa ophiolitic complex represents a dismembered ophiolite unit, which is superimposed on a basement consisting of rocks belonging to the Pelagonian and Axios (Almopias subzone) isopic zones in northern Greece. Mantle peridotites are composed of variably serpentinised lherzolite and harzburgite intruded by a sparse network of pyroxenitic dykes. The serpentinised lherzolite and harzburgite contain Al-spinels (Cr#=38.83-42.52 and Mg#=58.94-64.77), Cr-spinels (Cr#=43.37-64.92 and Mg#=49.20-58.66) and magnesiochromites (Cr#=53.93-57.13 and Mg#=55.73-61.71). All of them display commonly richer-in-Cr cores rimmed by secondary ferrian chromite and magnetite. Whole-rock geochemicall compositions and primary spinel chemical composition of these peridotites are analogous to peridotites that formed in a suprasubduction zone. It is supported that the Mantle peridotites of the Veria-Naousa ophiolitic complex formed in a back-arc basin.
Keywords: *Almopias subzone, backarc basin, Mantle impregnation.*

Περίληψη

Το οφιολιθικό σύμπλεγμα της περιοχής ανάμεσα στη Βέροια και τη Νάουσα αντιπροσωπεύει μια διαμελισμένη οφιολιθική ενότητα, η οποία είναι υπερκείμενη σε μία βάση που αποτελείται από πετρώματα της Πελαγονικής ζώνης και μερικώς της υποζώνης Αλμωπίας, της ζώνης Αξιού στη βόρεια Ελλάδα. Οι μανδυακοί περιδοτίτες αποτελούνται από σερπεντινιωμένους λερζόλιθους και χαρτσβουργίτες, στους οποίους διεισδύει ένα αραιό δίκτυο πυροξενιτικών φλεβών. Οι σερπεντινιωμένοι λερζόλιθοι και χαρτσβουργίτες αποτελούνται από Al-σπινέλιους (Cr#=38.83-42.52 and Mg#=58.94-64.77), Cr-σπινέλιους (Cr#=43.37-64.92 and Mg#=49.20-58.66) και μαγνησιοχρωμίτες (Cr#=53.93-57.13 and Mg#=55.73-61.71). Εμφανίζουν συχνά πιο πλούσιους σε Cr πυρήνες, οι οποίοι περιβάλλονται από σιδηροχρωμίτη και μαγνητίτη. Οι γεωχημικές συστάσεις και η αρχική σύσταση των σπινελίων είναι όμοια με περιδοτίτες, οι οποίοι σχηματίστηκαν σε μία ζώνη καταβύθισης. Έτσι, οι μανδυακοί περιδοτίτες του Οφιολιθικού Συμπλέγματος στην περιοχή ανάμεσα στη Βέροια και τη Νάουσα αρχικά σχηματίστηκαν σε μία οπισθοτοξική λεκάνη.
Λέξεις κλειδιά: *υποζώνη Αλμωπίας, οπισθοτοξική λεκάνη, εμποτισμένος Μανδύας.*

1. Introduction

Spinels are commonly used as "petrogenetic indicators", occurring in ultramafic rocks of ophiolite complexes. They display a wide range of compositions reflecting their primary magmatic or secondary origin (Barnes and Roeder, 2001; Ghosh *et al.*, 2013). Primary spinel can be well maintained during serpentinisation, hence unaltered spinels in serpentinite can be used as a petrogenetic and geotectonic indicator because their chemical composition depends on the petrogenesis and physical conditions of the host peridotites (Zhou *et al*., 1994; Karipi *et al.*, 2007; Oh *et al.*, 2010). The prime purpose of this paper is to present new data on the chemical variability of spinel-group minerals occurring in serpentinised peridotites from the Veria-Naousa ophiolite, north Greece, aiming also to unravel the petrogenetic processes during their formation.

2. Geological setting

Extensive fieldwork in the Veria-Naousa ophiolitic complex focused mainly on the distribution and mode of development of the ophiolitic rocks, as well as their relation to the adjacent formations. These rocks extend throughout the area between Veria and Naousa towns and belong geotectonically to the Almopias subzone of the Axios isopic zone, in northern Greece (Fig. 1).

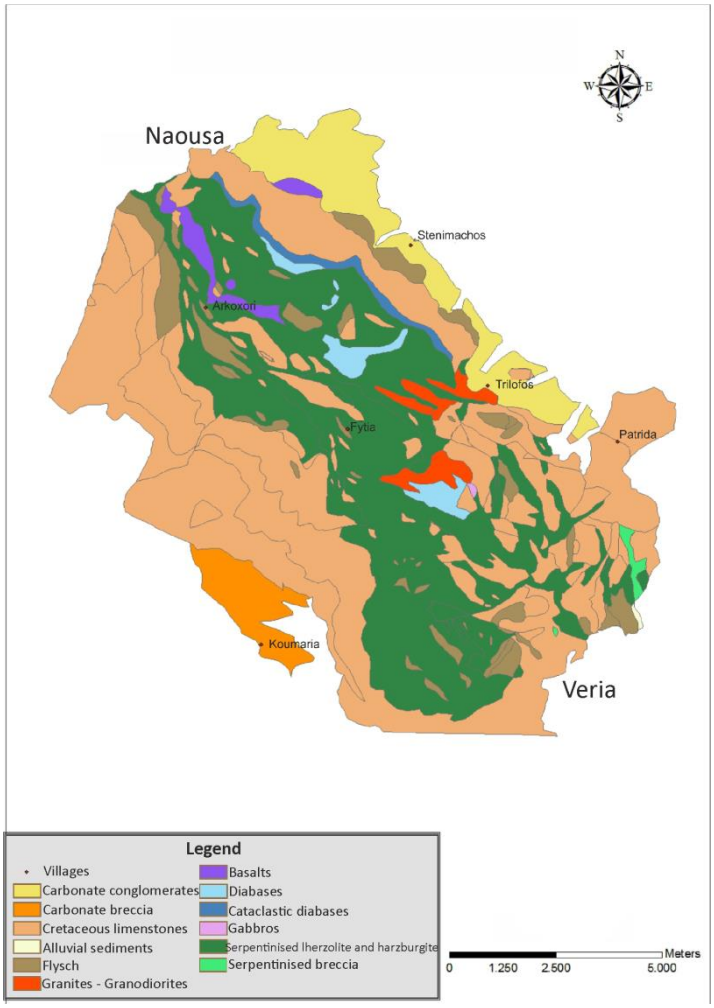

Figure 1 - Geological map of the Veria-Naousa region.

They represent remnants of oceanic lithosphere which were thrust from one or more ocean basins. They have been obducted onto the Cretaceous platform carbonates and a flysch succession of the Pelagonian Zone during Upper Jurassic to Lower Cretaceous time (Mercier *et al.*, 1975; Economou, 1983; Michailidis, 1990; Economou-Eliopoulos, 2003; Tsoupas and Economou-Eliopoulos, 2008). The ophiolite suite includes, from base to top, serpentinised lherzolite and harzburgite, intruded by a sparse network of pyroxenitic dykes, as well as gabbros, diabases and pillow basalts. It is dismembered and scattered due to intensive tectonism of the area. The serpentinised peridotites are intensely tectonised, showing a dense network of joints. Rare rodingite dykes occur in the serpentinised ultramafic rocks. The ophiolite is unconformably overlain by sediments (conglomeratic limestone, flysch). Also, a granitic intrusion in the serpentinised mass is observed near the village of Trilofos.

3. Analytical methods

The mineralogical and textural characteristics of the samples were studied in polished-thin sections in optical and scanning electron microscopes (SEM). Spinel microanalyses were performed using a JEOL JSM-6300 SEM equipped with EDS and WDS and THETA software at the Laboratory of Electron Microscopy and Microanalysis, University of Patras. Operating conditions were accelerating voltage 15 kV and beam current 3.3 nA, with 4 μm diameter beam. Whole-rock chemical analyses for major and trace elements were performed at ACME Analytical Laboratories LTD in Canada. Whole-rock major element analyses were carried out using a XRF spectrometer and a sequential spectrometer (ICP-ES). Trace elements were determined on totally digested samples by inductively coupled plasma-mass spectrometry (ICP-MS). Detection limits for major elements is 0.01 wt. % and for trace elements is 1 and 0.1 ppm. The analytical precision calculated from replicate analyses is better than 3% for most major elements and better than 5% for trace elements.

4. Results

4.1. Petrographic features

4.1.1. Serpentinised Lherzolite

The lherzolite samples are intensively serpentinised, therefore their classification was made based on their normative mineralogical composition and whole-rock geochemical analyses. Serpentine is the dominant alteration product forming mesh, hourglass, ribbon and bastite textures; lesser amounts of chlorite and magnetite occur, too. Their primary modal mineralogical assemblage has been mostly obliterated by alteration and only few relics of olivine, orthopyroxene, clinopyroxene and spinel are present. They have two types of spinels, Al-spinel and Cr-spinel, both forming subhedral to euhedral grains with lobate boundaries (Fig. 2a, b, c), and are usually frequently veined and surrounded by thin rims of ferrian chromite and magnetite, due to alteration (Fig. 2c). A scarce network of calcite veins occurs, too.

4.1.2. Serpentinised Harzburgite

The primary assemblage of the harzburgite constitutes less than 20% of the mode and comprises relics of orthopyroxene, rare clinopyroxene, olivine, as well as magnesiochromite and Cr-spinel (Fig. 2d). Serpentine is the main alteration product showing mesh, ribbon and intersertal textures. Chlorite and magnetite are also products of hydrothermal alteration of the harzburgite. Orthopyroxene appears as subhedral porphyroclasts and most of them show exsolution lamellae of clinopyroxene, typical feature of mantle peridotites. The magnesiochromite and Cr-spinel crystals are subhedral to euhedral and scanning electron microscopic observation revealed that infrequently they show an irregular distribution of ferrian chromite compositional areas, at their rims (Fig. 2e, f). The boundary between the magnesiochromite and Cr-spinel (either unaltered or altered) and the ferrian chromite is curved and lobate.

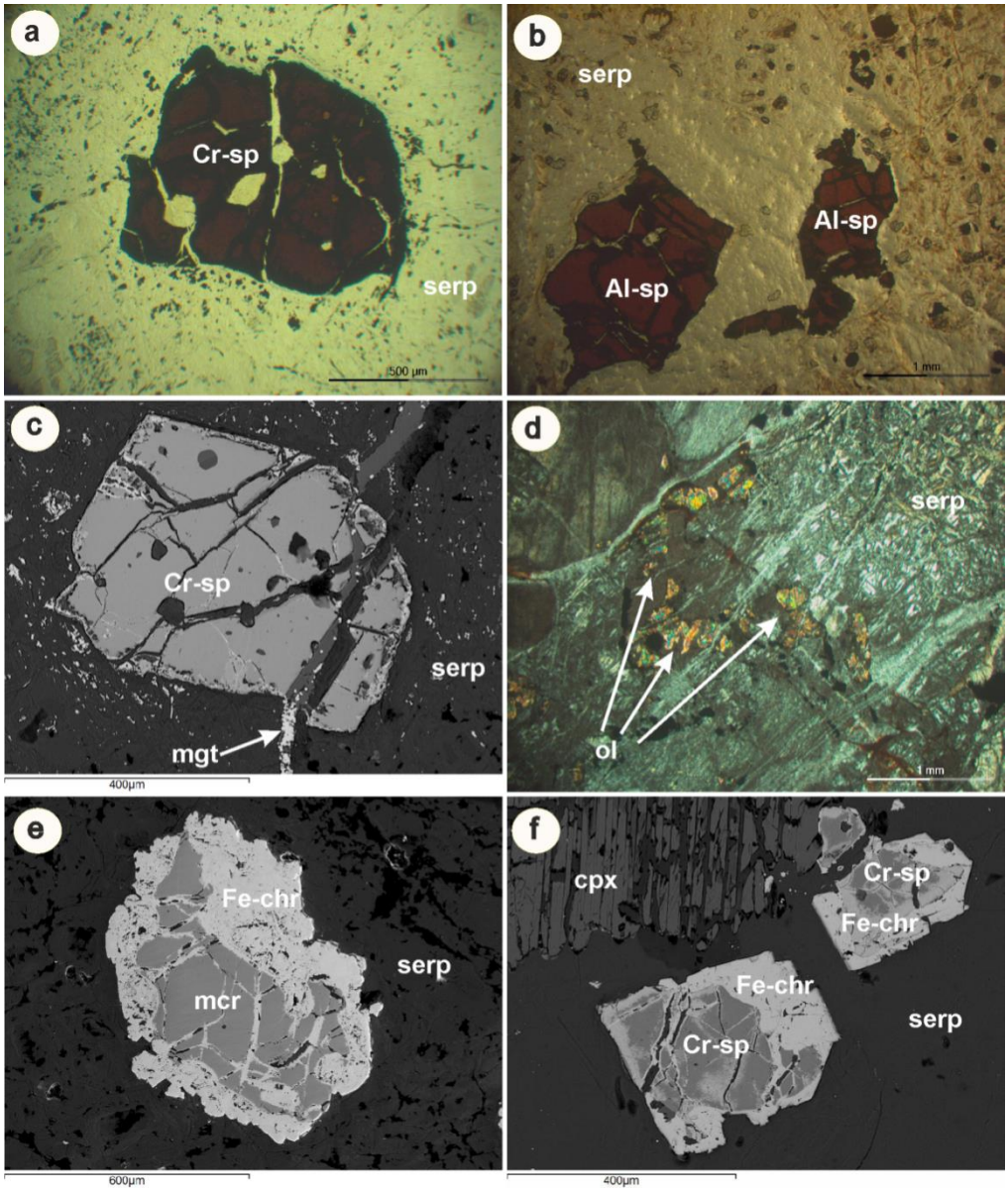

Figure 2 - Textural characteristics of the serpentinised peridotites from Veria-Naousa: a. Photomicrograph of a Cr-spinel (Cr-sp) in serpentinised mass (lherzolite sample BE.8B, PPL), b. Photomicrograph of Al-spinel (Al-sp) crystals (serpentinised lherzolite BE.58, PPL), c. Backscattered electron image of a Cr-spinel crystal with irregular distribution of poorer-in-Cr compositional areas, at its rim (sample BE.8B) d. Photomicrograph of relics of olivine (ol) surrounded by ribbon and intersertal serpentine (serp) in serpentinised harzburgite (sample BE.12), e. Backscattered electron image of a severely altered magnesiochromite (mcr) crystal surrounded by thick ferrian chromite (Fe-chr) in serpentinised harzburgite (sample BE.14), f. Backscattered electron image of Cr- Spinel (Cr-Sp) crystals surrounded by ferrian chromite and altered clinopyroxene (cpx) to chlorite in serpentinised harzburgite (sample BE.12).

4.2. Chemical composition of spinel-group minerals

Representative compositions of spinel-group minerals from the Veria-Naousa serpentinised peridotites are given in Tables 1 and 2. Cationic ratios were calculated on the basis of 8 oxygen atoms assuming spinel stoichiometry.

Table 1 - Representative electron microanalyses of spinel-group minerals from serpentinised lherzolites of Veria-Naousa.

Sample	**Spinel**					**Ferrian chromites**	
	BE.8B	BE.8B	BE.58	BE.58	BE.58	BE.8B	BE.8B
Oxide wt. %	1	2	1	2	3	1	2
SiO_2	-	-	-	-	-	-	-
TiO_2	0.11	0.16	-	-	-	-	-
Al_2O_3	18.34	17.56	32.44	35.85	34.44	-	-
Cr_2O_3	47.09	48.45	35.49	33.93	34.98	43.89	42.23
FeO^t	21.56	22.76	17.27	18.16	15.90	43.67	46.01
MnO	-	-	-	-	-	9.01	8.57
MgO	11.76	10.45	14.39	13.82	15.06	0.81	0.66
CaO	-	0.04	-	-	-	0.12	-
ZnO	0.28	0.22	-	-	-	2.21	1.86
Total	99.14	99.64	99.59	101.76	100.38	99.71	99.33
Structural formula on the basis of 8 O							
Si	-	-	-	-	-	-	-
Al	0.686	0.662	1.122	1.209	1.171	-	-
Cr	1.182	1.225	0.824	0.767	0.798	1.298	1.250
Fe^{3+}	0.113	0.094	0.054	0.024	0.031	0.580	0.647
Ti	0.003	0.004	-	-	-	-	-
Mg	0.557	0.498	0.630	0.589	0.648	0.045	0.037
Fe^{2+}	0.456	0.515	0.370	0.411	0.352	0.787	0.794
Mn	-	-	-	-	-	0.286	0.272
Zn	0.007	0.005	-	-	-	0.061	0.051
Ca	-	0.001	-	-	-	0.005	-
Total	3.007	3.005	3.000	3.000	3.000	3.061	3.007
Cr#	63.27	64.92	42.33	38.83	40.52	100.00	100.00
Mg#	54.80	49.20	62.98	58.94	64.77	5.43	4.43

Table 2 - Representative electron microanalyses of spinel-group minerals from serpentinised harzburgites of Veria-Naousa.

Sample	Spinel					Ferrian chromites	
	BE.12	BE.14	BE.14	BE.14	BE.14	BE.12	BE.14
Oxide wt. %	1	1	2	3	4	1	1
SiO_2	0.75	-	-	-	-	2.24	-
TiO_2	0.09	0.19	0.20	0.28	0.01	0.03	0.53
Al_2O_3	31.34	24.01	22.67	24.29	24.89	3.40	-
Cr_2O_3	35.78	47.51	45.03	46.6	43.43	25.78	40.42
FeO^t	17.36	17.32	17.29	17.90	17.03	58.26	51.56
MnO	-	-	-	0.05	-	5.03	5.36
MgO	13.68	12.23	13.63	12.71	13.78	3.16	-
NiO	-	-	-	-	-	0.10	-
ZnO	0.20	0.37	0.30	0.11	0.31	1.08	1.64
Total	99.20	101.63	99.12	101.94	99.45	99.08	99.51
Structural formula on the basis of 8 O							
Si	0.022	-	-	-	-	0.080	-
Al	1.080	0.860	0.824	0.862	0.894	0.142	-
Cr	0.841	1.142	1.098	1.109	1.046	0.724	1.198
Fe^{3+}	0.004	-	0.055	0.011	0.046	0.916	0.681
Ti	0.002	0.004	0.005	0.006	-	0.001	0.015
Mg	0.606	0.554	0.627	0.570	0.626	0.167	-
Ni	-	-	-	-	-	0.003	-
Fe^{2+}	0.427	0.440	0.391	0.439	0.388	0.815	0.936
Mn	-	-	-	0.001	-	0.151	0.170
Zn	0.004	0.008	0.007	0.002	0.007	0.028	0.045
Total	3.004	3.008	3.007	3.002	3.007	3.028	3.045
Cr#	43.37	57.03	57.13	56.27	53.93	83.18	100.00
Mg#	58.66	55.73	61.55	56.49	61.71	17.39	0.00

Chemical classification in spinel-group minerals of the serpentinised peridotites from Veria-Naousa region is illustrated in a $Mg/(Mg+Fe^{2+})$ *vs.* $Cr/(Cr+Al)$ diagram (Fig. 3a). The lherzolitic Al-spinel and harzburgitic Cr-spinel plot in the field of "spinel", while the lherzolitic Cr-spinel and magnesiochromite plot in the field of "magnesiochromite" (Fig. 3a).

The serpentinised lherolite contains Cr-poor and Mg-rich, Al-spinels, with Cr# [=100×Cr/(Cr+Al)] in the range from 38.83 to 40.52 (Table 1) and Mg# [=100×Mg/(Mg+Fe^{2+})] ranging from 58.94 to 64.77. The chemical composition of the analysed Al-spinels is characterised by poorer FeO^t (15.9 0-18.16 wt. %) than the Cr-spinels. Furthermore, the lherzolitic Cr-spinels contain appreciable amo unts of ZnO (0.22-0.28 wt. %) and TiO_2 (0.11-0.16 wt. %).

The serpentinised harzburgites display magnesiochromites and rare Cr-spinels. Magnesiochromite is distinguished from Cr-spinel in containing a considerable amount of Fe^{2+} replacing Mg, and displaying Fe^{2+}>Mg (Deer *et al.*, 1992). The Cr-spinels are richer in Al_2O_3, MgO and poorer in Cr_2O_3, TiO_2, ZnO, FeO than the magnesiochromites.Cr# in the harzburgitic magnesiochromites and Cr-spinels ranges from 54.55 to 57.78 whereas Mg# ranges from 55.73 to 61.07 (see table 2 and Fig.

3). They contain noticeable amounts of TiO_2 (generally 0.10 to 0.28 wt. %, with few exceptions that contain lesser TiO_2) and ZnO (0.11 to 0.37 wt. %), too.

Secondary spinels were formed during serpentinisation along fractures in the primary spinel crystals, in both rocks. Two groups of secondary spinels are observed: the first group includes magnetite and Cr-magnetite, which are rich in FeO^t, whereas the second group includes ferrian chromite enriched in Cr_2O_3, TiO_2 and MnO and poorer in FeO^t compared to the magnetite.

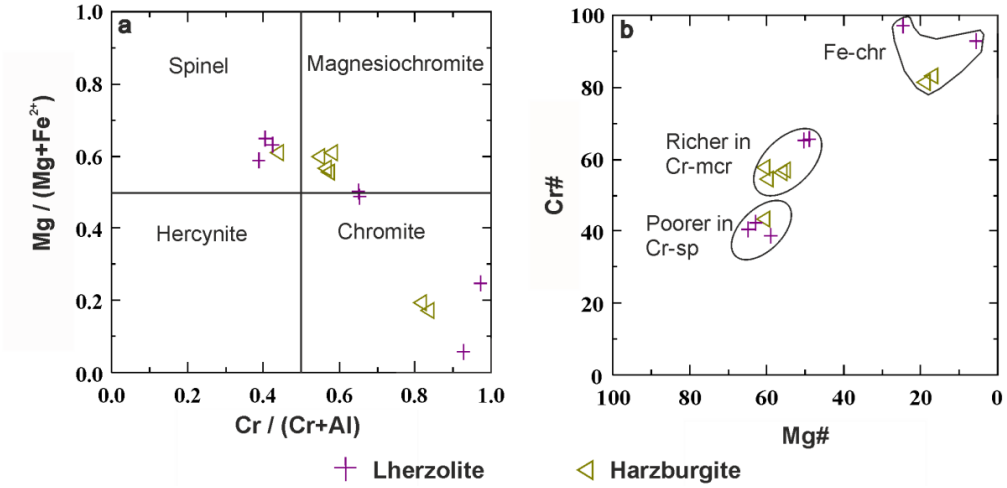

Figure 3 - a. Chemical classification diagram for the spinel-group minerals of the Veria-Naousa serpentinised peridotites, b. Spinel compositions from Veria-Naousa serpentinised peridotites, in terms of Cr# against Mg#.

Table 3 - Representative geochemical analyses of serpentinised peridotites from Veria-Naousa ophiolite. - Below detection limit.

	Lherzolite BE.58	Harzburgite BE.14		Lherzolite BE.58	Harzburgite BE.14
Major elements (wt. %)			**Trace elements (ppm)**		
SiO_2	41.45	40.83	Zn	25	24
TiO_2	0.09	-	Rb	1.3	0.3
Al_2O_3	1.33	0.46	Sr	57.0	0.8
$Fe_2O_3^t$	7.42	9.18	Y	1.8	0.2
MnO	0.11	0.12	Zr	8.4	0.2
MgO	29.56	35.11	Nb	1.0	-
CaO	3.29	0.06	Pb	0.6	2.7
Na_2O	0.01	-	Ba	8	1
K_2O	-	-	V	42	16
P_2O_5	0.01	-	Sc	8	6
LOI	15.6	13.1	Ga	2.1	2.9
Total	98.87	98.86	Hf	0.2	-
Trace elements (ppm)			Ta	-	-
Cr	2374	1669	Th	0.2	-
Co	82.5	114.3	U	0.3	-
Ni	1944.6	2743.7	MgO/FeO^t	4.43	4.25
Cu	5.1	8.3			

4.3. Whole-rock geochemical features

Whole-rock compositions of representative serpentinised peridotite samples from the Veria-Naousa ophiolite are given in Table 3. The high degree of serpentinisation is reflected by high loss-on-ignition (LOI) values. Both samples are Mg-rich, Al-poor and alkali poor rocks. The serpentinised harzburgite is characterised by depletion in TiO_2 and Na_2O and low amounts of Al_2O_3 and CaO. These values correspond to highly depleted upper mantle peridotites (McDonough and Sun, 1995; Niu, 1997). The lherzolite is richer in the incompatible elements Rb, Sr, Y and Zr relative to the harzburgite, further evidence for the relatively fertile character of the first compared to the last rock (Table 3). However, this enrichment is not as high as in chondritic lherzolites, fact that along with the enrichment in the compatible Cr indicate that the lherzolite has also undergone a stage of depletion.

5. Discussion

Spinel-group minerals from the serpentinised rocks of Veria-Naousa ophiolite reveal a multi-stage genesis in the different types of their host peridotites. Textural and chemical features of the studied spinel-group minerals indicate that an early partial melting process and a subsequent episode of melt-rock interaction in the mantle section played a decisive role in their genesis. The partially depleted character of the lherzolite is also compatible with an early stage of melting and depletion. This less depleted lherzolite has spinels poorer in Cr# (Al-spinels and Cr-spinels), compared with the highly depleted harzburgite, that contains Cr-spinel and magnesiochromite with increased Cr.

Unlike the Al-spinels, which are depleted in TiO_2 and ZnO, Cr-spinels (including magnesiochromites) have rather high amounts of these oxides, which reflects the involvement of impregnating melts during the evolution of both peridotites (Farahat *et al.*, 2011). The development of subhedral to euhedral Cr-spinel grains in the serpentinised harzburgite, as well as lack of significant correlation between Cr# and Mg# in the magnesiochromite and Cr-spinel are also consistent with a melt-peridotite interaction episode and their crystallisation from magmatic processes (Zhou *et al.*, 1994, 2005).

The Cr-spinels and magnesiochromite in the lherzolite and harzburgite display Cr# <60, which is typical of oceanic ophiolites (including backarc basins; Dick and Bullen, 1984). The composition and textural characteristics of the Al-spinels suggest that they can be considered as a residual phase after a first stage melting episode of a fertile peridotite, during adiabatic decompression under a mid-ocean spreading center. The textural features and composition of Cr-spinels (including magnesiochromites combined with the highly depleted nature of the harzburgite are consistent with evolution in a back-arc basin. The analysed spinel-group minerals from the Veria-Naousa serpentinised peridotites display similar chemical characteristics from the Othrys and Vourinos ophiolite complexes of analogous SSZ origin (Karipi *et al.*, 2006; Kapsiotis, 2013).

Furthermore, the formation of ferrian-chromite and chromian magnetite alteration rims around the Al-spinels, Cr-spinels and magnesiochromites is assigned to secondary processes that typically occur during serpentinisation (Khedr and Arai, 2011; Singh *et al.*, 2013; Banerjee *et al.*, 2015; Maulana *et al.*, 2015). Notable Mn-erichments in the ferrian chromite zones involve interaction of hydrothermal fluids that were likely rich in Mn, similarly to other ophiolite complexes (e.g., Gahlan and Arai, 2007).

6. Conclusions

Three different types of primary spinel compositions have been distinguished within the Veria-Naousa serpentinised peridotites: Al-spinel, Cr-spinel and magnesiochromite, occurring as subhedral to euhedral crystals, surrounded by secondary ferrian chromite and magnetite rims. The serpentinised peridotites of the Veria-Naousa ophiolite represent a mantle part of an SSZ ophiolite complex and their evolution involves an early depletion stage followed by melt impregnation in a back-arc basin tectonic

setting. During the incipient stages of spreading variable degrees of melting depleted the lherzolite and harzburgite at different degrees. Subsequent evolution of the basin, along with the involvement of subduction-related hydrous fluids are thought to be responsible for the production of melts that triggered the formation of Cr-spinels and magnesiochromites and refertilised the harzburgite. After the igneous stage, the peridotites underwent a hydrothermal alteration event that caused alteration of the primary spinel-group minerals to ferrian chromite and magnetite.

7. References

Banerjee, R., Ray, D. and Ishii, T., 2015. Mineral Chemistry and Alteration Characteristics of Spinel in Serpentinised Peridotites from the Northern Central Indian Ridge, *Jour. Geol. Soc. India*, 86, 41-51.

Barnes, S.J. and Roeder, P.L., 2001. The Range of Spinel Compositions in Terrestrial Mafic and Ultramafic Rocks, *J. Petrol*., 42, 2279-2302.

Deer, W.A., Howie, R.A. and Zussman, S., 1992. The rock-forming minerals, Library of Congress Cataloguing in Publication Data, 558-568.

Dick, H.J.B. and Bullen, T., 1984. Cr-spinel as a petrogenetic indicator in abyssal and alpine-type peridotites and spatially associated lavas, *Contrib, Mineral. Petrol*., 86, 54-76.

Economou, M., 1983. A short note on the evolution of the Vermion ophiolite complex (Macedonia-Greece), *Ofioliti*, 8, 333-338.

Economou-Eliopoulos, M., 2003. Apatite and Mn, Zn, Co-enriched chromite in Ni-laterites of northern Greece and their genetic significance, *Journal of Geochemical Exploration*, 80, 41-54.

Farahat, E.S., Hoinkes, G. and Mogessie, A., 2011. Petrogenetic and geotectonic significance of Neoproterozoic suprasubduction mantle as revealed by the Wizer ophiolite complex, Central Eastern Desert, Egypt, *Int. J. Earth Sci*., 100, 1433-1450.

Gahlan, H.A. and Arai, S., 2007. Genesis of peculiarly zoned Co, Zn and Mn-rich chromian spinel in serpentinite of Bou-Azzer ophiolite, Anti-Atlas, Morocco, *Jour. Min. Petrol. Sci*., 102, 69-85.

Ghosh, B., Morishita, T. and Bhatta, K., 2013. Significance of chromian spinels from the mantle sequence of the Andaman Ophiolite, India: Paleogeodynamic implications, *Lithos*, 164-167, 86-96.

Kapsiotis, A., 2013. Origin of mantle peridotites from the Vourinos Ophiolite Complex, Greece, as deduced from Cr-spinel morphological and chemical variations, *Journal of Geosciences*, 58, 217-231.

Karipi, S., Tsikouras, B. and Hatzipanagiotou, K., 2006. The petrogenesis and tectonic setting of ultramafic rocks from Iti and Kallidromon Mountains, continental Central Greece: vestiges of the Pindos ocean, *Can. Mineral*., 44, 267-287.

Karipi, S., Tsikouras, B., Hatzipanagiotou, K. and Grammatikopoulos, T.A., 2007. Petrogenetic significance of spinel-group minerals from the ultramafic rocks of the Iti and Kallidromo ophiolites (Central Greece), *Lithos*, 99, 136-149.

Khedr, M.Z. and Arai, S., 2011. Petrology and geochemistry of chromian spinel-bearing serpentinites in the Hide Marginal Belt (Ise area, Japan): characteristics of their protoliths, *J. Miner. Petrol. Sci*., 106, 225-260.

Maulana, A., Christy, A.C. and Ellis, D., 2015. Petrology, geochemistry and tectonic significance of serpentinised ultramafic rocks from the South Arm of Sulawesi, Indonesia, *Chem. Erde*, 75, 73-87.

Mcdonough, W.F. and Sun, S.S., 1995. The composition of the Earth. *Chem. Geol*., 120, 223-253.

Mercier, J., Vergely, P. and Bebien, J., 1975. Les ophiolites helleniques "obductees" au Jurassique superieur sont-elles les vestiges d'un ocean tethysien ou d'une mer marginale perieuropeenne, *C.R. Somm. Soc. Geol. France*, 17, 108-112.

Michailidis, K.M., 1990. Zoned chromites with high Mn-contents in the Fe-Ni-Cr-laterite ore deposits from the Edessa area in Northern Greece, *Mineral. Deposita*, 25, 190-197.

Niu, Y., 1997. Mantle melting and melt extraction processes beneath ocean ridges: evidence from abyssal peridotites, *J. Petrol*., 38, 1047-1074.

Oh, C.W., Rajesh, V.J., Seo, J., Choi, S.G. and Lee, J.H., 2010. Spinel compositions and tectonic relevance of the Bibong ultramafic bodies in the Hongseong collision belt, South Korea, *Lithos*, 117, 198-208.

Singh, N.I., Devi, L.D. and Chanu, Th.Y., 2013. Petrological and Geochemical Study of Serpentinised Peridotites from the Southern Part of Manipur Ophiolitic Complex, Northeast India, *Jour. Geol. Soc. India*, 82, 121-132.

Tamura, A. and Arai, S., 2005. Unmixed spinel in chromitite from the Iwanai-dake peridotite complex. Hokkaido, Japan: a reaction between peridotite and highly oxidized magma in the mantle wedge, *Am. Mineral*., 90, 473-480.

Tsouras, G. and Economou-Eliopoulos, M., 2008. High PGE contents and extremely abundant PGE-minerals hosted in chromitites from the Veria ophiolite complex, Northern Greece, *Ore Geol. Rev*., 33, 3-19.

Zhou, M.F., Robinson, P.T. and Bai, W.J., 1994. Formation of podiform chromitites by melt/rock iteraction in the upper mantle, *Mineralium Deposita*, 29, 98-101.

Δελτίο της Ελληνικής Γεωλογικής Εταιρίας, τόμος L, σελ. 2009-2017
Πρακτικά 14ου Διεθνούς Συνεδρίου, Θεσσαλονίκη, Μάιος 2016

Bulletin of the Geological Society of Greece, vol. L, p. 2009-2017
Proceedings of the 14th International Congress, Thessaloniki, May 2016

MINERALOGICAL AND SPECTROSCOPIC STUDY OF NESQUEHONITE SYNTHESIZED BY REACTION OF GASEOUS CO_2 WITH MG CHLORIDE SOLUTION

Skliros V.[1], Anagnostopoulou A.[2], Tsakiridis P.[1] and Perraki M.[1]

[1]*National Technical University of Athens, School of Mining* and *Metallurgical Engineering, 15780, Athens, Greece, sklirosbill@metal.ntua.gr, ptsakiri@metal.ntua.gr, maria@metal.ntua.gr*

[2]*Hellenic Open University, School of Science* and *Technology, 26 335, Patra, Greece, kanagnostopoulou@windowslive.com*

Abstract

Nesquehonite, a hydrous carbonate with promising uses such as building raw material and *treatment of wastewaters, was synthesized under low pressure conditions by reaction of gaseous CO_2 with Mg chloride solution* and *it was studied by means of X-Ray Diffraction, optical* and *scanning/transmission electron microscopy*, and *FT-IR* and *Raman spectroscopic methods. Synthesized nesquehonite forms elongated fibers, exhibiting transparent to translucent diaphaneity* and *vitreous luster. It is characterized by high crystallinity. IR* and *Raman spectroscopy indicated the presence of OH^-* and *HCO_3^- in the crystal structure of nesquehonite. The nesquehonite synthesis described herein constitutes a potential permanent storage of CO_2 emissions.*

Keywords: *nesquehonite, hydrous magnesium carbonate, low-pressure mineralization, CO2 storage.*

Περίληψη

Στην παρούσα εργασία πραγματοποιήθηκε η σύνθεση νεσκεχονίτη, ενός ένυδρου ανθρακικού ορυκτού, υπό χαμηλές συνθήκες πίεσης με αντίδραση CO_2 σε διάλυμα χλωριούχου μαγνησίου. Ο νεσκεχονίτης μπορεί να αξιοποιηθεί ως πρώτη ύλη σε δομικά υλικά και επιπλέον στην διαχείριση υγρών αποβλήτων. Ο νεσκεχονίτης μελετήθηκε με περιθλασιομετρία ακτίνων-Χ, υπέρυθρη φασματοσκοπία (FT-IR) και φασματοσκοπία Raman, διοφθάλμιο στερεοσκόπιο, Ηλεκτρονικό Μικροσκόπιο Σάρωσης και Ηλεκτρονικό Μικροσκόπιο Διερχόμενης Δέσμης Ηλεκτρονίων. Ο παραγόμενος νεσκεχονίτης αναπτύσσει επιμήκεις διαφανείς έως ημιδιαφανείς βελονοειδείς κρυστάλλους με υαλώδη λάμψη. Η υπέρυθρη φασματοσκοπία (FT-IR) και η φασματοσκοπία Raman υπέδειξαν την παρουσία OH^- και HCO_3^- στην κρυσταλλική δομή του νεσκεχονίτη. Η διαδικασία σύνθεσης που περιγράφεται στην παρούσα εργασία μπορεί να χρησιμοποιηθεί στην διαδικασία της ορυκτοποίησης για μόνιμη αποθήκευση των εκπομπών CO_2.

Λέξεις κλειδιά: *νεσκεχονίτης, ένυδρο ανθρακικό ορυκτό του μαγνησίου, ορυκτοποίηση, αποθήκευση του διοξειδίου του άνθρακα.*

1. Introduction

Nesquehonite is a magnesium carbonate mineral with proposed chemical formula either $MgCO_3*3H_2O$ (Kloprogge *et al.*, 2003; Dong *et al.*, 2009; Stephan and McGillavry, 1972) or $Mg(OH)(HCO_3)*2H_2O$ (Hales *et al.*, 2008; Hales *et al.*, 2008; Frost and Palmer, 2011), named after a location in Pennsylvania, USA, where found for first time. It is crystallized in the monoclinic crystal structure in space group P21/n, Z = 4 and it has unit cell parameters of a = 7.70Å, b = 5.37Å, c = 12.12 Å and β= 90º, 45´as described by Stephan and MacGillavry (1972) and by Giester *et al.* (2000). Its structure consists of infinite flat ribbons of corner-sharing MgO_6 octahedra (Fig. 1a) along the b axis of the crystal, which is the fiber axis, linked by hydrogen bonds and contains only one crystallographically inequivalent carbon (Fig.1b). Within the chains, CO_3 groups link three MgO_6 octahedra by one edge and two common corners. The Mg atoms are in a distorted coordination, and each atom is coordinated by two H_2O ligands; one free H_2O molecule is located between the chains as shown in Figure 2 (Wang *et al.*, 2008; Ferrini *et al.*, 2009; Ballirano *et al.*, 2009; Giester *et al.*, 2000; Moore *et al.*, 2015; Stephan and McGillavry, 1972). In Greece, natural nesquehonite has been reported in Lavrion (Giester *et al.*, 2000).

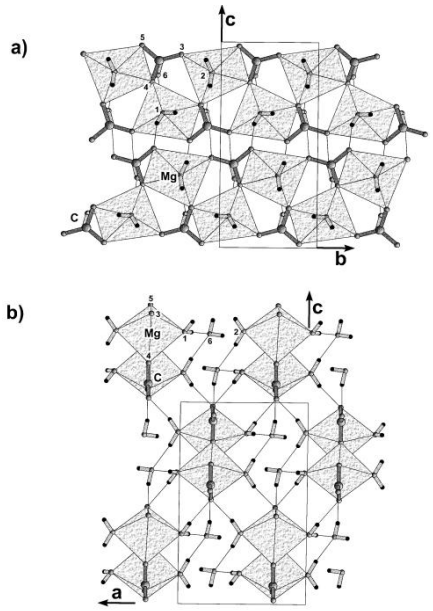

Figure 1 – Crystal structure of nesquehonite in projections parallel to a [100] and b [010] (Giester *et al.*, 2000).

Nesquehonite exhibits promising uses as a raw material of magnesium cement (Ferrini *et al.*, 2009) as well as in wastewater treatment (Shan *et al.*, 2013). Besides, recent studies showed that nesquehonite can be the product of CO_2 mineralization under low pressure conditions (Ferrini *et al.*, 2009; De Vito *et al.*, 2012). Given that nowadays, the reduction of CO_2 emissions has become a first priority for all industrial activities, CO_2 mineralization, i.e. CO_2 carbonation, constitutes one of the main carbon capture and sequestration (CSS) methods (Verduyn, 2011). Whereas, first studies dealt with the laboratorial reaction of CO_2 with the Mg-rich minerals of ultramafic rocks under high pressure conditions to form pure magnesite (Lackner *et al.*, 1995) followed by studies on the in-situ storage of high pressure CO_2 gas in ophiolite complexes (Kelemen and Matter, 2008; Kelemen *et al.*, 2011), an increasing interest on CO_2 mineralization under low pressure conditions is coming up (Ferrini *et al.*, 2009; De Vito *et al.*, 2012). Apart from the synthesis procedure, of great interest is the detailed characterization of the synthesized nesquehonite.

In this work, nesquehonite was synthesized under low pressure conditions by reaction of gaseous CO_2 with Mg chloride solution and its characterization was carried out by means of X-Ray Diffraction, optical and scanning/transmission electron microscopy, and FT-IR and Raman spectroscopic methods.

2. Materials and Methods

1.1 Analytical methods

X-Ray Diffraction patterns were obtained with a Bruker D8 Focus diffractometer in a θ-θ configuration employing CuKα radiation (λ = 1.5406 Å) with a fixed divergence slit size of 0.5° and a rotating sample stage. The samples were scanned between 4 and 70° 2θ. The step size and time per step were set to 0.017° 2θ and 80 s, respectively. Stereoscopic study was carried out under a Leica MZ8 binocular stereoscope. Scanning Electron Microscopy (SEM) was performed using a JEOL 6380LV-SEM equipped with an Oxford EDS-WDS. Transmission Electron Microscopy was performed with a JEOL 2100 HR–TEM at 200kV. A Fourier-transform infrared FT-IR spectrophotometer, Perkin Elmer Spectrum GX, and a Renishaw's inVia-micro-RAMAN (532 nm excitation laser wavelength) were employed to obtain additional information on nesquehonite composition and structure.

1.2 Synthesis of Nesquehonite

Nesquehonite was synthesized at laboratory conditions by using a gas cylinder of CO_2 and chemical reagents $MgCl_2*6H_2O$ and $NaHCO_3$. 80g $MgCl_2*6H_2O$ were dissolved into 500 ml of dionized water. CO2 gas was then introduced into the solution at pressure of 0.1kbar under continuous magnetic stirring at 1100rpm. A solution of 60g $NaHCO_3$ was added by using peristaltic pump. CO_2 gas was continually added into the solution for an hour under stirring. After that, the solution was left to precipitate for 24 hours. During the experiment solution temperature was kept stable at 25 ºC. The chemical reaction that took place was

$$MgCl_2*6H_2O + 2NaHCO_3 + 3CO_2 \rightarrow MgCO_3*3H_2O + 2NaCl + 4H_2CO_3$$

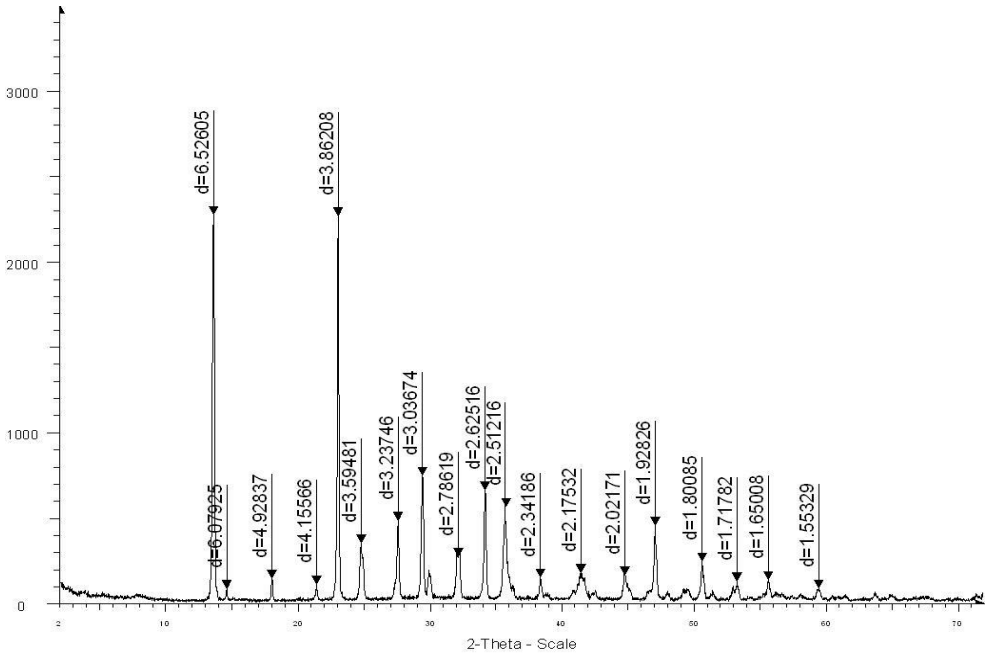

Figure 2 - XRD pattern of the nesquehonite synthesized herein.

The precipitated nesquehonite was then separated from the solution by using a vacuum pump and suitable paper filters and washed out with dionized water to dissolve any salts that might have been remained. Moisture was removed from the sample by putting it into an oven at 50ºC for 24 hours.

3. Results and Discussion

As can been seen in the representative XRD diagram (Fig. 2) the produced precipitate is pure nesquehonite, with characteristic peaks at d= 6.52, 3.86, 3.04, 2.62, 2.51 and 1.92 Å, which corresponds to [-101], [200], [-211], [021], [-301] and [400] Miller indices (Stephan and McGillavry, 1972).

Nesquehonite formed as a white precipitate. Study under the binocular stereoscope, showed that it exhibits transparent to translucent diaphaneity and vitreous luster and it forms elongated fibers (Fig. 3).

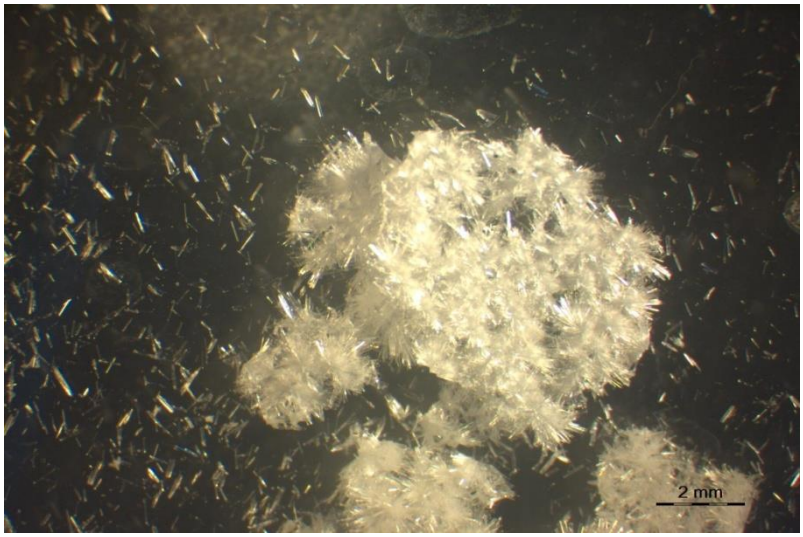

Figure 3 – Stereoscopic view of the nesquehonite synthesized herein.

Scanning Electron Microscopy (SEM) showed that nesquehonite fibers were developed around a centerpiece creating a structure called rosettes (Fig. 4). EDS point analyses (Fig. 5) showed the presence of only one chemical phase; any salts might have been removed during the sample preparation.

Transmission Electron Microscopy (TEM) study showed that nesquehonite is highly crystalline (Fig. 6). The Selected Area Diffraction (SAED) pattern (Fig.7) confirms the high crystallinity of the nesquehonite crystals and the absence of any amorphous phase (Egerton, 2005).

Fourier-Transform Infrared (FTIR) and Raman analyses were performed in the samples, to obtain additional information on their chemistry and structure. IR spectra (Fig. 8) showed the symmetric stretching (*v1*) and the bending (*v2*) modes of CO_3^{2-} at 1097.94 cm^{-1} and at 853.61 cm^{-1}, respectively. The three bands at 1520, 1466.06, 1420.06 cm^{-1} are ascribed to the split *v3* antisymmetric stretching mode (Kloprogge *et al.*, 2003; Coleyshaw *et al.*, 2003; Morgan *et al.*, 2015).The stretching of the O-H and the H_2O molecule gives rise to broad bands in the region between 2500-4000 cm^{-1} (Ferrini *et al.*, 2008; Kloprogge *et al.*, 2003). The bands at 3326.33, 3455.14, 3564.25 cm^{-1} can be ascribed to OH-stretching modes of water in the crystal structure of the nesquehonite (Hopkinson *et al.*, 2012; Hopkinson *et al.*, 2008). At 1653.43 cm^{-1} a H-O-H bending band is observed, which is associated with structural H_2O (Lanas and Alvarez, 2004; Hopkinson *et al.*, 2008; Hopkinson *et al.*, 2012) and absorbed H_2O (Kloproggre *et al.*, 2003).

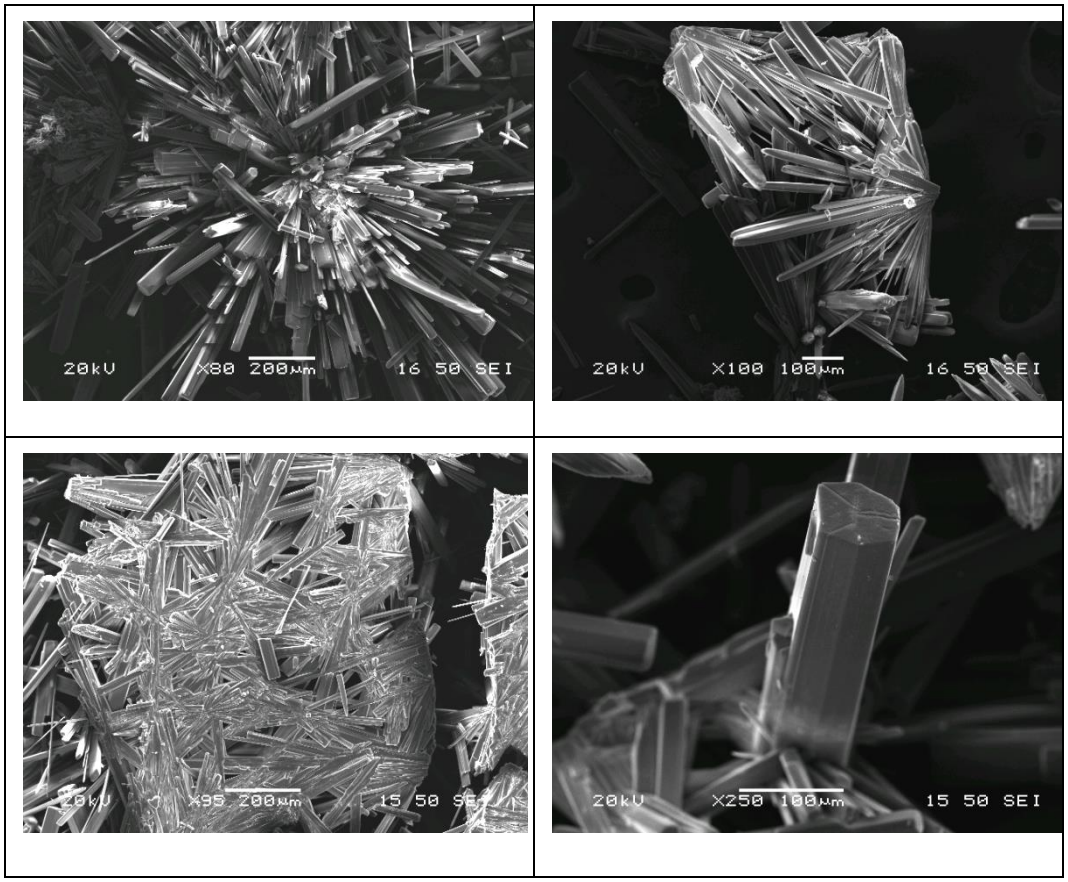

Figure 4 – Secondary electron (SE) images of nesquehonite showing prismatic crystals in the form of rosettes.

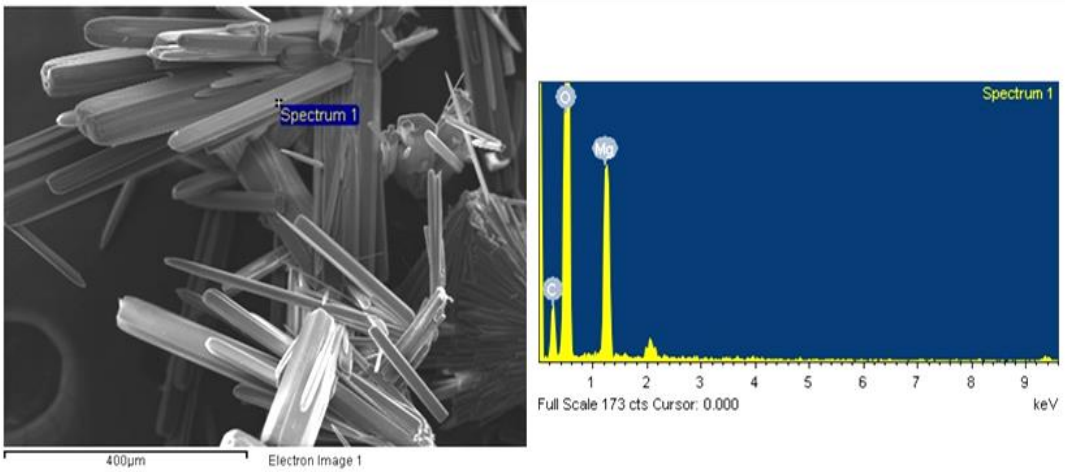

Figure 5 – Nesquehonite SE image (left) and the respective EDS spectrum (right), showing the presence of a magnesium carbonate mineral phase.

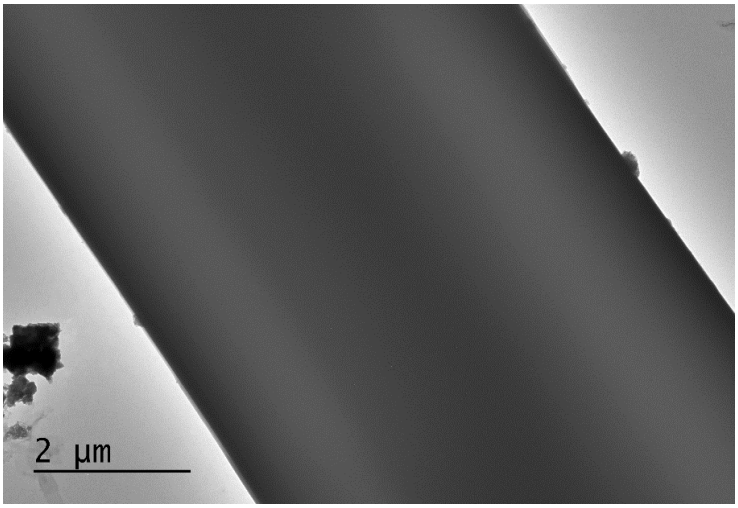

Figure 6 – TEM image showing the highly crystalline structure of the nesquehonite sample.

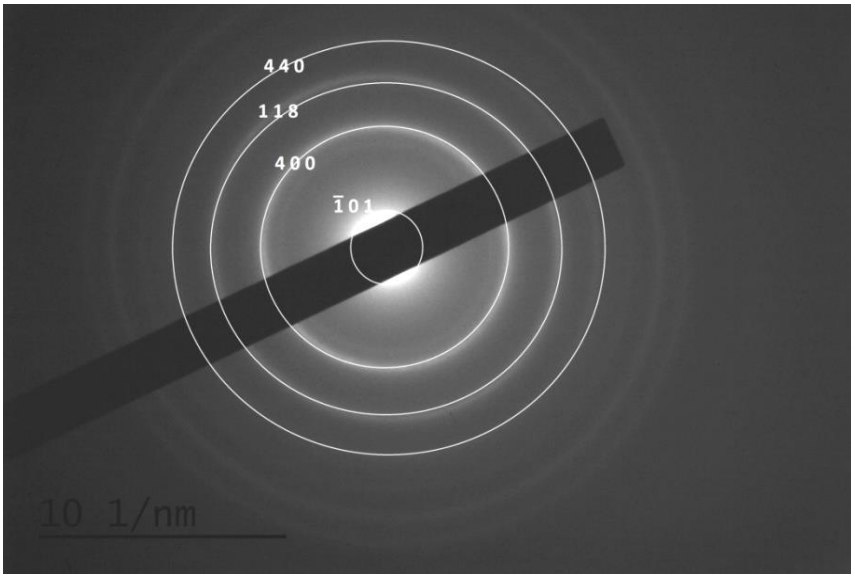

Figure 7 – SAED pattern of nesquehonite crystal indicating a highly crystalline structure. Each ring is created by Hall Effect and is assigned to d-spacing values which correspond to a certain set of hkl, compared with the diffraction data from literature (Egerton, 2005; American Mineralogy Crystal Structure Database; Stephan and McGillavry, 1972).

The two peaks observed at 699.97 cm^{-1} and 607.12 cm^{-1} are assigned to the *v4* in-plane bending mode of the HCO_3^- (Hales *et al.*, 2008; Frost and Palmer, 2011).

Raman spectra showed a very strong vibration at 1100 cm^{-1} (Fig. 9) that is ascribed to the *v1* symmetric stretching vibration of the CO_3^{2-} (Hales *et al*., 2008). The peak at 1515 cm^{-1} (Fig. 9) corresponds to *v1* antisymmetric stretching vibration of CO_3^{2-} and appears less intense. The two bands at 3123 cm^{-1}(Fig. 9) and 3444 cm^{-1}(Fig. 10) are assigned to the stretching vibration of H_2O molecules. The peak at 3556 cm^{-1} (Fig. 10) corresponds to the vibration tendency of O-H hydroxyl. The vibration at 1423 cm^{-1} (Fig. 9) is ascribed to the antisymmetric stretching of the HCO_3^- (Hales *et al.*, 2008; Frost and Palmer, 2011).

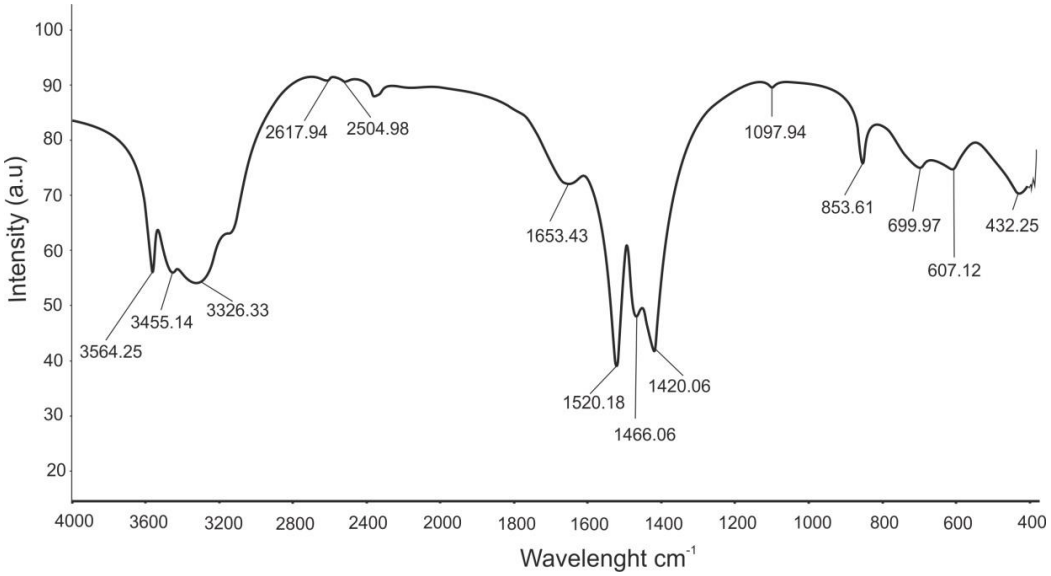

Figure 8 – FTIR spectrum of the nesquehonite synthesized herein.

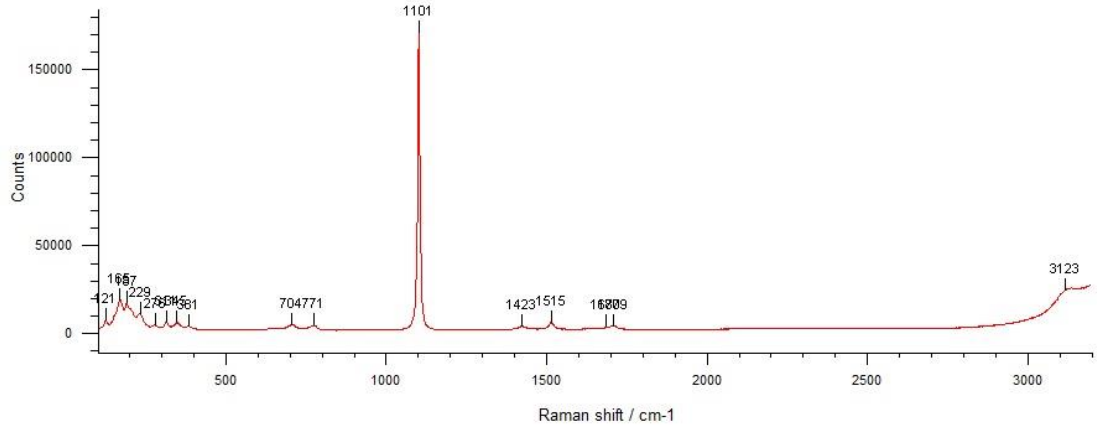

Figure 9 – Raman spectrum of the nesquehonite synthesized herein, from 50-3200 cm^{-1} wavelengths.

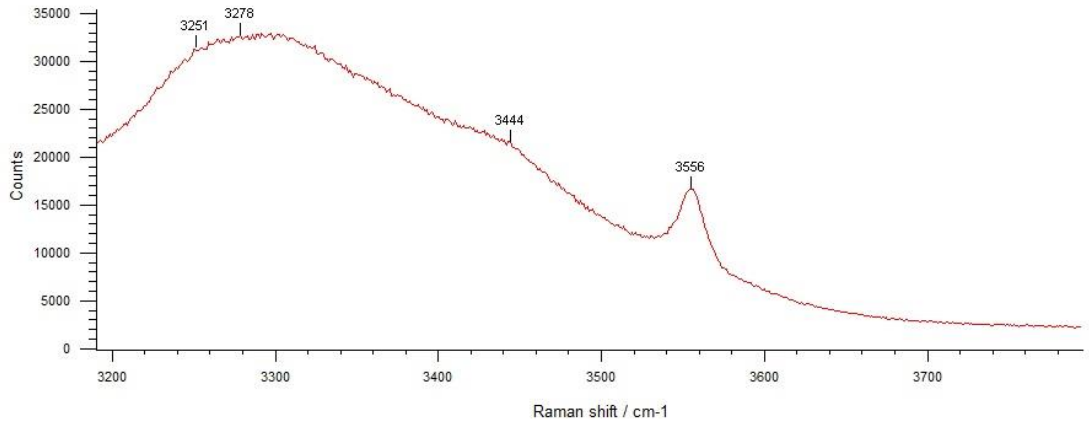

Figure 10 – Raman spectrum of the nesquehonite synthesized herein, from 3200-4000 cm^{-1} wavelengths.

Nesquehonite has a chemical composition of $MgCO_3$*$3H_2O$ (Kloprogge *et al.*, 2003; Dong *et al.*, 2009; Stephan and McGillavry, 1972), but has been described also as $Mg(OH)(HCO_3)$*$2H_2O$ (Hales *et al.*, 2008; Hales *et al.*, 2008; Frost and Palmer, 2011). Our IR and Raman results showed the presence of OH^- and HCO_3^- in the crystal structure of nesquehonite.

4. Conclusion

Nesquehonite, a hydrous carbonate, was synthesized under low pressure conditions by reaction of gaseous CO_2 with Mg chloride solution. Detailed study by means of X-Ray Diffraction, optical and scanning/transmission electron microscopy, and FT-IR and Raman spectroscopic methods showed that the synthesized nesquehonite

- forms elongated fibers developed as rosettes around of centerpieces with transparent to translucent diaphaneity and vitreous luster
- exhibits high crystallinity
- is characterized by the presence of OH^- and HCO_3^- in its crystal structure.

Nesquehonite is a thermodynamically and chemically stable solid product. The nesquehonite synthesis described herein is simple, fast and environmentally friendly and it constitutes a potential long-term CO_2 storage method. It might be applied in larger/industrial scale with the aim to capture and permanent store CO_2 emissions.

5. References

Ballirano, P., De Vito, C., Ferrini, V. and Mignardi, S., 2010. The thermal behaviour and structural stability of nesquehonite, MgCO3·3H2O, evaluated by in situ laboratory parallel-beam X-ray powder diffraction: New constraints on CO2 sequestration within minerals, *Journal of hazardous materials*, 178(1-3), 522-528.

Coleyshaw, E., Crump, G. and Griffith, W., 2003. Vibrational spectra of the hydrated carbonate minerals ikaite, monohydrocalcite, lansfordite and nesquehonite, *Spectrochimica Acta Part A: Molecular and Biomolecular Spectroscopy*, 59(10), 2231-2239.

De Vito, C., Ferrini, V., Mignardi, S., Cagnetti, M. and Leccese, F., 2012. Progress in carbon dioxide sequestration via carbonation of aqueous saline wastes, *Periodico di Mineralogia*, 81(3), 333-344.

Dong, M., Li, Z., Mi, J. and Demopoulos, G.P., 2009. Solubility and stability of nesquehonite ($MgCO_3·3H_2O$) in mixed NaCl + $MgCl_2$, NH_4Cl + $MgCl_2$, LiCl, and LiCl + $MgCl_2$ solutions, *Journal of Chemical* and *Engineering Data*, 54(11), 3002-3007.

Egerton, R., 2005. Physical Principles of Electron Microscopy. Boston, MA, Springer Science and Business Media, Inc.

Ferrini, V., De Vito, C. and Mignardi, S., 2009. Synthesis of nesquehonite by reaction of gaseous CO_2 with Mg chloride solution: Its potential role in the sequestration of carbon dioxide, *Journal of hazardous materials*, 168(2-3), 832-837.

Frost, R.L. and Palmer, S.J., 2011. Infrared and infrared emission spectroscopy of nesquehonite $Mg(OH)(HCO_3)·2H_2O$-implications for the formula of nesquehonite, *Spectrochimica Acta - Part A: Molecular* and *Biomolecular Spectroscopy*, 78(4), 1255-1260.

Giester, G., Lengauer, C.L. and Rieck, B., 2000. The crystal structure of nesquehonite, $MgCO_3$ $3H_2O$, from Lavrion, Greece, *Mineralogy* and *Petrology*, 70(3-4), 153-163.

Hales, M.C., Frost, R.L. and Martens, W.N., 2008. Thermo-Raman spectroscopy of synthetic nesquehonite - Implication for the geosequestration of greenhouse gases, *Journal of Raman Spectroscopy*, 39(9), 1141-1149.

Hopkinson, L., Kristova, P., Rutt, K. and Cressey, G., 2012. Phase transitions in the system MgO-CO_2-H_2O during CO_2 degassing of Mg-bearing solutions, *Geochimica et Cosmochimica Acta*, 76, 1-13.

Hopkinson, L., Rutt, K. and Cressey, G., 2008. The transformation of nesquehonite to hydromagnesite in the system CaO-MgO-H_2O-CO_2: An experimental spectroscopic study, *Journal of Geology*, 116(4), 387-400.

Kelemen, P.B. and Matter, J., 2008. In situ carbonation of peridotite for CO_2 storage, *Proceedings of the National Academy of Sciences of the United States of America*, 105(45), 17295-17300.

Kelemen, P.B., Matter, J., Streit, E.E., Rudge, J.F., Curry, W.B. and Blusztajn, J., 2011. Rates and mechanisms of mineral carbonation in peridotite: Natural processes and recipes for enhanced, in situ CO2 capture and storage.

Kloprogge, J.T., Martens, W.N., Nothdurft, L., Duong, L.V. and Webb, G.E., 2003. Low temperature synthesis and characterization of nesquehonite, *Journal of Materials Science Letters*, 22(11), 825-829.

Lackner, K.S., Wendt, C.H., Butt, D.P., Joyce Jr., E.L. and Sharp, D.H., 1995. Carbon dioxide disposal in carbonate minerals, *Energy*, 20(11), 1153-1170.

Lanas, J. and Alvarez, J.I., 2004. Dolomitic lime: Thermal decomposition of nesquehonite, *Thermochimica Acta*, 421(1-2), 123-132.

Moore, J., Surface, J., Brenner, A., Skemer, P., Conradi, M. and Hayes, S., 2015. Quantitative Identification of Metastable Magnesium Carbonate Minerals by Solid-State 13 C NMR Spectroscopy, *Environmental Science and Technology*, 49(1), 657-664.

Morgan, B., Wilson, S.A., Madsen, I.C., Gozukara, Y.M. and Habsuda, J., 2015. Increased thermal stability of nesquehonite ($MgCO_3 \cdot 3H_2O$) in the presence of humidity and CO_2: Implications for low-temperature CO2 storage, *International Journal of Greenhouse Gas Control*, 39, 366-376.

American Mineralogist Crystal Structure Database, 2015. Available online at: http://rruff.geo.arizona.edu/AMS/amcsd.php [Accessed 6 Oct. 2015].

Shan, Q., Zhang, Y. and Xue, X., 2012. Removal of copper from wastewater by using the synthetic nesquehonite, *Environental Progress and Sustainable Energy*, 32(3), 543-546.

Stephan, G. and MacGillavry, C., 1972. The crystal structure of nesquehonite, $MgCO_3.3H_2O$, *Acta Crystallographica Section B*, 28(4), 1031-1033.

Verduyn, M., Geerlings, H., Van-Mossel, G. and Vijayakumari, S., 2011. Review of the various CO_2 mineralization product forms, *Energy Procedia*, 2885.

Wang, Y., Li, Z. and Demopoulos, G.P., 2008. Controlled precipitation of nesquehonite ($MgCO_3 \cdot 3H_2O$) by the reaction of MgCl2 with $(NH4)_2CO_3$, *Journal of Crystal Growth*, 310(6), 1220-1227.

Δελτίο της Ελληνικής Γεωλογικής Εταιρίας, τόμος L, σελ. 2018-2024
Πρακτικά 14ου Διεθνούς Συνεδρίου, Θεσσαλονίκη, Μάιος 2016

Bulletin of the Geological Society of Greece, vol. L, p. 2018-2024
Proceedings of the 14th International Congress, Thessaloniki, May 2016

COMPOSITIONAL AND MORPHOLOGICAL EVALUATION OF EDIBLE SALTS: PRELIMINARY RESULTS

Stergiou C.[1], Karageorgiou S.[1], Theodoridou S.[1], Giouri K.[1], Papadopoulou L.[1] and Melfos V.[1]

[1]Aristotle University of Thessaloniki, School of Geology, Department of Mineralogy-Petrology-Economic Geology, 54124, Thessaloniki, Greece, christer@geo.auth.gr, stamatik@geo.auth.gr, steltheo@geo.auth.gr, agiouri@geo.auth.gr, lambrini@geo.auth.gr, melfosv@geo.auth.gr

Abstract

Nutritional habits have as a result the uptake of the elemental content of various foods in the human body. Salt (NaCl) constitutes an integral part of human diet needs. As a consequence, knowledge concerning the composition of edible salt is critical. The aim of the present study is to evaluate the components of 8 edible salt samples that are available in the Greek retail market. Samples were classified according to their color as follows: white (WS1, WS2), black (BS1, BS2), pink (PS1), red (RS1), blue (BLS1) and pale brown (BRS1). The research revealed that all samples mainly consist of Cl and Na. Himalayan Black Salt (BS2) also contains S, whereas the Hawaiian Red Salt (RS1) contains Fe. Additionally, most of the samples contain low levels of Al, Ca, K, Mg, P, S, Si and O as impurities. Concerning the morphological characteristics, salt particles appear irregular, rounded and in two cases as cubic crystals referring to the crystal structure of NaCl. Backscattered images confirm the presence of other mineral phases besides NaCl.

Keywords: *Sea salt, Rock salt, Sodium chloride, Human consumption.*

Περίληψη

Οι διατροφικές συνήθειες του ανθρώπου έχουν ως αποτέλεσμα την πρόσληψη των ουσιών που περιέχονται στις διάφορες τροφές, από τον ανθρώπινο οργανισμό. Το αλάτι (NaCl) αποτελεί ένα αναπόσπαστο συστατικό των αναγκών της ανθρώπινης διατροφής. Επομένως, είναι σημαντικό να είναι γνωστό το περιεχόμενο της σύστασής του. Ο στόχος της παρούσας εργασίας είναι η αξιολόγηση της σύστασης 8 διαφορετικών δειγμάτων αλατιών προς κατανάλωση, τα οποία διατίθενται στην ελληνική αγορά. Τα δείγματα αυτά ταξινομήθηκαν με βάση το χρώμα, χρησιμοποιώντας τους εξής χαρακτηρισμούς: λευκό (WS1, WS2), μαύρο (BS1, BS2), ρόδινο (PS1), ερυθρό (RS1), κυανό (BLS1) και ανοιχτό καστανό (BRS1). Όλα τα δείγματα αποτελούνται κυρίως από Cl και Na. Το μαύρο αλάτι Ιμαλάϊων (BS2) περιέχει επιπλέον και S, ενώ το κόκκινο αλάτι Χαβάης (RS1) περιέχει Fe. Ενώ, ως προσμίξεις συμμετέχουν τα Al, Ca, K, Mg, P, S, Si και O. Μορφολογικά τους χαρακτηρίζονται ως τυχαία, έως στρογγυλεμένα και σε μόνο δυο περιπτώσεις σχηματίζουν κυβικές δομές, παρόμοιες με αυτές του NaCl.

Λέξεις κλειδιά: *Θαλασσινό αλάτι, Ορυκτό αλάτι, Χλωριούχο νάτριο, Ανθρώπινη διατροφή.*

1. Introduction

The word salt relates to the ancient Greek word *άλς* (genitive: *αλός*). *Άλς* means either "salt", the substance which enhances the flavour in food, or "sea" (Babiniotis, 2010). However, nowadays salt refers to any salty material despite its relation to the sea.

Edible salt (NaCl) is worldwide the most commonly used food additive, providing improvement of taste and preservation of food. Its biological necessity lies on the fact that sodium and chlorine, the two main elements that it provides, are very important for the human body (Musaiger *et al.,* 2008; Soylak *et al.,* 2008; Cheraghali *et al.,* 2010). Since food chain is a common pathway for human exposure to many elements, the analysis of food samples for their elemental concentration is very important and has been continuously performed (Haddy, 2006; Steinhauser *et al.,* 2006; Tuzen and Soylak, 2007). The various properties of the chemical elements are essential for human life. However, when some elements are found in high concentrations, they can be considered as toxic. Edible salt may contain various chemical substances and due to its excessive use, information about its elemental content is critical (Zukowska and Biziuk, 2008; Zarei *et al.,* 2011).

The aim of the present study is to determine the general and morphological characteristics of 8 different types of edible, refined and unrefined, salts available in the Greek retail market and to evaluate their mineralogical and chemical composition.

2. Materials and Methods

A variety of refined and unrefined edible salts was examined in this study. Eight pre-packed salt sa mples available in the Greek market were purchased, either directly from the market or from vendo rs. Salts were examined in their bulk form, since they are used for human consumption in the way t hey are packed.

2.1. Sample Identification

The salt samples that were studied represented various origin locations, grain sizes, particle shapes, colors, sources and prices. However, as presented in Table 1, they were classified according to the ir color since it has been probably affected by their composition (which will be further investigated). Salts were classified in 6 groups: white (WS1, WS2), black (BS1, BS2), pink (PS1), red (RS1), b lue (BLS1) and pale brown (BRS1).

2.2. Sample Analyses

Elemental analyses of the salt samples, as well as their particle size and morphology, were evaluated with a JEOL JSM-840A scanning electron microscope (SEM) at the Electron Microscopy Laboratory in the Faculty of Sciences, Aristotle University of Thessaloniki. The microscope was equipped with an energy dispersive spectrometer (EDS) INCA 300, providing spot analyses. The samples were coated with carbon with an average thickness of 200A°, using a vacuum evaporator JEOL-4X. The operating conditions were 20 kV accelerating voltage and 0.4 mA beam current. Beam diameter was 1 μm while the time of each measurement was 60sec.

3. Results and Discussion

Organoleptic characteristics and some physical properties of all the salt samples are presented in Table 1. Samples represented 8 commercial types of edible salts, originating from 5 different locations. Half of them (samples WS1, WS2, BS1, RS1) are, essentially, products obtained by the evaporation of seawater when heated by the sun. The rest of the samples (BS2, PS1, BLS1, BRS1) are simply crystallized salts, mainly mineral deposits known as rock salts. Classification of the rock samples was based on their color, leading to 1 sample from each locality, with the exception of white and black, out of which 2 samples were recognized (WS1 and WS2 for white, BS1 and BS2 for

black). Concerning their odor, only the Himalayan Black salt smelled like sulfur, while the Hawaiian Red Salt gave away a slightly earthy smell.

Table 1 – Organoleptic characteristics of the studied salt samples.

Sample	Commercial Type	Location	Source	Color	Odor	Grain Size
WS1	Table Salt	Mediterranean Sea	Sea Salt	White	None	Very fine crystals ≤1 mm
WS2	Fleur de Sel	Mediterranean Sea	Sea Salt	White	None	Small crystals ≤2 mm
BS1	Hawaiian Black Salt	Hawaii	Sea Salt	Black	None	Very large crystals 3-10 mm
BS2	Himalayan Black Salt	Himalayas (India)	Mineral Salt	Black	Sulfur	Very fine crystals ≤1 mm
PS1	Himalayan Pink Salt	Himalayas	Mineral Salt	Pink	None	Small crystals ≤2 mm
RS1	Hawaiian Red Salt	Hawaii	Sea Salt	Red	Slightly earthy	Large crystals 2-3 mm
BLS1	Persian Blue Salt	Iran	Mineral Salt	Blue	None	Large crystals 2-5 mm
BRS1	Alpine salt	Austrian Alps	Mineral Salt	Pale Brown	None	Large crystals 1-3 mm

Many variations were observed in the grain size of the salt samples, as presented in Table 1. Figure 1 illustrates grains of each one of the 8 salt samples that were studied. Images were taken under a ZEISS stereoscope. The common table salt (WS1) and the Himalayan Black salt (BS2) are recognized as the most fine grained, since their crystal size is ≤1 mm. Small crystals are observed in the Fleur de Sel (WS2) and the Himalayan Pink salt (PS1), with their size not exceeding 2 mm. The grain sizes of all of the other samples vary between 1 and 5 mm. The only exception is the Hawaiian Black salt (BS2), since its impressively large and pyramid shaped crystals vary from 3 to 10 mm (Fig.1).

Figure 1 – Grains of the studied salt samples.

Table 2 presents qualitative characteristics, as obtained by numerous spot analyses on the edible salt samples. It is concluded that all samples mainly consist of Cl and Na. A differentiation was defined for the Himalayan Black Salt (sample BS2) since it also contains a sufficient amount of S, which can explain the odor of this sample, as indicated in Table 1 and Figure 2 . The same occurs for Fe, since it was defined as an abundant element in the Hawaiian Red Salt (sample RS1, Fig. 3). However, apart from their main elemental concentration, impurities were determined in most of the edible salts and they are mentioned in Table 2. The common Mediterranean Sea table salt and the Alpine salt were identified as the purest ones, since they contained no impurities. On the other hand, Himalayan Black salt (BS2) and Persian Blue salt (BLS1) comprise more impurities than the rest of the samples (Table 2). It should also be mentioned that oxygen was determined in the composition of all the edible salts. Thus, further investigation is required in order to define the mineral phases in which oxygen participates.

Table 2 – Qualitative characteristics of the studied salt samples.

Sample	Cl	Fe	Na	S	Impurities
WS1	+		+		-
WS2	+		+		Ca, Mg, S
BS1	+		+		K
BS2	+		+	+	Al, Ca, Fe, K, Mg, P
PS1	+		+		K, Mg, S
RS1	+	+	+		Al, Ca, Mg, S, Si
BLS1	+		+		Ca, K
BRS1	+		+		-

The results obtained by the elemental analyses of the studied samples are presented in Table 3. The most abundant elements are Cl and Na, as revealed by their mean values (in weight %) which are the highest ones (67.1 and 28.8, respectively). They take part in the composition of all the salt samples and the range of their percentage is 14.1-95.8% for Cl and 4.2-44.3% for Na. As mentioned above, S and Fe are abundant in samples BS2 and RS1, respectively. Moreover, they are present in lower amounts in some other samples (Table 2). Overall, S ranges from 0.7% to 65.7% with its mean value reaching up to 9.7%, while Fe ranges from 1.2% to 43.9% with a mean of 8.0%.

SEM observations of representative salt samples with their corresponding spectrums are illustrated in Figures 2 and 3. All samples consist of irregular, rounded particles with sizes ranging from 2 mm to less than 500 μm. In the black samples of Himalayan (BS1) and Hawaiian (BS2) salts, cubic crystals are present with cubic blemishes referring to the crystal shape of NaCl (face-centered cubic structure). Backscattered images show the presence of different mineral phases (dark grey areas) both on the surface of the salt particles (samples BS1 and PS1) as well as individual grains (sample RS1, lower left side), pointing to the existence of other mineral phases besides NaCl, as determined by EDS analyses. These mineral phases will be determined through further investigation.

The concentrations of all other elements are relatively low, since they are present as impurities. The next predominant elements are K and Ca and that were determined in 4 samples. The range of their percentage is 1.3-50.7% for K and 1.0-26.5% for Ca, while their corresponding mean values are 14.5% and 8.6%. Magnesium was determined in 4 samples with a range of 1.5-11.8% and a mean value of 4.5%. The percentage of Al ranges from 1.0% to 2.7% in 2 samples, with a mean of 1.7%. In only 1 sample (RS1) Si was determined, with a range of 1.3-2.7% and a mean value of 2.0%. Finally, it should be noted that in 1 sample (BS2) and in only 1 spot analysis, 0.9% of P was determined.

Table 3 – Results of the elemental analysis of the studied edible salts and notable samples.

Element	Min (Weight %)	Max (Weight %)	Mean (Weight %)	Sample with Lower Percentage	Sample with Higher Percentage
Al	1.0	2.7	1.7	RS1	BS2
Ca	1.0	26.5	8.6	BLS1	WS2
Cl	14.1	95.8	67.1	BS1	BS1
Fe	1.2	43.9	8.0	RS1	RS1
K	1.3	50.7	14.5	BS1	BLS1
Mg	1.5	11.8	4.5	WS2	BS2
Na	4.2	44.3	28.8	BS1	WS1
P	0.9	0.9	0.9	BS2	BS2
S	0.7	65.7	9.7	BS1	BS1
Si	1.3	2.7	2.0	RS1	RS1

The lowest and highest percentage of some elements was observed in the same sample (Table 3). T his is reasonable in the case of P and Si, since they were detected in only 1 sample. Although Cl is one of the main components of the salt samples, its minimum and maximum values are observed in the same sample (BS1). Despite the fact that they were determined in almost half of the samples, l owest and highest contents of Fe and S were determined in samples RS1 and BS1, respectively (Fi g. 2, 3). Sample BS1 contains the lowest K and Na values, while the highest values were observed in sample BLS1 and WS1, respectively. The lowest amount of Al was observed in sample RS1 and the highest in sample BS2. The Mg content ranges from 1.5 wt% in the sample WS2 to 11.8 wt% i n the sample BS2. As for Ca, its lowest and highest values were determined in samples BLS1 (1.0 wt%) and WS2 (26.5 wt%), respectively.

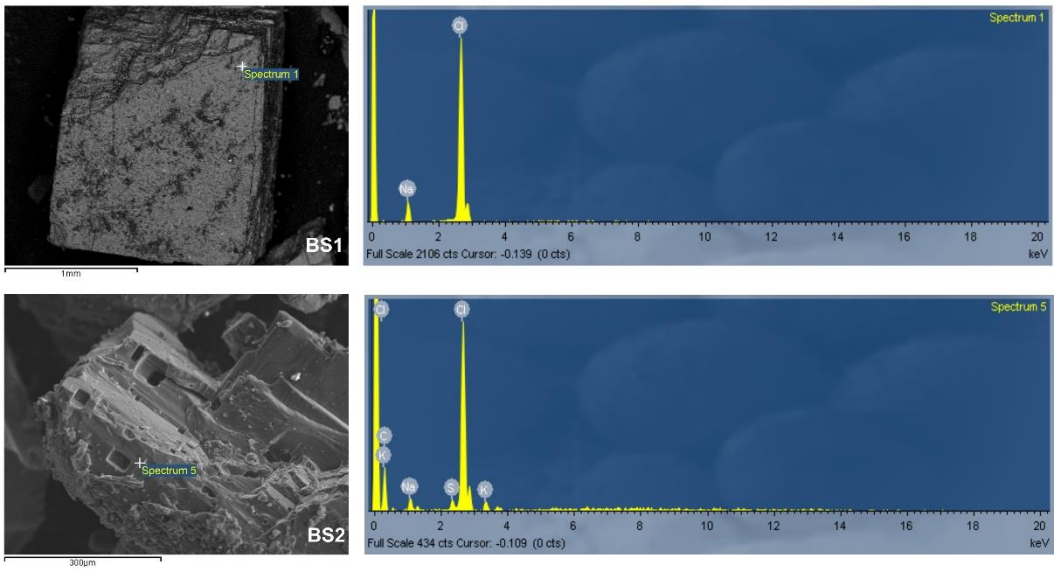

Figure 2 – SEM microphotographs of the studied samples, with representative X-ray spectrums. Sample BS1: backscattered image; BS2: secondary image.

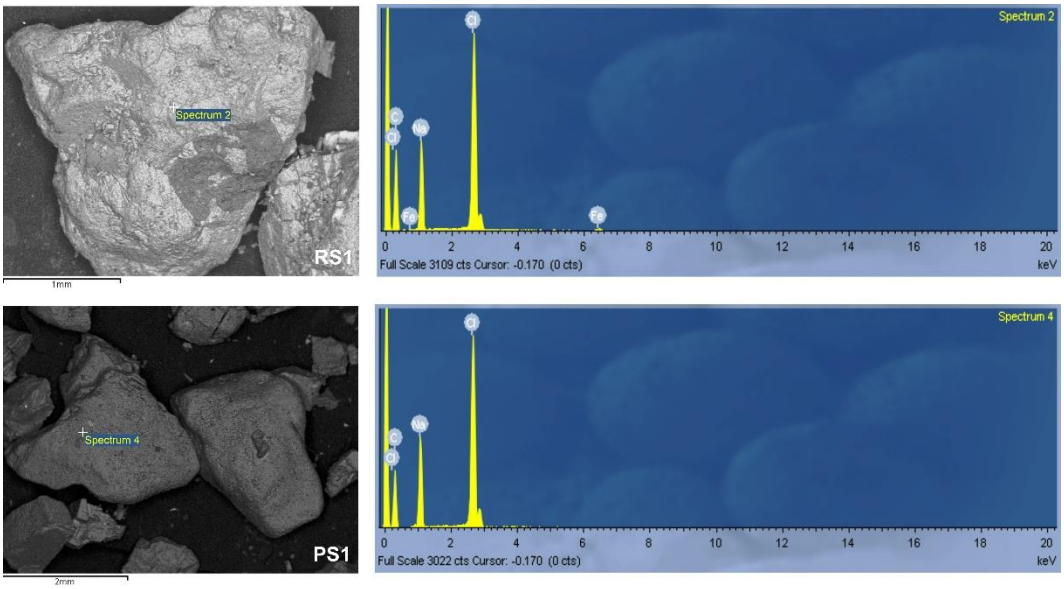

Figure 3 – SEM microphotographs of the studied samples, with representive X-ray spectrums. Samples RS1 and PS1: backscattered images.

4. Conclusions

The studied samples represent 8 commercial types of edible salts, of 6 different colors and originating from 5 different locations (Mediterranean Sea, Hawaii, Himalayas, Iran and Austrian Alps). Four samples include sea salts and four samples are rock salts. The size of their grains varies from very fine (≤1 mm) to very large (10 mm).

Bulk chemical analyses of the samples revealed that all of them consist mainly of Cl and Na. Additionally, samples BS2 and RS1 contain sufficient amounts of S and Fe, respectively. Apart from their main chemical composition, most of the edible salt samples contain low levels of Al, Ca, K, Mg, P, S, Si and O as impurities.

Concerning morphological characteristics, salt grains in all samples appear irregular and rounded with sizes ranging from <2 μm to 2 mm. Backscattered images certify the existence of different mineral phases other than NaCl.

However, the research is in progress since a more detailed evaluation of the composition of the salt samples is required, especially concerning the trace elements that they may comprise.

5. References

Babiniotis, G., 2010. Etymological Dictionary of the Modern Greek Language: History of Words, Athens, Lexicology Centre Ltd, 1652 pp.

Cheraghali, A.M., Kobarfard, F. and Faeizy, N., 2010. Heavy metals contamination of table salt consumed in Iran, *Iranian Journal of Pharmaceutical Research*, 9(2), 129-132.

Haddy, F.J., 2006. Role of dietary salt in hypertension, *Life Sciences*, 79, 1585-1592.

Musaiger, A.O., Al-jedah, J.S. and D'souza, R., 2008. Occurrence of contaminants in foods commonly consumed in Bahrain, *Food Control*, 19(9), 854-861.

Soylak, M., Peker, D. and Turkoglu, O., 2008. Heavy metal contents of refined and unrefined table salts from Turkey, Egypt and Greece, *Environmental Monitoring and Assessment*, 143, 267-272.

Steinhauser, G., Sterba, J.H., Poljanc, K., Bichler, M. and Buchtela, K., 2006. Trace elements in rock salt and their bioavailability estimated from solubility in acid, *Journal of Trace Elements in Medicine and Biology*, 20, 143-153.

Tuzen, M. and Soylak, M., 2007. Evaluation of trace element contents in canned foods marketed from Turkey, *Food Chemistry*, 102, 1089-1095.

Zarei, M., Eskandari, M.H. and Pakfetrat, S., 2011. Determination of heavy metals content of refined table salts, American-Eurasian, *Journal of Toxicological Sciences*, 3(2), 59-62.

Zukowska, J. and Biziuk, M., 2008. Methodological evaluation of method for dietary heavy metal intake, *Journal of Food Sciences*, 73(2), R21-R29.

Δελτίο της Ελληνικής Γεωλογικής Εταιρίας, τόμος L, σελ. 2025-2036
Πρακτικά 14ου Διεθνούς Συνεδρίου, Θεσσαλονίκη, Μάιος 2016

Bulletin of the Geological Society of Greece, vol. L, p. 2025-2036
Proceedings of the 14th International Congress, Thessaloniki, May 2016

IRON-OXIDE MINERALIZATION OF SESI, KOROPI (S. HYMITTOS, GREECE): MINERALIZATION WITHIN A DETACHMENT ZONE

Stouraiti C.[1], Lekkas S.[2], Lozios S.[2] and Kanellopoulos C.[3]

[1]Department of Geology and Geoenvironment, Division of Economic Geology and Geochemistry, National and Kapodistrian University of Athens, Panepistimiopolis, Ano Ilissia, Athens 15784, Greece, chstouraiti@geol.uoa.gr

[2]Department of Geology and Geoenvironment, Division of Dynamic Tectonic and Applied Geology, National and Kapodistrian University of Athens, Panepistimiopolis, Ano Ilissia, Athens 15784, Greece, slozios@geol.uoa.gr

[3]Institute of Geology and Mineral Exploration, 1st Spirou Louis St., Olympic Village, 13677, Acharnae, Greece, ckanellopoulos@gmail.com

Abstract

Small occurrences of iron-oxide deposits at Sesi-Koropi in S. Hymittos, are hosted by an extensional brittle detachment zone between carbonate rocks of "Vari-Kirou Pira" and "Hymittos" units. Another low-angle fault separates a heterogeneous formation of schists, containing meta-ophiolitic blocks ("Lavrion" Unit), which is cut by high-angle normal faults that root in the detachment zone, reducing the total structural thickness of "Hymittos" marbles and bringing in contact the meta-ophiolitc lithologies with the "Vari-Kirou Pira" dolomites. Three mine caves were found along the detachment zone indicating that these iron deposits were possibly mined on a very small scale in the past. The mineralization is developed in a cataclastic zone a few meters thick (3-5m), forming thin rusty black encrustations and larger zones of alteration with a reddish to yellow brown hue. Scanning Electron Microscope (SEM) mineralogical study of the iron-ore deposit indicated that hematite is the primary iron-oxide mineral extensively replaced by goethite. Goethite appears with the typical colloidal form within voids showing typical open-space filling type microstructures. According to field evidence and the tectonic macro-structure of the area, the mineralization is associated with hydrothermal fluid circulation along the brittle detachment zone between meta-ophiolitic lithologies and carbonate rocks. Similar type iron-oxides mineralization in cataclastic zones were observed along other detachment zones in northern and southeastern Hymittos Mt. and further south towards Lavrion. This suggests that this type of mineralization is not local but has a broader development and regional implications for the tectonic evolution of the central and SE Attica.

Keywords: *iron-oxides, hematite, goethite, mineralization, brittle detachment zone, low-angle fault.*

Περίληψη

Μικρές εμφανίσεις μεταλλοφορίας οξειδίων του σιδήρου στην περιοχή Σέσι, Κορωπί, Ν. Υμηττός, αναπτύσσονται κατά μήκος μιας κατακλαστικής ζώνης αποκόλλησης ανάμεσα σε ανθρακικούς σχηματισμούς των ενοτήτων "Υμηττού" και "Βάρης-Κύρου Πύρα". Ένα

άλλο μικρής κλίσης ρήγμα, φέρνει σε επαφή του σχιστολίθους της υπερκείμενης ενότητας "Λαυρίου" που περιλαμβάνουν τεμάχη από μετα-βασικά πετρώματα και σερπεντινίτες. Η όλη δομή κόβεται από μεγάλης κλίσης κανονικά ρήγματα, που ριζώνουν στην κατακλαστική ζώνη αποκόλλησης, συντελώντας στην τεκτονική εκλέπτυνση της ενότητας "Υμηττού", με αποτέλεσμα σε αρκετές περιπτώσεις να έρχονται σε επαφή οι μετα-οφιολιθικές λιθολογίες με τα ανθρακικά της ενότητας "Βάρης-Κύρου Πύρα". Η εμφάνιση του σιδηρομεταλλεύματος εντοπίστηκε μέσα σε τρείς μικρές διερευνητικές στοές εξόρυξης όπου υπάρχουν ενδείξεις για περιορισμένη εξόρυξη στο πρόσφατο παρελθόν. Η μεταλλοφορία αναπτύσσεται στην κατακλαστική ζώνη του ρήγματος αποκόλλησης, έχει πάχος λίγων μέτρων (3-5μ), και σχηματίζει λεπτούς μαύρους φλοιούς και ζώνες εξαλλοίωσης με χαρακτηριστική καφέ-κόκκινη έως κίτρινη απόχρωση. Η ορυκτολογική μελέτη της μεταλλοφορίας του σιδηρομεταλλεύματος έδειξε ότι αποτελείται από αιματίτη (πρωτογενής μεταλλοφορία) και γκαιτίτη (δευτερογενής μεταλλοφορία από αντικατάσταση). Μελέτη των μικροδομών του γκαιτίτη έδειξε ότι παρουσιάζει τυπική μορφολογία κολλοειδούς μορφής, που είναι χαρακτηριστική πλήρωσης κοιλοτήτων του ανθρακικού πετρώματος (ξενιστής). Σύμφωνα με τις παρατηρήσεις υπαίθρου και την τεκτονική μακροδομή της ευρύτερης περιοχής, η ανάπτυξη της σιδηρούχου μεταλλοφορίας συνδέεται με κυκλοφορία υδροθερμικού ρευστού κατά μήκος της κατακλαστικής ζώνης αποκόλλησης. Η σιδηρούχος εξαλλοίωση των ανθρακικών σχηματισμών είναι έντονη σε συγκεκριμένες ζώνες κατάκλασης κατά μήκος τέτοιου τύπου μικρής κλίσης κατακλαστικών ζωνών αποκόλλησης σε όλη την κεντρική και ΝΑ Αττική, από τον Β. Υμηττό μέχρι το Λαύριο. Αυτό υποδηλώνει ότι αυτού του τύπου η μεταλλοφορία δεν παρατηρείται μόνο τοπικά, αλλά έχει μια ευρύτερη ανάπτυξη και επομένως σημασία για την τεκτονική εξέλιξη της ΝΑ Αττικής.
Λέξεις κλειδιά: *οξείδια σιδήρου, αιματίτης, γκαιτίτης, μεταλλοφορία, κατακλαστική ζώνη αποκόλλησης, μικρής κλίσης κανονικό ρήγμα.*

1. Introduction

This study describes for the first time, the occurrence of an iron-oxide deposit in the Sesi area, south Hymittos Mt., along the brecciated contact of the "Lower Marble" ("Hymittos" Unit) with the underlying dolomitic marbles ("Vari-Kirou Pira" Unit). Oxidized mineralization related to brittle detachment faulting (low-angle normal faults), having characteristic structural features as well as mineral assemblage, have recently been recognized in many cases in the Attic Cycladic massif, from Lavrion to western Cyclades and further south in western Crete (Lavrion: Berger *et al*, 2013; Kea: Rice *et al*., 2012; Kithnos, Serifos: Grasemann *et al*., 2012; W Crete: Seidel *et al*., 2005). Similar iron-oxide deposits associated with detachment faulting in western Crete have been correlated, by Seidel *et al*. (2005) with the extension model of Basin and Range Province in the western United States. Previous authors (Seidel *et al*., 2005) suggested that this type of mineralization may be an indication of deep crustal fluid flow resulting from retrograde metamorphism in hot lower plate rocks. Alternatively, it may represent low-temperature circulation of fluids at shallower crustal levels.

In some of the above mentioned cases of detachment-related mineralizatiosn there is a strong localization of detachment faulting and interaction of brittle deformation with the injection of fluids related to granitoid intrusions (e.g. Lavrion, Serifos). In south Hymittos Mt. (Sesi-Koropi) small iron oxide deposits are also located within a detachment zone and hosted by carbonate rocks. However, the origin of the lower temperature Fe-mineralization (e.g. Kea and Sesi-Hymittos Mt.) is not straight-forward and remains speculative regarding the heat source that triggered hydrothermal circulation and Fe-oxide deposition at the upper crustal levels.

Here we report mineralogical and petrographic data of the iron-ore samples which allow categorization of goethite into different textural types and make a preliminary examination of its possible origin. Moreover, in order to understand the interrelations between the mineralization and the detachment tectonics, a detailed geological mapping of the Sesi area was carried out and the

project will continue on other key areas in Hymittos Mt and southern Attica, where both detachment structures and Fe-oxide mineralization are spatially closely associated.

2. Geological Setting

The Hymittos Mt. (located to the east of Athens) belongs to the Attic-Cycladic crystalline massif (ACCM), which in turn belongs to the Intermediate Tectonometamorphic Zone of the Hellenides orogen (Dörr, 1978 and Papanikolaou, 1988). Lepsius (1893) was the first to propose a complete lithostratigraphic structure of Attica, which is nowadays accepted with some alterations. Marinos and Petrascheck (1956), for the first time and Katsikatsos (1977, 1990) later, suggest the existence of two main geotectonic units in Attica – one relative autochthonous and an allochthonous – and prove that all metamorphic rocks of south and central Attica are both of Mesozoic age.

Based on systematic mapping and detailed litho-stratigraphic correlations, Lekkas and Lozios (2000) proposed a refined model of the tectonic structure of Hymittos Mt., by integrating all previous structural and petrological data for the area (Fig. 1). According to these authors, from bottom to top the structural sequence of Hymitos Mt. consists of: a) the lower "Vari-Kirou Pira" Unit, b) the overlying "Hymittos" Unit (both represent the relative autochthonous of Marinos and Petrascheck, 1956 and Katsikatsos, 1977) and c) the allochthonous "Lavrion-Athens" Unit.

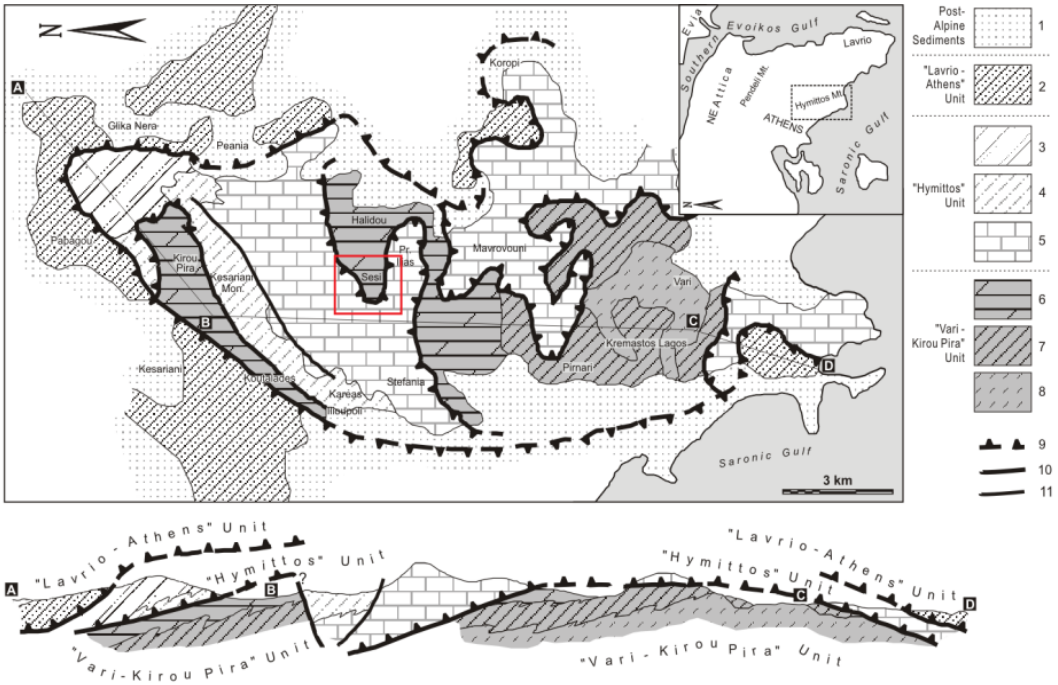

Figure 1 - Simplified geological map of Hymittos Mt., after Lekkas and Lozios (2000), showing the area of study in the red colored frame. 1: post-alpine sediments, 2: "Lavrion-Athens" Unit, 3, 4 and 5: "Hymittos" Unit (3: marble and alternations of marble and schists, 4: "Kessariani Schists", 5: "Lower Marble"), 6, 7 and 8: "Vari-Kirou Pira" Unit (6: white massive dolomite, 7: impure dolomite marble, 8: "Vari Schist"), 9: brittle detachment, 10: tectonic contact, 11: fault.

The lower "Vari-Kirou Pira" Unit consists of the following litho-stratigraphic units, from base to top (Fig. 1): a) calc- and micaschists (equivalent to "Vari Sshists" of Lepsius, 1893), b) an intermediate horizon of grey to black, thin-bedded impure dolomitic marble and c) an upper thick

horizon of white massive dolomitic marble (equivalent to "Pirnari Dolomite" of Lepsius). The latter unit crops out at central Hymittos (including the study area of Sesi) (Fig. 2).

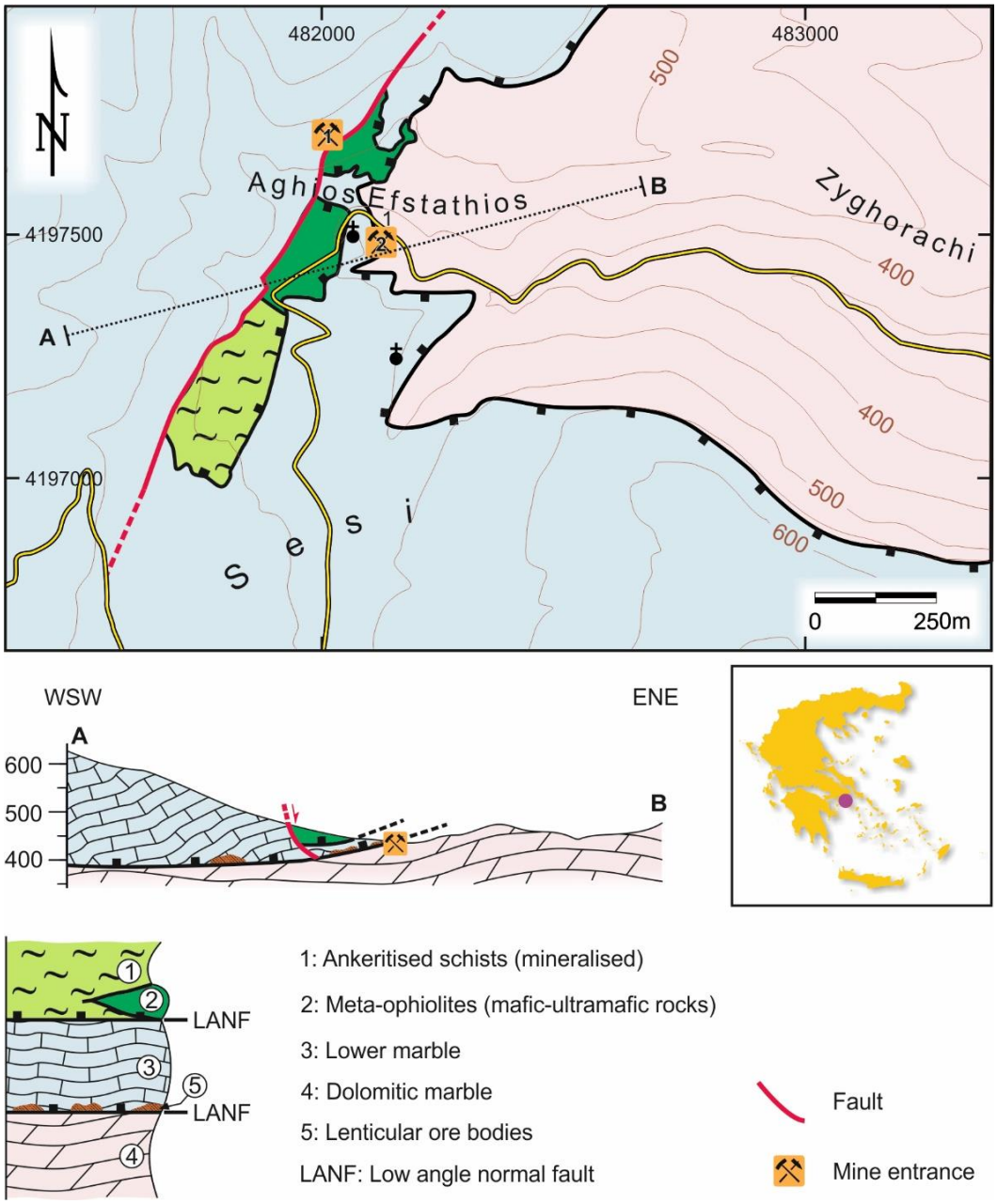

Figure 2 - Detailed geological map of Sesi area, Koropi, central Hymittos. Location of mine caves close to the tectonic contact of Lower Marble with the underlying dolomites, are shown with numbers (1, 2) and cross section A-B is also shown.

The overlying "Hymittos" Unit, consists of the following tectonostratigraphic succession, from base to top: a) white, light blue or grey, massive to thick-bedded marble (equivalent to the "Lower Marble" of Lepsius), outcropping at central and northern Hymittos Mt. (including the study area of Sesi), b) a continuous sequence of various types of schists (mica-, calc-, epidote-chlorite and actinolite schists) alternating with quartzites, cipolines and thin marble horizons (equivalent to

"Kessariani Schists" of Lepsius) including also blocks of meta-basic rocks and serpentinites and c) dark blue or grey marbles and impure marbles including a lot of intercalations of calc- and mica-schists. This formation outcrops at the northernmost of Hymittos Mt.

The upper "Lavrio-Athens" Unit is a very heterogeneous formation including mainly schists or phyllites, as the predominant lithology, alternating with quartzites, dark coloured marbles, impure marbles and marbles with silex, dark thin-layered marbles, crystalline limestones and variable size blocks of metabasic rocks and serpentinites, giving the "chaotic" image of a tectonic melange. This unit mainly located around the flanks of Hymittos Mt., although relics of schists, serpentinites and metabasic rocks found along the central axis of the mountain, as in the study area of Sesi (Fig. 2).

According to the same authors the above mentioned tectonic units are separated by brittle low-angle normal faults (or brittle detachment zones) and the overall tectonic macrostructure of Hymittos Mt. corresponds to a km-scale very gentle anticlinical macro-fold or dome (with a N-S main axis), where the core of this dome consists of the lower "Vari-Kirou Pira" tectonic unit (Fig. 1). The most impressive low-angle fault is the lower one, where the sharp and geometric contact between the "Lower Marble" of "Hymittos" Unit (hanging wall) and the dolomitic marbles and impure marbles of "Vari-Kirou Pira" Unit (foot-wall) outcropped in many places, along the E-W gorges and small valleys that cross the mountain, mainly at the central part (e.g. the study area of Sesi), or more to the south (e.g. Ano Glifada-Terpsithea). The other (upper) low-angle normal fault brings together the various lithologies of "Lavrio-Athens" Unit (hanging wall) with the "Lower Marble" or "Kessariani Schists" of "Hymittos" Unit (foot-wall), outcropping mainly along the western or eastern flanks of Hymittos Mt. Younger high-angle normal faults cut this upper low-angle fault and root in the lower detachment zone, producing tilting of the hanging wall fault-blocks and reducing the total structural thickness of "Lower Marble". A result of this is to bring in contact the lithologies of the "Lavrion-Athens" Unit (including the meta-ophiolitc blocks) with the lower detachment zone and the dolomitic marble, as in the case of Sesi area (Fig. 2).

The cataclastic rocks of this lower detachment forming up a brittle zone of few meters thick (3-5 m) (Fig. 3). It is characterised by reddish tectonic breccias, including marble and rarely dolomitic clasts and producing cargneule formation which mark the marble (hanging wall) and the dolomitic marble (foot wall) adjacent to the contact. It is within this tectonic zone that small iron-hydroxide deposits have been identified in the area of Sesi (south Hymittos) and described herein for the first time (Fig. 4). Recent exploration and small scale mining activity in the study area is evidenced by three small galleries, bearing traces of excavation and drilling with modern instrumentation.

3. Iron-oxide mineralization

The mineralization in the study area occurs mostly along foliation plains within a brecciated zone of the carbonate host rocks, of variable thickness (1m up to 3m) (Fig. 3). Iron-oxide mineralization consists mainly of goethite.

Hematite has a subordinate and relic occurrence within the goethite matrix. Goethite forms porous hard crusts within the carbonate host rock. In the study area of Sesi, massive hematite/goethite mineralization forms lenses of up to 0.5m thick. The goethite (initially hematite) itself, is brecciated and surrounded by a matrix of fine-grained goethite (Fig. 3, 4).

Gangue minerals are mostly calcite (Table 1) and minor aluminosilicates. Traces of barite and base metal sulfides, sphalerite, galena (sample M-2), and chalcopyrite (sample CS15-M1-B) were identified only by Scanning Electron Microscopy analysis, as very fine grains within voids of massive goethite samples (see section below).

Figure 3 - Field photos from the Sesi area (S. Hymittos), showing: (A) the low-angle normal fault (brittle detachment, in red-dashed line) separating the "Lower Marble" (hanging wall) and the dolomitic marble (foot-wall). (B) Fe-ore (hematite) occurrence in the small mining excavations along the detachment zone. (C) Surface outcrop of Fe-ore encrustations within the carbonate host rock (locality 1 of map Fig. 2). (D) Detail of Figure B (center-left) showing brecciated zone of the carbonate host, fragments of Fe-ore (dark brown-black) and matrix filled with goethite.

The carbonate host rock (pure and dolomitic marble) is strongly altered due to fluid-rock interaction along the detachment zone as evidenced by the highly porous and a brown coloration. The host rocks are extensively impregnated by limonite which causes a ubiquitous yellow-brown hue. Goethite from the study area has been examined in terms of its morphology and microstructure in relation to chemical composition. Scanning electron microscopy study indicated several goethite morphotypes.

4. Materials and Methods

2.1. Sampling

Sampling of Fe-ore from breccias as well as, of the marble host rocks was carried out. Representative samples were collected from three exploratory cavities in the Sesi area. Sampling locations are shown in the detailed map of Figure 2.

2.2. Analytical methods

The mineralogy of the oxidized Fe-ore was studied by conventional X-ray diffraction (XRD) techniques on bulk samples and Scanning Electron Microscopy (SEM) on thin sections. XRD analyses were carried out at the University of Athens (Geology Dept.), using a Siemens D-5005 diffractometer with Cu K _ radiation.

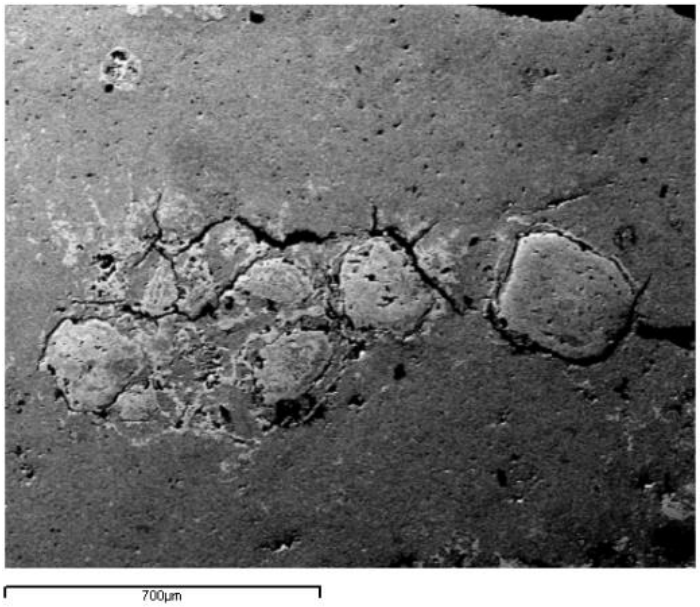

Figure 4 - Electron micro-photographs of brecciated iron oxides: fragments of goethite (with relic hematite, in light grey color) in a very fine grained matrix of goethite [sample M-2(9)].

SEM analyses and electron micro-photographs were conducted using a JEOL JSM-5600 scanning electron microscope (SEM) in energy-dispersive mode (EDS) in order to obtain semi-quantitative analysis [Institute of Geological and Metallurgical Exploration - Athens, (IGME)]; running acceleration voltage at 15 kV. The study utilized semi- quantitative analysis using appropriate standards.

3. Results

XRD analysis of the ore samples revealed (Fig.5) that the major iron bearing mineral is goethite followed by hematite. The other gangue minerals identified are calcite ($CaCO_3$). Traces of Barite ($BaSO_4$) and aluminosilicates were identified only by SEM analysis.

3.1. Characteristics of goethite

Goethite samples were examined by scanning electron microscopy (SEM) and analyses were obtained on a semi-quantitative basis. Different types of goethite morphology have been distinguished in the Sesi Fe-ore formation. These are botryoidal, spheroidal and massive (Fig. 6). Some microanalytical differences among these morphologies were observed on the basis of Fe content of goethite (see Table 1).

3.2. Microstructures

The microstructures of goethite can be broadly categorized mostly as open space filling type (Fig. 6). Open space filling textures (Fig. 6) indicate shallow depths of formation, where brittle rocks deform by fracturing. Fe-enriched fluids circulate freely within fractures and precipitate along with gangue constituents during sudden changes in pressure/temperature.

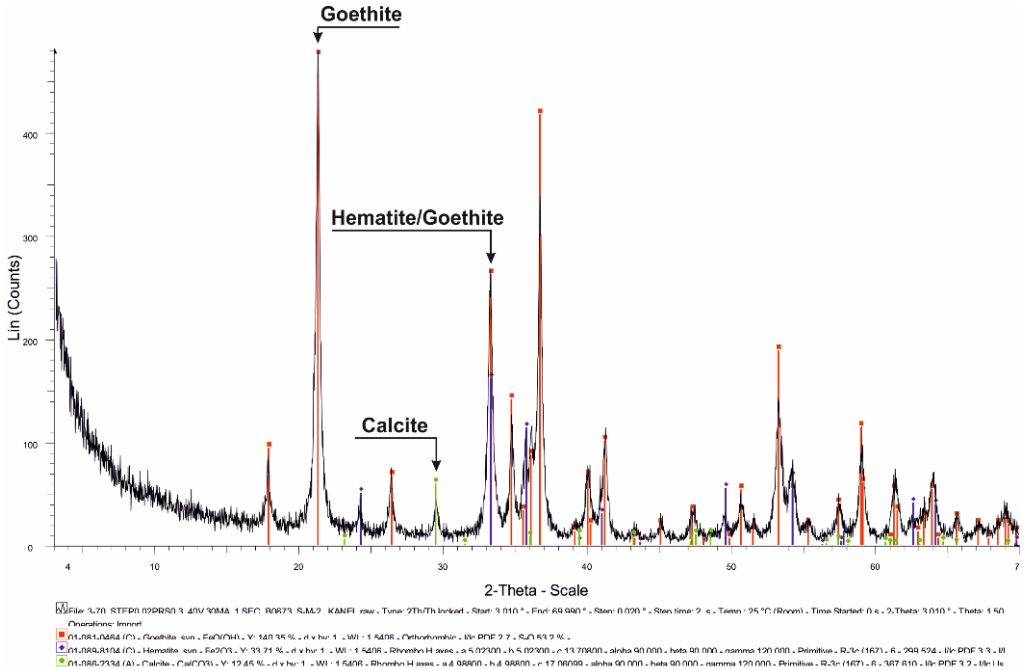

Figure 5 - Evaluated XRD pattern of representative Fe-ore samples from the Sesi area (S. Hymittos). The major peaks of the main mineral phases are underlined and shown in order of abundance: goethite, hematite calcite.

The most typical form of this type is the colloform texture which occurs as rhythmic concentric thin layers of goethite in different shades (Fig. 6C). Different grey colored layers in the SEM images (photomicrographs, Fig. 6) are due to slight difference in iron content (Table 1). Moreover, thin encrustations of goethite lining a cavity and small beads of goethite are common types of open space fillings in the Sesi iron-ore formation.

Evidence for replacement type textures is not common. In most cases, hematite grains appear cracked, weathered and almost completely replaced by goethite, where only an outline of the original Fe-oxide is seen. Replacement is more common at high temperature, where open spaces are very limited. The fact that there is scant evidence for remaining replacement texture indicates for the low temperature of formation of the Sesi iron-ore.

3.3. Compositional variations between various types

The different morphology of goethite in terms of Fe (wt.%), as obtained using SEM microanalysis, are given in Table 1. Results show relative compositional variation between these types.

The botryoidal and reniform morphotypes of goethite are the more iron rich types (av. Fe is 75 wt.%). The colloform type and the massive porous type (limonite) are the less enriched in Fe content. Other elements, commonly adsorbed in goethite mineral, such as Al, Si, P and Mn were not detected in goethite samples by SEM analysis.

4. Discussion

Evidence for ferruginous alteration along the detachment zone between the "Lower Marble" (of "Hymittos" Unit) and the underlying dolomitic marbles (of "Vari-Kirou Pira" Unit) is widespread along the entire contact from the central Hymittos Mt. to Ano Glyfada (Lekkas and Lozios, 2000) and further south to Panion hill (Bassi et al., 2004), indicating that this characteristic zone is not local but has a regional development. However, associated small Fe-oxide deposits along this zone

are described, for the first time in the Sesi area. This observation came into light after detailed mapping. According to microscopic observations, the iron-ore development in the area of Sesi exhibit open space filling textures and extensive fracturing of the primary Fe-oxide mineralization (Fig. 6). Such textures indicate shallow depths of formation, where brittle rocks deform by fracturing. Fe-enriched fluids circulate freely within fractures and precipitate along with gangue constituents during sudden changes in pressure/temperature.

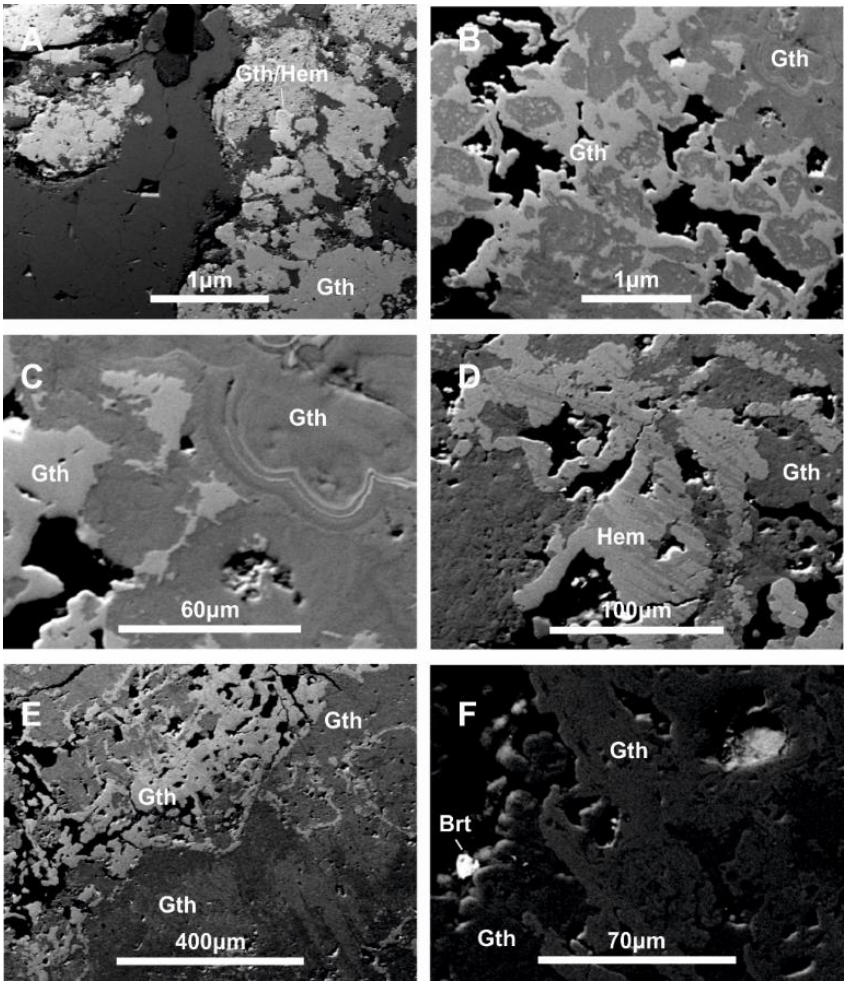

Figure 6 - Electron photo micropgraphs showing different microstructures of goethite developed as open space filling. (A) Amorphous Goethite (Gth) occupying the pore spaces of the carbonate host rock. Relic hematite (noted as Gth/Hem) occurs as lighter colored areas [sample CS15-M1-A(1)]. (B) Goethite (Gth) filling open space of the carbonate host. Lighter grey edges of goethite mass are richer in iron content than dark grey matrix [CS15-M1-A(4)]. (C) Alternate colloform layers of goethite forming thin laminations. Different grey colored layers are due to slight difference in iron content (see text for detail). The layers have different thickness and reflectivity [CS15-M1-A (5)]. (D) Botryoidal form (center) of hematite (Hem) and smaller beads (bottom) of goethite in a matrix of goethite (Gth) [CS15-M2(5)]. (E) Goethite forming in two generations, a dark grey matrix (Fe-poor) and light grey goethite filling the porous area (Fe-rich) [M-2 (6)]. (F) Porous goethite matrix and barite crystal (Brt) forming in the void [M-2 (15)]. Thin encrustation of goethite (Gth). Abbreviations from Whitney and Evans (2010).

Table 1 - Elementary goethite compositional variation from the Sesi iron-oxide deposit and associated minerals through SEM - EDS semi-quantitative analyses (wt%).

	Sample no.	Fe (wt %)	O (wt %)	Subtotal (Fe_2O_3 wt.%)	Morphology
Goethite/Hematite					
1	M-2 (3)-2	74.16	21.24	95.40	*Light colored diffuse areas (Hem)*
2	M-2 (5)-1	77.90	22.32	100.21	*Botryoidal (Gth/Hem)*
3	M-2 (2)-3	71.70	20.54	92.24	*Light colored patches in goethite*
4	M2 (16)-2	75.95	21.76	97.71	*lining cavities*
5	CS-15-M1A (3)	71.50	20.50	92.00	*Light colored patches (reniform)*
6	CS-15-M1A (1)	70.94	20.32	91.26	*Light colored patches*
7	CS-15-M1A (5)-1	71.32	20.43	91.76	*Light colored patches*
8	CS-15-M1A (7)-1	70.46	20.18	90.64	*Light colored patches*
9	CS-15-M1A (7)-3	67.80	19.42	87.22	*Light colored patches*
10	CS-15-M1A (7)-4	66.20	19.14	85.96	*Light colored patches*
11	CS-15-M1A (8)-4	69.56	19.93	89.49	*Light colored edge of encrustation*
12	CS-15-M1-B (3)-1	67.97	19.47	87.45	*Light colored areas within goethite*
Goethite Colloform layers					
13	CS-15-M1A (2)	62.31	18.55	80.86	*Layer*
14	CS-15-M1A (2)	68.86	19.73	88.58	*Layer*
15	CS15-M1A (10)-4	62.29	17.85	80.14	*Massive grey matrix (Goethite)*
16	CS15-M1A (9)-3	61.59	17.64	79.23	*Massive grey matrix*
17	CS15-M1A (7)-5	62.14	17.18	79.94	*Massive grey matrix*
Goethite/Limonite matrix					
18	CS15-M1A (7)-6	59.33	17.00	76.32	*Porous matrix of carbonate host (Limonite)*
19	CS15-M1A(7)-7	50.31	15.84	66.15	*Porous matrix of carbonate host (Limonite)*
20	CS15-M1A (7)-2	59.74	17.14	76.86	*Porous matrix of carbonate host (Limonite)*
21	CS15-M1B (4)	59.01	17.01	76.02	*Porous matrix (Limonite) of Fe-ore*
22	CS15-M1B(10)-2	57.59	16.5	74.08	*Grey porous matrix of Fe-ore*
Other minerals					
		Ba (wt%)	**S (wt%)**	**O (wt%)**	**Total**
1	M-2 (8)-1	58.34	15.050	30.03	103.4	*Barite grain in void*
2	M-2 (15)-1	57.00	16.00	31.08	104.8	*Barite grain in void*

The ore mineralogy (hematite), the prominent structural control and the distinctive suite of minor elements e.g. Zn, Pb, Cu, Co, Ag (preliminary data) classify this deposit into the category of Iron-Oxide Copper Gold hydrothermal deposits (IOCG) (Barton and Johnson, 2004). Similar type mineralization of Fe-oxide ore with barite along detachment zones have been recorded in almost all western Cyclades (Kea, Kythnos, Serifos) by Graseman *et al*. (2012). Rice *et al*. (2012) reported for the Kea detachment related mineralization that fluid infiltration processes particularly affected the porous parts of the detachment zone, where many of the cataclastic carbonate rocks have been strongly ankeritised. In the latter case deposition of Fe-Mn-Pb-Au ores occur along brittle/ductile to brittle high-angle faults (Rice *et al*., 2012) and have been correlated to unexposed magmatic activity, as in the Lavrion mining district of Attica (Skarpelis, 2007; Skarpelis *et al*., 2008; Voudouris *et al*., 2008a,b and Bonsall *et al*. 2011).

The underground occurrence of the Fe-ore deposits within the carbonate host rocks indicate that similar type deposits may be hidden all along the detachment zone in south Hymittos Mt. Hence systematic and thorough investigation should be carried in the future.

In the Attic Cycladic Massif evidence for fluid infiltration of hot Fe-rich fluids during and after greenschist facies metamorphism (M2) has been documented in different Cycladic islands, strongly affecting the country rock (e.g Kea: Rice *et al*., 2012; Serifos: Grasemann *et al.*, 2012; Mykonos: Menant *et al*. 2013). In the case of Kea (e.g. Aghios Theodhoros), Rice *et al*. (2012) reported that iron deposits (hematite mineralization) were large enough to be mined on a very small-scale and are also associated with barite deposits.

In the case of Sesi the restricted occurrence of iron-oxide deposits (south Hymittos) and the scant occurrence of barite and base metal sulfide mineralization do not allow correlations to the Lavrion-type mineralization. The meta-ophiolitic rocks which immediately overly the marble formation ("Lower Marble") and bear widespread Fe-mieneralization, could be a potential local source for the iron mineralization. However, this suggestion remains speculative and further research should be carried out in order to make regional scale correlations of the detachment related mineralization of southern Attica.

5. Conclusion

Field evidence and mineralogical study of the small Fe-oxide deposits of the Sesi, Koropi, S. Hymittos, revealed that mineralization is structurally controlled and developed along a brittle detachment zone (low-angle normal fault). The mineralogical study showed that the mineralization consists mainly of goethite, with subordinate hematite. Several types of microstructures of goethite formation are recognized. These are broadly grouped as open space cavity-filled types: Botryodal, cavity-line and reniform.

The source of iron and the conditions of ore formation remains speculative and needs further investigation. The observations substantiate replacement of hematite by goethite due to oxidation-hydration processes at shallow crustal levels and secondary substantial open space filling within fractured and porous carbonate host.

Fluid interaction of the iron-enriched fluid with the carbonate rocks along the detachment zone and brecciation of goethite itself, indicates a structural control on the ferrigenous alteration and iron-ore formation. The ferruginous alteration of the carbonate rocks along the detachment zone is evidenced by their transformation to porous ankeritic carbonates and an extensive limonite impregnation.

6. Acknowledgments

We would like to thank Dr G. Oikonomou from IGME for his collaboration with SEM facility. The authors would also like to thank Dr. Sofia Pasa (IGME) for her assistance with microphotographs.

7. References

Bassi, E.K., Soukis, K. and Lekkas, S., 2014. The presence of Vari - Kirou Pira Unit at Panion Hill (SE Attica, Greece), *Bulletin of the Geological Society of Greece 34, Proc. of the X International Congress*, Thessaloniki, Greece, 1608-1617.

Bakopoulou, A., 2004. Kinematic and dynamic analysis of the tectonic contacts of Mt. Hymittos. Dissertation thesis, National and Capodistrian University of Athens, 188 pp.

Berger, A., Schneider, D., Grasemann, B. and Stockli, D., 2012. Footwall mineralization during Late Miocene extension along the West Cycladic Detachment System, Lavrion, Greece, *Terra Nova*, 25(3), 181-191, doi: 10.1111/ter.12016.

Bonsall, T.A., Spry, P.G., Voudouris, P., Seymour, K.St., Tombros, S. and Melfos, V., 2011. The Geochemistry of Carbonate-Replacement Pb-Zn-Ag Mineralization in the Lavrion District,

Attica, Greece: Fluid Inclusion, Stable Isotope, and Rare Earth Element Studies, *Econ. Geology*, 106, 619-651.
Deer, W.A., Howie, R.A. and Zussman, J., 1966. Rock-forming minerals, non-silicates, 532–672.
Grasemann, B., Schneider, D.A., Stockli, D.F. and Iglseder, C., 2012. Miocene bivergent crustal extension in the Aegean: evidence from the western Cyclades (Greece), *Lithosphere*, 4, 23-39.
Katsikatsos, G., 1977. La structure tectonique d' Attique et de l' ile d' Eubee, *Proceedings of VIth Coll. on the Geol. of the Aegean Reg.*, Athens 1977, (I.G.M.E. Publ.), V/1, 211-228.
Katsikatsos, G., 1990. Geology of Greece, Athens, 451 pp. (in Greek).
Lekkas, S. and Lozios, S., 2000. Tectonic structure of Mt. Hymittos (Attica-Greece), *Annales Géologiques des pays Helléniques*, 38, 47-62.
Lepsius, R., 1893. Geologie von Attica. Ein Beitrag zur Lehre von Metamorphismus der Gesteine, *Berlin Zeitschr. F. parkt. Geol*., 4, 196-592.
Marinos, G. and Petrascheck, W., 1956. Laurium. I.G.M.E. *Geol. Geoph. Res.*, V/1, 247 pp.
Menant, A., Jolivet, L., Augier, R. and Skarpelis, N., 2013. The North Cycladic Detachment System and associated mineralization, Mykonos, Greece: Insights on the evolution of the Aegean domain, *Tectonics*, 32, 433-452, doi: 10.1002/tect.20037.
Papanikolaou, D., 1986. *Geology of Greece*, Eptalofos publications 240 pp. (In Greek).
Rice, A.H.N., Iglseder, C., Grasemann, B., Zamolyi, A., Nikolakopoulos, K.G., Mitropoulos, D., Voit, K., Muller, M., Draganits, E., Rockenschaub, M. and Tsombos, P.A., 2012. A new geological map of the crustal-scale detachment on Kea (western Cyclades, Greece), *Austrian Journal of Earth Sciences*, 105, 108-124.
Skarpelis, N., 2007. The Lavrion deposit (SE Attica, Greece): geology, mineralogy and minor elements chemistry, *Neues Jahrbuch für Mineralogie Abhandlung*, 183, 22-249.
Skarpelis, N., Tsikouras, B. and Pe-Piper, G., 2008. The Miocene igneous rocks in the basal unit of Lavrion (SE Attica, Greece): petrology and geodynamic implications, *Geological Magazine*, 145, 1-15.
Seidel, M., Pack, A., Share, Z. and Seidel, E., 2005. The Kakopetros and Ravdoucha iron-oxide deposits, western Crete, Greece: fluid transport and mineralization within a detachment zone, *Economic Geology*, 100, 165-174.
Voudouris, P., Melfos, V., Spry, P.G., Bonsall, T., Tarkian, M. and Economou-Eliopoulos, M., 2008. Minealogy and fluid inclusion constraints on the evolution of the Plaka intrusion-related ore system, Lavrion, Greece, *Mineralogy and Petrology*, 93, 79-110.
Voudouris, P., Melfos, V., Spry, P.G., Bonsall, T.A., Tarkian, M. and Solomos, Ch., 2008. Carbonate replacement Pb-Zn-Ag±Au mineralization in the Kamariza area, Lavrion, Greece: Mineralogy and thermochemical conditions of formation, *Mineralogy and Petrology*, 94, 85-106.
Whitney, D.L. and Evans, B.W., 2010. Abbreviations for names of rock-forming minerals, *American Mineralogist*, 95, 185-187, doi: 10.2138/am.2010.3371 185.

Δελτίο της Ελληνικής Γεωλογικής Εταιρίας, τόμος L, σελ. 2037-2046
Πρακτικά 14ου Διεθνούς Συνεδρίου, Θεσσαλονίκη, Μάιος 2016

Bulletin of the Geological Society of Greece, vol. L, p. 2037-2046
Proceedings of the 14th International Congress, Thessaloniki, May 2016

GOLD METALLOGENY OF THE SERBOMACEDONIAN-RHODOPE METALLOGENIC BELT (SRMB)

Tsirambides A.[1] and Filippidis A.[1]

[1]Aristotle University of Thessaloniki, Faculty of Sciences, School of Geology, Department of Mineralogy-Petrology-Economic Geology, 54124 Thessaloniki, Greece, ananias@geo.auth.gr, anestis@geo.auth.gr

Abstract

The Alpine-Balkan-Carpathian-Dinaride (ABCD) metallogenic belt, which tectonically evolved during Late Cretaceous to the present, is Europe's premier metallogenic province, especially for gold. Three spatially distinct tectonic and metallogenic belts are associated with this belt. One of them is the Serbomacedonian-Rhodope Metallogenic Belt (SRMB) which intersects with a NNW-SSE trend the south eastern Balkan countries. This belt includes the geotectonic zones of Vardar (Axios), Circum-Rhodope, and the Serbomacedonian and Rhodope Massives. It comprises dominantly carbonate replacement or porphyry metal deposits, stratiform volcano-sedimentary deposits, skarns and various isolated magmatic-hydrothermal deposits. The most significant Au metallogeny centers of this belt are found in Bulgaria (i.e., Madjarovo, Ada Tepe, Madan, Lozen), Greece (i.e., Perama Hill, Sapes, Maronia, Olympias-Stratoni-Skouries, Gerakario-Vathi-Pontokerasia), F.Y.R.O.M. (i.e., Buchim, Ilovitza, Alshar), Kosovo (i.e., Trepca), and Serbia (i.e., Lece District: Kiseljak, Bakrenjaca). The metal reserves of all categories in the SRMB are 24 t Au, 14 t Ag and >100 Mt (Pb+Zn) ore in Bulgaria, 743 t Au, 4100 t Ag, 5345 th.t Cu and 3125 th.t (Pb+Zn) in Greece, 106 t Au, 96 t Ag and 834 th.t Cu in F.Y.R.O.M., >150 Mt (Pb+Zn) ore in Kosovo, 118 t Au and 1270 th.t Cu in Serbia. In addition many other sites inside this belt exist which are very promising for precious metals.
Keywords: *Precious metals, metal concentrations, reserves.*

Περίληψη

Η μεταλλογενετική ζώνη Alpine-Balkan-Carpathian-Dinaride (ABCD), η οποία τεκτονικά εξελίχθηκε κατά τη διάρκεια του τέλους του Κρητιδικού έως σήμερα, είναι η κύρια μεταλλογενετική επαρχία της Ευρώπης, ιδιαίτερα για το χρυσό. Τρεις χωρικά διακριτές τεκτονικές και μεταλλογενετικές ζώνες συσχετίζονται με αυτή τη ζώνη. Μία από αυτές είναι η Σερβομακεδονική-Ροδοπική Μεταλλογενετική Ζώνη (SRMB), η οποία διατέμνει με κατεύθυνση ΒΒΔ-ΝΝΑ τις νοτιοανατολικές Βαλκανικές χώρες. Αυτή η ζώνη περιλαμβάνει τις γεωτεκτονικές ζώνες του Βαρδάρη (Αξιού), της Περιροδοπικής, και τις Μάζες της Σερβομακεδονικής και Ροδοπικής. Περιλαμβάνει κυρίως κοιτάσματα μετάλλων αντικατάστασης ανθρακικών ή πορφυρικά, στρωματόμορφα ηφαίστειο-ιζηματογενή κοιτάσματα, skarns και ποικίλα απομονωμένα μαγματικά-υδροθερμικά κοιτάσματα. Τα πιο σημαντικά κέντρα μεταλλογένεσης χρυσού αυτής της ζώνης βρίσκονται στη Βουλγαρία (π.χ. Madjarovo, Ada Tepe, Madan, Lozen), Ελλάδα (π.χ. Λόφος Περάματος, Σάπες, Μαρώνεια, Ολυμπιάδα-Στρατώνι-Σκουριές, Γερακαριό-Βάθη-Ποντοκερασιά), Π.Γ.Δ.Μ. (π.χ. Buchim, Ilovitza, Alshar), Κόσοβο (π.χ. Trepca) και Σερβία (π.χ. Lece District: Kiseljak, Bakrenjaca). Τα

αποθέματα μετάλλων όλων των κατηγοριών στη SRMB είναι 24 t Au, 14 t Ag και >100 Mt κοιτάσματος (Pb+Zn) στη Βουλγαρία, 743 t Au, 4100 t Ag, 5345 th.t Cu και 3125 th.t (Pb+Zn) στην Ελλάδα, 106 t Au, 96 t Ag και 834 th.t Cu στην Π.Γ.Δ.Μ., >150 Mt κοιτάσματος (Pb+Zn) στο Κόσοβο, 118 t Au και 1270 th.t Cu στη Σερβία. Επιπλέον μέσα σ' αυτή τη ζώνη υπάρχουν πολλές άλλες περιοχές οι οποίες είναι πολύ ελπιδοφόρες για πολύτιμα μέταλλα.
Λέξεις κλειδιά: *Πολύτιμα μέταλλα, συγκεντρώσεις μετάλλων, αποθέματα.*

1. Introduction

The Alpine-Balkan-Carpathian-Dinaride (ABCD) metallogenic and geodynamic belt is considered Europe's premier Pb-Zn-Cu (-Mo-Sb-Ag-Au) province, especially for gold-rich deposits. This orogenic system is the result of convergence of the African, Arabian and Indian plates and their collision with Eurasia. This belt tectonically evolved from Late Cretaceous to the present. The segmented geodynamic character of the orogen is reflected in a discontinuous distribution of ore deposits. Three spatially and temporally distinct tectonic and metallogenic belts are associated with the ABCD belt (Heinrich and Neubauer, 2002). One of them is the Serbomacedonian-Rhodope Metallogenic Belt (SRMB), which intersects with a NNW-SSE trend south western Serbia, Kosovo, F.Y.R.O.M., north eastern Greece and south Bulgaria. This arcuate belt is about 500 km long and 130-180 km wide and includes the geotectonic zones of Vardar (Axios), Circum-Rhodope, and the Serbomacedonian and Rhodope Massives (Fig. 1).

The SRMB comprises dominantly carbonate-replacement Pb-Zn-Ag-Au deposits, several porphyry Cu-Mo-Au deposits, stratiform volcano-sedimentary deposits, skarns, and various isolated magmatic-hydrothermal deposits. All are genetically related to Oligocene-Miocene post-subduction magmatism (Kalogeropoulos *et al*., 1989; Frei, 1995; Mitchell, 1996; Kroll *et al.*, 2002; Serafimovski *et al*., 2010). Several other types of gold mineralization (e.g., intrusion-related systems, epithermal, Carlin-type), are, in general, genetically related to arc- magmatic rocks, and, in part, are controlled by exhumation structures in this belt (Melfos *et al.*, 2002; Marchev *et al.*, 2005; Eliopoulos and Kilias, 2011; Fornadel *et al.*, 2011).

The gold metallogeny of the Serbomacedonian-Rhodope Metallogenic Belt (SRMB) is the focus of this paper.

2. Bulgaria

The Madjarovo ore district is located within the Madjarovo volcanic center of the eastern Rhodope Massif (Fig. 1). This district is characterized by abundant low-sulphidation epithermal base and precious metal (Pb-Zn-Cu-Ag-Au) deposits and sub-economic porphyry Cu-Mo deposits. Advanced argillic, sericitic, silicic and propylitic alterations were recognized in the area. In the last 55 years of mining, more than 10 Mt of (Pb+Zn) ore have been extracted, while another 6.5 Mt of (Pb+Zn) ore reserves remain unexploited. Although the probable reserves are about 2 Mt grading at 3.9 g/t Au, a feasibility study completed in 1995 by Euraust Mineral Developments indicated that the ore is economically not viable for gold (Harkovska *et al.*, 1989; Marchev *et al.*, 2005). Most of the gold occurs as small crystal inclusions with sizes up to 100 μm and is associated with pyrite, galena and sphalerite (Melfos *et al.*, 2003).

The Ada Tepe gold deposit is located approximately 3 km south of Krumovgrad and 15 km east of Zvezdel in the Kardjali District (Fig. 1). The region belongs to the Kessebir metamorphic complex of the eastern Rhodope Massif. Its basement consists of Precambrian and Paleozoic rocks such as metasediments, gneisses, and amphibolites. These rocks are unconformably overlain by Tertiary conglomerates, sandstones, siltstones and limestones. The Sharovo Formation, which primarily hosts the Au-Ag mineralization, consists of a large accumulation of breccias and sands. The Pb-Zn (Au-Ag) epithermal vein deposits are related to the volcanic activity of the Upper Eocene to Upper

Oligocene, which affected all the south-eastern Bulgaria and north-eastern Greece. Ada Tepe is a t ypical sedimentary-hosted low-sulfidation epithermal mineralization associated mainly with detach ment faults (Márton *et al.*, 2010). Its proven / probable reserves are 7.2 Mt (Au+Ag) of ore with 3.4 g/t Au (~24 t Au) and 1.9 g/t Ag (~14 t Ag) (Balkan Mineral and Mining EAD 2012).

The Madan district (Fig. 1) comprises the largest and richest Pb-Zn ore accumulation in the Rhodopes. During the second half of 20th century the extensive underground mining in more than 50 deposits in this area led to a production of more than 100 Mt of ores with mean content of 2.5% Pb and 2.1% Zn. Another 95 Mt of (Pb+Zn) ores have been left unexploited. Additional minor components are 300-1200 ppm Ag and 130-1410 ppm Sb (Table 1). Due to the economic crisis after 1990 most of the deposits were ranked unprofitable and many of the underground mines were closed. Considerable ore reserves are still available and some mines have a potential for development (Marchev *et al.*, 2005; Bonev, 2007; Vassileva *et al.*, 2009).

In the Lozen (Fig. 1) low-sulphidation epithermal Pb-Zn-Cu ore veins and lenses are hosted by Ca-alkaline volcanic complex. Adularia-sericite host rock alterations are dominant, while chlorite is more abundant close to the contacts of the ore bodies. The mode of gold occurrence is similar to the adjacent Madjarovo epithermal mineralization. The gold is associated with pyrite, galena and sphalerite and its grain sizes vary from 10 μm to 100 μm (Melfos *et al.*, 2003).

3. Greece

Greece presents a large number of occurrences and ores of Pb, Zn, and Cu, which are often accompanied by Mo, Sb, Ag and Au. Occurrences of placer gold exist in many regions of Macedonia and Thrace (northern Greece), such as in Langadas and along the riverbeds of Strymon and Gallikos. The deposits of Gallikos River (Thessaloniki-Kilkis area, Fig. 1) were the only Au-bearing deposits of Greece exploited in modern times. During the period of 1953-1960, 1355 kg of gold were collected. Placer gold and minerals of the platinum group (alloys of Os-Ir-Ru, Os-Ir-Rh, Os-Ir-Pt, and Pt-Fe) were also found in Servia Kozani and along the riverbeds of Aliakmonas and Axios and their tributaries. The most important and economically significant ores of gold are located in the regions of Thrace and Macedonia (Kalogeropoulos *et al*., 1989; Michael, 2004; Shawh and Constantinides, 2001; Charistos, 2010; Voudouris *et al*., 2011; Tsirambides and Filippidis, 2012).

The Pagoni Rachi/Kirki Cu-Mo±Re±Au deposit (Fig. 1) is a porphyry-epithermal system that contains molybdenite with up to 4.7 wt% Re. Tellurides and Ag-Au alloy occur in the epithermal veins. The D-type veins contain the highest Au grades (up to 5 g/t) and include Ag-, Bi-, Te-, and Se-bearing minerals. Based on the Au and Re grades, Cu/Mo ratios, and the extremely high Re content in molybdenite, Pagoni Rachi may be considered as a distinct Cu-Mo±Re±Au porphyry deposit derived from rocks transitional between calc-alkalic and alkalic porphyries (Voudouris *et al.*, 2009, 2013a).

In Sapes area (Fig. 1) three high epithermal mineralizations with significant ores have been discovered: the “St. Demetrios”, the “Viper” and the “Scarp” prospects. Tertiary volcanic and pyroclastic rocks of andesitic and rhyodacitic composition are the dominant rock types of the area. The main alterations recognized are silicic, argillic, sericitic, and rarely a zone of adularia. The proven / probable reserves are 1.32 Mt of ore at an average grade of 15.1 g/t Au (~16 t Au), 8.2 g/t Ag (~8 t Ag), and 0.3% Cu (~3000 th.t Cu) (Table 1) (Shawh and Constantinides, 2001; Glory Resources, 2012).

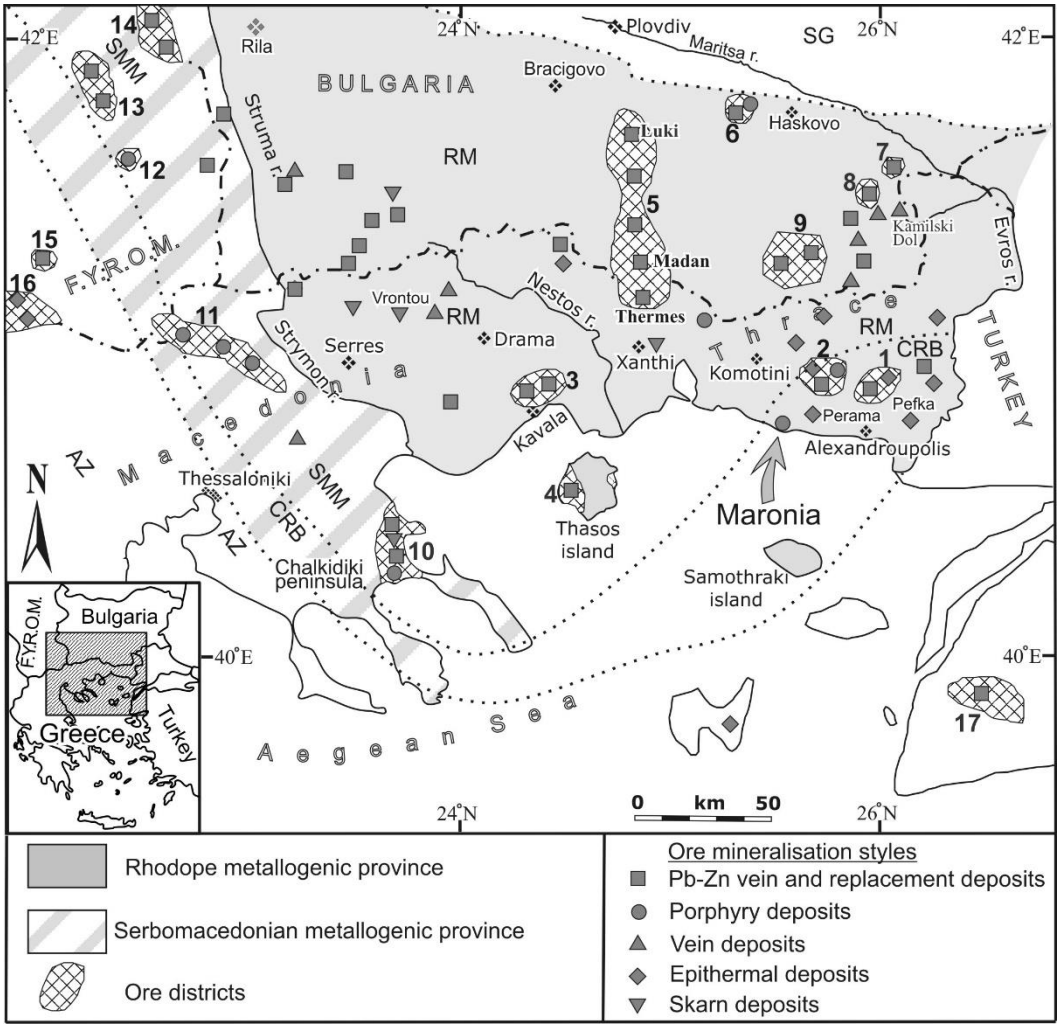

Figure 1 - Geologic sketch map showing the gold metallogeny centers of the Serbomacedonian Rhodope Metallogenic Belt (SRMB). AZ = Axios (Vardar) Zone, CRB = Circum Rhodope Zone, SMM = Serbomacedonian Massif, RM = Rhodope Massif, SG = Srednogorie Zone. 1. Esymi, 2. Kirki-Sapes, 3. Palea Kavala, 4. Thasos, 5. Thermes-Madan-Luki, 6. Spahievo, 7. Lozen, 8. Madjarovo, 9. Zvezdel, 10. Chalkidiki (Olympias-Stratoni-Skouries), 11. Kilkis (Gerakario-Vathi-Pontokerasia), 12. Buchim, 13. Kratovo-Zletovo, 14. Osogovo-Sasa-Toranica, 15. Borov Dol, 16. Aridea-Kozuf, 17. Balikesir (Melfos *et al.*, 2002).

The Perama Hill deposit (Fig. 1) is a high-sulphidation Au-Ag-Te-Se epithermal system hosted in silicic and argillic altered andesitic rocks and in sandstones. The deposit covers an area of approximately 700 m in length to 300 m in width and is oxidized. Sulphides are found at a depth of approximately 120 m. The probable / indicated reserves of this deposit are ~11.7 Mt of ore at an average grade of 3.1-3.5 g/t Au (~74 t Au) and 2.8-4.2 g/t Ag (~62 t Ag) (Table 1). Eighty percent of the gold is hosted by sandstones (oxidized upper part of the deposit) and the rest is associated with base metal sulphides and tellurides hosted within andesitic breccias and conglomerates (Michael, 2004; Voudouris *et al.*, 2011).

The Maronia Cu-Mo deposit (Fig. 1) is located in an area dominated by metamorphic rocks (marbles, calc-schists, and schists) and plutonic to subvolcanic intrusions. The marbles and schists are intruded by an Oligocene pluton of gabbroic to monzonitic composition and younger porphyry microgranite,

which hosts the Cu-Mo mineralization. Surface samples of altered rock contain as much as 7600 ppm Mo, 5460 ppm Cu and 1 ppm Au. Geochemical data from a drill core revealed a 10-m-thick horizon containing up to 12 ppm Au, up to 17 ppm Ag and up to 2.0% Cu. The Maronia deposit presents the potential of containing large quantities of high-grade Cu-Mo porphyry ore, as well as economic grades of Au (Melfos *et al.*, 2002).

Table 1 - Gold metallogeny of the Serbomacedonian-Rhodope Metallogenic Belt (SRMB)[1].

Country	Region/Site	Type	Metals	Metal concentrations	Metal reserves[2]
Bulgaria	Madjarovo	EV	Pb, Zn, Au	3.9 g/t Au	6.5 Mt (Pb+Zn) ore
	Ada Tepe	EV	Au, Ag	3.4 g/t Au, 1.9 g/t Ag	24 t Au, 14 t Ag
	Madan	EV	Pb, Zn, Ag, Sb	2.5% Pb, 2.1% Zn, 300-1200 ppm Ag, 130-1410 ppm Sb	95 Mt (Pb+Zn) ore
Greece	Thrace/ Perama Hill	DED	Au, Ag	3.1-3.5 g/t Au, 3.8-4.2 g/t Ag	74 t Au, 62 t Ag
	Thrace/ Sapes	DED	Cu, Au, Ag	0.3% Cu, 15.1 g/t Au, 8.2 g/t Ag	3000 th.t Cu, 16 t Au, 8 t Ag
	Thrace/ Maronia	CAP	Cu, Mo, Au, Re	2.0% Cu, 0.8% Mo, 12 ppm Au, 17 ppm Ag	
	Macedonia/ Olympias-Stratoni[3]	RBMS	Pb, Zn, Au, Ag	4.4-6.2% Pb, 5.9-8.6% Zn, 8.7-10.0 g/t Au, 132.1-176.7 g/t Ag	3125 th.t (Pb+Zn), 250 t Au, 4030 t Ag
	Macedonia/ Skouries	CAP	Cu, Au	0.49% Cu, 0.67 g/t Au	1205 th.t Cu, 166 t Au
	Macedonia/ Gerakario-Vathi-Pontokerasia	CAP	Cu, Au	0.4% Cu, 0.9 g/t Au	1140 th.t Cu, 237 t Au
F.Y.R.O.M.	Ilovitza	CAP	Cu, Au	0.2% Cu, 0.3 g/t Au	474 th.t Cu, 70 t Au
	Buchim[3]	CAP	Cu, Au, Ag, Mo	0.3% Cu, 0.3 g/t Au, 0.8 g/t Ag	360 th.t Cu 36 t Au, 96 t Ag
	Alshar	Carlin	Au, Sb, As, Tl	2.5% Sb, 1.5% As, >1 g/t Au	
Kosovo	Trepca	RBMS	Pb, Zn, Ag, Au	6% Pb, 4% Zn	>150 Mt (Pb+Zn) ore
Serbia	Kiseljak	CAP	Cu, Au	0.2% Cu, 0.2 g/t Au	1270 th.t Cu[4], 118 t Au[4]
	Bakrenjaca	EV	Cu, Au		

[1]references are presented in the text, [2](proven/probable)+(measured/indicated) reserves,[3]mines in operation, [4]reserves from both sites. EV = Epithermal Vein, DED = Disseminated Epithermal Au-Ag Deposit, CAP = Cu-Au Porphyry, RBMS = Replacement Base Metal Sulphide.

The Palea Kavala is considered an intrusion-related gold system (Fig. 1). Here the Miocene pluton contains ~150 minor hydrothermal and precious-metal occurrences. The presence of the

metallogenic assemblage of Bi–Te–Pb–Sb±Au, as well as of the magnetite and ilmenite, are consistent with this intrusion-related gold system (Fornadel *et al.*, 2011).

The Olympias carbonate-replacement Pb-Zn (-Au-Ag) sulphide ore (Fig. 1) is regionally distributed and structurally controlled. The deposit strikes NNE for 1500 m, dips 30-35º southeast to a depth of at least 300 m, and has an average thickness of 12 m. Both deformed and undeformed ore varieties formed during Tertiary by replacement of base metals from fluids of primarily magmatic derivation through reaction with the host marbles at low pressures (300-800 bars) and relatively high temperatures (300-400ºC) (Kalogeropoulos *et al.*, 1989). Current mining activity in the area produces about 220000 t/y of (Pb+Zn) concentrate. The ore contains 4.4-6.2% Pb, 5.9-8.6% Zn, 8.7-10 g/t Au, and 132.1-176.7 g/t Ag. The probable / indicated reserves of this deposit are 3125 th.t (Pb+Zn), 250 t Au and 4030 t Ag (Table 1) (Tsirambides and Filippidis, 2012).

Skouries is a typical Cu-Au porphyry deposit associated with alkaline magmatism (Fig. 1). The deposit occurs as a pipelike mineralized subvolcanic body with surface dimensions of 180 m north-south and 200 m east-west with a vertical extent of at least 700 m (Frei, 1995). The measured / indicated reserves of this deposit are 246 Mt of ore grading by average at 0.49% Cu (~1205 th.t Cu) and 0.67 g/t Au (~166 t Au) (Table 1) (European Goldfields Ltd 2011). This ore is hosted by at least four hypabyssal monzonite-porphyry phases. All four phases present specific compositions, such as high SiO_2, low MgO and low mg# [mg# = MgO/(FeOt+MgO)×100], as well as variable but low contents of mantle-compatible elements such as V, Ni and Co. Their mg# suggests increasing degrees of fractionation of the parental melts with decreasing age. Their high K_2O (up to 5.8 wt%) and K_2O/Na_2O ratios (>1), as well as their high Ce/Yb and Th/Yb ratios (>34 and >21 respectively), are typical of alkaline rocks of the shoshonite association. In addition the high initial $^{87}Sr/^{86}Sr$ ratios (0.7082) for the Skouries intrusions suggest crustal contamination during emplacement (Kroll *et al.*, 2002).

The Stanos area of the Chalkidiki Peninsula hosts several Cu-Bi-As-Au ore bodies, which are dissimilar to the existing Cu-Au porphyry and carbonate-replacement Pb-Zn-Au-Ag deposits of the same Peninsula, since these ores are syn-deformational and related to major shear zones. The ores are polymetallic featuring a wide mineralogical variety including native bismuth, bismuthinite, cosalite, and emplectite associated with native gold, galena, and chalcopyrite (Voudouris *et al.*, 2013b; Bristol *et al.*, 2015).

The potential for gold metallogeny in other areas extends further to the NW of the Serbomacedonian Zone (in Greece and F.Y.R.O.M.) for more than 250 km, where the Drakontio and Paliomylos (Thessaloniki regional unity), the Laodikino and Koronouda (Kilkis regional unity), and the Ilovitza and Buchim prospects occur (Vavelidis *et al.*, 1994, 1999, 2000; Serafimovski *et al.*, 1996, 2010).

The Cu-Au porphyry deposits of Gerakario-Vathi-Pontokerasia Kilkis may be considered the second most important center for gold in Macedonia Greece. The probable / indicated reserves are about 258 Mt of ore grading up to 0.4% Cu (~1140 th.t Cu) and up to 0.9 g/t Au (~237 t Au) (Kelepertsis *et al*,. 1986; Arvanitidis, 2012; Tsirambides and Filippidis, 2012).

The probable / indicated reserves of gold from Macedonia and Thrace Regions of Greece are approximately 743 t Au and their gross value exceeds €24 b. Sites, deposit types, metal concentrations and metal reserves are presented in Table 1. The first gold production in Greece is expected in 2018.

4. F.Y.R.O.M.

Ilovitza is an isolated Cu-Au porphyry deposit, located in a NW-SE striking Tertiary magmatic arc in the south eastern part of the country. The porphyry deposits are in close spatial and temporal association with intermediate to felsic, medium to high potassium (K) calc-alkaline igneous rocks. The deposit, which was emplaced 29 Ma ago, is located about 20 km west of the 33-38 Ma Osogovo-Besna-Kobila Pb-Zn belt and about 30 km east of the 22-27 Ma Lece-Buchim-Chalkidiki Cu-Au metallogenic zone (Fig. 1). The Ilovitza deposit is about 1.5 km in diameter and is associated with

a poorly exposed dacite-granodiorite plug, emplaced along the NW-SE elongate Strumitza graben. The measured / indicated reserves are 237 Mt of ore with 0.3 g/t Au and 0.2% Cu containing 2.54 moz Au (~70 t Au) and 1.1 b lb Cu (~474 th.t Cu) (Table 1) (Euromax Resources, 2014).

The Buchim Cu porphyry deposit (Fig. 1) is located in the border of the Serbomacedonian Massif and Circum Rhodope Belt. Primary Cu mineralization exists around magmatic cross-cuts. The deposit occupies approximately 150 km^2. It belongs to the Lece-Chalkidiki metallogenic zone (part of the SRMB) which is characterized by widespread Tertiary volcanic rocks of calc-alkaline composition. These rocks are accompanied by Pb, Zn, Cu, Fe, Mo, Au and Ag ore mineralization as it happens in Ilovitza F.Y.R.O.M. and Kilkis (Gerakario-Vathi-Pondokerasia) and Chalkidiki (Olympias-Stratoni-Skouries) Macedonia Greece (Serafimovski *et al.,* 1996, 2010). The Buchim mine is the only one in F.Y.R.O.M. that operates nowadays. Its Cu mineralization covers an area of 0.5 km^2 and is traced to a depth of 300 m. The probable / indicated reserves are 120 Mt of ore with an average grade of 0.3% Cu (~360 th.t Cu), 0.3 g/t Au (~36 t Au) and 0.8 g/t Ag (~96 t Ag) (Table 1). The deposit has been mined since 1979. At present, ore with 0.21% Cu, 0.2 g/t Au, and 0.8 g/t Ag is being mined. Thirty-two thousand tons of concentrate containing 18-21% Cu and 18 g/t Au (Au recovery is 50%) have been produced. The concentrate is delivered by trucks to smelters at Bor in Serbia and Pirdop in Bulgaria (Serafimovski *et al.,* 2010; Palinkaš *et al.,* 2013).

The complex Au-As-Sb-Tl Alshar deposit is unique in its mineral composition. In addition to economic Sb and As grades, the ore is substantially enriched in Tl. Furthermore, Alshar is the first Carlin type gold deposit discovered in the Balkan Peninsula in the late 1980s. The volcanic-plutonic complex of calc-alkaline rocks was emplaced in Pliocene on a basement of Precambrian gneisses, Triassic rocks (dominant), Jurassic ophiolites, and Cretaceous formations. The deposit is located at the intersection of the Vardar (Axios) and Kozuf-Aridea metallogenic zones at the western flank of the Vardar Graben and the Pelagonian crystalline massif approximately 50 km SW of the town of Kavadarsi and 3 km from the Greek-F.Y.R.O.M. border (Fig 1). The ore field covers an area of 21 km^2. It is a significant deposit that contains economic grades of Sb (up to 2.5%), As (1.5%), Tl (0.1-0.5%) and Au (>1 g/t) (Table 1) (Volkov *et al.,* 2006).

5. Kosovo

The Trepca mines are located in northern Kosovo near the village Stari Trg. They are within the Vardar zone of the Trepça mineral belt, consisting of Paleozoic basement rocks, Jurassic-Cretaceous sediments and ophiolites. This tectonic zone, within which the Pb, Zn, Ag and Au deposits are located, is marked by very strong lineaments and a fracture zone striking NW-SE. Trepça has >150 Mt of probable / indicated reserves of ores containing by average 6% Pb and 4% Zn (Table 1). Current primary product is (Pb+Zn) concentrate with significant content of Ag and Au. The company's production capacity is around 100000 t/month; currently production is around 10000 t/month, only a tenth of what it is capable because of lack of new processing technologies (Heinrich and Neubauer, 2002; Hyseni *et al.,* 2012).

Trepca Mines and Minerals is the enterprise that has long played the key role in the Kosovo's economic development. The enterprise dates back to 1927 when Kosovo's mining resources were first exploited by a British firm. In 1948 Trepca became the biggest mining complex in the Balkans. Stari Trg was at the heart of the complex, which produced half of the complex's 3 Mt Pb, 2 Mt Zn, and 4500 t Ag (Feraud *et al.,* 2007). Until 1985 Trepca produced 8.7 t Au and 4000 t Ag. The Ag was mainly recovered from Pb concentrates in which it assayed between 1000 g/t and 1100 g/t (Monthel *et al.,* 2002).

During the 1970s Trepça had assets all around the ex-Yugoslavia. The complex began to have problems by the end of 1970s. Funds were poorly invested, deteriorating equipment was neglected, and little regulation of ore grades was done. Kosovo has never recovered from the 1999 civil war. Trepça itself was hardly damaged. Nowadays the company is in the process of restructuring.

6. Serbia

The Serbomacedonian Metallogenic Province in Serbia appears to have been under-explored for gold, particularly with the availability of modern methods. Most of the Pb-Zn deposits are largely endowed with Ag, associated with galena and Pb sulphosalts.

The Lece District in SW Serbia is without doubt one of the most promising for precious metals. It is centered on a Tertiary volcanic complex, with several nested volcanic cones and calderas. The gold mineralization at Lece, Djavolija Varos, Tulare and Sijarinska Banja is found in veins and silicified breccia of the adularia-sericite type. Between 1953 and 1959 the Lece deposit produced about 470 th.t of ore at 2.0% Pb, 4.5% Zn, 6 g/t Au, and 19 g/t Ag (Jankovic *et al.*, 1992; Serafimovski, 2000).

The Tulare Porphyry Cluster (TPC) area lies within the Lece Volcanic Complex and belongs to the SRMB. The most significant prospect defined is the Kiseljak Cu-Au porphyry, which was drilled predominantly during the 1980s. In total, 32 vertical drillholes, ranging from 109 m to 450 m depth, were completed between 1969 and 1990. This is a typical calc-alkaline Cu-Au porphyry deposit, forming a north plunging (~70°) dike intruded into amphibolite and biotite schist country rock. Mineralization within the potassic zone primarily comprises chalcopyrite veinlets (0.1 mm to 10 mm thick) and disseminated chalcopyrite and bornite. Gold mineralization occurs as native gold associated with gangue minerals and as blebs within sulphide minerals. The Kiseljak deposit extends at an area of 800 m by 300 m and has been traced to a vertical depth of 450 m. The total ore is estimated at 300 Mt grading an average of 0.2% Cu and 0.2 g/t Au in the inferred resource category, for 1.8 b lbs Cu and 2.5 moz Au (AMC Consultants UK Ltd 2013).

Drillings in late 2012 have identified a carbonate-base metal gold epithermal vein system at Bakrenjaca (Yellow Creek), located approximately 3 km south of the Kiseljak deposit. Dunav Co plans to commence a detailed drilling program area in order to determine the mineral ore potential of that epithermal system. The combined Kiseljak and Yellow Creek mineral inferred resources have been estimated at 547 Mt of ore grading an average of 0.2% Cu and 0.2 g/t Au, for 2.8 b lbs Cu (~1270 th.t Cu) and 3.8 moz Au (~118 t Au) (Table 1) (AMC Consultants UK Ltd 2013).

7. Conclusions

The metallogeny centers of the Serbomacedonian-Rhodope Metallogenic Belt (SRMB) in the Balkan Peninsula present world interest nowadays. Large global mining companies have invested significant funds in the research and exploitation of precious and basic metals in this area. The indicated and probable reserves of gold and silver in these regions are very promising. The most important of them are found in Macedonia Greece (Olympias-Stratoni-Skouries and Gerakario-Vathi-Pontokerasia) with 653 t Au and 4030 t Ag, Serbia (Kiseljak and Bakrenjaca) with 118 t Au and F.Y.R.O.M. (Ilovitza and Buchim) with 106 t Au and 96 t Ag.

8. References

AMC Consultants UK Ltd, 2013. Tulare Porphyry Project (Kiseljak Deposit), NI 43-101 Technical Report, Serbia, 145 pp.

Arvanitidis, N., 2012. State mining areas of the Prefecture Unit of Kilkis, http://nikolaosarvanitidis.eu/?p=316.

Balkan Mineral and Mining EAD, 2012. Krumovgrad Gold Project (Ada Tepe Deposit). Definitive Feasibility Study, NI 43-101 Technical Report, Bulgaria, 400 pp.

Bonev, I.K., 2007. Crystal habit of Ag-, Sb- and Bi-bearing galena from the Pb-Zn ore deposits in the Rhodope Mountains, *Geoch. Miner. Petrology, Bulgaria*, 45, 1-18.

Bristol, S., Spry, P., Voudouris, P., Melfos, V., Mathur, R., Fornadel, A. and Sakellaris, G., 2015. Geochemical and geochronological constraints on the formation of shear-zone hosted Cu-A

u-Bi-Te mineralization in the Stanos area, Chalkidiki, northern Greece, *Ore Geology Revie ws*, 66, 266-282.
Charistos, V., 2010. Study of placer gold in the regions of Servia Kozani and of rivers Aliakmonas and Axios, PhD thesis, Aristotle University, Thessaloniki, 372 pp.
Eliopoulos, D. and Kilias, S.P., 2011. Marble-hosted submicroscopic gold mineralization at Asimotrypes area, Mount Pangeon, southern Rhodope Core Complex, Greece, *Econ. Geol.*, 106, 751-780.
Euromax Resources Ltd, 2014. Pre-Feasibility Study. Technical Report for the Ilovitza Gold-Copper Project in Southeast Macedonia, 311 pp.
European Goldfields Ltd, 2011. Skouries Cu/Au Project. NI 43-101 Technical Report, Greece, 118 pp.
Feraud, J., Maliqi, G. and Meha, V., 2007. Famous mineral localities: the Trepca mine, Stari Trg, Kosovo, *Mineralogical Record*, 38(4), 267-278.
Fornadel, A.P., Spry, P.G., Melfos, V., Vavelidis, M. and Voudouris, P., 2011. Is the Palea Kavala Bi-Te-Pb-Sb±Au district, northeastern Greece, an intrusion-related system? *Ore Geology Reviews*, 39, 119-133.
Frei, R., 1995. Evolution of mineralizing fluid in the porphyry copper system of the Skouries deposit, northeast Chalkidiki (Greece): evidence from combined Pb-Sr and stable isotope data, *Econ. Geol.*, 90, 746-762.
Glory Resources, 2012. High Grade Gold in Greece. Sapes Project Overview, www.gloryresources.com.au, 31 pp.
Harkovska, A., Yanev, Y. and Marchev, P., 1989. General features of the Palaeogene orogenic magmatism in Bulgaria, *Geol. Balcanica*, 19, 37-72.
Heinrich, C.A. and Neubauer, F., 2002. Cu-Au-Pb-Zn-Ag metallogeny of the Alpine-Balkan-Carpathian-Dinaride geodynamic province, *Miner. Deposita*, 37, 533-540.
Hyseni, S.M., Durmishaj, B.N., Bytyqi, A.X., Krasniqi, R. and Abazi, S., 2012. Lost metals through processing polymineral lead and zinc in the flotation Stan Terg, Trepca, *ARPN J. Eng. & Applied Sci.*, 7(3), 251-255.
Jankovic, S., Milovanovic, D., Jelenkovic, R. and Hrkovic, K., 1992. Gold Deposits and Occurrences in Serbia: Types, Metallogenic Units and Outlook, Chair of Economic geology, Faculty of Mining and Geology, University of Belgrade, Belgrade, 285 pp.
Kalogeropoulos, S., Kilias, S., Bitzios, D., Nicolaou, M. and Both, R., 1989. Genesis of the Olympias carbonate-hosted Pb-Zn (Au, Ag) sulphide ore deposit, eastern Chalkidiki Peninsula, northern Greece, *Econ. Geol.*, 84(5), 1210-1234.
Kelepertsis, A.E., Reeves, R. and Andrulakis, J., 1986. Geochemical studies of porphyry type mineralization at Gerakario-Vathi of Kilkis area, Northern Greece, *Mineral Wealth*, 42, 43-48.
Kroll, T., Muller, D., Seifert, T., Herzig, P.M. and Schneider, A., 2002. Petrology and geochemsitry of the shoshonite-hosted Skouries porphyry Cu-Au deposit, Chalkidiki, Greece, *Miner. Deposita*, 37, 137-144.
Marchev, P., Kaiser-Rohrmeier, M., Heinrich, C., Ovtcharova, M., von Quadt, A. and Raicheva, R., 2005. Hydrothermal ore deposits related to post-orogenic extensional magmatism and core complex formation: the Rhodope Massif of Bulgaria and Greece, *Ore Geology Reviews*, 27, 53-89.
Márton, I., Moritz, R. and Spikings, R., 2010. Application of low-temperature thermochronology to hydrothermal ore deposits: Formation, preservation and exhumation of epithermal gold systems from the Eastern Rhodopes, Bulgaria, *Tectonophysics*, 483, 240-254.
Melfos, V., Vavelidis, M. and Bogdanov, K., 2003. Occurrence, mineralogy and chemical composition of primary gold from Tertiary ore mineralisations in the Rhodope massif (Greece-Bulgaria). *In:* Eliopoulos *et al., eds.*, Mineral Exploration & Sustainable Development, Millpress, Rotterdam, 1201-1204.
Melfos, V., Vavelidis, M., Christofides, G. and Seidel, E., 2002. Origin and evolution of the Tertiary Maronia porphyry copper-molybdenum deposit, Thrace, Greece. *Miner. Deposita*, 37, 648-668.
Michael, C., 2004. Epithermal systems and gold mineralization in Western Thrace (North Greece), *Bull. Geol. Soc. Greece*, 36(1), 416-423.

Mitchell, A.H.G., 1996. Distribution and genesis of some epizonal Zn-Pb and Au provinces in the Carpathian and Balkan region, *Trans. Inst. Mineral. Metall.*, 105, B127-B138.

Monthel, J., Vadala, P., Leistel, J.M. and Cottard, F., 2002. Mineral deposits and mining districts of Serbia. Compilation map and GIS databases, BRGM/RC-51448-FR (with the collaboration of M. Ilic, A. Strumberger, R. Tosovic, A. Stepanovic).

Palinkaš, S., Palinkaš, L., Renac, C., Spangenberg, J., Lüders, V., Molnar, F. and Maliqi, G., 2013. Metallogenic model of the Trepča Pb-Zn-Ag Skarn Deposit, Kosovo: Evidence from fluid i nclusions, rare earth elements, and stable isotope data, *Econ. Geol.*, 108(1), 135-162.

Serafimovski, T., 2000. The Lece-Chalkidiki metallogenic zone: geotectonic setting and metallogenic feature, *Geologijia*, 42, 159-164.

Serafimovski, T., Stefanova, V. and Volkov, A.V., 2010. Dwarf Copper-Gold Porphyry Deposits of the Buchim-Damian-Borov Dol Ore District, Republic of Macedonia (FYROM), *Geology of Ore Deposits*, 52(3), 179-195.

Serafimovski, T., Cifliganec, V., Jankovic, S. and Boev, B., 1996. Genetic model of the Buchim porphyry copper deposit, Republic of Macedonia, *Proc. Annual Meeting I.G.C.P. (No 356)*, Sofia, 1, 63-74.

Shawh, A. and Constantinides, D., 2001. The Sappes gold project, *Bull. Geol. Soc. Greece*, 34(3), 1073-1080.

Tsirambides, A. and Filippidis, A., 2012. Metallic mineral resources of Greece, *Cent. Eur. J. Geosci.*, 4(4), 641-650.

Vassileva, D.R., Atanassova, R. and Bonev, K.I., 2009. A review of the morphological varieties of ore bodies in the Madan Pb-Zn deposits, Central Rhodopes, Bulgaria, *Geochemistry, Mineralogy and Petrology, Sofia*, 47, 31-49.

Vavelidis, M., Boboti-Tsitlakidis, I. and Melfos, V., 1994. The gold-silver-copper mineralization a nd the placer gold in Koronouda area, northern Greece, *Eur. J. Mineral.*, 6, 293.

Vavelidis, M., Melfos, V. and Kilias, A., 1999. The gold-bearing quartz veins in the metamorphic rocks at the Drakontio area, central Macedonia, northern Greece. *In:* Stanley, C.J., *et al., eds.*, Mineral Deposits: Processes to Processing, Balkema, Rotterdam, 209-212.

Vavelidis, M., Melfos, V. and Arikas, K., 2000. Mineralogy and structural control of the Au-Ag-rich copper mineralization in the Serbomacedonian Massif, Paliomylos area, Greece, *Beih. zum Eur. J. Mineral.*, 12, 220.

Volkov, A.V., Serafimovski, T., Kochneva, N.T., Tomson, I.N. and Tasev, G., 2006. The Alshar Epithermal Au-As-Sb-Tl Deposit, Southern Macedonia, *Geology of Ore Deposits*, 48(3), 175-192.

Voudouris, P., Melfos, V., Spry, P., Moritz, R., Papavassiliou, C. and Falalakis, G., 2011. Mineralogy and geochemical environment of formation of the Perama Hill high-sulfidation epithermal Au-Ag-Te-Se deposit, Petrota Graben, NE Greece, *Miner. Petrol.*, 103, 79-100.

Voudouris, P., Melfos, V., Spry, P., Kartal, T., Schleicher, H., Moritz, R. and Ortelli, M., 2013a. The Pagoni Rachi / Kirki Cu-Mo±Re±Au deposit, Northern Greece: mineralogical and fluid inclusion constraints on the evolution of a telescoped porphyry-epithermal system, *Can. Miner.*, 51, 253-284.

Voudouris, P., Spry, P., Mavrogonatos, C., Sakellaris, G., Bristol, S., Melfos, V. and Fornadel, A., 2013b. Bismuthinite derivatives, lillianite homologues, and bismuth sulfotellurides as indicators of gold mineralization in the Stanos shear-zone related deposit, Chalkidiki, Northern Greece, *Can. Miner.*, 51, 119-142.

Voudouris, P., Melfos, V., Spry, P., Bindi, L., Kartal, T., Arikas, K., Moritz, R. and Ortelli, M., 20 09. Rhenium-rich molybdenite and rheniite (ReS_2) in the Pagoni Rachi-Kirki Mo-Cu-Te-Ag -Au deposit, Northern Greece: Implications for the rhenium geochemistry of porphyry style Cu-Mo and Mo mineralization, *Can. Miner.*, 47, 1013-1036.

Δελτίο της Ελληνικής Γεωλογικής Εταιρίας, τόμος L, σελ. 2047-2056
Πρακτικά 14ου Διεθνούς Συνεδρίου, Θεσσαλονίκη, Μάιος 2016

Bulletin of the Geological Society of Greece, vol. L, p. 2047-2056
Proceedings of the 14th International Congress, Thessaloniki, May 2016

MINERAL CHEMISTRY AND FORMATION OF AWARUITE AND HEAZLEWOODITE IN THE XEROLIVADO CHROME MINE, VOURINOS, GREECE

Tzamos E.[1], Filippidis A.[1], Michailidis K.[1], Koroneos A.[1], Rassios A.[2], Grieco G.[3], Pedrotti M.[3] and Stamoulis K.[4]

[1]Aristotle University of Thessaloniki, Faculty of Sciences, School of Geology, Department of Mineralogy-Petrology-Economic Geology, 541 24, Thessaloniki, Greece, tzamos@geo.auth.gr, anestis@geo.auth.gr, kleopas@geo.auth.gr, koroneos@geo.auth.gr

[2]Institute of Geology and Mineral Exploration, Lefkovrisi, Kozani, 501 00, Kozani, Greece, rassannie@gmail.com

[3]Department of Earth Sciences, Università degli Studi di Milano, Via Botticelli, 23, Milano, Italy, giovanni.grieco@unimi.it, maria.pedrotti84@gmail.com

[4]Geologist, Kastania, Servia, 505 00, Kozani, Greece, stamoul@hotmail.gr

Abstract

The Serpentinite between the chromite bodies 4 and 5 of Xerolivado mine (Vourinos, Greece), contains sparsely very small grains (<20μm) of awaruite ($Fe_{0.91}Cu_{0.06}Co_{0.03}Ni_3$), heazlewoodite ($Ni_{2.91}Fe_{0.06}S_2$), magnetite and Co-pentlandite ($Ni_{3.79}Fe_{2.98}Co_{2.38}S_8$). The olivine contains 0.40 wt% NiO and 6.91 wt% FeO, while the serpentine 0.18 wt% NiO and 3.02 wt% FeO. The Co-content of awaruite is 1.31 wt% and that of heazlewoodite 0.12 wt%. Heazlewoodite is a product of the primary Co-pentlandite reduction, resulting from the serpentinization of the ultramafic rock. The Ni content of awaruite is derived both from olivine and from Co-pentlandite. The reducing environment resulting from serpentinization and the low sulphur fugacity, favour the formation of awaruite, heazlewoodite and magnetite.
Keywords: *Pentlandite, olivine, serpentine, magnetite.*

Περίληψη

Ο σερπεντινίτης μεταξύ των χρωμιτικών σωμάτων 4 και 5 στο μεταλλείο Ξερολίβαδο (Βούρινος, Ελλάδα) περιέχει σποραδικούς πολύ μικρούς κόκκους (<20μm) αβαρουίτη ($Fe_{0,91}Cu_{0,06}Co_{0,03}Ni_3$), χεζλεγουδίτη ($Ni_{2,91}Fe_{0,06}S_2$), μαγνητίτη και Co-πεντλανδίτη ($Ni_{3,79}Fe_{2,98}Co_{2,38}S_8$). Ο ολιβίνης περιέχει 0,40 %κβ NiO και 6,91 %κβ FeO, ενώ ο σερπεντίνης 0,18 %κβ NiO και 3,02 %κβ FeO. Η περιεκτικότητα Co του αβαρουίτη είναι 1,31 %κβ και του χεζλεγουδίτη 0,12 %κβ. Ο χεζλεγουδίτης είναι ένα προϊόν της αναγωγής του πρωταρχικού Co-πεντλανδίτη, που προκύπτει από τη σερπεντινίωση του υπερβασικού πετρώματος. Το περιεχόμενο Ni στον αβαρουίτη προέρχεται τόσο από τον ολιβίνη και από τον Co-πεντλανδίτη. Το αναγωγικό περιβάλλον που προκύπτει από τη σερπεντινίωση και η χαμηλή μερική πίεση του θείου, ευνοούν τον σχηματισμό αβαρουίτη, χεζλεγουδίτη και μαγνητίτη.
Λέξεις κλειδιά: *Πεντλανδίτης, ολιβίνης, σερπεντίνης, μαγνητίτης.*

1. Introduction

The paragenesis and the chemical composition of the opaque minerals (e.g., sulphides, metal alloys) formed during serpentinization, depend on the initial chemical composition of the olivine and the oxygen and sulfur fugacities (fO_2 and fS_2). The Ni^{2+} commonly display preference in the M1 site of olivine, and the serpentinized olivine is proposed as the source of nickel (Brown, 1980; Filippidis and Annersten, 1981; Annersten *et al.*, 1982; Filippidis, 1982, 1985, 1991; Nord *et al.*, 1982; Deer *et al.*, 1997), whereas, the origin of the sulfur is attributed to the fluid phase that causes the serpentinization. The sulfur either exists in the fluid phase, or comes from sources outside of the ultramafic body and transferred by the fluid phase along with H_2O, CO_2 and Cl (Ashley, 1973; Groves and Keays, 1979; Groves *et al.*, 1979; Donaldson, 1981; Donaldson and Bromley, 1981; Seccombe *et al.*, 1981; Pasteris, 1984).

The "internal" sulfur, which originates from magmatic sulphides, immigrates during serpentinization (Shima and Naldrett, 1975; Donaldson, 1981; Seccombe *et al.*, 1981). Sulfur can occur under reducing conditions from these magmatic sulphides (e.g., pentlandite, pyrrhotite) with the process of desulfurization, producing H_2S, sulphides and alloys at temperatures of 365-445^oC. The produced H_2S, reacts with the metallic elements that are released during the serpentinization of the silicate minerals and Ni-Fe-sulphides are produced. Further serpentinization, can lead to the formation of violarite and/or millerite (Krishna Rao, 1964, Kanehira *et al.*, 1975).

The maximum thermal stability of pentlandite is at the temperature of 610^oC, however pentlandites frequently contain amounts of Co substituting Fe and Ni. The presence of Co raises the thermal stability of pentlandites (up to 630^oC) and the confining pressure reduces it to 425^oC. The maximum thermal stability of heazlewoodite is 556^oC, but metal deficiency lowers it to 524^oC The Ni content of awaruite and heazlewoodite is interpreted as being derived both from primary silicates and from a primary sulphide such as pentlandite; under reducing conditions pentlandite is desulphurized (Craig and Scott, 1974).

The present study investigates the mineral-chemistry and formation of awaruite (Ni-Fe alloy) and heazlewoodite, found in the serpentinite of the Xerolivado chrome mine, Vourinos, Greece.

2. Geologic setting

The Vourinos ophiolite complex is located in western Macedonia of northern Greece (Fig. 1). It covers an area of 400 km^2 dominated by mantle rocks and it constitutes a complete ophiolite sequence with a well-exposed petrologic moho (Grieco and Merlini, 2012). The crustal sequence consists of mafic and ultramafic cumulates, gabbro, dykes, pillow lavas and carbonate sediment cover (Liati *et al.*, 2004; Rassios and Moores, 2006). The age of the Vourinos oceanic crust was found to be 168.5±2.4 my and 172.9±3.9 my via U/Pb analyses of zircons within plagiogranite (Liati *et al.*, 2004). Mantle rocks are strongly depleted and dominated by harzburgite with abundant irregular chromitite-hosting dunite bodies (Saccani *et al.*, 2004; Bortolotti *et al.*, 2004; Grieco and Merlini, 2012). Some areas, several close to the eastern emplacement margin, are serpentinized (Margaras and Vacondios, 1996, Grieco and Merlini, 2012).

Many authors have worked on Vourinos geological and petrological/geochemical characteristics and evidence confirms the existence of multiple magma chambers and that the harzburgites represent mantle residue, remaining after a high degree of partial melting (Moores, 1969; Jackson *et al.*, 1975; Harkins *et al.*, 1980; Beccaluva *et al.*, 1984; Paraskevopoulos and Economou, 1986; Konstantopoulou and Economou-Eliopoulos, 1991). The chromite formation in dunite occurred at about 1300^oC with re-equilibration at about 600^oC (Rassios and Kostopoulos, 1990). The successive stages of the structural evolution and deformation of the chromite-hosting dunite bodies were: a) Dunite and chromite formation within the upper mantle, b) High-temperature plastic deformation resulting from mantle flow, c) Low-temperature plastic to semi-brittle deformation resulting in folding of dunite and chromite and d) Brittle deformation (faults and thrusts) displacing the dunites

and chromite ore bodies (Ross *et al.*, 1980; Roberts, 1988; Konstantopoulou, 1993; Filippidis, 1996, 1997; Grieco and Merlini, 2012). Serpentinization processes controlled the final mineralogical composition of the rocks and resulted in the serpentinization of the former dunite and its alteration to serpentinite and/or serpentinized peridotite.

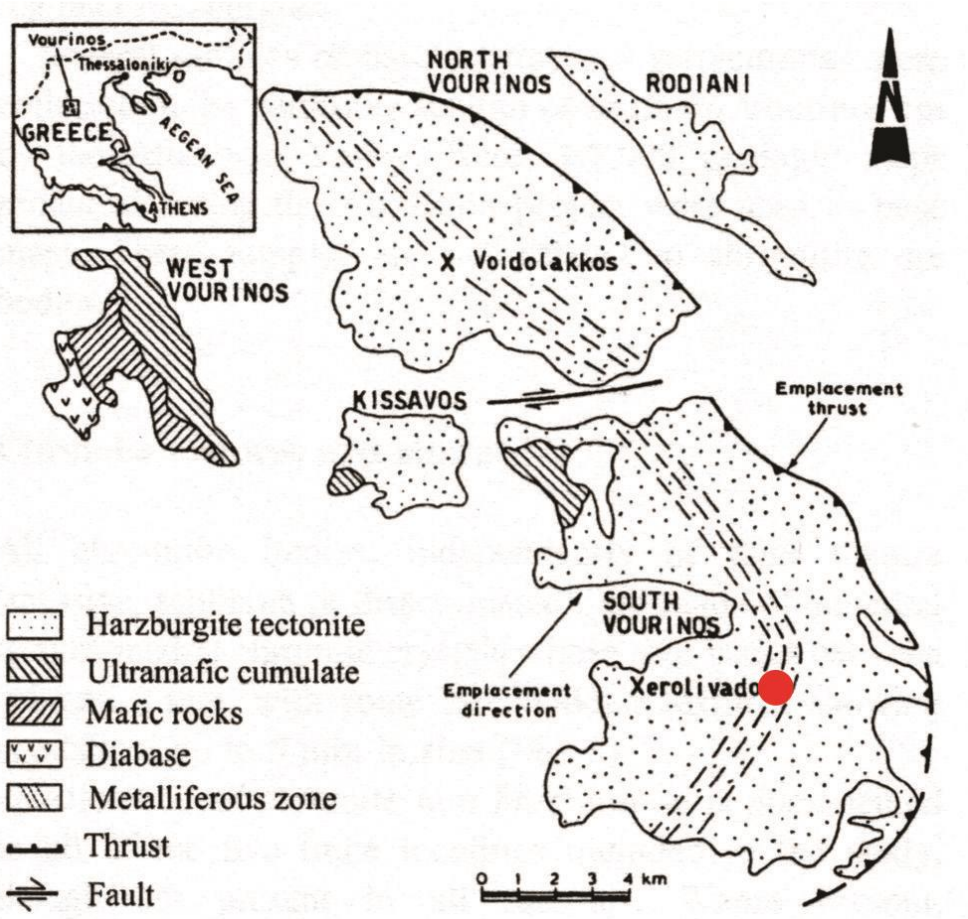

Figure 1 - Major petrologic units of the Vourinos ophiolite complex and location of the Xerolivado mine (red circle) (after Grivas *et al*., 1993).

The largest dunite body of Vourinos occurs at Xerolivado locality (Fig. 1). It has an approximate surface exposure of 3 km^2 (3 x 1 km). Harzburgite tectonite hosts the dunite body but also outcrops within the dunite, occurring as elongated masses, with length up to 300 m, striking NE-SW (Apostolidis *et al.*, 1981; Roberts, 1988; Stamoulis, 1990; Filippidis, 1996, 1997). The Xerolivado chromite mine, hosted in the ultramafic body, is one of the world's largest alpine type chromite deposit, with a known potential of 6 million tons of schlieren ore averaging 22 modal percent chromite-schlieren chromitite bodies contain bands of schlieren ore, each being 1 to 15 cm thick, alternating with the ultramafic rock (Stamoulis, 1990; Filippidis, 1996).

Three main normal fault zones (F1, F2 and Fm) divide the Xerolivado mine into four sectors: the northern, the central, the southern and the southwestern (Fig. 2). These fault zones down throw the ultramafic body and the hosted chromitite bodies to the SW with horizontal and vertical dislocations (Stamoulis, 1990; Filippidis, 1996, 1997). The schlieren chromite bodies with thickness ranging between 1 and 12 m strike NE-SW and steeply dipping towards NW.

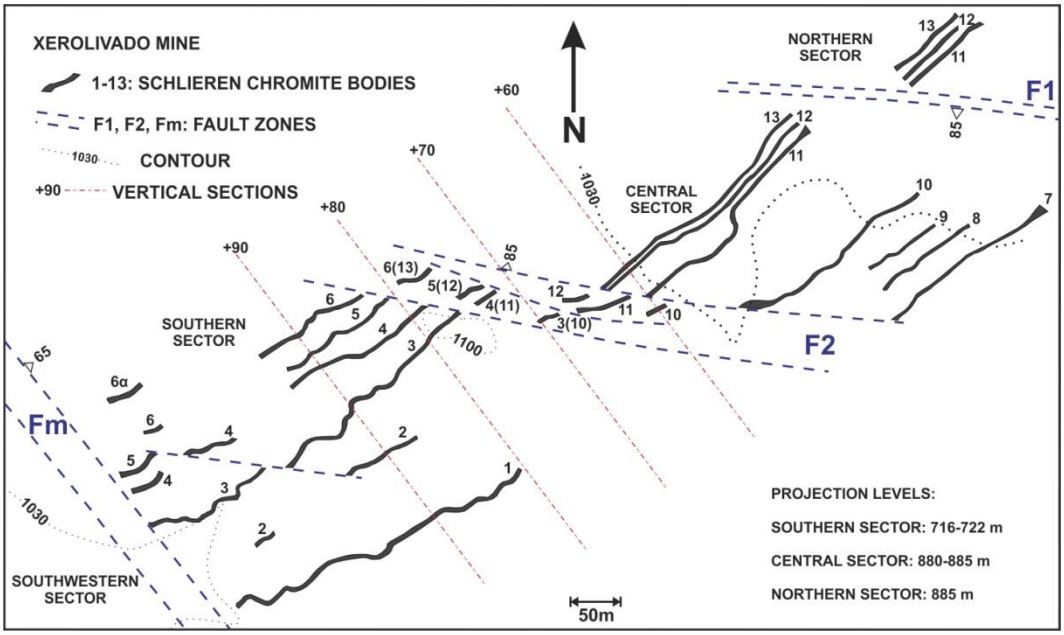

Figure 2 - Distribution and form of the schlieren chromite ore bodies of the Vourinos Xerolivado mine (modified after Filippidis, 1996).

3. Materials and methods

The serpentinite samples were collected from the underground tunnels of the Xerolivado chromite mine, between chromite bodies 4 and 5 (Fig. 2). Thin and thin-polished sections were mounted from these samples and they were investigated by optical microscopy, scanning electron microscope and electron microprobe for their textures as well as their mineralogical and chemical composition.

Mineral chemistry of sulphides and metal alloys was determined with a JEOL 8200 electron microprobe at the University of Milan. For the analyses the system was operated using an accelerating voltage of 15 kV, a sample current on brass of 15 nA and a counting time of 20 s on the peaks and 10 s on background. A series of natural minerals were used as standards.

4. Results

The microscopic examination of the samples shows that they are dominated by the presence of serpentine. Modal analyses of the samples shows that presence of serpentine makes up more than 90% v/v of total silicates, thus all samples are characterized as serpentinites. Serpentine has a typical mesh texture, the position of the original fractures and grain boundaries of olivine are marked by a simple parting or by a string of magnetite, sulphides and metal alloys. Sulphides, magnetite and metal alloys grains are found disseminated in the serpentinite matrix having a relatively small size of no more than 20 μm (Fig. 3). Awaruite and heazlewoodite are also found substituting primary pentlandite (Fig. 3b, c and d). Chromite is also present in disseminated grains. Some chromite grains are altered to ferrochromite in spots on their rims.

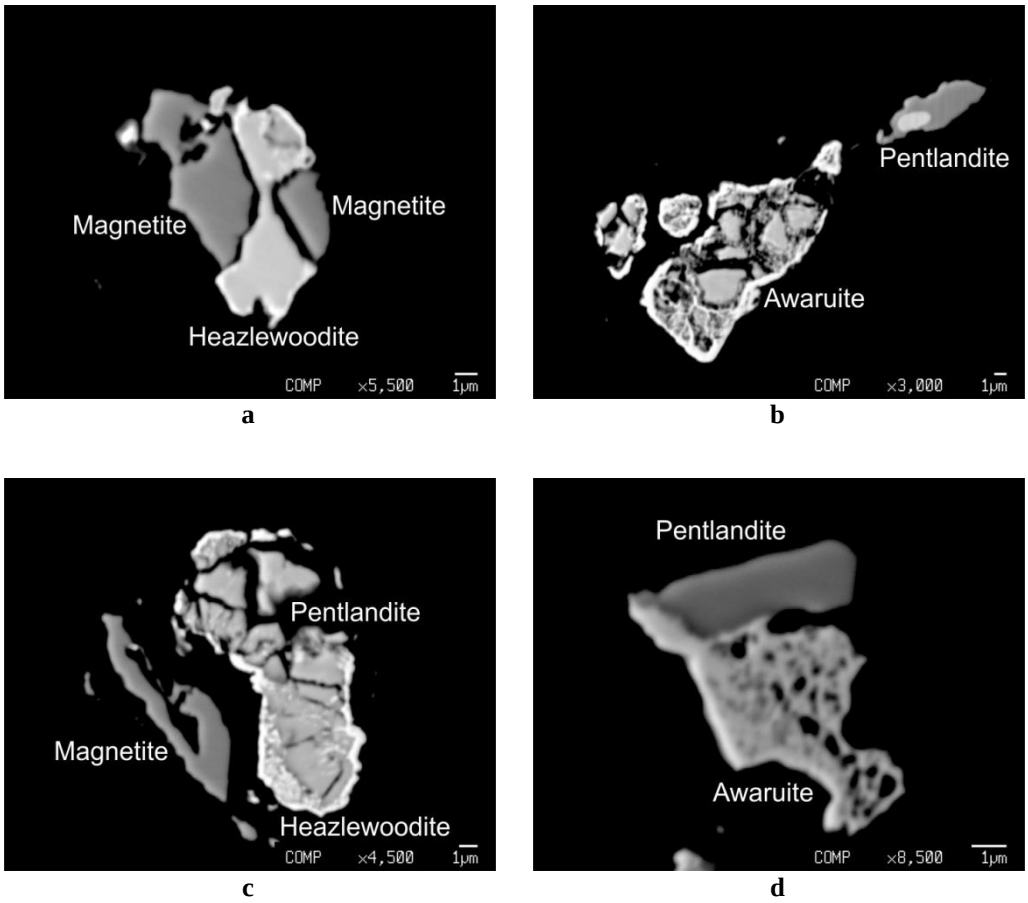

Figure 3 - Microphotographs from scanning electron microscope (SEM) with back-scattered electron image (BSI) from Xerolivado serpeninites. a) Sample D4-5/717, magnetite (gray) and heazlewoodite (light gray), b) Sample D4/765, awaruite (light gray) and pentlandite (gray), c) Sample D4-5/738, magnetite (gray), pentlandite (light gray) and heazlewoodite (white rim), d) Sample D4-5/765, awaruite (light gray) and pentlandite (gray).

The chemical compositions of awaruite, heazlewoodite, and pentlandite are presented respectively in Tables 1, 2, and 3.

Awaruite contains on average 75.71 wt% Ni, 21.67 wt% Fe, 1.53 wt% Cu and 1.31 wt% Co (Table 1). Heazlewoodite contains 71.32 wt% Ni, 1.48 wt% Fe and 0.12 wt% Co (Table 2). Pentlandite contains 28.14 wt% Ni, 21.02 wt% Fe and 17.71 wt% Co (Table 3). Olivine present in the samples contains 0.40 wt% NiO and 6.91 wt% FeO, while serpentine contains 0.18 wt% NiO and 3.02 wt% FeO (Tzamos, unpublished PhD thesis).

Table 1 - Chemical composition (wt%) of Awaruite (Xerolivado mine serpentinite).

Sample	D4-5/717A	D4-5/717B	D4-5/738	C1/745A	C1/745B	C3/717B	Average
As	Bdl	0.03	Bdl	N/A	N/A	N/A	0.01
Sb	0.03	Bdl	Bdl	N/A	N/A	N/A	0.01
Co	0.95	1.06	1.91	N/A	N/A	N/A	1.31
Cu	1.44	3.63	1.29	0.93	1.52	0.35	1.53
Fe	22.17	21.45	16.38	24.74	20.18	25.10	21.67
Ni	74.65	73.42	80.13	74.76	77.52	73.76	75.71
Total	99.24	99.59	99.71	100.43	99.22	99.21	100.24
Structural formulae based on 3 (Ni)							
As	-	-	-	-	-	-	-
Sb	-	-	-	-	-	-	-
Co	0.04	0.04	0.07	0.00	0.00	0.00	0.03
Cu	0.05	0.14	0.04	0.03	0.05	0.01	0.06
Fe	0.94	0.92	0.64	1.04	0.82	1.07	0.91
Ni	3.00	3.00	3.00	3.00	3.00	3.00	3.00
Total	4.03	4.10	3.75	4.07	3.87	4.08	4.00

Bdl: Below detection limit, N/A: not analyzed

Table 2 - Chemical composition (wt%) of Heazlewoodite (Xerolivado mine serpentinite).

Sample	D4-5/717A	D4-5/717B	D4-5/717C	D4/765	D4-5/738A	D4-5/738B	C1/745	C1/745	Average
As	Bdl	Bdl	Bdl	Bdl	0.02	0.02	N/A	N/A	0.01
Sb	Bdl	Bdl	Bdl	Bdl	0.04	Bdl	N/A	N/A	0.01
Co	0.06	0.14	0.12	0.04	0.27	0.10	N/A	N/A	0.12
Cu	Bdl	Bdl	Bdl	Bdl	Bdl	Bdl	Bdl	Bdl	Bdl
Fe	1.42	1.14	2.11	1.27	1.82	1.52	1.07	1.48	1.48
Ni	72.01	70.95	70.71	70.94	70.99	71.10	72.14	71.75	71.32
S	27.44	27.81	27.43	27.40	27.20	27.39	25.06	24.81	26.82
Total	100.93	100.04	100.37	99.65	100.34	100.13	98.27	98.04	99.76
Structural formulae based on 2 (S)									
As	-	-	-	-	-	-	-	-	-
Sb	-	-	-	-	-	-	-	-	-
Co	-	0.01	-	-	0.01	-	-	-	-
Cu	-	-	-	-	-	-	-	-	-
Fe	0.06	0.05	0.09	0.05	0.08	0.06	0.05	0.07	0.06
Ni	2.87	2.79	2.82	2.83	2.85	2.84	3.15	3.16	2.91
S	2.00	2.00	2.00	2.00	2.00	2.00	2.00	2.00	2.00
Total	4.93	4.85	4.91	4.88	4.94	4.90	5.19	5.23	4.99

Bdl: Below detection limit, N/A: Not analyzed

Table 3 - Chemical composition (wt%) of Pentlandite (Xerolivado mine serpentinite).

Sample	D4-5/765A	D4-5/738	D4/765	D4-5/765B	Average
As	Bdl	Bdl	0.01	0.04	0.01
Sb	Bdl	Bdl	Bdl	0.08	0.02
Co	18.18	17.50	19.56	15.58	17.71
Cu	Bdl	0.02	Bdl	Bdl	0.01
Fe	21.70	22.57	22.10	17.70	21.02
Ni	26.09	27.97	23.34	35.17	28.14
S	33.30	31.56	34.33	30.52	32.43
Total	99.27	99.62	99.34	99.09	99.34
Structural formulae based on 8 (S)					
As	-	-	-	-	-
Sb	-	-	-	0.01	-
Co	2.38	2.41	2.48	2.22	2.38
Cu	-	-	-	-	-
Fe	2.99	3.28	2.96	2.66	2.98
Ni	3.42	3.87	2.97	5.03	3.79
S	8.00	8.00	8.00	8.00	8.00
Total	16.79	17.56	16.41	17.92	17.15

Bdl: Below detection limit

5. Discussion and conclusions

The chemical formulae of the studied opaque minerals are $Fe_{0.91}Cu_{0.06}Co_{0.03}Ni_3$ for awaruite, $Ni_{2.91}Fe_{0.06}S_2$ for heazlewoodite and $Ni_{3.79}Fe_{2.98}Co_{2.38}S_8$ for Co-pentlandite. In figures 4 and 5, the relative compositions of the studied mineral phases in Fe-(Ni+Co)-S and Fe-Ni-Co are shown respectively.

The formation of heazlewoodite, awaruite and magnetite as a result of the serpentinization is clearly shown by the rock texture, with disseminated small grains of the opaque minerals in the serpentinite, with the formation of rims of heazlewoodite (Fig. 3c) and awaruite (Fig. 3b) around Co-pentlandite and by even more severe substitution of Co-pentlandite grains from awaruite (Fig. 3d).

Nickel was contained in the original Mg-Fe olivine and the primary Co-pentlandite. The initial chemical composition of the (Mg,Fe,Ni) olivine, the reducing environment during serpentinization, the oxygen and sulfur fugacity (fO_2 and fS_2), controlled the formation and chemical composition of the heazlewoodite and the Ni-Fe alloy (awaruite). Heazlewoodite is a product of the primary Co-pentlandite reduction, resulting from the serpentinization of the ultramafic rock which contained traces of pentlandite (Craig and Scott, 1974; Brown, 1980; Filippidis and Annersten, 1981; Annersten *et al.*, 1982; Filippidis, 1982, 1985, 1991; Nord *et al.*, 1982; Deer *et al.*, 1997).

The serpentinization of (Mg,Fe,Ni) olivine and the alteration of primary Co-pentlandite, converted some of Ni and Fe into the serpentine, and some of Ni, Fe and Co into heazlewoodite and awaruite. At very low sulfur and oxygen fugacity to sulfur and oxygen free serpentinization system, awaruite and heazlewoodite were formed. Heazlewoodite, awaruite and magnetite were formed as a result of the serpentine and brucite being unable to incorporate as much Fe and Ni into their lattices as the original olivine. The Ni content of awaruite is derived both from primary olivine and from primary Co-pentlandite. The reducing environment resulting from serpentinization yields a low sulphur fugacity, which favour the formation of the reduced opaque assemblage heazlewoodite-awaruite-magnetite.

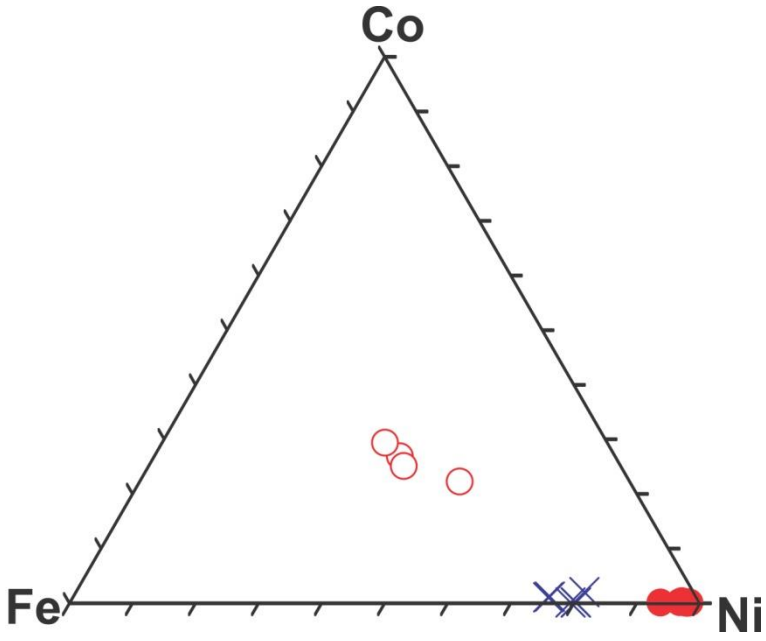

Figure 4 - Ternary diagram Fe-(Ni+Co)-S showing the relative compositions of the Xerolivado mine pentlandites (o), heazlewoodites (•) and awaruites (x).

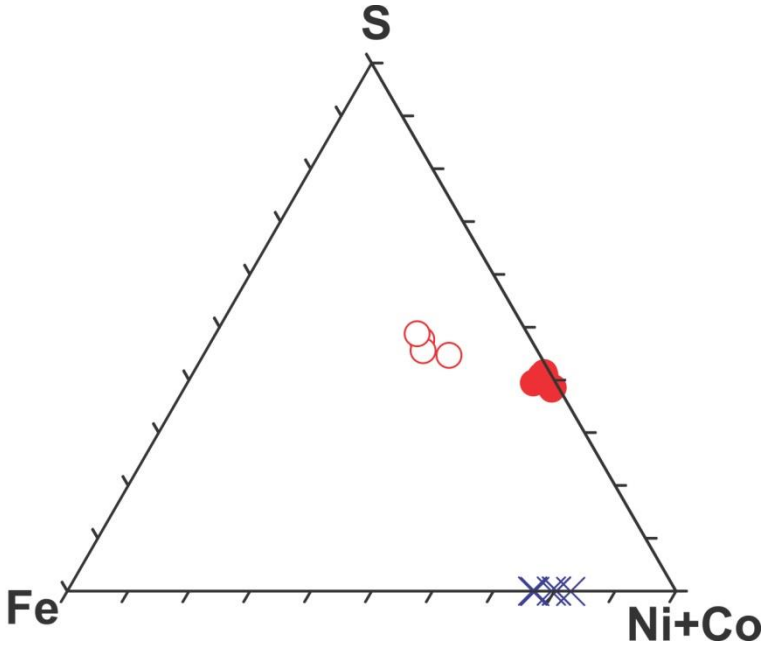

Figure 5 - Ternary diagram Fe-Ni-Co showing the relative compositions of the Xerolivado mine pentlandites (o), heazlewoodites (•) and awaruites (x).

6. Aknowledgments

E. Tzamos would like to thank the Greek State Scholarship Foundation (IKY) for partly financing his PhD research, a part of which is presented in this paper. Andrea Risplendente from University of Milan is thanked for helping with the micro-analyses.

7. References

Annersten, H., Ericsson, T. and Filippidis, A., 1982. Cation ordering in Ni-Fe olivines, *Amer. Miner.*, 67, 1212-1217.

Apostolidis, G., Mastoris, K. and Vgenopoulos, A.G., 1981. Exploration of the Xerolivado-chromite deposits and their chemical, mineralogical and physical properties, *Proc. of the Intern. Symp. Metallogeny of Mafic* and *Ultramafic complexes*, 9-11 Oct.1980 Athens, 1, 1-20.

Ashley, P. M., 1973. Pedogenesis of sulphide bearing reaction zones in the Coolac ultramafic belt, New South Wales, Australia, *Mineral. Depos.*, 8, 370-378.

Beccaluva, L., Ohnenstetter, D., Ohnenstetter, M. and Paupy, A., 1984. Two magmatic series with island arc affinities within the Vourinos ophiolite, *Contrib. Mineral. Petrol.*, 85, 253-271.

Bortolotti, V., Chiari, M., Marcucci, M., Marroni, M., Pandolfi, L., Principi, G. and Saccani, E., 2004. Comparison among the Albanian and Greek ophiolites; in search of constraints for the evolution of the Mesozoic Tethys Ocean, *Ofioliti*, 29, 19-35

Brown, G.E.Jr., 1980. Olivines, *In:* Ribbe, P.H., *ed.*, Orthosilicates, Miner. Soc. America, Washington D.C. *Reviews in Mineralogy*, 5, 275-381.

Craig, J.R. and Scott, S.D., 1974. Sulfide phase equilibria, *In*: Ribbe, P.H., *ed.*, Sulfide Mineralogy, Miner. Soc. America, 1, CS1-110.

Deer, W.A., Howie, R.A. and Zussman, J., 1997. Orthosilicates. Rock-forming minerals vol. 1A, *The Geol. Soc*., London, 919 pp.

Donaldson, M.J., 1981. Redistribution of ore elements during serpentinization and talc-carbonate alteration of some Archean dunites, Western Australia, *Econ. Geol.*, 76, 1698-1713.

Donaldson, M.J. and Bromley, G.J., 1981. The Honeymoon well nickel sulfide deposits, western Australia, *Econ. Geol.*, 76, 1550-1564.

Filippidis, A., 1982. Experimental study of the serpentinization of Mg-Fe-Ni olivine in the presence of sulphur, *Can. Miner.*, 20, 567-574.

Filippidis, A., 1985. Formation of awaruite in the system Ni-Fe-Mg-Si-O-H-S and olivine hydration with NaOH solution: An experimental study, *Econ. Geol.*, 80, 1974-1980.

Filippidis, A., 1991. Further comments on the opaque mineral assemblages in ultramafic rocks: an experimental study, *Ofioliti*, 16, 1-6.

Filippidis, A., 1996. Chemical variation of olivine in the serpentinite of the central section in the Xerolivado chrome mine of Vourinos, Greece, *N. Jb Miner. Mh.*, 170(2), 189-205.

Filippidis, A., 1997. Chemical variation of chromite in the central sector of Xerolivado chrome nine of Vourinos, western Macedonia, Greece, *N. Jb Miner. Mh.*, 354-370.

Filippidis, A. and Annersten, H., 1981. Mineral chemical investigation of an ultramafic nickel bearing body in the Swedish Caledonides, *Proc. of the Intern. Symp. Metallogeny of Mafic* and *Ultramafic complexes*, 9-11 Oct.1980 Athens, 2, 115-130.

Grieco, G. and Merlini, A., 2012. Chromite alteration processes within Vourinos ophiolite, *Int. J. Earth Sci.*, 101(6), 1523-1533.

Grivas, E., Rassios, A., Konstantopoulou, G., Vacondios, I. and Vrahatis, G., 1993. Drilling for "blind" podiform chrome orebodies at Voidolakkos in the Vourinos ophiolite complex Greece, *Econ. Geol.*, 88(2), 461-468.

Groves, D.I. and Keays, R.R., 1979. Mobilization of ore-forming elements during alteration of dunites, Mt. Keith-Betheno, Western Australia, *Can. Mineral.*, 17, 373-389.

Groves, D.I., Barret, F.M. and McQueen, K.G., 1979. The relative roles of magmatic segragation, volcanic exhalation and regional metamorphism in the generation of volcanic associated nickel ores of Western Australia, *Can. Mineral.*, 17, 319-336.

Harkins, M.E., Green, H.W. and Moores, E.M., 1980. Multiple intrusive events documented from the Vourinos complex, Northern Greece, *Amer. J. Sci.*, 280A, 284-295.

Jackson, E.D., Green, H.W. and Moores, E.M., 1975. The Vourinos ophiolite, Greece: cyclic unit of lineated cumulates overlying harzburgite tectonite, *Geol. Soc. America Bull.*, 86, 390-398.

Kanehira, K., Banno, S. and Yui, S., 1975. Awaruite, heazlewoodite, am native copper in serpentinized peridotite from the Mineoka district southern Boso Peninsula, *J. Japan, Assoc. Mineral. Petrol. Econ. Geol.*, 70, 388-394.

Konstantopoulou, G., 1993. Structural criteria in locating chromite ores: evidence from the Rizo district, Vourinos ophiolite, Greece, *Bull. Geol. Soc. Greece*, 28, 381-392.

Konstantopoulou, G. and Economou-Eliopoulos, M., 1991. Geochemistry of the Vourinos chromite ores, Greece. *In:* Malpas, J., Moores, E., Panayiotou, A. and Xenophontos, C., *eds*, Ophiolites, Oceanic Crustal Analogues, *Proc. Symp. "Troodos 1987"*, Nicosia, Cyprus, 605-613.

Krishna Rao, J.S.R., 1964. Native nickel-iron alloy, its mode of occurrence, distribution and origin, *Econ. Geol.*, 59, 443- 448.

Liati, A., Gebauer, D. and Fanning, C.M., 2004. The age of ophiolitic rocks of the Hellenides (Vourins, Pindos, Crete): first U-Pb ion microprobe (SHRIMP) zircon ages, *Chem. Geol.*, 207(3-4), 171-188.

Margaras, S. and Vacondios, I., 1996. Metallogenic map of the Vourinos ophiolite complex (West Macedonia, Greece), IGME, Greece.

Moores, E.M., 1969. Petrology and structure of the Vourino ophiolite complex of Northern Greece, *Geol. Soc. America, Special Paper*, 118, 1-74.

Nord, A.G., Annersten, H. And Filippidis, A., 1982. The cation distribution in synthetic Mg-Fe-Ni olivines, *Amer. Miner.*, 67, 1206-1211.

Paraskevopoulos, G. and Economou, M., 1986. Genesis of magnetite ore occurrences by metasomatism of Chromite ores in Greece, *N. Jb. Miner. Abh.*, 140, 29-53.

Pasteris, J.D., 1984. Further interpretation of the Cu-Fe-Ni sulfide mineralization in the Duluth Complex, norteastern Minnesota, *Can. Miner.*, 22, 39-53.

Rassios, A. and Kostopoulos, D., 1990. The geochemistry of dunite and its relation to the position of chromitites in the Vourinos ophiolite complex, Greece, *In:* Malpas, J., Moores, E., Panayiotou, A. and Xenophontos, C., *eds*, Ophiolites, Oceanic Crustal Analogues. *Proc. Symp. "Troodos 1987"*, Nicosia, Cyprus, 593-604.

Rassios, A.H.E. and Moores, E.M., 2006. Heterogeneous mantle complex, crustal processes, and obduction kinematics in a unified Pindos-Vourinos ophiolitic slab (northern Greece), *Geol. Soc., London, Special Publ.*, 260, 237-266.

Roberts, S., 1988. Ophiolite chromite formation: a marginal basin phenomenon?, *Econ. Geol.*, 83, 1034-1036.

Ross, R., Mercier, J., Ave Lallemant, H., Carter, N. and Zimmerman, J., 1980. The Vourinos ophiolite complex, Greece: the tectonite suite, *Tectonophysics*, 70, 63-83.

Saccani, E., Beccaluva, L., Coltorti, M., Siena, F., 2004. Petrogenesis and tectono-magmatic significance of the Albanide-Hellenide subpelagonian ophiolites, *Ofioliti*, 29, 75–93

Seccombe, P.K., Groves, D.I., Marston, R.J. and Barrett, E.M., 1981. Sulfide paragenesis and sulfur mobility in Fe-Ni-Cu sulfide ores at Lunnon and Juan Main shoots, Kambalda: textural and Sulfur isotopic evidence, *Econ. Geol.*, 76, 1675-1685.

Shima, H. and Naldrett, A.J., 1975. Solubility of sulfur in an ultramafic melt and the relevance of the system Fe-S-O, *Econ. Geol.*, 70, 960-967.

Stamoulis, K., 1990. Observations on the formation of the chromitite bodies of the Xerolivado mine (in Greek), *EL.SI. S.A.*, Unpubl. internal report, 184 pp.

Δελτίο της Ελληνικής Γεωλογικής Εταιρίας, τόμος L, σελ. 2057-2067
Πρακτικά 14ου Διεθνούς Συνεδρίου, Θεσσαλονίκη, Μάιος 2016

Bulletin of the Geological Society of Greece, vol. L, p. 2057-2067
Proceedings of the 14th International Congress, Thessaloniki, May 2016

GEOCHEMICAL CHARACTERISTICS OF THE ERENLERDAGI VOLCANICS, KONYA, CENTRAL TURKEY

Uyanık C.[1] and Koçak K.[2]

[1]*N. Erbakan University, 54124, Konya, TURKEY, cuyanik@konya.edu.tr*

[2]*Selcuk University Konya, TURKEY, kkocak@yahoo.com, kkocak@selcuk.edu.tr*

Abstract

Late Miocene to Pliocene volcanism produced lava domes with mafic microgranular enclaves (MMEs), nuée ardentes and pyroclastic fall and flow (ignimbrites) deposits in the WSW and NW of Konya city. All samples are predominantly high K-calc alkaline in composition but calc-alkaline and shoshonitic composition also exist. The felsic volcanics are mainly dacite, andesite, basaltic trachyandesite and rare trachyandesite in compositon. But, the MMEs have basaltic andesite and andesite compositon. SiO_2 increases with decreasing TiO_2, FeOt, MgO and CaO, suggesting fractional crystallization of mafic minerals. All samples have fractionated chondrite-normalised REE pattern (La/Yb_N: 6.7-18.1), and negative Eu anomaly (Eu/Eu: 0.67-0.89), indicating plagioclase fractionation. In primitive mantle-normalized spider diagram, the samples show an enrichment in large ion litophile elements (LILE) such as Cs and Ba, and depletion in high field strength elements (HFSE), e.g. Dy and Y. They show negative Nb, Ta and Ti anomalies, indicating a subduction signature for their genesis.*

Based on geochemical data, the volcanics are suggested to have been formed by Assimilation-Fractional Crystallization (AFC) and/or magma mixing process. Various geotectonic diagrams imply volcanic arc to post collisional setting for the samples.

Keywords: *Erenlerdağı, volcanism, enclave.*

1. Introduction

The collision of Eurasian and Arabian plates along the Miocene thrust front caused deformation of the Anatolian plate, determines the beginning of the Neotectonic period, which shortened the Eastern Anatolia and is followed by the formation of the East and North Anatolian faults. The Anatolian block begins to move to the west along these two major faults (McKenzie, 1972; McKenzie and Yilmaz, 1991). Intensive volcanic activity developed in Turkey during the Neotectonic period, producing volcanic rocks covered an area of about 85,000 km^2 in East, Central and West Anatolia (Ketin, 1983).

In Central Anatolia, calc-alkaline volcanic units cover large areas located in the WSW and NW of Konya city (Figure 1), in where transtensive and transpressive tectonic regimes have been effective since the Late Miocene (Kempler and Garfunkel, 1991). Keller *et al.* (1977), suggests that volcanism had been active from Late Miocene 11.9 Ma. to Pliocene 3.35 Ma. A limited number of studies related to the Konya volcanics have been done (Ota and Dincel, 1975; Keller *et al.*, 1977; Ulu *et al*., 1994; Temel *et al*., 1996; Kurt *et al*., 2003).

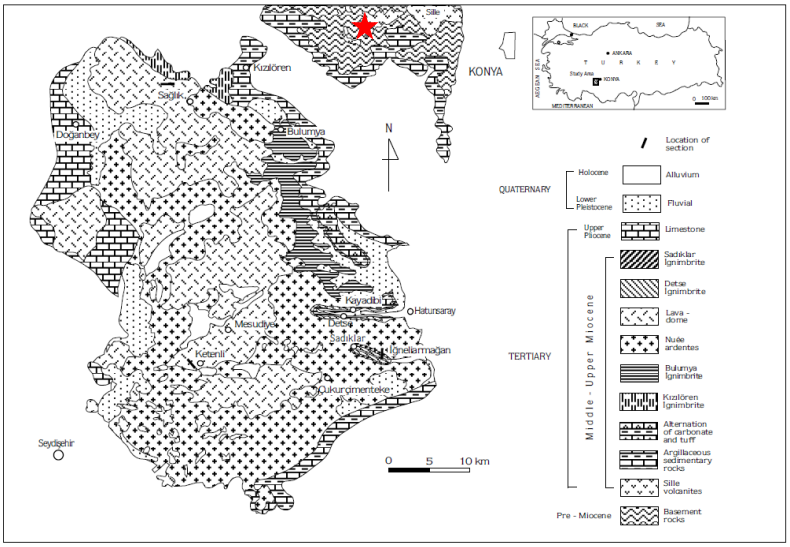

Figure 1 - Location and geological map of the study area (modified from Keller *et al*., 1977)

★ : sill.

The volcanics form as lava domes, sill, nue´e ardentes and ignimbrite deposits. It is aimed to explain the origin of magmas in the Konya region, with new data obtained from the sill.

Pre- Miocene basement is represented by phyllite, schist, quartzite and dolomitic limestone, metavolcanic rocks, diorite, diabase, gabbro, peridotite and serpentinite (Özcan *et al*., 1990; Eren, 1993; Kurt, 1994). It is unconformably overlain by Upper Miocene-Lower Pliocene aged Ulumuhsine formation (Eren, 1993), which is made up by limestone, limestone-mudstone alternation, marl, bands of chert and trace fossils- bearing limestone. The pyroclastic rocks, which consist of volcanic breccia, agglomerate, tuffite and tuffs, conformably overlaid the Ulumuhsine formation. The youngest volcanic rocks are andesite, dacite, and basaltic andesite. Lower Pliocene aged Yürükler formation overlies unconformably volcanic rocks, and contains red conglomerate, red and caliche nodulled mudstone deposites. All these lithologies are overlined unconformably by the Upper Pliocene- Holocene Topraklı formation with conglomerate, and caliche nodulled mudstone formation.

2. Materials and Methods

Twenty one samples were analyzed to determine contents of major oxides, trace and rare earth elements (REE) by ICP-MS at ACME Analytical laboratories in Canada, and fourteen of which are presented in Table 1, with analyses of various volcanic samples in previous studies (Tables 2-5).

2.1. Geochemistry

In an AFM ternary diagram (Figure 2a), the samples clearly define a calc-alkaline trend. The samples are concentrated on high K calc-alkaline series (Figure 2b), but some samples were also found on shoshonite, particularly sill samples, and calc-alkaline areas in a SiO2 vs K2O diagram. The felsic samples are predominantly dacite and andesite, and rare trachyandesite in composition though the sill samples have basaltic trachyandesite composition (Figure 3a). MMEs are however mostly basaltic andesite and andesite in composition. The SiO2 increases with decreasing TiO2, FeOt, MgO, CaO, Ni and Co, suggesting fractional crystallization of pyroxene (±olivine), ilmenite and magnetite (not shown). Primitive mantle normalized spider trace element diagram of the samples from Sağlık lava domes, Takkeli tepe volcanics and sill (Figure 3b) are characterized by an enrichment in large ion litophile elements (LILEs), particularly Cs and Ba, and depletion in high field strength elements

(HFSEs). The rocks show progressively decreasing negative Nb, P and Ti anomalies, which are typical of subduction related magmas (Pearce, 1983). Chondrite-normalized REE patterns (Figure 4a) for the three rock groups usually exhibit a strongly fractionated REE pattern with high LREE/ HREE for the rocks. The samples are LREE enriched with (Ce / Sm) N=2.77-3.04, which are similar to those of subduction-related magmas (Pearce 1982, 1983). The more fractionated and LREE-enriched character of the volcanic rocks indicates that the evolution of the rocks involved continental crust (Watters and Pearce, 1987). Plagioclase fractionation is evident from the slight development of a negative Eu anomaly (Eu/Eu*) N:= 0.84-0.90. Figure 4 b-c shows that the samples have mostly volcanic arc geotectonic setting, but some samples have also post collisional setting.

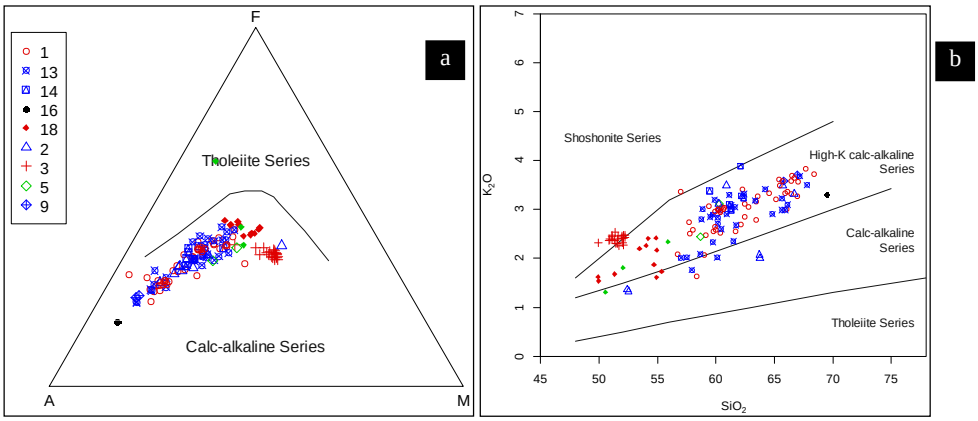

Figure 2 - a) AFM classification of the samples (Irvine and Baragar, 1971) b) SiO_2 vs K_2O diagram of the samples (after Peccerillo and Taylor, 1976).

Symbols; 1: Sağlık lava domes, 2: Takkeli tepe volcanics (Kurt *et al.*, 2003), 3: sill, 5: two-pyroxene andesite, 9: Kızıloren ignimbrite (Temel *et al.*, 1996), 13: Nueerdant (Temel *et al.*, 1996), 14: Erenkaya ignimbrite (Temel *et al.*, 1996), 16: Sille lava dome (Temel *et al.*, 1996), 18: MMEs.

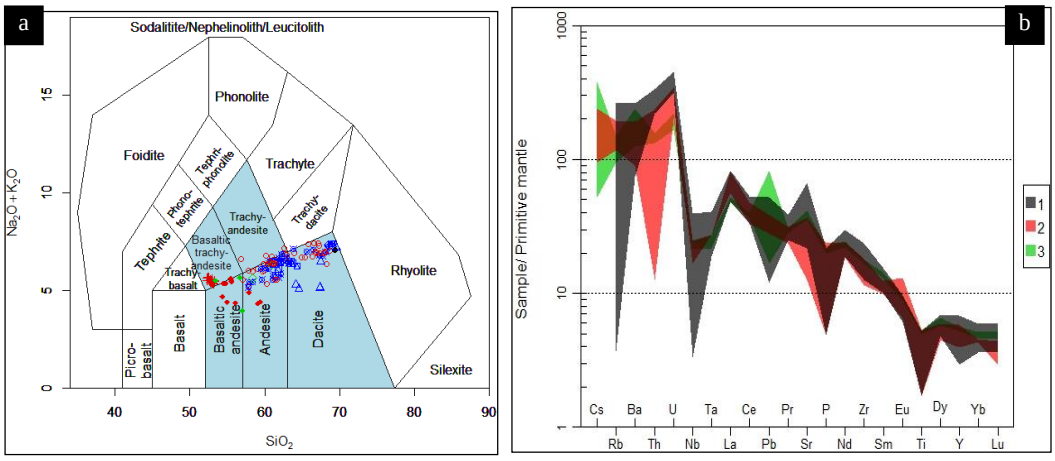

Figure 3 - a) Total alkaline vs SiO2 diagram (Middlemost, 1994) of the samples. b) Primitive mantle normalized spider trace element diagram (McDonough and Sun, 1995) of the Sağlık lava domes (1), Takkeli tepe volcanics (2) and sill (3).

The symbols are as in Fig.2.

Table 1 - Geochemical analyses of the sill samples.

Sample	S2A	S4	T1.1	T1.4	S2B	S5	F2	T1.5	S6	T2.7	F3	T2.2	T2.8	T2.5
SiO2	49.95	50.83	50.95	51.1	51.34	51.44	51.56	51.63	51.71	51.96	52.04	52.09	52.21	52.23
TiO2	1.06	1.04	1.07	1.06	1.06	1.05	1.04	1.04	1.03	1	1.04	1.01	1	1.04
Al2O3	15.92	15.52	15.51	15.37	15.64	15.63	15.48	15.08	15.56	14.93	15.45	15.01	14.7	14.96
Fe2O3	6.67	8.17	7.3	7.67	7.8	7.82	7.9	7.76	7.57	8.09	7.58	8.22	8.37	8.21
MgO	3.86	7.35	5.8	5.52	7.19	7.3	7.27	6.35	7.22	7.1	7.13	7.27	6.98	7.11
CaO	11.9	8.36	10.63	10.49	8.46	8.57	8.28	9.95	8.68	9.16	8.6	8.94	9.17	9.23
Na2O	3.08	2.96	3.11	3.04	3.02	3	2.95	2.93	2.97	2.82	3.07	2.88	2.82	2.93
K2O	2.32	2.37	2.39	2.47	2.37	2.3	2.31	2.46	2.26	2.42	2.32	2.47	2.43	2.47
P2O5	0.42	0.42	0.43	0.44	0.42	0.41	0.42	0.44	0.42	0.42	0.42	0.42	0.43	0.43
MnO	0.11	0.13	0.12	0.14	0.13	0.13	0.13	0.13	0.12	0.14	0.13	0.14	0.14	0.14
LOI	4.3	2.4	2.3	2.3	2.1	1.9	2.2	1.8	2	1.5	1.8	1.1	1.3	0.8
Sum	**99.6**	**99.62**	**99.63**	**99.64**	**99.61**	**99.61**	**99.61**	**99.62**	**99.58**	**99.59**	**99.61**	**99.61**	**99.62**	**99.6**
Ni	79	106	114	99	113	99	108	82	107	80	104	76	83	78
Co	27	29	37	30	29	30	30	30	29	30	30	31	30	31
Pb	9	3	5	8	12	5	6	8	6	4	6	3	4	3
Rb	61	75	73	79	74	60	72	82	59	90	61	88	88	90
Sr	775	748	821	748	745	742	701	765	789	736	756	747	726	770
Ba	1583	846	898	941	849	862	864	919	1079	904	830	921	899	952
Hf	4.8	4.3	5.3	5.3	4.3	4.6	5	5.3	5.1	5	4.8	5.2	4.8	5
Nb	15.6	15.5	15.9	14.4	15.5	15.7	16	14.6	15.3	14.1	15.7	14.3	14.4	15.3
Ta	0.9	0.9	0.9	0.9	1	0.8	1	0.8	0.9	0.8	0.9	0.9	0.8	0.8
Th	11.4	10.6	10.9	11	11.2	11.7	11	12	11.4	10.9	11	11.6	12.1	12.5
U	4	3.5	3.8	3.9	3.7	3.9	3.6	4	3.4	4	3.7	4	4.2	4
Zr	184.6	179.1	184.5	179.6	179.5	180.6	177.3	183.3	176.9	181.3	177	183.7	175.1	186.3
Y	23.9	23.2	23.1	23	22.7	23.4	22.7	23.3	23.1	23.8	23.2	23.6	23.3	24.1
Cs	7.1	7.1	1.1	2.2	6.4	7.1	5.8	3.2	6.6	4.8	8	4.7	5.1	4.8
La	32.5	31.4	31.2	31.1	31.8	33.1	32.5	31.9	32.5	31.6	32.1	32.4	31.6	33
Ce	64.9	63	64.3	63.5	63.4	65.9	64.7	63.9	63.5	63.7	63.2	66.5	64.3	66.4
Pr	7.41	7.18	7.36	7.37	7.31	7.51	7.37	7.44	7.37	7.43	7.34	7.6	7.35	7.79
Nd	29.8	28.6	29	30	29	29.3	29.3	28.8	28.5	27.8	29.9	30.2	28.4	29.8
Sm	5.37	5.49	5.48	5.42	5.19	5.43	5.35	5.46	5.24	5.32	5.26	5.66	5.31	5.74
Eu	1.42	1.45	1.44	1.41	1.39	1.44	1.4	1.44	1.4	1.4	1.36	1.44	1.41	1.48
Gd	4.74	4.54	4.5	4.7	4.5	4.72	4.47	4.77	4.65	4.69	4.55	4.74	4.59	4.63
Tb	0.73	0.73	0.75	0.75	0.73	0.75	0.74	0.74	0.74	0.75	0.72	0.76	0.74	0.77
Dy	4.16	4.08	4.09	4.11	3.88	4.44	4.14	3.9	4.09	4.16	4.11	4.33	4.02	4.1
Ho	0.81	0.8	0.82	0.8	0.82	0.8	0.82	0.82	0.8	0.85	0.81	0.83	0.77	0.79
Er	2.36	2.27	2.4	2.25	2.2	2.34	2.37	2.35	2.41	2.32	2.38	2.32	2.29	2.35
Tm	0.34	0.33	0.34	0.34	0.34	0.37	0.36	0.33	0.35	0.34	0.36	0.35	0.32	0.35
Yb	2.17	2.11	2.14	2.17	2.14	2.17	2.16	2.05	2.28	2.2	2.28	2.16	2.13	2.17
Lu	0.31	0.32	0.32	0.33	0.32	0.35	0.34	0.32	0.34	0.32	0.34	0.33	0.31	0.34

Table 2 - Results of the geochemical analyses of the samples from the Sağlık lava domes (Kocak and Zedef, 2016)

Samp.	1B	2C	3B	4B	5B	7B	8B	9C	11B	40B	41B	42B	43B	44B	46B	47B
SiO2	66.11	59.9	67	64.57	65.75	65.44	65.39	59.76	66.46	60.18	60.35	60.69	60.38	60.67	60.15	59.89
TiO2	0.45	0.8	0.45	0.47	0.47	0.47	0.48	0.83	0.43	0.8	0.79	0.79	0.78	0.79	0.8	0.83
Al2O3	15.52	15.91	15.23	15.43	15.39	15.15	15.24	16.07	15.54	16.94	17.07	16.64	16.53	16.8	16.94	16.97
Fe2O3	3.76	6.3	3.68	3.74	3.78	3.84	3.95	6.27	3.57	6.11	5.99	5.95	6.12	6.04	6.01	6.19
MgO	1.61	3.37	1.58	1.54	1.7	1.56	1.73	3.33	1.42	2.54	2.45	2.39	2.51	2.38	2.61	2.69
CaO	3.73	5.26	3.44	4.73	4.1	4.48	4.01	5.38	3.51	5.93	5.77	5.68	5.88	5.77	5.78	6.04
Na2O	3.39	2.73	3.26	3.22	3.27	3.26	3.23	2.84	3.19	3.39	3.39	3.3	3.33	3.33	3.4	3.34
K2O	3.37	2.64	3.57	3.34	3.58	3.49	3.62	2.56	3.58	2.99	2.97	3.04	2.94	3	3.01	2.96
P2O5	0.17	0.13	0.16	0.17	0.18	0.18	0.18	0.16	0.16	0.25	0.24	0.24	0.25	0.26	0.25	0.25
MnO	0.08	0.13	0.07	0.1	0.08	0.1	0.1	0.12	0.07	0.11	0.11	0.1	0.11	0.11	0.11	0.11
LOI	1.6	2.6	1.3	2.4	1.4	1.8	1.8	2.4	1.8	0.4	0.5	0.9	0.8	0.5	0.6	0.4
Sum	**99.75**	**99.79**	**99.75**	**99.75**	**99.75**	**99.75**	**99.75**	**99.74**	**99.75**	**99.64**	**99.65**	**99.67**	**99.66**	**99.66**	**99.65**	**99.65**
Ni	3.4	2.1	3.2	3	3.4	3.2	3.5	2.6	3.2	2	1.9	2.4	2.6	2.3	1.8	1.9
Co	6.7	12.2	7.7	8.7	8.4	7.3	7.7	14.3	8	14.6	13.7	12.8	14	14.7	13.8	14.1
Hf	4	4	4.1	3.5	4.7	4.1	4.8	4.3	4.2	3.9	5	4.5	4.4	5.2	5.2	4.1
Nb	13.9	12.8	14.6	14.1	15	14.1	13.4	12.2	13.3	12.5	13.5	13.1	12.1	12.6	13.8	11.4
Rb	125.9	93.4	130.5	115.2	131.6	122.7	130.4	99.6	135.3	92.3	91.9	95.5	94.4	96.9	93	90.3
Ba	1024	490	1027	984	1015	980	988	621	981	1151	1103	1055	1120	1176	1134	1087
Sr	529.2	524.9	501.8	514.5	503.7	541	479.4	577.4	518.8	949.5	906.7	858.2	906.4	878.4	900.7	925.6
Pb	3.2	5.4	3.5	2.4	2.8	3.5	2.5	5	7.8	2.3	1.9	1.8	1.8	1.9	2	2.1
Zn	27	35	23	30	31	25	26	39	35	19	15	17	20	18	16	14
Ta	1.3	1	1.5	1.1	1.4	1.2	1.3	1	1.2	1	0.7	1.2	1	1	0.9	0.9
Th	23.3	20.4	26.8	23.7	26.7	24.4	24.6	17.7	25.7	21.2	21.3	20.7	22	22.3	21.3	20.7
U	7.7	6.3	8.8	7.7	9	8.9	9	7.3	8.1	6.6	6.3	6.3	6.2	6.5	6.5	6.4
Zr	151.2	133.7	166.7	143.6	168.6	155.5	170.3	146.1	157.6	173.2	168.1	164.1	174.5	175.2	170.2	164.5
Y	17.5	21.2	18.5	18.6	19.1	18.2	18.6	23.2	17.8	23.9	24.9	21.6	22.1	25.1	21.9	22.8
La	42.5	31.6	46.9	42.8	46.6	44.1	41.4	32	42.1	49.1	51.4	46	49	53	51.4	49.8
Ce	71.5	56.7	80.9	75.2	82	76.9	72	58.8	73	86.4	84.6	83.1	84.4	86.7	88.4	85
Pr	7.3	6.32	8.32	7.83	8.47	7.96	7.56	6.49	7.38	9.6	9.35	9	9.26	9.75	9.51	9.41
Nd	28.6	23.7	26.8	26.9	29.8	26.8	25.8	23.9	27.3	37.1	33.8	34.6	34.1	35.5	35.5	36.3
Sm	4.41	4.25	4.48	4.41	4.79	4.09	4.7	4.48	4.2	5.94	5.54	5.71	5.78	6.16	5.82	5.69
Eu	1.04	1.1	0.97	0.97	1.03	0.96	0.97	1.02	0.95	1.42	1.37	1.38	1.42	1.49	1.45	1.4
Gd	3.88	4.07	4.22	4.14	4.49	3.86	4.09	4.32	3.64	5	5.07	4.95	5.3	5.22	5.08	5.08
Tb	0.54	0.64	0.59	0.56	0.6	0.57	0.58	0.68	0.53	0.7	0.7	0.67	0.72	0.77	0.7	0.73
Dy	3.3	3.71	3.76	3.46	3.21	3.43	3.47	4.18	3.3	3.84	3.93	4.15	3.58	4.68	3.62	3.79
Ho	0.6	0.88	0.58	0.56	0.65	0.64	0.68	0.84	0.56	0.8	0.86	0.69	0.79	0.98	0.81	0.77
Er	1.96	2.32	2.03	1.92	1.91	1.74	1.92	2.63	1.91	2.23	2.74	1.98	2.29	2.36	2.49	2.42
Tm	0.27	0.4	0.27	0.29	0.29	0.34	0.3	0.33	0.26	0.31	0.37	0.31	0.36	0.38	0.32	0.36
Yb	1.6	2.2	1.99	1.69	1.87	1.88	1.77	2.12	2	2.31	1.91	2.23	2.21	2.59	2.23	2.3
Lu	0.29	0.41	0.33	0.31	0.33	0.29	0.28	0.39	0.25	0.32	0.33	0.32	0.3	0.35	0.33	0.39

Table 3 - Results of the geochemical analyses of the samples from MMEs (Kocak, 2016; Temel *et al*., 1998).

Samples	Kocak, 2016											Temel *et al.*, 1998		
	5A	**8A**	**4A**	**42A**	**43A**	**41A**	**1A**	**40A**	**2A**	**47A**	**9A**	**KO-39**	**KO-50**	**KO-53**
SiO2	49.92	49.95	51.33	53.46	54.02	54.19	54.71	54.88	54.93	54.94	55.35	55.89	52.06	50.54
TiO2	0.81	0.8	0.9	1.17	1.14	1.11	0.93	1.11	0.89	1.13	0.87	0.83	0.86	0.76
Al2O3	14.66	14.79	15.4	17.59	17.53	17.94	16.19	17.69	16.17	17.73	16.1	16.24	16.4	14.31
Fe2O3	6.23	6.2	7.22	8.54	8.37	8.16	7.4	8.18	7.1	8.08	6.69	7.33	8.41	8.61
MgO	3.5	3.65	4.24	3.79	3.9	3.08	4.31	3.49	4.2	3.44	4.01	4.57	4.13	1.09
CaO	11.93	10.91	8.06	7.91	7.98	7.21	6	7.61	5.3	7.74	5.72	7.79	9.82	9.39
Na2O	2.68	2.45	2.29	3.05	3.02	3.05	2.76	3.12	2.41	3.23	2.38	3.23	3.54	2.2
K2O	1.62	1.54	1.68	2.2	2.26	2.41	1.87	2.42	1.61	2.17	1.73	2.34	1.81	1.31
P2O5	0.17	0.16	0.2	0.28	0.27	0.3	0.16	0.27	0.17	0.29	0.17	0.27	0.27	0.24
MnO	0.37	0.4	0.23	0.13	0.13	0.13	0.18	0.12	0.18	0.13	0.15	0.123	0.193	0.17
LOI	7.8	8.9	8.2	1.5	0.9	2	5.2	0.7	6.8	0.7	6.5	0.98	1.87	0.83
Sum	99.74	99.75	99.72	99.58	99.55	99.58	99.71	99.58	99.73	99.58	99.73	99.59	99.36	99.25
Ni	2.2	1.4	2.3	2.6	2.9	2.2	2.9	2.4	2.8	2.1	2.4	10.8	19.1	184.5
Co	14.4	13.6	15.8	21.9	21.2	20.6	16	21.3	15.5	20.1	15.2	34.4	27.6	46.9
Pb	4.4	2.7	5.5	2.9	2.6	2.9	5.4	2.5	6.1	2.9	6.9			
Rb	57.3	47.9	57.2	62.2	65	70.5	66.6	71	50.4	63.5	52.2	62.2	51.5	25.9
Sr	615.3	548.6	577.1	1213	1221	1222	635.5	1207	495.9	1249	541.5	1195	637.7	1162
Hf	3.6	2.4	3.2	4.1	3.6	4.8	3.2	3.9	3.3	4.3	3.6			
Nb	8.7	7.6	9.1	11.6	11.8	11.9	10.2	10.3	8.4	13.6	8.1	9.2	14.7	5.3
Ta	0.7	0.4	0.5	0.5	0.6	0.7	0.5	0.9	0.5	0.8	0.6			
Th	8.5	7.5	7.3	14.4	16.2	16.4	8	15.7	8.9	16.2	9			
U	8.3	3	3.5	3.8	5	4.5	4.3	4.5	2.8	5.4	2.8	175.5	153.9	164.4
Zr	128.7	113.3	125.2	148.7	152.7	156.5	116.8	149.2	115	151.7	124	150	113.5	127.6
Y	23.3	20.3	24.2	24.9	25.1	28.4	23.2	22.8	18.9	23.8	20.2	21.1	30.5	16.4
La	25.8	24.6	28.4	47.3	49.1	53.7	25.7	46.2	22.8	49.2	25.4			
Ce	46.6	43.6	53.2	81.8	86.8	91.4	50	85.3	45.9	87.4	48.1			
Pr	5.39	5.25	6.29	9.8	10.11	10.73	5.87	9.82	5.25	10.28	5.66			
Nd	22.7	23.3	26.6	40.6	39.7	38.7	21.6	32	19.3	37.9	23.2			
Sm	4.12	4.01	4.84	6.68	6.87	6.76	4.62	6.66	4.27	6.73	4.57			
Eu	1.11	1.04	1.27	1.67	1.59	1.83	1.26	1.71	1.11	1.65	1.01			
Gd	3.99	3.58	4.68	5.36	6.09	6.19	4.4	5.63	3.89	5.65	4.48			
Tb	0.63	0.6	0.72	0.82	0.82	0.83	0.69	0.81	0.59	0.81	0.65			
Dy	4.09	3.52	4.28	4.23	4.47	5.09	4.04	4.23	3.37	4.16	3.76			
Ho	0.79	0.79	0.91	0.89	0.8	1	0.89	0.92	0.71	0.82	0.72			
Er	2.28	2.14	2.62	2.68	2.82	2.96	2.61	2.49	2.13	2.52	2.33			
Tm	0.3	0.29	0.34	0.39	0.36	0.39	0.42	0.4	0.32	0.35	0.31			
Yb	2.13	1.87	2.34	2.38	2.64	2.26	2.6	2.36	2.09	2.68	2.17			
Lu	0.38	0.3	0.35	0.34	0.35	0.33	0.4	0.32	0.32	0.35	0.34			

Table 4 - Results of the average geochemical analyses of the samples ignmbrite, Nue´e ardentes, two pyroxene andesites, Sille lava dome (Temel *et al*., 1998).

	Lava domes		Kızıloren Ignimbrite		Nue´e ardentes		Erenkaya Igni.		Two pyrx. Andes.		Sille
Sample	ave.	std(26)	ave.	std (n:2)	ave	std (n:34)	Aver.	Std(7)	Ave.	Std(n:2)	
SiO2	62.0	3.60	66.4	0.58	61.4	2.9	61.4	0.92	59.5	0.81	69.5
TiO2	0.6	0.19	0.4	0.00	0.7	0.2	0.7	0.06	0.8	0.09	0.5
Al2O3	16.5	0.76	15.6	0.25	16.5	0.6	16.5	0.59	16.3	0.03	16.9
Fe2O3	5.4	1.41	3.0	0.00	5.5	1.3	5.5	0.52	6.3	0.60	1.9
MgO	4.0	7.74	1.0	0.02	2.5	0.8	2.2	0.46	3.7	0.47	0.7
CaO	5.5	1.50	3.3	0.01	5.4	1.2	5.2	0.40	7.0	0.76	3.4
Na2O	3.5	0.29	3.4	0.03	3.4	0.3	2.9	0.47	3.2	0.02	3.8
K2O	4.5	7.87	3.6	0.06	2.8	0.5	3.3	0.29	2.8	0.34	3.3
P2O5	0.2	0.07	0.2	0.01	0.2	0.1	0.2	0.02	0.2	0.00	0.2
MnO	0.5	1.92	0.1	0.00	0.1	0.0	0.2	0.25	0.1	0.01	0.0
Cr2O3	0.0	0.00	0.0	0.00	0.0	0.0	0.0	0.00	0.0	0.00	0.0
LOI	2.8	9.86	2.4	0.12	1.0	0.6	1.9	0.81	0.7	0.29	1.0
Sum	**99.9**	**0.64**	**99.3**	**0.78**	**97.1**	**15.2**	**99.8**	**0.51**	**100.1**	**0.79**	**101.1**
Nl	12	7	6	0	11	4	9	2	49	30	5
Ba	1057	268	990	95	987	247	950	97	759	15	957
Co	19	8	26	1	20	6	17	5	23	3	11
Ga	18	1	18	0	22	27	17	0	17	1	22
Nb	14.6	5.7	24.9	0.1	14.2	3.9	13.1	1.6	12.2	0.7	13.3
Rb	91.0	29.5	131.6	8.1	90.6	20.3	123.7	19.7	96.1	17.8	122.2
Sr	791.1	238.5	771.7	13.6	845.5	768.5	591.9	36.5	515.5	19.5	468.8
V	104.8	43.9	35.0	1.1	103.5	39.6	77.3	9.8	126.8	21.7	73.7
Zr	178.7	25.4	158.9	0.3	164.2	17.1	178.3	7.2	160.7	18.3	174.9
Y	21.7	3.3	15.2	0.8	22.2	3.4	22.4	1.6	21.8	1.7	23.9

Table 5 - Results of the geochemical analyses of the samples from Takkeli tepe volcanics (Kurt *et al.*, 2003).

sample	M1	M2	M3	M4	M5	M6	M7	M8	M9	M10
SiO2	63.73	63.79	52.52	52.40	63.39	60.26	60.90	66.70	65.72	65.94
TiO2	0.34	0.35	1.03	1.07	0.58	0.60	0.68	0.56	0.44	0.42
Al2O3	16.84	16.80	15.34	15.46	15.59	16.35	*16.5*	14.64	16.13	15.75
Fe2O3	3.47	3.50	7.73	7.78	4.50	5.82	5.0	4.14	3.72	3.67
MgO	1.39	1.40	6.4S	6.55	2.01	2.87	2.5	1.74	1.44	1.42
CaO	3.71	3.82	8.7S	8.9	4.7	*6*	5.10	4.45	.3.86	3.85
Na2O	2.82	2.86	2.82	2.96	3.14	3.10	3.13	3.10	3.29	3.26
K2O	2.07	2	1.32	1.36	3.39	3.12	3.49	3.32	3.49	3.6S
P2O5	0.11	0.10	0.47	0.49	0.17	0.21	0.20	0.19	0.15	0.14
MnO	0.06	0.06	0.14	0.16	0.07	0.08	0.08	0.07	0.07	0.07
LOI	5.2	5	2.4	2.46	2.2	1.60	2.2	0.9	1.5	1.6
Sum	**99.74**	**99.68**	**99.78**	**99.59**	**99.74**	**99.99**	**99.78**	**99.81**	**99.81**	**99.80**
Ni	6	6	98	99	15	14	*10*	9	5	6
Ba	35	36	49	51	28	50	55	32	23	26
Rb	18	18	18	18	19	17	17	16	20	20
Sr	11	11	16	16	12	11	12	13	14	13
Hf	7.2	7	30	30	8	13	6	8	8	8
Nb	4.1	4	2	2	3	3	3.1	*5*	4	4.2
Ta	88	88	70	70	103	110	100	84	111	117
Th	2	2	2	2	2	3	2	1	1	2
U	251	252	730	735	613	620	565	625	555	552
Zr	5	5	4	4	6	*5*	6	6	7	7
Y	58	60	150	155	78	70	*75*	71	43	49
La	2	2	1	1	*2*	2	2	2	2	2
Ce	134	134	174	174	135	190	155	122	165	154
Pr	19	19	24	25	20	23	20	17	20	19
Nd	49.0	50.0	37.0	37.0	*36.0*	42.0	39.0	37.0	42.0	52.0
Sm	75.0	75.0	60.0	60.0	*55.0*	60.0	80.0	57.0	64.0	79.0
Eu	7.0	7.0	7.0	7.0	6.0	6.0	6.3	6.0	7.0	8.0
Gd	28.0	28.0	30.0	30.0	*25.0*	25.0	25.0	23.0	27.0	30.0
Tb	4.0	4.0	5.0	5.0	4.0	4.0	4.0	4.0	4.0	5.0
Dy	1.0	I	*2.0*	2.0	I	1.0	1.0	1.0	1.0	1.0
Ho	4.0	4.0	5.0	5.0	4.0	4.0	4.0	4.0	4.0	4.0
Er	1.0	I	1.0	1.0	0.6	0.5	0.6	0.5	0.6	0.6
Tm	3.0	3.0	4.0	4.0	3.0	3.0	3.0	3.0	3.0	3.0
Yb	0.6	0.6	1.0	1.0	0.7	0.6	0.7	0.5	0.6	0.6
Lu	2.0	2.0	2.0	2.0	1.7	1.7	1.8	1.5	1.8	1.7

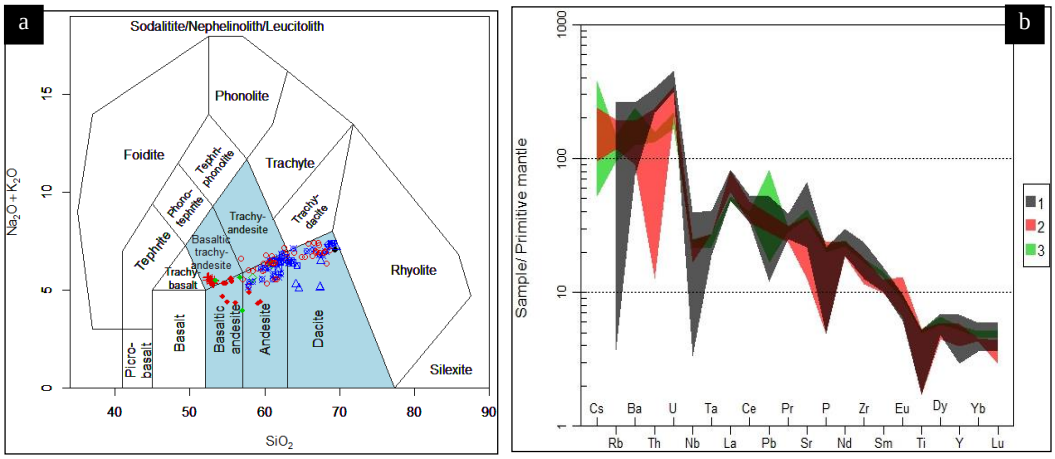

Figure 4 - a) Total alkaline vs SiO2 diagram (Middlemost, 1994) of the samples. b) Primitive mantle normalized spider trace element diagram (McDonough and Sun, 1995) of the Sağlık lava domes (1), Takkeli tepe volcanics (2) and sill (3).

The symbols are as in Fig.2

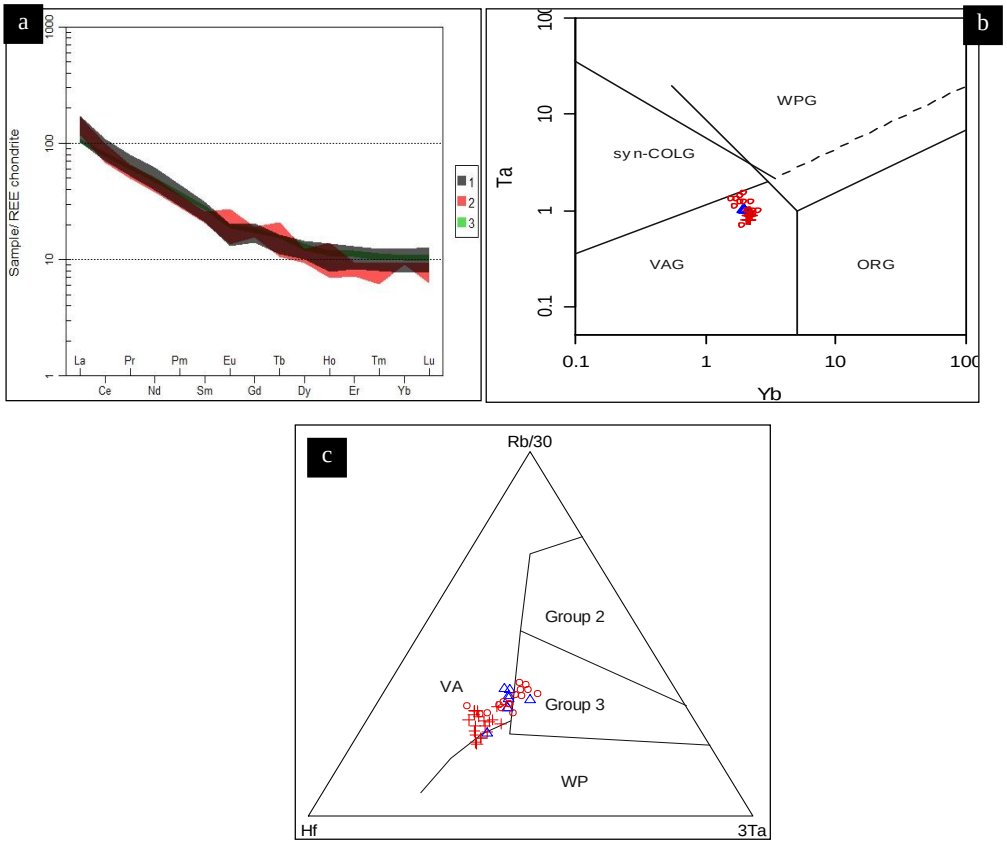

Figure 5 - a) Chondrite normalized REE pattern of the Sağlık lava domes (1), Takkeli tepe volcanics (2) and sill (3). Normalized values are from Boynton, 1984. b) Ta vs Yb diagram (after Pearce *et al.*, 1984) c) Hf-Rb/30-Ta*3 (Harris *et al.*, 1986).

Group 2: syncollisional, Group 3: Post collisional, WP: Within plate, The symbols are as in Fig.2.

3. Discussions and Conclusions

Fractional crystallization is evident in the the Harker variation diagrams and chondrite normalized REE diagrams (negative Eu anomaly). However, presence of MMEs in volcanics proposes mafic-felsic interaction and mingling (Barbarin and Didier, 1992; Kocak, 2006) by injection hot mafic magma injected into felsic magma. Dusty zone on the plagioclase phenocryst rims and reverse zoning in plagioclases (Temel *et al.*, 1998) strong enrichments in incompatible elements e.g., Rb, Sr, Ba and K_2O also support this suggestion. Combined AFC and/or magma mixing between mantle-derived magmas and crustal components are proposed for the Erenlerdagi volcanics by Temel *et al.* (1998).

The samples are characterized by high K_2O (1.32-3.83 wt.%), Rb (2-157 ppm), Ba (490-1715 ppm), K_2O/Na_2O (0.5 -1.2) and FeO_t/MgO (0.94-8.00) ratios, which is comparable to Andean type andesites series developed in relation with a subduction event. The samples have mostly High-K calc-alkaline in composition, which is typical of continental orogenic regions. Accordingly, Large ion lithophyle elements e.g., K, Rb, Ba, Sr, and Zr, are high in orogenic series (Gill, 1981). In various geotectonic diagrams, volcanic arc is dominated, but there is a tendency from Volcanic arc to Post collisional area. Existence of shoshonitic sill samples may indicate a change of the compressional regime into an extensional one. Similarly, the trachytic rocks formed in Anatolia such as Galata Galatia Volcanic Province, and Oglakci (Sivrihisar, Eskisehir) area are postulated to be formed in the extensional tectonic regime (Temel, 2001). The volcanics have relatively high Rb/Y (0.1-9.7), and low Nb/Y (0.17-1.7) ratios, indicating a subduction zone enrichments or by crustal contamination, as Rb is enriched giving elevated Rb/Nb ratios. Within-plate type enrichments induce development of Nb/Y(~1) ratio (Edwards *et al.*,1991).

4. Acknowledgments

Thanks to Selcuk University (BAP, Konya/Turkey) Research Fund for the financial support of the study.

5. References

Barbarin, B. and Didier, J., 1992. Genesis and Evolution of Mafic Microgranular Enclaves through Various Types of Interaction between Coexisting Felsic and Mafic Magmas, *Transactions of the Royal Society of Edinburgh-Earth Sciences*, 83,145-153.

Boynton, W.V., 1984. Cosmochemistry of the rare earth elements: meteorite studies. *In*: Henderson, P., *ed*., *Rare earth elements*, Elsevier, 63-114.

Edwards, C., Menzies, M. and Thirlwall, M., 1991. Evidence from Muriah, Indonesia, for the inter play of supra-subduction zone and intraplate processes in the genesis of potassic alkaline m agmas, *Journal of Petrolo*gy, 32, 555-592.

Eren, Y., 1993. Eldes - Derbent - Tepeköy - Söğüttözü (Konya) arasinin jeolojisi, Doktora Tezi, 5. Fen Bilimleri Enstitüsü, Konya, 224 s. (yayinlanmamis).

Harris, N.B.W., Pearce, J.A. and Tindle, A.G., 1986. Geochemical characteristics of collision-zone magmatism. *In:* Collision tectonics, Coward, M.P. and Ries, A.C., *eds*., *Geological Society (of London)*, Special Publication, 19, 67-81.

Gill, J.B., 1981. Orogenic Andesites and Plate Tectonics. Springer, Berlin, 390 pp.

Irvine, T.N. and Baragar, W.R., 1971. A guide to the chemical classification of the common igneous rocks, *Canadian Journal of Earth Sciences*, 8, 523-548.

Keller, J., Jung, D., Burgath, K. and Wolf, F., 1977. Geologie und petrologie des Neogenen kalkalkali-vulkanismus von Konya (Erenler Dağ-Alaca Dağ-Massiv Zentral-Anatolian), *Geo. Jb. B*, 25, 37-117.

Kempler D. and Garfunkel Z., 1991. The northeast Mediterranean triple junction from a plate kinematics point of view, *Bull. Tech. Univ*., Istanbul, 44, 203-232.

Ketin, İ., 1983, Türkiye Jeolojisine Genel Bir Bakış, *Istanbul Technical Univercity Publications*, Istanbul, 595 pp.

Kocak, K., 2006. Hybridization of mafic microgranular enclaves: mineral and whole-rock chemistry evidence from the Karamadazi Granitoid, Central Turkey, *International Journal of Earth Sciences*, 95(4), 587-607.

Kurt, H.K., Özkan, A.M. and Koçak, K., 2003. Geology, Petrography and Geochemistry of the Subduction Related Volcanic Rocks, West of Konya, Central Anatolia, *Geological Bulletin of Turkey*, 46(2), 39-51.

Kurt, H., 1994. Petrography and geochemistry of Kadinhani (Konya) area, Central Turkey, PhD th esis, Glasgow University (unpublished), UK, 191 pp.

McDonough, W.F. and Sun, S.-S., 1995. Composition of the Earth, *Chemical Geology*, 120, 223-253.

McKenzie, D. and Yılmaz, Y., 1991. Deformation and volcanism in Western Turkey and the Aege an, *Bulletin of Technical University*, İstanbul, 44(1/2), 344-373.

McKenzie, D., 1972. Active tectonics of the Mediterranean region, *Geophys. J. R. Astr. Soc.*, 30, 1 09-185.

Middlemost, E.A.K., 1994. Naming materials in the magma/igneous rock system, *Earth Science Reviews*, 37(1), 215-224.

Ota, R. and Dincel, A., 1975. Volcanic rocks of Turkey, *Bull. Geol. Survey of Japan*, 26, 19(393)-45(419).

Özcan, A., Göncüoglu, M.C., Turhan, N., Sentürk, K., Uysal, S. and Isık, A., 1990. Konya- Kadınhan ı-Ilgın dolayının temel jeolojisi, *M.T.A. Rapor.*, No: 9535 (in Turkish, unpublished).

Pearce, J.A., 1982. Trace element characteristics of lavas from destructive plate boundaries, 525-548, *In*: Thorp, R.S., *ed*., *Andesites: Orogenic Andesites and Related Rocks*, John Wiley and Sons, New York, 724 pp.

Pearce, J.A., Harris, N.B.W. and Tindle, A.G., 1984. Trace element discrimination diagrams for the tectonic interpretation of granitic rocks, *Journal of Petrology*, 25, 956-983.

Pearce, J.A., 1983. Role of the sub-continental lithosphere in magma genesis at acrive continental margins, 230-249, *In*: Hawkesworth, C.J. and Norry, M.J., *eds*., *Continental Basalts and Mantle Xenoliths*, Shiva Publishing Ltd., Cambridge, Mass., 272 pp.

Peccerillo, A and Taylor, S.R. 1976. Geochemistry of Eocene calcalkaline volcanic rocks from the Kastamonu area, northern Turkey, *Contrib. Mineral Petrol.*, 58, 63-81.

Temel, A., Gündoğdu, M.N. and Gourgaud, A., 1998. Petrological and geochemical characteristics of Cenozoic high-K calc-alkaline volcanism in Konya, Central Anatolia, Turkey, *J. Volcanol. Geotherm. Res.*, 85, 327-354.

Temel, A., 2001. Post-collision Miocene alkaline volcanism in the Oglakçi Region, Turkey: petrology and geochemistry, *International Geology Review*, 43, 640-660.

Ulu, Ü., Bulduk, A.K., Ekmekçi, E., Karakafl, M., Öcal, H., Arbas, A., Saçlı, L, Taşkıran, A., Adir, M., Sözeri, Fi. and Karabıyıkoğlu, M., 1994. İnlice-Akkise ve Cihanbeyli-Karapınar Alanının Jeolojisi, *Maden Tetkik ve Arama Genel Müdürlüğü Rapor,* 9720, 219 pp. (in Turkish; unpublished).

Watters, B.R. and Pearce, J.A., 1987. Metavolcanic rocks of La Ronge domain in the Churchill Province, Saskatchewan: geochemical evidence for a volcanic arc origin, *Geol. Soc. Lond.*, 33, 167-182.

Δελτίο της Ελληνικής Γεωλογικής Εταιρίας, τόμος L, σελ. 2068-2078
Πρακτικά 14ου Διεθνούς Συνεδρίου, Θεσσαλονίκη, Μάιος 2016

Bulletin of the Geological Society of Greece, vol. L, 2068-2078
Proceedings of the 14th International Congress, Thessaloniki, May 2016

MN-ANDALUSITE, SPESSARTINE, MN-GROSSULAR, PIEMONTITE AND MN-ZOISITE/CLINOZOISITE FROM TRIKORFO, THASSOS ISLAND, GREECE

Voudouris P.[1], Graham I.[2], Mavrogonatos K.[1], Su S.[2], Papavasiliou K.[3], Farmaki M.-V.[1] and Panagiotidis P.[1]

[1]Department of Mineralogy and Petrology, Faculty of Geology and Geoenvironment, National and Kapodistrian University of Athens, voudouris@geol.uoa.gr, kmavrogon@geol.uoa.gr,mbfarmaki@yahoo.gr, parispanagiotidis@yahoo.gr

[2]School of Biological, Earth and Environmental Sciences, University of New South Wales, Sydney, NSW 2052 Australia, i.graham@unsw.edu.au, z3308907@zmail.unsw.edu.au

[3]Department of Economic Geology & Geochemistry, Faculty of Geology and Geoenvironment, National and Kapodistrian University of Athens, kpapavas@geol.uoa.gr

Abstract

Mylonitized manganiferous schists and calc-silicate layers intercalated within amphibolite- to greenschist facies mica schists from the Trikorfo area (Thassos Island, Greece), host an unusual Mn-rich paragenesis of metamorphic silicate minerals, most of them in large, gemmy crystals. The silicates occur both in layers subparallel to the foliation and within discordant veins cross-cutting the metamorphic fabric. Piemontite (up to 12.7 wt. % Mn_2O_3), Mn-rich epidote (up to 7.8 wt. % Mn_2O_3), Mn-rich andalusite (up to 15.6 wt. % Mn_2O_3), Mn-poor pink clinozoisite-epidote (up to 0.87 wt. % Mn_2O_3), Mn-poor pink zoisite (up to 0.21 wt. % Mn_2O_3), spessartine (up to 47.7 wt. % MnO) and Mn-rich grossular (up to 3.6 wt. % MnO) are associated with diopside, hornblende, phlogopite, muscovite, tourmaline, hematite and iron-bearing kyanite. The studied assemblages are indicative of high fO_2 conditions due to the presence of highly-oxidized pre-metamorphic Mn-rich mineral associations. They developed during prograde metamorphism of a Mn-rich sedimentary protolith(s), followed by re-equilibration to post-peak metamorphic conditions, vein formation and metasomatism during retrograde metamorphism accompanying the exhumation of the Thassos Island during the Oligocene-Miocene. Alternatively, the skarn-similar mineralogy of the calc-silicate layers could have been formed by fluids released by granitoids during contact metamorphism. The studied area represents a unique mineralogical geotope. Its geological-mineralogical heritage should be protected through establishment of a mineralogical-petrological geopark that will also promote sustainable development of the area.

Keywords: *Mn-andalusite (viridine), Mn-zoisite (thulite), spessartine, geotope, Thassos Island.*

Περίληψη

Μυλωνιτιωμένοι πλούσιοι σε μαγγάνιο σχιστόλιθοι και ασβεστοπυριτικά στρώματα που απαντούν ως ενδιαστρώσεις εντός αμφιβολιτικής έως πρασινοσχιστολιθικής φάσης μεταμόρφωσης μαρμαρυγιακούς σχιστόλιθους στο Τρίκορφο της Θάσου,

χαρακτηρίζονται από μία ασυνήθιστη Mn-ούχο παραγένεση μεταμορφικών ορυκτών τα περισσότερα από τα οποία σε ιδιαίτερα μεγάλους κρυστάλλους και σε ποικιλία πολύτιμων λίθων. Τα Mn-ούχα πυριτικά ορυκτά απαντούν τόσο σε στρώσεις παράλληλα με την φύλλωση όσο και σε φλέβες που τέμνουν τη μεταμορφική δομή. Τα ορυκτά πιεμοντίτης (έως 12.7 % κ.β. Mn_2O_3), Mn-ούχο επίδοτο (έως 7.8 % κ.β. Mn_2O_3), Mn-ούχος ανδαλουσίτης (έως 15.6 % κ.β. Mn_2O_3), φτωχός σε Mn ροζ κλινοζοϊσίτης/επίδοτο (έως 0.87 % κ.β. Mn_2O_3), φτωχός σε Mn ροζ έως κόκκινος ζοϊσίτης (έως 0.21 % κ.β. Mn_2O_3), σπεσσαρτίνης (έως 47.7 % κ.β. MnO) και Mn-ούχος γροσσουλάριος (έως 3.6 % κ.β. MnO), συνοδεύονται από διοψίδιο, κεροστίλβη, φλογοπίτη, μοσχοβίτη, τουρμαλίνη, αιματίτη και σιδηρούχο κυανίτη. Η παραγένεση που μελετήθηκε είναι ενδεικτική υψηλών τιμών πτητικότητας του οξυγόνου λόγω της παρουσίας προϋπάρχουσας έντονα οξειδωτικής προ-μεταμορφικής ορυκτολογικής παραγένεσης πλούσιας σε μαγγάνιο. Σχηματίσθηκε κατά την πρόδρομη μεταμόρφωση ιζηματογενών πρωτόλιθων πλούσιων σε Mn, με ακόλουθη επανισσορόπηση απο τις μέγιστες συνθήκες πίεσης και θερμοκρασίας, σχηματισμό φλεβών και μετασωμάτωσης κατά την ανάδρομη μεταμόρφωση που συνόδευσε την ανάδυση της Θάσου στο Ολιγόκαινο-Μειόκαινο. Εναλλακτικά, η προσφορά ρευστών από γρανιτοειδή κατά την διάρκεια μεταμόρφωσης επαφής δεν πρέπει να αποκλειστεί. Η περιοχή μελέτης αντιπροσωπεύει μοναδικό ορυκτολογικό Γεώτοπο. Η γεωλογική-ορυκτολογική αυτή κληρονομιά μπορεί να προστατευθεί μέσω της ίδρυσης ενός Γεωπάρκου που θα συμβάλλει επιπλέον και στην προώθηση φιλικής προς το περιβάλλον ανάπτυξης της Θάσου.
Λέξεις κλειδιά: *Mn-ανδαλουσίτης (βιριδίνης), Mn-ζοϊσίτης (θουλίτης), σπεσσαρτίνης, γεώτοπος, Θάσος.*

1. Introduction

Greece hosts several sites containing manganiferous minerals that formed in metamorphic environments, such as the Mn-rich metasediments of Andros and Evia islands (Reinecke, 1986), the high P/T Mn-bearing meta-conglomerates from northern Syros Island (Altherr *et al*., 2013) and the Mn-bearing meta-skarn on Paros Island (Paraskevopoulos, 1958). The Trikorfo area, Thassos Island, is characterized by an unusual manganiferous mineralogical assemblage hosted within metamorphic rocks of the Rhodope Massif, first described by Zachos (1982), and consist of piemontite, braunite, spessartine, dravite, thulite, epidote, kyanite, staurolite, titanite and hematite. Dimitriadis (1989) reported on the presence of pink pleochroic manganoan epidote in mica schists, as well as, biotite-muscovite-kyanite-sillimanite bearing schists, thus limiting peak metamorphic conditions to 600-650 °C at 4-7 kbar. Voudouris (2005) and Voudouris *et al*. (2006, 2012, 2013), described in some detail the mineralogy and mineral-chemistry of the above manganiferous minerals and other silicates from Trikorfo (kyanite, tremolite, tourmaline, chlorite, etc) and reported on the discovery of Mn-rich andalusite ((better known as viridine) in the area occurring within piemontite-spessartine schists and quartz veins as deep emerald-green-colored crystals up to 7cm. The Mn-andalusite, spessartine and thulite from Trikorfo are of world class museum quality, and can be considered as potential gemstones (Voudouris *et al*., 2012). The aim of the current study is to present new data on the manganiferous silicate association(s) of Trikorfo, to describe the mineralogical and mineral-chemical characteristics and discuss the role of various mechanisms in their formation through comparison it with other similar assemblages from elsewhere.

2. Geology

Thassos Island consists mainly of Permo-Carboniferous orthogneisses and marbles intercalated with amphibolites and metapelites interpreted as members of the Southern Rhodope Core Complex, and display an intense, penetrative top-to-the-southwest shearing under amphibolite and greenschist facies conditions (Brun and Sokoutis, 2007). The island comprises three dominant rock units from base to top, separated by two SW-dipping low-angle normal fault systems (Wawrzenitz and Krohe,

1998; Brun and Sokoutis, 2007): (1) a lower unit, consisting mainly of marbles with intercalations of paragneisses and micaschists; (2) an intermediate unit consisting of orthogneisses, marbles with intercalations of paragneisses, mica-schists and amphibolites and (3) an upper unit, dominated by migmatites and gneisses. Two major tectonic events affected the above mentioned lithologies: a compressional phase (of pre-Mid-Eocene age) resulted in the thrusting of the gneisses and migmatites on top of the intermediate unit and an extensional ductile to brittle event that took place from 26-24 to 12 Ma, creating a NE-trending stretching lineation, foliated fabric and widespread boudinage formation (Wawrzenitz and Krohe, 1998; Brun and Sokoutis, 2007; Kounov *et al*., 2015). Rb-Sr and U-Pb dating by the above authors revealed a continuous cooling history of the ductile metamorphic rocks from 700°C to 300°C from 26 to 12 Ma.

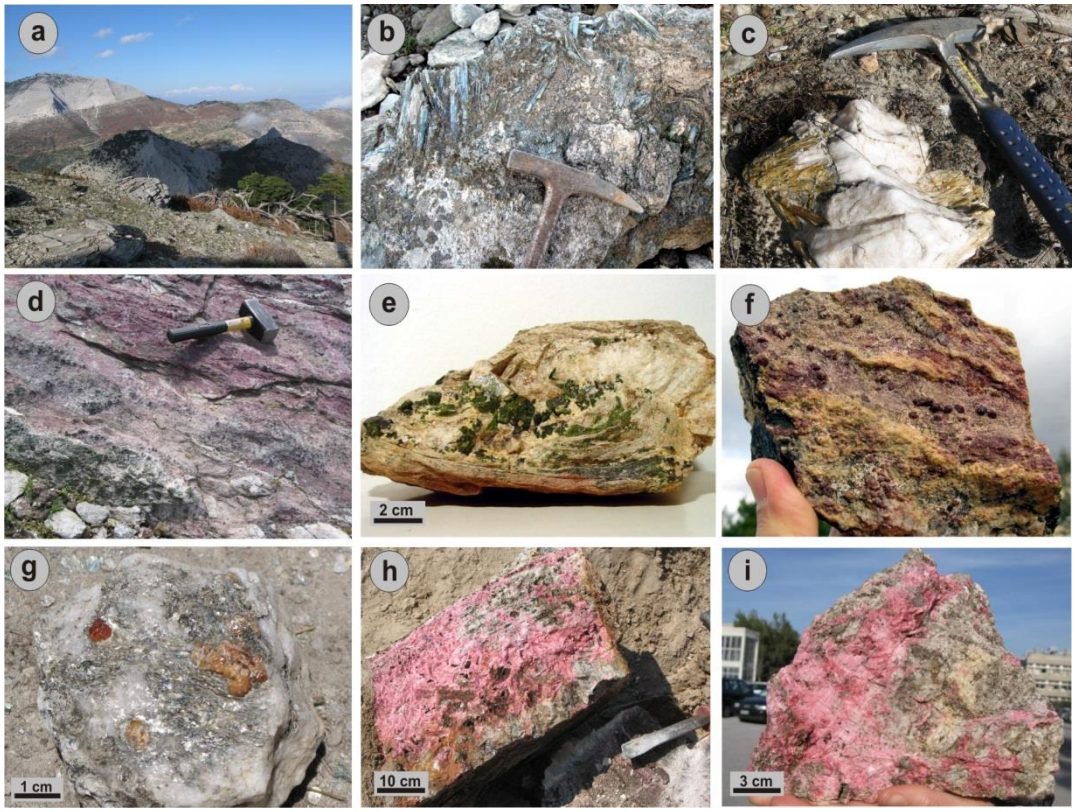

Figure 1 - (a) Panoramic view of the Trikorfo area, Thassos Island. (b) Blue kyanite crystals from quartz-feldspar lenses within mica schists. (c) Orange kyanite in quartz lense. (d) Outcrop of piemontite (purple) and Mn-andalusite (green) bearing schists. (e) Mn-andalusite crystals in quartz-feldspar lense. (f) Spessartine from piemontite-spessartine assemblage. (g) Gemmy spessartine with muscovite in quartz. (h,i) Mn-zoisite crystals with grossular and quartz from calc-silicate layers hosted within the mica schists.

The study area at Trikorfo is located along the major SW-dipping low-angle normal detachment zone (e.g. reactivated thrust) separating the lower from the intermediate unit at Thasos (Fig. 1a). Mica schists and orthogneisses predominate and tectonically overlay the marbles of Theologos (e.g. lower unit; Fig. 1a). Kyanite-sillimanite micaschists which are close to the main shear zone have formed in P-T conditions of 5.5±1.5 kbar and 600±50°C and bear signs of incipient partial melting contemporaneous with the ductile fabric that is related to extensional deformation (Brun and Sokoutis, 2007). Quartz lenses within the mica schists mostly contain blue kyanite crystals, but in some cases green, yellow and orange kyanite are present (Fig. 1b, c), along with uncommon zoned kyanite crystals with dark blue cores and yellow-green rims. Piemontite-andalusite-muscovite, piemontite-spessartine-braunite-

and kyanite-spessartine-muscovite schists are intercalated within the kyanite-bearing mica schists (Fig. 1d). Quartz- and quartzofeldspathic lenses inside the schists contain large crystals of Mn-andalusite, spessartine and piemontite (Fig. 1e to g). Calc-silicate layers (up to 80 cm wide) intercalated within the kyanite-bearing mica schists are mainly composed (from an outer band adjacent to host mica schists towards the centre of the layer) of tremolitic hornblende, diopside, quartz, plagioclase, Mn-clinozoisite/epidote, grossular, titanite and Mn-zoisite (Figs 1h, i and 2a). An orthogneiss exposed in the area is composed of orthoclase, plagioclase (oligoclase-andesine) along with biotite, quartz, hematite, epidote and allanite and is surrounded by a transitional zone with the same mineralogy as the above mentioned calc-silicate layers (e.g. amphibole, plagioclase, Mn-clinozoisite/epidote from granitoid outwards; Fig. 2b, c). Allanite is an accessory mineral of the orthogneiss and is associated with andesine, epidote and biotite (Fig. 2d).

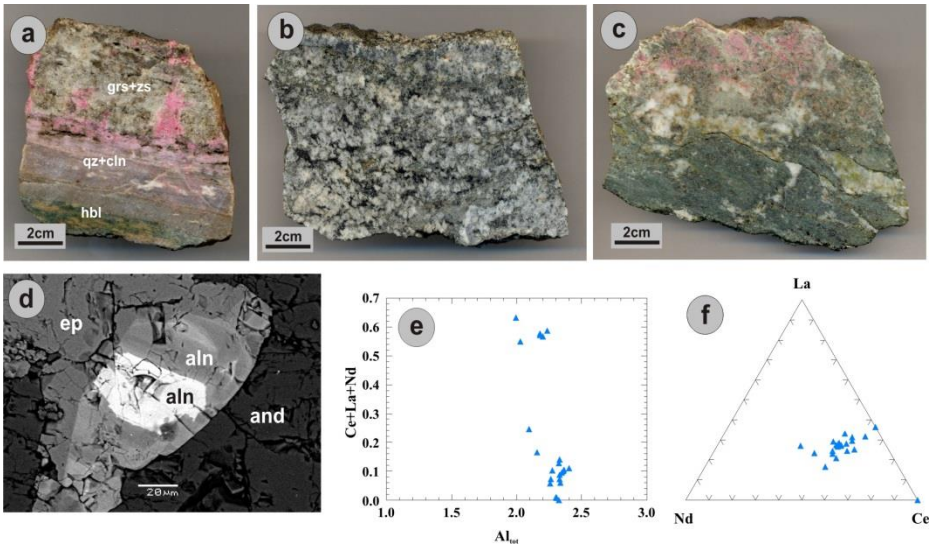

Figure 2 - (a) Hand-specimen of calc-silicate layer demonstrating mineralogical zonation with a tremolitic hornblende (hbl), diopside and plagioclase rich zone proximal to the mica schist, grading into a quartz- pink clinozoisite/epidote (qz+cln) zone and then into a Mn-grossular – Mn-zoisite (grs+zs) zone in the centre of the layer. (b) Hand-specimen of mylonitized orthogneiss consisting of biotite and feldspars, sample GA6. (c) Hand-specimen from the transitional zone between the orthogneiss and the mica schists, consisting of tremolitic hornblende, feldspar, quartz, green epidote and Mn-poor pink epidote/clinozoisite, sample GA7, 7a. (d) Photomicrograph (BSE-image) showing chemically-zoned allanite (aln) in association with epidote (ep) and andesine (and), sample GA6. (e) REE (Ce+La+Nd) vs Al_{tot} plot of the analysed allanite and REE-poor epidote from the previous sample, demonstrating negative correlation between Al^{3+} and REE^{3+}. (f) Ternary La-Nd-Ce plot demonstrating chemical variation of analysed allanites.

3. Materials and Methods

Twenty five thin and polished sections from 11 representative samples (TH1-8, GA6, GA7, GA7a) of Mn-rich minerals and their host rocks were studied in detail by optical microscopy. Sample TH1, TH2 and TH3 are calc-silicate rocks consisting of grossular, Mn-clinozoisite/epidote, Mn-zoisite, tremolitic hornblende and quartz. Sample TH4 is spessartine-piemontite-braunite-hornblende schist. Sample TH5 is piemontite-Mn andalusite-muscovite schist. Sample TH6 represents quartz lenses inside mica schists including green epidote. Sample TH7 consists of blue kyanite and TH8 represents quartz lenses with orange kyanite. Sample GA6 is an orthogneiss. Samples GA7, GA7a are from the transitional zone between the orthogneiss and the surrounding metapelites. A total of fifteen thin-and-polished

sections were studied by scanning electron microscopy using a Jeol-JSM 5600 SEM equipped with back-scattered imaging capabilities and a Cameca SX 100 wavelength-dispersive electron microprobe, at the universities of Athens and Hamburg, respectively. Operating conditions were as follows: for the Jeol-JSM 5600 SEM, accelerating voltage was 20kV, beam current 0.5nA, time of measurement 50sec and beam diameter 1-2μm; for the Cameca SX 100, accelerating voltage was 20kV, beam current 0.2nA and beam diameter 1μm. In addition, XRD analyses were carried-out using a Siemens (Brooker) 5005 X-ray diffractometer at the University of Athens. Operating conditions were: Cu Kα radiation at 40kV, 40nA and 0.02º step time. The XRD patterns were evaluated using the EVA 10.0 program of the Siemens DIFFRACplus and the D5005 software package.

4. Mineralogy and mineral chemistry

Kyanite in blue, green, yellow to orange coloured crystals up to 20 cm, is found in quartz±feldspar lenses intercalated with the schists (Fig. 1b, c). Orange kyanite also occurs in association with spessartine, biotite (phlogopite), muscovite and oligoclase. Kyanite forms euhedral prisms rimmed by muscovite (Fig. 3a). Microprobe analyses for orange kyanite indicate no Mn_2O_3 and up to 1.07 wt. % Fe_2O_3 in the structural formula, which probably contributes to the coloration of the crystals (Table 1).

Mn-andalusite (formerly Viridine) in dark green-colored euhedral to subhedral crystals up to 7cm is found in piemontite mica schists or quartz-feldspar lenses (Fig. 1d, e). Mn-andalusite also occurs in massive quartz lenses in association with muscovite, and in kyanite-muscovite schists, where it replaces orange kyanite. In andalusite-piemontite schists the viridine is associated with piemontite and quartz (Fig. 3b), or with plagioclase (anorthite), phlogopite and muscovite (Fig. 3c), or with spessartine and muscovite (Fig. 3d) and accompanies opaque Mn-oxides. Microprobe data revealed relatively elevated Mn_2O_3 contents, up to 15.55 wt. %, corresponding up to 0.351 apfu (Table 1). The substitution of Al^{3+} by Mn^{3+} in the mineral formula is demonstrated in Figures 4a,b.

Spessartine and Mn-grossular are usually found (a) in "piemontite"-spessartine-braunite-quartz and spessartine-muscovite-quartz lenses intercalated within andalusite-piemontite-spessartine schists and within mica schists respectively (Fig. 1f,g), (b) in the andalusite-piemontite-spessartine schists and (c) in the calc-silicate layers consisting mainly of Mn-clinozoisite/epidote, Mn-zoisite and Mn-grossular (Figs 1h, i and 2a). Spessartine and Mn-grossular are also found in fissure veins crosscutting the above lithologies and were described in a previous study (Voudouris *et al*., 2010). Within the "piemontite"-spessartine-braunite-quartz aggregates, the spessartine commonly forms large euhedral crystals with numerous inclusions of piemontite and is surrounded by piemontite and magnesio-hornblende (Fig. 3e). Spessartine from the andalusite-piemontite-spessartine schists is also associated with muscovite, phlogopite, anorthite and hematite. Spessartine from quartz-muscovite lenses within mica schists forms translucent, orange-coloured, gem-quality euhedral crystals up to 1 cm. Electron microprobe analyses of spessartine indicate MnO contents in the range of 37.75.12 - 47.7 wt. % (Table 1). Mn-bearing grossular from the calc-silicate layers, forms euhedral yellowish crystals of gem-quality in close association with pink to red coloured Mn-zoisite and quartz (Figs. 1i, 2a and 3h,i). MnO content ranges from 1.92 to 3.60 wt. % (Table 1). All data are plotted in the ternary Mn-Ca-Fe diagram (Fig. 4c).

Epidote group minerals are represented in the study area by the Mn-bearing minerals piemontite, red-purple Mn-epidote, pink to red Mn-clinozoisite/epidote, typical green epidote and allanite. Electron microprobe analyses are presented in Table 1 and all data are plotted in Figures 2 and 4d.

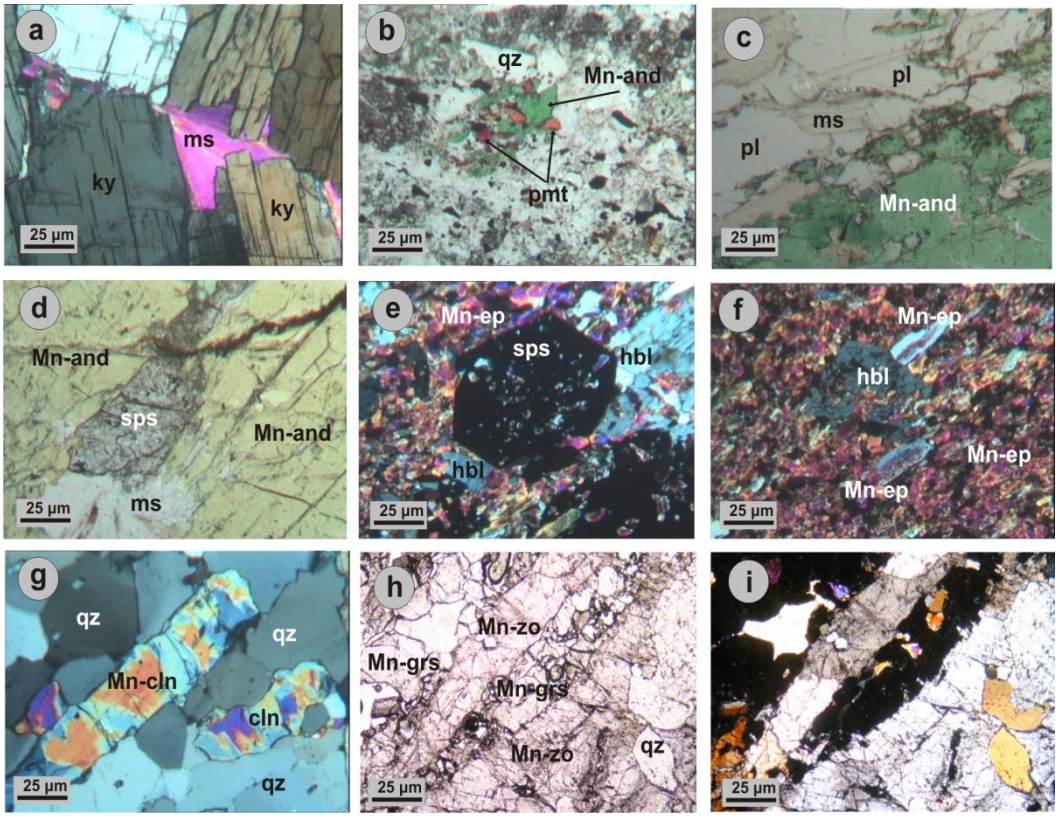

Figure 3 - Photomicrographs demonstrating mineralogical assemblages from the studied area. (a) kyanite (ky) in association with muscovite (ms), sample TH8, # nicols. (b) piemontite (pmt) and Mn-andalusite (Mn-and) set in a fine-grained matrix dominated by quartz (qz), sample TH5, // nicols. (c) Mn-andalusite in association with plagioclase (pl) and muscovite, sample TH5, // nicols. (d) Mn andalusite associated with spessartine (sps) and muscovite, sample TH5, // nicols. (e) spessartine associated with Mn-rich epidote (Mn-ep) and magnesio-hornblende (hbl) from "piemontite"-spessartine-braunite-quartz aggregates, sample TH4, # nicols. (f) Magnesio-hornblende surrounded by Mn-rich epidote, some of which are intensely zoned, sample TH4, # nicols. (g) Mn-poor clinozoisite (Mn-cln) from the intermediate part of the calc-silicate layers, sample TH2, # nicols. (h, // and i, # nicols respectively) typical assemblage of Mn-zoisite (Mn-zo), Mn-grossular (Mn-grs) and quartz from the innermost part of the calc-silicate layers, samples TH3.

Piemontite and **Mn-rich epidote** usually accompany Mn-andalusite, spessartine, quartz, hematite and Mn-oxides in piemontite-spessartine-andalusite mica schists and in "piemontite"-spessartine-braunite-quartz aggregates, respectively (Fig. 1d). Within the piemontite-spessartine-andalusite schists, the piemontite is associated with Mn-andalusite (Fig. 3b).

Mn-rich epidote from the "piemontite"-spessartine-braunite-quartz aggregates occurs with spessartine and magnesio-bearing hornblende (Fig. 3e,f). In both cases piemontite and Mn-rich epidote forms dark purple-coloured prismatic crystals with typical piemontite pleochroism. Microprobe analyses revealed true piemontite (sensu-stricto) for the andalusite-bearing schists with Mn_2O_3 content up to 12.69 wt. % and Mn-rich epidotes for the "piemontite"-spessartine-braunite-quartz aggregates with Mn_2O_3 in the range of 1.9 to 7.8 wt. % (Table 1 and Fig. 4d).

Table 1 - Representative electron microprobe data of Spessartine (1-3), Mn-Grossular (4-6), Piemonite (7-9), Mn-rich epidote (10,11) Mn-Clinozoisite (12-14), Zoisite (15-17), Mn-Andalusite (18-20) and Fe-Kyanite (21). (bd): below detection.

Wt%	1	2	3	4	5	6	7	8	9	10	11	12	13	14	15	16	17	18	19	20	21
SiO_2	35.87	35.71	34.31	39.85	39.70	40.18	36.01	36.51	36.36	37.06	36.73	37.34	37.05	37.17	39.23	39.11	39.42	34.57	34.63	34.26	36.73
Al_2O_3	20.65	20.78	23.40	22.27	22.46	22.65	21.48	20.98	20.89	22.69	25.40	26.83	25.59	26.11	32.71	32.11	32.78	48.26	49.01	48.03	62.92
MgO	1.94	0.31	0.41	bd	bd	bd	0.06	0.07	0.06	0.11	0.06	0.10	0.04	0.05	0.02	0.10	0.01	0.13	0.15	0.13	bd
FeO	0.53	0.08	0.52	0.90	0.87	0.73	-	-	-	-	-	-	-	-	-	-	1.54	-	-	-	-
Fe_2O_3	-	-	-	-	-	-	6.53	6.83	6.32	8.44	10.46	9.28	9.84	10.83	1.55	2.01	-	3.38	2.80	2.79	1.06
MnO	41.12	47.70	44.95	2.46	3.60	1.92	-	-	-		3.63	0.24	-	-	-	-	-	-	-	-	-
Mn_2O_3	-	-	-	-	-	-	12.38	12.12	11.75	6.97	-	-	0.23	0.26	0.15	0.21	0.17	15.26	15.01	15.55	bd
CaO	3.47	0.55	0.93	34.07	33.08	34.43	21.27	21.34	21.56	21.60	21.40	23.78	23.40	23.60	24.78	24.73	24.66	0.01	0.01	bd	bd
K_2O	bd	bd	bd	bd	bd	bd	bd	bd	bd	bd	0.06	0.01	bd	bd	bd	bd	bd	bd	bd	bd	bd
Na_2O	bd	bd	bd	0.09	0.32	0.06	bd	0.01	bd	bd	0.07	bd	bd	bd	bd	bd	bd	bd	bd	bd	bd
TiO_2	0.25	0.09	0.05	bd	bd	bd	bd	bd	bd	0.06	0.06	bd	bd	bd	0.02	0.04	0.05	0.02	0.04	0.02	bd
Total	99.71	100.38	100.07	99.74	100.12	100.08	97.73	97.86	96.94	96.93	95.87	97.28	97.15	98.02	98.44	98.31	98.58	100.11	100.09	99.21	100.71
			24 (O)								8 cations								5 (O)		
Si	5.849	5.880	5.616	6.019	5.985	6.018	3.006	2.969	2.967	2.983	2.913	2.930	2.940	2.924	2.970	2.970	2.920	1.015	1.013	1.015	0.987
Al	3.968	4.032	4.517	3.967	3.984	4.000	2.151	2.006	2.009	2.153	2.374	2.481	2.393	2.420	2.918	2.874	2.920	1.671	1.690	1.678	1.994
Mg	0.471	0.083	0.100	0.000	0.000	0.000	0.008	0.089	0.008	0.014	0.007	0.011	0.005	0.006	0.003	0.011	0.001	0.006	0.007	0.006	0.000
Fe^{2+}	0.073	0.011	0.071	0.120	0.120	0.102	0.418	0.417	0.388	0.000	0.000	0.000	0.000	0.000	0.000	0.000	0.000	0.000	0.000	0.000	0.000
Fe^{3+}	0.000	0.000	0.000	0.000	0.000	0.000	0.000	0.000	0.000	0.512	0.624	0.643	0.647	0.643	0.088	0.115	0.089	0.074	0.062	0.062	0.021
Mn^{2+}	5.103	5.980	5.603	0.308	0.462	0.239	0.000	0.000	0.000	0.000	0.270	0.016	0.000	0.000	0.000	0.000	0.000	0.341	0.334	0.351	0.000
Mn^{3+}	0.000	0.000	0.000	0.000	0.000	0.000	0.800	0.749	0.730	0.475	0.000	0.000	0.016	0.012	0.010	0.014	0.011	0.000	0.000	0.000	0.000
Ca	0.606	0.160	0.163	5.506	5.352	5.540	1.936	1.854	1.886	1.862	1.790	1.999	1.989	1.990	2.010	2.013	1.998	0.000	0.000	0.000	0.000
K	0.000	0.000	0.000	0.000	0.000	0.000	0.000	0.000	0.000	0.000	0.000	0.000	0.000	0.000	0.000	0.000	0.000	0.000	0.000	0.000	0.000
Na	0.000	0.000	0.000	0.034	0.086	0.017	0.000	0.001	0.000	0.000	0.011	0.000	0.000	0.000	0.000	0.000	0.000	0.000	0.000	0.000	0.000
Ti	0.030	0.008	0.006	0.000	0.000	0.000	0.000	0.000	0.000	0.010	0.003	0.000	0.000	0.000	0.001	0.002	0.003	0.008	0.004	0.000	0.000

Mn-poor clinozoisite/epidote occurs in euhedral to subhedral crystals that vary in colour from light pink to red, usually found in the intermediate zone of the calc-silicate layers (Fig. 2a) mostly associated with quartz (Fig. 3g), plagioclase (anorthite-bytownite), titanite, diopside and tremolitic hornblende. Available microprobe data revealed Fe_2O_3 content varying from 1.84-10.83 wt. %, and minor Mn_2O_3 content ranging from 0.02 to 0.87 wt. %.

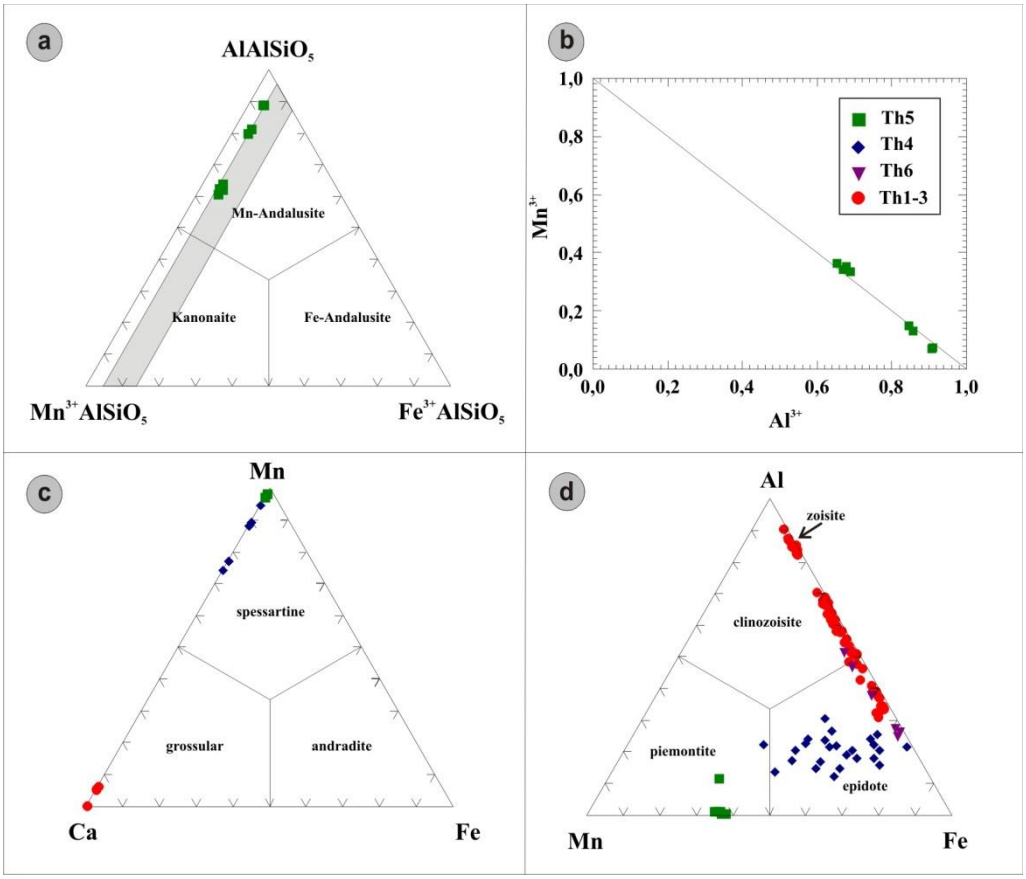

Figure 4 - (a) Compositions of the analysed Mn-andalusite plotted in the ternary Al_2SiO_5-Fe_2O_5-Mn_2SiO_5 diagram. Shaded area demonstrates chemical compositions of andalusite-kannonaite from Novák and Škoda (2007). (b) binary plot demonstrating partial substitution of Al^{3+} by Mn^{3+} in the analysed Mn-andalusite. (c) Compositions of garnets plotted in the ternary Mn-Fe-Ca diagram. (d) Ternary Al-Mn-Fe plot of the analysed epidote-group minerals from the studied area. Al refers to X_{cln}, Mn to X_{pmt} and Fe to X_{ep}. Mn-poor zoisite is also plotted for comparison (based on Franz and Liebscher, 2004, Armbruster *et al.*, 2006).

Mn-poor zoisite (var. thulite) is found in the inner part of the calc-silicate layers, intergrown with Mn-grossular, titanite and quartz, both in the matrix of the rock and in fissures cross-cutting the foliation. It occurs in light pink to red colors and forms translucent subhedral to euhedral crystals up to 10cm (Figs. 1h, i and 2a, 3h, i). Available electron microprobe data revealed low Fe_2O_3 content (1.52-2.00 wt. %) and very low Mn_2O_3 values from 0.15-0.21 wt. %, enough to be responsible for the pink-red coloration (see Discussion).

Green epidote is often formed at the outer margins of the calc-silicate layers and in the orthogneiss and (meta)skarn (Fig 2c, d), along with hornblende and feldspar (andesine). It contains 0.15 to 0.58 wt. % MnO.

REE-bearing epidote and allanite occur as accessory minerals in the orthogneiss and are rimmed by REE-free epidote, in association with andesine, orthoclase and biotite (Fig. 2d). Analytical data revealed that allanite from the Trikorfo area is rich in Ce_2O_3, La_2O_3 and Nd_2O_3 (up to 9.4, 5.1 and 7.2 wt. % respectively) and has relatively poor Al_2O_3 content, as incorporation of trivalent rare earth elements in the A2 (divalent) site is compensated by an increase of Fe^{2+} in the M3 site with concomitant decrease of Al^{3+} (Fig. 2e, f).

Mn-bearing varieties of **diopside** (up to 1.0 wt. % MnO), **tremolitic hornblende** (up to 0.7 wt. % MnO), **magnesio-hornblende** (up to 2.3 wt. % MnO), **phlogopite** (up to 2.2 wt. % MnO) and **chlorite** (up to 1.4 wt. % MnO), accompany the manganiferous association at Trikorfo. Accessory phases include monazite (relatively abundant in discrete layers), sphene and zircon. Tourmaline is very abundant in quartz-feldspar lenses within mica schists, where it occurs in black crystals (var. schorlite) up to 10 cm and is associated with muscovite and chlorite. Olive green-colored tourmaline (crystals up to 3cm) is also present, however these were not analysed in the present study. Tourmaline is also present in fissures intergrown with chlorite, titanite and quartz (Voudouris et al., 2010). Finally, tremolite in white crystals up to 10 cm was observed in sheared marbles.

5. Discussion and Conclusions

Co-existing Al_2SiO_5 polymorphs occur in various metamorphic rocks and formed either during regional metamorphism or a combination of regional and contact metamorphism (Larson and Sharp, 2003; Sepahi *et al*., 2004). The peak metamorphic conditions at Trikorfo are muscovite-sillimanite-kyanite facies, at about 5.5 ±1.5 kbar and 600 ±50°C and occur along the shear zone separating the lower from the intermediate units on the island (Dimitriadis, 1989; Brun and Sokoutis, 2007). Among the studied mineralogical assemblages at Trikorfo, high-medium grade associations include kyanite-garnet-muscovite-biotite-plagioclase and these were retrogressed to lower-grade assemblages (e.g. epidote group minerals, titanite, chlorite, albite) during the exhumation stage of decompression and cooling, in accordance to Dimitriadis (1989) and Wawrzenitz and Krohe (1998). Mn-andalusite might have formed during decompression in veins within host rocks containing kyanite (e.g. Kerrich, 1990).

Field and mineralogical evidence suggest that the zoisite-grossular-bearing calc-silicate layers represent local inhomogeneities in the bedding of the sedimentary protoliths and/or compositional changes that have been produced by metasomatic processes during regional metamorphism, as suggested for similar layers at Therapio, Evros area by Kassoli-Fournaraki *et al*. (1995). In this sense, the mineralogy of the calc-silicate layers could have developed during prograde metamorphism of a Mn-rich, calcareous pelitic protolith, followed by vein formation and metasomatism during retrograde metamorphism accompanying the exhumation of the Thassos Island during the Oligocene-Miocene.

Alternatively, the skarn-similar mineralogy of the calc-silicate layers could have been formed by fluids released by granitoids during contact metamorphism. With the lack of radiometric data, the exact age (e.g. Hercynian?) of the orthogneiss at Trikorfo is not known. Miocene granitoids are not exposed at Thassos Island, however a burried granitoid is considered by Melfos and Voudouris (2016) to be genetically related to the widespread Miocene intrusion-related gold mineralization in the area. Tourmaline at Trikorfo also occurs as a retrograde mineral, and according to van Hinsberg *et al*. (2011) metasomatic introduction of boron on the retrograde path, is most commonly associated with the intrusion of late granites in orogenic belts. This is in accordance to Kassoli-Fournaraki and Michailidis (1994) who stated that the tourmaline-quartz veins formed prior to deformation and metamorphism, but they do not exclude a further retrograde development.

In addition to the calc-silicate layers, the piemontite-andalusite-spessartite-hornblende-hematite in the schists are typical metamorphic mineral assemblages characteristic of highly oxidized pre-metamorphic Mn-rich sedimentary rocks, metamorphosed under amphibolite- to greenschist facies

conditions, as for example at Tanzania, the Hidaka area/ Japan and New Mexico/USA (Meinhold and Frish, 1970; Bonazzi and Menchetti, 2004).

The presence of Mn-bearing andalusite in the studied assemblage indicates very high fO_2 values, as experimentally demonstrated for the incorporation of Mn^{3+} into the andalusite structure (Abs-Wurmbach and Peters, 1999). Electron microprobe analyses of Mn-andalusites from the Trikorfo revealed that Mn_2O_3 can reach up to 15.55 wt. % (0.351 apfu). The Mn^{3+} substitutes for Al^{3+} in the formula of the mineral which corresponds to $(Al,Mn)_2SiO_5$ as also reported by Novák and Škoda (2007). The Mn-poor clinozoisite/epidote and Mn-poor zoisite from the Trikorfo area contain up to 0.9 wt. % Mn_2O_3 which is responsible for their pink to red color, in accordance to Bonazzi and Menchetti (2004) and Franz and Liebscher (2004) that coloration in pink epidotes/clinozoisites is due to Mn^{3+} and not Mn^{2+} in the mineral structure. Future petrographic, isotopic and geochemical studies will help better understand the genetic implications of manganiferous minerals at Thasos Island. Some of these minerals can be considered as gemstones, however, the Trikorfo site is a worldwide unique Geotope that should be protected through integration in a mineralogical Geopark under promotion of sustainable development in the broad area.

6. Acknowledgments

The authors would like to thank Stefanie Heidrich (Institute for Mineralogy and Petrography, University of Hamburg) for the support at the electron microprobe and Peter Stutz (Institute for Mineralogy and Petrography, University of Hamburg) for the preparation of polished thin sections. Finally we greatly thank the reviewers Prof. A. Magganas and Assist. Professor L. Papadopoulou for constructive comments which highly improved the initial manuscript.

7. References

Abs-Wurmbach, I. and Peters, T., 1999. The Mn-Al-Si-O system: an experimental study of phase relations applied to paragenesis in manganese-rich ores and rocks, *Eur. J. Mineral.*, 11, 45-68.

Altherr, R., Soder, C., Panienka, S., Peters, D. and Meyer, H.P., 2013. Pink manganian phengite in a high P/T meta-conglomerate from northern Syros (Cyclades, Greece), *Contrib Mineral Petro*l, 166, 1323-1334.

Armbruster, T., Bonazzi, P., Akasaka, M., Bermanec, V., Chopin, C., Giere, R., Heuss-Assbicheler, S., Liebscher, A., Menchetti, S., Pan, Y. and Pasero, M., 2006. Recommended nomenclature of epidote-group minerals, *Eur. J. Mineral.*, 18, 551-567.

Bonazzi, P. and Menchetti, S., 2004. Manganese in Monoclinic Members of the Epidote Group: Piemontite and Related Minerals, *Rev. Miner. Geochem.*, 56, 495-551.

Brun, J.P. and Socoutis, D., 2007. Kinematics of the Southern Rhodope Core Compex (North Greece), *Int. J Earth Sci*., 96, 1079-1099.

Dimitriadis, E., 1989. Sillimanite grade metamorphism in Thasos island, Rhodope massif, Greece and its regional significance, *Geologica Rhodopica*, 1, 190-201.

Franz, G. and Liebscher, A., 2004. Physical and chemical properties of the epidote minerals - an Introduction, *Rev. Miner. Geochem*., 56, 1-81.

Kassoli-Fournaraki, A. and Michailidis, K., 1994. Chemical composition of tourmaline in quartz veins from Nea Roda and Thasos areas in Macedonia, northern Greece, *Can. Mineral*., 32, 607-615.

Kassoli-Fournaraki, A., Michailidis, K., Zannas, I. and Zachos, S., 1995. Titanite-rich carbonates from the Therapio area in Thrace, Northern Greece: contraints of the mineral assemblage formation, *Schweiz. Mineral. Petrogr. Mitt*., 75, 387-398.

Kerrick, D.M., 1999. The Al_2SiO_5 polymorphs, *Reviews in Mineralogy*, 406 pp.

Kounov, A., Wüthrich, E., Seward, D., Burg, J.P. and Stockli, D., 2015. Low-temperature constraints on the Cenozoic thermal evolution of the Southern Rhodope Core Complex (Northern Greece), *Int. J. Earth Sci*., 104, 1337-1352.

Larson, T.E. and Sharp, Z.D., 2003. Stable isotope constraints on the Al_2SiO_5 "triple-point" rocks from

the Proterozoic Priest pluton contact aureole, New Mexico, USA, *J. Metam. Geol*., 21, 785-798.
Meinhold, K.D. and Frisch, T., 1970. Manganese-silicate-bearing metamorphic rocks from central Tanzania, *Schweiz. Mineral. Petrogr. Mitt*., 50, 493-507.
Melfos, V. and Voudouris, P., 2016. Fluid evolution in Tertiary magmatic-hydrothermal ore systems at the Rhodope metallogenic province, NE Greece, A review, *Geologia Croatica*, 69(1), 157-167.
Novák, M. and Škoda, R., 2007. Mn^{3+}-rich andalusite to kannonaite and their breakdown products from metamamganolite at Kojetice near Trebic, the Moldanubian Zone, Czech Republic. *Journal of Geosciences*, 52, 161-167.
Paraskevopoulos, G., 1958. Die Entstehung der Manganlagerstaetten auf der Insel Paros, Griechenland, *N. Jb. Min. Abh*., 90(3), 367-380.
Reinecke, T., 1986. Phase relationships of sursassite and other manganese-silicates in highly oxidized low-grade metamorphic rocks from Evia and Andros Islands, Greece, *Contrib. Mineral. Petrol*., 94, 110-126.
Sepahi, A.A., Whitney, D.L. and Baharifar, A.A., 2004. Petrogenesis of andalusite-kyanite-sillimanite veins and host rocks, Sanandaj-Sirjan metamorphic belt, Hamadan, Iran, *J. Metam. Geol*., 22, 119-134.
Van Hinsberg, V.J., Henry, D.J. and Dutrow, B.L., 2011. Tourmaline as a petrologic forensic mineral: a unique recorder of its geologic past, *Elements*, 7, 327-332.
Voudouris, P., 2005. Minerals of Eastern Macedonia and Western Thrace: Geological framework and environment of formation, *Bull. Geol. Soc. Greece*, 37, 62-77.
Voudouris, P., Melfos, V. and Katerinopoulos, A., 2006. Precious stones in Greece: Mineralogy and geological environment of formation. Understanding the genesis of ore deposits to meet the demand of the 21st century, 12th Quadrennial IAGOD symposium, Moscow, 6p, CD-ROM volume.
Voudouris, P., Graham, I., Melfos, V., Sutherland, L. and Zaw, K., 2012. Gemstones in Greece: Mineralogy and crystallizing environment, 34th IGC conference, Brisbane, Australia, August 2012.
Voudouris, P., Constantinidou, S., Kati, M., Mavrogonatos, C., Kanellopoulos, C. and Volioti, E., 2013.Genesis of alpinotype fissure minerals from Thasos Island, northern Greece. Mineralogy, mineral chemistry and crystallizing environment, *Bull. Geol. Soc. Greece*, 47, 468-476.
Wawrzenitz, N. and Krohe, A., 1998. Exhumation and doming of the Thasos metamorphic core complex (S Rhodope, Greece): structural and geochronological constraints. *Tectonophysics*, 285, 301-332.
Zachos, S., 1982. Geological map of Greece, Thassos sheet. Scale 1:50000, Greek Institute of Geological and Mining Research, Athens, Greece.

Δελτίο της Ελληνικής Γεωλογικής Εταιρίας, τόμος L, σελ. 2079-2087
Πρακτικά 14ου Διεθνούς Συνεδρίου, Θεσσαλονίκη, Μάιος 2016

Bulletin of the Geological Society of Greece, vol. L, p. 2079-2087
Proceedings of the 14th International Congress, Thessaloniki, May 2016

TOURMALINITE VEINS AND BRECCIAS FROM THE SYMVOLON-KAVALA PLUTON, NORTHERN GREECE: PETROGENETIC PRELIMINARY RESULTS

Xydous S., Magganas A., Pomonis P. and Kokkinakis A.

National and Kapodistrian University of Athens, Department of Geology and GeoEnvironment, Department of Mineralogy and Petrology, 15784, Athens, Greece, stxydous@geol.uoa.gr, amagganas@geol.uoa.gr, ppomonis@geol.uoa.gr

Abstract

A previously undescribed tourmalinite rock consisting of tourmaline-rich veins and breccias occurs within the Lower Miocene Symvolon-Kavala granodiorite pluton, which intrudes the Lower Tectonic Unit of the Rhodope Metamorphic Province. Tourmaline, usually with crypto- to micro-crystalline grain size, is abundant within the matrix of breccias, also forming along with quartz and host rock clasts massive veins and injections in the fractures of the pluton. Field relations indicate that the tourmaline veins and breccias most likely formed in a brittle deformation regime, overprinting the previously developed foliation of the pluton. In addition, mineralogical and textural observations indicate that the precipitation of tourmaline was a result of cooling of B-rich hydrothermal fluids, implying for a possible magmatic-hydrothermal origin for the studied tourmalinite.
Keywords: *Tourmaline, hydrothermal, fluid, metasomatism, cataclasite.*

Περίληψη

Περιγράφεται για πρώτη φορά η παρουσία ενός τουρμαλινίτη με τη μορφή φλεβών και λατυποπαγών που εμφανίζεται μέσα στον Κατω-Μειοκαινικό γρανοδιοριτικό πλουτωνίτη της Καβάλας, ο οποίος διεισδύει στην κατώτερη τεκτονική ενότητα της ζώνης της Ροδόπης. Ο τουρμαλίνης, που συνήθως είναι κρυπτο- ως μικροκρυσταλλικός, είναι άφθονος στην κύρια μάζα των λατυποπαγών, ενώ απαντά ακόμη μαζί με κλάστες χαλαζία και γρανοδιορίτη σε μορφή συμπαγών φλεβών και εγχύσεων μέσα σε ρωγμές του πλουτωνίτη. Με βάση παρατηρήσεις υπαίθρου το σύστημα με τα τουρμαλινικά λατυποπαγή συνήθως διακόπτει την προϋπάρχουσα φύλλωση του πλουτωνίτη, υποδεικνύοντας πιθανή δημιουργία σε καθεστώς εύθραυστης παραμόρφωσης. Επιπρόσθετα, ορυκτολογικές και ιστολογικές παρατηρήσεις οδηγούν στο συμπέρασμα πως η απόθεση του τουρμαλίνη έγινε λόγω της απόψυξης πλούσιων σε βόριο υδροθερμικών ρευστών, υποδεικνύοντας μια πιθανή μαγματική-υδροθερμική προέλευση για τους υπό εξέταση τουρμαλινίτες.
Λέξεις κλειδιά: *Τουρμαλινίτης, υδροθερμικό, ρευστό, μετασωμάτωση, κατακλασίτης.*

1. Introduction

Although tourmaline is a common accessory phase in igneous, metamorphic and sedimentary rocks, it can locally become the main constituent of particular rock-types, such as tourmalinite (e.g., Slack *et al.*, 1984), tourmaline-bearing granite, pegmatite, greisen (e.g.,Trumbull and Chaussidon, 1999),

tourmaline-quartz breccias and breccia pipes within granites (e.g., London and Manning, 1995, Williamson *et al.*, 2000) and metasomatic blackwalls around eclogite knockers within serpentinite mélanges (e.g., Altherr *et al*., 2004; Marschall *et al.*, 2006). Tourmaline can be formed as a magmatic mineral, as a subsolidus phase and as a late hydrothermal mineral, especially at the exocontacts of granitoid plutons. The presence of tourmalines is a marker of high B activity and their chemical composition reflects the character of source rocks and might help to define the origin of the boron (Henry and Guidotti 1985; van Hinsberg *et al.*, 2011a, b).

Tourmalinite, commonly consisting of tourmaline-quartz assemblages, usually forms cross-cutting veins and veinlets as well as pervasive replacements on a very fine scale, so that the smallest features and textures are perfectly preserved. Tourmalinization, is a special kind of alteration, characteristic of W-Sn deposits, which is commonly related to the emplacement and crystallization of peraluminus granitic magmas, with the possibility that the B-enrichment can be derived from a source containing evaporites or tourmaline-rich protolith (Harlov and Austrheim, 2013). Boron in granitic magma, particularly in combination with P and F, increases intensely the solubility of H_2O, and reduces the viscosity of melt. This effects in enhanced partitioning of B into the fluid phase, the incremental solubility of silica in the fluid phase and high hydrostatic pressure during final crystallization (Pollard *et al.*, 1987; London, 2009). The circulation of the released B-rich fluids from the crystallizing granitoid magma, in the contact aureoles causes metasomatic reactions (tourmalinization and silicification) and/or hydrofracturing in both the granite and the host rocks (Müller and Halls, 2005; Dini *et al.*, 2008; Slack and Trumbull, 2011). When the internal pressure of the fluids exceeds the lithostatic load, the hydrofracturing triggers a breccia pipe and stockwork formation, usually associated with Cu, Au, Mo, Zn and Sn ores and barren types, at the apices of granitic bodies (Derham and Feely, 1988; Williamson *et al.*, 2000; Skewes *et al.*, 2003; Dini *et al.*, 2008; Feely *et al.*, 2010). In the hydrofractured zones the solid rocks are fragmented and cemented by minerals crystallizing from the exsolved fluid, forming tourmaline-bearing breccias (Skewes *et al.*, 2003; Müller and Halls, 2005; Dini *et al.*, 2008).

In this study we present juvenile mineralogical and textural data of a previously undescribed system of tourmalinite veins and tourmaline-rich breccias from selected outcrops inside the Symvolon-Kavala granodiorite pluton, Northern Greece. Some preliminary implications for the petrogenesis of these peculiar and rarely found tourmaline-rich rocks are herein also reported.

2. Regional Geology

The Rhodope Metamorphic Province (RMP) is a polymetamorphic geological complex located in northeast Greece to southwest Bulgaria, in the hinterland of the Hellenic Subduction System (Burg *et al.*, 1990; Bonev *et al.*, 2006; Krenn *et al.*, 2010; Jahn-Awe *et al.*, 2010; Nagel *et al.*, 2011). RMP consists of three allochthon tectonic units (Lower, Middle and Upper) and is bordered by Servomacedonian Massif in the west and Circum-Rhodope Belt in the east (e.g. Krohe and Mposkos, 2002; Bonev *et al.*, 2006; Froitzhaim *et al.*, 2014). Several metamorphic core complexes have been recognized in these units. The studied tourmaline-rich rocks of the Symvolon-Kavala pluton are located within the Southern Rhodope Core Complex (SRCC) representing the Lower Tectonic Unit (LTU), which is also named as Pangaeon Unit. The LTU, which comprises massive marbles, micaceous gneisses, mica schists, calc-silicate schists and amphibolites, was metamorphosed up to the upper greenschist / lower amphibolite facies. The Middle and Upper tectonic units have been metamorphosed up to ultra high pressure conditions, while during retrogration migmatization, as well as granulite to amphibolite and greenschist facies assemblanges formed.

Cenozoic igneous activity in the Rhodope is represented by Oligocene to Miocene volcanic rocks and Upper Eocene to Middle Miocene plutonic rocks. Plutonic rocks, mainly monzonite and granodiorite with lesser amounts of gabbro, are widespread in the Rhodope, although they dominate in the eastern and central parts (e.g., Christofides, 1995; Dinter *et al.*, 1995; Eleftheriadis and Koroneos, 2003). In Kavala area the metamorphic rocks of the LTU of RMP were concordantly to

discordantly intruded by the Kavala-Symvolon pluton along the SW-NE trend of the Kavala–Komotini fault zone (Dimadis and Zachos, 1989). Kokkinakis (1977) suggests that the pluton is mainly consisting of hornblende-biotite granitic and granodioritic blastomylonites, occupying respectively the northern and the southern part of the pluton (Fig. 1). Other subordinate lithologies of the pluton include tonalitic, quartz monzonitic and quartz monzodioritic compositions. Both the pluton and the country rock are penetrated by aplitic, pegmatitic and more basic usually porphyritic dikes, the latter having an average modal composition of biotite-hornblende quartz monzodiorite. According to Christofides (1995) and Neiva *et al.*, (1996) the pluton is a metaluminous, alpine I-type granodiorite intrusion, with lensoidal enclaves of metaluminous tonalite and diorite particularly towards its margins. Geochronological data based on U-Pb dating of titanite and $^{40}Ar/^{39}Ar$ dating of hornblende yielded an about 21 Ma, emplacement age for Kavala pluton (Dinter *et al.*, 1995). The K-Ar biotite ages of 15.5±0.5 Ma (Dinter and Royden, 1993) and 17.8± 0.8 Ma (Kokkinakis, 1980) along with the 14-16 Ma Rb-Sr biotite age (Kyriakopoulos *et al.*, 1989) originally suggested as reset metamorphic ages, are in fact the cooling ages related to the emergence of the SRCC in the footwall of the Strymon valley detachment system.

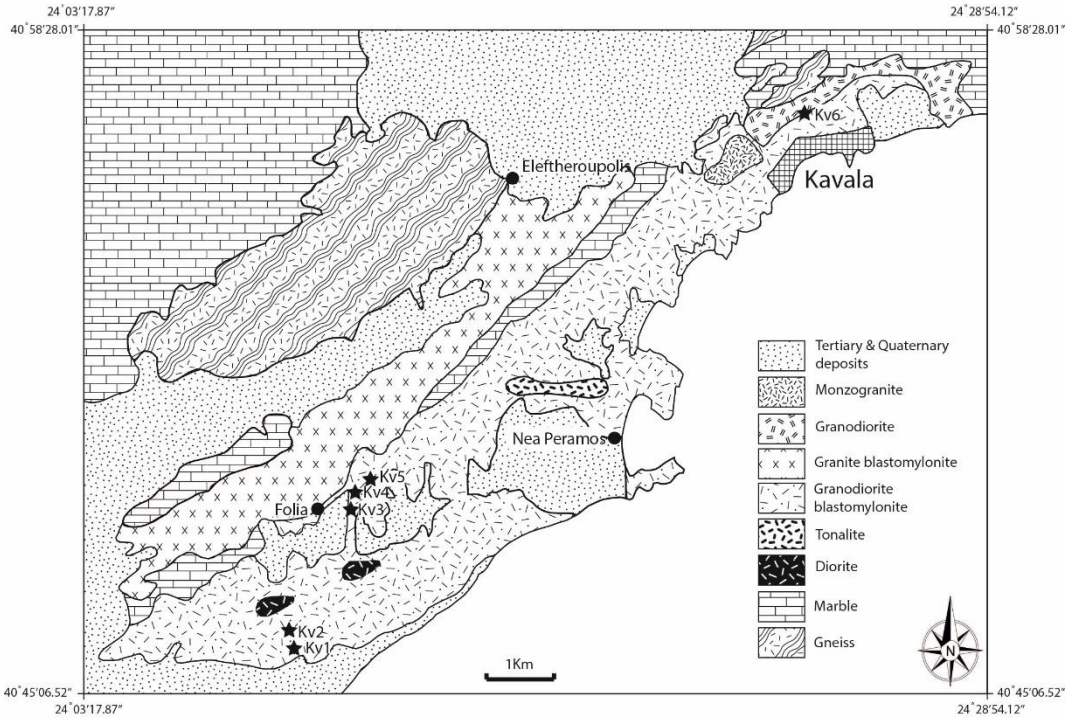

Figure 1 - Simplified geological map of the Symvolon-Kavala pluton (modified after Kokkinakis (1977) and Neiva *et al.* (1996). Sample locations are shown with the filled star symbol.

2.1. Tourmaline-rich rocks

The studied tourmaline-rich rocks occur with different frequency in the plutonic and metamorphic rocks occurring nearby Kavala city and the Symvolon Mt (Fig. 1). They are mainly found in three different forms: a) massive veins, b) cataclasites/breccias and c) injection veins (Fig. 2). The massive tourmaline veins have a blue-black colour and are completely aphanitic with a glassy fabric (Fig. 2a), which makes the discrimination from pseudotachylites extremely difficult without laboratory X-ray diffraction methods. In cataclasites/breccias the angular clasts have a granitic or pure quartz composition, while tourmaline constitutes their matrix. This second rock type also shows a vein or

layered structure with thickness that varies from few mm to about one meter. Their tourmaline matrix, which also shows a dark blue to black colour, is locally disrupted by the grey to white clasts occurring with greater abundance in breccias thicker than 1 cm (Fig. 2b, c). Tourmaline injection veins (Fig. 2d) are commonly developed into a complicated network, which finally seems to feed/infiltrates the breccias. Another type of tourmaline-rich rock maybe represented by fracture filling tourmaline-rich material spatially associated with microfault and joint systems. It frequently has a thickness not exceeding few cm and a mirror like polished surface with slickensides indicating a movement which is postdating the tourmaline precipitation.

The most important occurrence of the tourmaline-rich rocks is in the area of Mavri Petra in the Symvolon Mt (sample locations Kv1-Kv5, in Fig. 1). In this area the massive veins and breccias are abundant and are found within the granodioritic blastomylonite, and in close spatial association with aplitic dikes. The tourmaline-rich vein system is mostly developed along a NW-SE to NNW-SSE trend with moderate to steep dip angles (Fig.2a), under a brittle deformation regime. Field relations show that the tourmaline bearing cataclastic system seems to be overprinting the previous mylonitic foliation of the pluton.

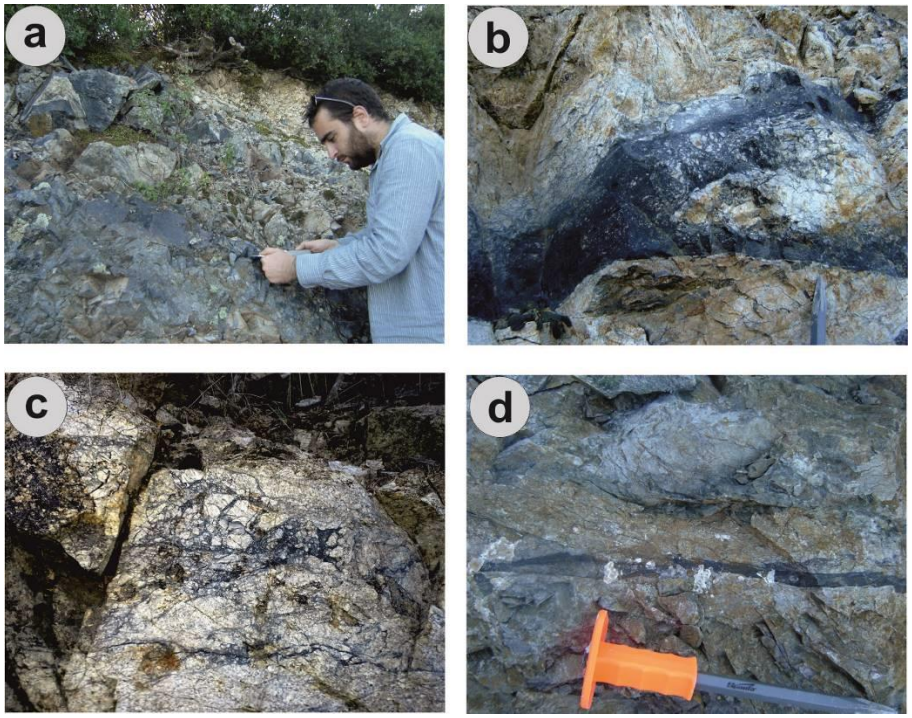

Figure 2 - Outcrop photographs of the tourmaline-rich rocks in the field. Fine-grained tourmaline is found in the forms of: a) massive veins, b, c) matrix within granitic cataclasites/breccias and d) injection veins. Field of view for picture (c) is about 1m.

3. Materials and Methods

Fifteen samples of tourmaline-rich rocks (both veins and breccias) and host granodiorite were pulverized for X-Ray Diffraction analysis, obtained using a SIEMENS D-5005 type diffractometer with Cu tube, in order to verify the presence of tourmaline. The mineralogical phases were determined with the software DIFRAC PLUS 2004, EVA ver. 10 at the laboratories of the NKUA, Faculty of Geology and Geo-Environment. Except the evaluation of the bulk mineralogy on the XRD, more than twenty-five thin sections of the most representative tourmaline bearing rocks were

constructed in order to investigate the textural relationships of the studied material mostly under a ZEISS AXIOSKOP 40 polarizing microscope.

4. Results

4.1. X-Ray Diffraction analysis

X-Ray Diffraction patterns of orientated powder mounts revealed the bulk mineralogy of the massive tourmaline veins and tourmaline breccias. Tourmaline and quartz are essentially present in all the studied samples. Other components are orthoclase, plagioclase and white mica, which represent alongside quartz the granodioritic clasts inside the breccias. Based on XRD patterns morphology and recognized mineral phases we can divide the studied samples in two groups: Group 1 (Fig. 3a), represented by samples composed only of tourmaline and quartz and Group 2 (Fig. 3b) where tourmaline coexists with quartz, orthoclase, albite and white mica. In combination with hand specimen and thin section petrography Group 1 samples are interpreted as massive tourmaline-quartz veins and Group 2 as tourmaline-cemented granodioritic breccias. However, as semi-quantitative analysis reveals the tourmaline amount in both groups exceeds 15%, moreover being higher than 50% in massive veins, most of the studied rocks can be characterized as tourmalinites (cf. Harlov and Austrheim, 2013).

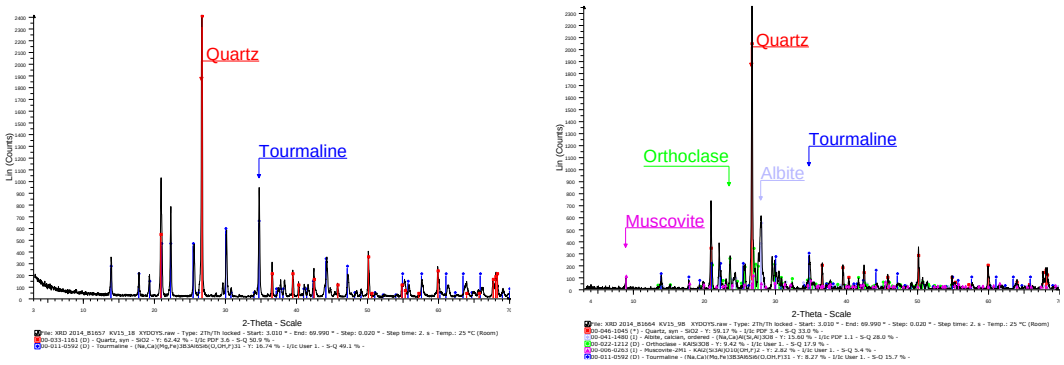

Figure 3 - XRD patterns of two selected tourmalinite samples (Kv15-9B, Kv15-18).

4.1.2 Petrography

All the studied samples are mainly composed of angular granodioritic rock fragments, mineral clasts and a fine-grained to aphanitic matrix. Even the massive tourmaline veins reveal under the microscope a cataclastic texture, in a similar manner as the tourmaline breccias. Microscopic textures are quite similar to macroscopic-scale textures, and effects of brittle deformation and cataclasis are very clear in most of the samples. Clear evidence of ductile deformation seems to be absent from the studied samples, in contrast to the host granodiorite, which presents a well-defined gneissic texture. However, in places tourmaline crystals and quartz fragments present orientation of their elongated c-axes.

The clastic material inside the breccias is mainly composed of angular to subrounded granodioritic fragments and monomineralic clasts, mainly quartz and K-feldspar, derived from the host rocks, giving the rock a poorly sorted appearance (Fig.4a). The fragments are characterized by ribbon quartz textures, K-feldspars with deformation twins and domino fragmented porphyroclasts of K-feldspars and plagioclase (Fig.4b). It should be noticed that plagioclase occurs mainly inside the rock clasts, and it is nearly absent in the form of isolated grains inside the matrix. Quartz generally has angular outlines with numerous internal fractures; recrystallization and subgrain formations are visible and undulose extinction is widespread.

Between the rock and mineral fragments, a fine-grained to aphanitic tourmaline-rich matrix is present covering at least 15% of the surface in the studied thin sections (see Fig.4a).

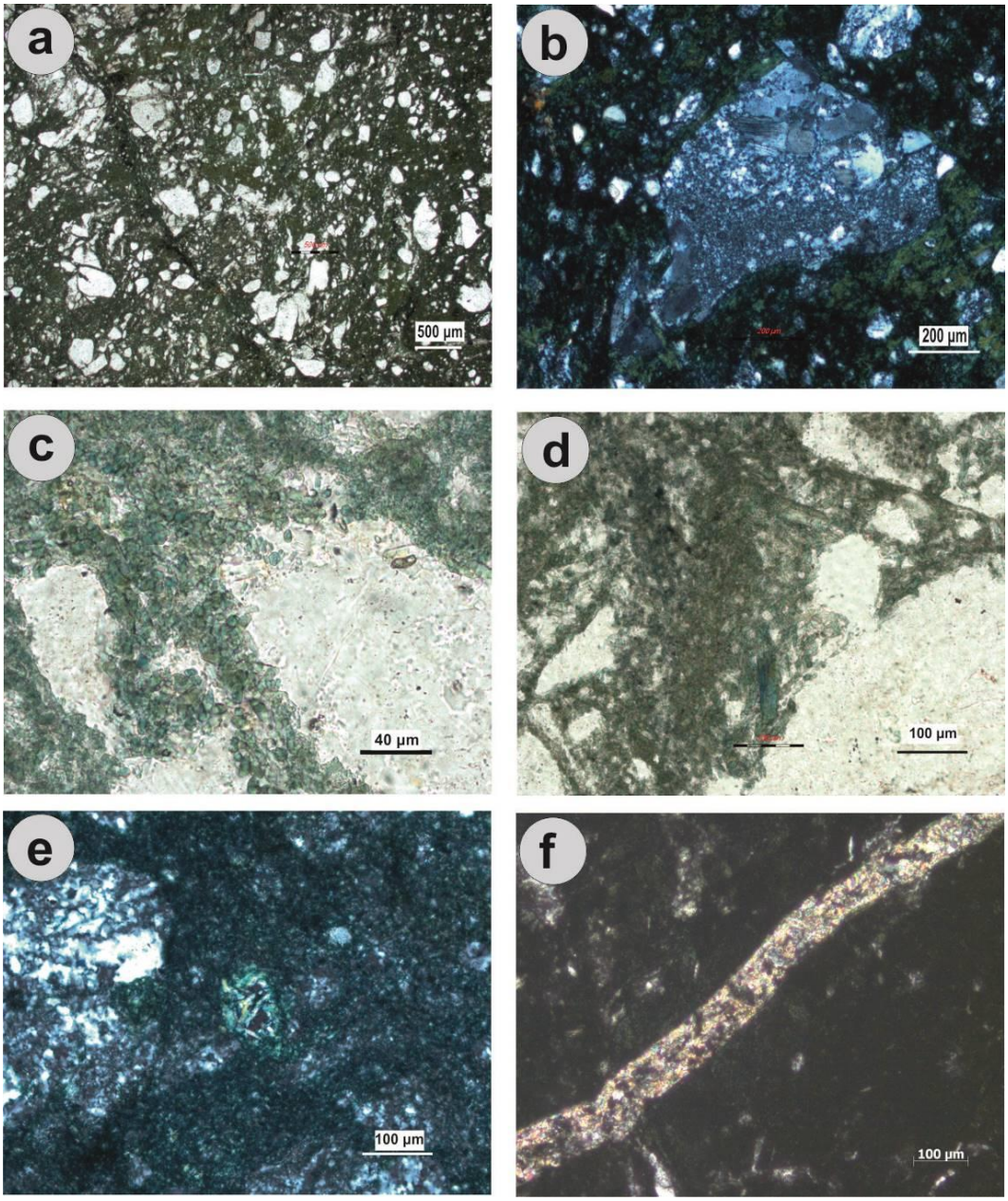

Figure 4 - Photomicrographs of the studied samples under the polarizing microscope: a)Typical view of the tourmaline-breccias showing abundant rock and mineral fragments embedded in a aphanitic tourmaline matrix (KV15/9, PPL), b) Angular fragment of the host granodiorite (KV15/9, XPL), c) Euhedral tourmaline microcrystals of the matrix surrounding subrounded quartz clasts (KV15/9, PPL), d) Tabular, subhedral tourmaline crystal with distinct zoning surrounded by the matrix (KV15/9, PPL), e) Orbicular intergrowth of tourmaline and quartz crystals (KV15/9, XPL), f) White mica + K-feldspar + quartz veinlet crosscutting the matrix of the tourmaline breccias (KV15/18, XPL).

The tourmaline-rich matrix appears with a light- to dark green color under plane polarized light and with a blue-green color in crossed polars, presenting subsequently a weak to moderate green pleochroism. In some cases, the aphanitic matrix appears nearly isotropic. Under high magnifications (500x), tiny (up to 30 μm long and 5-10 μm wide) euhedral to subherdral tiny tourmaline crystals are present, forming a nearly equigranular crypto- to microcrystalline matrix (Fig.4c). Besides the aphanitic matrix, tourmaline is present in two other distinct but rarely occurring forms in the studied thin sections, namely zoned and orbicular tourmalines. Zoned tourmalines are subhedral to anhedral, elongated (up to 120 μm long), corroded tourmaline crystals with distinct zonation. They are present within the aphanitic matrix (Fig.4d) forming a microporphyric texture, resembling clasts in a similar manner with the host rock fragments. The orbicular tourmalines consist of light green euhedral tourmaline microcrystals surrounding a core of undeformed quartz grains (Fig.4e).

Another noteworthy petrographic feature is the presence of secondary quartz, K-feldspar and white mica in fractures and veinlets with crosscutting relation to the tourmaline matrix (Fig.4f).

5. Discussion and Conclusions

The tourmalinite rocks of the Symvolon-Kavala pluton, can be broadly classified as magmatic-hydrothermal breccias, as they match distinguishing criteria such as the presence of angular to subrounded rock fragments and high temperature cementing phases (Sillitoe, 1985; Lawless *et al.*, 1998). Lawless *et al.* (1990) suggested that this kind of breccias are likely formed by the release of juvenile magmatic volatiles derived from partial melting of crustal rocks.

Field relations indicate formation rather in a brittle deformation regime, postdating the mylonitization event, which is responsible for the widespread gneissic texture of the intrusion. The locally occurring oriented c-axes of tourmaline crystals and quartz can be interpreted as a result of cataclastic flow. Hydrofracturing of the granodioritic host rock and fracture propagation seems to be a result of B-rich hydrothermal solution responsible for the pervasive tourmalinization. This is commonly resulting from the formation of mineralized or barren breccias pipes and stockworks around granitic cupolas. These structures lack from the study area, probably due to focused fluid flow within shear zones parallel to the regional NW-SE trending, as suggested by Demirel *et al.* (2009) for a similar case within the Kerkenez monzonite-granite massif (Central Anatolian Crystalline Complex, Turkey**).**

Mineralogical and textural observations during this study, revealed two types of tourmaline-bearing rocks: a) tourmaline-cemented granitic breccias and b) massive tourmaline-quartz veins. Massive tourmaline-quartz veins are depleted in material derived from the host rock, probably due to high water/rock ratios. Penetrative B-rich fluid circulation triggered metasomatic reactions that resulted in the precipitation of tourmaline in the aphanitic matrix. Although replacement textures have not been observed, the absence of biotite and hornblende from the studied samples, could be attributed to the formation of idiomorphic tiny tourmaline crystals at the expense of biotite and hornblende. The decomposition of the later phases could have probably contributed to the offer of the essential Fe and Mg amounts for the tourmaline crystallization. The small size of tourmaline, combined with its great abundance, indicates precipitation from a rapidly cooling hydrothermal fluid under high nucleation and low crystal growth rates.

Corroded tourmaline porphyroclasts (up to 120 μm) within the aphanitic matrix (see Fig.4d) may represent an early boron-rich metasomatic event, as tourmaline has not been identified as an accessory phase in the magmatic rocks of the study area. In opposite, euhedral tourmaline crystals followed by crystallization of undeformed quartz grains may indicate formation within open space miarolithic microcavities under low pressure and by late stage boron-bearing fluids. In addition, the presence of white mica, K-feldspar and quartz in late veinlets crosscutting the tourmaline matrix probably suggests that the circulation of hydrothermal fluids is continued after the successive tourmalinization events.

The preliminary results presented in this study, verify the presence of tourmaline in the studied breccias and suggest a magmatic-hydrothermal origin. Several plausible scenarios can be suggested for the source of boron, including exsolution of B-rich magmatic-hydrothermal fluids from the host granodioritic rock. Upcoming work should include detailed electron probe microscopy in order to classify the tourmaline species and make more accurate hypothesis for their formation environment. In addition, stable and radiogenic isotopic studies, which also are anticipated for the near future, can provide valuable information about the source of boron and the genetic relationship of the breccias with the host granodiorite.

6. References

Altherr, R., Topuz, G., Marschall, H., Zack, T. and Ludwig, T. 2004. Evolution of a tourmaline-beari ng lawsonite eclogite from Elekdag area (Central Pontides, N Turkey): evidence for infiltratio n of slab-derived B-rich fluids duringexhumation, *Contrib. Mineral. Petrol*., 148, 409-425.

Bonev, N., Burg, J.-P. and Ivanov, Z., 2006. Mesozoic-Tertiary structural evolution of an extension al gneiss dome-The Kesebir-Kardamos dome, eastern Rhodope (Bulgaria-Greece), *Int. J. E arth Sci. (Geol Rundsch*), 95(2), 318–340, doi: 10.1007/s00531-005-0025-y.

Burg, J.-P., Ivanov, Z., Ricou, L.-E., Dimov, D. and Klain, L., 1990. Implications of shear-sense criteria for the tectonics evolution of the Central Rhodope massif, southern Bulgaria, *Geology*, 18, 451-454, doi: 10.1130/0091-7613(1990)018.

Christofides, G., 1996. Tertiary magmatism in the Greek Rhodope Massif, northern Greece: Granitic pl utons. *In:* Knezevic, V. and Krstic, B., *eds*., Terranes of Serbia: The Formation of the Geologic F ramework of Serbia and the Adjacent Regions, University of Belgrade, Belgrade, 1, 55-160.

Christofides, G., Neiva, A., Soldatos, T. and Eleftheriadis, G., 1995. Petrology of the Kavala plutonite (Eastern Macedonia, Greece), *Proc. XV Congress CBGA*, Athens, *Bull. Geol. Soc. Greece*, Spec. Publ., 4(2), 489-494.

Demirel, S., Göncüoĝlu, C., Topuz, G. and Isik, V., 2009. Geology and chemical variations in Tourmaline from the Quartz-Tourmaline Breccias within the Kerkenez Granite-Monzonite Massif, Central Anatolian Crystalline Complex, Turkey, The Canadian Mineralogist, 47, 787-799.

Derham, J.M. and Feely, M., 1988. A K-feldspar breccia from Mo-Cu stockwork deposit in the Galway granite, west of Ireland, *J. Geol. Soc*., London, 145, 661-667.

Dimadis, E. and Zachos, S., 1989. Geological and tectonic structure of the metamorphic basement of the Greek Rhodope, *Geologica Rhodopica*, 1, 122-130.

Dini, A., Mazzarini, F., Musumeci, G. and Rocchi, S., 2008. Multiple hydrofracturing by boron-rich fluids in the Late Miocene contact aureole of eastern Elba Island (Tuscany, Italy), *Terra Nova*, 20, 318-326.

Dinter, D., MacFarlane, A., Hames, W., Isachsen, C., Bowring, S. and Royden, L., 1995. U-Pb and 40Ar/39Ar geochronology of the Symvolon granodiorite: implications for the thermal and structural evolution of the Rhodope metamorphic core complex, northeastern Greece, *Tectonics*, 14, 886-908.

Dinter, D.A. and Royden, L, 1993. Late Cenozoic extension in northeastem Greece: Strymon Valley detachment and Rhodope metamorphic core complex, *Geol*., 21, 45-48.

Eleftheriadis, G. and Koroneos, A., 2003. Geochemistry and petrogenesis of post-collisonal Pangeon granitoids in central Macedonia, northern Greece, *Chemie der Erde*, 63, 364-389.

Feely, M., Selby, D., Hunt, J. and Conliffe, J., 2010. Long-lived granite-related molybdenite mineralization at Connemara, western Irish Caledonides, *Geol. Mag*., 147, 886-894.

Froitzheim, N., Jahn-Awe, S., Frei, D., Wainwright, A., Maas, R., Georgiev, N., Nagel, T.J. and Pleuger, J., 2014. Age and composition of meta-ophiolite from the Rhodope Middle Allochthon (Satovcha, Bulgaria): a test for the maximum-allochthony hypothesis of the Hellenides, *Tectonics*, 32.

Harlov, D.E. and Austrheim, H., 2013. Metasomatism and the Chemical Transformation of Rock, Lecture Notes in Earth System Sciences, doi: 10.l007/978-3-642-28394-9_l, Springer-Verlag, Berlin, Heidelberg.

Henry, D.J. and Guidotti, C.V., 1985. Tourmaline as a petrogenetic indicator mineral: an example from the staurolite- grade metapelites of NW Maine, A*merican Mineralogist*, 70, 1-15.

Jahn-Awe, S., Froitzheim, N., Nagel, T.J., Frei, D., Georgiev, N. and Pleuger, J., 2010. Structural and geochronological evidence for Paleogene thrusting in the western Rhodopes, SW Bulgaria: Elements for a new tectonic model of the Rhodope Metamorphic Province, *Tectonics*, 29.

Kokkinakis, A., 1977. Das Intrusivgebiet des Symvolon-Gebirges und yon Kavala in Ostmakedonien, Griechenland. - Diss. Univ. Miinehen. - 255 + XIII S., 208 Abb., 29 Tab., 8 Kt., 1 B1, Miinehen.

Kokkinakis, A., 1980. Altersbeziehungen zwischen Metamophosen, mechanischen Deformationen und Intrusionen am Südrand des Rhodope-Massivs (Makedonien, Griechenland) Geol, *Rundschau*, 69, 726-144.

Krenn, K., Bauer, C., Proyer, A., Klötzli, U. and Hoinkes, G., 2010. Tectonometamorphic evolution of the Rhodope orogen, *Tectonics*, 29, TC4001.

Krohe, A. and Mposkos, E., 2002. Multiple generations of extensional detachments in the Rhodope Mountains (N. Greece): evidence of episodic exhumation of high-P rocks. *In*: Blundell, D.J., Neubauer, G. and Von Quadt, A., *eds*., The Timing and Location of Major Ore Deposits in an Evolving Orogen, Geological Society of London, Special Publication 204, 151-178.

Kyriakopoulos, K., Pezzino, A. and Del Moro, A., 1989. Rb-Sr geochrological, petrological and structural study of the KavaIa plutonic complex (N. Greece), *Bu1l. Geo1. Soc. Greece*, 23, 545-560.

Lawless, J.V. and White, P.J., 1990. Ore-Related Breccias: A Revised genetic classification, with particular reference to epithermal deposits, 12th New Zealand Geothermal Workshop.

Lawless, J.V., White, P.J., Bogie, I., Paterson, L.A. and Cartwright, A.J., 1998. Appendix 1: Genetic Classification of Breccias, Ore Deposits and Magmatic-Hydrothermal Processes (Workshop manual), Kingston Morrison consulting, 20 pp.

London, D., 2009. The origin of primary textures in granitic pegmatites, *Canad. Mineral*, 47, 697-724.

Marschall, HR, Ludwig, T, Altherr, R, Kalt, A. and Tonarini, S., 2006. Syros metasomatic tourmaline: Evidence for very high-δ11B fluids in subduction zones, *Journal of Petrology*, 47, 1915-1942.

Müller, A. and Halls, C., 2005. Rutile - the tin-tungsten host in the intrusive tourmaline breccia at Wheal Remfry, SW England. *In*: Jingwen, M and Bierlein, F.P., *eds*., *Mineral Deposit Research*, Meeting the Global Challenge, 441-444.

Nagel, T.J., Schmidt, S., Janak, M., Froitzheim, N., Jahn-Awe, S. and Georgiev, N., 2011. The exposed base of a collapsing wedge: The Nestos Shear Zone (Rhodope Metamorphic Province, Greece), *Tectonics*, 30, TC4009, doi: 10.1029/2010TC002815.

Neiva, A., Christofides, G., Eleftheriadis, G. and Soldatos, T., 1996. Geochemistry of granitic rocks and their minerals from the Kavala pluton, northern Greece, *Chemie der Erde*, 56, 117-142.

Pollard, P.J., Pichavant, M. and Charoy, B. 1987. Contrasting evolution of fluorine- and boron-rich systems, *Miner Depos*, 22, 315-321.

Sillitoe, R.H., 1985, Ore-related breccias in volcanoplutonic arcs, *EconomicGeology*, 80, 1467-1514.

Skewes, M.A., Holmgren, C. and Stern, C.R., 2003. The Donoso copper-rich, tourmaline-bearing breccia pipe in central Chile: petrologic, fluid inclusion and stable isotope evidence for an origin from magmatic fluids, *Miner Depos*, 38, 2-21

Slack, J.F. and Trumbull, R.B., 2011. Tourmaline as a recorder of ore-forming processes, *Elements*, 7, 321-326.

Trumbull, R.B. and Chaussidon, M., 1999. Chemical and boron isotopic composition of magmatic and hydrothermal tourmalines from the Sinceni granite–pegmatite system in Swaziland, *Chem. Geol*., 153, 125-137.

van Hinsberg, V.J., Henry, D.J. and Dutrow, B.L., 2011a. Tourmaline as a petrologic forensic mineral: A unique recorder of its geologic past, *Elements*, 7, 327-332.

van Hinsberg, V.J., Henry, D.J. and Marschall, H.R., 2011b. Tourmaline: An ideal indicator of its host environment, *Canadian Mineralogist*, 49, 1-16.

Williamson, B.J., Spratt, J., Adams, J.T., Tindle, A.G. and Stanley, C.T., 2000. Geochemical constraints from zoned hydrothermal tourmalines on fluid evolution and Sn mineralization: an example from fault breccias at Roche, *SW England. J Petrol*, 41, 1439-1453.

Δελτίο της Ελληνικής Γεωλογικής Εταιρίας, τόμος L, σελ. 2088-2097
Πρακτικά 14ου Διεθνούς Συνεδρίου, Θεσσαλονίκη, Μάιος 2016

Bulletin of the Geological Society of Greece, vol. L, p. 2088-2097
Proceedings of the 14th International Congress, Thessaloniki, May 2016

MINERALOGICAL AND GEOCHEMICAL CHARACTERIZATION OF THE OLYMPIAS MINE TAILINGS, NE CHALKIDIKI, GREECE

Zaimis S.[1], Vavelidis M.[1], Alifragkis D.[2], Melfos V.[1], Kantiranis N.[1], Daftsis E.[3] and Gazea E.[3]

[1]Aristotle University of Thessaloniki, School of Geology, 54124, Thessaloniki, Greece, szaimis@gmail.com

[2]Aristotle University of Thessaloniki, Faculty of Forestry and Natural Environment, 55134, Thessaloniki, Greece

[3]Hellas Gold S.A., Stratoni, 63082, Chalkidiki, Greece

Abstract

The Olympias tailings of NE Chalkidiki, Greece represent the mine wastes produced by the beneficiation of the Pb-Zn-Au-Ag ore deposit, which is hosted within the carbonate rocks of the Kerdylia Unit. In the present study X-Ray diffraction (XRD), scanning electron microscopy (SEM), optical microscopy, chemical analyses and pH measurements were conducted to determine the tailings mineralogy and chemical composition. The results indicated that they consist of gangue (quartz, rhodochrosite, calcite, dolomite, feldspars, micas, kaolinite and actinolite) and sulfide minerals (pyrite, arsenopyrite, sphalerite, chalcopyrite and galena), reflecting the source ore and its host rock composition, accompanied by traces of Fe-oxides (magnetite, hematite), Fe-oxyhydroxides (goethite) and Mn-oxides, often enriched in Zn and Pb and in some cases Fe, Sb and As. Secondary sulfates (gypsum, jarosite) and surface efflorescent salts (ferrohexahydrite, hexahydrite, halotrichite) have also been recognized. The Olympias tailings are generally unoxidized, generating an alkaline environment. However, variations in composition result in the formation of restricted separate phases, such as thin layers and lenses of oxidized material that generates an acidic environment. In terms of precious metals content, the Olympias tailings are enriched in Au (up to 12 g/t) and Ag (up to 20 g/t).
Keywords: *Mine wastes, secondary minerals, efflorescent salts.*

Περίληψη

Τα τέλματα της Ολυμπιάδας στην ΒΑ Χαλκιδική, αποτελούν τα κατάλοιπα του εμπλουτισμού του κοιτάσματος Pb-Zn-Au-Ag που εντοπίζεται στα ανθρακικά πετρώματα της Ενότητας Κερδυλίων. Στην παρούσα εργασία, η ορυκτολογική σύσταση των τελμάτων προσδιορίστηκε με τη χρήση περιθλασιμετρίας ακτίνων-Χ (XRD), ηλεκτρονικής μικροσκοπίας σάρωσης (SEM) και οπτικής μικροσκοπίας, ενώ επιπλέον πραγματοποιήθηκαν χημικές αναλύσεις και μετρήσεις pH. Τα αποτελέσματα έδειξαν πως τα τέλματα συνίστανται από σύνδρομα ορυκτά (χαλαζίας, ροδοχρωσίτης, ασβεστίτης, άστριοι, μαρμαρυγίες, καολινίτης και ακτινόλιθος) και σουλφίδια (σιδηροπυρίτης, αρσενοπυρίτης, σφαλερίτης, χαλκοπυρίτης και γαληνίτης), κάτι που δείχνει ότι υπάρχει σχέση με την ορυκτολογική σύσταση της μεταλλοφορίας και των

μητρικών πετρωμάτων. Επίσης, τα τέλματα αποτελούνται από ίχνη οξειδίων Fe (μαγνητίτης, αιματίτης), οξείδια-υδροξείδια Fe (γκαιτίτης) και οξείδια Mn, συχνά εμπλουτισμένα σε Zn και Pb και σε ορισμένες περιπτώσεις Fe, Sb και As. Επιπλέον εντοπίστηκαν δευτερογενή θειικά άλατα (γύψος, ιαροσίτης) και επανθίσματα θειικών αλάτων (σιδηροεξαϋδρίτης, εξαϋδρίτης, αλοτριχίτης). Τα τέλματα της Ολυμπιάδας είναι γενικά μη οξειδωμένα, δημιουργώντας ένα αλκαλικό περιβάλλον. Παρόλα αυτά, λόγω μεταβολών στη σύσταση, σχηματίζονται ξεχωριστές φάσεις περιορισμένης έκτασης, όπως λεπτές στρώσεις και φακοί οξειδωμένου υλικού, οι οποίες δημιουργούν όξινο περιβάλλον. Από την άποψη της περιεκτικότητας σε πολύτιμα μέταλλα, τα τέλματα της Ολυμπιάδας είναι εμπλουτισμένα σε Au (έως 12 g/t) και Ag (έως 20 g/t).
Λέξεις κλειδιά: *Στείρα μεταλλευτικά κατάλοιπα, δευτερογενή ορυκτά, επανθίσματα.*

1. Introduction

Tailings constitute the residues of ore deposits beneficiation process and are generally located close to mine districts, being the most common mine wastes. They are usually used as backfill underground or stored in open pits, dried and stacked, or pumped into tailings impoundments (Hudson-Edwards *et al.*, 2011). Today, due to the increased demand for precious metals and the availability of improved and more effective beneficiation methods, tailings are often re-assessed and treated as sources of raw materials.

In Olympias, which is part of the "Kassandra mining district" in NE Chalkidiki, Greece, the tailings impoundments are under removal and retreatment (Figure 1a), since 2012, for the production of gold-bearing pyrite-arsenopyrite concentrate by the company Hellas Gold, 95% owned by Eldorado Gold. After the complete removal, the area, which was used to host the tailing pond and then the tailings impoundments in Olympias, will be returned to its natural greenfield state after replanting (Forward *et al.*, 2011; Alifragkis *et al.*, 2012a, b). The re-process and beneficiation of Olympias tailings in the local concentrator will *produce* fine tailings, which will be filter-pressed at Olympias and disposed on the existing tailings management facilities in Stratoni, 10 km southeastern, whereas the coarse residues will initially be sold as aggregates (Forward *et al.*, 2011). The current study is part of a research project for the reclamation of disturbed lands in the wider area of Kassandra mining district, providing an insight in the mineralogical and geochemical composition of the mine tailings. The study was conducted at the Olympias mine tailings, where planting experiments by the Faculty of Forestry and Natural Environment of the Aristotle University of Thessaloniki are in progress, investigating remedial practices on these materials by chemical stabilization using a material rich in Fe-Mn oxides and phytoremediation (Alifragkis *et al.*, 2012a, b) (Figure 1b).

The exposure of mine wastes to the atmosphere and hydrosphere along with the action of microorganisms generates drainage that may be acid and rich in dissolved metals and sulfates (Jamieson, 2011). However, the chemical reactivity and the mobility of heavy metals can be controlled by the mineralogical composition of the tailings. Jamieson (2011) states that in the presence of sufficiently high amounts of carbonate minerals, such as calcite and/or dolomite, the acid drainage may be neutralized. Furthermore, tailings usually contain secondary oxyhydroxides, oxides, sulfates, sulfides, carbonates and silicates (Alpers *et al.*, 1994; Lottermoser, 2010), many of which are fine grained, exhibiting a high capacity for adsorption of potentially toxic metals (Jamieson, 2011). At the surface of the tailings impoundments, secondary minerals are precipitated in the form of soluble sulfate salts after the evaporation of cycling water, caused by the heat produced either by the strongly exothermic reaction of pyrite oxidation or the intense sunlight.

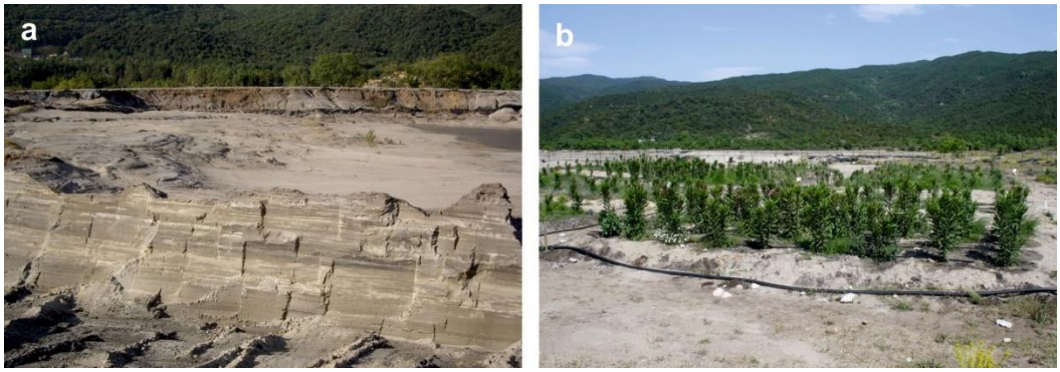

Figure 1 - Olympias mine tailings in NE Chalkidiki. (a) Tailings impoundments in the stage of removal, (b) Planting experiments on the tailings impoundments by the Faculty of Forestry and Natural Environment of the Aristotle University of Thessaloniki.

These minerals are known in the literature as "efflorescent salts" and common examples are melanterite, rozenite, szomolnokite, copiapite, rhomboclase, halotrichite and chalcanthite (Nordstrom, 2011). In this paper we attempt to examine the mineralogy and geochemistry of these materials, for the understanding of tailings mineralogical and chemical composition, theassociation with the primary ore and the host rocks and the nature of secondary mineral phases formed under weathering conditions.

2. Regional geology and ore deposits in NE Chalkidiki

The Olympias mining district is part of the broader Kassandra mining district at the NE Chalkidiki Peninsula of northern Greece and geotectonically lies to the Greek part of the Serbo-Macedonian massif (SMM). The SMM is subdivided in two major lithostratigraphic units; the predominant Vertiskos Unit in the northwest and the Kerdylia Unit in the east (Kockel *et al.*, 1977; Burg *et al.*, 1995; Himmerkus *et al.*, 2009). The SMM has been subjected to a metamorphism that reaches upper amphibolite facies (Kilias *et al.*, 1999) and the Kerdylia Unit, where Olympias and the local orebodies are situated, is composed of migmatitic biotite gneisses with intercalations of hornblende gneisses, amphibolite lenses and marbles (upper, intermediate and lower horizon) (Kockel *et al.*, 1977) (Figure 2).

Regarding the igneous activity, the region of NE Chalkidiki is characterized by a post-orogenic acid magmatism with intrusions of porphyry calc-alkaline to shosonitic igneous rocks in SMM during Tertiary (Kockel *et al.*, 1975; Kockel *et al.*, 1977; Fytikas *et al.*, 1984; Tompouloglou *et al.*, 1986; Gilg and Frei, 1994). In the Kassandra mining district, three major Tertiary magmatic rocks have been distinguished by Gilg and Frei (1994); the Stratoni granodiorite (27.9 ±1.2 Ma, U/Pb on zircons), the phyllically altered granodioritic to quartz-dioritic porphyry dikes and stocks (minimum age span of 25.4 ±0.6 to 24.4 ±0.6 Ma, biotite K/Ar) between Fisoka and Aspra Chomata, including Skouries porphyry, and the latest andesite porphyry dikes (19.1 ±0.6, K/Ar biotite-whole rock isochrones) at Stratoni region.

The economically most important mineral resources in NE Chalkidiki were/are the Pb-Zn (Au-Ag) carbonate-replacement deposits of Madem Lakkos, Mavres Petres, Olympias and the porphyry Cu-Au mineralization in Skouries. The Olympias Pb-Zn-Au-Ag ore deposit, which is intrusion related (e.g. Kalogeropoulos *et al.*, 1989; Gilg and Frei, 1994) and associated to our study, is a stratabound (manto) and locally stratiform or fracture controlled sulfide mineralization, hosted mainly within the lower marble horizon of the Kerdylia Unit and along the contact with the overlying biotite gneiss (Kalogeropoulos *et al.*, 1989). The main host rock of the mineralization is a calcitic and rhodochrosite- and/or Mn calcite-bearing marble.

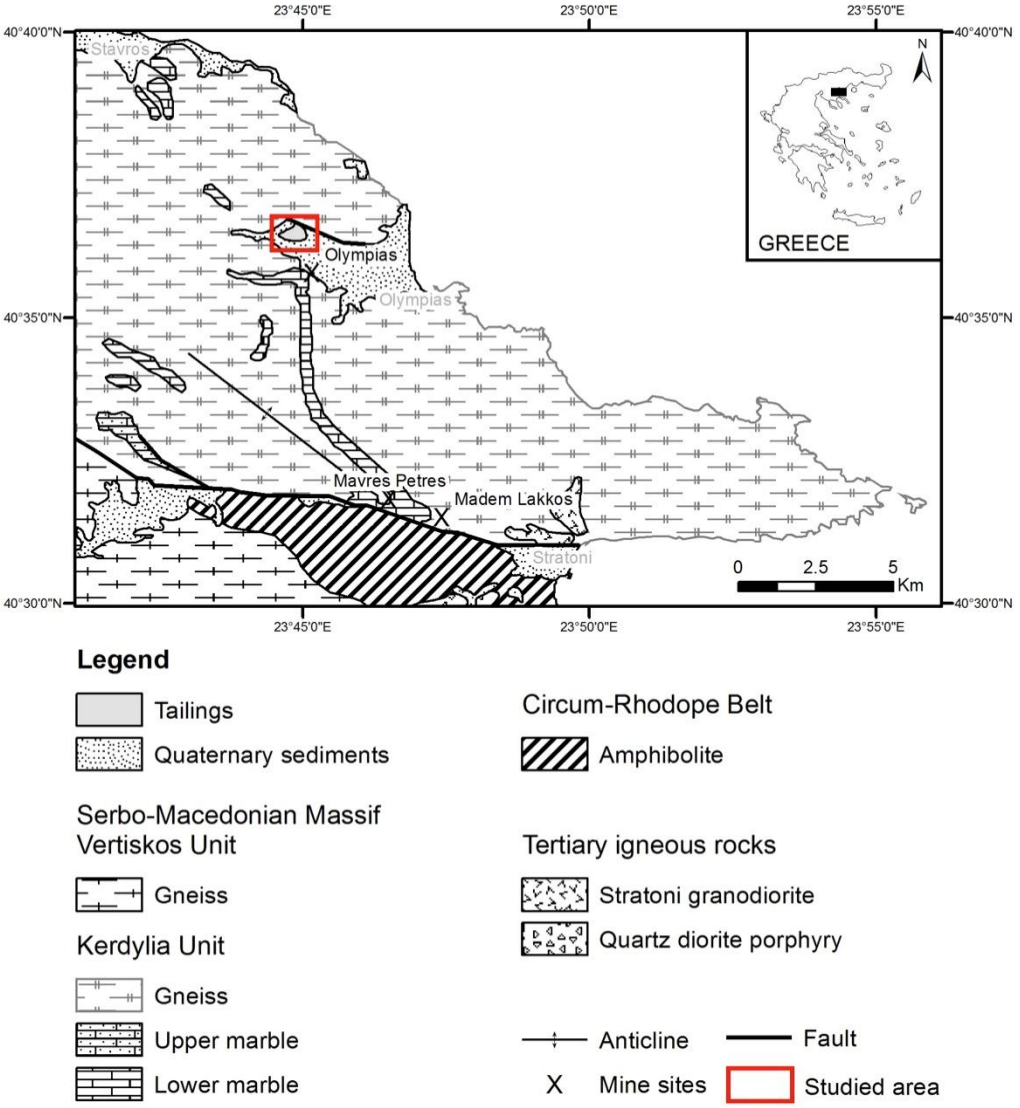

Figure 2 - Simplified geological map of the Kassandra mining district in NE Chalkidiki, Greece (modified after Kockel *et al.*, 1978a, b and Nebel *et al.*, 1991).

Kalogeropoulos *et al.* (1989), report that the Olympias orebodies consist mainly of pyrite, sphalerite, galena and arsenopyrite, accompanied by sulfides and sulfosalts such as chalcopyrite, tetrahedrite, boulangerite, bournonite, pyrrhotite, marcasite, geocronite and enargite, whereas the gangue minerals consist mainly of quartz, rhodochrosite and calcite. According to Chryssoulis and Cabri (1990), the bulk of the gold in Olympias is "invisible" and is predominantly carried by arsenopyrite and arsenian pyrite.

The broader region of NE Chalkidiki is a historic mining center, as the exploitation of mineral resources for lead and silver started during the archaic period (Vavelidis *et al.*, 1983). Mining, along with gold and silver metallurgy continued during the Byzantine and Ottoman times (Vavelidis and Melfos, 2012). In the modern history, the exploration in the Olympias area commenced in 1954, whereas full production in the Olympias ore deposit started in 1970. It is estimated that 3.64 Mt of mixed sulfide ore were mined between 1976 and 1995, since production stopped, for the production

of concentrates of galena, sphalerite and pyrite-arsenopyrite, after beneficiation in the local facilities by crushing, milling and differential flotation processes (Papagrigoriou *et al.*, 2010; Forward *et al.*, 2011). Separation of the minerals was achieved in the Olympias concentrator plant through a combination of pH control and conventional reagents for the depression and activation of the various mineral species (Papagrigoriou *et al.*, 2010; Forward *et al.*, 2011).

The waste residuals, exclusively derived from the Olympias deposit and partially free of the four separated minerals, were discharged in the tailing pond, 500 m north of the beneficiation facilities in Olympias (Papagrigoriou *et al.*, 2010). Today, the Olympias mine tailings represent the residuals from the former local tailing pond, which cover a geographic area of 26.5 hectares, upon Quaternary sediments (Figure 2).

According to Papagrigoriou *et al.* (2010) and Forward *et al.* (2011), apart from the remaining underground resources in Olympias, the operation and development project includes the re-milling and re-processing of the historic tailings in the Olympias concentrator in a rate of 720,000 dry tonnes per annum, for the production of payable gold in concentrate. Forward *et al.* (2011) report that a drilling campaign of 83 holes indicated a total tonnage of 2,408,403 tonnes, with concentrations of 3.42 g/t Au and 14.25 g/t Ag.

3. Materials and Methods

The samples used in the current study, are derived from the Olympias tailings disposal area (40°36'28.31"N, 23°44'51.70"E). The mineralogical composition of tailings was determined by X-ray diffraction (XRD) (9 samples), scanning electron microscopy (SEM) and reflected-light optical microscopy (5 samples).

The X-ray diffraction analyses were carried out at the Physics Department and the School of Geology, Department of Mineralogy-Petrology-Economic Geology, Aristotle University of Thessaloniki, using a Rigaku Ultima+ and a Philips PW1710 X-ray diffractometer, respectively, both with CuKa radiation, 1.54056 Å wave length and Ni filter. Scanning electron microscopy (SEM, JEOL JSM-840A) with associated energy dispersive spectroscopy (EDS, Link AN10000) was performed at the Laboratory of Scanning Electron Microscopy of the Aristotle University of Thessaloniki. Optical microscopy was performed at the School of Geology, Department of Mineralogy-Petrology-Economic Geology of Aristotle University of Thessaloniki using a Leitz Laborlux 11 Pol S polarized- and reflected-light microscope.

Sixteen chemical analyses were carried out for the determination of major and trace elements at the Quality Control Laboratory of Hellas Gold S.A. (Stratoni, Chalkidiki) and the ACME Analytical Laboratories Ltd. (Vancouver, Canada). In the first laboratory the analyses of base and trace elements were carried out by inductively coupled plasma atomic emission spectrometry (ICP-AES) and atomic absorption spectroscopy (AAS), Au by fire-assay, Ag by fire-assay/AAS and total S by LECO furnace, whereas in the latter, base and trace elements were also analyzed by inductively coupled plasma atomic emission spectrometry (ICP-AES). The samples were examined for their pH value at the School of Geology, Department of Mineralogy-Petrology-Economic Geology, Aristotle University of Thessaloniki, using a digital pH meter (pH301 HANNA Instruments). The pH was measured by glass-calomel electrode in water: sample pastes (McLean, 1982) of 1:1 ratio (20 g: 20 ml), whereas samples of small quantity measured in 1:5 ratio (5 g: 25 ml).

4. Results and Discussion

4.1 Structure and features of the Olympias mine wastes

The gradual removal of tailings from the depositional site resulted in the exposure of vertical sections (Figure 1a), giving access for sampling from a depth up to 2 m in average, but also an opportunity for the observation of deeper levels. The Olympias mine tailings consist of parallel

layers with a thickness of up to 30 cm, often with lenticular intercalations with variant compositions. There are no indications for rhythmical precipitation or graded bedding; in fact it seems that the stratigraphic features were determined by the random disposal of beneficiation residuals from the local concentrator plant. The Olympias tailings are generally unoxidized, exhibiting a light-grey to grey and greyish-yellow to greyish-olive color. However, variations in composition result in the formation of separate oxidized phases, in the form of yellow to brown lenses and thin layers of very limited extend. The texture of the tailings is mainly classified as sandy-silt and silty-sand, while it seems that the coarser components are mainly concentrated at the outer part of the impoundments, close to the termination points of the disposal pipes (Zaimis, 2013). This can be explained by the early precipitation of larger particles and heavier minerals at the margins of the pond, where was the end of the feeding tubes. At the surface of tailings impoundments, secondary minerals are precipitated in the form of white botryoidal aggregates consist of soluble sulfate salts.

4.2 Mineralogy and mineral chemistry

The examination of the Olympias tailings indicated that the mineralogical composition in the whole disposal area exhibits a significant resemblance. They mainly consist of gangue minerals (quartz, rhodochrosite, calcite, dolomite, feldspars, micas, actinolite and kaolinite), which are accompanied by sulfides (pyrite, arsenopyrite, chalcopyrite, sphalerite and galena) from the primary ore mineralization, Fe oxides (magnetite, hematite), Fe oxyhydroxides (goethite), Mn oxides, sulfates (gypsum, jarosite) and efflorescent salts (ferrohexahydrite, halotrichite, hexahydrite), formed at the surface of the impoundments. The oxidized tailings are distinguished from the fresh unoxidized, as they represent the materials that contain high amounts of iron sulfates, such as jarosite, formed by the oxidation of the sulfides, providing a characteristic yellow to brown color to the material.

As indicated by the current study, the mineralogy of the Olympias orebody and its host rocks (Kalogeropoulos *et al.*, 1989) is strongly reflected on the Olympias tailings, which contain both primary and secondary minerals. The formation of secondary minerals in Olympias tailings is predominantly associated with the weathering of the included sulfides and the dissolution of primary carbonates. However, the use of CaO and /or $Ca(OH)_2$ during the ore beneficiation process may have had an important contribution in the formation of certain secondary phases, such as gypsum.

The Olympias tailings are dominated by quartz (17 to 44 wt.%) and carbonate minerals, which consist of rhodochrosite (up to 25 wt.%), calcite (up to 23 wt.%) and dolomite (up to 17 wt.%). Feldspars, mainly albite (up to 11 wt.%) and microcline (up to 10 wt.%) have also been observed. Mica flakes consist mainly of muscovite (up to 10 wt.%) and biotite (up to 10 wt.%). Minor amounts of kaolinite have only been determined by XRD (up to 5 wt.%), whereas from the amphibole group, Ca-Mg-amphibole has been identified by XRD in traces, only in one sample.

Pyrite is the dominant sulfide mineral in the tailings (up to 9 wt.%), containing 46.71 to 46.92 wt.% Fe. Pyrite occurs either in the form of separate grains or incorporated with carbonates or silicates and/or other sulfides, such as sphalerite and galena. In the oxidized tailings, the alteration of pyrite is more extensive than in the unoxidized, replaced by Fe oxyhydroxides, mainly goethite. Arsenopyrite is the second most common sulfide (up to 4 wt.%). It is often found as separate grains, usually fractured, or intergrown with gangue minerals.

Sphalerite occurs in traces (up to 2 wt.%), as separate grains or intergrown with quartz and sulfides such as pyrite and galena. Chalcopyrite blebs have also been observed in sphalerite, which is a typical texture for the sphalerite from Olympias, according to Kalogeropoulos and Economou (1987). Regarding the chemical composition, sphalerite contains 54.86 to 60.99 wt.% Zn, 5.04 to 10.96 wt.% Fe and traces of Mn (up to 0.66 wt.%). Galena is found rarely as separate grains. It is mostly intergrown with other sulfides such as sphalerite and pyrite, but also with gangue minerals mainly quartz and calcite. Chalcopyrite, besides forming blebs in sphalerite, occurs in traces containing 33.65 to 35.49 wt.% Cu and 29.50 to 30.50 wt.% Fe.

Goethite occurs mainly in the form of replacement rims around pyrite or in co-existence with jarosite. As indicated by SEM-EDS microanalyses, it contains FeO (62.25 to 94.93 wt.%) with ZnO (up to 10.37 wt.%), PbO (up to 8.77 wt.%), As_2O_3 (up to 10.34 wt.%) and MnO (up to 3.27 wt.%).

Manganese oxides have been observed in traces, in the form of sub-rounded to rounded grains of up to 2.5 mm in length. They are often enriched in Zn and Pb and in some cases Fe, Sb and As, as well as K and Ca. Due to their extensive elemental variation, the Mn oxides exhibit various mineral phases, which were difficult to identify. The majority of the Mn oxides grains consist of MnO (70.51 to 100.00 wt.%), being rich in ZnO (up to 19.81 wt.%), PbO (up to 7.82 wt.%), K_2O (up to 4.7 wt.%) and CaO (up to 3.74 wt.%), whereas Fe-Mn oxides phases (FeO 10.05 - 62.18 wt.%, MnO 12.45 - 71.85 wt.%) occur as intergrowths. Occasionally, coatings of highly enriched phases in Zn, Pb, Fe, Sb and As, were observed under the SEM, around the Mn oxide grains. These rims contain various concentrations of MnO (48.33 to 89.76 wt.%), ZnO (2.25 to 38.49 wt.%) and PbO (up to 22.35wt.%), along with FeO (up to 7,88 wt.%), Sb_2O_3 (up to 7.60 wt.%) and As_2O_3 (up to 5.28 wt.%). The most sufficient assumptions for the formation of the Mn oxides are to be secondary phases, controlled by adsorption/co-precipitation mechanisms.

Leckie *et al.* (1980) report that co-precipitation and adsorption reactions with $Fe(OH)_3$ can be effective in the removal of metals such as Cd, Cu, Zn, As and Se from waste-water streams. Likewise in Olympias, the presence of Zn, Pb, Sb and As in Fe and Mn oxides enhances the role of these materials as trace elements retentive agents.

Jarosite is found only in the oxidized tailings, where is the predominant constituent (up to 18 wt.%), coexisting sometimes with goethite, exhibiting replacement textures on grains of obscure origin. The SEM-EDS microanalyses indicated that jarosite contains K_2O (9.77 to 10.50 wt.%), FeO (50.95 to 51.48 wt.%) and SO_3 (38.02 to 39.28 wt.%). Another common sulfate mineral in tailings is gypsum (up to 18 wt.%), which often forms euhedral crystals of up to 2 mm in length, indicating a secondary formation.

Blowes and Jambor (1990), suggest that minor amounts of ferrous sulfates ($FeSO_4 \cdot nH_2O$) in dried tailings, may form as ephemeral precipitates on the sun-baked surface crust, a phenomenon that has also been observed in Olympias tailings. White botryoidal aggregates of up to 1 mm in diameter have been observed at the surface of the Olympias tailings impoundments as efflorescent salts. On the basis of qualitative and semi-quantitative identification, the white aggregates, collected from an exposure in the surface of tailings piles, consist mainly of ferrohexahydrite (67 wt.%) and gypsum (4 wt.%), whereas quartz (15 wt.%) and calcite (13 wt.%) probably represent impurities, as observed in the SEM. Additionally, Mg- and Fe-Al-sulfates have been observed under the SEM, identified, based on their chemistry, as hexahydrite and halotrichite, respectively.

4.3 Geochemistry

The results from bulk chemical analyses indicate that there is a strong relation between the geochemistry and the mineralogy. Within tailings, high Fe concentrations (1.19 - 7.43 wt.%) are associated with the presence of iron sulfides, their alteration products and the contained ferromagnesian silicates. Total S is also elevated (0.80 - 5.28 wt.%), reflecting the contribution of sulfides and sulfate salts. Arsenic occurs in elevated amounts (up to >1 wt.%) and is associated with the Fe-sulfides, mainly arsenopyrite, on the basis of mineralogical results. Manganese (up to >1 wt.%) is mainly associated with rhodochrosite, while Mg (0.14 to 1.67 wt.%) mainly reflects the presence of dolomite. Calcium (1.87 - 11.97 wt.%) is associated with Ca-carbonates and sulfates.

In the Olympias tailings several metals are associated with the contained sulfides and are of particular economic importance such as Au and Ag. Gold reaches 12 g/t and silver varies from 4 to 20 g/t, being strongly associated with galena, as indicated by the chemical analyses. The most abundant trace metals, considering only the absolute values (excluding the above upper detection limits values) were As (2684 - 26960 g/t), Pb (1318 - 8802 g/t), Zn (709 - 7733 g/t), Sb (147 - 672 g/t) and Cu (62 - 665 g/t).

The mineralogical composition affects the grade of acidity, which is measured in pH. The Olympias mine tailings, which are predominantly unoxidized, do not indicate significant pH deviation, ranging from 7.5 to 8.1. The increased amount of carbonates, that prevails in the majority of samples of the unoxidized tailings and the relatively low concentration of sulfides and sulfates are factors that determine their alkaline nature. However, the oxidized type of tailings, which exhibit lower content in carbonate minerals, has significantly lower pH, equal to 3.0, suggesting an acidic environment.

5. Conclusions

The mine wastes deposited in Olympias, NE Chalkidiki, were derived from the beneficiation of the Olympias Pb-Zn-Au-Ag carbonate-replacement ore and their mineralogical composition shows a significant resemblance with the source ore and host rocks. The results indicate that they predominantly consist of gangue minerals such as quartz, rhodochrosite, calcite and dolomite and minor sulfides, such as pyrite, arsenopyrite, sphalerite, chalcopyrite and galena. Due to the increased amount of contained carbonate minerals the tailings generate an alkaline environment with pH values between 7.5 and 8.1. However, variations in composition result in the formation of separate phases, such as thin layers and lenses of oxidized material that generates an acidic environment. This oxidized material is characterized by its yellow colour, the high content in jarosite and the low content in carbonates. The tailings also contain minor quantities of iron and manganese oxides, often enriched in Zn and Pb and in some cases Fe, Sb and As, most probably after adsorption/co-precipitation mechanisms. Sulfates, such as gypsum and jarosite and surface efflorescent salts, identified as ferrohexahydrite, hexahydrite and halotrichite constitute the main secondary phases. Arsenic, Pb, Zn, Sb and Cu have been detected in high concentrations, whereas in terms of precious metals content, the Olympias tailings are enriched in Au (up to 12 g/t) and Ag (up to 20 g/t).

6. Acknowledgements

We would like to thank Professor Dr. G. Voutsas from the Physics Department, Aristotle University of Thessaloniki for providing XRD analyses. For the XRD analyses, provided by the School of Geology, Department of Mineralogy-Petrology-Economic Geology, Aristotle University of Thessaloniki, we would like to thank Prof. Dr. A. Filippidis. Assistant Professor Dr. L. Papadopoulou, School of Geology, Aristotle University of Thessaloniki, is especially thanked for her valuable assistance with the SEM. We would also like to express our gratitude to Hellas Gold S.A. for providing part of the chemical analyses and the permission for obtaining the samples. Finally, special thanks are due to Dr. I. Georgiadis for his useful comments on the entire study.

7. References

Alifragkis, D., Voulgaridou, H., Orfanoudakis, M., Daftsis, E., Characlias, J., Papaioannou, A., Vavelidis, M., Alifragkis, E., Voulgaropoulou, M. and Galatsianou, A., 2012a. Reclamation of mining waste (cake) of Kassandra Chalkidikis mines after stabilization with rich in Fe and Mn oxides materials, 14th Congress of the Hellenic Soil Science Society (HSSS), Thessaloniki, *Proceedings of the Hellenic Soil Science Society (HSSS)*, (in Greek with English abstract) (in press).

Alifragkis, D., Voulgaridou, H., Orfanoudakis, M., Daftsis, E., Papaioannou, A., Vavelidis, M., Characlias, J., Alifragkis, E., Voulgaropoulou, M. and Galatsianou, A., 2012b. Reclamation of old tailing disposal area of Olympias Halkidiki mine after stabilization with rich in Fe and Mn oxides materials, 14th Congress of the Hellenic Soil Science Society (HSSS), Thessaloniki, *Proceedings of the Hellenic Soil Science Society (HSSS)*, (in Greek with English abstract) (in press).

Alpers, C.N., Blowes, D.W., Nordstrom, D.K. and Jambor, J.L., 1994. Secondary minerals and acid mine-water chemistry. *In*: Jambor, J.L. and Blowes, D.W., *eds.*, Environmental Geochemistry of Mine Wastes, *Mineralogical Association of Canada Short Course*, 247-270.

Blowes, D.W. and Jambor, J.L., 1990. The pore-water geochemistry and the mineralogy of the vadose zone of sulfide tailings, Waite Amulet, Quebec, Canada, *Applied Geochemistry*, 5(3), 327-346.

Burg, J.P., Godfriaux, I. and Ricou, L.E., 1995. Extension of the Mesozoic Rhodope thrust units in the Vertiskos-Kerdillion Massifs (Northern Greece), *C. R. Acad. Sci.*, Paris. 320(9), 889-896.

Chryssoulis, S.L. and Cabri, L.J., 1990. Significance of gold mineralogical balances in mineral processing, *Trans. Inst. Min. Metall.*, 99, C1-C10.

Forward, P., Francis, A. and Liddell, N., 2011. Technical Report on the Olympias Project, Au Pb Zn Ag Deposit, Northern Greece, European Goldfields Ltd., Whitehorse, Yukon, 213 pp.

Fytikas, M., Innocenti, F., Manetti, P., Peccerillo, A., Mazzuoli, R. and Villari, L., 1984. Tertiary to Quaternary evolution of volcanism in the Aegean region, *Geological Society, London, Special Publications*, 17(1), 687-699.

Gilg, H.A. and Frei, R., 1994. Chronology of magmatism and mineralization in the Kassandra mining area, Greece: The potentials and limitations of dating hydrothermal illites, *Geochimica et cosmochimica acta*, 58(9), 2107-2122.

Himmerkus, F., Reischmann, T. and Kostopoulos, D., 2009. Serbo-Macedonian revisited: a Silurian basement terrane from northern Gondwana in the Internal Hellenides, Greece, *Tectonophysics*, 473(1), 20-35.

Hudson-Edwards, K.A., Jamieson, H.E. and Lottermoser, B.G., 2011. Mine wastes: Past, present, future, *Elements*, 7(6), 375-380.

Jamieson, H.E., 2011. Geochemistry and mineralogy of solid mine waste: essential knowledge for predicting environmental impact, *Elements*, 7(6), 381-386.

Kalogeropoulos, S.I. and Economou, G.S., 1987. A study of sphalerite from the carbonate-hosted Pb-Zn sulfide deposits of the Eastern Chalkidiki Peninsula, Northern Greece, *Canadian Mineralogist*, 25, 639-646.

Kalogeropoulos, S.I., Kilias, S.P., Bitzios, D.C., Nicolaou, M. and Both, R.A., 1989. Genesis of the Olympias carbonate-hosted Pb-Zn (Au, Ag) sulfide ore deposit, eastern Chalkidiki Peninsula, northern Greece, *Economic Geology*, 84(5), 1210-1234.

Kilias, A., Falalakis, G. and Mountrakis, D., 1999. Cretaceous-Tertiary structures and kinematics of the Serbomacedonian metamorphic rocks and their relation to the exhumation of the Hellenic hinterland (Macedonia, Greece), *International Journal of Earth Sciences*, 88(3), 513-531.

Kockel, F., Mollat, H. and Walther, H.W., 1977. Erläuterungen zur Geologischen Karte der Chalkidhiki und angrenzender Gebiete 1:100.000 (Nord-Griechenland), *Bundesanstalt für Geowissenschaften und Rohstoffe*, Hannover.

Kockel, F., Mollat, H. and Gundlach, H., 1975. Hydrothermally altered and (copper) mineralized porphyritic intrusions in the Serbo-Macedonian Massif (Greece), *Mineralium deposita*, 10(3), 195-204.

Kockel, F., Mollat, H., Walther, H.W., Antoniades, P. and loannides, K., 1978a. Stavros sheet (1:50,000), geological map of Greece, Athens, Greece, Inst. Geol. Mining Research.

Kockel, F., Mollat, H., Walther, H.W., Antoniades, P. and loannides, K., 1978b. Stratoniki sheet (1:50,000), geological map of Greece, Athens, Greece, Inst. Geol. Mining Research.

Leckie, J.O., Benjamin, M.M., Hayes, K., Kaufman, G. and Altmann, S., 1980. Adsorption/coprecipitation of trace elements from water with iron oxyhydroxide, Rep. prepared for the Electric Power Research Institute, EPRI-RP-910.

Lottermoser, B., 2010. Mine wastes: Characterization, Treatment and Environmental Impacts, Springer-Verlag Berlin Heidelberg, 400 pp.

McLean, E.O., 1982. Soil pH and lime requirement. Methods of soil analysis. Part 2, *Chemical and microbiological properties*, 199-224.

Nebel, M.L., Hutchinson, R.W. and Zartman, R.E., 1991. Metamorphism and polygenesis of the Madem Lakkos polymetallic sulfide deposit, Chalkidiki, Greece, *Economic Geology*, 86(1), 81-105.

Nordstrom, D.K., 2011. Mine Waters: Acidic to Circmneutral, *Elements*, 7(6), 393-398.

Papagrigoriou, S., Papadaki, A., Katselis, I., Kotzageorgis, G., Mpekiaris, I., Tentes, G., Manitara, K., Meletiou, A., Mprousti, P., Mpakouras, X., Kavvadia, A., Sfikas, G., Adamopoulos, T., Apostolidis, I., Hallmann, B., Ivovic, M., Vogiatzis, K., Kassomenos P., Charalampopoulou, M. and Toris, N., 2010. Environmental impact assessment of the mining and metallurgical plants of Hellas Gold S.A. in Chalkidiki, ENVECO S.A., Athens, (in Greek), 1074 pp.

Tompouloglou, C., Campiglio, C. and Bellon, H., 1986. Les manifestations magmatiques dans le Massif Serbo-Macédonien (Grèce) à l'Oligo-Miocène. Précisions apportées par l'analyse radiométrique 40K-40Ar. Comptes rendus de l'Académie des sciences. Série 2, Mécanique, Physique, Chimie, Sciences de l'univers, *Sciences de la Terre*, 302(7), 431-436.

Vavelidis, M. and Melfos, V., 2012. Study of the ancient metallurgical works in Kipouristra, Olympiada (Ancient Stageira), NE Chalkidiki, *Scientific Annals of the Faculty of Geology, School of Science, Aristotle University of Thessaloniki*, Special Volume 101, 9-16 (in Greek).

Vavelidis, M., Pernicka, E. and Wagner, G.A., 1983. Untersuchungen in den Pb-Ag und Au-Vorkommen von NE-Chalkidiki (Nordgriechenland), *Beihefte zum Eurp. J. Miner.*, 212-213.

Zaimis, S., 2013. Mineralogical and geochemical investigation at reclamation sites of old tailings disposal area at Olympias mining district, NE Chalkidiki. Master thesis, Faculty of Geology, Aristotle University of Thessaloniki, Greece (in Greek with English abstract).

Special Session

Environmental Geochemistry: mobility and speciation of chemical elements in the system rock-soil-water-plant (endorsed by SEGH)

Conveners
Ariadne Argyraki
Athanasios Godelitsas

Δελτίο της Ελληνικής Γεωλογικής Εταιρίας, τόμος L, σελ. 2100-2107
Πρακτικά 14ου Διεθνούς Συνεδρίου, Θεσσαλονίκη, Μάιος 2016

Bulletin of the Geological Society of Greece, vol. L, p. 2100-2107
Proceedings of the 14th International Congress, Thessaloniki, May 2016

RARE ELEMENTS (ZR, NB, LA, CE AND HF) IN TRAFFIC EMITTED FERRIMAGNETIC PARTICLES FROM ROAD DUSTS

Bourliva A.[1], Papadopoulou L.[1], Aidona E.[2] and Pipera K.[1]

[1]Department of Mineralogy-Petrology-Economic Geology, School of Geology, Aristotle University of Thessaloniki, 54124, Thessaloniki, Greece, annab@geo.auth.gr, lambrini@geo.auth.gr, piperakir@gmail.gr

[2]Department of Geophysics, School of Geology, Aristotle University of Thessaloniki, 54124 Thessaloniki, Greece, aidona@geo.auth.gr

Abstract

In the present study, the presence and the elemental contents of some rare elements such as zirconium (Zr), niobium (Nb), lanthanum (La), cerium (Ce) and hafnium (Hf) in different fractions (bulk samples, non-magnetic fraction-NMF and magnetic fraction-MF) of road dusts from the city of Thessaloniki, were investigated. The mean Zr, Nb, La, Ce and Nb concentrations in the bulk road dust samples were 32.1, 5, 16.4, 40 and 0.9 μg g^{-1},αντίστοιχα.. On the other hand, the studied rare elements concentrations in magnetic fractions (MFs) were enriched and the enrichment ratios, defined as the concentration ratio of metals in MFs and NMFs, ranged between 1.9 (Ce) and 7.9 (Nb). Pearson's correlation coefficients in the MFs indicated 3 groups of elements originating from common source: a) Zr-Hf-Cr-Cu-Mo-Sn-Sb, b) Nb-Ni-Cu-Mo-Sn and c) La-Ce. The significant correlations of the Zr, Hf and Nb with elements such as Cu, Sb, Sn and Mo which are characteristic of brake wear emissions indicated that the emission of these elements in the urban environment can also be attributed to vehicular traffic as they are highly associated with traffic emitted ferrimagnetic particles.

Keywords: *road dust, rare metals, magnetic particles, traffic emissions, Thessaloniki.*

Περίληψη

Στην παρούσα εργασία, μελετήθηκαν η παρουσία και οι συγκεντρώσεις ορισμένων σπάνιων στοιχείων όπως το ζιρκόνιο (Zr), το νιόβιο (Nb), το λανθάνιο (La), το σέριο (Ce) και το χάφνιο (Hf) σε διαφορετικά κλάσματα (ολικό, μη-μαγνητικο και μαγνητικό) δειγμάτων σκόνης δρόμων από την πόλη της Θεσσαλονίκης. Οι μέσες συγκεντρώσεις των Zr, Nb, La, Ce και Hf στις σκόνες των δρόμων (ολικό δείγμα) ήταν 32.1, 5, 16.4, 40 and 0.9 μg g^{-1},αντίστοιχα. Απο την άλλη πλευρά, οι συγκεντρώσεις των μελετούμενων στοιχείων στο μαγνητικό κλάσμα ήταν σχετικά αυξημένες και ο λόγος εμπλουτισμού που προκύπτει από το λόγο των συγκεντρώσεων στο μαγνητικό και το μη-μαγνητικό κλάσμα κυμαίνεται μεταξύ 1.9 (Ce) και 7.9 (Nb). Οι συντελεστές συσχέτισης μεταξύ των στοιχείων στο μαγνητικό κλάσμα υπέδειξαν 3 ομάδες στοιχείων με κοινή προέλευση: α) Zr-Hf-Cr-Cu-Mo-Sn-Sb, β) Nb-Ni-Cu-Mo-Sn και γ) La-Ce. Η σημαντική συσχέτιση των Zr, Hf και Nb με τα στοιχεία Cu, Sb, Sn και Mo που κυριαρχούν σε εκπομπές σωματιδιών από την φθορά των φρένων, αποδεικνύει ότι η παρουσία των σπάνιων αυτών στοιχείων στο αστικό περιβάλλον σχετίζεται άμεσα με

την κυκλοφορία των αυτοκινήτων και έχουν άμεση σχέση με τα εκπεμπόμενα από την κυκλοφορία των αυτοκίνητων σιδηρομαγνητικά σωματίδια.
Λέξεις κλειδιά: *σκόνη δρόμων, σπάνια στοιχεία, μαγνητικά σωματίδια, εκπομπές αυτοκινήτων, Θεσσαλονίκη.*

1. Introduction

In recent years the anthropogenic magnetic particles contained in suspended dusts have been studied with an increased frequency (Sagnotti *et al.*, 2006; Bućko *et al.*, 2010). In urban areas, in the absence of heavy industry, circulation of motor vehicles is considered among the most important sources of magnetic particles emission into the environment (Shilton *et al.*, 2005; Bućko *et al.*, 2010; Yang *et al.*, 2010). The past investigations concentrated mostly on the correlation of traffic emitted ferrimagnetic particles with toxic heavy metals (Goddu *et al.*, 2004). However, a number of other rare elements i.e. Zr, Nb, La, Ce and Hf are also released into the environment and are identified as traffic emitted elements.

Rare earth elements such as La and Ce have become extremely interesting in the last decades, owing to increasing use of these elements in car catalysts. The vehicles catalytic converters contain also a number of stabilizers, commonly oxides of rare earth elements and alkaline earth elements such as Ce, La and Zr, which stabilize the catalyst support (a γ-alumina based honeycomb) and enhance the oxidation of pollutants (Lyubomirova *et al.*, 2011). On the other hand zirconium (Zr) and hafnium (Hf) are less studied although their concentrations in road dust are also correlated with traffic emissions. On the contrary, appears to be very little information on Nb in the urban environment and as concluded it is unlikely that motor vehicles are significant sources of Nb in the urban environment (Kennedy, 2003).

Since vehicular emission of rare elements has received little attention so far and the obtained results are mainly based on whole dust samples and not on individual separated magnetic phases, the present study attempts to offer insight into their concentration and enrichment in magnetic extracts from urban road dust samples.

2. Materials and Methods

2.1. Sample Collection and Magnetic Separation

Road dust samples (each weighting almost 100 g) were collected from selected roads in Thessaloniki's city core (5 sampling locations) (Fig. 1). Road dusts were collected twice within a gap of 5 months before and almost at the end of the dry season (April and September) in the year 2014. The dust samples were mainly collected by gently sweeping at all sites a comparable area of one square meter (1 m^2) from pavement edges using clean plastic dustpans and brushes for each sampling site. Care was taken to reduce the disturbance of fine particles. Samples (bulk sample) were dried in an oven at 35ºC for 3 days and mechanically sieved and the <250-μm size fraction was used for subsequent analyses. The magnetic extracts were obtained by using a hand magnet sealed with a propylene bag. The extraction procedure was run continuously until no magnetic particles were attached to the magnet. The extracted magnetic fractions (MFs) and the residue (hereafter called non-magnetic fractions, NMFs) were collected and weighed.

2.2. Geochemical Analyses and Magnetic Measurements

The concentration of a total of 45 elements including the studied rare metals (Zr, Nb, La, Ce, and Hf) were determined in different road dust fractions (bulk sample, magnetic fraction-MF and non-magnetic fraction-NMF) using inductively coupled plasma mass spectrometry (ICP-MS) after a multi acid digestion procedure at the accredited Acme Analytical Laboratories, Canada. Specifically, about 0.25 g of the prepared dust sample was heated in a concentrated HF-HNO_3-$HClO_4$ mixture to fuming and taken to dryness. The residue was dissolved in HCl. Quality assurance and quality

control (QA/QC) included reagent blanks, analytical duplicates and analyses of certified reference materials (multi-element soil standard OREAS25A-4A and OREAS45E). Results of the method blanks were always below detection limits. The recovery rates were estimated within ±10 % of the certified value, and analytical precision was better than ±5 %. Mass specific magnetic susceptibility (χ) of dust samples was measured at low (0.46 kHz) and high (4.6 kHz) frequency using a Bartington MS2 laboratory magnetic susceptibility meter (Bartington Ltd., UK), equipped with a dual frequency MS2B sensor. Magnetic susceptibility value provides an indication of the concentration within the sample of strongly ferrimagnetic minerals, such as magnetite.

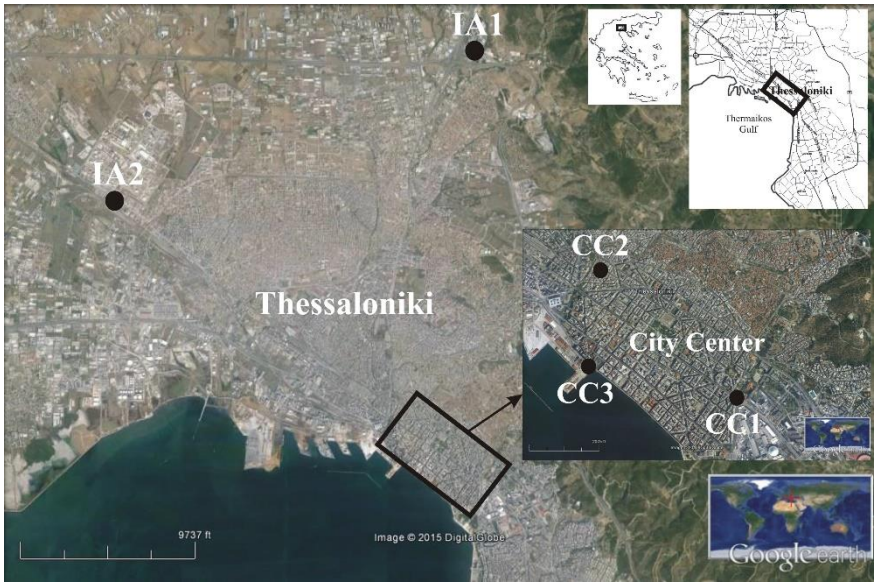

Figure 1 - Map of study area and sampling sites of road dust samples. CC: city center, IA: industrial area.

3. Results and Discussion

3.1. Magnetic Properties and Elemental Contents of Road Dust Samples

Road dusts exhibited values of mass specific magnetic susceptibility (χ_{lf}) ranging between 122.5×10^{-8} and 638.7×10^{-8} m^3 kg^{-1}, indicating the presence of a considerable amount of ferrimagnetic iron oxides (Bourliva *et al*., 2015). The contents of MFs in road dusts varied between 2.2 and 14.7 wt%.

Road dusts are dominated by Ca (12.08-27.72%), while lower abundances of Al and Fe occurred with their concentrations ranging between 1.04 and 3.92% and 0.61 and 3.91%, respectively. Mg, Na, K and Ti presented lower quantities with mean values below 1% (Bourliva *et al.*, 2015). In order to have a clear view and to differentiate between natural and anthropogenic loads, the elemental concentrations of the different road dust fractions (bulk samples, NMFs and MFs) were normalized to the bulk continental crust values (Taylor and McLennan, 1995) and the results are presented in Figure 2.

As shown, large-ion lithophile elements (LILE) such as potassium, rubidium, strontium, and barium along with some light rare earth elements (LREE) such as lanthanum (La) and cerium (Ce) which are considered as crustal components, were depleted in the bulk road dusts. Iron as it was expected, was depleted in NMFs and highly enriched in MFs, while Ca, Al, Na, and K were depleted in the MFs, indicating that these elements are associated with the non-magnetic dust particles mainly of crustal origin (Bourliva *et al*., 2015). The elements of considerable anthropogenic impacts in road dusts (both bulk samples and MFs) are Cu, Zn, As, Mo, Sn, Sb, Pb and Bi (Fig. 2). On the other

hand, elements such as Cr and W which reflect anthropogenic input were not presented highly enriched in the bulk road dusts, while their normalized elemental concentrations were significantly higher in the MFs exhibiting an anthropogenic origin related to the ferrimagnetic dust particles.

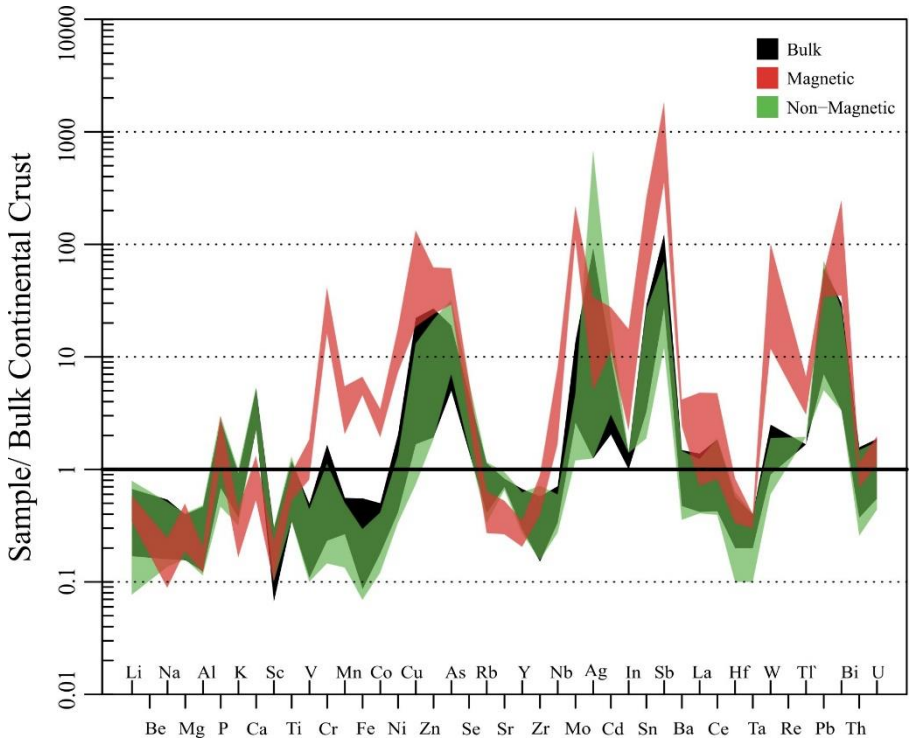

Figure 2 - Elemental concentrations of the different road dust fractions (bulk sample, non-magnetic fraction and magnetic fraction) normalized to bulk continental crust values. Normalization values after Taylor and McLennan (1995).

Elevated concentrations of metals such as Cu and Zn in road dusts are attributed to tire and break wear (Thorpe and Harrison 2008). Furthermore, Cr, Cu, Ni, Pb and Zn are abundant metals in brake lining materials (Westerlund and Johansson, 2002), while brake wear emissions have been cited as a potentially important source of Sb and Sn emissions to the environment (Thorpe and Harrison 2008). Kennedy and Gadd (2003) presented evidence to suggest that brake dust is enriched in Cr, Cu, Fe, and Sn. On the other hand, molybdenum (Mo) is used primarily in steel alloys, many of which are used in automotive industry, while tires and brake pads contained low concentrations of Mo (Kennedy and Gadd, 2003). As far as Pb is concerned, after the prohibition of its use as a fuel additive for gasoline, brake wear emissions may represent a significant source of airborne Pb (Westerlund and Johansson, 2002).

3.2. Rare Elements Content in Road Dust Samples

The range and the mean concentrations of the rare elements Zr, Nb, La, Ce and Hf in bulk road dusts and the non-magnetic and magnetic fractions are presented in Table 1. As shown in Table 1, bulk road dusts exhibited concentration ranges from 15.1 to 57.4 μg/g for Zr, from 3.7 to 7.8 μg/g for Nb, from 6.7 to 22.1 μg/g for La, from 14 to 61 μg/g for Ce and from 0.60 to 1.70 μg/g for Hf respectively. The mean concentrations of these rare elements decreased in the order Ce > Zr > La > Nb > Hf.

Table 1 - Minimum, Maximum, Mean and Median Concentrations of Rare Elements in different fractions of road dust samples from the city of Thessaloniki.

Elements	Bulk				Non-Magnetic Fraction				Magnetic Fraction			
	Min	Max	Mean	Median	Min	Max	Mean	Median	Min	Max	Mean	Median
Zr	15.1	57.4	32.1	25.0	15.6	71.6	32.8	31.8	39.0	88.8	70.6	72.6
Nb	3.7	7.8	5.0	4.2	3.0	6.6	4.3	4.1	18.4	88.2	31.2	21.8
La	6.7	22.1	16.4	16.3	6.5	19.8	14.2	14.8	11.4	76.8	30.2	23.9
Ce	14	61	40	32	13	62	41.4	43	27	157	71.2	64.5
Hf	0.60	1.70	0.90	0.70	0.30	1.90	0.95	0.95	1.00	2.50	1.82	1.85

According to the elemental concentrations normalized to bulk continental crust, zirconium (Zr), niobium (Nb), lanthanum (La), cerium (Ce) and hafnium (Hf) are depleted in the bulk road dusts (Fig. 2). Furthermore, cerium (Ce) appeared more enriched compared to lanthanum, which is not normal for crustal rocks and enforced the fact that there were low crustal influences in road dust samples. On the contrary, in the MFs and taking into account the normalized values niobium (Nb) appeared enriched, while La and Ce are enriched in most of the cases in the MFs. On the other hand, Zr and Hf though presenting higher concentrations in the MFs are considered still depleted in the MFs (Fig. 2).

In order to evaluate the correlation of the studied rare elements with the NMFs and MFs, the enrichment ratios of the studied rare elements, which are defined as the concentration ratio of elements in magnetic fraction to non-magnetic fraction, were determined and are presented in Figure 3.

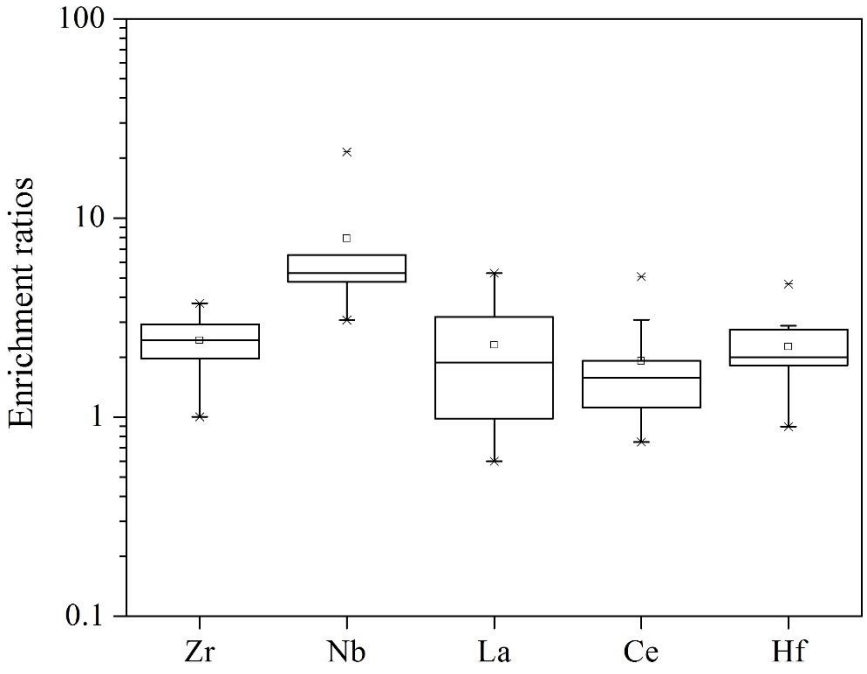

Figure 3 - Enrichment ratios of rare elements of road dusts.

As shown, the mean enrichment ratios ranged between 1.9 (Ce) and 7.9 (Nb) decreasing in the order Nb > Zr > La > Hf > Ce. Though the enrichment ratios presented low values for some of the studied rare elements, these elements could be considered related to the ferrimagnetic dust particles. Specifically, niobium which presented significantly high enrichment ratios exhibiting in some cases concentrations more than 15 times higher in the MF, its correlation with the ferrimagnetic particles could be considered certain. Furthermore, the positive anomaly of Nb compared to the negative

anomaly of tantalum (Ta) in the MFs, which are transition metals almost always paired together in nature, enforced the anthropogenic origin of Nb in road dust samples (Fig. 2).

3.3. Traffic Related Rare Elements in Road Dusts Magnetic Fractions

In order to identify the possible sources of Zr, Nb, La, Ce and Hf in the ferrimagnetic dust particles, inter-element relations in the magnetic fraction were determined and the correlation diagrams of the pairs which presented significant correlations ($p<0.05$) are illustrated in Figure 4. As shown, zirconium and hafnium presented good correlation with the same elements i.e. Cr, Cu, Mo, Sn and Sb and along with their strong positive correlation ($r_{Zr\text{-}Hf}= 0.976$) indicated a group of elements with probable common source. Additionally, niobium (Nb) presented good correlations with Ni, Cu, Mo and Sn. Generally, the good correlation of the studied rare metals with metals which were highly enriched in the road dusts MFs also suggested an anthropogenic origin of these elements in the ferrimagnetic particles.

Specifically, the strong correlations between Zr, Hf, and Nb with elements such as Cu, Sb, Cr, Sn, and Mo which are attributed to brake wear emissions, enforce the fact that Zr, Hf and Nb in the road dusts magnetic fraction are traffic related, originating from brake wear emissions. Zr ($ZrSO_4$ as abrasive) and Sb (i.e. Sb_2S_3 as solid lubricant) are used in friction materials for an automotive brake system (Jang and Kim, 2000). Additionally, metals such as Ti, Cr, Zr, Al and Hf can be used as coating materials in automotive brake pads. On the other hand, niobium is used as a microalloying element in high strength steels for automotive applications (Mohrbacker, 2006) and along with chromium, nickel, copper, titanium and molybdenum, can be used in grey iron alloys for vehicle brake disc (http://www.niobelcon.com).

As far as the rare earth elements lanthanum (La) and cerium (Ce) are concerned, they exhibited a high positive correlation ($r_{La\text{-}Ce}=0.958$) indicating their chemical association and their derivation from a common source which probable is the catalytic converters. La and Ce are important components of the catalysts wash coat as they are added in order to improve or stabilize the catalytic activity of platinum group elements (PGEs). Ce is employed as a promoter in catalytic converters and is also a fuel additive (Jarvis *et al.*, 2001; Rauch *et al.*, 2002; Kan and Tanner, 2005; Lough *et al.*, 2005).

4. Conclusions

In this present study, the presence of rare metals such as Zr, Nb, La, Ce and Hf in road dusts from the city of Thessaloniki and its relation to traffic emitted iron-rich magnetic particles were investigated. Road dusts (bulk samples) exhibited significantly high contents in Cu, Zn, As, Mo, Sn, Sb, Pb with their concentrations being significantly higher than the background levels, reflecting anthropogenic influences in the road dusts. The mean concentrations of the studied rare elements decreased in the order Ce > Zr > La > Nb > Hf, while according to the normalized values were depleted in the bulk road dusts. The enrichment ratios of the Zr, Nb, La, Ce and Hf in the MFs indicated their preferred gather in the magnetic fractions and enforced the fact that are highly associated with the ferrimagnetic particles. Finally, the significant correlations among Zr, Hf and Nb with elements associated with brake wear emissions such as Cu, Sb, Sn and Mo, suggested their anthopogenic origin related to vehicular traffic.

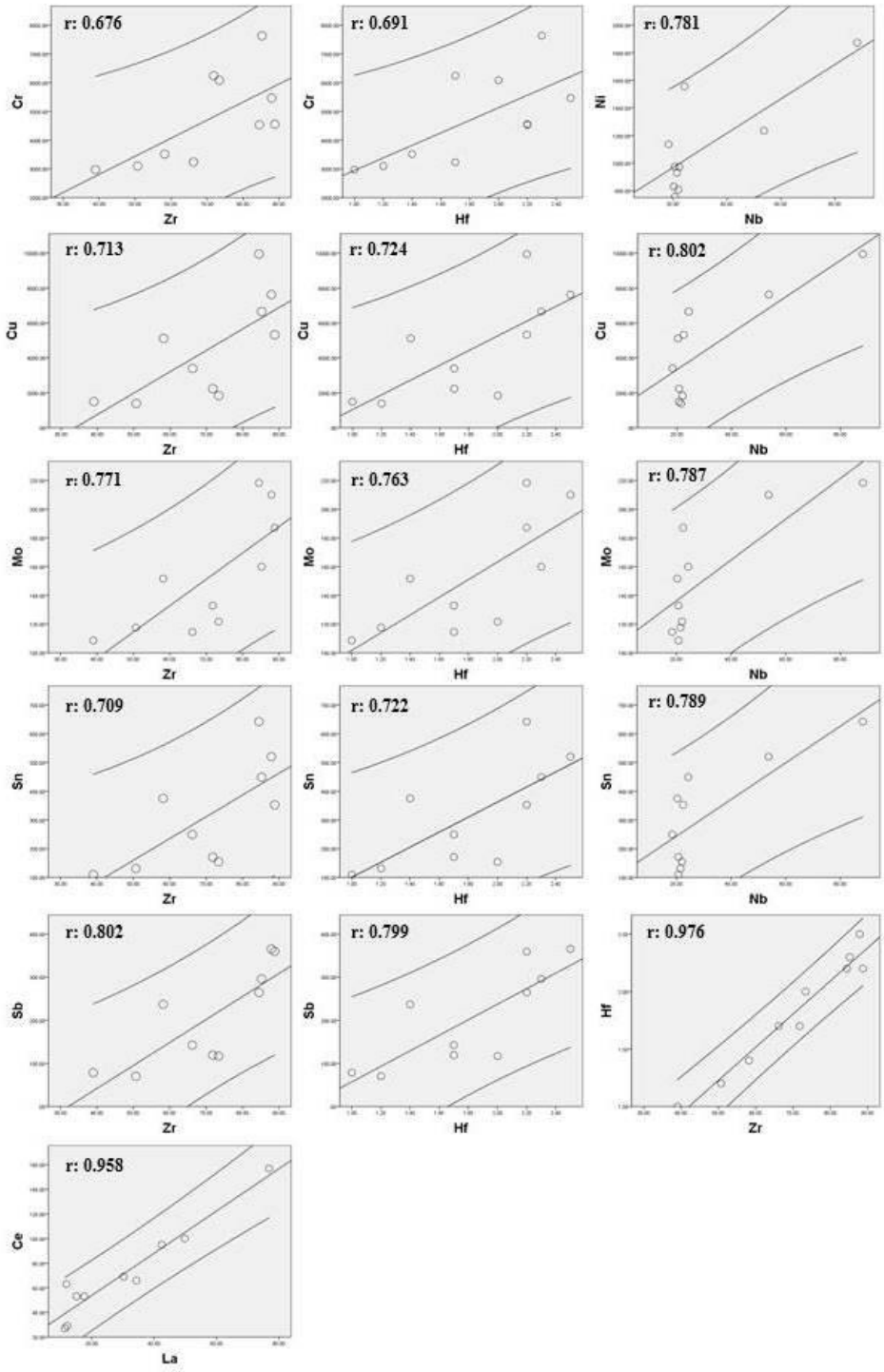

Figure 4 - Inter-element relations in the magnetic fraction of road dusts. The r value is the Pearson's correlation coefficient.

5. Acknowledgments

The first author acknowledges financial support from IKY Fellowships of Excellence for Postgraduate Studies in Greece-Siemens Program.

6. References

Bourliva, A., Papadopoulou, L. and Aidona, E., 2015. Heavy metal content and health risk associated with magnetic particles in urban road dusts from Thessaloniki city center, Greece: Preliminary results, *Proceedings of the 14th International Conference on Environmental Science and Technology*, e-Proceedings, CEST2015_00655.

Bućko, M.S., Magiera, T., Pesonen, L.J. and Janus, B., 2010. Magnetic geochemical, and microstructural characteristics of road dust on roadsides with different traffic volumes-case study from Finland, *Water Air Soil Pollut.*, 209, 295-306.

Goddu, S.R., Appel, E., Jordanova, D. and Wehland, F., 2004. Magnetic properties of road dust from Visakhapatnam (India): relationship to industrial pollution and road traffic, *Phys. Chem. Earth*, 29, 985-995.

Jang, H. and Kim, S.J., 2000. The effects of antimony trisulfide (Sb_2S3) and zirconium silicate ($ZrSiO_4$) in the automotive brake friction material on friction characteristics, *Wear*, 239, 229-236.

Jarvis, K., Parry, S. and Piper, J., 2001. Temporal and spatial studies of autocatalyst-derived platinum, rhodium, and palladium and selected vehicle-derived trace element in the environment, *Environ. Sci. Technol.*, 35, 1031-1036.

Kan, S.F. and Tanner, P.A., 2005. Platinum concentrations in ambient aerosol at a coastal site in South China, *Atmos. Environ.*, 39, 2625-2630.

Kennedy, P. and Gadd, J., 2003. Preliminary examination of trace elements in tyres, brake pads, and road bitumen in New Zealand, Report, Ministry of Transport, New Zealand.

Kennedy, P., 2003. Metals in particulate material on road surfaces, Report, Ministry of Transport, New Zealand.

Lough, G.C., Schauer, J.J., Park, J.S., Shafer, M.M., Deminter, J.T. and Weinstein, J.P., 2005. Emissions of metals associated with motor vehicle roadways, *Environ. Sci. Technol.*, 39, 826-836.

Lyuborinova, V., Djingova, R. and van Elteren, J. T., 2011. Fractionation of traffic-emitted Ce, La and Zr in road dusts, *J. Environ. Monit.*, 13, 1823-1830.

Mohrbacker, H., 2006. Niobium microalloyed automotive sheet steel-a cost effective solution to the challenges of modern body engineering. *Proceedings of the International Symposium on Niobium Microalloyed Sheet Steel for Automotive Application*, The Minerals, Metals & Materials Society.

Rauch, S., Morrison, G.M. and Moldovan, M., 2002. Scanning laser ablation ICP-MS tracking of platinum group elements in urban particles, *Sci. Total Environ.*, 286, 243-251.

Sagnotti, L., Macrì, P., Egli, R. and Mondino, M., 2006. Magnetic properties of atmospheric particulate matter from automatic air sampler stations in Latium (Italy): toward a definition of magnetic fingerprints for natural and anthropogenic PM10 sources, *Geophys. Res.*, 111, B12S22, doi: 10.1029/2006JB004508.

Shilton, V.F., Booth, C.A., Smith, J.P., Giess, P., Mitchell, D.J. and Williams, C.D., 2005. Magnetic properties of urban street dust and their relationship with organic matter content in the West Midlands, UK, *Atmos. Environ.*, 39, 3651-3659.

Taylor, S.R. and McLennan, S.M., 1995. The geochemical evolution of the continental crust, *Reviews Geophys.*, 33, 241-265.

Thorpe, A. and Harrison, R.M., 2008. Sources and properties of non-exhaust particulate matter from road traffic: A review, *Sci. Tot. Environ.*, 400, 270-282.

Westerlund, K.G. and Johansson, C., 2002. Emission of metals and particulate matter due to wear of brake linings in Stockholm, *Air Pollut.*, 10, 793-802.

Yang, T., Liu, Q., Li, H., Zeng, Q. and Chan, L., 2010. Anthropogenic magnetic particles and heavy metals in the road dust: magnetic identification and its implications, *Atmos. Environ.*, 44, 1175-1185.

http://www.niobelcon.com

Δελτίο της Ελληνικής Γεωλογικής Εταιρίας, τόμος L, σελ. 2108-2117
Πρακτικά 14ου Διεθνούς Συνεδρίου, Θεσσαλονίκη, Μάιος 2016

Bulletin of the Geological Society of Greece, vol. L, p. 2108-2117
Proceedings of the 14th International Congress, Thessaloniki, May 2016

HEAVY METALS IN CULTIVATED SOIL AND PLANTS OF DAMOUR URBAN AREA - LEBANON

Fadel D.[1], Argyraki A.[2], Papageorgiou S.[2] and Kelepertzis E.[2]

[1]Lebanese University, Facutly of Agriculture, Department of Plant Production. Dekwaneh – Lebanon, dr.danifadel@gmail.com

[2]National & Kapodistrian University of Athens, Faculty of Geology & Geoenvironment, Panepistimiopolis Zographou, 15784, Athens, Greece, argyraki@geol.uoa.gr, papagstamatia@hotmail.com, kelepert@geol.uoa.gr

Abstract

Preliminary data on heavy metals concentrations in soil and edible plants of Damour-Lebanon are presented for the first time. Concentration ranges of Zn, Cu, Ni, Cr, Co, Mn, Fe, Ba, Pb and Cd in soils and vegetables collected from urban allotments in Damour were determined and assessed taking into account the pseudototal (extracted by aqua regia) and mobilizable (0.43 M acetic acid extractable) concentrations of the elements in the rhizosphere soil of the plants as well as the total concentrations in edible plant tissue. Average elemental concentrations in urban allotments are low in general. No detectable concentrations of the non-essential heavy metals Pb and As were measured in the studied plants while concentrations of micronutrient elements in plants were within normal ranges. The collected data indicate that previous land use is an important factor controlling heavy metal content in soil and that there is a complex mechanism controlling micronutrient uptake by plants.
Keywords: *vegetables, harmful elements, mobility, phytoavailability.*

Περίληψη

Παρουσιάζονται για πρώτη φορά δεδομένα συγκεντρώσεων βαρέων μετάλλων στο έδαφος και καλλιέργειες της περιοχής Νταμούρ Λιβάνου. Μετρήθηκαν οι ψευδοολικές και κινητοποιήσιμες συγκεντρώσεις των Zn, Cu, Ni, Cr, Co, Mn, Fe, Ba, Pb και Cd σε δείγματα εδαφών καθώς και οι αντίστοιχες ολικές συγκεντρώσεις των ίδιων στοιχείων σε φυτικούς ιστούς λαχανικών που καλλιεργούνται στην περιοχή Δεν ανιχνεύθηκαν συγκεντρώσεις των μη απαραίτητων στοιχείων Pb και As ενώ αυτές των υπόλοιπων στοιχείων που μελετήθηκαν βρίσκονται εντός των φυσιολογικών ορίων. Οι συγκεντρώσεις στο έδαφος φαίνεται να επηρεάζονται από την προηγούμενη χρήση γης και αυτές στα φυτά φαίνεται να ρυθμίζονται μέσω της λειτουργίας σύνθετων μεταβολικών μηχανισμών.
Λέξεις κλειδιά: *οπωροκηπευτικά, βλαβερά στοιχεία, κινητικότητα, φυτοδιαθεσιμότητα.*

1. Introduction

Heavy metals are among the most common chemical constituents in soil that are associated with human activities (Rodríguez Martín *et al.*, 2015; Tahmasbian *et al.*, 2013). Some of these potentially harmful elements, such as zinc (Zn), copper (Cu), manganese (Mn), chromium (Cr), nickel (Ni) and cobalt (Co), are known as essential trace metals because they are required only in minute amounts by living

organisms for normal growth while others such as lead (Pb), arsenic (As) and cadmium (Cd) are toxic even at low concentrations (Kelepertzis and Argyraki, 2015). Bioavailability of heavy metals in soils is critically dependent on the chemical speciation of the metals and plants respond only to the fraction that is "phytoavailable" (Yao-Tsung *et al.,* 2014). The readily soluble fraction of heavy metals in soil is generally considered to be phytoavailable, but there is growing awareness that the various methods for assessment of "soluble" and "phytoavailable" fractions need reevaluation. It is generally known that there are variations in the rates of soil to plant transfer between different plant species but also between the same plant species from different areas (McLaughlin and Singh, 1999). It has been reported that previous land uses of the cultivated areas have a significant contribution to the levels of heavy metal contamination of soil and plants (Srour, 2000).

The Lebanese National Center for Scientific Research (2006) published "the soil map of Lebanon" and the most widely represented soils reported, were calcareous Terra-Rossa and Rendzina soils located in the agricultural plains of Bekaa, Aakkar, Koura, Sour, Saida, Rachaya and Hasbaya while outcropping rocks include sandstone, basalt and similar older volcanic material. Most of Lebanese soils are high in active clays with the exception of some marly and sandy soils. Active clays are clays with the ability to adsorb and immobilize positively charged ions, namely heavy metals. Earlier studies with reference to the dynamics of some heavy metals (Cd, Ni, and Cr) in four Lebanese soils (Samad, 2000) and effect of acidifying fertilizers on Cd, Cr and Ni mobility and uptake by radish plants grown on four different Lebanese soils (Srour, 2000) were published. In 2008, Darwish analyzed the soil-groundwater vulnerability to contamination by heavy metals in the central Bekaa plain. Generally, soils in Lebanon are young and characterized by fragility, poor consistency and shallowness, especially on sloping terrains. A few publications exist on the soil database and mapping (Darwish *et al*., 1999; Samad, 2000); however, there are no published data related to the specific area of Damour, south of Beirut. This study is the first to present preliminary data on the interaction between soil and edible plants with respect to heavy metal concentrations in Damour, Lebanon. The main objectives were to determine the concentration range of heavy metals (Zn, Cu, Ni, Cr, Co, Mn, Fe, Ba, Pb and Cd) in 16 samples of the edible parts of cultivated plants collected from urban allotments in Damour, and to assess the pseudototal and mobilizable concentrations of the same elements in the rhizosphere soil of the collected plants.

2. Materials and Methods

2.1. Description of the study area

The study area is located in Damour, a Lebanese town 24 km south of central Beirut, and a part of Greater Beirut (Fig. 1). The region has a Mediterranean climate with intensive precipitation between January and May (600-900 mm). The city is located in one of the few flat areas of the Lebanese coast. It is built to the north of the river, the ancient Tamyrus. This region of the southern coastal hills is a typical horticultural area, with large-scale greenhouse production of many fruits and vegetables. The pilot study area pulls water exclusively from groundwater wells due to the absence of any collective irrigation network.

Since this area is located in the central part of Lebanon, it is characterised by the intimate contact between the mountain and the sea, as well as the quasi absence of the coastal plain (Sanlaville, 1977). Concerning the pedology of the area around Damour, the karstic parent rock is covered by red soils "Terra Rossa" (El Moujabber *et al.*, 2005; Darwish and Zurayk, 1997). Red soils are consisted of residual clay after calcareous material loss that can facilitate water intrusion. The northern part of Damour (Hadeth-Choueifat) consists of large patches of gravely sandy soils. Those soft fluvial deposits belong to the Quaternary and enhance horizontal water infiltration. The southern part of Damour belongs to the Cenomanian-Turanian (C4-5) karstified hard limestone (Dubertret, 1955) which is susceptible to seawater intrusion (FAO, 1973). The rock mineralogy is simple including calcite. Metallic minerals appear to be confined to the iron ores of haematite and limonite (Walley,

1998). No data exist on the pollution status of Damour as the area is not included in the Lebanese pollutant release and transfer register (El-Jisr, 2014).

Figure 1 - Air photograph of the study area showing the location of sampled allotments (A, B, C).

2.2. Sampling methodology and preparation for analyses

Soil and plant samples were collected in the spring of 2015 from several urban allotments in the city of Damour, Lebanon. The samples were collected from three communal allotments within Damour: site A, site B and site C (Fig. 1). The distance between them is a few hundred meters. Sixteen different plant species were selected for plant sampling and each one was accompanied by its rhizosphere soil sample (depth 0-10 cm). After collection the soil samples were air dried at a constant temperature of 40 °C for 3 days in a thermostatically controlled oven at the Laboratory of Soil Sciences in the Faculty of Agriculture of the Lebanese University. The soil was subsequently sieved using a 2 mm nylon sieve. Also, the edible parts of plants were selected, thoroughly washed three times with deionized water and air dried at room temperature. All dried samples were stored in plastic bags at room temperature in a dark room for transportation. Soil and relevant plant samples were finely ground using automated agate mill for further analyses in the Laboratory of Economic Geology and Geochemistry in the National and Kapodistrian University of Athens. The total concentrations of heavy metals (Pb, Zn, Cu, Mn, Cr, Ni, Co, Cd) and of trace elements (Fe, Ba) in plants were measured by Inductively Coupled Plasma Optical Emission Spectroscopy (ICP-OES) following microwave digestion by HNO_3/ H_2O_2, 6:1 v/v. Pseudototal heavy metal concentrations in soil were measured by ICP-OES following digestion by a mixture of HNO_3, H_2O_2 and HCl (US-EPA, 2002). Also, acetic acid (0.43 M) extractable concentrations of same heavy metals and trace elements were measured by the same analytical technique after mixing 1g of each soil sample with 40 ml acetic acid and shaking for 16 h at room temperature in an overhead shaker. All used utensils were thoroughly washed between the samples to avoid any cross contamination. Analytical quality control procedures including duplicate analysis performance, blank solutions inclusion and soil certified reference materials (NIST SRM 2709 and NIST SRM2711a for the total analysis and BCR-483 and BCR-484 for the acetic acid extraction) were performed at random positions within the analytical batches. The obtained results from analytical control were found within acceptable limits for all geochemical results.

2.3. Assessment of physicochemical soil parameters

The major physicochemical properties of topsoil were measured including pH, organic matter content and texture (sand, silt, clay). Soil pH was measured after mixing the sieved soil samples (<2 mm) with deionized water in a solid -to-liquid ratio of 1:2.5 (ISO, 1994). Organic matter content of the soil samples was estimated by the loss-on-ignition (LOI) method (US-EPA, 2002) by heating 1 g of each sample to 450^0C for 4 hours in a furnace oven. Since the method determines the organic matter content in the soil, a conversion factor of 1.724 has been used to convert organic matter to

organic carbon based on the assumption that organic matter contains 58% organic C (i.e., g organic matter/l .724 = g organic C). The grain size distribution in the sand, silt and clay fractions was determined using the Bouyoucos Hydrometer Method (Bouyoucos, 1962).

3. Results and Discussion

3.1. Heavy metals in soil samples

The measured pseudototal concentrations of heavy metals in soil (S) samples and their sampling sites (coded as A, B and C) are presented in Table 1. The statistical summary of physicochemical properties including pH, total carbon (TOC) and texture (sand, silt, clay %) and acetic acid extractable concentrations of heavy metals for the investigated soil samples from Damour city are shown in Table 2.

Mean values of the pseudototal elemental concentrations in soil are following the decreasing order Fe>Mn>Cu~Zn>Ba>Cr>Ni>Sb. Iron registered the highest concentration in all the extracts among the metals (Table 1). Most of soil textures shown in Table 2 are loamy sand (means of sand and clay are 81.8 and 6.3 % respectively). The minimum sand percentage is 69.92 giving a sandy loam texture to soils grown with potatoes and the maximum sand percentage is 94.72 giving a sandy texture to soils grown with Armenian cucumbers. For example, potatoes grow in any of all these well drained soils. The TOC average value of 2.8 % is considered normal for urban agriculture soils. However, in contrast to other studies (Rodrigues *et al.,* 2009) no significant correlations were detected between the key soil properties and the pseudototal concentrations of heavy metals. The pH values of soil samples ranged from 7.4 (slightly alkaline) to 8.4 (moderate alkaline). The decreasing order of soil extractable concentrations differs from the order of pseudototal concentrations and is as follows: Mn>Ba>Zn>Co>Fe>Ni>Cu. Manganese presents the highest extractability ratio while Fe is hardly extractable by the dilute acetic acid (Fig. 2). The low extractability ratio of Cu is also worth noting as if combined with the relatively low pseudototal concentrations in soil might be indicative of Cu deficiency in the plants grown in the study area.

3.2. Heavy metals in plant samples

The myriad of parameters controlling the chemical fate of specific elements in soils determine their solubility and availability for plant uptake. The elemental concentrations in plant tissues are presented in Table 1.

Plant tissue average content of heavy metals is generally lower than the respective content of rhizosphere soil with some exceptions in our study. The highest concentration of Zn (135 mg/kg) was found in potato tubers of site A and the lowest (16.6 mg/kg) in cucumber. The rate of Zn absorption differs greatly among both plant species and growth media (Kabata-Pendias *et al.,* 2001; Warren *et al.,* 1970). The levels of Cu in cucumbers (368.8 and 359.1 mg/kg) are also extremely high when compared to other edible plant tissues (average 46.8 mg/kg). The levels of Cu in spring onion were also high (94.4 mg/kg) when compared to the normal levels recommended by WHO/FAO and NAFDAC for metals in foods and vegetables (in the order of 30 mg/kg). High levels of Cu in soil have been reported by various researchers (Kakulu, 2003 and Awofolu, 2005) and may explain high concentrations in plant tissue, however, in the present study

Table 1 – Sample codes, plant species and their respective pseudototal concentrations (mg/kg) of elements in soil (S) and plant (P) tissues. Sampling areas are coded as (A), (B) and (C). bdl = below detection limit.

Sample code	Scientific name	Common name	Area	Zn S	Zn P	Cu S	Cu P	Ni S	Ni P	Cr S	Cr P	Co S	Co P	Sb S	Sb P	Mn S	Mn P	Fe S	Fe P	Ba S	Ba P
DS1	*Cucumis sativus*	cucumber	A	114	27.4	32	5.1	23	1.9	26	bdl	54	11.1	1.5	0.5	384	19.9	19386	485	108	22.2
DS2	*Allium cepa*	green onion	A	119	25.4	15	3.2	21	13.7	23	18.5	51	94.2	8.4	0.9	352	16.3	18932	561	105	16.8
DS3	*Solanum tubersosum*	potato	A	129	134.8	16	17.6	19	4.4	21	bdl	63	17.4	3.2	0.8	343	46.4	17907	763	97	45.0
DS4	*Cucurbita pepo*	kousa squash	A	59	47.6	10	9.2	21	5.0	22	bdl	54	10.4	0.8	0.6	367	39.4	20237	2153	69	26.0
DS6	*Brassica oleracea*	cabbage	A	62	73.8	12	5.2	44	4.0	37	bdl	63	2.2	bdl	0.4	573	72.6	21686	225	61	56.8
DS7	*Mentha spicata*	spearmint	A	171	31.0	22	7.6	24	3.8	25	bdl	55	6.6	1.1	0.6	372	41.6	20144	235	139	33.6
DS8	*Phaseolus vulgaris*	common beans	A	56	32.6	11	5.4	43	7.6	36	bdl	69	17.6	bdl	0.8	607	115.0	21754	2938	69	34.0
DS9	*Phaseolus vulgaris*	white kidney beans	B	63	41.4	11	13.8	22	6.0	24	bdl	54	2.2	bdl	0.6	405	22.0	19869	119	71	11.6
DS10	*Cichorium intybus*	chicory	B	64	49.4	13	7.6	41	4.2	36	bdl	68	5.0	bdl	0.4	552	78.8	21616	371	74	14.4
DS12	*Solanum melongena*	eggpalnt	B	74	21.8	14	2.6	23	4.8	25	bdl	48	10.0	bdl	0.8	396	30.0	20397	690	102	40.6
DS13	*Cucumis melo*	armenian cucumber	B	48	44.8	13	11.6	20	6.0	27	bdl	56	30.4	1.6	1.0	252	19.2	17110	423	105	13.4
DS14	*Solanum lycopersicum*	tomato	C	63	46.0	7	12.0	17	3.2	14	bdl	54	5.0	0.3	0.4	302	64.4	18772	576	44	27.8
DS15	*Beta vulgaris*	chard	C	67	27.0	16	6.2	24	2.8	26	bdl	52	8.2	bdl	0.8	392	121.6	20674	525	76	31.8
DS16	*Raphanus sativus*	radish	C	64	44.4	14	31.0	21	16.6	21	12.0	59	25.2	1.7	0.6	371	16.8	19724	934	78	12.0
DS17	*Abelmoschus esculentus*	okra	C	46	bdl	12	bdl	19	bdl	26	bdl	46	bdl	bdl	bdl	258	bdl	17203	bdl	111	bdl
DS18	*Lactuca sativa*	lettuce	C	59	29.0	9	9.0	21	3.8	21	bdl	61	21.2	1.1	1.0	354	72.8	20280	648	62	48.8
DS19	*Cucumis sativus*	cucumber	A	122	59.4	37	359.1	25	4.0	31	bdl	49	18.0	bdl	6.6	423	85.2	20358	1366	130	51.2
DS21	*Mentha spicata*	spearmint	A	65	37.0	13	2.8	48	2.0	46	bdl	72	7.4	bdl	0.6	605	21.0	21724	177	72	9.2
DS23	*Cucumis sativus*	cucumber	A	117	16.6	33	368.8	25	2.2	29	bdl	53	5.6	bdl	0.4	419	17.8	20224	410	124	26.8
DS24	*Mentha spicata*	spearmint	A	61	29.0	13	11.8	48	4.0	46	bdl	70	35.6	bdl	1.0	609	79.4	21740	790	73	61.0

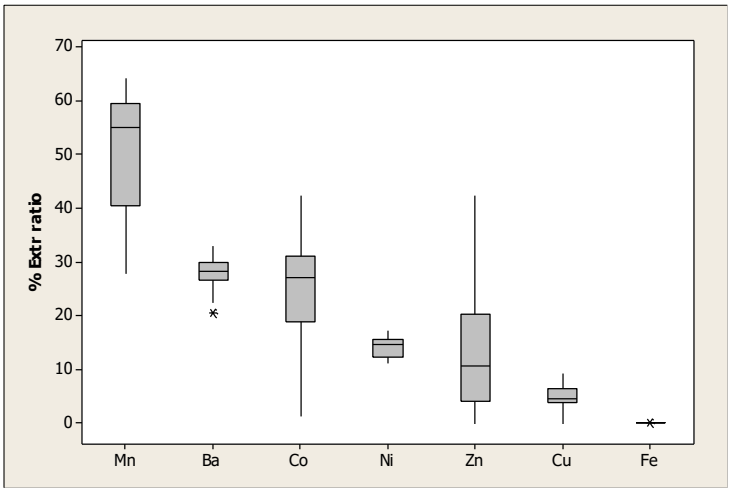

Figure 2 - Box plots of extractability ratios of the studied elements in soils of Damour, based on pseudototal and dilute acetic acid extractable concentrations. The elements are ordered according to decreasing median value (horizontal lines).

soil Cu is relatively low and high plant concentrations are sporadic. This is indicative of a different source of Cu in the specific samples, possibly related to crop management practices.

The highest concentrations of Fe were found in kousa squash (2153 mg/kg), common beans (2938 mg/kg) and cucumber (1366 mg/kg) grown in site A. Also, radish (934 mg/kg), spearmint (790 mg/kg) and lettuce (648 mg/kg) grown in site B and site C had relatively high Fe concentration compared to the normal levels recommended by WHO/FAO and NAFDAC for metals in food and vegetables ranging between 400 and 500 mg/kg. Nickel, Co, Sb and Mn concentrations were all below the levels recommended by WHO/FAO and NAFDAC for metals in foods and vegetables and are also within the normal range of metals in plants despite their remarkable variation in soil. Chromium concentrations were below the detection levels in most of studied plants with the exception of spring onions (18.5 mg/kg) grown in site C and in radish (12 mg/kg) grown in site A.

Table 2 - Statistical summary of physicochemical properties and extractable concentrations (mg/kg) of heavy metals for the investigated soil samples from Damour city (n = 20).

Parameter	Mean	Median	Standard deviation	Maximum	Minimum
pH	7.9	7.96	0.29	8.06	7.45
TOC (%)	2.8	2.65	1.16	6.29	1.52
Sand (%)	82	83	8.4	90	70
Silt (%)	12	12	7.1	12	0.8
Clay (%)	6	5	2.5	6	4.5
Zn ex	18	11	19	72	1
Cu ex	0.9	0.6	0.7	3.0	0.4
Ni ex	3.9	3.5	1.4	6.7	2.1
Co ex	15	16	5	26	1
Mn ex	204	223	44	250	103
Fe ex	11	9	9	44	3
Ba ex	24	22	6	35	15

3.3 Metal interaction between soil and plants

The correlation between concentrations of pseudototal and extractable heavy metals in soils, physicochemical soil properties (including pH, total carbon and texture) and concentrations of heavy metals in plants was calculated. Significant positive correlation between pseudototal concentrations of soil samples and the concentrations of plant tissues, was observed only for Cu levels (r^2 = 77.47%). There was no correlation between the physicochemical soil properties (pH, TOC, texture) and elemental concentrations. Regarding the soil samples a strong inter-correlation was observed between Ni, Cr, Co, Mn and Fe.

Based on average concentrations of the total study area, the acetic acid soil extraction provided a reasonable prediction of bioavailable Ni and Ba, however, the bioavailability of Zn, Cu and Fe was underestimated while the bioavailability of Co and Mn was overestimated (Fig. 3). A possible explanation for these differences might be that metal uptake by plants involves much more complex mechanisms compared to the potential of dilute acetic acid which only affects metals of specific soil phases, including the release of specifically adsorbed metals on mineral surfaces as well as the dissolution of carbonate minerals.

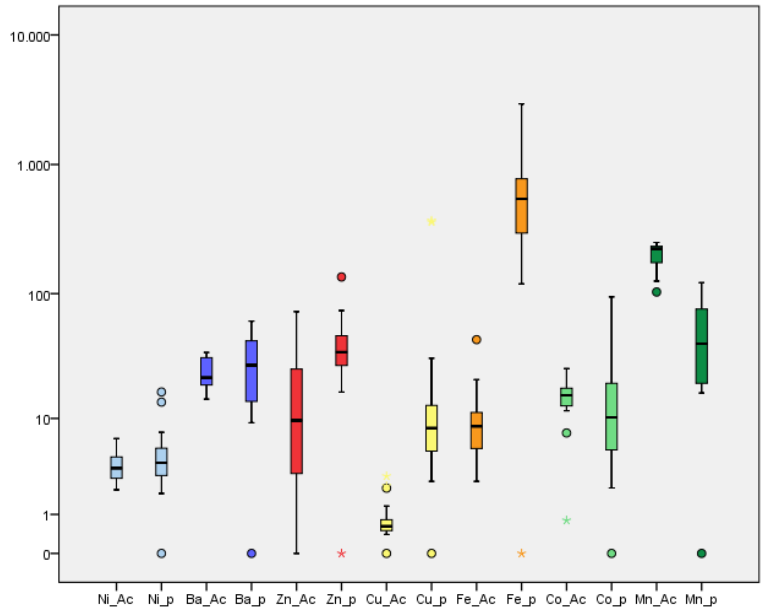

Figure 3 - Box plot comparison of elemental concentrations (mg/kg) of heavy metals in acetic acid extracted soil (denoted by Ac) and plant tissues (denoted by p).

The three communal allotments within Damour areas (site A, site B and site C) were studied in this research in terms of land management and micronutrient concentrations in their produce since urban agriculture is a cosmopolitan upcoming trend. Based on a questionnaire that was distributed to the local managers it was found out that organic crop growing is practiced in all three of them without any application of chemical soil improvers, fertilizers and pesticides. Plants are irrigated with water originating from municipal boreholes. Previous land use varied from parking areas to unused urban space in Damour to horse stables and traditional cultivated parcels. In the first, the surface soil layer (0-70 cm) had been removed and new soil was brought in before starting the cultivation. All three allotments were used for communal agriculture for the past five years.

The average physicochemical topsoil properties from site A, site B and site C were similar. The average pH of every site was 7.8, the average TOC % was 3.1 and the average sand, silt and clay

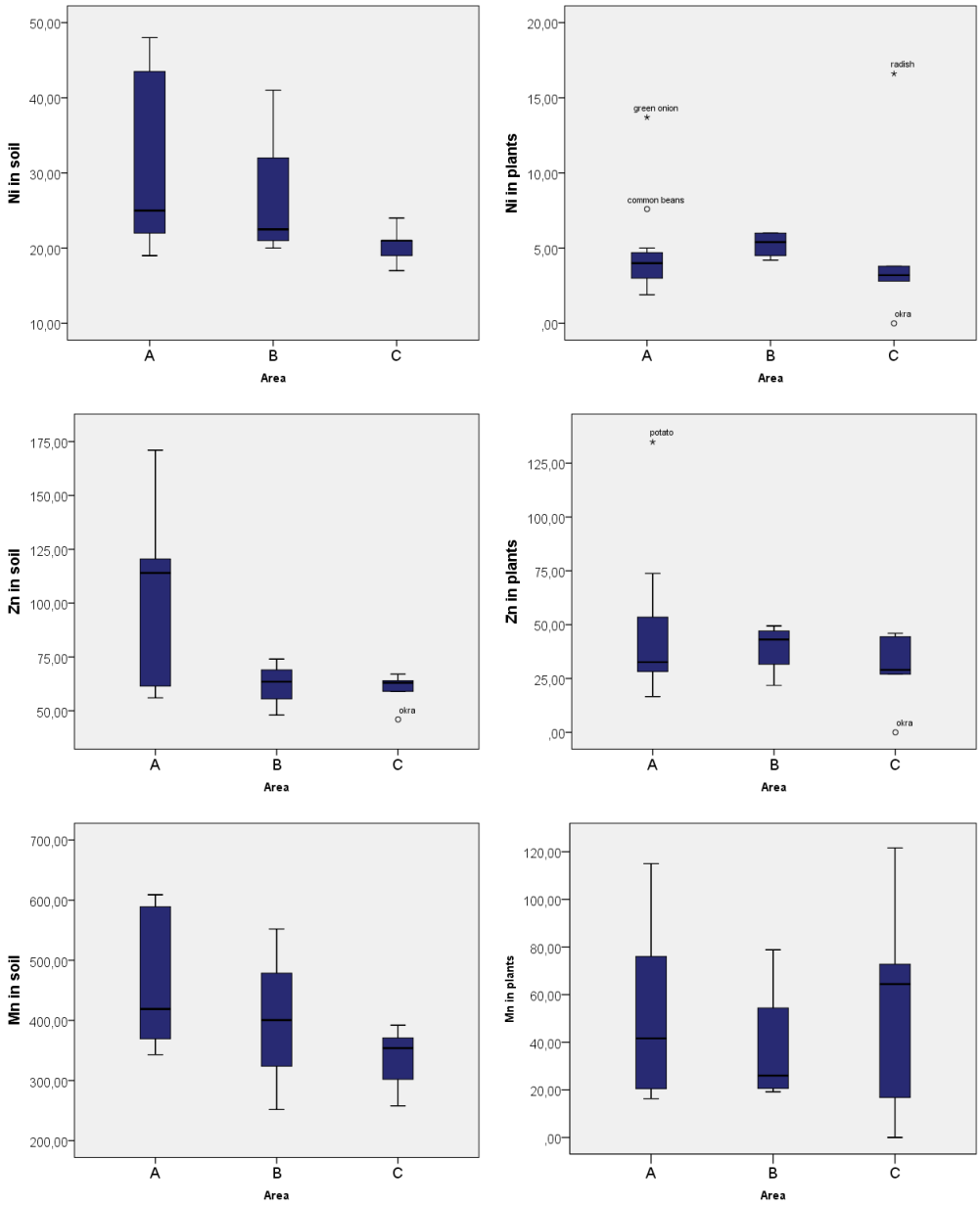

Figure 4 - Boxplot comparison of concentration ranges of Ni, Zn and Mn in soil and plants in the three studied sites.

percentage were 82, 12 and 6 percent respectively. Significant variation of the median concentration values of the studied elements was only observed in site A but not in between sites B and C. Differences of elemental concentrations in soils were also well realized in the first site if compared to the others and this might be related to the previous use of the three studied areas (Fig. 4). Taking into account that different plant species were sampled in each allotment it is difficult to pinpoint any specific factors affecting micronutrient uptake by plants in the three areas. However, with the exception of few outliers elemental concentrations in plants are relatively uniform between the three sites when compared to their respective values in soil (Fig. 4). This observation is indicative of the ability of plant metabolic processes to balance the uptake of micronutrients according to their needs.

3. Conclusions

Data on concentrations of heavy metals in soil and plants from urban agriculture areas in the city of Damour are presented for the first time. The geochemical signature of soil in three communal allotments was studied with respect to Fe, Mn, Ba, Zn, Ni, Cr, Co, Sb, Pb, Cu and Cd and concentration levels in the edible parts of produced vegetables were measured. Heavy metal concentrations in plant tissues were below detection limit for Pb, Cr, and As and within normal ranges for healthy plant growth regarding the rest of the studied elements. Significant correlation was observed between pseudototal and acetic acid extractable concentrations in soil but there was no significant correlation between soils and plants, indicating that a more complex mechanism is controlling micronutrient uptake from soils to plants. Vegetable produce from the communal allotment of the first site contained higher concentrations of Cu, Co, Mn, Fe and Ba compared to the other two communal agriculture areas. Further research is needed in order to determine the controlling factors of micronutrient uptake within the urban environment.

4. Acknowledgments

The authors would like to thank Dr. Ioannis Mitsis for his help and guidance during the plant tissue digestions. Special thanks are given to Dr. Adil Bakir for his involvement in chemical analysis of geochemical solutions at the analytical facilities of School of Earth & Environmental Sciences, University of Portsmouth, UK.

5. References

Awofolu, O.R., 2005. A survey of trace metals in vegetation, soil, and lower animals along some selected major roads in Metropolitan City of Lagos, *Environmental Monitoring and Assessment in Nigeria*, 105, 431-447.

Argyraki, A. and Kelepertzis, E., 2014. Urban soil geochemistry in Athens, Greece: The importance of local geology in controlling the distribution of potentially harmful trace elements, *Science of The Total Environment*, 482-483, 366-377.

Bouyoucos, G.J., 1962. Hydrometer method improved for making particle size analysis of soils, *Agronomy Journal*, 54, 464-465.

Darwish, T. and Zurayk, R., 1997, 'Distribution and nature of red Mediterranean soils in Lebanon along altitudinal sequence', *Catena*, 28, 191-202.

Darwish, T., Haddad, T., Faour, G. and Aboudaher, M., 1999. Environmental changes due to land use changes in Tripoli area, North Lebanon. 6th International meeting on Soils with Mediterranean Type of Climate, Barcelona, Sopain, 4-9 July, 845-847.

Darwish, T.M., Jomaa, I., Awad, M. and Boumetri, R., 2008. Preliminary contamination hazard assessment of land resources in Central Bekaa Plain of Lebanon, *Lebanese Science Journal*, 9(2), 3-13.

Dubertret, L., 1955. Carte Géologique du Liban au 1/200,000, Note Explicative.

El Jisr, K., 2014. Polluant release and transfer register (PRTR) Lebanon, Final Project for UNEP, ECODIT, 2014.

El Moujabber, M., Atallah, T., Bou Samra, B., Fayssal, S., El-Chami, D., Mefleh, J. and Darwish, T., 2012. Seawater intrusion and crop response to salinity in coastal Lebanon, *Lebanese Science Journal*, 14(1), 2013.

FAO, 1973. Results of an airborne thermal infrared survey of the coast of Lebanon for marine sweet water springs. United nation, USA.

ISO 10390, 1994. Soil quality- determination of pH.

Jaworowski. C., 1981. The effect of copper and fertilization with various forms of nitrogen on some physiological indices in maize, *Acta Agrar. Silvistria*, 20, 95 pp.

Kabata-Pendias, A. and Pendias, H., 2001. Trace Elements in Soils and Plants (third edition), CRS Press, Boca Raton, FI.

Kakulu, S.E., 2003. Trace metal concentration in roadside surface soil and tree bark: a measurement of local atmospheric pollution in Abuja, Nigeria, Environmental Monitoring and Assessment, 89(3), 233-242.

Kelepertzis, E. and Argyraki, A., 2015. Geochemical associations for evaluating the availability of potentially harmful elements in urban soils: Lessons learnt from Athens, Greece, *Applied Geochemistry*, 59, 63-73.

Manta, D.S., Angelone, M., Bellanca, A., Neri, R. and Sprovieri, M., 2002. Heavy metals in urban soils: a case study from the city of Palermo (Silicy), Italy, *Sci. Total Environ.*, 300, 229-43.

McLaughlin, M.J. and Singh, B.R., 1999. Cadmium in soil and plants: a global perspective. *In*: McLaughlin, M.J. and Singh, B.R., *eds*., Cadmium in soils and plants, Dordrecht, The Netherlands, Kluwer *Academic Publishing*, 13-21.

Opaluwa, O.Da., Aremu, M.Oa., Ogbo, L.Ob., Abiola, K.Ab., Odiba, I.Ec., Abubakar, M.Ma. and Nweze, N.Od., 2012. Heavy metal concentrations in soils, plant leaves and crops grown around dump sites in Lafia Metropolis, Nasarawa State, Nigeria, *Advances in Applied Science Research*, 3(2), 780-784.

Rodrigues, S., Urquhart, G., Hossack, I., Pereira, M.A., Duarte, A.C. and Davidson, C., 2009. The influence of anthropogenetic and natural geochemical factors of urban soil quality variability: a comparison between Glasgow, UK and Aveiro, Portugal, *Environ. Chem. Lett.*, 7, 141-8.

Samad, F., 2000. Dynamics of Cd, Ni, and Cr in Four Lebanese Soils, M.Sc, Thesis, Faculty of Agricultural and Food Sciences, AUB, October 2000.

Sanlaville, P., 1977, Etude géomorphologique de la région littorale du Liban. Tome II, publication de l'université libanaise, section des ´études géographiques, Beyrouth-Liban, 402-859.

Srour, R., 2000. The Effect of Acid-Forming Fertilizers on the Mobility & Uptake of Cd, Cr, and Ni by Radish Plants in Four Lebanese Soils, M.Sc. Thesis, Faculty of Agricultural and Food Sciences, AUB. May 2000.

Tahmasbian, I., Nasrazadani, A., Shoja, H. and Safari Sinegani, A.A., 2013. The effects of human activities and different land use on trace elements pollution in urban topsoil of Isfahan (Iran), *Environ. Earth Sci*., 71(4), 1551-1560.

US-EPA, 2002. Methods for the determination of total organic carbon (TOC) in soils and sediments, *Report No. NCEA-C- 1282, EMASC-001*, Las Vegas, April 2002, United States Environmental Protection Agency.

Yao-Tsung, C., Zeng, Y.H. and Franz, Z., 2014. Evaluation of Phytoavailability of Heavy Metals to Chinese Cabbage (*Brassica chinensis L.*) in Rural Soils, *The Scientific World Journal*, 2014, Article ID 309396, 10 pp.

Warren, H.V., Delavault, R.E., Fletcher, K. and Wilks, E., 1970. Variation in the copper, zinc, lead and molybdenum content of some British Columbia vegetables. *In*: *Trace Subst. environ. Health*, Vol.4, Hemphill, D.D., Ed., University of Missouri Columbia, MO, 94.

Walley, C.D., 1998. The geology of Lebanon. A summary. Digital Documentation Center at AUB in collaboration with Al Mashriq of Høgskolen in Østfold, Norway, 980429 MB. 10 pp.

Δελτίο της Ελληνικής Γεωλογικής Εταιρίας, τόμος L, σελ. 2118-2126
Πρακτικά 14ου Διεθνούς Συνεδρίου, Θεσσαλονίκη, Μάιος 2016

Bulletin of the Geological Society of Greece, vol. L, p. 2118-2126
Proceedings of the 14th International Congress, Thessaloniki, May 2016

MOBILITY OF MERCURY IN THE VOLCANIC/GEOTHERMAL AREA OF NISYROS (GREECE)

Gagliano A.L.[1], Calabrese S.[2], Daskalopoulou K.[2], Cabassi J.[3-4], Capecchiacci F.[3-4], Tassi F.[3-4], Bonsignore M.[5], Sprovieri M.[5], Kyriakopoulos K.[6], Bellomo S.[1], Brusca L.[1] and D'Alessandro W.[1]

[1]Istituto Nazionale di Geofisica e Vulcanologia, sezione di Palermo, via U. La Malfa 153, 90146, Palermo, Italy, antoninalisa.gagliano@gmail.com, sergio.bellomo@ingv.it, lorenzo.brusca@ingv.it, walter.dalessandro@ingv.it

[2]University of Palermo, Dip. Scienze della Terra e del Mare, via Archirafi 36, 90129, Palermo, Italy, sergio.calabrese@gmail.com, kdaskalopoulou@hotmail.com

[3-4]University of Florence, Dip. Scienze della Terra, and Consiglio Nazionale delle Ricerche, IGG, Via La Pira 4, 50121 Florence, Italy, jacopo.cabassi@unifi.it, francesco.capecchiacci@unifi.it, franco.tassi@unifi.it

[5]Consiglio Nazionale delle Ricerche, IAMC, UOS di Capo Granitola, via del Mare 3, 91021, Campobello di Mazara (TP), Italy, maria.bonsignore@iamc.cnr.it, mario.sprovieri@iamc.cnr.it

[6]National and Kapodistrian University of Athens, Dept. Geology and Geoenvironment, Panestimioupolis, 15784, Ano Ilissia, Greece, ckiriako@geol.uoa.gr

Abstract

In the summer 2013, mercury concentrations in soils and air from Nisyros (Greece), an active volcanic island located in the Aegean Sea, were determined. Up to 102 samples of soil were collected in the Lakki plain caldera and analyzed for mercury by using a cold vapour atomic absorption analyzer, following 7473 US EPA method. Concentrations of mercury in air were also investigated in the same sites with a portable spectrophotometer (Lumex RA-915M). Soil mercury concentrations were in the range from 0.023 to 13.7 μg/g. The mercury concentrations in air showed high background values in the Lakki plain caldera, ranging from 21 to 36 ng/m^3 and maximum values up to 493 ng/m^3 in the proximity of the fumarolic areas, in contrast with the relatively low values (from 2 to 5 ng/m^3) measured in the distal sites outside of the caldera. The positive correlation between mercury and CO_2 and H_2S in the atmosphere highlights the important role of fumarolic gases as carrier for gaseous mercury (Hg^0). On the contrary, mercury does not show significant correlations with CO_2 and H_2S in the soil gases. This finding evidences the complexity of the processes affecting mercury in hydrothermal gases passing through the soil.
Keywords: *soil mercury, atmospheric mercury, hydrothermal gases, carbon dioxide, hydrogen sulphide.*

Περίληψη

Το καλοκαίρι του 2013, προσδιορίστηκαν οι συγκεντρώσεις υδραργύρου στο έδαφος και τον αέρα του ενεργού ηφαιστείου της Νισύρου (Ελλάδα), το οποίο ανήκει στο ενεργό ηφαιστειακό τόξο του νοτίου Αιγαίου. 102 δείγματα εδάφους συλλέχθηκαν και

αναλύθηκαν για υδράργυρο με τη χρήση ψυχρού ατμού ατομικής απορρόφησης αναλυτή, σύμφωνα με τη μέθοδο EPA 7473. Ταυτόχρονα, στα ίδια σημεία πραγματοποιήθηκαν συγκεντρώσεις υδραργύρου στον αέρα, με φορητό φασματοφωτόμετρο (Lumex RA-915M). Οι τιμές των εδαφικών συγκεντρώσεων υδραργύρου κυμαίνονται από 0.023 έως 13.7 mg/g. Οι συγκεντρώσεις υδραργύρου στον αέρα έδειξαν υψηλότερες τιμές υποβάθρου στην περιοχή Λακκί της καλδέρας, μεταξύ 21 και 36 ng/m^3 και μέγιστες τιμές μεγαλύτερες από 493 ng/m^3 κοντά στις φουμαρολικές περιοχές, σε αντίθεση με τις σχετικά χαμηλότερες τιμές (από 2 μέχρι 5 ng/m^3) που μετρήθηκαν σε σημεία μακριά από την Καλδέρα. Η θετική συσχέτιση μεταξύ υδραργύρου, διοξειδίου του άνθρακα και υδροθείου στην ατμόσφαιρα υποδηλώνει το σημαντικό ρόλο των φουμαρολικών αερίων ως φορείς αερίου υδραργύρου (Hg^0). Αντίθετα ο υδράργυρος δεν παρουσιάζει σημαντική συσχέτιση με το CO_2 και H_2S των εδαφικών αερίων δειγμάτων. Αυτό το συμπέρασμα υποδηλώνει την πολυπλοκότητα των διαδικασιών που επηρεάζει τον υδράργυρο που βρίσκεται στα υδροθερμικά αέρια εντός του εδάφους.
Λέξεις κλειδιά: *εδαφικός υδράργυρος, ατμοσφαιρικός υδράργυρος, υδροθερμικά αέρια, διοξείδιο του άνθρακα, υδρόθειο.*

1. Introduction

Volcanoes and geothermal areas are natural sources of compounds that are potentially dangerous for the environment and for the human health. High amounts of gases such as of CO_2, H_2S, SO_2, HF and other including gaseous mercury (Hg^0), are emitted both actively and due to the passive degassing., Trace metals were found at significant concentrations in hydrothermal fluids, being associated with uprising gases. Trace metals even if in very low amount have a significant impact on the biosphere, atmosphere and hydrosphere.

Among the volcanic trace volatile elements, mercury (Hg) is one of the most environmentally-significant (Mason *et al*., 1994) because of its extreme mobility and toxicity (Lamborg *et al*., 2003). The biogeochemistry of Hg is a highly complex issue due to the exchanges between atmospheric, terrestrial and marine pools (Fitzgerald *et al*., 1991). These exchanges are mainly driven by microbial activity, dark abiotic and photochemical reactions affecting the Hg speciation and bioaccumulation (Morel *et al*., 1998). Mercury is emitted in several forms: elemental (metallic) mercury, inorganic mercury compounds, and organic mercury compounds. Metallic mercury (Hg^0) is highly volatile due to its high vapour pressure that permits a long-range transport in the air. Monovalent and divalent mercury are soluble in the water; the divalent mercury, Hg(II), is more stable than monovalent Hg(I), and common in the environment, it may undergo complexation, precipitation with inorganic ligands, and sorption onto the soil matrix. The toxicological properties of mercury for environment and human health depend on the physical and chemical form in which it occurs. Hg vapors, for example, are very dangerous if inhaled, due to their ability to reach the lungs causing pulmonary edema, pain and peeling of the respiratory epithelium of the bronchi.

Mercury, as constituent of volcanic and geothermal fluid (Barnes and Seward, 1997; Bagnato *et al*., 2007), is discharged in the water and released into the atmosphere as Hg^0 being in association with the reducing non-condensable gases (Nimik *et al*., 2013; Robertson *et al*., 1977).

Since in the last decades, authors underlined the correlation in hydrothermal fluid discharged between mercury and hydrogen sulphide (e.g. Vitolo and Saggiani, 2002) related to the formation of solid HgS. Hydrogen sulphide is an odorous pollutant and it is commonly regarded as toxic; it is corrosive and poses severe concerns for human health.

Nisyros Island is a quiescent volcano emitting hydrothermal gases from fumaroles and through soil degassing. Its hydrothermal fluids are particularly rich in H_2S, causing a low pH on soils they permeate (Daskalopoulou *et al*., 2014). The main aim of this work is to calculate the Hg emitted from the hydrothermal area of Nisyros (Greece) in its gaseous form and measure the concentrations

of this pollutant in the soil. These results were compared with H_2S and CO_2 data measured in soil gases and in the air.

2. Study area

Nisyros Island is a quiescent volcano located in the easternmost volcanic group of the South Aegean active volcanic arc. The volcanic edifice developed in the last 200 ka through five distinguished stages (Hunziker and Marini, 2005) that led to the formation of a caldera about 4 km in diameter. The most recent activity is represented by hydrothermal explosions forming several phreatic craters, the last of which occurred in 1887 (Hunziker and Marini, 2005). The Lakki Plain represents the south-eastern remnants of the calderic depression after the emplacement of a series of volcanic domes filling up the north-western part. Fumarolic fields are currently present in this area, mainly within the hydrothermal craters strongly controlled by fracturing along the main NW- and NE-trending active fault systems (Papadopoulos *et al*., 1998) and are fed by a >1000 m deep hydrothermal system having a temperature of 300-350°C. The fumarolized hydrothermal craters can be subdivided into three main groups: The oldest one comprises the Kaminakia craters, the second consists of the Stephanos crater, whereas the third one corresponds to the youngest area where a post-calderic dome (Lophos) is placed and includes the Phlegeton, Polybotes Megalos and Polybotes Micros craters (Caliro *et al*., 2005; D'Alessandro *et al*., 2013). Water vapour (91-99%) is the main component of the fumarolic fluids, followed by CO_2 and H_2S. The estimated total output of CO_2 and H_2S is close to 1 kg/s and <0.3 kg/s, respectively (Caliro *et al*., 2005; D'Alessandro *et al*., 2013).

3. Materials and Methods

A multidisciplinary field campaign was carried out on June 2013 at Lakki Plain, Nisyros Island, where soil gases and soils were sampled and Hg^0, H_2S and CO_2 in the air were measured. A total of 102 soil gas samples were collected at Lakki plain mostly in the fumarolic areas of Kaminakia, Stephanos, Micro Polibotes and Phlegeton craters, and in the areas of Ramos and Lophos (Fig. 1).

Gases were sampled at 50 cm depth using a Teflon tube of 5 mm ID equipped with a tight plastic syringe to avoid air contamination. The over-pressured vials were used for H_2S and CO_2 analysis by using Micro Gas Chromatography with a Micro GC MSHA CP-4900 having 3 independent modules.

Ground temperature was measured at 20 cm depth by using thermal probes and a digital thermometer; these measurements were carried out 10-15 min after the insertion of the thermal probe in the soil in order to achieve thermal equilibrium.

Soils were collected from the first 3 cm of depth at 119 spots at Lakki Plain. Soil samples were homogenized and powdered. Homogenized samples were used for the analysis of total Hg, performed using a DMA-80 analyzer (an atomic absorption spectrophotometer, Milestone, Wesleyan University, Middletown, CT, USA). About 10 mg of dry soil were loaded into specific nickel boats and analyzed according to the US-EPA 7473 method. Accuracy was checked by running replicates of the reference materials NCSDC7701 (0.015±0.006 mg/kg) and MESS3 (0.091±0.009 mg/kg). Bench quality control material was measured at the start of each analytical run (set of 15 samples) for quality assurance and control. The measured values were, on average, within ±8% of the recommended values.

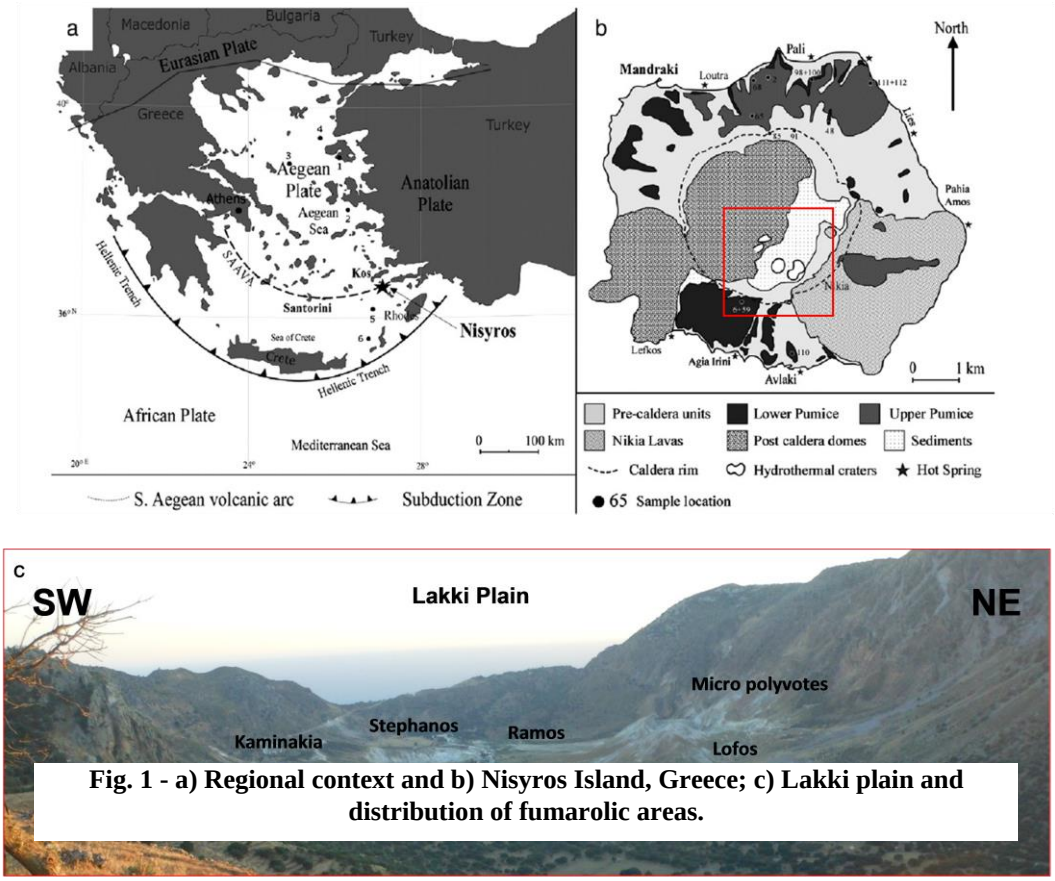

Fig. 1 - a) Regional context and b) Nisyros Island, Greece; c) Lakki plain and distribution of fumarolic areas.

Figure 1 - a) Regional context and b) Nisyros Island, Greece; c) Lakki plain and distribution of fumarolic areas.

The simultaneous real-time measurements of Hg^0, CO_2, H_2S and meteorological parameters (air temperature, pressure and relative humidity) were carried out by coupling a portable Zeeman atomic absorption spectrometer with high frequency modulation of light polarization (Lumex RA-915M) and a Multi-GAS analyzer (manufactured by INGV-Palermo). The acquisition of the GPS signal at the same time allowed to obtain spatial coordinates for each concentration value. All instruments were synchronized and set to high-frequency acquisition (every two seconds). Measurements were carried out along three (Kaminakia, Stephanos and Lofos) transects-walk (about 15 km path, with a mean speed 1.5 km/h) across Lakki plain caldera.

All data were processed by GSA approach (Sinclair, 1974) and plotted by using GIS platform.

4. Results and Discussion

4.1. Soils

Hg data in soils, soil gases and real-time measures of Hg^0, CO_2 and H_2S in the air were integrate to describe, as first step of a deeper study, the behavior of the hydrothermal gases once released and the Hg transportation processes through the soil and into the atmosphere.

Soil temperatures provided indication for the hydrothermal uprising gases, allowing to identify the anomalous areas. High temperatures were considered related to high fluxes of hydrothermal fluids and enhanced enrichment of the hydrothermal component in the soil gases. The temperature distribution map at 20 cm depth indicate temperature above 30°C at all the investigated sites, with the exception of some points along the western flank of Kaminakia crater. Higher temperature, in the range of 50 to 100°C were recorded at the southern part of Stefanos crater, at Phlegeton and Micro Polibotes (Fig. 2).

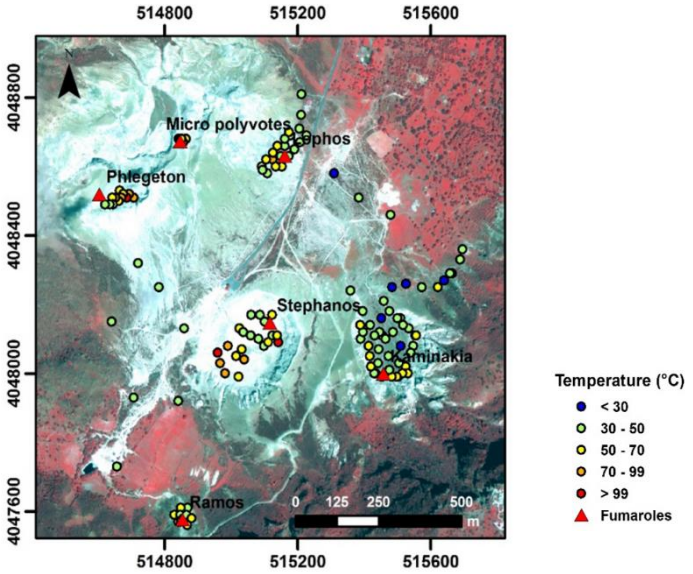

Figure 2 - Temperature distribution at Lakki Plain; temperature measurements were acquired at 20 cm depth.

The GSA approach (Sinclair, 1974) was applied on the CO_2 and H_2S dataset and the obtained probability plot allowed to estimate the source of the gas mixture. On the basis of CO_2 content, gases can be divided in three main families: background values (close to atmosphere), moderately high values (hydrothermal component and air mixing, CO_2 up to 47%) and very high values (hydrothermal component, CO_2 up to 75%) (Fig. 3). The H_2S probability plot shows the same three populations, the highest values being up to 18%.

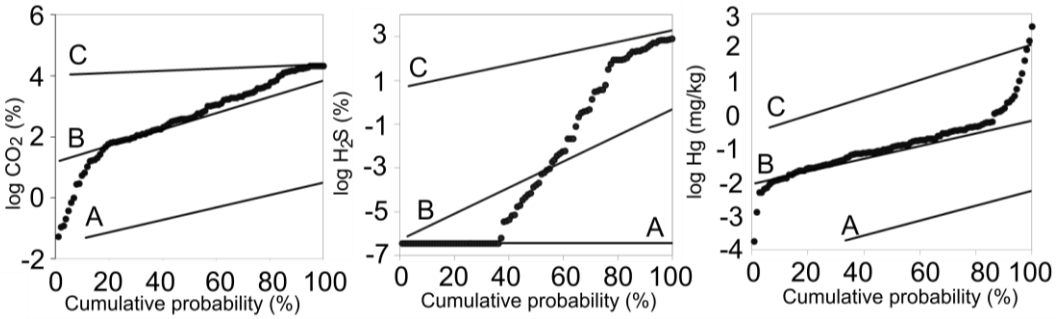

Figure 3 - Probability plots of CO_2 and H_2S in soil gases and total Hg in top soils.

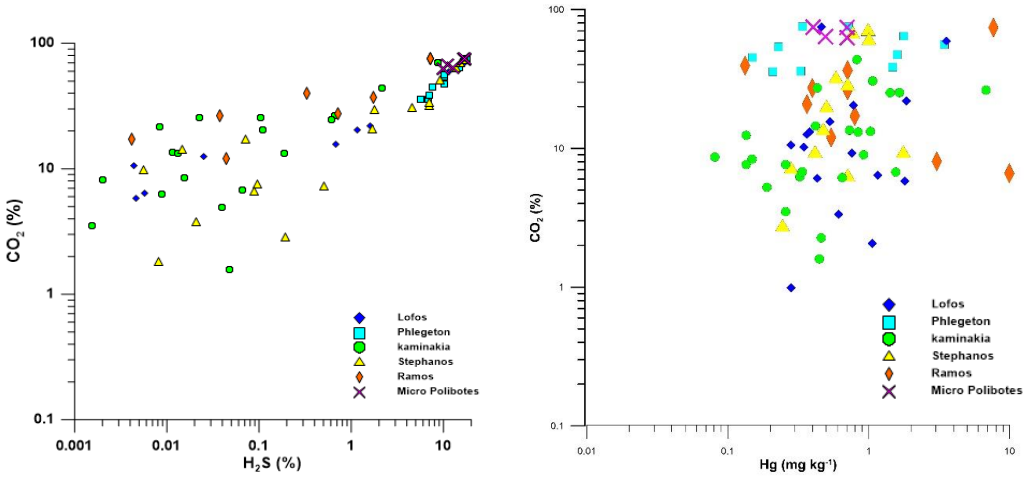

Figure 4 – CO_2-H_2S and CO_2-Hg binary plots.

The CO_2 and H_2S contents in the soil gases show a positive correlation, especially at high concentrations (Fig. 4). The general trend indicates that when CO_2 values are lower than 30%, H_2S content does not exceed 2% due to the influence of the diffusive flux. On the contrary, samples with CO_2 higher than 30%, show high H_2S concentrations, up to 18%, indicating that a convective regime and reducing condition dominate.

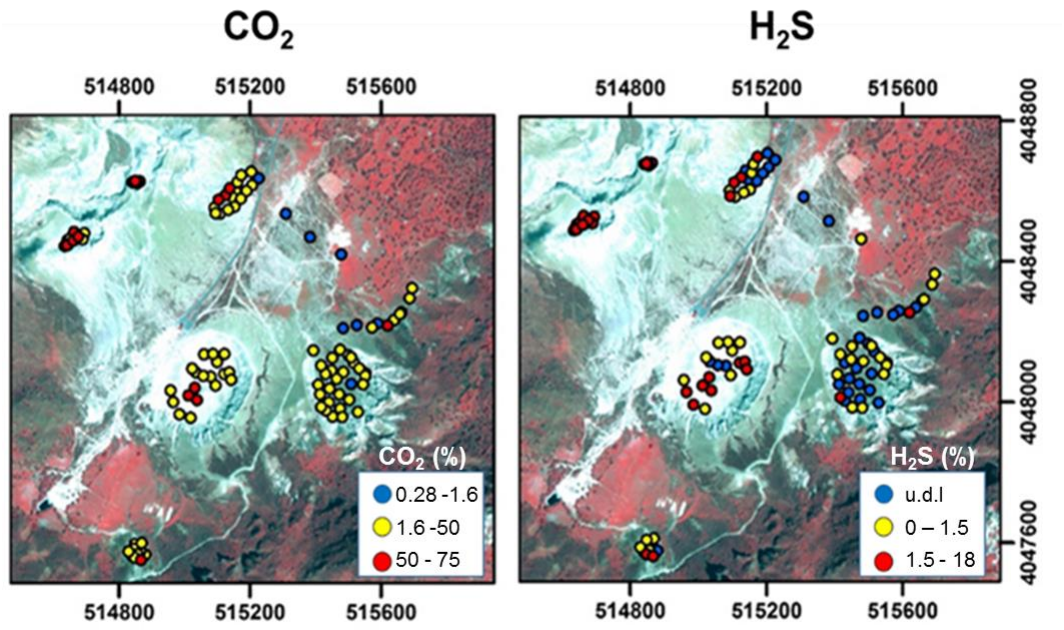

Figure 5 – CO_2 and H_2S distribution at the Lakki Plain in soil gases.

High concentrations of CO_2 and H_2S were measured at Phlegeton and Micro Polyvotes craters (Fig.5), with values close to the fumarolic compositions. Measurements at Lofos and Stefanos

craters showed variable concentrations of H_2S ranging from high concentrations, close to the relative fumarolic composition, down to concentrations below the detection limit.

The distribution of the temperatures and CO_2 and H_2S concentrations seems to be controlled by the fracturing pattern along the main NW- and NE-trending active fault systems, since the highest values were measured in correspondence of the main fumarolic manifestation, such as in the Stefanos, Micro Polyvotes and Phlegeton craters.

Soils were used to measure the total amount of Hg trapped in the soils; Hg value were plotted in a probability plot according to the GSA method and, as for CO_2 and H_2S, three population of data were detected. High Hg concentrations were also measured at the main fumarolic areas, without showing a clear correlation with CO_2 (Fig.4) and H_2S (not shown). It is worth noting that all samples have been taken at the same time and in the same place, but CO_2 and H_2S have been measured on the gas phase collected at 50 cm depth, while Hg has been measured on the solid phase at the soil surface. Nevertheless a better correlation was expected. The accumulation of Hg in the soil matrix does not depend solely on the amount of Hg carried by the upflowing hydrothermal gases but also on the capability of the soil to fix a part of it. Accumulation of Hg in soils depends on the amount of complexing phases within the soil. Mercury in soils shows generally a good correlation with soil organic matter (SOM) (Martin *et al*., 2012 and references therein). The latter, which is the best Hg sink in the soil, was not determined in the soil samples of Nisyros but it is probably very scarce due to the absence of vegetation in the area. Sulphide, which could react with Hg, is also very scarce in the surface soil levels due to the oxidising environment (Daskalopoulou *et al*., 2014). Soil temperatures are though to play a role in Hg retention in soils. This parameter has probably a contrasting effect because higher soil temperatures indicate stronger hydrothermal gases that transport more Hg from depth, but at the same time higher soil temperatures presuppose also a faster remobilization of Hg from the soils because of its high volatility (Engle *et al*., 2006).

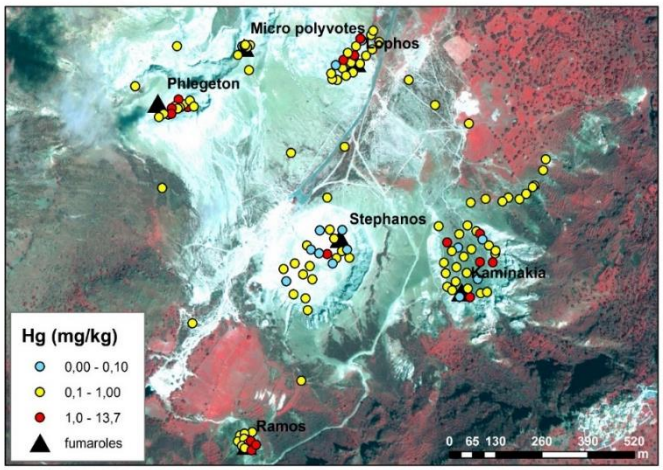

Figure 6 - Total Hg distribution in the top soils of Lakki Plain.

4.2. Atmosphere

The data acquired in the atmosphere were processed by using the GSA approach (Sinclair, 1974) and are showed in Figure 7. The CO_2 probability plot identifies three main populations (A, B and C). The A population groups value up to 440 ppm and refers to the background atmospheric CO_2. Population B (CO_2 up to 690 ppm) is the population with CO_2 level slightly higher than average atmospheric air, probably due to a weak degassing quickly diluted in the air. Population C includes the highest values (up to 4490 ppm) indicating a significant fumarolic contribution to the atmosphere.

Similarly to CO_2, H_2S probability plot suggests that the dataset can be divided in three populations; A includes very low H_2S concentrations, B values up to 30 ppm, indicating a significant H_2S emission into the atmosphere, and C population includes values reaching 63 ppm of H_2S in the air, suggesting the significant contribution of the hydrothermal fluids released from the subsurface. Also for Hg^0 concentrations in the air, measured with the Lumex instrumentation, three populations were detected (A up to 16.5, B up to 40 and C up to 490 ng/m^3).

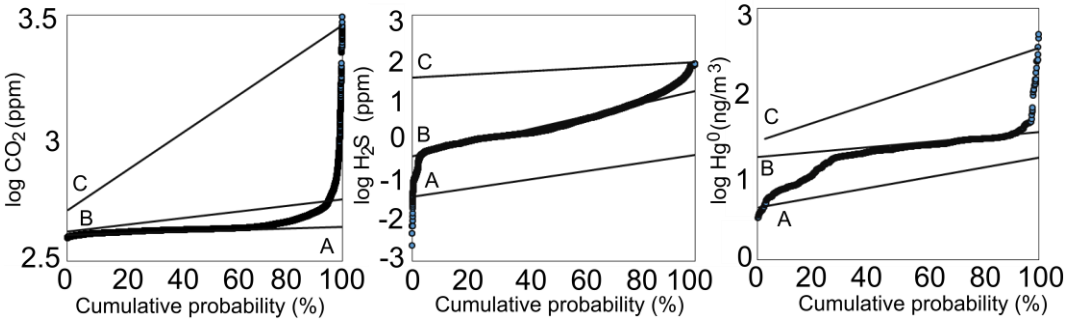

Figure 7 - Probability plots of CO_2, H_2S and Hg^0 in the atmosphere.

In Fig. 8, atmospheric concentrations of H_2S, CO_2 and Hg^0 against the number of measures over time, carried out through transect walk inside Stefanos crater, are shown. The main fumarolic emissions inside the crater were clearly highlighted by anomalously high Hg^0 concentrations (up to ~500 ng/m^3) with respect to the surrounding air masses (~30 ng/m^3). Part of the released mercury is probably immediately retained within the soil, where it tends to form organo-metallic complexes (e.g. Landa, 1978). A good match between Hg^0, H_2S and CO_2 concentration peaks was achieved, confirming the interdependence of these gaseous compounds and their common fumarolic origin. The variability in the continuous concentration signal probably depends on: i) different emission mechanisms among the gases, having a direct impact on their atmospheric dispersion (e.g. Witt et al., 2008); ii) the effect of wind direction and intensity; iii) the dilution of the fumarolic plumes; iv) the presence of multiple emission sources, which include both the fumaroles and the crater floor whose soil is characterized by a diffuse release of hydrothermal gases resulting also in the absence of vegetation.

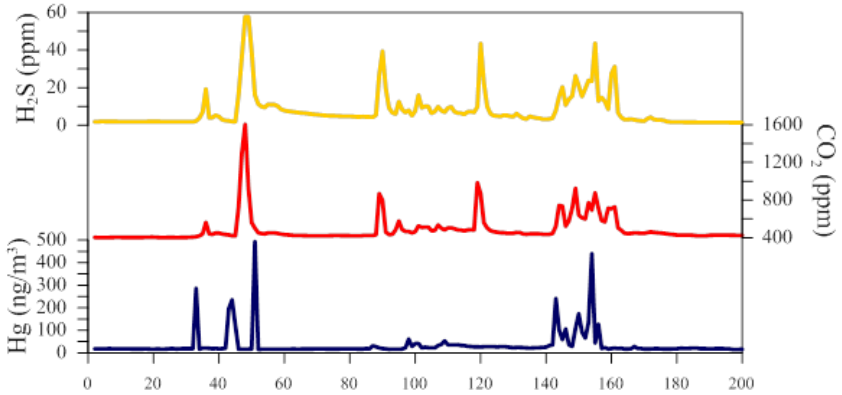

Figure 8 - CO_2, H_2S and Hg^0 atmospheric concentrations against the number of measures over time within Stefanos crater.

5. References

Bagnato, E., Aiuppa, A., Parello, F., Calabrese, S., D'Alessandro, W., Mather, T.A., McGonigle, A.J.S., Pyle, D.M. and Wängberg, I., 2007. Degassing of gaseous (elemental and reactive) and particulate mercury from Mount Etna volcano (Southern Italy), *Atmos. Environ*., 41(35), 7377-7388.

Barnes, H.L. and Seward, T.M., 1997. Geothermal systems and mercury deposits. *In:* Barnes, H.L., *ed.*, Geochemistry of hydrothermal ore deposits (3rd ed.), *John Wiley & Sons, New York,* 699-736.

Caliro, S., Chiodini, G., Galluzzo, D., Granieri, D., La Rocca, M., Saccorotti, G. and Ventura, G. 2005. Recent activity of Nisyros volcano (Greece) inferred from structural, geochemical and seismological data, *Bull. Volcanol*., 67, 358-369.

D'Alessandro, W., Gagliano, A.L., Kyriakopoulos, K. and Parello, F., 2013. Hydrothermal methane fluxes from the soil at Lakki plain (Nisyros, Greece), *Proceedings of the 13th International Congress of the Geological Society of Greece*, Chania, Crete, Greece, 5-8 September 2013, *Bull. Geol. Soc. Greece,* 47(3), 1920-1928.

Daskalopoulou, K., Calabrese, S., Milazzo, S., Brusca, L., Bellomo, S., D'Alessandro, W., Kyriakopoulos, K., Tassi, F. and Parello, F., 2014. Trace elements mobility in soils from the hydrothermal area of Nisyros (Greece), *Annals Geophys.,* 57 Fast Track 2, doi: 10.4401/ag-6623.

Engle, M.A., Gustin, M., Goff, F., Counce, D.A., Janik, C., Bergfeld, D. and Rytuba, J.J., 2006. Atmospheric mercury emissions from substrates and fumaroles associated with three hydrothermal systems in the western United States, *J. Geophys. Res.,* 111, D17304.

Fitzgerald, W.F., Mason, R.P. and Vandal, G.M., 1991. Atmospheric cycling and air- water exchange of mercury over mid-continental lacustrine regions, *Water Air Soil Pollut*., 56, 745-767.

Hunziker, J.C. and Marini, L., *eds,* 2005. The geology, geochemistry and Evolution of Nisyros Volcano (Greece). Implications for the volcanic hazards, *Memoires de Geologie (Lausanne),* 44, 192.

Lamborg, C.H., Tseng, C.M., Fitzgerald, W.F., Balcom, P.H. and Hammerschmidt, C.R., 2003. Determination of the mercury complexation characteristics of dissolved organic matter in natural waters with "reducible Hg" titrations, *Environ. Sci. Technol*., 37, 3316-3322.

Landa, E.R., 1978. The retention of metallic mercury vapour by soils, *Geochim. Cosmochim. Acta,* 42, 1407-1411.

Mason, R.P., Fitzgerald, W.F. and Morel, F.M.M., 1994. The biogeochemical cycling of elemental mercury: anthropogenic influences, *Geochim. Cosmochim. Acta,* 58(15), 3191-3198.

Morel, F.M.M., Kraepiel, A.M.L. and Amyot, M., 1998. The chemical cycle and bioaccumulation of mercury, *Annu. Rev. Ecol. Syst*., 29, 543-566.

Nimik, D.A., Caldwell, R.R., Skaar, D.R. and Selch, T.M., 2013. Fate of geothermal mercury from Yelloestone National Park in the Madison and Missouri Rivers, USA, *Sci. Total Environ*., 4463, 40-54.

Papadopoulos, G.A., Sachpazi, M., Panopoulou, G. and Stavrakakis, G., 1998. The volcanoseismic crisis of the 1996-97 in Nisyros, SE Aegean Sea, Greece, *Terra Nova* ,10, 151-154.

Park, C.M., Kats, L.E. and Liljestrand, E.M., 2015. Mercury speciation during in situ thermal desorption in soil, *J. Haz. Materials,* 300, 624-632.

Robertson, D.E, Crecelius, E.A., Fruchter, J.S. and Ludwick, J.D., 1997. Mercury emissions from geothermal power plants, *Science,* 196, 1094-1097.

Sinclair, A.J., 1974. Selection of threshold values in geochemical data using probability graphs, *J. Geochem. Explor*., 3, 129-149.

Vitolo, S. and Saggiani, M., 2002. Mercury removal from geothermal exhaust gas by sulfur-impregnated and virgin activated carbons, *Geothermics*, 31, 431-442.

Witt, M.L.I., Fischer, T.P., Pyle, D.M., Yang, T.F. and Zellmer, G.F., 2008. Fumarole compositions and mercury emissions from the Tatun Volcanic field, Taiwan: results from multi-component gas analyser, portable mercury spectrometer and direct sampling techniques, *J. Volcanol. Geotherm. Res.,* 178, 636-643.

Δελτίο της Ελληνικής Γεωλογικής Εταιρίας, τόμος L, σελ. 2127-2136
Πρακτικά 14ου Διεθνούς Συνεδρίου, Θεσσαλονίκη, Μάιος 2016

Bulletin of the Geological Society of Greece, vol. L, p. 2127-2136
Proceedings of the 14th International Congress, Thessaloniki, May 2016

REDUCTION OF TOXIC ELEMENT MOBILITY IN MINING SOIL BY ZEOLITIC AMENDMENTS

Giannatou S.[1], Vasilatos Ch.[1], Mitsis I.[1], Koukouzas N.[2], Itskos G.[3] and Stamatakis G.M.[1]

[1]Department of Geology and Geoenvironment, National & Kapodistrian University of Athens, Panepistimiopolis, Ano Ilissia, GR-15784, Athens, Greece, spiridoula_14@hotmail.com

[2]Centre for Research and Technology Hellas, Chemical Process and Energy Resources Institute, 52 Egialias str., GR-151 25, Maroussi, Athens, Greece, koukouzas@certh.gr

[3]Nazarbayev University, School of Engineering, 53 Kabanbay batyr ave., Astana, 010000, Republic of Kazakhstan, gregoryitskos@gmail.com

Abstract

The aim of this study is to examine the effectiveness of natural and synthetic zeolitic materials as potential amendments for the rehabilitation of mine degraded areas. Two types of natural zeolite tuffs, clinoptilolite- and mordenite-rich originating from Samos Island, Greece, were used as low cost modifiers. In addition, the synthetic zeolite Na-P1, produced from lignite fly ash of the Meliti Lignite fired Power Station (Florina, Greece), was used. Fly ash was converted into synthetic zeolite via a low temperature alkaline hydrothermal treatment. In order to evaluate the aquatic solubility and potential bioavailability of heavy metals in contaminated soils of the mining area of Lavrion, specific soil amendments were used in leaching experiments. The Na-P1zeolite proved to be the most effective among the tested amendments for in situ de-contamination of mining soils. Comparing the two natural zeolites used, the mordenite-rich tuff exhibited better results than the clinoptilolite-rich, for the reduction of the potential bioavailability of almost all the studied heavy metals. Despite the high trace element content of the specific soils, it was observed that the Glaucium flavum, a plant that grows in the contaminated soils of Lavrion, does not accumulate high concentrations of metals; therefore the high toxic element content of soils does not always influence the physiology of the plants.
Keywords: *Contaminated soils, synthetic zeolite, fly ash, leaching, bioavailability.*

1. Introduction

A significant problem in mining areas is the local pollution of the soil close to the mining or dumping area with hazardous heavy metals and metaloids. In general, soils have the natural capacity to mitigate the bioavailability and mobility of metals through mechanisms of precipitation, adsorption processes and/or redox reactions (Vasilatos *et al*., 2015). Nevertheless, when the concentration of heavy metals is significantly increased, soil's capacity to mobilize the contaminants becomes limited. Thus, there is a contamination risk of agricultural lands, vegetation, and/or groundwater. A notorious example of local but extremely contaminated area is the Lavrion region, Attica Greece, where mining activities had been taking place from antiquity up until the 20th century. Besides fluorite that was extracted for its use as flux in the cement industry in the '70s, the major metals

extracted from Lavrion were lead, silver and zinc. These metals derived from the mining and metallurgical processing of sulfide ores (Ag-bearing galena, sphalerite and arsenopyrite) of the area. Those activities had produced over the centuries a vast amount of tailings that were generally deposited upon the soil surface in forms of smelting waste, slags, sulfur compounds, etc., all rich in hazardous metals and metalloids. These kinds of tailings usually provide an unfavorable substrate for plant growth because of their low pH, high concentrations of toxic elements and low nutrient content (Ha *et al*., 2011). Specifically, mining, processing and dumping of wastes, in several cases have produced severe heavy element pollution (Baker *et al*., 1994). Heavy metals are generally immutable, non-degradable and persistent in soils, unlike any organic contaminants (Adriano *et al*., 2004; Shi *et al*., 2009; Sunarso and Ismadji, 2009 and Peng *et al*., 2009). Consequently, it's necessary to take action in order to remediate heavily polluted soils. For the stabilization of contaminated soils, a variety of methods have been suggested and developed. However, soil clean-up technologies are often expensive, energy consuming and usually soil can rarely be used after the treatment. Moreover, the economic limitations related to the removal of the contaminated soil and its ex-situ treatment have led to a closer investigation of potential in-situ treatment techniques including stabilization/solidification processes. Those techniques usually involve mixing of the contaminated soil or waste in situ with appropriate amendments and curing for the reactions to proceed (Conner, 1990). Many stabilization techniques including the application of lime, cement, coal fly ash and phosphates among other natural and synthetic additives employing various fixation mechanisms, have been tested in mining soils with varying degrees of contamination (Stouraiti *et al*., 2002 and Martinez-Sanchez *et al*., 2011).

Zeolite tuffs have been extensively studied for their potential use as remediation agents in contaminated soils, soil amendments and as substrates in hydroponics (e.g. Stamatakis *et al*., 2001; Savvas *et al*., 2004; Castaldi *et al*., 2005; Filippidis and Kantiranis, 2005; Kumpiene *et al*., 2008 and Fillipidis, 2010). Zeolite is a group of porous aluminosilicate minerals with a negative charge, having a three-dimensional framework, neutralized by introducing exchangeable cations in their crystal structure. The ion exchanging efficiency depends on the micro-porosity and mineral structure of each particular zeolitic type. Moreover, it has been referred that zeolites may be more suitable for rehabilitation of heavy metal-contaminated soils than other amendments, because of their property to regulate modestly soil's pH and do not import any new pollutants (Castaldi *et al*., 2005 and Kumpiene *et al*., 2008).

The idea of utilizing the coal (with a broad sense, including lignite) fly ash as a low-cost sorbent for the removal of heavy metals (e.g. Srivastava *et al*., 2006; Pehlivan *et al*., 2006; Itskos *et al*., 2010 and Alexopoulos *et al*., 2013), radionuclides, and organic pollutants as well (e.g. Sun *et al*., 2010; Karagozoglu *et al*., 2007 and Janos *et al*., 2003), has been extensively discussed. Even though raw coal fly ashes usually have low sorption capacity, physical and/or chemical modifications have often been examined for their enhancement. Coal fly ash is a suitable material for zeolite synthesis, when it is of aluminosilicate composition.

The fly ash low temperature hydrothermal zeolitization processes implemented in the present study, are based on the chemical attack of Al-Si bearing phases of the fly ash by alkaline solutions and the subsequent transformation to zeolitic material (Querol *et al*., 2002; Mouhtaris *et al.*, 2003; Koukouzas *et al*., 2010 and Itskos *et al.*, 2015). Products of such transformation have been described by better ion-exchange properties and several fold-enlarged surfaces (Remenarova *et al*., 2014 and Giannatou *et al*., 2015).

The current study deals with the evaluation of water solubility and potential bioavailability of heavy metals in the Lavrion contaminated soil, after its amendment with natural and synthetic zeolitic materials. In addition, *Glaucium flavum*, a plant species, which grows naturally in Lavrion highly contaminated soils was sampled and analyzed in order to determine its heavy metal accumulation capability and investigate if it could be used in bio-remediation processes.

2. Materials and Methods

The laboratory tests were performed at the Economic Geology and Geochemistry Laboratory of National and Kapodistrian University of Athens. The mineralogical composition of the materials used was identified by X-ray diffraction (XRD) analysis on a Bruker Model 5005 X-ray diffractometer in combination with the DIFFRACplus software package. The diffractometer was operated using Cu K-a radiation at 40kV and 40mA, with graphite monochromator, and employing the following scanning parameters: 0.020° step size and 2.0 sec. step time. The output files were evaluated for mineralogical identifications by the EVA 10.0 program of the Bruker DIFFRACplus software package. The measurement of pH in the solid samples was performed by dilution of the solid in dionized water at a ratio of 1:1 solid:liquid. Then, the Consort 561 multimeter was used for the pH determination.

Natural and synthetic zeolitic materials were used as amendments in contaminated soils from an abandoned mine site. The natural zeolites used, clinoptilolite-rich tuff (ZCS) and mordenite-rich tuff (ZMS), originated from Samos Island, Greece. Clinoptilolite is widely used in several applications worldwide. The porous structure of clinoptilolite has a heterogeneous nature and is classified as sorbent. Several authors classified it in heulandite family (Breck, 1974), but its Si/Al ratio and thermal stability is different than heulandites (Mansouri *et al*., 2013). On the other hand, mordenite from the Late Miocene rhyolitic tuffs of Samos is remarkably rich in K and depleted in Na. The needle-like mordenite crystals drapes across smectite; other silica mineral such as quartz and cristobalite are also present. The use of mordenite type zeolite rocks is an ambiguous issue, as in some countries it is classified as fibrous mineral (e.g. Suzouki, 1982 and Spurny, 1983), while in others is used extensively in construction and environmental applications (i.e. Hungary, Romania, Japan, Australia and Philippines). The lignite fly ash sample (CFA) used, derived from the electrostatic precipitators of the lignite-fired Meliti Power Station (Florina, Greece). The CFA was converted to synthetic zeolitic material (FAZ) via a low temperature alkaline hydrothermal treatment with 1M NaOH. The hydrothermal treatment, proposed by Koukouzas *et al*. (2010) and Itskos *et al*. (2015) took place at 90-100^{0}C. The zeolite produced was Na-P1($Na_6Al_6Si_{10}O_{32}\cdot 12H_2O$), a synthetic mineral with high ion exchange capacity due to the substitution of Si (IV) by Al (III) in its structure, which results in an increased overall negative charge. Heavily contaminated soil samples (LSoil) were collected near the Lavrion harbor, (Figure 1). The soil samples were air dried for 5-6 days.

In order to evaluate the effectiveness of natural and synthetic zeolitic materials as amendments to reduce the solubility and potential bioavailability of heavy metals in the contaminated soil, the following experiment was conducted: a quantity of 4kg of contaminated soil and each amendment (ZCS, ZMS and FAZ) at a rate of 10% by weight was used, to produce the CLS, MLS and FLS soil mixtures accordingly. The mixtures were equilibrated for 1 week, moistened to 40% of their water holding capacity. Control pots without any amendment (Control) were also set up. All treatments in the experiment were replicated 3 times. The experiment lasted ten weeks under natural environmental conditions. The moisture was maintained throughout the ten weeks by irrigation twice a week. Afterwards a compliance test for leaching of heavy metals was conducted in the soil treatments. According to the European Standard 12457-2, the solid matter and distilled water were placed in a bottle at a liquid to solid ratio of 10 l/kg. The bottle was agitated for 24 h and the suspended solids were let to settle for 15 min. Filtration of the eluate followed and the metals in the leachates were analyzed with a Perkin Elmer 1100b atomic absorption spectrophotometer (AAS). The potential bioavailable fraction was determined by leaching with 0,05N EDTA (ethylenediaminetetraacetic acid, $C_{10}H_{16}N_2O_8$). Five grams of each solid sample were mixed with 25 ml of extraction solution in a 50 ml flask and the slurry was agitated for 1 h at 150 rpm. Following the filtration of the slurries, the metals in the leachates were analyzed by the AAS method.

Figure 1 – Contaminated soil sampling in Lav rion area.

Figure 2 – The *Glaucium flavum* plant grows naturally in the s ampling area.

During this study, plant species of Glaucium flavum were sampled from the same area of Lavrion (Figure 2). Plant samples, were separated into root and above-ground (flower and shoots and leaves) biomass and then lyophilized. 0,5 g of the lyophilized plant tissue were placed in Teflon vessels with 1 ml of 30% H2O2 (perhydrol) and 6 ml of concentrated HNO3 acid solution. When digestion was complete (25 minutes at 1000 W in an ETHOS 1600 MILESTONE Microwave System), the samples were left to cool and then transferred to a volumetric flask to a final volume of 100 mL with distilled water. Cd, Pb, Zn, Cu, Mn and Fe content were determined by the AAS method.

3. Results

The mineralogical composition of both natural and synthetic zeolitic materials used, is presented in Table 1. These results for the natural zeolitic tuffs are in accordance with those reported by Filippidis *et al.*, 2007, (ZCS may contain approx. 60 wt% clinoptilolite and ZMS may contain 21-64 wt% mordenite). The high degree of zeolitization of the lignite fly ash (CFA) after the alkaline hydrothermal treatment is demonstrated in the XRD patterns (Figure 3). While the CFA (upper pattern in blue) consists mainly of quartz and feldspar, the synthetic zeolite (FAZ) (bottom pattern in black) consists mainly of Na-P1 zeolite. The specific zeolite has an affinity with the cations that are generally found in acid mine drainage effluents (Cardoso *et al.*, 2015). The pH values of all materials used are presented in Table 2. The synthetic zeolitic material exhibits higher pH values in comparison to the natural zeolites samples. As expected, the untreated contaminated soil from Lavrion (LSoil) has acidic [3.82] pH value. The untreated soil sample (Control), had a pH value as low as 4.52, after the equilibration.

The amended soil mixtures have showed an increased pH. This was particularly evident in FLS sample (amended with synthetic zeolite) that had the highest pH value but close to MLS pH value that goes after. The pH value of the FLS is attributed to the high pH of the FAZ component used in the mixture. It is noted that Control sample pH that has the same composition with LSoil, presents higher values after the equilibration. In Table 3 is illustrated that the concentrations of heavy metals in water leachat of amended soil samples were lower than those of the untreated soil sample (Control). Among the soil treatments the FLS one (amended with synthetic zeolite) exhibited the lowest concentrations for all studied heavy metals.

The potential bioavailability of heavy metals expressed with EDTA values (Table 3), exhibited higher values as expected.

The EDTA buffers a lower soil pH and, consequently, a higher percentage of the heavy metals content of the soil may be mobilized to the leachates. Between the two natural zeolites, MLS sample (amended with Mordenite-rich material) had better performance excibiting lower potential bioavailability for all the heavy metals, compared to the Control. On the other hand, the synthetic zeolitic amended FLS, exhibited lower potential bioavailability for Cd, Cu, Mn and Fe. Moreover,

the concentration of heavy metals in different parts of Glaucium flavum is presented in Table 4. The root exhibited the highest values for all heavy metals, in contrast with the flower which had the lowest values.

Table 1 - Mineralogical composition of the zeolitic materials (+: presence of mineral, -: absence of mineral, MJ: Major mineral phase).

	Zeolitic materials		
Mineral species	**ZCS**	**ZMS**	**FAZ**
Clinoptilolite	+ **MJ**	+	-
Mordenite	+	+ **MJ**	-
Zeolite P1, (Na)	-	-	+ **MJ**
Sanidine	+	+	-
Orthoclase	-	+	-
Anorthoclase	-	-	+
Albite	-	-	+
Opal CT	-	+	-
Quartz	-	-	+ **MJ**
Hematite	-	-	+
Maghemite	-	-	+
Calcite	-	-	+

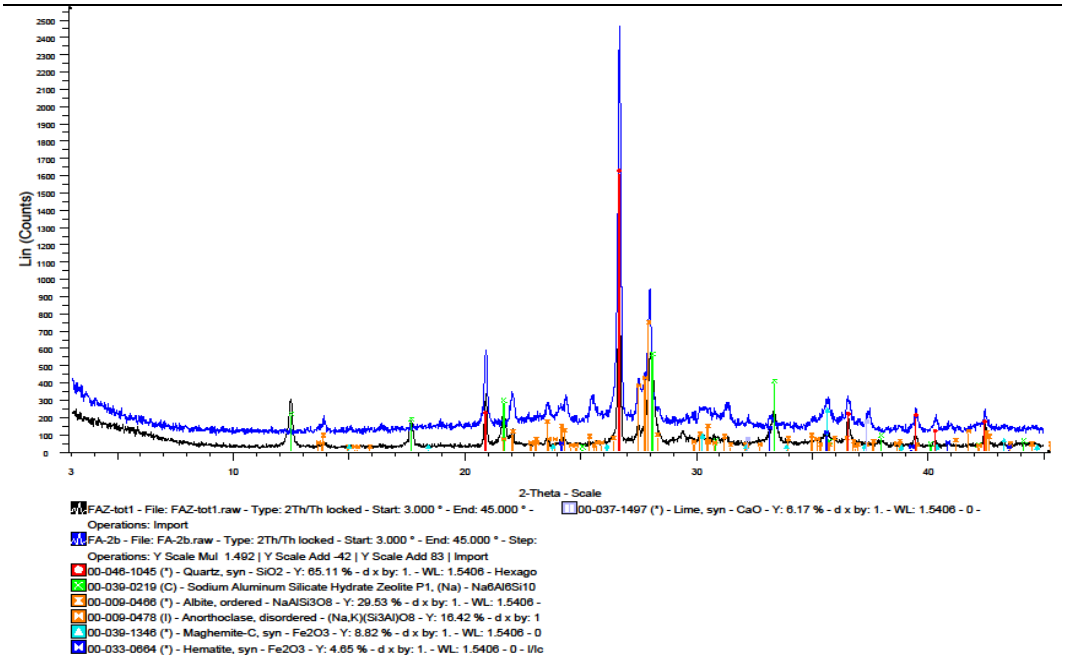

Figure 3 - XRD patterns of the materials used. The upper pattern (in blue) is from the coal fly ash (CFA) before the alkaline hydrothermal treatment and the lower (in black) is from the synthetic zeolite rich material (FAZ) after the treatment.

Table 2 - pH values of natural and synthetic zeolitic materials, along with the contaminated soil sample and soil treatments after the 10 weeks experimental period.

Soil & zeolitic amendments	pH	Soil Treatments	pH
Lsoil	3.82	Control	4.52
ZCS	8.18	CLS	4.94
ZMS	7.55	MLS	5.38
FAZ	12.25	FLS	5.62

Table 3 – Concentration of heavy metals in soil (μg/g) and in the leachates (μg/ml) after leaching with water and EDTA.

	Soil	Water leachates				EDTA leachates			
		Soil Treatments							
	Lsoil	CLS	MLS	FLS	Control	CLS	MLS	FLS	Control
Pb	42000	0.94	1.00	0.58	0.77	110	75	126	61
Cd	91.5	0.52	0.42	0.25	0.73	4.3	3.7	3.5	4.3
Zn	29800	206	170	97	231	700	555	817	673
Cu	1366.6	0.08	0.06	0.05	0.14	14	10	10	16
Mn	4600	16	13	8	28	107	100	61	107
Fe	215900	3	3	2	3	71	62	48	96

Table 4 – Concentration (μg/gr in dry basis) and bio-concentration factor (BCF), of heavy metals in *Glaucium flavum.*

	Plant parts			BCF
	Flower	Shoots & Leaves	Root	
Pb	82	246	887	0.02
Cd	<0.5	8	18	0.19
Zn	337	1250	1720	0.06
Cu	38	35	84	0.06
Mn	66	205	227	0.05
Fe	357	978	3740	0.02

4. Discussion

A comparative presentation of the effect of natural and synthetic zeolitic amendments to the solubility of the studied heavy metals in the contaminated soil is illustrated in Figure 4. It is evident that the FLS treatment presented reduced solubility of all studied metals (Pd, Cd, Zn, Cu and Mn) except Fe. The negative effectiveness for Pb and Fe may be attributed to their release from the original amendments, as they exhibited high content of these metals (ZCS: 70.5 μg/g Pb, 1.3% Fe, ZMS: 57.3 μg/g Pb, 0.8% Fe, FAZ: 13.6 μg/g Pb, 4.7% Fe), in combination with their pH (Table 2). Among the natural zeolites, the mordenite exhibited better effect in the reduction of the solubility of heavy metals. The crystal structure of zeolite grains constitutes the primary porosity (microporosity) of zeolites, while the grain

sizes of zeolite and other minerals in the zeolite rocks are connected with the secondary porosity (mesoporosity and macroporosity) (Sprynskyy *et al*., 2010). The primary porosity is defined as the microporosity displayed by the mineral 3-dimensional alumino-silicate framework. The mesoporosity is formed by slot pores determined mainly by cleavability of the zeolite crystals. The macropores consist of pores of various forms which are located between blocks of the zeolite crystallite and other minerals in the zeolite bearing rocks. For example, the heterogeneity of the clinoptilolite bearing rocks porosity is caused by the presence of associated minerals (albite, mordenite, etc.) and heterogeneity of crystalline structure of those minerals (Mansouri *et al*., 2013). The mesopores are active surfaces for catalysis, transport channels and adsorption of relatively large molecules. Besides some technological properties which may not be explained by adsorption in micropores, they might be explained by secondary porosity (Mansouri *et al*., 2013). Moreover, zeolite soil amendments in mining areas may provide sufficient alkalinity to neutralize the acid polluted soils, causing the precipitation of insoluble phases (Chen *et al*., 2000). The newly formed phases may accommodate the metal pollutants either as major constituents (Chen *et al*., 2000) or as minor components co-precipitated in hydroxides (Chlopecka and Adriano, 1997 and Boisson *et al*., 1999). The increase of alkalinity enhances the metal sorption via surface complexation processes. Although mineral surfaces have a positive charge at low pH values due to the sorption of protons, as pH increases owing to the deprotonation of the surface unsaturated bonds, they acquire a negative charge (e.g. Basaldella *et al*., 2007; Peng *et al*., 2009; Shi *et al*., 2009). The complexion of cations by stable bonds with the negative radicals on the mineral surfaces is promoted by higher pH values. Zeolite minerals can play a significant role in thus surface complexion because of their high specific surface (Korkuna *et al*., 2006 and Sponer *et al*., 2001). The increase pH value of treated soil by the tested amendments (Table 2) confirmed the buffering effect (Radulescu, 2013) and suggested the opportunity of using zeolitic materials for conditioning and remedying contaminated soil from sulfide mines.

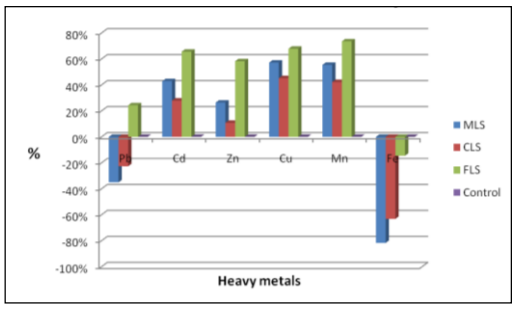

Figure 4 – The % effect in the solubility of heavy metals in the different soil treatments.

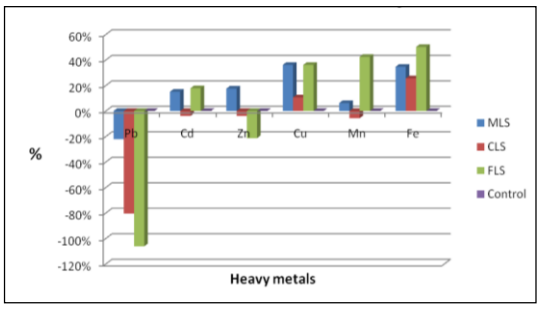

Figure 5 – The % effect in potential bioavailability of heavy metals in the different soil treatments.

The effect of natural and synthetic zeolitic materials in potential bioavailability of studied heavy metals is displayed in Figure 5. The treatment with the synthetic material (FLS) exhibited the highest effectiveness in reduction of potential bioavailability of Cd, Cu, Mn and Fe. The synthetic zeolitic material originated from the alkaline hydrothermal treatment of fly ash, resulted to a significant decrease of the contaminants leachability and potential bioavailability. The increase of pH, as also indicated by Stouraiti *et al*. (2002) may be a key factor for the toxic elements immobilization. As regards the natural zeolites, mordenite proved to be more effective in controlling the potential bioavailability of all studied heavy metals except Pb, in contrast to the clinoptilolite which presented a poor effect for almost all heavy metals. The potential bioavailability of Pb and Zn (Table 3) in the amended samples was higher in comparison to the untreated soil sample (Control). However, it is widely accepted that the EDTA test overestimates the bioavailable content of pollutants (Stouraiti *et al*., 2002).

The plant response to heavy metals in soil depends on the plant species, the total soil metal concentration, and the bioavailability of the metal (Martinez-Sanchez *et al*., 2012). For example, excluders have an avoidance (or restriction) mechanism which prevents element uptake, while

accumulators have mechanisms of metal accumulation in their aboveground biomass (Perez-Sirvent *et al.*, 2008). The bioconcentration factor (BCF), defined as the ratio of metal concentration in plant shoots to metal concentration in soil, is a measure of the ability of a plant to take up and transport metals to the shoots, which are the parts that can be easily harvested. With rare exceptions, most plants have a BCF for heavy metals and metalloids of less than 1 (McGrath and Zhao, 2003).

Glaucium flavum is a plant species that grows naturally in the contaminated fields of Lavrion, region. It is abundant along the roadsides and it is a short cycle plant. For all the studied elements, root concentrations were higher than those of shoots & leaves as expected for most of the plant species. BCF in that plant was found lower than 1 (almost by two factors) for all the studied elements (Table 4). According to Martinez-Sanchez *et al.* (2012) *Glaucium flavum* is considered as a hypertolerant plant. Our findings suggest that *Glaucium flavum* does not accumulate high concentrations of metals and may inherit an avoidance/restriction mechanism that not only prevents all the studied toxic elements uptake but tolerates the low soil pH of the acid mine soil. Hence the presence of bioavailable trace elements in soils is not a critical factor that controls the uptake ability of the plants. It is therefore suggested the implementation of such measurements on specific plant species, in order to avoid misleading results that might influence the farming activity.

5. Conclusions

The synthetic zeolitic material originated from alkaline hydrothermal treatment of fly ash, resulted in a significant decrease of contaminants leachability and potential bioavailability. The pH increase of the amended soil confirmed the buffering effect of the zeolitic materials, along with the reduction of the heavy metals mobility, indicating their possible use in conditioning and remediating mining soils. The zeolite produced by Meliti's lignite fly ash was the most effective among the tested amendments. Our results suggest that those low temperature synthetic zeolites are suitable for in situ de-contamination of mining soils. Comparing the natural zeolitic materials from Samos Island, mordenite-rich tuff proved to be the most efficient at reducing the potential bioavailability of almo st all the heavy metals studied. The need for a low-cost amendment for the in-situ remediation of Lavrion mine degraded soils, may be effectively fulfilled with a large scale use of zeolitic materials. The plant species *Glaucium flavum* does not accumulate high concentrations of metals, exhibiting an avoidance/restriction mechanism that prevents the uptake of all the studied toxic elements from the contaminated soil.

6. Acknowledgements

University of Athens (NKUA) is acknowledged for the support of this work. The RFCS of the European Commission is thanked for funding a part of this research [Research Project MANAGER (Management of mine water discharges to mitigate environmental risks for post-mining period-RFCR-CT-2013-00005)]. Dr. Pinelopi Delipetrou, Department of Botany, NKUA is kindly thanked for the identification of the plant specimens. Mrs Stefania Stamataki, chemist is thanked for language editing.

7. References

Adriano, D.C., Wenzel, W.W., Vangronsveld, J. and Bolan, N.S., 2004. Role of assisted natural remediation in environmental cleanup, *Geoderma*, 122, 121-142.

Alexopoulos, D., Itskos, G., Vasilatos, Ch., Koukouzas N. and Stamatakis, M.G., 2013. Mine wastewater treatment by highly calcareous and siliceous fly ash: a comparative study. World of Coal Ash Conference, Lexington, Kentucky, April 2013.

Baker, A.J.M., McGrath, S.P., Sidoli, C.M.D. and Reeves, R.D., 1994. The possibility of in situ heavy-metal decontamination of polluted soils using crops of metal accumulating plants, *Resources Conservation Recycling*, 11, 41-49.

Basaldella, E.I., Vazquez, P.G., Iucolano, F. and Caputo, D., 2007. Chromium removal from water using LTA zeolites: effect of pH, *J. Colloid Interface Sci.*, 313, 574-578.

Boisson, J., Mench, M., Vangronsveld, J., Ruttens, A., Kopponen, P. and Koe, T., 1999. Immobilization of trace metals and arsenic by different soil additives: evaluation by means of chemical extractions, *Commun. Soil Sci. Plant Anal.*, 30, 365-387.

Breck, D.W., 1974. Zeolite Molecular Sieves: Structure, *Chemistry and Use*, New York, John Wiley and Sons Press.

Cardoso, A.M., Paprocki, A., Ferret, L.S., Azevedo, C.M.N. and Pires, M., 2015. Synthesis of zeolite Na-P1 under mild conditions using Brazilian coal fly ash and its application in wastewater treatment, *Fuel*, 139, 59-67.

Castaldi, P., Santona, L. and Melis, P., 2005. Heavy metal immobilization by chemical amendments in a polluted soil and influence on white lupin growth, *Chemosphere*, 60, 365-371.

Chen, Z.S., Lee, G.J. and Liu, J.C., 2000. The effects of chemical remediation treatments on the extractability and speciation of cadmium and lead in contaminated soils, *Chemosphere*, 41, 235-242.

Chlopecka, A. and Adriano, D.C., 1997. Influence of zeolite, apatite and Fe-oxide on Cd and Pb uptake by crops, *Sci. Total Environ.*, 207, 195-206.

Conner, J.R., 1990. Chemical Fixation and Solidification of Hazardous Wastes, Van Nostrad Reinhold, New York, 692 pp.

Filippidis, A., 2010. Environmental, industrial and agricultural applications of Hellenic Natural Zeolite, *Hellenic Journal of Geosciences*, 45, 91-100.

Filippidis, A., Kantiranis, N., Stamatakis, M., Drakoulis, A. and Tzamos, E., 2007. The cation exchange capacity of the Greek zeolitic rocks. Bulletin of the Geological Society of Greece, 40, 723-735, *Proceedings of the 11th International Congress*, Athens, May, 2007.

Filippidis, A. and Kantiranis, N., 2005. Industrial, agricultural and environmental uses of the natural zeolites of Thrace, *Bull. Geol. Soc. Greece*, 37, 90-101.

Giannatou, S., Vasilatos, Ch., Mitsis, I. and Koukouzas, N., 2015. Use of natural and synthetic zeolitic materials as soil amendments in abandoned mine sites. *In*: Stamatakis, M.G., *eds.*, Coastal Landscapes, *Mining Acitivities and Preservation of Cultural Heritage*, Cambridge Scholars Publishing.

Ha, N.T.H., Sakakibara, M., Sano, S. and Nhuan, M.T., 2011. Uptake of metals and metalloids by plants growing in a lead-zinc mine area, Northern Vietnam, *Journal of Hazardous Materials*, 186, 1384-1391.

Itskos, G., Koukouzas, N., Vasilatos, Ch., Megremi, I. and Moutsatsou, A., 2010. Comparative uptake study of toxic elements from aqueous media by the different particle-size-fractions of fly ash, *Journal of Hazardous Materials*, 183, 787-792.

Itskos, G., Koutsianos, A., Koukouzas, N. and Vasilatos, Ch., 2015. Zeolite development from fly ash and utilization in lignite mine-water treatment, *Journal of Mineral Processing*, 139, 43-50, doi: 10.1016/j.minpro.2015.04.011.

Janos, P., Buchtova, H. and Ryznarova, M., 2003. Sorption of dyes from aqueous solutions onto fly ash, *Water Res.*, 37, 4938-4944.

Karagozoglu, B., Tasdemir, M., Demirbas, E. and Kobya, M., 2007. The adsorption of basic dye (Astrazon Blue FGRL) from aqueous solutions onto sepiolite, fly ash and apricot shell activated carbon: kinetic and equilibrium studies, *J. Hazard Mater.*, 147, 297-306.

Korkuna, O., Leboda, R., Skubiszewska-Ziemba, J., Vlublevska, T., Gunko, V.M. and Ryczkowski, J., 2006. Structural and physicochemical properties of natural zeolites: clinoptilolite and mordenite, *Microporous Mesoporous Mater.*, 87, 243.

Koukouzas, N., Vasilatos, Ch., Itskos, G., Mitsis, I. and Moutsatsou, A., 2010. Removal of heavy metals from wastewater using CFB-coal fly ash zeolitic materials, *Journal of Hazardous Materials*, 173, 581-588.

Kumpiene, J., Lagerkvist, A. and Maurice, C., 2008. Stabilization of As, Cr, Cu, Pb and Zn in soil using amendments - a review, *Waste Manage.*, 28, 215-225.

McGrath, S.P. and Zhao, F.J., 2003. Phytoextraction of metals and metalloids from contaminated soils, *Current Opinion in Biotechnology*, 14, 1-6.

Mansouri, N., Rikhtegar, N., Panahi, H.A., Atabi, F. and Shahraki, K.B., 2013. Porosity, characterization and structural properties of natural zeolite-clinoptilolite-as a sorbent, *Environment Protection Engineering*, 39, doi: 10.5277/EPE130111.

Martinez-Sanchez, M.J., Garcia-Lorenzo, M.L., Perez-Sirvent, C. and Bech, J., 2012. Trace element accumulation in plants from an aridic area affected by mining activities, *Journal of Geochemical Exploration*, 123, 8-12.

Martinez-Sanchez, M.J., Martinez-Lopez, M.L., Garcia-Lorenzo, L.B., Martinez-Martinez, C. and Perez-Sirvent, C., 2011. Evaluation of arsenic in soils and plant uptake using various chemical extraction methods in soils affected by old mining activities, *Geoderma*, 160, 535-541.

Mouhtaris, Th., Charistos, D., Kantiranis, N., Filippidis, A., Kassoli-Fournaraki, A. and Tsirambidis, A., 2003. GIS-type zeolite synthesis from Greek lignite sulphocalcic fly ashes promoted by NaOH solutions, *Microporous and Mesoporous Materials*, 61, 57-67.

Pehlivan, E., Cetin, S. and Yanik, B.H., 2006. Equilibrium studies for the sorption of zinc and copper from aqueous solutions using sugar beet pulp and fly ash, *J. Hazard Mater.*, B135, 193-199.

Peng, J.F., Song, Y.H., Yuan, P., Cui, X.Y. and Qiu, G.L., 2009. The remediation of heavy metals contaminated sediment, *J. Hazard. Mater.*, 161, 633-640.

Perez-Sirvent, C., Martinez-Sanchez, M.J., Garcia-Lorenzo, M.L. and Bech, J., 2008. Uptake of Cd and Pb by natural vegetation in soils polluted by mining activities, *Fresenius Environmental Bulletin*, 17, 106.

Querol, X., Moreno, N., Umana, J.C., Alastuey, A. and Hermandez, E., 2002. Synthesis of zeolites from fly ash: an overview, *J. Coal Geol.*, 50, 413-423.

Radulescu, H., 2013. Soil treatment effects of zeolitic volcanic tuff on soil fertility, *Research Journal of Agricultural Science*, 45(2).

Remenarova, L., Pipiska, M., Florkova, E., Hornik, M., Rozloznik, M. and Augustin, J., 2014. Zeolites from Coal Fly Ash as efficient Sorbents for cadmium ions, *CleanTechn Environ Policy*, Berlin, Heidelberg, Springer-Verlag, doi: 10.1007/s10098-014-0728-5.

Savvas, D., Samantouros, K., Paralemos, D., Vlachakos, G., Stamatakis, M.G. and Vassilatos, Ch., 2004. Yield and nutrient status in the root environment of tomatoes (Lycopersicon esculentum) grown on chemically active and inactive inorganic substrates, *Acta Hortic.*, 644, 377-383.

Shi, W.Y., Shao, H.B., Li, H., Shao, M.A. and Du, S., 2009. Progress in the remediation of hazardous heavy metal-polluted soils by natural zeolite, *Journal of Hazardous Materials*, 170(1), 1-6.

Sponer, J.E., Sobalik, Z., Leszczynski, J. and Wicthterlova, B., 2001. Effect of metal coordination on the charge distribution over the cation binding sites of zeolites: A combined experimental and theoretical study, *J. Phys. Chem.*, B105, 8285-8290.

Spurny, K.R., 1983. Natural fibrous zeolites and their carcinogenicity - a review, *The Science of the Total Environment*, 30, 147-166.

Sprynskyy, M., Golembiewski, R., Trykowski, G. and Buszewski, B., 2010. Heterogeneity and hierarchy of clinoptilolite porosity, *J. Phys. Chem. Solids.*, 71, 1269.

Srivastava, V.C., Mall, I.D. and Mishra, I.M., 2006. Equilibrium modeling of single and binary adsorption of cadmium and nickel onto bagasse fly ash, *Chem. Eng. J.*, 117, 79-91.

Stamatakis, M.G., Koukouzas, N., Vassilatos, C., Kamenou, E. and Samantouros, K., 2001. The zeolites from Evros region, Northern Greece: A potential use as cultivation substrate in hydroponics, *Acta Hortic.*, 548, 93-104.

Stouraiti, C., Xenidis, A. and Paspaliaris, I., 2002. Reduction of Pb, Zn and Cd availability from tailings and contaminated soils by the application of lignite fly ash, *Water, Air and Soil Pollution*, 137, 247-265.

Sun, D., Zhang, X., Wu, Y. and Liu, X., 2010. Adsorption of anionic dyes from aqueous solution on fly ash, *J. Hazard. Mater.*, 181, 335-342.

Sunarso, J. and Ismadji, S., 2009. Decontamination of hazardous substances from solid matrices and liquids using supercritical fluids extraction: a review, *J. Hazard. Mater.*, 161, 1-20.

Suzuki, Y., 1982. Carcinogenic and fibrogenic effects of zeolites: Preliminary observations, *Environmental Research*, 27, 433-445.

Vasilatos, C., Koukouzas, N. and Alexopoulos, D., 2015. Geochemical Control of Acid Mine Drainage in Abandoned Mines: The Case of Ermioni Mine, Greece, *Procedia Earth and Planetary Science*, 15, 945-950.

Δελτίο της Ελληνικής Γεωλογικής Εταιρίας, τόμος L, σελ. 2137-2144
Πρακτικά 14ου Διεθνούς Συνεδρίου, Θεσσαλονίκη, Μάιος 2016

Bulletin of the Geological Society of Greece, vol. L, p. 2137-2144
Proceedings of the 14th International Congress, Thessaloniki, May 2016

ASSESSMENT OF SELECTED METALS ENRICHMENT IN SEDIMENTS FROM PALEA KAVALA RIVER, NE MACEDONIA, NORTHERN GREECE

Giouri K.[1], Vavelidis M.[1], Melfos V.[1] and Papadopoulou L.[1]

[1]Aristotle University of Thessaloniki, School of Geology, Department of Mineralogy-Petrology-Economic Geology, 54124, Thessaloniki, Greece, agiouri@geo.auth.gr, vavelidi@geo.auth.gr, melfosv@geo.auth.gr, lambrini@geo.auth.gr

Abstract

In surface aquatic systems, trace elements and especially heavy metals accumulate in sediments. Thus, the determination of sediment chemical characteristics is critical in the assessment of an aquatic environment's quality. Thirteen sediment samples from Palea Kavala river (NE Macedonia, Greece) were studied for their content in Al, Fe, Cu, Cd, Mn, Pb, Zn. In order to evaluate the metal enrichment for environmental purposes, two geochemical indices were employed: Enrichment Factor (EF) and Geo-accumulation Index (I_{geo}). According to the results, Al was the most abundant major element in sediments with Fe and Mn to follow. Trace element content followed the order Pb>Zn>Cu>Cd. EF values revealed that samples are enriched in Cd and Pb, while I_{geo} values also suggested that there is considerable contamination concerning Cd and Pb. It is concluded that ore mineralizations which occur in Palea Kavala region contribute to the elevated concentrations of all the studied elements, since they comprise mainly Fe-Mn metal assemblages including minerals such as pyrite, goethite, chalcopyrite, galena, sphalerite and pyrolousite.

Keywords: *Environmental geochemistry, Sediment contamination, Enrichment Factor, Northern Greece.*

Περίληψη

Δεκατρία δείγματα ιζήματος από το ρέμα Παλαιάς Καβάλας στην ΒΑ Μακεδονία μελετήθηκαν ως προς το περιεχόμενό τους σε Al, Fe, Cu, Cd, Mn, Pb και Zn. Προκειμένου να εκτιμηθεί η περιβαλλοντική επιβάρυνση των υπό μελέτη ιζημάτων σε μέταλλα, προσδιορίστηκαν για το κάθε δείγμα δύο γεωχημικοί δείκτες: ο Συντελεστής Εμπλουτισμού (EF) και ο Δείκτης Γεωσυσσώρευσης (I_{geo}). Όσον αφορά τα κύρια στοιχεία, από την χημική ανάλυση των ιζημάτων προέκυψε πως τις υψηλότερες συγκεντρώσεις εμφανίζει το Al, ενώ ακολουθούν οι συγκεντρώσεις των Fe και Mn. Όσον αφορά τα ιχνοστοιχεία, οι συγκεντρώσεις που προσδιορίστηκαν ακολουθούν τη σειρά Pb>Zn>Cu>Cd. Με βάση τις τιμές των δεικτών, τα ιζήματα είναι εμπλουτισμένα σε Cd και Pb. Οι περιεκτικότητες όλων των μετάλλων είναι αναμενόμενες, καθώς οφείλονται στις μεταλλοφορίες Fe-Mn που εντοπίζονται στην ευρύτερη περιοχή έρευνας και περιέχουν ορυκτά όπως ο σιδηροπυρίτης, ο γκαιτίτης, ο χαλκοπυρίτης, ο γαληνίτης, ο σφαλερίτης και ο πυρολουσίτης.

Λέξεις κλειδιά: *Περιβαλλοντική γεωχημεία, Ρύπανση ιζημάτων, Συντελεστής Εμπλουτισμού, Βόρεια Ελλάδα.*

1. Introduction

Natural environment's contamination by trace elements, especially heavy metals, is of major concern to the society. These elements are not biodegradable and their presence in surface aquatic environment is attributed either to natural or anthropogenic sources. Heavy metals can be adsorbed by sediments through complex physical and chemical processes, acting both as carriers and potential sources of contaminants. The mechanisms by which metals accumulate in sediments, depend on the nature of the sediment and the properties of the adsorbed compounds. Hence, the determination of sediments' physicochemical characteristics is very important in the assessment of both the bioavailability of metals and the quality of the aquatic environment (Förstner, 1989; Laws, 1993; Calmano *et al*., 1996; Kabata-Pendias, 2010). Various reference materials and enrichment calculation methods have been used by many researchers for the assessment of metal contamination in aquatic environments (Müller, 1981; Hakanson, 1980; Salomons and Förstner, 1984). Therefore, there is a considerable variation of methodologies in order to quantify metal contamination on a specific site.

The aim of the present study is to evaluate the enrichment of Fe, Cu, Cd, Mn, Pb and Zn in the sediments of Palea Kavala river and also to make a primary approach on the evaluation of its contamination status. Palea Kavala river is located 6 km north of the Kavala city, in northeastern Greece (Fig. 1). It emanates from the Lekani mountains and passing through the Palea Kavala village it flows towards the Philippoi plain. When entering the plain, due to the extensive karst formations, the river disappears into the sediments.

2. Geological Setting

Geotectonically the study area belongs to the lower Pangeon unit part of the Southern Core Complex and consists mainly of gneisses overlain by intercalations of marbles and schists. In the Palea Kavala area the metamorphic rocks were intruded by the Kavala pluton of a Lower Miocene age (21-22 Ma). The Kavala Pluton has the characteristics of an I-type intrusion and is mainly composed of amphibole-biotite granodiorite. Alluvial deposits which consist of clays, sands and gravels overlie the crystalline rocks (Christofides, 1996; Krohe and Boskos, 2002; Brun and Sokoutis, 2007; Burg, 2012; Melfos *et al*., 2008) (Fig. 1).

The Palea Kavala region contains ~ 150 minor magmatic-hydrothermal base- and precious-metal occurrences within the Kavala pluton and the surrounding metamorphic rocks. These occurrences have variable metal assemblages that include Fe-Mn-(Pb±Zn±Ag), Fe-Mn-Au, Fe-As-Au, Fe-Cu-Au and Bi-Te, but they are mostly weathered and oxidized. Primary metallic minerals comprise pyrite, arsenopyrite, chalcopyrite, pyrrhotite, galena, sphalerite, tetrahedrite-tennantite, scorodite. Cosalite, pyrrhotite, bismuthinite, petzite, lillianite, proustite, pyrargyrite, argentite, jalpaite, stephanite and native gold are also included. Moreover, secondary minerals like goethite, covellite, arseniosiderite, pyrolusite, manganite, manganosite and cryptomelane contribute to the Fe and Mn content in the sediments resulting by the weathering of the surrounding rocks and the mineralizations that they comprise (Arvanitidis *et al.*, 1989; Vavelidis *et al*., 1996a, b; Vavelidis *et al*., 1997; Melfos *et al*., 2008; Brun and Sokoutis, 2007; Fornadel *et al*., 2011). As Palea Kavala river flows towards the exit of its catchment area, it passes through extensive agricultural cultivated lands that grow on the Quaternary formations of the area and finally enters the sedimentary deposits of the Philippoi plain (Fig. 1).

3. Materials and Methods

3.1. Sample Collection

Thirteen sites were sampled for their sediment (PK1 to PK13) downstream the Palea Kavala river (Figure 1). Sediment samples were collected at the top of the riverbeds and their banks, avoiding the input of other materials. All sediment samples were collected with a plastic shovel and were placed in plastic bags, until they were delivered at the laboratory.

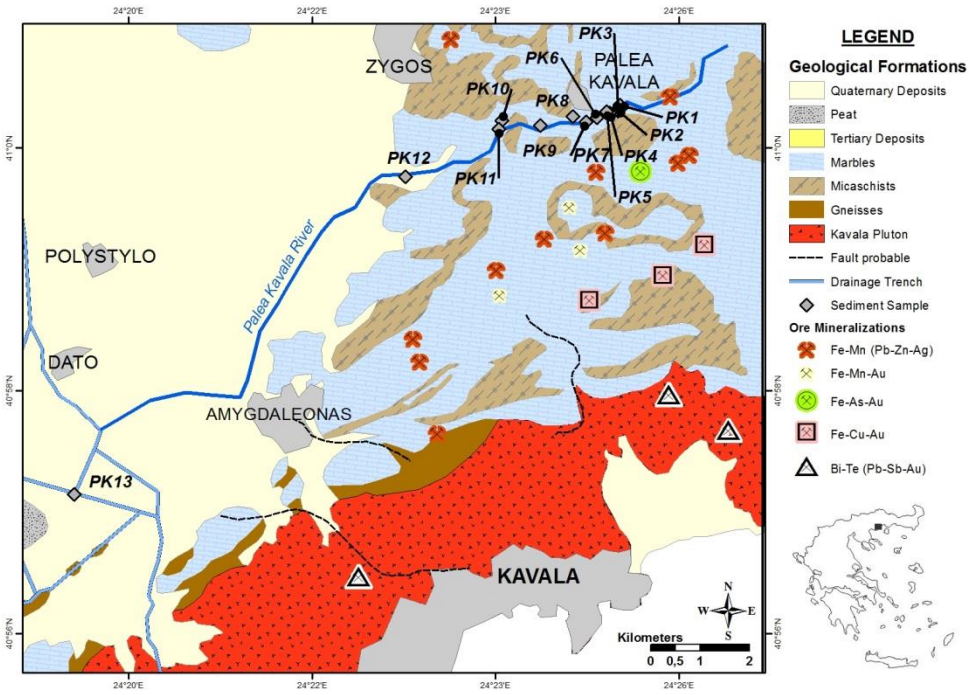

Figure 1 - Geological map of the studied area, including Palea Kavala river and sampling sites (according to Kronberg, 1970; Kronberg and Melidonis, 1970; Vavelidis, 1996a, b, 1997, with modifications).

3.2. Sample Preparation

In the laboratory the sediment samples were dried in an oven at 60˚ C, so as to remove the adsorbed moisture. They were gently ground with pestle and mortar, in order to disaggregate the samples but not to break the grains themselves. Afterwards, the samples were sieved through a 0.063 mm sieve and stored in polyethylene bags until they were sent for analysis. Fine-grained sediments reveal large specific area. Consequently, inorganic contaminants and especially the environmentally available trace elements, remain mainly in this fraction. For that reason the <0.063 mm fraction has been used by many researchers in order to investigate river pollution and likewise in the present study (Förstner and Salomons, 1991; Salomons, 1995; Kabata-Pendias, 2010).

3.3. Sample Analysis

In order to obtain their total content, determination of the major elements Al, Fe and Mn was performed by X-Ray Fluorescence (XRF) at the Electron Microscopy Laboratory in the Faculty of Sciences, Aristotle University of Thessaloniki. For the application of the method, fused discs with a mixture of 35% $Li_2B_4O_7$/65% $LiBO_2$ as a flux and NH_4I as releasing agent were prepared for every sample. The mixture was placed into an Au-Pt alloy crucible and heated at 1100˚C with simultaneous agitation. Afterwards it was cast in an Au-Pt disc, mould and cooled in order to obtain the fused disc.

The concentrations of the trace elements Cd, Cu, Pb and Zn were determined by Inductively Coupled Plasma-Mass Spectrometry (ICP-MS), at the Acme Analytical Laboratories, in Vancouver, Canada. Metals in the sediments were extracted by using the aqua regia digestion, in order to solubilize all the elements that could become environmentally available.

3.4. Data Analysis

To determine the metal enrichment in the sediments, Enrichment Factor (EF) and Geo-accumulation Index (I_{geo}) were employed. The choice of background is very important in the calculation of both used indices. The normalizing elements often considered are Fe and Al, because their concentrations are not affected by any contaminant inputs. But as it was mentioned above, the study area contains numerous Fe-enriched metal occurrences due to the presence of iron minerals (mainly pyrite, arsenopyrite, chalcopyrite, pyrrhotite, goethite). It is apparent therefore that there might be a slight enrichment in Fe in the Palea Kavala region, so Al was chosen as the reference element to normalize the metal concentrations. The geochemical background values used for calculating the indices are derived from those that were introduced by Turekian and Wedepohl (1961) as average shale content (Table 1).

The normalized enrichment factors (EF) were calculated according to the original Salomons and Förstner (1984) equation:

$$EF = \frac{\left(Metal/Al\right)_{Sample}}{\left(Metal/Al\right)_{Background}}$$

EF values were interpreted as suggested by Sakan *et al*. (2009), where: EF<1 indicates no metal enrichment; 1-3 there is minor enrichment; 3–5 there is moderate enrichment; 5–10 there is moderately severe enrichment; 10–25 there is severe enrichment; 25–50 there is very severe enrichment; and >50 there is extremely severe enrichment.

The geo-accumulation Index (I_{geo}) is defined as follows:

$$I_{geo} = \log_2\left(\frac{C_n}{1.5 \times B_n}\right)$$

where Cn is the measured concentration of the examined metal in sediment samples and Bn is the geochemical background concentration of the metal for the average shale. The 1.5 factor is the background matrix correction factor due to lithogenic effects (Muller, 1981; Loska and Wiechula, 2003). The Igeo values are classified in seven classes, according to Müller (1981). Class 0 (practically uncontaminated): $I_{geo} \leq 0$; Class 1 (uncontaminated to moderately contaminated): $0<I_{geo}<1$; Class 2 (moderately contaminated): $1<I_{geo}<2$; Class 3 (moderately to heavily contaminated): $2<I_{geo}<3$; Class 4 (heavily contaminated): $3<I_{geo}<4$; Class 5 (heavily to extremely contaminated): $4<I_{geo}<5$; Class 6 (extremely contaminated): $I_{geo}>5$.

4. Results and Discussion

The results of this study are presented in Table 1 and Figure 2. Among the major elements, Al is th e most abundant demonstrating an average content of 6.61±1.65 wt%. The second most abundant e lement is Fe with an average content of 4.46±1.05 wt%. Concentrations of Mn (0.17±0.20 wt% in average) are very low in relation to Al and Fe. In terms of the trace elements, the highest detected c oncentrations correspond to Pb (avg. 651.36±1104.89 μg/g) and Cu (avg. 559.04±1772.46 μg/g). T he lowest content corresponds to Cd (avg. 1.84±1.68 μg/g) and Zn (avg. 189.22±123.76 μg/g).

Table 1 - Statistical characteristics of the determined elements concentrations in all the studied samples.

	Al (wt%)	Fe (wt%)	Mn (wt%)	Cd (μg/g)	Cu (μg/g)	Pb (μg/g)	Zn (μg/g)
Min	3.49	2.37	0.06	0.50	38.38	75.68	74.50
Max	8.42	5.87	0.79	6.34	6457.96	4240.92	539.80
Mean	6.61	4.46	0.17	1.84	559.04	651.36	189.22
SD	1.65	1.05	0.20	1.68	1772.46	1104.89	123.76
Average Shale	8.00	4.72	0.085	0.3	45	20	95

The elevated standard deviation that is mainly demonstrated by Cu, Pb and to a lesser extent by Zn content is attributed to the extremely elevated concentrations that were determined for these elements in only one sample. That is the sample PK13, which was collected downstream Palea Kavala river in the sedimentary deposits of the Philippoi plain (Fig. 1). The concentrations determined in that sample are 6457.96 μg/g for Cu, 4240.92 μg/g for Pb and 539.80 μg/g for Zn. In order to evaluate if those concentrations affect the statistical characteristics, the calculation of mean and standard deviation values was repeated excluding the sample PK13.

According to the results, no significant variation was observed concerning the major elements. More specifically, by excluding sample PK13 the average content is 6.74±1.64 wt% for Al, 4.59±0.97 wt% for Fe and 0.17±0.21 wt% for Mn, remaining in the same level with the corresponding values presented in Table 1. Similarly for Cd, its concentration determined in PK13 does not affect strongly the statistical characteristics, since its exemption decreases the average Cd content slightly, from 1.84±1.68 μg/g to 1.74±1.71 μg/g. Concerning the rest of the trace elements, significant variations were observed both in average content and standard deviation of Cu, Pb, and Zn. By excluding sample PK13, Cu decreases from 559.04±1772.46 μg/g in average to 67.47±15.31 μg/g. The average content of Pb decreases from 651.36±1104.89 μg/g to 352.23±250.56 μg/g. Although in a smaller degree, variation is also observed in the calculated statistical parameters for Zn, since its average content decreases from 189.22±123.76 μg/g to 160.01±67.86 μg/g.

It is apparent, therefore, that Cu, Pb and Zn content in sample PK13 is extremely high compared to all the other studied samples. This is probably attributed to the fact that between the sampling sites PK12 and PK13, the Palea Kavala river passes through extensive agricultural cultivated lands. So, the use of pesticides, fertilizers and other agrochemical products which contain significant Cu, Pb and Zn components, may explain such an elevated content (Baker, 1990; Ramalho *et al*., 2000).

The resulting EF and I_{geo} values are presented in Figure 2a and 2b, respectively. According to the EF values, Fe exhibits minor enrichment. As demonstrated in Fig. 2a, there is a minor to extremely severe enrichment for Cu, moderate to extremely severe enrichment for Pb and minor to moderately severe enrichment for Zn. It must be mentioned though, that these three elements show elevated concentrations in only one sample, PK13. As presented in Table 1 and discussed above, PK13 reveals maximum concentrations for Cu, Pb and Zn which are extremely higher than their corresponding mean values, elevating EF values as well. Minor to very severe enrichment is observed for Cd and minor to severe enrichment for Mn. In that case, maximum concentrations of Cd and Mn are not determined in sample PK13. They occur in other samples along Palea Kavala river since, as mentioned above, by excluding PK13 the mean content and standard deviation values of Cd and Mn do not demonstrate significant variation.

Overall, as demonstrated in Figure 2a it can be assumed that Fe, Cu, Mn and Zn enrichment is characterized as minor, since most of the EF values concerning those elements are plotted in that field. On the contrary, Cd and Pb appear to be enriched in the Palea Kavala river sediments (Fig. 2a).

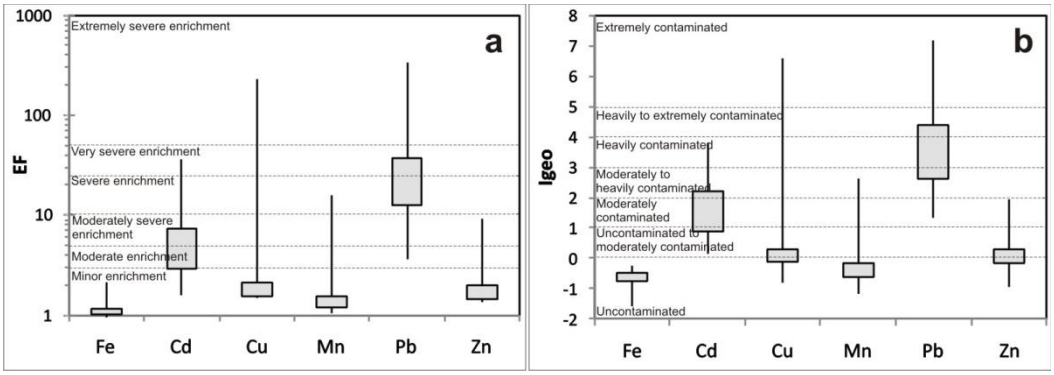

Figure 2 - Variations of values that resulted for (a) enrichment factors-EF and (b) geo-accumulation indexes -I_{geo}.

Calculated I_{geo} values present similar distribution with EF values (Fig. 2b). The results indicate that the sediments are not contaminated with respect to Fe. Moreover, Cu, Mn and Zn levels range from uncontaminated to extremely contaminated, moderately-heavily contaminated and moderately contaminated, respectively. Finally, the sediments are uncontaminated-moderately to heavily contaminated with respect to Cd and moderately to extremely contaminated concerning Pb. I_{geo} values of most elements demonstrate similar effect with EF values. Maximum concentrations that in certain cases are extremely higher than the corresponding mean values have as a consequence the elevation of I_{geo} values. Based on the classification of most of the I_{geo} values (Fir. 2b), sediments are mainly considered as uncontaminated regarding Fe and Mn with a degree of uncontaminated to moderately contaminated for Cu and Zn. Concerning Cd and Pb, most of I_{geo} values suggest that sediments are moderately to heavily contaminated.

Generally, the concentrations of all the studied elements are expected to be elevated, since they participate in the composition of metallic minerals contained in the ore mineralization that occurs in the study area. Minerals like pyrite, goethite and chalcopyrite increase the enrichment of Fe and Cu, while Pb and Zn are attributed in galena and sphalerite, respectively. Since that ore mineralization includes mainly Fe-Mn metal assemblages (Vavelidis *et al*., 1997; Fornadel *et al*., 2011), Mn concentrations are expected as well due to the presence of pyrolousite, manganosite and manganite. Concerning Cd, it is a common content of sphalerite, a mineral which is abundant in the region (Vavelidis *et al*., 1996a, b; Vavelidis *et al*., 1997; Melfos *et al*., 2008; Fornadel *et al*., 2011). Moreover, the extremely elevated concentrations of Cu, Pb and Zn in site PK13 are more related with anthropogenic activities since they probably result due to the extensive use of agrochemical products, whereas Cd and Mn enrichment is mainly attributed to the geological environment.

5. Conclusions

The present study imposes a primary approach on the evaluation of the enrichment that sediments from Palea Kavala river (NE Macedonia, Northern Greece) may demonstrate, with respect to selected metals.

Concerning major elements, the most abundant is Al with Fe to follow. Among the trace metals, Cd and Cu reveal the lowest concentrations. As demonstrated by enrichment factor (EF) values, Palea Kavala river sediments are enriched in Cd and Pb. The same result is also revealed by the I_{geo} values, according to which the sediments are uncontaminated-moderately to heavily contaminated with respect to Cd and moderately to extremely contaminated concerning Pb. The presence of extended ore mineralization which among others includes as primary metallic minerals pyrite, chalcopyrite, galena, sphalerite, pyrolusite, manganosite and manganite, probably affect the Fe, Cu, Pb, Zn, Cd and Mn content in sediments. However, maximum concentrations of Cu, Pb and Zn, which are extremely higher than their corresponding mean values, do not seem having a natural origin. Unlike

all the other determined metals, they are probably related with anthropogenic activities and more specifically with the use of agrochemical products.

However, the research in the study area is in progress for a more detailed evaluation on the mineralogical composition of the sediments and on the correlation among the metal concentrations that they comprise.

6. Acknowledgments

The first author (Giouri K.) would like to thank the State Scholarships Foundation of Greece for the financial support during her post-graduate studies.

7. References

Arvanitidis, N., Kosmas, C., Eliopoulos, D., Perdikatsis, V. and Economou, G., 1989. Gold mineralization associated with carbonate-hosted polymetallic gossans in the area of Kavala, *Geologica Rhodopica*, 340-349.

Baker, D.E., 1990. Copper, *In*: Alloway, B.J., *eds*., Heavy metals in soils, 151-176, Glasgow/London/New York, Blackie/Wiley, 339 pp.

Brun, J.P. and Sokoutis, D., 2007. Kinematics of the Southern Rhodope Core Complex (North Greece, *International Journal of Earth Sciences*, 96(6), 1079-1099.

Burg, J.P., 2012. Rhodope: From Mesozoic convergence to Cenozoic extension, Review of petrostructural data in the geochronological frame. *In:* Skourtsos, E. and Gordon, S.L., *eds*., The Geology of Greece, *Journal of the Virtual Explorer*, 42(1), 44 pp.

Calmano, W., Ahlf, W. and Förstner, U., 1996. Sediment quality assessment: chemical and biological approaches. *In:* Calmano, W. and Förstner, U., *eds.*, Sediments and Toxic Substances, 1-35. Springer Verlag, Berlin.

Christofides, G., 1996. Tertiary magmatism in the Greek Rhodope Massif, northern Greece: Granitic plutons. *In:* Knezevic, V. and Krstic, B., *eds.*, Terranes of Serbia: *The Formation of the Geologic Framework of Serbia and the Adjacent Regions*, University of Belgrade, Belgrade, 155-160.

Fornadel, A.P., Spry, P.G., Melfos, V., Vavelidis, M. and Voudouris, P., 2011. Is the Palea Kavala Bi–Te–Pb–Sb±Au district, northeastern Greece, an intrusion-related system? *Ore Geology Reviews*, 39, 119-133.

Förster, U. and Salomons, W., 1991. Mobilization of metals from sediment. *In:* Merian, E., *ed.*, Metals and their compounds in the environment, 379-398, VCH, Weinheim.

Förstner, U., 1989. Contaminated sediment. *In:* Bhattacharij, S. *ed.*, Lecture Notes in Earth Sciences, 1-157, Springer, Berlin.

Hakanson, L., 1980. Ecological risk index for aquatic pollution control, a sedimentological approach, *Water Research*, 14, 975-1001.

Kabata-Pendias, A., 2010. *Trace elements in soils and plants*, 4th Edition, CRC Press, 548 pp.

Krohe, A. and Mposkos, E., 2002. Multiple generations of extensional detachments in the Rhodope Mountains (northern Greece): evidence of episodic exhumation of high-pressure rocks. *In*: Blundell, D.J., Neubauer, F. and von Quadt, A., *eds.*, The timing and location of major ore deposits in an evolving orogen, 204, 151-178, Geological Society, London.

Kronberg, P., 1970. Geological map of Greece: Kavala Sheet, Scale 1:50.000. IGME, Athens.
Kronberg, P. and Melidonis, N., 1970. Geological map of Greece: Krinidhes Sheet, Scale 1:50.000. IGME, Athens.
Laws, E.A., 1993. Aquatic Pollution: An Introductory Text, 2nd Edition, John Wiley and Sons, Inc., New York, 611 pp.
Loska, K. and Wiechula, D., 2003. Application of principal component analysis for the estimation of source of heavy metal contamination in surface sediments from the Rybnik Reservoir, *Chemosphere*, 51, 723-733.
Melfos, V., Voudouris, P., Vavelidis, M. and Spry, P.G., 2008. Microthermometric results and formation conditions of a new intrusion-related Bi–Te–Pb–Sb±Au mineralization in the Kavala Pluton, Greece, Joint 13th All-Russian Conference on Thermobarogeochemistry/ *4th Asian and Pacific International Fluid Inclusion Society Symposium*, Moscow, Abstracts.
Müller, G., 1981. Die Schwermetallbelstung der sedimente des Neckars und seiner Nebenflusse: eine Bestandsaufnahme, *Chemicer-Zeitung*, 105, 157-164.
Ramalho, J.F.G.P., Sobrinho, N.M.B. and Velloso, A.C.X., 2000. Heavy metals contamination of a watershed in Caetés by the use of agrochemicals, *Pesquisa Agropecuária Brasileira*, 35(7), 1289-1303.
Sakan, S.M., Djordjevic, D.S., Manojlovic, D.D. and Polic, P.S., 2009. Assessment of heavy metal pollutants accumulation in the Tisza river sediments, *Journal of Environmental Management*, 90(11), 3382-3390.
Salomons, W., 1995. Environmental impact of metals derived from mining activities: processes, predictions, preventions, *Journal of Geochemical Exploration*, 52, 5-23.
Salomons, W. and Förstner, U., 1984. Metals in the hydrocycle, Berlin/Heidelberg/Tokyo, Springer, 349 pp.
Turekian, K.K. and Wedepohl, K.H., 1961. Distribution of the elements in some major units of the earth's crust, *Bulletin of the Geological Society of America*, 72, 175-192.
Vavelidis, M., Christofides, G. and Melfos, V., 1996a. The Au-Ag-bearing mineralization and placer gold of Palea Kavala (Macedonia, N. Greece). *In:* Knežević-Dorđević, V. and Krstić, B., *eds.*, Terranes of Serbia, *The Formation of the Geologic Framework of Serbia and the Adjacent Regions*, University of Belgrade, Belgrade, 311-316.
Vavelidis, M., Gialoglou, G., Melfos, V. and Wagner, G.A., 1996b. Goldgrube in Palaea Kavala-Griechenland: Entdeckung von Skaptehyle? *Erzmetall*, 49, 547-554.
Vavelidis, M., Melfos, V. and Eleftheriadis, G., 1997. Mineralogy and microthermometric investigations in the Au-bearing sulphide mineralization of Palea Kavala (Macedonia, Greece). *In:* Papunen, H., *eds.*, Mineral Deposits: *Research and Exploration - Where do They Meet?* 343-346, Balkema, Rotterdam.

Δελτίο της Ελληνικής Γεωλογικής Εταιρίας, τόμος L, σελ. 2145-2154
Πρακτικά 14ου Διεθνούς Συνεδρίου, Θεσσαλονίκη, Μάιος 2016

Bulletin of the Geological Society of Greece, vol. L, p. 2145-2154
Proceedings of the 14th International Congress, Thessaloniki, May 2016

THE USE OF HEU-TYPE ZEOLITIC TUFF IN SUSTAINABLE AGRICULTURE: EXPERIMENTAL STUDY ON THE DECREASE OF NITRATE LOAD IN VADOSE ZONE LEACHATES

Hatzigiannakis E.[1], Kantiranis N.[2], Tziritis E.[1], Filippidis A.[2], Arampatzis G.[1] and Tzamos E.[2]

[1]Hellenic Agricultural Organization, Soil and Water Resources Institute 57400, Sindos-Thessaloniki, Greece, hatzigiannakis@gmail.com, tziritis@gmail.com, arampgeo@gmail.com

[2]Aristotle University of Thessaloniki, Faculty of Sciences, School of Geology, Department of Mineralogy-Petrology-Economic Geology, 54124, Thessaloniki, Greece, kantira@geo.auth.gr, anestis@geo.auth.gr, tzamos@geo.auth.gr

Abstract

A HEU-type zeolitic tuff of very-high quality (88 wt.% clinoptilolite-heulandite) has been used as an additive to natural soils, aiming to reduce the produced nitrate load in leachates, following a common irrigation scheme. Zeolitic tuff has been added and mixed with agricultural soil in three different proportions (0.2, 0.4 and 0.6%) corresponding to an application of 500, 1000 and 1500 kg per acre. The control soil (without zeolitic tuff) and the three mixtures were exposed in a ten weeks experiment, in which, specific doses of irrigation water enriched in nitrates were added. Results of leachates analyses revealed that the addition of 0.2% zeolitic tuff is not effective and the mixture of soil-zeolitic tuff appears to have similar behaviour with the untreated (reference) soil sample. On the contrary, zeolitic tuff additions by 0.4% and 0.6% showed remarkable results and reduced the nitrate load of leachates by 81 and 86%, respectively. Hence, the impacts from the application of very-high quality HEU-type zeolitic tuff in agricultural soils could be rather positive towards environmental protection and rational farming, an in line with the goals and objectives of the new common agricultural policy imposed by European Union.
Keywords: *zeolite, agriculture, nitrates, environmental protection, leachates.*

Περίληψη

Στην παρούσα εργασία χρησιμοποιήθηκε ένας πολύ υψηλής ποιότητας ζεολιθικός τόφφος τύπου-HEU (88% κ.β. κλινοπτιλόλιθος-ευλανδίτης) ως πρόσθετο υλικό σε φυσικά εδάφη, με στόχο την ελάττωση της συγκέντρωσης των παραγόμενων εκπλυμάτων νιτρικών ιόντων, υπό συνήθεις συνθήκες άρδευσης. Ο ζεολιθικός τόφφος αναμίχθηκε με το έδαφος σε τρεις αναλογίες (0.2, 0.4 και 0.6%) οι οποίες αντιστοιχούν σε εφαρμογή 500, 1000 και 1500 kg ανά στρέμμα. Στο δείγμα αναφοράς (μάρτυρας – απουσία ζεολιθικού τόφφου) και στα τρία μίγματα εδάφους-ζεολιθικού τόφφου πραγματοποιήθηκε πείραμα διάρκειας 10 εβδομάδων, στο οποίο, διοχετεύτηκαν σταθερές δόσεις αρδευτικού νερού εμπλουτισμένου με νιτρικά ιόντα. Τα αναλυτικά αποτελέσματα των εκπλυμάτων έδειξαν ότι η προσθήκη ζεολιθικού τόφφου κατά 0,2% δεν ήταν αποτελεσματική και το μίγμα συμπεριφέρθηκε ανάλογα του δείγματος

αναφοράς. Αντιθέτως, η προσθήκη ζεολιθικού τόφφου σε περιεκτικότητες 0,4% και 0,6% έδωσε σημαντικά αποτελέσματα, καθώς η συγκέντρωση νιτρικών ιόντων μειώθηκε κατά 81% και 86% αντίστοιχα, σε σχέση με το έκπλυμα του μάρτυρα. Συνεπώς, οι επιπτώσεις από την εφαρμογή πολύ υψηλής ποιότητας ζεολιθικού τόφφου στα αγροτικά εδάφη, μπορεί να έχει σημαντικά θετικές επιπτώσεις στην περιβαλλοντική προστασία και στην αειφόρο γεωργία, γεγονός που είναι συνδεδεμένο άμεσα με τους στόχους της νέας κοινής αγροτική πολιτικής της Ε.Ε και την σχετική νομοθεσία.
Λέξεις κλειδιά: *Ζεόλιθος, καλλιέργεια, νιτρικά, περιβαλλοντική προστασία, εκπλύματα.*

1. Introduction

Soil and water quality deterioration has become a significant challenge due to population growth combined with other man-made activities, like e.g. irrational agriculture and industrialization. As a result, a considerable increment of contaminants has been recorded worldwide in the aforementioned compartments, denoting a significant impact to their overall quality and environmental characteristics.

Agricultural areas are by definition vulnerable to environmental pressures related with excessive use of fertilizers and agrochemicals. Nitrogen leaching from cropland contributes to increased nitrate levels in ground and surface water (Lichtenberg and Shapiro, 1997) and constitutes a focal point for European legislation (Council Directive, 1991) in terms of environmental protection and mitigation of potential threats. Depending on the concentration, elevated N levels may cause adverse effects to aquatic ecosystems and humans, particularly to infants and also result in collateral financial impacts for farmers due to the expense of fertilizers (Perrin *et al.*, 1998).

Nitrates (NO_3) are present to some degree in almost all cropland, except flooded soils. Depending on soil's leaching potential, when water is added in excess of the soil's field capacity (e.g. through precipitation and/or irrigation) it will carry nitrate and other salts downward. Controlling nitrate leaching can be a challenge for farmers because it requires simultaneous management of two essentials of plant growth; nitrogen (N) and water. Any factor influencing soil moisture (such as rainfall, irrigation, evaporation and transpiration) will impact nitrate movement. In general, more water infiltration results in nitrate moving deeper in the profile. Soil properties also have a major impact on the extent of nitrate movement. However, the extent of nitrate movement to groundwater depends on the underlying soil and bedrock conditions, as well as depth to groundwater.

Nitrate in a field may originate from many sources, including manures, composts, decaying plants, septic tanks, or from fertilizer which is rather common in agricultural soils. Nitrate behaviour does not depend on its sources; the simple fact is that any nitrate available for plant uptake is vulnerable to leaching loss. One key practice for reducing leaching losses is to minimize the amount of nitrate present in the soil at any given time. This goal can be difficult to achieve because rapidly growing crops require adequate N. Hence, integrated agriculture is seeking for alternatives in order to achieve optimal conditions for both plants and their environment. Such an alternative may be considered the use of zeolitic tuffs as a soil conditioner to reduce nitrate leaching, and in parallel, to improve critical parameters for crops like soil humidity.

Zeolites exist in nature in many forms; a common form is the zeolitic tuff which corresponds to a rock that contains high amounts of one or more from the different (>65) phases of zeolites. The zeolite with the numerous applications is the HEU-type zeolite (clinoptilolite-heulandite) that shows tabular crystals and contains micro/nanopores in a framework of channels with 10- and 8-member rings, in dimensions of 7.5×3.1 Å, 4.6×3.6 Å and 4.7×2.8 Å (Baerlocher *et al.*, 2007; Mitchell *et al.*, 2012). Very-high quality HEU-type zeolitic tuffs, display unique physical and chemical features and have a great variety of environmental, industrial and agricultural applications (Tsitsishvili *et al.*, 1992; Colella and Mumpton, 2000; Filippidis and Kantiranis, 2007; Filippidis *et al.*, 2008a, 2015a, b; Kantiranis *et al.*, 2011; Tzamos *et al.*, 2011; Vogiatzis *et al.*, 2012; Filippidis, 2013).

Using very-high quality HEU-type zeolitic tuff, the nitrate load reduction were found to be 86-92% in batch treatments of Kilkis city urban wastewaters (Filippidis *et al.*, 2008b, 2012, 2015a; Filippidis, 2008, 2009, 2010; Filippidis and Tsirambides, 2012), 94% in batch treatment of Thessaloniki dyeing industry wastewater (Filippidis *et al.*, 2015b), 54-60% in batch treatments of Sindos industrial area wastewaters (Filippidis *et al.*, 2011a,b, 2013, 2014), 57% in batch treatment of nitrate-solutions (Filippidis, 2007, 2010), 55% in batch treatment of groundwater (Filippidis *et al.*, 2006; Filippidis, 2010), and using surfactant modified clinoptilolitic zeolitic tuff, 96-97% in batch and column treatments of groundwater (Masukume *et al.*, 2011). In leaching experiments, 100% of the nitrate were leached from Kilkis city sewage sludge and Thessaloniki dyeing industry sludge (Filippidis *et al.*, 2008b, 2015a, b; Filippidis, 2009; Filippidis and Tsirambides, 2012). Mixing very-high quality zeolitic tuff with sewage and dyeing industry sludge, the nitrate leaching was reduced 81-91% in the case of Zeolitic tuff + sewage sludge (Filippidis *et al.*, 2008b, 2015a; Filippidis, 2009; Filippidis and Tsirambides, 2012) and 82% in the case of zeolitic tuff + dyeing industry sludge (Filippidis *et al.*, 2015b). The present paper investigates the possibility of reducing the nitrate leaching by the addition-mixing the very-high quality zeolitic tuff in the agricultural soils.

2. Materials and Methods

2.1. Description of experimental processing

The field experiment was performed in the premises of Soil and Water Resources Institute (ISWR) of Hellenic Agricultural Organization "Demeter" in Sindos-Thessaloniki, Greece. The goal of the experiment was to assess nitrate leaching of irrigated agricultural soils after been treated-mixed with zeolitic tuff in different proportions; irrigation water was enriched in nitrates (totally 80L with 100 mg/L concentration) and was applied in doses following a common irrigation scheme for cultivations (see details below). The experiment took place between May and July of 2015 (10 weeks), resembling the dry conditions of a hydrological year.

The experimental procedure included the following intermediate steps:

Four (4) prototype devices were constructed; the devices included a cylinder pipe (column) of 500mm diameter (internal diameter 470mm) and total length of 50cm, which subsequently would be filled with soil and soil-zeolitic tuff mixture in different proportions. To the lower part of the cylinder was attached a fine mesh in order to prevent sediment transport. The cylinder was based on a protected metal pan, which was intended to collect leachates from the column. The columns were roof-protected and not exposed to precipitation or any other external water source.

The next step included the sampling (bulk) of reference agricultural soils with medium soil texture from the wider area of Sindos. Samples belonged to the same soil unit, but were further homogenized with mechanic means and dried naturally (sun exposure). The lower 30cm of the columns were filled with the homogenized reference soil, whilst the upper 20 cm were filled with the zeolitic tuff-soil mixture in three (3) different proportions, namely 0% (reference) (R), 0.2% (A), 0.4% (B) and 0.6% (C) zeolitic tuff in the mix, respectively. The above quantities were selected intentionally as they correspond to application of 500, 1000 and 1500 kg of zeolitic tuff per acre. These quantities are higher than the common applications used annually in agriculture, but may be achieved through the cumulative additions of zeolitic tuff quantities, hence remain on the verge of financial viability for the farmers (depending on the case).

A prototype solution of KNO_3 with 100mg/L of NO_3^- was used as irrigation water. Each irrigation dose included 2.5 litres of the prototype solution; in order to increase soil saturation and acquire efficient volume of leachates, 3 extra application doses (4 ½, 5 ½ and 6 ½ weeks) were added between the 4th and the 7th week whilst the amount of irrigation water was doubled (5lt) for the applications of 5th, 5 ½th and 6th week. Leachates were scheduled to be collected in a weekly time-span, but eventually a sufficient volume was acquired at the fourth week of the experiment; hence six (6) leachate samples were collected in total, from the 5 ½th to 10th week. The total volume of

irrigation water used was 40L and corresponds to 260mm per year. Samples were analysed immediately in the laboratories of ISWR with the use of a LAMBDA35 PERKIN-ELMER spectrophotometer.

2.2. Analysis and characterization of soil and zeolitic tuff

A bulk soil sample was collected from the same soil unit used in the described experimental process, for further physicochemical and mineralogical analysis. The sample was air–dried and a fraction (<2 mm) was used for laboratory determinations. Particle size distribution was determined by the Bouyoucos hydrometer method (Gee and Bauder, 1986) and pH was measured in a saturation paste (Alexiadis, 1967). Cation exchange capacity (CEC) was determined by CH_3COONa saturation solution of 1N and pH of 8.5 or 7 (Bower *et al.*, 1952). Organic matter was determined by liquid oxidation method. Finally NO_3-N was determined through KCl extraction and N total with Kjeldahl method. The same methodologies were applied in zeolitic tuff physicochemical analyses.

The zeolitic tuff sample (grain-size <0.8 mm) used was supplied by ZEOVET Ouzoundis and GEO-VET N. Alexandridis & Co O.E. The mineralogical composition of the zeolitic tuff and soil sample was determined by X-Ray Powder Diffraction (XRPD). The XRPD analysis was performed using a Philips PW1710 diffractometer with Ni-filtered CuK_α radiation on randomly oriented samples. The counting statistics were: start angle 3º, end angle 63º (2θ), step size 0.02º (2θ), time per step 1 sec and scan speed 0.02º/sec. Semi-quantitative estimates of the abundance of the mineral phases were derived from the XRPD data, using the intensity (counts) of certain reflections, the density and the mass absorption coefficient of the identified minerals for CuK_α radiation, the software MAUD-Material Analysis Using Diffraction with the RIETVELD method. Clay mineralogy was identified from air-dried, glycolated and heat-treated oriented samples scanned from 3º to 23º 2θ at a scanning speed of 1.2º/min. The semi-quantitative estimation of the percentage of total amorphous materials was achieved by comparing the area of each broad background hump, which represented the amorphous materials in each sample, with the analogous area of standard mixtures of minerals with different contents of natural amorphous material, scanned under the same conditions (Filippidis and Kantiranis, 2007; Kantiranis *et al.*, 2004, 2005, 2006).

3. Results and Discussion

The physicochemical determinations of soil and zeolitic tuff are presented in Table 1. Based on its texture and organic content (USDA 1987) soil sample is characterized as Sandy-Loam (SaL) with slightly alkaline pH (7.8); organic content is 0.6% and cation exchange capacity (CEC) is 9.5 meq/100g; total nitrogen content (Kjeldahl) is 767 mg/kg and and NO_3-N is 48 mg/kg. Regarding zeolitic tuff, total nitrogen is 178 mg/kg and NO_3-N 13 mg/kg, respectively.

Table 1 - Physicochemical characteristics of soil and zeolitic tuff samples.

	Texture			**CEC**	**pH**	**Organic C**	**N_{total} (Kjeldahl)**	**NO_3-N**
	Sand (%)	Silt (%)	Clay (%)	meq/100g		%	mg/kg	mg/kg
Soil	62	22	16	9.5	7.8	0.6	767	48
zeolitic tuff	-	-	-	-	-	-	178	13

The semi-quantitative mineralogical compositions of the zeolitic tuff and soil sample are presented in Table 2 and Figures 1 and 2. Zeolitic tuff contains 88 wt.% HEU-type zeolite (clinoptilolite-heulandite), 5 wt.% mica + clay minerals, 4 wt.% quartz, 2% amorphous materials and 1% feldspars. Soil sample contains 59 wt.% quartz, 21 wt.% feldspars, 15 wt.% micas+clay minerals and 5 wt.% amphibole.

Based on the analytical results of leachates, nitrate load is decreased significantly in zeolite treated soils compared with the reference (untreated) sample. The initial concentration (5.5 week) of nitrates

in R sample is 894 mg/L, whilst the initial concentrations in leachates of A, B and C samples are 554, 471 and 458 mg/L respectively, corresponding to a decreased concentration of 38, 47% and 49% of initial R leachates (Table 3 and Figure 3).

Table 2 - Semi-quantitative mineralogical composition of Zeolitic tuff and soil samples.

Zeolitic tuff		Soil	
Minerals	**Wt.%**	**Minerals**	**Wt.%**
HEU-type zeolite (clinoptilolite-heulandite)	88	Quartz	59
Micas + Clay-minerals	5	Feldspars	21
Quartz	4	Micas + Clay-minerals	15
Feldspars	1	Amphibole	5
Amorphous	2		
Total	100	Total	100

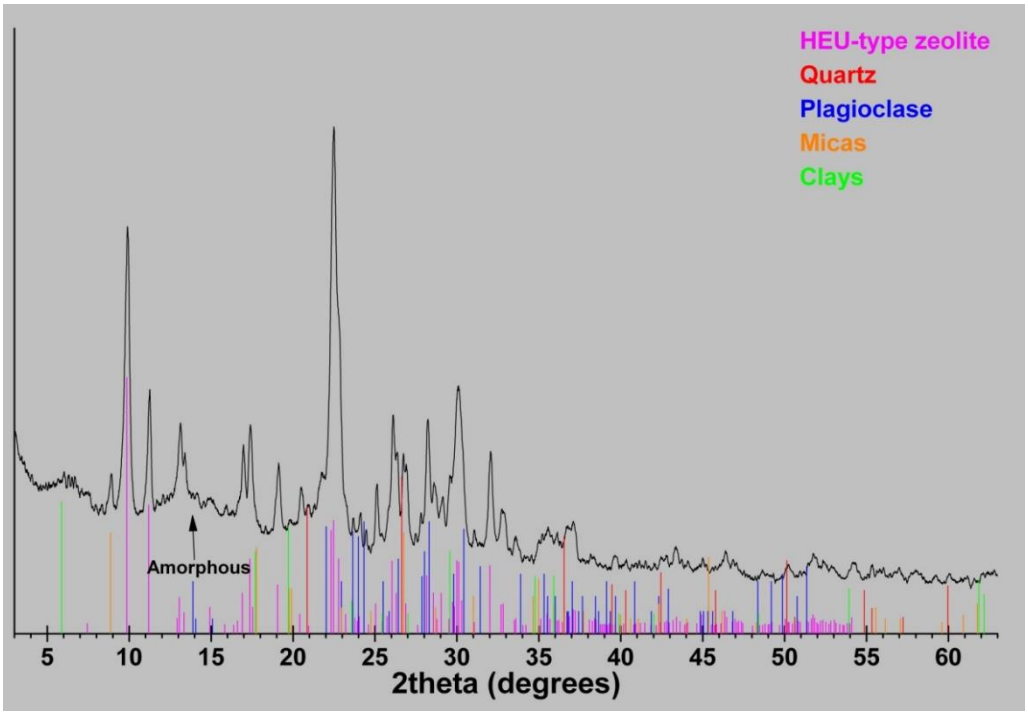

Figure 1 - X-Ray Powder Diffraction pattern of zeolitic tuff sample.

Taken into account that experimental conditions are similar and that soil organic content is in general low (0.6%), it is evident that this significant decrease should be attributed to zeolitic tuff impact. Subsequently, intermediate of the experimental process (8th week), nitrate load concentrations decrease with different rates for A, B and C samples, corresponding to a reduction of 26%, 50% and 55% compared to R leachates. In general, R and A samples follow similar decrease rates for nitrates, denoting an insignificant impact of the 0.2% zeolitic tuff content in soil. This may also be deduced by the concentrations of nitrate load at the end of experiment (10th week), which differ only by 2 mg/L (2%), corresponding to a negligible variation within the standard analytical error. On the contrary, it is rather promising that the final concentrations of nitrate load in samples B and C, has been decreased significantly compared to R sample by 81% and 86%, respectively.

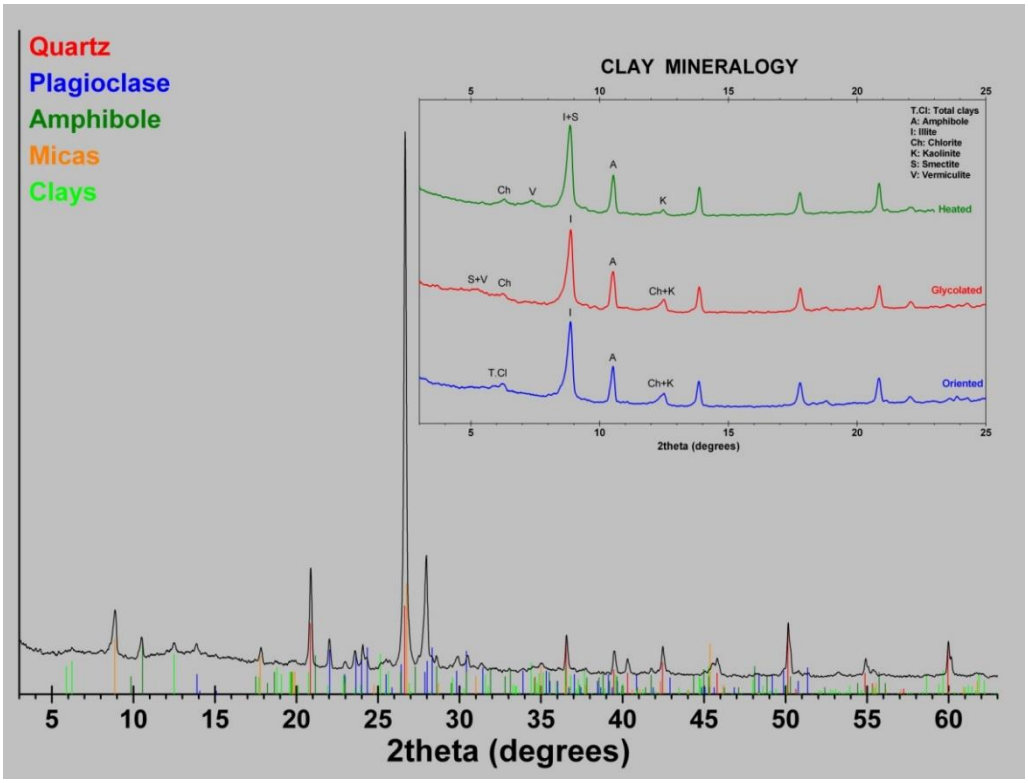

Figure 2 - X-Ray Powder Diffraction pattern of soil sample. Clay mineralogy: Illite, smectite, kaolinite, vermiculite and chlorite.

Table 3 - Percentages of nitrate load reduction in leachates compared to reference sample.

	Start (5.5th week)	Intermediate (8th week)	End (10th week)
Reference (R)	894 mg/L	162 mg/L	81 mg/L
0.2 % Z (A)	38%	26%	2%
0.4 % Z (B)	47%	50%	81%
0.6 % Z (C)	49%	55%	86%

The results of nitrate load reduction obtained from soil mixing with natural HEU-type zeolitic tuff (ZT) are rather successful; nitrate load was decreased in 0.4% ZT sample by 81%, whilst in 0.6% ZT sample by 86%. So far, similar decrease percentages have been recorded using very-high quality HEU-type zeolitic tuff and surfactant modified clinoptilolitic zeolitic tuff, (86-92%) in batch treatments of urban wastewaters (Filippidis *et al.*, 2008b, 2012, 2015a; Filippidis, 2008, 2009, 2010; Filippidis and Tsirambides, 2012), (94%) in batch treatment of dyeing industry wastewater (Filippidis *et al.*, 2015b), (54-60%) in batch treatments of industrial area wastewaters (Filippidis *et al.*, 2011a,b, 2013, 2014), (57%) in batch treatment of nitrate-solutions (Filippidis, 2007, 2010), (55%) in batch treatment of groundwater (Filippidis *et al.*, 2006; Filippidis, 2010), and (96-97%) in batch and column treatments of groundwater (Masukume *et al.*, 2011). In leaching experiments, 100% of the nitrate were leached from Kilkis city sewage sludge and Thessaloniki dyeing industry sludge (Filippidis *et al.*, 2008b, 2015a, b; Filippidis, 2009; Filippidis and Tsirambides, 2012). Mixing very-high quality zeolitic tuff with sewage and dyeing industry sludge, the nitrate leaching was reduced 81-91% in the case of Zeolitic tuff + sewage sludge (Filippidis *et al.*, 2008b, 2015a; Filippidis, 2009; Filippidis and Tsirambides, 2012) and 82% in the case of zeolitic tuff + dyeing

industry sludge (Filippidis *et al.*, 2015b); nevertheless zeolite modification is a non viable process in financial terms for common agricultural practices. In comparison with this study, nitrate removal with a zeolitic rock (70-75 wt.% clinoptilolite) achieved percentages of less of than 10% (Mazeikiene *et al.*, 2008), and proved to be an insufficient for nitrate retention.

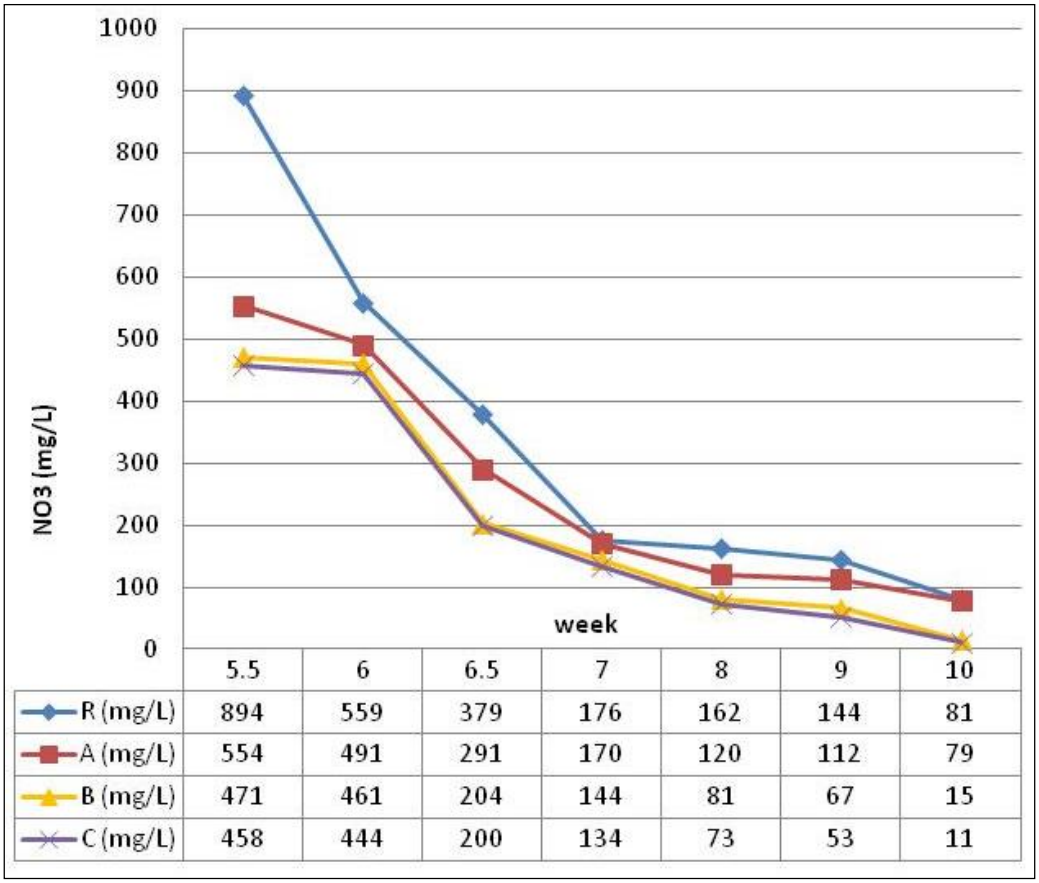

	5.5	6	6.5	7	8	9	10
R (mg/L)	894	559	379	176	162	144	81
A (mg/L)	554	491	291	170	120	112	79
B (mg/L)	471	461	204	144	81	67	15
C (mg/L)	458	444	200	134	73	53	11

Figure 3 - Nitrate load concentrations in leachates.

On the contrary, the used very-high quality HEU-type zeolitic tuff has proven to be a unique sorbent of bacteria, gases, inorganic, organic and organometallic compounds, and achieves to buffer pH of soils and waters to neutral (e.g., Filippidis and Kantiranis, 2007; Filippidis *et al.*, 2008a, b, 2015a, b; Filippidis, 2010, 2013). The sorption and fixation of the different components from their solutions by the micro/nano-pores of HEU-type zeolite, as well as from meso- and macro-pores of the zeolitic tuff, is attributed to absorption (ion exchange), adsorption and surface precipitation processes (Godelitsas *et al.*, 1999, 2001, 2003; Fu and Wang, 2011; Kantiranis *et al.*, 2011; Malamis and Katsou, 2013). The HEU-type zeolite is characterized by Brønsted acidic and the Lewis basic active sites, that react with the negatively or/and positively charged chemical components, even with molecules in gas condition. These chemical processes are related to sorption and fixation physicochemical phenomena of ions and molecules, and are related both to the structural void spaces (micro/nano-pores) and the surface of the HEU-type zeolite crystals, consequently the meso- and macro-pores of the zeolitic tuff. Finally, HEU-type zeolite shows an ability to neutralize the pH of acidic and basic waters, acting either as a proton acceptor or donor, exhibiting thus an amphoteric character (Misaelides *et al.*, 1995; Godelitsas *et al.*, 1999, 2001, 2003; Kantiranis *et al.*, 2011).

4. Conclusions

A very-high quality HEU-type zeolitic tuff containing 88 wt.% clinoptilolite-heulandite, has been used as a mixing material with soil samples from Sindos area, Thessaloniki. Zeolitic tuff-soil mixture was added on the top 20cm of a totally 50cm column (the remaining covered with untreated soil) in different proportions (0.2, 0.4 and 0.6%) corresponding to an application of 500, 1000 and 1500 kg per acre. Samples were subjected to common irrigation scheme with stable doses, simulating a total volume of 40 L or 260 mm per year. Results revealed that zeolitic tuff mixture may act as an efficient natural sorbent with a remarkable ability to retain nitrate leachates from soils, up 86% of the initial leachates of the reference (untreated) sample. The maximum retention percentage was achieved with a 0.6% addition of zeolitic tuff, which is still under conditions within the margins of financial viability form common farmers. However, results should be further exploited and verified in field conditions, with real irrigation and cultivations schemes, and external effects. Nevertheless, the results obtained in laboratory scale from this study are quite promising for the efficacy of zeolitic tuff as natural sorbent and its contribution to rational agricultural practices against nitrate contamination. The latter is in line with the objectives of the new common EU agricultural policy, and may act as a supplementary tool for integrated fertilization, water resources management and environmental protection.

5. Acknowledgments

The authors wish to thank GEO-VET N. Alexandridis & Co O.E. for the supply of the zeolitic tuff.

6. References

Alexiadis, K., 1967. Physical and chemical soil analysis. Thessaloniki, 78 pp. (in Greek).

Baerlocher, Ch., McCuster, L.B. and Olson, D.H., 2007. Atlas of Zeolite Framework Types. Amsterdam, Elsevier, 301 pp.

Bower, C.A., Reitemeier, R.F. and Fireman, M., 1952. Exchangeable cation analysis of saline and alkali soils, *Soil Sci*. 73, 251-261

Colella, C. and Mumpton, F.A., 2000. Natural Zeolites for the Third Millenium, Napoli, De Frede Editore, 481 pp.

Council Directive 1991/676/EEC of 12 December 1991 concerning the protection of waters against pollution caused by nitrates from agricultural sources.

Filippidis, A., 2007. Zeolites of Trigono Municipality of Evros Prefecture in industrial, agricultural, cattle-raising and environmental technology (in Greek), *Proc. Sci. Meet. Development Perspectives of Northern Evros*, Petrota, Evros, Greece, 4 Aug., 89-107.

Filippidis, A., 2008. Treatment and recycling of municipal and industrial waste waters using Hellenic Natural Zeolite: A Review, *Proc. AQUA, 3rd Intern. Conf. Water Sci. & Technology*, Athens, 16-19 Oct., 5 pp.

Filippidis, A., 2009. Management of urban and industrial wastewaters using Hellenic Natural Zeolite. Review article (in Greek with English summary), *Proc. Congr. Integrated Manag. Water Res. Climatic Change Conditions*, Volos, Greece, 27-30 May, II, 829-836.

Filippidis, A., 2010. Environmental, industrial and agricultural applications of Hellenic Natural Zeolite, *Hellenic J. Geosci.*, 45, 91-100.

Filippidis, A., 2013. Industrial and municipal wastewater treatment by zeolitic tuff, Water Today V(X), 34-38.

Filippidis, A. and Kantiranis, N., 2007. Experimental neutralization of lake and stream waters from N. Greece using domestic HEU-type rich natural zeolitic material, *Desalination*, 213, 47-55.

Filippidis, A. and Tsirambides, A., 2012. Quality characteristics of the Greek zeolites, environmental, industrial, agricultural and aquacultural uses of Hellenic natural zeolite: A review (in Greek with English abstract), *Scientific Annals*, School of Geology, Aristotle University of Thessaloniki, 101, 125-133.

Filippidis, A., Kantiranis, N., Drakoulis, A. and Vogiatzis, D., 2006. Improvement and protection of the lake Koronia using natural zeolite (In Greek with English summary), *Proc. 2nd Congr. Aristotle Univ. Environ. Council*, Thessaloniki, 1-4 June, 273-279.

Filippidis, A., Apostolidis, N., Paragios, I. and Filippidis, S., 2008a. Zeolites clean up, *Industrial Minerals*, 487, 68-71.

Filippidis, A., Apostolidis, N., Paragios, I. and Filippidis, S., 2008b. Safe management of sewage sludge, produced by treatment of municipal sewage with Hellenic Natural Zeolite, *Proc. AQUA, 3rd Intern. Conf. Water Sci. & Technology*, Athens, 16-19 Oct., 5 pp.

Filippidis, A., Tsirambides, A., Kantiranis, N., Tzamos, E., Vogiatzis, D., Papastergios, G., Papadopoulos, A. and Filippidis S., 2011a. Purification of wastewater from Sindos industrial area of Thessaloniki (N. Greece) using Hellenic Natural Zeolite, *Proc. 9th Intern. Hydrogeol. Congr.*, Kalavrita, Greece, 5-8 Oct., Environ. Earth Sci., Springer, Berlin, *Adv. Res. Aquatic Environ.*, 2, 435-442.

Filippidis, A., Tsirambides, A., Tzamos, E., Vogiatzis, D., Papastergios, G., Georgiadis, I., Papadopoulos, A. and Filippidis, S., 2011b. Purification of wastewater from Thessaloniki industrial area using Hellenic natural zeolite (in Greek with English abstract), *Proc. 21st Panhellenic Chemistry Congr.*, Thessaloniki, 9-12 Dec., 8 pp.

Filippidis, A., Kantiranis, N., Vogiatzis, D., Tzamos, E., Papastergios, G. and Filippidis, S., 2012. Odourless-cohesive zeosewage sludge production and urban wastewater purification by natural zeolite, *Proc. Intern. Conf. Protection & Restoration Environment XI*, Thessaloniki, 3-6 July, 582-588.

Filippidis, A., Godelitsas, A., Kantiranis, N., Gamaletsos, P., Tzamos, E. and Filippidis, S., 2013. Neutralization of sludge and purification of wastewater from Sindos industrial area of Thessaloniki (Greece) using natural zeolite, *Bull. Geol. Soc. Greece*, 47(2), 920-926.

Filippidis, A., Kantiranis, N., Tziritis, E., Tzamos, E., Vogiatzis, D. and Filippidis, S., 2014. The use of Hellenic Natural Zeolite (HENAZE) in the purification of Thessaloniki industrial area wastewaters, *Proc. 10th Intern. Hydrogeol. Congr.*, Thessaloniki, 8-10 Oct., 187-193.

Filippidis, A., Kantiranis, N., Papastergios, G. and Filippidis, S., 2015a. Safe management of municipal wastewater and sludge by fixation of pollutants in very high quality HEU-type zeolitic tuff, *J. Basic Appl. Res. Intern.*, 7(1), 1-8.

Filippidis, A., Papastergios, G., Kantiranis, N. and Filippidis, S., 2015b. Neutralization of dyeing industry wastewater and sludge by fixation of pollutants in very high quality HEU-type zeolitic tuff, *J. Global Ecol. Environ.*, 2(4), 221-226.

Fu, F. and Wang, Q., 2011. Removal of heavy metal ions from wastewaters: A review, *J. Envir. Manag.*, 92, 407-418.

Gee, G. and Bauder, J., 1986. Particle Size Analysis. *In:* Klute, A., *eds*., Methods of Soil Analyses, Part 2, 2nd American Society of Agronomy and Soil Science Society of America: Madison, WI, 9, 383-411.

Godelitsas, A., Charistos, D., Dwyer, J., Tsipis, C., Filippidis, A., Hatzidimitriou, A. and Pavlidou, E., 1999. Copper (II)-loaded HEU-type zeolite crystals: characterization and evidence of surface complexation with N,N-diethyldithiocarbamate anions. *Microporous & Mesoporous Materials*, 33, 77-87.

Godelitsas, A., Charistos, D., Tsipis, A., Tsipis, C., Filippidis, A., Triantafyllidis, C., Manos, G. and Siapkas, D., 2001. Characterisation of zeolitic materials with a HEU-type structure modified by transition metal elements: Definition of acid sites in Nickel-loaded crystals in the light of experimental and quantum-chemical results, *Chemistry-A European Journal*, 7, 3705-3721.

Godelitsas, A., Charistos, D., Tsipis, C., Misaelides, P., Filippidis, A. and Schindler, M., 2003. Heterostructures patterned on aluminosilicate microporous substrates: Crystallisation of cobalt (III) tris (N,N-diethyl-dithiocarbamato) on the surface of HEU-type zeolite. *Microporous & Mesoporous Materials*, 61, 69-77.

Kantiranis, N., Filippidis, A. and Georgakopoulos, A., 2005. Investigation of the uptake ability of fly ashes produced after lignite combustion, *J. of Environmental Management*, 76, 119-123.

Kantiranis, N., Filippidis, A., Mouhtaris, T., Paraskevopoulos, K.M., Zorba, T., Squires, C. and Charistos, D., 2006. EPI-type zeolite synthesis from Greek sulphocalcic fly ashes promoted by H_2O_2 solutions, *Fuel*, 85, 360-366.

Kantiranis, N., Georgakopoulos, A., Filippidis, A. and Drakoulis, A., 2004. Mineralogy and organic matter content of bottom ash samples from Agios Dimitrios power plant, Greece, *Bull. Geol. Soc. Greece*, 36(1), 320-326.

Kantiranis, N., Sikalidis, K., Godelitsas, A., Squires, C., Papastergios, G. and Filippidis, A., 2011. Extra-framework cation release from heulandite-type rich tuffs on exchange with NH4+, *J. Environ. Management*, 92, 1569-1576.

Lichtenberg, E. and Shapiro, L.S., 1997. Agriculture and nitrate concentrations in Maryland community water system wells, *J. Environ. Qual.*, 26, 145-153.

Malamis, S. and Katsou, E., 2013. A review on zinc and nickel adsorption on natural and modified zeolite, bentonite and vermiculite: Examination of process parameters, kinetics and isotherms, *J. of Hazar. Mater.*, 252/253, 428-461.

Masukume, M., Onyango, M.S., Aoyi O. and Otieno, F., 2011. Nitrate removal from groundwater using modified matural zeolite, Tshwane University of Technology, Department of Chemical and Matallurgical Engineering, South Africa, *Res. Rep.*, 13 pp.

Mazeikiene, A., Valentukeviciene, M., Rimeika, M., Matuzevicius, A.B. and Dauknys, R., 2008. Removal of nitrates and ammonium ions from water using natural sorbent zeolite (clinoptilolite), *J. Envir. Eng. Landsc. Manag.*, 16, 38-44.

Misaelides, P., Godelitsas, A., Filippidis, A., Charistos, D. and Anousis, I., 1995. Thorium and uranium uptake by natural zeolitic materials, *Sci. Total Environment*, 173/174, 237-246.

Mitchell, S., Michels, N.L., Kunze, K. and Perez-Ramirez, J., 2012. Visualization of hierarchically structured zeolite bodies from macro to nano length scales, *Nature Chemistry*, 4, 825-831.

Perrin, S., Drost, D., Boettinger, J. and Norton, J., 1998. Ammonium-Loaded Clinoptilolite: A Slow-Release Nitrogen Fertilizer for Sweet Corn, *J. of PNutrition*, 21(3), 515-530.

Tsitsishvili, G.V., Andronikashvili, T.G., Kirov, G.N. and Filizova, L.D., 1992. Natural Zeolites, Chichester, England, Ellis Horwood Ltd, 295 pp.

Tzamos, E., Kantiranis, N., Papastergios, G., Vogiatzis, D., Filippidis, A. and Sikalidis, C., 2011. Ammonium exchange capacity of the Xerovouni zeolitic tuffs, Avdella area, Evros Prefecture, Greece, *Clay Minerals*, 46,179-187.

Vogiatzis, D., Kantiranis, N., Filippidis, A., Tzamos, E. and Sikalidis, C., 2012. Hellenic Natural Zeolite as a replacement of sand in mortar: mineralogy monitoring and evaluation of its influence on mechanical properties, *Geosciences*, 2, 298-307.

USDA, 1987. United States Department of Agriculture (USDA), Textural Soil Classification (Module 3), Soil Mechanics Level -1, Technical report, 48 pp.

Δελτίο της Ελληνικής Γεωλογικής Εταιρίας, τόμος L, σελ. 2155-2162
Πρακτικά 14ου Διεθνούς Συνεδρίου, Θεσσαλονίκη, Μάιος 2016

Bulletin of the Geological Society of Greece, vol. L, p. 2155-2162
Proceedings of the 14th International Congress, Thessaloniki, May 2016

ORGANIC POLLUTANTS IN THE GROUNDWATERS USED FOR IRRIGATION PURPOSE WITHIN A COAL-BEARING BASIN OF NORTHERN GREECE

Iordanidis A.[1], Schwarzbauer J. [2] and Gudulas K. [1]

[1]Department of Geotechnology and Environmental Engineering, Technological Educational Institute (TEI) of Western Macedonia, Kila, 50100 Kozani, Greece, aiordanidis@yahoo.co.uk, kgudulas@teikoz.gr

[2]Institute of Geology and Geochemistry of Petroleum and Coal, RWTH Aachen University, Lochnerstrasse 4-20, 52056 Aachen, Germany, jan.schwarzbauer@emr.rwth-aachen.de

Abstract

The aim of this study is to identify potential toxic or environmentally relevant organic compounds in the aquifers of the Amynteo hydrogeological basin and to investigate a possible link of the identified organic contaminants with the Pliocene Amynteo lignites. For these purposes ten groundwater samples were collected from this area. A sequential liquid-liquid extraction procedure was applied to approximately 1000 mL aliquots of the groundwater samples using dichloromethane as extractant. All extracts were analysed by Gas Chromatography (GC) and Gas-Chromatography-Mass Spectrometry (GC-MS) by means of a non-target screening approach. The results of the GC-MS analyses of the extracts are presented and discussed in this work. The identified organic compounds with a potential environmental relevance are: 2, 2, 4-trimethyl-1, 3-pentanediol diisobutyrate (TXIB), triacetine, isopropyl palminate, isopropyl myristate, tributyl-, triethyl- and trioctylphosphates, N, N-dibutyl formamide, methyl dihydrojasmonate, nonylphenols and bumetrizole. However, all these organic micro-pollutants can derive either by anthropogenic emissions (plasticizers, industrial pollutants, pesticides etc.) or by contaminations from the pump and the borehole structure itself. Noteworthy, coal derived organic molecules (such as anthracene, fluorene, pyrene, phenanthrene etc.) have not been detected. Hence, an influence of coal deposits to the groundwater quality is considered negligible.
Keywords: *organics, liquid-liquid extraction, GC-MS, Amynteo.*

Περίληψη

Σκοπός της παρούσας μελέτης είναι ο εντοπισμός τοξικών οργανικών ενώσεων στα υπόγεια ύδατα της υδρογεωλογικής λεκάνης Αμυνταίου και η έρευνα μιας πιθανής σύνδεσης αυτών των οργανικών ρυπαντών με τους λιγνίτες της περιοχής. Δέκα δείγματα υπόγειων υδάτων συλλέχθηκαν και υπέστησαν μία διαδοχική διαδικασία εκχύλισης υγρού-υγρού με διχλωρομεθάνιο. Όλα τα εκχυλίσματα αναλύθηκαν με αέρια χρωματογραφία-φασματομετρία μάζας (GC-MS). Οι οργανικές ενώσεις που προσδιορίστηκαν είναι: 2,2,4-τριμεθυλο-1,3-πεντανοδιόλη διισοβουτυρική (TXIB), τριακετίνη, ισοπροπυλικά παλμινικά, μυριστικό ισοπροπύλιο, τριβουτυλ-, τριαιθυλ- και τριοκτυλ- φωσφορικά, N, N-διβουτυλ- φορμαμίδιο, μεθυλο- διυδροϊασμονικό, εννεϋλοφαινόλες και μπουμετριζόλη. Ωστόσο, όλες αυτές οι ενώσεις μπορεί να έχουν ανθρωπογενή προέλευση (πλαστικοποιητές, βιομηχανικοί ρύποι, παρασιτοκτόνα κλπ.)

ή να προέρχονται από επιμολύνσεις από τα δομικά μέρη της υδρογεώτρησης. Αξιοσημείωτο είναι ότι δεν προσδιορίστηκαν χαρακτηριστικές οργανικές ενώσεις που συνδέονται με γαιάνθρακες, όπως ανθρακένιο, φθορένιο, πυρένιο, φαινανθρένιο κλπ. Ως εκ τούτου, η επίδραση των λιγνιτικών κοιτασμάτων στην ποιότητα των υπόγειων υδάτων θεωρείται αμελητέα.
Λέξεις Κλειδιά: *οργανικοί ρυπαντές, εκχύλιση υγρή-υγρής φάσης, αέρια χρωματογραφία.*

1. Introduction

Groundwater use represents 42% of the total demanded hydraulic resources in Greece including 36% in agriculture, 5% in public supply and 1% in self-supplied industries, while in some cases nearly 100% of the drinking water requirements are met from groundwater (Vryzas *et al.*, 2012). A wide range of organic contaminants are present in groundwaters, which originate from many sources (industrial, municipal, agricultural, surface water exchange etc.). Despite the aforementioned significance of groundwaters for Greece, only limited information is published regarding the organic contamination of groundwaters.

Besides, a large number of coal-bearing geological basins exist in Greece, which are exploited by opencast mining and feed nearby lignite-fired power stations. The contribution of lignite to the total electric power output of the country exceeds 60% (Iordanidis *et al.*, 2014). The pumped groundwater is used either for irrigation or for the drainage of the open-pit lignite mines. However, the organic pollutants originating from aquifers within lignite deposits are accused for endemic diseases, such as Balkan Endemic Nephropathy (Orem *et al.*, 1999, 2007). Thus, there is an additional interest and environmental concern for the organic contamination assessment of these groundwaters.

The aim of the present study is to identify potential toxic or environmentally relevant organic compounds present in the aquifers of this region and to investigate a possible link of the identified organic contaminants with the Pliocene Amynteo lignites, i.e. whether leaching of lignite seams transferred organic micro-pollutants in the groundwater. It should be noted that the publications regarding organic pollutants of groundwaters from Greece are scarce and there has not been a similar study related to organic contamination in the groundwaters of this area so far.

2. Description of study area

Most Greek lignite deposits are located in the Florina-Ptolemais-Kozani basin, a large intensively exploited area, in northern Greece. The elongated intermontaine Florina-Ptolemais-Kozani basin is a NNW-SSE trending graben, which extends over a distance of 250 km from Bitola, in the Former Yugoslavian Republic of Macedonia to Servia, southeast of Kozani, Greece. Within this basin, Pliocene lignite beds alternate with marls, clays and sands. There is a great variance in the thickness of the overburden, intermediate and floor rocks as well as in the thickness of lignite seams. The average thickness of the overburden is approximately 260 m and of the lignite beds approx. 20 m (Iordanidis *et al.*, 2014).

The Amynteo hydrogeological basin has a total surface of 228 km^2 and belongs to the aforementioned coal-bearing basin (Gudulas, 2012). Numerous wells are located in the area, some of them employed for the drainage of the Amynteo open-pit lignite mine. The pumped groundwater is mainly used for irrigation.

3. Materials and Methods

Ten groundwater samples were collected from the study area (Figure 1) and were stored in glass bottles in the dark at a temperature of approximately 4 ºC. The samples were transferred in a portable fridge to the Laboratories of the Institute of Geology and Geochemistry of Petroleum and Coal, RWTH University, Aachen, Germany. Prior to extraction, water samples were filtered through pre-cleaned filters (0.45 μm pore size) in order to remove suspended particulate matter from the aqueous phase.

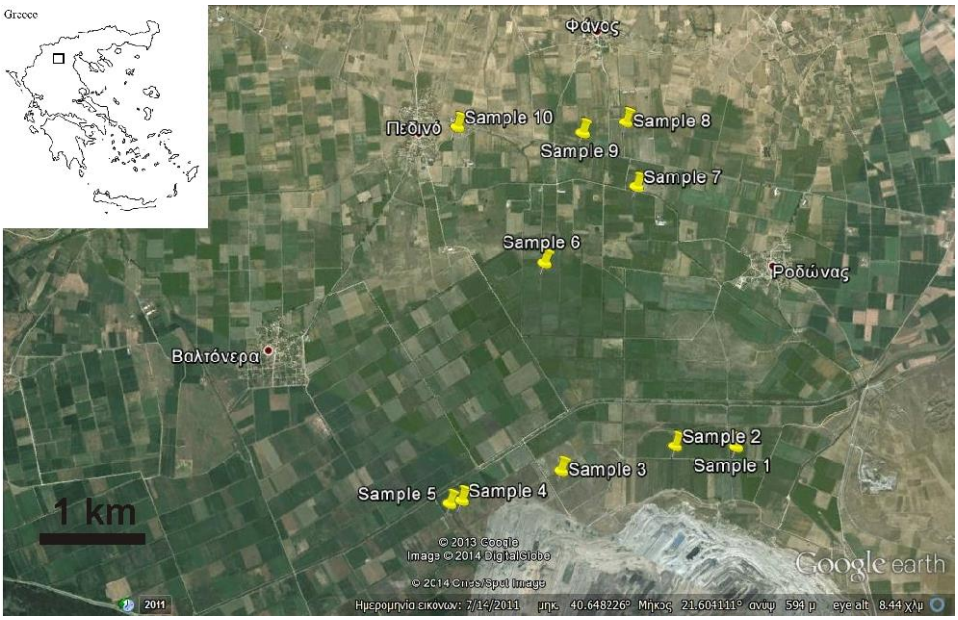

Figure 1 - Sampling sites of groundwaters from ten wells within Amynteo coal-bearing basin of northern Greece. The Amynteo lignite mine is clearly observed at the lower bottom of the image.

A sequential liquid-liquid extraction procedure was applied to approximately 1000 mL aliquots of the groundwater samples, dichloromethane (DCM) and dichloromethane after acidification to pH2 with hydrochloric acid. 50 mL of solvent were used for each extraction step. Thereafter, the organic layers were concentrated to approx. 1 mL by rotary evaporation at room temperature under reduced pressure and dried by filtration over 1 g of anhydrous granulated sodium sulphate. The analytical results of the non-polar and polar extracts are presented in this study. Prior to GC and GC/MS-analyses all extracts were further concentrated down to 50μL at room temperature under ambient pressure.

Gas chromatographic analyses were carried out on a Carlo Erba 6000 vega series 2 gas chromatograph, equipped with a ZB5 capillary column (30 mX0.25 mm IDX0.25 μm film). Flow velocity of the carrier gas (hydrogen) was 25 cm s1. The GC oven was programmed from 60 to 310 ºC at a rate of 3 ºC/ min, after 3 min at the initial temperature. The injection was carried out on a split/splitless injector at 310 ºC, splitless time was 60 s. Detection was conducted by a flame ionization detector (FID). GC/MS analyses were carried out with a Finnigan Trace MS mass spectrometer linked to a Carlo Erba HRGC 5160 gas chromatograph, employing the same conditions used for GC analysis.

4. Results and Discussion

The results of the GC and GC/MS analyses of the DCM extracts are presented in Figures 2, 3 and 4. It should be noted that in our study a non-target screening approach has been applied, hence only qualitative information are given.

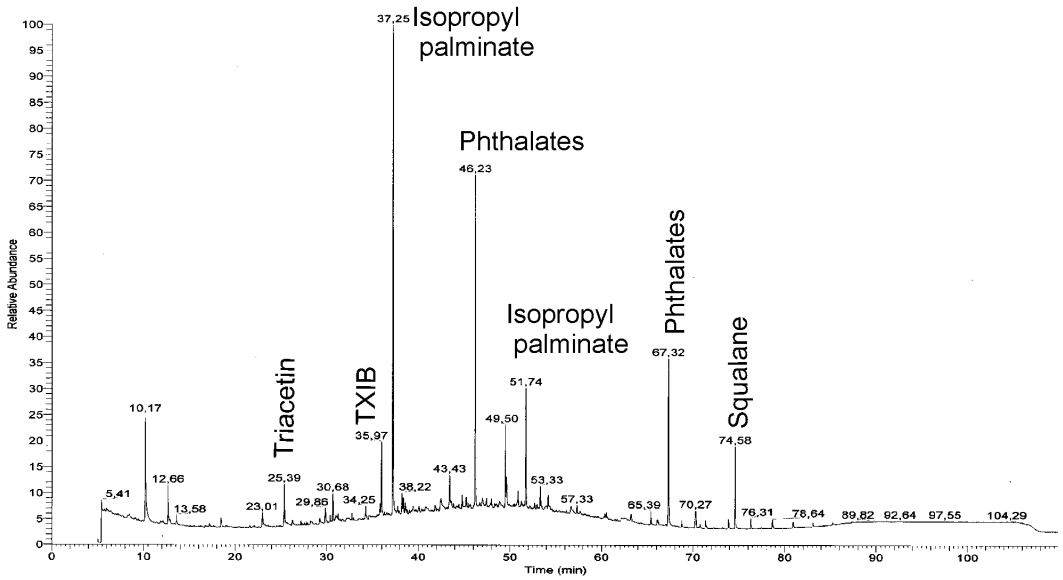

Figure 2 - Gas chromatogram of the DCM extract of the groundwater sample No 4. Specific organic compounds are assigned on the chromatogram (Triacetin, TXIB, Isopropyl palminate, Phthalates and Squalane).

Some of the identified organic compounds are shown in Figure 2, which is the gas chromatogram of the DCM extract of sample No 4. Very similar chromatograms were obtained by GC analyses of all other samples. The organic molecules presented in Fig. 2 are triacetin, TXIB, isopropyl palmitate, phthalates and squalane.

Under careful processing of the GC/MS results, some specific compounds were revealed. The assignment of the obtained mass spectra to specific molecules is shown in Figures 3 and 4. In particular, the TXIB, tributyl phosphates and N, N-dibutyl formamide are shown in Figure 3 and methyl dihydrojasmonate, bumetrizole and nonyl phenols are encountered in Figure 4. A synopsis of the most significant compounds found in the DCM extracts of the samples of our study is shown in Table 1.

The identified organic compounds with a potential environmental relevance are: 2, 2, 4-trimethyl-1, 3-pentanediol diisobutyrate (TXIB), triacetine, isopropyl palminate, isopropyl myristate, tributyl-, triethyl- and trioctylphosphates, N, N-dibutyl formamide, methyl dihydrojasmonate, nonylphenols and bumetrizole.

TXIB is used as a plasticizer or the manufacture of PVC and vinyl plastics and its medium toxicity to fish was indicated in previous reports (Botalova *et al.*, 2011). Triacetin detected in most of the studied samples. It is a known contaminant in propellant and industrial wastewaters as well as in surface water (Botalova *et al.*, 2011). It is mainly used as a cellulosic plasticizer in the manufacture of cigarette filters, plasticizer for laminating resins, vinylidene polymers and copolymers. It is also used as a solvent and carrier in pharmaceutical preparations, in the compounding of perfumes and flavors, as well as an ingredient for printing inks and useful reagents in textile dyeing and the manufacture of photographic films. Therefore, it can be suggested to act as a potential indicator for these industrial processes. Triethyl phosphate was detected in several extracts of our samples. It is used as an industrial solvent, plasticizer for resins, plastics, gums, fire-retarding agent, defoamer and raw material for insecticides water (Botalova *et al.*, 2011). Nonyl phenols, which are used as detergents and bumetrizole, which is used in cosmetics, were detected only in sample No 9 and are indeed frequently found in groundwaters (Lapworth *et al.*, 2012).

Table 1 - Abundance of organic pollutants in the groundwater samples of the present study.

	sample 1	sample 2	sample 3	sample 4	sample 5	sample 6	sample 7	sample 8	sample 9	sample 10
TXIB	+	+	+	+	+	+	+	+	+	
Triacetin			+	+		+	+		+	+
Isopropyl palminate		+	+	+	+	+	+			+
Isopropyl myristate						+				+
Tributyl-, triethyl- and trioctyl- phosphate		+			+				+	+
N, N-Dibutyl formamide			+			+	+			+
Methyl dihydro jasmonate						+				+
Nonylphenols									+	
Bumetrizole									+	

Some detected compounds are also known as: Bumetrizole=Uvazol 236, Tinuvin 326, Benazol PBK4, Lowitite 26, Hydroxybutylmethylphenylchlorobenzotriazole; TXIB= Propanoic acid, 2, 2, 4-trimethyl-1, 3-pentanediol diisobutyrate, Kodaflex

Likewise, methyl dihydrojasmonate, which is used for flavours and fragrances and isopropyl palminate and isopropyl myristate, which are used in cosmetics and personal care products were found in several samples of our study (Jurado *et al.*, 2012). Phthalates are very common organic compounds (Schwarzbauer, 2006) with a versatile use (plastics etc.) and while some authors have attributed them to lignite extractable compounds (Orem *et al.*, 1999), this could not be suggested in our study.

Compounds such as cycloalkanes/alkenes, steranic structures, mono aromatic and polyaromatic terpanes, polycyclic aromatic hydrocarbons, aromatic amines, and N-, S-, and O-containing heterocyclic compounds are often related to leachates from lignite deposits (McElmurry *et al.*, 2004; Orem *et al.*, 2007; Kapusta and Stanczyk, 2011; Iordanidis *et al.*, 2012). Many of these compounds have attached oxygen-based functional groups (hydroxy-, phenol-, keto-, methoxy), and some of them contain heterocyclic nitrogen or amino groups, structural features that could make them nephrotoxic and carcinogenic. None of the aforementioned compounds were encountered in the DCM extracts of our samples.

In conclusion, all these organic micro-pollutants could have been derived either by anthropogenic emissions (plasticizers, industrial pollutants, pesticides etc.) or could be contamination from the pump and the borehole structure itself. Noteworthy, coal derived organic molecules have not been detected, such as anthracene, fluorene, pyrene, phenanthrene etc. (Kapusta and Stanczyk, 2011; Iordanidis *et al.*, 2012). Hence, an influence of coal deposits to the groundwater quality is considered negligible.

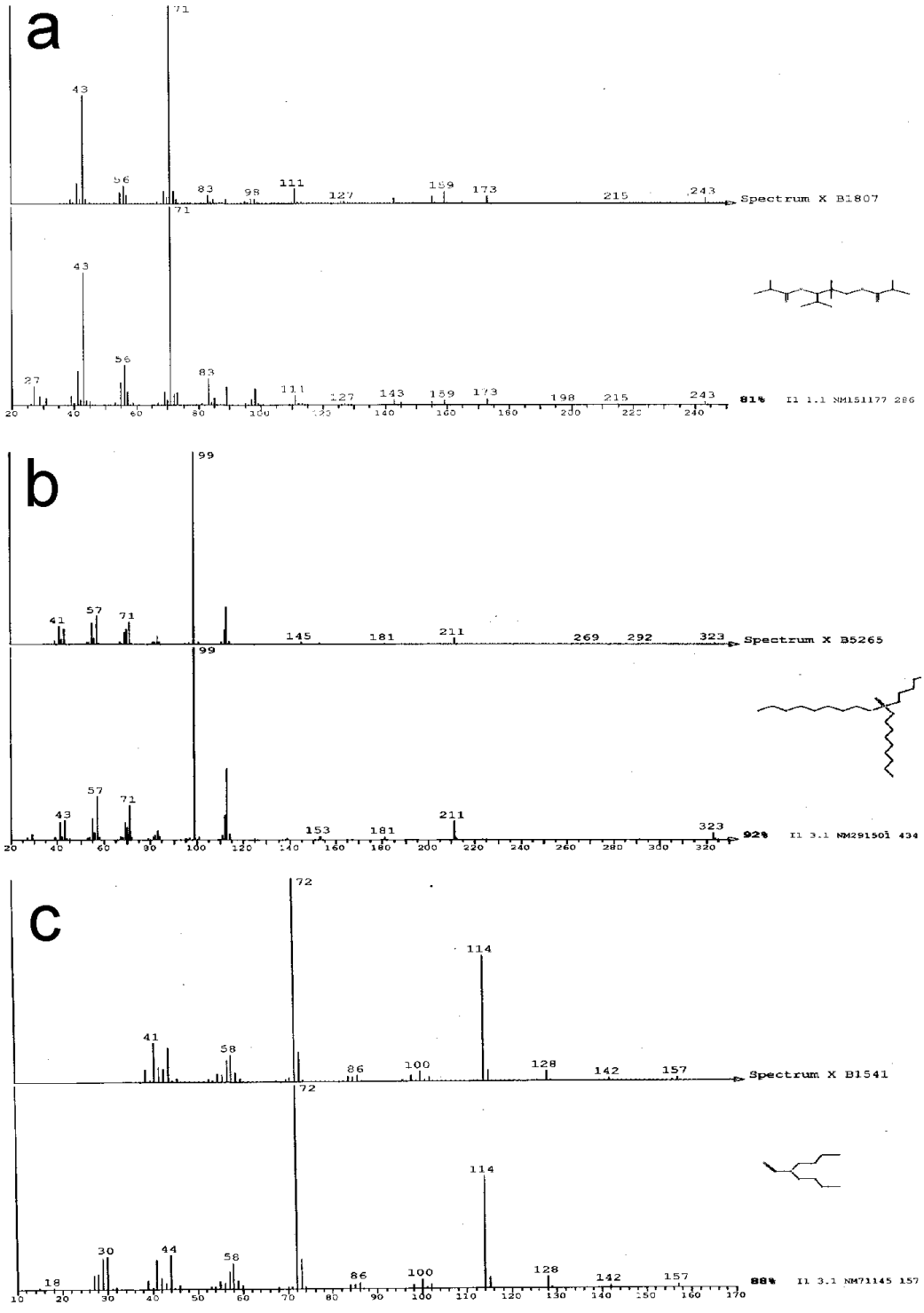

Figure 3 - Mass spectra assignment of specific organic molecules found in the GC-MS analysis of the DCM extracts of the groundwater samples: a) TXIB, b) Tributyl phosphate, c) N, N-dibutyl formamide.

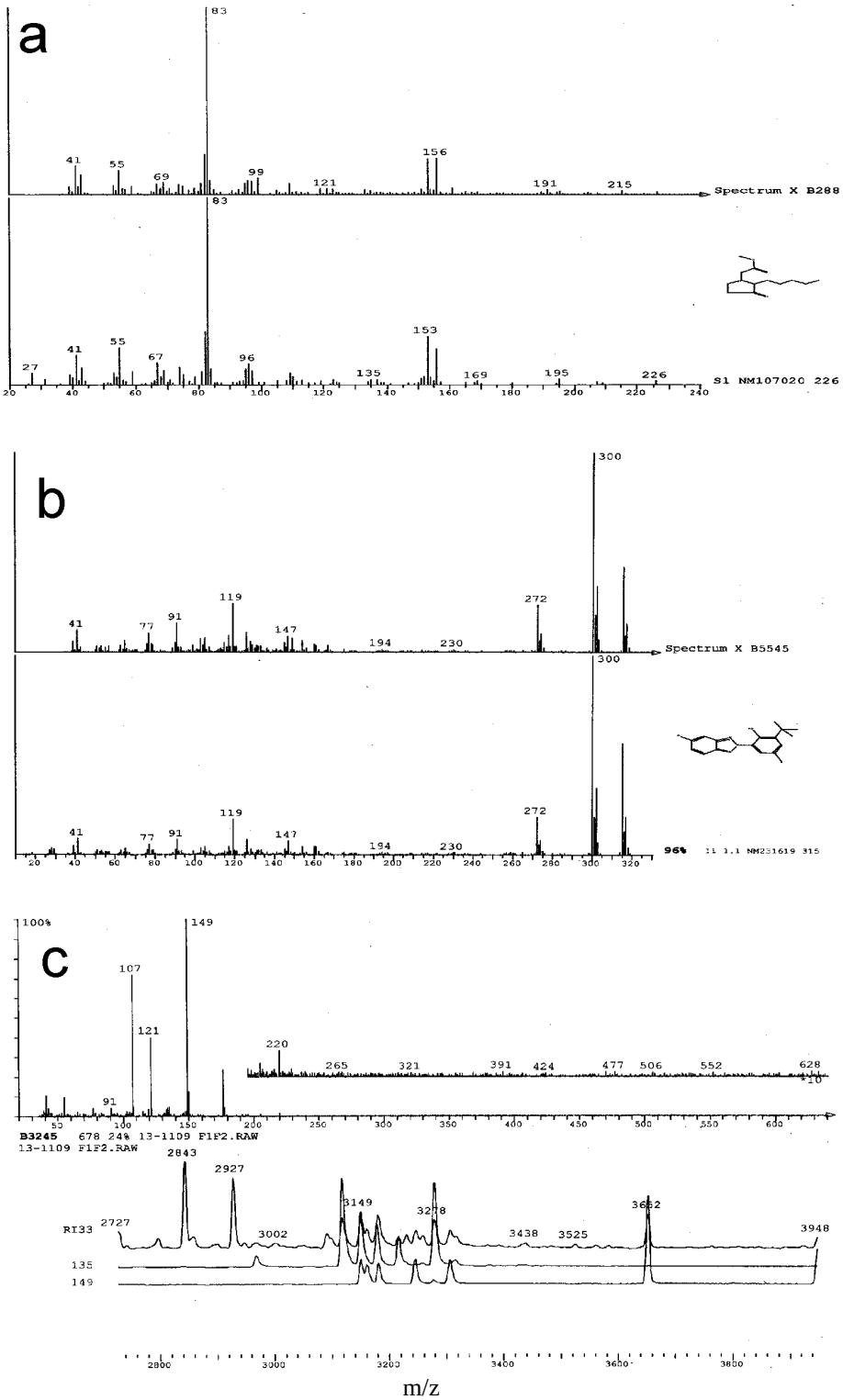

Figure 4 - Mass spectra assignment of specific organic molecules found in the GC-MS analysis of the DCM extracts of the groundwater samples: a) Methyl dihydrojasmonate, b) Bumetrizole, c) Nonyl phenols.

5. Acknowledgements

The financial support of the German Academic Exchange Service (DAAD) through a short-term scholarship (A/13/04441) awarded to the first author for a research stay at RWTH, Aachen, Germany is gratefully acknowledged.

6. References

Botalova, O., Schwarzbauer, J. and Al Sandouk, N., 2011. Identification and chemical characterization of specific organic indicators in the effluents from chemical production sites, *Water Research*, 45, 3653-3664.

Gudulas, K., 2012. Investigation of the mechanisms of operation of lakes Cheimaditida and Zazari, located in the Amyntaio basin, of Florina County, from a hydrogeological and environmental point of view, PhD Thesis, School of Geology, Aristotle University of Thessaloniki, Greece.

Iordanidis, A., Georgakopoulos, A. and Kalaitzidis, S., 2014. Petrographic composition and palaeoenvironment of the Amynteo lignite deposit, northern Greece, *Energy Sources, Part A Recovery, Utilization, and Environmental Effects*, 36, 2715-2724.

Iordanidis, A., Schwarzbauer, J., Georgakopoulos, A. and Van Lagen, B., 2012. Organic geochemistry of Amynteo lignite deposit, northern Greece: a multi-analytical approach, *Geochemistry International*, 50(2), 159-178.

Jurado, A., Vàzquez-Suñé, E., Carrera, J., López de Alda, M., Estanislao Pujades, E. and Barceló, D., 2012. Emerging organic contaminants in groundwater in Spain: A review of sources, recent occurrence and fate in a European context, *Science of the Total Environment*, 440, 82-94.

Kapusta, K. and Krzysztof, S., 2011. Pollution of water during underground coal gasification of hard coal and lignite, *Fuel*, 90, 1927-1934.

Lapworth, D.J., Baran, N., Stuart, M.E. and Ward, R.S., 2012. Emerging organic contaminants in groundwater: A review of sources, fate and occurrence, *Environmental Pollution*, 163, 287-303.

McElmurry, S.P. and Voice, T.C., 2004. Screening methodology for coal derived organic contaminants in water, *International Journal of Environmental Analytical Chemistry*, 84, 277-287.

Orem, W., Tatu, T., Pavlovic, N., Bunnell, J., Lerch, H., Paunescu, V., Ordodi, V., Flores, D., Corum, M. and Bates, A., 2007. Health Effects of Toxic Organic Substances from Coal: Toward "Panendemic" Nephropathy, *AMBIO: A Journal of the Human Environment*, 36(1), 98-102.

Orem, W.H., Feder, G.L. and Finkelman, R.B., 1999. A possible link between Balkan endemic nephropathy and the leaching of toxic organic compounds from Pliocene lignite by groundwater: preliminary investigation, *International Journal of Coal Geology*, 40, 237-252.

Schwarzbauer, J., 2006. Organic contaminants in riverine and groundwater systems - aspects of the anthropogenic contribution, Springer Verlag, Berlin/Heidelberg, 464 pp.

Vryzas, Z., Papadakis, E.N., Vassiliou, G. and Papadopoulou-Mourkidou, E., 2012. Occurrence of pesticides in trans boundary aquifers of North-eastern Greece, *Science of the Total Environment*, 441, 41-48.

Δελτίο της Ελληνικής Γεωλογικής Εταιρίας, τόμος L, σελ. 2163-2170
Πρακτικά 14ου Διεθνούς Συνεδρίου, Θεσσαλονίκη, Μάιος 2016

Bulletin of the Geological Society of Greece, vol. L, p. 2163-2170
Proceedings of the 14th International Congress, Thessaloniki, May 2016

PRELIMINARY SPECTROSCOPIC STUDY OF FE-BEARING CLAY MINERALS IN ALTERED PILLOW LAVAS FROM LAMIA AREA, GREECE[1]

Katranidou B.[1], Godelitsas A.[1] and Sanakis I.[2]

[1]*National and Kapodistrian University of Athens, Faculty of Geology and Geoenvironment, 15784, Zografou campus, Athens, Greece, vera.katranidou@gmail.com, agodel@geol.uoa.gr*

[2]*NCSR "Demokritos", Institute of Materials Science, 15310, Agia Paraskevi, Attiki, Greece, sanakis@ims.demokritos.gr*

Abstract

Geological material, of greenish color, filling interspaces in altered Triassic pillow lavas of Lamia area (central Greece) was studied, for the first time in the literature. According to XRD and SEM-EDS data it predominantly consists of calcite, zeolites and clay minerals. The zeolites concern thomsonite and analcime. The clay minerals, on the basis of XRD, FTIR and Mössbauer spectroscopic measurements, constitute a Fe-bearing phase of the illlite-glauconite-celadonite group (most likely Fe-illite).
***Keywords**: Altered pillow lavas, clay minerals, iron, Mössbauer spectroscopy.*

Περίληψη

Γεωλογικό υλικό, πρασινωπού χρώματος, το οποίο απαντά σε εξαλλοιωμένες μαξιλαροειδείς λάβες του Τριασικού στην περιοχή της Λαμίας, μελετάται για πρώτη φορά στη βιβλιογραφία. Σύμφωνα με τα δεδομένα XRD και SEM-EDS αποτελείται κυρίως από ασβεστίτη, ζεόλιθους και ορυκτά της αργίλου. Από την ομάδα των ζεολίθων, απαντούν τομσονίτης και ανάλκιμο. Τα ορυκτά της αργίλου, σύμφωνα με XRD και φασματοσκοπικές μετρήσεις FTIR και Mössbauer, συνιστούν Fe-ούχα φάση της ομάδας ιλλίτη-γλαυκονίτη-σελαδονίτη (πιθανότατα Fe-ιλλίτη).
***Λέξεις κλειδιά:** Μαξιλαροειδείς λάβες, ορυκτά της αργίλου, σίδηρος, φασματοσκοπία Mössbauer.*

1. Introduction

Iron-bearing clay minerals mainly concern Fe-illlite, glauconite and celadonite (e.g. Buckley *et al*., 1978; Bailey *et al*., 1980; Odin *et al*., 1988; Martin *et al*., 1991; Meunier, 2005; Zhukhlistov, 2005; Drits *et al*., 2010). According to the international clay nomenclature (AIPEA committee), celadonite and glauconite are dioctahedral micas with the following general composition:

$$[Si_{4-x}Al_x]\,O_{10}\left(Mg_{1+y}Fe^{3+}_{1-y}\right)(OH)_2K \quad \text{with } x\,(=y) < 0.2$$

$$[Si_{4-x}Al_x]\,O_{10}\left(R^{3+}_{2-y}R_{2+y}\right)(OH)_2K_{x+y} \quad \text{with } x > 0.3 \text{ and } Fe^{3+} \gg Al$$

[1] Part of the the BSc Thesis of B.K.

Glauconite is a low-temperature mica that grows at the sediment-seawater interface (the term glaucony indicate the green pellets either rounded or retaining the form of bioclasts: sponge spicules, foraminifer shells etc). Celadonite-group minerals are extensively occurring in deep-sea floor basalts, such as those sampled in the present study. Fe-bearing (ferric) illites, glauconite micas, and hyper-aluminous glauconites do not grow in the marine environment like glaucony but in a continental environment in salt lakes or lagoons, as well as in arid soils. The layer charge of Fe-illites varies from 1 to 0.7 per Si_4O_{10}. The charge originates both in the tetrahedral sheet by substitutions of Al for Si and in the octahedral sheet by substitution of bivalent elements R^{2+} (Mg, Fe^{2+}) for trivalent elements R^{3+} (Al, Fe^{3+}). The iron content (Fe^{3+} + Fe^{2+}) varies between 0.5 and 1 ion per half unit cell. The presence of a continuous solid solution domain between Fe-illites and glauconites seems unlikely for crystallographic reasons. In fact, the exact chemical composition of illites is somewhat difficult to define, despite the plenty of data in the literature. Subsequently, under the term "illite" are hidden various phases, according to whether they are defined by X-ray diffraction criteria only (absence of expandable sheets) or by a combination of criteria (XRD, morphology, composition). The general formula unit of an illite is the following:

$$[Si_{4-x}Al_x]\,O_{10}\left(R^{3+}_{2-y}R^{2+}_{y}\right)(OH)_2K_{x+y} \quad \text{with } 0.75 \le x+y \le 0.95$$

This formula can be distinguished from that of glauconites whose charge is predominantly octahedral. There is apparently no continuous solid solution, as mentioned above, between illite and glauconite. In general, illites form in different natural environments: weathering environments, geothermal fields, and diagenetic environment. The scope of the present paper was a first attempt to characterize, mainly by means of Mössbauer spectroscopy, Fe-clays occurring as interpillow greenish material, together with zeolites, in Triassic pillow lavas in the area north of Lamia city, central Greece (e.g. Pe-Piper and Piper, 2002; Barth, *et al*., 2003; Barth and Gluhak, 2008; Tsikouras *et al*., 2008; Koutsovitis *et al*., 2012). These parent rocks are actually basalts (Figure 1).

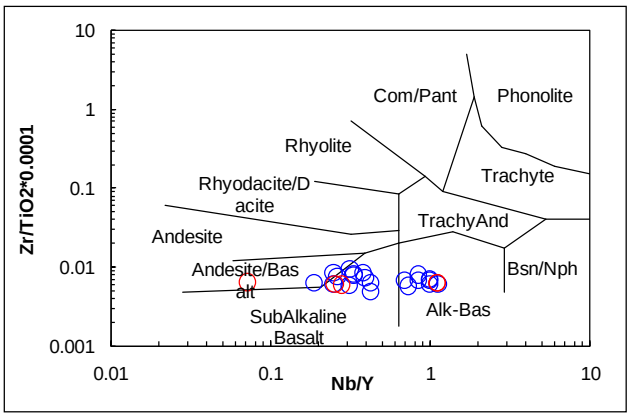

Figure 1 - Discrimination of the parent rocks using analytical data by Tsikouras *et al*. (2008) and Barth and Gluhak (2009).

2. Materials and Methods

The geological material, examined in the present study, was sampled in Triassic pillow lavas occurring in the area north of Lamia (Figure 2). A portion of the material was embedded in epoxy resin and polished, in order to be examined by Scanning Electron Microscope with Energy Dispersive Spectrometer (SEM-EDS). Moreover, the "white" part of the material as well as the greenish part, were carefully separated using an optical stereomicroscope and further pulverized for powder-XRD (PXRD), Fourier-Transform Infrared Spectroscopy (FT-IR) and Mössbauer spectroscopy investigation.

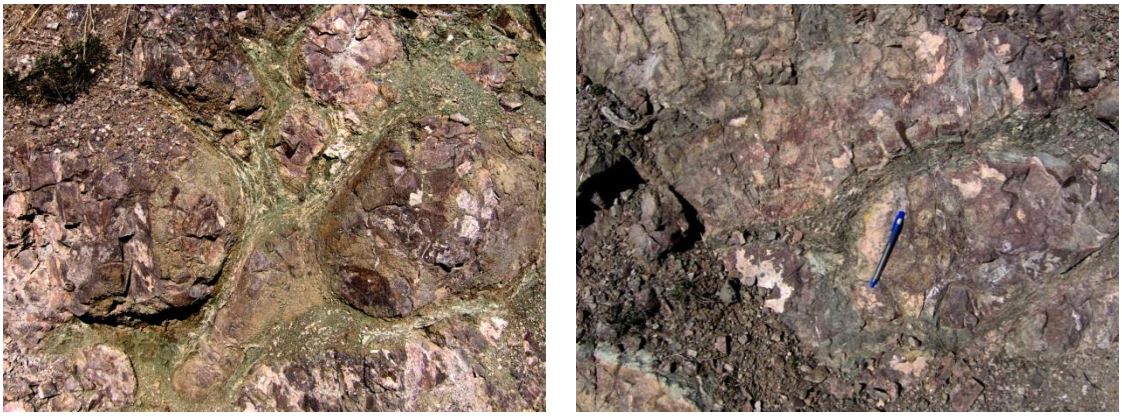

Figure 2 - Altered pillow lavas and the greenish interpillow clayey material.

The PXRD patterns were recorded by means of a Siemens D5005 (Bruker AXS) using CuK_α radiation. The SEM-EDS investigation was carried out using a Jeol JSM-5600 microscope equipped with an Oxford EDS. The FT-IR spectroscopic measurements were performed using a Perkin Elmer Spectrum One spectrometer in the frequency range 4000–450 cm^{-1}, at 2 cm^{-1} resolution, using KBr pellets. The Mössbauer spectra, of the previously characterized Fe-clays, were obtained using a Bruker ER-200D spectrometer at the Institute of Materials Science of NCSR "Demokritos" (Athens, Greece).

3. Results and Discussion

The PXRD of the initial interpillow material, containing both "white" and greenish phases, showed the presence of calcite, zeolites (analcime) and clays of the the celadonite group (Figure 3). A further investigation of the "white" part of the material revealed the presence of more zeolite group minerals, namely thomsonite (Figure 4). The presence of zeolites in altered basalts is rather common in the literature (e.g. Keith and Staples, 1985). More detailed study of the separated greenish clayey part of the material proved the existence of illlite-glauconite-celadonite group clay minerals (Figure 5). The chemical composition, and particularly the increased Fe-content of the clays, prior to spectroscopic study, was confirmed by the SEM-EDS investigation (Figure 6). It should be mentioned that it was rather unfeasible to determine the exact phase by conventional SEM-EDS, due to the nature of the clayey material limiting the application of precise microanalyses. That was attempted, after the FT-IR characterization, by cautious Mössbauer spectroscopic measurements.

The FT-IR spectra of the greenish clayey material (Figure 7) showed a peak at 3578 cm^{-1}, featuring the hydrous components (O-H bonds) of Fe-clays and possibly of celadonite. Another characteristic peak at 1000 cm^{-1} is common in many silicate minerals, including Fe-clays, whereas the lack of a peak at 800 cm^{-1} is probably an indication of celadonite (e.g. Slonimskaya *et al*., 1986 and references therein). Nevertheless, it was not clearly stated, as in the case of SEM-EDS investigation, the exact phase in concern.

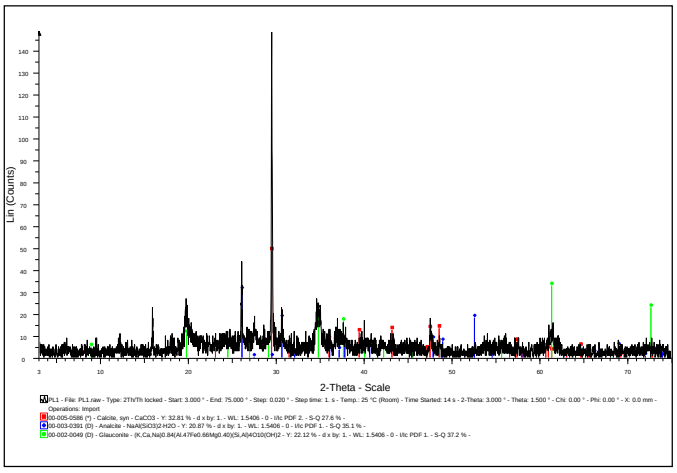

Figure 3 - PXRD pattern of the interpillow material.

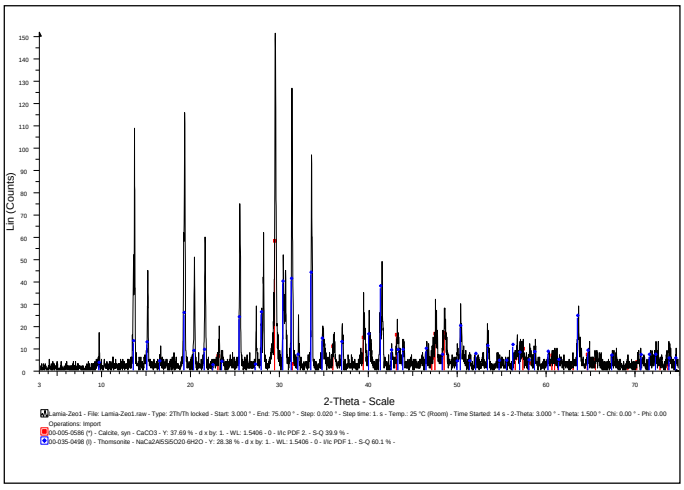

Figure 4 - PXRD of the "white" part of the material.

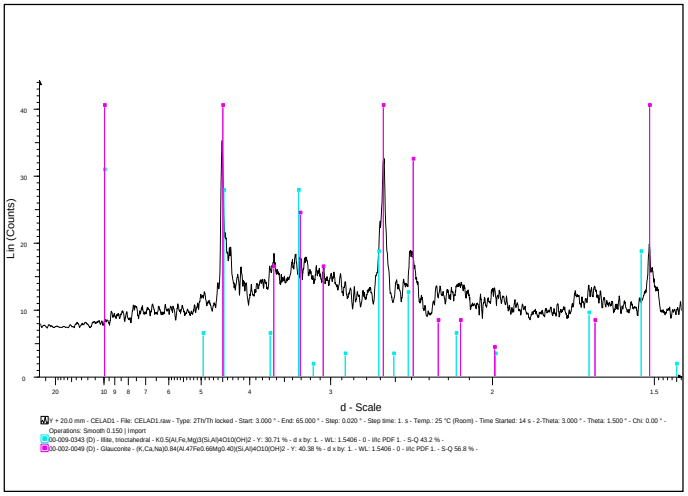

Figure 5 - PXRD of the separated greenish clayey part of the material.

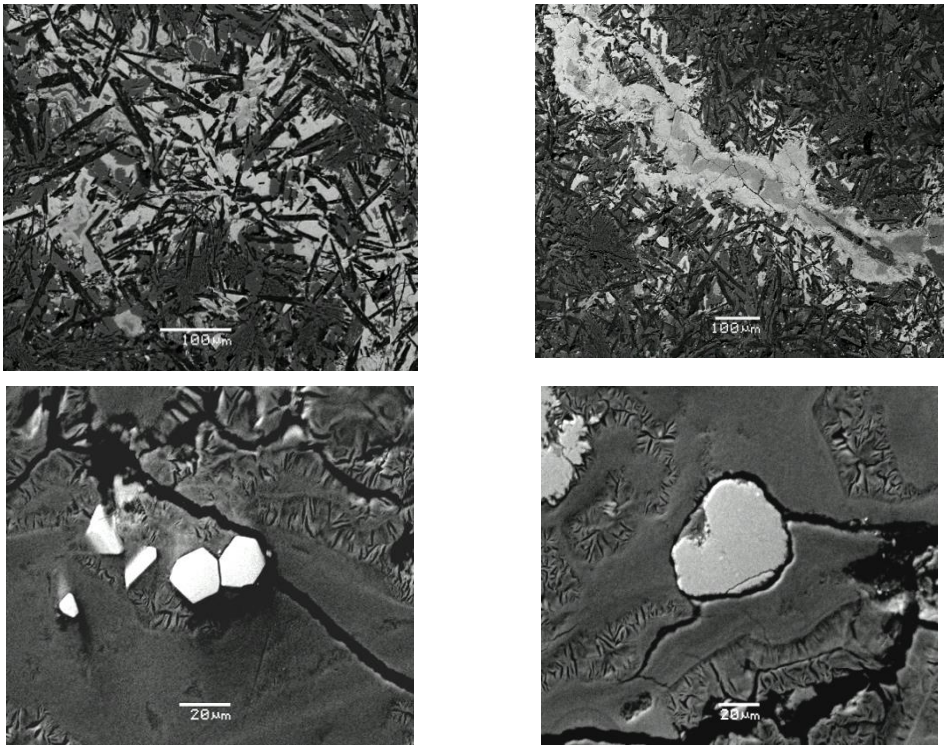

Figure 6 - SEM-EDS data concerning the studied material. Upper left: fresh parent rock; upper right: altered micro-zone containing Fe-oxides/oxyhydroxides; lower left & right: Cr-spinel crystals included into the Fe-clay phase.

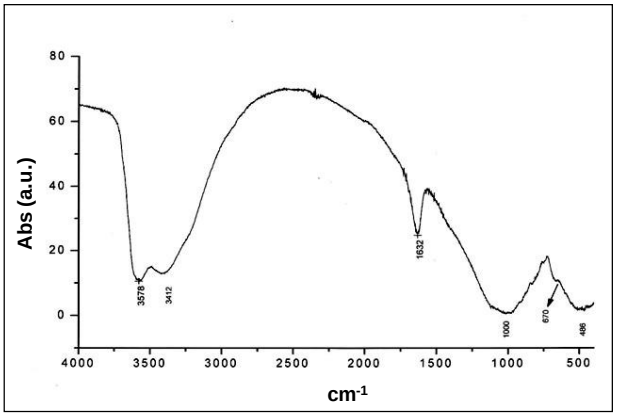

Figure 7 - Representative FT-IR spectrum of the greenish clayey material.

In the subsequent Mössbauer study, it was indicated, for first time in the literature, that the Fe-clays from Lamia altered pillow lavas contain 92% Fe^{3+} and 8% Fe^{2+} and may be Fe-illites than celadonites (Figure 8; Table 1; Figure 9; e.g. Dainyak and Drits, 1987 and references therein; Drits *et al*., 1997 and references therein; Dyar *et al*., 2006 and references therein). In particular, the Mössbauer spectra show two quadrupole splitting peaks, where δ=0.36 mm/s and ΔE_Q=0.58 correspond to Fe^{3+} and δ=1.15 and ΔE_Q=2.57 correspond to Fe^{2+}. It should be mentioned, that the above preliminary data, regarding nature of the Lamia Fe-clays, are going to be supported by further research, including X-ray Absorption Spectroscopy measurements in the Fe *K*-edge and Transmission Electron Microscopy (TEM).

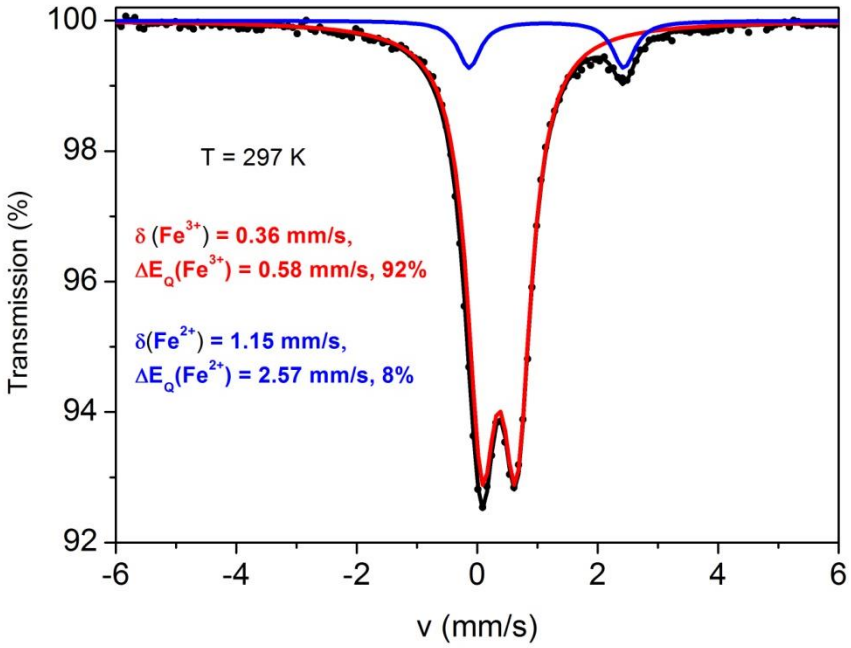

Figure 8 - Mössbauer spectrum of the greenish clayey material.

Table 1 - Fe^{3+} and Fe^{2+} content and Fe^{3+}/Fe^{2+} ratios in Fe-illlite-glauconite-celadonite group clay minerals (Bailey *et al.*, 1980; Odin *et al.*, 1988; Martin *et al.*, 1991; Meunier, 2005; Zhukhlistov, 2005; Drits *et al.*, 2010; Dainyak and Drits, 1987 and references therein; Drits *et al.*, 1997 and references therein; Dyar *et al.* 2006 and references therein). 1: Celadonite; 2: Celadonite; 3: Glauconite; 4: Glauconite; 5: Celadonite; 6: Fe-illite; 7: Glauconite; 8: Glauconite; 9: Fe-illite; 10: Fe-clay from the present study.

Number	Fe^{3+}	Fe^{2+}	Fe^{3+} %	Fe^{2+} %	Fe^{3+}/Fe^{2+}
1	0.96	0.26	78.69	21.31	3.69
2	1.15	0.36	76.16	23.84	3.19
3	0.93	0.21	81.58	18.42	4.43
4	0.89	0.18	83.18	16.82	4.94
5	0.58	0.46	55.77	44.23	1.26
6	0.74	0.07	91.36	8.64	10.57
7	1.10	0.12	90.16	9.84	9.17
8	0.79	0.10	88.76	11.24	7.90
9	0.41	0.13	75.93	24.07	3.15
10	-	-	92.00	8.00	11.50

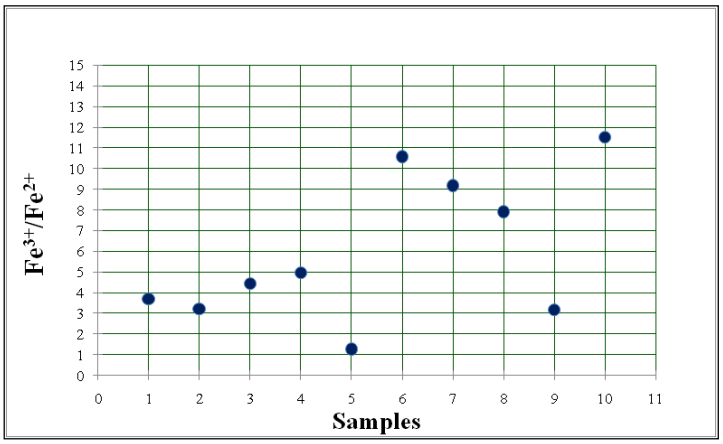

Figure 9 - Fe^{3+}/Fe^{2+} ratios in Fe-illlite-glauconite-celadonite group clay minerals on the basis of chemical analyses and Mössbauer spectroscopic data (see Table 1).

4. References

Bailey, S., 1980. Summary of recommendations of AIPEA nomenclature committee on clay minerals. Available at: http://www.clays.org/journal/archive/volume%2028/28-1-73.pdf.

Barth, M., Mason, P., Davies, G., Dijkstra, A. and Drury, M., 2003. Geochemistry or the Othris Ophiolite, Greece: Evidence for Refertilization? *J. Petrol*., 44, 759-1785.

Barth, M. and Gluhak, M., 2008. Geochemistry and tectonic setting of mafic rocks from the Othris Ophiolite, Greece, *Contrib. Mineral. Petrol.*, 157, 23-40.

Buckley, H.A., Bevan, J.C., Brown, K.M., Johnson, L.R. and Farmer, V.C., 1978. Glauconite and celadonite: two separate mineral species, *Min. Mag*., 42, 373-82.

Dainyak, L.G. and Drits, V.A., 1987. Interpretation of Mössbauer spectra of notro-nite, celadonite and glauconite, *Clays Clay Mineral*., 35, 363-372.

Drits, V.A., Dainyak, L.G., Muller, F., Besson, G. and Manceau, A., 1997. Isomorphous cation distribution in celadonites, glauconites and Fe-illites determined by infrared, Mössbauer and EXAFS spectroscopies, *Clay Minerals*, 32, 153-179.

Drits, V.A., Zviagina, B.B., McCarty, D.K. and Salyn, A.L., 2010. Factors for crystal-chemical variations in the solid solutions from illite to aluminoceladonite and from glauconite to celadonite, *Am. Mineral*., 85, 348-361.

Dyar, M.D., Agresti, D.G., Schaefer, M.W., Grant, C.A. and Sklute, E.C., 2006. Mössbauer Spectroscopy of Earth and Planetary Materials, *Annual Review of Earth and Planetary Sciences*, 34, 83-125.

Keith T.E.C. and Staples, L.W., 1985. Zeolites in Eocene Basaltic Pillow Lavas of the Siletz River Volcanics, Central Coast Range, Oregon, *Clays Clay Mineral*., 33/2, 135-144.

Koutsovitis, P., Magganas, A. and Ntaflos, Th., 2012. Rift and intra-oceanic subduction sig-natures in the Western Tethys during the Triassic: The case of ultramafic lavas as part of an unusual ultramafic-mafic-felsic suite in Othris, Greece, *Lithos*, 144-145, 177-193.

Martin, R.T., Bailey, S.W., Eberl, D.D., Fanning, D.S., Guggenheim, S., Kodama, H., Pevear, D.R., Srodoń, J. and Wicks, F.J., 1991. Report of the clay mineral society nomenclature committee: Revised classification of clay minerals. Available at: http://www.clays.org/journal/archive/volume%2039/39-3-333.pdf.

Meunier, A., 2005. Clays, Springer, Berlin-Heidelberg-New York.

Odin, G.S., Desrairies, A., Fullagar, P.D., Bellon, H., Decarreau, A., Frohlich, F. and Zelvelder, M., 1988. Nature and geological significance of celadonite, *Green Marine Clays-Developments in Sedimentology*, 45, 337-398.

Pe-Piper, G. and Piper, D.J.W., 2002. The Igneous Rocks of Greece, *Beiträge zur regionalen Geologie der Erde*, Band 30, 537 pp.

Slonimskaya, M.V., Besson, G., Dainyak, L.G., Tchoubar, C. and Drits, V.A., 1986. Interpretation of the IR spectra of celadonites nad glauconites in the region of OH-stretching frequencies, *Clay Mineral*., 21, 377-388.

Tsikouras, V., Pe-Piper, G., Piper, D.J.W. and Hatzipanagiotou, K., 2008. Triassic rist-related komatiite, picrate and basalt, Pelagonian continental margin, Greece, *Lithos*, 104, 199-215.

Zhukhlistov, A.P., 2005. Crystal structure of Celadonite from the Electron Diffraction Data, Crystallography Reports, 50/ 6, 902-906.

Δελτίο της Ελληνικής Γεωλογικής Εταιρίας, τόμος L, σελ. 2171-2181
Πρακτικά 14ου Διεθνούς Συνεδρίου, Θεσσαλονίκη, Μάιος 2016

Bulletin of the Geological Society of Greece, vol. L, p. 2171-2181
Proceedings of the 14th International Congress, Thessaloniki, May 2016

POTENTIAL TOXIC ELEMENTS (PTES) IN GROUND AND SPRING WATERS, SOILS AND SEDIMENTS: AN INTERDISCIPLINARY STUDY IN ANTHEMOUNTAS BASIN, N. GREECE

Kazakis N.[1], Kantiranis N.[1], Kaprara M.[2], Mitrakas M.[2], Vargemezis G.[1], Voudouris K.[1], Chatzipetros A.[1], Kalaitzidou K.[2] and Filippidis A.[1]

[1]Aristotle University of Thessaloniki, School of Geology, 54124, Thessaloniki, Greece, kazakis@geo.auth.gr

[2]Aristotle University of Thessaloniki, School of Chemical Engineering, Thessaloniki, Greece

Abstract

Ground and spring waters, soils and sediments of Anthemountas basin in Northern G reece were analyzed for Potential Toxic Elements (PTEs). In total, twenty three soil and sediment samples, three groundwater (boreholes) and two spring water samples, were analyzed. Contents of Ni in soils and sediments can be as high as 2169 mg/kg. The high correlation coefficient of Ni and Cr, indicates the geogenic origin of Ni, which originates from ophiolitic rocks. Arsenic concentration ranges from 3 to 110 mg/kg in soils and sediments, with the highest contents observed in travertine. The spring waters are characterized by elevated concentrations of As (up to 235 μg/L), N a, K, Fe and Zn, indicating that hydrothermal fluids are responsible for feldspar alte ration of the Monopigado granodiorite. On the contrary, in groundwaters, As conten ts are low (up to 18 μg/L). Electrical resistivity tomographies performed around the groundwater boreholes, revealed the presence of normal faults, locally allowing the mixing of geothermal fluids with the shallow porous aquifer (SPA). The presence of As in the SPA is probably due to inputs from geothermal waters through normal faulting.

Keywords: *Arsenic, Nickel, Travertine, Geothermal water, Faults, Ophiolites.*

Περίληψη

Υπόγεια και πηγαία νερά, εδάφη και ιζήματα της λεκάνης του Ανθεμούντα (Βόρεια Ελλάδα) αναλύθηκαν για την πιθανή παρουσία τοξικών στοιχείων (PTEs: Potential Toxic Elements). Συνολικά αναλύθηκαν, 23 δείγματα εδαφών και ιζημάτων, 3 υπόγειων (γεωτρήσεων) και 2 πηγαίων νερών. Η συγκέντρωση του Ni σε εδάφη και ιζήματα έφθασε τιμές έως τα 2169 mg/kg και ο υψηλός συντελεστής συσχέτισής του με το Cr, δηλώνει τη γηγενή προέλευση του Ni απο τα οφιολιθικά πετρώματα. Η συγκέντρωση του As κυμαίνεται από 3 έως 110 mg/kg σε εδάφη και ιζήματα, με την υψηλότερη συγκέντρωση να παρατηρείται στον τραβερτίνη. Τα πηγαία νερά χαρακτηρίζεται από υψηλές συγκεντρώσεις As (έως 235 μg/L), Na, K, Fe και Zn, δηλώνοντας ότι τα υδροθερμικά ρευστά επηρεάζουν άμεσα και επιδρούν στους αστρίους του γρανοδιορίτη του Μονοπήγαδου. Αντίθετα, στα υπόγεια νερά, η συγκέντρωση του As έφθασε τιμές έως και 18 μg/L. Οι γεω-ηλεκτρικές τομογραφίες που πραγματοποιήθηκαν γύρω από τις γεωτρήσεις των υπόγειων υδάτων, αποκάλυψαν την παρουσία κανονικών ρηγμάτων, που τοπικά συνδέουν τα γεωθερμικά ρευστά με το

επιφανειακό πορώδη υδροφορέα. Η παρουσία του As στον επιφανειακό πορώδη υδροφορέα, οφείλεται στις εισροές από τα γεωθερμικά νερά διαμέσου αυτών των κανονικών ρηγμάτων.
Λέξεις κλειδιά: *Αρσενικό, Νικέλιο, Τραβερτίνης, Γεωθερμικά ρευστά, Ρήγματα, Οφιόλιθοι.*

1. Introduction

Natural environments such as water, soil and air are under a constant risk of pollution due to population growth, agricultural activities and accelerated industrialization process (Morrison *et al.*, 1990). Heavy metals are considered as one of the most serious environmental pollutants due to their persistence in the environment, bioaccumulation and high toxicity (Esmaeili *et al.*, 2014; Assubaie, 2015). Heavy metals and Potential Toxic Elements (PTEs) can originate from two primary sources; anthropogenic such as agricultural practices, vehicle exhaust emissions, metalliferous mining and associated industries, whereas rock weathering and thermal springs constitute natural or geological inputs (Zhang *et al.*, 1999; Gallego *et al.*, 2002; Micó *et al.*, 2006, Rodríguez Martín *et al.*, 2007; Esmaeili *et al.*, 2014). However, heavy metals and PTEs pollution in soils, sediments, plants, surface and groundwater is due to both natural processes and human activities and depends, among other things, on rock chemistry and mineral chemistry, the bioavailability of heavy metals and the different metallic and industrial mineral deposits that are exploited by humans (Papastergios *et al.*, 2011; Petrotou *et al.*, 2012; Skordas *et al.*, 2013). Hexavalent chromium and arsenic are two of the most toxic elements in the environment and their consumption leads to carcinogenesis (Mandal and Suzuki, 2002; Linos *et al.*, 2011). Weathering and erosion of ultramafic rocks has been recognized as a natural source of chromium in sediments and groundwater (Fantoni *et al.*, 2002; Kaprara *et al.*, 2015; Kazakis *et al.*, 2015; Dermatas *et al.*, 2015). The release of arsenic in groundwater can be due to the reductive dissolution of arsenic-bearing iron oxides (Harvey *et al.*, 2002), the released As through sulfide oxidation reactions (Chowdhury *et al.*, 1999) and the result of geothermal inputs (Nimik *et al.*, 1998; Pique *et al.*, 2010). Geothermal fluids circulating through faults can also be a source of As on groundwater and soils (Gamaletsos *et al.*, 2013).

The Anthemountas river basin is characterized by a complex hydrogeological and hydrochemical regime with elevated concentrations of arsenic and chromium in groundwater (Kazakis, 2013). The geogenic origin of chromium and its distribution in aquifers has been clarified from previous studies (Kazakis *et al.*, 2015). Nimfopoulos *et al.* (2002) reported elevated concentrations of heavy metals, PTEs and arsenic in the Geothermal springs water of the Anthemountas basin. Additionally, Tzamos *et al.* (2014) and Tziritis *et al.* (2015) reported low concentrations of heavy metals, PTEs and arsenic on tap water of Thermi Municipality.

This study aiming to explain the presence of the PTEs and heavy metal concentrations in soils, sediments, groundwater and geothermal springs' water in the Anthemountas basin. Therefore, previous studies (Kazakis, 2013; Kazakis *et al.*, 2015) and new analytical data of soils, sediments a nd water were used to study the leaching mechanism of the most toxic elements Cr(VI) and As(III) (McCleskey *et al.*, 2004). Additionally, this study focused in leaching from soils and sediments of the most toxic elements Cr(VI) and As. Moreover, electrical resistivity tomographies (ERT) were performed in selected sites in order to determine the hydrogeological conditions favoring elevated arsenic concentrations.

2. Study site

Anthemountas basin is placed in the eastern part of the Thermaikos Gulf in Northern Greece (Fig. 1). The site is characterized by a complex geological, hydrogeological and hydrochemical status due to the coexistence of various geological formations and aquifer types. Mesozoic igneous and metamorphic rocks, ultramafic rocks, together with granodiorite and recrystallized carbonates rocks are placed in the mountainous area surrounding the basin. The lowland comprises Quaternary and

Neogene sediments of variable thickness. The Quaternary sediments consist of terrace systems (gravels, sands, pebbles and clays) and alluvial deposits (sands, gravels and sands with clay), whereas the Neogene sediments are composed of conglomerates, sandstones, marls and red-clay series. The sedimentary formations are the hosts of confined and unconfined porous aquifers with variable morphological characteristics. Fissured rock aquifers are developed in the crystalline and metamorphic rocks, whereas a karstic aquifer is located in the carbonate rocks. A detailed description of these aquifers' characteristics can be found in previous studies (Kazakis *et al.*, 2015). In the study area, the water demands are met with groundwater resources and therefore aquifers' quality is of the utmost importance for the sustainability of the site. Consequently the origin and spatial distribution of pollutants are essential so as to prevent exposure of the population to toxic elements.

3. Materials and Methods

3.1. Soil and sediment sampling, mineralogical and chemical characterization

The soil and sediment sample sites were the same as those used in the study of Kazakis *et al.* (2015) in order to supplement the geochemical analysis of Cr and Mn. Additionally, a sediment sample of travertine was collected from the Voskina spring. In total, 23 soil and sediment samples were collected at depths up 0.7 m by using a Dutch auger.

For the aluminosilicate mineral samples, a subsample of 0.2 g was placed in an open PTFE beaker where 1 mL of concentrated HClO4 and 20mL of concentrated HF (Merck, pro-analysis) were added. The solution was then heated to fully evaporate HF and HClO4. Subsequently, 20 mL of HCl 6 N were added and the sample was heated for 30 min. The solution was diluted to a final volume of 200 mL (Sparks *et al*., 1996). Metal concentrations were determined either by flame or graphite furnace atomic absorption spectrophotometry using a Perkin Elmer AAnalyst 800 instrument (GF-AAS). For the determination of water-soluble fraction of As and Cr a 20 g sub-sample of soil was shaken with 60 mL deionized water for 15 min and then was filtered through a 0.45 μm pore-size membrane filter. As and Cr concentrations in filtrate were determined by GF-AAS.

The morphological and mineralogical characteristics of the travertine sample were accurately deter mined by microprobe analysis of its minerals were determined by Scanning Electron Microscopy (SEM, JEOL JSM-840A) with associated Energy Dispersive Spectroscopy analysis (EDS, Link AN10000). To minimize volatilization of alkalis in the minerals framework, the electron beam spot size was enlarged and the counting time decreased. Different minerals (micas, carbonates, feldspars) and pure metals were used as probe standards.

3.2 Water sampling and analysis

Groundwater samples were collected from 2 springs (Voskina 1S and Agiasma 2S) and three boreholes from the shallow porous aquifer, following a two-hour (at least) pumping session for the boreholes (Fig. 1). All samples were collected in September 2015. The water samples were filtered through 0.45 μm membrane filters. One part of each sample was acidified at pH 2 using HNO_3 and the other was analyzed immediately or refrigerated at 4 ^{0}C to be analyzed later. All analyses were conducted according to Clesceri *et al.* (1989). In particular, the parameters pH and electric conductivity (EC) were analyzed according to the methods APHA 4500-H^+ and 2520 B, respectively. The anions of bicarbonate (HCO_3^-), chloride (Cl^-), nitrate (NO_3^-), nitrite (NO_2^-), phosphate (PO_4^{3-}) and sulfate (SO_4^{2-}) were determined according to the methods 2320 B, 4500 Cl^- F, 4500 NO_3^- C, 4500 NO_2^- B, 4500 P C and 4500 SO_4^{2-} B respectively. The ammonium cation NH_4^+ was determined according to the 4500 NH_3 C method. The concentration of water soluble metals was determined either by flame or GF-AAS. Cr(VI) concentrations were determined by the diphenylcarbazide method (3500-Cr D) using a Perkin Elmer Lambda 2 UV/VIS spectrophotometer version 3.7 equipped with 10 cm path-length measurement cells. Boron determination was

performed by the azomethine H method and total organic carbon (TOC) content was measured to a Shimadzu TOC-V_{CSN} Total Organic Carbon Analyzer.

3.3 Electrical resistivity tomography (ERT)

Three ERT lines were measured during the period of September 2011 near to the groundwater sample sites to detect structure which can facilitate the mixing between geothermal waters and fresh water of the upper aquifers system. Twenty-one stainless steel electrodes were used 50 m apart, forming a total length of 1000 m for each ERT line. Electrical resistivity measurements were performed using a SYSCAL Pro resistivity meter which was located in the center of the electrode array. Wenner array and configuration was used to accurately delineate the predicted horizontal structures and their interfaces (Loke, 2011), whereas dipole-dipole array configuration was also used to examine if lateral changes are significant. The reliability of the ERTs was tested with available lithological profiles and geological data and the best fitting array configuration was selected. The inversion of the mixed resistivity data set was performed using DC2DPRO software (Kim, 2009) and 2-D resistivity images were produced. Finally, the RMS error values of all ERTs ranged between 2 and 8% indicating the reliability of the measured data.

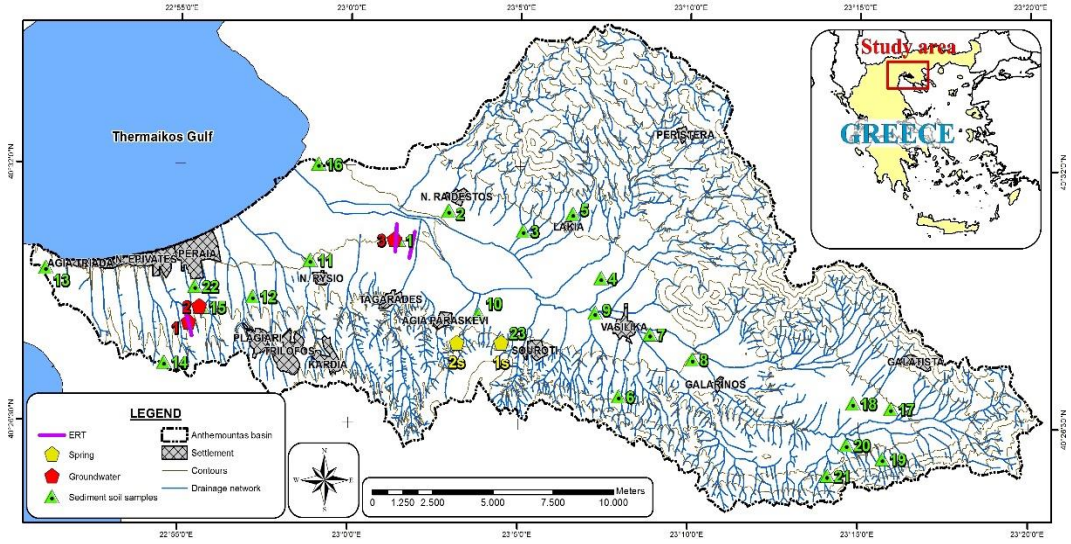

Figure 1 - Topographic map of Anthemountas river basin showing the sampling points.

4. Results and discussion

The minimum, maximum and mean values of the geochemical composition of soils and sediments are shown in Table 1. Total arsenic concentration in soils and sediments varies from 5 to 110 mg/kg, whereas the highest concentration was recorded in the travertine sample, and leachable arsenic ranges between 3 and 58 mg/kg. It is worth mentioning that leachable amounts of As from travertine were below the detection limit. Chromium and manganese content of travertine were 2 and 384 mg/kg respectively which are low in comparison to the rest of samples from the study area. The leachable Cr(VI) concentration of soils and sediments range between 3 and 46 mg/kg; the higher leachable amounts of Cr(VI) were observed in the samples with high serpentine content.

The concentrations of Ni, Pb and Zn range between 7 and 2169 mg/kg, 1 and 35 and 39 and 123 mg/kg, respectively. Mg contents range between 1.6 and 5.6 g/kg, while the higher values for Mg and Ni are located in the areas near the ophiolitic rocks. Sodium and potassium concentrations in soils and sediments range between 8.7 to 27.2 and 2.2 to 16.3 g/kg, respectively. Calcium varies from 13 to 375 g/kg with an average concentration of 194 g/kg. The higher concentrations of calcium

are found in soils and sediments nearby the carbonate rocks of the study area. Lead (Pb) and zinc (Zn) range between 1 to 35 and 39 to 123 mg/kg, respectively.

Table 1 - Leachable As and Cr(VI) and geochemical composition of the studied soils and sediments.

Values	Cr[1]	Mn[1]	Ni	As	Pb	Zn	Al	Ca	Fe	K	Mg	Na	As[2]	Cr[2]
	mg/kg						g/kg						mg/kg	
Min	2	384	7	5	ND[3]	39	4.4	13	1.9	2.2	1.6	8.7	ND	ND
Max	959	1630	2169	110	35	123	62.0	375	15.2	16.3	5.6	27.2	58	46
Mean	303	964	350	22	20	74	33.2	194	8.6	9.3	3.6	18.0	15	8
SD[4]	245	314	524	28	9	17	13	78	3.2	3.4	1.2	5.9	11	9
DL[3]	50	50	1	1	1	1	1	0.1	0.05	0.05	0.1	0.05	1	1

[1] Includes data from Kazakis et al., 2015; [2] Leachable As and Cr(VI); [3] Not detected; [4] Standard deviation; [5] Detection limit.

A correlation analysis was performed between the elements and is shown in Table 2. The high correlation between Cr and Mn has been also referred in the study of Kazakis *et al*. (2015). Ni has high correlation with Cr, Mn, Fe and Mg and thus, it is concluded the geogenic origin of Ni from the weathering products of ophiolitic rocks. In contrast, the highest correlation of As was observed with Na and K. This is probably an indication of the influence of hydrothermal fluids in feldspar-rich clastic sediments and/or directly to the Monopigado granodiorite, causing the alteration of feldspars which enriches these fluids in Na and K. The interaction between the geothermal field of Monopigado granodiorite field and the springs' hydrothermal fluid has been proposed by Nimfopoulos *et al*. (2002) based on Michard *et al*. (1998) study. Furthermore, the existence of a system of faults running through this igneous rock with ESE-NW direction favors the circulation of these fluids and the enrichment of groundwater in As and other heavy metals such as Fe, Mn and Zn. Additionally, high correlation coefficient is observed between Fe and Mn.

Table 2 - Correlation matrix of the elements from soils and sediments of the Anthemountas basin.

	Cr	Ni	Mn	Pb	Zn	As	Al	Ca	Fe	Mg	Na	K
Cr	1											
Ni	**0.847**	1										
Mn	**0.859**	**0.764**	1									
Pb	-0.244	-0.172	-0.122	1								
Zn	-0.145	0.034	0.044	0.224	1							
As	0.072	-0.006	0.070	-0.635	0.192	1						
Al	-0.577	-0.713	-0.311	-0.086	0.187	0.370	1					
Ca	-0.388	-0.313	-0.502	0.095	-0.198	-0.177	-0.265	1				
Fe	**0.798**	**0.737**	**0.837**	-0.470	0.177	0.539	-0.201	-0.450	1			
Mg	**0.842**	**0.886**	0.698	-0.203	-0.068	0.039	-0.772	-0.053	0.700	1		
Na	-0.094	-0.161	-0.040	-0.555	0.219	**0.968**	0.531	-0.180	0.414	-0.146	1	
K	-0.277	-0.302	-0.226	-0.422	0.351	**0.901**	0.570	-0.108	0.222	-0.306	**0.943**	1

Scanning electron microscopy (Fig. 2) of the travertine sample revealed the presence of an amorph ous Fe-As rich phase deposited as irregular masses scattered throughout the surface of travertine. T his denotes the arsenic deposition together with iron oxides-hydroxides (oxidized forms of iron) on

the carbonate phases of travertine (Nimfopoulos *et al.*, 2002). The latter is rich in $CaCO_3$ phases, e specially calcite, as revealed from the X-ray diffraction analysis.

Groundwater samples were collected from two springs and three boreholes. Their statistical values ar e presented in Table 3. The electrical conductivity varies from 1127 to 6334 μS/cm, the higher values being observed in spring waters. In the spring waters and borehole 3, the pH is slightly acidic (6.2-6. 5), while in boreholes 1 and 2 is neutral to slightly alkaline (7.8). Nitrate concentrations are mainly lo w (<22 mg/L), while the highest concentration was observed in borehole 3. Sodium and potassium co ncentrations range from 105 to 950 and 2.6 to 70.9 mg/L, respectively, while the highest concentratio ns were observed in the spring waters. These confirm our opinion that the hydrothermal fluids directl y affect and alter the feldspars of the Monopigado granodiorite. Also, the highest concentrations of Cl (up to 1325 12 mg/L) were observed in spring waters.

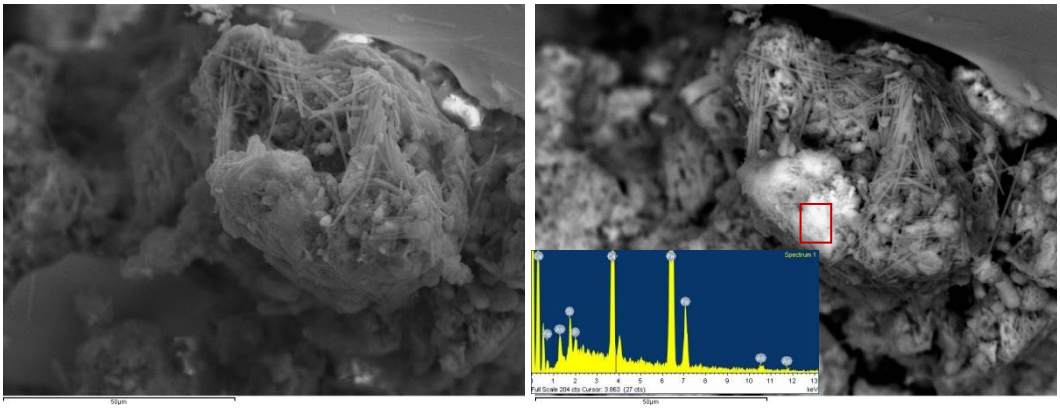

Figure 2 - Microphotograph (normal-left, backscattered-right) of travertine sample and micr oprobe analysis of Fe-As rich phase deposit on the Ca-rich travertine surface.

The concentrations of Hg, Pb, Cu, Cr, Cr(VI) and Sb were below the corresponding detection limit. Cobalt was detected only in the spring water of Agiasma (6 μg/L). Iron and manganese vary from 204 to 6667 and 96 to 1264 mg/L, respectively. The highest concentration of boron was observed in the borehole 3 (9.5 mg/L), whereas in the Voskina and Agiasma springs the concentrations were 8.3 and 7.8 mg/L, respectively. In borehole 2 the concentration of B was below detection limit, while in borehole 1 the concentration was 2.4 mg/L. Arsenic concentrations in the studied samples range from 3 to 235 μg/L. The highest concentration was observed in Agiasma spring and the lowest in the borehole 3. Concentration in the Voskina spring was 30 μg/L, 18 μg/L in borehole 1 and 7 μg/L in borehole 2.

Electrical resistivity tomographies were performed near the boreholes 1 and 3 in order to detect faults which can serve as paths for geothermal waters in the course of being mixed with the fresh waters of the shallow porous aquifers. Figure 3 depicts the electrical conductivity (Kazakis, 2013) of the boreholes around the ERT lines and the ERT. ERTs confirm the existence of faults with resistivity values up to 10 Ohm-m. The low resistivity value in the fault bodies is due to the circulation of geothermal fluids.

The fault orientation in the site of borehole 3 is ENE-WSW, whereas the faults are normal and parallel to the Anthemountas fault. It is located in the boundary between the alluvial deposits and the terrace system. In the site of borehole 1, the orientation of the fault wasn't determined due to the absence of a second ERT. The fault is located in the sandstone-marl series two kilometres south of the Peraia town.

Summarizing the results of this study, the groundwater quality of the shallow porous aquifer is locally affected by geothermal fluids. The geothermal water connected through the faults with the upper aquifer and mixed with fresh groundwater. The elevated concentrations of As and the related trace elements in groundwater of the study area are probably associated with the geothermal waters.

Table 3 - Statistical characteristics of groundwater and spring water samples.

Parameter	Units	Detection Limit	Mean	Max	Min	St. Dev
pH			6.9	7.8	6.2	0.83
E.C.	μS/cm		3326	6334	1127	2209
Total Hardness	ºF		69.5	106.7	27.3	34.6
Carbonate Hardness	ºF		62.4	106.7	27.3	38.4
Non-Carbonate Hardness	ºF		17.7	24.7	10.7	10.88
Alkalinity (M)			12.3	25.2	6.9	7.81
Alkalinity (P)			ND	ND	ND	ND
(HCO_3^-)	mg/L	5	847	1537	418	547
(CO_3^{2-})	mg/L	5	ND	ND	ND	ND
(Cl^-)	mg/L	2	629.2	1325.0	110.0	518.14
(SO_4^{2-})	mg/L	2	66.8	144.0	35.0	45.21
(NO_2^-)	mg/L	0.01	0.1	0.2	0.01	0.08
(NO_3^-)	mg/L	2	8.8	22.0	2.0	8.89
(PO_4^{3-})	mg/L	0.01	0.1	0.2	0.0	0.07
(Na^+)	mg/L		434	950	105	351
(K^+)	mg/L		22.9	70.9	2.6	28.96
(Ca^{2+})	mg/L		190	375	35	160
(Mg^{2+})	mg/L		53.5	97.0	31.4	26.77
(Li^+)	mg/L	0.01	1.0	2.6	0.04	1.11
(Sr^{2+})	mg/L	0.05	1.5	2.0	1.2	0.35
(NH_4^+)	mg/L	0.05	3.1	5.0	1.2	2.17
(Sb)	μg/L	2	ND	ND	ND	ND
(As)	μg/L	1	58.6	235.0	3.0	99.2
(Cd)	μg/L	0.1	0.2	0.2	0.2	0.09
Cr(VI)	μg/L	1	ND	ND	ND	ND
(Cr)	μg/L	1	ND	ND	ND	ND
(Cu)	μg/L	50	ND	ND	ND	ND
(Fe)	μg/L	50	1594	6667	204	2840
(Pb)	μg/L	1	ND	ND	ND	ND
(Mn)	μg/L	20	427	1264	96	481
(Ni)	μg/L	1	11.0	21.0	1.8	9.56
(Co)	μg/L	1	6.0	6.0	6.0	-
(Mo)	μg/L	2	4.1	6.3	2.0	2.48
(Zn)	μg/L	10	70.8	194.0	22.0	72.03
(Hg)	μg/L	0.2	ND	ND	ND	ND
(B)	mg/L	0.05	7.0	9.5	2.4	4.15
SiO_2	mg/L	2	23.8	27.0	20.0	2.77
T.O.C.	mg/L	0.5	3.5	7.4	0.7	3.12

The geothermal origin of As is also supported by the elevated concentrations of As, Na, K, Fe and Zn in the travertine sample. The Ni in soils and sediments of the study area has a geogenic origin from the weathering products of the ophiolitic rocks.

The small number of the groundwater samples is the main limitation of this study in order to make a representative map of As concentration in the aquifers of the Anthemountas basin. However, it is important to the origin of As in porous aquifers from geothermal waters. The geological sources of As in Greece are reported by Gamaletsos *et al.* (2013). Geothermal inputs of As in groundwater have been also reported from Mitrakas (2001) and Pique et al. (2010) in the Caldes de Malavella geothermal area in Spain. A future study, with a higher number of groundwater samples would be

beneficial for the determination of As distribution in porous aquifers of the study area. In Greece, elevated concentration of arsenic in groundwater have been reported in many regions (Katsoyiannis *et al*., 2007; Voudouris *et al*., 2014) indicating the need for a consistent and detailed monitoring of As in groundwater. Additionally, speciation of As should be performed in future studies in order to determine the form of arsenic (As(III) or As(V)) on groundwater considering that the toxicity of As(V) is significantly lower from As(III).

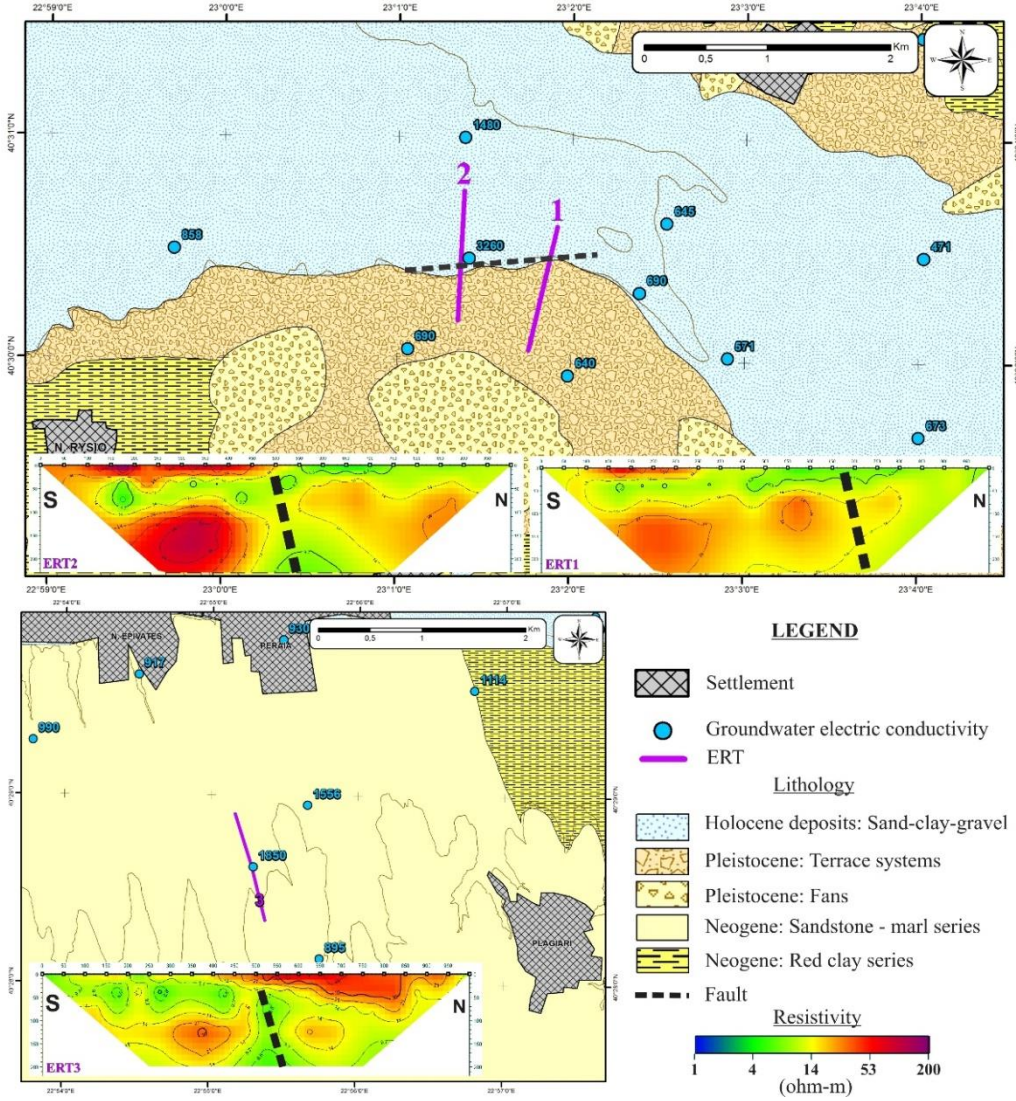

Figure 3 - Geological maps with ERTs and groundwater electrical conductivity.

5. Conclusions

In the Anthemountas river basin, a variable geochemical composition was occurred in soils and sediment samples. Nickel concentrations were up to 2169 mg/kg and the highest values located near to the ophiolitic rocks. The high correlation coefficient between Cr and Ni indicates the geogenic origin of Ni in the Anthemountas basin. Arsenic concentrations range from 3 to 110 mg/kg in soils and sediments, while the highest concentration observed in travertine. Spring waters are characterized by elevated concentrations of As (up to 235 μg/L), Na, K, Fe and Zn, and can be

assumed, particularly by the presence of Na and K, that hydrothermal fluids directly affect and alter the feldspars of the Monopigado granodiorite. In groundwater samples from the studied boreholes As concentrations are equal or below 18 μg/L. Electrical resistivity tomographies have revealed the existence of normal faults which facilitate the mixing between geothermal waters and fresh water of the upper porous aquifers.

The interdisciplinary approach and results of this study can be used as a tool to identify aquifers prone to high As concentrations originating from geothermal waters. However, a more detailed mapping of As distribution in the aquifers of Anthemountas basin is necessary in order to prevent exposure of the population to As.

6. Acknowledgements

This research was carried out within the framework of the Post Doc of Nerantzis Kazakis and was funded by the State Scholarships Foundation of Greece (I.K.Y.) through the Program "IKY FELLOWSHIPS OF EXCELLENCE FOR POSTGRADUATE STUDIES IN GREECE - SIEMENS PROGRAM".

7. References

Assubaie, F.N., 2015. Assessment of the levels of some heavy metals in water in Alahsa Oasis farms, Saudi Arabia, with analysis by atomic absorption spectrophotometry, *Arabian Journal of Chemistry*, 8, 240-245.

Chowdhury, T.R., Basu, G.K., Mandal, B.K., Biswas, B.K., Samanta, G., Chowdhury, U.K., Chanda, C.R., Lodh, D., Roy, S.L., Saha, K.C., Roy, S., Kabir, S., Quamruzzaman, Q. and Chakraborti, D., 1999. Arsenic poisoning in the Ganges Delta, *Nature*, 401, 545-546.

Clesceri, L., Greenberg, A. and Trussell, R., 1989. Standard Methods for the Examination of Water and Wastewater, *17th edition. APHA-AWWA-WEF*, Washington DC.

Dermatas, D., Mpouras, T., Chrysochoou, M., Panagiotakis, I., Vatseris C., Linardos, N., Theologou, E., Boboti, N., Xenidis, A., Papassiopi, N. and Sakellariou, L., 2015. Origin and concentration profile of chromium in a Greek aquifer, *Journal of Hazardous Materials*, 281, 35-46.

Esmaeili, A., Moore, F., Keshavarzi, B., Jaafarzadeh, N. and Kermani, M., 2014. A geochemical survey of heavy metals in agricultural and background soils of the Isfahan industrial zone, Iran, *Catena*, 121, 88-98.

Fantoni, D., Brozzo, G., Canepa, M., Cipolli, F., Marini, L., Ottonelo, G., Vetuschi and Zuccolini, M., 2002. Natural hexavalent chromium in groundwaters interacting with ophiolitic rocks, *Environmental Geology*, 42(8), 871-882.

Gallego, J.L.R., Ordonez, A. and Loredo, J., 2002. Investigation of trace element sources from an industrialized area (Aviles, northern Spain) using multivariate statistical methods, *Environ. Int*., 27, 589-596.

Gamaletsos, P., Godelitsas, A., Dotsika, E., Tzamos, E., Gotthlicher, J. and Filippidis, A., 2013. Geological sources of As in the Environment of Greece: A review. *In*: The Handbook of Environmental Chemistry, vol. 40. Threats to the Quality of Groundwater Resources: Prevention and Control, Scozzari, A. and Dotsika, E., *eds*., *Springer-Verlag*, Berlin Heidelberg, 77-113.

Harvey, C.F., Swartz, C.H., Badruzzaman, A.B.M., Keon-Blute, N., Yu, W., Ali, M.A., Jay, J., Beckie, R., Niedan, V., Brabander, D., Oates, P.M., Ashfaque, K.N., Islam, S., Hemond, H.F. and Ahmed, M.F., 2002. Arsenic mobility and groundwater extraction in Bangladesh, *Science*, 298, 1602-1606.

Kazakis, N., 2013. Groundwater Pollution Risk Assessment in Anthemountas Basin, PhD thesis, Department of Geology, Aristotle University of Thessaloniki (in Greek).

Kazakis, N., Kantiranis, N., Voudouris, K.S., Mitrakas, M., Kaprara, E. and Pavlou, A., 2015. Geogenic Cr oxidation on the surface of mafic minerals and the hydrogeological conditions influencing hexavalent chromium concentrations in groundwater, *Science of the Total Environment*, 514, 224-238.

Kaprara, E., Kazakis, N., Simeonidis, K., Coles, S., Zoumboulis, A.I., Samaras, P. and Mitrakas, M., 2015. Occurrence of Cr (VI) in drinking water of Greece and relation to the geological background, *J. Hazard. Materials*, 281, 2-11.

Katsoyiannis, I., Hug, S., Ammann, A., Zikoudi, A. and Hatziliontos, C., 2007. Arsenic speciation and uranium concentrations in drinking water supply wells in Northern Greece: Correlation s with redox indicative parameters and implications for groundwater treatment, *Science of the Total Environment*, 383, 128-140.

Kim, J.H., 2009. DC2DPro-2D Interpretation System of DC Resistivity Tomography, *User's Manual and Theory*, KIGAM, S. Korea.

Linos, A., Petralias, A., Christophi, C.A., Christoforidou, E., Kouroutou, P., Stoltidis, M., Veloudaki, A., Tzala, E., Makris, K.C. and Karagas. M.R., 2011. Oral ingestion of hexavalent chromium through drinking water and cancer mortality in an industrial area of Greece - an ecological study, *Environ*., Health 10(50), 1-8.

Loke, M.H., 2011. Electrical resistivity surveys and data interpretation. *In*: Gupta, H.K., *ed*., Encyclopedia of Solid Earth Geophysics. 2nd edition, *Springer*, 276-283.

Mandal, B.K. and Suzuki, K.T., 2002. Arsenic round the world: a review, *Talanta*, 58, 201-235.

McCleskey, R.B., Nordstrom, D.K. and Maest, A.S., 2004. Preservation of water samples for arsenic(III), *Applied Geochemistry*, 19, 995-1009.

Methods of Soil Analysis, 1996. Part 3 - Chemical Methods. *In*: Sparks, D.L., *ed*., *Soil Science Society of America*, Madison, WI, USA.

Michard, A., Feinberg, H. and Montigny, R., 1998. The Chalkidiki supra-ophiolitic formations, and their bearing on the Vardarian obduction process, *Bull. Geol. Soc. of Greece*, 32(1), 59-64.

Micó, C., Recatalá, L., Peris, M. and Sánchez, J., 2006. Assessing heavy metal sources in agricultural soils of an European Mediterranean area by multivariate analysis, *Chemosphere*, 65, 863-872.

Mitrakas, M., 2001. A survey of arsenic levels in tap, underground, and thermal mineral waters of Greece, *Fresenius Environmental Bulletin*, 10(6), 717-721.

Morrison, G.M.P., Revitt, D.M. and Ellis, J.B., 1990. Metal Speciation in Separate Stormwater Systems, *Water Science Technology*, 22, 53.

Nimik, D.A., Moore, J.N., Dalby, C.E. and Savka, M.W., 1998. The fate of geothermal arsenic in the Madison and Missouri Rivers, Montana and Wyoming, *Water Resources Research*, 34(11), 3051-3067.

Nimfopoulos, M.K., Hadjispyrou, S.A., Polya, D.A., Michailidis, K.M. and Trontsios, G., 2002. Geochemical conditions and environmental pollution from hydrothermal waters of the Anthemous basin, Thessaloniki district, N. Greece, 6th Pan-Hellenic Geographical Conference (Volume II), Thessaloniki 2002, 428-435.

Papastergios, G., Filippidis, A., Fernandez-Turiel, J.L., Gimeno, D. and Sikalidis, C., 2011. Surface soil geochemistry for environmental assessment in Kavala Area, northern Greece, *Water, Air, & Soil Pollution*, 216, 141-152.

Petrotou, A., Skordas, K., Papastergios, G. and Filippidis, A., 2012. Factors affecting the distribution of potentially toxic elements in surface soils around an industrialized area of northwestern Greece, *Environmental Earth Sciences*, 65, 823-833.

Pique, A., Grandia, F. and Canals, A., 2010. Processes releasing arsenic to groundwater in the Caldes de Malavella geothermal area, NE Spain, *Water Research*, 44, 5618-5630.

Rodríguez Martín, J.A., Vázquez de la Cueva, A., Grau Corbí, J.M. and López Arias, M., 2007. Factors controlling the spatial variability of copper in topsoils of the Northeastern Region of the Iberian Peninsula, Spain, *Water, Air, & Soil Pollution*, 186, 311-321.

Voudouris, K., Melfos, V., Aidona, E., Kazakis, N., Giouri, K. and Stratis, J., 2014. Arsenic concentration in groundwater and sediments of Velestino area, Thessaly, Central Greece. *Proc. of 10th International Hydrogeological Conference*, 8-10 October 2014, Thessaloniki, 1, 759-770.

Skordas, K., Papastergios, G. and Filippidis, A., 2013. Major and trace element contents in apples from a cultivated area of central Greece, *Environ. Monitoring & Assessment*, 185, 8465-8471.

Tzamos, E., Tziritis, E., Vogiatzis, P., Matzari, C., Kantiranis, N., Filippidis, A., Theodosiou, N. and Fytianos, K., 2014. Suitability of potable groundwater reserves of Thermi Municipality (Macedonia, Northern Greece) and definition of main hydrogeochemical signatures, *Proc. of 12th Intern. Conf. "Protection & Restoration of the Environment"*, Skiathos, 6-3 July, 272-276.

Tziritis, E., Tzamos, E., Vogiatzis, P., Matzari, C., Kantiranis, N., Filippidis, A., Theodosiou, N. and Fytianos, K., 2015. Quality assessment and hydrogeochemical status of potable water resources in a suburban area of northern Greece (Thermi Municipality, central Macedonia), *Desalination and Water Treatment*, doi: 10.1080/19443994.2015.1052993.

Zhang, C., Selinus, O. and Kjellstrom, G., 1999. Discrimination between natural background and anthropogenic pollution in environmental geochemistry - exemplified in an area of south-eastern Sweden, *Science of the Total Environment*, 243-244, 129-140.

Δελτίο της Ελληνικής Γεωλογικής Εταιρίας, τόμος L, σελ. 2182-2191
Πρακτικά 14ου Διεθνούς Συνεδρίου, Θεσσαλονίκη, Μάιος 2016

Bulletin of the Geological Society of Greece, vol. L, p. 2182-2191
Proceedings of the 14th International Congress, Thessaloniki, May 2016

INTERACTION OF HEAVY METALS IN THE SOIL-PLANT SYSTEM OF URBAN GARDENS IN ATHENS, GREECE

Kazantzoglou A.[1], Argyraki A.[1], Papageorgiou S.[1] and Fadel D. [2]

[1]National & Kapodistrian University of Athens, Faculty of Geology & Geoenvironment, Panepistimiopolis Zographou, 15784, Athens, Greece, nancykaza1993@hotmail.com, argyraki@geol.uoa.gr, papagstamatiou@hotmail.com

[2]Lebanese University, Faculty of Agricultural Engineering, Damour, Lebanon, dr.danifadel@gmail.com

Abstract

Preliminary data on the interaction between soil and edible plants with respect to heavy metal concentrations in Athens, Greece are presented. Concentration ranges of Zn, Cu, Ni, Cr, Co, Mn, Fe, Ba, Pb and Cd in soils and vegetables collected from urban allotments in Athens are determined and assessed taking into account the pseudototal (extracted by aqua regia) and mobilizable (0.43 M acetic acid extractable) concentrations of the elements in the rhizosphere soil of the collected plants as well as the total concentrations in plant tissue. Average elemental concentrations in urban allotments are lower than the ones previously reported for Athens urban soil. No detectable concentrations of the non-essential heavy metals Pb and Cd were measured in the studied plants while concentrations of micronutrient elements in plants are within normal ranges. The collected data indicate that previous land use is an important factor controlling heavy metal content in soil and that there is a complex mechanism controlling micronutrient uptake by plants.
Keywords: *Biogeochemistry, soil contamination, micronutrient elements, urban agriculture.*

Περίληψη

Παρουσιάζονται προκαταρκτικά δεδομένα που αφορούν την αλληλεπίδραση μεταξύ εδάφους και βρώσιμων φυτών ως προς τις συγκεντρώσεις βαρέων μετάλλων στην πόλη των Αθηνών. Προσδιορίστηκε το εύρος των συγκεντρώσεων των στοιχείων Zn, Cu, Ni, Cr, Co, Mn, Fe, Ba, Pb και Cd σε εδάφη και φυτά αστικών καλλιεργειών περιοχών της Αθήνας και συγκεκριμένα μελετήθηκε το ψευδο-ολικό περιεχόμενο (εξαγωγή με βασιλικό ύδωρ) και το κινητοποιήσιμο (εξαγωγή με 0.43 M οξικό οξύ) κλάσμα των στοιχείων στο έδαφος καθώς και η ολική συγκέντρωση των στοιχείων στους φυτικούς ιστούς. Οι εδαφικές συγκεντρώσεις που μετρήθηκαν είναι γενικά χαμηλότερες αυτών που αναφέρονται για τα εδάφη της ευρύτερης περιοχής της Αθήνας. Οι συγκεντρώσεις των μη απαραίτητων ιχνοστοιχείων Pb και Cd δεν ανιχνεύτηκαν στα φυτικά δείγματα, ενώ αυτές των μικροθρεπτικών κυμαίνονται σε κανονικά πλαίσια. Τα δεδομένα καταδεικνύουν τη σημασία της προηγούμενης χρήσης γης στον καθορισμό των επιπέδων συγκέντρωσης των στοιχείων στο έδαφος και την περιπλοκότητα των μηχανισμών που ελέγχουν την απορρόφηση των στοιχείων από τα φυτά.
Λέξεις κλειδιά: *Βιογεωχημεία, ρύπανση εδάφους, μικροθρεπτικά στοιχεία, αστική γεωργία.*

1. Introduction

In recent years, the application of urban agriculture has risen dramatically and is at a climax. Not only have municipalities taken an active role on that matter, but also much domestic cultivation is apparent in urban areas. At the same time the urban ecosystem is being weakened by excessive heavy metal loadings in the environment, resulting from the continuous production and use of industrial commodities. Furthermore, a growing body of scientific evidence shows that heavy metal contamination in the urban soil might be related to the natural geochemical background (e.g. Manta *et al.*, 2002; Rodrigues *et al.*, 2009; Argyraki and Kelepertzis, 2014). All of the above might lead to soil pollution. Through plant uptake and the food chain, heavy metals may be passed on to humans resulting in possible adverse health effects. The concentration of heavy metals in plant tissue largely depends on the soil-plant transfer. It is generally known that there are variations in the rates between different plant species but also between the same plant species from different areas (Kabata-Pendias and Pendias, 1992). It has also been observed that previous land uses of the cultivated areas have a significant contribution to the levels of heavy metal contamination of soil and plants (Tahmasbian *et al.*, 2013).

The aim of the present study is to present preliminary data on the interaction between soil and edible plants with respect to heavy metal concentrations in Athens, Greece. The specific objectives were: a) to determine the concentration range of Zn, Cu, Ni, Cr, Co, Mn, Fe, Ba, Pb and Cd in vegetables collected from urban allotments in Athens, and b) to assess the pseudototal and mobilizable concentrations of the same elements in the rhizosphere soil of the collected plants.

2. Materials and Methods

2.1. Field sampling and chemical analyses

Twenty composite plant and 20 rhizosphere soil samples were collected from cultivated communal allotments in Athens, Greece organized by the municipalities of Agios Dimitrios, and Maroussi in the respective areas and by the NGO "The Center of Earth" in Tritsis Park, Ilion. Additional samples were collected from cultivated house gardens in Filothei, Neo Irakleio and Elliniko. All sampling took place during the spring of 2015.

In the laboratory, plants were thoroughly washed three times with deionized water and air dried at room temperature. The edible parts of the plants were separated before drying and kept for further analysis. All plant samples were ground in an agate mill and concentrations of heavy metals (Zn, Cu, Ni, Cr, Co, Mn, Fe, Ba, Pb and Cd) were measured by Inductively Coupled Plasma Optical Emission Spectroscopy (ICP-OES) in the University of Porthsmouth, UK following microwave digestion by HNO_3/ H_2O_2, 6:1 v/v. Soil samples were oven dried at 40ºC for 3 days, sieved using a 2mm nylon sieve and ground using an automated agate mill. Pseudototal heavy metal concentrations in soil were measured by ICP-OES following digestion by a mixture of HNO_3, H_2O_2 and HCl (US-EPA, 2002). Acetic acid (0.43 M) extractable concentrations of heavy metals were also measured by the same analytical technique after mixing 1g of the soil samples with 40 ml acetic acid and shaking for 16 h at room temperature in an overhead shaker.

All utensils which were used during laboratory work, were thoroughly cleaned between the samples in order to avoid cross contamination. Analytical quality control procedures included the performance of duplicate analysis, the inclusion of blank solutions and certified reference materials of soils (NIST SRM 2709 and NIST SRM2711a for the total analysis and BCR-483 and BCR-484 for the acetic acid extraction) at random positions within the analytical batches. The results of the analytical control were found within acceptable limits for all analyses and all elements.

2.2. Measurement of physicochemical parameters of soil

The major physicochemical soil properties were measured including pH, organic matter content and texture (sand, silt, clay). Soil pH was measured after mixing each <2 mm soil sample with deionized

water in a solid -to-liquid ratio of 1:2.5 (ISO, 1994). Organic matter content of the soil samples was estimated by the loss-on-ignition (LOI) method (US-EPA, 2002) by heating 1 g of each sample to 450^0C for 4 hours in a furnace oven. Since the method determines the organic matter content in the soil, a conversion factor of 1.724 has been used to convert organic matter to organic carbon based on the assumption that organic matter contains 58% organic C (i.e., g organic matter/l .724 = g organic C). The grain size distribution in the sand, silt and clay fractions was determined using the Bouyoucos Hydrometer Method (Bouyoucos, 1962).

3. Results and Discussion

3.1. Heavy metals in soil samples

The measured pseudototal concentrations of heavy metals in soils samples are presented in Table 1. The summary statistics of elemental concentrations as well as the major physicochemical properties including pH, total organic carbon (TOC) are presented in Table 2. The alkaline soil pH values in this study, ranging from 8.0 to 9.0, are in agreement with data reported in earlier studies of Athens soil (Argyraki and Kelepertzis, 2014), reflecting the abundant presence of calcite in bedrock (Kelepertzis and Argyraki, 2015). The TOC average value of 3 % is considered normal for urban agriculture soils and is slightly over the 2 % TOC average reported by Kelepertzis and Argyraki (2015) for Athens soil. However, in contrast to other studies (Rodrigues *et al.*, 2009) no significant correlations were detected between the key soil properties and the pseudototal concentrations of heavy metals.

Median values of the pseudototal elemental concentrations in soil are following the decreasing order Fe>Mn>Ba>Zn>Ni>Cr>Co~Pb~Cu>Cd. In comparison with median values in Athens soil reported by Kelepertzis and Argyraki (2015), all elements present significantly lower concentrations except Co and Cd that display comparatively elevated levels in the studied urban agriculture soil. Acetic acid extractability ratios expressed as % percentages of the pseudototal concentrations are presented in Figure 1. The decreasing order of extractable concentrations is somehow similar to that of pseudototal concentrations except for Fe which has the lowest extractability ratio despite being the element with the highest pseudototal concentration. Similar acetic acid extractability ratios of Zn (~15%) and Ni (~5%) have been reported by Kelepertzis and Argyraki (2015) however, relatively higher extractabilities of Mn and Co were measured in the present study. It is noted that the anthropogenic influence has been shown to be the dominant factor controlling Pb, Zn, Cd and Cu concentrations in Athens soil (Argyraki and Kelepertzis, 2014).

3.2. Heavy metals in edible plant tissues

The elemental concentrations in plant tissues are presented in Table 1. Plant tissue content of heavy metals is generally much lower than the respective content of rhizosphere soil (Table 1 and Figure 2). Concentrations of Pb and Cd were below detection limit in all plant samples. Normal concentrations of Cu in plants are in the order of 6 mg/kg for lettuce and 4 mg/kg for carrots and onions (Jaworowski, 1981). Relatively lower Cu content was measured in the present study for the respective vegetables. Barium is reported to be commonly present in plants, but it apparently is not an essential component of plant tissues. Barium concentration in the present study was within the normal ranges in plants from 1 to 198 mg/kg (Kabata-Pendias and Pendias, 1979). The rate of Zn absorption differs greatly among both plant species and growth media (Kabata-Pendias and Pendias, 2001).

The measured concentrations of Zn are similar to those mentioned in the bibliography for selected species, i.e. 44 mg/kg Zn in lettuce, 24 mg/kg in carrots and 22 mg/kg in onion (Warren *et al.*, 1970). Most soils contain significant amounts of Cr but its availability to plants is highly limited. Data from the present study totally agree with this fact. The Mn content shows a remarkable variation depending on plant species, stage of growth and different organs as well as for different ecosystems; the range of Mn in samples of the present study is 80 mg/kg. It is known that when Fe is easily

soluble, plants may take up a very large amount of Fe. Measured concentrations of Fe in lettuce, cabbage, carrots and onions are very close to those reported by Kabata-Pendias and Pendias (1979). The rates of Co are very low and the ability of plant species to absorb Co varies considerably (Kabata-Pendias and Pendias, 2001). An extreme outlying value has been observed for this element in sample KZ16 (beetroot). This value was not taken into account in statistical calculations.

Finally, the Ni content of plants growing on uncontaminated soils may vary considerably because it reflects both environmental and biological factors. However, the Ni concentrations in certain food products from different countries do not differ widely (Kabata-Pendias and Pendias, 2001). Generally, Ni levels in plants of the present study are very low. In general, the elements that are more easily absorbed by plants in the present study include Fe, Zn, Mn and Ba while the uptake of Co, Cu, Ni and Cr is very low. In terms of plant species, spinach and chicory- especially the Italian variety- seem to preferably concentrate Zn, Cu and Fe in their leaves (Figure 2), although the small number of plant samples does not allow to draw any general conclusions.

The main sources of trace elements in plants are their growth media, for example, nutrient solutions or soils. One of the most important factors that determine the biological availability of trace element is its binding to soil constituents. In general, plants take up the species of trace elements that are dissolved in soil solution in either ionic or chelated and complex forms (Kabata-Pendias and Pendias, 2001). Furthermore, each plant species responds differently and according to its specific metabolic functions regarding the uptake of micronutrients. Following this, one can explain why there is no correlation between pseudototal elemental concentrations in soil and plant tissue (Figure 2). Also, when the rates of acetic acid extractable concentrations in soil samples are compared with the rates of concentrations in plant samples no significant correlation is noticeable for any of the studied elements. This observation indicates that the particular reagent is not effective for dissolving the chemical forms of elements that are up taken by plants. This in turn, might be related to the rather alkaline soil conditions prevailing in the study area as well as the speciation of the studied elements in soil samples.

3.3. Comparison of heavy metal plant uptake between the studied communal urban allotments

Since urban agriculture is an upcoming trend in modern cities it is of interest to compare the three communal allotments within the Athens urban net that were studied in this research in terms of land management and micronutrient concentrations in their produce. Based on a questionnaire that was distributed to the allotment managers it was found out that organic crop growing is practiced in all three of them without any application of chemical soil improvers, fertilizers and pesticides. Plants are irrigated with water originating from municipal boreholes. Previous land use varied from unused urban space in Maroussi, to horse stables in Parko Tritsi and parking area in Agios Dimitrios. In the later, the surface soil layer (0-50 cm) had been removed and new soil was brought in before starting the communal garden. All three allotments are used for communal agriculture for the past three years.

Table 1 - Sample codes, plant species and their respective pseudototal concentrations of elements in soil (S) and plant tissue (P). Concentrations are expressed in mg/kg. Sampling sites are coded as E: Elliniko, AD: Agios Dimitrios, PT: Parko Tritsi, F: Filothei, M: Maroussi, NI: Neo Irakleio. bdl= below detection limit.

Sample code	Scientific name	Common name	Area	Zn S	Zn P	Cu S	Cu P	Ni S	Ni P	Cr S	Cr P	Co S	Co P	Mn S	Mn P	Fe S	Fe P	Ba S	Ba P	Pb S	Cd S
KZ37	*Allium cepa*	onion	E	101	19	32	3	61	4.0	56	0.8	37	11	395	16	13038	78	138	11	31	2.2
KZ16	*Beta vulgaris*	beetroot	AD	79	39	26	7	56	23	40	9.8	37	2800	546	28	13870	186	185	79	28	2.6
KZ28	*Beta vulgaris*	beetroot	PT	99	43	28	12	70	2.6	65	0.7	33	6.0	292	29	8870	181	143	97	34	2.4
KZ20	*Beta vulgaris var sicla*	mangel	AD	74	46	18	7	61	2.8	46	1.5	44	2.6	506	49	15751	273	150	27	25	2.5
KZ25	*Brassica oleracea*	cabbage	PT	98	41	76	bdl	65	2.2	67	0.2	34	2.2	345	20	10539	64	181	12	52	2.2
KZ24	*Cichorium endivia*	endive	PT	66	41	31	9	75	2.7	77	1.0	35	4.8	328	57	9956	72	144	14	77	2.3
KZ5	*Cichorium indybus*	chicory	F	81	66	27	12	47	3.2	32	1.0	43	1.6	319	40	13057	166	149	19	31	2.4
KZ6	*Cichorium indybus*	chicory	F	77	58	24	11	39	4.2	29	1.2	43	2.4	320	55	12861	149	186	23	45	2.5
KZ22	*Cichorium indybus*	chicory	PT	66	81	38	5	66	3.2	69	0.5	34	3.4	334	59	10310	131	159	24	35	2.3
KZ15	*Cichorium indybus*	italian chicory	AD	78	92	28	7	53	4.0	39	2.7	44	8.6	523	84	14745	356	187	33	24	2.4
KZ18	*Cichorium indybus*	italian chicory	AD	72	116	18	10	54	3.8	47	1.3	37	5.8	464	63	12989	159	164	18	29	2.3
KZ23	*Dacus carota*	carrot	PT	61	30	35	3	63	2.6	66	1.4	34	1.2	323	4	9998	66	144	31	27	2.3
KZ33	*Dacus carota*	carrot	M	61	21	20	bdl	29	2.0	22	1.0	45	6.8	321	7	12332	92	101	19	17	2.3
KZ29	*Lactula sativa*	iceberg	M	109	40	54	5	78	2.6	79	1.1	43	6.4	385	39	11589	191	161	21	60	2.4
KZ12	*Lactula sativa*	lettuce	NI	96	43	43	3	49	3.0	41	1.3	44	24	270	14	12895	183	104	18	21	2.3
KZ27	*Lactula sativa*	lettuce	PT	64	38	39	5	98	2.6	80	0.7	35	4.0	352	28	10390	162	132	18	31	2.3
KZ26	*Petroselinum crispum*	parsley	PT	64	32	27	2	56	3.0	37	0.8	39	3.8	439	21	12341	84	142	137	17	2.4
KZ21	*Spinacia oleracea*	spinach	AD	62	124	19	13	51	3.4	40	1.9	37	5.4	448	42	13878	331	162	16	21	2.4
KZ17	*Vicia faba*	beans	AD	72	47	20	9	55	3.6	41	2.5	40	4.6	494	46	14064	336	189	21	22	2.4
KZ32	*Vicia faba*	beans	M	71	22	24	5	69	2.4	50	1.3	44	7.8	425	62	14381	213	119	18	21	2.3

Table 2 - Summary statistics (*n* =20) of pseudototal heavy metal concentrations in soil (S) and plants (P), soil pH and soil OC. Concentrations are expressed in mg/kg.

	Minimum	Maximum	Median	Std.Deviation
Zn S	61	109	78	15
Zn P	19	124	52	30
Cu S	18	76	31	14
Cu P	2	13	7	3
Ni S	29	98	60	15
Ni P	2	23	4	4
Cr S	22	80	51	18
Cr P	0	10	2	2
Co S	33	45	39	4
Co P	1	24	6	5
Mn S	270	546	391	83
Mn P	4	84	38	21
Fe S	9000	15800	12410	1866
Fe P	64	356	174	91
Ba S	101	189	152	26
Ba P	11	137	33	33
Pb S	17	77	32	15
Cd S	2.2	2.6	2.3	0.1
Soil pH	7.83	8.82	8.43	0.23
Soil OC	2	5	3	1

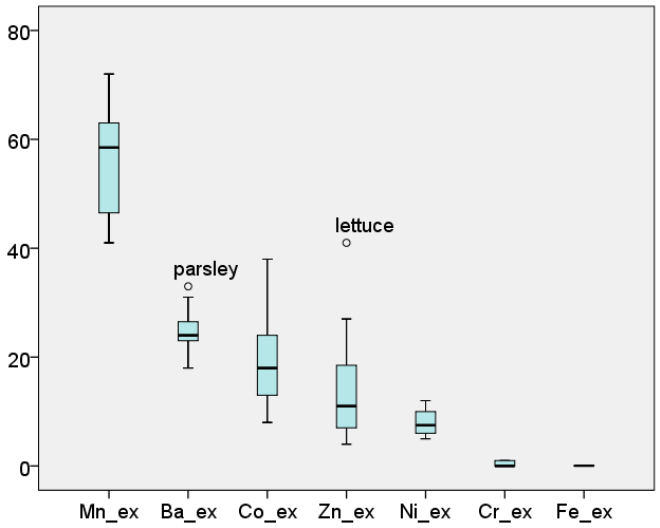

Figure 1 - Boxplot comparison of acetic acid extractability ratios of heavy metal concentrations and variation in the studied soil samples. The elements are ordered according to decreasing median value (horizontal lines). The y axis scale shows % extractability. Two outlying values are denoted by circles (one for parsley and one for lettuce).

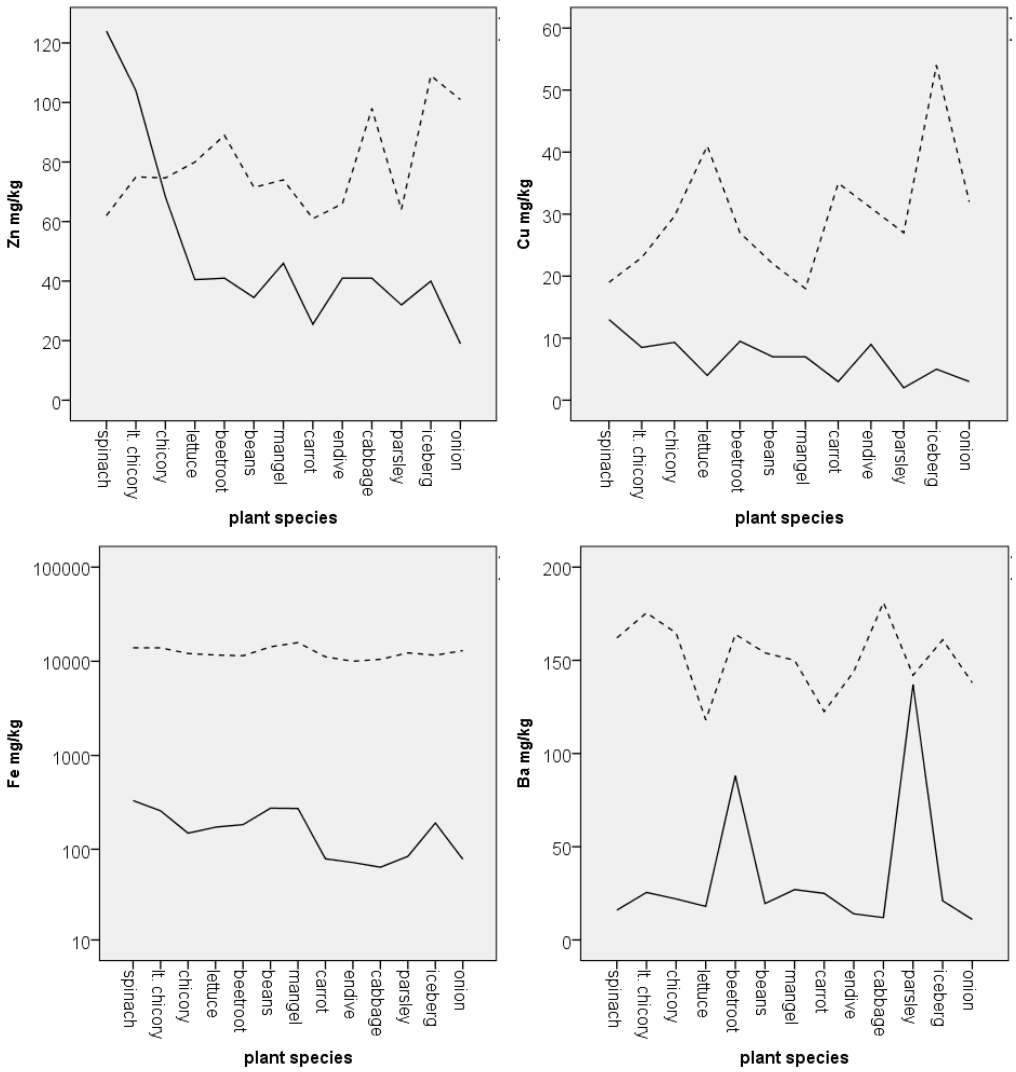

Figure 2 - Comparison the various plant species collected in this study with respect to selected elements' concentrations in plant tissues (continuous lines) and their respective rhizosphere soil (dotted lines).

Elemental concentrations in soil and plants of the three studied areas are compared using side by side box-plots in Figure 3. Although no specific trend is observed, a noticeable greater variance exists for most of the elements in Maroussi soil compared to the other two areas, while the opposite holds for plant elemental content. Differences of elemental concentrations in soil might be related to the previous land use of the study areas. Also, variation of the median values in plants exceeds the respective variation in soil medians between the three areas. The vegetable produce in Agios Dimitrios contains the highest concentrations of Zn, Cu, Cr and Fe. However, taking into account that different plant species were sampled in each allotment it is difficult to pinpoint any specific factors affecting micronutrient uptake by plants in the three areas.

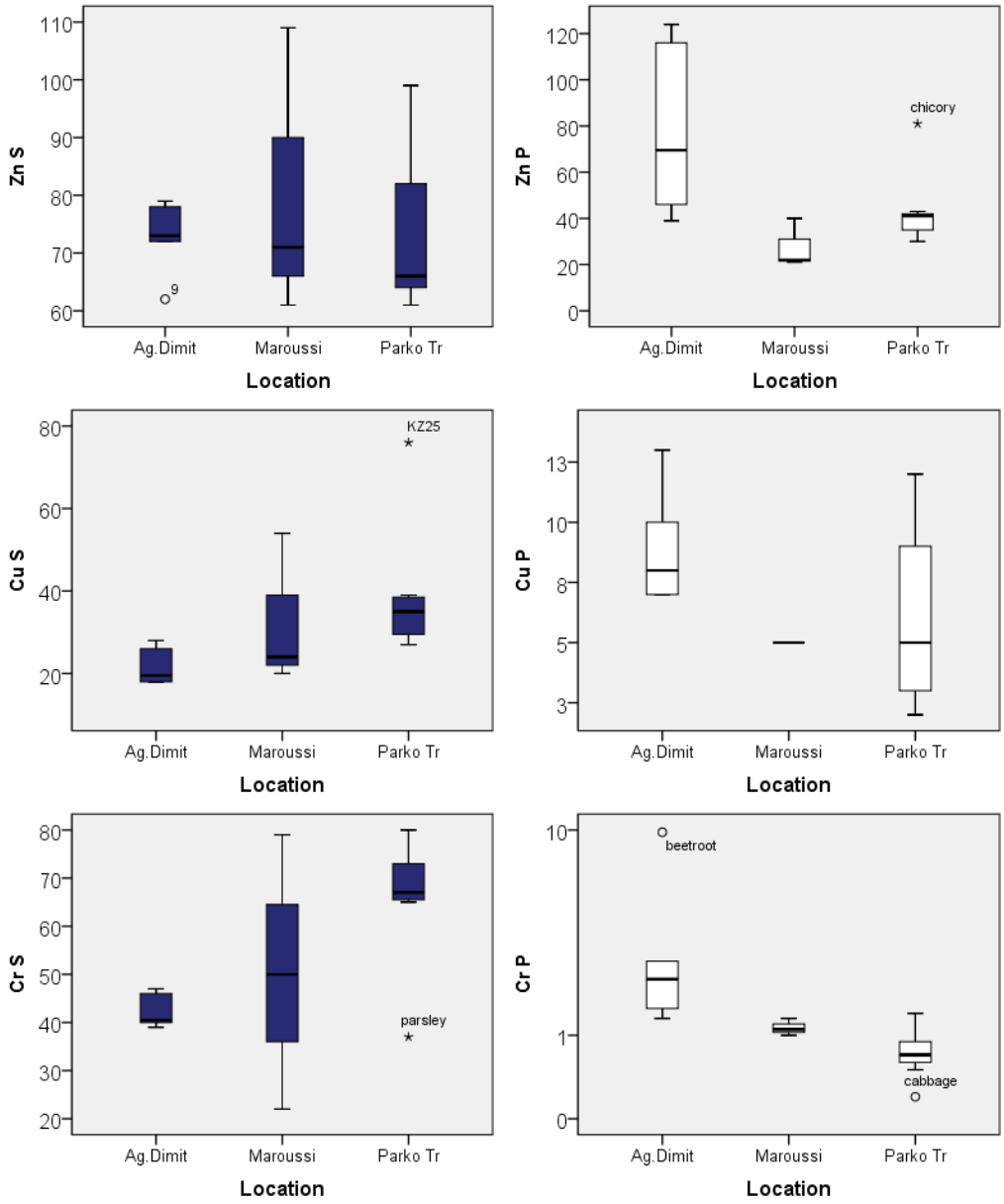

Figure 3 - Boxplot comparisons of soil (S- dark boxes) and plant (P- white boxes) concentrations of selected elements between the three communal allotment study areas (Agios Dimitrios (n=8), Maroussi (n=6) and Tritsis Park n=7)). Concentrations are expressed as mg/kg except for Cr in plants which is in µg/kg.

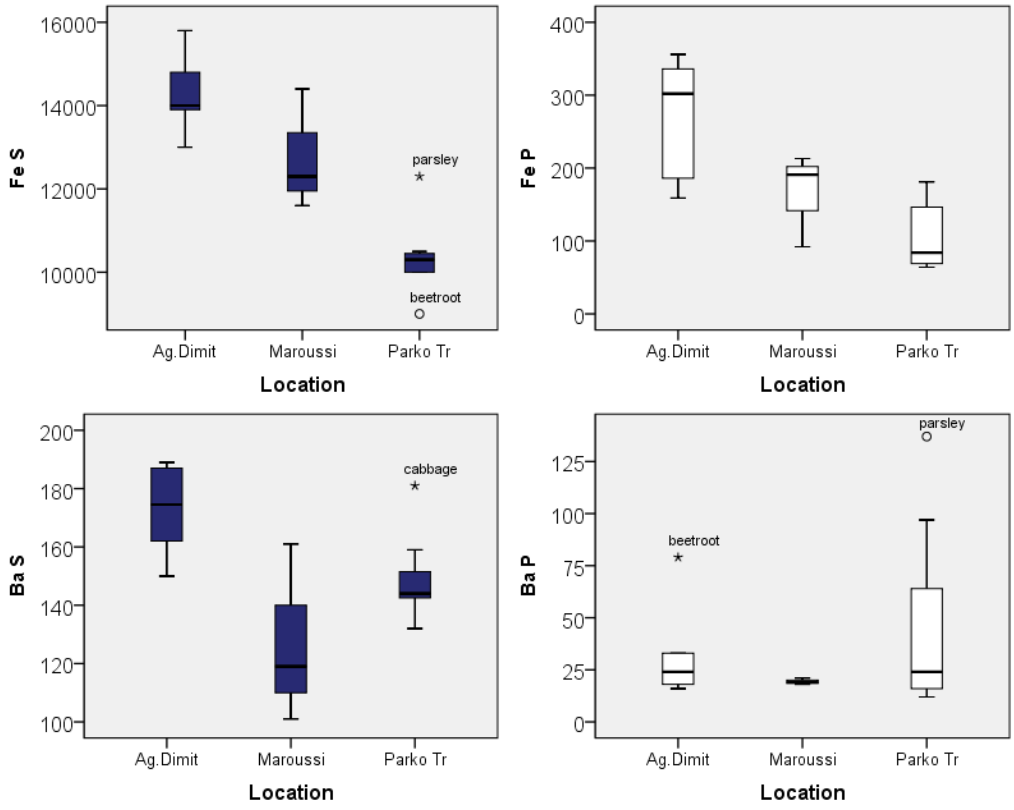

Figure 3 - ***continue***

4. Conclusions

Data on concentrations of heavy metals in soil and plants from urban agriculture areas in the city of Athens are presented for the first time. The geochemical signature of soil in three communal allotments and three private house gardens was studied with respect to Fe, Mn, Ba, Zn, Ni, Cr, Co, Pb, Cu and Cd and concentration levels in the edible parts of produced vegetables were measured. Although no systematic pattern was observed, concentration levels in soil were in general lower than the median values previously reported for Athens soils (Kelepertzis and Argyraki, 2015). Heavy metal concentrations in plant tissues were below detection limit for Pb and Cd and within normal ranges for healthy plant growth regarding the rest of the studied elements. No significant correlation was observed between pseudototal or acetic acid extractable concentrations in soil and plants, supporting that a more complex mechanism controls micronutrient uptake by plants. Vegetable produce from the communal allotment of Agios Dimitrios contains higher concentrations of Zn, Cu, Cr and Fe compared to the other two communal agriculture areas. Further interdisciplinary research is needed in order to determine the controlling factors of micronutrient uptake within the urban environment.

5. Acknowledgments

The authors would like to thank Dr. Ioannis Mitsis of the Laboratory of Economic Geology and Geochemistry, University of Athens for his invaluable help and guidance during the plant tissue digestions. Also Dr. Efstratios Kelepertzis for his help during sample preparation and analytical procedures. Special thanks are given to Dr. Adil Bakir for his involvement in chemical determinations of geochemical solutions at the analytical facilities of School of Earth &

Environmental Sciences, University of Portsmouth, UK. Ms. Asimakopoulou of the Municipality of Agios Dimitrios, Ms. Koroni of the Municipality of Maroussi, Mr. Dritsoulas of the NGO "The Center of the Earth" as well as the owners of the private gardens are greatly acknowledged for their help during field sampling.

6. References

Argyraki, A. and Kelepertzis, E., 2014. Urban soil in Athens, Greece: The importance of local geology in controlling the distribution of potentially harmful trace elements, *Science of The Total Environment*, 482-483, 366-377.

Bouyoucos, G.J., 1962. Hydrometer method improved for making particle size analysis of soils, *Agronomy Journal*, 54, 464-465.

ISO 10390, 1994. Soil quality- determination of pH.

Jaworowski, C., 1981. The effect of copper and fertilization with various forms of nitrogen on some physiological indices in maize, Acta Agra, Silvistria, 20, 95 (Po).

Kabata-Pendias, A. and Pendias, H., 1979. Trace elements in the Biological environment, Wyd. Geol., Warsaw, 300 (Po).

Kabata-Pendias, A. and Pendias, H., 1992. Trace Elements in Soils and Plants, CRS Press, Boca Raton, FI.

Kabata-Pendias, A. and Pendias, H., 2001. Trace Elements in Soils and Plants (third edition), CRS Press, Boca Raton, FI.

Kelepertzis, E. and Argyraki, A., 2015. Geochemical associations for evaluating the availability of potentially harmful elements in urban soils: Lessons learnt from Athens, Greece, *Applied Geochemistry*, 59, 63-73.

Manta, D.S., Angelone, M., Bellanca, A., Neri, R. and Sprovieri, M., 2002. Heavy metals in urban soils: a case study from the city of Palermo (Silicy), Italy, *Science Total Environ*., 300, 229-43.

Rodrigues, S., Urquhart, G., Hossack, I., Pereira, M.A., Duarte, A.C., Davidson, C., Hurtshouse, A., Tucker, P. and Roberston, D., 2009. The influence of anthropogenetic and natural geochemical factors of urban soil quality variability: a comparison between Glasgow, UK and Aveiro, Portugal, *Environ. Chem. Let.*, 7, 141-8.

Tahmasbian, I., Nasrazadani, A., Shoja, H. and Safari Sinegani, A.A., 2013. The effects of human activities and different land use on trace elements pollution in urban topsoil of Isfahan (Iran), *Environ Earth Sci*.

US-EPA, 2002. Methods for the determination of total organic carbon (TOC) in soils and sediments. *Report No. NCEA-C- 1282, EMASC-001*, Las Vegas.

Warren, H.V., Delavault, R.E., Fletcher, K. and Wilks, E., 1970. Variation in the copper, zinc, lead and molybdenum content of some British Columbia vegetables, *In:* Trace Subst. environ. Health, Vol.4, Hemphill, D.D., *ed.*, University of Missouri Columbia, MO, 94.

Δελτίο της Ελληνικής Γεωλογικής Εταιρίας, τόμος L, σελ. 2192-2199
Πρακτικά 14ου Διεθνούς Συνεδρίου, Θεσσαλονίκη, Μάιος 2016

Bulletin of the Geological Society of Greece, vol. L, p. 2192-2199
Proceedings of the 14th International Congress, Thessaloniki, May 2016

COPPER ACCUMULATION IN VINEYARD SOILS FROM NEMEA, GREECE

Kelepertzis E.[1], Massas I.[2], Fligos G.[1], Panagiotou M.[2] and Argyraki A.[1]

[1]*Department of Geology and Geoenvironment, University of Athens, Panepistimiopolis, 15784, Athens, Greece, kelepert@geol.uoa.gr, giorgos_fligos@yahoo.com, argyraki@geol.uoa.gr*

[2]*Department of Natural Resources and Agricultural Engineering, Agricultural University of Athens, 75 Iera Odos St., 11855, Athens, Greece, massas@aua.gr, stud609027@aua.gr*

Abstract

We present for the first time the extent and magnitude of Cu accumulation in calcareous vineyard soils from Nemea, Greece, as result of intensive application of Cu-based fungicidal sprays. Surface (0-20 cm) soil samples were collected from 40 vineyard plots covering the whole agricultural region of Nemea devoted to viticulture. In 20 randomly selected vineyards, we also collected soil at 50 cm depth. Major soil properties were determined (pH, electrical conductivity, organic carbon and equivalent calcium carbonate contents, particle size distribution). Copper concentrations in Nemea vineyard soils (33.1 - 291 mg kg^{-1}) were similar to those reported in the soils of vineyards in other parts of Europe. Copper has migrated down the soil profile since the levels at 50 cm depth are higher than the known background concentrations, probably as result of soil disturbance by tillage practices. We did not find differences in Cu availability between the surface and deep soil samples after applying the DTPA chemical extraction. The DTPA-extracted Cu concentrations were largely dependent on the total soil Cu content. The excessive application of Cu-based fungicides should be avoided with the aim to ensure that Cu accumulation does not reach levels that may inhibit plant growth.

Keywords: *chemical extractions, heavy metals, soil contamination, agricultural activities.*

Περίληψη

Στην εργασία αυτή παρουσιάζουμε το μέγεθος και τη σημασία της συσσώρευσης χαλκού σε ασβεστούχα εδάφη αμπελώνων στη Νεμέα της Ελλάδας, ως αποτέλεσμα της εντατικής εφαρμογής χαλκούχων μυκητοκτόνων. Συλλέχθηκαν επιφανειακά (0-20 cm) δείγματα εδαφών από 40 αμπελώνες αντιπροσωπεύοντας το σύνολο της γεωργικής γης της Νεμέας το οποίο είναι αφιερωμένο στην αμπελοκαλλιέργεια. Επίσης, σε 20 τυχαία επιλεγμένους αμπελώνες συλλέξαμε έδαφος μέχρι το βάθος των 50 cm. Στα εδαφικά δείγματα προσδιορίστηκαν βασικές ιδιότητες των εδαφών. Οι συγκεντρώσεις του χαλκού (33.1 - 291 mg kg^{-1}) στους αμπελώνες της Νεμέας είναι παρόμοιες με αυτές που αναφέρονται σε εδάφη αμπελώνων και σε άλλες περιοχές της Ευρώπης. Ο χαλκός έχει μετακινηθεί σε βαθύτερες στρώσεις του εδάφους με τα επίπεδά στο βάθος 50 cm να παραμένουν υψηλότερα από τις γνωστές συγκεντρώσεις αναφοράς, πιθανόν ως αποτέλεσμα της ανατάραξης του εδάφους λόγω καλλιεργητικών τεχνικών (άροση).Η εκχύλιση των διαθέσιμων μορφών του χαλκού επιτεύχθηκε με τη βοήθεια του εκχυλιστικού DTPA. Δεν εντοπίσαμε διαφορές στη διαθεσιμότητα χαλκού ανάμεσα στα

επιφανειακά δείγματα εδάφους και στα δείγματα βάθους 50 cm. Προτείνονται ο έλεγχος της εφαρμογής και η αποφυγή υπερβολικής χρήσης χαλκούχων μυκητοκτόνων διασφαλίζοντας ότι η συσσώρευση του χαλκού στα εδάφη να μην φτάσει σε επίπεδα που να εμποδίζουν την ανάπτυξη φυτών.
Λέξεις κλειδιά: *εκχυλίσεις, βαρέα μέταλλα, ρύπανση εδάφους, αγροτικές δραστηριότητες.*

1. Introduction

Since the end of the 19th century, the intensive application of copper (Cu)-based fungicides in vineyards to fight vine fungal diseases, such as downy mildew caused by *Plasmopara viticola*, has resulted to increased Cu concentrations in the receiving soils (Komárek *et al.*, 2010). The wash-off of Cu from the vine leaves, the deposition of the senescent leaves and the accidental spills of the fungicides are the major source processes of Cu to the vineyard soils. However, the Cu accumulation in the soil over the years is the result of its strong fixation to soil organic matter, Fe- and Mn-(hydr)oxides and clay minerals (Komárek *et al.*, 2008 and Pietrzak and McPhail, 2004). This geochemical behavior combined with the neutral-alkaline soil pH of most of vineyard soil (Mackie *et al*., 2012) do not favor the migration of Cu throughout the soil profile. As a result, a decrease in Cu concentrations with increasing depth has been reported, and Cu commonly reaches background levels within 40-50 cm depth (Deluisa *et al*., 1996 and Pietrzak and McPhail, 2004). Referring to the chemical methods used in the laboratory to determine the Cu content in vineyard soil, the *aqua regia* extraction is frequently applied, especially in the European studies, but with low correlation with the phytoavailability of this element. For that reason, a variety of single stage chemical extractions has been proposed for mimicking the processes that operate at the soil-plant interface providing more useful information for the fraction of Cu that is available for plant uptake (Kelepertzis *et al*., 2015).

In Greece, the favorable calcareous substrate and the Mediterranean climatic conditions have allowed the wide spread of viticulture since the early historic years. In North Peloponnese, the region of Nemea has enjoyed a long tradition of intensive grapevine growing for the production of its indigenous *Agiorgitiko* red wine variety. In this area, Cu-based fungicides, such as copper sulfate ($CuSO_4$), have been extensively applied to the vineyards, and as a result there is a high potential risk for soil contamination with Cu. An investigation regarding the Cu concentration levels in agricultural soils from different regions of Greece, including some vineyard soils located in Nemea, has previously been undertaken (Vavoulidou *et al.*, 2005). Nevertheless, this study was based on a reduced set of samples without delineating the magnitude of Cu accumulation throughout this region and without investigating the potential Cu migration in deeper soil layers. The aim of the present survey was to assess the extent and magnitude of Cu accumulation in Nemea vineyard soils by using the *aqua regia* and diethylene triamine pentaacetic acid (DTPA) chemical extractions and to investigate the potential for the soil to retain Cu at greater depths.

2. Materials and Methods

2.1. Soil sampling and preparation

Soil samples were collected during May and June 2015 from a total of 40 vineyard plots evenly distributed throughout the Nemea agricultural region devoted to grapevine production (Fig. 1). We specifically followed the recommendations given by Wightwick *et al.* (2006) who suggested the collection of one composite sample from as many vineyards in a region as possible instead of collecting many samples from fewer vineyards. In each vineyard, soil samples were collected from the surface soil (20 cm depth) from the middle row in the vineyard. Within this row, soil was collected from locations one-fourth, halfway and three-fourths of the way down the row, and the sub-samples were mixed in order to constitute a representative composite sample from each vineyard. Following the conclusions reached by Pietrzak and McPhail (2004) and Mirlean *et al*. (2007) who

claimed that Cu concentrations are higher at the vines than between the vine lines, we collected the surface soil samples within 30 cm of the vine line instead of collecting soil from the middle of the row. This soil sampling strategy was accomplished with the aim to detect the highest concentrations of accumulated Cu in the studied vineyard soil. Additionally, at 20 randomly selected vineyards, we collected soil at a depth of 50 cm using a soil auger. The samples were air dried at 45ºC for three days, sieved through a 2 mm plastic sieve and well homogenised. Representative portions obtained by quartation were further sieved through a 100-μm sieve and stored in room temperature.

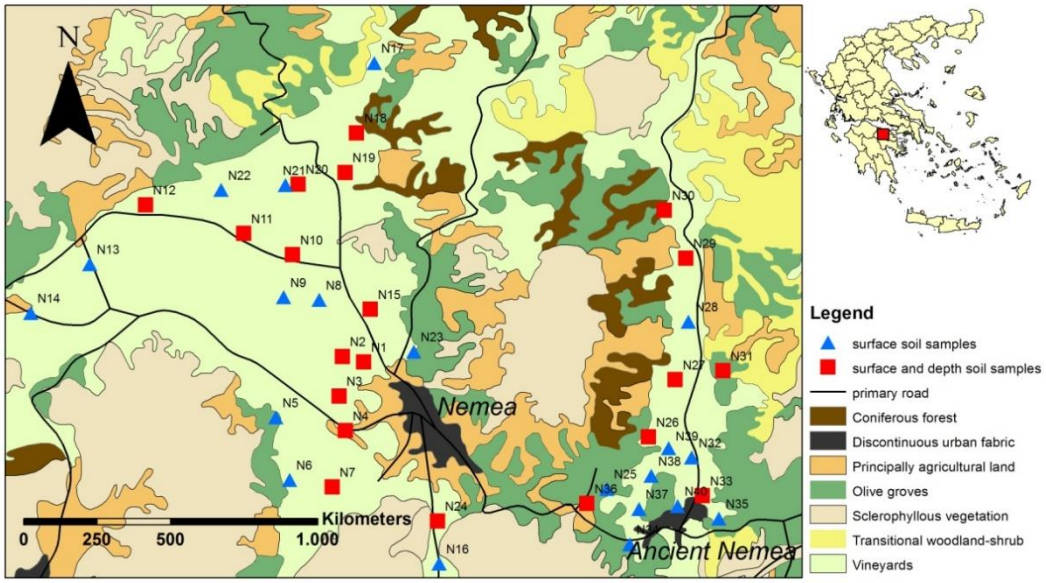

Figure 1 - Land use map of the area according to the CORINE database showing the location of the investigated vineyard plots.

2.2. Soil analysis

Soil pH and electrical conductivity were determined using a 1:1 ratio (w/v) of soil and deionised water based on the < 2 mm sample fraction. Total organic carbon (TOC) was determined on the < 100 μm fraction according to the method described by Walkley and Black (1934). Particle size distribution in the sand, silt and clay fractions was determined using the hydrometer sedimentation method. The equivalent calcium carbonate content was determined by HCl attack. The applied chemical extractions were performed on the < 100 μm fraction. Copper was extracted from soil samples using the *aqua regia* attack (HNO_3/HCl, 1:3) at the Acme Analytical Laboratories of Canada and Cu concentrations were measured using Inductively Coupled Plasma-Mass Spectrometry (ICP-MS). Hereafter and for simplicity reasons, the Cu concentrations determined by this method will be referred to as total. The availability of Cu was evaluated by the DTPA extraction because of its effectiveness in neutral to alkaline soils (Lindsay and Norvell, 1978). Concentrations of Cu in the DTPA extracts were determined by flame atomic absorption spectrometry.

3. Results

Basic physico-chemical properties and extracted Cu concentrations of the studied vineyard surface soils are given in Table 1. The strong influence of the carbonate bedrock on soil chemistry is reflected by the alkaline soil pH (median 7.8) and the high eq. $CaCO_3$ content (up to 68.9%). The soils exhibit a low TOC content (median 1.34%, max 1.99%) and a wide variation in the electrical conductivity values ranging from 256 to 1150 μS/cm. The texture in most of the vineyard-devoted soils is characterised by the predominance of the clay fraction (median 44.3%), which is expected

given that the weathering of carbonate rocks result to soil parent materials that give rise to soils with a fine texture.

Table 1 - Descriptive statistics of the analysed soil properties and Cu concentrations extracted by the aqua regia and DTPA chemical extractions for the surface soil samples (*n*=40).

Variable	Mean	Median	Minimum	Maximum
pH	7.8	7.8	7.4	8.1
Electrical Conductivity (μS/cm)	484	465	256	1150
Sand (%)	26.7	25.5	12.8	51.8
Silt (%)	31.4	31.6	20.6	39.6
Clay (%)	41.9	44.3	24.6	58.6
$CaCO_3$ (%)	42.7	41.0	9.8	68.9
TOC (%)	1.35	1.34	0.68	1.99
Cu (aqua regia), mg kg^{-1}	116	111	33.1	291
Cu DTPA, mg kg^{-1}	22.6	21.3	3.2	59.4

The total Cu concentrations in the surface vineyard soils varied from 33.1 to 291 mg kg^{-1} with a median value of 111 mg kg^{-1}. The average Cu content observed in the 0-20 cm soil layer by the DTPA extraction was 22.6 mg kg^{-1}, with a maximum concentration of 59.4 mg kg^{-1}. No significant differences could be found in Cu variation with depth ($p > 0.05$, one way ANOVA) based on the results from the 20 vineyard plots where soil samples were collected from both the surface and deeper soil horizons. An inspection of the variation in Cu amounts as a function of soil depth (Figure 2a and 2b) indicates that the classical expected decrease with depth is not evident for all the vineyards; for some vineyards, the Cu concentrations (for both metal forms) can remain either the same (e.g. for the investigated vineyards coded as N7, N11 and N18) or considerably increased (e.g. for the vineyards coded as N15 and N10).

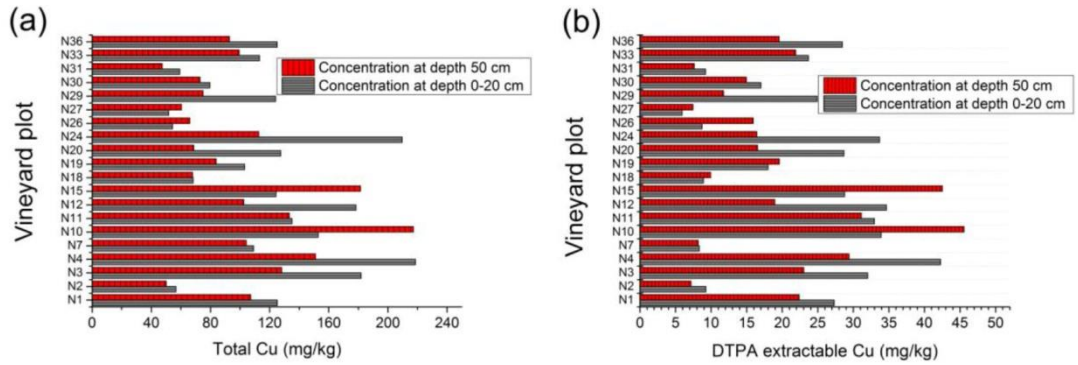

Figure 2 - Total (a) and DTPA (b) extractable Cu concentrations at two depths (0-20 cm and 50 cm) in 20 vineyard soils from Nemea.

4. Discussion

The vineyard soils from Nemea presented elevated Cu concentrations when compared to the world average Cu content of 20 mg kg^{-1} for non-contaminated soils (Kabata-Pendias and Pendias, 2001). Copper has a tendency to be excluded from carbonate rocks, sandstones and calcareous shales (Kabata-Pendias and Pendias, 2001). Since the local geology is characterised by the presence of such rocks we consider that weathering and erosion has minimum contribution to the observed soil

Cu enrichment. Moreover, Cu concentrations in background uncultivated soil samples from the adjacent Argolida area, which is characterized by occurrences of similar rock types and therefore similar soil parent material, ranged from 17.24 to 42.81 mg kg^{-1} (Kelepertzis, 2014). Such data clearly demonstrate that the source of Cu in the studied vineyard soils could be attributed to the application of Cu-based fungicides. Furthermore, the low contents of Zn and Cd in the studied soils (data not presented in this study) provide further evidence that the fungicide treatments should be regarded as the principal source for the established soil Cu enrichment. These elements are typical tracers of fertilizer and manure application in agricultural soils (Kelepertzis, 2014).

Our results are comparable to those reported from studies in vineyards within other European countries. In particular, the total Cu concentrations in the present study are consistent with those found in the soils of vineyards in Italy (mean 130 mg kg^{-1}, Deluisa *et al.*, 1996), France (mean 99 mg kg^{-1}, Brun *et al.*, 1998) and NW Iberian Peninsula (mean 163 mg kg^{-1}, Fernández-Calviño *et al.*, 2009). The levels of concentrations tend to be lower than those found in our study for the Australian vineyards (Wightwick *et al*., 2006) and for vineyards from the Czech Republic (Komárek *et al*., 2008), probably due to the lower average annual usage of Cu-based fungicides. On the contrary, Cu concentrations in Brazilian vineyards and in vineyards from Champagne area, France, can reach up to 3200 mg/kg^{-1} and 1500 mg/kg^{-1} respectively, because of the exceptionally high volumes of fungicides that are needed in areas with greater humidity and precipitation for diminishing downy mildew attacks (Mirlean *et al*., 2007).

Interestingly, a wide variation in the Cu concentrations is observed for the soils of the studied vineyards since the values are fluctuating from 33.1 to 291 mg kg^{-1} (Table 1). In general, differences in the Cu concentrations among vineyards from the same region could be ascribed to variation in soil properties, topography and Cu application history. In the present study and in line with findings by Vavoulidou *et al.* (2005) and Deluisa *et al.* (1996), no significant correlation was found between the analysed soil parameters and the Cu concentrations, probably due to the relatively narrow range of values of the soil properties. Only a weak positive correlation was found between the organic content and the Cu total concentrations (r=0.37, p=0.02) indicative though of Cu-humic complexes as a result of the long history of Cu application and the humification processes. The dispersion of Cu-enriched soil particles via runoff and soil erosion could be an influencing factor for the observed variation in Cu concentrations; nonetheless, the majority of the studied vineyards is exclusively located in the plain area (approximately 300 m a.s.l.), and as a result the topography can be reasonably regarded to have a relatively minor influence on the extent of Cu accumulation. According to Mackie *et al.* (2012) the effect of topography on Cu accumulation in vineyard soil is rather unclear and probably is masked when other determinants are taken into consideration. We speculate that the vineyard age is the main parameter that determines Cu concentrations since some vineyards in the Nemea region have been cultivated for more than 100 years. Previous studies have demonstrated that as vineyards age they are subjected to prolonged periods of fungicide treatments resulting to a more pronounced Cu accumulation (Romić *et al*., 2014; Rusjan *et al*., 2007). The Bordeaux mixture [$CuSO_4$+$Ca(OH)_2$] has been widely used since the end of 19th century in various countries, for example in Croatia (Romić *et al*., 2014) and in France (McBride *et al*., 1981), but we have not been able to verify the exact time period that this material was first used in the area of Nemea.

Copper accumulates mainly in the topsoil following fungicidal sprays application because of its complexation with organic matter and affinity for Fe oxyhydroxides and decreases with depth (Komárek *et al*., 2010); this pattern was also seen for almost half of the vineyard plots where a soil sample from a deeper soil horizon was obtained (Fig. 2a). However and contrary to the general concession that Cu eventually returns to natural levels at a maximum depth of -50 cm, the studied vineyards at this particular depth exhibited a median soil Cu concentration of 96.1 mg kg^{-1} (n=20) which is considerably higher than the background concentrations (Kelepertzis, 2014). Furthermore, in some cases Cu concentrations remain either the same or even increase down to 50 cm depth (Fig. 2a) pointing out to a specific process that results to Cu migration deeper into the soil profile.

Considering the alkaline pH of the investigated vineyard soils that does not favor the mobility of Cu, leaching should be excluded. Moreover, the predominance of clay fraction provides plethora of cation exchange sites for Cu adsorption and neither promotes the opening of transport routes of water for the removal of minerals and soil particles nor shows any cracks during the dry summer period due to minor water application in vines; as a result, the process of Cu eluviation in these soils should be restricted. Soil disturbance by tillage should be the key reason for the redistribution of Cu-enriched particles within the profile (Romić *et al*., 2014) resulting to the significant accumulated Cu levels at 50 cm depth.

In the present study, we applied the DTPA chemical extraction for assessing the Cu availability. This chemical reagent uses a strong ligand that allows Cu desorption from the solid matrix through the mechanism of complexation. It was originally developed for the determination of Cu, Zn, Fe and Mn deficiency in neutral and alkaline soils (Lindsay and Norvell, 1978), and is has been frequently adopted for assessing Cu availability in vineyard soils (examples given by Brun *et al*., 1998; Deluisa *et al*., 1996 and Romić *et al*., 2014). The average available Cu concentrations were almost identical for both the surface and deep soil samples (18.7 and 22.6 mg kg^{-1}, respectively) and were quite similar with the mean value of 15.4 mg kg^{-1} reported by Vavoulidou *et al.* (2005) for vineyard soils from the same area. The availability ratios that were calculated by dividing the Cu amounts obtained by the DTPA extraction over the total soil content, were almost the same for both the surface soils and the soils collected at 50 cm depth (Fig. 3). Such data further support the evidence for soil disturbance in Nemea area, as result of vineyard soil tilling by the local landowners. In the case of vineyard soils from Czech Republic (Komárek *et al*., 2008) and Italy (Deluisa *et al*., 2006), the Cu availability, both in terms of the actual values and relative to the total content, was significantly higher in the superficial soil layer, perhaps as a result of specific local cultivation tillage implements that are restricted to the surface soil. In addition, an excellent positive correlation coefficient (r=0.94, p=0.000) was found between the DTPA-extractable Cu and the respective total Cu content for the investigated soil samples from Nemea, in agreement with findings by Deluisa *et al.* (1996) and Romić *et al*. (2014). Linear regression analysis demonstrated that the available Cu concentrations can be accurately predicted by the corresponding total content ($Cu_{DTPA} = -2.82 + 0.220Cu_{total}$, R^2_{adj} = 87.4 %). Considering that the available Cu is part of the total Cu concentration, this strong correlation indicates a common source of both metal forms, which is the intensive fungicide application in the vineyards of Nemea area.

Copper is an essential micronutrient for plants and is involved in several metabolic processes. Despite its essentiality, excess Cu in soil has phytotoxic effects, including plant growth retardation and leaf chlorosis (Kabata Pendias and Pendias, 2001). The range of Cu concentrations determined in this study is not expected to cause phytotoxicity considering both monocotyledon and dicotyledon plants (toxicity thresholds are 18-537 mg kg-1 and 36-698 mg kg-1, respectively) (Oorts, 2013). In addition and based on the threshold of human dietary toxicity for Cu (10 mg kg^{-1}), the critical concentrations of total and available (DTPA) Cu in the soil were found to be 430 and 269 mg kg^{-1} for pakchoi, 608 and 313 mg kg^{-1} for celery, and 835 and 339 mg kg^{-1} for Chinese cabbage, respectively (Yang *et al*., 2002). The total and DTPA-extracted Cu concentrations as well as the alkaline pH values that determined in the investigated soils do not support potential phytotoxicity problems in the agricultural region of Nemea.

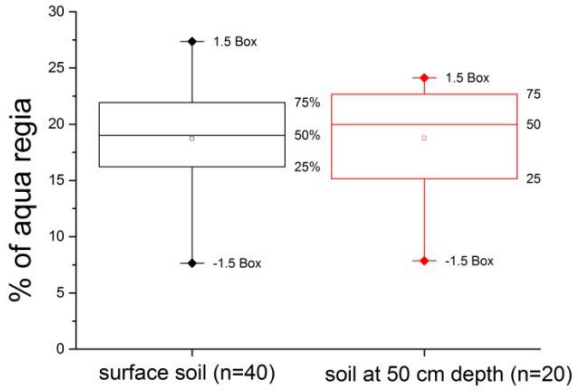

Figure 3 - Ratio of the Cu concentrations extracted by the DTPA method relative to the total soil content in the vineyard soils from Nemea.

5. Conclusions

Similar to agricultural areas around the world where Cu-based fungicides have been extensively applied, the calcareous vineyard soils from Nemea display elevated Cu concentrations that are much higher than the background levels. A wide range of Cu concentrations has been determined and the extent of Cu accumulation could be linked to the age of individual vineyard and the associated Cu application history, but such information cannot be easily acquired. Copper has been migrated through the soil profile, at least to a 50 cm depth, and this pattern is attributed to soil disturbance by tillage agricultural practices. As a consequence, the availability of Cu, as was evaluated by the DTPA extraction, does not demonstrate differences between the surface and the deeper soil samples. The DTPA-extracted Cu concentrations correlate significantly with the respective Cu total content in the soil indicating a common source of both metal forms in the soils of the area. Although the alkaline nature of the studied vineyard soils is certainly a limiting factor of plant uptake, the application rates of Cu-based fungicidal sprays should be reduced in order Cu accumulation does not reach levels that can inhibit plant growth.

6. Acknowledgments

The Municipality of Nemea is acknowledged for financial support covering the geochemical analyses at the ACME Analytical Laboratories.

7. References

Brun, L.A., Maillet, J., Richarte, J., Herrmann, P. and Remy, J.C., 1998. Relationships between extractable copper, soil properties and copper uptake by wild plants in vineyard soils, *Environmental Pollution*, 102, 151-161.

CORINE land cove, 1994, Technical Guide Office for Official Publications of the European Communities, Luxembourg (1994).

Deluisa, A., Giandon, P., Aichner, M., Bortolami, P., Bruna, L., Lupetti, A., Nardelli, F. and Stringari, G., 1996. Copper pollution in Italian vineyard soils, *Communications in Soil Sciences and Plant Analysis*, 27, 1537-1548.

Fernández-Calviño, D., Nóvoa-Muñoz, J.C., Díaz-Raviña, M. and Arias-Estévez, M., 2009. Copper accumulation and fractionation in vineyard soils from temperate humid zone (NW Iberian Peninsula), *Geoderma*, 153, 119-129.

Kabata-Pendias, A. and Pendias, H., 2001. Trace elements in soils and plants, Third edition, CRC Press, NW.
Kelepertzis, E., 2014. Accumulation of heavy metals in agricultural soils of Mediterranean: Insights from Argolida Basin, Peloponnese, Greece, *Geoderma*, 221-222, 82-90.
Kelepertzis, E., Paraskevopoulou, V., Argyraki, A., Fligos, G. and Chalkiadaki, O., 2015. Evaluation of single extraction procedures for the assessment of heavy metal extractability in citrus agricultural soil of a typical Mediterranean environment (Argolida, Greece), *Journal of Soils and Sediments*, in press.
Komárek, M., Száková, J., Rohošková, M., Javorská, H., Chrastný, V. and Balík, J., 2008. Copper contamination of vineyard soils from small wine producers: A case study from the Czech Republic, *Geoderma*, 147, 16-22.
Komárek, M., Čadková, E., Chrastny, V., Bordas, F. and Bollinger, J.-C., 2010. Contamination of vineyard soils with fungicides: A review of environmental and toxicological aspects, *Environment International*, 36, 138-151.
Lindsay, W.L. and Norvell, W.A., 1978. Development of a DTPA soil test for zinc, iron, manganese and copper, *Soil Science Society of America Journal*, 42, 421-428.
Mackie, K.A., Müller, T. and Kandeler, E., 2012. Remediation of copper in vineyards - A mini review, *Environmental Pollution*, 167, 16-26.
McBride, M., Tiller, K. and Merry, R., 1981. Copper in soils and plants, Academic Press, Sydney.
Mirlean, N., Roisenberg, A. and Chies, J.O., 2007. Metal contamination of vineyard soils in wet subtropics (southern Brazil), *Environmental Pollution*, 149, 10-17.
Oorts, K., 2013. Copper. *In:* Alloway, B.J., *ed*., Heavy metals in soils, Trace metals and metalloids in soils and their bioavailability, 3rd edition, Springer Dordrecht Heidelberg.
Pietrzak, U. and McPhail, D.C., 2004. Copper accumulation, distribution and fractionation in vineyards soils of Victoria, Australia, *Geoderma*, 122, 151-166.
Romić, M., Matijević, L., Bakić, H. and Romić, D., 2014. Copper accumulation in vineyard soils: Distribution, fractionation and bioavailability assessment. *In*: Hernandez-Soriano, M.C., *ed*., Environmental Risk Assessment of Soil Contamination, doi: 10.5772/57086.
Rusjan, D., Strlič, M., Pucko, D. and Korošec-Koruza, Z., 2007. Copper accumulation regarding the soil characteristics in Sub-Mediterranean vineyards of Slovenia, *Geoderma*, 141, 111-118.
Vavoulidou, E., Avramides, E.J., Papadopoulos, P., Dimirkou, A., Charoulis, A. and Konstantinidou-Doltsinis, S., 2005. Copper content in agricultural soils related to cropping systems in different regions of Greece, *Communications in Soil Science and Plant Analysis*, 36, 759-773.
Walkley, A. and Black, I.A., 1934. An examination of the Degtjareff method for determining soil organic matter, and a proposed modification of the chromic acid titration method, Soil Science, 37, 29-37.
Wightwick, A., Mollah, M., Smith, J. and MacGregor, A., 2006. Sampling considerations for surveying copper concentrations in Australian vineyard soils, *Australian Journal of Soil Research*, 44, 711-717.
Wightwick, A.M., Mollah, M.R., Partington, D.L. and Allinson, G., 2008. Copper fungicide residues in Australian vineyard soils, *Journal of Agricultural and Food Chemistry*, 56, 2457-2464.
Yang, X-E., Long, X-X., Ni, W-Z., Ye, Z-Q., He, Z-L., Stoffella, P.J. and Calvert, D.V., 2002. Assessing copper thresholds for phytotoxicity and potential dietary toxicity in selected vegetable crops, *Journal Environmental Science and Health Part B*, B37, 625-635.

Δελτίο της Ελληνικής Γεωλογικής Εταιρίας, τόμος L, σελ. 2200-2209
Πρακτικά 14ου Διεθνούς Συνεδρίου, Θεσσαλονίκη, Μάιος 2016

Bulletin of the Geological Society of Greece, vol. L, p. 2200-2209
Proceedings of the 14th International Congress, Thessaloniki, May 2016

ANTIMONY FIXATION IN SOLID PHASES AT THE HYDROTHERMAL FIELD OF KOLUMBO SUBMARINE ARC-VOLCANO (SANTORINI): DEPOSITION MODEL AND ENVIRONMENTAL IMPLICATIONS

Kilias S.P.[1], Gousgouni M.[1], Godelitsas A.[1], Gamaletsos P.[2], Mertzimekis T.J.[3], Nomikou P.[1], Argyraki A.[1], Goettlicher J.[4], Steininger R.[4] and Papanikolaou D.[1]

[1]National and Kapodistrian University of Athens(NKUA), Department of Geology and Geoenvironment,15785, Athens, Greece, mgousgouni@gmail.com, kilias@geol.uoa.gr, agodel@geol.uoa.gr, evinom@geol.uoa.gr, argyraki@geol.uoa.gr, dpapan@geol.uoa.gr
[2]National Technical University of Athens (NTUA), Athens, Greece, platongamaletsos@metal.ntua.gr
[3]National and Kapodistrian University of Athens, Department of Physics, 15785, Athens, Greece tmertzi@phys.uoa.gr
[4]Karlsruhe Institute of Technology, ANKA Synchrotron Facility, Hermann-von-Helmholtz-Platz 1, 76344 Eggenstein, Germany, joerg.goettlicher@kit.edu, ralph.steininger@kit.edu

Abstract

Antimony, an emergent global contaminant, that is hydrothermally discharged along with other epithermal metals(-loids) (Au, As, Hg, Ag, Tl, Ag) onto Kolumbo volcano's shallow (<500 m water depth) crater seabed, is fixed either in pyrite, orpiment-like As-sulfides, and ferrihydrite-like Fe-oxy(hydro)oxides, or forms independent Pb(Zn)-Sb sulfosalts, of layered Sb-rich (up to 2.2 wt%) chimneys. High concentrations of Sb (≤ 27.2 wt%) are found in early colloform chemically-zoned hydrothermal pyrite, and later orpiment (As_2S_3)-type As-sulfide phases (≤16.09 wt %), along individual micron-scale growth zones. Antimony in pyrite may occur in the relatively more toxic trivalent (or lower valence) (Sb^{3+}) rather than pentavalent (Sb^{5+}) forms. Lead (Pb) always occurs with Sb in growth zones where the abundances of Sb and Pb vary inversely with Fe and S, suggesting that Sb and Pb occur either as homogeneously distributed sulfosalt nanoparticles of Sb and Pb and/or lattice bound trace elements. These findings indicate the solid phases that fix Sb on the seafloor are crucial for high- grade concentration during shallow-water hydrothermal polymetallic mineralization, and reducing the high hydrothermal flux of this notorious environmental toxin to seawater, near the fishing area of Santorini that is also one of the most popular tourist places in the world.
Keywords: *contaminant, epithermal, Aegean.*

Περίληψη

Αντιμόνιο, ένας αναδυόμενος παγκόσμιος ρυπαντής, που εκλύεται υδροθερμικά μαζί με επιθερμικά μέταλλα/μεταλλοειδή (Au, As, Hg, Ag, Tl, Ag) στον πυθμένα του κρατήρα του υποθαλάσσιου ηφαιστείου Κολούμπο σε βάθος <500 m, ενσωματώνεται σε σιδηροπυρίτη, σε αρσενικούχα σουλφίδια τύπου σανδαράχης και οξυ-υδροξείδια Fe τύπου σιδηρουδρίτη,

ή σχηματίζει ανεξάρτητα θειοάλατα Pb(Zn)-S, από καμινάδες πλούσιες σε Sb (≤ 2.2 % κ.β). Υψηλές συγκεντρώσεις αντιμονίου (≤ 27.2 wt%) μετρήθηκαν στον πρώιμο κολλοφορμικό σιδηροπυρίτη, και φάσεις σουλφιδίων τύπου σανδαράχης (≤16.09 wt %), σε ζώνες κλίμακας μικρόμετρων (μm) . Το αντιμόνιο στον σιδηροπυρίτη μπορεί να υφίσταται σαν τοξικό τρισθενές Sb^{3+} (ή χαμηλότερου σθένους) παρά σαν πεντασθενές Sb^{5+}. Ο μόλυβδος (Pb) συνυπάρχει πάντα με το Sb σε ζώνες ανάπτυξης όπου οι περιεκτικότητες των Sb και Pb ποικίλλουν αντίστροφα σε σχέση με Fe και S, προτείνοντας ότι τα Sb και Pb απαντώνται είτε σαν νανοσωματίδια θειοαλάτων Sb και Pb με ομοιογενή κατανομή ή ιχνοστοιχεία υπό μορφή στερεού διαλύματος. Τα ευρήματα αυτά υποδεικνύουν ότι οι στερεές φάσεις που ενσωματώνουν Sb έχουν κρίσιμη σημασία τόσο στον σχηματισμό υδροθερμικής πολυμεταλλικής μεταλλοφορίας υψηλών συγκεντρώσεων σε μικρά βάθη πυθμένα, όσο και στην ελάττωση της υδροθερμικής έκλυσης αυτού του τοξικού μετάλλου στο θαλασσινό νερό, κοντά σε περιοχές αλιείας της Σαντόρίνης που αποτελεί επίσης δημοφιλή τουριστικό προορισμό.
Λέξεις κλειδιά: *ρυπαντήςς, επιθερμικό, Αιγαίο*.

1. Introduction

Antimony (Sb) bears economic and environmental importance: it belongs to the critical raw materials that are crucial to Europe's economy; then again Sb is an emerging toxic pollutant of priority interest (e.g. EU Commission, 2014; Filella *et al.*, 2009; Amarasiriwardena and Wu, 2011).

High amounts of Sb can be discharged into the oceans by continental riverine runoff affected by mining or industrial effluents (Filella *et al.*, 2002a, b) and seafloor hydrothermal fluids which may discharge Sb at concentrations up to several hundred times those of seawater (e.g. Fouquet *et al.*, 2010). The toxicity, the solubility, and adsorption properties of Sb to natural minerals depend on the oxidation state (Sb^{3+} and Sb^{5+}) (Filella *et al.*, 2002a), however, key aspects of the environmental chemistry and the mechanisms of concentration of Sb in natural systems, and its global biogeochemical cycle, remain poorly understood. More specifically, despite its importance for understanding the genesis and metal enrichment of currently explored ancient VMS deposits (e.g. Au, which is often associated with As and Sb), understanding the distribution of Sb and related trace metals during the formation and transformation of massive sulfides on the modern seafloor, and especially shallow submarine hydrothermal systems, remains tentative (Filella *et al.*, 2002a; Filella *et al.*, 2009; Majzlan and Fillela, 2012; Meleketseva *et al.*, 2014; Wohlgemuth-Ueberwasser *et al.*, 2015; Keith *et al.*, 2016).

A recent study by Kilias *et al.* (2013) has highlighted the active Kolumbo Hydrothermal Field (KHF) of the Kolumbo shallow-submarine (<600 m) arc-volcano, Santorini, as an Sb (±Tl, Hg) geochemical and potential economic anomaly compared to the rest of the Hellenic Volcanic arc (HVA), and the importance of seafloor hydrothermal activity as a source of potentially toxic trace metals in areas exploited by fishing in the Aegean Sea. The 5 Ma-to-present HVA is unique in as much that arc-volcanism and seafloor hydrothermal activity occur in thinned continental crust (Kilias *et al.*, 2013a, and references therein).

The Kolumbo active shallow-submarine arc-volcano, Santorini (Cantner *et al.*, 2014; Hubscher *et al.*, 2015) belongs to an active volcano-tectonic field that runs sub-parallel to the NE-SW Christianna-Santorini-Kolumbo tectonic zone in the central HVA (Nomikou *et al.*, 2013). The KHF (600X1200 m) was discovered (Sigurdsson *et al.*, 2006) at 492-504 m depth on the N floor of the density-stratified acidic (pH~ 5) Kolumbo crater (Carey *et al.*, 2013), and consists of Fe (oxy)hydroxide rich sediments (T<70 ^{o}C), and polymetallic diffuser chimneys and mounds, some with active bubble streaming (99% CO_2) and aqueous fluid shimmering at T_{max} 220^{o}C. The chimneys are uniquely enriched in Sb+Tl+Hg [Sb, avg.: 8,330 ppm; max: 2.2 wt%; Tl, avg.:510 ppm; max: 1,000 ppm; Hg, avg.: 397 ppm; max:1,070)](Kilias *et al.*, 2013a), and comprise epithermal geochemical association (Au, As, Sb, Hg, Ag, Tl, Ag) and a new active analogue style of hybrid epithermal-VMS mineralization (Kilias *et al.*, 2013a). Hydrothermal chimneys are typically layered

comprising: (a) a thick "inner sulfide-sulfate core" (ISSC), (b) a thin outer As-sulfide dominated layer (OAsL), and, (c) an Fe oxyhydroxide-dominated microbial Fe crust (SFeC); interior hydrothermal conduit networks are lined by unidentified Sb-Zn-S phases (IPCN). ISSC sulfides comprise, according to powder-XRD (PXRD) and SEM-EDS, crystalline pyrite, sphalerite and galena, and a PXRD-amorphous (hereafter amorphous) Pb-Sb sulphosalts, in a barite matrix. The OAsL consists of amorphous orpiment (As_2S_3)-type phases within a barite and gypsum matrix, whereas amorphous ferrihydrite-type phases dominate the SFeC; the interior IPCN are lined by barite and gypsum overgrown by metallic aggregates of amorphous Sb-Zn-S phases which are overgrown by amorphous K-Mg-Al-silicate, and/or Al-K-Fe-sulphate phases (Kilias *et al.*, 2013a).

This paper will focus on the concentration and modification of Sb in hydrothermal mineral phases of the KHF, and the genetic and environmental significance.

2. Materials and Methods

2.1. Sampling

The studied samples were recovered in September 2011 during the NA014 ("Hellenic Volcanic Arc and Cretan Basin") oceanographic expedition of the "New Frontiers in Ocean Exploration 2011" project (Principal Investigator Robert Ballard, Ocean Exploration Trust (OET), University of Rhode Island URI, USA). Chief scientists for NA014 were Katherine Croff Bell (Ocean Exploration Trust, University of Rhode Island (URI) USA, and Paraskevi Nomikou (NKUA, Dept. of Geology and Geoenvironment, Greece). The expedition used Exploration Vessel (E/V) Nautilus and was sponsored by: (1) Institute for Exploration (IFE), a division of Mystic Aquarium and Institute for Exploration (MAIFE); (2) National Geographic Society; (3) NOAA Office of Ocean Exploration and Research; (3) Ocean Exploration Trust (OET); (4) Office of Naval Research (ONR). The E/V Nautilus is owned and operated by the Ocean Exploration Trust and University of Rhode Island (URI)-Center for Ocean Exploration and is equipped with the remotely operated vehicles (ROVs) Hercules and Argus. Sampling campaign and methods are detailed in Ocean Exploration Trust and URI Center for Ocean Exploration-State File No. F2011-049 (2012) and Kilias *et al.* (2013a).

2.2. Optical microscopy and Scanning electron microscopy

Optical microscopy in transmitted and reflected light and Scanning Electron Microscopy-Energy Dispersive Spectrometry (SEM-EDS) techniques were used for mineral identification and textural interpretation. SEM-EDS investigation of carbon-coated free surfaces and polished thin sections and blocks was performed using a Jeol JSM-5600 SEM equipped with an Oxford EDS, at the Department of Geology and Geoenvironment, N.K.U.A. The conditions for semi-quantitative analyses were: Accelerating Voltage: 20 kV, Beam Current: 0,5 nA, Livetime: 50 sec, Beam Diameter: < 2 μm.

2.3. Synchrotron micro-X-ray Absorption Near Edge Structurespectroscopy

The Synchrotron Radiation (SR) study was conducted at the SUL-X beam line of ANKA Synchotron facility, Karlsruhe Institute of Technology (KIT), Germany. In order to determine the chemical and structural character of Sb an X-ray Absorption Near Edge Structure spectroscopic investigation was performed on the ISSC material in microscale at the Sb L_3-edge (4132 eV). Micro-XANES spectra were obtained in the polished blocks after logging of micro-areas using a Zeiss Axio Imager.Z1m (with Axiovision 4.7 software) motorized optical microscope in reflected light. . Elemental Sb, stibnite ($Sb^{3+}{}_2O_3$) and tripuhyite ($Fe^{3+}Sb^{5+}O_4$), were used as reference materials of various Sb species. The spectra were processed using Athena software (Ravel *et al.*, 2005).

3. Results

3.1. Mineralogy and textures

Three pyrite (according to SEM-EDS and PXRD; Kilias *et al.* 2013a) textures representing relevant generations are distinguished which are linked with initial crystallization and following recrystallization (Wohlgemuth-Ueberwasser *et al.*, 2015). Pyrite 1 includes the most immature textures which are distinctly banded and/or concentrically laminated colloform, as well as oncoid-like and microstromatolite-like (Figs. 1A, B, D, E, F, H, I). More compact but fine-grained porous pyrite aggregates (pyrite 2) (Figs. 1D, I) represents an intermediate stage of the modification of primary precipitates (pyrite 1) to fully massive subhedral to euhedral pyrite 3 (Fig. 1C), as porosity is reduced during replacement and recrystallization processes (Wohlgemuth-Ueberwasser *et al.*, 2015).

3.2. Mineral chemistry and Sb enrichment (SEM-EDS)

Antimony is selectively partitioned in pyrite 1 or forms autonomous antimoniferous sulphosalt phases and rare stibnite needles (Fig. 1). Concentrically laminated pyrite 1 shows µm-scale compositional variations along the laminae, representing growth zones with different Fe and S, as well as Sb and Pb trace element compositions (Fig. 2). The Fe and S contents vary from 24.26 to 46.36 wt% and 40.60 to 54.83 wt%, respectively, related to trace metal substitution in pyrite 1(Reich *et al.*, 2013) (Fig. 2; Table 1).

Table 1 - Summary of chemical composition (semi-quantitative EDS data) for pyrite 1, pyrite 2, orpiment-like phases and unidentified Pb-Sb sulfosalts.

Mineral/Analysis No.	Fe	S	As	Sb	Pb	Total
	wt%					
Pyrite 1/1	43.26	52.7	–	3.79	–	99.75
Pyrite 1/2	43.81	54.83	–	1.26	–	99.9
Pyrite 1/3	43.33	53.3	–	1.98	1.52	100.13
Pyrite 1/4	34.66	46.26	–	8.36	11.26	100.24
Pyrite 1/5	34.64	44.93	–	9.08	11.53	100.18
Pyrite 1/6	44.29	53.54	–	2.13	–	99.96
Pyrite 1/7	34.87	44.91	–	8.47	12.30	100.55
Pyrite 1/8	40.70	49.12	–	3.76	6.44	100.02
Pyrite 1/9	39.31	48.40	–	4.39	8.29	100.39
Pyrite 1/10	40.89	49.53	–	3.58	6.31	100.31
Pyrite 1/11	41.66	49.92	–	2.76	5.65	99.99
Pyrite 1/12	41.65	50.22	–	2.58	5.80	100.26
Pyrite 1/13	24.26	40.60	–	27.21	8.22	100.29
Pyrite 1/14	39.64	51.68	–	8.95	–	100.27
Pyrite 1/15	28.37	43.40	–	22.01	6.32	100.00
Pyrite 1/16	44.36	53.20	–	2.44	–	100.00
Pyrite 1/17	40.57	54.29	–	5.13	–	100.00
Pyrite 2/7	46.36	52.79	1.84	–	–	100.99
Pyrite 2/8	45.35	53.28	1.2	–	–	99.83
Orpiment-like/1	–	42.10	57.47	0.33	–	99.9
Orpiment-like/2	–	41.11	58.74	0.25	–	100.1
Orpiment-like/3	–	36.98	46.97	16.09	–	100.09
Pb-Sb sulfosalt/1		18.83		31.84	49.22	99.89
Pb-Sb sulfosalt/2		18.14		29.07	51.42	98.64
Pb-Sb sulfosalt/3		18.81		30.35	48.77	97.94
Pb-Sb sulfosalt/4		18.37		32.81	46.40	97.59

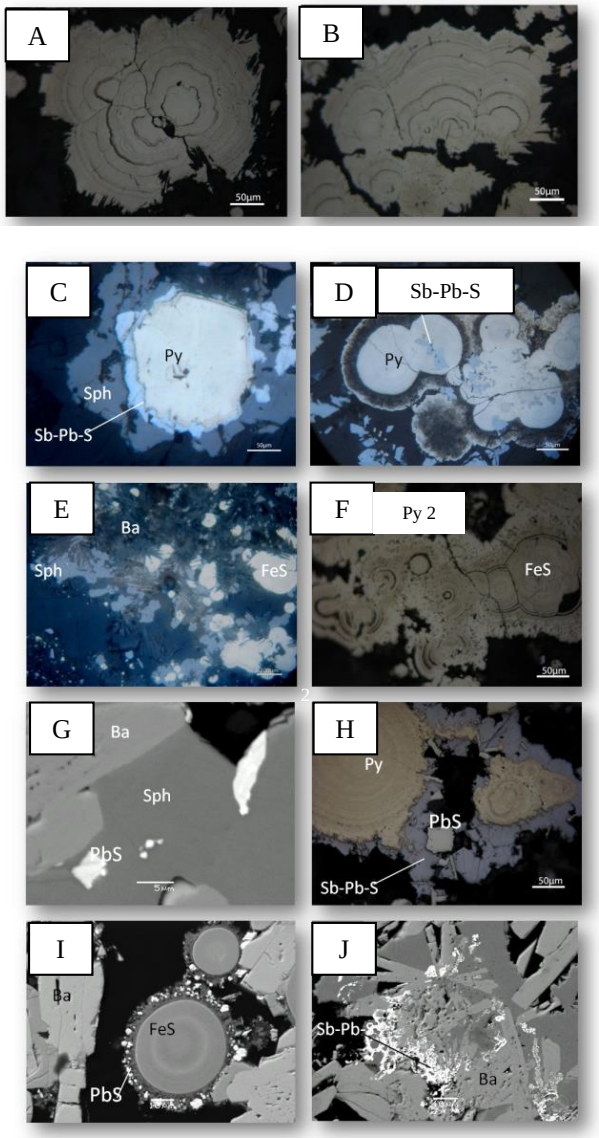

Figure 1 - Photomicrographs in reflected light (RLP) and BSE images of ISSC phases. (A, B) RLP of closely-packed aggregates of bulbous, oncoid-like and microstromatolite-like pyrite 1; (C) RLP of idiomorphic crystal of pyrite 3 (Py) mantled by Sb-Pb-sulfosalts (Sb-Pb-S) and later sphalerite (Sph); (D) RLP of anhedral Sb-Pb-sulfosalt inclusions in concentrically laminated pyrite 1overgrown by thin porous pyrite 2; Sb-Pb-sulfosalts also shown; (E) RLP of clusters of pyrite 1(FeS_2) set in a barite matrix mantled by sphalerite; (F) RLP of zoned colloform pyrite 1 (FeS_2) overgrown by a layer of spongy/porous pyrite 2(Py 2); (G) BSE image showing galena (PbS) inclusions in sphalerite (Sph) intergrown with concentrically laminated pyrite 1; (H) concentrically laminated pyrite 1 (Py) mantled by pyrite 2 and anhedral to subhedral intergrowths of Sb-Pb-sulfosalts and galena (PbS); (I) BSE image of pyrite 1 surrounded by highly porous pyrite 2 with inclusions of galena (PbS); (J) BSE image of dendritic Sb-Pb sulphosalts (Sb-Pb-S, white) mantling pyrite 1, sphalerite (dark grey) and barite laths (light gray).

Zones “bright” in BSE are enriched in Sb (up to 27.21 wt %) and Pb (up to 12.30 wt %) (Table 1), whereas zones ‘’dark grey’’ in BSE are trace element-poor (Sb up to 2.13 wt%, Pb was not detected). Porous pyrite 2 overgrowths contains As (up to 1.84 wt %), but no detectable Sb or Pb. Euhedral pyrite 3 is nearly stoichiometric devoid of detectable amounts of Sb and trace metals. Antimony contents up to 16.09 wt % have been measured along “bright” in BSE growth zones of orpiment (As_2S_3)-type As-sulphide phases of the OAsL (Table 1); moreover, SEM-EDS spectra collected from amorphous ferrihydrite-type Fe-(hydrated)-oxyhydroxides of the SFeC, and amorphous Sb-Zn sulfosalt phases of the IPCN have revealed clear signals for Sb (Gousgouni, 2014). It should be noted that the data presented in Table 1 concern preliminary semi-quantitative analyses whereas accurate EPMA (SEM-WDS) analyses, aiming in the elucidation of the exact chemical formula of the phases, will be a subject of future research.

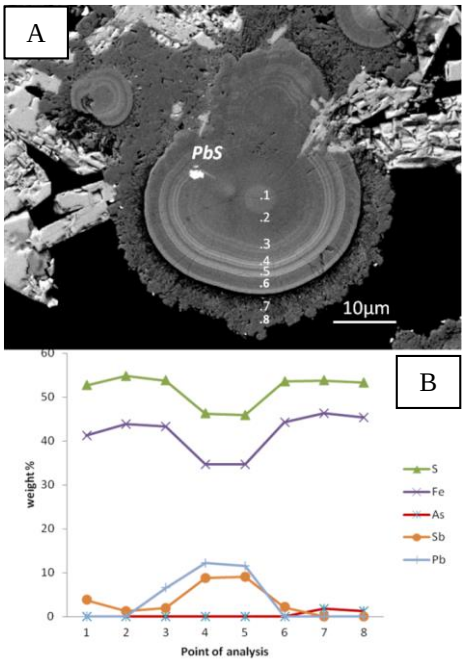

Figure 2 - (A) Backscattered electron (BSE) image, and elemental profiles (EDS semi-quantitative analyses) across concentrically laminated pyrite 1 with embedded galena (white), overgrown by thin porous spongy pyrite 2. (B) Element profile across pyrite 1 oncoid, by EDS spot analyses (Numbers on x-axis refer to analysis points) (see text for discussion).

3.3. Speciation of Sb in pyrite 1 by micro-XANES

Figure 3A shows the normalized Sb L_3-edge XANES spectra recorded from pyrite 1 of the ISSC material, and Figure XB shows derivatives of the normalized Sb L_3XANES spectra of the sample, compared to selected reference Sb spectra. Note that Sb_2O_3 is not pure and seems to contain some Sb^{5+} (see the peak in its derivative at about 4143.6 eV) which may have shifted the position of the SB_2S_3 flank to a higher energy position than for pure Sb_2S_3. The position of the second derivative peak of the sample spectrum plots significantly before the Sb^{3+} peak.

4. Discussion

Four (4) distinct modes of Sb enrichment of various minerals of ore-grade samples ($\leq$2 wt% Sb) belonging to different mineralogical zones of the Kolumbo chimneys (i.e. ISCC, OAsL, SFeC,

IPCN): **(A)** High concentrations (up to 27.2 wt% Sb) occur in µ-scale concentric zones of colloform pyrite 1 (ISSC). Here, micro-XANES spectra at the Sb L_3-edge (Fig. 3) confirms the

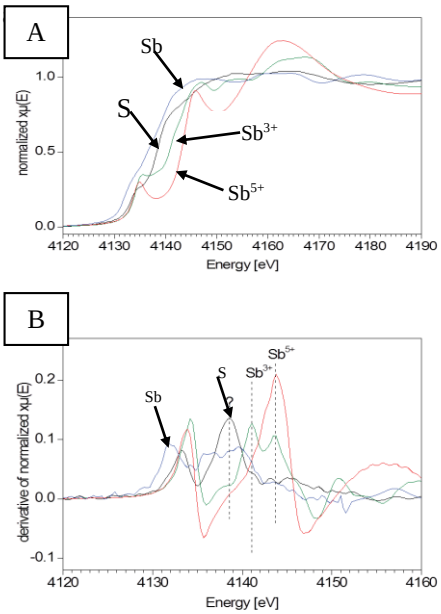

Figure 3 - (A) Normalized (edge jump of 1) Sb L_3 XANES spectra and derivatives of the normalized Sb L_3 XANES spectra(B) of the sample (S) compared to the spectra of elemental Sb (Sb), $Sb^{3+}{}_2O_3$ (Sb^{3+}) and Tripuhyite ($Fe^{3+}Sb^{5+}O_4$)(Sb^{5+}) (Kilias *et al.*, 2013b) (see text for discussion).

preferential partitioning of Sb within pyrite 1, and further reveals the possible dominance of the reduced relatively more toxic trivalent (or lower valence) (Sb^{3+}), rather than pentavalent (Sb^{5+}) species; this comes in accordance with the high organic carbon content of the ISCC ($C_{org} \leq 5.3$ % TOC) (Kilias *et al.*, 2013a); **(B)** Unidentified non-stoichimetric Pb–Sb sulphosalt phases; **(C)** High concentrations of Sb (up to 16 wt %) are also found in growth zones of amorphous colloform banded orpiment (As_2S_3)-type sulfide phases (OAsL); and, **(D)** Antimony is hosted by poorly ordered ferrihydrite-type Fe (oxy)hydroxides (SFeC), and amorphous Zn–Sb sulphosalt phases (IPCN).

The systematic Sb (and Pb) variations between different growth zones (Fig. 2) may be explained by variable fluid conditions during pyrite 1 growth or changes in the physicochemical parameters of the discharging parental fluids linked to the episodic nature of the Kolumbo hydrothermal vent system (cf. Maslennikov *et al.*, 2009; Wohlgemuth-Ueberwasser *et al.*, 2015; Keith *et al.*, 2016). Variations in the physicochemical parameters of hydrothermal fluids, namely temperature, pH, redox conditions, salinity and ligand availability, coupled by magmatic volatile contribution, are known to influence trace element composition of pyrite from modern submarine hydrothermal sulfide ores (e.g. Wohlgemuth-Ueberwasser *et al.*, 2015; Keith *et al.*, 2016, *and references therein*). Alternatively, these variations can evolve from ultra-local fluid composition variations due to short-lived fluid flow events linked to a seismic cycle, or they may suggest different chemical microenvironments within chimneys that may arise from geomicrobiological processes (Kristall *et al.*, 2011).

For seafloor hydrothermal vent precipitates, mineral texture is a measure of the maturity of the precipitates (i.e.variations in the crystallization sequence and texture of pyrite and other sulphides/sulfosalts depicted in Fig.1), which also influences the mobility of trace metals during the course of dissolution–reprecipitation processes within the vent edifices during later stage

hydrothermal activity, alteration and recrystallization; the latter might liberate trace elements to be incorporated into different phases (Wohlgemuth-Ueberwasser *et al.* 2015). The most immature textures are those of pyrite 1 (Fig. 1) which may have formed directly from hydrothermal fluids during the early stages of chimney growth (Wohlgemuth-Ueberwasser *et al.* 2015; Keith *et al.*, 2016). The final stage of recrystallization during the mature stage of chimney growth are represented by samples with well-defined, massive textures consisting of interlocking subhedral to euhedral minerals (i.e. pyrite 3; Pb-Sb sulfosalts; Fig. 1) which formed at different (higher?) temperature (Wohlgemuth-Ueberwasser *et al.* 2015). Consequently, pyrite 1 may have liberated Sb and Pb during hydrothermal recrystallization to form galena, and Pb-Sb sulfosalt phases. Because, pyrite 2 and pyrite 3 are devoid of Pb and Sb (Gousgouni, 2014), it appears that more compact but porous pyrite 2 represents an intermediate stage of the modification of primary precipitates (pyrite 1) to fully massive texture (pyrite 3), as porosity is reduced during recrystallization processes (Wohlgemuth-Ueberwasser *et al.* 2015). The tendency for a trace element depletion in late pyrite compares well with that reported for several ancient massive sulfide deposits (e.g. Maslennikov *et al.*, 2009) and the modern seafloor (Keith *et al.*, 2016).

Previous studies suggested different mechanisms for the incorporation of trace elements in pyrite. For Sb these possible mechanisms include substitution into the pyrite lattice at low temperature, non-stoichiometric substitution, and the possibility that Sb may simply be present as nanoparticles (e.g. Maslennikov *et al.*, 2009; Deditius *et al.*, 2011). Synchrotron radiation μ-XRF elemental distribution maps for Sb, Fe, Zn, and As in concentrically laminated pyrite 1 (Kilias et al 2013b) has revealed that Fe, Zn, As and Sb show laminae parallel quasi-linear distributions. Zn and Fe partly positively correlate, and As and Sb are also positively correlated in a linear manner parallel to the Fe and Zn distribution with some spots of elevated concentrations. These correlations in conjunction with the abundances of Sb and Pb that vary inversely with Fe and to S along geochemical profiles across pyrite 1 globules (Fig. 2), suggest that Sb and Pb occur either as homogeneously distributed nano-inclusions and/or lattice bound trace elements (Reich *et al.*, 2013; Keith *et al.*, 2016).

Antimony fixation in solid phases at submarine hydrothermal vents is essential for reducing the high hydrothermal flux of this toxic element to seawater and is an important part of the biogeochemical Sb-cycle. The solid phases that were found to fix Sb on the Aegean seafloor at Kolumbos are proved crucial for reducing the high hydrothermal flux of this notorious environmental toxin to seawater, near the fishing area of Santorini that is also one of the most popular tourist places in the world. Moreover, the observed enrichment of Sb^{3+} (toxic trivalent species) emphasize the weight of shallow-submarine geothermal activity as a potential source of toxic metals (Sb^{3+}) during seafloor weathering, and/or natural disasters (i.e. explosive volcanic/hydrothermal, and seismic activity).

5. Acknowledgments

Support for the operation of the E/V Nautilus was provided by the U.S. National Oceanic and Atmospheric Administration (NA06OAR4600140, NA10OAR4600127), Office of Ocean Exploration (OCE-0452478), and the Ocean Exploration Trust. The officers and the crew of the E/V Nautilus are gratefully acknowledged for their important and effective contribution to the field work and sampling. We acknowledge funding from the Special Account for Research Grants, National and Kapodistrian University of Athens (70/4/11078, 70/3/11401) and the Karlsruhe Institute of Technology-ANKA Synchrotron Radiation Facility (ENV-199).

6. References

Amarasiriwardena, D. and Wu, F., 2011. Antimony: Emerging toxic contaminant in the environment, *Microchemical Journal*, 97, 1-3.

Cantner, K., Carey, S. and Nomikou, P., 2014. Integrated volcanologic and petrologic analysis of the 1650AD eruption of Kolumbo submarine volcano, Greece, *Journal of Volcanology and Geothermal Research*, 269, 28-43.

Carey, S., Nomikou, P., Croff-Bell, K., Lilley, M., Lupton, J., Roman, C., Stathopoulou,E., Bejelou, K. and Ballard, R., 2013. CO2 degassing from hydrothermal vents at Kolumbo submarine volcano, Greece and the accumulation of acidic crater water, *Journal of Geochemical Exploration*, 20, 223-302.

Deditius, A., Utsunomiya, S., Reich, M., Kesler, S.E., Ewing, R.C., Hough, R. and Walshe, J., 2011. Trace metal nanoparticles in pyrite, *Ore Geol. Rev*., 42, 32-46.

EU Commission, 2014. Report on critical raw materials for the EU. Available online at: http://mima.geus.dk/report-on-critical-raw-materials_en.pdf.

Filella, M., Belzile, N. and Chen Yu-Wei., 2002a. Antimony in the environment: a review focused on natural waters, I Occurrence, *Earth-Science Reviews*, 57, 125-176.

Filella, M., Belzile, N., and Chen, Yu-Wei., 2002b. Antimony in the environment: a review focused on natural waters, II Relevant solution chemistry, *Earth-Science Reviews*, 59, 265-285.

Filella, M., Williams, P.A. and Belzile, N., 2009. Antimony in the environment: Knows and unknowns, *Environ, Chem*., 6, 95-105.

Fouquet, Y., Cambon, P., Etoubleau, J., Charlou, J.L., Ondréas, H., Barriga, F.J.A.S., Cherkashov, G., Semkova, T., Poroshina, I., Bohn, M., Donval, J.P., Henry, K., Murphy, P. and Rouxel, O., 2010. Geodiversity of hydrothermal processes along the Mid-Atlantic Ridge and ultramafic-hosted mineralization: a new type of oceanic Cu-Zn-Co-Au volcanogenic massive sulfide deposit. *In*: Rona, P.A., Devey, C.W., Dyment, J. and Murton, B.J., *eds*., Diversity of Hydrothermal Systems on Slow Spreading Ocean Ridges, *Geophysical Monograph*, 188, 321-367.

Gousgouni, M., 2014. Antimony fixation in solid phases at the hydrothermal field of the Kolumbo submarine arc-volcano (Santorini): Deposit model and environmental implications, Unbubl. M.Sc. thesis, National and Kapodistrian University of Athens, 167 pp.

Hübscher, C., Ruhnau, M. and Nomikou, P., 2015. Volcano-tectonic evolution of the polygenetic Kolumbo submarine volcano/Santorini (Aegean Sea), *Journal of Volcanology and Geothermal Research*, 291, 101-111.

Keith, M, Häckel F., Haase, K.M., Schwarz-Schampera, U. and Klemd, R., 2016. Race element systematics of pyrite from submarine hydrothermal vents, *Ore Geology Reviews*, 72(1), 728-745, doi:10.1016/j.oregeorev.2015.07.012.

Kilias, S.P., Godelitsas, A., Gamaletsos, P., Mertzimekis, T.J, Nomikou, P., Goettlicher, J., Steininger, R., Argyraki, A., Gousgouni, M. and Papanikolaou, D., 2013b. Antimony in hydrothermal chimneys of Kolumbo shallow-submarine vent field (Santorini, Greece) Goldschmidt 2013 Conference Abstracts, Goldschmidt 2013 Conference Abstracts, www.minersoc.org, doi:10.1180/minmag.2013.077.5.11.

Kilias, S.P., Nomikou, P., Papanikolaou, D., Polymenakou,P.N., Godelitsas, A., Argyraki, A., Carey, S., Gamaletsos, P., Mertzimekis, T.J, Stathopoulou E., Goettlicher, J., Steininger, R., Betzelou, K., Livanos, I., Christakis, C., Bell, K.C. and Scoullos, M., 2013a. New insights into hydrothermal vent processes in the unique shallow-submarine arc-volcano, Kolumbo (Santorini), *Greece. Sci. Rep*., 3, 2421, doi: 10.1038/srep02421.

Kristall, B., Nielsen, D., Hannington, M.D., Kelley, D.S. and Delaney, J.R., 2011. Chemical microenvironments within sulfide structures from the Mothra hydrothermal field: Evidence from high resolution zoning of trace elements, *Chemical Geology*, 290, 12-30.

Majzlan, J. and Fillela, M., 2012, Editorial, *In*: Antimony, Majzlan, J. and Filella, M., *eds*., Chemie der Erde - *Geochemistry*, 72(4), 1-66, doi: 10.1016/j.chemer.2012.04.002.

Maslennikov, V.V., Maslennikova, S.P., Large, R.R. and Danyushevsky, L.V., 2009. Study of trace element zonation in vent chimneys from the Silurian Yaman-Kasy volcanic hosted massive sulfide deposit (Southern Urals, Russia) using laser ablation-inductively coupled plasma mass spectrometry (LA-ICPMS), *Econ. Geol*., 104, 1111-1141.

Melekestseva, I.Y., Tret'yakov, G.A., Nimis, P., Yuminov, A.M., Maslennikov, V.V., Maslennikova, S.P., Kotlyarov, V.A., Beltenev, V.E., Danyushevsky, L.V. and Large, R., 2014. Barite-rich massive sulfides from the Semenov-1 hydrothermal field (Mid-Atlantic

Ridge, 13° 30.87′ N): Evidence for phase separation and magmatic input, *Marine Geology*, 349, 37-54.

Nomikou, P., Papanikolaou, D., Alexandri,M., Sakellariou, D. and Rousakis, G., 2013. Submarine volcanoes along the Aegean Volcanic Arc, *Tectonophysics*, 507-508, 123-146.

Ravel, B. and Newville, M., 2005. ATHENA, ARTEMIS, HEPHAESTUS: data analysis for X-ray absorption spectroscopy using IFEFFIT, *J. Synchrotron Radiat*., 12, 537-541.

Reich, M., Deditius, A., Chryssoulis, S., Li, J.-W., Ma, C.-Q., Parada, A.P., Barra, F. and Mittermayr, F., 2013. Pyrite as a record of hydrothermal fluid evolution in a porphyry copper system: a SIMS/EPMA trace element study, *Geochim. Cosmochim. Acta*, 102, 42-62.

Sigurdsson, H., Carey, S., Alexandri, M., Vougioukalakis, Croff, K., Roman, C., Sakellariou, D., Anagnostou, C., Rousakis, G., Ioakim, C., Gogou, A., Ballas, D., Misaridis, T. and Nomikou, P., 2006. Marine Investigations of Greece's Santorini Volcanic Field, EOS 87, 337-339.

Wohlgemuth-Ueberwasser, C.C., Viljoen, F., Petersen, S. and Vorster, C., 2015. Distribution and solubility limits of trace elements in hydrothermal black smoker sulfides: An in-situ LA-ICP-MS study, *Geochimica et Cosmochimica Acta*, 159, 16-41.

Δελτίο της Ελληνικής Γεωλογικής Εταιρίας, τόμος L, σελ. 2210-2220
Πρακτικά 14ου Διεθνούς Συνεδρίου, Θεσσαλονίκη, Μάιος 2016

Bulletin of the Geological Society of Greece, vol. L, p. 2210-2220
Proceedings of the 14th International Congress, Thessaloniki, May 2016

GEOCHEMICAL MODELING FOR THE ASSESSMENT OF THE CO_2 STORAGE POTENTIAL IN THE MESOHELLENIC TROUGH, NW GREECE

Koukouzas N.[1], Kypritidou Z.[2], Purser G.[3], Rochelle C.A.[3] and Vasilatos C.[2]

[1]Centre for Research and Technology Hellas, Chemical Process and Energy Resources Institute, 15125, Maroussi, Greece, koukouzas@certh.gr

[2]Department of Economic Geology and Geochemistry, Faculty of Geology and Geoenvironment, National and Kapodistrian University of Athens, 15724, Athens, Greece, zach-kyp@geol.uoa.gr

[3]Environmental Science Center, British Geological Survey, Keyworth, NG12 5GG, Nottingham, England, gemm@bgs.ac.uk, caro@bgs.ac.uk

Abstract

Sandstone of the Pentalofos formation from the Mesohellenic Trough was examined as a potential reservoir for CO_2 sequestration. Experiments were carried out into batch reactors for 6 months by mixing a simplified porewater solution saturated with CO_2 (150 bar, 70°C) with crushed sandstone. The sandstone is mainly composed of carbonates, feldspars and quartz, and secondly of clays and phyllosilicates. Chemical analysis of aqueous samples showed an increase in the concentration of dissolved ions as the experiment progressed. Geochemical kinetic models that were constructed using the PHREEQC geochemical code showed that the fluid chemistry is controlled by carbonate and feldspar dissolution, clay and quartz precipitation and cation exchange reactions. The proposed models were also used to estimate the future changes in mineralogy of the sandstone in order to evaluate its suitability as a CO_2 reservoir.
Keywords: *sequestration, sandstone, PHREEQC, reservoir, dissolution.*

Περίληψη

Κονιοποιημένο ψαμμιτικό υλικό από το σχηματισμό Πενταλόφου της Μεσοελληνικής Αύλακας χρησιμοποιήθηκε σε πειράματα αυτοκλείστου όπου αντέδρασε με άλμη (0,5M NaCl) κορεσμένη με CO_2 (150 bar, 70 °C) για 6 μήνες. Το ψαμμιτικό υλικό αποτελείτο κυρίως από ανθρακικά, αστρίους και χαλαζία, με δευτερεύοντα αργιλικά και φυλλοπυριτικά. Οι χημικές αναλύσεις των ρευστών έδειξαν αύξηση των ιόντων, ενώ στο υλικό διαπιστώθηκαν αλλαγές στην αναλογία των φάσεων. Χρησιμοποιώντας το λογισμικό PHREEQC κατασκευάστηκε γεωχημικό κινητικό μοντέλο σύμφωνα με το οποίο οι κύριες αντιδράσεις που λαμβάνουν χώρα είναι η διάλυση των ανθρακικών και αστρίων, καθώς και η ιοντοανταλλαγή. Το μοντέλο χρησιμοποιήθηκε στην πρόβλεψη της πιθανής εξέλιξης του υδροφόρου σε βάθος χρόνου για την εκτίμηση της καταλληλότητας του πετρώματος ως αποθηκευτικός χώρος CO_2.
Λέξεις κλειδιά: *δέσμευση, ψαμμίτης, PHREEQC, ταμιευτήρας, διάλυση.*

1. Introduction

CO_2 capture and underground storage (CCS) has been proposed as a satisfactory method to reduce the atmospheric CO_2 concentrations, that play the key role in greenhouse phenomenon. Storage can be attained through injection into deep saline aquifers or gas depleted reservoirs. However the selection of the proper reservoir and its caprock is not trivial as CO_2 can cause a number of geochemical reactions that can affect their integrity and trapping potential. Some of them include the acidification of pore waters, dissolution of the primary minerals and precipitation of secondary, less stable, phases, changes in porosity and permeability of the whole (Black, *et al.*, 2015; Gaus, 2010).

A useful way to study geochemical processes, and water-rock reactions linked to CO_2 storage, is through geochemical modeling applied to the lithology encountered in the Mesohellenic Trough (MT) in NW Greece. The MT is a basin with a length of over 200 km and a width of 30-40 km in NW Greece. It is characterized as the largest and most important basin of the last orogenic stage (molasse basin) of the Hellenides (Figure 1).

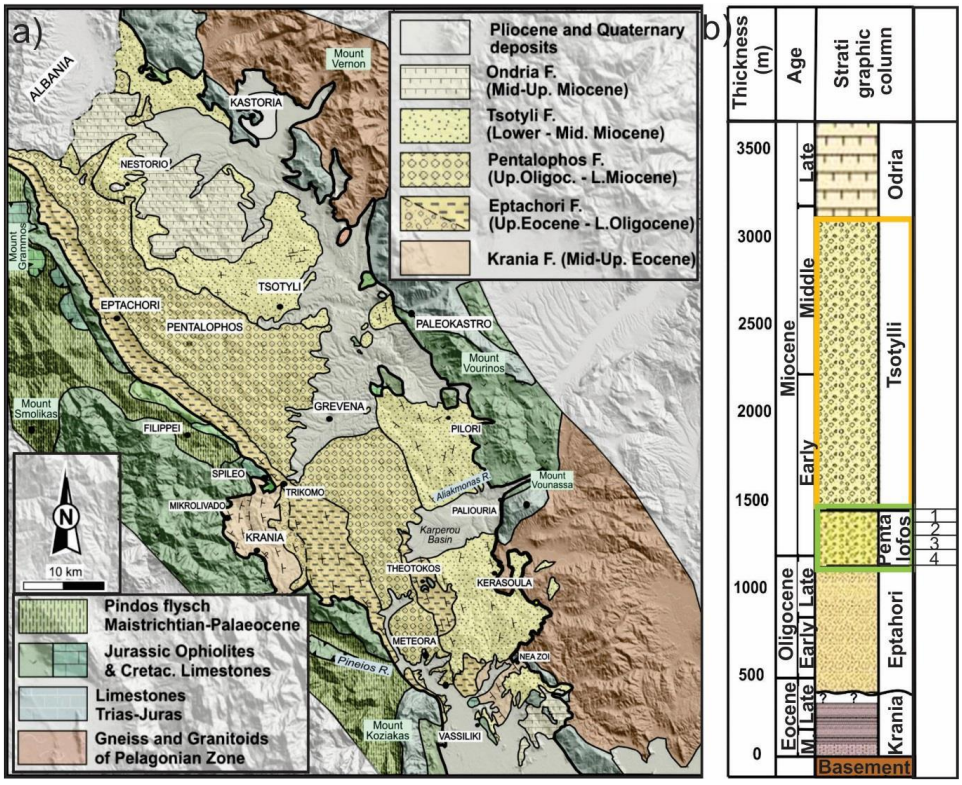

Figure 1 - Geological map (a) and stratigraphic column (b) of Mesohellenic trench (modified after Brunn (1956) and I.G.M.E. (1983) Tsotylli and Pentalofos Formations are highlighted - see text).

The sedimentary formations of the basin include deltaic conglomerates, alluvial scree, sandstones and clays of turbiditic and deltaic origin, floodplain and sandy shelf sediments, with a maximum thickness of 4 kilometers. The Tsotylli and Pentalofos Formations, correspond to local cap rock and reservoir respectively. The current work focuses on the Pentalofos Formation, with an age of Late Oligocene-Lower Miocene (25-23 Ma), which can be used as a reservoir due to its composition consisting mainly of loam and fine-grained sandstones (Vamvaka, 2009; Zelilidis *et al.*, 2002).

2. Materials and Methods

2.1. Materials

A sandstone sample from the Pentalofos Formation was used in batch reactor experiments. Quantitative mineralogical analysis of the sample before and after the reaction with CO_2 was attained by XRD analysis and data were processed using the Rietveld method.

2.2. Experimental set up and procedure

The sandstone sample was crushed and sieved to give 3 size fractions (<250, 250-500 and >500 μm). The 250-500 μm fraction was rinsed with acetone and filtered using a Buchner funnel containing a Whatman no.1 filter paper. 20g of this crushed and cleaned sandstone was mixed with 200ml of 0.5M NaCl solution (simplified porewater) inside the reaction vessel and heated in the oven to 70ºC. In order to ensure good rock-fluid mixing, it was stirred with a magnetic stirrer for 2 minutes every 4 hours (Figure 2). Periodic, rather than continuous, stirring ensured that the sandstone powder did not suffer too much mechanical abrasion.For the initial 37 days the sandstone and solution were allowed to partially equilibrate on CO_2-free conditions, with 15 bar of inert nitrogen in the headspace of the reaction vessel aiding sampling of the fluid. By day 37, the fluid had been sampled twice and addition of supercritical CO_2 (sCO_2) followed, which displaced the nitrogen initially present. CO_2 was maintained at a pressure of 150 bar for the rest of the experiment using a Teledyne ISCO 500D pump running in constant pressure mode. An additional number of 8 fluid samples were taken over this period. After a total duration of 184 days all the remaining aqueous solution that could be drained from the experiment was removed via a 'dip tube' that reached to the close to the bottom of the vessel, and its volume recorded. It was then slowly depressurised and dismantled to allow sandstone to be collected.

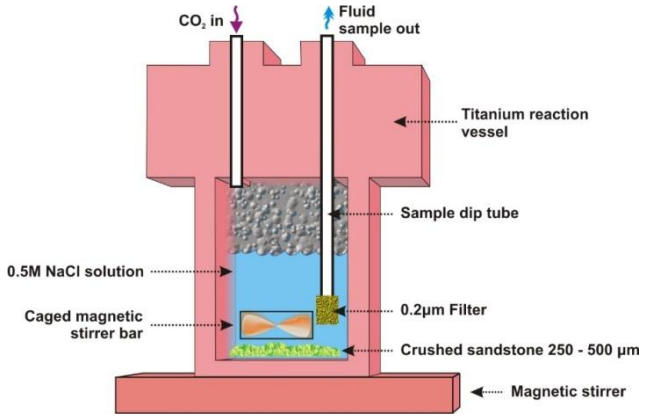

Figure 2 - Experimental arrangement for crushed sandstone sample.

2.3. Chemical Analysis

The experiment ran for approximately 6 months, during which a total of 10 fluid samples were collected. These were sub-sampled and prepared for analysis of pH, Eh (redox), anions, cations, alkalinity and iron (II) using the following methods. Most were pre-filtered through a 0.2 μm nylon Acrodisc filter. pH was measured at room temperature and pressure by an Orion bench top meter and glass pH probe calibrated using pH buffers of 4, 7 and 10 prior to sample analysis. The calibration of a Ag/AgCl Eh probe was checked using Zobell's solution prior to analysis of Eh. Alkalinity was measured using potentiometric titration as soon as practicable after sampling (usually within 1-3 days). The cation, anion and iron (II) samples were stored in a fridge at 4°C prior to analysis. Cations were analyzed using inductively coupled plasma mass spectrometry, anions by ion chromatography and reduced iron by UV-visible spectrophotometry.

2.4. Geochemical kinetic modelling

Geochemical models were constructed using the PHREEQC v.3.1 geochemical code with the llnl.dat database (Parkhust *et al.*, 1999). The parameters of reaction rates of each mineral were defined and solved by Ordinary Differential Equation (ODE) solver. The methodology followed is summarized in Figure 3. Speciation calculations were conducted on the basis of measured final solution composition for the base anions (Cl^-, HCO_3^-) and cations (Ca^{+2}, Mg^{+2}, Na^+, K^+, Al, Si, Fe_{total}). In each step, the data of previous calculations were used.

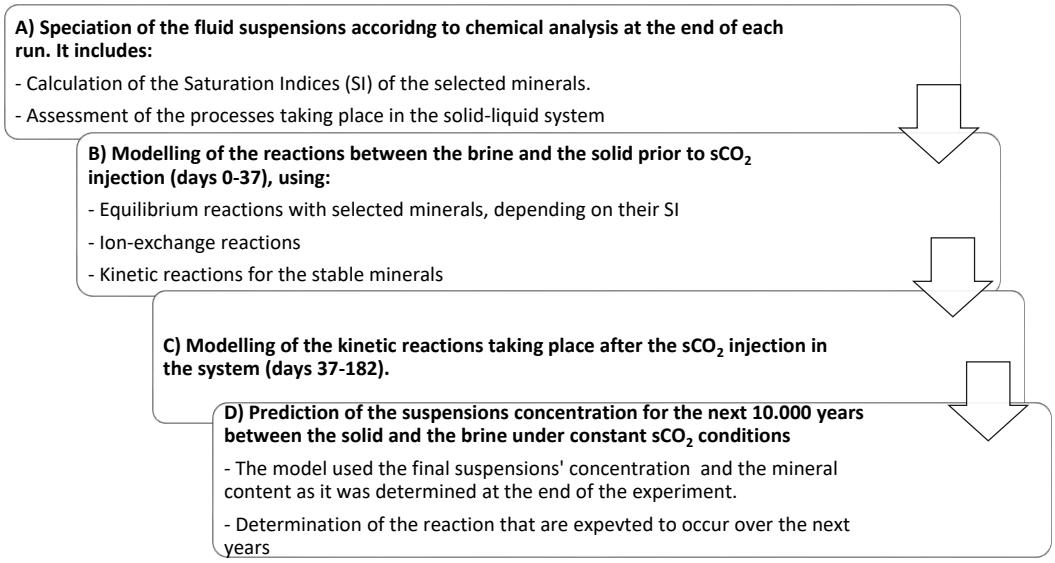

Figure 3 - Diagram showing the steps followed in constructing the geochemical models.

All simulations took into consideration the experimental conditions. The fugacity coefficient and solubility of the sCO_2 in 0.5M NaCl were calculated as 0.57 and 0.78 mol/kg H_2O respectively (Duan *et al.*, 2003). The reactive mineral mass was determined according to %wt mineral content of the sample and the solid/liquid ratio of 1:10. The effective diameter of the solid particles and their reactive surface area were calculated for the 250-500 μm particle size (assuming a spherical shape of the grains) and density of each mineral (Tester *et al.*, 1994). Reactive surface area (Equation 1) is the fraction of the mineral surface area that reacts with the solution and idealy is considered equal to the whole surface area.

Equation 1 – Reactive surface area

$$RS_A = \lambda n M S_A,$$

where n represents the number of moles and M the molar mass of the mineral respectively, and λ the reactive fraction (usually estimated experimentally). The values of λ were not measured, but defined to fit the models.

Reaction dissolution and precipitation rates were calculated using the Transition State Theory (TST) (Equations 2 and 3). Both dissolution (r_d) and precipitation (r_p) reactions are subject to the system temperature and pH which influence the reaction constants (Arrhenius Law), separating an acid, neutral and base part respectively.

Equation 2 – Dissolution rate kinetics (Lasaga, 1984)

$$r_d = RS_A * \left(k_0^{nu} \exp\left[\frac{-E_a}{R}\left(\frac{1}{T} - \frac{1}{298.15}\right)\right] + k_0^{acid} \exp\left[\frac{-E_a}{R}\left(\frac{1}{T} - \frac{1}{298.15}\right)\right] a_H^{acid} + k_0^{base}\left[\frac{-E_a}{R}\left(\frac{1}{T} - \frac{1}{298.15}\right)\right] a_{OH}^{base}\right) * \left|1 - \Omega_n^p\right|^q ,$$

where k_0 is the rate constant at 25 °C (mol m^{-2} s^{-1}), Ea the activation energy (J mol^{-1}), a_i the activity of ion i, R the gas constant (8.314 J mol^{-1} K^{-1}) and T the absolute temperature (K). Ω is the mineral saturation index and p,q are constants.

Equation 3 – Precipitation rate kinetics (Van Pham *et al.*, 2011)

$$r_p = -(k_{pre} + k_{add}) * RSA * \left|\Omega_n^p - 1\right|^q - k_N \exp\left[-\Gamma_{ij}\left(\frac{1}{\sqrt[3]{T^2}\ln\Omega}\right)^2\right],$$

where k_{pre} and k_N are the precipitation and nucleation constants respectively (mol m^{-2} s^{-1}), Γ_{ij} the nucleation constant and k_{add} the influence of additional mechanisms, such as carbonates or hydroxyl ions (Hellevang *et al.*, 2013). Kinetic dissolution and precipitation kinetic parameters were taken from Palandri and Kharaka (2004), Marty *et al*. (2015) and Van Pham *et al.* (2011).

3. Results

3.1. Sandstone mineralogy

The mineralogy of the samples before and after the interaction with sCO_2-brine was determined through XRD analysis. The bulk sample are consisted mainly of calcite (38.2%), quartz (20.9%), albite (14.9%) and orthoclase (10.2%). Secondary phases include dolomite (4.5%), clinochlore (8.2%) and montmorillonite (2.8%). Kaolinite (0.2%) and muscovite (0.1%) are of little importance. After the reaction with sCO_2, new phases were not formed, instead there was a mass transfer among the pre-existing mineral phases. More specifically, albite, orthoclase, clinochlore, calcite and dolomite dissolved to 12.7%, 9.9%, 34.8% and 2.1% respectively. The dissolution led to precipitation of clay minerals and silica (in the form of quartz) increasing their percentages to 0.7% for kaolinite, 3.6% for montmorillonite and 27.7% for quartz. Using the initial mineral contents of the sample, the specific surface was calculated for each mineral (Table 1).

Table 1 - Mineral parameters for the kinetic modelling.

Mineral phase	m (moles/kg H_2O)	ρ (g/cm^3)	S_A (m^2/g)
Albite	0.0566	2.62	6.35E-03
Orthoclase	0.0366	2.56	6.50E-03
Calcite	0.3817	2.71	6.14E-03
Dolomite	0.0244	2.65	6.28E-03
Montmorillonite	0.0051	2.35	7.08E-03
Kaolinite	0.0008	2.60	6.40E-03
Muscovite	0.0003	2.82	5.90E-03
Chlorite	0.0138	2.65	6.28E-03
Quartz	0.3479	2.62	6.35E-03

Ion exchange capacity was calculated by the CEC (meq/100g) reported in literature for each mineral and their relative mass. The calculated CEC ranges from 2.5 to 6 meq/100g. The average value used is 4.31 meq/100g resulting to 0.0008 moles per 20g of solid.

3.2. Fluid chemistry

The initial brine concentration, as well as the suspensions' composition prior to and after the sCO_2 injection were determined. sCO_2 injection increases calcium, magnesium and bicarbonate concentrations, (which are most likely caused by calcite and dolomite dissolution) and the solution pH decreases. K and Na are well correlated with silica, which suggests feldspar dissolution (Figure 4).

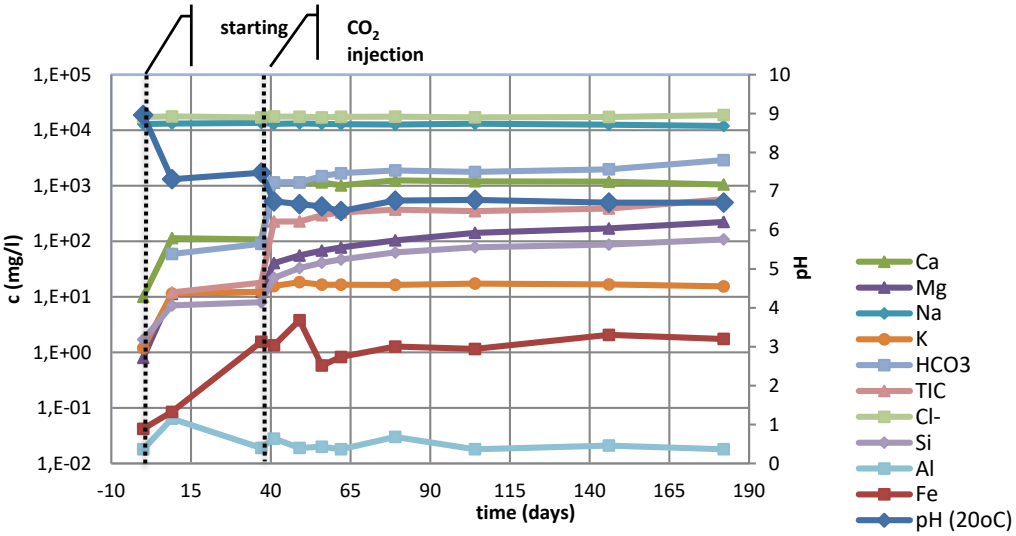

Figure 3 - Evolution of fluid chemistry as a function of time during the 6 months of the experiment (Purser *et al.*, 2015).

3.3. Geochemical modelling

3.3.1. Fluid speciation

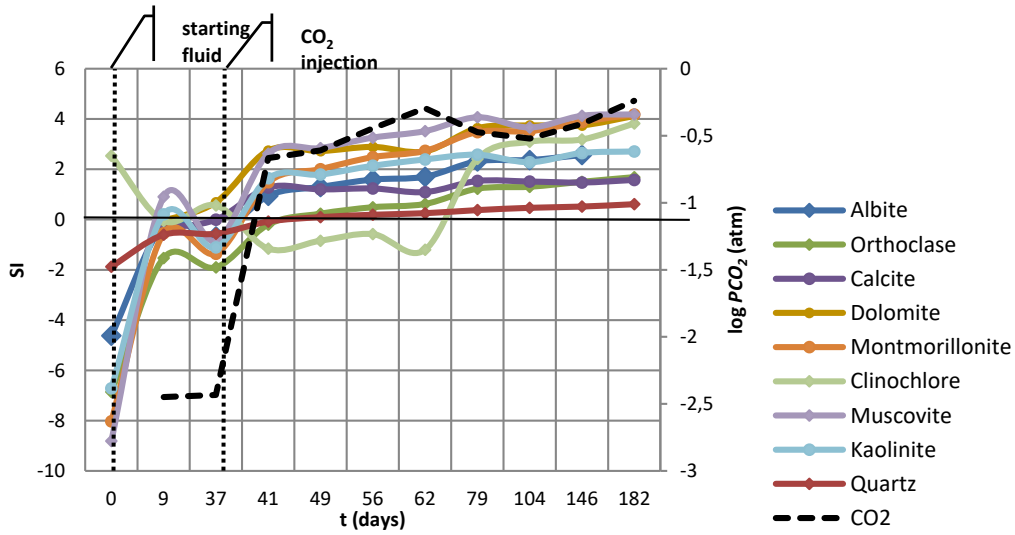

Figure 4 - Saturation indices (SI) for the mineral phases of the sandstone sample.

Geochemical modelling involved using the measured fluid compositions and calculating mineral saturation indices (Figure 5). The brine was undersaturated with respect to most minerals (SI<0) prior to sCO_2 injection, and saturated with respect to calcite (SI=0). After the addition of CO_2, many phases were oversaturated (SI>0).

3.3.2. Equilibrium modelling

Equilibrium calculations for brine-rock interaction were based on the experimental data at 37, i.e. before addition of CO_2.

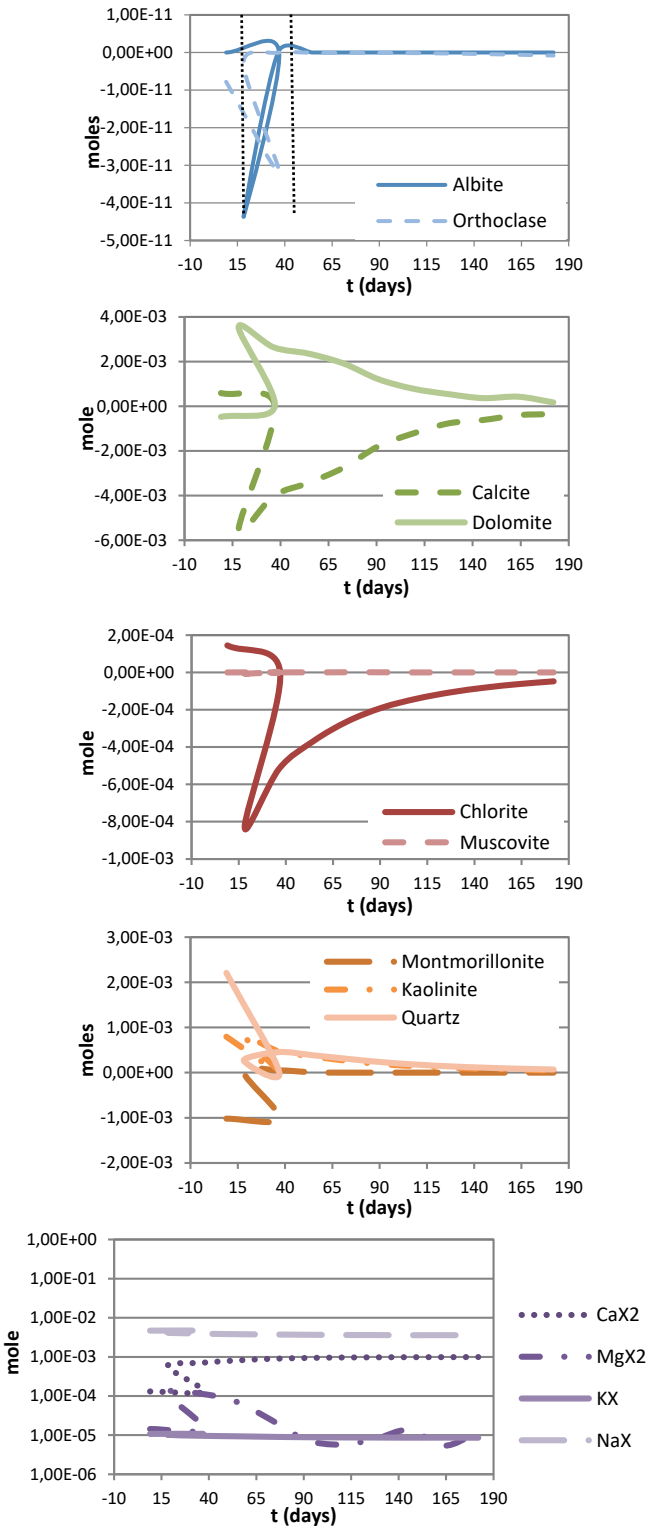

Figure 5 - Mole transfer prior to (equilibrium) and after (kinetics) the sCO_2 injection as a function with time from the beginning to the end of the experiment.

Whilst we recognise that this is a relatively short period of reaction time, it is informative to undertake these calculations to ascertain which reactions may have neared steady state conditions. The model used primarily equilibrium and cation exchange reactions. Taking into account the above speciation calculations, calcite, albite, dolomite, clinochlore were considered at equilibrium with the initial fluid and ion-exchange was attributed to surface sites occupied by Ca.

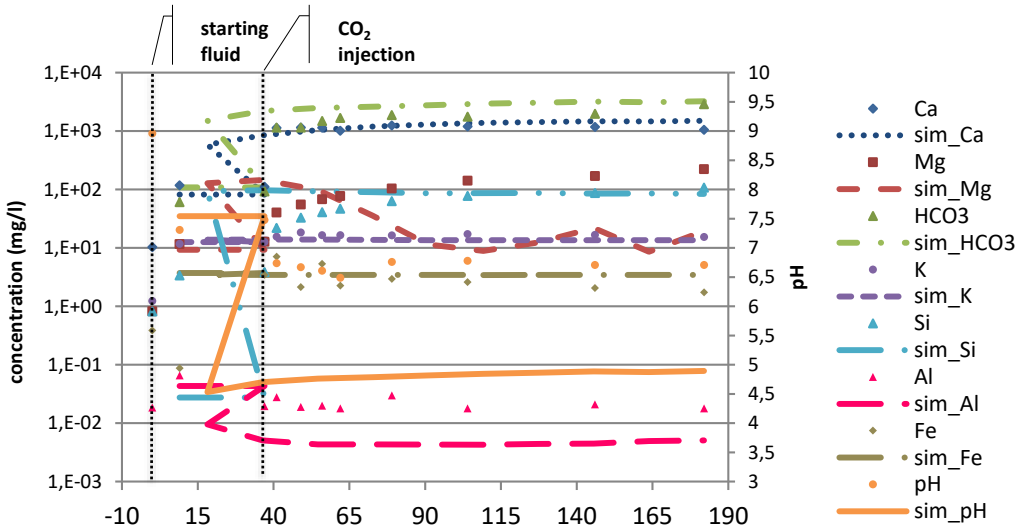

Figure 6 - Modelled and experimental suspensions composition as a function of time from the start (equilibrium reactions) to the end (kinetic reaction) of the experiment.

3.3.3. Kinetic model

A kinetic model was constructed based on the above equilibrium observations and fluid chemical changes between injection of CO_2 and the end of the experiment. According to the calculated SIs at the speciation, no equilibrium occurs after the sCO_2 injection. The kinetic modelling consists of kinetic reactions and ion-exchange. All input data were kept constant, except the reaction mineral mass which was adjusted to the equilibrium model results.

The simulated liquid is slightly acidic in respect to the experimental pH (Figure 7). The experimental pH measurement was of the degassed fluid that was extracted from the experiment, so its value is expected to be higher than the pH calculated by the model. Generally, the experimental data fit very well to the model results, with minor deviations. It must be noted that the constant suspension sampling during the experiment results in changing the solid/liquid ratio resulting in condensation.

The kinetic simulations show that albite, muscovite and orthoclase undergo limited dissolution (Figure 6). Silicates dissolution is followed by the precipitation primarily of kaolinite, montmorillonite and secondary silica (expressed as “quartz” in the model). Calcite, which was precipitating before CO_2, dissolve after the injection. Dolomite precipitates in contrast to the experimental data. Na and K are released from the surface sites, and are replaced by Ca and Mg.

3.3.4. Prediction model

The prediction model used the concentration of the final suspension sampled and the mineral mass determined by the XRD analysis for the solid after the reaction with sCO_2. Kinetic constants remained unchanged. The mineral evolution was simulated over a 10.000 year timescale. We recognise that this is extending an experimentally-derived model far in excess of its validated time period, and the results should be seen as tentative. However, this is a useful exercise as it helps identify the possible long-term fate of stored CO_2 and its impact on the host lithologies.

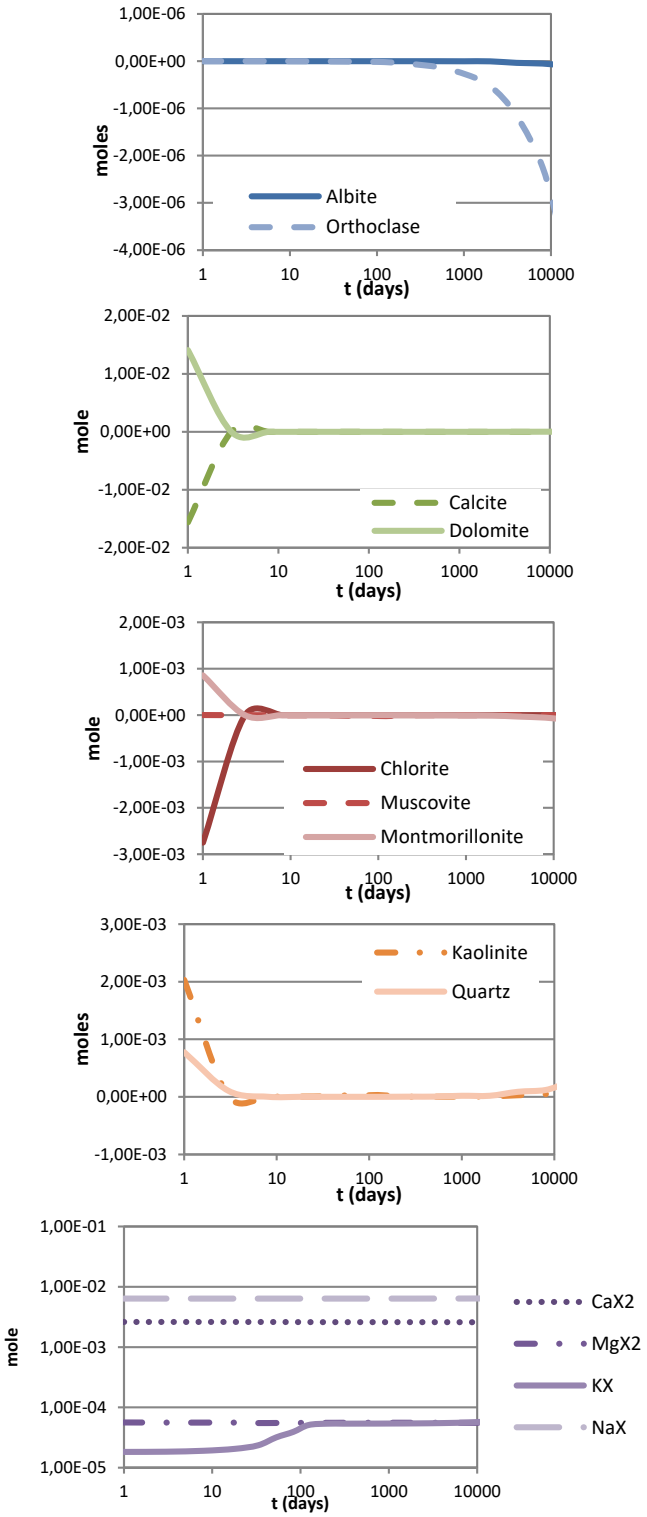

Figure 7 - Predictions of mineral evolution with the sandstone.

Albite remains unreactive. Chlorite and muscovite react for 10 years, then chlorite is being exhausted, and muscovite reacts again after 7000 years. Orthoclase is reactive till the end of the simulation.

Silicates dissolution result in precipitation primarily of montmorillonite and quartz, and secondly of kaolinite. Dolomite precipitates and calcite dissolves for 10 years, until it is exhausted. Then dolomite begins to dissolve. Generally, the phases of the solid seem to reach equilibrium after 10 years of reaction with sCO_2 (except orthoclase) leading to stabilization of the sandstone mineralogy (Figure 8).

4. Conclusion

The kinetic model, which was proposed to simulate the rock-brine interactions with sCO_2, showed that the fluid and sandstone chemistry is controlled primarily by the carbonates and secondly by the clinochlore and muscovite dissolution. The dissolution of feldspars is of less importance. These reactions are expected to continue for another 10 years (except orthoclase dissolution), after which the system tends towards equilibrium.

The above suggested models are based on a number of uncertainties. Surface area and ion-exchange were not measured but rather they were estimated using reference data Moreover, the ideal chemical compositions of the mineral phases were used instead of the real ones, especially in the case of chlorite and montmorillonite. The knowledge of the exact mineral stoichiometry would have given more accurate results regarding the fluids' chemistry. Despite these uncertainties, the proposed model provides a first estimation of the geochemical reactions occurring between the sandstone and a CO_2-saturated brine, helping in its evaluation as a potential CO_2 reservoir.

5. Acknowledgments

This research has been co-financed by the European Union (European Social Fund - ESF) and Greek national funds through the Operational Program "Education and Lifelong Learning" of the National Strategic Reference Framework (NSRF) - Research Funding Program: Thales. Investing in knowledge society through the European Social Fund. The authors would also specifically like to thank all the staff of the British Geological Survey (BGS) that were involved in the batch experiments on samples of Greek sandstone, limestone and borehole cement and that contributed to the sample preparation and provided the fluid analysis results. Special thanks should also be given to Alexandros Tasianas and Nikolas Tsoukalas from CERTH for their contribution in redacting this paper, as well as the National and Kapodestrian University of Athens for its support in this work. GP publish with the permission of the Executive Director of the British geological Survey, NERC.

6. References

Black, J.R., Caroll, S.A. and Haese, R.R., 2015. Rates of mineral dissolution under CO2 storage conditions, *Chemical Geology*,399, 134-144.

Brunn, J., 1956. Contribution a l' étude geologique du Pinde serpentrional et d' une partie de la Macedoine occidentale, *Annales Géologique des Pays Hellénique,* 7, 1-346.

Duan, Z. and Sun, R., 2003. An imroved model calculating CO2 solubility in pure water and aqueous NaCl solutions from 273 to 533 K and from 0 to 2000 bar, *Chemical Geology*, 193, 257-271.

Gaus, I., 2010. Role and impact of CO2-rock interactions during CO2 storage in sedimentary rocks, (Review), *International Journal of Greenhouse Gas Control*, 4, 73-89.

Hellevang, H., Pham, V.T. and Aaagaard, P., 2013. Kinetic modelling of CO2-water-rock interactions, *International Journal og Greenhouse Gas Control*, 15, 3-15.

I.G.M.E. (Institute of Geology and Mineral Exploration), 1983. Geological Map of Greece, Redaction from: Bornovas, J. and Rondogianni-Tsiambaou, Th., s.l.s.n.

Lasaga, A., 1984. Chemical kinetics of water-rock interactions, *Journal of Geophysical Research*, 89, 4009-4025.

Marty, N.C.M., *Claret, F., Giffaut, E., Madé, B. and Tournassat, C.,* 2015. A database of siddolution and precipitation rates for clay-rocks minerals, *Applied Geochemistry*, 55, 108-118.

Palandri, J. and Kharaka, Y., 2004. A compilation of rate parameters of water-mineral interaction kinetics for application to geochemical modeling, Mento Park, California: U.S. Geological Survey.

Parkhust, D. and Appelo, C., 1999. User's guide to PHREEQC (Version 2) - A computer program for speciation, batch-reaction, one-dimensionla transport, and inverse geochemical calculations, s.l.: U.S. Geologcal Survey-Resources Investigations, Report 99-4259, 310.

Purser, G. and Rochelle, C., 2015. A brief note describing batch experiments on samples of Greek sandstone, limestone and borehole cement., s.l.: British Geological Survey Commercial Report, CR/15/035, 22 pp.

Soave, G., 1972. Equilibrium constants from modified Redlich-Kwong equation of state, *Chemical Engineering Science*, 1197-1203.

Tester, J.W., Worley, W.G., Robinson, B.A., Grigsby, C.O. and Feerer, J.L., 1994. Correlating quartz dissolution kinetics in pure water from 25 to 625oC, *Geochemica et Cosmochimica Acta*, 58(11), 2407-2420.

Vamvaka, A., 2009. Geometry of deformation and kinematic analysis in Mesohellenic Trough, s.l., PhD Thesis, Aristotle University of Thessaloniki, Department of Geology.

Van Pham, T., Lu, P., Aagaard, P., Zhu, C. and Hellevang, H., 2011. On the potential of CO2-water-rock interactions for CO2 storage using a modified kinetic model, *International Journal of Greenhous Gas Control*, 5, 1002-1015.

Zelilidis, A., Piper, D. and Kontopoulos, N., 2002. Sedimentation and basin evolution of the Oligocene-Miocene Mesohellenic basin, Greece, *AAPG Bulletin*, 86(1), 161-182.

Δελτίο της Ελληνικής Γεωλογικής Εταιρίας, τόμος L, σελ. 2221-2230
Πρακτικά 14ου Διεθνούς Συνεδρίου, Θεσσαλονίκη, Μάιος 2016

Bulletin of the Geological Society of Greece, vol. L, p. 2221-2230
Proceedings of the 14th International Congress, Thessaloniki, May 2016

INTERACTION OF CLAY MATERIALS WITH LEAD IN AQUEOUS SOLUTIONS

Kypritidou Z.[1], Argyraki A.[1], Chryssikos G.[2] and Stamatakis M.[1]

[1]*Faculty of Geology and Geoenvironment, University of Athens, Panepistimiopolis Zografou, Athens 157 84, Greece, zach-kyp@geol.uoa.gr*

[2]*Theoretical and Physical Chemistry Institute, National Hellenic Research Foundation, 48 Vass. Constantinou Avenue, Athens 11635, Greece, gdchryss@eie.gr*

Abstract

Five bulk clay samples were characterized by XRD, XRF, FTIR and SEM and tested for their effectiveness in removing lead ions from aqueous solutions. These were pal ygorskite, smectite and mixed palygorskite/smectite clays from Macedonia, Greece, as well as a montmorillonite-rich sample from Kimolos, Greece, and a palygorskite-rich sample from Western Australia]. Lead removal was investigated as a function of the pH and ionic strength of the suspensions, the amount of sorbent and time, at con stant Pb^{2+} concentration (50mg/L) and temperature (22ºC). The greatest potential fo r Pb^{2+} removal was found for the natural palygorskite/smectite clay.
Keywords: *palygorskite, smectite, montmorillonite, removal, lead.*

Περίληψη

Πέντε αργιλικά υλικά χαρακτηρίστηκαν με XRD, XRF, FTIR και SEM και μελετήθηκα ν συγκριτικά ως προσροφητικά υλικά για την απομάκρυνση ιόντων μολύβδου από υδα τικά διαλύματα. Αυτά είναι παλυγορσκίτης, σμεκτίτης και παλυγορσκίτης/σμεκτίτης απ ό τη Μακεδονία (Ελλάδα), καθώς επίσης μοντμοριλλονίτης από την Κίμωλο (Ελλάδα) και παλυγορσκίτης από τη Δυτική Αυστραλία. Παράγοντες που ελέχθησαν ήταν η ποσό τητα του προσροφητικού μέσου, το pH του αρχικού διαλύματος και ο χρόνος αλληλεπί δρασης των δύο υπό σταθερή θερμοκρασία 22 ºC και συγκέντρωση μολύβδου (50mg/ L). Η μεικτή παλυγορσκιτική/σμεκτιτική άργιλος επέδειξε τη μεγαλύτερη αποτελεσματι κότητα ως προς την απομάκρυνση του Pb^{2+}.
Λέξεις κλειδιά: *παλυγορσκίτης, σαπωνίτης, μοντμοριλλονίτης, απομάκρυνση, μόλυβδος.*

1. Introduction

Clay minerals are well-known for their removal ability. Many laboratory studies have been conducted to investigate the ability of clay minerals to remove heavy metals including Pb, Cu and Cd from monometallic or polymetallic ideal solutions (e.g. Bourliva *et al.*, 2013; Malamis *et al.*, 2013; Potgieter *et al.*, 2006). The ultimate goal of such studies is the fundamental understanding of the factors and mechanisms that control the interaction between metal ions and clay materials. In this way, conclusions can be drawn about the impact of ion-exchange, removal and precipitation on the mobility and distribution of contaminants in the environment.

Within this framework, the main objective of the present work is to present preliminary data on the comparison of different clay materials regarding their effectiveness in the removal of lead from aqueous solutions.

2. Materials and Methods

2.1. Materials

The tested palygorskite (PCM), smectite (SCM) and mixed palygorskite-smectite (MCM) clay samples originate from the Ventzia Basin clay deposits, Grevena (West Macedonia, Greece), exploited by Geohellas S.A. They are considered alteration products of primary ultramafic rocks of the Vourinos complex (Kastritis *et al.*, 2003). An additional palygorskite sample (AT_AUS) originating from the Lake Nerramyne deposit in Western Australia, exploited by Hudson Resources Ltd. was used for comparison, as it is considered of sedimentary origin. Finally, the montmorillonite clay sample (KIM) was extracted by one of the authors (MGS) from the Prassa Quarry (Bentomine Enterprises), north Kimolos Island (SW Cyclades, Greece). The Kimolos clay deposit was formed by the alteration of volcanic ash in a shallow marine environment (Christidis, 1998). All samples were milled and sieved below 250μm particle size.

2.2. Methods

Clay morphology was examined by scanning electron microscopy (SEM) (JSM-5600) operating at 25-30 kV. Sample mineralogy was determined by powder X-Ray Diffraction (XRD) analysis (Siemens D5005, with Cu radiation operating at 40kV and 40mA) with 2-theta range from 3 to 45°, step 0.02° and step time 2sec at ambient condition. Mineralogical evaluation was conducted using the DIFRAC PLUS v2.2 software by Siemens. SEM and XRD analysis was performed in the Laboratory of Economic Geology and Geochemistry, NKUA. Mid-infrared (ATR) and near-infrared (NIR) spectra were measured using Fourier transform instruments equipped with a single reflection diamond accessory (Equinox 55 by Bruker Optics) and a powder probe optical fiber (Vector 22N by Bruker Optics), respectively, at the Theoretical and Physical Chemistry Laboratory of the National Hellenic Research Foundation. Measurements were obtained at 4 cm^{-1} spectral resolution and averaging a total of 100 and 200 scans for ATR and NIR respectively. The spectra are presented in the 2^{nd}-derivative mode (for better resolution of sharp weak bands) calculated by the OPUS v4.2 software (Bruker Optics).

Chemical analysis of the samples was carried out by X-Ray Florescence (XRF) in the laboratories of Titan Cement Company SA. The following analytical procedures were carried out at the Laboratory of Economic Geology and Geochemistry, NKUA. Cation exchange capacity (CEC) was determined by the ammonium acetate extraction method (Rhoades, 1990). It is noted that the used method is developed for soils and represents the "early" CEC, at least for the smectite-rich clay materials, rather than the complete CEC due to insufficient saturation of exchangeable cation sites with ammonium cations. Batch removal experiments were carried out to study the removal of lead. An appropriate quantity of $Pb(NO_3)_2$ (analytical grade) was dissolved in highly purified water (Milli-Q) to make a 50mg/L Pb^{+2} solution. The calculated amounts of solid, weighted after equilibration at ambient (moisture content ~10%) were dispersed in 25ml of the Pb^{+2} solutions in 50ml Erlenmeyer flasks, shaken in a thermostatic chamber at constant temperature (22°C) for the desired amount of time and filtered through 0.45μm membrane filters. The effect of adsorbent content was studied using solid/liquid ratios of 1-20g/L and a shaking time of 24h, at natural solution (pH 4.5). Preliminary feasibility experiments led to kinetic measurements at 10g/L solids for up to 24h (1440min). The influence of the pH of the initial solution (pH = 2-6) was examined at 10g/L material with shaking time of 4h. The solution pH was adjusted prior to the addition of clay by adding drops of 0.1N HNO_3 or 0.1N NaOH and measured by a bench-top pH-meter (Jenway 3040 Ion Analyzer) calibrated by using buffer solutions of pH 4 and 7. The influence of ionic strength was studied by dissolving proper amounts of KNO_3 or $NaNO_3$ (analytical grade) to obtain 0.01-0.1M solutions. All

samples were analyzed in triplicate giving the average value and standard deviation for each set. Procedural blank solutions containing only $Pb(NO_3)_2$ as well as zero Pb concentration suspensions of clays were also included in the analysis for quality control purposes. Lead concentration was determined by flame atomic removal spectroscopy (F-AAS) using a Perkin Elmer 603 instrument. Filtered samples were stored at 4°C prior to analysis.

3. Results

3.1. Material characterization

Preliminary mineralogical analysis showed that the Grevena samples are composed mainly of palygorskite (PCM, ~70%; MCM, ~20%), smectite (SCM, ~70%; MCM, ~40%, PCM~20%) and contain additionally, quartz, serpentine (MCM, SCM, PCM) and plagioclase admixtures (Figure 1 & 2). Australian palygorskite sample consists of palygorskite (~50%), kaolinite (~20%), and quartz (~15%) with traces of halite, whereas the Kimolos sample (KIM) consists of montmorillonite (~60%), zeolite and opal-CT (Figure 3).

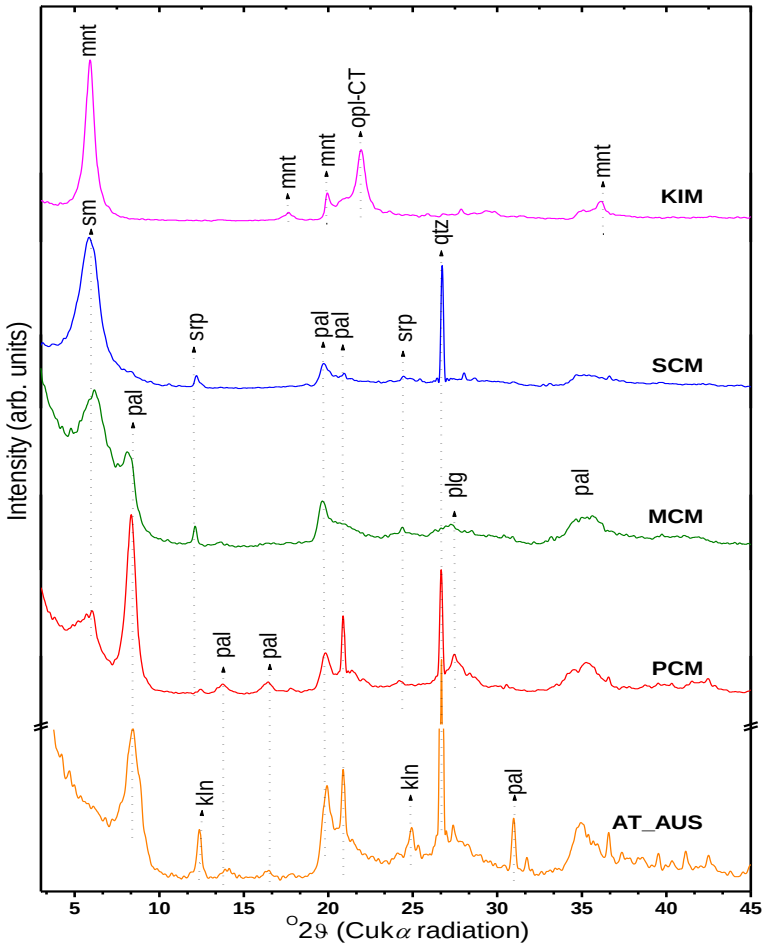

Figure 1 – XRD patterns of clay samples (sm=grevena smectite, mnt=montmorillonite, pal=palygorskite, kln=kaolinite, srp=serpentine, opl=opal-CT, qtz=quartz, plg=plagioclase).

The ATR and NIR spectra (Figure 2) exhibit the main stretching (overtone) modes of the various structural OH groups at 3685 (7212-7185) cm^{-1} for Mg_3OH, 3620 (7065) cm^{-1} for Al_2OH, 3585 (6995) cm^{-1} for AlFeOH, and 3545 (6927) cm^{-1} for Fe_2OH (Gionis *et al*., 2007; Madejova, 2003). The relative intensities of these bands indicate that the palygorskite in the Grevena samples has a mixed dioctahedral-trioctahedral character (Stathopoulou *et al*., 2011; Gionis *et al*., 2007) and is rich in Fe(III). On the contrary, AT_AUS is almost exclusively dioctahedral and of low Fe-content. With reference to the general formula:

$yMg_5Si_8O_{20}(OH)_2 \cdot (1 - y)[xMg_2Fe_2 \cdot (1 - x)Mg_2Al_2]\ Si_8O_{20}(OH)_2$

and the analysis in Chryssikos *et al.* (2009), palygorskite in PCM has (x, y) values of (0.41, 0.06), in comparison to (0.78, 0.48) for MCM, and (0.11, 0) for AT_AUS.

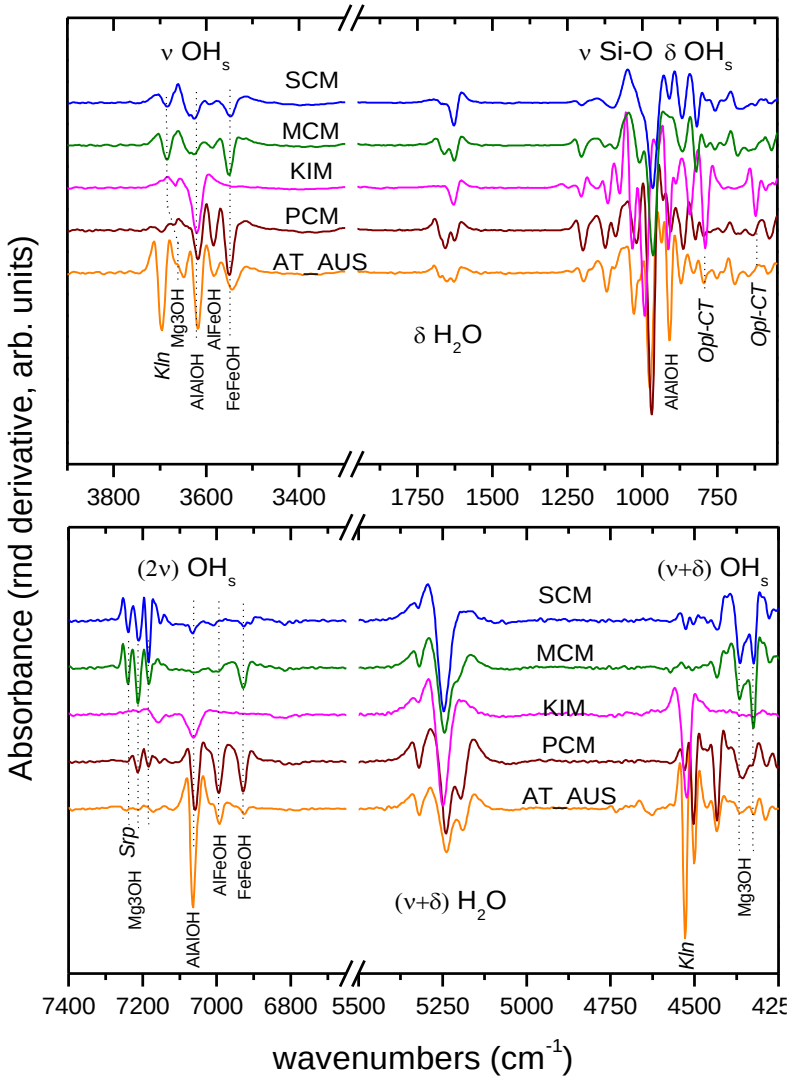

Figure 2 – 2nd derivative ATR (upper) and NIR (lower) spectra of the clays investigated. Main assignments are included, for details see text.

The smectite in KIM is clearly dioctahedral (montmorillonite). However, the nature of the smectite in SCM and MCM can be controversial and requires further investigation. On one hand, the presence

of Mg_3OH overtones at 7183 cm^{-1} and 7151 cm^{-1} in the spectra of SCM and MCM samples suggest the presence of a trioctahedral type, similar to talc or saponite (Gionis *et al*., 2007). On the other hand, the presence of the relatively broad band at ~3550 cm^{-1} in SCM (that contains no palygorskite) signals the presence of ferruginous smectite or nontronite, in agreement with Christidis *et al.* (2010).

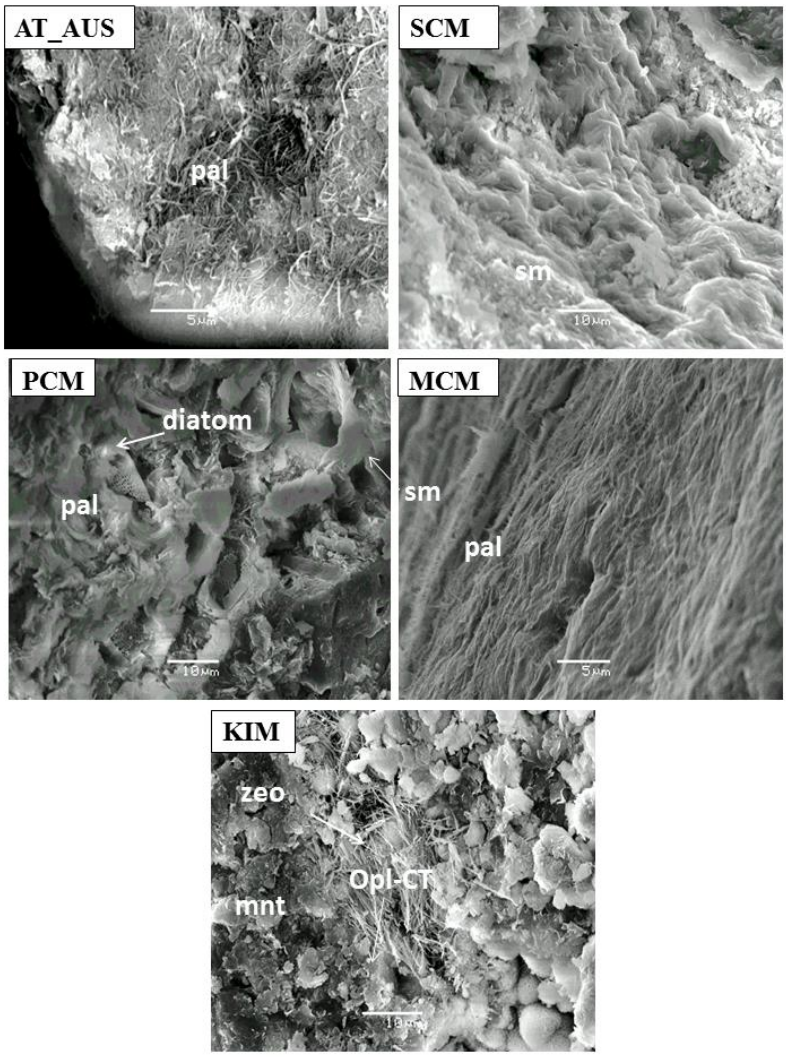

Figure 3 – SEM images of the clay samples (pal=palygorskite, sm=smectite, zeo=zeolite, mnt=montmorillonite, opl-CT=opal-CT).

SEM images show a typical fibrous texture for palygorskite (AT_AUS, PCM) and a flaky texture for smectites (SCM, KIM). In the MCM sample the palygorskite fibers are in contact with saponite flakes. In PCM samples diatom fragments and primary silicate minerals were detected. KIM samples show flakes of montmorillonite alongside with fibrous spheres of opal and acicular zeolite (mordenite) (Figure 3).

The chemical characteristics of clay samples are summarized in Table 1.

Table 1 – Chemical composition (%wt) and cation exchange capacity of clay samples.

Compound	PCM	AT_AUS	SCM	KIM	MCM
SiO_2	58.09	56.41	54.98	78.13	60.24
TiO_2	0.42	0.67	0.24	0.10	0.14
Al_2O_3	5.15	10.06	3.05	11.06	0
Fe_2O_3	5.91	2.91	9.30	0.89	9.90
MnO	0.04	0.03	0.15	0.01	0.15
MgO	12.16	5.71	18.92	6.14	27.52
CaO	3.09	1.77	1.36	0.74	1.17
Na_2O	0	0	0	1.81	0
K_2O	0.55	1.58	0.44	0.70	0.13
P_2O_5	0.03	0	0.025	0.01	0.03
SO_3	0.02	0.20	0.06	0.23	0.14
Cl	0	1.02	0	0.07	0.14
LOI	14.16	19.47	10.72	0	0
Total	99.64	99.85	99.19	99.87	99.55
CEC (meq/100g)	27	6	63	43	30

3.2. Removal experiments

3.2.1. Effect of adsorbent content

Removal increases with solid content for a constant metal concentration of 50mg/L (Figure 4). A plateau representing the complete removal of lead is reached at <2g/L for MCM and SCM, at ~5g/L for PCM and AT_AUS and at ~10g/L for KIM.

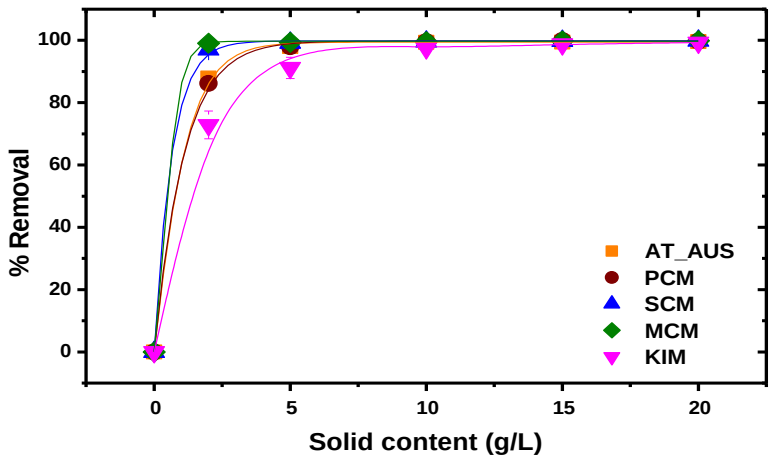

Figure 4 – Lead removal percentage (%), as a function of solid/liquid ratio (Pb=50 mg/L, contact time 24h, initial pH=4.5). Lines are guiding the eye.

At a solid content of 2g/L, sorbed metal loadings range from 15mg/g (KIM) to 21mg/g (MCM, SCM). At 10g/L and higher metal concentrations (Pb=1000 mg/L) the corresponding loadings

reached 45mg/g for both PCM and SCM samples (experimental data not shown). In general, at high mineral concentrations the available Pb concentration is insufficient to cover completely the exchangeable sites on the adsorbent, resulting in low heavy metal uptake. Also, higher mass of the adsorbent in the suspension may cause physical blockage of some removal sites, decreasing the removal efficiency (Malamis *et al*., 2013).

It is noted that the pH of the initial 50 mg/L lead solution is 4.5. The pH measured at the end of the removal experiments is higher and reaches 6.5 for KIM, 7.5 for AT_AUS and PCM, and ~8 for MCM and SCM samples. The respective values in clay lead-free suspensions range between 7.5 and 8.5. This increase has been attributed to a competition between protons and lead ions onto the clay surface due to the smaller hydrated radius of the former (H^+=0.28 nm, Pb^{2+}=0.4 nm) (Volkov *et al.*, 1997). The high pH of all suspensions indicates that precipitation of Pb phases is a very likely mechanism influencing the heavy metal removal from solution. This will be further discussed in paragraph 3.2.3.

3.2.2. Removal kinetics

Concluding that equilibrium is reached at adsorbent amount of 10 g/L, this amount was used in an attempt to study the kinetics of removal at initial solution pH 4.5 as a function of time (Figure 5). These studies indicated that SCM, MCM and PCM reached 100% removal instantaneously (t<5min). All other clay samples required longer times to disperse and, therefore, removal was heavily biased by clumping.

A pseudo-2nd order kinetic model seems to fit well the experimental data of KIM and AT_AUS samples (R^2=1).

Equation 1 – Pseudo-2nd order kinetic model

$$\frac{dq}{dt} = k(q_e - q)^2$$

where q and q_e the sorbed metal concentration (mg/g) at time t and at equilibrium respectively, k the kinetic constant (min mg^{-1} g^{-1}). The kinetic constants k and initial removal rates, $h=kq_e^2$, for KIM are 0.3 and 5.8, whereas for AT_AUS are 0.15 and 2.8. The above parameters are similar to those reported in the literature (Sen Gupta *et al.*, 2011).

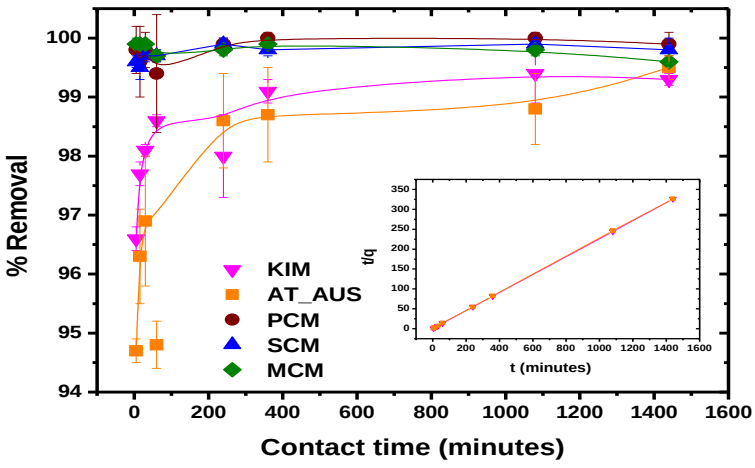

Figure 5 – Lead removal percentage (%) as a function of reaction time (Pb=50mg/L, s/l=10g/L, pH=4.5). Embedded graph corresponds to the 2nd-order kinetic removal model for KIM and AT_AUS. Lines are guiding the eye.

3.2.3. Effect of pH

The effect of the pH of the initial Pb^{+2} solution was tested in the range from 2 to 6. At pH <3, all clays show inferior removal percentage. The effect is more pronounced for all the studied samples with the exception of KIM sample. Specifically, at low pH (<2.5) KIM exhibits the best removal performance.

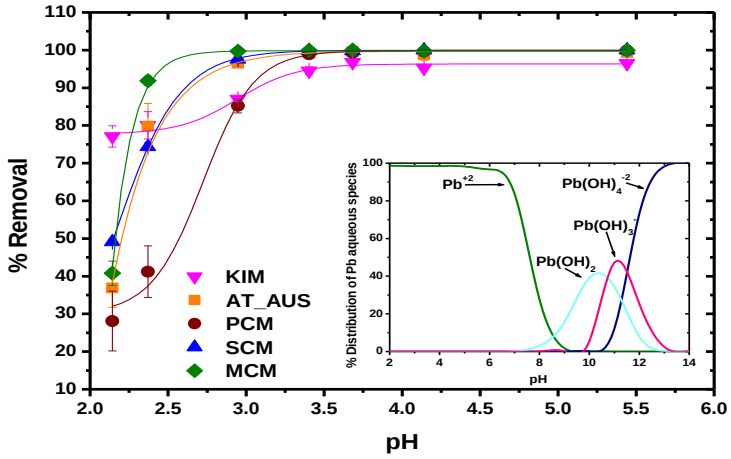

Figure 6 – Lead removal percentage (%) as a function of solution pH (Pb=50 mg/L, s/l 10 g/L, contact time 4h). Insert graph shows Pb speciation with respect to pH as calculated by PHREEQC.

According to speciation results for Pb solubility (calculated using PHREEQC v3.2 geochemical code), Pb^{2+} precipitates as $Pb(OH)_2$ at pH> 6 (Figure 6). The pH is an important removal parameter not only because it determines the speciation of Pb^{+2} in the solution (and therefore its precipitation), but also because it may affect the structure and morphology of the adsorbent. Extreme alkaline solutions promote the alteration of the adsorbent and induce the leaching of Si ions into the solution, whereas extreme acidic solutions leach the octahedral cations of the clay layers and create silanol groups.

3.2.4. Effect of Ionic Strength

The presence of additional ions in the solution affects removal in different ways for each material (Figure 7). Pb removal is inhibited at high ionic strengths, especially in KIM and to a lesser extent AT_AUS and PCM samples. On the contrary, MCM and SCM are unaffected by the K/Na presence.

The competition between the electrolyte cations, i.e. Na^+, K^+ and Pb^{2+} for the available removal sites can decrease the amount of the heavy metal ions adsorbed on the clay (Malamis et al., 2013). If ion-exchange between the exchangeable cations of the adsorbent and the Pb^{2+} was the primary mechanism, we should be observing a systematically large effect of ionic strength in smectites and a very small effect in palygorskites. This is observed in KIM, but not in SCM (or MCM). Furthermore, ion-exchange cannot be the main reason for the observed phenomenology, because removal performance is not correlated with the CEC. Based on the experimental observations discussed above, a mechanism involving the precipitation of Pb-bearing phases, such as Pb-hydroxides, on the large surface area of the alkaline adsorbent appears more plausible. In this case, removal performance would be mainly a function of the active surface of the adsorbent. The latter is determined mainly from the number of elementary particles present in the suspension (per constant mass of adsorbent in the suspension). Concerning the Grevena samples, it is noted that the active surface does not need to be a function of the mineralogical composition of the samples, and this may

explain why no systematic trends are observed between performance on one hand and the palygorskite/ smectite ratio on the other.

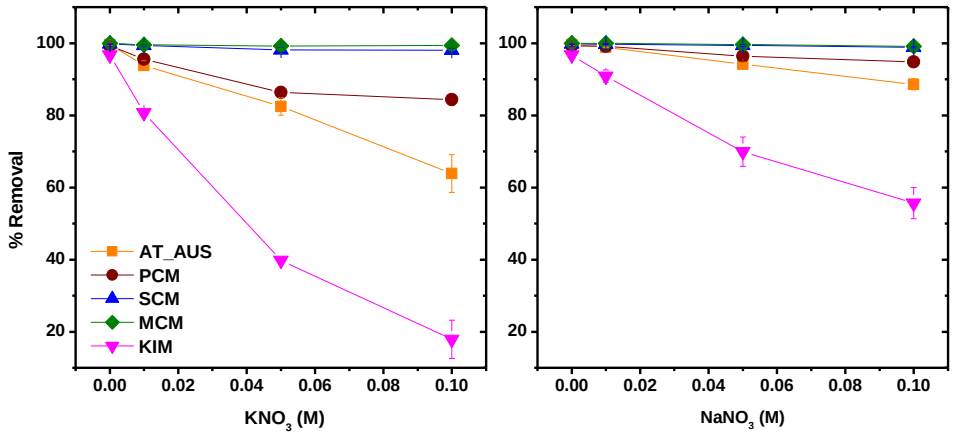

Figure 7 – Pb removal percentage (%) as a function of solution ionic strength (Pb=50 mg/L, pH=3.6, s/l=10g/L, t=4hr).

4. Conclusions

The performance of five clay materials has been assessed with respect to their effectiveness in removing Pb^{2+} from aqueous solutions. All adsorbents perform equally well at high solid to liquid ratios and long times (>4h) of interaction at pH>3, by adsorbing quantitatively the Pb^{2+} from 50mg/L solutions. However, based on their performance at low solids, and short reaction time it is evident that the adsorbents can be classified in the order MCM>=SCM>PCM=ATAUS>KIM. Further, at low pH, the removal properties are all deteriorating and KIM exhibits the best performance. Further studies are needed to elucidate the possible alteration of the adsorbent as a result of alkaline or acid leaching in the pH and time scales of the experiment, and its effect on removal. Also the maximum capacity of each adsorbent remains to be determined by plotting the removal isotherms with varying Pb concentrations in the solution. In terms of the mechanism controlling Pb removal from the solution our experimental data indicate that this is at least partially controlled by the active surface of the bulk clay which in turn might be related to the geological environment and type of processes that took place during the formation of the clay, e.g. hydrothermal or diagenetic alteration, precipitation etc.

5. Acknowledgments

The authors would like to thank Geohellas S.A. for providing the materials used in this study. Thanks are expressed to Mr. Panagiotis Oikonomou and Mr. Manolis Argyropoulos for providing us all facilities to work in bentonite Prassa Quarry at Kimolos Island, as well as Titan Cement Company S.A. for performing the XRF analysis of the samples. Last but not least, the authors acknowledge the reviewers for their comments and suggestions.

6. References

Bourliva, A., Michailidis, K., Sikalidis, C., Filippidis, A. and Betsiou, M., 2013. Lead removal from aqueous solutions by natureal Greek bentonites, *Clay Minerals*, 48, 771-787.

Christidis, G., 1998. Physical and chemical properties of some bentonite deposits of Kimolos Island, Greece, *Applied Clay Science*, 13, 79-98.

Christidis, G., Katsiki, P., Pratikakis, A. and Kacandes, G., 2010. Rheological properties of palygorskite-smectite suspensions from the Ventzia Basin, W. Macedonia, Greece, *Bulletin of the Geological Society of Greece, Proceedings of the 12th International Congress*, Patras.

Chryssikos, G.D., Gionis, V., Kacandes, G.H., Stathopoulou, E.T., Suárez, M., García-Romero, E., and Sánchez del Rio, M., 2009. Letter: Octahedral cation distribution in palygorskite, *American Mineralogist*, 94(1), 200-203.

Gionis, V., Kacandes, G., Kastritis, I. and Chryssikos, G., 2007. Combined near-infrared and X-ray diffraction investigation of the octahedral sheet composition of palygorskite, *Clays and Clay Minerals*, 55(6), 543-553.

Kastritis, I.D., Kacandes, G.H. and Mposkos, E., 2003. The palygorskite and Mg-Fe-smectite clay deposits of the Ventzia basin, western Macedonia, Greece, *Mineral exploration and sustainable development*, Millpress, Rotterdam, 891-894.

Madejova, J., 2003. FTIR techniques in clay mineral studies: Review, *Vibrational Spectroscopy*, 31, 1-10.

Malamis, S. and Katsou, E., 2013. A review on zinc and nickel adsorption on natural and modified zeolite, bentonite and vermiculite:Examination of process parameters, kinetics and isotherms, *Journal of Hazardous Materials*, 252-253 (Review), 428-461.

Potgieter, J., Potgieter-Vermaak, S. and Kalibantonga, P., 2006. Heavy metals removal from solution by palygorskite clay, *Minerals Engineering*, 19, 463-470.

Rhoades, J., 1990. Cation exchange capacity. *In:* A.L., P., Miller, R. and Keeney, D., *eds*., Methods of soil analysis, 2(9), 49-157, *Am. Soc. Agr., Soil Sc. Soc. Am*, Madison.

Sen Gupta, S. and Bhattacharyya, K., 2011. Kinetics of adsorption of metal ions on inorganic materials:A review, *Advances in Colloid and Interface Science*, 162, 39-58.

Stathopoulou, E.T., Suárez, M., García-Romero, E., Del Río, M.S., Kacandes, G.H., Gionis, V. and Chryssikos, G.D., 2011. Trioctahedral entities in palygorskite: Near-infrared evidence for sepiolite-palygorskite polysomatism, *European Journal of Mineralogy*, 23(4), 567-576.

Volkov, A., Paula, S. and Deamer, D., 1997. Two mechanisms of permeation of small neutral molecules and hydrated ions across phospholipid bilayers, *Bioelectrochemistry and Bioenergetics*, 42, 153-160.

Δελτίο της Ελληνικής Γεωλογικής Εταιρίας, τόμος L, σελ. 2231-2240
Πρακτικά 14ου Διεθνούς Συνεδρίου, Θεσσαλονίκη, Μάιος 2016

Bulletin of the Geological Society of Greece, vol. L, p. 2231-2240
Proceedings of the 14th International Congress, Thessaloniki, May 2016

DISTRIBUTION OF HEAVY METALS CONCENTRATIONS IN SOILS AROUND THE INTERNATIONAL ATHENS AIRPORT (GREECE). AN ASSESSMENT ON PRELIMINARY DATA

Massas I.[1], Ioannou D.[1], Kalivas D.[1] and Gasparatos D.[2]

[1]*Agricultural University of Athens, Laboratory of Agricultural Chemistry and Soil Science, Iera Odos 75, 11855, Athens, massas@aua.gr, dioannou@aua.gr, kalivas@aua.gr*

[2]*Aristotele University of Thessaloniki, Laboratory of Soil Science, gasparatos@agro.auth.gr*

Abstract

Soils are receptors of atmospheric metal depositions and hence reliable indicators of pollution phenomena, especially for cases that potential site specific pollution sources are detected in terrestrial ecosystems. The purpose of this study was to assess the distribution of Cu, Zn, Fe, Mn, Ni, Cr, Pb, and Ba concentrations in soils nearby the International Athens Airport "El. Venizelos", in Attica, Greece. Total metal concentrations were determined in 86 topsoil aqua regia extracts and the median values for Cu, Zn, Fe, Mn, Ni, Cr, Pb, and Ba concentrations were 23, 81, 22x10^3, 497, 87, 74, 75, and 423 mg kg^{-1} respectively. Though median values are not considered as high, the 90th percentile concentration values for some metals are high, indicating possible soil enrichment by these metals. A tendency for increased concentrations of Zn and Cr along the north-south axis and of Pb, Cu and Ni at the northern part of the studied area was also observed. As a first approach to discriminate between natural and anthropogenic metal contributions in the soils of the area, the obtained preliminary data were subjected to cluster analysis and to the evaluation of metals Enrichment Factors (EFs). Both EF values and cluster analysis results suggested secondary Pb, Cu and Zn site specific accumulation in the soils of the studied area.

Keywords: *Soil Characteristics, Heavy metals, Airport, Enrichment Factor, Cluster Analysis.*

Περίληψη

Τα εδάφη, ως αποδέκτες της ατμοσφαιρικής απόθεσης μετάλλων, αποτελούν αξιόπιστους δείκτες ρύπανσης, ιδιαίτερα στις περιπτώσεις που εντοπίζονται πιθανές σημειακές πηγές ρύπανσης σε χερσαία οικοσυστήματα. Σκοπός της παρούσας μελέτης ήταν η εκτίμηση της κατανομής των συγκεντρώσεων του Cu, Zn, Fe, Mn, Ni, Cr και Ba σε εδάφη κοντά στο Διεθνές Αεροδρόμιο Αθηνών «Ελ. Βενιζέλος», στην Αττική. Σε 86 επιφανειακά δείγματα προσδιορίστηκαν οι ολικές συγκεντρώσεις μετάλλων, στο εκχύλισμα που προέκυψε μετά από κατεργασία με «aqua regia». Οι διάμεσες τιμές των συγκεντρώσεων του Cu, Zn, Fe, Mn, Ni, Cr και Ba ήταν 23, 81, 22x10^3, 497, 87, 74, 75 και 423 mg kg^{-1} αντίστοιχα. Αν και οι διάμεσες τιμές δε θεωρούνται τόσο υψηλές, οι τιμές του ενενηκοστού εκατοστημόριου για ορισμένα μέταλλα θεωρούνται υψηλές, υποδεικνύοντας πιθανό εμπλουτισμό του εδάφους με τα μέταλλα αυτά. Επίσης,

παρατηρήθηκε μια τάση για αυξημένες συγκεντρώσεις του Zn και Cr κατά μήκος του άξονα Βορρά-Νότος καθώς και του Pb, Cu και Ni στο βόρειο τμήμα της περιοχής που μελετήθηκε. Τα προκαταρκτικά αποτελέσματα που προέκυψαν, υποβλήθηκαν σε ανάλυση κατά συστάδες και σε αξιολόγηση των συντελεστών εμπλουτισμού των μετάλλων, ως μια πρώτη προσέγγιση του διαχωρισμού μεταξύ φυσικής και ανθρωπογενούς συνεισφοράς των μετάλλων στα εδάφη της περιοχής. Τόσο οι συντελεστές εμπλουτισμού όσο και η ανάλυση κατά συστάδες, υποδηλώνουν δευτερογενή συγκέντρωση των Pb, Cu και Zn στα εδάφη της υπό μελέτη περιοχής.
Λέξεις κλειδιά: *Εδαφικές Ιδιότητες, Βαρέα μέταλλα, Αεροδρόμιο, Συντελεστής Εμπλουτισμού, Ανάλυση κατά Συστάδες.*

1. Introduction

Heavy metals occur naturally as chemical elements in the earth's crust and surface soils in varying concentrations (Alloway and Ayres, 1997). Total metal contents in soils are directly related to the nature of the parent material they are derived from (Swaine and Mitchell, 1960). Soils in urban and rural areas may become contaminated by accumulation of heavy metals through natural processes and/or human practices that may be high enough to pose risk to human health, plants, animals, and ecosystems (D'amore *et al.,* 2005). In terrestrial ecosystems many kinds of interactions between solids, liquids, gases and the biota take place as geochemical and biological processes (Giannakopoulou *et al.,* 2012) that evolved and affected by anthropogenic factors such as agricultural practices, industrial activities, waste treatments etc. (Kabata-Pendias, 2001).

Increased heavy metal concentrations in soils have been recorded for many industrial, urban, rural, and mixed land uses areas (Srinivasa Gowd *et al.,* 2010; Bretzel and Calderisi, 2006; Massas *et al.,* 2009; Koulourasis *et al.,* 2009). Considering that soils are not a renewable resource and that heavy metals do not biodegrade but accumulate in soils, it is necessary to monitor soil metal concentrations to prevent pollution situations and to propose remediation actions if necessary.

There are only few reports on the distribution of heavy metals in soils in the vicinity of international airports (Table 1). Thus, the purpose of this study was: (1) to determine the actual total concentration of Cr, Ni, Zn, Pb, Cu, Co, Mn, Ba, and Fe in soils around the International Athens airport area (2) to assess the spatial distribution of metals and (3) to discuss on possible relations between metals concentrations and soil properties.

2. Materials and Methods

2.1. Study area and sampling

The study area and the sampling sites are presented in Figure 1. Athens International Airport "El. Venizelos", is located in Mesogaia region, Eastern Attica, Greece, approximately 25 kilometers northeast of Athens. The climate of the area is typical subtropical Mediterranean, with prolonged hot and dry summers succeeded by considerably mild and wet winters. The mean annual precipitation is approximately 400 mm, while snowfall is rare. The drought period usually begins in May and lasts until October. The daily mean temperature ranges between 27^0C during the summer months and 11^0C during the winter months (Papathanasiou *et al.,* 2013a, b). Geologically, the study area is part of the Attico-Cycladic Massif. It is generally flat with low hills and consists of alluvial and diluvial deposits.

El. Venizelos airport operates since March 2001 and according to air traffic statistical data of the year 2013 has been ranked as the 35th airport in Europe. In 2014 the airport handled 154.530 aircraft movements, 15.196.369 passengers and 77.337.956 tons of cargo (http//www.aia.gr). The Municipalities of Spata, Koropi, Artemis and Markopoulo are located nearby. The airport facilities and infrastructure occupy an area of approximately 10 km^2 surrounded by agricultural land. Most of this land is covered by vineyards, but vegetable, olive and fruit tree cultivations are also present.

Topsoil samples (0-10 cm depth) were collected from the region around El. Venizelos airport during the summer of 2013. In order to obtain a distribution pattern of heavy metals concentrations in the soils of the area, a grid-type sampling scheme (cell size 1000x1000 m or 500x500 m in some cases) was followed, oriented by the presence of the airport. At every sampling site, three subsamples from 100 x 100 cm surface area were obtained and mixed to make each of the 86 bulk soil samples.

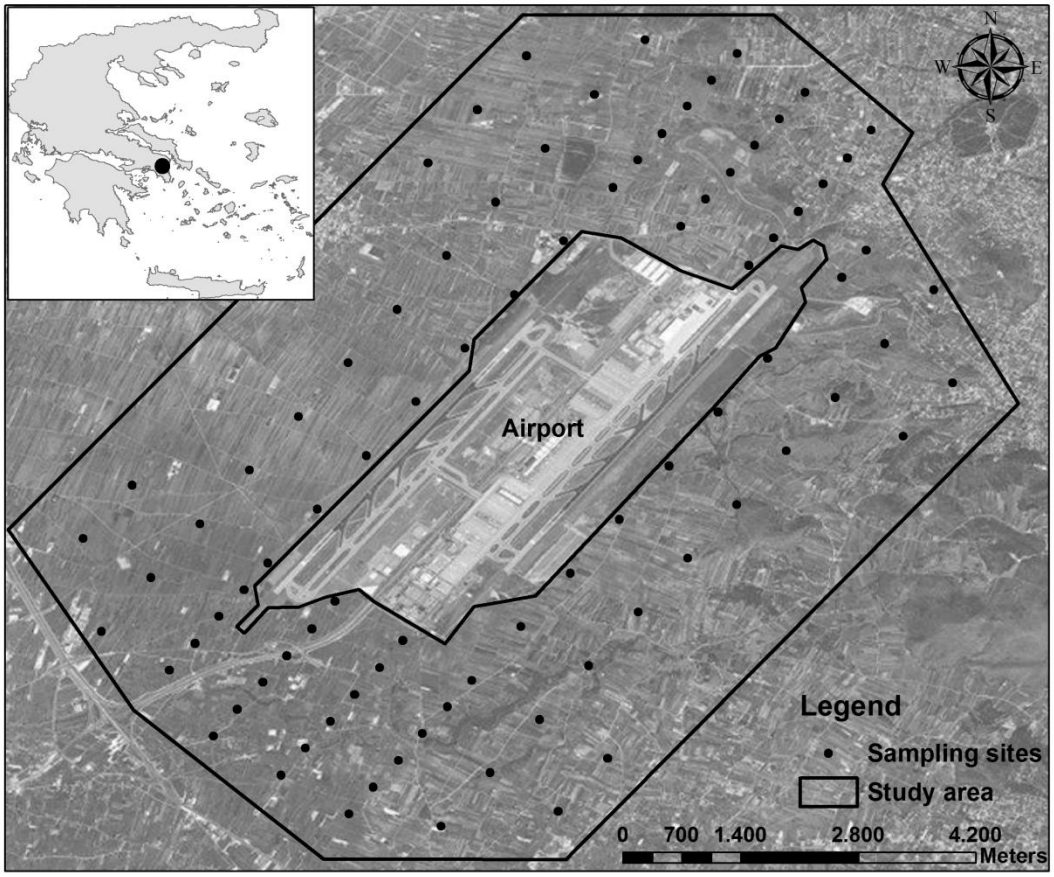

Figure 1 - Studied area and sampling sites.

2.2. Sample preparation and analysis

The soil samples were transferred to the laboratory in polyethylene bags, air-dried and sieved through a 2-mm sieve. The mechanical composition of the samples was determined by the Bouyoucos hydrometer method (Bouyoucos, 1951), while the organic matter content by the Walkley-Black procedure (Nelson and Sommers, 1982). Soil pH was determined in 1:1 v/w soil-water ratio slurries by the use of standard glass/calomel electrodes. The $CaCO_3$ equivalent percentage was estimated by measuring the evolved CO_2 following HCl dilution.

To obtain "pseudo-total" metal concentrations, the soil samples were digested with aqua regia (Gasparatos and Haidouti, 2001). "Pseudo-total" expression accurately describes the metal concentrations determined in aqua-regia extracts, because aqua-regia digestion does not completely destroy silicates (Facchinelli *et al.*, 2001). However, in the text of this study, the term "total" is used for simplicity.

All metal concentrations were determined by atomic adsorption spectrophotometer Varian spectra A300. The calibration standards were prepared in aqua-regia matrix which was used for the soil

samples. A control sample was analyzed for every ten samples, and reproducibility was tested by reanalyzing 30% of the samples. Analytical precision, estimated as relative standard deviation, ranged from 3% to 5% depending on the metal.

2.3. Enrichment factor (EF)

Table 1 - Total metal concentrations in soils close to international airports.

Location	Cu	Zn	Mn	Ni	Cr	Pb	Ba	Fe	References
	mg kg $^{-1}$							mg g $^{-1}$	
Shanghai Airport (China)	25	186	-	44	157	81	-	-	Rao *et al*., 2015
Pretoria Wonderboom Airport (South Africa)	98	88.9	1320		820	98.1	-	91.3	Olowoyo *et al*., 2013
Delhi (IGI) Airport (India)	21	97	391	44.2	127	37.5	-	4.38	Ray *et al*., 2012
Queen Alia Airport, (Jordan)	3.0	51.4			16.9	60.2	-	0.05	Al-Khashman & Shawabkeh, 2009
Athens Airport (Greece)	27	95.2	562.7	92.1	79.8	79	442	22.4	This study

Heavy metal enrichment factors (EFs) for the soil samples were calculated as described by Massas *et al.* (2010) and the following equation was used:

EF = Cit / Ait

where Cit, is the total metal concentration in the ith sampling site and Ait is the target metal A value of the Dutch guidelines system (Netherlands Ministry of Housing, Physical Planning and Environment (Netherlands M.H.P.P.E., 2000), obtained by adjusting the standard Atv value of the system for the ith sampling site according to the equation:

Ai =Atv x [{ a+(b x %clay) + (c x %organic matter)} / {(a+(b x 25) +(c x 10)}]

where:

Atv = standard A value of the metal in the Dutch guidelines system (Netherlands M.H.P.P.E., 2000)

% clay = percentage clay (grain size<2 mm) in the soil to be assessed

% organic matter = organic matter percentage (w/w) in the soil to be assessed.

a, b, c = metal dependent constants for each metal

EF values > 1 may be considered as possible soil enrichment.

2.4. Statistical Analysis and GIS

The descriptive statistical parameters, correlation analysis and cluster analysis were carried out by using the statistical software STATISTICA for Windows (StatSoft, Inc., USA, 1995, Version 7).

Spatial distributions of total metal concentrations in the soils of the tested area were visualized on maps produced by the ArcMap V9.3 software. The Geostatistical Analyst extension was used to

interpolate values between the sampling sites and to create interpolated surfaces by the Inverse Distance Weighted method.

3. Results

3.1 Soil properties

The soils of the studied area were developed mainly on alluvial deposits and their physicochemical key characteristics are presented in Table 2. The soils show light to medium texture as sand content ranged from 28.00 - 85.40 % and clay content ranged from 8.00 to 42.60 %. The pH does not vary much and is slightly basic (mean value=7.95) suggesting sub alkaline conditions and low metal mobility in the tested soils. Calcium carbonate equivalent ranges from 2.7 to 54.4 %, with an average value of 19%. High percentages of carbonates in soils are usually related to low bio-availability of heavy metals. Organic matter content highly fluctuated between traces and 21.06%, but most of the samples are poorly or moderately supplied by organic matter. These properties point to soils of adequate drainage that secure sufficient soil aeration and oxidizing conditions. Sand, clay, silt, organic matter, calcium carbonate equivalent content values and pH values are normally distributed, pointing to minimal site specific system disturbance.

Table 2 - Descriptive statistics of selected physicochemical properties of the studied soils (N=86).

	Sand (%)	**Silt (%)**	**Clay (%)**	**Org. matter (%)**	**$CaCO_3$ eq. (%)**	**pH (1:1)**
Mean	52.6	22.7	24.7	2.53	19.0	7.95
Median	52.8	23.5	24.3	2.24	19.8	7.96
Min.	28.0	2.6	8.0	traces	0.4	7.02
Max.	85.4	34.8	42.6	21.06	54.4	8.69
10^{th} percentile	40.0	14.0	15.5	1.01	2.7	7.64
90^{th} percentile	63.4	30.6	32.9	3.47	33.2	8.25
SD	9.6	6.5	6.7	2.38	11.8	0.26
CV%	18.2	28.6	27.0	94.12	61.8	3.30

3.2. Total metal concentrations

The descriptive statistics of the total Cu, Zn, Fe, Mn, Ni, Cr, Pb, and Ba concentrations are presented in Table 3. Though the mean total metal concentrations fall within the normal range for natural soils or for soils of low metal enrichment, the 90^{th} percentile and maximum values indicate that in some sampling sites (not necessary the same for all metals) concentration values exceed the reference "A values" or even the test "B values" of the Dutch System (Netherlands M.H.P.P.E., 2000). These increased metal concentrations, especially of Pb, Cu and Zn, point to secondary metal accumulation in the soils of the area, other than the presence of metals in soils due to soil formation processes. The observed high Ni mean total concentration is commonly detected in Greek soils and attributed to the soils' parent material. However, some soil samples showed clear indications of Ni enrichment.

Table 3 - Descriptive statistics for the total concentrations of the studied metals of the soils all around El. Venizelos airport (N=86).

	Cu	Zn	Mn	Ni	Cr	Pb	Ba	Fe*
				mg kg^{-1}				
Mean	27.02	95.21	562.72	92.13	79.77	78.96	442.53	22.39
Median	23.25	81.00	497.00	86.90	74.18	74.90	422.75	21.71
Min.	7.95	33.50	223.00	34.60	31.00	53.30	72.00	78.45
Max.	129.05	518.00	1491.00	177.10	154.35	271.20	1171.00	44.82
10^{th} percentile	17.70	61.50	363.00	60.35	52.90	62.35	257.50	15.45
90^{th} percentile	33.70	130.50	860.00	133.10	108.80	96.15	649.50	29.30
SD	16.66	56.59	232.17	28.75	24.35	26.24	174.155	62.00
CV%	61.66	59.43	41.26	31.20	30.53	33.23	39.35	27.69

*: Fe concentration in mg g^{-1}

4. Discussion

4.1. Distribution of metals

The interpolated studied area covered a land of 48 km^2 (including the airport). In Figures 2 and 3, the distribution of Pb, Ni, Cr, Ba, Cu, Zn, Mn and Fe total concentrations around the airport is presented. Not a clear unique pattern for the distribution of all metals can be detected. Spots of higher Pb and Cu concentrations are observed in the northern part of the studied area. Ni also shows a distribution pattern similar to that of Pb and Cu, while for Zn a south to north accumulation in the soils appears. Increased Cr, Ba and Mn concentrations observed in the western part though for Cr a north to south distribution is also apparent. Finally, the higher Fe concentration is clearly present in the south-west of the area. The interpolated maps that visualize the distribution of total metal concentrations in the soils around the El. Venizelos airport, can serve to relate the distribution pattern of each metal to specific potential metal sources. However, any discussion on the potential sources of the studied metals based on their distribution patterns in soils around the airport is beyond the scope of this preliminary assessment.

4.2 Enrichment Factors

Enrichment Factor (E.F.), as a soil pollution index that is calculated by metal concentration values normalized for clay and organic matter content of the soils, may provide a more precise approach to the data. The mean EF values for Pb, Cu, Zn, Ni, Cr and Ba are 1.03, 0.86, 0.75, 2.68, 0.80 and 2.29 respectively, indicating no or minor or moderate soil pollution, depending on the metal. Mean EF values suggest Ni and Ba accumulation in the soils of the area. However, the reference "A values" of the Dutch system (Netherlands M.H.P.P.E., 2000) that were used for the calculation of Ni and Ba EFs are lower than Ni and Ba background concentrations in most Greek soils, and this is probably the main reason for the high Ni and Ba EFs observed in the soils of the studied area (Geochemical Atlas of Europe, 2005). In Figure 4 the median, the 10^{th} and 90^{th} percentiles and the minimum and maximum EF values of the six metals are presented. Though median EF values are low (with the exception of the high Ni and Ba EF median values for reasons discussed earlier) the 90^{th} percentile and the maximum EF values for Pb, Cu and Zn indicate site specific soil enrichment by these metals. This argument is further supported by the fact that Pb, Cu and Zn EF values do not follow a normal distribution pattern (Kolmogorov-Smirnov & Lilliefors test for normality).

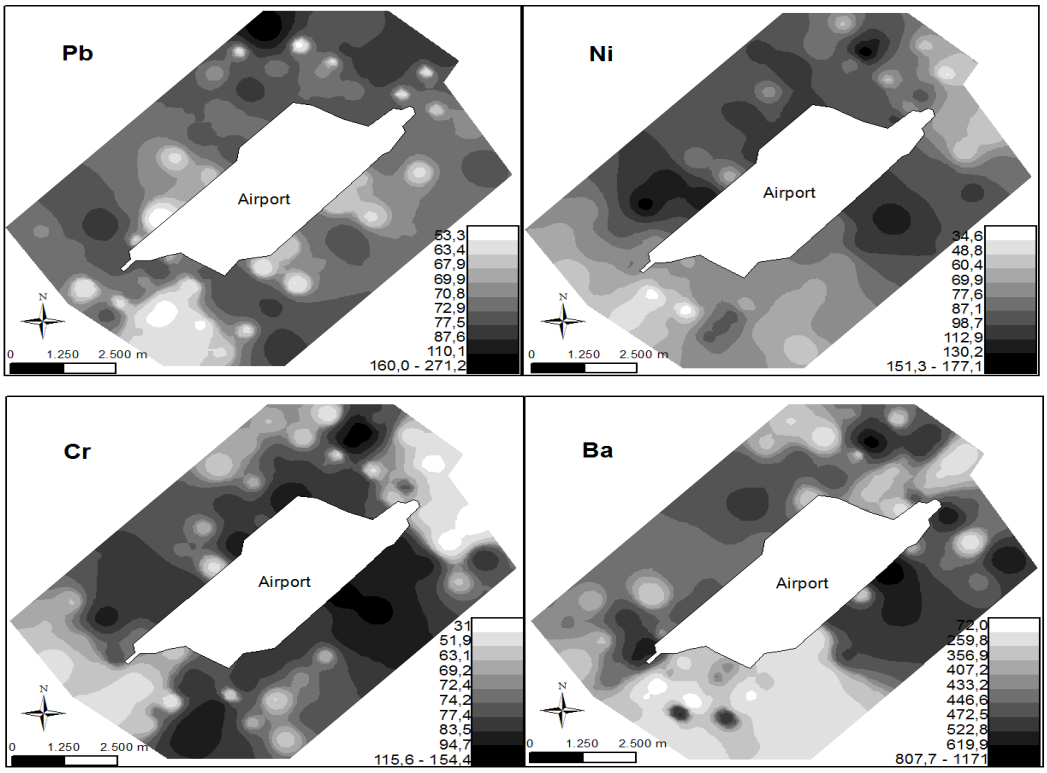

Figure 2 - Interpolated maps of the Pb, Ni, Cr, and Ba total concentrations in the soils around the El. Venizelos airport.

4.3. Cluster Analysis and Correlations

As it is presented in Figure 5, two main clusters were distinguished. The metals included in the first main cluster are Cr, Ni, Ba, Mn, Fe and Zn while the second main cluster consists of Pb and Cu. Within the first main cluster two clear sub-clusters observed indicating a strong relation between Cr and Ni and Mn and Ba, respectively. A weak connection of Fe with the second sub-cluster is also noticed and a very weak association of Zn with the metals of the first main cluster is apparent. Considering that the smaller the linkage distance the stronger the relation between metals, it can be supported that the metals in each of the following Cr-Ni, Ba-Mn and Pb-Cu groups originated from the same source. The significant but weak correlations between the clay content and Cr, Ni and Mn total concentrations (r values 0.34, 0.36 and 0.34 respectively, $p<0.05$) indicate that to some extent these metals derived from the soil's parent material. Clay content of the soils showed a significant correlation to the Fe total concentration ($r=0.60$, $p<0.05$) that strongly supports the geogenic origin of Fe. The physicochemical characteristics of the studied soils did not correlate to Ba, Cu, Zn and Pb total concentrations, pointing to secondary soil enrichment by these metals probably due to atmospheric depositions. However, to robustly support any assumptions relative to the origin of the metals in the studied soils the bioavaliable / exchangeable forms of the metals must be determined and soil samples must be subjected to fractionation schemes, since heavy metals from anthropogenic sources could be more mobile than from geogenic sources (Burt *et al.*, 2003; Gasparatos *et al.*, 2015).

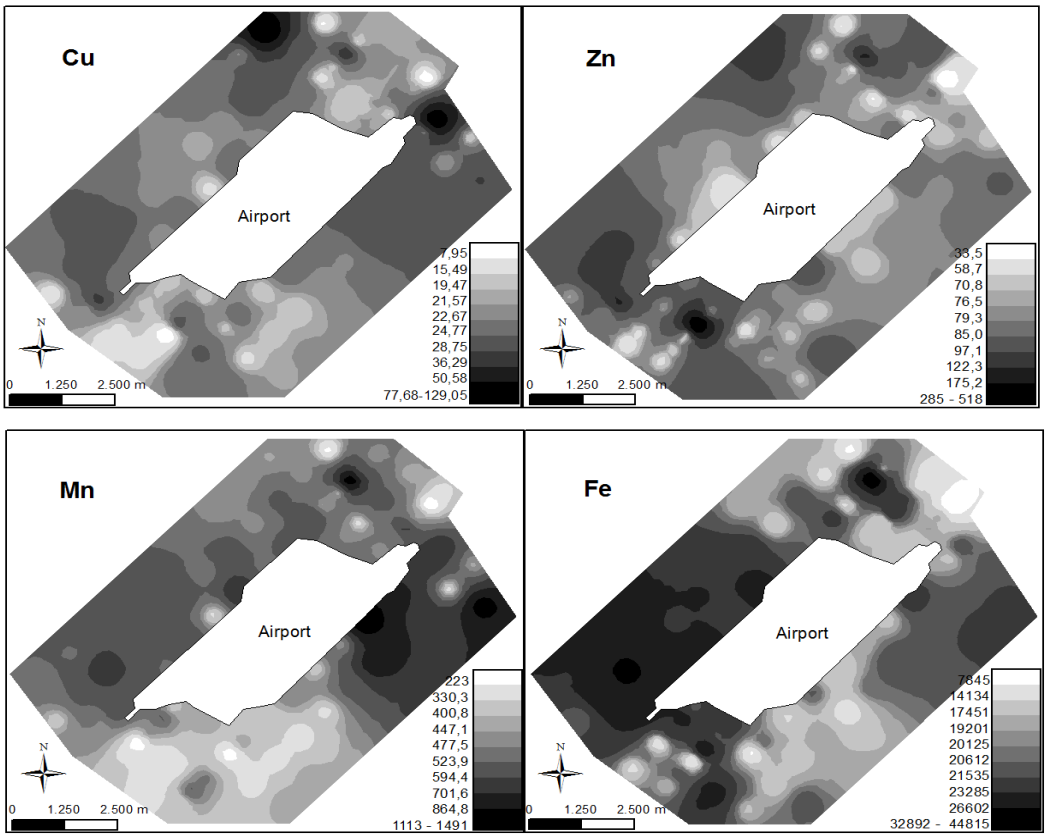

Figure 3 - Interpolated maps of Cu, Zn, Mn, and Fe total concentrations in the soils around the El. Venizelos airport.

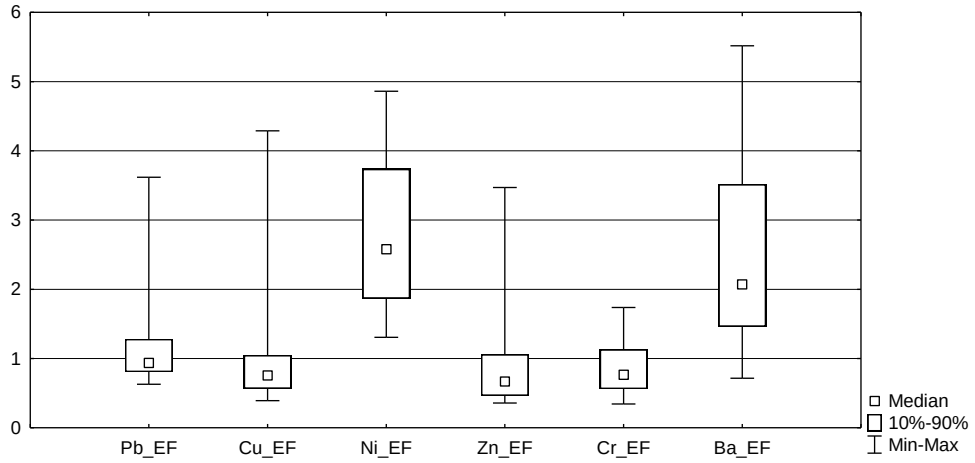

Figure 4 - Presentation of Enrichment Factors (EFs) statistics.

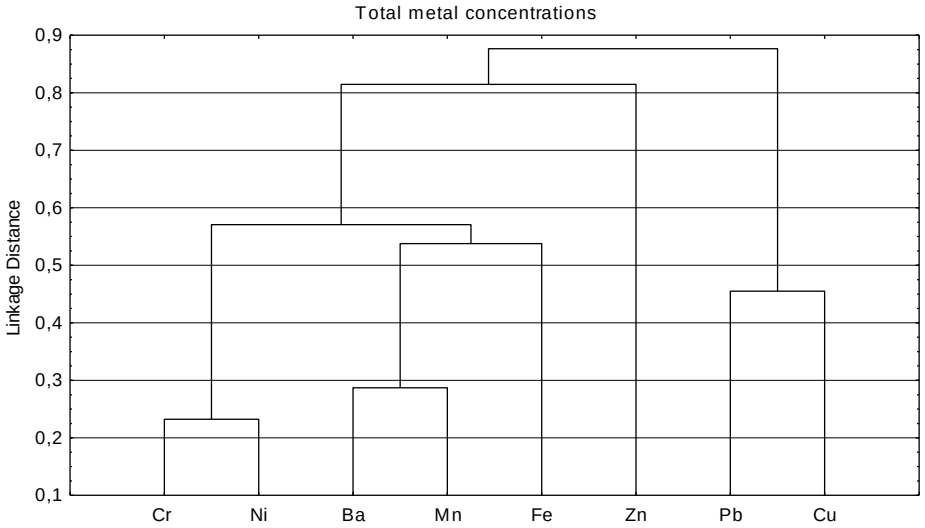

Figure 5 - Hierarchical clustering results (dendogram) of the total metal concentrations in the soils around the El. Venizelos airport.

5. Conclusions

This study attempted to record the levels of Pb, Cu, Zn, Ni, Cr, Ba, Mn and Fe in the soils around Athens International Airport after 13 years of airport operation. The mean metal concentrations were generally low but increased site specific Pb, Cu and Zn and to a lesser extent Ni concentrations were determined. Cluster and correlation analyses results and Enrichment Factor values support the assumption of secondary accumulation of the above metals in the soils of the studied area due to aerial depositions. The dense airplane landing and taking off, the maintenance of the aircrafts and the traffic burden within and nearby the airport area may contribute to the observed site specific soil enrichment by Pb, Cu and Zn. Considering that this study is an assessment on preliminary data, more scientific research is needed to clearly distinguish between the sources of the metals present in the studied soils.

6. References

Al-Khashman, O.A. and Shawabkeh, R.A., 2009. Metal distribution in urban soil around steel industry beside Queen Alia Airport, Jordan, *Environmental Geochemistry and Health*, 31, 717-726.

Alloway, B.J. and Ayres, D.C., 1997. *Chemical Principles of Environmental Pollution*, Blackie Academic and Professional, London.

Bouyoukos, G.H., 1951. A recalibration of the hydrometer method for making mechanical analysis of soils, *Agron. J.*, 43, 434-438.

Bretzel, F. and Calderisi, M., 2006. Metal contamination in urban soils of coastal Tuscany (Italy), *Environ. Monit. Assess.*, 118, 319-335.

Burt, R., Wilson, M.A., Keck, T.J., Dougherty, B.D., Strom, D.E. and Lindahl, J.A., 2003. Trace Element Speciation in Selected Smelter-Contaminated Soils in Anaconda and Deer Lodge Valley, Montana, USA, *Adv. in Environ. Res.*, 8/1, 51-67.

D'Amore, J.J., Al-Abed, S.R., Scheckel, K.G. and Ryan, J.A., 2005. Methods for speciation of metals in soils: a review, *J. Environ. Qual.*, 34(5), 1707-1745.

Facchinelli, A., Sacchi, E. and Mallen, L., 2001. Multivariate statistical and GIS-based approach to identify heavy metal sources in soils, *Environ. Pollut.*, 114, 313-324.

Gasparatos, D. and Haidouti, C., 2001. A comparison of wet oxidation methods for determination of total phosphorus in soils, *J., Plant Nutr. Soil Sc.*, 164, 435-439.

Gasparatos, D., Mavromati, G., Kotsovilis, S. and Massas, I., 2015. Fractionation of heavy metals and evaluation of the environmental risk for the alkaline soils of the Thriassio plain: a residential, agricultural, and industrial area in Greece, *Environmental Earth Sciences*, doi: 10.1007/s12665-015-4096-1.

Geochemical Atlas of Europe, 2005. Part 1: Background information, Methodology and Maps. Geological Survey of Finland.

Giannakopoulou, F., Gasparatos, D., Haidouti, C. and Massas, I., 2012. Sorption behavior of cesium in two Greek soils: effects of Cs initial concentration, clay mineralogy and particle size fraction, *Soil and Sediment Contamination*, 21(8), 937-950.

Kabata-Pendias, A. and Pendias, H., 2001.Trace elements in soils and plants, (3rd *eds.*) Boca Raton, CRC.

Koulourasis, M., Aloupi, M. and Angelidis, M.O., 2009. Total metal concentrations in atmospheric precipitation from the Nothern Aegean Sea, *Water Air Soil Poll.*, 209, 381-403.

Massas, I., Ehaliotis, C., Gerontidis, S. and Sarris, E., 2009. Elevated heavy metal concentrations in top soils of an Aegean island town (Greece): total and available forms, origin and distribution, *Environ. Monit. Assess*., 151, 105-116.

Massas, I., Ehaliotis, C., Kalivas, D. and Panagopoulou, G., 2010. Concentrations and availability indicators of soil heavy metals; the case of children's playgrounds in the city of Athens (Greece), *Water Air Soil Poll*., 212(1-4), 51-63.

Nelson, D.W. and Sommers, L.E., 1982. Total carbon, organic carbon and organic matter. *In:* Page, A.L., Miller, R.H. and Keeney, D.R., (e*ds.*), Methods of soil analysis, Chap. 29. Madison: Soil Science Society of America.

Netherlands Ministry of Housing, Physical Planning and Environment (Netherlands MHPPE). 2000. Annexes circular on target values for soil remediation. The Netherland: MHPPE.

Olowoyo, J.O., van Heerden, E. and Fischer, J., 2013. Trace metals concentrations in soil from different sites in Pretoria, South Africa, *Sustain. Environ. Res.*, 23, 93-99.

Papathanasiou, C., Makropoulos, C. and Mimikou, M., 2013a. The Hydrological Observatory of Athens: a state-of-the-art network for the assessment of the hydrometeorological regime of Attica, *Proc*. *13th International Conference on Environmental Science and Technology*, 5-7 September, Athens, Greece (full paper submitted and accepted for oral presentation).

Papathanasiou, C., Massari, C., Pagana, V., Barbetta, S., Brocca, L., Moramarco, T., Makropoulos, C. and Mimikou, M., 2013b. Hydrological Study of Rafina catchment, Technical report for Action B1: Catchment Hydrological Modelling of the FLIRE Project (LIFE11 ENV GR 975).

Rao, P., Zhu, A., Yao, W., Zhang, W., Men, Y. and Ding, G., 2015. Sources and risk assessment of metal contamination in soils at the international airport of Shanghai, China, *Toxicological & Environmental Chemistry*, 96, 1153-1161.

Ray, S., Khillare, P.S. and Kim, K.H., 2012. The Effect of Aircraft Traffic Emissions on the Soil Surface Contamination Analysis Around the International Airport in Delhi, India, *Asian Journal of Atmospheric Environment*, 6, 118-126.

Shrinivasa Gowd, S., Ramakrishna, M. and Govil, P.K., 2010. Assessment of heavy metal contamination in soils at Jajmau (Kanpur) and Unnao industrial areas of the Ganga Plain, Uttar Pradesh, India, *J. of Hazard. Mater*., 174, 113-121.

Swaine, D.J. and Micthell, R.L., 1960. Trace elements distribution in soil profiles, *J. Soil Sci.*, 11(2), 347-368.

Δελτίο της Ελληνικής Γεωλογικής Εταιρίας, τόμος L, σελ. 2241-2250
Πρακτικά 14ου Διεθνούς Συνεδρίου, Θεσσαλονίκη, Μάιος 2016

Bulletin of the Geological Society of Greece, vol. L, p. 2241-2250
Proceedings of the 14th International Congress, Thessaloniki, May 2016

ENVIRONMENTAL GEOCHEMISTRY OF PTOLEMAIS LIGNITES, INTERMEDIATE STERILES, AND COMBUSTION PRODUCTS

Megalovasilis P.[1], Godelitsas A.[2], Papastergios G.[3] and Filippidis A.[3]

[1]*Technological Educational Institute of Ionian Islands, Department of Environment Technologists, Division of Natural Environment Technologies, 29100, Zakynthos, Greece, pmegal@teiion.gr*

[2]*University of Athens, Faculty of Geology & Geoenvironment, 15784, Athens Greece, agodel@geol.uoa.gr*

[3]*Department of Mineralogy-Petrology-Economic Geology, Aristotle University of Thessaloniki, 131 Egnatia St. Thessaloniki 54124, Greece, gpapaste@geo.auth.gr; anestis@geo.auth.gr*

Abstract

The environmental geochemistry of lignite, intermediate sterile, fly ash and bottom ash samples from Ptolemais area, has been investigated. The chemical analyses of major elements, combined with SEM-EDS, showed that Si, Ca and Fe, are the most abundant elements and associated with various micro-particles. On average, the most abundant trace elements in the lignite samples are Ba (128 ppm), V (123 ppm), Cr (108 ppm), Sr (107), Ni (43 ppm), in intermediate sterile samples Ba (209 ppm), Sr (209 ppm), Cr (104 ppm), Ni (76 ppm), Zr (67 ppm), Zn (57 ppm), V (53 ppm), in fly ash samples Ba (455 ppm), Sr (336 ppm), Ni (180 ppm), Cr (160 ppm), V (110 ppm), Zr (102 ppm), Zn (74 ppm), Cu (71 ppm), Rb (62 ppm) and in bottom ash samples Ba (250 ppm), Cr (214 ppm), V (174 ppm), Sr (153 ppm), Ni (105 ppm), Zr (56 ppm), Zn (40 ppm).

Keywords: *Greece, trace element, bottom ash, fly ash, environment.*

Περίληψη

Διερευνήθηκε, η περιβαλλοντική γεωχημεία λιγνιτών, ενδιάμεσων στείρων, ιπτάμενης τέφρας και τέφρας εσχάρας, από την περιοχή της Πτολεμαΐδας. Οι χημικές αναλύσεις των κύριων στοιχείων, σε συνδυασμό με το SEM-EDS, έδειξαν ότι τα στοιχεία Si, Ca, και Fe είναι τα πιο άφθονα και συνδέονται με διάφορα μικρο-σωματίδια. Κατά μέσο όρο, τα πιο άφθονα ιχνοστοιχεία στα δείγματα των λιγνιτών είναι Ba (128 ppm), V (123 ppm), Cr (108 ppm), Sr (107), Ni (43 ppm), στα δείγματα των ενδιάμεσων στείρων Ba (209 ppm), Sr (209 ppm), Cr (104 ppm), Ni (76 ppm), Zr (67 ppm), Zn (57 ppm), V (53 ppm), στα δείγματα των ιπτάμενων τεφρών Ba (455 ppm), Sr (336 ppm), Ni (180 ppm), Cr (160 ppm), V (110 ppm), Zr (102 ppm), Zn (74 ppm), Cu (71 ppm), Rb (62 ppm) και στα δείγματα των τεφρών εσχάρας Ba (250 ppm), Cr (214 ppm), V (174 ppm), Sr (153 ppm), Ni (105 ppm), Zr (56 ppm), Zn (40 ppm).

Λέξεις Κλειδιά: *Ελλάς, Ιχνοστοιχείο, τέφρα εσχάρας, ιπτάμενη τέφρα, περιβάλλον.*

1. Introduction

Greece is second among EU countries for lignite coal production, with coal reserves of 3900 million tonnes at the end of 2007. The principal lignite production areas comprise the Ptolemais and Amyntaion lignite fields in Macedonia (N. Greece), which contribute 80%, and the Megalopolis area in the Peloponnese contributing 20%. In the greater area of Ptolemais six power stations operate with a total capacity 4388MWe (Petrotou *et al*., 2010, 2012; Megalovasilis *et al*., 2013). The geochemical character of coal deposits depends mainly on factors related with the coal (nature of the original plant material), the environment of deposition (geological setting and the physicochemical conditions applied after buried the age and rank of the coal, the activity of groundwater, and the weathering conditions of coal (Filippidis and Georgakopoulos, 1992; Georgakopoulos *et al*., 1994; Filippidis *et al*., 1996). All these factors control which elements are enriched, depleted or just present in the coal (Valcovic, 1983; Foscolos *et al.*, 1989; Swaine, 1990; Finkelman, 1999).

During lignite combustion the major, minor and trace elements may concentrate in fly ash, while the mineral matter undergoes a series of physical and chemical changes (Filippidis and Georgakopoulos 1992; Yan *et al*., 2001; Vamvuka *et al*., 2004; Koukouzas *et al*., 2007, 2009; Vamvuka *et al*., 2009; Vejahati *et al*., 2010). Lignite combustion processes result in emission of particulate matter to the environment resulting in high enrichment of certain elements against local soils or road dusts, such as S, Cl, Cu, As, Se, Br, Cd and Pb, and moderate enrichments in other elements e.g. Ti, Mn, Mg, Al, Si, P, Cr (Kolovos *et al*., 2002a, b; Zeevaert *et al.*, 2006; Petaloti *et al*., 2006; Iordanidis *et al*., 2008; Petrotou *et al*., 2010, 2012). One of the major problems that concerns the local authorities in the greater area of Ptolemais, and can easily be seen, is the respirable dust spread by winds from stock piles. In addition, lignite contains natural radionuclides ^{238}U, ^{226}Ra, ^{210}Pb, ^{232}Th and ^{40}K (Megalovasilis, 1994; Karangelos *et al*., 2003; Stoulos *et al*., 2004; Petropoulos *et al*., 2004) and lignite burning is a source of technologically enhanced exposure to man from natural radionuclides.

The continuous studying of the content of Potentially Toxic Elements as well as the understanding of the origin and behaviour of such elements is a priority in the EU (and worldwide), but even more in countries that utilize fossil fuels, such as lignite, as an energy source. The present study aims at contributing towards this priority.

2. Geological setting

Ptolemais basin is part of the Florina-Vegoritis-Ptolemais Graben which is a large basin, filled with Neogene-Quaternary sediments, that has been developed between the mountains of Voras-Vernon to the east and Vermion-Askio to the west, and extends from the northern Bitola plain (FYROM) in a SSE direction to the hills of the Kozani area. It is almost 100 km long and about 15-20 km wide covering approximately 155 km^2. In brief, the basin consists of Palaeozoic and Mesozoic rocks, either metamorphic or plutonic underlying limestone and flysch. The basement rocks can be divided into four tectonic units: 1. the pre-Alpine Pelagonian Basement, 2. the Almopia Unit, 3. the ultramafic-mafic Unit and 4. the Transgression Unit (Mountrakis *et al*., 1984).

3. Materials and Methods

3.1 Sampling and sample preparation

Amyntaion Power Station has two pulverised lignite-fired boilers. Samples were collected from the production lines and include pulverised lignite (PL), fly ash (FA) and bottom ash (BA). Black lignite samples (BL), wooden lignite (WL) and some intermediate steriles (i.e., conglomerates, sandstones, clays, marls, limestones, etc. that are interlayered with the lignite) samples (IS1, IS2, IS3, IS4) which were also collected from the stock piles just outside the production line. Lignite supplies for the power station vary even daily, in physical and chemical state because they originate from various

coal-fields; therefore, it was decided to take monthly average samples together with the corresponding fly ash and bottom ash. Each sample was grinded prior to any further preparation and the particle size was reduced to 90 meshes using a mortar and a pestle. A more detailed description can be found in Megalovasilis *et al.* (2013).

3.2. Bulk analyses and SEM-EDS

XRF methods were used for the determination of 10 major and 11 trace elements in all the fly ash and bottom ash samples as well as in all the rock samples. Geochemical results were obtained for: Si, Al, Fe, Mn, Mg, K, Na, Ca, P, Ti, and Pb, Zn, Cu, Ba, Cr, Co, Ni, V, U, Th, Rb, Sr, Y, Nb, Zr and Sc. Internal standards were used in all cases and analysis was carried out with the use of Philips PW 1400 X-ray generator. Instrumental conditions used for XRF analyses for major and trace elements are those followed in routine geochemical analyses. However, the preparation and analysis was performed in the same way as that for fly ash, bottom ash and rock samples and consequently is relevant. Arsenic was determined only on limited samples using AAS Absorption of Ultraviolet and Visible radiation in a Unicam 8625 UV/VIS Spectrometer and AAS graphite furnace (B.S. 1016:, 1977). Cadmium was also analysed on limited samples applied with Varian GTA 96 Graphite Tube Atomiser following the same B.S. 1016 standard. Based on laboratory procedures and operating conditions, trace elements results with 5% precision and major elements results an 1% precision, should be considered. SEM-EDS images taken using a Jeol SEM.

4. Results and Discussion

4.1. Major elements and related phases

Analysis was carried out with the use of TR1 & TR2 and MAJ software programmes, for trace and major elements respectively and analytical results stats are shown in Tables 1 and 2. The analytical results concerning major elements in intermediate steriles (IS), fly ash (FA) and bottom ash (BA), are presented in **Table 1**, whereas the solid related phases appearing in microscale, also in lignites, are shown in **Figures 1-6**.

Table 1 - Concentration (wt.%) of major elements in intermediate steriles (IS), fly ash (FA) and bottom ash (BA).

	SiO_2	TiO_2	Al_2O_3	Fe_2O_3	MnO	MgO	CaO	Na_2O	K_2O	P_2O_5	L.O.I.	Total
IS1	2.66	0.05	1.02	1.08	0.05	4.46	89.5	1.80	0.22	0.18	0.00	100.0
IS2	58.5	1.35	23.3	5.35	0.07	2.51	3.28	2.11	2.72	0.20	0.00	99.4
IS3	57.3	1.30	22.8	5.21	0.07	2.49	3.20	1.96	2.65	0.21	0.00	97.1
IS4	15.9	0.28	5.05	3.89	0.11	6.24	66.1	0.69	0.50	0.09	0.00	98.9
FA1	34.8	0.72	13.9	6.79	0.07	4.07	32.3	1.54	1.16	0.26	4.05	95.6
FA2	35.7	0.70	13.6	6.50	0.07	3.95	31.5	1.92	1.20	0.25	3.37	95.4
FA3	34.0	0.69	13.7	6.52	0.06	4.16	33.1	1.38	1.19	0.24	4.29	95.5
BA1	44.6	0.88	16.4	8.55	0.06	3.72	19.6	0.76	1.35	0.25	38.3	96.2
BA2	44.4	0.83	15.4	8.39	0.08	3.69	21.7	0.58	1.30	0.23	37.5	96.9
BA3	39.9	0.86	14.3	9.21	0.07	3.73	22.1	0.76	1.22	0.23	64.3	92.7

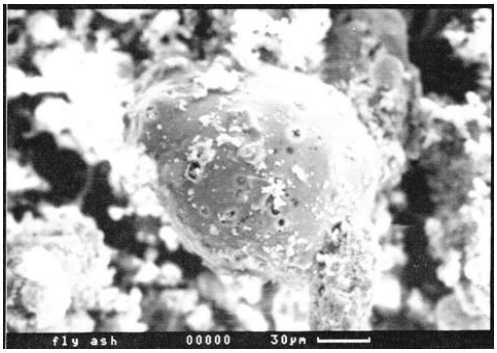

Figure 1 - Porous carbonaceous cenosphere.

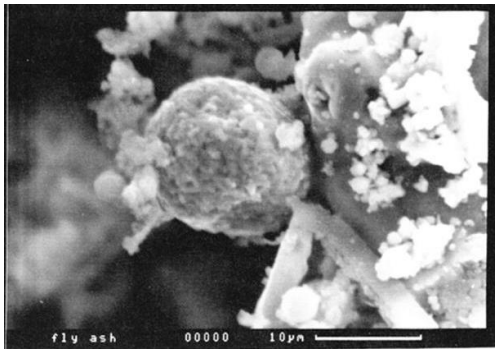

Figure 2 - Fe-oxide botryoidal spherule in F A.

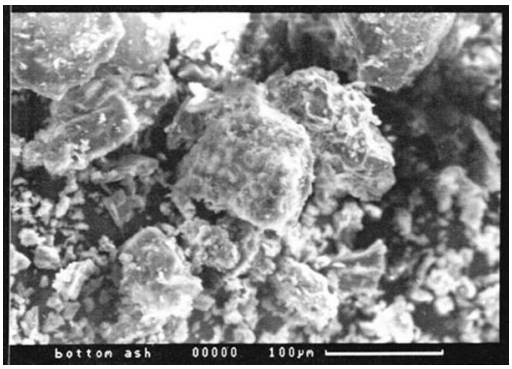

Figure 3 - Sulphate (gypsum-anhydrite) microparticles in BA.

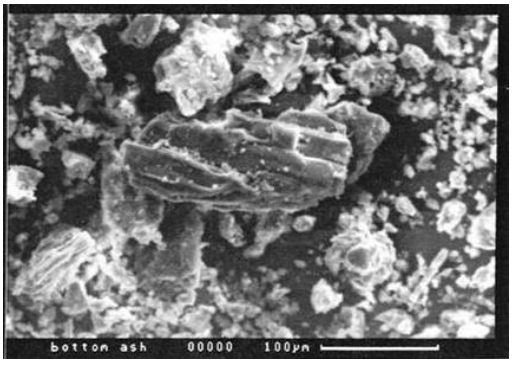

Figure 4 - Melilite (gehlenite-åkermanite) microparticle.

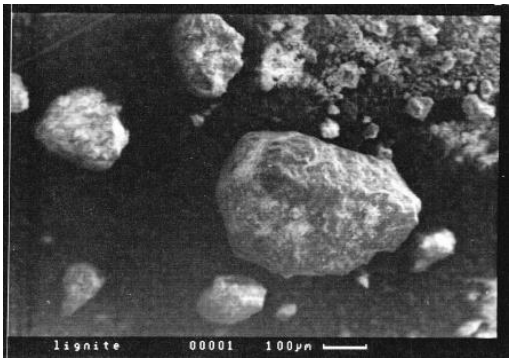

Figure 5 - Carbonaceous microparticles in lignite.

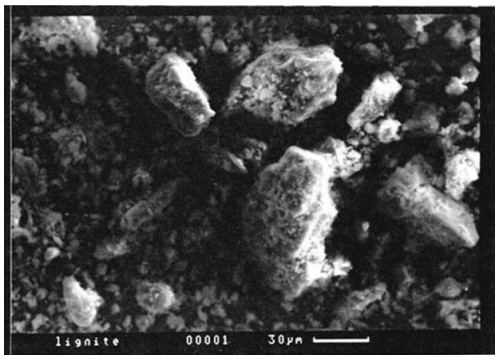

Figure 6 - Micro-fragments of feldspars in lignite.

It is evident that silicon is the predominant major element, in all types of samples examined by analytical and microscopic techniques. According to Koukouzas *et al.* (2009) the major lignite (inorganic) minerals are quartz and clays, whereas there are also organic minerals such as weddelite. Besides, calcium is also essential in all samples, occurring mainly in the form of Ca-carbonate, Ca-oxide, and Ca-sulphate microparticles. Moreover, iron seems to be essential in the case of ashes, forming porous and botryoidal Fe-oxide spherules. According to Filippidis *et al.* (1996), ashes may contain hematite together with a variety of Ca-Mg-silicates and Ca-Fe-/Ca-Al-Fe-oxides. It should be mentioned that, on the basis of the present results, and in accordance to previous works, there is

no clear indication of distinct phases composed by elements of environmental interest, such as Ni, V, Cr, As, U and Th.

4.2. Trace element geochemistry

The analytical results concerning trace elements in intermediate steriles (IS), lignites (BL, WL & PL), fly ash (FA) and bottom ash (BA) are presented in **Table 2** and **Figure 7**.

Table 2 - Summary of trace element concentrations (ppm) in intermediate steriles (IS), lignites (BL, WL & PL), fly ash (FA) and bottom ash (BA).

	Pb	Zn	Cu	Ba	Cr	Co	Ni	V	U	Th	Rb	Sr	Y	Nb	Zr	Sc	As	Cd
IS1	<5	14	<5	137	<5	3	4	<5	<3	4	4	263	<3	<2	<5	17		
IS2	35	166	40	543	298	40	169	184	<3	18	123	212	40	21	244	20		
IS3	<5	16	<5	40	18	3	20	8	<3	5	7	98	4	<2	6	21		
IS4	<5	31	13	114	98	8	109	20	<3	7	21	262	5	2	16	20		
BL	<5	11	21	91	64	17	11	70	5	4	14	106	5	4	32	8		
WL	<5	14	19	58	75	17	18	269	<3	3	<2	52	4	<2	<5	12		
PL																		
MIN	7	26	23	150	126	15	56	88	4	7	19	120	8	4	34	12	2	0.3
MAX	9	31	35	177	142	20	67	96	6	8	23	130	10	5	36	14	3	0.5
MEAN	8	28	28	166	135	18	62	91	5	8	21	126	9	4	35	13	3	0.4
FA																		
MIN	19	71	64	440	150	20	170	107	14	14	61	331	26	13	97	17	10	0.7
MAX	23	77	77	469	171	20	191	114	17	15	63	342	27	13	108	18	16	2.0
MEAN	21	73	71	457	160	20	178	110	15	15	62	335	26	13	102	17	14	1.2
BA																		
MIN	5	29	8	138	198	26	83	148	7	7	25	107	13	5	40	14	3	0.4
MAX	10	51	51	344	228	28	125	201	9	13	46	191	22	10	70	17	5	2.0
MEAN	7	41	33	267	216	27	108	173	9	10	38	160	18	8	59	15	4	0.9

Trace elements in coal can occur as components of either the organic constituents (macerals) or the inorganic constituents (minerals). The concentrations and distribution of the trace elements are important in order to understand the geochemical conditions in which the coal was formed and in predicting the environmental impact of burning particular coals. It has been found that coal combustion is a significant atmospheric pollutant source for lead (Petaloti *et al.*, 2006), but the amount of Pb emitted to the atmosphere from coal combustion is dependent upon its concentration in coal, type of boiler configuration and the effectiveness of control devices. The mode of occurrence of lead in coals, varies for different areas, and the main associations are with galena, pyrite, PbSe, and some Ba minerals, where Pb can replace Ba (sulphates, carbonates and phosphates). As mentioned above, all of these potential phases have not been determined in the SEM-EDS investigation performed in the present study. Organic association is (e.g. in low rank coals) expected as well but in lesser extent. It has been observed that no significant amount of lead is volatized upon ashing, and studies of lead distribution vs. fly ash particle size demonstrated maximum concentration in the sub micron range while coal combustion contributes 6% or more to total atmospheric lead

emissions (Valcovic, 1983). Lead average concentration in Ptolemais lignite is 8 ppm with a range of about 7-9 ppm. In fly ash the average concentration is 21 ppm ranging from 19 to 23 ppm and in bottom ash is 7 ppm ranging from 5-10 ppm.

Zinc is an essential element and is required by living organisms, but in very small amounts. In the Ptolemais lignite Zn concentrations vary from 26-31 ppm with an average value of 28 ppm. It has been suggested that Zn is organically bonded (i.e., in low-rank coals), but there have been many detections of sphalerite [(Zn,Fe)S], as well. In fly ash samples, Zn was found to be in the range of 71-77 ppm with an average of 73 ppm. In bottom ash, Zn levels are in the range 29-51 ppm while the average value is 41 ppm.

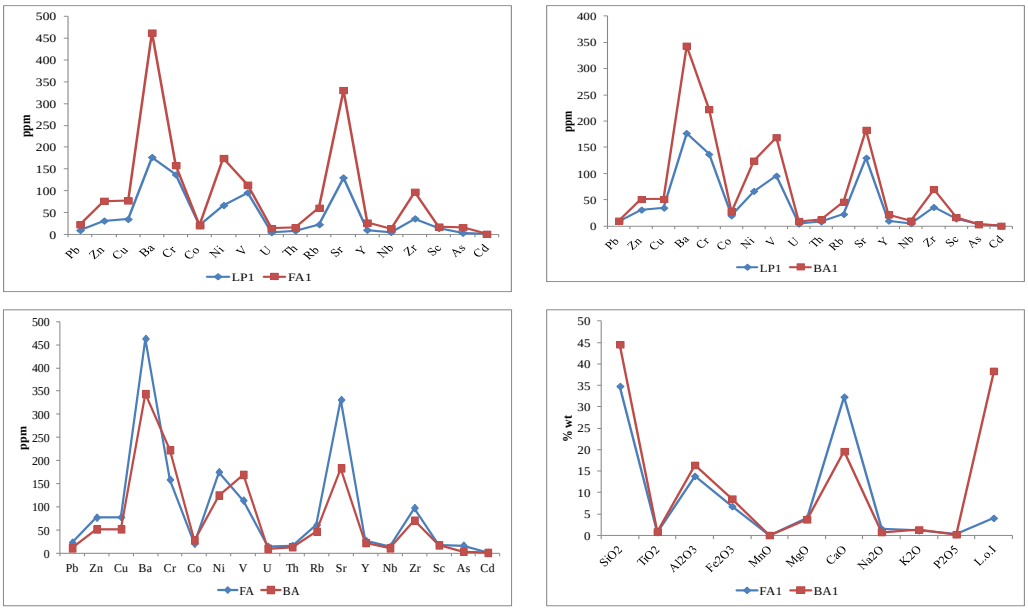

Figure 7 - Trace elements concentrations in lignite and combustion byproducts (FA and BA).

Copper is an essential element but excess is undesirable. Chalcopyrite is found in many coals, but other sulphide minerals of Cu occur occasionally (Swaine, 1990). The mode of occurrence of Cu in most coals is probably as a sulphide, usually Chalcopyrite [$CuFeS_2$] and associated with organic matter, especially in low-rank coals. In Ptolemais lignite, Cu concentration is between 23-35 ppm and while the average Cu content is 28 ppm. In the fly ash Cu has an average concentration of 71 ppm and a concentration range 64-77 ppm. In bottom ash samples Cu is within the range 8-51 and has an average concentration of 33 ppm.

Barium associates with Ba-bearing minerals e.g.: Barite [$BaSO_4$], Barytocelestine [$(Sr,Ba)SO_4$], Witherite [$BaCO_3$] and Gorceixite [$BaAl_3(PO_4)(PO_3OH)(OH)_6$], and thus has an inorganic affinity although in some cases there is evidence for the association of Ba with organic coaly matter via carboxyl groups. Barium in Ptolemais lignite varies from 150 to 177 ppm with an average concentration of 166 ppm Ba. In fly ash Ba has a range from 440-469 ppm and an average concentration of 457 ppm. In bottom ash samples, Ba concentration found between 138 to 344 with an average of 267 ppm.

Chromium is not regarded as toxic, except in the hexavalent state, which may occur in some waste waters and industrial situations, but not usually during coal mining or usage. It is partly complexed with organic matter in some US lignites, but in addition, mineral matter association has been observed as well. Chromium in Ptolemais Lignite was found being in a range from 126 to 142 ppm

and with average concentration 135 ppm. In fly ash Cr ranges from 150 to 171 ppm with average value 160 ppm, and in bottom ash from 198 to 228 ppm with an average of 216 ppm.

Cobalt may occur in coal associated with the mineral matter (linnaeite, other sulphides, clay) and with organic matter. The range for Ptolemais lignite is 15-20 ppm with a mean of 18 and for fly ash samples analysed the range is 16-23 with a mean of 20ppm. For the bottom ash sample Co found being in a range from 26-28 ppm with a mean of 27.

The major source of atmospheric Ni is form the combustion of fossil fuels. Nickel concentration in lignite is 56-67 ppm, with a mean of 62 ppm. In fly ash Ni concentration is ranging from 170-191 ppm with an average value 178 ppm and in bottom ash is ranging from 83-125 with a mean of 108 ppm. The mode of occurrence is associated with sulphides (millerite, linneaeite) and organically associated (Finkelman, 1999).

Vanadium could be responsible for corrosion effects during utilisation and health effects at high levels. Vanadium is bound organically in some coals, while in other cases an inorganic association has been proposed. In lignite, V has an average concentration of 91 ppm, ranging from 88-96 ppm while in fly ash the mean is 110 ppm and the range is 117-114 ppm. In bottom ash V has an average concentration of 173 ppm and a range from 148-201 ppm.

Uranium is an element of environmental importance because is a source of radioactivity. Its concentration in lignite is 5 ppm and it varies little (4 to 6 ppm). These values fall in range of other reported U concentrations from adjacent lignitic fields in the area (Papanicolaou *et al.*, 2004). In fly ash the mean is 15 and the fly ash samples fall in the range 14-17 ppm approximately. Regarding the bottom ash, the mean is 8.7 ppm and the range observed is around 7-9 ppm. The modes of occurrence of U in coal are diverse, but organic bonding seems general, together with associations with mineral matter (Swaine, 1990). Although U is not genetically associated with coaly substances (i.e., present in the original plant material), it may be picked up by coal during the course of migration and the fact that in some cases coalified wood materials in close proximity may or may not contain U demonstrates the effect of localised channelling of uranium- bearing waters. Uranium can form different minerals during its incorporation into coal e.g. uraninite and coffinite, depending on the composition of the original mineralizing fluid.

Thorium is another element that contributes to the radioactivity in coal and for that reason is of environmental importance. The mean value for the lignite samples is 7.5 ppm and the range is from 7 to 8 ppm. Although U is the main source of radioactivity for Greek lignites, Th levels in fly ash and bottom ash indicate that its contribution to radioactivity of coal by-products, result from coal combustion cannot be negligible. Thorium has a mean of 15 ppm in fly ash, while in bottom ash the mean value is 10ppm. The range is 14-15 ppm and 7-13 ppm for fly ash and bottom ash respectively. Thorium is associated with mineral matter in most coals, mainly as monazite, with lesser amounts in zircon, and xenotime (Finkelman, 1999).

Rubidium has no environmental or health significance, and is often associated with clays. In lignite, Rb has an average value of 21 ppm, ranging from 19-23 ppm. In fly ash and bottom ash the mean is 62 and 38 ppm respectively, and the range is 61-63 ppm for fly ash and 25-46 ppm for bottom ash.

It has been suggested (Finkelman, 1999), that Strontium is associated with organic matter in most low-rank coals, whereas other coals also contain Sr associated with phosphate minerals and in some cases, calcite. Strontium's mean value in lignite samples is 126, while in fly ash and bottom ash samples the average concentration is 335 and 160 ppm, respectively. The corresponding ranges were: 120-130 ppm, 331-342 ppm and 107-191.

Partly organic but mostly inorganic association has been proposed for the presence of Y in coals where Y found in fined-grained xenotime YPO_4. In lignite Y mean is 8 ppm , in fly ash is 26 ppm and in bottom ash is 18, while the corresponding ranges are: 8-10 ppm, 26-28 ppm and 13-22 ppm.

Accumulation of Y can be derived from leaching of the overlying sandstones and sorption by organic matter and Y undergoes local redistribution (Finkelman, 1999).

Niobium in lignite has an average concentration of 4 ppm. In fly ash and bottom ash samples analysed the mean is 13 and 8 ppm, respectively. The corresponding ranges are: 4-5 ppm, 12.8-13.4 ppm and 5-10 ppm approximately. The mode of occurrence of Nb in coals has not well defined yet and is different in various coals. In some coals Nb is organically associated and with mineral matter, whereas in some coal from USA, most of Nb was associated with Rutile (Finkelman, 1999). Both mineralogical and organic associations have been reported for this element although it is mainly associated with mineral matter (Swaine, 1990).

Zircon is regarded as the main mode of occurrence of Zr in most coals. Zr in lignite has an average concentration of 35 and a range from 34-36 ppm. In fly ash the mean is 102 ppm and in bottom ash the mean is 59 ppm while the range of Zr in fly ash and bottom ash is 92-108 ppm and 40-70 ppm, respectively.

Scandium is not considered to be essential or harmful in biological systems. There is an agreement that Sc occurs associated with the mineral matter and with the organic matter in varying proportions. Perhaps clays and phosphate minerals are sites for Sc in some coals (Finkelman, 1999). In lignite it has an average concentration of 13 ppm and a range from 12-14 ppm, in fly ash the mean is 17 and in bottom ash is 15 while the ranges are approximately: 17-18 ppm and 14-17 ppm, respectively.

Arsenic is an element of greatest concern, regarding its potential toxicity (Gamaletsos *et al.*, 2013). Both inorganic and organic forms of As are present in coal. Finkelman (1999), noted that As was predominantly in fractures in the coal and in microfractures in pyrite but it was, also found that As was present in solid solution in pyrite. The average concentration of As in lignite is approximately 3 ppm, in fly ash the mean is 14 and in bottom ash is 4 ppm, respectively.

Cadmium is an element of prime environmental concern and its levels in coal and its by-products are of great interest. Minor amounts of Cd are organically associated in most coals but the main mode of occurrence in most coals is associated with mineral matter i.e.: sphalerite, clay minerals and carbonate minerals or pyrite. Cadmium average concentration in those lignite samples analysed, is 0.411 ppm approximately. In fly ash the mean value is round 1.2 ppm and in bottom ash the mean is 0.9 ppm approximately, while values of 2 ppm were found in both ashes.

In general, the enrichments of the trace elements are in accordance with other related works (Megalovasilis *et al.*, 2013) and can be attributed to the local geology (Petrotou *et al.*, 2010, 2012). The same studies claim that a possible origin of U and Th could be from schists and other, similar, local rock types found in the area.

5. Conclusions

Considering the data presented herein, it can be concluded that the environmental geochemistry of Ptolemais lignites and intermediate steriles (IS), as well as of subsequent combustion by-products mainly concerns Cr, Ni, V, U, Th and As. Chromium concentration is rather low in IS samples, but the metal is particularly concentrated in lignites (max: 64 - 142 ppm) and additionally in FA and BA. Nickel and V concentrations are rather surprisingly high in IS samples (max: 169 and 184 ppm respectively), and of course, more accumulated in FA and BA. On the other hand, As is relatively absent in IS samples and elevated in ashes (min - max: 10 - 16 ppm), indicating lignites as the source. Actinides, namely U and Th, are also enriched in FA and BA (min - max: 14 - 17 ppm and 14 -15 ppm respectively). A perfect coupling between elemental concentration between lignites, FA and BA was observed, indicating similar chemical processes during combustion. Further investigation, by means of advanced microscopic and spectroscopic techniques (e.g. FEG-SEM, TEM, XAS) is need in order to clarify the trace element partitioning and speciation in all earth materials studied.

6. Acknowledgments

We would like to thank the Department of Earth Science and Environment of University of Leeds, UK, for permitting analyses of all samples using most analytical facilities available.

7. References

Filippidis, A. and Georgakopoulos, A., 1992. Mineralogical and chemical investigation of fly ash from the Main and Northern lignite fields in Ptolemais, Greece, *Fuel*, 71(4), 373-376.

Filippidis, A., Georgakopoulos, A., Kassoli-Fournaraki, A., Misaelides, P., Yiakkoupis, P. and Broussoulis, J., 1996. Trace element contents in composited samples of three lignite seams from the central part of the Drama lignite deposit, Macedonia, Greece, *International Journal of Coal Geology*, 29(4), 219-234.

Finkelman, R.B., 1999. Trace Elements in Coal Environmental and Health Significance, *Biological Trace Element Research*, 67(3), 197-204.

Foscolos, A.E., Goodarzi, F., Koukouzas, C.N. and Hatziyannis, G., 1989. Reconnaissance study of mineral matter and trace elements in Greek lignites, *Chemical Geology*, 76(1-2), 107-130.

Gamaletsos, P., Godelitsas, A., Dotsika, E., Tzamos, E., Gotthlicher, J. and Filippidis, A., 2013. Geological sources of As in the Environment of Greece: A review. *In*: Threats to the Quality of Groundwater Resources: Prevention and Control, Scozzari, A. and Dotsika, E., *eds.*, Springer, Berlin, *The Handbook of Environmental Chemistry*, 40, 77-113.

Georgakopoulos, A., Filippidis, A. and Kassoli-Fournaraki, A., 1994. Morphology and trace element contents of the fly ash from main and Northern lignite fields, Ptolemais, Greece, *Fuel*, 73(11), 1802-1804.

Giannouli, A., Kalaitzidis, S., Siavalas, G., Chatziapostolou, A., Christanis, K. and Papazisimou, S., 2009. Evaluation of Greek low-rank coals as potential raw material for the production of soil amendments and organic fertilizers, *International Journal of Coal Geology*, 77(3), 383-393.

Iordanidis, A., Buckman, J., Triantafyllou A.G. and Asvesta, A., 2008. Fly ash-airborne particles from Ptolemais-Kozani area, northern Greece, as determined by ESEM-EDX, *International Journal of Coal Geology*, 73(1), 63-73.

Karangelos, D.J., Petropoulos, N.P., Anagnostakis, M.J. Hinis, E.P. and Simopoulos, S.E., 2004. Radiological characteristics and investigation of the radioactive equilibrium in the ashes produced in lignite-fired power plants, *Journal of Environmental Radioactivity,* 77(3), 233-246.

Kolovos, N., Georgakopoulos, A., Filippidis, A. and Kavouridis, C., 2002a. The effects on the mined lignite quality characteristics by the intercalated thin layers of carbonates in Ptolemais mines, Northern Greece, *Energy Sources*, 24(8), 761-772.

Kolovos, N., Georgakopoulos, A., Filippidis A. and Kavouridis, C., 2002b. Utilization of lignite reserves and simultaneous improvement of dust emissions and operation efficiency of a power plant by controlling the calcium (total and free) content of the fed lignite. Application on the Agios Dimitrios power plant, Ptolemais, Greece, *Energy and Fuels*, 16(6), 1516-1522.

Koukouzas, N., Hämäläinen, J., Papanikolaou, D., Tourunen, A. and Jäntti, T., 2007. Mineralogical and elemental composition of fly ash from pilot scale fluidised bed combustion of lignite, bituminous coal, wood chips and their blends, *Fuel*, 86(14), 2186-2193.

Koukouzas, N., Ward, C.R., Papanikolaou, D., Li, Z. and Ketikidis, C., 2009. Quantitative evaluation of minerals in fly ashes of biomass, coal and biomass-coal mixture derived from circulating fluidised bed combustion technology, *Journal of Hazardous Materials*, 169(1-3) 100-107.

Koukouzas, N., Zeng, K.R., Perdikatsis, V., Xu, W. and Kakaras, E.K., 2006. Mineralogy and geochemistry of Greek and Chinese coal fly ash, *Fuel*, 85(16) 2301-2309.

Megalovasilis, P., 1994. Environmental aspects in relation to the lignite combustion at the Power Station of Amyntaion, Macedonia, Greece, *Bulletin of the Geological Society of Greece*, XXX/4, 45-55.

Megalovasilis, P., Papastergios, G. and Filippidis, A., 2013. Behavior study of trace elements in pulverized lignite, bottom ash and fly ash of Amyntaio power station, Greece, *Environmental Monitoring and Assessment*, 185, 6071-6076.

Mountrakis, D., Dixon, J.E. and Robertson, A.H.F., 1984. Structural evolution of the Pelagonian Zone in Northwestern Macedonia, Greece. *In*: The Geological Evolution of the Eastern Mediterranean, *Spec. Publs Geol. Soc. Lond*., 17, 581-591.

Papanicolaou, C., Kotis, T., Foscolos, A. and Goodarzi, F., 2004. Coals of Greece: a review of properties, uses and future perspectives, *International Journal of Coal Geology,* 58(3), 147-169.

Petaloti, C., Triantafyllou, A., Kouimtzis, T. and Samara, C., 2006. Trace elements in atmospheric particulate matter over a coal burning power production area of western Macedonia, Greece, *Chemosphere*, 65, 2233-2243.

Petrotou, A., Skordas, K., Papastergios, G., and Filippidis, A., 2010. Concentrations and bioavailability of potentially toxic elements in soils of an industrialised area of Northwestern Greece. *Fresenius Environmental Bulletin* 19(12), 2769-2776.

Petrotou, A., Skordas, K., Papastergios, G. and Filippidis, A., 2012. Factors affecting the distribution of potentially toxic elements in surface soils around an industrialized area of northwestern Greece, *Environmental Earth Sciences*, 65(3), 823-833.

Riga-Karandinos, A.N. and Karandinos, M.G., 1998. Assessment of air pollution from a lignite power plant in the plain of Megalopolis (Greece) using as biomonitors three species of lichens; impacts on some biochemical parameters of lichens, *The Science of The Total Environment*, 215(1-2), 167-183.

Skodras, G., Grammelis, P., Kakaras, E., Karangelos, D., Anagnostakis, M. and Hinis, E., 2007. Quality characteristics of Greek fly ashes and potential uses, *Fuel Processing Technology*, 88(1), 77-85.

Stoulos, S., Manolopoulou, M. and Papastefanou, C., 2003. Assessment of natural radiation exposure and radon exhalation from building materials in Greece, *Journal of Environmental Radioactivity*, 69(3), 225-240.

Stoulos, S., Manolopoulou, M. and Papastefanou, C., 2004. Measurement of radon emanation factor from granular samples: effects of additives in cement, *Applied Radiation and Isotopes*, 60(1), 49-54.

Swaine, D.J., 1990. Trace Elements in Coal, 278 pp.

Valcovic, V.T.E., 1983. Trace Elements in Coal Volume I and Volume II, CRC Press.

Vamvuka, D., Kastanaki, E., Lasithiotakis, M. and Papanicolaou, C., 2004. Combustion behavior of xylite/lignite mixtures, *Carbon*, 42(2), 351-359.

Vamvuka, D., Pitharoulis, M., Alevizos, G., Repouskou, E. and Pentari, D., 2009. Ash effects during combustion of lignite/biomass blends in fluidized bed, *Renewable Energy*, 34(12), 2662-2671.

Vejahati, F., Xu, Z. and Gupta, R., 2010. Trace elements in coal: Associations with coal and minerals and their behavior during coal utilization - A review, *Fuel*, 89(4), 904-911.

Yan, L., Gupta, R.P. and Wall, T.F., 2001. The implication of mineral coalescence behaviour on ash formation and ash deposition during pulverised coal combustion, *Fuel*, 80(9), 1333-1340.

Zeevaert, T., Sweeck, L. and Vanmarcke, H., 2006. The radiological impact from airborne routine discharges of a modern coal-fired power plant, *Journal of Environmental Radioactivity*, 85(1), 1-22.

Δελτίο της Ελληνικής Γεωλογικής Εταιρίας, τόμος L, σελ. 2251-2260
Πρακτικά 14ου Διεθνούς Συνεδρίου, Θεσσαλονίκη, Μάιος 2016

Bulletin of the Geological Society of Greece, vol. L, p. 2251-2260
Proceedings of the 14th International Congress, Thessaloniki, May 2016

HEAVY METALS IN URBAN PARK SOILS FROM ATHENS, GREECE

Papazotos P.[1,2], Chalkiadaki O.[1,3], Chatzistamatiou E.A.[1], Georgopoulos G.[1], Gkiouleka I.[1], Katsikis I.[1], Zygouri E.[1], Kelepertzis E.[1] and Argyraki A.[1]

[1]National and Kapodistrian University of Athens, Faculty of Geology and Geoenvironment, Panepistimiopolis, Zographou, 15784, Athens, Greece, argyraki@geol.uoa.gr, lina_chatzistamatiou@hotmail.com, giorgos_georgopoulos@hotmail.com, ireneski08@hotmail.com, johnkatsikis91@gmail.com, kelepert@geol.uoa.gr, eva12591@gmail.com

[2]National Technical University of Athens, School of Mining & Metallurgical Engineering, Heroon Polytechniou Str. 9, Zographou,15780, Athens, Greece, papazotos@metal.ntua.gr

[3]National and Kapodistrian University of Athens, Department of Chemistry, Panepistimiopolis, Zographou, 15441, Athens, Greece, ochalkiadaki@chem.uoa.gr

Abstract

Urban geochemistry is a scientific discipline which is growing in the recent years mainly because of the environmental impact caused by urbanization. The present study aims to determine the concentrations of potentially harmful elements (PHEs) on surface soils (0-10cm) in Athens parks. Soil sampling was carried out in public park areas within the Athens urban area. Twenty surface soil (0-10cm) samples were collected and the <100μm grain size fraction was analyzed by Flame Atomic Absorption Spectroscopy for Pb, Zn, Ni, Cu, Mn and Cr after a strong acid dissolution and partial extraction by 1M HCl. The organic soil matter content was determined by a combustion method. Two different inter-correlated groups of elements were identified, one including Pb, Zn, Cu showing the anthropogenic signature on urban soil and another including Cr, Ni and Mn showing geogenic origin. The mobility of the heavy metals determined in the present study follows the decreasing order: Pb> Mn >Ni≈ Cu≈ Zn> Cr. The data indicate that park areas seem to be important sinks of anthropogenic elements in urban soils.

Keywords: *Geochemistry, environmental pollution, potentially harmful elements.*

Περίληψη

Η αστική γεωχημεία είναι ένας επιστημονικός κλάδος ο οποίος αναπτύσσεται τα τελευταία χρόνια κυρίως λόγω των περιβαλλοντικών επιπτώσεων που προκύπτουν από την αστικοποίηση. Η παρούσα εργασία έχει ως στόχο τον προσδιορισμό των συγκεντρώσεων δυνητικά επιβλαβών στοιχείων (PHEs) των επιφανειακών (0-10 cm) εδαφών προερχόμενων από αλσύλια της Αθήνας. Η δειγματοληψία υπαίθρου πραγματοποιήθηκε σε 20 αλσύλια της Αττικής και κάλυψε συνολική έκταση περίπου 200km^2. Αναλύθηκαν 20 εδαφικά δείγματα κοκκομετρίας < 100μm χρησιμοποιώντας τη μέθοδο φασματοσκοπίας ατομικής απορρόφησης μετά από ολική διαλυτοποίηση και έκπλυση με 1M HCl και προσδιορίστηκαν τα στοιχεία Pb, Zn, Ni, Cu, Mn και Cr. Επίσης προσδιορίστηκε ο οργανικός άνθρακας των εδαφών με τη μέθοδο καύσεως. Αναγνωρίστηκαν δυο

διαφορετικές ομάδες στοιχείων. Στην πρώτη περιλαμβάνονται τα ανθρωπογενή στοιχεία (Pb - Zn - Cu) και στη δεύτερη τα λιθογενή (Cr - Ni - Mn). Η σειρά με την οποία κινητοποιούνται τα στοιχεία στο έδαφος ήταν: Pb> Mn >Ni≈ Cu≈ Zn> Cr. Τα δεδομένα της έρευνας υποδεικνύουν ότι το έδαφος των αλσυλίων μπορεί να είναι ένας σημαντικός ταμιευτήρας των ανθρωπογενών στοιχείων στο αστικό έδαφος.
Λέξεις κλειδιά: *Γεωχημεία, περιβαλλοντική ρύπανση, δυνητικά επικίνδυνα στοιχεία.*

1. Introduction

Soils of urban environment represent an integral part of the city landscape, with different and unique characteristics compared to the naturally developed soils (Wong *et al.*, 2006). Furthermore they receive higher than normal loads of contaminants from traffic and industrial activity, rapid development and urbanization (Yaylali-Abanuz, 2011). However, several studies have emphasized the influence of natural geochemical factors on soil chemistry in strongly urbanized regions (e.g., Argyraki and Kelepertzis, 2014).

Potentially harmful elements (PHE's) including heavy metals and metalloids, are among the most tenacious soil pollutants because of their non-biodegradable nature and the long term toxicity (Ajmone-Marsan and Biasioli, 2010; Massas *et al.*, 2013; Kelepertzis and Stathopoulou, 2013). Urban soils especially in public park areas may have an immediate impact on public health, mainly due to the direct contact with humans (Mielke *et al.*, 1999). In particular, the ingestion of dust and soil has been widely regarded as one of the key pathways by which children are exposed to the heavy metals and metalloids from paint, leaded gasoline, vehicles and local industry (Rasmussen *et al.*, 2001). Researchers found positive correlation between urban soil heavy metals concentration and intensive urbanization metrics (e.g., urban population density, length of roads and highways, traffic volume, and percent urban land use) (Pouyat *et al*., 2008). Consequently, the highest concentrations of the classical urban contaminants, found in Athens, were observed in the surface soil from roadside verges and in the older parts of the city, as well as the densely populated areas (Argyraki and Kelepertzis, 2014).

Athens is the Capital city of Greece and has one third of its population (around 3,000,000 city residents). Significantly higher concentrations of Pb have been previously observed in parks and woodland areas compared to other land uses in Athens (Argyraki and Kelepertzis, 2014). Following this, the central hypothesis of the present study is that vegetated, grove areas of Athens influence the concentration levels and the environmental mobility of heavy metals in urban soil. The specific objectives of this paper were: (a) to assess the concentration of heavy metals (Pb, Zn, Ni, Cu, Mn, Cr) in soil samples from 20 urban parks in Athens and (b) to investigate the availability of heavy metals by performing a single chemical extraction test using 1M HCl.

2. Materials and Methods

2.1 Soil Sampling

The target areas where soil sampling was performed were parks and specifically grove areas within the city of Athens. A common characteristic of all sampling areas is the presence of pine trees. A total of twenty composite topsoil (0-10cm) samples were collected during the spring of 2015 from locations presented in Figure 1. At each sampling site, one composite sample was collected by mixing five sub-samples from the corners and the center of a 10m square in sealable plastic bags. Samples were collected using a plastic spatula after removing debris and surface vegetation.

2.2 Laboratory procedures

The analytical experimental work presented below was performed at the Laboratory of Economic Geology and Geochemistry (Faculty of Geology and Geoenvironment, University of Athens) and the Laboratory of Environmental Chemistry (Faculty of Chemistry, University of Athens). All

samples were air dried at a constant temperature of 50°C for 3 days in a thermostatically controlled oven. They were subsequently gently disaggregated in a porcelain mortar and sieved to 2mm fraction. Each soil sample was further sieved through a nylon 100μm sieve in order to focus on geochemically reactive particles and stored at room temperature in a dark storeroom. The 100μm fraction was used for chemical analysis. All utensils were thoroughly cleaned between the samples to avoid cross contamination.

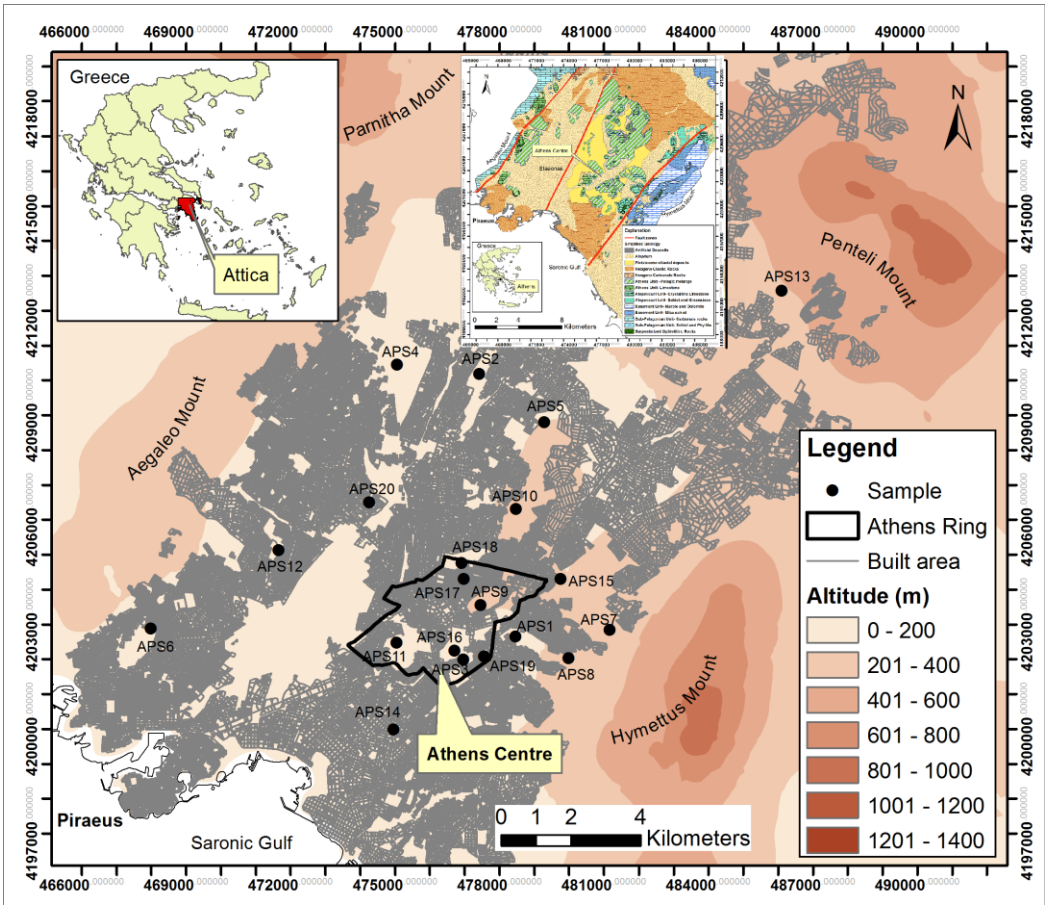

Figure 1 – Map of sampling locations. APS1: Ilissia "Black Grove", APS2: Nea Philadelphia Grove, APS3: National Garden, APS4: Tritsis Park, APS5: Veikos Park, APS6: Dexameni Park, APS7: NTUA Campus, APS8: NKUA Campus, APS9: Lycabettus Hill, APS10: Attikon Park, APS11: Filopappos Hill, APS12: Aegaleo Park, APS13: Syggros Park, APS14: Nea Smyrni Grove, APS15: Park of Hellenic Army, APS16: Ardittos Hill, APS17: Strefi Hill, APS18: Pedion Areos, APS19: Pagrati Grove, APS20: AUA Campus.

2.2.1 Chemical analysis

The total heavy metal content of the soil was determined after acid digestion with a mixture of three concentrated acids (HNO_3 - $HClO_4$ – HF) in Teflon beakers according to ISO 14869-1:2000 method. The digests were diluted appropriately with Milli-Q water and stored in polyethylene bottles at 4°C until measurement. All glassware and bottles used during the experiments were acid-washed in 10% nitric acid for at least 24 hours before use. It is noted that the mixture of acids that was used is regarded near total for some elements like Cr which is usually present in refractory minerals like chromite that is not completely dissolved.

A portion of the samples was subjected to 1M HCl extraction by shaking the samples for 18 hours at room temperature, in order to estimate the availability of the heavy metals, since metal content extracted by this treatment is considered to be easily mobilised and has major environmental significance. Single extractions can be considered as tools indicating potential release of elements from particular soil constituents to which they are associated. Soil washing with acids such as HCl relies on ion exchange and dissolution of soil components/discrete metal compounds to extract metals. Digestion in 1M HCl does not dissolve the silicate matrix. Such reagents do not mobilize trace elements from silicate parent materials but dissolve metal pollutants which largely enter the soil environment in non-silicate bound forms. The 1M HCl extractable metal content is commonly used for first-level screening in the risk assessment process, the rational being that total metal analysis includes all non-residual metals as well as metals in the silicate mineral matrix, which are not available to biota under normal environmental conditions (Massas *et al.*, 2010).

Concentrations of Pb, Zn, Ni, Cu, Mn and Cr for all the samples were measured by flame atomic absorption spectroscopy (FAAS), Perkin Elmer 110B, at the Laboratory of Economic Geology and Geochemistry, University of Athens. Analytical quality control for the strong acid digestion was assessed by including one reference material (NIST SRM2711) in the analytical batch for the estimation of analytical bias and performing duplicate analysis on 5 randomly selected samples for the estimation of analytical precision. Duplicate analysis of five randomly selected soil samples was also performed during the 1M HCl extraction to estimate analytical precision. The analytical quality of the result was found within acceptable limits.

2.2.2 Measurement of soil organic carbon

The organic matter content of the soil samples was estimated by the loss-on-ignition (LOI) method (US-EPA, 2002). The method is semi-quantitative and involves the heated destruction of all organic matter in the soil. A known weight of each sample (1g) was placed in a ceramic crucible which was then heated to 450^0C for 4 hours in a furnace oven. The samples were then cooled in a desiccator and weighed. Organic matter content was calculated as the difference between the initial and final sample weights divided by the initial sample weight times 100%. All weights were corrected for moisture/water content prior to organic matter content calculation. Since the method determines the organic matter content in the soil, a conversion factor of 1.724 has been used to convert organic matter to organic carbon based on the assumption that organic matter contains 58% organic C (i.e., g organic matter/l .724 = g organic C).

3. Results and Discussion

3.1 Total metal content

The total concentrations of heavy metals are presented in Table 1 along with a comparison with concentrations reported in older surveys from Athens and other cities of Europe. Heavy metal concentrations show positively skewed distributions. Manganese, Cr and Ni display the highest concentrations while the widest spread range is observed for Pb and Zn (Fig. 2). The concentrations of heavy metals from the studied parks are higher than the ones from Athens' soil (Argyraki and Kelepertzis, 2014) and also higher than the ones from Athens' playground top soil (Massas *et al*., 2010) for Ni, Cu, Mn and Cr. In comparison with other environmental pollution studies for park areas, e.g. Madrid *et al.*, 2002; Lacatucu *et al*., 2007 Cr, Ni and Mn are enriched in Athens. This might be attributed to the high geochemical background of these elements in Athens soil which is related to the presence of serpentinized ophiolithic rocks in local geology (Argyraki and Kelepertzis, 2014). Metal concentrations are relatively uniform with respect to the studied parks, with the exception of samples collected in the National Garden (APS 3) and Ardittos Hill (APS 16) which present statistically significantly higher values in all heavy metals than the other parks (one way ANOVA, $p<0.05$, Post hoc tests Tukey and Bonferroni).

3.2 Concentrations extracted by 1M HCl

In order to evaluate the degree of mobility of heavy metals in the soil samples from park areas, a single chemical extraction test was performed using 1M HCl. Trace elements accumulate in soil in various forms: water soluble, exchangeable, oxide-bound, carbonate-bound, organic matter- bound, and residual that is bound to resistant minerals (silicates) and non-extractable. The metals present in these forms have different mobility and bioavailability. Water-soluble and exchangeable fractions are readily released to the environment, but the residual fractions are immobile under natural conditions.

Table 1 and Figure 2(b) show the median values and the ranges of extractable metal concentrations respectively. Metal extractability expressed as the percentage of the metal fraction extracted by 1M HCl relative to the heavy metal content after total digestion is presented in Figure 3. The results show that extractable amounts of heavy metals by 1M HCl (as mean values) are <5% for Zn, Ni and Cu, around 10% for Mn and 14% for Pb. The percentages in the soil samples of the extracted Mn and Pb presented the highest range (3.4-24%). The order of heavy metals' potential for release from the studied soils into the dilute acid solution is Pb> Mn >Ni≈ Cu≈ Zn> Cr (one way ANOVA, $p<0.05$, Post hoc tests Tukey and Bonferroni). The decreasing order of the extractability ratios is in accordance with Kelepertzis and Argyraki (2015) and Lafuente *et al*. (2008).

Table 1 - Comparison of median values of extractable and total concentrations of heavy metals (mg kg^{-1}) from this study with total heavy metal concentrations (mg kg^{-1}) in park areas from other European cities.

	Pb	**Zn**	**Ni**	**Cu**	**Mn**	**Cr**
1M HCl extractable	9.8	3.2	6.8	1.8	55	2.0
Total concentration	59	105	166	44	603	270
Athens soils, 2014[1]	45	98	102	39	554	141
Athens playground top soils,2010[2]	101	146	78	42	311	84
Seville[3] *(Mean)*	137	145	22	68	471	39
Rostock[3] *(Mean)*	83	100	30	35	-	48
Madrid[3] *(Mean)*	161	210	14	72	437	75
Bucharest[4] *(Mean)*	11	59	21	14	-	18
Baia Mare[4] *(Mean)*	627	508	25	165	-	25
Target value[5]	85	140	35	36	-	100
Intervention value[5]	530	720	210	190	-	380

[1]Argyraki and Kelepertzis, 2014; [2]Massas *et al*., 2010; [3]Madrid *et al*., 2002; [4]Lacatucu *et al*., 2007; [5]VROM, 2000.

The low extractabilities of Zn and Cu are in accordance with findings by other researchers (Kelepertzis and Argyraki, 2015; Gasparatos *et al*., in press) who determined a large residual pool of these metals in Athens' soils. The low lability of Ni, Cu, Zn and Cr suggest that these contaminants in Athens park soils are sequestered in rather immobile fractions. Manganese is characterized by relatively high extractability probably due to the presence of Mn oxides in soils that are unstable under slightly acidic conditions. Also the relatively high extractability of Pb is could be at least partially related to its affinity to Mn-oxide phases as previously observed in Athens' soil by Kelepertzis and Argyraki, 2015.

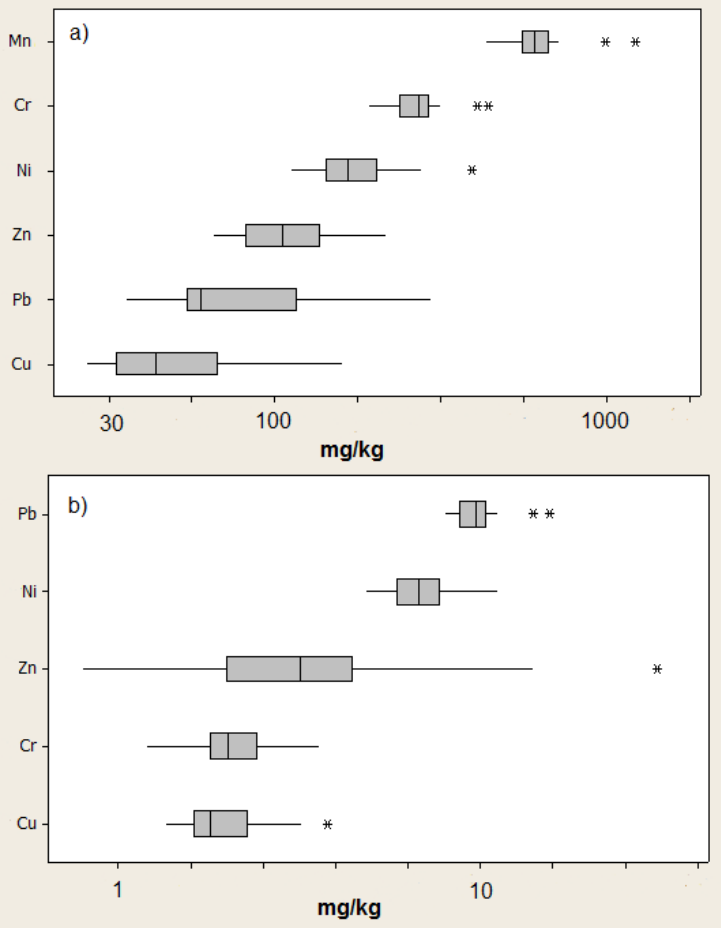

Figure 2 – Boxplot comparison of heavy metal concentrations and variation in the studied samples (log-transformed data) for a) total dissolution and b) 1M HCl extraction. The elements are ordered according to decreasing median value (vertical lines). The scale is back transformed to show concentrations in mg kg^{-1}.

3.3 Factors affecting concentrations of heavy metals in Athens Park soils

The correlations of heavy metals determined in the present study are presented in Table 2. The statistically significant positive correlation between Pb - Zn – Cu is indicative of the common origin of these elements; they are typical anthropogenic elements related to traffic or point source emissions in the urban environment (Albanese and Breward, 2011). Also, the observed positive correlations between Cr - Ni – Mn points to their natural origin in Athens' soil. Specifically, Cr, Ni and Mn are interpreted as geogenic elements associated with the ophiolithic parent rocks within the Athens Basin (Argyraki and Kelepertzis, 2014). Positive correlation coefficients were also observed between total and HCl extractable heavy metals with higher values for Cu, Zn and Pb (0.826, 0.793 and 0.600 respectively) and lower, insignificant values for Mn, Ni and Cr (0.444, 0.332 and 0.176 respectively). Furthermore, the organic carbon is positively correlated with the anthropogenic elements in both the extraction with HCl and the total digestion. However, the effect of organic carbon is far more pronounced for controlling the availability of Pb, Zn, Cu highlighting that soil organic matter effectively binds more heavy metals that are readily available in the applied leaching procedure.

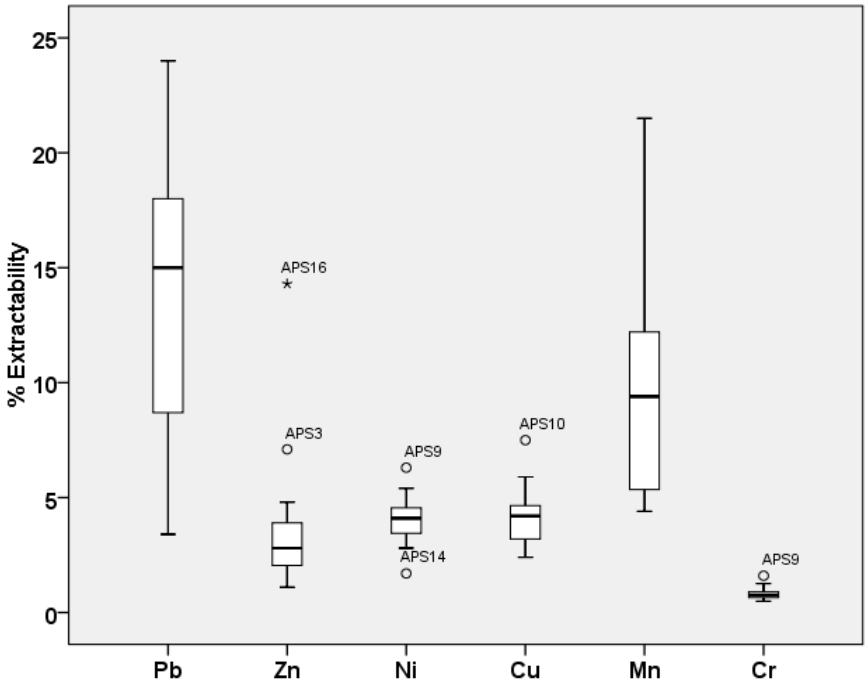

Figure 3 - Box plots of the extractability ratio for each heavy metal determined in soil samples (n=20) from Athens parks. The length of the box indicates the interquartile range whereas the horizontal line within each box represents the median. Whiskers extend to the maximum and minimum data point within 1.5 box heights from the top and the bottom of the box. The star characters are the extreme values which are more than 3 times the interquartile range above the third quartile.

Table 2 - Correlations of the studied elements (Cr, Ni, Mn, Pb, Zn, Cu).

Total concentration data						
	Pb	Zn	Ni	Cu	Mn	Cr
Pb	1.000					
Zn	***0.893***	1.000				
Ni	0.132	0.215	1.000			
Cu	***0.850***	***0.738***	-0.006	1.000		
Mn	0.197	0.158	0.417	0.082	1.000	
Cr	0.298	0.415	***0.814***	0.115	***0.530***	1
TOC	***0.759***	***0.673***	-0.111	***0.536***	-0.056	-0.180
HCl extractable concentration data						
	Pb	Zn	Ni	Cu	Mn	Cr
Pb	1.000					
Zn	***0.725***	1.000				
Ni	0.391	***0.710***	1.000			
Cu	***0.553***	***0.588***	0.321	1.000		
Mn	0.442	***0.866***	***0.737***	0.491	1.000	
Cr	0.009	-0.007	-0.057	0.152	-0.016	1
TOC	***0.686***	***0.723***	-0.056	***0.563***	0.192	-0.159

Statistically significant higher concentrations of Cu, Pb, and Zn (anthropogenic elements) are detected in parks located in the centre of Athens and overpopulated areas (APS3, APS6, APS11, APS14, APS16, APS18-20) in comparison to suburban areas (APS1,2,4,5,7,8,10,12,13,15) (see Fig. 1 for sample location). This indicates that vehicular traffic is the major contributory factor in urban soil contamination by the typical anthropogenic elements (Li *et al.*, 2001, 2004; Möller *et al.*, 2005; Morton-Bermea *et al.*, 2009; Andersson *et al.*, 2010). Leaded fuel for Pb and its use as a balance in the wheels of the cars (Harris and Davidson, 2005) and tire wear for Zn have been recognized as specific vehicular traffic-related sources (Albanese and Breward, 2011). Higher concentrations in the central parks could also be related to the age of park and site history as well as the distance of the sampling location from heavy traffic roads. Such data are not available in this study.

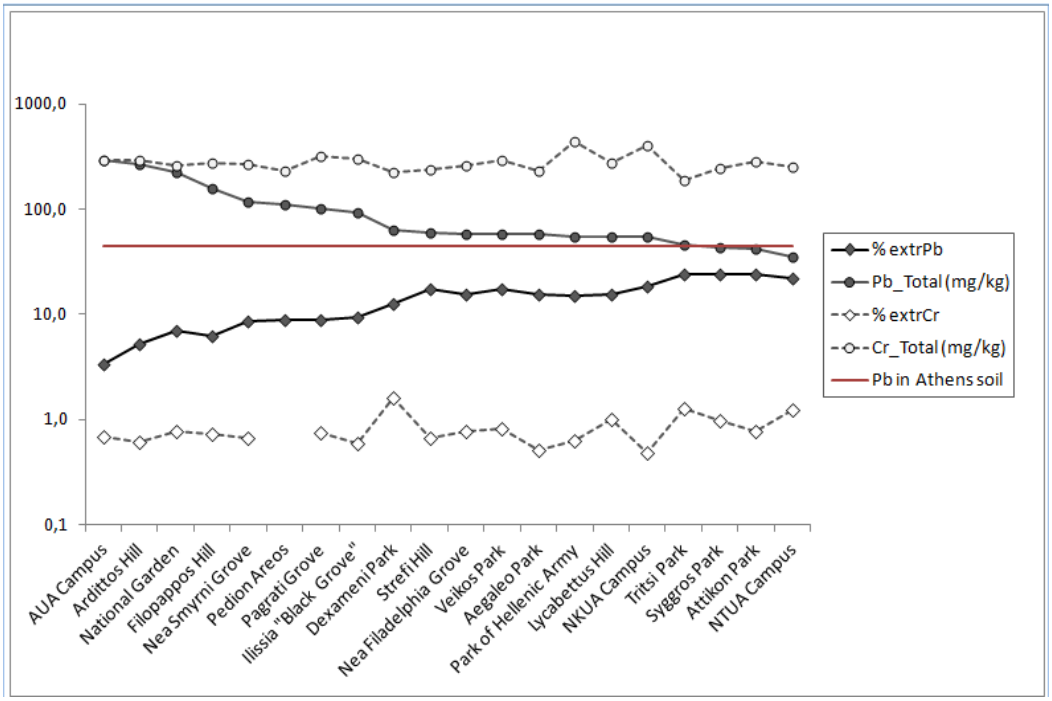

Figure 4 - Pattern of total and 1M HCl extractable concentration of Pb (dark symbols) and Cr (white symbols) with respect to sample location. The continuous horizontal line corresponds to the median concentration (45mg kg^{-1}) of total Pb in Athens soil reported previously by Argyraki and Kelepertzis (2014).

A comparison based on data of Pb and Cr concentrations in Athens' park soils as examples of anthropogenic and geogenic elements respectively reveals interesting patterns, showing the influence of elemental origin on their extractability behaviour (Fig. 4). Chromium, as a geogenic element, is characterized by low lability, reflecting its fixation to more stable chemical forms. This, explains the relative uniform pattern for both total concentration and extractability percentage of Cr (which is also <1% for most cases) resulting from the dissolution of rock forming minerals which are indifferent within the spatial scale of this study. In the instance of Pb a greater degree of variability is observed in both total concentrations and extractability ratios among the samples. Furthermore, only three samples have total Pb concentration lower than 45 mg kg^{-1} i.e. the median value previously reported for Pb in Athens top soil (Argyraki and Kelepertzis, 2014). This finding supports the hypothesis that top soil in park and woodland areas is enriched in airborne through either greater deposition (Ukonmaanaho *et al.*, 2001; Michopoulos *et al.*, 2005), or due to distinct point sources of pollution (Argyraki and Kelepertzis, 2014). Interestingly, samples from the parks with the highest total Pb concentrations demonstrate the lowest extractability ratios. Considering the

significant positive correlation between Pb and organic carbon as well as between Pb and Mn in soil, this pattern probably underlines the role of effective binders of Pb in park top soils.

4. Conclusions

The total and extractable concentrations of Pb, Zn, Ni, Cu, Mn and Cr in soils from parks in Athens, Greece were investigated in this study. The soil samples show significant levels of Ni and Cr content in agreement with the high geochemical background of these elements in Athens. The mean and median concentrations of all studied elements were above the median values previously reported for Athens soil. Among the investigated heavy metals in the studied soils, Mn, Ni and Cr are interpreted as geogenic and Pb, Zn and Cu as anthropogenic, with Pb and Mn showing significantly higher dilute acid extractable concentrations than the other metals. The concentrations of Pb, Zn and Cu were also more dependent on organic matter. The mobility of heavy metals determined in the present study by the 1M HCl extraction follows the decreasing order: Pb> Mn >Ni≈ Cu≈ Zn> Cr. Our data indicate that vegetated areas within the urban net of Athens have a significant effect on the sequestration of the anthropogenic heavy metals in soil.

5. References

Ajmone-Marsan, F. and Biasioli, M., 2010. Trace elements in soils of urban areas, *Water Air and Soil Pollution*, 213, 121-43.

Albanese, S. and Breward, N., 2011. Sources of anthropogenic contaminants in the urban environment. Chapter 8. *In*: Johnson, C.C., Demetriades, A., Locutura, J. and Ottesen, R.T., *eds*., Mapping the chemical environment of urban areas, Chichester, U.K., *John Wiley & Sons, Ltd*, 116-27.

Andersson, M., Ottesen, R.T. and Langedal, M., 2010. Geochemistry of urban soils - monitoring in Trondheim, Norway, *Geoderma*, 156,112-8.

Argyraki, A. and Kelepertzis, E., 2014. Urban soil geochemistry in Athens, Greece: The importance of local geology in controlling the distribution of potentially harmful trace elements, *The Science of the Total Environment*, 482-483, 366-377.

Cannon, W.F. and Horton, J.D., 2009. Soil geochemical signature of urbanization and industrialization - Chicago, Illinois, USA, *Appl. Geochem.*, 24, 1590-601.

Chen, T-B., Zheng, Y.-M., Lei, M., Huang, Z.-C., Wu, H.-T., Chen, H., Fan, K.-K., Yu, K., Wu, X. and Tian, Q.-Z., 2005. Assessment of heavy metal pollution in surface soils of urban parks in Beijing, China, *Chemosphere*, 60, 542-51.

Gasparatos, D., Mavromati, G., Kotsovilis, P. and Massas, I., in press. Fractionation of heavy metals and evaluation of the environmental risks for the alkaline soils of the Thriassio plain: a residential, agricultural and industrial area in Greece, *Environmental Earth Science*, doi: http://dx.doi.org/10.1007/s12665-015-4096-1.

Harris, A.R. and Davidson, C.I., 2005. The Role of Resuspended Soil in Lead Flows in the California South Coast Air Basin, *Environmental Science and Technology*, 39(19), 7410-7415.

Kelepertzis, E. and Argyraki, A., 2015. Geochemical associations for evaluating the availability of potentially harmful elements in urban soils: Lessons learnt from Athens, Greece, *Applied Geochemistry*, 59, 63-73.

Kelepertzis, E. and Stathopoulou, E., 2013. Availability of geogenic heavy metals in soils of Thiva town (central Greece), *Environmental Monitoring and Assessment*, 185, 9603-9618.

Lacatusu, R., Breaban, I., Carstea, S., Lungu, M. and Bretan, A., 2007. Abundance of heavy metals in urban soils as concerns genesis and polluting impact, *Scientific Paper Journal, Agronomy Series*, 50, 141-149.

Lafuente, A.L., González, C., Quintana, J.R., Vázquez, A. and Romero, A., 2008. Mobility of heavy metals in poorly developed carbonate soils in the Mediterranean region, *Geoderma*, 145, 238-244.

Lee, C.S.I., Li, X., Shi, W., Cheung, S.Cn. and Thornton, I., 2006. Metal contamination in urban, suburban, and country park soils of Kong Kong: a study based on GIS and multivariate statistics, *Sci. Total. Environ.*, 356, 45-61.

Li, X., Lee, S.-L., Wong, S.-C., Shi, W. and Thornton, I., 2004. The study of metal contamination in urban soils of Hong-Kong using a GIS-based approach, *Environ. Pollut.*, 129, 113-24.
Li, X., Poon, C.-S. and Liu, P.S., 2001. Heavy metal contamination of urban soils and street dusts in Hong Kong, *Appl. Geochem.*, 16, 1361-8.
Madrid, L., Diaz-Barrientos, E. and Madrid, F., 2002. Distribution of heavy metal contents of urban soils in parks of Seville, *Chemosphere*, 49, 1301-1308.
Massas, I., Ehaliotis, C., Kalivas, D. and Panagopoulou, G., 2010. Concentrations and Availability Indicators of Soil Heavy Metals; the Case of Children's Playgrounds in the City of Athens (Greece), *Water Air Soil Pollut.*, 212, 51-63.
Massas, I., Kalivas, D., Ehaliotis, C. and Gasparatos, D., 2013. Total and available heavy metal concentrations in soils of the Thriassio plain (Greece) and assessment of soil pollution indexes, *Environmental Monitoring and Assessment*, 185, 6751-66.
Michopoulos, P., Baloutsos, G., Economou, N., Nikolis, N., Bakeas, E.B. and Thomaidis, N.S., 2005. Biogeochemistry of lead in an urban forest in Athens, Greece. *Biogeochemistry*, 73, 345-57.
Mielke, H., Gonzales, C., Smith, M. and Mielke, P., 1999. The urban environment and children's health: soils as an integrator of lead, zinc and cadmium in New Orleans, Louisiana, USA. *Environ. Res.*, 81, 117-129.
Möller, A., Müller, H.W., Abdullah, A., Abdelgawad, G. and Utermann, J., 2005. Urban soil pollution in Damascus, Syria: concentrations and patterns of heavy metals in the soils of the Damascus Ghouta, *Geoderma*, 124, 63-71.
Morton-Bermea, O., Hernández-Álvarez, E., González-Hernández, G., Romero, F., Lozano, R. and Beramendi-Orosco, L.E., 2009. Assessment of heavy metal pollution in urban topsoils from the metropolitan area of Mexico City, *J. Geochem. Explor.*, 101, 218-24.
Pouyat, R., Yesilonis, I., Szlavecz, K., Csuzdi, C., Hornung, E., Korsós, Z., Russell-Anelli, J. and Giorgio, V., 2008. Response of forest soil properties to urbanization gradients in three metropolitan areas, *Landscape Ecol.*, 23, 1187-1203.
Rasmussen, P., Subramanian, S. and Jessiman, B., 2001. A muti-elements profile of housedust in relation to exterior dust and soils in the city of Ottawa, Canada, *The Science of the Total Environment*, 267, 125-140.
Ukonmaanaho, L., Starr, M., Mannio, J. and Ruoho-Airola, T., 2001. Heavy metal budgets for two headwater forested catchments in background areas of Finland, *Environ. Pollut.*, 114, 63-75.
US-EPA, 2002. Methods for the determination of total organic carbon (TOC) in soils and sediments, *Report No. NCEA-C- 1282, EMASC-001*, Las Vegas.
VROM, 2000. Circular on target values and intervention values for soil remediation: DBO/1999226863, *Netherlands Government Gazette*, 39, 1-11.
Wong, C., Li, X. and Thorton, I., 2006. Review on urban environmental geochemistry of trace metals, *Environmental Pollution*, 142, 1-16.
Yaylali-Abanuz, G., 2011. Heavy metal contamination of surface soil around Gebze industrial area, Turkey, *Microchemical Journal*, 99, 82-92.

Δελτίο της Ελληνικής Γεωλογικής Εταιρίας, τόμος L, σελ. 2261-2270
Πρακτικά 14ου Διεθνούς Συνεδρίου, Θεσσαλονίκη, Μάιος 2016

Bulletin of the Geological Society of Greece, vol. L, p. 2261-2270
Proceedings of the 14th International Congress, Thessaloniki, May 2016

OCCURENCE OF HEXAVALENT CHROMIUM IN THE OPHIOLITE RELATED AQUIFERS OF LOYTRAKI AND SCHINOS AREAS

Pyrgaki K.[1], Argyraki A.[2], Kelepertzis E.[2], Paraskevopoulou V.[1], Botsou F.[1], Dassenakis E.[1], Mitsis I.[2] and Skourtsos E.[2]

[1]National and Kapodistrian University of Athens, Faculty of Chemistry, 15784, University Campus, Zografou, Greece, konstantinapyrgaki@gmail.com, vparark@chem.uoa.gr, fbotsou@chem.uoa.gr , edasenak@chem.uoa.gr

[2]National and Kapodistrian University of Athens, Faculty of Geology and Geoenvironement, Panepistimiopolis Zographou 15784, Athens, Greece, email: argyraki@geol.uoa.gr, kelepert@geol.uoa.gr, mitsis@geol.uoa.gr, eskourt@geol.uoa.gr

Abstract

The main objective of the present study is to assess Cr(VI) concentrations in groundwater and surface water of Loutraki and Schinos areas. Totally, 38 samples were collected from both areas from April to May 2015. Both surface water and groundwater are of bicarbonate-magnesium type (Mg-HCO_3^-) and present very high concentrations of Mg^{2+} (up to 266mg/L) whereas the Cr(VI) concentrations vary among the different water groups (<1,6μg/L-120μg/L). Only 2 out of 15 boreholes of Loutraki area have chromium concentrations above the permissible level for drinking water (50μg/L for Cr(tot)) with the maximum Cr(VI) concentration being 74μg/L. In the area of Schinos, three wells have also high concentrations of Cr(VI) ranging from 40μg/L to 120μg/L. The absence of industrial activity in both areas is indicative of the geogenic origin of Cr(VI) in groundwater which is probably related to the dissolution and oxidation of primary Cr bearing minerals derived from ophiolithic rocks of Geraneia Mountains.

Keywords: *hydrogeochemistry, geogenic contamination, chromium mobility.*

Περίληψη

Η παρούσα εργασία έχει ως στόχο να μελετήσει τόσο τα υπόγεια όσο και τα επιφανειακά ύδατα των περιοχών Λουτρακίου και Σχίνου ως προς τις συγκεντρώσεις τους σε εξασθενές χρώμιο. Η δειγματοληψία πραγματοποιήθηκε κατά τους μήνες Απρίλιο και Μάϊο 2015 όπου συλλέχθησαν συνολικά 38 δείγματα. Τόσο τα επιφανειακά όσο και τα υπόγεια ύδατα είναι πολύ μαγνησιούχα με μέγιστη ανιχνεύσιμη συγκέντρωση τα 266mg/L. Αντιθέτως, οι συγκεντρώσεις Cr(VI) κυμαίνονται από 1,6μg/L έως 120μg/L στα διάφορα δείγματα ανάλογα με την προέλευση τους. Από τις συνολικά 15 γεωτρήσεις του Λουτρακίου μόνο σε 2 ανιχνεύθηκαν συγκεντρώσεις Cr(VI) πάνω από το ανώτατο αποδεκτό όριο (50μg/L για το ολικό χρώμιο) με τη μέγιστη συγκέντρωση να είναι 74μg/L. Στον Σχίνο και στα τρία φρεάτια από τα οποία συλλέχθησαν δείγματα ανιχνεύθηκαν υψηλές συγκεντρώσεις Cr(VI) μεταξύ 40μg/L και 120μg/L.Η απουσία βιομηχανικής δραστηριότητας στην ευρύτερη περιοχή δείχνει ότι η παρουσία του Cr(VI)

στα υπόγεια ύδατα είναι γεωγενούς προέλευσης και σχετίζεται άμεσα με το γεωλογικό υπόβαθρο της περιοχής που είναι τα υπερβασικά πετρώματα των Γερανείων.
Λέξεις κλειδιά: *Υδρογεωχημεία, γεωγενής ρύπανση, κινητικότητα χρωμίου.*

1. Introduction

Chromium occurs naturally but also enters the environment through emissions from human activities such as metallurgy and metal-finishing industries as well as from its use as a chemical intermediate. In water, chromium exists in two oxidation states, 3+ (III) and 6+ (VI), but the more thermodynamically stable state is Cr(VI). Hexavalent chromium is far more mobile than Cr(III) and more difficult to remove from water. It is also the toxic form of chromium, being approximately 10 to 100 times more toxic than Cr(III) by the acute oral route. Until recently human activities were considered the only Cr(VI) source in groundwater, however, latest research has shown that relatively high levels of Cr(VI) can also be attributed to natural processes (Kazakis *et al.,* 2015; Dermatas *et al.* 2015; Megremi *et al.*, 2013; Moraitis *et al.*, 2012; Margiota *et al.*, 2012; Oze *et al.* 2007; Fantoni *et al.*, 2002). Weathering and erosion of ultramafic rocks are possibly the main responsible mechanisms for the mobility of chromium from the bedrock to soils and aquifers. According to the Water Framework Directive 2000/60/EC, the upper limit of Cr(tot) in drinking water is 50 μg/L for the countries of European Union including Greece. However, Italy has regulated a maximum permissible level of Cr(VI) in drinking water at 5 μg/L.

Hexavalent chromium contamination in groundwater has been reported at several areas of Greece. Elevated concentrations have been attributed to natural processes within ophiolite related aquifers (Kazakis *et al.*, 2015; Kaprara *et al.*, 2015; Dermatas *et al.*, 2015), anthropogenic activities in industrial zones such as the notorious case of the Oinofyta- Asopos groundwater contamination (Panagiotakis *et al.*, 2015) or a combination of both, such as the ultramafic rock rich area of central Euboea which is also characterized by intensive agriculture (Voutsis *et al.,* 2015; Megremi *et al.,* 2013). Previously published data from the area of Schinos, which is one of study areas of the present study, reported high concentrations of Cr(VI) in a few domestic water wells within the village and attributed contamination to uncontrolled waste disposal (Papadopoulos and Lappas, 2014).

Taking into account that further study is required in order to assess Cr(VI) contamination in areas with suspect to geology, the objective of the present study is to present newly collected data regarding Cr(VI) concentrations in surface and groundwater samples from the area of Loutraki and Schinos and discuss Cr(VI) contamination in the context of the general hydrogeological and hydrogeochemical profile of the study areas.

2. Materials and Methods

2.1 Study Areas

The study areas (Loutraki and Schinos) are located in the Perachora peninsula at the eastern part of Corinthian Gulf (Fig.1). Loutraki lies at the southern part of Perachora peninsula and it is surrounded by the Gulf of Lechaio. The drainage basin of Loutraki covers an area of approximately 53.27 km^2 and has a perimeter of 35 km. The maximum elevation is 1068 m a.s.l. while the mean elevation is approximately 470 m a.s.l. The main geological formations of Loutraki's drainage basin are carbonate rocks (limestone) which cover an area of approximately 11.8 km^2, ophiolitic rocks (peridotite and serpentinite) which cover an area of 20.4 km^2, Neogene carbonate clay formations (marl) which cover an area of 1.1km^2, functioning as a barrier due to their impermeability controlling the groundwater flow and finally Quartenary conglomerate and alluvial deposits which cover an area of approximately 16km^2 (Bornovas *et al.*,1969). The above rock formations can be classified as permeable (limestone, quaternary conglomerates and alluvial deposits), partially permeable (marly sandstones and fractured ophiolites) and impervious (clay and marl). The main streams of Loutraki drainage network are Loumpiniaris and Agia Triada. The metallic aquifer is located in the alluvial

deposits consisting of ophiolite material (mainly serpentinite and pyroxenite) from the weathering and erosion of the ophiolite complex of Geraneia Mountains and covers approximately an area of 7.45km^2 with a maximum depth level of water at 150m (Kounis and Vitoriou, 2003a). The main sources of metallic groundwater are the direct infiltration of precipitation water, the runoff water of the whole drainage basin, the runoff water of ophiolite riverbeds from Geraneia Mountains as well as the underground source of conglomerates aquifer in the southeast part of Loutraki's drainage basin.

The area of Schinos is located in the northeastern part of Perachora peninsula and it is surrounded by the Alkyonides Gulf. The drainage area of Schinos covers approximately an area of 22,4 km^2 where the main geological formations are Jurassic limestone which is heavily fractured and fissured due to alpine and post-alpine tectonic movements, the Boeotian flysch consisting of rhythmic series of sandstone, clastic limestone and chert, ophiolites (serpentinite and peridotite) and the schist-chert formation at the base of ophiolite mélange which consists of radiolarites containing thin Mn-layers and reddish or grey limestone with chert (Bornovas *et al.*,1979). The wider region of Pissia-Schinos is tectonically active with active normal faults of NW-SE and E-W directions and this is depicted at the geomorphology of the whole area with abrupt alternation of slopes. The upper post-alpine formations are alluvial deposits and talus cones where the Schinos aquifer occurs. The aquifer of Schinos is placed in scree for the upper 2m depth and in fractured peridotites until a depth of 100m approximately (Kounis and Vitoriou, 2003b). The quality of groundwater is low due to sea intrusion (Papadopoulos and Lappas, 2014) so it is used mainly for irrigation.

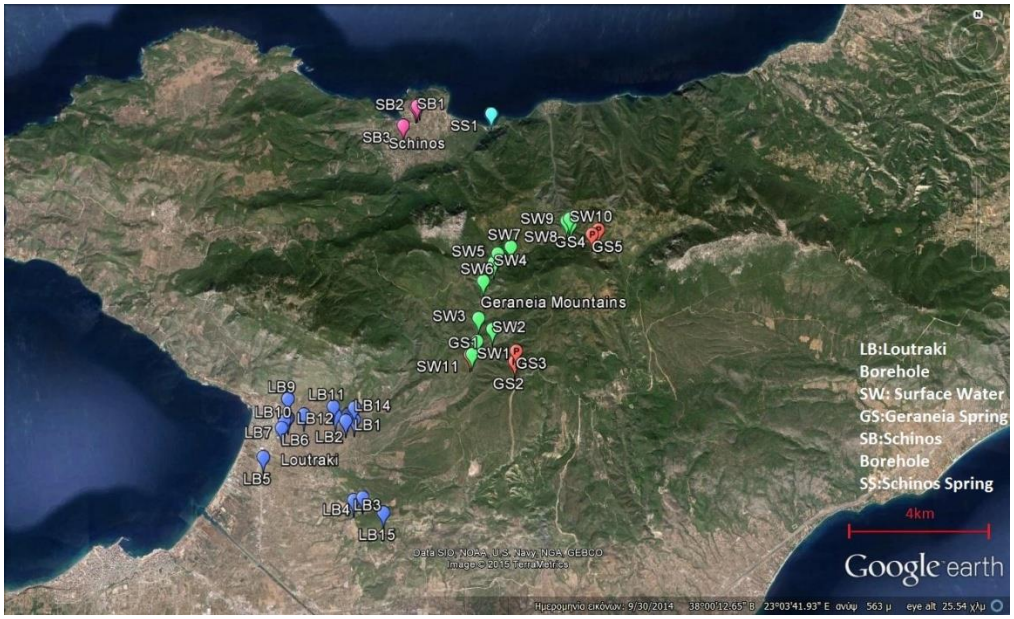

Figure 1 - Google earth map with sampling points.

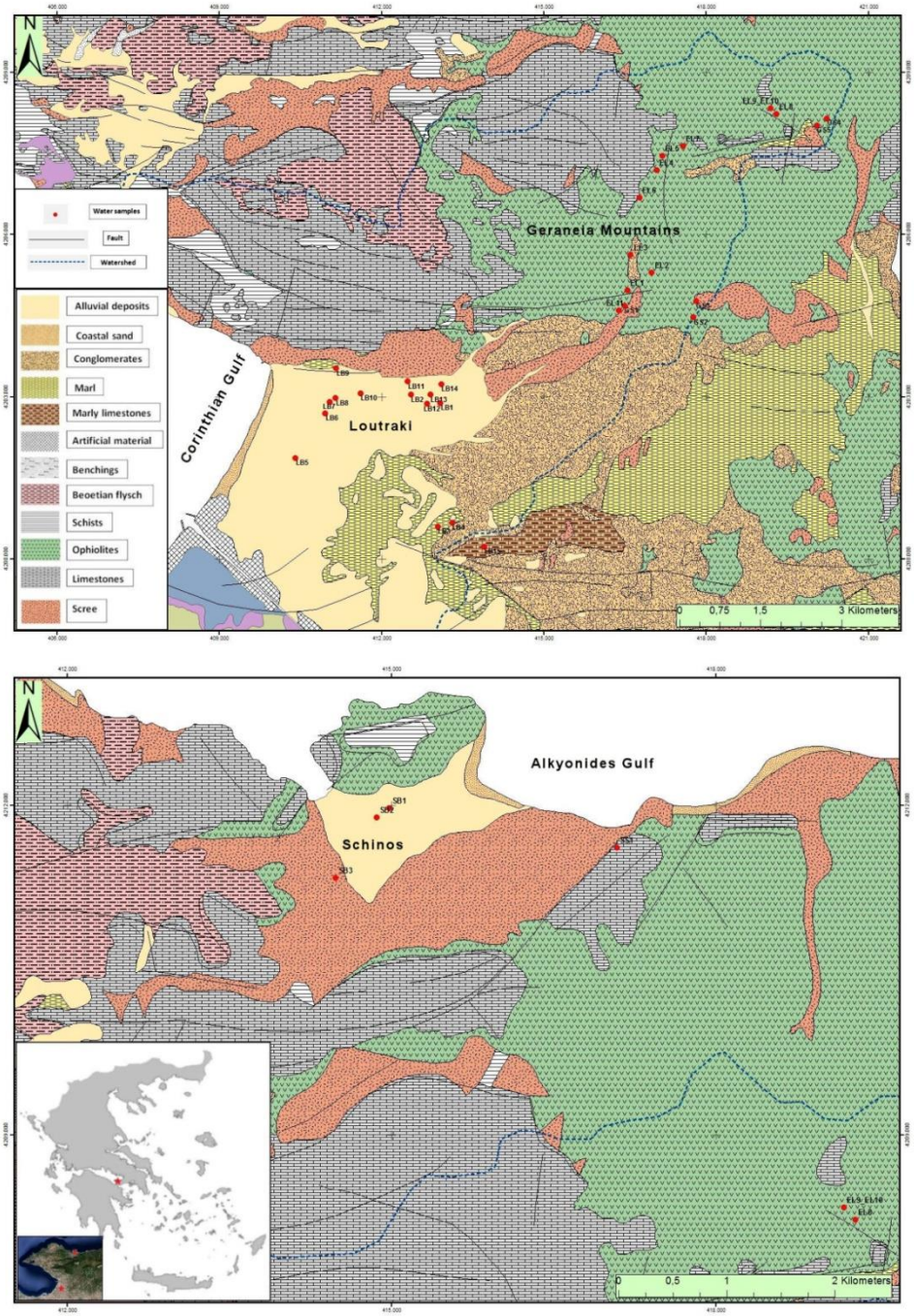

Figure 2 - Geological map of Loutraki and Schinos areas and location of sampling points.

2.2 Water Sampling and Analysis

A total of 38 water samples were collected from April to May 2015 (Fig. 1). Groundwater samples were collected from 15 boreholes from Loutraki area (LB) used to cover mainly the drinking water demands of Loutraki's residents. In addition, 5 groundwater samples (GS) were collected from natural springs of Geraneia Mountains, 11 surface water samples from the streams of Geraneia Mountains (SW), 1 surface water sample from the area of Sousaki (SSW) and 6 from the area of Schinos including 3 samples from wells (SB), 2 from springs (SS) and 1 from a borehole (SBF). In each sampling station three sub-samples were collected in separate bottles; one for cation analysis, one for Cr(VI) analysis and one for anion analysis. The water samples for cation and Cr(VI) analysis were filtered through 0.45 μm membrane filters *in situ* in order to collect only the soluble phases. The samples for cation analysis were acidified to pH<2 by adding a few drops of HNO_3. All samples were refrigerated during their transfer to laboratory. *In situ* measured parameters included pH, electrical conductivity (EC), total dissolved solids (TDS) and temperature. All major ions and trace elements were analyzed shortly after sampling in the laboratories of Environmental Chemistry, and Economic Geology and Geochemistry, University of Athens. In particular, Cr(VI) was determined by the DPC colorimetric method according to the ELOT-EN-ISO 18412 Standard (2006). The absorbance was determined at 540 nm on a double beam UV-vis Carry 1E spectrophotometer. The Method's Detection Limit (MDL), determined according to the EPA CRF 40B procedure (EPA 2008), is 0.6 μg L^{-1}. Nitric anions were measured with a photometric method which is based on the reduction of nitrates to nitrous using a cadmium column in a buffer solution and then the nitrous are measured according to the Griess-ilosvay process. Sodium and K^+ were determined by flame photometry, Mg^{2+} and Ca^{2+} were determined by means of Flame Atomic Adsorption Spectrometry (Varian SpectrAA-200) and finally the concentration of HCO_3^- was calculated by measuring the alkalinity of the samples through titration with H_2SO_4 1.16N using a HACH digital titrator.

3. Results and Discussion

3.1 Hydrogeochemical Features

The chemical analyses were tested for charge balance errors. Calculated charge balance errors were found to be less than or equal to ±10% for the majority of samples, which is an acceptable error for the purposes of the present study (Güler *et al.*, 2002). Only 3 samples balance errors were above ±10%. In general, the different water samples are classified into 6 groups according to their type (springs, boreholes, surface water) and physicochemical properties (Table 1). Among the different groups, mean pH values range from 7.5 to 9, conductivity (EC) ranges from 0.65 to 2.63 ms/cm, total dissolved solids (TDS) range from 0.33g/L to 1.34g/L and total hardness ($CaCO_3$) ranges from 329 mg/L to 606 mg/L. Relatively elevated values of conductivity have been measured at a Loutraki borehole, LB5 (13mS/cm) and at three Schinos boreholes-wells (SB1,SB2,SB3) ranging from 1.44 to 3.81mS/cm. These values are indicative of seawater intrusion because the same samples present elevated concentrations of Na^+ and Cl^-. As is shown in Figure 3, most samples are characterised by high concentrations of Mg^{2+} exceeding 100 mg/L whereas Ca^+ concentrations are significantly lower, ranging from 2 to 40 mg/L for most samples.

As a result it is concluded that the groundwater as well as surface water chemical composition is directly influenced by their interaction with ultramafic rocks and serpentinites. This is also justified by the high ratios of Mg/Ca for the different water groups (Table 1). The surface water samples (SW) are enriched in Mg^{2+} compared to Loutraki's alluvial aquifer groundwater (LB). The only sample with Mg/Ca ratio below 1 (0.15) is GS5 and this shows that probably this spring is related to the karstic aquifer. The highest Mg/Ca ratio is 149 and characterizes the spring Prathi (GS4). Plotting the samples' composition on a Piper plot (Fig. 4) revealed that all water samples are of bicarbonate magnesium type (Mg-HCO_3). Elevated concentrations of NO_3^- ranging from 16 mg/L to 207mg/L have been detected in certain samples within the built areas of Loutraki (LB5) and Schinos

(SB1,SB2,SB3) indicating most probably the deterioration of the water quality by wastewater i.e., contribution of organic effluents in water chemistry.

Table 1 - Mean values of physicochemical parameters and major ions in water samples.

Water groups	pH	EC ms/cm	TDS g/L	Ca^{2+} mg/L	Mg^{2+} mg/L	Mg/Ca	K^{+} mg/L	Na^{+} mg/L	HCO_3^{-} mg/L	NO_3^{-} mg/L	Cr(VI) µg/L
LB (n=15)	8.1	0.69	0.42	10.4	89.2	27.9	1.4	24.6	402	7.6	22.8
GS (n=5)	8.1	0.89	0.48	28	145	33.6	1.4	16.8	739	1.8	7.4
SW (n=11)	8.6	0.69	0.35	20.2	126	26.5	1.2	17.3	660	3.1	1.8
SSW (n=1)	8.3	1.1	0.54	35.8	145	6.7	1.5	27	825	1.3	3.5
SB (n=3)	7.5	2.63	1.34	59.9	225	7	1.86	254	676	107	65.3
SS (n=2)	9	0.65	0.33	2.07	105	55.3	1	20.6	580	1.3	1.3

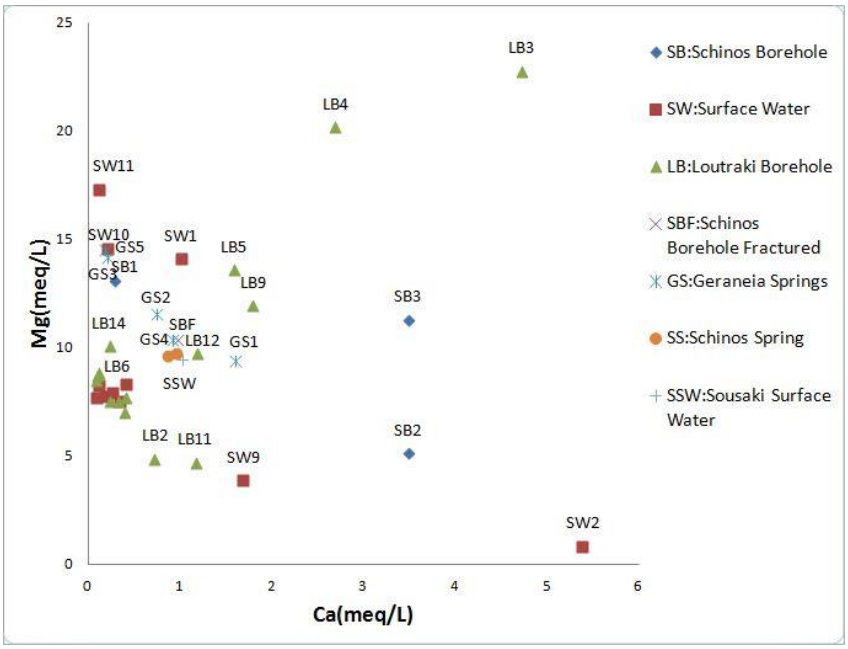

Figure 3 - Plot of Mg vs Ca.

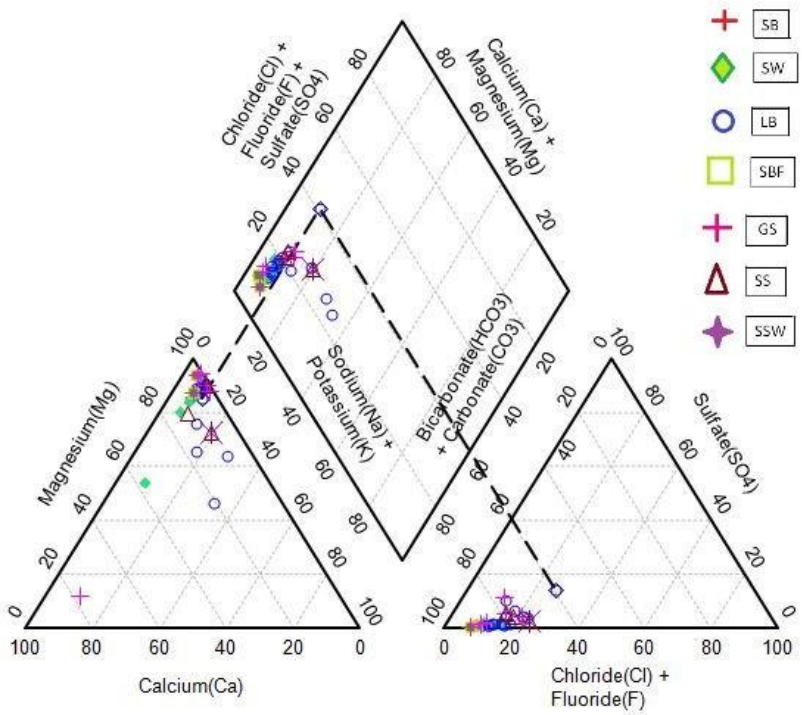

Figure 4 - Piper plot of different water groups indicating a bicarbonate magnesium water type.

3.2 Occurrence of Cr(VI) in water

The concentration of Cr(VI) in groundwater samples of Loutraki boreholes group (LB) were moderate to high ranging from 1.8 μg/L to 74 μg/L with a mean value of 23μg/L. Only 2 out of 15 samples had concentrations above the permissible level for drinking water. Dermatas *et al.* (2015) and Kazakis *et al.* (2015) have also found similar concentrations of Cr(VI) in the areas of Vergina (up to 64μg/L) and Anthemountas (up to 70μg/L) which also have an ophiolite-influenced geological background and aquifers which are related to ultramafic rocks. Furthermore, Dermatas *et al.* (2015) have reported much higher Cr(VI) concentrations, reaching 10 mg/L in groundwater from the area of Oinofyta where industrial activity is intense. The absence of industrial activities in the areas of Loutraki and Schinos as well as the concentrations levels of Cr(VI) are indicative of the natural source of this toxic element in water.

The highest Cr(VI) concentration of 120 μg/L was measured in one of the three water samples collected from domestic wells within the Schinos village. This is in agreement with data reported previously by Papadopoulos and Lappas (2014) who had measured up to 460 μg/L Cr(VI) in a water well at Schinos village. In contrast to domestic water wells Cr(VI) concentrations in the borehole sample of the area (SBF) as well as the two springs SS1 and SS2 which are the drinking water sources of Schinos village did not exceed 1.85μg/L. Moderate concentrations have been found in Geraneia springs (GS) with a maximum value of 14 μg/L Cr(VI) while low concentrations of Cr(VI) have been detected in surface water samples of Geraneia streams (SW) with a maximum concentration of approximately 4μg/L. The water samples with moderate to low concentrations of Cr(VI) (GS,SW,SBF,SS) are related to the aquifer of fractured ultramafic rocks of Geraneia Mountains, whereas the water samples with higher concentrations (GL, BS) are related with Loutraki's and Schino's alluvial aquifers. It is noted that alluvial sediments consist mainly of eroded ophiolite material derived from the upland areas surrounding the plains (Fig. 2). The enrichment of

alluvial aquifers in Cr(VI) has been also observed by Kazakis *et al.* (2015), Megremi *et al.* (2013) and Voutsis *et al.* (2015). Finally, Kelepertzis *et al.* (2013) have found that in Thiva basin which has a similar geological background, Cr(III) is mainly bounded within inherited chromite and to a lesser extent with Cr-magnetite and Cr silicates like enstatite, a conclusion which is in accordance to recent observations for this study.

Figure 5 presents a plot of Cr(VI) against Mg^{2+} concentrations in water samples. It is obvious that the increase of soluble Mg^{2+} does not influence soluble Cr(VI). This is probably explained by different sources of the two elements i.e., olivine for Mg and chromite for Cr as well as different processes affecting their release into the water, i.e. congruent dissolution of olivine and other silicate minerals for Mg and release of Cr(III) from chromite with subsequent oxidation to Cr(VI). According to the literature the release of Cr(VI) in the aqueous environment depends on several parameters such as the redox potential, the presence of MnO_2 and Fe_2O_3, the level of dissolved O_2 etc. Manganese oxides are likely to be responsible for chromium oxidation in aquatic environments through the following reaction (Fendorf, 1995):

$$Cr(OH)^{2+} + 1.5MnO_2 \rightarrow HCrO_4^- + 1.5Mn^{2+}$$

Also worth noting in Fig. 5 is the clustering of water samples according to their respective groups with stream water samples showing the lowest Cr(VI) concentrations and groundwater samples showing the highest Cr(VI) concentrations. This, indicates that the residence time of groundwater is a significant factor affecting Cr(VI) release into the water. Finally, the samples with relatively high conductivity (LB5,SB1,SB2,SB3) have also high concentrations of Cr(VI) ranging from 37μg/L to 120 μg/L.

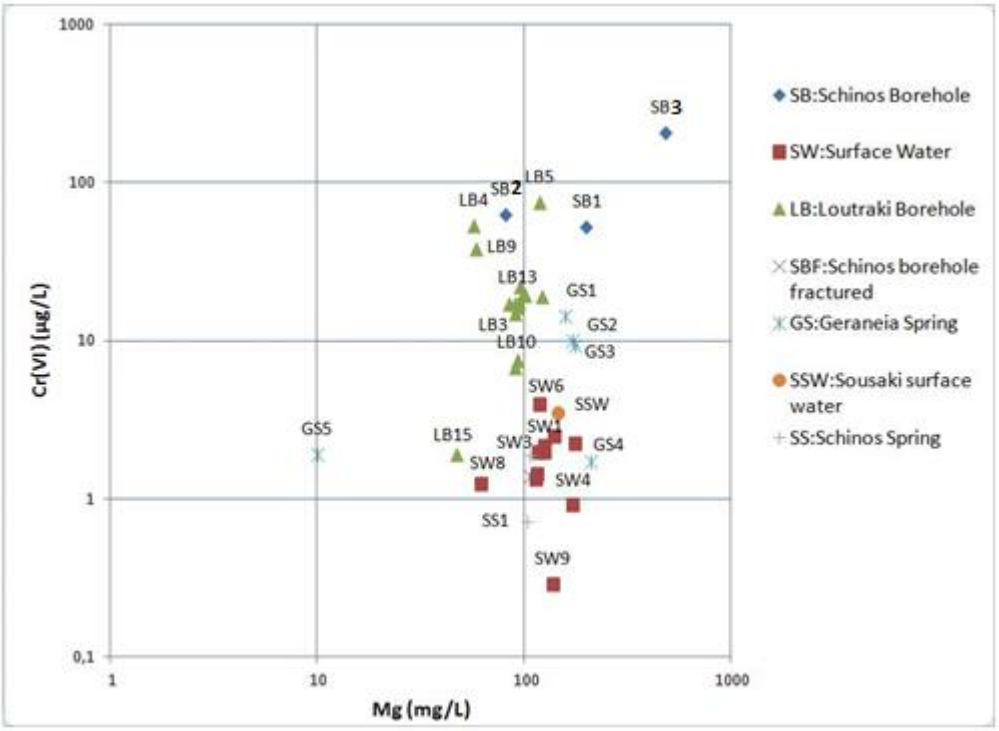

Figure 5 - Plot of Cr(VI) vs Mg.

4. Conclusions

Hexavalent chromium contamination of surface and groundwater in the areas of Loutraki and Schinos has been accessed in the context of local geology and hydrogeochemistry. Based on the data presented in the previous paragraphs the following conclusions have been drawn:

- The general chemical composition of all water samples is of $Mg\text{-}HCO_3$ type due to the interaction of both surface and groundwater with serpentinized ultramafic rocks that characterize the local geology.
- The release of Cr(VI) in groundwater is probably linked to natural processes and it is reflective of water–rock interaction within the ophiolite related aquifers in the study area.
- Alluvial aquifers present moderate to high concentrations of Cr(VI) in contrast to ophiolite fractured aquifers where the lowest Cr(VI) concentrations were measured.
- Groundwater of alluvial aquifers is enriched in Mg^{2+} and Cr(VI) in contrast to surface water which has only high concentrations of Mg^{2+}.
- Groundwater samples with higher conductivity exhibit the highest concentrations of Cr(VI).

Further research, looking into the mineralogy and weathering regime of chromium bearing phases in the serpentinized rocks as well as the hydrogeological features at local scale is needed in order to clarify the processes affecting Cr(VI) release into the water.

5. Acknowledgments

The authors would like to thank the Director of the Municipal Enterprise for Water and Sewage (MEWS) of Loutraki - Agioi Theodoroi Mr. Anastasios Mastrantonakis as well as the technical staff of MEWS for providing access to the Municipal boreholes and their help during the sampling survey. The help during field sampling of Mr Ioannis Ligouthis is also acknowledged.Dr. Sotirios Karavoltsos of the Laboratory of Environmental Chemistry, University of Athens is thanked for his help during water sample analysis.

6. References

Bornovas, J.I., Eleutheriou, A. and Gaitanakis, P., 1970-1980. Map of IGME Kaparellion.

Bornovas, J., Lalechos, N. and Filippakis, N., 1969. Map of IGME Korinthos.

Dermatas, D., Mpouras, T., Chrysochoou, M., Panagiotakis, I., Vatseris, C., Linardos, N. and Sakellariou, L., 2015. Origin and concentration profile of chromium in a Greek aquifer, *Journal of Hazardous Materials*, 281, 35-46.

Fantoni, D., Brozzo, G., Canepa, M., Cipolli, F., Marini, L., Ottonello, G. and Zuccolini, M., 2002. Natural hexavalent chromium in groundwaters interacting with ophiolitic rocks, *Environmental Geology*, 42(8), 871-882.

Fendorf, S.E., 1995. Surface reactions of chromium in soils and waters, *Geoderma*, 67(1), 55-71.

Güler, C., Thyne, G.D., McCray, J.E. and Turner, K.A., 2002. Evaluation of graphical and multivariate statistical methods for classification of water chemistry data, *Hydrogeology journal*, 10(4), 455-474.

Kaprara, E., Kazakis, N., Simeonidis, K., Coles, S., Zouboulis, A.I., Samaras, P. and Mitrakas, M., 2015. Occurrence of Cr (VI) in drinking water of Greece and relation to the geological background, *Journal of hazardous materials*, 281, 2-11.

Kazakis, N., Kantiranis, N., Voudouris, K.S., Mitrakas, M., Kaprara, E. and Pavlou, A., 2015. Geogenic Cr oxidation on the surface of mafic minerals and the hydrogeological conditions influencing hexavalent chromium concentrations in groundwater, *Science of the Total Environment*, 514, 224-238.

Kelepertzis, E., Galanos, E. and Mitsis, I., 2013. Origin, mineral speciation and geochemical baseline mapping of Ni and Cr in agricultural topsoils of Thiva valley (central Greece), *Journal of Geochemical Exploration*, 125, 56-68.

Kounis, G. and Vitoriou-Georgouli, A., 2003a. Water balance of Loutraki'smetallic aquifer.

Kounis, G. and Vitoriou-Georgouli, A., 2003b. Hydrogeological survey of Schinos area with implementation of pumping tests.

Margiotta, S., Mongelli, G., Summa, V., Paternoster, M. and Fiore, S., 2012. Trace element distribution and Cr (VI) speciation in Ca-HCO 3 and Mg-HCO 3 spring waters from the northern sector of the Pollino massif, southern Italy, *Journal of Geochemical Exploration*, 115, 1-12.

Megremi, I., Vasilatos, C., Atsarou, A., Theodoratou, C., Economou-Eliopoulos, M. and Mitsis, I., 2013. Geochemical evidences for the sources of the Cr (VI) contamination in groundwater in central Euboea and Assopos-Thiva basins, Greece: natural versus anthropogenic origin, *European Water*, 41, 23-34.

Moraetis, D., Nikolaidis, N.P., Karatzas, G.P., Dokou, Z., Kalogerakis, N., Winkel, L.H.E. and Palaiogianni-Bellou, A., 2012. Origin and mobility of hexavalent chromium in North-Eastern Attica, Greece, *Applied Geochemistry*, 27(6), 1170-1178.

Oze, C., Bird, D.K. and Fendorf, S., 2007. Genesis of hexavalent chromium from natural sources in soil and groundwater, *Proceedings of the National Academy of Sciences*, 104(16), 6544-6549.

Panagiotakis, I., Dermatas, D., Vatseris, C., Chrysochoou, M., Papassiopi, N., Xenidis, A. and Vaxevanidou, K., 2015. Forensic investigation of a chromium (VI) groundwater plume in Thiva, Greece, *Journal of Hazardous Materials*, 281, 27-34.

Papadopoulos, K. and Lappas, I., 2014. Groundwater quality degradation due to Cr^{6+} presence in Schinos area, prefecture of Corinth, Central Greece, 10th International Hydrogeological Congress of Greece, Thessaloniki.

Richard, F.C. and Bourg, A.C., 1991. Aqueous geochemistry of chromium: a review, *Water Research*, 25(7), 807-816.

Voutsis, N., Kelepertzis, E., Tziritis, E. and Kelepertsis, A., 2015. Assessing the hydrogeochemistry of groundwaters in ophiolite areas of Euboea Island, Greece, using multivariate statistical methods, *Journal of Geochemical Exploration*, 159, 79-92.

Δελτίο της Ελληνικής Γεωλογικής Εταιρίας, τόμος L, σελ. 2271-2280
Πρακτικά 14ου Διεθνούς Συνεδρίου, Θεσσαλονίκη, Μάιος 2016

Bulletin of the Geological Society of Greece, vol. L, p. 2271-2280
Proceedings of the 14th International Congress, Thessaloniki, May 2016

A GEOCHEMICAL INVESTIGATION OF SOILS, APPLES AND LEAVES IN AGIA AREA, CENTRAL GREECE

Skordas K.[1], Papastergios G.[2], Filippidis A.[2] and Kantiranis N.[2]

[1]*University of Thessaly, Department of Ichthyology and Aquatic Environment, Fitokou St., N. Ionia 38446, Greece, kskord@uth.gr*

[2]*Aristotle University of Thessaloniki, Department of Mineralogy-Petrology-Economic Geology, 131 Egnatia St. Thessaloniki 54124, Greece, gpapaste@geo.auth.gr*

Abstract

Forty two soil, apple and leaf samples from Agia area, central Greece, were collected and analyzed for their content in 7 major elements (Ca, Fe, K, Mg, Na, P and S). The average concentration of the determined elements follows the order: concentration in soils > concentration in leaves > concentration in apples. Elements, such as Fe that is found enriched in the soils of the study area, due to local geology, is not correlated with its concentrations in apples and leaves, possibly because of its association with resistant minerals. On the other hand, the relationship of some elements (i.e., K, P, S) that are constituents of the agrochemicals applied in the area, indicate that they are more readily available by the trees, either because they are associated with less resistant (clay) minerals, or because they derive through the application of agrochemical products (i.e., phosphate fertilisers, fungicides etc.).
Keywords: *mobility of chemical element, environment, fertilizer, agrochemical.*

Περίληψη

Σαράντα δύο δείγματα εδάφους, μήλων και φύλλων από την περιοχή της Αγιάς στην κεντρική Ελλάδα (Λάρισα) συλλεχτήκαν και αναλύθηκαν για το περιεχόμενο τους σε 7 κύρια στοιχεία (Ca, Fe, K, Mg, Na, P και S). Η επεξεργασία των δεδομένων έδειξε ότι η μέση συγκέντρωση των αναλυθέντων στοιχείων είναι μεγαλύτερη στα εδάφη, μετά στα φύλλα και τέλος, στα μήλα. Η στατιστική ανάλυση δεν έδειξε να υπάρχει κάποιος συσχετισμός μεταξύ των συγκεντρώσεων στοιχείων (π.χ., Fe) που είναι εμπλουτισμένα στα εδάφη, λόγω της τοπικής γεωλογίας και τη συγκέντρωση τους στα μήλα και φύλλα, πιθανότατα λόγω της σύνδεσης αυτών με ανθεκτικά ορυκτά. Αντίθετα, οι σχέσεις μεταξύ ορισμένων στοιχείων όπως K, P και S, τα οποία βρίσκονται στις διάφορες αγροχημικές ουσίες που εφαρμόζονται στην περιοχή δείχνουν πως μπορούν να απορροφηθούν πιο εύκολα από τα δέντρα, είτε γιατί σχετίζονται με λιγότερο ανθεκτικά (αργιλικά) ορυκτά, είτε γιατί προέρχονται από τη χρήση διάφορων αγροχημικών προϊόντων (π.χ., φωσφορικά λιπάσματα, ζιζανιοκτόνα κλπ.).
Λέξεις κλειδιά: *κινητικότητα χημικών στοιχείων, περιβάλλον, λίπασμα, αγροχημική ουσία.*

1. Introduction

Trees and plants and, consequently, their fruits and leaves, may contain and/or accumulate chemical elements depending on several attributes (i.e., soil chemical content, area of cultivation, method of

cultivation, individual fruit/plant properties and others), contributing this way to the daily need of humans in such nutrients (Wagner, 1993; Bobrowska-Grzesik and Jakobik-Kolon 2008; Skordas *et al.*, 2013). Some of these elements are called "*macronutrients*" (i.e., Ca, Fe, K, P etc.). They are considered as essential, or at least more essential than others, to the life cycles of organisms and are absorbed by them in significant amounts (Kabata-Pendias and Pendias, 2001).

At the same time, soils enriched in chemical elements, either through natural factors or through man-made procedures could be considered as an additional aspect to the problem as they could pass through it to fruits consumed by humans. The content of chemical elements in soils is highly affected and differentiated by the nature of parent materials (Kelepertsis *et al.*, 2001; Skordas and Kelepertsis, 2005; Papastergios *et al.*, 2009, 2010, 2011; Petrotou *et al.*, 2010, 2012; Skordas *et al.*, 2013). The latter controls, along with other factors (i.e., soil pH, Eh, absorptive power of soil constituents etc.) the level of the element availability and their uptake from plants and animals in sufficient and, in some cases, even toxic levels (Alloway *et al.*, 1988; Alloway, 1995; Hesterberg, 1998; Kabata-Pendias and Pendias, 2001; Newman and Unger, 2003).

The aim of the present research was to study the concentrations of seven major elements (Ca, Fe, K, Mg, Na, P, S) as well as, investigate the relationship between the content of these elements in soils, apples and leaves from Agia area, Thessaly, central Greece. This research advances the knowledge offered by a previous work (Skordas *et al.*, 2013) as it examines the interrelationships between three means (soils, apples and leaves), contrary to the previous one which offered data and analysis only for two (soils and apples).

2. Materials and Methods

2.1. Study area - Geological setting

The study area is located in the eastern part of the Regional Unit of Larissa, central Greece (Fig. 1). It is a region with a plain relief that is surrounded by low hills in the eastern and southern part. The large plain of Larissa lies to the west of the studied area. Most part of the surface is covered by apple tree orchards, while a large portion of the mountainous area and the hills are covered by mountainous forest.

The area consists of metamorphic rocks, belonging to the Pelagonian zone. The main geologic formations are (Skordas and Kelepertsis, 2005; Skordas *et al.*, 2010, 2013): Quaternary sediments, Neogene sediments, marbles, metamorphic rocks (i.e., gneisses-schists, amphibolite schists, amphibolites) and ophiolites.

Because of the extensive cultivation several agricultural products such as fertilizers and agrochemicals (i.e., pesticides, fungicides and insecticides) are applied. Some of the most common substances used are chlorpyrifos, diflubenzuron, dithianon, flufenoxuron, myclobutanil, paraffin oil, phosmet, pyriproxyfen, thiacloprid, copper oxychloride, sulphur etc. These substances are applied to the orchards most commonly between March and September, but sometimes application could take place all year long. Fertilizer application usually happens during January, while the fruits are harvested around September.

2.2. Sampling, sample preparation and methods

A total of 42 samples from each sample type (soil, apple, leaf) were collected covering an area of 65 km^2, approximately. During the sampling procedure the initial regular sampling grid of 500x500 m was impossible to follow accurately, because of the cultivated and, in some parts, mountainous terrain. However, care was taken to preserve a uniform distribution of sampling sites over the study area (Fig. 1). In the case of the apples and leaves, the samples were collected from the apple tree that was nearest to the location of the soil sample. A more detailed description of the sampling and treatment procedure is described in Skordas *et al.* (2013). Soil samples were analyzed for their elemental content by Inductively Coupled Plasma - Atomic Emission Spectrometry (ICP-AES),

while for the apples and leaves Inductively Coupled Plasma - Mass Spectrometry (ICP-MS) was used.

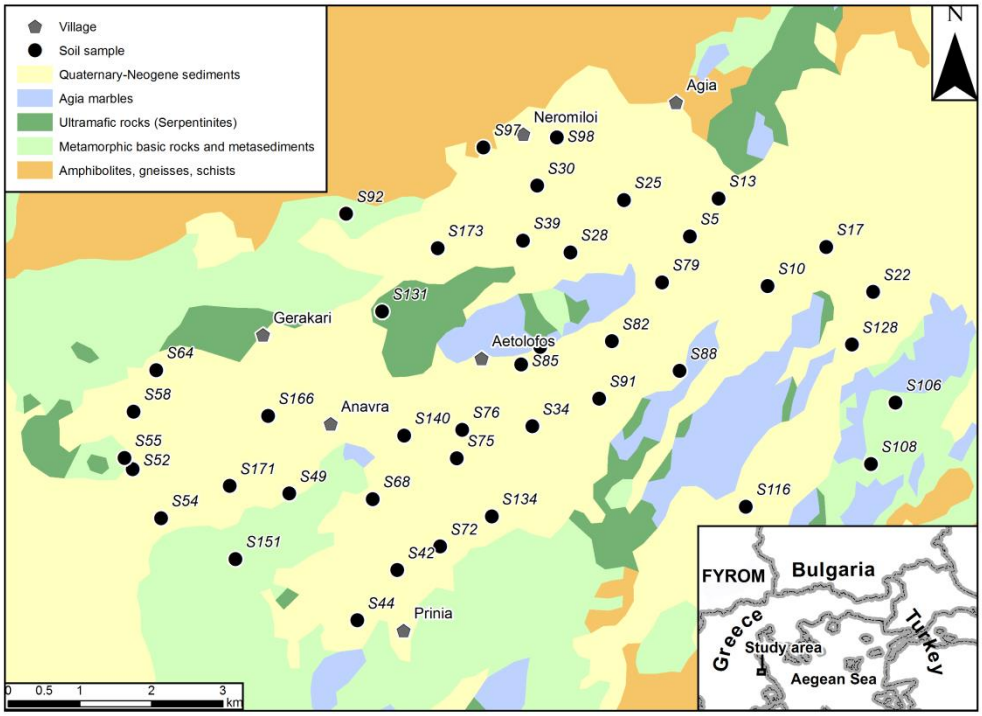

Figure 1 - Simplified geological map of the study area and sample locations (modified after Skordas *et al.*, 2013).

3. Results and Discussion

Descriptive statistics regarding the elements determined in the present study are given in Table 1. The most abundant element in soil is Fe, followed by Ca, Mg, Na, K and P. The rather elevated concentrations of Fe and Mg, were expected, as in the study area ophiolitic (ultramafic) rocks, which contain the above mentioned elements in noteworthy amounts, are present (Skordas and Kelepertsis, 2005; Petrotou *et al.*, 2010, 2012; Skordas *et al.*, 2010, 2013). A study (Kelepertzis, 2014) regarding agrcultural soils in Argolida, Greece, has reported slightly different average concentrations for Fe, P and K (27100 mg kg^{-1}, 3000 mg kg^{-1} and 900 mg kg^{-1}, respectively).

In apples, the most abundant element is K, followed by P, Mg, Ca, S, Na and Fe, while in leaves Ca is the element with the largest average concentration, followed by K, Mg, P, S, Fe and Na.

3.1. Overall assessment

For the majority of the determined elements their average concentrations follow the order: *concentration in soils* > *concentration in leaves* > *concentration in apples* (Table 1, Fig. 2). The same behaviour is demonstrated by the rest of the calculated statistic parameters, as well (Table 1). However, P is an exception to this behaviour. Its average concentration in soils (1119 mg kg^{-1}) is about the same as in apples (881.7 mg kg^{-1}) and lower than in leaves (2073 mg kg^{-1}). This could be a result of the excessive application of phosphoric fertilizers or/and organophosphate agrochemicals such as chlorpyrifos ($C_9H_{11}Cl_3NO_3PS$) and phosmet ($C_{11}H_{12}NO_4PS_2$). It also can be deducted that, probably, the determined elements accumulate more in leaves than in fruits (apples).

Table 1 - Descriptive statistics regarding the elements determined in soils, apples and leaves.

(mg kg^{-1})	Soil	Leaf	Apple	Soil	Leaf	Apple
Element	**Ca**			**Fe**		
median	25250	16350	400.0	45300	195.0	15.0
average	25390	16860	390.5	46486	228.1	28.3
geomean	23813	16593	383.5	45916	208.4	19.4
minimum	11600	11400	300.0	31200	110.0	10.0
maximum	70400	25700	600.0	65200	690.0	150.0
std deviation	10117	3078	75.9	7364	112.9	31.5
Element	**K**			**Mg**		
median	13950	11800	9550	20250	4935	480.0
average	13543	11964	9676	20088	5052	474.8
geomean	13303	11713	9545	19557	4976	470.8
minimum	8300	6600	6000	9900	3590	360.0
maximum	17300	16500	14700	32700	7440	610.0
std deviation	2448	2409	1632	4633	907.3	62.3
Element	**Na**			**P**		
median	15100	80.0	40.0	975.0	2040	865.0
average	14924	89.8	42.1	1119	2073	881.7
geomean	14629	83.8	40.5	1019	2043	869.4
minimum	8800	50.0	30.0	430.0	1410	590.0
maximum	23900	250.0	90.0	4290	3440	1190
std deviation	3040	37.9	13.2	619.4	378.5	148.3
Element		**S**				
median		1900	300.0			
average		1874	302.4			
geomean		1862	245.3			
minimum		1500	50.0			
maximum		2400	800.0			
std deviation		213.1	181.1			

Phosphate fertilizers are considered as an important source of heavy metals entering agricultural soils (Nicholson *et al.*, 2003; Rodriguez Martin *et al.*, 2006). Other elements (heavy metals) are also present in varying amounts in other inorganic fertilizers (i.e., nitrogen, potash) and in liming materials (Nicholson *et al.*, 2003; Rodriguez Martin *et al.*, 2006). The excessive application of such substances could lead to elevated concentrations in agricultural products cultivated over these soils (Otte *et al.*, 1993; Dudka *et al.*, 1994; Rodriguez Martin *et al.*, 2006; Skordas *et al.*, 2013). Hence, the elevated values of such elements in the apples of the present study could derive from the excessive amounts of fertilizers and agrochemicals applied to the local crops.

3.2. Elemental relationships between the sampled means

Additionally, correlation analysis was carried out to determine the nature of the relationships between the investigated elements. Because the data of the present research were not normally distributed the estimation of Spearman's rank correlation coefficient (also known as Spearman's *rho*) was selected (non-parametric statistics). Unless otherwise stated, correlations were considered significant at $p < 0.01$.

In soils, elements that are significantly correlated are Na and Ca (r: 0.52), Fe and Mg (r: 0.40) and P and Ca (r: 0.52) (Table 2). In apples (Table 3), the latter correlation applies for K and Mg (r: 0.61) and K and P (r: 0.44), while a correlation (at the 0.05 level) is also displayed by Ca and Mg (r: 0. 32) and Mg and P (r: 0.36). Finally, in leaves (Table 4), the only correlation present is between K a nd Mg (r: -0.36), which, is negative ($p < 0.05$).

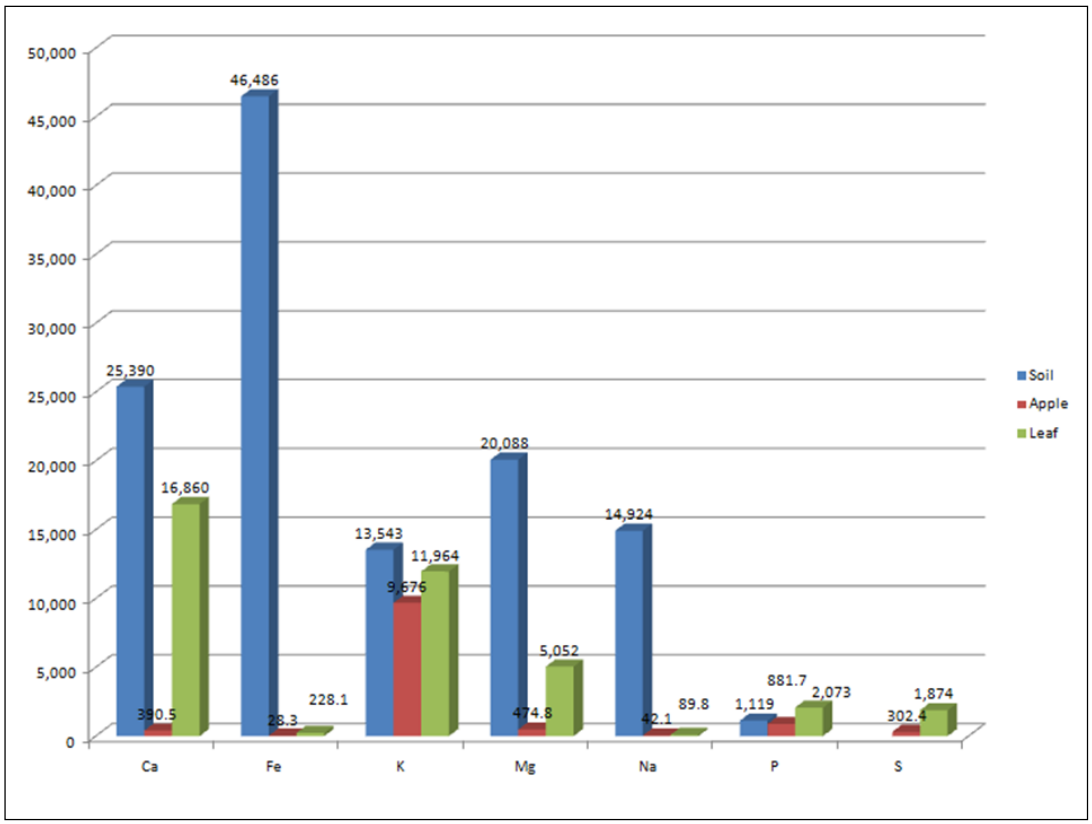

Figure 2 - Graphical representation of the average elemental concentrations determined in soils, apples and leaves.

Table 2 - Spearman's rank correlation coefficient (Spearman's *rho*) for the determined elements in soils (S) and apples (A).

	Ca_S	Ca_A	Fe_S	Fe_A	K_S	K_A	Mg_S	Mg_A	Na_S	Na_A	P_S	P_A
Ca_S	1											
Ca_A	-.242	1										
Fe_S	.111	.137	1									
Fe_A	-.004	-.231	-.134	1								
K_S	-.175	.112	-.133	-.104	1							
K_A	.170	-.021	.119	-.064	-.054	1						
Mg_S	.120	-.049	.401**	.070	.174	.012	1					
Mg_A	-.145	.316*	-.002	-.105	-.206	.612**	-.164	1				
Na_S	.520**	-.201	.010	.363*	-.198	.183	-.045	-.103	1			
Na_A	-.057	-.011	-.270	-.050	-.129	.051	-.159	.146	-.025	1		
P_S	.525**	-.049	.110	.027	-.078	.229	.099	.089	.268	-.154	1	
P_A	.162	-.034	-.203	.108	-.226	.441**	-.154	.356*	.370*	.159	.002	1

**. Correlation is significant at the 0.01 level (2-tailed).

*. Correlation is significant at the 0.05 level (2-tailed).

Table 3 - Spearman's rank correlation coefficient (Spearman's *rho*) for the determined elements in soils (S) and leaves (L).

	Ca_S	Ca_L	Fe_S	Fe_L	K_S	K_L	Mg_S	Mg_L	Na_S	Na_L	P_S	P_L
Ca_S	1											
Ca_L	.209	1										
Fe_S	.111	.006	1									
Fe_L	.011	-.139	-.168	1								
K_S	-.175	.073	-.133	.211	1							
K_L	-.003	-.256	-.071	-.001	.059	1						
Mg_S	.120	.167	.401**	.015	.174	-.006	1					
Mg_L	.310*	.226	-.126	.171	-.224	-.362*	.010	1				
Na_S	.520**	.008	.010	.035	-.198	-.033	-.045	-.061	1			
Na_L	.248	.097	.050	.225	-.058	-.299	-.009	.232	.249	1		
P_S	.525**	.043	.110	.159	-.078	.156	.099	-.004	.268	.016	1	
P_L	-.015	-.120	-.229	.015	.013	.191	-.038	-.129	.127	.025	-.316*	1

Table 4 - Spearman's rank correlation coefficient (Spearman's rho) for the determined elements in leaves (L) and apples (A).

	Ca_L	Ca_A	Fe_L	Fe_A	K_L	K_A	Mg_L	Mg_A	Na_L	Na_A	P_L	P_A	S_L	S_A
Ca_L	1													
Ca_A	-.022	1												
Fe_L	-.139	-.175	1											
Fe_A	.161	-.231	.350*	1										
K_L	-.256	-.146	-.001	-.243	1									
K_A	-.057	-.021	.145	-.064	.517**	1								
Mg_L	.226	-.052	.171	.162	-.362*	-.110	1							
Mg_A	-.265	.316*	.241	-.105	.261	.612**	-.083	1						
Na_L	.097	.027	.225	.165	-.299	.005	.232	.001	1					
Na_A	-.041	-.011	-.068	-.050	-.007	.051	.160	.146	.369*	1				
P_L	-.120	.025	.015	.120	.191	-.216	-.129	-.158	.025	.208	1			
P_A	-.107	-.034	.226	.108	.152	.441**	.066	.356*	.066	.159	.366*	1		
S_L	-.196	-.026	.237	-.198	.300	.097	-.416**	.257	-.132	.161	.072	-.222	1	
S_A	-.049	-.108	.290	.143	.264	.194	-.069	.172	-.325*	-.360*	.009	.109	.159	1

Nevertheless, when examining the elemental relationships amongst the different sampling in general, no significant correlation was found among the concentrations that the studied elements have in soils and apples, and in soils and leaves (Tables 2 and 3), indicating that for the studied elements their concentrations in apples and leaves is not strongly influenced by their concentration in soils. One would expect that, since these trees grow on soil enriched in Fe its elevated concentrations would be directly associated with their geogenic origin. Possibly, because Fe is found in resistant minerals is not readily available (Megremi, 2010; Petrotou *et al.*, 2010).

However, strong correlations between the concentrations of K and Mg, as well of Fe, Na and S (at $p < 0.05$), in apples and leaves has been noted (Table 4). Elements (i.e., Na, Ca) that are associated with clay minerals, such as montmorillonite, could be more easily extracted from the trees and accumulate in different parts, thus, the existing correlation between this elements in apples and leaves. Another way for this elements to accumulate in apples and leaves could be through the application of the various agrochemical substances applied, as the strong correlation between P and Na implies (Table 4).

4. Conclusions

The treatment of the data presented in this research has shown that the average concentration of the determined elements follows the order: *concentration in soils* > *concentration in leaves* > *concentration in apples*. Elements, such as Fe that is found enriched in the soils of the study area is not correlated with its concentrations in apples and leaves, possibly due to its association with resistant minerals. On the other hand, the relationship of some elements (i.e., K, P, S) that are constituents of the agrochemicals applied in the area, indicate that they are more readily available by the trees, either because they are associated with less resistant (clay) minerals, or because they derive through the application of agrochemical products (i.e., phosphate fertilisers, fungicides etc.).

5. References

Alloway, B.J., 1995. Heavy Metals in Soils, 2nd ed. Blackie, Glasgow.

Alloway, B.J., Thornton, I. and Smart, G.A., 1988. Metal availability, *Sci. Total Environ.*, 75, 41-69.

Bobrowska-Grzesik, E. and Jakobik-Kolon, A., 2008. Leaching of cadmium and lead from dried fruits and fruit teas to infusions and decoctions, *J. Food Compost. Anal.*, 21, 326-331.

Dudka, S., Piotrowska, M. and Chlopecka, A., 1994. Effect of elevated concentrations of Cd and Zn in soil on spring wheat yield and the metal contents of the plants, *Water Air Soil Pollut.*, 76, 333-341.

Hesterberg, D., 1998. Biogeochemical cycles and processes leading to changes in mobility of chemicals in soils, *Agric. Ecosyst. Environ.*, 67, 121-133.

Kabata-Pendias, A. and Pendias, H., 2001. Trace elements in Soils and Plants, 3rd ed. CRC Press, New York.

Kelepertsis, A., Alexakis, D. and Kita, I., 2001. Environmental geochemistry of soils and waters of Susaki area, Korinthos, Greece, *Environ. Geochem. Health*, 23, 117-135.

Kelepertzis, E., 2014. Accumulation of Heavy Metals in Agricultural Soils of Mediterranean: Insights from Argolida Basin, Peloponnese, Greece, *Geoderma*, 221-222, 82-90.

Megremi, I., 2010. Distribution and bioavailability of Cr in central Euboea, Greece, *Central Eur. J. Geosciences*, 2, 103-123.

Newman, M. and Unger, M., 2003. Fundamentals of Ecotoxicology, 2nd ed., Lewis Publishers.

Nicholson, F.A., Smith, S.R., Alloway, B.J., Carlton-Smith, C. and Chambers, B.J., 2003. An inventory of heavy metals inputs to agricultural soils in England and Wales, *Sci. Total Environ.*, 311, 205-219.

Otte, M.L., Haarsma, M.S., Broekman, R.A. and Rozema, J., 1993. Relation between heavy metal concentrations and salt marsh plants and soil, *Environmental Pollution*, 82, 13-22.

Papastergios, G., Fernandez-Turiel, J.L., Georgakopoulos, A. and Gimeno, D., 2009. Natural and anthropogenic effects on the sediment geochemistry of Nestos River, northern Greece, *Environmental Geology*, 58(6), 1361-1370.

Papastergios, G., Fernandez-Turiel, J.L., Georgakopoulos, A. and Gimeno, D., 2010. Arsenic background concentrations in surface soils of Kavala area, northern Greece, *Water, Air Soil Poll.*, 209(1), 323-331.

Papastergios, G., Filippidis, A., Fernandez-Turiel, J.L., Gimeno, D. and Sikalidis, C., 2011. Surface soil geochemistry for environmental assessment in Kavala area, northern Greece, *Water Air Soil Pollut.*, 216, 141-152.

Petrotou, A., Skordas, K., Papastergios, G. and Filippidis, A., 2010. Concentrations and bioavailability of potentially toxic elements in soils of an industrialised area of northwestern Greece, *Fresen. Environ. Bull.*, 19, 2769-2776.

Petrotou, A., Skordas, K., Papastergios, G. and Filippidis, A., 2012. Factors affecting the distribution of potentially toxic elements in surface soils around an industrialized area of northwestern Greece, *Environ. Earth Sci.*, 65, 823-833.

Rodriguez Martin, J.A., Lopez Arias, M. and Grau Corbi, J.M., 2006. Heavy metals contents in agricultural topsoils in the Ebro basin (Spain). Application of the multivariate geoestatistical methods to study spatial variations, *Environmental Pollution*, 144, 1001-1012.

Skordas, K. and Kelepertsis, A., 2005. Soil contamination by toxic metals in the cultivated region of Agia, Thessaly, Greece. Identification of sources of contamination, *Environmental Geology*, 48, 615-624.

Skordas, K., Pateras, D., Papastergios, G., Lolas, A. and Filippidis, A., 2010. Spatial distribution and concentrations of Fe, Mg, Co, Cr and Ni in surface soils of central Greece as affected by parent rocks, *Geochemistry, Mineralogy and Petrology, Sofia*, 48, 95-102.

Skordas, K., Papastergios, G. and Filippidis, A., 2013. Major and trace elements contents in apples from a cultivated area of central Greece, *Environ. Monit. Assess.*, 185, 8465-8471.

Wagner, G.J., 1993. Accumulation of cadmium in crop plants and its consequences to human health, *Adv. Agron.*, 51, 173-212.

Environmental Geosciences

Δελτίο της Ελληνικής Γεωλογικής Εταιρίας, τόμος L, σελ. 2283-2295
Πρακτικά 14ου Διεθνούς Συνεδρίου, Θεσσαλονίκη, Μάιος 2016

Bulletin of the Geological Society of Greece, vol. L, p. 2283-2295
Proceedings of the 14th International Congress, Thessaloniki, May 2016

NEW APPROACHES TO THE REVEGETATIONAND RECLAMATION OF OLD TAILING MANAGEMENT FACILITIES: THE EXAMPLE OF THE CASSANDRA MINES

Alifragkis D.[1], Vavelidis M.[2], Gazea B.[3], Voulgaridou E.[1], Galatsianou A.[3] and Daftsis E.[3]

[1]Aristotle University of Thessaloniki, Forestry and Natural Environment, Thessaloniki Greece, dalifrag@for.auth.gr, v_elena7@hotmail.com

[2]Aristotle University of Thessaloniki, vavelidi@geo.auth.gr

[3]Hellas Gold SA, EmmyGazea@gr, eldoradogold.com, anastasia galatsianou@ gr eldoradogold.com

Abstract

Vegetation cover is a cost effective method for reclaiming old mine wastes and tailings disposal sites. Physicochemical characteristics of wastes and tailings are often inimical to successful vegetation establishment. In this research revegetation and reclamation of old tailings management facilities at Cassandra Mines was investigated. The research was conducted in three stages. In the first stage, the physicochemical characteristics of the mining wastes were studied and methods for reduction of the bioavailability of heavy metals by adding various amendments such as material rich in Mn and Fe oxides (by-products of pyrolusite industry, zeolite, phosphates, Fe oxides, Fe^o etc.) were investigated. In the second stage, the suitability of different plant species for revegetation of the mine wastes in greenhouse conditions was investigated. The results of this stage showed that the species Nerium oleander can be used successfully to stabilize the surface of the old mining wastes followed by a reduction of heavy metals bioavailability. In the third stage (pilot experiment), the six best treatments of greenhouse experiment were used in two sites (Olympias, Karakoli) with three repetitions per treatment. The plants were fertilized and irrigated for two growth periods. Biometrical characteristics of Nerium oleander (leaf area, height of plants, weight of leaves and number of branches) and concentrations of the elements in the leaves of the plants were determined. One year after, a number of other plant species colonized the area with natural processes. These plants were recorded, collected and identified and the chemical compositions and bioaccumulation factors were determined. The growth of Nerium oleander was successful for almost all treatments. The revegetation and stabilization of the experimental plots resulted to a quick colonization by various plant species. Thirty five (35) different plant species were recorded in "old Olympias tailings pond" and forty (40) species in "old Karakoli tailings dam". Treatments affect the number of plant species colonized the experimental plots. The best treatments contained material rich in oxides of Fe and Mn.

Keyswords: *Mine wastes stabilization, revegetation of mine spoil, tails (TMF-tailing material facilities), phytoremediation.*

Περίληψη

Στην εργασία αυτή ερευνήθηκε η δυνατότητα φυτοαποκατάστασης των δύο χώρων απόθεσης μεταλλευτικών αποβλήτων στα μεταλλεία Κασσάνδρας Χαλκιδικής (Στρατώνι και Ολυμπιάδα). Η έρευνα διεξήχθη σε τρία στάδια. Στο πρώτο στάδιο μελετήθηκαν τα φυσικοχημικά χαρακτηριστικά των μεταλλευτικών αποβλήτων και διερευνήθηκαν οι τρόποι μείωσης της βιοδιαθεσιμότητας των βαρέων μετάλλων και μεταλλοειδών με τη χρησιμοποίηση διαφόρων πρόσθετων υλικών. Μεταξύ αυτών των υλικών ήταν οξείδια του Fe και Mn, υλικά πλούσια σε οξείδια των Fe και Mn (παραπροϊόντα του εργοστασίου της ηλεκτρολυτικής επεξεργασίας του πυρολουσίτη), ζεόλιθος, φωσφορικά άλατα, ρινίσματα του Fe, Fe^0 κ.ά. Στο δεύτερο στάδιο μελετήθηκε η αντοχή διαφόρων φυτικών ειδών σε συνθήκες θερμοκηπίου. Η επιλογή των ειδών βασίσθηκε στη δυνατότητα χρησιμοποίηση των ειδών αυτών σε προγράμματα φυτοαποκατάστασης μεταλλευτικών αποβλήτων. Τα αποτελέσματα του πειράματος του θερμοκηπίου έδειξαν ότι το φυτικό είδος Nerium oleander μπορεί να χρησιμοποιηθεί επιτυχώς. Από το πείραμα του θερμοκηπίου επιλέχτηκαν οι έξη καλύτερες μεταχειρίσεις. Οι μεταχειρίσεις αυτές αποτέλεσαν τη βάση του πιλοτικού σταδίου (τρίτο στάδιο). Για την αξιολόγηση των μεταχειρίσεων στην πιλοτική εφαρμογή χρησιμοποιήθηκαν διάφορα βιομετρικά χαρακτηριστικά των φυτών. Παράλληλα στο τέλος του πειράματος καταγράφηκαν τα φυτικά είδη που εγκαταστάθηκαν με φυσικό τρόπο . Τα είδη αυτά συλλέχθηκαν και αναλύθηκαν χημικά. Τα αποτελέσματα της έρευνας έδειξαν ότι το είδος Nerium oleander μπορεί να χρησιμοποιηθεί επιτυχώς. Παράλληλα τα αποτελέσματα έδειξαν ότι το είδος της μεταχείρισης επηρεάζει τον αριθμό των ειδών που εγκαθίστανται με φυσικές διεργασίες. Μερικά από τα είδη που εγκαταστάθηκαν με φυσικό τρόπο υπερβιοσυσσωρεύουν μέταλλα, ενώ ορισμένα ανήκουν στην κατηγορία των μεταλλοφύτων.

Λέξεις κλειδιά: *Σταθεροποίηση μεταλλευτικών αποβλήτων, Φυτοαποκατάσταση μεταλλευτικών αποβλήτων, tails (TMF-tailing material facilities), φυτοαποκατάσταση.*

1. Introduction

In recent years, a strong interest in the development of new methods and technologies for extraction and exploitation of minerals combining both the economic and the environmental dimension has been expressed (Rumenjak *et al.*, 2013; Van Zyl *et al.*, 2013; Shtiza *et al.*, 2013). It is now a requirement in most countries that reclamation schemes must be incorporated in mining proposals at the planning stage. At the same time, efforts are made to inform both citizens and stakeholders with scientific documentation and transparency of technologies that reduce environmental costs as well as how to deal with environmental problems, in order to accept the operation of mining activities (Craynon *et al.*, 2013; Kolovos, 2013). Old mine wastes or poor mining materials had, on the economic circumstances of their times, no value. Today these are raw material for new treatment. This was made possible by using new and improved methods of enrichment. These practices of reprocessing and exploitation of mining waste, are expected to be used in the future. According to Lottermoser (2010), «*waste of yesterday may be the mineral resources of the future*".

Mine waste disposal sites such tails and dumps must be reclaimed before the end of mine exploitation activities. In its broadest sense, as reclamation of mining waste disposal areas means the attempt to create a steady state or restore the soil functions in a deprived area, to a new land use that has been preselected for the region and that is possible (European Commission, 2006). There is a growing need to reclaim such sites in order to increase environmental quality. Remediation of large areas by conventional techniques, which were used for small areas of heavily contaminated sites, is not feasible economically. These areas, potentially, provide alternative equivalents of degraded natural resources. In these cases, it is suggested to create suitable conditions to allow re-settlement of a new ecological balance, thus reducing the risk to humans and the environment (European Commission, 2006).

Some basic techniques and methods (physical, chemical and biological) have been employed to reclaim a tail or a mine waste disposal area. Chemical stabilization involves use of chemical stabilizers as amendments such Fe^0, Fe_2O_3, $Fe(OH)_2$, $CaCO_3$, zeolite, MnO_2, red mud from bauxite processing organic matter etc. (Ladeira *et al.*, 2004; Chakravarty *et al.*, 2002), This technique for mine wastes stabilization is temporary but it is useful tool prior to revegetation. The use of chelating agents has disadvantages because in some cases complexes are toxic and poorly photo-, chemo- and bio-degradable and can cause ground water pollution by uncontrolled metal dissolution and metal leaching. Several efforts have been made to reduce soluble forms of heavy metals (Kumpiene *et al.*, 2006, 2008). The use of vegetation to stabilize mine wastes is a long term rehabilitation process. The unfavorable plant growth conditions that dominate in mine wastes sites have as a consequence these areas to be largely devoid of any natural vegetation, even many years after abandonment (Alifragkis *et al.*, 2013). Because of the great variation in physical, chemical and biological properties between mine wastes, revegetation of such areas is limited and needs more focused researches. Successful revegetation can be a permanent and visually attractive solution and, at the same time, relatively inexpensive. A vegetation cover can be effective in providing the necessary surface stability by preventing wind erosion of contaminated particulates, and in reducing water pollution by interception of a substantial proportion of precipitation.

Several different methods for revegetation of mine wastes have been developed. For example direct seedling with native plant species or commercially available plants, planting small plants, seedling or planting with metal tolerant plants or metallophytes, etc. Some of them are attractive methods and have advantages and disadvantages. In all cases ameliorants and stabilization agents must be used.

Selection of plant species is one of the most critical factors in revegetation applied on contaminated areas. It is associated with the facts that (a) the waste materials differ from site to site, (b) the climatic conditions such as temperature and humidity differ from site to site, and (c) only a limited number of plant species are tolerant in high salt and metal concentrations. The aim of this research is the reclamation via revegetation of abandoned mine wastes of the Cassandra Mines.

2. Material and Methods

In the Chalkidiki peninsula, abandoned mine working sites are typical features of landscape. Pb, Zn, Cu occur principally in the form of sulfide minerals galena (PbS), sphalerite (Zn, FeS), etc.

Northeastern Chalkidiki is the region of Greece with a great mining activity. Its mining history starts 2500 years ago since the time of Alexander the Great. Since the 90´s the mines were abandoned, leaving behind several old disposal areas.

The experimental sites were located in Northern Greece, 1) at Olympias- mine, and 2) at Stratoni mine. The materials that make up mine wastes are various minerals such as arsenopyrite, pyrite galena, sphalerite etc. In Olympias, in a specifically designed area (tailing material facilities -TMF), mine wastes were deposited in liquid form (area approximately 30 hectares). Tailing are fine-grained deposits (<2mm) from the final stage separators. After evaporation of the liquid phase the area covered with polyethylene sheets to reduce wind erosion temporarily. The variation of materials with depth is an important characteristic of the TMF. The texture of tailing materials is predominantly sandy loam. The chemical characteristics and bioavailability of nutrients are given in table 1. The Karakoli site, various mining waste (cake) in solid form were deposited (area approximately 3.5 hectares). Mine wastes came from the enrichment plant and sludge coming from the neutralization process. The chemical characteristics and bioavailability of nutrients are given in table 2.

Experiment was carried out at three levels. The first level experiment refers to purely laboratory investigation on the properties of the mine wastes materials in order to reduce the amount of soluble forms of heavy metals by extraction experiments, columns with suction microlysimeter, etc.

Table 1 - Mean chemical composition at Olympias site.

pH	Water soluble (μg/g)				Leachable DTPA (μg/g)				Exchangeable (cmol/Kg)				N (%)	P (Olsen) (μg/g)
	Zn	Cu	Mn	Fe	Zn	Cu	Mn	Fe	Mg	K	Na	Ca		
7,15	0,34	-	1,12	23,5	8,2	2,98	2,52	140,9	0,34	0,07	0,81	7,50	<0,01	15

Table 2 - Mean chemical composition of Karakoli mine wastes.

Location	pH	P (Olsen), μg/g	Exchangeable (cmol/kg)				
			N (%)	Ca	Mg	K	Na
1	4,10	3,58	0,03	59,63	1,866	0,004	0,127
2	2,81	3,55	0,044	34,56	0,899	0,012	0,510
3	4,13	3,56	0,04	58,88	1,377	0,009	0,244

Location	Water soluble (μg/g)				Leachable DTPA) (μg/g)				Water soluble (μg/g)
	Fe	Mn	Cu	Zn	Fe	Mn	Cu	Zn	Na
1	15,00	91,80	0,14	2,52	3,06	6150	3,24	782	22,70
2	28,70	68,60	0,72	7,15	237	6595	5,36	1650	14,60
3	14,25	33,10	0,48	5,12	2,92	3648	3,84	24,30	24,30

During this stage different amendments in varying proportions were used. More than 160 treatments were investigated and different materials, such as iron oxides, soil rich in iron oxides, manganese oxides material, rich in iron and manganese oxides like the by-product of the industry Tosoh-Hellas (as waste of the pyrolusite treatment), organic matter were tested. During this stage different plant species were selected which could potentially be used. The second level experiment refers to the greenhouse experiment, during which 36 treatments were initially used for each of the plant species chosen. The greenhouse experiment lasted two years, during which all necessary measurements of biometric characteristics of plants and the necessary chemical analyses have been done. This third level and most important experiment included pilot applications for the six best treatments (table 3). Each treatment comprised 36 plants with planting space 1x1 m. Each treatment was done in three replications (Voulgaridou, 2015).

The role of Fe and Mn oxides in the soil is significant not only because they are principal nutrient elements for the plants but also because they have the ability to stabilize heavy metals, to absorb anions such as As, Cr, P, cyanides, etc., to form chemical compounds, to oxidize various metals and to reduce the toxicity in the soil. The mechanism of chemical stabilization by Mn and Fe oxides as wastes of the pyrolusite industry Tosoh-Hellas has been described in the literature (Alifragkis *et al.* 2010, 2012a, 2012b, 2012c, 2013). The use of Fe oxides for reclamation of soil in polluted areas is referred, also, in the literature because they have the ability to absorb heavy metals and metalloids effectively (Mench *et al.*, 2004, Hartley *et al.*, 2004, Kumpiene *et al.*, 2006, Lidelow *et al.* 2007). For example, absorption isotherms showed that the use of a low cost material (50$/t), rich in Fe and Mn oxides (8% and 76,9%, respectively) including, also, other oxides (SiO_2, K_2O, Al_2O_3, etc.), removed significant quantities (up to 76%) of As(V) and As(III) from polluted soil.

Biometric characteristics such, survival, plant height, number of lateral shoots, leaf area and leaves weight of the species *Nerium oleander* were measured. In addition the weight of roots and root surface, type of mycorrhiza and degree of root colonization by fungi were measured. More over colonization of each plot by plant species with natural processes in various treatments was studied**.** Samples of all above mentioned plant tissues were used for all necessary chemical analyses.

Table 3 - Treatments and stratification of materials in the pilot experiment.

Treatment/Substrate material	1	2*	3	4**	5	6
Mine wastes (%)	50	50	60	60	100	-
Rich in Fe and Mn oxides materials as wastes of pyrolusite industry (%)	20	20	10	10	-	-
Soil (%)	10	10	10	10	-	100
Rice husk (%)	10	10	10	10	-	-
Skeleton material (%)	10	10	10	10	-	-

*****Mixture was inserted as layer at the bottom, while the tailing material with a thickness of 40cm at the top, ** Inoculation with *Glomus intraradices* fungus.

Stratification: Treatments 1, 3 and 4

Mixture of amendments (50% or 40%) and tailing material (50% or 60%).
**In treatment 4, inoculation with the fungus *Glomus intraradices*

Tailing disposal/mine waste area

*Stratification: Treatment 2

Tailing material, thickness ≈ 40 cm

Mixture of amendments (50 %) and tailing material/mine wastes (50 %)

Tailing disposal/mine waste area

2.1. Chemical analyses

2.1.1. Plant tissues

Nitrogen was measured by the Kjeldahl method. The elements Zn, Cu, Mn, Fe, K., Na., Mg, Ca and As were determined by the method of atomic absorption spectrophotometry after wet oxidation with a mixture of the HNO_3, H_2SO_4 and $HClO_4$ acids. P was measured by using a spectrophotometer.

2.1.2. Mine wastes materials

Nitrogen was determined by the method of Kjeldahl. The water-soluble elements and the extractable cations of Mn, Cu, Zn, Fe by the DTPA (Diethylenetriaminepentaceticacid) method, while the exchangeable cations K, Ca, Mg and Na by the method of atomic absorption spectrophotometry. The chemical composition of tail material was determined by ICP-MS (Inductively coupled plasma-mass spectrometry).

3. Results and discussion

3.1. Greenhouse experiment

Results showed that the treatment affects the biometric and the chemical characteristics of the plants. For example, results showed that treatments affect the length of the root system. The greatest root length was observed in treatments containing skeletal material (gneiss) in proportion of 30%

combined with rice husks, rich in Fe and Mn oxides material (wastes of the pyrolusite industry Tosoh-Hellas), and/or soil and mine wastes material (Fig. 1).

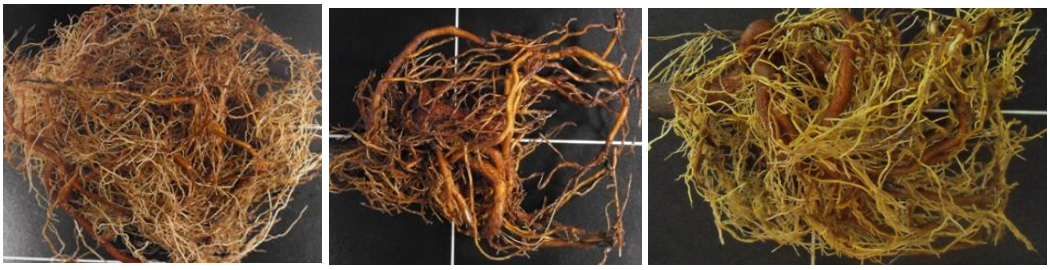

Figure 1 - Growth and development of plant root systems in the greenhouse experiment.

From the analytical data, it appears that all treatments containing by-products rich in Fe and Mn oxides in combination with mycorrhizal fungi cause greater root growth.

Regarding root biomass, the results showed that the biomass of the root system decreased slightly in all treatments. Regarding the frequency of mycorrhiza colonization, the results showed that all treatments with tailing material significantly increased the frequency of colonization by the fungus *Glomus intraradices*. The intensity of mycorrhiza colonization appears to increase in treatments containing rich in Fe and Mn oxide materials (by-product from the Tosoh-Hellas industry as waste of the pyrolusite treatment).

One of the very important result of the greenhouse experiment was that in all treatments containing rich in Fe and Mn oxides material, Zn accumulation in roots, even compared with that of the check treatment, decreases from 3.13 mg/ plant to 1.45 mg/plant, while accumulation of Mn increased from 11.92 to 14.29 mg/plant. The same result like Mn was observed for the accumulation of Cu. Mycorrhiza increased the accumulation of Fe from 38.52 to 100.02 mg/plant.

Between treatments, the best results were found in treatments with stratification of materials, i.e. by placing the rich in Fe and Mn oxides material mixed with the other materials on the bottom of the pots (as background) and the filling with tailings material. Thus, taking into account many of the data of the greenhouse experiment, a combination of treatments applied in the pilot experiment.

3.2. Main results from the pilot experiment.

Survival of *Nerium oleander* plants in the end of second growing season was 100% in Olympias site in contrast to Karakoli site in which the survival was less (table 4).

Table 4 - Mean survival of *Nerium oleander* (%).

Treatment	Olympias	Karakoli
1	100	82
2	100	92
3	100	86
4	100	94
5	100	0
6	100	95

3.2.1. Height

In Olympias site (TMF), the data showed that the mean height of the *Nerium oleander* plants was between 38.95 cm (treatment 3) and 80.36 cm (treatment 2) after the first growing season and between 80.07 (treatment 5) and 140.50 (treatment 2) after the second growing season (Fig. 2).

In Karakoli site data shows that, for the first growing season the mean height of *Nerium oleander* was between 35.92 cm (treatment 4) and 43.40 cm (treatment 6). For the second growth period mean height of plants for was between 50.80 cm (treatment 4) and 96.10 cm (treatment 1) (Fig. 3).

As in the greenhouse experiment, a good growth of plants roots (increase of their weight and length) was observed (Alifragkis *et al.*, 2013, Fig. 4).

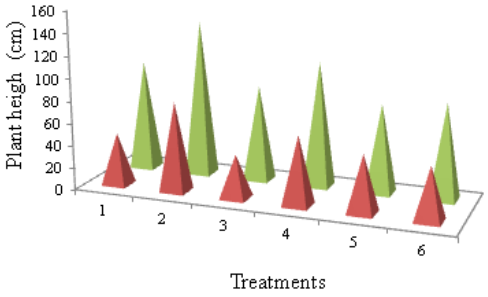

Figure 2 - Growth of Nerium oleander plants at "Olympias" site.

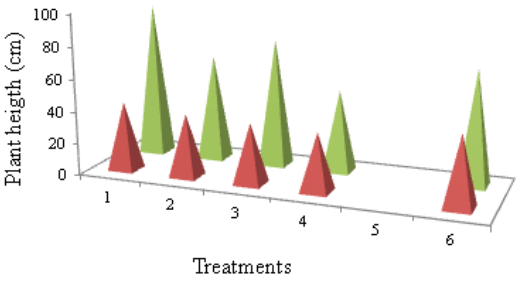

Figure 3 - Growth of Nerium oleander plants at "Karakoli" site.

Figure 4 - Growth and development of plant root systems at Olympias site in the pilot experiment.

3.2.2. Leaf area

Data from Olympias site showed that the mean leaf area of *Nerium oleander* was between 19.61 cm^2 (treatment 3) and 33.16 cm^2/leaf (treatment 2). Statistically significant differences (criterion Bonferroni) were observed between treatments 1 and 2, 1 and 4, 2 with all other treatments, 3 and 4, 4 with all other treatments, 5 and 2, 5 and 4, 6 and 2, and 6. For Karakoli site, the data showed that the mean leaf area of *Nerium oleander* was between 15.94 cm^2/leaf (treatment 2) and 22.09 cm2/leaf (treatment4). Differences in leaf area were relatively small between the two sites (Fig. 5).

The best treatments referred on leaf area for Karakoli site were the treatments 1 and 4, while for Olympias site were the treatments 2 and 4. These treatments contained rich in Fe oxides and Mn material from industrial byproducts, while treatment 4 was moreover inoculated with the fungus *Glomus intraradices* (mycorrhiza symbiosis).

3.2.3. Branching

For Olympias site (TMF), the data showed that the mean number of branches of *Nerium oleander* ranged between 2.75 (treatment 3) and 6.67 (treatment 2). Statistically significant differences, for significance level of 95%, were observed between treatments 1 and 2, 1 and 4, 2 and 3, 2 and 5, 2 and 6, 3 and 4, 4 and 5, and between 4 and 6.

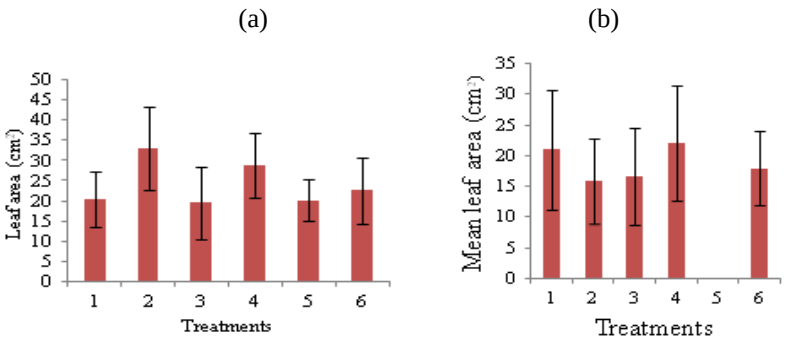

Figure 5 - Leaf area in different treatments (a. Olympias, b. Karakoli).

For Karakoli site, the mean number of branches of the *Nerium oleander* plant ranged between 2.75 (treatment 1) and 4.35 (treatment 4). Statistically significant differences, for significance level of 95%, were observed between treatments 1 and 2, 1 and 4, 1, and 6, 3 and 4, and 6 and 1 (fig. 6).

3.2.4. Leaves weight

The mean weight of *Nerium oleander* leaves to different treatments range between 10.46 and 15.57 g/100 leaves in Olympias site and between 6.1 and 10.13 g/100 leaves in Karakoli site. Statistically significant differences between treatments were not found within each site. Between the two mine waste disposal sites the largest differences in leaves weight were observed in treatments 1,4 and 6 (Fig. 7).

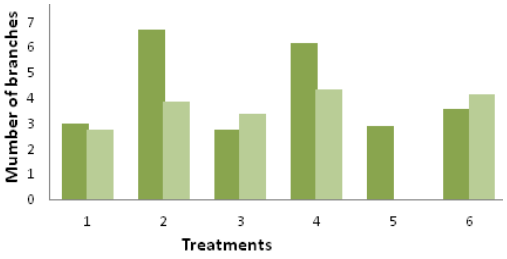

Figure 6 - Number of branches*

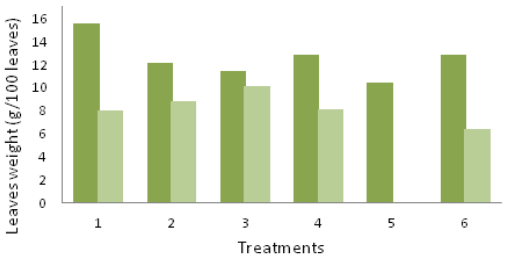

Figure 7 - Leaves weight*

(*1st column: Olympias site, 2nd column: Karakoli site).

3.2.5. Site colonization by plants

One of the key results of the present research was that from the first year of experiment different plant species colonized the area through natural processes (fig. 8). The total number of species that were recorded in Olympias tail was 35, namely *Polygonum aviculare, Tragus racemosus, Digitaria sanguinalis, Vebrasscum cylindrocarpum, Oxalis corniculata, Persicaria sp., Chenopodium album, Centaurea diffusa, Cynodon dactylon, Sorbum halepense, Cichorium intybus, Euphorbia cyparisias, Echinochloa column, Calystegia silvatica, Solanum nigrum, Cyperus longus, Solanum elaeagnifolium, Melilotus sp., Conyza bonariensis, Chenopodium botrys, Ailanthus altissima, Aster trifolium, Rumex pulcher, Cleone omithopodoides, Phytolacca americana, Rumex acetosa, Portulacca oleracea, Sanguisorba minor, Balota nigra, Dactylis glomerata, Piptatherum miliaceum, Rubus ulmifolius, Carduus acicularis, Xanthium spinosum.*

Forty (40) plant species were recorded in Karakoli mine waste deposit area (Fig. 8), namely *Persicaria sp., Cyperous longus, Amaranthus albus, Echinocloa column, Polygonum aviculare, Setaria viridis, Cynodon dactylon, Chenopodium album, Sorghum halepense, Euphorbia maculate, Solanum nigrum, Carthamus lanatus, Anagallis arvensis, Chenopodium sp., Cruciferae, Rosa sempervirens, Rubus ulmifolius, Rumex pulcher ssp.woodsii, Lolium perenne, Xanthium spinosum, Digitaria sanguinalis, Ranunculus muricatus, Arenaria leptoclados, Myosotis ramosissima,*

Portulaca oleracea, Campanula sparsa, Ruscus aculeatus, Chenopodium vulgare, Filago vulgaris, Boraginaceae, Verbascum undulatum , Apera spica-venti, Achillea sp., Sanguisorba minor, Rumex pulcher, Galium aparine, Hypericum perforatum, Pteridium aquilinum, Xanthium strumarium, Verbena officinalis.

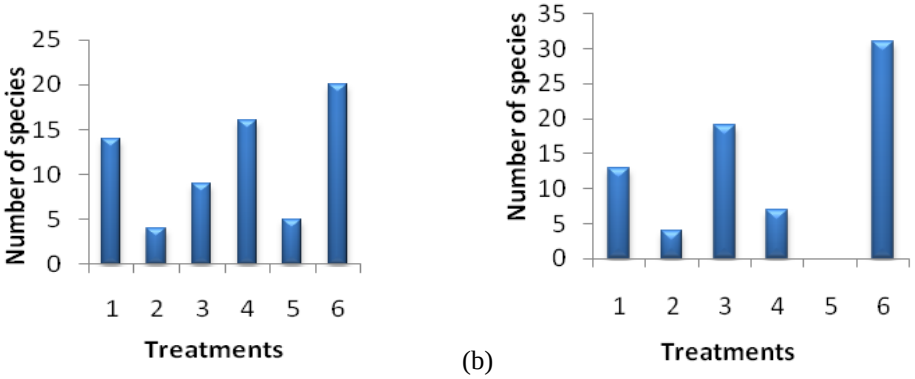

Figure 8 - Number of species colonized the experimental plots (a. Olympias, b. Karakoli).

After surface stabilization of mine wastes sites, they were colonized by different plant species with natural processes. The literature states that the greater the number of plant species installed in an area, the greater stability of plant communities occurred (Tilman *et al*., 1996, 1997; Hector *et al*., 2000). It is worthy to mention that no any plant species was installed with natural processes in Cassandra mine waste disposal sites during the last 35 years.

The type of treatment affected the number of species which may be used for phytoremediation effectively. Some of the plant species colonized the experimental sites behave as metal bioaccumulators. A typical case is *Vebrascum undulanum* in Olympias site, where Mn concentration in its tissues was 13,854 μg/g without showing any symptom of toxicity.

One of the criterions that characterized various plants as bioaccumulators is the bioaccumulation factor (Sarma, 2011). Analytical data indicated that in most cases, and in two experimental sites ("Olympias" and "Karakoli "), the bioaccumulation factor of heavy metal in most plants species was >1, a minimum value to characterize a plant species as metal bioaccumulator. In "Olympias" site, the Bioconcentration factor (BCF) of Cu ranged between 0.13 and 25.51 and for "Karakoli" site between 0.88 and 60.48 for different species and different treatments. For Zn, these values ranged between 2.50 and 29.07 ("Olympias" site) and between 1.13 and 52.30 ("Karakoli" site), and for Mn between 36.56 and 9,043.51 ("Olympias" site) and between 1.02 and 9,413.36 ("Karakoli" site). Between the two sites BCF was higher in Karakoli.

It should be noted that with the time and under continuous improvement of conditions, the composition of natural vegetation varies. It is also significant that, two years after the chemical stabilization and phytoremediation, mosses appeared to grow in some treatments (Fig. 9).

3.2.6. Plant evaluation as metal bioaccumulators

Plant evaluation as metal bioaccumulators based on the use of various indicators such as Bioconcentration factor. Bioconcentration factor (BCF) defined as the ratio between metal concentration in above ground biomass and metal concentration in soil. Greater bioaccumulation factor means that this species can be considered suitable to be used in phytoremediation programs (Ma *et al*., 2001).

Figure 9 - Appearance of mosses in some treatments two years after the chemical stabilization and phytoremediation showing the improvement of growth conditions of tailing materials at Karakoli site.

BCF varies with the plant species, metal, treatment and the type of mine wastes. For Cu this factor ranged between 0.13 and 25.51 for Olympias site and between 0.88 and 60.48 for "Karakoli" site. For Zn, BCF ranged between 2.50 and 29.07 and between 1.13 and 52.30 respectively. For Mn BCF ranged between 36.56 and 9,043 and between 1.02 and 9,413, respectively. Between two types of metal wastes Karakoli have maximum values of BCF. Between plant species BCF varied widely. For example BCF for Cu was low in *Ailanthus altissima* (0.51) and high in *Solanum nigrum* (24.55) for Olympias waste deposits. Bioconcentration factor for Zn was always > 1 in all treatments. For Olympias site, the BCF of Zn was higher (18.58) in *Cichorium intybus* and for "Karakoli" deposit area, the BCF was 52.30 in the species of *Echinocloa column*. BCF for Mn was highest for the species of *Rumex pulcher* (9,043) in “Olympias” site and in “Karakoli” for the species of *Solanum nigrum* (9,413). This means that many species of them colonized the mine wastes can be used for phytoremediation programs in contaminated areas by heavy metals.

3.2.7. Problems occurred during the pilot experiments in Karakoli disposal area

Two main problems emerged during the first year of the pilot experiment. One of them was increased concentration of various soluble salts (mainly sulphate) on the surface of the mine wastes (Fig. 10) and the other one was the formation hardpan and cemented horizons during the summer time, that did not allow root growth. Both are related to the texture and the mineralogical composition of the wastes.

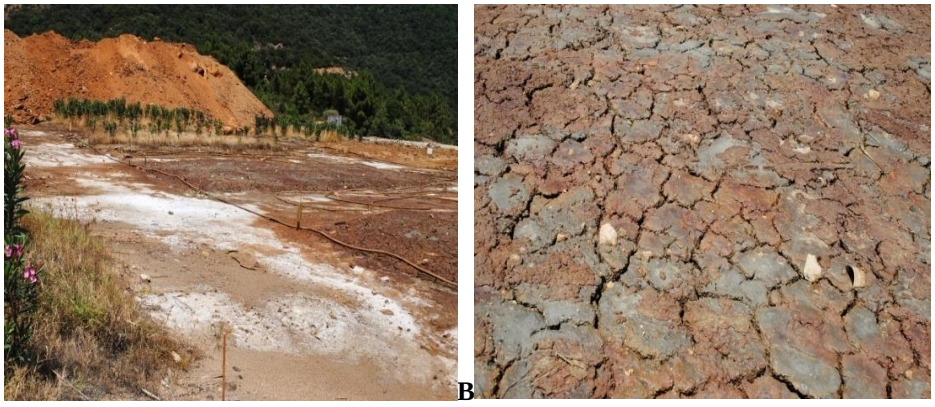

Figure 10 - A: Soluble salts concentrated on the surface of the mine wastes due to upward capillary movement of salt solution and evaporation, B: Cracks due to concentration of Na ions in the soil surface and water evaporation during the summer time.

These two problems were treated by adding limestone skeletal material in proportion of 10-15% v/v up to a depth of 40 cm, as shown in Figure 11, illustrating the additional experiments. Note that after the additional treatments, plant survival was 94% and the experimental plots were colonized by different plant species.

Figure 11 - Improvement of soil conditions by mixing limestone skeletal material with mine wastes for plants to grow in Karakoli site.

4. Conclusions

Phytoremediation of mine wastes in both sites is possible after chemical stabilization of wastes.

For chemical stabilization of mine wastes, by-products from of a pyrolusite industry, rich in iron and manganese oxides could be used with very good results. The use of these wastes as amendments had very good results improving the growth of plants.

The skeletal material such limestone gravel improved the growing conditions while rise husk improved the biological activity of mine wastes.

Mycorrhizal fungi improved growth of *Nerium oleander* under toxic conditions. The appearance of mosses in some treatments, two years after the chemical stabilization and phytoremediation, indicates the improvement of mine wastes conditions.

Reclamation of contaminated areas using phytoremediation processes includes several steps and materials such as study of mine wastes characteristics, use of amendments, increase of plant tolerance to high metal concentrations, etc., but it needs continuous monitoring of plants during the first period.

The type of treatment affects the biometric characteristics of the *Nerium oleander*, colonization of mine waste by plants and metal bioaccumulation factor.

Hardpan and cemented horizons can be avoided by adding skeletal material (rock fragments) that

Nerium oleander stabilizes metals and metalloids in root system and reduces phytotoxicity, while Fe and Mn oxides create complex substances, thus, limiting the adsorption and affecting the phytotoxicity. Analytical data of this research indicate that all treatments containing material rich in Fe oxides and Mn or Fe^0 affect heavy metals and metalloids concentration of root, stem and leaves *of Nerium oleander* while plants show richer root system.

5. Acknowledgements

The authors thank Hellas-Gold Company and the staff of Health-Safety and Environment Department for their support in performing this research.

6. References

Alifragkis, D., Gazea, E., Pavlidou, A., Papaioannou, A., Barbagiannis, N., Apostolidis, S. and Strouthopoulos, G., 2010. Reducing bioavailability of arsenic in ore enrichment materials with electrolytic pyrolusite process by-products, *Proceedings of 13th Congress of Hellenic Soil Science Society*, Thessaloniki 2012 Larissa, (in Greek), 161-175.

Alifragkis, D., Voulgaridou, E., Orfanoudakis, M., Daftzis, E., Charaklias, I., Papaioannou, A., Vavelidis, M., Alifragkis, E., Voulgaropoulou, M. and Galatsianou, A., 2012a. Phytoremediation of residual deposits of Kassandra mines after chemical stabilization by using materials rich in Fe and Mn oxides, *Proceedings of 14th Congress of Hellenic Soil Science Society*, Thessaloniki (In Greek).

Alifragkis, D., Voulgaridou, E., Pavlidou, A., Papaioannou, A. and Orfanoudakis, M., 2012b. The use of pyrolusite electrolytic process by-product for reclamation of limestone quarries, *Proceedings of 14th Congress of Hellenic Soil Science Society*, Thessaloniki (In Greek).

Alifragkis, D., Voulgaridou, E., Daftsis, E. and Characlias, I., 2012c. Reclamation of old tailing disposal area of Olympias, Halkidiki Mine, 3rd International Conference on Industrial and Hazardous Waste Management, Chania, Crete, Greece, 12-14 Sept. 2012.

Alifragkis, D., Vavelidis, M., Orfanoudakis, M., Galatsianou, A., Voulgaridou, E., Voulgaropoulou, M. and Alifragki, M., 2013. Installation of natural vegetation on old tailing disposal area at Olympias Halkidiki mine, after chemical stabilization and phytoremediation, 6th International Conference on Sustainable Development in the Minerals Industry, 30 June - 3 July 2013, Milos island, Greece, 435-445.

Chakravarty, S., Dureja, V., Bhattacharyya, G., Maity, S. and Bhattacharjee, S., 2002. Removal of arsenic from groundwater using low cost ferruginous manganese ore, *Water Research*., 36, 625-632.

Craynon, J.R., Sarver, E.A. and Karmis, M.E., 2013. The role of science in public ecology and sustainable development in mining, 6th International Conference on Sustainable Development in the Minerals Industry, 30 June - 3 July 2013, Milos island, Greece, 77-82.

European Commission (EC), 2006. European Pollutant Release and Transfer Register, Κανονισμός (EC Regulation 166/2006/EK).

Hartley, W., Edwards, R. and Lepp, N.W., 2004. Arsenic and heavy metal mobility in iron oxide-amended contaminated soils as evaluated by short-and long term leaching tests, *Environ. Pollution*., 131, 495-504.

Hector, A., Dobson, K., Minns, A., Bazeley-White, E. and Lawton, J. H., 2001. Community diversity and invasion resistance: An experimental test in a grassland ecosystem and a review of comparable studies, *Ecol. Res*., 16, 819-831.

Kolovos, C.J., 2013. Corporate social responsibility and the future of mining in Greece, 6th International Conference on Sustainable Development in the Minerals Industry, 30 June–3 July 2013, Milos island, Greece, 160-166.

Kumpiene, J., Ore, S., Renella, G., Menech, M., Lagerkvist, A. and Maurice, C., 2006. Assessment of zerovalent iron for stabilization of chromium, copper, and arsenic in soil, *Environ. Pollut*., 144, 62-69.

Kumpiene, J., Lagerkvist, A. and Maurice, C.M., 2008. Stabilization of As, Cr, Cu, Pb, and Zn on soil using amendments- A review, *Waste Management*, 28, 215-225.

Ladeira, A.C. and Cimineli, V.S.T., 2004. Adsorption and desorption of arsenic on an oxisols and its constituents, *Water Res*., 36, 2087-2094.

Lidelow, S., Ragnvaldsson, D., Leffler, P., Tesfalidet, S. and Maurice, C., 2007. Field trials to assess the use of iron-bearing industrial by-products for stabilisation of chromated copper arsenate-contaminated soil, *Science of the Total Environment*, 387, 68-78.

Lottermoser, B.G., 2010. Mine Wastes Characterization, Treatment, Environmental Impacts (3nd edition), Springer-Verlag, Berlin/London/NY.

Ma, L.Q., Komar, K.M., Tu, C., Zhang, W., Cai, Y. and Kenelly, E.D., 2001. A fern that hyper accumulates arsenic, *Nature*, 409, 579-582.

Marschner, H., 1995. Mineral nutrition of higher plants (2nd edition), Academic press, London/NY.

Mench, M., Bussiere, S., Boisson, J., Castaing, E., Vangronsveld, J. and Ruttens, A., 2002. Progress in remediation and revegetation of the barren Jales gold mine spoil after in situ treatments, *Plant Soil*, 249, 187-202.

Rumenjak, D., Rajković, D. and Štambuk, S., 2013. Some principles of expert systems for environment and mining, 6th International Conference on Sustainable Development in the Minerals Industry, 30 June - 3 July 2013, Milos island, Greece, 44-47.

Sarma, H., 2011. Metal hyperaccumulation in plants: a review focusing on phytoremediation technology, *J. Environ. Sci. Technol*., 4(2), 118-138.

Shtiza, A., Doome, R. and Wyart, M., 2013. Reducing the environmental footprint in the industrial mineral sector: Case studies and industry innovation initiatives, 6th International Conference on Sustainable Development in the Minerals Industry, 30 June-3 July 2013, Milos island, Greece, 527-531

Tilman, D., Wedin, D. and Knops, J., 1996. Productivity and sustainability influenced by biodiversity in grass-land ecosystems, *Nature*, 379, 718-720.

Tilman, D., Knops, J., Wedin, D., Reich, P., Ritchie, M. and Siemann, E., 1997. The influence of functional diversity and composition on ecosystem processes, *Science*, 277, 1300-1302.

Van Zyl, D., Chanda, M. and Brune, J., 2013. WFEO Task Force: Environmentally sound engineering technologies and practices in mining, 6th International Conference on Sustainable Development in the Minerals Industry, 30 June-3 July 2013, Milos island, Greece, 380-385.

Voulgaridou, E., 2015. Reclamation of soil in polluted areas, PhD Thesis, School of Forestry and Natural Environment, Aristotle University of Thessaloniki, Greece (In Greek), 266 pp.

Δελτίο της Ελληνικής Γεωλογικής Εταιρίας, τόμος L, σελ. 2296-2303
Πρακτικά 14ου Διεθνούς Συνεδρίου, Θεσσαλονίκη, Μάιος 2016

Bulletin of the Geological Society of Greece, vol. L, p. 2296-2303
Proceedings of the 14th International Congress, Thessaloniki, May 2016

ENVIRONMENTAL CONTAMINATION BY SUBSTRATA OF ORE MINING DUMPS, THEIR MONITORING AS WELL AS MEASURES OF REDUCTION

Blumenstein O.[1], Pustlauck F.[1] and Vavelidis M.[2]

[1]*University of Potsdam, Institute of Earth and Environmental Science, Research Group "Applied Geoecology", 14476, Potsdam, Germany, oblustei@uni-potsdam.de, pustlauc@uni-potsdam.de*

[2]*Aristotle University of Thessaloniki, Head of the School of Geology, 54006, Thessaloniki, Greece, vavelidi@geo.auth.gr*

Abstract

The main activity fields of the research group "Applied Geoecology" at the University of Potsdam are the development and tests of complex monitoring systems for water bodies and soils, together with the development of sustainable additives for vegetation restoration on ore mining dumps with extreme substratum parameters.
The dump substrata are translocated by surface waters and by aeolian processes to the surroundings affecting soil processes. A field spectrometer has been engineered, which can detect dam substrata in soils. Moreover, various soil additives were developed, enabling the establishment of vegetation on the extreme dump substrata. For all components there have been realised extensive tests in the framework of greenhouse and field experiments under different climate conditions on three continents, on various substrata and with varying plant species. All experiments were successful, even though no additional irrigation and no mineral fertilizer were allowed to be used, in order to realise the idea of a sustainable greening.
Keywords: *Detection of allochthonous soil matter, soil improvement, re-greening, components of different soil additives.*

1. Introduction

The main activity fields of the research group "Applied Geoecology", at the University of Potsdam are the development and tests of complex monitoring systems for water bodies, forestry and contaminated areas. Hereby, there is a close collaboration with international partners in Greece, Austria, China and South Africa.

For example, important hydrochemical data can be captured with the HYDROHERB-System for qanats and other water systems as well as with the complex monitoring system for gaseous and ionic water parameters.

Both systems have been developed for the industry market. With the help of them, it is possible to read out the data in situ, as well as transmit them to any computer in the world. All these systems can be programmed to capture the parameters automatically in a defined measurement interval (minutes to days). The data series can be efficiently processed further with Excel software.

Figure 1 - Complex monitoring system for gaseous and ionic water parameters in action.

The computer-based data logging system for forestry owns an integrated soil chemical tool. With its assistance, the vegetations' growth characteristics can be detected. With this integrated soil chemical tool the most important soil parameters, such as pH-value, soil moisture, conductivity and nitrate concentration can be captured quickly in situ. The tool can also be used separately. The data, in turn, can be transferred to any other computer.

However, one of the most important outcomes of the performed work is the development of sustainable additives for vegetation restoration on ore mining dumps with extreme substratum parameters. Why is it important?

These sites are characterised by

- extreme pH-value,
- insufficient buffer capacity,
- deficiency of nutrients,
- too less bonded nutrients,
- absence of soil organic matter (SOM),
- extreme substratum density,
- extreme soil water conditions and instability of structures.

The ecological consequences shall be proven using the example of Rustenburg region (South Africa, North West Province), where the mining of PGMs and Chromium is dominating. The exploitation follows mostly in a depth of 1500 to 2000 m and is associated with a severe pollution of the environment. A major problem occurs with the disposal of the extracted ores that were grinded up and later washed in suspension on so called "tailings dams". Only in the Rustenburg area, there exist 14 landfills, which extents hit several square kilometres. On the tailings dams of platinum ore mining, the excavated materials' grain size is to be assigned to the silt fraction. Here, the pH-value is in the alkaline range. Since there have only been extracted the PGMs, a considerable amount of heavy metals are still bound. Their contents exceed the internationally common boundary values many times over. Especially the chromium contents are extremely high (see fig. 2).

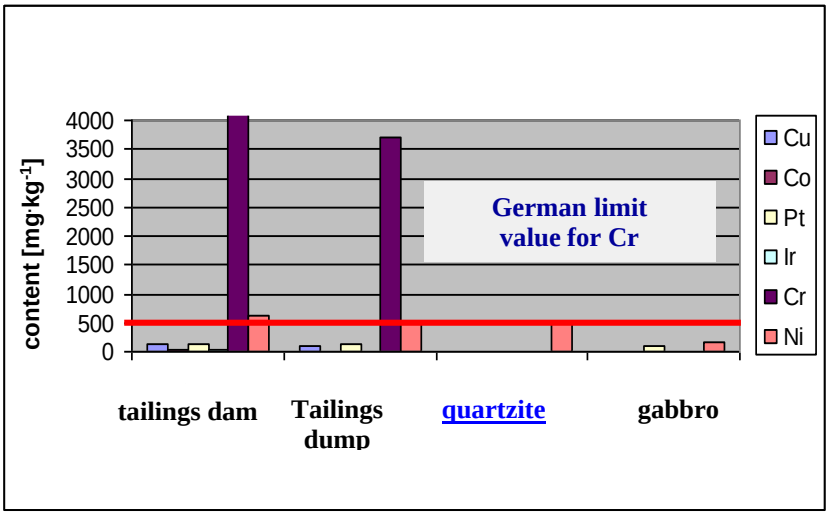

Figure 2 - Heavy metal contents of tailings substrata in comparison to regional genuine rocks.

2. Results

The fine substrate is shifted to the dams surroundings during rainy season by surface water and during dry season by aeolian processes. Those areas include settlements, water bodies and fields. In the farm soils there could be found substantial contents of platinum tailings substrate that is formed either diffusely or also as a layer (see fig. 3).

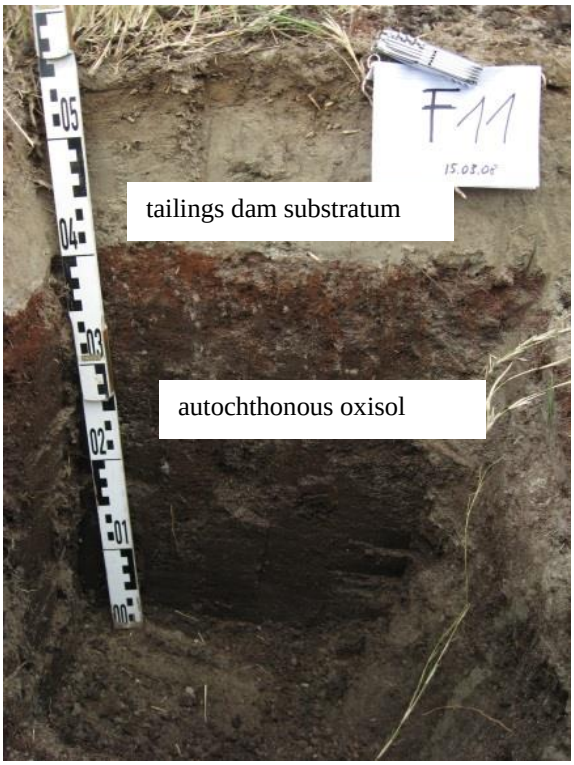

Figure 3 - Oxisol, overlaid by tailings dams subtrate (photo: S. Münzel).

Those allochthonous substrates massively affect the soil developments. Their impacts had been a first investigational focus.

A second field of research resulted from the necessity of being able to detect those inputs of ore mining dumps substrata in the surrounding soils. After their deposition, they can no longer be distinguished by the naked eye from the substrata of vertisols and oxisols (see fig. 4).

Figure 4 - Non contaminated vertisol (left), with platinum tailing dam substratum contaminated vertisol (right).

Therefore, a field spectrometer has been developed, which can detect substrata of gold tailings and platinum tailings in soils. At the test measurements in the Chalkidiki region, that served to the setup of the database, also partners from the Aristotle University Thessaloniki were involved. The user of this spectrometer (see fig. 5) can detect those substrata as well as organic compounds like mineral oils or paraffines in the soil.

Figure 5 - Test measurements with the field spectrometer near Stratoni (Chalkidiki).

A further working direction was geared to reduce the intensity of tailings dump substrata shifting processes. Therefore sustainable soil additives have been developed, which can be mixed with the extreme dump substrata and thus enable the establishment of vegetation.

According to the diverse demands of soil and climate, five components (C1 - C5) aiming different effects have been developed. These effects are described briefly in figure 6.

Moreover, a technique was developed, which consolidates the dump substrate by means of two solution components, so that its erosive shifting is substantially decreased.

For all components there have been realised extensive tests in the framework of greenhouse and field experiments under different climate conditions on three continents, on various substrata and with varying plant species. Certain examples are shown in figure 7. In any case the premise was that

no additional irrigation and no mineral fertilizer were allowed to be used, in order to realise the idea of a sustainable greening.

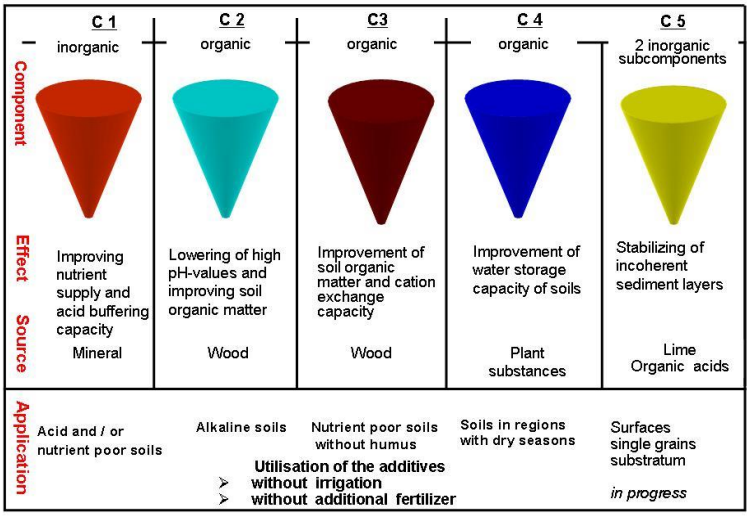

Figure 6 - Developed components (C1 - C5) of sustainable soil additives.

The aim was to evaluate biometric data like dry mass, growth rates and vitality (see for example fig. 8).

It became apparent, that one single component did not lead to an increase of biomass and an improvement of vitality in every case. The decisive factor was, that mixtures had to be com-pounded, which could then be optimised for individual substrate and climatic conditions.

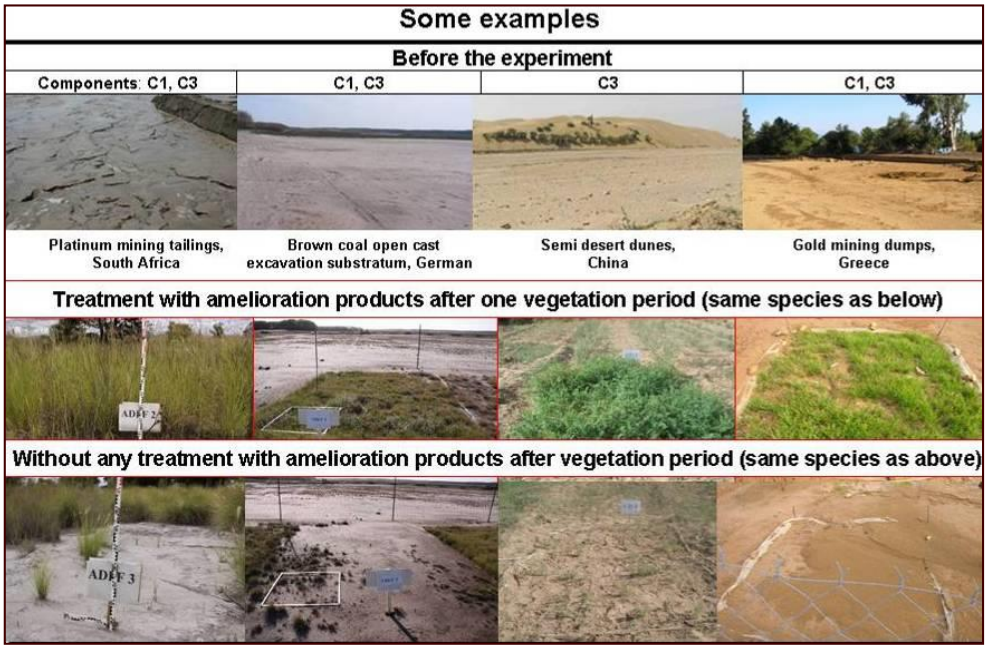

Figure 7 - Location of certain test sites and growth performances on various substrata.

Dump substrata mostly show a small water storage capacity. This is why component C4 is important for a sustainable vegetation development, especially in areas with long dry periods. Even with a mixing in of about 1%, an improvement of the water storage capacity in the soil occurs. The plants' drought stress can be decreased.

Results of the water retaining effect of component C4 are shown in figures 9 and 10. When mixed in to low-nutrient sand, all plants were no longer irrigated after growing off. In combination with components C1 and C3 it became evident, that the plants that grew on substrata mixed with component C4, had produced way more dry mass (see fig. 9). Some individuals of *Secale cereale* have survived after four weeks without water addition. This shows, that a survival during a longer dry period is possible (fig. 10).

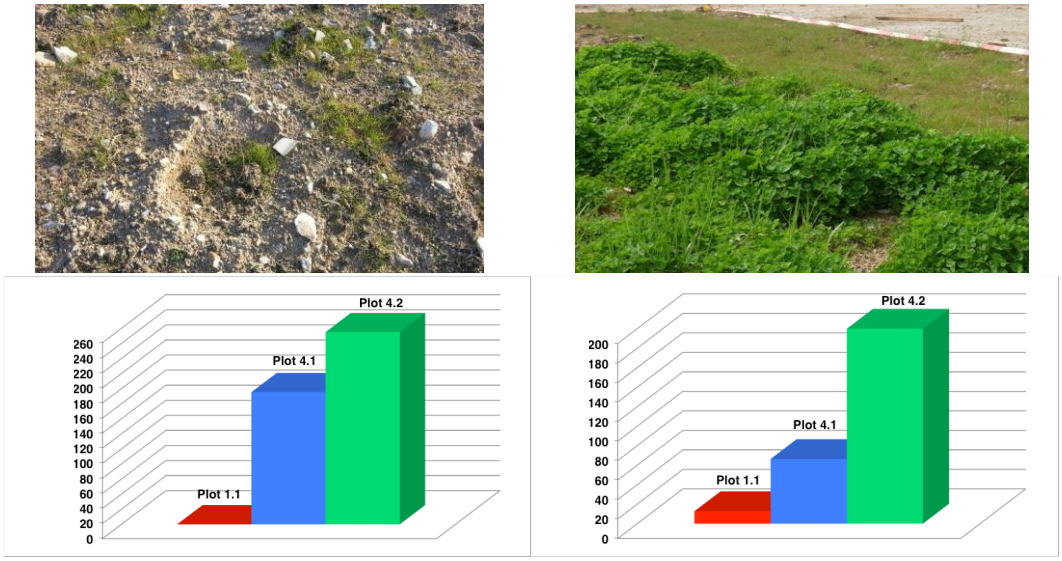

Figure 8 - Vegetation cover after one year development at the gold mining dump in Stratoni (Greece).

-above: without (plot 1.1, left) and with (plot 4.2, right) soil additives, but same species

-below: subterranean (left) and over ground (right) dry matter of grass, plot 4.1 contents additives in lower percentage.

- above: without component C4

- below: with 1% component C4

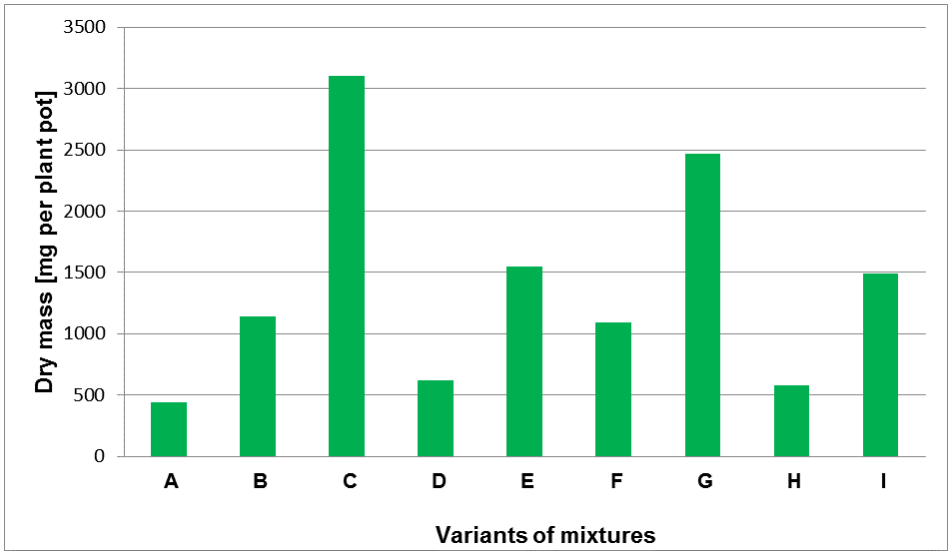

Figure 9 - Glasshouse experiment, average temperature 24°C: Overground dry mass of *Secale cereale* in plant pots with different contents of component C4 (trial C and G 1% content, trial A, D and H without C4) and components C1 and C3.

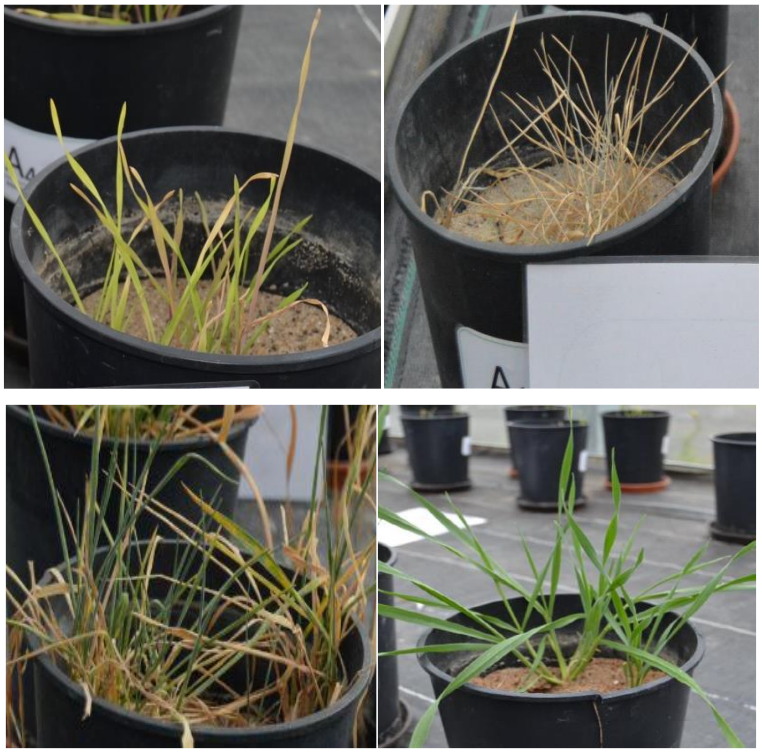

Figure 10 - Glasshouse experiment, average temperature 24°C: *Secale cereale* in plant pots by using different contents of component C4 after 14 days (left) and 28 days (right) without irrigation.

3. Summing up Discussion

Substrata of ore mining dumps are often shifted to the dump surroundings by aeolian and fluvial processes. These foreign substrata massively influence the soil development, contaminants can attain to the food web.

Therefore a field spectrometer was developed, which can detect gold tailings and platinum tailings substrata in the soil.

The intensity of shifting processes can be decreased, if a vegetation is established on the dumps. For this reason, five components of sustainable soil additives, that can be mixed with the extreme dump substrata, have been developed.

For all components there have been realised extensive tests in the framework of greenhouse and field experiments under different climate conditions on three continents, on various substrata and with varying plant species. Since dump substrata mostly show a small water storage capacity, in regions with long dry periods, a water storing component is important for vegetation development. It could be shown that even with a mixing in of about 1%, an improvement of water storage occurs in the soil. The drought stress of the plants can consequently be decreased.

4. Acknowledgments

An expression of thanks for scientific, technical or financial support is due to:

- Aristotle University of Thessaloniki (Greece), Laboratory of Forest Soil Science, Prof. Dimitris Alifragis
- Hellas Gold S.A., Stratoni (Greece), Ing. G. Bethlehem
- TOSOH Hellas A.I.C., Thessaloniki (Greece)
- Aquarius Platinum Lt. (South Africa), Ing. O. Faude
- North West University, Potchefstroom Campus, (South Africa), Unit Environmental Science and Management, Prof. L van Rensburg, P. van Deventer
- Beijing Forest University (China), College of Soil and Water Conservation, Prof. J. Guo
- Wurmitzer GmbH, Himmelberg (Austria)
- Universität Salzburg (Austria), Department of Geography and Geology, Ing. M. Marbach, Prof. H. Weingartner
- AIF Projekt GmbH, Berlin (Germany)
- UP Transfer GmbH, Potsdam (Germany)
- MLW intermed GmbH, Schöneiche (Germany)
- IPP Hydroconsult GmbH, Cottbus (Germany)

5. References

Since the research and development works are realised in the framework of industry projects, references only exist in the form of unpublished reports.

Δελτίο της Ελληνικής Γεωλογικής Εταιρίας, τόμος L, σελ. 2304-2313
Πρακτικά 14ου Διεθνούς Συνεδρίου, Θεσσαλονίκη, Μάιος 2016

Bulletin of the Geological Society of Greece, vol. L, p. 2304-2313
Proceedings of the 14th International Congress, Thessaloniki, May 2016

SAFETY ISSUES WHEN MONITORING CO_2 STORAGE IN THE PRINOS AREA, GREECE

Koukouzas N.[1], Lymperopoulos P.[1] and Tasianas A.[1]

[1]Centre for Research and Technology Hellas, Chemical Process and Energy Resources Institute, 15125, Maroussi, Greece, koukouzas@certh.gr, lymperopoulos@certh.gr, tasianas@certh.gr

Abstract

Geological storage of CO_2 in geological structures in the subsurface can mitigate global warming. A safe storage of CO_2 can be ensured through the development of comprehensive monitoring programs that prevent any possible leakage of CO_2. This paper presents various monitoring strategies of CO_2 subsurface movement in the Prinos reservoir, northern Greece, the results of a simulation of a CO_2 leak through a well, and an environmental risk assessment study related to the leakage of CO_2 or oil from the seafloor. After only 13.7 years, from the beginning of injection, the CO_2 leak reaches the seabed in the form of gas. For the assessment we set up a model, using ArcGIS software, based on the use of data regarding the speeds of the winds and currents encountered in the region. Assumptions were also made related to the flow rate of CO_2. Modeling results show that it only takes a period of 10 days from the start of oil leakage until the "Natura" protected areas start to be affected. CO_2 leakage modelling results show CO_2 to be initially flowing along a preferential flow direction, which is towards NE. However, 5 days after the start of leakage of CO_2, it is also flowing towards ENE. The consequences of a potential CO_2 leak are considered spatially limited and the ecosystem is capable of recovering by itself.
Keywords: *leakage, risk level, environmental impact.*

Περίληψη

Η γεωλογική αποθήκευση του CO_2 σε γεωλογικές δομές κάτω από την επιφάνεια της γης μπορεί να μετριάσει την υπερθέρμανση του πλανήτη. Μια ασφαλής αποθήκευση του CO_2 μπορεί να εξασφαλιστεί μέσω της ανάπτυξης ολοκληρωμένων προγραμμάτων παρακολούθησης που αποτρέπουν οποιαδήποτε πιθανή διαρροή CO_2. Η εργασία αυτή παρουσιάζει διάφορες στρατηγικές παρακολούθησης της υπόγειας μετακίνησης του CO_2 στον ταμιευτήρα του Πρίνου, στη Βόρεια Ελλάδα, τα αποτελέσματα προσομοίωσης μιας διαρροής CO_2 μέσω μιας γεώτρησης, και μια εκτίμηση των περιβαλλοντικών κινδύνων που σχετίζονται με πιθανή υποθαλάσσια διαρροή CO_2 ή πετρελαίου. Μετά από μόλις 13.7 χρόνια, από την αρχή της έγχυσης, η διαρροή του CO_2 φθάνει στον πυθμένα με τη μορφή αερίου. Για την περιβαλλοντική αξιολόγηση έχουμε δημιουργήσει ένα μοντέλο, με τη χρήση του λογισμικού ArcGIS, που βασίζεται στη χρήση των δεδομένων σχετικά με τις ταχύτητες των ανέμων και των ρευμάτων που συναντώνται στην περιοχή. Επίσης, έγιναν εκτιμήσεις σχετικά με τον ρυθμό ροής του CO_2. Τα αποτελέσματα της προσομοίωσης δείχνουν ότι αρκεί ένα διάστημα 10 ημερών από την έναρξη της διαρροής πετρελαίου μέχρι να αρχίσουν να επηρεάζονται οι προστατευόμενες περιοχές "Natura". Τα αποτελέσματα της προσομοίωσης δείχνουν το CO_2 που έχει διαρρεύσει να ρέει αρχικά κατά μήκος της επικρατούσας κατεύθυνσης ροής, η οποία είναι προς τα ΒΑ. Εντούτοις, 5 ημέρες μετά την έναρξη της διαρροής του CO_2, αυτό ρέει επίσης και

προς τα ΑΒΑ. Οι συνέπειες μιας ενδεχόμενης διαρροής CO_2 θεωρούνται χωρικά περιορισμένες και το οικοσύστημα είναι ικανό από μόνο του να επανέλθει στην πρωταρχική του κατάσταση.
Λέξεις κλειδιά: *διαρροή, επίπεδο κινδύνου, περιβαλλοντικές επιπτώσεις.*

1. Introduction

Geological storage of CO_2 is a valuable means of reducing greenhouse gases in the atmosphere and restricting the planet's global warming. The main aim of Carbon Capture and Storage (CCS) activities is to store CO_2 in geological structures, both onshore and offshore, which would be geologically secure without any CO_2 leaks from the reservoir to the overlying formations and at a later stage to the sea or atmosphere (Bachu *et al.*, 2003; Bentham *et al.*, 2005). The idea of underground CO_2 storage in an oil reservoir, such as that of Prinos, in northern Greece, is reinforced by the reality that the geological morphology of the area is known. Geotechnical studies have also already been carried out in the area, in order to find and exploit oil in the past, therefore facilitating further development of the area. After taking a look at the various stages involved in a safety and monitoring program for the Prinos area, we will focus on a hypothetical leak of oil and CO_2 from the Prinos reservoir and the potential consequences that it may have on the surrounding ecosystems.

To ensure the safety of CO_2 storage and to be able to control the monitoring techniques, there is a need to develop comprehensive monitoring programs (Chadwick *et al.*, 2014). The monitoring program proposed in this study should be designed in such a way that it can be applied during injection of CO_2 into the Prinos reservoir. This method will allow controlling the safety of CO_2 storage both during and after the injection phase. The proposed monitoring program would help prevent leakage of CO_2 that can occur at various stages of the project but we will also consider the possibility of CO_2 leakage and its effects on local ecosystems.

2. Geological setting

The study area concerns the Prinos - Kavala sedimentary basin which is located in the Northern Aegean Sea between the city of Kavala and the island of Thassos. The location of the basin and its hydrocarbon reserves is shown in Figure 1. The Prinos basin formed at the southern end of theRhodope Massif, between Thassos Island and the mainland. It has a length of 38 km and a width of 20 km (Pasadakis *et al.*, 2005; Kiomourtzi *et al.*, 2008). The main axis has a NE-SW direction covering an area of about 800 km^2. The maximum thickness of the sediments is about 5 km.

The Prinos-Kavala basin is characterized as a sub-basin and is evolved at a fast speed on an annual basis (Pasadakis *et al.*, 2005). It developed separately from the other areas of the North Aegean Sea; thus, it began to form in the lower Miocene and started to receive sediments from Middle to Upper Miocene and thereafter (Proedrou, 1986).

3. Material and Methods

3.1 Prinos CO_2 monitoring program

To prevent any potential CO_2 leakage and any possible negative effects on the environment, monitoring the reservoir in Prinos becomes a key component in the design of the security system. The monitoring program will cover the entire lifecycle of the project of geological storage of CO_2, and thus the total duration of the project. One of the main reasons for implementing a CO_2 monitoring program is for the protection of the environment and natural resources from leaks of CO_2. By monitoring, we can minimize or even prevent any impact on people, wildlife and ecosystems found in the area surrounding the Prinos field.

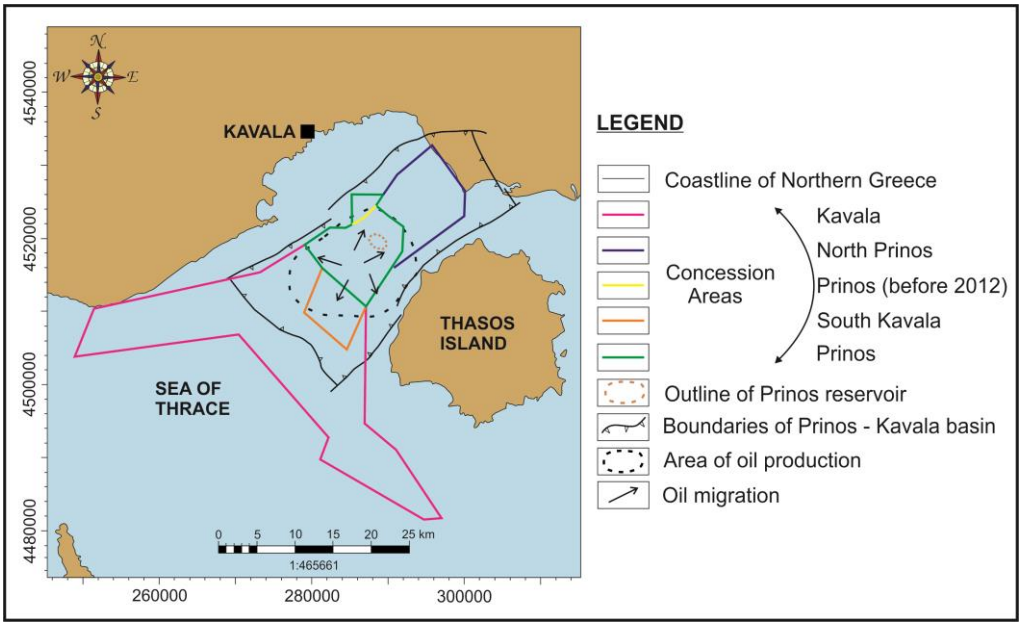

Figure 1 - Geologic sketch map of the Prinos - Kavala sedimentary basin in the Northern Aegean Sea, with the location of oil and gas resources.

3.2 Strategies for monitoring the subsurface

To detect any possible leakage of CO_2 in shallow waters close to the surface, background data related to the level of CO_2 in the atmosphere and in the shallow waters should be characterized prior to injection of CO_2. "Background" CO_2 values in the atmosphere vary between 350 ppm and 380 ppm. The CO_2 background concentration in shallow water does not exceed 320 ppm under a pH of 6-8. Recorded measurements that exceed the above values of "background" CO_2 could be interpreted as resulting from a CO_2 release. If the monitoring in the reservoir and the adjacent cap rock lithology shows an unexpected migration through the cap rock, then the monitoring of the overlying sediments will be necessary and the injection of CO_2 should be halted. The strategy that we propose to follow for baseline studies and monitoring of the seabed above the Prinos CO_2 storage area, in the wider basin of Kavala, includes the analysis of hydroacoustic data to see if bubbles of CO_2 are leaking from the seafloor during the course of the CO_2 injection in the reservoirs.

Another strategy corresponds to the use of seismic data to obtain information about the structures that exist beneath the seabed. This will allow to check the retention capacity of the cap rock at Prinos, the existence of channels, natural openings or other possible escape pathways for CO_2 or to even detect tectonic discontinuities. Monitoring of the sedimentary deposits overlying the reservoir in order to detect any leaks from the CO_2 storage reservoir, is best done by acquiring 3D seismic data over time (e.g. every year if possible or every few years) and then comparing them for discrepancies. Seismic data acquisition, using high resolution P-Cable seismic, (Figure 2), can also be used in order to focus on understanding the shallow subsurface and any leakage phenomena that may take place there.

The substitution of brine by CO_2 causes changes in the reflectance of the subsurface, which can be visualized in 3D seismic data. Analyzing the differences in signal between 3D seismic data that will be acquired over the years, the best opportunity to determine if there is a leak or not is provided. Moreover, the spatial and volumetric coverage provided by the seismic data (time-lapse), enables us to have a high detection capability (high resolution seismic, Figure 2).

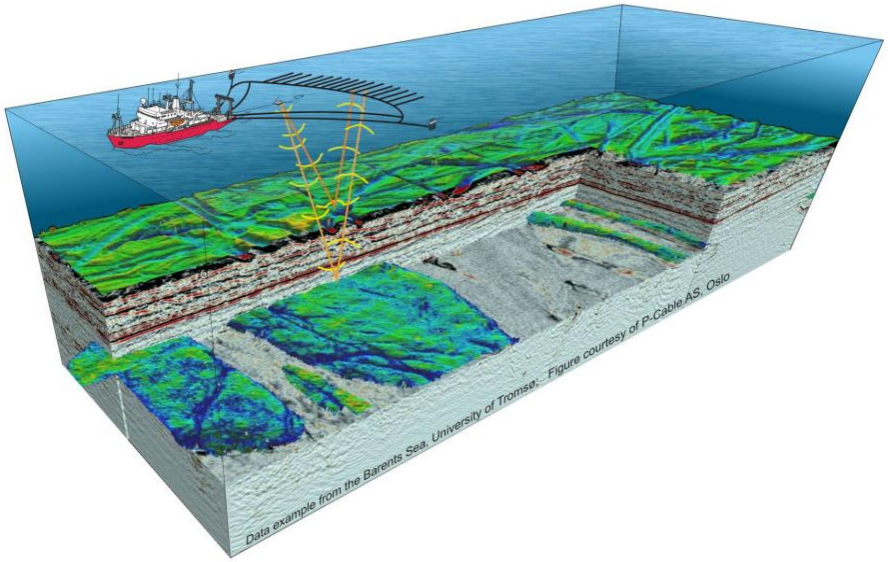

Figure 2 - Diagram of the P-cable high resolution seismic aquisition system using up to 24 streamers (from P-cable AS Oslo).

Possible CO_2 leakage can use the following escape pathways and it can be identified in the following ways: either in layers, which should produce observable seismic reflections or as diffuse flow of CO_2, with formation of "gas chimneys", which correspond to areas of chaotic reflections.

3.3 Monitoring CO_2 movement in the Prinos reservoir

It is important to focus our interest in monitoring the movement of the CO_2 also within the Prinos reservoir and identify any effects from the CO_2 injection. Sampling from oil production data from Prinos is the key instrument for monitoring the effects of CO_2 injection into the reservoir. Using a multibeam echosounder, we can obtain a better picture of the seabed bathymetry in the area of the Prinos field. The Multibeam echosounder is already on the market and usually available in many research vessels, something that enables us to create topographic maps of the seabed.

In the Prinos storage area we could also drill wells for monitoring the CO_2 storage. The monitoring wells could be positioned at some distance from the injector wells, in order to measure the temperature and pressure conditions in the reservoir and the underlying aquifer and analyse the composition of the subsurface fluids by taking samples

3.4 Simulation of a CO_2 leak in the Prinos field

With the aid of the ECLIPSE reservoir simulation software, we were able to carry out a simulation of the flow of CO_2 within a single injector well in the Prinos field and follow the development of the CO_2 plume through time over a few thousand years. We modelled a single injector well with an injection rate of 500,000 m^3/day. The injection period was for 3 years, followed by the post injection period.

The model contains 5 regions, with the upper most region 1 corresponding to the seabed, region 2 to the cap rock and regions 3, 4 and 5 to the reservoir. Region 3 is the top part of the reservoir, whereas region 5 corresponds to the bottom part of the reservoir. The limitations of the model include changes that we made to the properties of the top layer in the model. We assumed that this top layer corresponds to the seabed. In order to simulate a CO_2 leakage, we have also assumed that the cells located within the well have a higher permeability than the surrounding ones. We attributed a permeability of 10 mD to all cells in the well. We also assumed that CO_2 leakage is controlled by the leakage pathways in the subsurface.

3.5 Estimation of the level of risk in the Prinos field

Using the ArcGIS software, we will present a potential assessment model of the degree of risk to the Prinos field caused by a possible CO_2 or oil leak from the reservoir or through a pipeline penetrating it. This model was based on the use of data regarding the speeds of the winds and the currents encountered in the region and making certain assumptions as we will see below. Measurements and information received from the National Meteorological Service and the National Observatory of Athens, contributed significantly to a better understanding of the conditions in the Gulf of Kavala and generally in the region.

By estimating the speed of the flow of oil to be 20 cm/s and the wind speed to be 2 m/s, based on data collected by the National Meteorological Institute, we could then estimate the daily spread of oil into the sea. Assuming that the daily rate of oil spreading at sea is about 1.2 km/day and the prevailing direction of the currents and winds, we computed the possible spread of oil in the Prinos-Kavala basin and the time it would take for the spill to reach coastal areas as illustrated in the following sections. For the environmental risk assessment study related to the leakage of CO_2 we also used the ArcGIS software and based our study on some key elements such as the flow rate of CO_2 at the seabed level, the speed of CO_2 at the sea surface, the speed of the winds and currents and their predominant direction.

The maximum flow rate of CO_2 at the seabed is estimated to be at 0.75 m/s and the maximum flow rate of CO_2 at the sea surface to be at 1.5 m/s (close to the sea surface, within the water column). However, in our own calculations we used more moderate values, such as 0.3 m/s and 0.8 m/s, for each one of the above flow rates, respectively. The maximum wind speed can even reach a value of 15-20 m/s during the winter months. In this environmental risk assessment study, we used the value of 2 m/s. The wind speed recordings made by the National Meteorological Institute resulted to 6.9 km/h or 1.91 m/s for 2014 and to 7.1 km/h or 1.94 m/s for 2015. The wind direction is quite changeable so for this assessment we used the annual mean wind direction for 2014 which is ESE. It should be noted that when making our estimations of the flow rates of CO_2 or oil within the seawater we suggested that the contribution of the speed of sea currents was greater than that of the wind speed.

4. Results

4.1. Simulation of a CO_2 leak in the Prinos field

The results can be presented in terms of saturated CO_2, (Figure 3), in the form of free gas, or CO_2 as a mole fraction, corresponding to the dissolved liquid form of CO_2, partly dissolved in brine.

From the seabed curve on Figure 3 above, we observe that after approximately 5000 days or 13.7 years, from the beginning of injection, CO_2 reaches the seabed in the form of gas. From that point onwards the amount of CO_2 reaching the seabed increases until it reaches a peak at around 12000 days or 32.9 years. The impermeable cap rock curve is close to 0 relative gas saturation throughout the simulation as there is no pore space to host CO_2 in there. The top of the reservoir, region 3 in dark blue in Figure 3, shows how the CO_2 saturation rises steadily during the beginning of the experiment and how it remains almost constant during the entire injection and post injection period. Both regions 4, light blue curve, and 5, purple curve, show a higher saturation in the early years with the peak at the beginning corresponding to the end of the injection period. When comparing the 3 regions of the reservoir we notice the highest saturations in region 3, because this region is at the top of the reservoir. CO_2 gas migrates upwards, thus it is accumulated in the uppermost region just below the caprock (region 2). For both regions 4 and 5, CO_2 saturation drops after post injection because the CO_2 gas leaves these regions and migrates upwards into region 3, which is characterised by higher permeability.

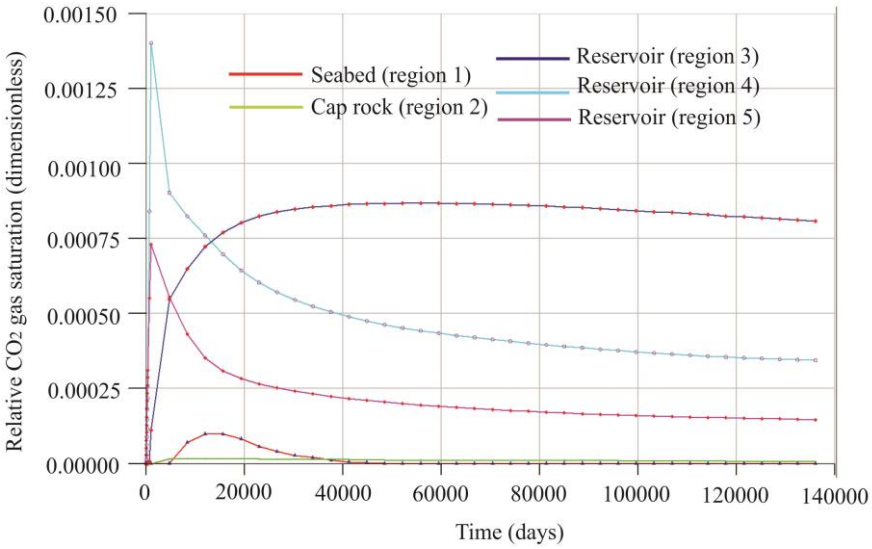

Figure 3 - Graph of relative CO_2 gas saturation for the various 5 regions of the model against time in days.

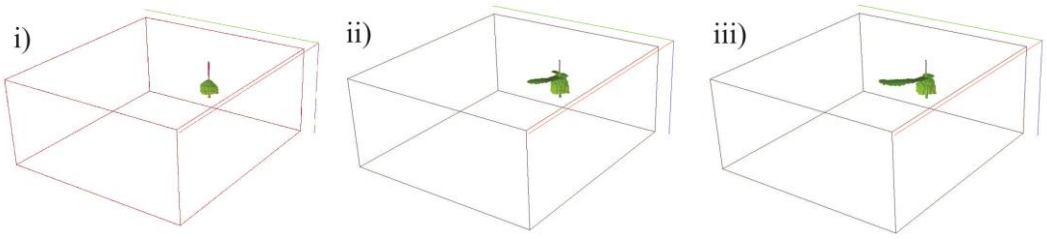

Figure 4 - Graph of the CO_2 plume development in terms of CO_2 saturation i) at the end of the injection, ii) 50 years and iii) 2363 years after the beginning of injection.

The CO_2 plume development in terms of CO_2 saturation graph above (Figure 4) shows that during the injection period (Figure 4i) the CO_2 plume develops only within the reservoir. We have perforated and injected CO_2 in the water leg of the reservoir, in the upper most part of the reservoir, corresponding to cells 45-52 of the model, and the plume's upward migration stops at the cap rock level. During the post injection period (Figure 4ii and 4iii), CO_2 has reached the seabed and develops side branches, corresponding to preferential lateral flow pathways of the CO_2 along certain formations characterised by better flow parameters.

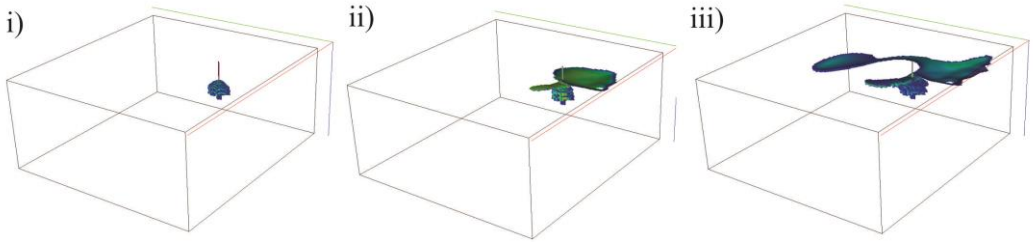

Figure 5 - Graph of the CO_2 plume development in terms of CO_2 mole fraction, i) at the end of the injection, ii) 50 years and iii) 2363 years after the beginning of injection.

Dissolved CO_2 tends to go downwards (Figure 5) whereas saturated CO_2 gas goes upwards (Fugure 4), thus explaining the difference in plume development between the previously mentioned 2 figures. Figure 5shows the plume distribution at various times after the beginning of injection. Both at 50 years and 2363 years from the beginning of injection, we see the CO_2 plume developing laterally across the seabed and in a more extensive way that for the saturated gas (Figure 4). From the simulation runs, we can actually determine that the CO_2 plume has actually reached the seabed surface at year 2028 from the beginning of injection, corresponding to 10 years after the end of the post injection period. This corresponds to a 2nd, less accurate estimation of the time the CO_2 has reached the seabed, as this estimation is based on visual detection than on a graphical method.

We will now present the results from the leakage model assessing the potential degree of risk and consequences to the study area, caused by a possible oil and/or CO_2 leak from the reservoir or through a pipeline penetrating it.

4.2. Potential leakage of oil and consequences

On the 2nd day after the beginning of the leakage process, we observe that the oil leak is being spread towards NE by the prevailing currents and winds blowing in the area (Figure 6). After eight days of oil leakage (Figure 7) we observe that the oil has covered more than half the distance, i.e. 9.2 km, between the point of storage and the coastal areas to the north of Thassos, which correspond to a total distance of 13 km.

Figure 6 - Direction of flow and magnitude of the oil leak during the 2nd day after the s tart of leakage.

Figure 7 - Extent of the leak 8 days after the start of leakage.

Twelve days after the onset of leakage, we start to observe the gradual contamination of "Natura" protected areas and thus the gradual pollution of the sea located between Thassos Island and the mainland (Figure 8). The rate of oil spreading in this closed sea is generally lower compared to the open sea and this is due to the fact that this area is protected from strong winds and severe weather.

Observing the area 16 days after the start of leakage and on the basis of the statistical data that we have and the assumptions that we made, we find that the oil spill reaches the northern coast of Thassos island (Figure 9).

From the above results obtained, we observe that there is only a period of 12 days (Figure 8) from the moment the leakage starts until the "Natura" areas start to be affected.

The public authorities have thus at their disposal a maximum of 12 days to take the necessary measures to protect the flora and fauna of the "Natura" sites from contamination. Also noting that the "Natura" areas in the above maps cover not only marine but also terrestrial areas we can thus understand that a possible leak would affect both marine and terrestrial ecosystems.

Figure 8 - Extent of the oil leak 12 days after start of leakage.

Figure 9 - Extent of the oil leak 16 days after the start of leakage.

4.3 Potential leakage of CO_2 and consequences

In the following figures we observe the dispersion of the CO_2 gas at various times since the start of leakage of CO_2. Already during the second day after the start of leakage, CO_2 flows along a preferential flow direction, which is towards NE (Figure 10), corresponding to the direction of surface sea currents and bottom sea currents in the area. Additionally, figure 8 illustrates a possible estimate of the expansion of CO_2, 5 days after the beginning of leakage of CO_2. The CO_2 continues to flow in accordance with the preferential flow direction, which is towards NE, but we observe also a part of the leaked gas to flow towards ENE (Figure 11).

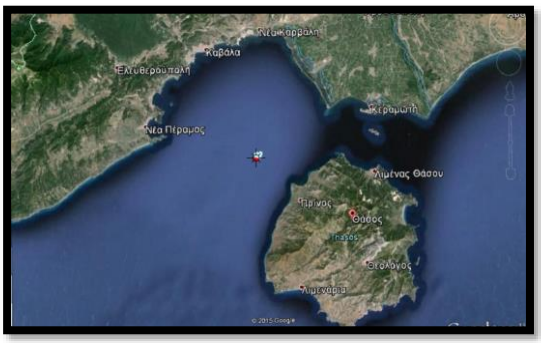

Figure 10 - Possible extent of CO_2 leak 2 days after the start of leakage.

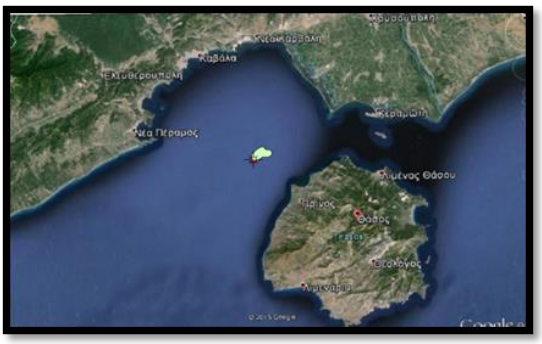

Figure 11 - Possible extent of CO_2 leak 5 days after the start of leakage.

The dispersion of the CO_2 gas 10 days from the start of leakage (Figure 12) shows that CO_2 has spread considerably compared to the previous days, now approaching the northeastern coast of Thassos. The quantities of gas to be released from the original source will play an important role in the spread of CO_2 and the impact that it will have on the environment.

5. Discussion

The simulation has shown that there is CO_2 leak in the well, which reaches the seabed. Even with a small leak, CO_2 would still reach the seabed. Therefore in terms of the quality of data that we possess, it's important to emphasise the development and application of monitoring techniques and invest on safety issues if we are to mitigate the risk of CO_2 leakage. In order to assure that there will be no CO_2 leakage around the wellbore, different monitoring techniques should be favoured. Also by assuring that the wells are cemented properly we will minimise the risk of leakage around the wellbore.

Figure 12 - Possible extent of CO_2 leak 10 days after the start of leakage.

A potential CO_2 leak in the marine area could also have negative effects on both the environment and the marine ecosystems. In our case study, a potential CO_2 leak from the Prinos reservoir will significantly affect the marine ecosystems, leading to a rapid local pH reduction. Related effects, primarily concern the animals that live attached on the seabed, which could not be removed in time and thus protected from the CO_2 spill. However, the consequences of a potential CO_2 leak are considered spatially limited and the ecosystem is capable of recovering by itself in a short time after the retreat of the leak.

One of the consequences that can result from the release of CO_2 is its ability to change the acidity of seawater in the area where the leak is taking place. The pH may decrease from 8.2 to 6.5, which can have various effects on marine ecosystems. Nevertheless, surveys carried out in areas where CO_2 is released naturally by bubbles in the ocean through leaking faults affecting submarine volcanoes have shown that after long periods of time the ecosystems can adapt to the new conditions (Apostolaki *et al.*, 2014). There is therefore no fear of any direct negative impacts of the dispersion of CO_2 on marine ecosystems. Possible long-term effects in the Prinos-Kavala basin will mainly concern shells and corals that will not be able to develop a shell.

However, it should be noted that due to the specific situation in which CO_2 is found in and its specific mode of dispersion, it is quite difficult to predict the way it will spread, the size of the leak and to what degree the ecosystems will be affected.

6. Acknowledgements

This research has been co-financed by funds from the Greek national project "NOVEL Technologies on the implementation of CCS". The authors are grateful to Dimitrios Alexopoulos and Nikolaos Tsoukalas, from CERTH, for their contributions regarding the graphic design and reading of the proof paper, as well as to Seyed Mohamed Shariatipour, from the University of Coventry, for running the CO_2 simulations in ECLISPE software. In additional they are grateful to the manufacturer of the software, the Schlumberger Co.

7. References

Apostolaki, E.T., Vizzini, S., Hendriks, I.E. and Olsen, Y.S., 2014. Seagrass ecosystem response to long-term high CO_2 in a Mediterranean volcanic vent, Marine Environmental Research, 99, 9-15.

Bachu, S. and Adams, J.J., 2003. Sequestration of CO_2 in geological media in response to climate change: capacity of deep saline aquifers to sequester CO_2 in solution, *Energy Conversion and Management*, 44, 20, 3151-3175.

Bentham, M. and Kirby, G., 2005. CO_2 storage in saline aquifers, *Oil & Gas Science and Technology. IFP Energies Nouvelles*, 60(3), 559-567.

Chadwick, R.A., Marchant, B.P. and Williams, G.A., 2014. CO_2 storage monitoring: leakage detection and measurement in subsurface volumes from 3D seismic data at Sleipner, *Energy Procedia*, 63, 4224-4239.

Kiomourtzi, P., Pasadakis, N. and Zelilidis, A., 2008. Source Rock and Depositional Environment Study of Three Hydrocarbon Fields in Prinos–Kavala Basin (North Aegean), *The Open Petroleum Engineering J.*,1, 16-29.

Pasadakis, N.A., Koutsotheodorou, E., Manoutsoglou, M., Papakonstantinou, K., Kiomourtzi, P. and Zelilidis, A., 2005. A comparative study of oils from Kavala basin using biomarkers analysis, *2nd Congress of the Commission of Economic Geology, Mineralogy and Geochemistry*, 309-317.

Proedrou, P., 1986. New age determination of the Prinos Basin, *Bull. Geol. Soc. Greece*, 20(2), 141-147.

Δελτίο της Ελληνικής Γεωλογικής Εταιρίας, τόμος L, σελ.2314-2322
Πρακτικά 14ου Διεθνούς Συνεδρίου, Θεσσαλονίκη, Μάιος 2016

Bulletin of the Geological Society of Greece, vol. L, p. 2314-2322
Proceedings of the 14th International Congress, Thessaloniki, May 2016

GEOMOPHOLOGICAL CHARACTERISTICS AND ENVIRONMENTAL SENSITIVITY INDEX FOR OIL SPILLS OF ANAVYSSOS BAY, ATTICA

Kourliaftis G. [1], Kapsimalis V.[2], Vandarakis D. [1,2] and Pavlopoulos K. [1,3]

[1] Harokopio University of Athens, Department of Geography, 70 El. Venizelou St., 17671, Kallithea-Athens, Greece, kourliaf@gmail.com, dbandarakis@hua.gr, kpavlop@hua.gr

[2]Hellenic Centre for Marine Research, Institute of Oceanography, 46.7th km Athens-Sounion Ave, 19013 Anavyssos, Attica, Greece, kapsim@hcmr.gr

[3]Paris-Sorbonne University Abu Dhabi, Department of Geography and Planning, P.O. Box 38044 AD UAE, Kosmas.Pavlopoulos@psuad.ac.ae

Abstract

The study of the coastal and shallow marine geomorphology of the adjacent bays of Anavyssos and Aghios Nikolaos (southeastern Attica) was carried out by acoustic scanning of the seafloor with an echo sounder and sonar side scan; topographical sections perpendicular to the shoreline, collection and analysis of surface sediments; determination of long-term shoreline displacements by comparing old and modern aerial photographs and satellite imagery. The terrestrial part of the coastal area consists of many landforms, such as lagoons, cliffs, beachrocks, tombola etc. The beaches affected by intense human activity have gentle slopes, low elevations and a coarse-grained texture. The remote sensing analysis showed that, over the last six decades, there are some small shoreline changes of the order of ± 2 meters. The bays have relatively gentle gradients covered by sand in their shallower parts and patches of Posidonia Oceanica towards the open sea. Taken into account the texture of sediments and landforms that make up the terrestrial part of the coasts, four categories (1st, 2nd, 3rd and 5th) of Environmental Sensitivity Index for oil spill (ESI) have been identified and an ESI map is created serving as a quick reference for oil spill responders and coastal zone managers.
Keywords: *Coastal topography, bathymetry, sediments, management.*

Περίληψη

Η διερεύνηση και η αποτύπωση της παράκτιας και υποθαλάσσιας γεωμορφολογίας των γειτονικών όρμων Αναβύσσου και Αγίου Νικολάου, στη νοτιοανατολική Αττική, πραγματοποιήθηκε με την ακουστική σάρωση του πυθμένα, με μονοδεσμικό βυθόμετρο και ηχοβολιστή πλευρικής σάρωσης, με τοπογραφικές τομές κάθετες στην ακτογραμμή, με τη συλλογή και ανάλυση θαλάσσιων και παράκτιων δειγμάτων ιζήματος καθώς και από τη μελέτη των ιστορικών αλλαγών της ακτογραμμής μέσω σύγκρισης παλιών αεροφωτογραφιών και νεώτερων δορυφορικών εικόνων. Το χερσαίο τμήμα της παράκτιας περιοχής αποτελείται από πλήθος γεωμορφών όπως λιμνοθάλασσες, κρημνούς, beachrocks, τόμπολο κ.ά. Οι αιγιαλοί παρουσιάζουν ήπιες κλίσεις και μικρές υψομετρικές διαφορές, με έντονη ανθρώπινη δραστηριότητα. Αποτελούνται από χαλαρά ιζήματα αμμώδους ή χαλικώδους σύστασης υποδηλώνοντας ένα ήπιο υδροδυναμικά

παράκτιο περιβάλλον. Τοπικά, καταγράφονται μικρές διαχρονικές μεταβολές της ακτογραμμής ενδείξεις μικρής διάβρωσης, της τάξης των ± 2 μέτρων. Το υποθαλάσσιο τμήμα της παραλίας εμφανίζει σχετικά ομαλές κλίσεις και μικρά βάθη, με την άμμο να κυριαρχεί στα ρηχότερα τμήματα του Όρμου και τις εκτενείς συστάδες της Posidonia Oceanica προς την ανοιχτή θάλασσα. Από την αποτύπωση της υφής των ιζημάτων και των γεωμορφών που συνιστούν το παράκτιο τμήμα της περιοχής προσδιορίστηκαν τεσσέρεις κατηγορίες (1η, 2η, 3η και 5η) του δείκτη περιβαλλοντικής ευαισθησίας στην πετρελαϊκή ρύπανση (E.S.I.) και προέκυψε ο αντίστοιχος διαχειριστικός χάρτης.
Λέξεις κλειδιά: *Παράκτια τοπογραφία, βαθυμετρία, ιζήματα, διαχείριση.*

1. Introduction

The coastal zone is an area of high environmental, cultural, social and financial value. In recent decades, the configuration of the coast is not only due to the interaction of terrestrial and marine processes (e.g., sediment supply, ripples, currents, etc.), but also to human activities and interventions (Bird, 2008).

The unregulated development of the coastal area (residential, tourist, industrial, maritime, etc.) modifies the long-standing morphodynamic regime of the coast enforcing the processes of erosion or deposition (Woodroff, 2002), as well as it degrades the local environment by discharging organic and inorganic contaminants on the land and/or at sea.

The purposes of the present study are: the mapping of the substrate types of the Anavyssos (Palaia Fokaia) coastal zone and bay, SW Attica (Figure 1); the designation of long-term shoreline displacements during the last seven decades and, consequently, the determination of areas undergoing erosion or deposition; the mapping of the Environmental Sensitivity Index (ESI) for oil spills used in planning to create cleanup strategies before an accident occurs, and to reduce the harmful consequences of oil spills and cleanup.

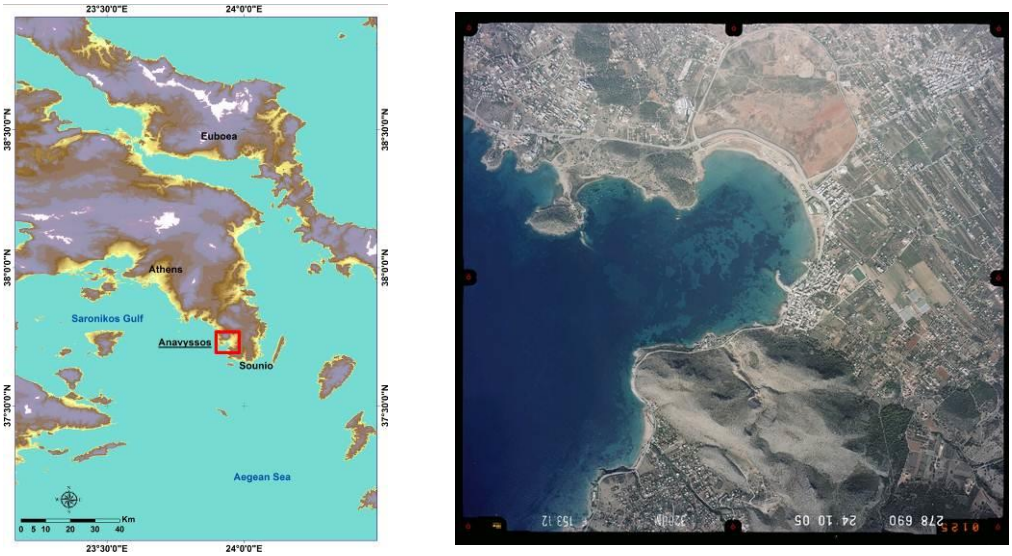

(a) **(b)**

Figure 1 - (a) Location map and (b) coloured aerial photograph of the Anavyssos and Aghios Nikolaos bays taken in 2005 by the Hellenic Military Geographical Service (HMGS).

2. The study area

The study area is the Anavyssos Bay and the adjacent Aghios Nikolaos inlet, located in southeastern Attica, 50 km south of Athens and 20 km north of Sounio (Figure 1). The coastal area of Anavyssos includes an extended lowland with a gradient of ≤5% (Gaki-Papanastasiou, 1985; Markopoulos, 1994). At the seaward end of this plain, there was a natural lagoon, which was operated as saltmarsh till the end of 1970s (Dalakoglou, 1996). The onshore section presents complex tectonic structure, while Quaternary formations are dominant (Pavlopoulos, 1992). The coasts are formed by waves resulting from the wind of south-eastern, southern, southwestern, and western direction. In addition, the large beaches of the area have been fully landscaped by humans for their summer tourist exploitation (Verikiou-Papaspiridakou *et al.*, 2004; Ladakis, 2006).

3. Materials and Methods

The bathymetry and seabed morphological features of the bay were conducted by the f/b "Triton I" (HCMR) in May 2015, using a single beam eco sounder (Humminbird 998c HD SI Combo) (Figure 2). The bathymetric and side imaging data were collected with the functional emission frequencies of 200 kHz and 450 kHz, respectively. The chosen coordinate system was the WGS84, while the projection system implemented was the UTM zone 34N. Beach survey was carried out in July 2015, and 7 descriptive shore-normal profiles, which extended from the sand dunes to the depth of ~2 m, were realized.

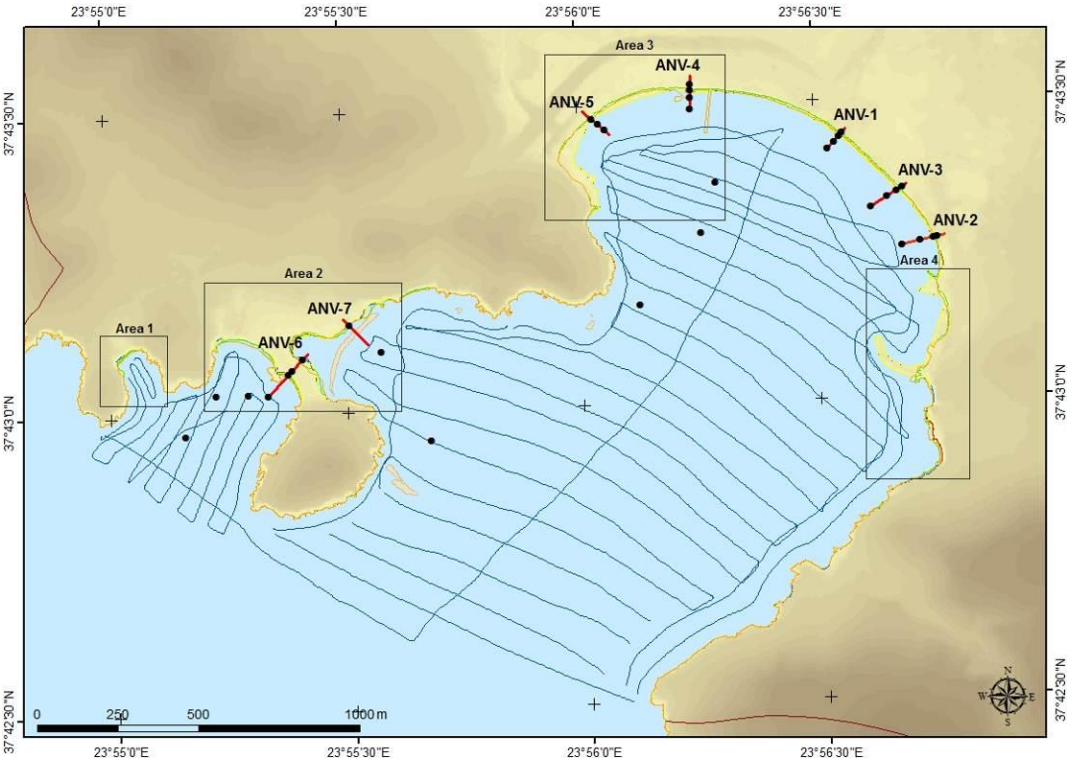

Figure 2 - Position of 7 topographic cross sections carried out along the shoreline (red lines); sampling sites of surface sediments (black dots); and tracks of the single-beam echo sounder and side imaging sonar in the Avavyssos Bay (blue lines).

Granulometric analysis was performed in 32 sediment samples obtained from the beaches (24 samples) and the bottom of bay (8 samples), while the extracted data were statistically processed on the basis of Folk and Ward (1957) method by the use of the GRATISTAT (v.8) software.

Shoreline spatial changes were identified with the comparison of three aerial photographs (of the years 1960, 1966 and 2008) and three satellite image (of the years 2006, 2011 and 2014). All aerial photographs and satellite images were geometrically corrected and digitized. A maximum total error of ±2 m was estimated.

The Environmental Sensitivity Index (ESI), firstly applied in 1976, is an integral component of oil-spill contingency planning and response and coastal resource management in many countries worldwide Jensen *et al.* (1998). The ESI is a spatial information system, which is composed of three main components: shoreline ranking system which ranks shoreline types on a scale of 1 to 10; oil-sensitive biological resources; and human-use resources of commercial, recreational, or subsistence value (NOAA, 2002).

4. Results

4.1. Historical shoreline displacements

On the eastern edge of the study area (Area 1), there is a total retreat of the shoreline by ~ 3 m, in the past 55 years. The shoreline imprinted in 2011 (Figure 3a, blue line) shows a further regression of 2-3 m, which is, however, due to high climbing waves resulting from relatively harsh weather conditions.

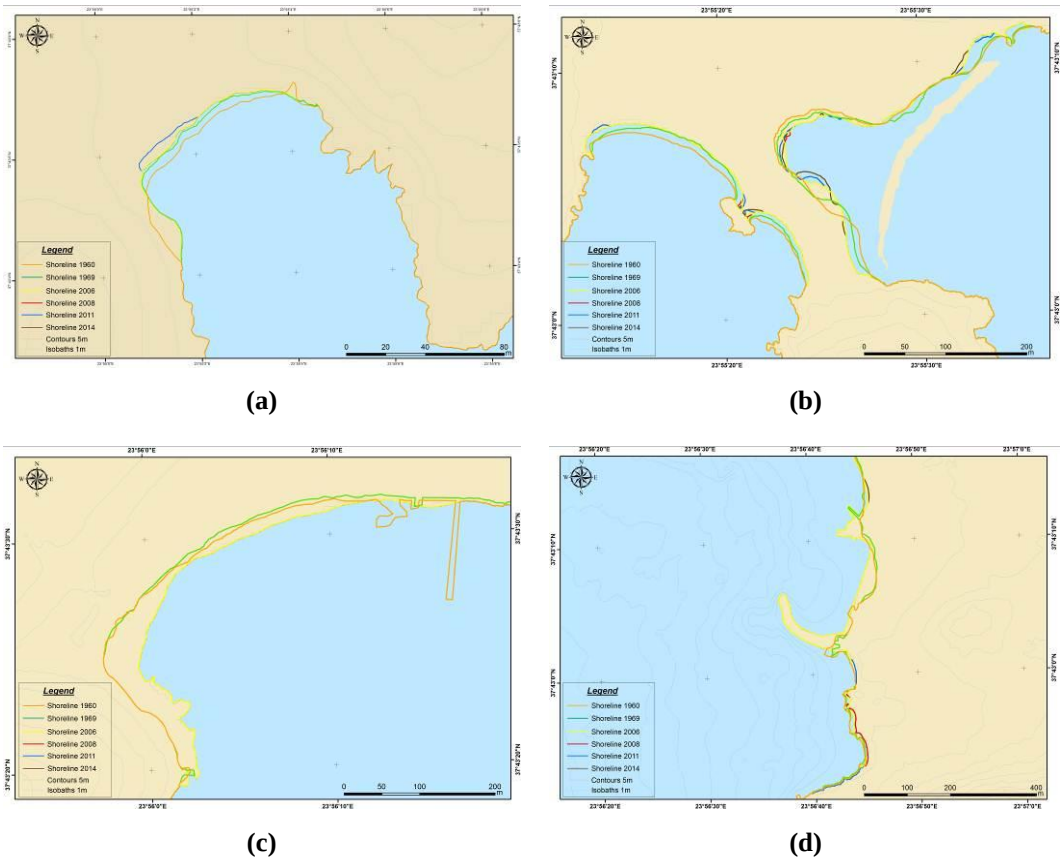

Figure 3 - Historical shoreline displacements in the Areas: (a) 1; (b) 2; (c) 3; and (d) 4. The locations of each Area are showed in Figure 2.

In Area 2 (tombolo), erosion (around 3 m) dominates across the west coast and the east side at the positions, where the lagoon meets the open sea (Figure 3b). On the contrary, the shoreline situated in front of the lagoon seems to be gaining ground progressively in recent years.

In the western part of the Anavyssos shore (Area 3, Figure 3c) there is a pier that was used to load the salt from the salt marshes. This structure was abandoned and destroyed with the closing of the operation of the saltmarsh, after the end of the 1960s - early 1970s. Furthermore, there seems to be a 35 m progradation of the coast, resulting from an artificial embankment presumably for the construction of the coastal highway after the closing of the saltmarsh.

Finally, in the eastern part of the Anavyssos Bay (Area 4) the construction of the Palaia Fokaia port stands out, while in its north and south shores there is a slight erosion in the range of ~ 1 m (Figure 3d).

4.2 Coastal Geomophology

The total length of the shoreline of the study area is 11 km. Almost all along it, there are beaches, the largest of which are the Anavyssos and Aghios Nikolaos (1500 and 400 meters, respectively). In addition, there are some small coasts that are the result of retreating erosion in front of small coastal cavernous recesses at the sea level. The beaches consist mainly of sand and gravel, and in places of pebbles and breccia. In the area there are also coastal cliffs, dunes, tombola, beachrocks and lagoons (Anavyssos and Aghios Nikolaos) (Figure 4).

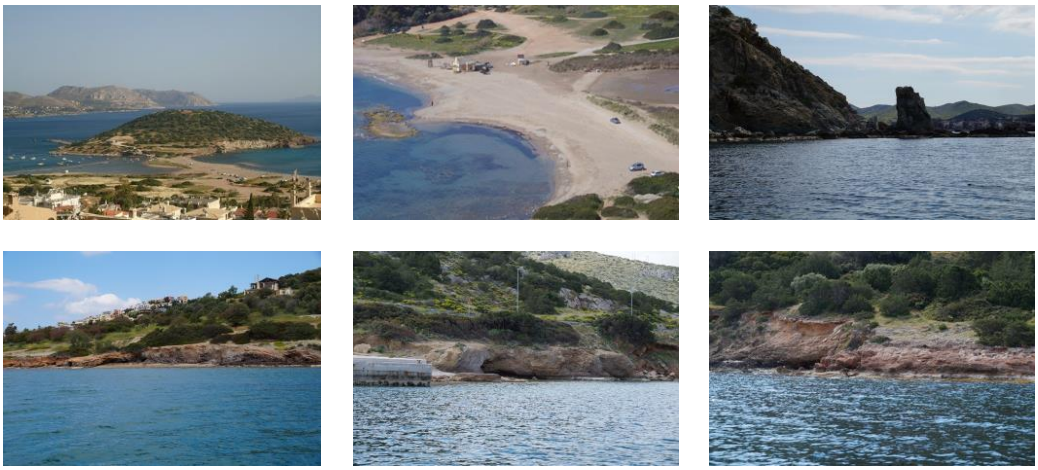

Figure 4 - Photographs showing various coastal landforms in the Anavyssos and Aghios Nikolaos, such as tombolo, beachrocks, stack, caves and cliffs.

Seven (7) topographic cross sections carried out along the shoreline of the study area, combined with the grain analysis of beach sediments (Figure 5). The terrain is low with gentle gradient, surface sediments are mainly sands with sporadic presence of gravel and pebbles, while human interference is present throughout the beaches. The backshore consists of consistent substrate (mainly of sandy composition) used as a parking lot. In the foreshore and offshore section of Anavyssos coast there is a number of longshore bars, at a distance of 20-40 m seaward of the shoreline, at a depth of 0.5-1 m. In the western part of Anavyssos beach (Section ANV-5) the ramp is absent, while in the center of the beach (Section ANV-4) there are numerous tile fragments and boulders, which are possibly from the damaged pier that stood in this position for the saltmarsh operation.

4.3. Submarine Geomorphology

The Anavyssos Bay present relatively shallow depths (maximum recorded depth 21 m), gentle slopes and non cohesive materials (mainly sand) (Figure 6a). In front of the steep shores of the bay, the depth is relatively low, probably due to the accumulation of landslide materials. The artificial

submerged breakwater plays a key role in the dynamics of sedimentology of the area preventing the seaward transport of the sand from nearshore.

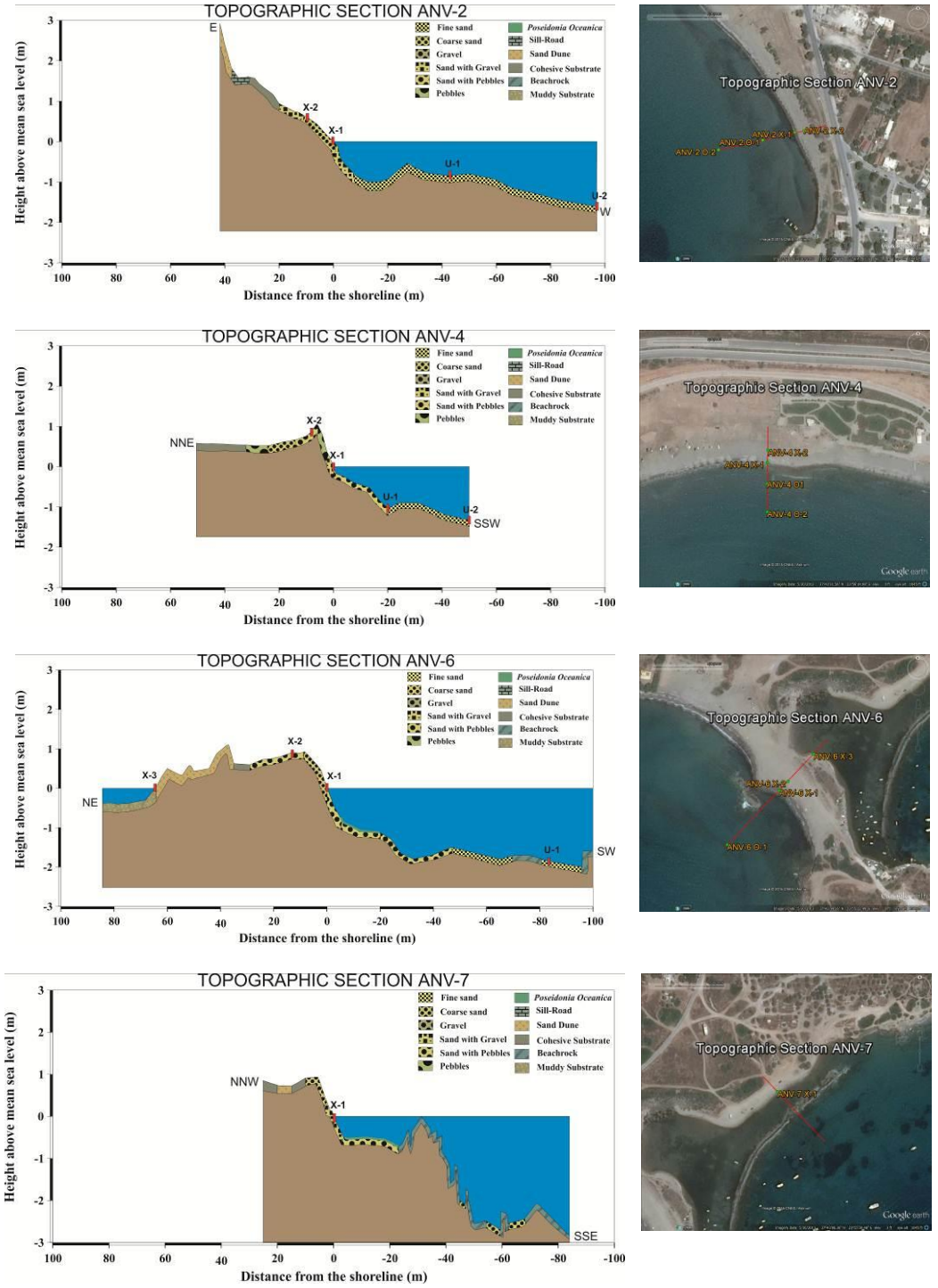

Figure 5 - Topographic sections of the Anavyssos and Aghios Nikolaos coasts. The locations of each section are showed in Figure 2.

The sand is mostly concentrated on the seafloor sites located in front of the beaches and tombolo sides. The presence of *Posidonia Oceanica* is detected at depths of more than 3 m covering the larger part of the seabed (Figure 6b). At depths of 3-17 m, some sandy patches are located, while in deeper waters a well-developed *Posidonia Oceanica* meadow is present.

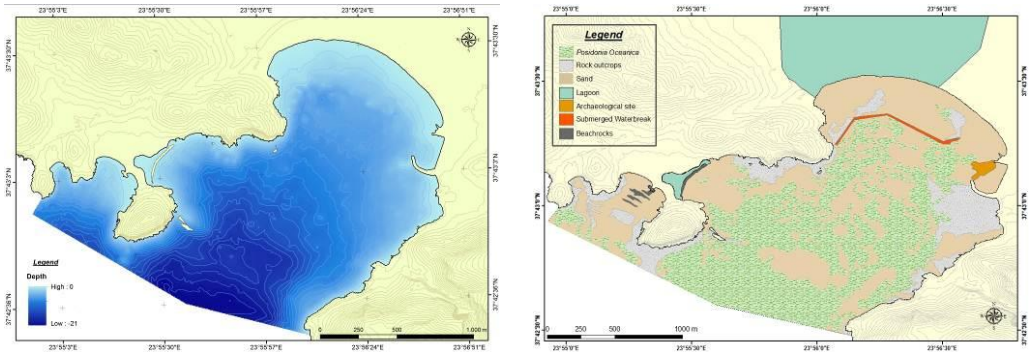

(a) (b)

Figure 6 - (a) Bathymetric map; and (b) Substrate type map of the Anavyssos and Aghios Nikolaos bays.

4.4. Environmental Sensitivity Index for oil spills

Based on the index of sensitivity to oil pollution (ESI), four categories of coastal habitats have been identified in the beaches of Anavyssos and Aghios Nikolaos that correspond to rocky shores exposed to wave and vertical impervious manmade structures (ESI = 1), beachrock and rocky platforms (ESI = 2), fine-grained and mid-grained sandy beaches (ESI = 3) and mixed sandy and pebbly beaches (ESI = 5).

5. Discussion

Small shoreline changes occurred in the last six decades, showing slight retreat in the range of ~2 m. These changes are a little larger than the statistical error of the method of aerial and satellite imagery analysis (± 2 m), therefore it cannot be concluded with certainty that the specific areas are eroded. In contrast, in the western part of the Anavyssos beach, strong advance of the coastline (~ 35 m) was recorded because of the artificial embankments made in the early 1970s.

The coastal environment of the area is strongly influenced by human activities. There is no longer available solid load at the coastal area because of reduced sediment supply from local rivers, since much of their riverbeds have been filled and built on.

The submarine morphology of the Anavyssos Bay probably owes its characteristics not only to modern morphodynamic factors, but also to processes in land before it was flooded by the sea during the post-Last Glacial Maximum period and the subsequent transgression phase of sea level. This assumption is derived by the examination of terrigenous sediments collected from depths of ~ 10 m.

As regards the environmental sensitivity index for the oil spill, the coastal cliffs and the port infrastructure belong to the 1st category (ESI = 1) and cover 5.45 km comprising 49% of the total shoreline. The 2nd category (ESI = 2) includes the shallow rocky coasts with slope ≤30°, the beachrocks located in Aghios Nikolaos Bay and the islets situated in the western part of the Anavyssos Bay. It covers 2 km, namely 19% of the whole littoral zone. The sandy beaches and the sandy banks of the Aghios Nikolaos lagoon belong to 3rd category (ESI = 3), and consist of 27% of the study area (2.9 km). Finally, the coastal systems included into the 5th category (ESI = 5) are the sandy-pebbly parts of the central and western beach of Anavyssos and the Aghios Nikolaos lagoon (5% or 0.45 km). The last category represents the most

sensitive coastal habitats of the Anavyssos-Aghios Nikolaos shores, and needs specific managerial action plans in order to face an oil spill pollution risk.

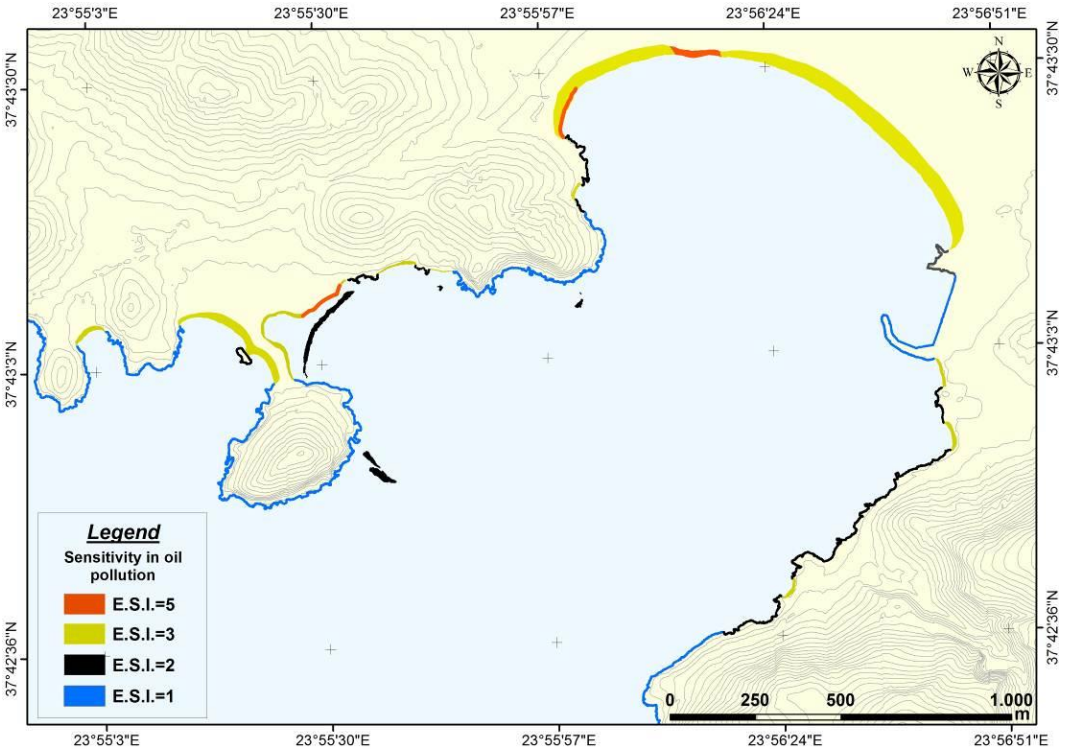

Figure 7 - Environmental Sensitivity Index (ESI) map of the Anavyssos and Aghios Nikolaos coasts.

The recommended actions for their cleaning are: complete purification is not necessary due to the action of the wave and inaccessibility, when ESI = 1; washing with high pressure or sandblasting since they are not particularly ecologically sensitive when ESI = 2, immediate cleaning and replacement of the sand and attention to the use of heavy machinery in order to avoid entrapment of the oil at greater depths when ESI = 3; and immediate cleaning is necessary with low-pressure washing and collecting the ingredients separated using the skimmer and sorbents when ESI = 5.

6. Conclusions

The gentle slopes and low elevations of the valley as well as the formation of the lagoon provide data on the deposition rates of the past. The sea shores and the underwater part of the region generally consist of fine material (except for some positions). The coastal and offshore part of the region consists of gentle slopes, loose particles, and small height differences with the recent landforms to be primarily attributable to marine processes of erosion and deposition. The Anavyssos Bay was created because of the land erosion before it submerged by rising sea levels and the low hydrodynamic regime which is unable to alter the characteristics of the underwater plain. In the seacoast region, there is small scale erosion in some places while intense seasonal human activity is present. The bottom cover verifies the low hydrodynamic regime in the bay with the existence of *Posidonia* (*Posidonia Oceanica*) from very shallow depths (3 m.). Finally, the mapping and classification of coastal habitats according to the Environmental Sensitivity Index is necessary information for responsible entities for a faster and more appropriate treatment of a possible oil spill.

7. Acknowledgments

The authors are grateful to Mr V. Mpampas for his valuable help in the fieldtrip work, BSc I. Stavrakaki for the laboratory treatment of the collected sediments, MSc H. Kyriakidou and MSc P. Drakopoulou for the manipulation of the data and G.I.S. analysis.

8. References

Bird, E., 2008. Coastal Geomorphology: an Introduction, *2nd Edition John Wiley, Chichester, U. K.*, 411 pp.

Dalakoglou, T., 1996. Anavyssos: The landscape, the people, the life, *Lithochrom*, Athens, Greece.

Folk, R.L. and Ward, W.C., 1957. Brazos bar: a study of significance of grain size parameters, *Journal of Sedimentary Petrology*, 27, 3-26.

Gaki-Papanastassiou, K., 1985. Coastal geomorphology of Anavyssos area (Attica) and study of modern marine sediments, MSc Thesis in Oceanography, Department of Geology, National and Kapodistrian University of Athens.

Jensen, J.R., Halls, J.N. and Michel, J., 1998. Systems Approach to Environmental Sensi-tivity lndex (ESI) Mapping for Oil Spill Contingency Planning and Response, *Photogrammetric Engineering and Remote Sensing*, 64 (10), 1003-1013.

Ladakis, E., 2006. Study of certain modern coastal organosedimentary forms, PhD Thesis, Department of Chemistry, National and Kapodistrian University of Athens.

Markopoulos, K., 1994. Coastal sedimentary formations in the area of Aghios Nikolaos-Anavyssos, Attica, MSc Thesis in Oceanography, Department of Geology, National and Kapodistrian University of Athens.

NOAA, 2002. Enviromental Sensitivity Index Guidelines, Version 3.0., NOAA Technical Memorandum NOS OR&R 11, Hazardous Materials Response Division, Office of Response and Restoration, NOAA Ocean Service.

Pavlopoulos, K., 1992. Geomorphological evolution of South Attika, Ph.D. thesis, Department of Geology, National and Kapodistrian University of Athens.

Verikiou-Papaspiridakou, E., Skilodimou, H. and Bathrellos, G., 2004. Recording of the changes of the natural geomorphological environment using maps of different issue date. An exam-ple from the coastal zone of the south-western Attica, *Bulletin of the Geological Society of Greece*, XXXVI, 968-977.

Woodroffe, C.D., 2002. Coasts, Form Process and Evolution, Cambridge University Press, Cambridge, 623 pp.

Δελτίο της Ελληνικής Γεωλογικής Εταιρίας, τόμος L, σελ. 2323-2331
Πρακτικά 14ου Διεθνούς Συνεδρίου, Θεσσαλονίκη, Μάιος 2016

Bulletin of the Geological Society of Greece, vol. L, p. 2323-2331
Proceedings of the 14th International Congress, Thessaloniki, May 2016

GEO-ELECTRICAL MAPPING OF BEACHROCK IN VATERA BEACH, LESVOS

Meligonitis R.[1,2], Galanopoulos D.[2], Hasiotis T.[1] and Velegrakis A.[1]

[1]*Department of Marine Sciences, University of the Aegean, University Hill, 81100, Mytilene, Lesvos, meligonitis@marine.aegean.gr, hasiotis@marine.aegean.gr, afv@aegean.gr*

[2]*Ministry of Marine & Island Policy, General Secretariat of Aegean & Island Policy, 2 Mikras Asias, 81100, Mytilene, Greece, ramel@ypai.gr, dgal@ypai.gr*

Abstract

Beachrock (Br) is encountered on the coastal zones, playing an important but also complex role in their morphodynamic evolution. Although Br has been widely studied, two important issues require further investigation. The first concerns the importance of the interaction of the dynamically changing coastal environment with the temporal changing surficial and underground hydrogeological balance. The second has to do with the spatial distribution and the evolution of Br with respect to the specific "host" coastal zone geo-environment. This paper designates the electrical resistivity method as a tool that contribute in arguing in the abovementioned issues. The research comprised subsurface measurements with the DC resistivity method along two profiles located on Vatera beach (Lesvos Island), where there is a significant Br outcrops. Twelve geoelectric soundings were carried out using the Axial Pole-Dipole electrode array. The electrical resistively measurements permitted an indirect estimation of TDS, which depicts the coastal interface of fresh water - sea water. The interpreted geoelectric model shows two thin formations attributed to Br. The first is the inland extension of the Br outcrop and the second it is believed to be a primary stage of Br build up.

Keywords: *beachrock, coastal zone, geophysics, prospecting, Lesvos.*

Περίληψη

Το Beachrock (Br ή παραλιακοί ψαμμίτες) εμφανίζεται σε παράκτιες ζώνες και έχει σύνθετο ρόλο όσον αφορά στη μορφοδυναμική εξέλιξη τους. Αν και το Br έχει μελετηθεί ευρέως, ωστόσο, δύο βασικά θέματα χρήζουν επιπρόσθετης έρευνας. Το πρώτο αφορά στη σημασία της αλληλεπίδρασης του δυναμικά μεταβαλλόμενου παράκτιου περιβάλλοντος με την χρονικά μεταβαλλόμενη επιφανειακή και υπόγεια υδρογεωλογική ισορροπία. Το δεύτερο θέμα έχει να κάνει με τη χωρική κατανομή και την εξέλιξη του Br σε σχέση με συγκεκριμένο περιβάλλον που το "φιλοξενεί". Η παρούσα εργασία αναδεικνύει τη μέθοδο της ειδικής ηλεκτρικής αντίστασης του υπεδάφους, ως ένα σύγχρονο εργαλείο που μπορεί να συμβάλει στη μελέτη των παραπάνω προβληματισμών. Η έρευνα περιέλαβε μετρήσεις με τη γεωηλεκτρική μέθοδο συνεχούς ρεύματος κατά μήκος δύο τομών στην παραλία των Βατερών της Λέσβου, όπου παρατηρούνται σημαντικές επιφανειακές εμφανίσεις Br. Πραγματοποιήθηκαν δώδεκα γεωηλεκτρικές βυθοσκοπήσεις, με ανάπτυγμα ηλεκτροδίων Axial Pole-Dipole. Οι μετρήσεις της ειδικής ηλεκτρικής αντίστασης επέτρεψαν μία έμμεση εκτίμηση του TDS, το οποίο απεικονίζει την διεπιφάνεια γλυκού-θαλασσινού νερού. Κατά την ερμηνεία του

γεωηλεκτρικού μοντέλου αναδείχθηκαν δύο σχηματισμοί που αντιστοιχούν σε Br. Ο πρώτος αποτελεί επέκταση του Br προς την ξηρά και ο δεύτερος πιστεύεται ότι είναι Br σε πρώιμο στάδιο ωρίμανσης.
Λέξεις κλειδιά: *beachrock, παράκτια ζώνη, γεωφυσική έρευνα, Λέσβος.*

1. Introduction

Beachrock (Br) (or coastal sandstone) is encountered on the coastal zones as a modern and dynamic-evolving phenomenon with a complex role of either degrading irreversibly the beach or in the case of submerged Br in protecting vulnerable beaches (Vousdoukas *et al.,* 2007). Overviews of the Br appearance worldwide, characteristics, origin and morphodynamic evolution and impacts and possible usage are mainly described in two review papers of Vousdoukas *et al.* (2007) and Danjo and Kawasaki (2012). Br is found mostly in the tropics - subtropics and temperate shores, its form and orientation varies greatly and they are mainly identified beneath a coastal sediment cover within the transitional mixing zone as a resulting effect of sea and coastal water interaction under the supratidal zone conditions (e.g.Erginal *et al.,* 2010; Caron, 2012).

The Gulf of Vatera is located on the south coast of Lesvos island in the northeastern Aegean Sea (Figure 1). It is a long curved beach, it has a total length of about 7 km, being less than 50m in width and it is confined in-between two small rivers -the Armyropotamos to the west and Vourkopotamos to the east-, whereas smaller ephemeral streams drain mainly to the eastern part of the beach. The wider coastal area is bounded by two rocky capes, Agios Fokas to the west and a high and tectonically affected coastal cliff to the east. Along specific parts of the beach there is significant appearance of Br, which has been the subject of previous studies (Vousdoukas *et al.,* 2007, 2009). However, it remains under investigation (i) the importance of the interaction of the dynamically changing coastal environment with the temporal changing surficial and underground hydrogeological balance (freshwater-saltwater mixing and its interaction/effect with the Br during its leakage) and (ii) whether the spatial distribution and the evolution of Br is in direct relation to the specific "host" coastal zone geo-environment. Within this framework a small scale geoelectrical survey was carried out, as part of an ongoing geophysical study, by using the Direct Current (DC) resistivity method in order to outline the subsurface spatial distribution of Br and adjacent coastal formations as well as their geoelectric characteristics, which could lead to useful conclusions regarding the geological host environment and to delineate the saline - fresh water transitional zone, so as to study its possible influence in the Br formation. Geophysical surveys focused on mapping Br are rather scarce (if absent) in the literature, with those of Psomiadis *et al.* (2009) and Kubo *et al.* (2013) being the most recent ones.

2. General Beachrock characteristics

The Br is either fragile or well laminated sedimentary rock or 'hard' coastal sedimentary formations or stratified sandstones, originating from the mixing of the various geological coastal materials (e.g. sand, pebbles etc.) (eg. Rey *et al.,* 2004). Br is formed within the coastal zone quickly (probably within a year). It can record any morphological change along the coastline (Cox*et et al.,* 2008). Moreover it can alter the physical nature of beaches and impact on the ecology (Brattström, 1992), the balance, the supply and the distribution of sediments along the coast, presenting seasonal morphological changes that differ from the expected ones (e.g. Rey *et al.,* 2004; Vousdoukas *et al.,* 2007; Psomiadis *et al.,* 2009). The changes in the transitional zone (mixing freshwater - seawater) in coastal areas play an important role in the genesis of Br. It exhibits a wide variation of physical characteristics related to a cementation process and therefore to the properties of the consolidated mass (Rutten, 2011). The connective - adhesive material of Br is carbonate, stemming from direct precipitation from seawater or fresh water (Kelletat, 2006). Porosity, permeability, energy conditions (waves, currents), the geographic location and the local weather conditions and water temperature determine the course of cementation (e.g. Chowdhury *et al.,* 1997). Dolomitization

andCO_2 degassing lead to mineralogical changes and create Br (e.g. Back *et al.*, 1983; Arrieta *et al.*, 2011). Also an important role must play the biological activity (role of bacteria in the cementing process) (e.g. Neumeier, 1999). Besides, the rainwater acts as the "carrier" of chemical and biological elements through surface and subsurface environments.Moreover, their formation might be affected by the morphology and the structure of the coastal zone and their interaction with the coastal hydrodynamics (Scoffin και Stoddart, 1983; Shinn, 2009; Vousdoukas *et al*., 2009; Arrieta *et al.*, 2011).

Figure 1 - (a) Location of the study area in Lesvos island, (b) position of the profiles presented in figure 4, (c) photo of profile 2 next to the Br outcrop and (d) a closer image of the Br outcrop along the shoreline.

3. Methodology

It is widely known that there is a relationship between the electrical conductivity and the physical characteristics and rock properties (e.g. the conductivity of the water filled pores, the porosity and the degree of saturation of the formation etc.). The DC resistivity method can determine the electrical properties of rocks and specifically the apparent electrical resistivity **ρ (**ohm.m) by measuring the intensity **I** of the electric current supplied to the subsoil by a pair of electrodes (current electrodes) and the voltage **ΔV** recorded in a separate pair of electrodes (potential electrodes) principally located in an intermediate position between the current electrodes (Figure 2 and Equation 1).

Equation 1 – apparent electrical resistivity ρ

$$\rho=K(\Delta V/I)$$

where **K** is a coefficient depending on the geometry of the electrode array being used (Telford *et al.*, 1981). The determination of electrical resistivity at different depths within the Earth is achieved by taking a series of measurements of the above physical quantities for successively increasing current and potential electrode spacing. This process is called Vertical Electrical Sounding (VES). One of the most common electrode configurations is that introduced by Schlumberger (Equation 2).

Equation 2 – geometric coefficient K

$K=\pi(AB/2)^2/MN$

where AB and MN are the distances between the two current and the two potential electrodes, respectively (Figure 2a).

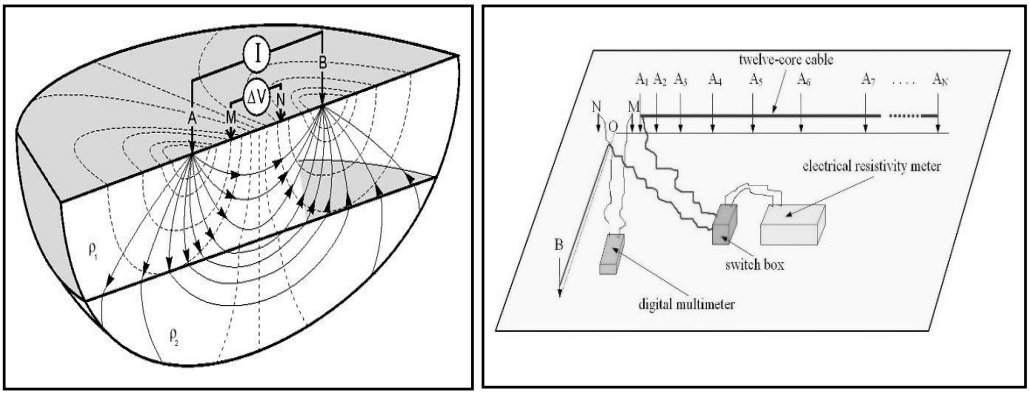

(a) (b)

Figure 2 - (a) The basic configuration of current (A, B) and potential (M, N) electrodes in the VES method (continuous curved lines: electric current lines; dashed curved lines: equipotential lines of electric field between current electrodes (from geoFact, 2014). (b) Equipment setup for the Axial Pole-Dipole array.

The electrical resistivity **ρ** of rocks can be determined as a function of depth by increasing successively the distance between the two current electrodes. For a total number of N distances between the current electrodes, the apparent electrical resistivity $\boldsymbol{\rho_n}$ corresponding to each distance using equation (1) is:

Equation 3 – apparent electrical resistivity ρ_n relative to the n-th measuring distance $A_nB/2$

$\rho_n=K_n(\Delta V_n/I_n)$

where n=1,2,3, ... N and $\boldsymbol{\Delta V_n}$ the potential difference, $\mathbf{I_n}$ the electric current intensity and $\mathbf{K_n}$the geometric coefficient relative to each current electrode distance $A_nB/2$.

In this study, **I** and **ΔV** measurements were performed using a version of the widely known Schlumberger electrode array (Telford et al., 1981) that is known either as «half-Schlumberger» (Akintorinwa and Abiola, 2012), or as «Axial Pole-Dipole» array (Chandra *et al.*, 2004). The main criteria for the selection of this particular electrode configuration was first ensuring less time and employees to conduct measurements and second the applicability of the method in a relatively limited space. According to this method, one of the two current electrodes (e.g. the current electrode B) is placed at a fixed point, at a large distance (about 3 times the maximum AB/2) away from the centre O of the array and in a way that OB is perpendicular to OA (Figure 2b). Then electrode A is moved successively at the prescribed positions A_1, A_2, A_3,...,A_N, where N is the total number of measurements. The apparent electrical resistivity $\boldsymbol{\rho_n}$, which corresponds to each of the distances $A_nB/2$ is calculated by combining equations (2) and (3), however, the potential difference **ΔV**is now doubled in order to balance for the loss of half of the voltage gradient measured at the potential electrodes M and N.

In order to demonstrate the sea water - fresh water mixing, the total dissolved salts (TDS) distribution was estimated (Bernard, 2006) by using equation 4 and under the assumption that the loose coastal geological formations (fluvial-alluvial, coastal sediments etc.) permit sea water presence in the coastal area.

Equation 4 – Total Dissolved Salts

TDS (mg/l) = 0.7σ

where σ = electrical conductivity (μS/cm) = 10000 / electrical resistivity (ohm.m).

3.1. Data Collection and Processing

The electrical resistivity measurements were carried out using a measuring system, consisting of a DC resistivity meter designed and developed by Galanopoulos and Kolettis (2005) and a twelve core cable connected to the meter via a mechanical switch box (Figure 2b). The field measurements were carried out during May 2014 and comprised 12 «Axial Pole-Dipole» VES, located along 2 profiles of SSW-NNE direction (Figure 1). All VES had a maximum AB/2 of 13m. Profile 1 is 25m long and consists of 7 VES having a spacing of 2-5m. Profile 2 is shorter (16m long) and consists of 5 VES having a spacing of 4m. Outcropping Br was detected only in profile 2 along the coastline and the measurements started directly next to the outcrop (Figure 1).

For each current electrode distance $A_nB/2$, the data collection consisted of measurements of electric current intensity **I**, the voltage **ΔV** and the self-potential (**SP**) of the Earth. **SP** is the potential difference measured between the potential electrodes M and N in the absence of any artificial current flow. This potential difference is due either to bioelectric activity in vegetation, varying electrolytic concentrations in ground water or to the flow of natural electric currents (telluric currents) within the Earth, which are induced by the varying magnetic field of the Earth as a result of various magnetospheric and ionospheric phenomena (Telford et al., 1981). **SP** was taken into account in each measurement of **I** and **ΔV**, by subtracting its value from the corresponding value of **ΔV**.

Application of equations (1)-(3) to the 12 VES data sets lead to the construction of an equal number of VES curves of apparent electrical resistivity versus AB/2 (Figure 3). The data processing of each VES was completed with the preparation of a one (1-D) dimensional geoelectric model (Figure 3) using JOINTEM, a geophysical modelling and interpretation software of EM and VES data made by Pirttijärvi (2014).

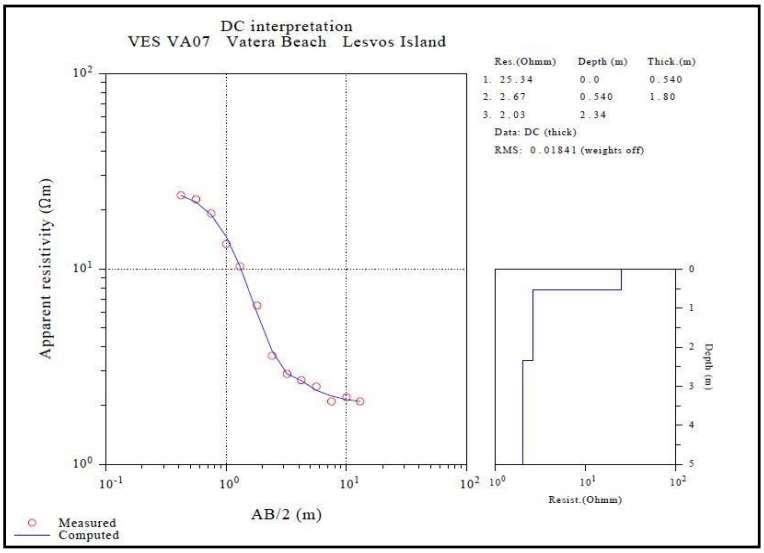

Figure 3 - Apparent electrical resistivity versus AB/2 and 1-D electrical model for VES7.

4. Results and Discussion

Appropriate combination of the derived 1-D models resulted in two geoelectric cross-sections showing the variation of the subsurface electrical resistivity with depth (Figure 4). Both geoelectric

cross-sections designate a similar subsurface electrical structure. The deepest common feature is a very low resitivity (0.5-2.0 ohm.m) geoelectric basement, whose thickness is 1-3m at Profile 1 and 1-5m at Profile 2. The depth to the top of the basement varies from sea level to ~4.5m below sea level. This figures the expected seawater intrusion, which has either filled the pores of the existing geological structures or has been mixed up with fresh water. In order to support the above interpretation with respect to the sea water - fresh water mixing the total dissolved salts (TDS) distribution below profile 1 is provided in figure 5.

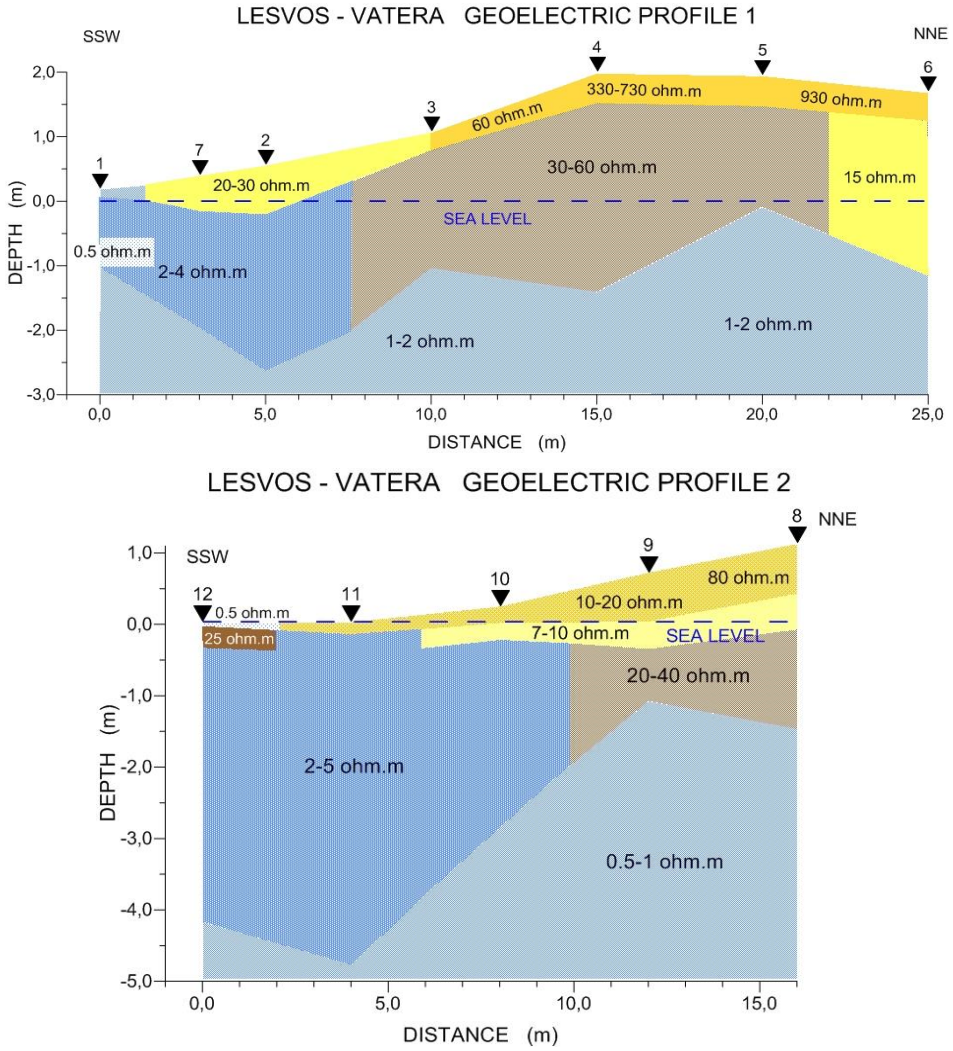

Figure 4 - Geoelectric cross sections compiled from 1-D models along Profile 1 (a) and Profile 2 (b).

The geoelectric basement is overlain by a less uniform and relatively more resistive (2.0-60.0 ohm.m) intermediate layer in both profiles, probably indicating a gradual decrease of the sea water content in the coastal aquifer. The main characteristic of this layer is the gradual, lateral increase in resistivity from 2.0 to 60.0 ohm.m at Profile 1 and 2.0-40.0 ohm.m at Profile 2, towards a NNE direction. The only difference is that at the NNE end of profile 1, the resistivity of this layer drops to 15.0 ohm.m, suggesting a different geoelectical formation that can be attributed to an alluvial-fluvial deposit, where fresh water content is most probably higher, also due to its geographical position, near the adjacent Armyropotamos river.

On top of this intermediate layer there is a surficial more resistive unit (10.0-900.0 ohm.m), which is also characterized by a gradual, lateral increase in electrical resistivity, towards the NNE. This feature is interpreted in terms of the expected gradual lateral decrease of the sand moisture that is more prominent along Profile 1, because of the more intense topography and the distance from the coastline.

Along profile 2, which is situated immediately next to a surface Br outcrop along the shoreline (at VES12), the following geoelectical characteristics are figured: (i) there is a 25.0ohm.m thin (0.35m) structure that is the subsurface extension of the adjacent Br outcrop, (ii) a 7-10.0 ohm.m geoelectric structure is observed to the NNE, which is believed to be the lateral extension of Br, sandwiched in between the surficial highly resistive unit and the intermediate layer, and (iii) the 7-10.0 ohm.m geoelectric structure has the same geometrical characteristics (thickness) and it is detected almost at the same elevation relative to the mean sea-level, with the observed Br.

The 25.0 ohm.m block underlies a 0.5 ohm.m surficial layer that correlates with the presence of a sea-water saturated, unconsolidated sand.

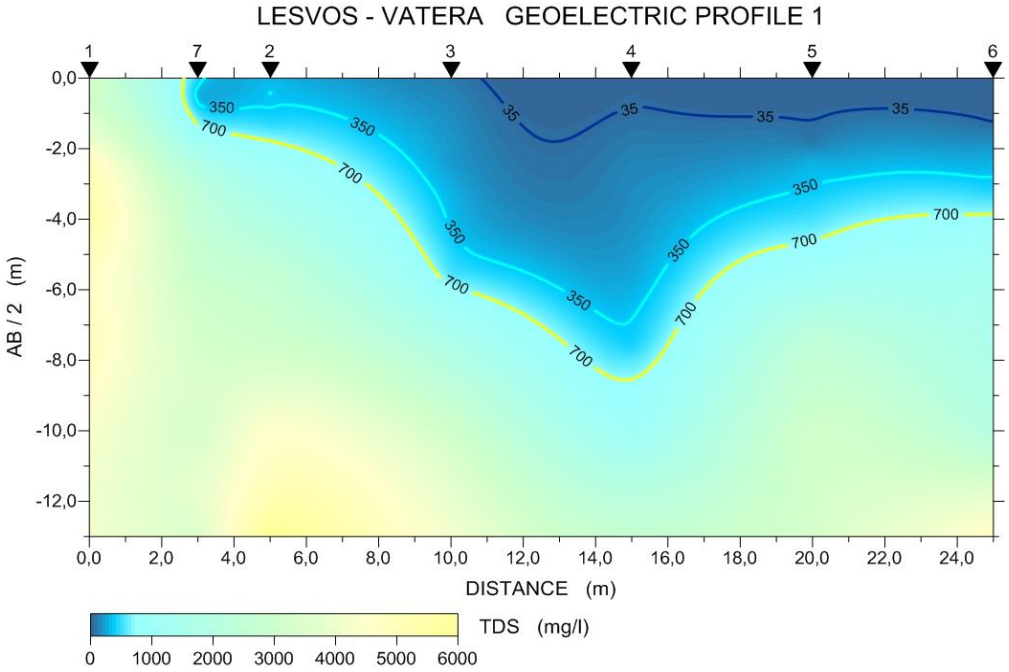

Figure 5 - Distribution of TDS as a function of AB/2, bellow profile 1.

Psomiadis *et al.* (2009) used electrical resistivity tomography for mapping the subsurface extend of Br between the villages Sotira and Kallirahi, in the western part of Thasos Island in Greece. The method gave reliable results in relation to in situ observations of the depth and dimensions of Br, which was identified with rather very low electrical resistivities of about 2-15 ohm.m. Kubo *et al.* (2013) employed both the DC resistivity and seismic methods to investigate Br on Yagaji Island in Japan, where it was found to have low electrical resistivities of about 4-40 ohm.m, small thickness of about 1m with a tendency to become thicker closer to the sea. During this survey in Vatera beach two thin formations with different geoelectrical characteristics, but being almost similar in thickness and in topographic level are attributed to Br of successive maturity stages. The submerged formation near the coastline, although limited in extent, has a uniform electrical resistivity value of 25ohm.m, whereas the buried formation towards the inner part of the beach has low electrical resistivity values (7-10 ohm.m), however within the range observed elsewhere (Psomiadis *et al.*, 2009; Kubo *et al.*, 2013) and probably resembles to a primary stage of Br build up. This hypothesis is supported by

Vousdoukas *et al*. (2007, figure 4 of that paper), who ground-truthed a buried beachrock, about 1000m besides profile 2, after mechanical removal of the overlying unconsolidated beach sediments. The surficial sediments had a wedge-shape, similar to those of profile 2, whereas the detected Br had a similar texture to that of the ambient sedimentary material.

Employment also of other geophysical methods (dipole-dipole geoelectric method, magnetic, seismics) together with geotechnical and geochemical testing of the different Br formations and monitoring in different seasons would support and verify the findings of successive stages of Br build up and extend.

5. References

Akintorinwa, O.J. and Abiola, O., 2012. Comparison of Schlumberger and modified Schlumberger arrays VES interpretation results, *Research Journal in Engineering and Applied Sciences*, 1(3), 190-196.

Arrieta, N., Iturregi, I., Martinez-Arkarazo, X., Murelaga, J.I., Baceta and Madariaga, J.M., 2011. Spectroscopic characterization of ferruginous cements in a temperate beachrock formation close to Nerbioi-Ibaizabal estuary (Tunelboka cove, Bay of Biscay), *CORALS II Conference*.

Back, W., Hanshaw, B.B., Plummer, L.N., Rahn, P.H., Rightmire, C.T. and Rubin, M., 1983. Process and rate of dedolomitization Mass transfer and 14C dating in a regional carbonate aquifer, *Geological Society of America Bulletin*, 94, 1415-1429.

Bernard, J., 2006. Training course on electrical methods, *IRIS instruments*, 1-29 pp.

Brattstrom, H., 1992. Marine biological investigations in the Bahamas. Littoral zonation at three Bahamian beachrock localities, *Sarsia*, 77, 81-109.

Caron, V., 2012. Geomorphic and Sedimentologic Evidence of Extreme Wave Events Recorded by Beachrocks: A Case Study from the Island of St. Bartholomew (Lesser Antilles), *Journal of Coastal Research*, 811-828.

Chandra, S., Anand Rao, V. and Singh, V.S., 2004. A combined approach of Schlumberger and axial pole-dipole configurations for groundwater exploration in hard-rock areas, *Current Science*, 86(10), 1437-1443.

Chowdhury, S.Q., Fazlul Haq, A.T.M. and Hasan, K., 1997. Beachrock in St. Martin's Island, Bangladesh: Implication of sea level changes on beachrock cementation, *Marine Geology*, 120, 89-104.

Cox, R.T., Lumsden, N.D., Gough, K., Lloyd, R. and Talnagi, J., 2008. Investigation of late Quaternary fault block uplift along the Motagua/Swan Islands fault system: Implications for seismic/tsunami hazard for the Bay of Honduras, *Tectonophysics*, 457, 30-41.

Danjo, T. and Kawasaki, S., 2014. Characteristics of Beachrocks: A Review, *Geotech. Geol. Eng*., 32, 215-246.

Erginal, A.E., Kiyak, N.G. and Ozturk, B., 2010. Investigation of beachrock using microanalyses and OSL dating: a case study from Bozcaada Island, Turkey, *Journal of Coastal Research*, 26(2), 350-358.

Galanopoulos, D. and Kolettis, G., 2005. Investigating the formation of a superficial fracture on Nisyros Island, Greece with the DC resistivity method. *In:* Fytikas, M. and Vougiougalakis, G., *eds.*, THE SOUTH AEGEAN ACTIVE VOLCANIC ARC, 7, Present Knowledge and Future Perspectives, *Developments in Volcanology*, 7, 227-240.

GeoFact, 2014. Geoelectrics, geoFact GmbH, Available online at: http://www.geofact.de/?page_id=110&language=en.

Kelletat, D., 2006. Beachrock as Sea-Level Indicator? Remarks from a Geomorphological Point of View, *Journal of Coastal Research*, 22(6), 1558-1564.

Kubo, R., Kawasaki, S., Suzuki, K., Yamaguchi, S. and Hatta, T., 2013. Beachrock mapping by geophysical exploration: Application to Yagaji Island in Okinawa, Japan. *Rock Mechanics for Resources, Energy and Environment*, Kwasniewski and Lydzba, *eds.*, Taylor & Francis Group, London, ISBN 978-1-138-00080-3.

Neumeier, U., 1999. Experimental modelling of beachrock cementation under microbial influence, *Sedimentary Geology*, 126(1-4), 35-46.

Pirttijärvi, M., 2014. Free Software from Markku Pirttijärvi, *Joint Inversion of EM and VES data*, Available online at: https://wiki.oulu.fi/pages/viewpage.action?pageId=20677943.

Psomiadis, D., Tsourlos, P. and Albanakis, K., 2009. Electrical resistivity tomography mapping of CS: application to the island of Thassos (N. Greece), *Environmental Earth Sciences*, 59(1), 233-240.

Rey, D., Rubio, B., Bernabeu, A.M. and Vilas, F., 2004. Formation, exposure, and evolution of a high-latitude beachrock in the intertidal zone of the Corrubedo complex (Ria de Arousa, Galicia, NW Spain), *Sedimentary Geology*, 169(1-2), 93-105.

Rutten, L.G., 2011. Interactions between beachrock formations and shoreline evolution. Case study: Togo, *Section for Geo-Engineering, Department of Applied Earth Sciences*, Delft University of Technology, The Netherlands.

Scoffin, T.P. and Stoddart, D.R., 1983. Beachrock and intertidal sediments. *In*: Goudie, A.S. and Pye, K., *eds*., Chemical Sediments and Geomorphology, *Academic Press*, London, 401-425.

Shinn, E.A., 2009. The Mystique of Beachrock, *IAS Special Publication*, 41, 19-28.

Telford, W.M., Geldart, L.P., Sheriff, R.E. and Keys, D.A., 1981. Applied Geophysics, Cambridge University Press.

Vousdoukas, M.I., Velegrakis, A.F. and Plomaritis, T.A., 2007. Beachrock occurrence, characteristics, formation mechanisms and impacts, *Earth-Science Reviews*, 85, 23-46.

Vousdoukas, M., Velegrakis, A. and Karambas, T., 2009. Morphology and sedimentology of a microtidal beach with beachrocks: Vatera, Lesbos, NE Mediterranean, *Continental Shelf Research*, 29(16), 1937-1947.

Δελτίο της Ελληνικής Γεωλογικής Εταιρίας, τόμος L, σελ. 2332-2341
Πρακτικά 14ου Διεθνούς Συνεδρίου, Θεσσαλονίκη, Μάιος 2016

Bulletin of the Geological Society of Greece, vol. L, p. 2332-2341
Proceedings of the 14th International Congress, Thessaloniki, May 2016

NATURAL RADIOACTIVITY OF WESTERN ANATOLIAN PLUTONS, TURKEY

Papadopoulos A.[1], Altunkaynak S.[2], Koroneos A.[1], Unal A.[2] and Kamaci O.[2]

[1]*Department of Mineralogy, Petrology and Economic Geology, School of Geology, Aristotle University of Thessaloniki, 541 24 Thessaloniki, Greece, koroneos@geo.auth.gr,* argpapad@geo.auth.gr

[2]*Department of Geological Engineering, Faculty of Mines, Istanbul Technical University, 34469 Maslak, İstanbul, Turkey, safak@itu.edu.tr, alp.unal@itu.edu.tr, kamaciom@itu.edu.tr*

Abstract

The natural radioactivity of the Western Anatolian plutonic bodies (Turkey), as well as the assessment of any potential health hazard due to their usage as decorative building materials is studied. Seventy samples from Western Anatolian plutonic bodies, including various rock-types from quartz-monzodiortie to syenogranite, have been measured for their natural radioactivity using γ-spectrometry. According to the experimental results the natural radioactivity levels were ranged up to 229.62 Bq.kg^{-1} for ^{226}Ra, up to 207.32 Bq.kg^{-1} for ^{232}Th and up to 2541.95 Bq.kg^{-1} for ^{40}K, with a mean value of 57.67 (±38.13), 80.30 (±42.00) and 1071.92 (±405.24) Bq.kg^{-1} respectively, which are below the international representative mean values for granite stones. The increment on the external γ-radiation effective dose rate appears a mean value of 0.27 (±0.19) mSv.y^{-1}, scattering below 1 mSv.y^{-1}. In case of the internal α-radiation a mean value of 0.14 (±0.10) mSv.y^{-1}, scattering below 0.5 mSv.y^{-1} was estimated. The majority of the samples increase the external and the internal dose less than 30% of the maximum permitted limit of the effective dose rate. Therefore, at least from radiological point of view, the plutonic rocks of Western Anatolia could be safely used as decorative building materials.

Keywords: *Building materials, External-Internal exposure, Radiation Index.*

Περίληψη

Εξετάζεται η φυσική ραδιενέργεια αξιολογούνται οι πιθανοί κίνδυνοι για την υγεία λόγω της χρήσης ως δομικών υλικών των πλουτωνικών πετρωμάτων της Δυτικής Ανταόλιας (Τουρκία). Εβδομήντα δείγματα από πλουτωνίτες της Δυτικής Ανατολίας συμπεριλαμβανομένων διαφόρων πετρογραφικών τύπων, από χαλαζιακό μονζοδιορίτη έως συηνογρανίτη, εξετάστηκαν για τα επίπεδα της φυσικής ραδιενέργειας, χρησιμοποιώντας γ-φασματοσκοπία. Σύμφωνα με τα αποτελέσματα, τα επίπεδα φυσικής ραδιενέργειας κυμαίνονται έως τα 229,62 Bq.kg^{-1} για το ^{226}Ra, έως 207,32 Bq.kg^{-1} για το ^{232}Th και έως 2541,95 Bq.kg^{-1} για το ^{40}K, με μέσες τιμές 57,67 (±38,13), 80,30 (±42,00) και 1071,92 (±405,24) Bq.kg^{-1} αντίστοιχα, τιμές που βρίσκονται κάτω από τις αντιπροσωπευτικές διεθνείς που αφορούν πλουτωνικά πετρώματα. Η αύξηση στην εξωτερική ισοδύναμη δόση γ-ακτινοβολίας εμφανίζει μια μέση τιμή 0,27 (±0,19) mSv.y^{-1}, αρκετά κάτω από το όριο του 1 mSv.y^{-1}. Στην περίπτωση της εσωτερικής δόσης από α-ακτινοβολία, η μέση τιμή των 0,14 (±0,10) mSv.y^{-1}, βρίσκεται επίσης αρκετά χαμηλότερα από το όριο του 0,5 mSv.y^{-1}. Η πλειονότητα των δειγμάτων αυξάνει την

εξωτερική και την εσωτερική δόση σε ποσοστό μικρότερο του 30% του μέγιστου επιτρεπόμενου ορίου της ισοδύναμης δόσης. Συνεπώς, τουλάχιστον από ραδιολογικής απόψεως, τα πλουτωνικά πετρώματα της Δυτικής Ανατολίας θα μπορούσαν να χρησιμοποιηθούν με ασφάλεια ως δομικά υλικά.
Λέξεις κλειδιά: *Δομικά υλικά, Εξωτερκή-Εσωτερική έκθεση, Δείκτης Ακτινοβολίας.*

1. Introduction

Plutonic rocks (gabbro to granite) are widely used as decorative building materials due to their durability and appearance. These rocks, due to their mineralogical composition, are likely to contain high concentrations of natural radionuclides. The purpose of setting controls on the radioactivity of building materials is to limit the radiation exposure due to materials with enhanced or elevated levels of natural radionuclides.

Several works present in the literature, are referred to radiation risks of granite used as decorative building material (Papadopoulos *et al.*, 2013 and references therein), while several authors have studied the natural radioactivity of plutonic bodies of Turkey e.g. Örgün *et al.* (2007). In the present work, the natural radioactivity of the major Western Anatolian plutonic bodies in Turkey as well as the assessment of any potential health hazard in case they were used as decorative building materials are studied.

2. Materials and Methods

2.1. Geological Setting

The Cenozoic geology of western Anatolia (Turkey) is characterized by intensive magmatic activity producing volcanic and plutonic rocks that can be used as decorative building materials (Fig. 1). Nature, origin and tectonic setting of these magmatic rocks have been studied in detail previously by various researchers (i.e. Yılmaz, 1989; Güleç, 1991; Altunkaynak and Yılmaz, 1998; Aldanmaz *et al.*, 2000; Okay and Satır, 2000, 2006; Köprübaşı and Aldanmaz, 2004; Altunkaynak and Dilek, 2006, Altunkaynak, 2007; Dilek and Altunkaynak, 2007; Altunkaynak and Genç, 2008; Boztuğ *et al.*, 2009; Ersoy *et al.*, 2009; Hasözbek *et al.*, 2010; Altunkaynak *et al.*, 2012a,b; Erkül and Erkül, 2012; Erkül, 2010).

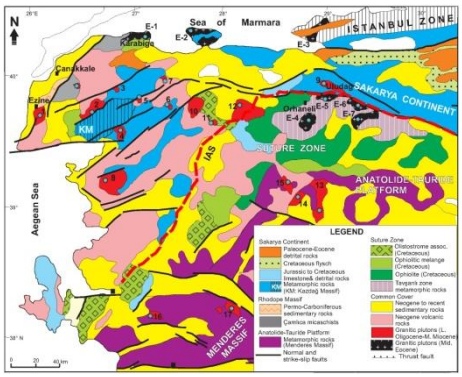

Figure 1 - Simplified geological map of western Anatolia showing the distribution of Granitoids (Modified from Yılmaz et al., 2000; Okay and Satır, 2006 and Altunkaynak et al., 2012a). IAS; Izmir-Ankara-Erzincan suture zone. E1 to 7: Eocene granitoids (E1: Karabiga, E2: Kapıdağ, E3: Fıstıklı, E4: Orhaneli, E5:Yopuk, E6:Göynükbelen, E7: Gürgenyayla), 1 to 15: Oligo-Miocene granitoids (1- Kestanbol 2-Evciler 3-Hıdırlar-Katrandag 4-Eybek 5-Yenice 6-Danisment, 7-Sarıoluk, 8-Kozak 9-Uludag 10, Ilica-Samli 11-Davutlar, 12-Çataldag 13-Egrigoz 14-Koyunaoba 15-Çamlik 16-Turgutlu 17-Salihli granitoids).

Western Anatolia and adjacent regions (Greece and Bulgaria) are situated along the eastern continuation of the Alpine collisional belt and are affected dominantly by convergent tectonics preceding current extensional tectonics. The final demise of the northern branch of Neo-Tethyan Ocean at a subduction zone dipping northwards beneath the Sakarya continent resulted in a continent-continent collision between the Sakarya and Anatolide-Tauride continental fragments during the Late Cretaceous-pre-Eocene. (Şengör and Yılmaz, 1981; Yılmaz, 1989; Güleç, 1991; Harris *et al.*, 1994). The Izmir-Ankara Suture Zone (IASZ) represents the collision zone between the Anatolide-Tauride platform (ATP) in the south and the Sakarya continent (SC) in the north.

Following the closure of the Neo-Tethyan Ocean, two major magmatic episodes producing granitic plutons occurred within the Cenozoic evolution of western Anatolia. The first episode of post-collisional magmatism developed during the early-late Eocene, and produced mainly medium to high-K calc-alkaline, I-type granitoid plutons and associated extrusive rocks (Harris *et al.*, 1994; Koprubasi and Aldanmaz, 2004; Altunkaynak, 2007; Altunkaynak *et al.*, 2012a). The Eocene granitic plutons occur within and north of the IASZ. Among these, Orhaneli, Topuk, Gürgenyayla plutons exposed along the IASZ and are intruded into the Cretaceous blueschist rocks and overlying ophiolitic units. They range in composition from quartz diorite, granodiorite to syenite. Kapıdağ, Fıstıklı (Armutlu), Karabiga plutons, on the other hand, crop out along the southern margin of the Marmara Sea. These plutons are intruded into the basement rocks of Sakarya continent north of the IASZ and are composed of monzogranite, granodiorite and granite. The Eocene granitic and volcanic rocks are rare and restricted to NW Anatolia. The following magmatic phase occurred during the late Oligocene and middle Miocene and is known to have produced the widespread granitic plutons (i.e., Kozak, Evciler, Cataldag, Kestanbol, Ilica, Eybek, Egrigoz, Çamlık, Uludağ) and volcanic rocks in western Anatolia (Yilmaz, 1989; Altunkaynak *et al.*, 2012b; Yilmaz, *et al.*, 2001; Ozgenc and Ilbeyli, 2008; Akay 2009). They are represented mostly by medium to high-K calc-alkaline to shoshonitic I-type granitic plutons emplaced into the continental blocks on both side of the IASZ. The Kozak, Evciler, Ilıca, Eybek, Çataldağ, granites are the representatives of the granites that were emplaced into the metamorphic basement rocks of the Sakarya continent. The Çamlık and Eğrigöz plutons, on the other hand, were emplaced into the Anatolide-Tauride Platform (i.e. the metamorphic rocks of the Menderes Massif). Late Oligocene- Middle Miocene granitoid plutons and associated volcanic rocks are widespread in the entire west Anatolia (Yılmaz, 1989; Altunkaynak and Dilek, 2006; Altunkaynak *et al.*, 2012b; Erkül and Erkül, 2012; Erkül, 2010). Most of the late Oligocene-middle Miocene granites are represented by caldera type, shallow level intrusions showing close relationships with their co-genetic volcanic rocks in time and space (Yılmaz, 1989; Altunkaynak and Yilmaz, 1998, 1999; Genç, 1998; Yılmaz *et al.*, 2001).

2.2. Gamma-ray spectroscopy

The measurements of activity concentrations were undertaken in Low Level Radioactivity Measurement Laboratory in the Istanbul Technical University Energy Institute by using copper lined lead shielding (10cm) detector (GAMMA-X HPGe coaxial n-type germanium detector, 45.7% efficiency and 1.84 keV full width at half maximum for 1.3 MeV of 60Co) with the integrated digital gamma spectrometer (DSPEC jr. 2.0). Statistical confidence level and range were adjusted to 2σ and 8K, respectively. In order to make the energy and efficiency calibration of the gamma spectroscopy system that are necessary for activity determination, the certificated multiple gamma ray emitting large volume source standard was used; including Am^{241}, Cs^{137}, Co^{60}, Pb^{210}, Cd^{109}, Co^{57}, Ce^{139}, Hg^{203}, Sn^{113}, Sr^{85}, Y^{88} radioisotopes in the sand matrix in Marinelli geometry as 500 mL volume, with a density of $1.7 g \cdot cm^{-3}$ and an activity of 1μCi. Samples and standard in Marinelli beakers were counted at the top of the detector. Counting times were adjusted to 15 to 24 h. Peak areas were determined by using GAMMA VISION-32 software program. After measurements, standards and samples were corrected for decay time and mass.

2.3. Major elements

The whole-rock powders were split from 1 to 5kg of crushed rocks. Chemical compositions of the samples were determined by using Spectro Ciros Vision ICP-ES for major oxides is given in Table 1.

Table 1 - Major element content (% w.t.) of the samples (*Altunkaynak *et al.*, 2012a, b).

	SiO_2	TiO_2	Al_2O_3	Fe_2O_3	MnO	MgO	CaO	Na_2O	K_2O	P_2O_5	LOI	Sum
AS209	65.17	0.47	15.41	4.45	0.08	1.96	4.08	3.23	3.68	0.19	0.90	99.62
AS211	67.09	0.40	15.42	3.82	0.10	1.54	3.90	3.45	3.11	0.15	0.70	99.68
AS234	65.31	0.47	15.20	4.56	0.09	2.09	4.56	3.33	3.13	0.21	0.70	99.65
AS236	64.26	0.49	15.94	4.42	0.08	2.08	4.43	3.37	3.67	0.19	0.70	99.63
AS238	63.00	0.50	16.60	4.88	0.10	1.95	4.82	3.59	2.94	0.22	1.10	99.70
AS239	62.42	0.57	15.84	5.42	0.11	2.68	5.01	3.42	2.91	0.18	1.10	99.66
AS240	62.71	0.52	16.16	4.78	0.10	2.25	4.51	3.38	3.18	0.16	1.90	99.65
AS241	62.40	0.53	16.64	5.07	0.10	2.30	5.39	3.44	2.75	0.20	0.80	99.62
AS245	62.75	0.56	16.21	5.33	0.10	2.64	5.13	3.37	2.89	0.16	0.50	99.64
AS248	63.51	0.50	16.08	4.77	0.09	2.21	4.65	3.46	3.07	0.17	1.20	99.71
ÇAT1	68.90	0.27	15.06	3.10	0.07	0.82	2.58	3.10	4.22	0.11	2.05	100.28
ÇAT2	74.51	0.03	13.68	0.63	0.16	0.05	1.08	4.43	3.56	< 0.01	0.70	98.83
ÇAT3	68.02	0.38	14.75	3.17	0.07	0.99	2.51	3.46	4.04	0.14	1.01	98.53
ÇAT4	67.68	0.35	15.49	3.25	0.09	0.77	3.36	4.08	2.94	0.17	0.70	98.87
ÇAT5	73.57	0.04	14.29	0.66	0.03	0.22	1.11	3.45	4.06	0.08	1.89	99.40
ÇAT6	77.25	0.04	13.58	0.45	0.02	0.11	0.82	3.76	3.92	0.06	0.86	100.88
OS388	73.34	0.22	15.10	1.71	0.04	0.43	2.09	3.90	3.17	0.07	1.01	101.08
OS409	72.64	0.09	14.88	0.80	0.01	0.19	1.12	3.63	5.37	0.09	1.10	99.92
ULU3	71.39	0.26	15.39	1.72	0.04	0.73	2.16	4.26	2.73	0.12	0.90	99.70
ULU5	71.08	0.27	15.65	1.56	0.02	0.52	1.75	3.97	3.63	0.11	1.10	99.66
ULU6	71.67	0.26	15.14	1.59	0.03	0.63	2.08	4.21	3.20	0.11	0.80	99.72
ULU8	71.91	0.23	15.30	1.37	0.03	0.48	1.82	4.08	3.41	0.10	1.00	99.73
ULU11	71.42	0.25	15.13	1.52	0.03	0.63	2.01	4.11	3.28	0.11	1.30	99.79
ULU12	72.03	0.24	15.25	1.44	0.03	0.50	1.36	3.96	3.91	0.13	0.90	99.75
EYB10	58.26	0.68	17.53	6.90	0.14	3.05	6.96	3.91	1.61	0.17	0.50	99.71
EYB14	60.41	0.69	16.22	6.50	0.13	3.00	5.39	3.75	2.17	0.14	1.30	99.70
EYB15	63.10	0.64	16.02	5.62	0.11	2.31	5.33	3.63	1.94	0.14	0.90	99.74
EYB24	61.18	0.52	17.21	5.19	0.11	1.80	4.48	4.80	1.49	0.12	2.80	99.70
EYB30	58.13	0.79	17.05	7.25	0.14	3.41	6.72	3.65	1.66	0.18	0.70	99.68
EYB34	60.73	0.66	16.72	6.28	0.13	2.40	5.33	3.76	2.09	0.15	1.40	99.65
EYB35	61.80	0.58	16.52	5.69	0.12	2.22	5.05	3.64	2.40	0.14	1.50	99.66
EYB38	61.19	0.66	16.52	6.14	0.12	2.60	5.67	3.67	2.01	0.15	1.00	99.73
KOZ1	66.01	0.42	16.09	3.61	0.06	1.58	3.50	3.62	3.40	0.16	1.20	99.65
KOZ2	63.04	0.53	16.08	4.32	0.07	2.29	4.38	3.47	3.58	0.22	1.70	99.68
KOZ4	64.60	0.51	15.62	4.02	0.07	2.27	4.05	3.35	3.77	0.20	1.10	99.56
KOZ5	71.44	0.29	14.47	2.14	0.05	0.64	2.16	3.59	4.15	0.09	0.60	99.62
KOZ8	65.32	0.51	15.73	4.00	0.07	2.18	3.98	3.41	3.84	0.21	0.40	99.65
KOZ9	64.19	0.50	16.18	4.14	0.07	2.21	4.16	3.53	3.90	0.22	0.50	99.60
KOZ10	65.63	0.49	15.37	3.94	0.07	2.14	3.83	3.27	3.85	0.21	0.80	99.60
EVC1	61.99	0.57	16.73	5.78	0.10	2.41	4.95	3.36	2.83	0.16	0.80	99.68
EVC2	64.06	0.49	15.94	4.90	0.11	1.95	4.47	3.37	2.87	0.13	1.50	99.79
EVC3	63.68	0.50	16.40	5.04	0.11	1.94	4.71	3.50	2.76	0.12	1.00	99.76
EVC5	65.38	0.44	15.43	4.28	0.10	1.94	4.03	3.22	3.77	0.17	0.90	99.66
EVC6	64.42	0.45	15.67	4.50	0.10	2.02	4.39	3.27	3.45	0.18	1.20	99.65

EVC8	66.69	0.41	15.12	1.69	0.06	2.14	4.80	4.01	0.47	0.16	4.20	99.75
ORH1	63.47	0.39	17.24	4.60	0.09	1.80	5.39	3.74	2.17	0.10	0.67	99.66
ORH3	63.81	0.38	17.44	4.29	0.09	1.66	5.16	4.01	1.98	0.12	0.71	99.64
ORH5	65.50	0.32	17.05	3.44	0.08	1.36	4.80	3.94	2.05	0.10	0.93	99.57
ORH6	64.93	0.37	16.59	2.76	0.06	0.77	2.00	4.77	6.42	0.12	1.08	99.87
KAP42	71.61	0.23	14.60	2.06	0.07	0.51	2.57	3.71	3.10	0.04	0.81	99.31
KAP43*	71.54	0.19	14.21	1.99	0.08	0.51	2.26	3.39	3.38	0.06	1.78	99.40
KAP45	64.18	0.50	16.83	4.78	0.10	1.84	5.12	3.54	2.15	0.10	0.48	99.64
KAP46	63.43	0.51	16.19	4.76	0.09	2.25	4.83	3.43	3.16	0.16	0.80	99.61
KAP47*	63.30	0.61	16.15	5.43	0.13	2.01	5.11	3.14	2.12	0.11	0.85	98.97
KAP52*	69.17	0.27	16.02	2.43	0.07	0.53	3.41	4.39	2.30	0.07	0.62	99.27
CAM28*	71.99	0.21	14.35	1.86	0.06	0.59	1.77	3.29	4.12	0.09	1.21	99.56
CAM29*	68.63	0.31	15.40	2.91	0.04	1.01	2.61	2.52	5.07	0.17	0.64	99.32
CAM30*	65.20	0.44	16.66	4.00	0.05	1.50	3.75	3.68	3.26	0.25	0.80	99.59
TOP9	64.55	0.38	16.59	4.34	0.14	1.40	5.26	3.77	1.88	0.12	0.67	99.09
TOP11	66.49	0.34	16.83	3.67	0.11	0.99	4.93	3.99	1.73	0.11	0.44	99.64
TOP12	67.37	0.29	16.44	3.32	0.10	1.05	4.37	3.38	2.71	0.08	0.70	99.81
TPL1	61.16	0.60	16.79	5.73	0.13	2.15	5.41	4.18	1.89	0.16	0.92	99.12
TPL13*	70.20	0.28	14.51	2.60	0.08	0.92	2.73	4.27	3.50	0.05	0.61	99.75
TPL14	54.94	0.76	17.37	7.39	0.15	4.52	8.63	3.42	1.19	0.16	0.89	99.42
GÜR18*	64.00	0.48	16.00	4.89	0.12	1.99	4.97	3.77	2.40	0.10	1.13	99.84
GÜR19	64.23	0.38	17.24	4.58	0.11	1.56	5.14	3.72	1.96	0.12	0.70	99.74
GÜR20*	64.10	0.42	16.38	4.47	0.12	1.70	4.96	3.70	1.97	0.13	1.13	99.08
EGR23	66.72	0.53	15.62	4.03	0.09	1.35	3.51	3.52	3.53	0.15	0.70	99.75
EGR24*	69.73	0.36	14.57	2.68	0.06	0.82	2.29	4.06	3.97	0.10	0.77	99.41
EGR27*	67.84	0.45	15.18	3.17	0.07	1.03	2.94	3.45	3.89	0.12	1.06	99.19

2.4. Rock-types and mineralogical composition

As shown in Fig. 2, a variety of rock-types, from quartz monzodiorite to syenogranite has been studied. These may contain hornblende, biotite and muscovite as major mineral phases. The accessory minerals present are zircon, apatite, titanite, allanite and epidote.

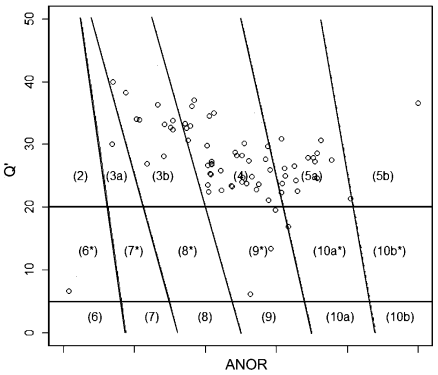

Figure 2 - Q'ANOR diagram (Streckeisen and Le Maitre, 1979) showing the classification of the samples. (2 Alkali-feldspar granite, 3a Syenogranite, 3b Monzogranite, 4 Granodiorite, 5a Tonalite, 5b Calcic Tonalite, 6* Alkali-feldspar Quartz-Syenite, 7* Quartz Syenite, 8* Quartz Monzonite, 9* Quartz Monzodiorite, 10a* Quartz diorite, 10b* Quartz Gabbro, 6 Alkali-feldspar Syenite, 7 Syenite, 8 Monzonite, 9 Monzogabbro, 10a Diorite, 10b Gabbro.

3. Results

3.1. Radiation indices and dose estimations

For each pluton of the Western Anatolia studied, the average values of the specific activities of ^{226}Ra, ^{232}Th and ^{40}K ($Bq{\cdot}kg^{-1}$), the external gamma index, the internal alpha index and the effective dose rate ($mSv{\cdot}y^{-1}$) received indoors and outdoors due to the usage of the studied samples as decorative building materials are given in Table 2.

Table 2 - ^{226}Ra, ^{232}Th and ^{40}K ($Bq.kg^{-1}$), I_γ, I_α, H_{ext} and H_{int} ($mSv.y^{-1}$) values.

		^{226}Ra	^{232}Th	^{40}K	I_γ	I_α	H_{ext}	H_{int}
AVERAGE	**Ilıca**	67.05	106.19	1210.22	1.16	0.34	0.33	0.17
MIN		33.01	0.12	854.58	0.40	0.17	0.16	0.09
MAX		100.58	185.66	1998.43	1.93	0.50	0.49	0.26
N		10						
AVERAGE	**Çataldağ**	108.18	101.16	1344.76	1.31	0.54	0.53	0.28
MIN		39.07	23.76	772.27	0.51	0.20	0.19	0.10
MAX		229.62	158.98	1894.11	2.19	1.15	1.13	0.60
N		8						
AVERAGE	**Uludağ**	74.86	77.80	1072.50	1.00	0.37	0.37	0.19
MIN		57.37	63.90	914.15	0.82	0.29	0.28	0.15
MAX		92.96	99.30	1235.47	1.22	0.46	0.46	0.24
N		6						
AVERAGE	**Eybek**	35.48	53.51	680.78	0.61	0.18	0.17	0.09
MIN		b.d.l.	35.40	462.73	0.43	0.14	0.14	-
MAX		42.93	70.10	811.71	0.76	0.21	0.21	0.11
N		7						
AVERAGE	**Kozak**	59.95	106.26	1267.88	1.15	0.30	0.29	0.16
MIN		b.d.l.	87.12	1153.13	0.98	0.24	0.24	-
MAX		86.31	131.11	1498.80	1.44	0.43	0.42	0.22
N		6						
AVERAGE	**Evciler**	61.92	107.00	874.26	1.03	0.31	0.30	0.16
MIN		b.d.l.	70.52	141.97	0.54	0.21	0.21	-
MAX		83.96	135.43	1261.58	1.38	0.42	0.41	0.22
N		6						
AVERAGE	**Orhaneli**	40.87	74.26	1192.70	0.91	0.20	0.20	0.11
MIN		15.26	27.57	704.81	0.42	0.08	0.07	0.04
MAX		116.58	207.32	2541.95	2.27	0.58	0.57	0.30
N		4						
AVERAGE	**Kapıdağ**	28.40	38.66	885.71	0.58	0.14	0.14	0.07
MIN		11.76	14.13	372.76	0.23	0.06	0.06	0.03
MAX		61.75	57.59	1385.18	0.96	0.31	0.30	0.16
N		6						
AVERAGE	**Çamlık**	66.54	67.62	1338.40	1.01	0.33	0.33	0.17
MIN		b.d.l.	59.61	1011.72	0.86	0.33	0.33	-
MAX		66.54	73.82	1597.66	1.12	0.33	0.33	0.17
N		3						
AVERAGE	**Topuk**	37.48	56.62	834.54	0.69	0.19	0.18	0.10
MIN		18.46	36.16	647.67	0.46	0.09	0.09	0.05
MAX		56.51	71.35	956.47	0.86	0.28	0.28	0.15

		^{226}Ra	^{232}Th	^{40}K	I_γ	I_α	H_{ext}	H_{int}
N		3						
AVERAGE	**Tepeldağ**	16.75	79.40	1180.81	0.85	0.08	0.08	0.04
MIN		b.d.l.	18.05	414.65	0.27	0.06	0.05	0.03
MAX		22.49	143.81	1768.80	1.38	0.11	0.11	0.06
N		3						
AVERAGE	**Gürgenyayla**	23.69	33.07	662.47	0.47	0.12	0.12	0.06
MIN		21.64	19.96	532.84	0.35	0.11	0.11	0.06
MAX		25.74	41.10	863.33	0.58	0.13	0.13	0.07
N		3						
AVERAGE	**Eğrigöz**	41.64	76.66	1346.05	0.97	0.21	0.20	0.11
MIN		33.93	66.55	1205.92	0.85	0.17	0.17	0.09
MAX		49.15	95.08	1484.57	1.13	0.25	0.24	0.13
N		3						

According to the experimental results, the natural radioactivity levels were ranged up to 229.62Bq.kg^{-1} for ^{226}Ra, up to 207.32Bq.kg^{-1} for ^{232}Th and up to 2541.95Bq.kg^{-1} for ^{40}K, with a mean value of 57.67 (±38.13), 80.30 (±42.00) and 1071.92 (±405.24)Bq.kg^{-1} respectively. Comparing the activities of ^{226}Ra and ^{232}Th of the samples analyzed with the average granite concentrations (UNSCEAR 2000), it can be seen that the activities of the majority of the samples studied are below the average values of 78 and 111Bq.kg^{-1} in most cases (Table 2). Consequently, the granites studied are be competitive to the commercial granites worldwide. A radiological study, concerning radiation index and dose estimation is required in order to strengthen the above conclusion.

Aiming to protect the public from excessive exposure to radioactivity, various radioactivity indices have been proposed in order to assess the natural radioactivity of building materials. Radionuclides in building materials are the sources of both external exposure due to gamma-rays emitted by ^{40}K, ^{226}Ra and ^{232}Th as well as internal exposure caused by alpha-particles deposited on the respiratory tract tissues due to inhalation of radon indoors. Indoors environment is generally described by a standard room model. Three typical room models have been adopted up to now, (a) a parallelepiped room (4x5x2.8m) with wall density 2350kg.m^{-3} and thickness 0.2m; (b) a spherical shell with radius 2.7m, peripheral thickness 0.223 m and density 1890 kg.m^{-3}, and (c) a hole surrounded by an infinite thickness medium (Krisiuk *et al.*, 1971; Stranden, 1979; Koblinger, 1984). In the present study the indices adopted by the European Commission (E.C., 1999) were applied considering a standard parallelepiped room model with no doors and windows. Taking into account that the external exposure due to the building materials has a limit of 1 mSv.y^{-1} then the following formula of external gamma index (I_γ) is calculated as:

$$I_\gamma = \frac{C_{Ra}}{300 Bq.kg^{-1}} + \frac{C_{Th}}{200 Bq.kg^{-1}} \frac{C_K}{3000 Bq.kg^{-1}} \quad (1)$$

Materials having I_γ<2 would increase the annual effective dose by 0.3mSv, while for 2<I_γ<6, the gamma-ray index corresponds to an increase in effective dose by 1mSv·y^{-1}. Building materials used superficially rather than in bulk amounts should be exempted from all restrictions concerning radioactivity, if the excess of gamma radiation originating from them increases the annual effective dose of a member of the public by 0.3mSv at the most. On the other hand, dose rates higher than 1mSv.y^{-1} are allowed only in exceptional cases, where materials are locally used. Finally, samples with I_γ>6 cannot be recommended for use in buildings (E.C., 1999). In case of internal alpha radiation exposure the following formula has been applied, taking into consideration that a building material with ^{226}Ra concentration lower than 200 Bq.kg^{-1} could not cause indoor radon concentration higher than 200 Bq.m^{-3}, which is the recommended action level of indoor radon exposure by EU and ICRP for dwellings (E.C., 1990; ICRP, 1994; Righi and Bruzzi, 2006).

$$I_\alpha = \frac{C_{Ra}}{200 Bq.kg^{-1}} \leq 1 \quad (2)$$

The index factors estimated above, correspond to a standard room with massive granitic walls and could be applied more to workers in a well-ventilated granite mine than inhabitants. For the estimation of the actual dose received annually indoors, due to granite tiles usage, a more realistic case has to be considered where granite tiles with ~2 cm in thickness cover only the floor of the standard room (Anjos *et al.*, 2005, 2011; Salas *et al.*, 2006; Mao *et al.*, 2006). In this case, the absorbed gamma dose rate (D_a, $nGy.h^{-1}$), denoted as the energy transfer rate by ionizing radiation absorbed per unit mass of the tissue, due to granite floor could be calculated as:

$$D_a(nGy.h^{-1}) = 0.172 \cdot C_{Ra} + 0.217 \cdot C_{Th} + 0.015 \cdot C_K \quad (3)$$

where C_{Ra}, C_{Th} and C_K are the activity concentrations ($Bq.kg^{-1}$) of ^{226}Ra, ^{232}Th and ^{40}K in the samples. Then, taking into account the indoor occupancy factor (T, 7000 $h.y^{-1}$), which implies that 80% of time is spent indoors, and the doses conversion factor (F, 0.7 $Sv.Gy^{-1}$), the increment of the effective dose rate due to gamma radiation received indoors derives as follows:

$$H_{ext}(mSv.y^{-1}) = 10^{-6} \cdot (0.7 \cdot C_{Ra} \cdot 7000) \quad (4)$$

The effective dose rate due to radon exposure indoors is estimated as:

$$H_{\text{int}}(mSv.y^{-1}) = 10^{-3} \cdot (f_{P-eq} \cdot D_c \cdot B \cdot F \cdot C_{Rn}) \quad (5)$$

where C_{Rn} is the radon concentration indoors ($Bq.m^{-3}$), F is the appropriate equilibrium factor between radon and its daughters, $f_{p\text{-}eq}$ is the conversion factor from equilibrium equivalent radon concentration ($F \cdot C_{Rn}$) to potential alpha energy concentration ($5.56.10^{-9}$ $J.m^{-3}$ per $Bq.m^{-3}$), D_c is the conversion factor from potential alpha energy concentration to the effective dose (2 Sv/J), and B is the annual breathing rate (7013 $m^3.y^{-1}$). For a well ventilated room the equilibrium factor F ranges from 0.5 to 0.7, hence using equation (5) results in 1 $Bq.m^{-3}$ of radon which corresponds to an effective dose rate 0.039 - 0.055 $mSv.y^{-1}$ due to alpha radiation (ICRU, 1994; E.C., 1990).

The radon concentrations indoor due to radon exhalation from the granitic floor existing in the room can be determined by the following formula:

$$C_{Rn}(Bq.m^{-3}) = \frac{(1/2) \cdot C_{Ra} \cdot \varepsilon \cdot \lambda \cdot \rho \cdot d \cdot S}{V \cdot (\lambda_v + \lambda)} \quad (6)$$

Considering the parallelepiped standard room with ventilation rate λ_v=1h^{-1} (that corresponds to an equilibrium factor F=0.7) and the floor covered by granite tiles with 1.5cm in thickness (d), 2650$kg.m^{-3}$ density (ρ) and 8% emanation factor (ε) as representative values, the internal effective dose rate is calculated as: (Bruzzi *et al.*, 1992; Stoulos *et al.*, 2003; Anjos *et al.*, 2011):

$$H_{\text{int}}(mSv.y^{-1}) = 0.0026 \cdot C_{Ra} \quad (7)$$

The range, standard deviation, standard error, average and median values of I_γ, I_α, H_{ext} and H_{int} for each of the Western Anatolian plutons studied are given in Fig. 2.

4. Conclusions

The excess on the effective dose received annually indoors due to granite tiles usage is estimated considering a standard room model where granite tiles with few cm in thickness cover only the floor of the room. The increment on the external γ-radiation effective dose rate appears a mean value of 0.27 (± 0.19) $mSv.y^{-1}$, scattering well below 1 $mSv.y^{-1}$. In case of the internal α-radiation a mean value of 0.14 (± 0.10) $mSv.y^{-1}$, scattering below 0.5 $mSv.y^{-1}$ has been found. The majority of the granite samples increase the external as well as the internal dose less than 30% of the maximum permitted limit of the effective dose rate. Only one sample from Cataldag pluton seems to exceed the effective dose received outdoors and indoors. Moreover, Cataldag pluton shows the highest average activities of radionuclides and thus, values of radioactive indices. Therefore, at least from radiological point of view, the majority of granitic rocks studied could be safely used as decorative building materials.

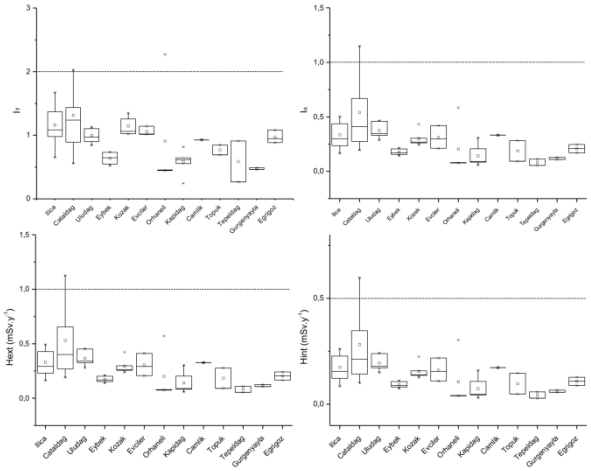

Figure 2 – I_{γ}, I_{α}, H_{ext} and H_{int} values of the samples studied for each Western Anatolian pluton. (The box corresponds to the standard error while the whisker to the standard deviation). X: max and min values, black star: mean value, dashed lines: permitted limits.

5. Acknowledgments

This study has been funded by grants from the Istanbul Technical University (BAP Project No: 37883 and 36010) and the Turkish Research Council (TUBITAK-CAYDAG-112Y093) that are gratefully acknowledged.

6. References

Akay, E., 2009. Geology and Petrology of the Simav Magmatic Complex (NW Anatolia) and its comparison with the Oligo-Miocene granitoids in NW Anatolia: implications on Tertiary tectonic evolution of the region, *Int. J. Earth Sci.* (GeolRundsch), 98, 1655-1675.

Aldanmaz, E., Pearce, J., Thirlwall, M.F. and Mitchell, J., 2000. Petrogenetic evolution of late Cenozoic, post-collision volcanism in western Anatolia, Turkey, *J. Volcanol. Geoth. Res.*, 102, 67-95.

Altunkaynak, Ş., 2007. Collision-driven slab breakoff magmatism in northwestern Anatolia, Turkey, *J. Geol.*, 115, 63-82.

Altunkaynak, Ş. and Yılmaz, Y., 1998. The Kozak magmatic complex; western Anatolia, *J. Volcanol. Geoth. Res.*, 85/1-4, 211-231.

Altunkaynak, Ş. and Dilek, Y., 2006. Timing and nature of post collisional volcanism in Western Anatolia and Geodynamic Implications. *In*: Dilek, Y. and Pavlides, S., *eds*., Post-Collisional Tectonics and Magmatism of the Eastern Mediterranean Region, *Geological Society of America Special Paper*, 409, 321-351.

Altunkaynak, Ş. and Genç, Ş.C., 2008. Petrogenesis and time-progressive evolution of the Cenozoic continental volcanism in the Biga Peninsula, NW Anatolia (Turkey), *Lithos*, 102, 316-340.

Altunkaynak, S., Dilek, Y., Genç, S.C., Sunal, G., Gertisser, R., Furnes, H., Foland, K.A. and Yang, J., 2012a. Spatial, temporal and geochemical evolution of OligoMiocene granitoid magmatisin western Anatolia, Turkey, *Gondwana Res.*, 21 (2012A), 961-986.

Altunkaynak, S., Sunal, G., Aldanmaz, E., Genç, S.C., Dilek, Y., Furnes, H., Foland, K.A., Yang, J. and Yıldız, M., 2012b. Eocene Granitic Magmatism in NW Anatolia (Turkey) revisited: New implications from comparative zircon SHRIMP U-Pb and 40Ar-39Ar geochronology and isotope geochemistry on magma genesis and emplacement, *Lithos*, 155, 289-309.

Anjos, R.M, Veiga, R., Soares, T., Santos, A.M.A, Aguiar, J.G., Frasca, M.H.B.O., Brage, J.A.P., Uzeda, D., Mangia, L., Facure, A., Mosquera, B., Carvalho, C. and Gomes, P.R.S., 2005. Natural radionuclide distribution in Brazilian commercial granites, *Rad. Measur.*, 39, 245-253.

Anjos, R.M., Ayub, J.J., Cid, A.S., Cardoso, R. and Lacerda, T., 2011. External gamma-ray dose rate and radon concentration in indoor environments covered with Brazilian granites, *J. Envir. Radioact.*, 102,1055-1061.

Boztuğ, D., Harlavan, Y., Jonckheere, R., Can, I. and Sarı, R., 2009. Geochemistry and K-Ar cooling ages of the Ilıca, Cataldag (Balıkesir) and Kozak (Izmir) granitoids, west Anatolia, Turkey.

Dilek, Y. and Altunkaynak, Ş., 2007. Cenozoic crustal evolution and mantle dynamics of post-collisional magmatism in western Anatolia, *Int. Geol. Rev.*, 49(5), 431-453.

Erkül, F., 2010. Tectonic significance of synextensional ductile shear zones within the Early Miocene Alaçamdağ granites, northwestern Turkey, *Geol. Mag.*, 147, 611-637.

Erkül, S.T. and Erkül, F., 2012. Magma interaction processes in syn-extensional granitoids: The Teriary Menderes Metamorphic Core Complex, western Turkey, *Lithos*, 142-143, 16-33.

Ersoy, Y.E., Helvacı, C. and Palmer, M.R. Petrogenesis of the Neogene volcanic units in the NE-SW-trending basins in western Anatolia, Turkey, *Contrib. to Mine and Petrol.*, 163, 379-401.

European Commission (E.C.), 1999. Radiation Protection 112: Radiological Protection Principles Concerning the Natural Radioactivity of Building Materials Directorate -General Environment, Nuclear Safety and Civil Protection.

Genç, Ş.C. and Yılmaz, Y., 1997. An example of post-collisional magmatism in northwestern Anatolia: the Kizderbent Volcanics (Armutlu Peninsula, Turkey), *Turk. J. Earth. Sci.*, 6, 33-42.

Güleç, N., 1991. Crust-mantle interaction in western Turkey: implications from Sr and Nd isotope geochemistry of Tertiary and Quaternary volcanics, *Geol. Mag.*, 23, 417-435.

Harris, N.B.W., Kelley, S. and Okay, A.I., 1994. Post-collisional magmatism and tectonics in northwest Anatolia, *Contrib. to Mine and Petrol.*, 117, 241-252.

Hasözbek, A., Satır, M., Erdoğan, B., Akay, E. and Siebel W., 2010. Early Miocene post-collisional magmatism in NW Turkey: geochemical and geochronological constraints, *Int. Geol. Rev.*, 1-22.

Köprübaşı, N. and Aldanmaz, E., 2004. Geochemical constraints on the petrogenesis of Cenozoic I-type granitoids in Northwest Anatolia, Turkey: Evidence for magma generation by lithospheric delamination in a post-collisional setting, *Int. Geol. Rev.*, 46, 705-729.

Mao, Y., Liu, Y., Fu, Y. and Lin, L., 2006. Physical models and limits of radionuclides for decorative building materials, *Health Physics*, 90, 471-476.

Okay, A.I. and Satır, M., 2000. Coeval plutonism and metamorphism in a latest Oligocene metamorphic core complex in northwest Turkey, *Geol. Mag.*, 137, 495-516.

Okay, A.I. and Satır, M., 2006. Geochronology of Eocene plutonism and metamorphism in northwest Turkey: evidence for a possible magmatic arc, *Geodin. Acta*, 19(5), 251-266.

Özgenç, İ. and İlbeyli, N., 2008. Petrogenesis of the Late Cenozoic Eğrigöz Pluton in Western Anatolia, Turkey: implications for magma genesis and crustal processes, *Int. Geol. Rev.*, 50, 375-391.

Papadopoulos, A., Christofides, G., Koroneos, A., Papadopoulou, L., Papastefanou, C. and Stoulos, S., 2013. Natural radioactivity and radiation index of the major granitic plutons in Greece, *J. Envir. Radioact.*, 124, 227-238.

Streckeisen, A. and Le Maitre, R.W., 1979. A chemical approximation to the modal QAPF classification of the igneous rocks, Egypt, *Neues Jahrb. Mineral Abh.*, 136, 169-206.

Salas, H.T, Nalini Jr, H.A. and Mendes, J.C., 2006. Radioactivity dosage evaluation of Brazilian ornamental granitic rocks bases on chemical data, with mineralogical and lithological characterization, *J. Radioanal. Nucl. Chem.*, 267, 669-673.

Şengör, A.M.C. and Yılmaz, Y., 1981. Tethyan evolution of Turkey: a plate tectonic approach, *Tectonophysics*, 75, 181-241.

UNSCEAR, 2000. United Nations Scientific Committee on the Effects of Atomic Radiation. Sources and Effects of Ionising Radiation, Vol. I. United Nations, New York.

Yılmaz, Y., 1989. An approach to the origin of young volcanic rocks of western Turkey. *In*: Şengör, A. M. C., *eds.*, Tectonic evolution of the Tethyan region: The Hague, Kluwer Academic, 159-189.

Yılmaz, Y., Genç, Ş.C., Gürer, O.F., Bozcu, M., Yılmaz, K., Karacik, Z., Altunkaynak, Ş. and Elmas, A., 2000. When did the western Anatolian grabens begin to develop? *In*: Bozkurt, E., Winchester, J.A. and Piper, J.A.D., *eds*., Tectonics and Magmatism in Turkey and the Surrounding Area, Geological Society, London, Special Publication, 173, 353-384.

Δελτίο της Ελληνικής Γεωλογικής Εταιρίας, τόμος L, σελ. 2342-2351
Πρακτικά 14ου Διεθνούς Συνεδρίου, Θεσσαλονίκη, Μάιος 2016

Bulletin of the Geological Society of Greece, vol. L, p. 2342-2351
Proceedings of the 14th International Congress, Thessaloniki, May 2016

GEOCHEMICAL MODELING OF ABANDONED SULFIDIC FLOTATION MILL TAILINGS: THE CASE OF KIRKI, NE GREECE

Triantafyllidis S.

National Technical University of Athens, School of Mining and Metallurgical Engineering, 157 80, Zografou, Athens, Greece, striantafyllidis@metal.ntua.gr

Abstract

The Kirki flotation plant is located approximately 5 km south of the Agios Filippos open pit mine (Thrace, NE Greece), and unconfined mill tailings are exposed to atmospheric conditions. Rain water accumulates on the surface of the tailings and interacts with the solids, resulting in highly acidic and oxidative surface solutions with increased heavy metal content. The tailings material is dominated by gangue minerals with very low acid buffering capacity, including quartz, kaolinite/dickite, pyrophyllite and minor orthoclase. Secondary phases identified include mainly species of the jarosite group, gypsum and anglesite. No primary ore minerals besides pyrite are identified. The finegrained character of the tailings material favors fast reactions between the surface waters and the solids. The speciation/mass transfer computer code PHREEQC-2 and the MINTEQ database were employed for geochemical modeling of the acidic surface waters of the tailings dams T1 and T2. Three different scenarios were employed, "Direct Precipitation", "Mixing with Rainwater" and "Evaporation" to check the equilibrium between the developed surface solutions and the secondary minerals identified in the tailings. The purpose of this work is to understand the way heavy metals may be locked to the lattice of secondary minerals, or dispersed/dissolved after dissolution of unstable secondary phases.
Keywords: *Acidic surface waters, secondary minerals, geochemical modelling.*

Περίληψη

Το εργοστάσιο εμπλουτισμού της Κίρκης εντοπίζεται περίπου 5 km νότια του μεταλλείου του Αγίου Φιλίππου. Τα απορρίμματα της επεξεργασίας του μεταλλεύματος είναι εκτεθειμένα στις ατμοσφαιρικές συνθήκες, με αποτέλεσμα τη συσσώρευση μετεωρικού νερού στην επιφάνειά τους. Τα επιφανειακά ρευστά αλληλεπιδρούν με το λεπτόκοκκο υλικό με υψηλό φορτίο βαρέων μετάλλων, με τελικό αποτέλεσμα τη δημιουργία όξινων και οξειδωτικών διαλυμάτων με υψηλό φορτίο μετάλλων στην επιφάνεια των απορριμμάτων. Τα απορρίμματα της επεξεργασίας αποτελούνται κυρίως από σύνδρομα ορυκτά της μεταλλοφορίας (χαλαζίας, δικίτης/καολινίτης, πυροφυλλίτης και άστριοι), ενώ τα κυριότερα δευτερογενή ορυκτά που εντοπίζονται αφορούν ορυκτά της ομάδας του γιαροσίτη, γύψο και αγκλεσίτη. Μοναδική πρωτογενής φάση της μεταλλοφορίας που εντοπίζεται στα απορρίμματα είναι ο σιδηροπυρίτης. Ο λεπτόκοκκος χαρακτήρας των απορριμμάτων της επεξεργασίας ευνοεί ταχύτατες αντιδράσεις μεταξύ των επιφανειακών ρευστών με το υλικό των απορριμμάτων. Το γεωχημικό πρόγραμμα PHREEQC, με χρήση της βάσης δεδομένων MINTEQ, εφαρμόσθηκε για τη διερεύνηση της λειτουργίας του συστήματος «επιφανειακό διάλυμα - δευτερογενή ορυκτά», με την

ανάπτυξη τριών διαφορετικών μοντέλων, «Άμεση Καθίζηση», «Ανάμιξη με Μετεωρικό Νερό» και «Εξάτμιση». Σε κάθε μοντέλο εξετάζεται ο μηχανισμός με τον οποίο βαρέα μέταλλα δεσμεύονται στο πλέγμα δευτερογενών ορυκτών, αλλά και αποδεσμεύονται/διαλυτοποιούνται μετά από διαλυτοποίηση μετασταθών φάσεων.
Λέξεις κλειδιά: *Όξινα επιφανειακά νερά, δευτερογενή ορυκτά, γεωχημικό μοντέλο.*

1. Introduction

A major issue the mining industry faces is the safe disposal of ore processing waste or tailings. Tailings are defined as the processing waste from a mill, washery or concentrator where the economic metals or minerals from the mined resource are removed (Lottermoser, 2010). During the early years of ore exploitation, the produced processing wastes were usually dumped in nearby streams or creeks without consideration of their environmental impact (Plumlee and Logsdon, 1999). In recent years and following processing, the tailings are usually disposed as slurry or paste to certain facilities and present unique environmental and physical characteristics. Mill tailings originating form sulfide ores present challenges namely because of the high oxidation potential of sulfides remaining in the tailings (Fergusson, 1990; Larsen *et al.*, 2001; Lacal *et al*., 2003) and possible generation of Acid Rock Drainage (ARD). The flow of meteoric water over sulfidic tailings may further increase the potential for metal leaching from tailings due to the fine to very fine-grained character of the tailings material (Mohamed *et al*., 2002) but also due to dissolution of heavy-metal bearing secondary phases that develop at the surface and near the surface of the tailings (Wray, 1998). Therefore, abandoned mine waste disposal sites containing sulfide minerals may pose significant environmental threats and may severely contaminate surface and groundwater as well as soils and ecosystems (Bigham and Nordstrom, 2000; Draves and Fox, 1998; Groudev *et al.* 1999; Hudson-Edwards *et al.*, 2003; Komnitsas *et al.* 1998; Adam, 2003).

2. Site description

The Kirki (Agios Filippos) high sulfidation deposit is hosted into the Eocene-Oligocene rock sequences of SE Evros county and is associated with orogenic calc-alkaline to high-potassium calc-alkaline magmatism. The epithermal mineralization is developed between two sub-parallel fault zones that form the western and the eastern part of the open pit. An advanced argillic alteration with alunite and pyrophyllite followed an early pervasive grey silicification of the rocks. The base metal sector has been exposed due to erosion of the upper part of the epithermal system (Skarpelis, 1999). The mineralization is characterized by complex mineralogy with several Pb-bearing and Pb-As-bearing sulfosalts (Moelo *et al.*, 1985; Moelo *et al.*, 1990).

The Kirki flotation plant and tailings ponds, built approximately 5 km south of the Agios Filippos mine (Fig. 1), are founded on Tertiary clastic sediments, including mainly breccio-conglomerates, sandstones, shales and marls (Michael and Dimadis, 2006). The flotation plant comprises eight tailings ponds in total (4 of them depicted in Fig.1) built in favorable locations that required minimum earthworks, while no measures to protect the environment were taken (Directives 2006/21/EC and 98/83/EC) (Triantafyllidis *et al*., 2007). Sandstones, conglomerates and fine-grained tailings were used for the construction of the tailing dump walls with questionable results regarding their stability, as evident by the collapse of the walls at dumps T2, T3 and T4 (Triantafyllidis, 2006). Additionally, the dumps were constructed without consideration of a drainage system thus favoring accumulation of rain water on their surface (Loupasakis and Konstantopoulou, 2010).

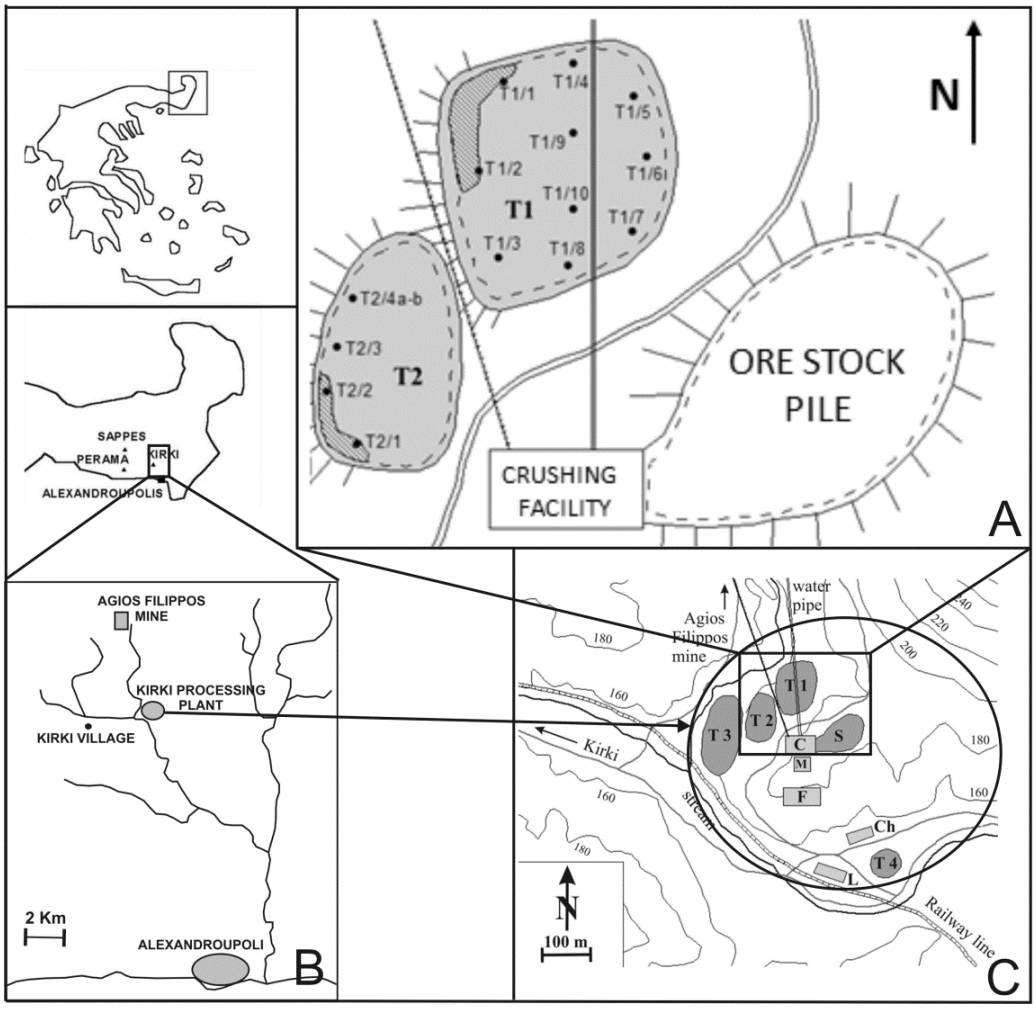

Figure 1 – Location map of the Kirki processing plant. A. Sampling points for tailings dams T1 and T2. Small water ponds formed on the surface of the dams appear with dashed lines. C. Kirki flotation plant.

3. Sampling – Analytical methods

Water samples were collected from the surface of tailings dams T1 and T2 (Fig.1A) in September 2001 and June 2003, applying standard sampling techniques. Temperature, pH and Eh were measured on site using a WTW pH 320/Set-2 electronic pH-meter. Water samples were filtered through a 0.45 μm Millipore filter and acidified with 1 M HNO_3 for cation analyses. Concentrations of Pb, Cu, Zn, Fe, Cd, Ni, Co, As, Hg, Mn and Sb were measured commercially with an inductively coupled plasma atomic emission spectrometer (ICP-AES), whereas SO_4 concentrations using a Hach DR 2000 spectrophotometer. Bulk samples from successive tailings layers were collected up to a depth of 1.6 m (Fig.1A). Samples were dried at room temperature, and sieved to achieve collection of the finer-grained material for more reliable identification of the secondary phases with X-RAY diffraction. The samples were then pulverized, homogenized and split in two so that analyses were done in duplicate. Mineral identification was carried out at the Laboratory of Economic Geology and Geochemistry, University of Athens by X-ray Diffractometry and Scanning Electron Microscopy (SEM). X-ray diffractometry included the use of a SIEMENS D5005 X-ray

Diffractometer with Cu(kα) radiation at 40kV/20mA operating conditions. Scanning Electron Microscopy involved the use of a Jeol JSM 5600 scanning electron microscope combined with energy dispersive X-ray spectrometry (EDS) (OXFORD ISIS Link electron microprobe) and equipped with a Jeol Analytical back scattered electron detector. Operating conditions for the SEM were 20kV accelerating voltage and 0.5 nA beam current. Counting time for each analysis was 50 sec, with 15 sec dead time.

4. Analytical data used

The geochemical characteristics of surface waters accumulated on the surface of tailings dams T1 and T2 are given in table 1. In table 2 selected major and trace elements analyses are given for tailings dams T1 and T2, whereas the secondary phases identified by X-ray Diffraction and Scanning Electron Microscopy are presented in table 3.

Table 1 – Physicochemical characteristics of stagnant surface waters on tailings dams T1 and T2, after Triantafyllidis (2006) (dissolved ions in mg/L, Eh in mV).

	pH	**Eh**	**SO_4**	**As**	**Cd**	**Co**	**Cu**
Tailings dam T1							
Min	3.1	160	2600	b.d.l.	1.9	0.12	1.0
Max	4.4	256	6300	0.12	14.7	1.10	18.0
Mean	3.7	239	4450	-	8.3	0.56	8.1
Stand. Dev.	0.6	37	1752	-	5.5	0.45	7.5
Tailings dam T2							
Min	3.0	226	2450	b.d.l.	3.8	0.25	5.0
Max	3.4	235	17500	0.33	35.3	2.90	11.6
Mean	3.3	229	9975	-	19.6	1.61	8.3
Stand. Dev.	0.1	4	7261	-	15.5	1.25	3.0

Table 1 continued

	Fe	**Mn**	**Ni**	**Pb**	**Zn**	**Sb**
Tailings dam T1						
Min	0.1	121	0.9	1.0	193	b.d.l.
Max	130	613	5.2	3.7	1398	b.d.l.
Mean	64.6	385	3.1	2.4	798	-
Stand. Dev.	64.1	230	2.1	1.2	575	-
Tailings dam T2						
Min	1.0	188	1.6	2.8	278	b.d.l.
Max	4.8	2852	17.5	4.8	4298	0.15
Mean	2.7	1518	8.8	3.4	2223	-
Stand. Dev.	1.3	1166	7.3	0.7	1955	-

b.d.l.: below detection limit
As< 0.01 mg/lt
Sb< 0.002 mg/lt
Hg< 0.001 mg/lt (Hydride/cold vapor technique)
Ag< 0.002 mg/lt

Table 2 – Selected major and trace elements analyses of tailings dam material in wt % and ppm respectively, after Triantafyllidis (2006).

	SiO_2	Al_2O_3	CaO	Na_2O	Fe_2O_3	K_2O	TiO_2	L.O.I.
Min	63,0	9.12	0.27	0.09	2.77	0.74	0.44	5.6
Max	84.1	20.95	0.54	0.31	3.61	1.82	0.49	10.9
Mean	73.9	14.5	0.43	0.15	3.1	0.84	0.46	7.7
Stand. Dev.	8.5	5.0	0.11	0.07	0.3	0.39	0.02	2.2
	Pb	**Zn**	**Cu**	**Cd**	**As**	**Mn**	**Bi**	**Sb**
Min	2597	2082	57	14	92	200	38	13
Max	13991	11013	526	122	238	6828	339	60
Mean	4465	6086	109	45	127	1545	60	16.5
Stand. Dev.	3818	3285	149.6	38.8	46.8	2002	101	15.8
L.O.I. Loss on Ignition								

Table 3 – Secondary phases identified in the tailings material of dumps T1 and T2.

Mineral phase	**Empirical Formula**	**Tailing dump T1**	**Tailing dump T2**
Jarosite group*	$(K,Na,Pb,H_3O)Fe^{+3}{}_3(SO_4)_2(OH)_6$	+++++	+++++
Gypsum	$CaSO_4x2H_2O$	+++++	+++++
Anglesite	$PbSO_4$	+++	+
Butlerite	$Fe^{+3}(SO_4)(OH)x2H_2O$	+	+
Ktenasite	$Zn(Cu,Zn)_4(SO_4)_2(OH)_6x6H_2O$		+
Giniite	$Fe^{2+}Fe^{3+}{}_4(PO_4)_4(OH)_2x2(H_2O)$	+	
Zykaite	$Fe^{3+}{}_4(AsO_4)_3(SO_4)(OH)x15(H_2O)$	+	
Osarizawaite	$PbCuAl_2(SO_4)_2(OH)_6$	+	
* Namely K-jarosite with minor Pb-jarosite, Na-jarosite and Hydronium-jarosite Mineral abundances: +++++ major, +++ minor, + trace			

5. Application of PHREEQC geochemical code

The correlation between the chemistry of the surface waters on tailing dumps T1 and T2 (examined separately) and the mineralogy and geochemistry of the tailings material from each dam was investigated with the use of the geochemical code PHREEQC-V2 (Parkhurst and Appelo, 1999). Thermodynamic data was taken from MINTEQ database (Allison *et al.*, 1991). Saturation Indices were calculated only for jarosite group species, anglesite and gypsum, since thermodynamic data for ktenasite, butlerite, giniite, zykaite and osarizawaite are not included in the MINTEQ database. Imported parameters in the system (Table 4) include: Eh (as pe), pH, As, Ag, Cd, Cu, Fe (total), K, Na, Ni, Mn, Pb, Sb, Zn, Cu and SO_4^{-2}. The dissolved concentrations for Ca, Na, K for the PHREEQC models were based on estimate after geochemical analyses performed on acid mine drainage samples from the Agios Filippos mine (Liakopoulos, 2009). The pe (Eh) values employed in the PHREEQC tests are changed relative to those measured during sampling. At a center point surface stagnant waters are not equilibrated with atmosphere, thus preserving significantly higher pe conditions than normal measured values (Heikkinen *et al.*, 2009). As stated by Manchester *et al.* (2008), near the surface of sulfide tailings disposal facilities pe values may be high and approach the theoretical maximum of 13.75 for O_2 at pH=7. Several different scenarios were employed for the system "tailings surface waters – tailings secondary mineralogy" (Fig. 2), including:

- "Direct Precipitation"
- "Mixing with Rainwater"
- "Evaporation".

Table 4 – Physicochemical characteristics of solutions applied for PHREEQC modelling.

Parameter added to the program	Meteoric water* (applied on model "Mixing with Rainwater")	Tailings dam T1 surface water	Tailings dam T2 surface water
Temperature	25	28.2	29.4
pH	5.5	3.7	3.3
Eh	4	6	9
Density	1	1	1
Ca	0.2	100	100
K	0.35	10	10
Na	0.6	20	20
SO_4	0.18	4450	9975
Ag		0.002	0.002
As		0.063	0.168
Cd		8.3	19.6
Co		0.6	1.6
Cu		8	8.3
Fe		65	2.7
Hg		0.005	0.005
Mn		385	1520
Ni		3.1	8.8
Pb		2.4	3.4
Sb		0.02	0.08
Zn		798	2212

* After Carroll (1962)
Temperature in °C
Density in gr/cm^3
Eh in pε
All ions in mg/lt

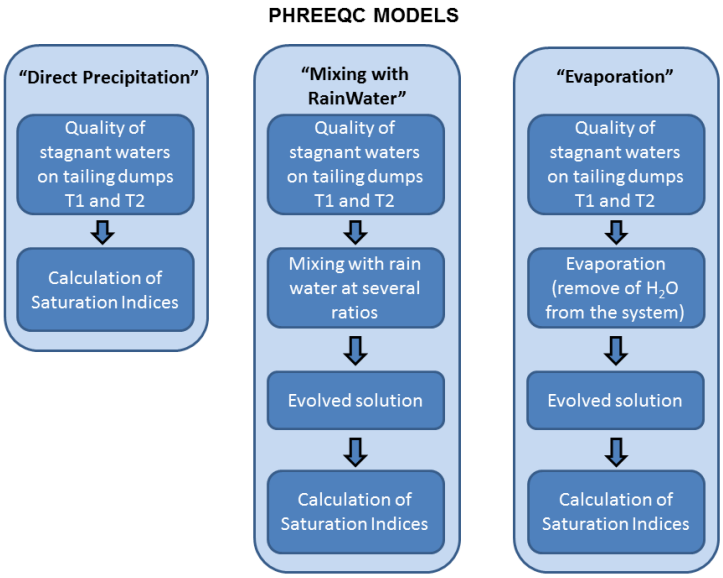

Figure 2 – Schematic representation of PHREEQC models applied in the study.

6. Results of PHREEQC tests

6.1. Direct precipitation

The first model (*Direct Precipitation*) examines the equilibrium between the stagnant surface waters on the tailing ponds and the secondary phases identified in the tailings material, and calculates the Saturation Indices (SI) of specific phases based on the MINTEQ database (Fig. 2, Table 5). This model showed that anglesite is saturated and slightly undersaturated for dams T2 and T1 respectively, whereas only in dam T2 K-jarosite precipitates (SI > 0). All other secondary phases identified by XRD and SEM are undersaturated (SI < 0).

Table 5 – Calculated Saturation Indices for model "Direct Precipitation" for tailings dams T1 and T2.

Mineral phase	**Tailings dump T1**	**Tailings dump T2**
Anglesite	-0.11	**0.03**
H-jarosite	-4.43	-1.61
Na-jarosite	-4.96	-2.66
K-Jarosite	-1.95	**0.32**
Gypsum	-0.60	-0.57

6.2. Mixing with rainwater

The second model (*Mixing with Rainwater*) examines mixing of the surface stagnant waters with rain water (geochemical data for rain water were taken from Carroll, 1962) at several ratios, and checks the equilibrium between the solution produced after mixing and the secondary phases developed in the tailings material (Fig.2, Table 6). This model revealed that if surface solutions mix with rain water, at any ratio, all secondary phases identified show negative SI values (Table 6), indicating possible dissolution and release of heavy metals to solution.

Table 6 – Calculated Saturation Indices for model "Mixing with Rainwater" for tailings dams T1 and T2 for several Rainwater/Surface water ratios.

Mineral phase	Tailings dump T1 (1/1 ratio)	Tailings dump T2 (1/1 ratio)	Tailings dump T1 (4/1 ratio)	Tailings dump T2 (4/1 ratio)
Anglesite	-0.41	-0.25	-0.85	-0.66
H-jarosite	-5.36	-1.74	-6.30	--2.11
Na-jarosite	-5.89	-2.60	-6.85	-2.99
K-Jarosite	-2.86	**0.25**	-3.79	-0.10
Gypsum	-0.96	-0.91	-1.47	-1.38

6.3. Evaporation

The third model (*Evaporation*) examines the evolution of the system and the possible secondary phases resulting from evaporation, at several ratios, of the sampled surface waters and may control the solubility of several toxic metals (Fig.2, Table 7). If the surface waters become more condensed, then the resulting solutions are highly acidic and oxidative with increased metal content. In such conditions precipitation of anglesite, K-jarosite and gypsum is favored, as evident by the positive SI values (Table 7).

Table 7 – Calculated Saturation Indices for model "Evaporation" for tailings dams T1 and T2 for several evaporation ratios.

Mineral phase	**Tailings dump T1 (x10)**	**Tailings dump T2 (x10)**	**Tailings dump T1 (x40)**	**Tailings dump T2 (x40)**
Anglesite	**0.89**	**1.24**	**1.96**	**3.04**
H-jarosite	-1.14	-2.28	-0.99	-2.01

Table 7 continued

Na-jarosite	-1.35	-2.94	-0.86	-2.15
K-Jarosite	**0.38**	-0.08	**1.94**	**0.39**
Gypsum	**0.56**	**0.69**	**1.49**	**2.35**

7. Conclusions

The Kirki flotation dams T1 and T2 show high Pb and Zn content, and lower Mn, As, Cu and Cd load (Table 2). On site observations revealed that the tailings material is weakly cemented, with alternations of reddish-brown with grayish layers. The secondary phases identified with X-ray Diffraction are only identified in the reddish-brown layers, whereas only gangue and minor gypsum and pyrite are present in the grayish layers. The tailings material is fine-grained with particle size ranging from fine sand to fine silt (Triantafyllidis *et al.*, 2007), thus favoring high rates of reaction between surface waters and tailings solids. Oxidation reactions result in the development of a surface reddish-brown layer prior to the deposition of the next slurry layer in the dams.

The three PHREEQC models employed in this study are focused on the major secondary phases identified in the tailings material of the dams T1 and T2, and in particular jarosite group species, anglesite and gypsum (Table 3). The models showed that interaction between surface solutions and tailings material plays a very important role in the fate and transport of certain pollutants.

Jarosite group phases, and in particular K-jarosite, are the major secondary phases identified in the reddish-brown layers of the tailings dams T1 and T2. Jarosite is stable in highly acidic and oxidative conditions (especially after significant degree of evaporation - Table 7), and plays a key role in controlling dissolved metal concentration when it precipitates. On the other hand, if the geochemical environment becomes less acidic (e.g. mixing with rain water - Table 6), jarosite is metastable and dissolves (Lottermoser, 2010). Jarosite dissolution after mixing of surface solutions with rainwater favors metal mobility in two ways:

- Direct release of heavy metals and sulfates to solution (e.g. Pb^{+2} from plumbojarosite in the case of dam T1).
- The dissolved Fe (III) may hydrolyze and precipitate as ferric hydroxide (e.g. goethite). Goethite precipitation causes solution pH to decrease (production of H^{+}), enhancing heavy metal mobility. Although goethite was not identified by XRD or SEM studies, employed PHREEQC models showed that after mixing with rainwater at any ratio, goethite is supersaturated relative to the developed solution (SI > 0).

Anglesite is also identified in the reddish-brown layers of dams T1 and T2, in lower content relative to jarosite (Table 3). Anglesite may control dissolved concentrations of Pb more effectively than plumbojarosite (minor secondary phase in tailings dam T1). Anglesite is rather insoluble in the Kirki tailings dams, since it is metastable to cerussite and hydrocerussite only in mildly acidic to alkaline environments with increased CO_2 content (Krauskopf and Bird, 1995). No cerussite or hydrocerussite are identified in the tailings material by XRD or SEM, so it is reasonable to assume that such conditions are not developed in the surface environment of the Kirki tailings dams.

Gypsum behaves in a similar manner as anglesite and jarosite. During mixing with rainwater, gypsum is undersaturated relative to the produced solutions, whereas it precipitates when surface solutions become more condensed. Moreover, based on the results of the PHREEQC models applied, hematite and goethite precipitation is favored when conditions turn less acidic, especially after mixing of surface solutions with rainwater, although none of these phases were identified by XRD and SEM in dams T1 and T2.

Finally, it is very important to state that the PHREEQC models applied for the Kirki flotation plant tailings dams T1 and T2 are based on several critical limitations:

- Systematic sampling is required to focus on the geochemical conditions of the solid-water interface.
- Limited thermodynamic data for other secondary minerals identified in the tailings material.
- Microbial and organic activity within the tailings material. It is known that the role of aerobic bacteria is critical in the initial oxidation/weathering of primary sulfides and sulfosalts (Stokes, 1954; Walsh and Mitchell, 1972; Evangelou, 1983), as well as their catalytic behavior in the formation of secondary phases present in tailings dams.

8. Acknowledgements

Part of the research work was funded through the program "IRAKLEITOS - Fellowships for Research of National and Kapodistrian University of Athens - ENVIRONMENT".

9. References

Adam, K., 2003. Solid Wastes Management in Sulphide Mines: from Waste Characterisation to Safe Closure of Disposal Sites, *Minerals & Energy*, 18(4), 25-35.

Allison, J.D., Brown, D.S. and Novo-Gradac, K.J., 1991. MINTEQA2/PRODEFA2, A geochemical assessment model for environmental systems, Version 3.0 User's Manual, Environmental Research Laboratory, Office of Research and Development, *US Environmental Protection Agency*, EPA/600/3-91/021, Athens, Georgia, 30605, 92 pp.

Bigham, J.M and Nordstrom, D.K., 2000. Iron and aluminum hydroxysulfates from acid sulfate waters. *In*: Alpers, C.N., Jambor, J.L. and Nordstrom, D.K., *eds.*, Sulfate minerals. Crystallography, geochemistry and environmental significance, *Mineralogical Society of America Reviews in mineralogy and geochemistry*, 40, 351-403.

Carroll, D., 1962. Rainwater as a Chemical Agent of Geologic Processes - A Review, *U.S. Geological Survey*, Washington, Water-Supply Paper 1535-G, 23 pp.

Draves, J.F. and Fox, M.G., 1998. Effects of a mine tailings spill on feeding and metal concentrations in yellow perch (Perca flavescens), *Environ. Toxicol. Chem*., 17, 1626-1632.

Evangelou, V.P., 1983. Pyritic coal spoils: Their chemistry and water interactions. *In:* Augustithis, S.S., *ed*., Leaching and *diffusion in rocks and their weathering products*, Theophrastus Publications S.A., Athens, Greece, 175-228.

Fergusson, J.E., 1990. The heavy metal elements: chemistry, environmental impact and health effects, Pergamon Press, Oxford, 614 pp.

Groudev, S., Batkova, S.G. and Komnitsas, K., 1999. Treatment of waters polluted with radioactive elements and heavy metals by means of a laboratory passive system, *Minerals Engineering*, 12(3), 261-270.

Heikkinen, P.M., Räisänen, M.L. and Johnson, R.H., 2009 Geochemical Characterisation of Seepage and Drainage Water Quality from Two Sulphide Mine Tailings Impoundments: Acid Mine Drainage versus Neutral Mine Drainage, *Mine Water Environ*, 28, 30-49.

Hudson-Edwards, K.A., Macklin, M.G., Jamieson, H.E., Brewer, P.A., Coulthard, T.J., Howard, A.J. and Turner, J.N., 2003. The impact of tailings dam spills and clean-up operations on sediment and water quality in river systems: the Rios Agrio-Guadiamar, Aznalcollar, Spain, *Applied Geochemistry*, 18, 221-239.

Komnitsas, K., Kontopoulos, A., Lazar, I. and Cambridge, M., 1998. Risk assessment and proposed remedial actions in coastal tailings disposal sites in Romania, *Minerals Engineering*, 11(12), 1179-1190.

Krauskopf, K.B. and Bird, D.K., 1995. Introduction to geochemistry, *McGraw-Hill*, New York, USA, 645 pp.

Larsen, T.S., Kristensen, J.A., Asmund, G. and Bjerregaard, P., 2001. Lead and zinc in sediments and biota from Maarmorilik, west Greenland: an assessment of the environmental impact of mining wastes on an Arctic fjord system, *Environmental Pollution*, 114, 275-283.

Lacal, J., Da Silva, M.P., Garcia, R., Sevilla, M.T., Procopio, J.R. and Hernandez, L., 2003. Study of fractionation and potential mobility of metal sludge from pyrite mining and affected river sediments: changes in mobility over time and use of artificial ageing as a tool in environmental impact assessment, *Environmental Pollution*, 124(2), 291-305.

Liakopoulos, A., 2009. Environmental study of the former Kirki mines area. Pollution extension and proposed abatement measures, *Institute of Geology and Mineral Exploration*, Athens, Greece, 257 pp., (in Greek).

Loupasakis, C. and Konstantopoulou, G., 2010. Safety assessment of abandoned tailings ponds: an example from Kirki mines, Greece, *Bull. Eng. Geol. Environ*., 69, 63-69.

Lottermoser, B.G., 2010. Mine Wastes. Characterization, treatment and environmental impact, *Springer-Verlag*, Berlin, 400 pp.

Manchester, J.B., Eykholt, G.R., Donohue, S.V. and Cherry, J.C., 2008. Water chemistry and metal cycling in a subaqueous tailings disposal facility. *In*: Tailings and Mine Waste '08, *Taylor & Francis Group*, London, 449 pp.

Michael, K. and Dimadis, E., 2006. Geological study of the area around the Kirki beneficiation plant, *Institute of Geology and Mineral Exploration*, Athens. Greece, 40 pp., (in Greek).

Moelo, Y., Oudin, E., Makovicky, E., Karup-Moller, S., Pillard, F., Bornuat, M. and Evanghelou, E., 1985. La Kirkiite, Pb10Bi3As3S18, une nouvelle espece minerale homologue de la jordanite, *Bull. Mineral*., 108, 667-677.

Moelo, Y., Makovicky, E., Karup-Moller, S., Cervelle, B. and Maurel, C., 1990. La levyclaudite, Pb8Sn7Cu3(Bi,Sb)3S28, une nouvelle espece a structure incommensurable, de la serie de la cylindrite, *Eur. J. Mineral*., 2, 711-723.

Mohamed, A.M.O., Hossein, M. and Hassani, F.P., 2002. Hydro-mechanical evaluation of stabilized mine tailings, *Environmental Geology*, 41, 749-759.

Parkhurst, D.L. and Appelo, C.A.J., 1999. User's guide to PHREEQC (version 2) - a computer program for speciation, batch-reaction, one-dimensional transport and inverse geochemical calculations, *U.S. Geological Survey*, Denver, Colorado, report 99-4259.

Plumlee, G.S. and Logsdon, M.J., 1999. An earth system science toolkit for environmentally friendly mineral resource development. *In*: Plumlee, G.S. and Logsdon, M.J., *eds*., The Environmental Geochemistry of Mineral Deposits. Part A: Processes, Techniques, and Health Issues, *Society of Economic Geologists*, Reviews in Economic Geology, 6A, 1-27.

Skarpelis, N., 1999. The Agios Filippos ore deposit, Kirki (Western Thrace). A base metal part of a high sulfidation epithermal system, *Bull. Geol. Soc. Greece*, XXXIII, 51-60.

Stokes, J.L., 1954. Studies in the filamentous iron bacterium Sphaerotilus natans, *Journal of Bacteriology*, 67, 278-291.

Triantafyllidis, S., 2006. Environmental risk assessment of mining and processing activities and rehabilitation proposals in Evros and Rhodope Prerefectures (Thrace, NE Greece), Unpublished Doctoral Thesis (in Greek), Faculty of Geology and Geoenvironment, University of Athens, Athens, Greece, 378 pp.

Triantafyllidis, S., Skarpelis, N. and Komnitsas K., 2007. Environmental characterization and geochemistry of Kirki, Thrace, NE Greece, abandoned flotation tailings dumps, *Environ Forensic*, 8(4), 351-359.

Walsh, F. and Mitchell, R., 1972. A pH-dependent succession of iron bacteria, *Environmental Science and Technology*, 6, 809-812.

Wray, D.S., 1998. The impact of unconfined mine tailings and anthropogenic pollution on a semiarid environment - an initial study of the Rodalquilar mining district, southeast Spain, *Environmental Geochemistry and Health*, 20, 29-38.

Abstracts of Keynote Lectures

Δελτίο της Ελληνικής Γεωλογικής Εταιρίας, τόμος L, σελ. 2355-2355
Πρακτικά 14ου Διεθνούς Συνεδρίου, Θεσσαλονίκη, Μάιος 2016

Bulletin of the Geological Society of Greece, vol. L, p. 2355-2355
Proceedings of the 14th International Congress, Thessaloniki, May 2016

NEOTECTONICS OF THE WESTERN ANATOLIA EXTENDED TERRANE (WAET): IMPLICATIONS FOR EARTHQUAKE POTENTIAL OF WESTERN TURKEY

Çemen I.

University of Alabama, United States, icemen@as.ua.edu

The Western Anatolia Shear Zone (*WASZ)* separates the WAET from the Central Anatolia Extended Terrain where timing of the Cenozoic extension is younger and extension rates are probably less than the WAET. The shear zone contains mostly normal faults in the vicinity of the Gulf of Gokova. However, its movement is mostly oblique-slip from the vicinity of the town of Tavas towards the Lake of Acigol where it makes a northward bend and possibly joins the Eskisehir fault zone to the north of the town of Afyon. The WASZ bounds the Denizli Graben to the east where E-W striking normal faults and N-S striking oblique to strike-slip fault are common structural features. The WASZ is similar in its structural/tectonics setting to the Eastern California Shear zone of the Basins and Ranges of North America Extended terrane which is also composed of many normal to oblique-slip faults and separates two extended terrane with different timing and rates of extension.

Western Anatolia, Turkey experienced many devastating earthquakes during the historical times. Many of the ancient Greek/Roman city states, including Ephesus, Troy, and Hierapolis were destroyed several times by large earthquakes. During the second half of the 20th century, the region experienced two major large earthquakes giving normal fault focal mechanism solutions. They are the 1969, M=6.9 Alasehir and the 1970, M=7.1 Gediz earthquakes. These earthquakes had caused substantial damage and loss of life in the region. Although a M=7.4 earthquake similar to the 1999 Izmit Earthquake is unlikely to happen in western Turkey because of the size and nature of active fault zones in the region, the active faults in the regions are capable of producing devastating earthquakes with M~7.0. Therefore, a comprehensive understanding of the kinematics of the Cenozoic extensional tectonics and earthquake potential of the major active faults zone, including the WASZ in the region, is very important.

Δελτίο της Ελληνικής Γεωλογικής Εταιρίας, τόμος L, σελ. 2356-2356
Πρακτικά 14ου Διεθνούς Συνεδρίου, Θεσσαλονίκη, Μάιος 2016

Bulletin of the Geological Society of Greece, vol. L, p. 2356-2356
Proceedings of the 14th International Congress, Thessaloniki, May 2016

THE SIGNIFICANT AND NECESSARY ROLE OF THE GEOLOGIST FOR THE STUDY OF THE COASTAL SECTOR AND THE MARINE SUB-BOTTOM. THE EXPERIENCE FROM THE INSTITUTE OF GEOLOGY AND MINERAL EXPLORATION OF GREECE (IGME)

Perissoratis C.

Institute of Geology and Mineral Exploration, perissoratis@yahoo.gr

The detailed Marine Geological studies in Greece by IGME and other Greek Institutes started in the 1970s and was particularly extensive up to a few years ago. The main activity was mainly based in the funding of projects proposed and accepted by the European Commission and carried out in cooperation with other institutes in Greece and Europe. In parallel a number of applied researches were also carried out for the public and private sectors. The recent development of the ideas of the impacts of the forthcoming Climate Changes, mainly in the coastal areas, gave a new initiative in the applied marine geological studies increasing the required role of the marine geologists.

In this presentation the results and experience are presented in these main fields of Marine Geology: Upper Quaternary to Holocene Geology of the Greek seas, Researches for Useful Minerals, Earthquakes and Tsunamis, Definition of the new and old shoreline and Impacts of the Climatic changes, Prognostic Geology.

Ο σημαντικός αλλά και αναγκαίος ρόλος του Γεωλόγου στις μελέτες στον παράκτιο και θαλάσσιο χώρο. Εμπειρίες από το ΙΓΜΕ.

Οι μελέτες Θαλάσιας Γεωλογίας από το ΙΓΜΕ, όπως και άλλα Ινστιτούτα, άρχισαν στα μέσα της δεκαετίας του 1970 και ήταν αρκετά ανεπτυγμένη μέχρι πριν από μερικά χρόνια. Η κυριότερη πηγή χρηματοδοτήσεων ήταν από την έγκριση ανταγωνιστικών προγραμμάτων από την Ευρωπαϊκή Επιτροπή, μετά από σωστά τεκμηριωμένες προτάσεις. Σε αυτά πάντα συμμετείχαν και αλλά ελληνικά και ευρωπαικά Ιδρύματα. Παράλληλα πραγματοποιήθηκαν βέβαια και επί μέρους ειδικές μελέτες εφαρμοσμένης Θαλάσσιας Γεωλογίας για τεχνικά έργα.Κατά τα τελευταία έτη η άποψη περί κλιματικών αλλαγών και των συνεπειών τους είχαν σαν αποτέλεσμα την ανάγκη γεωλογικών μελετών για τις αναμενόμενες συνέπειες , κυρίως στην παράκτια ζώνη, λόγω της αναμαινόμενης ανόδου της στάθμης της θάλασσας.

Στην παρούσα ομιλία θα παρουσιαστούν αποτελέσματα και εμπειρείες τα εξης πεδία: Μεταβολές της παράκτιας ζώνης στην Ελλάδα από το Αν. Τεταρτογενες έως σήμερα, έρευνες για Ορυκτούς Πόρους, Σεισμοί και Παλίρροιες (Τσουνάμι), Καθορισμός Νέου και Παλαιού Αιγιαλού και συνέπειες των κλιματικών αλλαγών, Προγνωστική Γεωλογία.

Δελτίο της Ελληνικής Γεωλογικής Εταιρίας, τόμος L, σελ. 2357-2357
Πρακτικά 14ου Διεθνούς Συνεδρίου, Θεσσαλονίκη, Μάιος 2016

Bulletin of the Geological Society of Greece, vol. L, p. 2357-2357
Proceedings of the 14th International Congress, Thessaloniki, May 2016

RESPONDING TO ENVIRONMENTAL RISKS TO HEALTH: THE MULTIDISCIPLINARY CHALLENGES

Stewart A.G.

Ex-Public Health England, Consultant in Health Protection, Liverpool, UK

Honorary Senior Research Associate, College of Life and Environmental Science, University of Exeter, UK

Visiting Lecturer, Faculty of Health and Social Care, University of Chester, UK

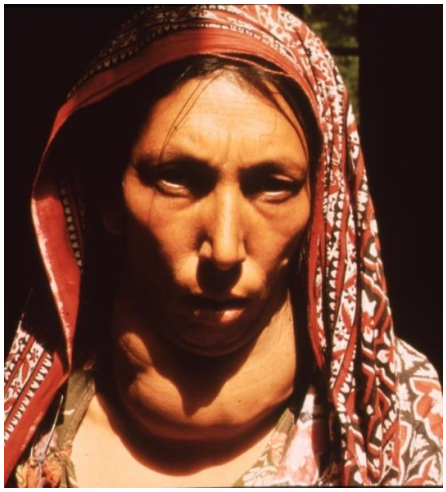

The environment has long been known to affect health, with the details beginning to become clear over the past 300 years, through such developments as verifiable theory (e.g. the emergence of the germ theory of infection), comprehensive observations (all sciences) and enhanced analytical techniques (e.g. in chemistry, clinical sciences, epidemiology).

Health is multi-factorial, with influences ranging from genes and diet through lifestyle and culture to international pressures (including trade and war). Nevertheless, our understanding has largely been built through a reductionist approach to ill-health and disease, by focussing on ever narrower spheres of interest. This method has been very successful in detailing the health effects of many substances: metals and metalloids (e.g. Pb, As, Cr); asbestos, radioactivity (e.g. U, Rn, Cs) and organic compounds (petroleum hydrocarbons, pesticides).

Public Health action arising from this knowledge concentrates on communities rather than individuals, resulting in the prevention paradox, where the majority of cases of a disease come from a population at low or moderate risk, with only a minority of cases arising from the much smaller population at high risk. So, in environmental terms, interest is often focussed on high profile situations with, as yet, not enough attention paid to more moderate risks and exposures. The burden of disease approach pioneered by the World Health Organization is starting to resolve this, showing that, globally, from a few chemicals with available data, there are around five million deaths annually, with over 50% of them in children under 15 years of age.

Communicating such scientific understandings to the lay community (which really includes scientists of other disciplines as well as the public) brings particular joys and problems, some arising from different perceptions and paradigms. The challenges (and delights) of partnership working between environmental scientists and health professionals have never been greater, nor more rewarding: chemical mixtures and statistical confounders, new sciences such as genomics and environmental toxicology, social and health inequalities and deprivation. How will this affect future research opportunities? What is the role of health professionals? What can they offer environmental scientists, including geologists?

Δελτίο της Ελληνικής Γεωλογικής Εταιρίας, τόμος L, σελ. 2358-2359
Πρακτικά 14ου Διεθνούς Συνεδρίου, Θεσσαλονίκη, Μάιος 2016

Bulletin of the Geological Society of Greece, vol. L, p. 2358-2359
Proceedings of the 14th International Congress, Thessaloniki, May 2016

THE IMPORTANCE OF FAULT INTERACTIONS IN THE LONG-TERM AND SHORT-TERM GROWTH OF FAULT SYSTEMS

Walsh J.J.[1], Nicol A.[2], Childs C.[1], Mouslopoulou V.[3] and Manzocchi T.[1]

[1]*Fault Analysis Group, School of Earth Sciences, University College Dublin, Ireland*

[2]*Department of Geological Sciences, University of Canterbury, Private Bag 4800, Christchurch, New Zealand*

[3]*GeoForschungsZentrum (GFZ), Helmholtz-Centre Potsdam, Germany*

Faults typically form components of complex systems in which dynamic and kinematic interactions are an essential element of fault growth on earthquake and geological timescales. These interactions, which on geological timescales are typically manifest as displacement transfer associated with fault intersection (hard-linkage) or distributed deformation (soft-linkage), influence fault dimensions, displacement patterns and growth (Nicol *et al.*, 2010; Journal of Structural Geology 32, 1101-1113). Fault interaction and growth over timescales of up to millions of years have been constrained by analysis of faulting with displacements of millimetres to kilometres using outcrop and seismic-reflection data. Many of the faults analysed experienced rapid fault propagation followed by prolonged displacement accumulation. The resulting near-constant lengths established from an early stage in the fault history are attributed to retardation of lateral propagation by interaction between fault tips. These interactions are interpreted to result in near-linear along strike displacement profiles and increasing displacement gradients with fault size (i.e. length and maximum displacement). The increase in displacement gradients is associated with a steepening of slope on fault displacement vs length (D-L) plots and with rising strain across fault systems. For immature low-strain fault systems in which individual faults have experienced few slip events the slope of D-L plots is typically <1, while in mature higher-strain systems this slope is generally >1. The increasing D-L slopes is interpreted to primarily reflect a combination of tip-line retardation arising from interactions and preferential death (or longer recurrence intervals between individual slip increments) of smaller faults. As a consequence, large faults accrue their cumulative displacement in many more slip events than small faults. The available data are consistent with fault growth models in which the hierarchy of fault size is established rapidly, perhaps in many cases due to fault reactivation, with the longest faults moving fastest, for the longest duration and being most likely to benefit from strain localisation.

Despite the relatively systematic nature of fault growth on longer time scales, the established importance of fault interaction as indicated by displacement transfer (whether by hard- or soft-linkage) requires that stress-dependent fault interactions must also be occurring on shorter time scales. These stress-dependent interactions should, in principle, be reflected in temporal and spatial variations in fault displacement rates. Here we examine the relations between fault displacement rates on short (<25 kyr) and long (>1 Myr) timescales in the Taranaki Rift, New Zealand, using trench and coastal outcrop together with onshore and offshore deep (~<5 km) seismic-reflection lines (Mouslopoulou *et al.*, 2012; Journal of Structural Geology 36, 71-80). Displacement rates on many individual faults become increasingly variable on shorter time scales, a characteristic which is attributed to a combination of variable earthquake behaviour (i.e. recurrence interval and single event slip) and sampling artefacts. Comparison between paleoearthquake and million-year (seismic-

reflection) displacements on faults in the Taranaki Rift, and elsewhere (Mouslopoulou *et al.*, 2009; EPSL 278, 186-197), shows that the number of faults in the system, their lengths, displacement rates and earthquake recurrence interval differ significantly for different observational time windows. More specifically, short-term fault data (< 25 kyr) generally overestimate the long-term average displacement rates of individual faults and underestimate the number of active faults as well as their total length and their associated earthquake recurrence interval. Active faults that displace the ground surface by <~1 m are not routinely resolved, resulting in underestimates of fault lengths by up to 85% and incomplete temporal and spatial sampling of paleoearthquakes on faults with short-term displacement rates of ~<0.1 mm/yr. Variations of earthquake recurrence interval and slip of up to an order of magnitude contribute to undersampling of those faults which have experienced few earthquakes during the Holocene (Nicol *et al.*, 2009; Geology 37, 911-913). In these circumstances, seismic reflection data have been used to improve estimates of maximum fault rupture lengths and to identify potential low displacement rate (<0.1 mm/yr) active faults that were not previously recognised. Our study shows that integrated datasets provide much improved estimates of seismic hazard in the rift, a conclusion which is supported by earthquake studies in other tectonically active areas, including Christchurch, New Zealand (see below).

Our analysis In the Taranaki Rift has important implications for earthquake predictions and is consistent with the notion that the catastrophic earthquakes that recently (September 4th, 2010 and February 22nd, 2011) hit Christchurch, New Zealand, show that active faults hidden beneath the Earth's surface are capable of generating large-magnitude earthquakes (Mouslopoulou *et al.*, 2012; Journal of Structural Geology 36, 71-80). Analysis of the Taranaki Rift shows that the integration of different timescale datasets provides a basis for identifying active faults not observed at the ground surface, estimating maximum fault-rupture lengths, inferring maximum short-term displacement rates and improving earthquake hazard assessment. Because fault displacement rates become increasingly irregular (both faster and slower) on shorter timescales, this inevitably leads to incomplete sampling of the active-fault population. Surface traces have been recognised for <50% of the active faults and along 50% of their lengths. By contrast, the similarity of along-strike displacement profiles for short and long time intervals suggests that fault lengths and maximum single-event displacements have not changed over the last 3.6 Ma. Therefore, rate changes are likely to reflect temporal adjustments in earthquake recurrence intervals due to fault interactions and associated migration of earthquake activity within the rift. An appreciation of these rate changes is an essential requirement for improved earthquake risking.

AUTHOR INDEX